

“Engineering Meets Dreams”



ICME-20

INTERNATIONAL CONFERENCE ON MECHANICAL ENGINEERING

Edited by:

***Prof. Dr. Tauseef Aized
Dr. Muhammad Farooq
Mr. Syed Sohail Rehman***

ORGANIZED AND SPONSORED BY:



FACULTY OF MECHANICAL ENGINEERING

UNIVERSITY OF ENGINEERING AND TECHNOLOGY (UET) LAHORE, PAKISTAN

All Rights Reserved. No part of this publication may be reproduced, stored in retrieval system or transmitted in any form without permission of the International Conference on Mechanical Engineering.

ISBN: 978-969-23447-0-8

Proceedings of the International Conference on Mechanical Engineering (ICME-20).

Published By: Faculty of Mechanical Engineering, University of Engineering & Technology
Lahore



ICME-20

INTERNATIONAL CONFERENCE ON MECHANICAL
ENGINEERING

PROCEEDINGS OF THE

INTERNATIONAL CONFERENCE ON MECHANICAL ENGINEERING (ICME-20)

ORGANIZED BY

Faculty of Mechanical Engineering

University of Engineering and Technology (UET) Lahore, Pakistan

29-31 January 2020

FOREWORD

International Conference on Mechanical Engineering-2020 (**ICME-20**) is a **multi-module, multi-track double blind peer-reviewed** International Conference which will be held on January 29-31, 2020 in Main Auditorium, UET, Lahore, Pakistan.

This conference will showcase Research/Policy/Industry Papers, Posters and Projects, Industrial Products Exhibition, Students Professional development from all disciplines of Mechanical Engineering including but not limited to Thermo-fluids, Energy systems, Design Engineering and Stress Analysis, Industrial and Manufacturing Engineering, Engineering Management, Mechatronics, Control and Robotics, Textile Engineering, Aerospace and Metallurgy and Materials Engineering.

Following are **Six Modules** of the Conference:

Module 1:	Plenary Sessions by industry leaders on issues related to national importance
Module 2:	Research Presentations by researchers, experts, Academics and Industry Staff focusing state of the art research findings in theory and applications
Module 3:	Interactive Workshops for students, academic and industry
Module 4:	Posters/ Projects Exhibition by researchers, experts, Academics and Industry Staff focusing state of the art research findings in theory and applications
Module 5:	Exhibition: <i>Industrial products/ Education Expo/ Book Fare</i> by various industries showcasing their products and technologies
Module 6:	Entertainment and networking activities like Sky Lantern, drama, stage performance and Lahore sight- seeing trips.

We would like to express our sincere gratitude to our sponsors Higher Education Commission of Pakistan (HEC), Punjab Higher Education Commission (PHEC), HVACR Society, United States Education Foundation in Pakistan, Education USA, Commonwealth Scholarships and KK Power Company, for providing financial and technical support.

Dr. Muhammad Farooq
Secretary, ICME-20

Prof. Dr. Tauseef Aized
Convener, ICME-20

EDITORIAL BOARD

PROCEEDINGS OF THE ICME-20

Editor-in-Chief

Dr. Tauseef Aized

Professor, Mechanical Engineering
Department, UET Lahore



Managing Editor

Dr. Muhammad Farooq

Assistant Professor, Mech. Engg.
Department, UET Lahore New Campus



Editors

Prof. Dr. Shahid Imran

Thermo-Fluids & Energy Systems



Dr. Ali Hussain Kazim

Editor Publications (Thermo)



Dr Amjad Hussain

Manufacturing & Management



Dr. Qamar Mahboob

Editor Publications (M&M)



Dr. Jaffar Hussain

Mechanics and Stress Analysis



Dr. Tariq Nawaz

Editor Publications (Design)



Dr. Hafiz Farhan Maqbool

Mechatronics and Control



Engr. Syed Sohail Rehman

Associate Managing Editor



Review Editors

Dr. Salman Abbasi

Dr. Hasan Izhar Khan

Dr. Imran Mehmood

Dr. Jawad Sarwar

Engr. Ahmed Naveed

Dr. Qasim Ali Ranjha

Mr. Adnan Qamar

Dr. Muhammad Amjad

Dr. Muhammad Usman

REVIEWERS

Prof. Dr Fiaz Hussain Shah

Dr Muhammad Asim

Dr Fahad Noor

Dr Ghulam Moeen Uddin

Dr. Zahid Anwer

Ms. Tamseela

Dr Wakil Shahzad

Dr Fahad Riaz

Dr Imran Mehmood

Dr Saif Ur Rehman

Dr Saad Nawaz

Muhamamd Ali Shahbaz

Dr. John M Andresen

Dr. Ummul Baneen

Dr. Muhammad Ahsan

Dr. Nasir Ahmad

Dr. Imran Mahmood

Dr. Muhammad Khurram Saleem

Dr. Zohaib Aftab

Dr. Nadeem Ahmad Mufti

Dr. Muhammad Salman Habib

Dr. Rakhshanda Naveed

Dr. Sarmad Ali Khan

Prof. Dr M. Asif Mahmood Qureshi

Dr Naseer Ahmad

Dr Awais Ahmad Khan

Dr. Muhammad Farhan

Dr. Jawad Sarwar

Dr. Hasan Ali

Dr. Zia Ul Rehman

Dr Salman Raza Naqvi

Dr Tahir Qureshi

Dr Huma Bilal

Dr. Farhan Raza Rizvi

Dr. Muhammad Imran

Dr. Ali Raza

Dr. Mohsin Rizwan

Dy. Syed Abbas Zilqurnain Naqvi

Dr. Muhammad Usman

Dr. Asif Ishfaq

Dr. Ahmed Nouman

Dr. Mohammed Ibrahim Awad

Dr. Kashif Ishfaq

Dr. Sadaf Zahoor

Dr. Muhammad Qaisar Saleem

Dr. Naveed Ahmad

Editorial Assistance

Ms. Saba Ajmal

Ms. Zahra Waseem

Abdul Wahhab

Engr. Luqman Razzaq

Muhammad Hamza Zulfiqar

TECHNICAL COMMITTEE

- Dr. Sedat İRİÇ, Turkey
- Prof. Dr Pascal Biwole, France
- Professor Philip Longhurst, United Kingdom
- Dr Muhammad Rehan, Saudi Arabia
- Dr. Alberto Pettinau, Italy
- Dr. Ahmet Turan, Turkey
- Prof. Dr. Daniel Straub, Germany
- Prof. Dr. Muhammad Tufail, Karachi
- Prof. Dr. Riffat Pasha, Taxila
- Prof. Koji Takahashi, Japan
- Dr. Zuhail ERDEN, Turkey
- Prof. Dr. Mahmut ÖZACAR, Turkey
- Prof. Dr. John M. Andresen, United Kingdom
- Dr Jabbar Gardy, United Kingdom
- Prof. Dr Qi Liu, China
- Prof. Dilshad Hussain, Lahore
- Prof. Dr. Saleem Abid Tabussum, Lahore
- Prof. Dr. Ahmad Hassan, Karachi
- Prof. Ichiro Hagiwara, Japan
- Prof. Bijan Shirinzadeh, Melbourne
- Dr. Jagjit Singh Srail, UK
- Prof. Yiliu, Norway
- Dr. Osman İYİBİLGİN, Turkey
- Dr. Muhammad Imran, UK
- Prof. M.H. Zuberi, Lahore
- Prof. Dr. Ijaz A. Ch., Lahore
- Prof. Dr. Mian Muhammad Awais, LUMS
- Dr Gabriel Anandarajah, London
- Prof. Dr. Fehim Findik, Turkey
- Dr. M. İskender ÖZSOY, Turkey
- Prof Dr Dongsheng Wen, China
- Prof. Dr. Yi Zhang, China
- Dr. Nurudeen Almustapha, Nigeria
- Prof. Dr. Arshad H. Qureshi, Lahore
- Prof. Dr. Mirza Jehanzeb, Taxila
- Prof. Dr. Ejaz M. Shahid, Lahore

LIFE TIME SERVICES AWARD

Prof. M. H. Zubari

Prof. Dilshad Hussain

Prof. Dr. A. H. Qureshi

Prof. Dr. Iqbal Hussain

Prof. Dr. Saleem Iqbal Alvi

Prof. Dr. Ijaz Ahmed Chaudhary

Prof. Dr. Younis Jamal

Prof. Dr. Fiaz Hussain shah

Prof. Dr Saleem Abid Tabassum

Prof. Dr. Ijaz Mehmood Shahid

Prof. Dr. Hameed Ullah Mughal

Prof. R. M. Yahya

Mr. Javed Anwar

Prof. Dr. A. H. Qureshi (Late)

Prof. Dr. Ikram Khan (Late)

Prof. Dr. Sultan Hussain (Late)

Prof. Dr. Nazir (Late)

Prof. Dr. Khawaja Masood Ul Hassan(Late)

Prof. Dr. Shoukat Ali (Late)

Prof. Dr. Riaz Mirza (Late)

Prof. Dr. Khalid Rasheed Opal (Late)

Prof. Dr. Islam Ud Din Saleem (Late)

Prof. Asif Aslam

Mr. Shahid Pervez Malik

Prof. Javed Latif Paracha

ORGANIZING COMMITTEE

Convener

Prof. Dr. Tauseef Aized

Secretary

Dr. Muhammad Farooq

Members

Prof. Dr. Fiaz H. Shah

Prof. Dr. Nadeem Ahmad Mufti

Prof. Dr. Nasir Hayat

Prof. Dr. Younas Jamal

Prof. Dr. Asad Naeem Shah

Prof. Dr. Asif Qureshi

Prof. Dr. Shahid Imran

Dr. Amjad Hussain

Dr. Ali Raza

Dr. Muhammad Qaiser Saleem

Dr. Naseer Ahmad

Dr. Ummul Baneen

Dr. Muhammad Farhan

Dr. Muhammad Amjad

Dr. Ghulam Moeen ud Din

Dr. Rana Hassan Ali

Dr. Qasim Ali Ranjha

Dr. Tariq Nawaz

Dr. Nasir Ahmad

Dr. Hafiz Farhan Maqbool

Dr. Qamar Mahboob

Dr. Mohsin Rizwan

Mr. Muhammad Moeen Sultan

Engr. Nazim Waheed

Engr. Ahmed Naveed

Engr. Syed Saqib

Engr. Gulzar Ahmed

Engr. Abdul Sattar

ORGANIZERS AND SPONSORS



University of Engineering
& Technology, Lahore



Higher Education
Commission



Pakistan Engineering
Council



Punjab Higher
Education Commission



Management & Business
Excellence Constancy



KK Power International
(PVT) Ltd



Commonwealth
Scholarships



Education USA



The United States
Educational Foundation in
Pakistan



The Institute of Engineers
Pakistan



Sakarya University Turkey



Pakistan Science
Foundation



Pakistan HVACR Society



Government of Punjab



ASME UET



ASME UET KSK



TABLE OF CONTENTS

● Invited Abstracts	01
1. Characterization of Ti-Ha Biocomposite Produced by Powder Metallurgy <i>Görkem Kahramana, Eren Yılmazb, Fehim Findika,</i>	<i>02</i>
2. Design and Production of Reinforced Chain in Areas Exposed to High Stress According to the Results of Finite Element Analysis <i>Dr. Sedat İRİÇ.....</i>	<i>03</i>
3. Experimental Investigation of Test Samples' Mechanical Properties Produced from Pure Titanium with Binder Jet 3D Metal Printer <i>Osman İYİBİLGİNa,b, Engin GEPEKb.....</i>	<i>04</i>
4. Sliding Wear Behavior of Carbon Fiber Reinforced Polyphenylene Sulfide Composites <i>Dr. M. İskender ÖZSOY.....</i>	<i>05</i>
5. A Novel Nanocomposite Photocatalyst for Hydrogen Production <i>Soner Çakar and Mahmut Özacar.....</i>	<i>06</i>
6. Unlocking the Mystery of Desalination Processes <i>Muhammad Wakil Shahzad, Muhammad Burhan and Kim Choon Ng2</i>	<i>07</i>
7. Recent advances in the use of phase change and silica aerogel based materials for energy applications in buildings. <i>Prof. Pascal Henry Biwole.....</i>	<i>08</i>
8. The Road Towards Flexible Smart Materials <i>Dr Jibran Khaliq.....</i>	<i>09</i>
9. Hybrid Piezo-Pyroelectric Energy Scavenging by High β -phase Poly (Vinylidene fluoride) Membrane <i>Mohd Faizul Bin Mohd Sabri.....</i>	<i>10</i>
10. Industry 4.0 – Need of Current Era <i>Prof. Dr. Muhammad Tufail.....</i>	<i>11</i>
11. Potential and Prospects of Energy Transition in Pakistan <i>Khanji Harijan</i>	<i>12</i>
12. Focus towards Mission Oriented Research to Benefit Pakistan <i>Muhammad Abid.....</i>	<i>13</i>
13. Mechanism and role of module design upon osmotically driven module operation at pilot and bench scale <i>Dr. Farrukh Arsalan Siddiqui</i>	<i>14</i>
14. Transformation of Industry in the wake of Smart Manufacturing/Industry 4.0 <i>Prof. Dr. Mirza Jahanzaib</i>	<i>15</i>
15. Functional Reverse Engineering of Machine Tools <i>Professor Dr. Wasim Ahmed Khan</i>	<i>16</i>
16. Natural Air Conditioning – Innovative air cooling with renewable energy integration <i>Dr. Nadeem Ahmed Sheikh.....</i>	<i>17</i>
17. Advanced Nuclear Reactors and their Role in Meeting Growing Energy Demand of Pakistan <i>Kamran Rasheed Qureshi</i>	<i>18</i>



18. Influence of Plain and N ₂ Purging Conditions on Corrosion Mechanism Correlated With Microstructures of Low Alloy Steel Multipass Weldments <i>Riffat Asim Pasha, Kamran Ghafoor, Aneela Wakeel, Rizwan Malik</i>	19
● Thermo-Fluid and Energy Track	20
19. Assessment of Wind Potential in South Punjab <i>Muhammad Sumair, Tauseef Aized, Muhammad Usman</i>	21
20. Thermodynamic performance of vapor compression refrigeration cycle (VCRC) retrofitted with low-GWP refrigerants <i>Ameer Hamza, Sadaf Mehdi, Tauseef Aized Khan</i>	29
21. Modelling The Penetration Of Electric Vehicles As An Alternate Mode Of Road Transport In Pakistan <i>Sher Asif Khan, Tanzeel ur Rashid, Ubaid ur Rehman Zia, Waqas Nazir Awan, Talal Bin Ahmed</i>	38
22. Performance Analysis of Four Concentrated Solar Power Technologies for Quetta <i>Ahmad Nabeel Hafeez, Mudassar Hassan, Muhammad Sajid, Zia ul Rehman Tahir, Muhammad Asim, Muhammad Umair Siddique</i>	44
23. Contribution of different factors in the production of smog in major cities of Pakistan <i>Syed Muhammad Sohail Rehman, Syed Ubaid Ur Rehman, Tauseef Aized, Syed Junaid Ur Rahman</i>	50
24. Design, Analysis and Optimization of 50MW Solar Thermal Parabolic-Trough Power Plant in Multan <i>Kamran Mahboob, Farman Ali, Hassan Mehmood, Awais Khan, Tauseef Azid</i>	55
25. Collaborating Sharing Decentralized Solar Energy System in Pakistan <i>Syed Muhammad Kashif Shah, Tanzeel-ur-Rashid</i>	63
26. Analysis of Wind Energy Potential of Southern Punjab using Measured Data <i>Arslan Ahmad, Usama Bin Saeed, Ammara Kanwal, Zia ul Rehman Tahir, Muhammad Asim, Hafiz Ameer Hamza, Naeem ullah Khan, Muhammad Zeeshan Jamil and Muhammad Abdullah</i>	69
27. Energy saving potential of evaporative cooling systems compared to traditional air conditioners <i>Hadeed Ashraf, Shazia Noor, Muhammad Sultan, Zahid M. Khan</i>	75
28. Passive Cooling based Thermal Management System of Lithium-ion Batteries employing Copper foam/Paraffin Composite <i>Muhammad Ramzan, Abid Hussain</i>	82
29. Selection and Characterization of PV Cell Material for Thermophotovoltaic Application <i>Zertasha Shoukat, Mohsina Asif, Khujista Nadeem, Aqsa Shabbir, Rabia Nazir, Muhammad Farooq, Ali H. Kazim</i>	87
30. Modeling and Optimization of Solar Absorption Cooling System for Cold Storages in Pakistan <i>Musannif Shah, Adeel javed, Hamid Ikram</i>	93
31. Experimental study on the thermal management of electronics using phase change material integrated metallic foam and heat pipe <i>Muhammad Aamer Hayat, Hafiz Muhammad Ali</i>	99
32. Evaluation of Eight Reflected Solar Radiations Models to find Daily Optimum Tilt Angle for Lahore <i>Muhammad Hamza Faisal, Arsalan Naveed, Huzaiifa Maqsood, Zia ul Rahman Tahir, Muhammad Asim, Bilal Mahmood, Zeeshan Arif, Muzammil Aslam and Saiqa Hafeez</i>	104



33. Assessment of Relative Humidity, Temperature, Carbon Dioxide & Particulate Materials in Labs <i>Tahir Nawaz, Muhammad Bilal Sajid</i>	111
34. Analysis of Temperature Distribution and Phase Change Time Inside Iron-Nickel Foam Infiltrated with Paraffin <i>Muhammad Mehboob, Abid Hussain</i>	117
35. Improvement in Generation Economics by the Application of Selected Thermal Power Plant Repowering Strategies in Pakistan – A Case Study <i>Ahmad Jamil, Adeel Javed</i>	122
36. Comparing the performance of wet-bulb and dew-point evaporative cooling systems <i>Hafiz S. Ullah, Hafiz M.U. Raza, Khawar Shahzad, Muhammad Sultan, Muhammad H. Mahmood, Zahid M. Khan</i>	129
37. Experimental evaluation of desiccant dehumidification unit for air conditioning applications <i>Muhammad Ishaq, Akash Siddique, Hafiz M.U. Raza, Muhammad Sultan, Zahid M. Khan, Muhammad H. Mahmood</i>	134
38. Techno-Economic Analysis of Conventional & Variable Refrigeration Flow (VRF) for Hot Climatic Condition of Lahore <i>Haider Latif, Muhammad Asim, Hafiz Muhammad Waqas Badar, Muhammad Farooq, Yasir Rashid</i>	139
39. Life cycle assessment of Solar Assisted Geothermal Heat Pump for the Residential buildings in Pakistan <i>Ali Farooq & Dr. Tauseef A. Khan</i>	148
40. Experimental Investigation on Effect of YSZ Coated Piston Crown on the Performance of a Petrol Engine <i>Hafiz Liaqat Ali, Muhammad Tahir Hassan, Farrukh Arsalan Siddiqui, Syed Asad Raza Gardezi, Muhammad, Farooq Zaman, Muhammad Sanwal and Muhammad Jaon Haider</i>	156
41. Experimental Investigation of Passive Cooling Techniques to Reduce Cooling Load in Residential Building in Lahore <i>Muhammad Asim, Ahmed Zohaib Zaidi, Muhammad Sajid Kamran</i>	164
42. Deformation of neutrally buoyant droplet with clean and Particle covered interface under an electric field <i>Muhammad Salman Abbasi, Haroon Farooq and Hassan Ali</i>	172
43. Effect of CTAB on stability, thermal conductivity and viscosity of 2D h-BN based nanofluids <i>Syed Nadeem Abbas Shah, Syed Shahabuddin and Mohd Faizul Mohd Sabri</i>	178
44. Thermal Characterization of Graphene coated Copper Foam Saturated with Phase Change Material <i>Ali Hasan, Abid Hussain,</i>	185
45. Thermal Conductivity Measurement of Graphene Coated Metal Foam Saturated with Phase Change Material <i>Awais Ahmed, Abid Hussain, Ali Hasan</i>	192
46. Optimization of the number of vanes of a centrifugal pump to improve hydraulic efficiency for calcium chloride solution <i>Hafiz Ahmad Hassan, Awais Ali, Muhammad Farooq</i>	197



47. Design and Performance Analysis of 500kW Solar Power Electric Vehicle Charging Station <i>Rauf Ahmad, Hafiz Liaqat Ali, Muhammad Tahir Hassan, Usama Bin Mehboob, Muzammil Asif, Muhammad Jaon Haider, Muhammad Mustahson Awasi, Muftooh Ur Rehman Siddiqi</i>	203
48. Effect of using nano-lubricant on COP of Vapor Compression System: An Experimental Study <i>Saif Ullah Khalid, Muhammad Saleem Khan</i>	211
49. Fossil fuel based Carbon footprint of Pakistan and its role towards sustainable development <i>Muhammad Wajid Saleem, Muhammad Hanzla Tahir, Muhammad Wajid Ashfaq</i>	216
50. Investigation Regarding Thermal Management of Electric Heater Using Different Geometry Configurations <i>Saad Saeed Minhas, Abid Hussain</i>	223
51. Recent advances in the use of phase change and silica aerogel based materials for energy applications in buildings <i>Biwole P. H., Nocentini K. and Achard P.</i>	227
52. A Novel Nanocomposite Photocatalyst for Hydrogen Production <i>Nuray Güy, Keziban Atacan, Mahmut Özacar</i>	235
53. Hybrid Piezo-Pyroelectric Energy Scavenging by High β - phase Poly(Vinylidene fluoride) Membrane <i>IA Fadzallah, NS Sabran, NV Toan, T Ono, SM Said, MFM Sabri</i>	240
54. Numerical Study of Subcooling Effect on Single Bubble Growth by Using Volume of Fluid Model <i>Zeeshan Ahmad Khan, Majid Ali</i>	244
55. Design and Simulation of a Scale Model Thermo-Acoustic System for Refrigeration Applications <i>Muhammad Mahmood Aslam Bhutta, Muhammad Farooq, Sajid Kamran, Syed Muhammad Sohail Rehman, Syed Murawat Abbas Naqvi</i>	250
56. Experimental Analysis of Alternative Hydrocarbons for R 134a by a Vapor Compression Cycle Based System <i>Muhammad Mahmood Aslam Bhutta, Nasir Hayat, Muhammad Farooq, Sajid Kamran, Syed Muhammad Sohail Rehman, Muhammad Umair Mirza</i>	254
57. Investigation and design of archemedes Screw turbine for run of the rive scenario <i>Ahmad Naveed, Umair Ashraf, Muhammad Farooq, Warda Ijaz, Mahnoor Amir, Zara Saqib</i>	266
• Design and Stress Analysis Track	272
58. Ti-HA Biocomposite Produced By Powder Metallurgy <i>Görkem Kahramana, Eren Yılmazb, Fehim Fındıka</i>	273
59. Experimental Study on Heat Storage Properties Comparison of Paraffin/Metal foams Phase Change Material Composites <i>W. Ahmed, A. Hussain</i>	279
60. Evaluation of Stability and Rheological Behavior of TiO ₂ -H ₂ O Nanofluid <i>Muhammad Assad Khan, Majid Ali, Waqas Ahmad</i>	285
61. Analysis of South Asian Electric Vehicle's Policies and Recommendations for Electric Vehicle's Policy for Pakistan <i>Zain Ul Hassan, Naseer Ahmad, Awais Ahmad Khan</i>	293
62. Comparative Analysis of a Medium Concentrated Photovoltaic/Phase Change Material System with a Flat Plate Photovoltaic System <i>Arshmah Hasnain, Jawad Sarwar, Ahmed E. Abbas, Konstantinos E. Kakosimos</i>	302



63. Performance Analysis of Constant Current Process of Capacitive Deionization with CFD Flow Simulation and AI Optimization <i>Shahrose Imran, Muhammad Nouman Zafar, Hira Naveed, Muhammad Wajid Saleem</i>	308
64. Derailment accidents due to SPAD in railways: Improv-ing modeling and analysis of risks quantification <i>Qamar Mahboob, Awais Ahmad Khan, Ghulam Moeen Uddin, Attiq ur Rehman</i>	318
65. Minimization of Warpage and Average Volumetric Shrinkage on a multi cavity Injection Molded Polymeric Nut using Taguchi Optimization Method <i>Bisma Ali, Yasir Qayyum Gill</i>	328
66. Sliding wear behavior of carbon fiber reinforced polyphenylene sulfide composites <i>Mehmet İskender ÖZSOY, Levent ESATOĞLU</i>	336
67. Comparison of Various Shapes of Internal Cut-outs in Gas Turbine Blades Using FEA Based Modal Analysis <i>Ahmed Naveed, Sohail Afzal, Ahmed Aqeel, Haziq Sajjad1 and Rafay Tariq</i>	343
68. Design and Fabrication of a Low Cost 3-Axes CNC Precision Router <i>Sarmad Ishfaq, Muhammad Ali Bhutto, Muhammad Shoaib Butt, Saad Ali, Khalid Rahman, Wasim Ahmed Khan</i>	350
• Manufacturing and Management Track.....	359
69. Design Parameters for Bio-absorbable Stent Production with Additive Manufacturing <i>Osman Iyibilgin, Muhammet Baran Çikılı, Fehim Findik</i>	360
70. Modeling and Simulation of a Spare Parts Production Line of Automobile using Promodel <i>Umair Nisar Malik, Tauseef Aized, Muhammad Shafiq, Muhammad Ibrar Mukhtar</i>	365
71. Improving performance of auto parts manufacturing plant using discrete event simulation modeling technique <i>Muhammad Ibrar, Tauseef Aized, Hafiz Liaqat Ali, Umair Nisar Malik, Mohib Ullah</i>	373
72. Discrete Event Simulation of a Tractor Assembly Line using PROMODEL <i>Syed Ubaid Ur Rehman, Dr. Tauseef Aized, Syed Muhammad Sohail Rehman</i>	379
73. Gap Analysis of Municipal Solid Waste Management System in Peshawar, Pakistan <i>Waqas Ahmad, Muhammad Hassan, Tahir Nawaz, Muhammad Ashfaq, Muhammad Assad Khan</i> ...	387
74. Process Improvement of Pet Bottle by Eliminating Bottlenecks <i>Eng. Daniyal Farooque, Shakeel Ahmed Shaikh, Sonia Irshad Marri, Muhammad Saad Memon</i>	396
75. Investigating the Effects of Process Parameters of FDM using RSM <i>Muhammad Arslan, Dr. Tauseef Aized, Muhammad Ahsaan ul Haq</i>	404
76. Surgical Instruments Manufacturing Sector in Pakistan – Current Scenario, Issues and Recommendations <i>M.J. Afzal and T.A. Khan</i>	411
77. Impacts of Electric Vehicle’s on Emissions & Economy for Developing Nations & Recommendations for Electric Vehicle’s Policy for Pakistan <i>Zain Ul Hassan, Dr. Naseer Ahmad</i>	419



78. Analysis of Overall Equipment Effectiveness by Implementing TPM Strategy and Equipment Reliability Approach <i>Muhammad Faisal, Tauseef Aized, Syed Muhammad Sohail Rehman</i>	427
79. Competitiveness Enhancement of SMEs by Integrating Lean and Corporate Social Responsibility (CSR) – A Case Study <i>Qasar Wasique Ahmad, Amjad Hussain, Amjad Mehmood, Muhammad Imran and Fahad Noor</i>	439
80. Application of Total Productive Maintenance (TPM) Technique in Improved Productivity of Industrial Equipment: A case study from Pakistan <i>Hamid Minhas, Usman Ghani, Shar Noor, Muhammad Usman and Zain Ul Hassan</i>	448
81. Experimental Investigation of Test Samples’ Mechanical Properties Produced from Pure Titanium with Binder Jet 3D Metal Printer <i>Osman İYİBİLGİN, Engin GEPEK</i>	457
82. Influence of Plain and N2 purging Conditions on Corrosion Mechanism correlated with Microstructures of Low Alloy Steel Multiphases Weldments <i>Kamran Ghafoor, Riffat Asim Pasha, Aneela Wakeel, Rizwan Ahmed Malik</i>	464
83. Development, up-gradation and maintenance of engineering laboratories for teaching and research in the universities of developing countries <i>Wasim Ahmad</i>	472
84. Functional Reverse Engineering of Machine Tools <i>Wasim Ahmed Khan</i>	479
85. The relationship among working hours per shift, worker productivity and errors in locksmith work <i>Benjamin Durakovic, Tauseef Aized Khan, Ramo Palalić</i>	483
86. Manufacturing of composite materials via 3D printers: Materials selection and process optimization <i>Osman İyibilgina,b, M. İskender Özsoya, Engin Gepek, Fehim Findikb,c,d</i>	491
• Mechatronics and Control Track	496
87. Implementation of Impedance Control Schemes for Position and Force Tracking on Redundant Manipulator <i>Muhammad Bilal, Mohsin Rizwan, Ali Raza and Muhammad Ali</i>	497
88. Design and Development of Sun Tracking System Using Programmable Logic Controller (PLC) <i>Hammad Farooq, Hafiz Muhammad Waqas Badar, Ahmad Hussain Safder</i>	506
89. Determining the Precise Work Area of Agriculture Machinery using Internet of Things and Artificial Intelligence <i>Dr. Tariq Kamal, Asima Bibi, Syed Muhammad Usman, Khubaib Ahmad, Dr. Bilal Habib, Dr. Zaka Ullah Zahid, Dr. Muhammad Tufail Khan, Adil Iqbal, and Abdullah Osama</i>	513
90. A Novel Spherical Actuator for Robotic Shoulder Joint <i>M. U. Khan, M. Rizwan</i>	521
91. Vibrational Analysis of Microcantilever Beams using Modeling and Simulation Technique <i>Dr. Tauseef Aized, Sania Azam, Mukhtiar Ahmad, Amna Azam</i>	527
92. Vision Based Gesture Controlled Robotic Arm <i>Saqib Zafar, Muhammad Usman, Fatima Ahmad, Nasir Ahmad, Hafiz Farhan Maqbool, Muhammad Imran</i>	533



• Abstracts.....	540
93. Assessment of Rain Water Harvesting System (Case study Sheikhul Bandi Abbottabad) <i>Mujahid Khan, Syed Adnan Shah, Ikramullah qayyum, Ashar Iqbal.....</i>	<i>541</i>
94. Selective exhaust gas recirculation for natural gas-fired power plant coupled with CO ₂ capture system <i>Yamina Qureshi, Usman Ali.....</i>	<i>541</i>
95. Thermal Investigation of Nanofluids in Heat Exchanger using Two Phase Approach <i>M Mubashir Farid, Tauseef Aized Khan, Shahid Farooq.....</i>	<i>542</i>
96. Numerical investigation of thermo-hydraulic characteristics of an indirect evaporative cooler <i>Attiq ur Rehman, Qamar Mahboob, Muhammad Asim, Muhammad Sajid Kamran, Jawad Sarwar..</i>	<i>542</i>
97. Visualization of Heliostat field of solar thermal tower power plant using virtual reality (VR) technologies <i>Kamran Mahboob, Muhammad Awais, Ahsan Naseem, Malik Safi Ullah, Awais Khan, Tauseef Azid.....</i>	<i>543</i>
98. Passive Temperature Excursion of Lithium Ion Batteries <i>Waqas Ahmed, Abid Hussain, Muhammad Rizwan.....</i>	<i>543</i>
99. Comparison of Flow-Solvers: Linear Vortex Lattice Method and Higher-Order Panel Method with Analytical and Wind Tunnel Data <i>Tahura Shahid, Faiza Sajjad, Muneeb Ahsan, Shuaib Salamat, Jehanzeb Masud.....</i>	<i>544</i>
100. Design and Analysis of Combined Darrieus Savonius Wind Turbine <i>Muneeb Ahsan, Syed Hassan Raza, Nadeem Shafi Khan.....</i>	<i>544</i>
101. Design a Solar Powered Air Conditioning system <i>M Rizwan Mehboob, M Imran Mehboob and Sumera Mehboob.....</i>	<i>545</i>
102. Computational Investigation of Turbulent Flow through Fractal Plates by Using COMSOL Multi-physics 5.2a <i>Hassan Raza, Ghulam Abbas Gohar, Muhammad Shahid Nazeer, Ali Zahid, Muhammad Muzammil Nazeer, Muhammad Saeed, Rashid Hussain Asif, Shiekh Adnan Atta.....</i>	<i>545</i>
103. Causes, Effects and Prevention Techniques for Smog in Pakistan <i>Syed Ubaid Ur Rehman, Dr. Tauseef Aized, Syed Muhammad Sohail Rehman, Syed Junaid Ur Rehman.....</i>	<i>546</i>
104. Analysis of the Spiral Bladed Vertical Axis Wind Turbine using Subsonic Wind Tunnel <i>Roshan Manghwar, Tanweer Hussain, Imran Nazir, Muhammad Sharif Jamali.....</i>	<i>546</i>
105. Scenario Analysis of the Potential for CO ₂ Mitigation and Energy Efficiency in Cement Industry of Pakistan Using LEAP <i>Amjad ullah khan, M. Bilal Sajid.....</i>	<i>547</i>
106. Fe-Polyphenol Complex Dyes for DSSCs <i>Soner Çakar and Mahmut Özacar.....</i>	<i>548</i>
107. Photoelectrochemical Water Splitting with Ag ₂ CrO ₄ /g- C ₃ N ₄ /MnFe ₂ O ₄ Nanocomposite <i>Keziban Atacan Nuray Güy and Mahmut Özacar.....</i>	<i>549</i>
108. Photocatalytic Degradation of Rhodamine B with CuFe ₂ O ₄ /Tannin/ZnO Magnetic Nanocomposite under Visible Light <i>Keziban Atacan, Nuray Güy and Mahmut Özacar.....</i>	<i>550</i>



109. Optimization of a Geothermal Multi-Generation Energy System: Energy, Exergy and Cost for Use in Coastal and Tropical Environments <i>Asif Mansoor, Tahir A. H. Ratlamwala, Muhammad A.M. Abdulmannan, Zaeem Shabbir, Muhammad S. Idrees, Sohail B. Qureshi</i>	551
110. Transformation of gasoline two-wheeler to electric two-wheeler; Energy and Environment perspective <i>Waqas Nazir Awan, Tanzeel Ur Rashid, Talal Bin Ahmed, Ubaid Ur Rehman, Sher Asif Khan, Muhammad Uzair Shah, Muhammad Hameed Ul Din</i>	551
111. Energy Management Practices of Pakistan's Glass Manufacturing Industry <i>Arslan Yousaf, Tauseef Aized Khan</i>	552
112. Energy Improvement Strategies in Coal Fired Chain Grate Boiler <i>Mr. Muhammad Khalil, Abid Hussain</i>	552
113. Energy and Exergy Analyses of Multi-Generation System using Renewable Energy <i>Tahir Abdul Hussain Ratlamwala, Jahanzeb Javed</i>	553
114. Analysis of Wind Turbine Blade's material using simulation <i>Saad Imran, Hamza Riaz</i>	554
115. Design and Experimentation of Sevonius Vertical Axis Wind Turbine for Roadside Applications <i>Muhammad Rizwan, Abid Hussain, Waqas Ahmed</i>	554
116. Design and Fabrication of Conductive Polymer Strain Sensor <i>Bakhtawar Maqsood, Muzamil Bokhari, Ajab Khan Kasi</i>	555
117. Modified and Cost-Efficient Design of the Permeameter Utilizing Indigenous Resources <i>Ghous Baksh, Hoor Ul Ain, Rabia Basry, Nayab Fareed and Atif Ismail</i>	555
118. Functional Reverse Engineering of Machine Tools <i>Wasim Ahmed Khan</i>	556
119. Design and Fabrication of Aluminum Anodizing Process <i>Saud Bin Zafar, Saadullah, Sajeel Tariq, Rao Muhammad Hamza</i>	556
120. Design and Fabrication of Charpy Impact Testing Machine <i>Muhammad Zeeshan, Ismail Khan, Muhammad Owais, Adam Khan</i>	558
121. Application of Total Productive Maintenance (TPM) Technique in Improved Productivity of Industrial Equipment: A case study from Pakistan <i>Hamid Minhas, Usman Ghani, Shar Noor, Muhammad Usman, and Zain Ul Hassan</i>	558
122. Productivity Enhancement of a Process Industry using Value Stream Mapping <i>Asif Mahmood, Dr. Tauseef Aized, Shoaib Muhammad</i>	559
123. Minimization of warpage in Plastic Part using Response Surface Methodology <i>Awais Ahmad Khan, Ramsha Kanwal, Muhammad Ismail Najib, Ghulam Moeenuddin, Hira Syed, Arooba Malik, Basit Mehmood, Muhammad Tahir Arshad</i>	559
124. Implementation of Lean Six Sigma in an Air Conditioning Industry: A case study <i>Arshad Khan, Ali.Hasnain, M.U Malkana</i>	560
125. Improving the Efficiency of Assembly Line using Line Balancing and Work Study Method in a Manufacturing Industry <i>Fareed Alam Chishti</i>	560



126.Design Modification of Power Cord of an Air Conditioner's Indoor Unit to Improve Productivity through Implementation of Lean Six Sigma <i>Ali Hasnain, J. Sarwar, A. Khan, Q.Z.Ahan, Awais A.Khan</i>	561
127.Implementation of lean six sigma to improve changeover time, machine availability and productivity <i>Arshad khan , J. Sarwar , A. Hasnain, Q. Z. Ahsan, and Awais A.Khan</i>	561
128.Design and Development of Cost Effective Prosthetic Hand using four stage gear Reduction with Infinite Fatigue Life <i>Usman Ali Khan, Saman Khan, M. Areeb Usman, Mohsin Ali, Umar S. Khan, Mohsin I. Tiwana</i>	562
129.Study of the Recent Developments and Trends of End- Effector Design for Fruit Harvesting Robot from 2013-2019 <i>Sadaf Jamshed, Tauseef Aized</i>	562
130.IOT based DATA Acquisition, Control and Performance Monitoring of 4-Stroke Diesel Engine <i>Muhammad Imran,S.M.Umair Rasheed,Tauseef Aized,Arslan Ahmad Chattha,Iftikhar Tumrani,Hassan Tanveer,Muhammad Furqan</i>	563
131.Optimized Sorting Robotic Arm: (Design for processing industry) <i>Muhammad Ihtisham Amin, Muhammad Adeel Hafeez, Adeel Ahmad</i>	563
132.Smart Visitor's Management System through ID Card in Pakistan <i>Ayesha Siddiqa, Usman Sheikh, Aneeq Asif, Zainab Riaz, Ali Asghar</i>	564
133.Automated Fruit Harvesting System using Digital Image Processing for Indoor Environment <i>Samrina Sarwar, Aisha Kanwal, Shaban Arshad, Zainab Riaz, Ali Usama, Usman Sheikh</i>	564
134.IoT Based Automatic Street Lights and Car Parking System <i>Engr. Saif Ullah, Engr. Jalal Khan, Dr. Mushtaq Ahmad Khan</i>	565
135.Image processing and Data storage for fire Alarm <i>Zainab Riaz, Aneeq Asif, Ayesha Saddiqa, Ali Asghar, Waqas Arshad, Muhammad Zia Ur Rahman</i>	565
136.An Approach to Measure Key Performance Indicators for Linear Servo Actuators <i>Naveed Riaz, Faisal Rehman</i>	566
137.Voice Recognition based Operation Theatre Assistive Robot <i>Arslan Ahmad, Amr Fazeel Baig, Iram Liaquat, Samavia Noor, Syed Muhammad Umer</i>	566
138.Towards the development of an Intelligent Smart Cane for Visually Impaired People <i>Rabia Samreen, Rimsha Perveen, Rida Fatima, Fatima Ahmad, Saqib Zafar, Aamir Mehmood, Hafiz Farhan Maqbool</i>	567
139.Human-robot teams in industrial assembly <i>Ali Ahmad Mali, Bilal Ahmad</i>	567
140.Design of G Code Interpreter Alogrithm for CNC Machines <i>Muhammad Ali Bhutto, Asif Ullah, Wasim A.Khan, Khalid Rehman</i>	568



INVITED SPEAKER



Characterization of Ti-Ha Biocomposite Produced by Powder Metallurgy



Görkem Kahraman^a, Eren Yılmaz^b, Fehim Findik^{a,b}

^aMetallurgy & Materials Engineering Department, Faculty of Technology, Sakarya Applied Sciences University, Sakarya, Turkey, E-mail: findik@sakarya.edu.tr

^bBiomedical, Magnetic and Semiconductor Materials Application & Research Center, Sakarya University, Sakarya, Turkey, E-mail: erenyilmaz@sakarya.edu.tr

Abstract:

In this study, titanium (Ti) - hydroxyapatite (HA) biocomposites sintered at 800 ° C and 1200 ° C in argon atmosphere and pure Ti sample were produced for comparison under the same conditions. The effects of the addition of hydroxyapatite into titanium on microstructure, phase content, surface wettability and corrosion behavior of titanium were investigated. While the density decreased with increasing sintering temperature, the density approached the bone with the addition of HA. Sintered titanium contains α -Ti and titanium oxide phases. The Ti-10HA composite contains α -Ti, titanium oxide and hydroxyapatite phases as well as hydroxyapatite decomposition phases depending on the sintering temperature. Furthermore, the water contact angle was reduced from about 71 ° to 30 ° by the addition of HA into the Ti. In addition, the mechanical properties and corrosion resistance of Ti-Ha biocomposite were found to be lower compared to pure titanium.

Keywords: Titanium, hydroxyapatite, biocomposite, powder metallurgy



Design and Production of Reinforced Chain in Areas Exposed to High Stress According to the Results of Finite Element Analysis



Dr. Sedat İRİÇ
Mechanical Engineering Department, Faculty of Engineering, Sakarya University,
Sakarya, Turkey

Abstract:

FDM technology, which is one of the additive manufacturing technologies, has many parameters affecting product quality and strength. These parameters include layer height, wall thickness and density. However, the strength increase obtained with these parameters remains limited. In this study, the tensile load was applied to the chain link and finite element analysis was performed and the regions with high stresses were determined. According to the results of the analysis, extra strengthening was performed in regions with high stress. The results obtained in the present case were compared experimentally with the tensile strength values in the reinforced sample. As a result, in case of additional strengthening, 20% strength increase was obtained in addition to the strength increase obtained by production parameters.

Keywords: Additive Manufacturing, Reinforced chain, FEM, Design, Tensile Strength.



Experimental Investigation of Test Samples' Mechanical Properties Produced from Pure Titanium with Binder Jet 3D Metal Printer

Osman İYİBİLGİN^{1,2}, Engin GEPEK^{2Mechanical}



¹Mechanical Engineering Department, Faculty of Engineering, Sakarya University, Sakarya, Turkey

²Biomedical, Magnetic and Semiconductor Materials Application & Research Center, Sakarya University, Sakarya, Turkey

¹Communication author, E-mail: ibilgin@sakarya.edu.tr, Tel: +90-264-295 7390

Abstract

Polymer, ceramic and metal powders are used in production with Binder jet 3D printer. Samples are subjected to sintering after pre-bonding using adhesive. This heat treatment process significantly affects the mechanical properties and strength values of the sample. In this study, test specimens were fabricated via pure Ti powders and the effect of heat treatment processes on mechanical properties was experimentally investigated. Ti powders are preferred because they are biocompatible, have sufficient strength, and especially have a high weight strength ratio in porous structures in implant manufacturing. After the experimental work, it was detected that the surface hardness of the sample increased with increasing sintering temperature. The powder distribution was close to homogeneous in the SEM micrographs. In the conventional powder metallurgy method, strength problems encountered due to the heterogeneous pore which are frequently encountered are overcome.

Keywords: Binder Jetting, Titanium, Metallic 3D Printer, Mechanical Properties



Sliding Wear Behavior of Carbon Fiber Reinforced Polyphenylene Sulfide Composites



Mehmet İskender ÖZSOY,

Levent ESATOĞLU

iozsoy@sakarya.edu.tr

*Department of Mechanical Engineering, Sakarya University,
Sakarya 54187, Turkey*

Abstract

In this study, sliding wear performance of polyphenylene sulfide polymer (PPS) and 40% and 50% weight ratio of chopped carbon fiber reinforced polyphenylene sulfide composites were investigated. In this context friction and wear tests were performed by pin-on-disc test arrangement. Test conditions are chosen as 50, 100, 200 N normal loads and 1, 2, 3 m/s sliding speeds. The counter face disc material is AISI 1040 steel. The results showed that adding fiber decreased the friction and wear rates. Furthermore increasing load decreased the friction coefficients of PPS and composites, however increasing speed increased the friction coefficients of PPS polymer but speed decreased the friction coefficients of fiber reinforced composites.

Keywords: *Polyphenylene sulfide, carbon fiber, composite materials, sliding wear*



Unlocking the Mystery of Desalination Processes



Muhammad Wakil Shahzad¹, Muhammad Burhan² and Kim Choon Ng²
Mechanical and Construction Engineering Department, Northumbria
University, Newcastle Upon Tyne, United Kingdom
Corresponding Author: Muhammad.w.shahzad@northumbria.ac.uk

Abstract:

For future sustainable seawater desalination, the importance of achieving better energy efficiency of the existing 19,500 commercial-scale desalination plants cannot be over emphasized. The major concern of desalination industry is the inadequate approach for energy efficiency evaluation of diverse seawater desalination processes by omitting the grade of energy supplied. These conventional approaches would suffice if the efficacy comparison were to be conducted for the same energy input processes. The misconception of considering all derived energies as equivalent in desalination industry has severe economic and environmental consequences. In the realms of the energy and desalination system planners, serious judgmental errors in process selection of green installations are made unconsciously as the efficacy data are either flawed or inaccurate. The inferior efficacy technologies implementation decisions were observed in many water stressed countries that can burdened a country's economy immediately with higher unit energy cost as well as causing greater undesirable environmental effects to the surroundings. In this article, a standard primary energy based thermodynamic framework is presented that addresses the energy efficacy fairly and accurately. It clearly shows that thermally driven process consume 2-3 % of SPE when combined with power plants. A standard universal performance ratio based evaluation method has been proposed that showed all desalination processes performance varies from 10-12% of thermodynamic limit. To achieve 2030 sustainability goals, innovative processes are required to meet 25-30% of thermodynamic limit.



A Novel Nanocomposite Photocatalyst for Hydrogen Production



Nuray Güy¹, Keziban Atacan², Mahmut Özacar^{1,2}

¹ Sakarya University, Science&Arts Faculty, Department of Chemistry,
54187 Sakarya, Turkey.

² Sakarya University, Biomedical, Magnetic, Semiconductor Materials Application and
Research Center (BIMAS-RC), 54187 Sakarya, Turkey.

Abstract

The growing demand for energy has led to strong research to grow a clean and renewable energy source. Hydrogen stands out as one of the most perfect fuels thanks to its excellent energy conversion performance and zero carbon emissions. Photoelectrochemical (PEC) water splitting is a sustainable energy production technique that converts solar energy to hydrogen in the form of fuel. Semiconductors such as ZnO, TiO₂, WO₃, and BiVO₄ have an important role in the conversion of solar energy into the hydrogen via the PEC water splitting. But, they exhibit low PEC activity owing to their wide band gap energy which restricts the absorption of the visible light. Some methods such as noble metal doping, surface photosensitization and combining with narrow band semiconductors were applied to develop the photocatalytic performance. Coupling of TiO₂ with other semiconductors such as Bi₂O₃-TiO₂, g-C₃N₄-TiO₂, CdS-TiO₂, CuFe₂O₄-TiO₂ has exhibited to increase the photoelectrochemical efficiency by hindering the recombination of charge carrier. NiFe₂O₄ as a magnetic oxide semiconductor, is one of the co-catalysts due to its low cost and visible light response for photocatalysis and PEC water splitting. In this work, NiFe₂O₄/Ag/TiO₂ ternary nanocomposite was prepared for the PEC water splitting under visible light. Compared the PEC water splitting performance of NiFe₂O₄/Ag/TiO₂ with the pure TiO₂, NiFe₂O₄ and Ag/TiO₂, the ternary nanocomposite displayed the great activity. The superior activity of NiFe₂O₄/Ag/TiO₂ is related to its more visible light absorption and influential interfacial electron flow thanks to the synergetic interactions of Ag nanoparticles and TiO₂ and NiFe₂O₄. In conclusion, this work demonstrates that NiFe₂O₄/Ag/TiO₂ nanocomposite is effective in PEC water splitting applications.

Keywords: PEC water splitting, Ag doping, NiFe₂O₄.



Recent advances in the use of phase change and silica aerogel based materials for energy applications in buildings.



*Prof. Pascal Henry Biwole,
Université Clermont Auvergne, France*

Abstract:

Phase change and silica aerogel based materials for thermal energy storage and thermal insulation in buildings have attracted a lot of attention as promising materials to reduce the energy consumption and carbon footprint of the building sector. Here, we present prototypes of several innovative building envelopes and systems integrating such materials. The complex modeling of the heat and mass transfers through the materials is detailed. Life cycle assessment and economic analysis are also presented. Results show that while phase change and silica aerogel based materials can dramatically increase the energy performance of buildings, their dissemination in the building sector is still hampered by high initial investment costs.



The Road Towards Flexible Smart Materials



Dr Jibrán Khaliq,

Senior Lecturer, Department of Mechanical and construction Engineering,
Faculty of Engineering and Environment, Northumbria University at
Newcastle, NE1 8ST, United Kingdom

Corresponding Author: Jibrán.khaliq@northumbria.ac.uk,

Abstract:

For large area flexible or printed electronics, the aim is to make electronic products on a flexible polymer, paper or metal substrate. Examples of these products can be Organic LEDs (OLEDS), solar cells, RFID tags, smart cards, wearables and on longer term even complete flexible smart phones. When more functionality is introduced in this field there will be a need for flexible electronic components like capacitors and all kinds of sensors. These electronic components are now typically based on ceramics. These class of electroceramics include the ferroelectrics which are used in capacitors and piezoelectrics but also Negative and Positive Temperature Coefficient (NTC, PTC) thermistors. All these Electroceramics are intrinsically non-flexible! In this course we will discuss various research and development which is being done to come to more flexible components. This can be achieved by making composites out of a polymer matrix and a filler material which can consists of electroceramic-powder. Specific materials can be designed by structuring of electroceramic powder in the polymer matrix, particle size and aspect ratio, and by the polymer which is used. This opens up new ways to make functional components.



Hybrid Piezo-Pyroelectric Energy Scavenging by High β -phase Poly (Vinylidene fluoride) Membrane



Mohd Faizul Bin Mohd Sabri,
Department of Mechanical Engineering, Faculty of Engineering, University of
Malaya, Malaysia
Corresponding Author: faizul@um.edu.my

Abstract:

A highly β -phase content poly-(vinylidene fluoride) (PVDF) membrane can be produced in a one-step electrospinning process, which eliminates a need for the post treatment [1,2]. Electrospinning was chosen to be the proposed method to produce piezo-pyroelectric membrane from polymer based starting material. Micro energy scavenging devices based on PVDF have attracted many interest due to their high sensitivity, low cost, easy preparation, excellent stability and good mechanical properties [3, 4]. This work reports a study on the fabrication and integration of PVDF microarrays for hybrid micro energy scavenging device [5,6]. The microarrays consists of electrospun PVDF membrane (Fig.1) were fabricated using MEMS approach. The micropatterning of the electrospun PVDF on a flexible substrate was done by dry reactive ion etching (RIE) with oxygen plasma. Progress claims include: (1) high etching rate value of $2\mu\text{m}/\text{min}$ on the electrospun (PVDF) membrane; (2) micropatterning of electrospun PVDF membrane on a flexible substrate. The results show that a rather higher etching rate of electrospun PVDF membrane with value of $2\mu\text{m}/\text{min}$; successfully micropatterned arrays with dimensions of $200/500/200\mu\text{m}$ with the height of over $50\mu\text{m}$ (Fig. 3). This work presented the possibilities of micropatterning of electrospun PVDF membrane for integration into MEMS and micro devices.



Industry 4.0 – Need of Current Era

Prof. Dr. Muhammad Tufail,
Pro-Vice Chancellor NED University Karachi, Pakistan

Abstract:

Industry 4.0 is a part of fourth industrial revolution initiated by the German Manufacturers. The whole concept is based on the coordination between machines and humans using the information technology. Transformation from first to fourth industrial revolution enormously changed the concepts of productivity, value addition, quality and product life cycles. Concepts of material transformation changed to; value addition, then value chains and now life cycles which traces the product up to its dispose off. Traceability of raw material from multi-tier supplier to manufacturing and manufacturing to distribution, retailer, customer and retirement has become essential part of product life cycle management. Although the components of Industry 4.0 are extending due to the continuous evolution but still the implementation of such a massive change is a question in backward countries such as Pakistan.

Being the fifth largest nation on the earth, Pakistan is enriched in demand and production of basic agriculturally based and other products, such as; wheat, cotton, milk, lentils, wood, cement, sugar, spices etc. Up to now the factories processing such products are still too old and not upgraded to cater the need of productivity due to increasing population. Agriculture, farming and other industries are still traditional, bearing the higher cost of quality and inefficient working practices, resulting in shortages, high imports and wastages of foreign reserves. To overcome these issues, it is the immense need of the country to implement smart industry or industry 4.0 concept.

Comparing the need of Industry 4.0 against the current infrastructure, Pakistan is one of the third world country lacking the basic requirements, such as; availability of fast internet, multi-tier cyber security, skill set of labours and management, availability of technological ready government protocol, cyber laws, load shedding of utilities etc. Hence in this keynote, recommendations for the implementations and limitations are discussed in detail.



Potential and Prospects of Energy Transition in Pakistan



Khanji Harijan,

*Meritorious Professor, Department of Mechanical Engineering, Dean Faculty of Engineering, Mehran University of Engineering and Technology, Jamshoro-76062, Pakistan.
Email: khanji.harijan@faculty.muett.edu.pk*

Abstract:

Economic Survey of Pakistan and various other reports recognize that for over a decade (2008-2018), around 2-3 percent of GDP was lost due to the power outages. The underperformance of energy and power sector both at planning and operation levels, as such, have seriously affected the masses. Globally, such challenge has been viewed and resolved with inclusive approach on economy, energy- technology, and energy-society. While energy, as the sector was recognized too late in Pakistan. As such, so far Pakistan does not have any integrated energy policy since its independence. During early days, power sector was primarily recognized as energy sector. However, within power sector planning in late 1960s onwards, water management remained top agenda for governments. In early 1990s, power sector reforms were promised and initiated as well. However, the reform process was not only too slow but at the same time outcome of reforms was little evidently relevant. Various energy and power sector plan and policies were announced thereafter; however, the results of such efforts remained adverse with increased demand-supply gap and evolution of circular debt. The key barriers, however, are not alone associated with government, yet these include unwillingness to pay the price of energy by the consumers, the political stubbornness to maintain the subsidies, administrative and line losses, and, most importantly lack of integrated energy planning and implementation. The failure of conformist approaches emphasis that country explores indigenous resources and adopt globally acknowledged energy transition pathway. An energy transition will have significant implications, as it will bring about essential changes in energy trade balances, and impact economic development. The resultant energy transformation will create new energy leaders and strengthening the significant investments in renewable energy technologies. At this juncture of time, Pakistan, with substantial renewable energy potential, also need to quickly adjust and adopt energy transition pathway as the future sustainability is linked with resilient and microeconomic landscape.

Keywords: Energy Transition, Renewables, Potential, Prospects, Pakistan



Focus towards Mission Oriented Research to Benefit Pakistan



Muhammad Abid,

*Director Interdisciplinary Research Center, COMSATS University Islamabad, Wah Cantt,
Pakistan.*

Abstract:

Interaction between academia, research and industry is observed at best limited in Pakistan. This has resulted mostly theoretical research, limited innovation and entrepreneurship and hence almost no opportunities for real world solution provisions to the industry. In addition it is observed that the current capabilities and resources of Pakistan in computational mechanics related areas are at best limited. The present practices are generally based on limited and simplified data and empirical models developed over years of experience. Such manufacturing and design practices fail to take advantage of the modern virtual prototyping technologies, thus making it difficult to optimize the design of products. In order for the Pakistani industry to become competitive in the emerging global economy that is taking shape under the umbrella of World Trade Organization, it is essential to modernize our design practices and procedures. In this paper some applications of computational mechanics is presented to highlight its use and importance for real world problems solving. This highlights potential of research in Pakistan and invites researchers for interdisciplinary research to benefit the community for tangible outcomes as Mission Oriented Research may be the only solution. Some of the case studies presented are regarding; bolted pipe joints for petrochemical, nuclear, and process industries to analyses and optimize their performance for no leak conditions addressing environmental impacts; simulate and optimize welding procedures to control deformations and residual stresses during pipe flange joint during single and multipass welding; simulation and optimization of Environmentally controlled poultry sheds; water and sediment flow simulations through tunnels and reservoirs for their life predictions; simulations of renewable energy systems for optimized performances; applications of high performance computing for large scale problems; industrial products such as overhead cranes, industrial trusses and others.



Mechanism and role of module design upon osmotically driven module operation at pilot and bench scale



Dr. Farrukh Arsalan Siddiqui,

Chairman, Department of Mechanical Engineering, Bahauddin Zakariya
University Multan, Pakistan

Email: farrukh.siddiqui@bzu.edu.pk

Abstract:

Forward Osmosis (FO) has globally attracted consideration because of its potential to reclaim water with low consumption of energy. However, membrane fouling still appears to be one of the major issues limiting the efficiency of FO. Although, a number of studies have been performed to investigate the FO membrane fouling, the majority of them focused on the use of synthetic water as feed which may well not sufficiently represent practical performance and underlying technology. FO membrane fouling by real waters is much more complicated and has been the focus of this study focussing role of module performance and its mechanism. The potential of a commercial forward osmosis (FO) module to recover water from NEWater brine, an RO retentate, was assessed by taking an innovative approach to obtaining the mass transfer coefficients. The performance comparison of the spiral wound (S-W) FO module with that of the flat sheet laboratory unit suggests that the winding involved in S-W construction can adversely affect performance; the values for the S-W mass transfer coefficients were half of those expected. This first-of-its-kind performance comparison utilised coupons of the membrane and spacers taken from the module. The module was used both in the conventional manner for FO and in the reverse manner with the active layer facing the draw solution. Estimates of membrane parameters and mass transfer coefficients experiments for the two orientations were obtained using pure water, 10 mM and 25 mM NaCl solution on the feed side and 1 M NaCl as draw solution. The fouling potential of NEWater brine per se was found to be low. These are the first results with a S-W module that suggest potential for this niche application; nevertheless the level of the water flux through the S-W module clearly indicates that industrial applications of S-W FO will be constrained to special cases.

Keywords: *Forward osmosis, module, fouling, pilot scale, bench scale, membrane orientation*



Transformation of Industry in the wake of Smart Manufacturing/Industry 4.0



Prof. Dr. Mirza Jahanzaib,

Dean Faculty of Industrial, Mechanical & Aeronautical Engineering, UET, Taxila

Abstract:

The smart manufacturing/Industry 4.0 is to drive manufacturing forward: to be faster, more efficient and customer-focused while pushing beyond mechanization and optimization to discover new business opportunities and models. Since, Industry 4.0, realization, it is pertinent to discover its usefulness in manufacturing systems. By entrenching modern technology into manufacturing, industry 4.0 objectives can be achieved. Workforce is another critical area where technology makes a big impact. With communication and networking, workforce needs to talk about what is happening in the manufacturing arena to find the solutions that work. The days of sitting in cubicles, sticking with desktop computers and physical presence on the shop floor are old days. Smart workers run everything, including business from mobile devices. Some key stepping stones in Industry 4.0 are: 1) Cloud Computing; which is a single instance, multi-tenant environment scales with your business. Companies are running on the same set of manufacturing software code and same database technology. This is the platform on which manufacturers build their Industry 4.0 environment. 2) Industrial Internet of Things; Receiving and shipping is carried out by automation. Within Industry, It's all done through PLC integration and controls, which is highly efficient, higher product quality, and better customer satisfaction. Industrial internet of things connects devices from the shop floor and to ERP. 3) Agility and Sequencing; Sequencing means best optimal use of components and parts which arrive at a production line, in a specific configuration, at the exact time the product is required for the customer's specific product configuration. This will be a requirement for all manufacturing companies across the industry spectrum. 4) On Demand- Manufacturing (Flexibility); Consumer preference and demand patterns assume customers and companies are going to provide products to the market. For competitiveness, manufacturing companies need to react and coping with rapidly changing the production process to align with the evolving demand patterns of its customer base. These variable demand patterns will be flowing through the enterprise business systems straight down to the shop floor manufacturing technology. This auto-configure the manufacturing production lines so the specific products can be manufactured. The days of large manufacturing plants making the same part or product, are gone. It's going to be localized and clustered manufacturing, supporting customers within a very specific region at regional level. All this is possible with future factories and one contemporary is Industry 4.0.



Functional Reverse Engineering of Machine Tools

Professor Dr. Wasim Ahmed Khan,

Faculty of Mechanical Engineering, GIK Institute of Engineering Sciences and
Technology, Topi-23640, Khyber Pakhtunkhwa, Pakistan.

E-mail: Wasim@giki.edu.pk

Cell: 0300-8217392



Abstract:

The purpose of this talk is to persuade academia to develop capacity building in strategic and non-strategic machine tool technology, and; machinery in other sectors. Strategic machines can produce non-strategic machines and any other discrete product. Nonstrategic machines directly or indirectly produce machines used in production of food, apparel and shelter. Functional Reverse Engineering of Machine Tools and Equipment is meant for acquiring self-sufficiency in discrete manufacturing sector. Same process is applicable to other sectors as well. Functional reverse engineering is a redesign and manufacturing procedure that does not violates anybody's intellectual property rights and allows incorporation of innovative features making the discrete product under consideration more viable for the client. Pakistan being one of the Next Eleven emerging markets, requires focus on more exports from the country and lessen the burden of imports. To achieve this and to move on to BRICS nations, the country has to have the capacity to develop machinery in sectors, such as machine tools, construction, food processing and packaging, textile, automobiles, home appliances, energy, biomedical engineering etc. The Faculty of Mechanical Engineering at the Ghulam Ishaq Khan Institute is fully aware of this necessity and the Machine Tool Research Group at the GIK Institute has spent three years working in this area. The responsibility of the group is to provide a general model for an enterprise of functional reverse engineering that can generate profit in less focused but advance areas of research and development in the country and share the model with peers working in other sectors. The work is being done with the support of Directorate of Science and Technology, Department of Science and Technology, Government of Khyber Pakhtunkhwa; and, Ghulam Ishaq Khan Institute of Engineering Sciences and Technology.



Natural Air Conditioning – Innovative air cooling with renewable energy integration



Dr. Nadeem Ahmed Sheikh,

Professor, Dept. of Mechanical Engg. IIUI, Islamabad

Abstract:

Steep growth in the demand for energy in building sector is seen over the past few decades primarily due to urbanization, population growth, climatic changes and improvements in living styles. On average, the consumption of electricity in building sector of Pakistan stands at around ~50%. Out of this huge percentage around 40-50% percent of the electricity is consumed in air conditioning and this share is expected to increase in coming years. One alternate of commonly used conventional technologies is to rely on air cooling through direct and/or indirect evaporative methods. This has been in practice for many decades but owing to health and high inlet humidity issues; these techniques have not been able to match conventional systems. However, the idea to use air as the heat transport fluid has recently gained attention owing to several advancements including efficient multi-stage indirect evaporation techniques such as Maisotsenko-cycle. In addition, efficient and cost effective ways of humidity control have also been achieved. Together with these two, in addition to solar energy for re-generation of desiccant system, the technology has gained significant attention owing to low operational cost and marginal carbon foot print. Since 2013, our team has worked on the idea and led to development of prototype which has demonstrated its capabilities in lab environment. Today, with the aid of our industrial partner and HEC TDF fund, the product shape of this idea is being prepared for domestic as well as industrial scale applications providing provision for solar integration. This is a classic example of how the local resources and human resource worked together to develop low cost, efficient & greener product to address local as well as global challenge.



Advanced Nuclear Reactors and their Role in Meeting Growing Energy Demand of Pakistan

Kamran Rasheed Qureshi,

Department of Mechanical Engineering, PIEAS



Abstract:

Nuclear power reactor is a clean source of electricity and provides a consistent base load power. Because of stable fuel supply and cheaper fuel cost, it reduces dependence on costly fossil fuel imports. In order to meet the global electricity demand, the share of nuclear in the electricity mix is growing because of these advantages. At present, there are 453 nuclear reactors operating in the world generating 399 GWe, and 55 units are under construction in 18 countries. In order to enhance the role of nuclear energy in future, advanced nuclear reactor designs have been proposed which involve improvements over existing designs or incorporates radical conceptual changes in the design of reactors. These advanced designs offer improved safety, improved economic competitiveness, less waste, and address many public health and safety risks. Pakistan has currently five operating nuclear power plants. According to MTRF-2005-10, PAEC has been tasked to enhance the current installed capacity by nuclear to 8,800 MWe by 2030. In order to meet this target, PAEC has been planning to build more reactors. The construction work for two units (1100 MWe each) near Karachi i.e. K-2 and K-3 has already started and sites for more nuclear power plants are being identified. However, in order to achieve this much high demand by nuclear in Pakistan, large-scale deployment of advanced nuclear reactors is required. In this talk, advanced nuclear reactor technologies available for immediate, near, and long term deployment will be presented. Furthermore, their innovative features with respect to safety, simplicity and economics will also be discussed. At the end, their potential role within the context of Pakistan will also be described.



Influence of Plain and N₂ Purging Conditions on Corrosion Mechanism Correlated With Microstructures of Low Alloy Steel Multipass Weldments

Riffat Asim Pasha, 2.Kamran Ghafoor, 3.Aneela Wakeel, 4.Rizwan
Malik,

1Mechanical Engineering Department University of Engineering and Technology Taxila.

Metallurgy and Materials Engineering Department, University of Engineering and
Technology Taxila, Pakistan.



Abstract:

The influence of plain and N₂ Purging conditions in plain water and 0.5 NaCl solutions of low alloy steel weldments have been investigated through electrochemical technique. Gas Tungsten arc welding (GTAW) as root / hot pass and submerged arc welding (SAW) as filling / capping was applied to SA 516 (grade 70) steels. To study effect of multipass welding cycles on Base Metal (BM), Heat Affected Zone (HAZ) and Weld Zone (WZ) , tensile testing, micro-vicker hardness, optical microscopy, X-ray diffraction (XRD) and potentiodynamic polarization scan was carried out. The attempt is made to correlate the corrosion kinetics with microstructural change in tap water and 0.5 % NaCl solution in both plain and N₂ purging conditions. The N₂ purging conditions both in water and saline environment accelerate corrosion damages. The base metal is more corrosion resistance than HAZ and HAZ is more corrosion resistance than WZ. The presence of acicular ferrite in weld zone shows higher corrosion rate in weld zone as compare to Base metal and Heat Affected Zone in water and 0.5 % NaCl solution both in plain and N₂ purging conditions.

Keywords: Boiler & Pressure vessel steel, Multipass GTAW Welding, HAZ, WZ, Corrosion and Microstructures



THERMO-FLUID AND ENERGY TRACK



Assessment of Wind Potential in South Punjab

Muhammad Sumair¹, Tauseef Aized¹, Muhammad Usman¹

1. Department of Mechanical Engineering, University of Engineering and Technology, Lahore

Abstract

The work is important as it is 1st of its kind conducted so far in Pakistan. The expectedly high wind potential area in Punjab i.e. South Punjab has never been assessed so far. Therefore, the current work focusses on the wind potential assessment in south Punjab. Eleven locations from South Punjab have been analyzed using two-parameter Weibull model and 5-years wind data which has been collected from Global Wind Atlas (GWA) and PMD (Pakistan Meteorological Department). The analysis showed that Rahim Yar Khan carries the highest wind speed, highest wind power density (WPD) and Wind Energy Density (WED) with values being 4.40 ms⁻¹, 77.2 W/m² and 677.76 kWh/m²/year respectively. Bahawalnagar observed the least wind speed i.e. 3.60 ms⁻¹ while Layyah observed the minimum WPD and WED as 38.96 W/m² and 352.24 kWh/m²/year respectively. Weibull frequency distributions and commulative probability diagrams were drawn and presented. Polar diagrams were also drawn to determine and show the optimum wind blowing directions at each location.

Keywords: Wind Energy, Wind Potential, Potential Assessment, South Punjab

1. Introduction

Wind energy, being a significantly economical and renewable form of energy, is seeking attention throughout the world these days. Currently the global wind installed capacity reaches about 597 GW in 2019 [1] with China as the leading one having a share of 37.01% in global installed capacity followed by USA (16.14%), Germany (9.93%), India (5.46 %) and Spain (3.85 %) [2]. According to International Renewable Energy Agency (IRENA) report, 2019 [3], India has total installed capacity of 35 GW whereas Pakistan has only 1186 MW which was only 106 MW in 2014 [4]. As Pakistan is energy deficient country, having a huge reliance on fossil fuels for both the primary energy (with 87% and 80% share as of 2014 and 2019 respectively) and electrical energy generation (61% and 64 %share as of 2014 and 2019 respectively) [5, 6], therefore, to achieve the sustainable development, there is a need to harness wind energy [7]. Before the exploitation of wind energy, accurate estimation of wind potential is important [8]. So far, numerous sites throughout the world have been investigated. Hong Kong, an island in China has been investigated to assess the wind potential and to determine the suitability of certain wind turbine models, presented in [9]. A potential site in Brazil i.e. Paraiba has been investigated and presented in [10]. Similarly, Firouzkooh county of Iran [11], Arizona [12], Tehran, Iran [13] and many others have been studied. In Pakistan, Gharo, Sindh [7], Baburband, Sindh [14], Jiwani, Balochistan [15] and other potential sites have been investigated. However, province of Punjab has not been investigated as no literature is available for that. Keeping in view the geographical location of south Punjab, high wind potential is expected there. The objective of this paper is to investigate the wind characteristics and to assess the wind potential in south Punjab. The output from this study may be useful for the feasibility of any wind power project going to be launched.

There are a number of distributions available to model various phenomenon [16, 17] but two-parameter Weibull model has been found the most accurate one throughout the literature to estimate the wind potential [18, 19]. 2-parameters Weibull model is given as follows [20-22].

$$f(V) = \frac{K}{c} \left(\frac{V}{c}\right)^{K-1} e^{-\left(\frac{V}{c}\right)^K} \quad (1)$$

world have been investigated. Hong Kong, an island in China has been investigated to assess the wind potential and to determine the suitability of certain wind turbine models, presented in [9]. A potential site in Brazil i.e. Paraiba has been investigated and presented in [10]. Similarly, Firouzkooh county of Iran [11], Arizona [12], Tehran, Iran [13] and many others have been studied. In Pakistan, Gharo, Sindh [7], Baburband, Sindh [14], Jiwani, Balochistan [15] and other potential sites have been investigated. However, province of Punjab has not been investigated as no literature is available for that. Keeping in view the geographical location of south Punjab, high wind potential is expected there. The objective of this paper is to investigate the wind characteristics and to assess the wind potential in south Punjab. The output from this study may be useful for the feasibility of any wind power project going to be launched.

2. Methodology

$$F(V) = 1 - e^{-\left(\frac{V}{c}\right)^K} \quad (2)$$

$f(V)$ = Probability Density Function

$F(V)$ = Commulative Density Function

K = Dimensionless Shape Parameter



$C = \text{Scale Parameter (ms}^{-1}\text{)}$

Whereas shape (K) and Scale (C) parameters can be estimated using energy pattern factor method [23]; one of the significantly accurate method [24] for the estimations of Weibull parameters

$$K = 1 + \frac{3.69}{E_{pf}^2} \quad (3)$$

$$C = \frac{\bar{V}}{\Gamma(1+\frac{1}{K})} \quad (4)$$

$$WEPF = E_{pf} = \frac{\sum \bar{V}_i^3}{(\sum \bar{V}_i)^3} \quad (5)$$

$$\bar{V} = \frac{1}{N} \sum_{i=1}^N V_i \quad (6)$$

2.1. Wind Potential

Wind potential is not only determined by wind speeds but also from wind power density and hence the wind energy density because average wind speeds can be identical for different locations irrespective of whether they possess same or different wind power or wind energy densities. Wind power and wind energy densities can be estimated using following mathematical relationships [11, 25]:

$$WPD_W = \frac{1}{2} \rho C^3 \Gamma \left(1 + \frac{3}{K}\right) \quad (7)$$

$$WED = \frac{1}{2} \rho C^3 \Gamma \left(1 + \frac{3}{K}\right) T \quad (8)$$

Two important speeds in the analysis of wind potential are Most Probable Wind Speed and the Optimum Wind Speed or the Speed Carrying the Maximum Wind Energy. Once the Weibull parameters are calculated, these speeds can be calculated using following mathematical relationships [7, 13]:

$$V_{mp} = C \left(\frac{K-1}{K}\right)^{1/K} \quad (9)$$

3.4. Wind speed distribution

Commulative frequency distribution has been shown in Figure 5 analysis shows that the highest wind potential area has a wind speed greater than 3 ms⁻¹ with commulative frequency of more than 75% whereas for Bahawalnagar the wind blows at a speed greater than 3 ms⁻¹ with ~62 % commulative frequency value.

$$V_{opt} = V_{max E} = C \left(\frac{K+2}{K}\right)^{1/K} \quad (10)$$

3. Results and discussions

3.1. Wind speeds

Yearly average wind speeds have been shown in Table 1 alongwith shape parameters, scale parameters and average wind power density values. The analysis of Table 1 and Fig.1 shows that RYK has the maximum 5-years average wind speed i.e. 4.40 ms⁻¹ (with highest value observed in 2018 was 4.56 and minimum value in 2016 was 4.20 ms⁻¹). On the other hand, Bahawalnagar carries the minimum wind speed as 3.60 ms⁻¹ (with highest value of 3.90 ms⁻¹ in 2018 and the least value of 3.38 ms⁻¹ in 2016).

3.2. Wind power and energy density

It has been observed from Table 1 and Figures 2-3 that RYK possesses the maximum WPD and maximum WED as 77.2 W/m² and 677.76 kWh/m²/year respectively. On the other hand, the minimum values of both the WPD and WED has been observed for Layyah as 38.96 W/m² and 677.76 kWh/m²/year respectively. The important point to note here is that minimum wind speed has been observed for Bahawalnagar but it is not the location with minimum WPD and WED which shows that wind speed is not the true representative of wind potential.

3.3. Most probable and optimum wind speed

The analysis of table 2 shows that RYK has the highest most probable wind speed of 4.25 ms⁻¹ and the minimum value 3.44 ms⁻¹ has been observed for Bahawalnagar. The highest optimum wind speed is observed for RYK as 5.62 ms⁻¹ and the minimum is for Layyah i.e. 4.57 ms⁻¹ (lower than that of Bahawalnagar i.e. 4.71 ms⁻¹). This is the reason why Layyah has the lower WPD and WED than Bahawalnagar although Bahawalnagar has the lower wind speed than Layyah.

3.5. Weibull distribution

Weibull distribution used to model the actual wind data estimates the actual wind data with significant accuracy. The Weibull diagrams for all 11 locations have been shown here in Fig. 4 which is consistent with shape and scale parameters listed in Table 1. The highest peak shown here is for Layyah (consistent with highest value of K i.e. 3.69). Similarly, the most widely spread curve on x-axis is for RYK (consistent with the highest value of scale parameter of 4.79 ms⁻¹).



3.6. Polar Diagrams:

Polar diagrams are very important to show the optimum direction in which the wind blows at a certain location. The determination of this direction is important as the amount of energy extraction surely relies on the direction in which the turbine is installed. In Fig.6, the polar diagrams have been shown for all 11 locations.

4. Conclusion

A region in south Punjab consisting of 11 districts has been investigated and analyzed for wind potential assessment. 2-parameter Weibull distribution with 5 years daily average wind data has been employed to estimate the potential of wind. The following conclusions have been drawn from the analysis:

- i. Rahim Yar Khan is the highly windy area with maximum wind speed, wind power density and wind energy density
- ii. Rahim Yar Khan is the highly windy area with maximum wind speed, wind power density and wind energy density.



Table 1. Annual Average Wind Speeds, Shape (K), Scale (C) parameters and Wind Power Densities (WPD) for South Punjab

Location	2014				2015				2016				2017				2018			
	V _{avg}	K	C	WPD	V _{avg}	K	C	WPD	V _{avg}	K	C	WPD	V _{avg}	K	C	WPD	V _{avg}	K	C	WPD
Bahwalnagar	3.68	3.2	4.05	46.37	3.51	2.81	3.9	40.04	3.38	3.18	3.72	34	3.5	2.98	3.87	40.1	3.9	3.23	4.26	51.06
Bahawalpur	4.35	3.2	4.77	80.29	4.12	2.99	4.53	62.89	3.94	2.97	4.16	50.1	3.96	2.89	4.38	61	4.42	3.12	4.85	83.57
D.G Khan	3.8	3.5	4.13	43.86	3.82	3.36	4.17	43.72	3.81	3.56	4.11	41	3.96	3.54	4.27	47.7	4.42	3.66	4.74	65.16
Muzaffargarh	3.78	3	4.17	52.73	3.75	2.9	4.16	46.97	3.62	2.97	3.99	41.1	3.81	3.03	4.21	51.8	4.33	3.22	4.72	74.59
Multan	3.72	3.02	4.1	51.67	3.62	2.87	4.02	43.12	3.43	2.93	3.8	36.57	3.6	2.98	3.98	45.77	4.19	3.26	4.57	68.22
Rahim Yar Khan	4.54	3.1	4.96	88.5	4.45	3.19	4.86	73.5	4.20	3.21	4.58	65.5	4.15	2.93	4.58	66.8	4.56	3.24	4.96	91.19
Khanewal	3.72	3.02	4.10	51.67	3.62	2.87	4.02	43.12	3.43	2.93	3.80	36.57	3.60	2.98	3.98	45.77	4.19	3.26	4.57	68.22
Layyah	3.66	3.72	3.92	35.74	3.60	3.54	3.90	35.80	3.67	3.67	3.93	35.99	3.77	3.71	4.03	38.31	4.23	3.80	4.50	53.96
Lodhran	4.08	3.12	4.49	67.27	3.92	2.94	4.33	54.68	3.69	2.92	4.09	45.94	3.81	2.93	4.22	54.43	4.36	3.20	4.76	77.19
Rajanpur	4.38	3.52	4.74	69.46	4.33	3.28	4.73	64.91	4.10	3.38	4.48	56.08	4.23	3.38	4.60	60.34	4.67	3.53	5.03	79.92
Vehari	3.75	3.12	4.12	51.14	3.60	2.89	3.99	42.21	3.45	3.03	3.80	36.42	3.57	2.97	3.93	43.50	4.22	3.36	4.58	66.20

Table 2. Annual Average Values of Most Probable and Optimum Wind Speeds for South Punjab

Locations	2014		2015		2016		2017		2018	
	V _{mp}	V _{maxE}	V _{mp}	V _{maxE}	V _{mp}	V _{maxE}	V _{mp}	V _{maxE}	V _{mp}	V _{maxE}
Bahawalnagar	3.55	4.8	3.31	4.75	3.28	4.36	3.32	4.66	3.76	5
Bahawalpur	4.22	5.6	3.92	5.44	3.61	4.96	3.75	5.3	4.27	5.72
D.G Khan	3.72	4.7	3.74	4.81	3.74	4.67	3.87	4.88	4.34	5.34
Multan	3.57	4.9	3.45	4.85	3.28	4.56	3.43	4.79	4.06	5.31
Muzaffargarh	3.61	5	3.59	4.99	3.44	4.79	3.65	5.02	4.2	5.5
Rahim Yar Khan	4.39	5.8	4.3	5.7	4.07	5.34	3.95	5.5	4.42	5.77
Khanewal	3.57	4.89	3.45	4.85	3.28	4.56	3.43	4.79	4.06	5.31
Layyah	3.59	4.41	3.54	4.45	3.60	4.43	3.69	4.54	4.15	5.03
Lodhran	3.94	5.28	3.73	5.21	3.52	4.92	3.62	5.09	4.21	5.57
Rajanpur	4.29	5.41	4.22	5.49	3.99	5.20	4.12	5.31	4.58	5.72
Vehari	3.61	4.87	3.45	4.85	3.31	4.53	3.37	4.74	4.12	5.27

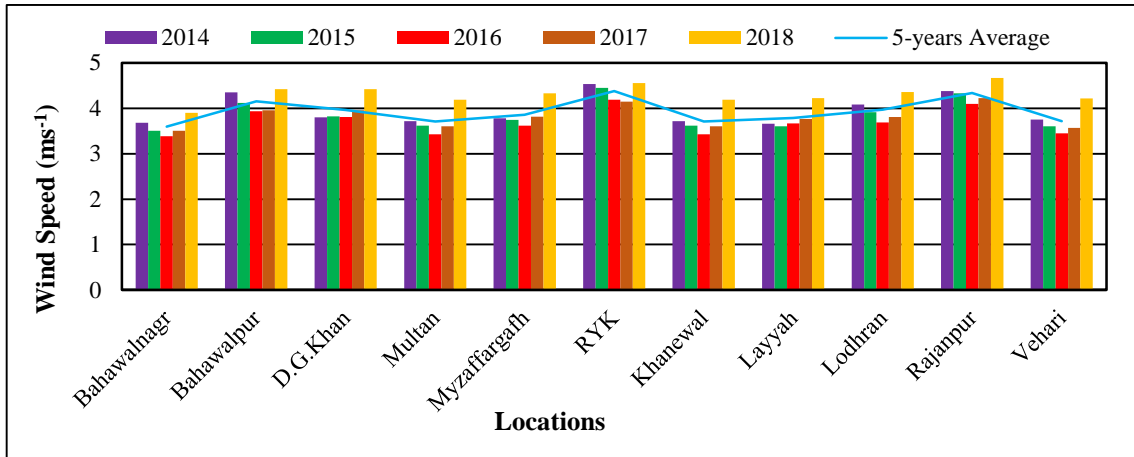


Fig. 1. Yearly Average and 5-years Average Wind Speeds (ms^{-1})

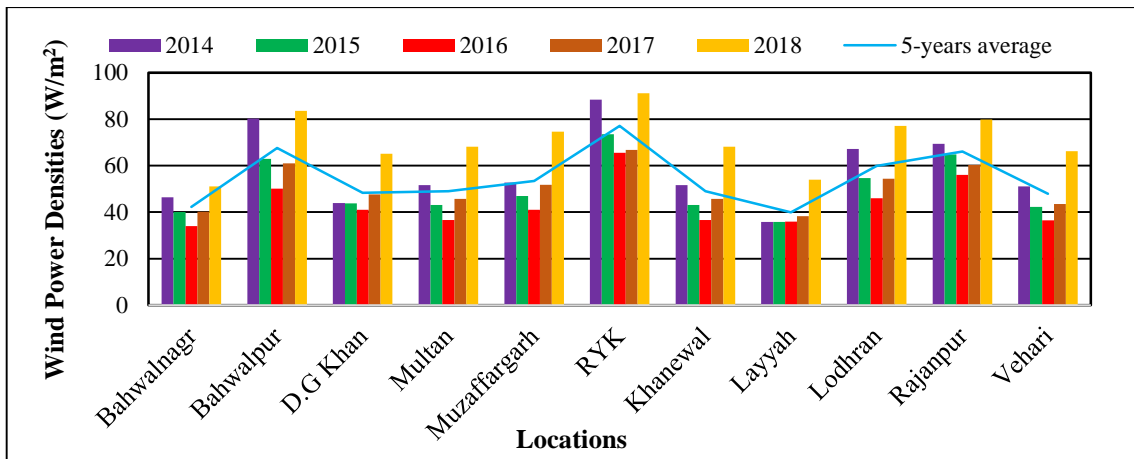


Fig. 2. Yearly Average and 5-years Average Wind Power Densities (W/m^2)

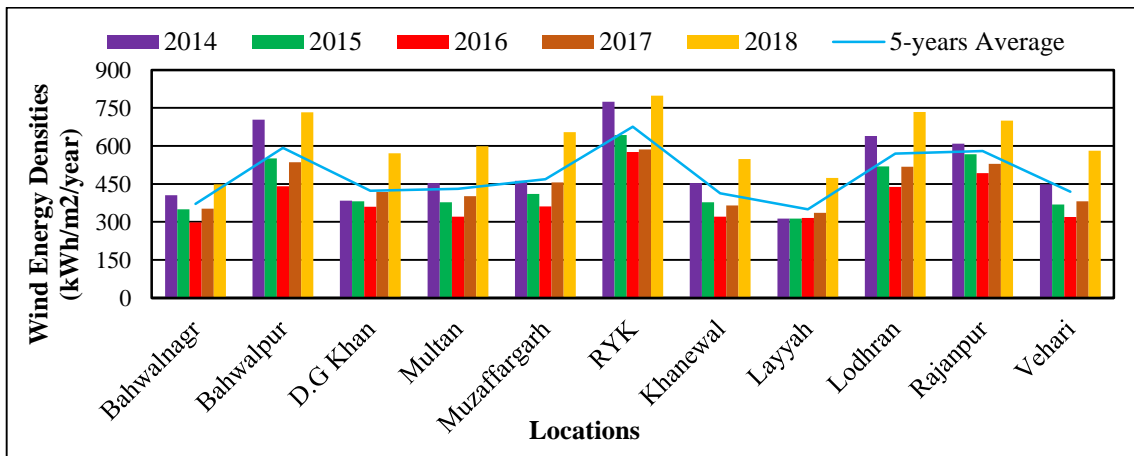


Fig. 3. Yearly Average and 5-years Average Wind Energy Densities ($kWh/m^2/year$)

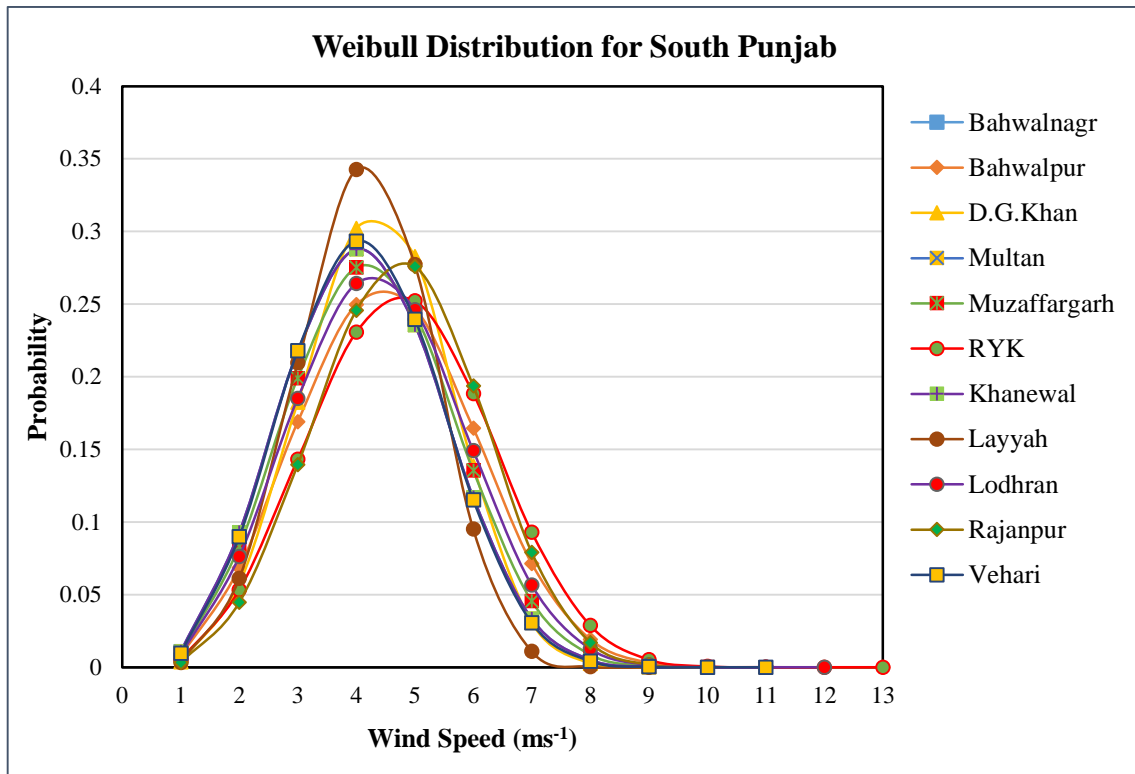


Fig. 4. Weibull Distribution for South Punjab

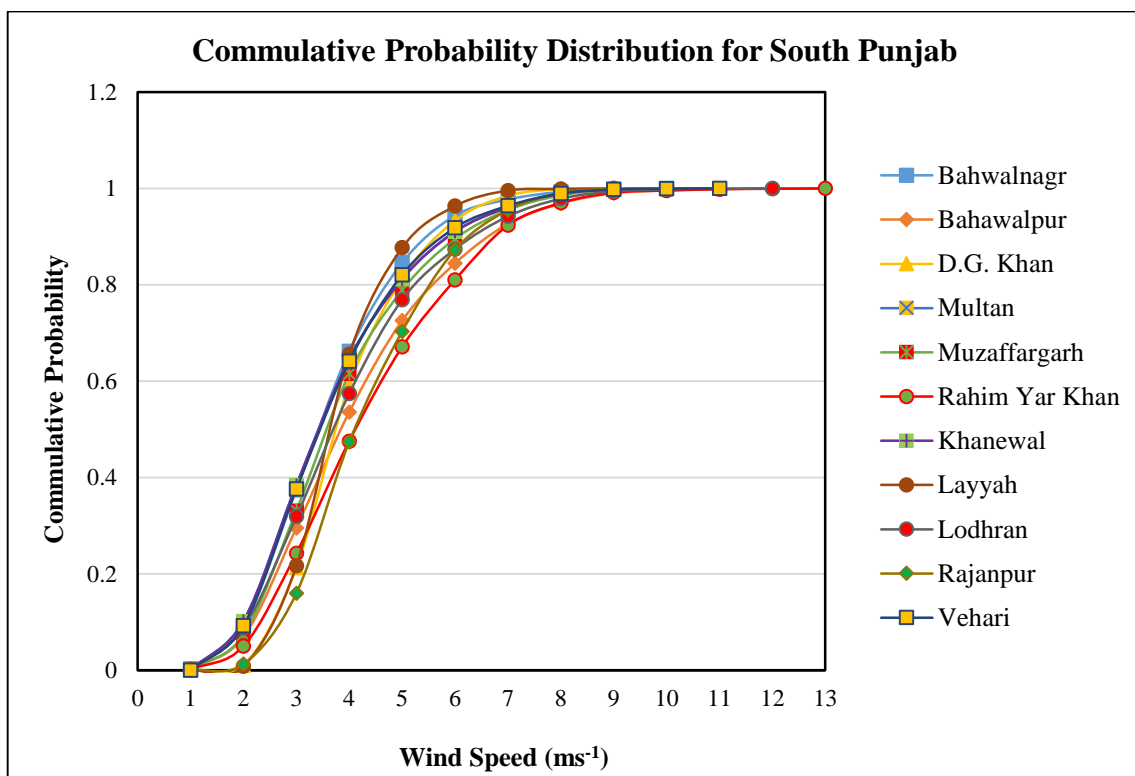


Fig. 5. Commulative Frequency Distribution for South Punjab

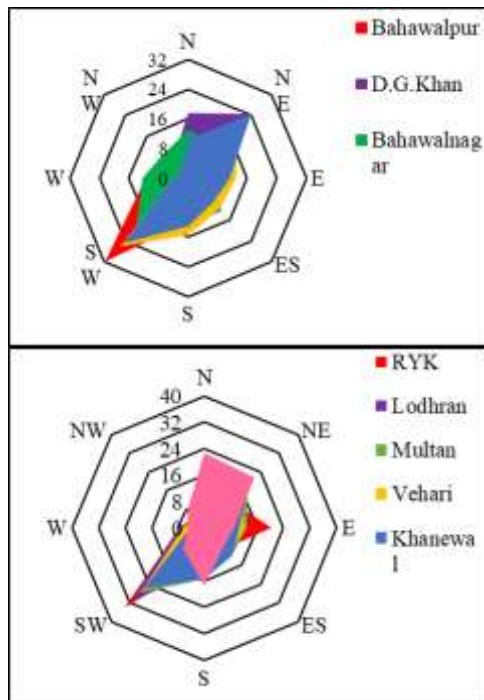


Fig. 6. Polar Diagram for South Punjab

- iii. On the other hand, Bahawalnagar is the poorest area as far as wind speed is concerned. But the minimum wind power density and wind energy density has been observed for Layyah rather than Bahawalnagar
- iv. Highest most probable and optimum wind speeds are observed for RYK while the lowest Most Probable speed is observed for Bahawalnagar and lowest Optimum Wind Speed is observed for Layyah.
- v. Weibull distribution, commulative frequency distribution and polar diagrams are also drawn for each location analyzed.

REFERENCES

[1] World Wind Energy Association. *Wind Power Capacity Worldwide Reaches 597 GW, 50.1 GW added in 2018*. 2019 15-10-2019]; Available from:

<https://wwindea.org/information-2/information/>.

[2] ETEnergyWorld. *World's top 10 countries in wind energy capacity*. 2019 12-11-2019]; Available from: <https://energy.economicstimes.indiatimes.com/news/renewable/worlds-top-10-countries-in-wind-energy-capacity/68465090>.

[3] IRENA, *RENEWABLE ENERGY STATISTICS 2019*. 2019.

[4] Khahro, S.F., et al., *Techno-economical evaluation of wind energy potential and analysis of power generation from wind at Gharo, Sindh Pakistan*. *Renewable and Sustainable Energy Reviews*, 2014. **35**: p. 460-474.

[5] Baloch, M.H., G.S. Kaloi, and Z.A. Memon, *Current scenario of the wind energy in Pakistan challenges and future perspectives: A case study*. *Energy Reports*, 2016. **2**: p. 201-210.

[6] Sarim, M. *Pakistan's energy mix*. 2019 15-10-2019]; Available from: <https://tribune.com.pk/story/1879268/6-pakistans-energy-mix/>.

[7] Khahro, S.F., et al., *Techno-economical evaluation of wind energy potential and analysis of power generation from wind at Gharo, Sindh Pakistan*. *Renewable and Sustainable Energy Reviews*, 2014. **35**: p. 460-474.

[8] Bilir, L., et al., *Seasonal and yearly wind speed distribution and wind power density analysis based on Weibull distribution function*. *international journal of hydrogen energy*, 2015. **40**(44): p. 15301-15310.

[9] Lu, L., H. Yang, and J. Burnett, *Investigation on wind power potential on Hong Kong islands—an analysis of wind power and wind turbine characteristics*. *Renewable Energy*, 2002. **27**(1): p. 1-12.

[10] Lima, L.d.A. and C.R.B. Filho, *Wind resource evaluation in São João do Cariri (SJC) – Paraíba, Brazil*. *Renewable and Sustainable Energy Reviews*, 2012. **16**(1): p. 474-480.

[11] Pishgar-Komleh, S., A. Keyhani, and P. Sefeedpari, *Wind speed and power density analysis based on Weibull and Rayleigh distributions (a case study: Firouzkooh county of Iran)*. *renewable and sustainable energy reviews*, 2015. **42**: p. 313-322.

[12] Acker, T.L., et al., *Wind resource assessment in the state of Arizona*:



- Inventory, capacity factor, and cost.* Renewable Energy, 2007. **32**(9): p. 1453-1466.
- [13] Keyhani, A., et al., *An assessment of wind energy potential as a power generation source in the capital of Iran, Tehran.* 2010. **35**(1): p. 188-201.
- [14] Shoaib, M., et al., *Evaluation of wind power potential in Baburband (Pakistan) using Weibull distribution function.* Renewable and Sustainable Energy Reviews, 2017. **70**: p. 1343-1351.
- [15] Shami, S.H., et al., *Evaluating wind energy potential in Pakistan's three provinces, with proposal for integration into national power grid.* Renewable and Sustainable Energy Reviews, 2016. **53**: p. 408-421.
- [16] Pobočíková, I., Z. Sedláčková, and M. Michalková, *Application of four probability distributions for wind speed modeling.* Procedia engineering, 2017. **192**: p. 713-718.
- [17] Carta, J.A., et al., *A review of wind speed probability distributions used in wind energy analysis: Case studies in the Canary Islands.* 2009. **13**(5): p. 933-955.
- [18] Bagiorgas, H.S., et al., *Wind power potential assessment for seven buoys data collection stations in Aegean Sea using Weibull distribution function.* 2012. **4**(1): p. 013119.
- [19] Kitaneh, R., H. Alsamamra, and A. Aljunaidi, *Modeling of wind energy in some areas of Palestine.* Energy Conversion and Management, 2012. **62**: p. 64-69.
- [20] Khahro, S.F., et al., *Evaluation of wind power production prospective and Weibull parameter estimation methods for Babaurband, Sindh Pakistan.* Energy conversion and Management, 2014. **78**: p. 956-967.
- [21] Aized, T., et al., *Design and analysis of wind pump for wind conditions in Pakistan.* 2019. **11**(9): p. 1687814019880405.
- [22] Costa Rocha, P.A., et al., *Comparison of seven numerical methods for determining Weibull parameters for wind energy generation in the northeast region of Brazil.* Applied Energy, 2012. **89**(1): p. 395-400.
- [23] Akdağ, S.A. and A. Dinler, *A new method to estimate Weibull parameters for wind energy applications.* Energy conversion and management, 2009. **50**(7): p. 1761-1766.
- [24] Akdağ, S.A. and Ö. Güler, *A novel energy pattern factor method for wind speed distribution parameter estimation.* Energy conversion and management, 2015. **106**: p. 1124-1133.
- [25] Azad, A.K., et al., *Analysis of wind energy conversion system using Weibull distribution.* Procedia Engineering, 2014. **90**: p. 725-732.



Thermodynamic performance of vapor compression refrigeration cycle (VCRC) retrofitted with low-GWP refrigerants

Ameer Hamza^{1*}, Sadaf Mehdi², Tauseef Aized Khan³

1. Department of Electrical Engineering, FAST National University of Computer and Emerging Sciences, Chiniot-Faisalabad Campus, Pakistan.
2. Department of Mechanical Engineering, Incheon National University 12-1 Songdo-Dong, Yeonsu-Gu, Incheon, 22012, Korea,
3. Department of Mechanical Engineering, University of Engineering and Technology Lahore, Pakistan.

* Corresponding author.

Email: ameer.hamza@nu.edu.pk

Abstract:

This study examines numerically the performance of the vapor compression refrigeration cycle (VCRC) retrofitted with low-GWP refrigerants as a substitute for R134a. The low-refrigerants investigated in this study are R152a (hydrofluorocarbon), R290 (hydrocarbon), and R1234yf (hydrofluoroolefin). A computer model was developed in the EES software and effect of output parameters was studied. The model simulated the performance of VCRC at fixed evaporation temperature of 5°C, condensation temperatures of 45°C and 50°C, and compressor speed of 1000-3000 rpm with interval of 1000 rpm. The effect of performance parameters of VCRC i.e. input power, compression ratio, cooling capacity, discharge temperature, COP and cooling capacity was investigated against the compressor speed and condensation temperatures. The EES model developed in this study was validated successfully with the published literature results. Results show that 152a and R1234yf are the suitable low-GWP replacement options as substitutes for R134a in VCRC. R290 is not appropriate replacement because its saturation temperature is much higher as compared to R134a. COP of R152a is found by 4.39-3.95% and 5.45-4.92% higher as compared to that of R134a at condensation temperature of 45°C and 50°C, respectively. R1234yf offers 4.83-4.51% and 5.85-5.45% lower COP at the same operating conditions. Finally, numerical results prove that R152a is the potential low-GWP replacement of R134a in VCRC.

Keywords: Alternative refrigerants, vapor compression refrigeration system, EES, low-GWP

Nomenclature

VCRC	Vapor compression refrigeration cycle (-)	η_{vol}	Compressor volumetric efficiency (-)
GWP	Global Warming Potential (-)	ρ	Density of refrigerant (kg/m ³)
EES	Engineering Equation Solver (-)	Subscripts	
COP	Coefficient of performance (-)	3,4	State point of refrigerant
HFC	Hydrofluorocarbon (-)	crit	Critical
CFC	Chlorofluorocarbon (-)	cond	Condenser
ODP	Ozone Depletion Potential (-)	evap	Evaporator
IHX	Internal heat exchanger (-)	inp	Input
NBP	Normal boiling point (°C)	comp	Compressor
T_{crit}	Critical temperature (°C)		
P_{crit}	Critical pressure (kPa)		
h	specific enthalpy (kJ/kg)		
P_{cond}	Condenser pressure (kPa)		
P_{evap}	Evaporator pressure (kPa)		
CR	Compression ratio (-)		
T	Temperature (°C)		
P_{inp}	Input power (kW)		
Q_{evap}	Evaporator capacity (kW)		
m_r	refrigerant mass flow rate (kg/s)		
N	Compressor speed (rpm)		
V_{comp}	Compressor displacement (m ³ /rev)		

1. Introduction

R134a, a hydrofluorocarbon refrigerant (HFC) is the working fluid used in domestic refrigerators and other refrigeration systems. This refrigerant offers good thermodynamic and thermophysical properties which make it suitable refrigerant in refrigeration systems [1-3]. The disadvantage associated with this refrigerant is its high value of global warming potential (GWP) of 1430 [4]. Kyoto Protocol of the



United Nations has put forward restriction on the use of substances which are responsible for the increasing global warming and ozone layer depletion [5, 6]. The R134a is increasing global warming because of its high value of global warming potential. This refrigerant is responsible for the increasing temperature of the earth's surface and hence causing climate change [7-9]. The ozone layer is affected by the refrigerants containing chlorine atoms, usually known as ozone-depleting substances. Initially, hydrofluorocarbons (HFC) were considered as eco-friendly, safe refrigerants and potential replacements of chlorofluorocarbons (CFCs) and hydrochlorofluorocarbons (HCFCs) [10-12]. But, now the increasing global warming of the earth has forced the authorities to phase out hydrofluorocarbon R134a from refrigeration systems as soon as possible [13, 14]. Worldwide, there is an urgent need to examine and search for the suitable low-GWP alternative of R134a in refrigeration systems. The replacement refrigerant should have zero or low ozone depletion potential (ODP) and low global warming potential (GWP). The maximum allowed value of GWP is 150. The required replacement refrigerant must have GWP of less than 150 [15, 16].

Various researchers have made their efforts to find out the feasible replacement of R134a in VCRC. Sanchez D. et al. [17] investigated experimentally the performance of R600a, R290, R1234ze (E), R1234yf and R152a as possible substitutes of R134a in vapor compression refrigeration system. Based on the experimental results, they concluded that R1234yf and R152a can be the possible replacement options of R134a. Belman Flores et al. [18] investigated exergy and energy performance of R1234yf to examine its possibility to replace R134a in refrigerator. Higher irreversibility losses were reported in case of R1234yf, when compared with the R134a and hence, they concluded that this might not be the appropriate replacement of R134a. Bolaji et al. [19] performed the theoretical investigation of three replacements (R450A, R440A, and R430A) as substitutes of R134a in vapor compression refrigeration system. They found that the highest COP was found with R440A which showed 10.70% higher COP as compared to R134a. Andrew et al. [20] investigated experimentally the performance of R430A as substitute for R134a in vapor compression refrigeration system. He performed the exergy analysis and found the system operating with R430 showed 12-18% less exergy destruction as compared to that R134a. Hence, the authors reported that R430A can be the feasible replacement of

R134a in VCRC. Meng et al. [21] conducted the experimental study to investigate the behaviour of R1234yf/R134a mixture as replacement of R134a in refrigeration system. They operated the system in heating and cooling mode and found that the investigated mixture shows 4-9% and 4-16% less COP in cooling and heating mode, respectively. Mota-Babiloni et al. [22] performed the experiments to analyze the performance of refrigerant mixture R513A in modified refrigeration cycle. They used the internal heat exchanger (IHx) in cycle and observed the COP improvement of 4% for R134a and 8% for R513A. Jatinder Gill et al. [22] conducted the experimental study to analyze the exergy performance of VCRC using R450A as possible potential replacement. They found that exergy efficiency and total irreversibility for R450A operating cycle were less as compared to R134a operating system. However, compressor was the least component and evaporator was the best component for both operating systems. JM et al. [23] conducted experimental study on the domestic refrigeration system using R1234yf and R134a. Exergy and energy analysis of the VCRC were conducted. Their results concluded that R1234yf may not be the possible replacement of R134a in the current refrigeration systems. Golzari et al. [24] conducted the second law exergy analysis of the vapor compression refrigeration cycle using R1234yf as potential replacement. They developed a computer program to observe the variation of performance parameters and found that exergy destruction in R1234yf operated system is less as compared to R134a operated system. Sumeru et al. [25] conducted study numerically to analyze the

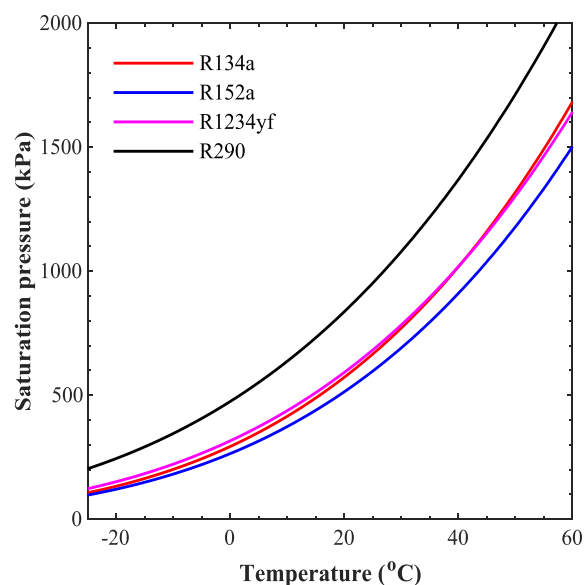


Figure 1. Saturation pressure vs temperature



thermodynamic performance of conventional refrigeration cycle using R152a as potential replacement. They found that R152a shows improvement of COP of 13.5% w.r.t R134a system. Jemaa et al. [26] carried out numerically the energy and exergy analysis of refrigeration chiller operated with R1234ze as feasible replacement option of R134a in system. They found the exergy losses and exergy destruction rates in the components of the unit. They concluded that total irreversibility found the unit operated with R1234ze is less as compared to that operated with R134a. Jankovic et al. [27] conducted study to simulate the performance of refrigeration system retrofitted with R1234yf and R1234ze(E) as possible replacements of R134a. They performed two different analyses based on the same condensation and evaporation temperature, and another on the basis of same cooling medium conditions. They reported that R1234yf may be the feasible replacement option of R134a in refrigeration system.

The properties of the investigated refrigerants are shown in table 1. Saturation pressures of these refrigerants against the temperature are plotted in figure 1. This figure shows that the saturation pressure of the refrigerant R1234yf closely matches that of R134a, while R290 and R152a show deviation from R134a. R290 shows the higher value of saturation pressure and R152a shows a little bit lesser value. From this figure, it seems that the refrigerant R1234yf may be the potential substitute for R134a in the refrigeration system.

In the present study, three low-GWP refrigerants i.e. R152a (GWP = 140), R290 (GWP = 20) and R1234yf (GWP = 4) are considered as the possible replacements of R134a in a VCRC [28] and among these, a potential replacement will be figured out through theoretical thermodynamic analysis. Computer code will be written in EES software and the performance parameters of the refrigeration cycle will be calculated and compared with R134a. The analysis will be performed with respect to compressor speed of 1000-3000 rpm with interval of 1000 rpm, evaporation temperature of 5°C and condensation temperatures of 45°C and 50°C. The performance parameters of the cycle will be computed and potential replacement will be concluded depending upon the numerical results.

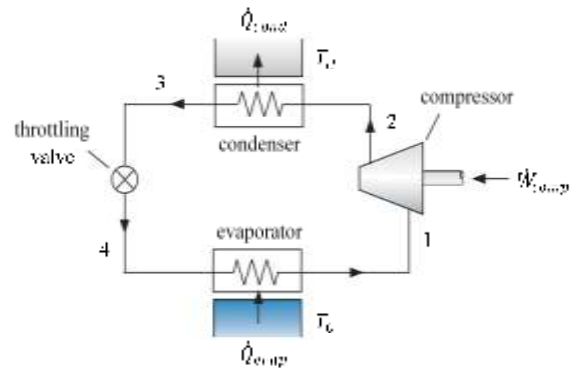


Figure 2. Schematic diagram of VCRC

Table 1. Properties of refrigerants [10, 23, 29]

Refrigerant	R134a	R290	R1234yf	R152a
GWP	1430	20	4	140
ODP	0	0	0	0
NBP (°C)	26.09	-42.2	-29.49	-24.05
T _{crit} (°C)	101	96.7	94.7	113.3
P _{crit} (kPa)	4059	4.25	3382	4520

2. Cycle analysis

The schematic diagram of the investigated vapor compression refrigeration system is shown in figure 2 and its representation on P-h diagram is shown in figure 3. The four major components of this cycle are: a compressor, condenser, expansion valve, and evaporator. The thermodynamic processes occurring in this cycle are: 1-2 isentropic compression in compressor, 2-3 constant pressure heat rejection in condenser, 3-4 isenthalpic expansion in expansion valve, and 4-1 constant pressure heat addition in evaporator. Initially the dry saturated vapor of refrigerant at state point 1 enters the compressor and is compressed to the superheated vapor at state point 2. The temperature of superheated vapor is decreased by passing it through the condenser and finally it becomes saturated liquid at state point 3. Saturated liquid is throttled by isenthalpic process ($h_3 = h_4$) from state 3 to state 4 in throttling valve. At state 4, refrigerant is wet vapor where it enters the evaporator and absorbs heat from the surrounding where cooling is required and changes its state to saturated vapor. Refrigerant in VCRC completes its cycle and produce the required cooling effect.

The refrigeration cycle shown in figure 2 was modeled in the EES software. There were certain assumptions which were supposed in the modeling which are described as follow: (a) steady-state



conditions exist; (b) changes in kinetic and potential energy are negligible; (c) pressure losses are insignificant; (d) compressor rotational speeds 1000-3000 rpm with interval of 1000 rpm; (e) evaporator temperature is 5°C; (f) condensation temperature of 45°C

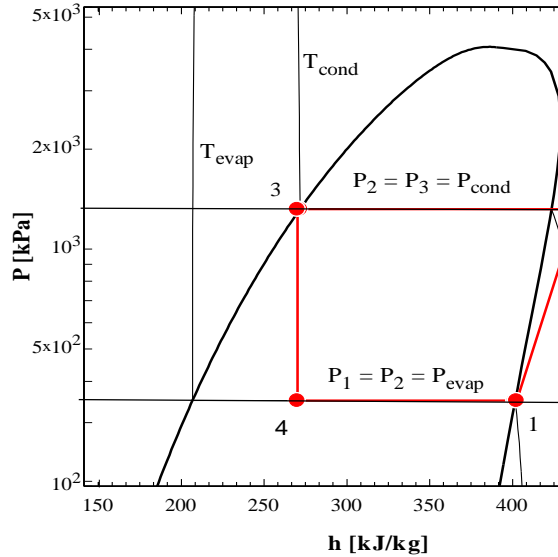


Figure 3. P-h diagram of VCRC

and 50°C; (g) degree of subcooling and superheating is equal and its value is 1 Kelvin, 2 Kelvin, and 3 Kelvin corresponding to compressor speeds of 1000-3000 rpm, with interval of 1000 rpm respectively; (i) compressor isentropic efficiency and volumetric efficiency are same and their values are 0.75, 0.65 and 0.55 corresponding to three compressor speeds from 1000-3000 rpm with interval of 1000 rpm respectively; (j) isenthalpic process takes place in expansion valve i.e. $h_3 = h_4$; (k) compressor has constant displacement of $120 \times 10^{-3} \text{ m}^3/\text{rev}$.

The output performance parameters of the simulation model were compression ratio, discharge temperature, input power, cooling effect and COP of the cycle. These parameters were calculated for each investigated refrigerant and compared with that of R134a. They were calculated using the following equations [19, 28, 30]:

$$CR = \frac{P_{cond}}{P_{evap}} \quad (1)$$

$$P_{inp} = m_r(h_2 - h_1) \quad (2)$$

$$Q_{evap} = m_r(h_4 - h_1) \quad (3)$$

$$COP = \frac{Q_{evap}}{P_{inp}} \quad (4)$$

where the mass of refrigerant, m_r , was calculated by [28]

$$m_r = \frac{N}{60} V_{comp} \eta_{vol} \rho_1 \quad (5)$$

where V_{comp} is the compressor volumetric displacement and η_{vol} is compressor volumetric efficiency.

3. Results and discussion

3.1 Validation of model

The model in this study was validated with the literature results of Sumeru et al. [25]. In validation, the results of COP and discharge temperature of R134a at various compressor speeds 1000-3000 rpm with interval of 1000 rpm, condensation temperature of 50°C, and evaporation temperature 5°C were validated with the literature results of authors. The validation results are shown in figure 4. It shows that both parameters COP and discharge temperature of the present study closely match with the literature values. The maximum difference of COP of R134a between the model and literature value is 2.96%, while that of discharge temperature is 2.57%, at a compressor speed of 3000 rpm. At other compressor

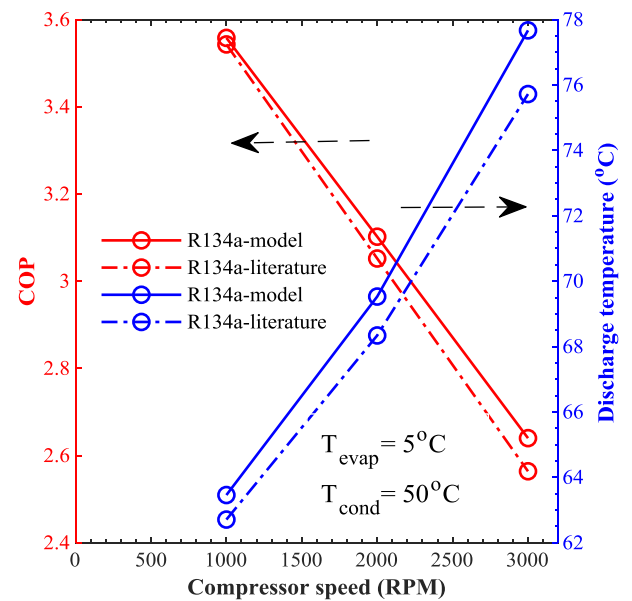


Figure 4. Model validation



speeds, this discrepancy is even smaller. This proves that the theoretical model of vapor compression refrigeration developed in this study is in good correspondence with the literature values and hence it can be used in further analysis of predicting the performance parameters of the cycle with low-GWP refrigerants.

The performance parameters of the cycle are described below:

3.2 Effect of compressor speed and condensation temperature on input power

The variation of the compressor's input power for the investigated refrigerants against the compressor speed and condensation temperature is shown in figure 5. This shows that input power for all refrigerants increases when the compressor speed is increased from 1000-3000 rpm at a given condensation temperature. Also, when the condensation temperature is increased, input power further increases. The input powers of refrigerants at condensation temperature of 45°C are shown by solid lines while that of condensation temperature of 50°C is shown by dotted lines in this figure. The input power of the refrigerant R1234yf closely matches that of R134a at both condensation temperatures. R152a shows almost 8% and 7.67-7.75% less input power at condensation temperatures of 45°C and 50°C, respectively. R290 shows almost 34% higher values of input power at condensation temperatures of 45°C and 50°C, respectively, when compared with R134a. At given compressor speed, input power depends upon the mass flow rate of refrigerant and difference of specific enthalpy between state points 2 and 1, as shown by Eq. (2). Further, the mass flow rate of refrigerant is a direct function of its density at the suction of compressor, as per Eq. (5). The increased mass flow rate and increased value of the difference of specific enthalpy between state points 2 and 1, compared to R134a, cause the increased value of input power for that refrigerant at the same compressor speed. Similarly, the decreased values of the mass flow rate of refrigerant and difference of specific enthalpy, compared to R134a, cause a reduction of input power for that refrigerant at the same compressor speed.

From this performance parameter, it seems that R1234yf is the most appropriate replacement of R134a since its input power closely matches that of R134a.

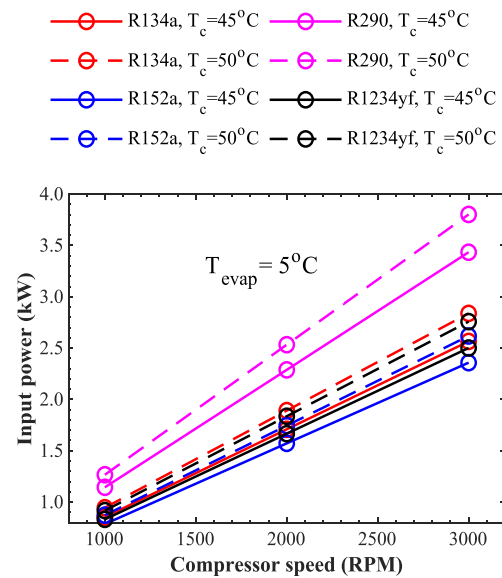


Figure 5. Input power vs compressor speed

3.3 Effect of compressor speed and condensation temperature on cooling capacity

The variation of the cooling capacity for the investigated refrigerants against the compressor speed and condensation temperature is shown in figure 6. This shows that cooling capacity for all refrigerants increases when the compressor speed is increased from 1000-3000 rpm at a given condensation temperature. Also, when the condensation temperature is increased, the evaporator's cooling capacity further increases. The cooling capacity of refrigerants at condensation temperature of 45°C are shown by solid lines while that of condensation temperature of 50°C is shown by dotted lines in this figure. The cooling capacity of R152a is 3.96-4.44% and 2.65-3.18% lower as compared to that of R134a at condensation temperature of 45°C and 50°C, respectively. The cooling capacity of R1234yf is 7.31-6.87% and 8.66-8.13% lower as compared to that of R134a at condensation temperature of 45°C and 50°C, respectively. R290 shows almost 31% higher values of cooling capacity at condensation temperatures of 45°C and 50°C, respectively, when compared with R134a. At given compressor speed, cooling capacity depends upon the mass flow rate of refrigerant and difference of specific enthalpy between state point 4 and 1, as shown by Eq. (3). Further, mass flow rate of refrigerant is a direct function of its density at suction of compressor, as per Eq. (5). The increased mass flow rate and increased value of difference of specific enthalpy between state point 4 and 1,



compared to R134a, cause the increased value of cooling capacity for that refrigerant at same compressor speed. Similarly, the decreased values of mass flow rate of refrigerant and difference of specific enthalpy, compared to R134a, cause reduction of cooling capacity for that refrigerant at same compressor speed. From this performance parameter, it seems that R152a is the most appropriate replacement of R134a since its cooling capacity closely matches that of R134a.

3.4 Effect of compressor speed and condensation temperature on COP

The variation of the COP for the investigated refrigerants against the compressor speed and condensation temperature is shown in figure 7. This shows that COP for all refrigerants decreases when the compressor speed is increased from 1000-3000 rpm at a given condensation temperature. Also, when the condensation temperature is increased, the COP further decreases. COP is the ratio of cooling capacity to the input power, as per Eq. (4). Both the cooling capacity and input power increase when the compressor speed is increased from 1000 rpm to 3000 rpm, as shown by Figures 5 and 6 respectively. The increase in cooling capacity is less than the increase of input power when the compressor speed changes by an interval of 1000 rpm, that's why COP decreases with the compressor speed. The COP values of refrigerants at condensation temperature of 45°C are shown by solid lines while that of condensation temperature of 50°C is shown by dotted lines in this figure. R152a shows 4.39-3.95%

and 5.45-4.92% higher COP with respect to R134a at condensation temperature of 45°C and 50°C, respectively. COP of R290 is 2.21-2.14% and 2.53-2.42% lower when compared with R134a at condensation temperature of 45°C and 50°C, respectively. R1234yf shows the minimum COP value among all refrigerants i.e. its COP is 4.83-4.51% and 5.85-5.45% lower as compared to that of R134a at condensation temperature of 45°C and 50°C, respectively. Since, higher value of COP is desirable, so VCRC retrofitted with R152a would be the most suitable replacement of R134a.

3.5 Effect of compressor speed and condensation temperature on discharge temperature

The variation of the discharge temperature for the investigated refrigerants against the compressor speed and condensation temperature is shown in figure 8. This shows that the discharge temperature for all refrigerants increases when the compressor speed is increased from 1000-3000 rpm at a given condensation temperature. Also, when the condensation temperature is increased, the COP further increases. The increasing trend of discharge temperature with compressor speed is related to increased input power for higher compressor speed as discussed before in figure 5. When the compressor speed increases, input power increases which causes the high discharge temperature at the exit of the compressor for given condensation temperature. The discharge temperatures of refrigerants at condensation temperature of 45°C are

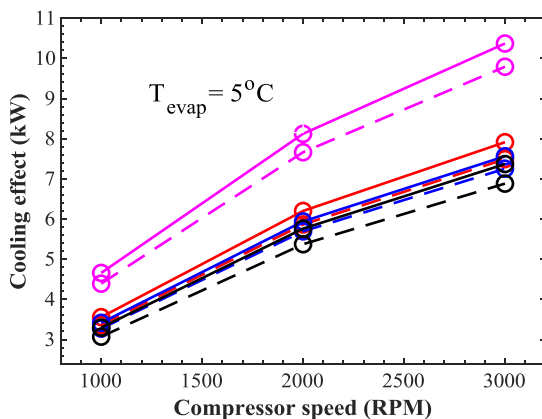
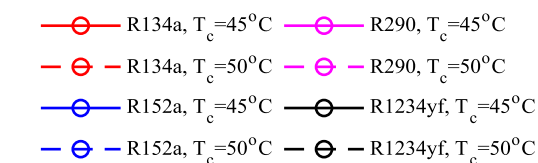


Figure 6. Cooling effect vs compressor speed

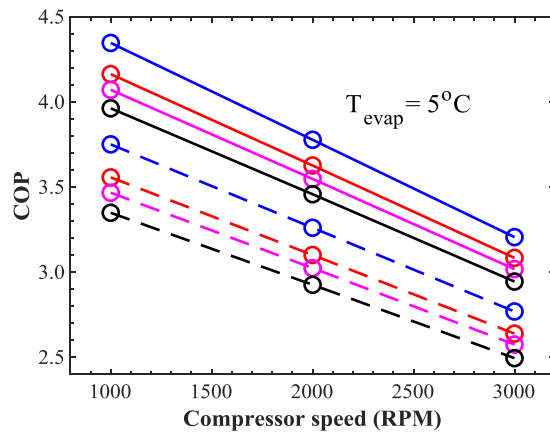
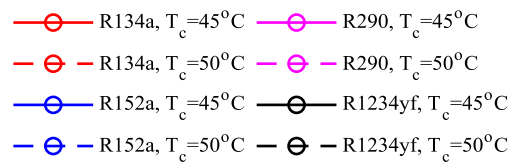


Figure 7. COP vs compressor speed



shown by solid lines while that of condensation temperature of 50°C is shown by dotted lines in this figure. R152a shows 15.46-17.05% and 15.38-17.15% higher discharge temperature as compared to that of R134a at condensation temperature of 45°C and 50°C, respectively. R290 shows 1.11-2.03% and 1.12-2.09% lower values of discharge temperature as compared to R134a at condensation temperature of 45°C and 50°C, respectively. R1234yf shows the minimum values of discharge temperatures among all refrigerants i.e. its discharge temperature is 14.97-16.25% and 14.80-16.27% lower as compared to R134a at condensation temperature of 45°C and 50°C, respectively. Since lower value of discharge temperature is preferable, so the refrigerant R290 can be retrofitted in the current refrigeration system considering only the discharge temperature.

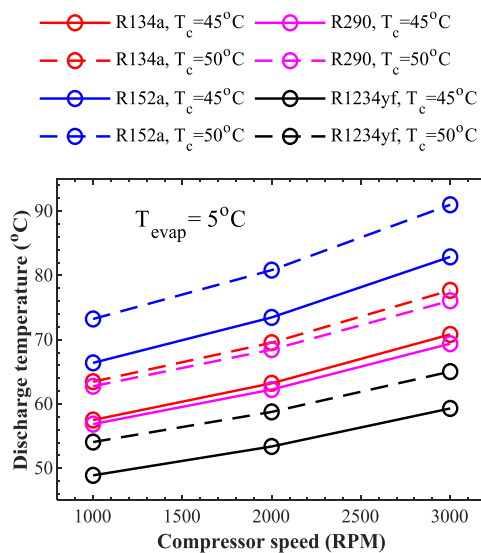


Figure 8. Discharge temperature vs compressor

3.6 Effect of compressor speed and condensation temperature on compression ratio

Compression ratio is simply the ratio of condenser pressure to the evaporator ratio. Its value dictates that how much work has to be done by the compressor for compressing the refrigeration from state 1 to state 2 to in figure 2. Higher value means the higher input power and vice versa. Since the evaporator temperature is 5°C for all cases, so the evaporator pressure is the saturation pressure corresponding to this temperature of refrigerant. Condenser pressure is also a unique value corresponding to the condenser temperature. Therefore, at fixed temperatures of evaporator and condenser, the compression ratio remains the same

when compressor speed is increased from 1000 rpm to 3000 rpm. It only changes when the condenser or evaporator temperature is changed. The variation of compression ratio for all refrigerants against the compressor speed and condensation temperature is shown in figure 9. This shows the compression ratio of R134a and R152a is almost same. R1234yf shows 6.72% and 7.35% lower value of compression ratio when compared with R134a at condensation temperature of 45°C and 50°C, respectively. R290 shows 16.10 and 17.54% lower value of compression ratio as compared to that of R134a at condensation temperature of 45°C and 50°C, respectively.

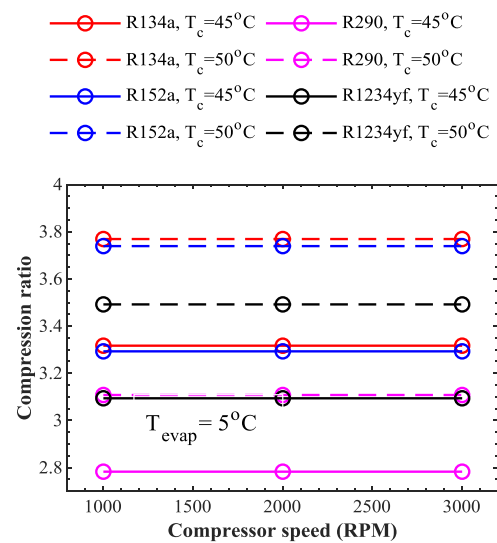


Figure 9. Compression ratio vs compressor speed

4. Conclusion

In this numerical study, three low-GWP refrigerants (R152a, R290, and R1234yf) were investigated as possible substitutes of R134a in VCRC. Effect of input power, cooling capacity, discharge temperature, COP, and compression ratio were studied against the compressor speed and condenser temperature, for the fixed evaporator temperature of 5°C. Based on the numerical results, following conclusions are drawn:

- The saturation pressure of R1234yf closely matches that of R134a, while that of R152a is a little bit less than that of R134a. The saturation pressure of R290 is much higher than that of R134a, so it cannot be suitable replacement. However, R152a and R1234yf might be good replacement options depending upon the other parameters.



- The input power of R1234yf closely matches that of R134a while that of R152a is 8% and 7.67-7.75% less at condensation temperatures of 45°C and 50°C, respectively.
- The cooling capacity of R152a is 3.96-4.44% and 2.65-3.18% lower as compared to that of R134a at condensation temperature of 45°C and 50°C, respectively. R1234yf offers 7.31-6.87% and 8.66-8.13% lower cooling effect as the same operating conditions. This shows that R152a is the suitable replacement of R134a in current refrigeration systems.
- R152a shows 4.39-3.95% and 5.45-4.92% higher COP with respect to R134a at condensation temperature of 45°C and 50°C, respectively. R1234yf offers 4.83-4.51% and 5.85-5.45% lower COP at the same operating conditions. Since, higher value of COP is desirable, so VCRC retrofitted with R152a would be the most suitable replacement of R134a.
- R152a shows 15.46-17.05% and 15.38-17.15% higher discharge temperature as compared to that of R134a at condensation temperature of 45°C and 50°C, respectively. R1234yf offers 14.97-16.25% and 14.80-16.27% lower discharge temperature at the same operating conditions.
- The compression ratio of R134a and R152a is almost same. R1234yf shows 6.72% and 7.35% lower value of compression ratio as compared to R134a at condensation temperature of 45°C and 50°C, respectively.

The numerical results of this study conclude that R152a is the most suitable low-GWP potential replacement of R134a in the current vapor compression refrigeration system.

REFERENCES

- [1] Cabello, R., et al., *Experimental comparison between R152a and R134a working in a refrigeration facility equipped with a hermetic compressor*. international journal of refrigeration, 2015. **60**: p. 92-105.
- [2] Wongwises, S., A. Kamboon, and B. Orachon, *Experimental investigation of hydrocarbon mixtures to replace HFC-134a in an automotive air conditioning system*. Energy Conversion and Management, 2006. **47**(11-12): p. 1644-1659.
- [3] Sánchez, D., et al., *Energy performance evaluation of R1234yf, R1234ze (E), R600a, R290 and R152a as low-GWP R134a alternatives*. International Journal of Refrigeration, 2017. **74**: p. 269-282.
- [4] Cho, H. and C. Park, *Experimental investigation of performance and exergy analysis of automotive air conditioning systems using refrigerant R1234yf at various compressor speeds*. Applied Thermal Engineering, 2016. **101**: p. 30-37.
- [5] Tsai, W.-T., *An overview of environmental hazards and exposure risk of hydrofluorocarbons (HFCs)*. Chemosphere, 2005. **61**(11): p. 1539-1547.
- [6] Li, G., et al., *Experimental investigation of energy and exergy performance of secondary loop automotive air-conditioning systems using low-GWP (global warming potential) refrigerants*. Energy, 2014. **68**: p. 819-831.
- [7] Prabakaran, R. and D.M. Lal, *A novel exergy based charge optimisation for a mobile air conditioning system*. Journal of Thermal Analysis and Calorimetry, 2018. **132**(2): p. 1241-1252.
- [8] Paradeshi, L., et al., *Exergy analysis of direct-expansion solar-assisted heat pumps working with R22 and R433A*. Journal of Thermal Analysis and Calorimetry, 2018. **134**(3): p. 2223-2237.
- [9] Daviran, S., et al., *A comparative study on the performance of HFO-1234yf and HFC-134a as an alternative in automotive air conditioning systems*. Applied Thermal Engineering, 2017. **110**: p. 1091-1100.
- [10] Meng, Z., et al., *Performance of low GWP R1234yf/R134a mixture as a replacement for R134a in automotive air conditioning systems*. International Journal of Heat and Mass Transfer, 2018. **116**: p. 362-370.
- [11] Lee, Y. and D. Jung, *A brief performance comparison of R1234yf and R134a in a bench tester for automobile applications*. Applied Thermal Engineering, 2012. **35**: p. 240-242.
- [12] Zhao, Y., et al., *Experimental analysis of the low-GWP refrigerant R1234yf as a drop-in replacement for R134a in a typical mobile air conditioning system*. Proceedings of the Institution of Mechanical Engineers, Part C: Journal of Mechanical Engineering Science, 2012. **226**(11): p. 2713-2725.
- [13] Austin, N., *Different refrigerants and their impact on vapour-compression refrigeration systems*. Journal of Advances in Mechanical Engineering and Science, 2016. **2**(3): p. 29-39.



- [14] Zilio, C., et al., *The refrigerant R1234yf in air conditioning systems*. Energy, 2011. **36**(10): p. 6110-6120.
- [15] Vakiloroya, V. and Q. Ha. *Energy-efficient air-cooled DX air-conditioning systems with liquid pressure amplification*. in *ISARC. Proceedings of the International Symposium on Automation and Robotics in Construction*. 2014. IAARC Publications.
- [16] Mota-Babiloni, A., et al., *Drop-in energy performance evaluation of R1234yf and R1234ze (E) in a vapor compression system as R134a replacements*. Applied Thermal Engineering, 2014. **71**(1): p. 259-265.
- [17] Sánchez, D., et al., *Energy performance evaluation of R1234yf, R1234ze(E), R600a, R290 and R152a as low-GWP R134a alternatives*. International Journal of Refrigeration, 2017. **74**: p. 269-282.
- [18] Belman-Flores, J.M., et al., *Energy and exergy analysis of R1234yf as drop-in replacement for R134a in a domestic refrigeration system*. Energy, 2017. **132**: p. 116-125.
- [19] Bolaji, B.O., et al., *Theoretical Investigation of Energy-Saving Potential of Eco-Friendly R430A, R440A and R450A Refrigerants in a Domestic Refrigerator*. Iranian Journal of Science and Technology, Transactions of Mechanical Engineering, 2019. **43**(1): p. 103-112.
- [20] Andrew Pon Abraham, J.D. and M. Mohanraj, *Thermodynamic performance of automobile air conditioners working with R430A as a drop-in substitute to R134a*. Journal of Thermal Analysis and Calorimetry, 2019. **136**(5): p. 2071-2086.
- [21] Meng, Z., et al., *Performance of low GWP R1234yf/R134a mixture as a replacement for R134a in automotive air conditioning systems*. International Journal of Heat and Mass Transfer, 2018. **116**: p. 362-370.
- [22] Mota-Babiloni, A., et al., *Experimental influence of an internal heat exchanger (IHx) using R513A and R134a in a vapor compression system*. Applied Thermal Engineering, 2019. **147**: p. 482-491.
- [23] Belman-Flores, J., et al., *Energy and exergy analysis of R1234yf as drop-in replacement for R134a in a domestic refrigeration system*. Energy, 2017. **132**: p. 116-125.
- [24] Golzari, S., et al., *Second law analysis of an automotive air conditioning system using HFO-1234yf, an environmentally friendly refrigerant*. International Journal of Refrigeration, 2017. **73**: p. 134-143.
- [25] Sumeru, K., et al., *Comparative performance between R134a and R152a in an air conditioning system of a passenger car*. Jurnal Teknologi, 2016. **78**(10-2).
- [26] Jemaa, R.B., et al., *Energy and exergy investigation of R1234ze as R134a replacement in vapor compression chillers*. International Journal of Hydrogen Energy, 2017. **42**(17): p. 12877-12887.
- [27] Janković, Z., J. Sieres Atienza, and J.A. Martínez Suárez, *Thermodynamic and heat transfer analyses for R1234yf and R1234ze(E) as drop-in replacements for R134a in a small power refrigerating system*. Applied Thermal Engineering, 2015. **80**: p. 42-54.
- [28] Aized, T. and A. Hamza, *Thermodynamic Analysis of Various Refrigerants for Automotive Air Conditioning System*. Arabian Journal for Science and Engineering, 2019. **44**(2): p. 1697-1707.
- [29] Mohanraj, M., S. Jayaraj, and C. Muraleedharan, *Comparative assessment of environment-friendly alternatives to R134a in domestic refrigerators*. Energy Efficiency, 2008. **1**(3): p. 189-198.
- [30] Vaghela, J.K., *Comparative evaluation of an automobile air-conditioning system using R134a and its alternative refrigerants*. Energy Procedia, 2017. **109**: p. 153-160.



Modelling The Penetration Of Electric Vehicles As An Alternate Mode Of Road Transport In Pakistan

Sher Asif Khan¹, Tanzeel ur Rashid¹, Ubaid ur Rehman Zia^{2,*}, Waqas Nazir Awan,² Talal Bin Ahmed¹

1. University of Engineering and Technology, Taxila.
2. The University of Lahore (UOL), Pakistan

*Corresponding Author: Email: ubaid2k13_137@yahoo.com

Abstract

Transport sector is one of the major drivers of energy consumption and plays an important role in environmental stability of a country. Approximately half of global oil conversation is through this sector. In Pakistan, transport sector constitutes 48.8 % of total oil consumption. Considering the industrial development of Pakistan and a constantly increasing urbanization rate, this sector has emerged as the fastest means of energy utilization, revenue generation and CO₂ emissions. Currently, due to the constraints applied by Kyoto Protocol and sustainability, this emission control is a long and gruelling task for Pakistan. To overcome this problem, TIMES model is used to identify those radical changes we can bring to ensure a sustainable and environment friendly system for transport sector of Pakistan. The model results showed that penetration of electric vehicles in current scenario is very low due to upfront cost and below par technology. For a considerable change to occur, a large portion of our vehicle stock has to shift from diesel and gasoline to electric fuel. This research also assesses the potential of electricity to appear as a sustainable source in Transport sector of any country. By allotting more capital in this sector, the energy saving innovations can be advanced resulting in a better energy balance and a decrease in CO₂ emissions subsequently.

Key Words: Electric Vehicles, Energy Modeling, Transport Sector, TIMES

1. Introduction

Transport of Pakistan is currently the fastest growing sector in terms of energy consumption and CO₂ emissions. Oil and Gas are major fuels for this sector and Pakistan along with man counties is expecting to run out of them by 2030-2040. In 2017, Pakistan spent approximately \$9 Billion on import of petroleum products and LNG [1]. According to IEA Sankey diagram, Pakistan imported a total of 15.32 MTOE through oil and petroleum and the consumption of transport sector alone was 15.65 MTOE. This resulted in an increased gap between demand and supply that just ballooned in to a huge energy crisis.

Even on a universal front, this sector consumed above 60% of world's oil demand and 27% of overall energy utilization. Hence, there is need for a paradigm shift towards a more sustainable solution [2], [3]. To account for this ordeal, most of the developed countries have shifted towards the solution of Hybrid and Electric Vehicles. In 2015, the global stock of electric vehicles was 1 million. This value rose above 2 million in the following year [4]. For a sustainable transition, this growth rate has to be even faster. Currently, the contribution of electric vehicles in transport sector of Pakistan is negligible. This study investigates the penetration of electric vehicles (cars) in to the energy system of

Pakistan and the potential of electricity to serve as a sustainable energy source.

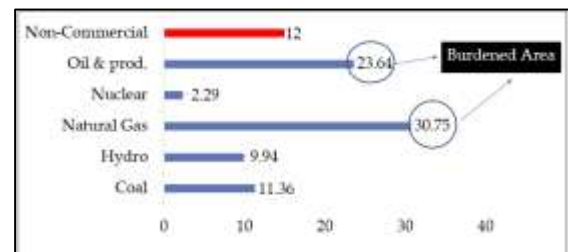


Figure 1 Energy Supplies of Pakistan FY 2015 [3]

Now transport sector is one of the fastest developing sector as far as revenue, energy utilization and CO₂ emissions are considered. It contributes to around 10 percent of the GDP and employs 6 percent of the population. To overcome this problem a paradigm shift is needed from an unsustainable approach to possible sustainable energy alternative. In developing world, strong momentum in Electric Vehicle sales puts this technology on track to meet the sustainability goals.

2. Evolution of Global EV Stock

As depicted in figure-2, infrastructure increase for available charging in 2016 was 72% with 320,000 units globally. Norway had the highest (29%)

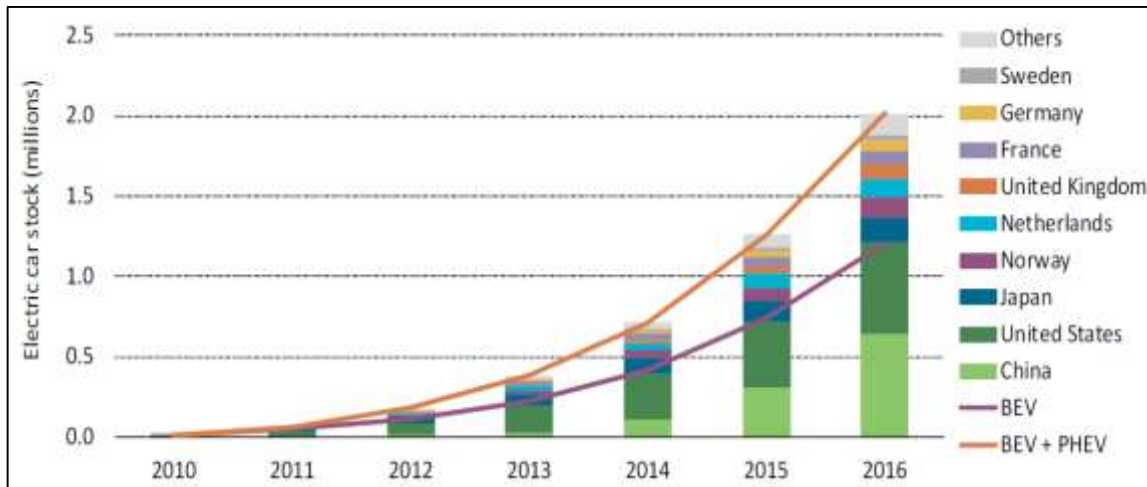


Figure 2 Global increase in Stock of Electric Vehicles

Market share while China had the stock. The electric car stock shown here is primarily estimated on the basis of cumulative sales since 2005 [5], [6].

Neighbouring countries such as China and India have a population of 1.386 billion and 1.339 billion respectively in 2017, also doing their efforts to curtail consumption such as Gov. of India is looking to end the petrol and diesel vehicles up to 2030 [7]. After 2030 every car sold will be electric in India and carbon emissions will be decreased round about 37% up to 2030 [8]. To overcome the demand for oil and diesel which has bad health hazards effects China policymakers are looking to see one car electric out of four at least in 2040. Also, the countries such as Norway in 2025, Netherlands, Slovenia, Ireland, in 2030, Scotland in 2032, Srilanka, California, France, and the United Kingdom in 2040 target to reduce the fossil fuel vehicles. Countries such as Spain, India Germany, Portugal, and South Korea are aiming to have a full share of Battery Electric Vehicles (BEVs) cars in 2020 having 2.5 million, 1million, 1million, 750,000 million, and 200,000 million respectively. [4], [8]–[13]The countries which have the target for 2030 including Malaysia goal of 100,000 electric vehicles, Finland aiming for 250,000 and South Africa plans to have a 20% of shares of BEVs (cars). Out of all these countries, Norway is leading. Norway is going to eliminate the petrol and diesel car in 2016 and there will be no sale at all of diesel and petrol cars after 2025. By 2050, Germany goal is to reduce the CO2 emissions by 92% by introducing Bev's cars. By 2050, France is also aiming for the restriction on diesel and petrol cars [19]. The Government and

Policymakers of Norway are all set to build a zero-emission control area (ZECA) for the first time in the world after 2026 [20]. In recent times, the United States and China have the biggest vehicle markets having a sale of round about 120 million vehicles over the span of 8 years. After that Japan has the biggest sale market having a sale of 40 million cars over the same period of time. Sale of diesel vehicles cars is more than petrol cars in countries such as Thailand, Spain, Turkey, France, Italy, and United Kingdom. In these countries list Brazil is also included which mainly has predominantly flex-fuel cars. Compare to these markets sales of EVs is very small less than 1% [14]–[23].

3. Methodology and Data Collection

3.1. Transport Sector of Pakistan

Currently, energy sector of Pakistan consumes approximately 10 MTOE of energy and emits approximately 30 Mt of CO2 emissions with Diesel and Gasoline providing the largest shares. Based on the data statistics of 2015, although electric does not occupy any share, new policies indicate this increase to up to 30% y 2030.

This chapter includes the purposed methodology for this research, research stages, model development in which energy demand equations number of vehicles, vehicles kilometre travel, fuel economy, cost (capital, fuel and operational) and the environmental data equations. We have used TIMES model for the analysis of all types of cars including gasoline, hybrid, plugged in hybrid cars, and electric cars based on their power. Different scenarios have been

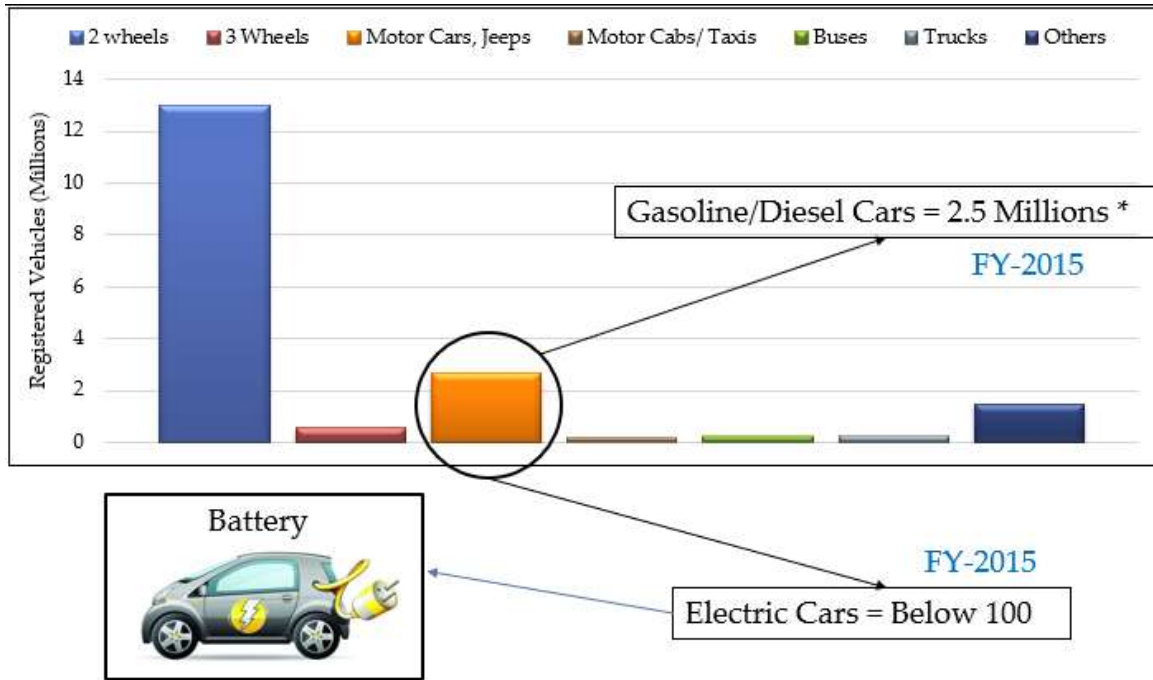


Figure 3 Fig. Stock of Vehicles in Pakistan

discussed such as business as usual and electric penetration scenario.

In this study, TIMES model is used to identify those radical changes we have to make to bring a significant change in our transport market. Base year was taken as 2007 and the analysis was performed under the baseline scenario. Following parameters were used as input to the model.

- Current stock of Electric and ICE (non-hybrid) cars.
- Energy Consumption
- Vehicle Travel

According to PES and PBS, total stock of registered cars in Pakistan is 2531600 and 2577858 respectively and their percentage change from the projected stock is -3.3% and -1.54% respectively. Now Useful Demand of these vehicles was calculated by using the following formula

$$V_s = (UD)/A * P$$

Where V_s represents the “vehicle stock”, UD represents the “useful demand”, A is the “annual activity” and P represents the “passengers per vehicle”.

Now, the penetration of electric vehicles starts from 2018 growing with an annual compound growth rate

of 2% (taken from the literature) to forecast the demand up to year 2045. This was followed by calculations of energy consumption using the below mentioned equation.

$$EC = (V_k * V_s) / (mv * 1000)$$

Where E_c is the energy consumption, and mv is the million-vehicle kilometre per Petajoule.

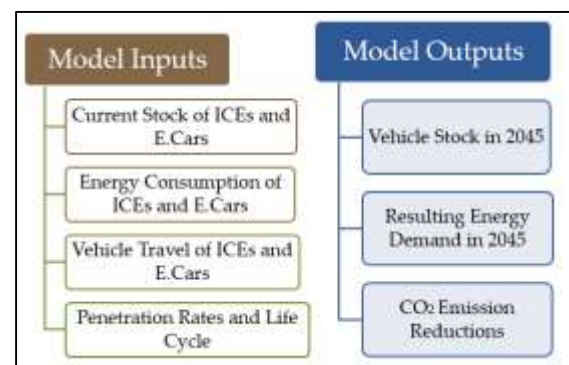


Figure 4 Input and Outputs of TIMES Model

4. Results and Discussion

Results of the model show the year-wise developing trends of electric cars considering the inputs defined in previous section. The results show an increasing trend for stock of electric vehicles and a comparatively decreasing trend of ICE cars while



the total number of vehicles keep on increasing. A similar trend was observed for the energy consumption of these vehicles. The results obtained for three major scenarios of Full Penetration, Business as usual and Sustainable development are as given below

almost same but these results are limited for the case of Pakistan.

The study is based on a real time problem of Pakistan. Pakistan is already under severe energy crisis. Implementation of policies based on results obtained from this analysis can provide a sustainable

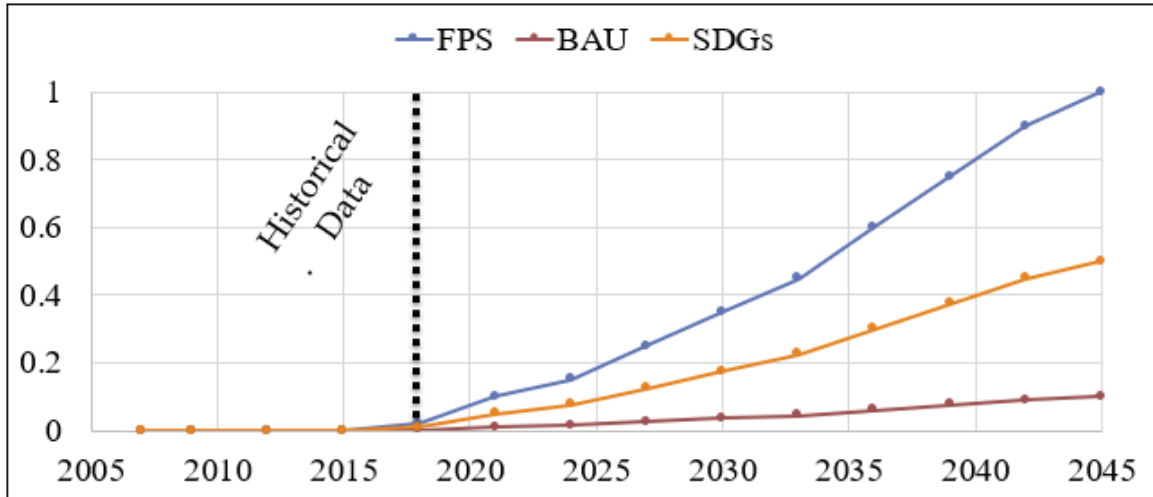


Figure 5 Percentage share of Electric Cars under three hypothetical scenario of Full Penetration, business As Usual and Sustainable Development.

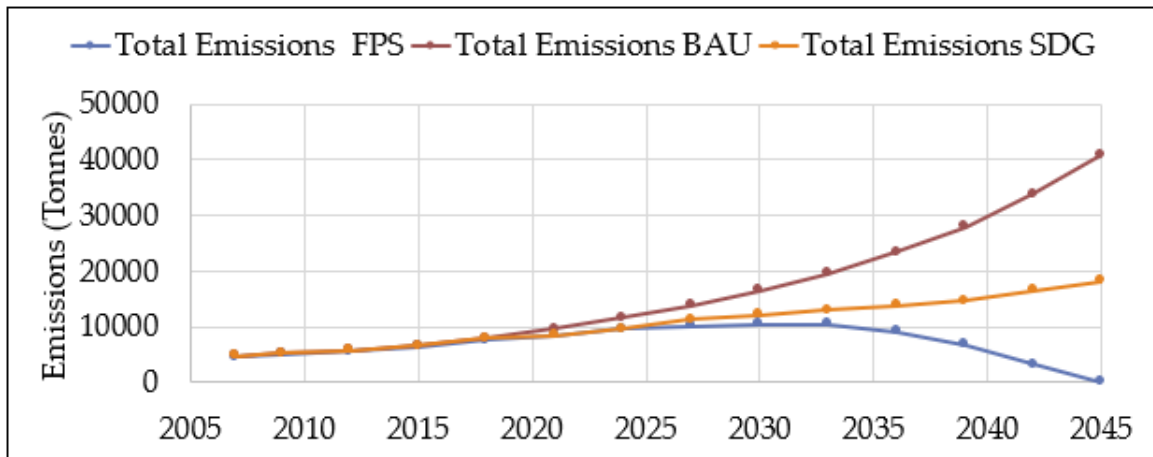


Figure 7 Emission Reduction through penetration of EVs under these Scenarios.

The energy limitation produced from each of such scenario has also been calculated. However, only an average assessment will be given here.

The results of the analysis shown above are highly dependent on the scenario considered. In case of strong or a weak economy, high urbanization rate, status quo of energy sector of a country, these results can vary significantly. Hence, this research is limited for a single country. Although, the modelling approach for TIMES model in different countries is

energy mix of Pakistan. Moreover, other than providing a sustainable energy alternative, penetration of electric vehicles will reduce GHG emissions to a significant extent. The results of the analysis also depict the emission reductions due to this penetration. However, currently Pakistan lack in technological advancement in this field. To commence any such policies, there is a need for technological advancement.



Currently, the involvement of electric vehicles in the transport sector of Pakistan is almost negligible. For a policy implementation, there is a need to advance the research regarding this topic by using different modelling tools. According to current scenario, no policy implications for Pakistan exist that determines the effect of penetrating electric vehicles in to the system.

and is best conceived when coupled with other instruments that allow the scale-up of production.

- 4- Description of Targets, Mandates and Regulations.
- 5- Financial Incentives.

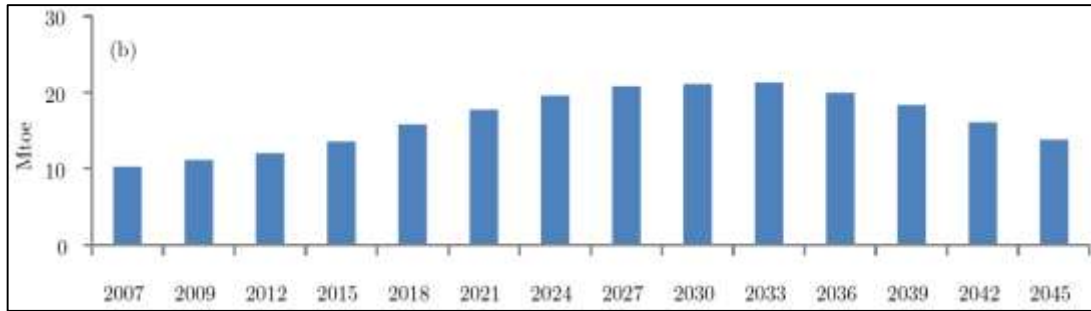


Figure 8 Average Energy Reductions through Penetration of EVs in Transport Sector of Pakistan

5. Conclusion

This study signifies the outlook obtained through penetration of EVs in Transport sector of Pakistan. Currently, transport sector of Pakistan is highly dominated by Oil and Gas sector. However, the larger portion of these resources is imported thus resulting in a high import cost. Now although, currently electric vehicles does not hold any share in transport sector but it utilization will improve both environmental and energy sector of Pakistan. This study discusses the energy and environment outlook through penetration of electric vehicles under different scenarios. Full Penetration scenarios signifies a 100% share by 2045 while SDG signifies a share of approximately 45% by 2045. TIMES model is used to identify those radical changes through which we can bring that penetration level. The results of the model explain that by making these penetrations, energy consumption can significantly drop. However, to bring these changes, we have to perform the following policy implementations:

- 1- The scale-up of policy research, including policy efficacy analysis, information and experience sharing, and capacity building
- 2- Establishing a program that aims the replication of best practices for promotion of EVs in Pakistan.
- 3- Research support is key to achieving cost declines and performance improvements

6. References

- [1] M. Kamran, "Current status and future success of renewable energy in Pakistan," *Renew. Sustain. Energy Rev.*, vol. 82, no. October 2017, pp. 609–617, 2018.
- [2] IEA, "Summary and Conclusions from IEA Bioenergy ExCo17 Workshop," 2013.
- [3] H. Qudrat-Ullah, "Independent power (or pollution) producers? Electricity reforms and IPPs in Pakistan," *Energy*, vol. 83, pp. 240–251, 2015.
- [4] A. Priessner, R. Sposato, and N. Hampl, "Predictors of electric vehicle adoption: An analysis of potential electric vehicle drivers in Austria," *Energy Policy*, vol. 122, no. July, pp. 701–714, 2018.
- [5] G. Bauer, "The impact of battery electric vehicles on vehicle purchase and driving behavior in Norway," *Transp. Res. Part D Transp. Environ.*, vol. 58, no. December 2017, pp. 239–258, 2018.
- [6] M. Dugdale, "European countries banning fossil fuel cars and switching to electric," 2018.
- [7] X. Chang, T. Ma, and R. Wu, "Impact of urban development on residents' public transportation travel energy consumption in China: An analysis of hydrogen fuel cell vehicles alternatives," *Int. J. Hydrogen Energy*, pp. 1–13, 2018.



- [8] A. López-Arquillos, J. C. Rubio-Romero, M. Suárez-Cebador, and M. del C. Pardo-Ferreira, "Comparative risk assessment of vehicle maintenance activities: Hybrid, battery electric, and hydrogen fuel cell cars," *Int. J. Ind. Ergon.*, vol. 47, pp. 53–60, 2015.
- [9] Ö. Simsekoglu, "Socio-demographic characteristics, psychological factors and knowledge related to electric car use: A comparison between electric and conventional car drivers," *Transp. Policy*, vol. 72, no. March, pp. 180–186, 2018.
- [10] Y. Wang, Z. Bian, K. Qin, Y. Zhang, and S. Lei, "A modified building energy model coupled with urban parameterization for estimating anthropogenic heat in urban areas," *Energy Build.*, p. 109377, 2019.
- [11] H. Fathabadi, "Novel battery/photovoltaic hybrid power source for plug-in hybrid electric vehicles," *Sol. Energy*, vol. 159, no. November 2017, pp. 243–250, 2018.
- [12] L. H. Björnsson, S. Karlsson, and F. Sprei, "Objective functions for plug-in hybrid electric vehicle battery range optimization and possible effects on the vehicle fleet," *Transp. Res. Part C Emerg. Technol.*, vol. 86, no. February 2017, pp. 655–669, 2018.
- [13] W. Liu, H. He, and Z. Wang, "A comparison study of energy management for a plug-in serial hybrid electric vehicle," *Energy Procedia*, vol. 88, pp. 854–859, 2016.
- [14] I. Nastjuk, J. Werner, M. Marrone, and L. M. Kolbe, "Inaccuracy versus volatility – Which is the lesser evil in battery electric vehicles?," *Transp. Res. Part F Traffic Psychol. Behav.*, vol. 58, pp. 855–870, 2018.
- [15] X. Hu, Y. Zou, and Y. Yang, "Greener plug-in hybrid electric vehicles incorporating renewable energy and rapid system optimization," *Energy*, vol. 111, pp. 971–980, 2016.
- [16] J. Saarenpää, M. Kolehmainen, and H. Niska, "Geodemographic analysis and estimation of early plug-in hybrid electric vehicle adoption," *Appl. Energy*, vol. 107, pp. 456–464, 2013.
- [17] B. W. Lane, J. Dumortier, S. Carley, S. Siddiki, K. Clark-Sutton, and J. D. Graham, "All plug-in electric vehicles are not the same: Predictors of preference for a plug-in hybrid versus a battery-electric vehicle," *Transp. Res. Part D Transp. Environ.*, vol. 65, pp. 1–13, 2018.
- [18] T. E. Lipman, M. Elke, and J. Lidicker, "Hydrogen fuel cell electric vehicle performance and user-response assessment: Results of an extended driver study," *Int. J. Hydrogen Energy*, vol. 43, no. 27, pp. 12442–12454, 2018.
- [19] Z. Wu, M. Wang, J. Zheng, X. Sun, M. Zhao, and X. Wang, "Life cycle greenhouse gas emission reduction potential of battery electric vehicle," *J. Clean. Prod.*, vol. 190, pp. 462–470, 2018.
- [20] L. L. P. de Souza, E. E. S. Lora, J. C. E. Palacio, M. H. Rocha, M. L. G. Renó, and O. J. Venturini, "Comparative environmental life cycle assessment of conventional vehicles with different fuel options, plug-in hybrid and electric vehicles for a sustainable transportation system in Brazil," *J. Clean. Prod.*, vol. 203, pp. 444–468, 2018.
- [21] Y. Xia, J. Yang, F. Wang, and Q. Cheng, "Impact of Battery Size and Energy Cost on the Market Acceptance of Blended Plug-in Hybrid Electric Vehicles," *Procedia Comput. Sci.*, vol. 131, pp. 377–386, 2018.
- [22] F. J. Pino, D. Marcos, C. Bordons, and F. Rosa, "Car air-conditioning considerations on hydrogen consumption in fuel cell and driving limitations," *Int. J. Hydrogen Energy*, vol. 40, no. 35, pp. 11696–11703, 2015.
- [23] A. R. Gopal, W. Y. Park, M. Witt, and A. Phadke, "Hybrid- and battery-electric vehicles offer low-cost climate benefits in China," *Transp. Res. Part D Transp. Environ.*, vol. 62, no. March, pp. 362–371, 2018.



Performance Analysis of Four Concentrated Solar Power Technologies for Quetta

Ahmad Nabeel Hafeez¹, Mudassar Hassan¹, Muhammad Sajid¹, Zia ul Rehman Tahir^{1*}, Muhammad Asim¹,
Muhammad Umair Siddique¹

¹Department of Mechanical Engineering, University of Engineering and Technology, Lahore.

ziartahir@uet.edu.pk

Abstract:

This paper provides the best solar concentrated solar power (CSP) technology for Quetta with perspectives of optimization total annual energy, capacity factor and levelized cost of electricity. The commercial software System Advisor Model (SAM) was used for the simulations of the data for four technologies. Selection of best technology is based on different parameters like collectors, receivers, heat transfer fluid (HTF), single unit capacity and optical characterization methods. By comparing the above given parameters, some trends showing the best results were analyzed. The capacity factors for Parabolic Trough (PT), Linear Fresnel (LF), Dish Stirling (DS) and Solar Power Tower (SPT) systems for 50 MW plant was estimated as 48.1, 44.6, 21.1 and 78.2% whereas and levelized Cost of Electricity (LCOE) as 3.71, 12.86, 3.14 and 14.52 ¢/kWh, respectively.

Keywords: National Renewable Energy Laboratory, Concentrated Solar Power, Parabolic Trough, Linear Fresnel Reflector, Solar Power Tower

1. Introduction

Energy demand is increased day by day with the growth of the world's population. Electricity production from fossil fuels makes environment polluted. There is need of clean energy resources in future to protect the environment from pollution. Solar is the big source of clean energy for earth. Concentrating solar power (CSP) use different mirrors or reflecting materials to focus sunrays on a receiver. This receiver contains a fluid that delivers heat to a power cycle for electric power generation. CSP is one of the promising, future-oriented renewable energy technologies. In the last ten years, CSP attracted more and more interest from energy utilities all over Europe and in the United States. Typically, the sun's power coming to earth is about 1000 W/m² every year but it depends upon the location [1]. Pakistan has enormous potential to use this free and clean source of energy. In Pakistan, there is one major solar power plant using PV technology in Bahawalpur. Now, there is need to design CSP technology for different location of Pakistan which is successfully working in the developed countries. This technology, although expensive, but have a great efficiency and will be a great demand in the coming years. Because the coal deposits will deplete within next 200 years and that of petroleum will deplete in next few decades. The energy from the sunrays is clear, efficient, clean and environment friendly. Today, Pakistan is facing the issue of shortage of electricity and pollution. The use of solar energy using CSP technologies is better solution for Pakistan to meet the energy demand and avoid environment from greenhouse gases (pollution).

2. Literature Review

World is moving towards solar thermal power plants to meet the energy demands. There was no existence of electricity production from solar through CSP technology until 1980s. The interest towards solar power was developed due to oil crisis in 1970s [2]. The first commercial CSP plant was constructed in Mojave Desert in California by Luz International Ltd in between 1984 to 1991. But after that progress of CSP was collapsed at that time due to reduction in oil prices. USA and Spain pursued CSP plant development initiatives in 2006 to meet the future needs [3]. Many developed countries use CSP technology for solar resources. Spain and the US are surely leading the commercialization of solar thermal energy. Spain installed 2400 MWe plant and connected to grid in 2013. Many others commercial solar projects lead by Spain with the USA to achieve the target of 4500 MWe in the same year. India was also in this race and approved its "Solar Mission" in 2010 to connect grid 20,000 MWe solar power [4]. Many other countries like Australia, China and Italy are working on solar commercial plants. There is huge potential of solar thermal energy in the world like only southern Europe produce more than 1000 GW. Pakistan is also rich in solar radiation to deploy this source for electricity production. Solar energy is clean energy source to replace fossil fuels that produce large CO₂. Solar power of 1 MWe capacity is used instead of natural gas to save environment from 688 tons of CO₂ and 1360 tons in case of coal power plant [5]. 1 m² mirror produce 400 kWh annually and saves 2.5 tons of fossil fuels in its 25 years lifetime. International Energy Agency have interesting solar thermal energy to create scenario of low carbon dioxide in future [5]. In 1912, first



parabolic power plants were installed for a pump of 73 KW in Egypt. Temperature achieved by this technology is from 350 to 550 °C. In 1980, a PT power plant of 354 MW capacity was connected to grid in California. The performance of parabolic trough power plants was continuously improved by introducing new collector, receiver and HTF [6].

The first simple model of LFR in form of fixed receiver having array of rotating reflectors was created by Francia in 1961 but there was a little progress in this field until Australia and Belgium started development on design of LFR. First Solarmundo was built in 2001 which was started in 1997 [2].

The idea of the solar based Stirling engine was first given by Roelf J. Meijer in 1987 [7]. It comprised of a large parabolic dish of specific diameter and one main focal point, pointing towards the Sun. The solar radiations were reflected from every point of the dish to its focal point at which there was the main cylinder of the Stirling engine[8]. The gas inside the cylinder heated up starting the power cycle. Further compressions and expansions drove the wheel which was further attached to a generator producing electricity [6].

This is one of the most efficient (about 30%) and powerful CSP technologies. There is an engine used for this purpose. So, we can say, it is itself a small power plant. It has a dual axis tracking system and can, therefore, be able to track the sun for whole day time (sunrise to sunset). The heat transfer fluids (HTFs) used in dish Stirling is usually air or hydrogen gas. This technology is not bounded to the generation of electricity only. There are other applications of this technology in daily life mechanical things. For example, water pumping in sunbelt areas, heat pumps etc. [9]. This is a small plant of low capacity (25 kW or 50 kW). So, a large capacity can be taken by applying several dishes to fulfill the energy requirements.

Concentrated power tower technology is one the four CSP technologies which run on the similar principle and working. It contains a long tower on the top of which the molten salt or other HTFs are placed. Instead of only one mirror, solar power tower contains many mirrors reflecting the sunrays to the top of the tower. These mirrors or reflecting materials are collectively known as heliostat [10]. It has lesser efficiency than CSP dish Stirling, but its production rate is very high. One plant can produce up to 50 MW or more electricity for 24 hours a day. From this thermal storage point of view, it is the most suitable technology for demanding area [7].

3. Methodology

3.1 Design PT Power Plant

To design a PT power plant suitable for Quetta, use available collector, receiver and HTF combination for optimum results. Use different combination of these components to get best solution for Quetta. SAM software is used to calculate this data and choose the best 20 combinations having maximum energy, high capacity factor and low LCOE. First select the PT technology for commercial usage.

Choose the location like Quetta.

Import the data files from the national renewable energy laboratory (NREL) National solar radiation Database.

Use solar multiple 2.7 for optimum solution.

Select the collector (i.e. Euro Trough ET150, Luz LS-2, Luz LS-3, Solargenix SGX-1, Albiassa Trough AT150, Siemens SunField 6, Skyfuel Sky trough (with 80-mm OD receiver), FLABEG Ultimate Trough RP6(with 89-mm OD receiver for oil HTF) and FLABEG Ultimate Trough RP6(with 70-mm OD receiver for molten-salt HTF).

Select the receiver (i.e. Schott PTR70, Schott PTR70 2008, Solel UVAC 3, Siemens UVAC 2010, Schott PTR80, Royal Tech CSP RTUVR 2014, Royal Tech CSP RTUVR 70M4 and TRX-Solar TRX70-125).

Select the HTF (i.e. Hitec Solar Salt, Hitec, Hitec XL, Dowtherm RP, Dowtherm Q, Caloria HT 43, Therminol VP-1, Therminol 59 and Therminol 66).

Simulate each combination & get output data.

Compare the combination CRF based on annual energy, capacity factor and levelized cost of electricity.

Select top 20 results of best collector, receiver and HTF for Quetta.

3.2 Design LFR Power Plant

This section represents the method to extract the result for LFR using SAM. As SAM basically is used to give the analysis of total amount of energy, levelized cost of energy, capacity factor, capital cost with respect to capacity of plant and how these values were calculated, the method is described below.

In the SAM software, first step is to select the technology which is CSP linear fresnel molten salt (commercial).

Download the weather file (location and resources) for Quetta for multiples years which is 60 minutes data.



Select HTF and optimum solar multiple (2.7).

Select one by one optical characteristics method (solar position, collector incidence table and IAM polys) and perform simulation for one by one for each HTF.

Put the plant capacity (e.g. 50MWe) and suitable operating boiling pressure.

In thermal storage, define the value of full load thermal storage hours and HTF.

Update the system cost, lifetime, financial parameters, electricity rates and electric load according to standards and then perform the possible simulations which are 27 and select the best results.

3.3 Design Dish Stirling Power Plant

Following steps are done during the simulation of the data for Quetta for different total capacities and different single unit capacities.

The location was selected, and the weather files were downloaded from the official website of NREL, using SAM. The downloaded files contain the required parameters like annual energy, levelized cost of electricity (real and nominal) direct normal irradiance (DNI), global horizontal irradiance (GHI), and capacity factors for 15 years (from 2000 to 2014). Select the year for which the simulation is to be performed.

In the solar field menu, the parameters were defined. Some parameters are chosen to be default. Such as, wind stow speed, slot gap (width and height) and some losses. The other parameters are;

Total numbers of collectors (N_{Coll}) are calculated by

$$N_{Coll} = N_{Coll(N-S)} \times N_{Coll(E-W)}$$

Where;

N_{Coll} : number of collectors

$N_{Coll, N-S}$: number of collectors north-south

$N_{Coll, E-W}$: number of collectors east-west

Total surface area of field (A_{SF}) is calculated by

$$A_{SF} = d_{coll, sep, N-S} \times d_{Coll, sep, E-W} \times N_{coll}$$

Where;

A_{SF} : total surface area of field

$d_{coll, sep, N-S}$: collector separation north-south

$d_{Coll, sep, E-W}$: collector separation east-west

Further, some properties of collector were adjusted. The collector consists of parabolic mirrors, two-axis tracking system and a support structure. Some parameters are, projected mirror area (m^2), total mirror area (m^2) and mirror reflectance. These parameters can be taken as default or can be changed accordingly.

Then comes some properties of receiver. Important parameters are, aperture, insulation, absorber and cavity. Some sub-parameters are changed accordingly.

There are some important parameters of stirling engine. Heater head-set temperature (K), heater head lowest temperature (K), engine operating speed (rpm), displaced engine volume (m^3) and most important single unit nameplate capacity (kW), these parameters are to be concerned. All other co-efficient are used as default.

Next the cost parameters are managed if needed, but the recommendations are in USD (\$).

3.4 Design Solar Power Tower Power Plant

For solar CSP power tower molten salt, only few steps are needed as follows;

Select and download the weather data file using SAM for Quetta by simply writing the name of the location. It contains all the parameters like DNI, GHI, annual energy, capacity factor and levelized costs (For 15 years).

Within system design module, some parameters are to be changed, like solar multiple, design turbine gross output and HTF hot and cold temperatures. All other parameters are kept default.

In heliostat field, simply use SAM to run solar pilot and it will automatically generate heliostat positions given as a tower height, heliostat geometry and optical properties, and receiver geometry and properties. Hence all the parameters can be used as default.

In tower and receiver option, we must decide and select the HTF type (nitrates or fluorides). Flow pattern and material type can also be change according to desire and availability but mostly kept default. Other parameters such as, system design parameters, tower and receiver dimensions, receiver heat transfer properties, design operations, receiver flux modeling parameters and piping losses are used as default.



Only Rankine power cycle is selected for power cycle option. All the general and system design parameters are selected to be default as provided by SAM.

Defining the system cost in USD (\$) is recommended as per international market. Other currency can also be selected.

4. Results and discussion

4.1 Parabolic trough

The top 15 best combination of collector, receiver and HTF for Quetta having maximum annual energy generation, high capacity factor and low LCOE are given in the table below. The range of annual energy for top combinations is 188.1GWh to 188.969 GWh, capacity factor is 47.7% to 48.1% & range of LCOE is from 3.71¢/kWh to 3.73¢/kWh for 50MWe power plant.

Table 1-Top 15 best results for Parabolic trough power plant

1	C3R3F9	Luz LS-3	Solel UVAC 3	Therminol 66
2	C3R3F2	Luz LS-3	Solel UVAC 3	Caloria HT 43
3	C3R3F7	Luz LS-3	Solel UVAC 3	Dowtherm RP
4	C3R7F4	Luz LS-3	Royal Tech CSP RTUVR 70M4 (Manufacturing Specifications)	Therminol VP-1
5	C3R3F8	Luz LS-3	Solel UVAC 3	Therminol 59
6	C3R7F9	Luz LS-3	Royal Tech CSP RTUVR 70M4 (Manufacturing Specifications)	Therminol 66
7	C3R7F2	Luz LS-3	Royal Tech CSP RTUVR 70M4 (Manufacturing Specifications)	Caloria HT 43
8	C3R7F7	Luz LS-3	Royal Tech CSP RTUVR 70M4 (Manufacturing Specifications)	Dowtherm RP
9	C3R6F4	Luz LS-3	Royal Tech CSP RTUVR 2014 (Manufacturing Specifications)	Therminol VP-1
10	C7R3F9	SkyFuel SkyTrough	Solel UVAC 3	Therminol 66
11	C3R6F9	Luz LS-3	Royal Tech CSP RTUVR 2014 (Manufacturing Specifications)	Therminol 66
12	C3R6F2	Luz LS-3	Royal Tech CSP RTUVR 2014 (Manufacturing Specifications)	Caloria HT 43
13	C6R7F4	Siemens SunField 6	Royal Tech CSP RTUVR 70M4 (Manufacturing Specifications)	Therminol VP-1
14	C3R6F7	Luz LS-3	Royal Tech CSP RTUVR 2014 (Manufacturing Specifications)	Dowtherm RP
15	C3R7F6	Luz LS-3	Royal Tech CSP RTUVR 70M4 (Manufacturing Specifications)	Dowtherm Q

annual energy generation depends upon the DNI for parabolic trough. DNI is varied from location to location. Its value for Quetta is about 2311kWh/m². DNI must be greater than 1800kWh/m² for location suitable for CSP technology. Hence, climate condition of Quetta is best for this PT technology.

method didn't give satisfactory results but other gives better results for LFR solar plant and best capacity factor is 44.6% for Caloria HT 43 using IAM Polys. The minimum cost came out 12.86¢/kWh. There is negligible change in capacity factor by changing the total capacity of the plant.

4.2 Linear Fresnel Reflector

Using SAM, 27 simulations were performed according to the above described methodology in section 3.2 for Quetta by varying optical characterization methods and changing HTF. Then capacity factor, levelized cost of electricity, capital cost and annual energy were observed and compared and best four results of each optical characterization method are shown in the form of graph as shown in Fig. 1. This graph shows Caloria HT 43 is best HTF in all aspects. Solar position optical characterization

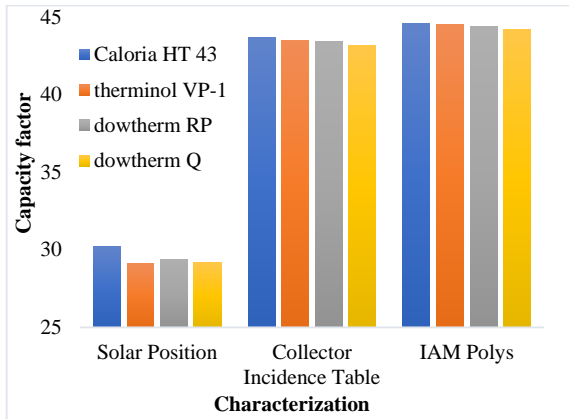


Fig. 1 Best result of capacity factor for LFR for Quetta

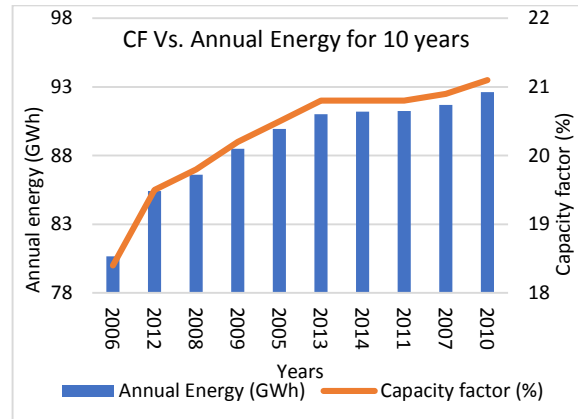


Fig. 3 Trend of capacity factor with annual energy for 10 years in Quetta

4.3 Dish Stirling

In Fig. 2, there is a comparison of capacity factors is done against 10 years for two single units having different single unit capacities. The simulations were performed for 25 kW and 50 kW of single capacity units. As compared, the unit with 25kW capacity has greater capacity factor (about double) gives economical energy than that of 50kW capacity. This comparison leads us to choose which single unit will be feasible in the selected location. So, 25kW of single capacity unit is best with Quetta environment.

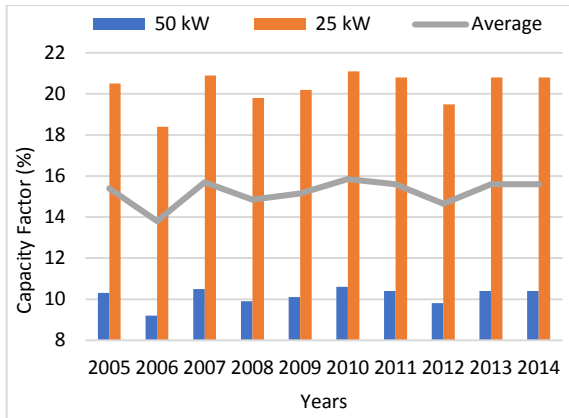


Fig. 2 Graphical comparison of capacity factor.

Next the trend of the capacity factor and annual energy is studied for latest 10 years data provided by SAM. Annual energy increases as the capacity factor increases as shown by the Fig. 3. The value of capacity factor comes out 21.1%. This can be interpreted that the maximum value of annual energy as well as maximum value of capacity factor is in 2010. So, the properties and parameters (GHI, DNI, etc.) that were in 2010 are best suitable for Quetta. At these properties, the levelized cost of electricity was estimated to be 3.14 ¢/kWh.

4.4 Solar Power Tower

For the best and feasible power tower plant, we compared the total plant capacity with respect to cost and capacity factor. In Fig. 4, it is shown that capacity factor is inversely proportional to the levelized cost. But there is a bit different trend that for larger total capacity, the capacity factor lesser than the that of smaller total capacities and levelized cost is lesser as well. This means that we must compromise on one of the two factors. If we must maximize the capacity factor, it will be costly and vice versa.

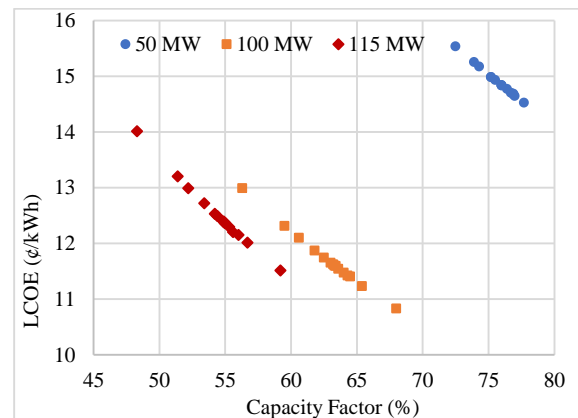


Fig. 4 Comparison for cost and capacity factor for different total capacities

The levelized cost for 50MW of total capacity for maximum capacity factor of 78.2% comes out to be 14.52 ¢/kWh. For maximum capacity factor of 59.2% for 115MW of total capacity, the cost is calculated to be 11.51 ¢/kWh.

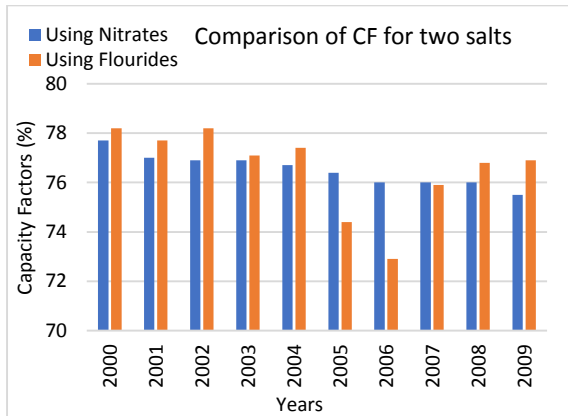


Fig. 5 Comparison of salts for 50 MW of total capacity for 15 years

In Fig. 5, there is a comparison of two salts for 50 MW of total plant capacity. One of the two salts is nitrate (60% NaNO_3 40% KNO_3) and the other one is fluoride (46.5% LiF 11.5% NaF 42% KF). The best salt for this total capacity is found out that is fluorides. But there is a small difference in the values using both salts. So, any salt can be used if there is availability. Moreover, the results are best suitable in 2000, 2002 and 2004. So, for Quetta, the best parameters should be what that were in the year 200 using fluorides salt.

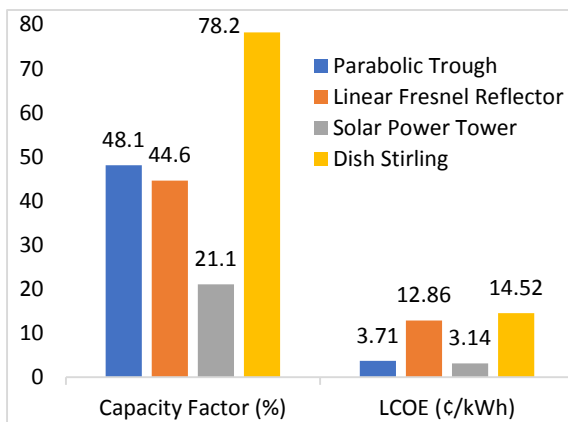


Fig. 6 Comparison of four CSP technologies

5. Conclusion

This study is conducted to analyze the best CSP technology for Quetta. System advisory model (SAM) is used to calculate the annual energy, capacity factors and LCOE. Solar power tower generates maximum energy than others for 50MW. LFR produces energy and LCOE in between other technologies. Solar tower and parabolic trough also generate suitable energy having maximum capacity factors. But parabolic trough has optimum values of all the factors like annual energy, capacity factor and LCOE as compared to other technologies, so the best technology to be suggested for Quetta is parabolic trough. Parabolic trough is mature technology used

all over the world and it is also suitable for Quetta as described in Fig. 6. So, it is best option to install in Quetta to overcome the energy shortage and prevent environment from more polluted.

REFERENCES

- [1] Poullikkas, A., et al., *The cost of integration of parabolic trough CSP plants in isolated Mediterranean power systems*. 2010. **14**(5): p. 1469-1476.
- [2] Mills, D.J.S.e., *Advances in solar thermal electricity technology*. 2004. **76**(1-3): p. 19-31.
- [3] Islam, M.T., et al., *A comprehensive review of state-of-the-art concentrating solar power (CSP) technologies: Current status and research trends*. 2018. **91**: p. 987-1018.
- [4] Rathore, P.K.S., et al., *Solar power utility sector in india: Challenges and opportunities*. 2018. **81**: p. 2703-2713.
- [5] Romero, M., J.J.W.I.R.E. González-Aguilar, and Environment, *Solar thermal CSP technology*. 2014. **3**(1): p. 42-59.
- [6] Müller-Steinhagen, H. and F.J.A.r.o.t.t.I.I.Q.A.E. Trieb, *Concentrating solar power*. 2004. **18**: p. 43-50.
- [7] Soomro, M.I., et al., *Performance and Economic Analysis of Concentrated Solar Power Generation for Pakistan*. 2019. **7**(9): p. 575.
- [8] Robert F. Boehm, U.o.N.L.V., *Performance and Economic Analysis of Concentrated Solar Power Generation for Pakistan*. *Journal of Solar Energy Engineering*, 2019. **Volume 141**(Issue 6).
- [9] Dobos, A., T. Neises, and M.J.E.P. Wagner, *Advances in CSP simulation technology in the System Advisor Model*. 2014. **49**: p. 2482-2489.
- [10] Lovegrove, K. and W. Stein, *Concentrating Solar Power Technology: Principles, Developments and Applications*. 2018: Elsevier Science.



Contribution of different factors in the production of smog in major cities of Pakistan

Syed Muhammad Sohail Rehman¹, Syed Ubaid Ur Rehman¹, Tauseef Aized¹, Syed Junaid Ur Rahman²

1- Department of Mechanical Engineering, University of Engineering and Technology Lahore

2- Department of Food Sciences and Technology, Khwaja Fareed University of Engineering and Information

Technology Rahimyar Khan

Corresponding author: syedsohailrehman89@gmail.com

Abstract:

Smog has become the serious concern to the health of people living in major cities of Pakistan for last decade. This research work is an attempt to estimate the contribution of different factors including transport, industry, crop residue burning and brick kilns in the production of smog in major cities of Pakistan naming Lahore, Faisalabad and Multan. A relation has been developed in the form of percentage showing the contribution of different factors in the production of smog. Results derived for the three cities show that transport sector is the major source of pollution and contributes approx. 40-45% in smog production. Moreover industries, burning of crops residue and brick kilns also contribute up to 25-30%, 20-25% and 8-12% respectively in smog production.

Keywords: Smog, traffic emission, crop residue, brick kiln, Pakistan

1. Introduction

Health is the main concern of all human being and any hazard to it can never be compromised. Smog has become a crucial problem for last five years for the residents of populated cities in the country especially in Punjab province. It prevails during the months of November and December.

With the increase of population in big cities, areas are becoming more congested to live and greenery is eliminated. Besides that sudden increase in daily traffic, industries, non-conserved human activities and urbanization have led to the inclusion of unfavourable matter into the air. Presence of air pollutant i.e. CO, NO_x, SO_x, PM and VOC is increasing each year from 2014-19. Studies showed that the amount of NO_x present in the air of Lahore in 2019 is 17 times compared to that in 2014. Similarly the content of other pollutants like SO_x, VOC, PM_{2.5} is found to be increased 400% during the last five years. [1].

Vehicles running on the roads of affected cities have a significant contribution towards production of smog. Xie et al. [2] and Wang et al. [3] proposed his study in China and revealed that there is a U-shaped relation between traffic density and smog production. Meaning that the production of smog is high during the time when a large number of vehicles are present on the roads. Low quality of fuel in Pakistan also adds to the harmful emissions from vehicle. Oil refineries in the country provide Euro 2 compliant fuel instead of Euro 4 compliant fuel which is provided throughout the world.

With the rise in construction and infrastructure development in Pakistan, production of bricks is on the high every year. Bricks are produced in kiln which emits very harmful gas and unburned matter in a very high quantity. Presence of such kilns is among the main contributors of smog production. CO, CO₂ and SO₂ are the main constituents of the smoke produced by kiln and have very adverse effect on environment. Incomplete burning of coal in kiln emits unburned carbon which causes severe damage to respiratory system [4].

Industrial emissions are another cause of smog production. Lahore and Faisalabad are two big industrial cities which have industrial areas close to residential locations. During the winter season, smoke and harmful gases ejecting from the chimneys are trapped in the lower layer of the atmosphere and provide a potential source for smog production.

Ramisha et al.[5] investigated that due to changing social and economic reasons, burning of crops residue is becoming more frequent activity in the countries like Pakistan over the last 10 years. Pakistan emission inventory was developed to find out the level of crops burning annually during the years 2008 to 2018. Due to intense agricultural activities, quantity of crops residue and rate of burning of this residue was found to be high in the province of Punjab and Sindh. Thus CO₂ emissions produced due to stated activities are high in that area. Combined with the other factors, most of the cities in Punjab and Sindh being highly populated, suffer more from the air pollution [6].



Standard air quality for the healthy breathing is less than 50 AQI. According to Environment Protection Department Punjab, air quality during the first week of November was reported to reach 600AQI. Average level of the air quality was found to be 250-300 AQI in November and December during the last 5 years[7].

With increasing environmental concerns and changing global trends, it is very important to focus on the factors, present and affecting in any form, which deteriorate the human habitat. So there has been a dire need of such an investigation, especially in Pakistan, to evaluate today's great environmental problem i.e. smog.

Table 1: Air Quality Index

AQI	Breathing quality	Color code	Precautions
0 to 50	Good		None. Go out, walk and exercise.
51 to 100	Moderate		Usually patient are affected, people having medical history should remain inside.
101 to 150	Unhealthy for children and aged people		Children and older people with already existing respiratory disease are affected badly. They should limit outdoor activities.
151 to 200	Unhealthy		This air quality is unhealthy for all. Face mask and goggles should be used while going in open air.
201 to 300	Very unhealthy		Avoid outdoor activity, no outside walk and play. Children should remain at home.
301 to 500	Hazardous		AQI of this level should not be inhaled.

Data taken from Mayo Hospital Lahore reveals that out of 2100 patients 200 were reported in 2015 and 500 were reported in 2016, 600 were reported in 2017 and 800 during 2018-19 with smog-borne diseases including irritation (21%), throat problem (29.5%), dry eyes (23%), corneal diseases (7%), lid erosion (6%), uveitis (2.5%) and lacrimation (11%) on average. The study ultimately revealed that there was a 60% increase in the number of patients reported over the past five years. Moreover health department is insisting on precautionary measures which considerably decreases the number of affected people. A careful estimation showed that breathing the pollutant air in smog areas is equally dangerous as 20 cigarettes smoked a day [8].

2. Methodology and data collection

To conduct this research work following methodology has been followed.

Table 2: Average Air Quality Index for Lahore, Faisalabad and Multan during years 2015-18

Name of City	Months	2015	2016	2017	2018
Air Quality Index (AQI)					
Lahore	November	275	350	325	390
	December	250	280	270	280
Faisalabad	November	190	300	220	280

- i. Collection of AQI for the last years 2015-18 from Air Visual application
- ii. Finding the number of vehicles running on the roads of Lahore, Faisalabad and Multan, and emissions from the burning of fuels
- iii. Industrial unit estimation in three major cities in Punjab
- iv. Finding the number of brick kiln not using zigzag technology in the suburb of cities
- v. Estimation of contribution of transport, industry, crops residue burning and kiln emissions in the production of smog
- vi. Representation of results in the form of tables and charts

Average AQI for the months of November and December during last five years in three cities is given in table 2.



	December	180	280	180	300
	November	160	180	200	210
Multan	December	150	200	175	160

According to City Traffic Police department 1.3, 0.5 and 0.15 million vehicles runs daily on the roads of Lahore, Faisalabad and Multan respectively. According to United States Environmental Protection Agency (EPA) [9] a typical passenger vehicle emits about 4.5 metric ton of CO₂ in a year provided the quality of fuel is compliant with Euro 4. There are 1100, 512 and 60 industrial units in Lahore, Faisalabad and Multan respectively which are listed as major units producing air pollution. Studies showed that CO₂ production in Pakistan would reach 278 million ton in 2035 [10].

To find out the overall contribution of each factor in smog production in each particular city, individual contributors in each factor are addressed. For example to find out the contribution of vehicle emissions in smog production, first number of vehicles in the city and emissions from each vehicle are calculated. After that overall estimation is done. Same is followed for the estimation of contribution of other factors.

3. Results and discussions

Analysis of the emissions data collected through different concerned institutes and surveys in the

desired cities shows that high density of traffic in these cities is the major source of pollution coming into air.

In Lahore, contribution of transport sector in air pollution and smog production was found to be 45%. Second major contributor is industrial sector comprising about 24% part in smog production. Emissions from the industrial sector are mainly because of power and processing industries established in the suburb of the city. Punjab being an agricultural province produces 0.73 million ton of crops residue annually that is burnt to make the land spare for next crop. The most vulnerable months of November and December are the harvest season of rice and maize, and some quantity of vegetable-plants so these are the major crops residue. Thus the burning of this residue makes the air pollutant and has 19% contribution towards smog production. Another factor of smog production is brick kilns working on conservative methods of operation. There are approx. 90 brick kilns in the suburb of Lahore that are not using zigzag technology and having adverse effect on environment throughout the year.

Details about the all four smog producing factors and their percentage contribution in smog production in Lahore, Faisalabad and Multan are given in table 3.

Table 3. Smog producing factors and their contribution in smog production

City	Factor	No. of source units	%age contribution in smog production
Lahore	Transport (including HTV and LTV)	1.3 million	45
	Industry (power, processing)	1100 units	24
	Crop residue	0.1 ton	19
	Brick kiln	78	12
Faisalabad	Transport (including HTV and LTV)	0.5 million	40
	Industry (power, textiles, processing)	512 units	28
	Crop residue	0.12 ton	23
	Brick kiln	55	9
Multan	Transport (including HTV and LTV)	0.15 million	38
	Industry (power, processing)	60 units	25
	Crop residue	0.15 ton	25
	Brick kiln	45	12

Figure 1 shows the number of emission sources units in Lahore, Faisalabad and Multan. It is evident that

emission sources in Lahore are high as compared to Faisalabad and Multan.

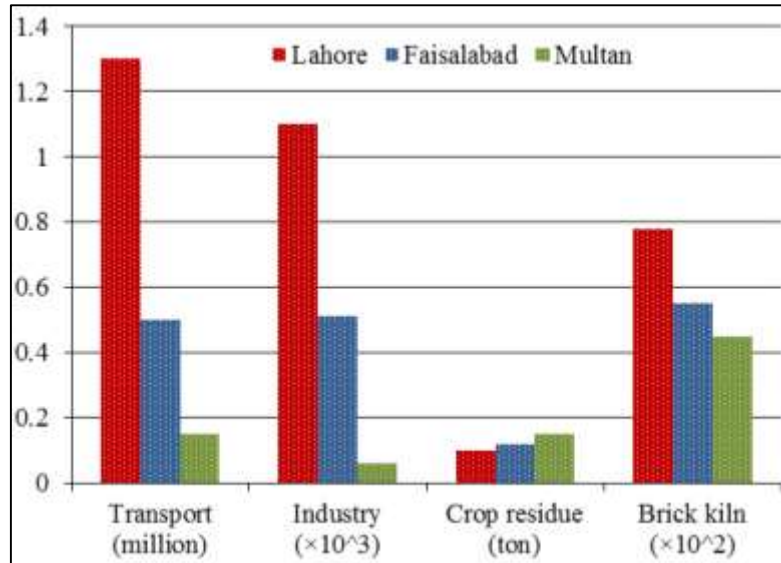


Figure 1. No. of emission sources in Lahore, Faisalabad and Multan

Similarly, pictorial representation of the data presented in above table is given in figure 2. It shows

that transport sector has the maximum contribution in the production of smog.

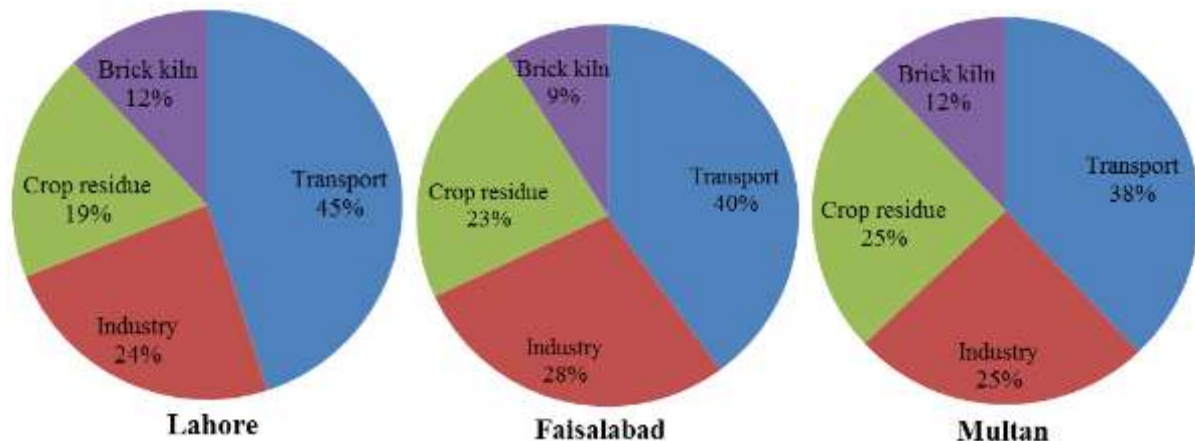


Figure 2. Percentage contribution of different factors in production of smog in the cities of Lahore, Faisalabad and Multan

4. Conclusions

All the big cities in Punjab are affected from smog and it generally prevails during the start of November and sustains till the end of December. Total four major contributors to the smog production including transport, industry, crops residue and brick kilns are addressed in this research study. Following conclusions have been made out of this research.

- i. Smog results mainly from human activities and it sustains in cities having high and congested population.
- ii. Lahore is at the top of list among the smog affected cities in the world. Transport is the major source of smog pollution and contributes up to 45%. Other factors are Industry (24%), crops residue (19%) and brick kilns (12%).

- iii. Faisalabad being a populated and industrial city is also affected from smog in the months of November and December. Main contributors are transport (40%), industry (28%), crops residue (23%) and brick kilns (9%).
- iv. Multan is the major city of South Punjab and it is both agricultural and industrial area. Transport, industry, crops residue and brick kiln contribute 38, 25, 25 and 12% respectively in smog production.

It is obvious from the above conclusions that transport sector is the key constituent in smog production. AQI of the city is directly proportional to traffic density and industrial units. Updated legislation is required to control the emissions from the vehicle and industrial, and there is a dire need to devise an Environment



Protection policy based on current environmental scenario in the major cities of Pakistan.

REFERENCES

- [1] Ashraf A., Butta A., Khalid I., Alam R.U., and Ahmad S.R., "Smog analysis and its effect on reported ocular surface diseases: A case study of 2016 smog event of Lahore," *Atmospheric Environment*, vol. 198, pp. 257-264, 2019.
- [2] Xie R., Wei D., Han F., Lu Y., Fang J., Liu Y., and Wang J., "The effect of traffic density on smog pollution: Evidence from Chinese cities," *Technological Forecasting and Social Change*, volume 144, pp. 421-427, 2019
- [3] Wang F., Zheng P., Dai J., Wnag H., and Wang R., "Fault tree analysis of the causes of urban smog events associated with vehicle exhaust emissions: A case study in Jinan, China," *Science of The Total Environment*, vol. 668, pp. 245-253, 2019.
- [4] Khan M.W., Ali Y., Felice F.D., Salman A., and Petrillo A., "Impact of brick kilns industry on environment and human health in Pakistan," *Science of The Total Environment*, vol. 678, pp. 383-389, 2019.
- [5] Azhar R., Zeeshan M., and Fatima K., "Crop residue open field burning in Pakistan; multi-year high spatial resolution emission inventory for 2000–2014," *Atmospheric Environment*, vol. 208, pp. 20-33, 2019.
- [6] Sawlani R., Agnihotri R., Sharma C., Patra P.K., Dimri A.P., Ram K., and Verma R.L., "The severe Delhi SMOG of 2016: A case of delayed crop residue burning, coincident firecracker emissions, and atypical meteorology," *Atmospheric Pollution Research*, vol. 10 (3), pp. 868-879, 2019.
- [7] Environment Protection Department Punjab, <https://epd.punjab.gov.pk/>, 15.11.2019.
- [8] Punjab health department, <https://pshd.punjab.gov.pk/>, 20.11.2019.
- [9] Environmental Protection Agency, <https://www.epa.gov/>, 21.11.2019.
- [10] Lin B., and Raza M.Y., "Analysis of energy related CO2 emissions in Pakistan," *Journal of Cleaner Production*, vol. 219, pp. 981-993, 2019.

Acknowledgements

We thank all the colleagues whose help has been a source of light for us.



Design, Analysis and Optimization of 50MW Solar Thermal Parabolic-Trough Power Plant in Multan

Kamran Mahboob^{1,2}, Farman Ali², Hassan Mehmood², Awais Khan¹, Tauseef Azid¹

¹ Dept. of Mechanical Engineering, University of Engineering and Technology Lahore, Pakistan

² Dept. of Mechanical Engineering, Chenab College of Engineering and Technology Gujranwala, Pakistan

* Corresponding Author: Email: mahboobccet@gmail.com

Abstract

Fossil fuels, air pollution, emission of greenhouse gasses affect our climate and cause different diseases. Solar energy is the best and common way to produce clean renewable electricity generation. Solar thermal Power Plant is an effective and eco-friendly system to produce electricity. Parabolic trough technology is the advanced and commercially used for power plant in the world. The southern region of Pakistan is receiving perfect amount of solar radiations comparable to one of the best in the world. These areas have suitable environment and optimistic potential for Concentrated Solar Power (CSP) and Photovoltaic (PV) energy productions. Southern region of Pakistan has appropriate and effective amount of solar radiation for proposed project. Multan is situated in the same region of Pakistan with the highest value of DNI. The purpose of this paper is to design 50MWe Solar Power Plant using parabolic trough collector technology; it will be the first step towards clean energy production in Pakistan. This plant uses Therminol VP-1 as high temperature fluid. Storage tanks that can be used as energy storage are designed in that way; this plant is operative at night time and capable of producing electricity for 24 hours. The monthly and yearly production from proposed CSP power plant is found by performance analysis. It is revealed in this research that maximum energy production is achieved from March to October due to high solar radiation during these months. The minimum energy production is recorded in December and January. It is concluded that the efficiency of the Concentrated Solar Power (CSP) is feasible compared to other renewable energy resources. It is recommended that Government should take interest in this type of projects as renewable energy CSP plant is pollution free process to produce electricity.

Keywords: energy; solar; renewable energy production; parabolic trough technology; CSP parabolic trough power plant.

1. Introduction

With the population and industrial growth of the world, energy needs are growing. This has forced the world to produce energy from fossil fuels in past century [1-3]. One of the major drawbacks of fossil fuels is emission of green house gases [4-6]. The quest for clean energy production has forced many industrial economies to shift to renewable energy from fossil fuels [7-9].

Recent growths in renewable shows shift of the world to renewable energy resources. There is a major shift in electricity generation and share of renewable has increased considerably. Europe and Eurasia region is leading in this regard and has the largest share [10].

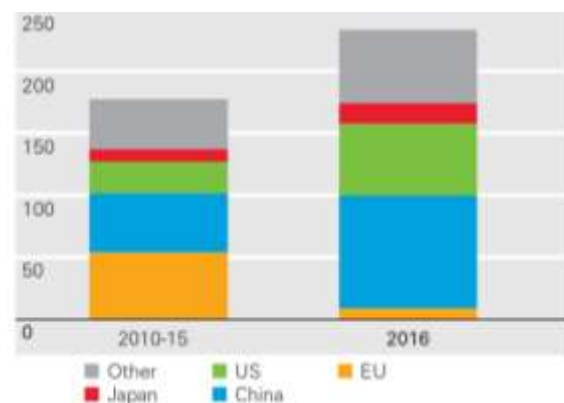


Fig. 1: Growth and diffusion of renewable [10]

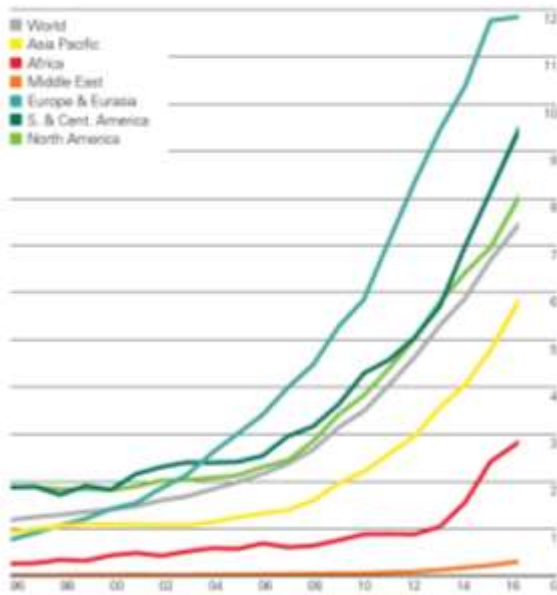


Fig. 2: Share of renewable (other than hydro) in power generation in different regions of the world [10].

Pakistan has followed the footsteps of developed countries and has greater dependencies on the fossil fuels currently. Nearly two third of the resources used in electricity generation is thermal. As major part of electricity generation and transportation [11] is using fossil fuels that is damaging the atmosphere severely. It has polluted the environment in all populated region severely. There is a dire need to shift great portion of energy production to renewable resources instead of fossil fuels, whose share is negligible [12].

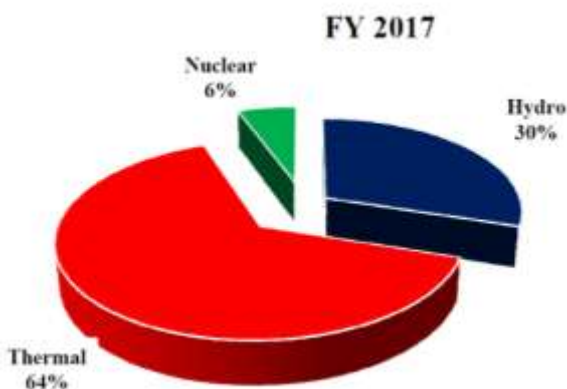


Fig. 3: Share in Electricity Generation FY2017, Pakistan [13].

2. SOLAR ENERGY

Solar energy can be used to harness energy from the sun into other forms of energies like thermal, electric etc. [14-17]. There are different ways to convert solar energy into electrical energy like PV panel, solar tower power plants, Linear Fresnel, parabolic troughs, and parabolic dishes [18-26].

Pakistan is blessed with solar energy and has huge potential to harness this clean and free source of energy. By utilizing solar energy we can enhance power generation capacity and there will be little fossil fuel emission [27].

2.1. Global Horizontal Irradiance (GHI) for Pakistan

Nearly all regions of Pakistan and especially southern regions of the country are suitable for having greater solar radiations. More than 90% of the land has a GHI value greater than 1500 kWh/m² suitable for solar energy applications. It is estimated that annual mean GHI value of Pakistan is 2071kWh/m². It is clear from GHI value that Pakistan can be listed amongst countries which are rich in solar energy [28].

Southern areas of Pakistan like Sindh, Balochistan, and Southern Punjab are best suited for CSP plant installation. These areas have around eight hour of daily sunshine and higher DNI values. Punjab is most populist region of Pakistan and has greatest demand of electricity. By installing a generation plant in southern Punjab can help in harnessing solar resources of the areas as well as reducing environment pollution.

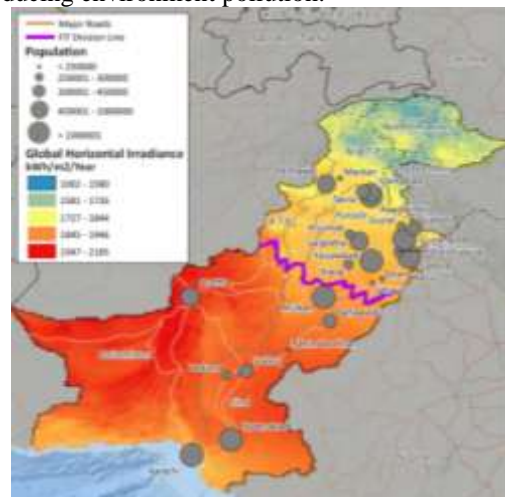


Fig. 4: Global horizontal irradiance of Pakistan [29].

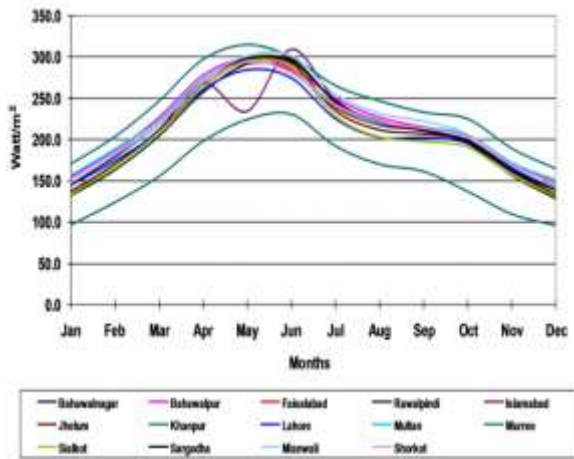


Fig. 5: Solar radiation in Punjab[30]

Solar radiation intensity value higher than 200 W/m² is observed in most region of the Punjab between March and September. Multan lies in southern Punjab region and has high sunshine values therefore it is selected for CSP plant installation.

2.2. Parabolic Trough

PTC is a parabolic shape structure covered with mirrors or reflective film which reflects the rays coming from sun onto its focal line [31]. At its focal line there is a glass enclosed metallic tube receiver, which is coated with a high solar radiation absorber and low heat emission material. The receiver tube contains the heat transfer fluid, which is different for different applications. The Parabolic Trough Collectors are arranged parallel in the solar field to track the sun whole day [32-37].



Fig. 6: Sky Fuel Parabolic Trough collector [38].



Fig. 7: Andasol Solar Power Station Project [39].

3. 50MWe CSP plant design

The designing of PTC 50MW plant is initiated by selecting the suitable and appropriate site. Selection of site is a vital aspect for better production in any renewable energy project. The efficiency of the plant depends upon the DNI radiation intensity and solar field aperture area. For the initial designing of PTC plant the selected parameters are given as follows;

3.1. Collector Type

The collector preferred for the PTC plant is SkyFuel Trough. The characteristics of the SkyFuel Trough collector are given in Table 1. It is selected for the plant due to following features;

- 1) Low cost of the reflective film
- 2) Rigid and sustainable structure against severe climate
- 3) Better Thermal and optical efficiency
- 4) High torsion stiffness than Luz-1 and Luz-2 troughs.

Table 1: Characteristics of the SkyFuel Trough (with 80-mm OD receiver).

Parameters	Values
Aperture Area	656 m ²
Total-Structure-Width	6 m
Collector-Assembly-Length	115 m
Modules-Per-Assembly	8
Single-Module-Length	14.375 m
Design-Optical-Efficiency	0.8484
Focal-Length	2.15 m
Mirror-Reflectance	0.93

3.2. Heat Transfer Fluid (HTF)

The HTF preferred for proposed PTC is Therminol VP-1 due to following characteristics;



- 1) Thermal stable operating temperature of the VP-1 ranges from 12 to 400°C.
- 2) Better thermal efficiency than other heat transfer fluid like Hitec Solar Salt etc.
- 3) Significant annual increase in energy production by using Therminol VP-1.

3.3. Receiver (Schott PTR80)

Another important aspect for better production in CSP plants is selection of receiver. Schott PTR80 is selected for the PTC plant. Schott PTR80 receiver characteristics are listed in Table 2.

Table 2: All design parameters of the PTC plant

Parameters	Values
Total capacity of the PTC plant	50 MWe 413 acres
Total covered land area	Air Cooled
Condenser Type	
HTF properties and Receiver	
Filed HTF fluid	Therminol VP-1
Design-loop-inlet-Temp.	293°C
Design-loop-outlet-Temp.	391°C
Pressure of Boiler	86 bar
Receiver Type	Schott PTR80
Inner Dia. of Absorber Tube	0.076 m
Outer Dia. of Absorber Tube	0.08 m
Glass-envelope inner Dia.	0.115 m
Glass-envelope outer Dia.	0.12 m
Absorber-Material	304L
Solar and Collector Field	
Solar Multiple	2
Single loop aperture	5248 m ²
Row Spacing	15 m
Field Subsection	2
Total field reflector area	477568 m ²
Number of loops	91
Water usage per wash	0.7 L/m ²
Washes per year	63
Thermal Energy Storage	
Storage fluid	Therminol VP-1
Storage type	2 tanks
Thermal Storage (hr) (TES)	6 hr

Tank Diameter	20.1584 m
Thermal Capacity	943.82MWht
Tank loss coefficient	0.4 W/m ² -K
Storage tank heater efficiency	0.98
Estimated heat loss	0.4087MWt

4. Performance Analysis of PTC plant

The performance analysis is done by analyzing the monthly energy generation from the PTC plant in Multan, Pakistan. Annual energy generation from the proposed PTC plant is obtained 90,484,504 KWh.

Maximum monthly energy generation from March to October varies from 10.28 GWh to 6.718 GWh. The energy production during July is pointedly low due to the rainy season in Multan. From November to February minimum energy production received from PTC plant varies from 3.953 GWh in December and 3.47 GWh in January as shown in Fig. 8.

Fig. 9 illustrates the data of field-thermal-power incident, cycle-thermal-power-output and cycle-electric-power-output.

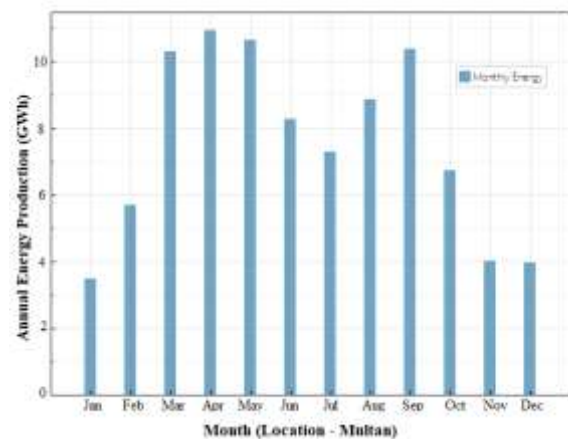


Fig. 8: Monthly energy generation from PTC in Multan.

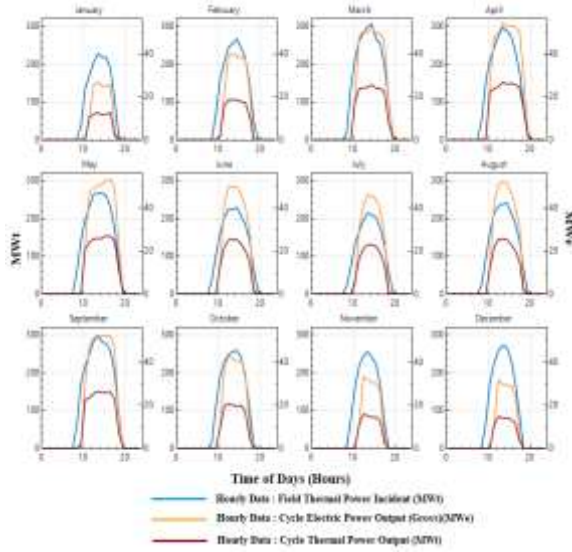


Fig. 9: Plot of Thermal-power-incident, cycle-electric-power-output and cycle-thermal-power-output

The values of these cycles depend upon the intensity of solar radiations in the region selected for the proposed PTC plant. The maximum and minimum values recorded for the thermal power incident are 315.7064 MW and 197.239 MW in March and December respectively. 59.8192 MW is the highest value of the electric power output received from March to October.

The mean efficiency (Gross) 0.1088 and maximum efficiency 0.393 are recorded for the proposed PTC plant as shown in Fig. 10.

Annual energy production for the proposed CSP Parabolic trough plant is found out 90,484,504 KWh with a capacity factor of 20.5%. The gross to net recorded efficiency of the plant is 88.8%. The detailed information after simulation of the plant is shown in Table.3.

Table.3. Annual energy production for PTC plant.

Characteristics	Values
Annual energy production	90.48
Capacity Factor	GWh
Gross to net efficiency	20.5%
	88.8%

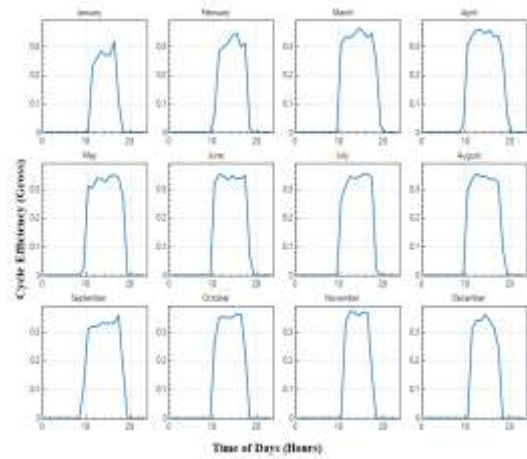


Fig. 10: Cycle Efficiency (Gross)

5. Results after optimization

Optimization of the initial design of Parabolic trough plant is performed by changing the values of solar multiple and thermal storage (TES) (Fig. 11 and 12) and the results are illustrated for varying solar multiple and thermal storage (TES).

From Fig. 11 it is clear that by increasing solar multiple, the annual energy production will increase. Actually, by increasing solar multiple, we directly increase the reflective aperture area of solar field.

It is observed that, there is a significant change appeared in annual energy production by changing the values of solar multiple. The solar multiple selected for the initial designing of proposed PTC plant with a corresponding energy generation is 90.4 GWh is 2. If we increase the value from 2 of solar multiple, a substantial change will occur. The optimum value of solar multiple for the PTC plant is around 8 for better energy generation.

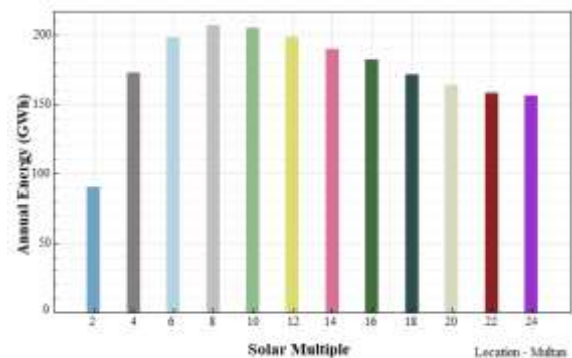


Fig. 11: Variation of solar multiple with annual energy production for PTC plant in Multan

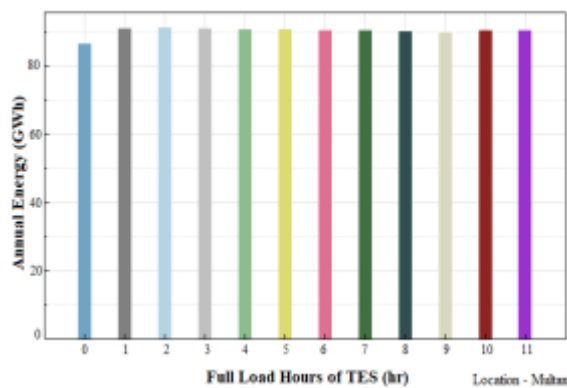


Fig. 12: Variation of thermal storage (TES) with annual energy production for PTC plant in Multan

Another constraint of optimization is thermal energy storage (TES), which provides energy during the period of low radiation or in night time to the power block to produce electricity. Moreover, the main reason of using thermal storage in the plant is to avoid energy generation breakdown.

Fig. 12 shows the variation of thermal energy storage (TES) with annual energy production. The thermal energy storage time for the selected plant is 6 hours, corresponding annual energy production is 90.4 GWh. Increase in the storage time simply means the increment of investment in the plant and reduction in the annual energy production. The optimum value of TES for the proposed plant is 2 hours with energy generation of 101.64 GWh. Energy generation can be increased by increasing the thermal energy storage of the plant within certain condition.

6. Final result summary

The optimization simulation has revealed improvement in net energy generation. A comparison between initial designing and optimize final result is shown in Table 4.

Table.4. Comparison between initial and optimized designing of PTC

Parameters	Multan, Pakistan	Punjab
	Initial	Optimized
Annual Energy GWh	90.48	101.64
Capacity Factor	20.5 %	23 %
Solar multiple	2	2.2

Load hours	6 hrs.	2 hrs.
Gross to net efficiency	88.8%	89.8 %

7. Conclusions

It is evident from survey of the location that southern Punjab region is suited for solar energy production. The optimized result has shown that 101.64 GWh of energy is produced with storage load hours of 2 hrs. It is evident that increase in solar multiple will increase the production and maximum generation can be achieved at point where solar multiple is 8. Design and optimization has shown that Multan has good potential for solar energy production and also this area is suitable for CSP plant installation.

Punjab is most populated region and Multan is one amongst the mega cities of Pakistan. A Clean and green house free plant in this region will overcome energy demand with no emission. This will help in reducing the pollution.

Special subsidies from Govt. are requested in this regard. It will also helpful in human and capital development of the country. A designing, fabrication and installation will create new jobs.

REFERENCES

- [1] X. Li, E. Xu, L. Ma, S. Song, and L. Xu, "Modeling and dynamic simulation of a steam generation system for a parabolic trough solar power plant," *Renewable Energy*, vol. 132, pp. 998-1017, 2019.
- [2] N. Mahlangu and G. A. Thopil, "Life cycle analysis of external costs of a parabolic trough Concentrated Solar Power plant," *Journal of cleaner production*, vol. 195, pp. 32-43, 2018.
- [3] D. Ferruzza, M. Topel, B. Laumert, and F. Haglind, "Impact of steam generator start-up limitations on the performance of a parabolic trough solar power plant," *Solar Energy*, vol. 169, pp. 255-263, 2018.
- [4] M. Mehrpooya and A. Dadak, "Investigation of a combined cycle power plant coupled with a parabolic trough solar field and high temperature energy storage system," *Energy conversion and management*, vol. 171, pp. 1662-1674, 2018.
- [5] D. Popov and A. Borissova, "Innovative configuration of a hybrid nuclear-parabolic trough solar power plant," *International*



- Journal of Sustainable Energy*, vol. 37, pp. 616-639, 2018.
- [6] F. Calise, M. D. d'Accadia, L. Libertini, and M. Vicidomini, "Thermoeconomic analysis of an integrated solar combined cycle power plant," *Energy conversion and management*, vol. 171, pp. 1038-1051, 2018.
- [7] M. S. B. Fares and S. Abderafi, "Water consumption analysis of Moroccan concentrating solar power station," *Solar Energy*, vol. 172, pp. 146-151, 2018.
- [8] L. Guzman, A. Henao, and R. Vasquez, "Simulation and optimization of a parabolic trough solar power plant in the city of Barranquilla by using system advisor model (SAM)," *Energy Procedia*, vol. 57, pp. 497-506, 2014.
- [9] A. A. AlZahrani and I. Dincer, "Energy and exergy analyses of a parabolic trough solar power plant using carbon dioxide power cycle," *Energy conversion and management*, vol. 158, pp. 476-488, 2018.
- [10] B. P. Global, "BP statistical review of world energy June 2017," 2017.
- [11] A. Waheed Bhutto, A. Ahmed Bazmi, K. Qureshi, K. Harijan, S. Karim, and M. Shakil Ahmad, "Forecasting the consumption of gasoline in transport sector in Pakistan based on ARIMA model," *Environmental Progress & Sustainable Energy*, vol. 36, pp. 1490-1497, 2017.
- [12] S. Saleem and A. ul Asar, "Analysis & Design of Parabolic Trough Solar Thermal Power Plant for Typical Sites of Pakistan," *IOSR Journal of Electrical and Electronics Engineering*, vol. 9, pp. 2320-3331, 2014.
- [13] F. D. Economic Adviser's Wing, Government of Pakistan, "Pakistan Economic Survey 2016-2017," Islamabad, 2017.
- [14] R. Praveen, Abdul Baseer, Mohammad, A. B. Awan, and M. Zubair, "Performance analysis and optimization of a parabolic trough solar power plant in the middle east region," *Energies*, vol. 11, p. 741, 2018.
- [15] K. Mahboob, M. M. Aslam, A. Qaddus, A. Ahmad, U. Mushtaq, and A. Khan, "Design and Analysis of Tower Structure for Solar Thermal Power Plant," in *2018 2nd International Conference on Energy Conservation and Efficiency (ICECE)*, 2018, pp. 30-36.
- [16] K. Mahboob, A. Qaddus, M. M. Aslam, A. Ahmad, U. Mushtaq, and A. Khan, "Structural Design of Heliostat for Solar Thermal Power Plant," in *2018 2nd International Conference on Energy Conservation and Efficiency (ICECE)*, 2018, pp. 23-29.
- [17] F. Sorgulu and I. Dincer, "Design and analysis of a solar tower power plant integrated with thermal energy storage system for cogeneration," *International Journal of Energy Research*, 2018.
- [18] J.-Q. Guo, M.-J. Li, J.-L. Xu, J.-J. Yan, and K. Wang, "Thermodynamic performance analysis of different supercritical Brayton cycles using CO₂-based binary mixtures in the molten salt solar power tower systems," *Energy*, vol. 173, pp. 785-798, 2019.
- [19] E. C. Okonkwo, C. F. Okwose, M. Abid, and T. A. Ratlamwala, "Second-Law Analysis and Exergoeconomics Optimization of a Solar Tower-Driven Combined-Cycle Power Plant Using Supercritical CO₂," *J. Energy Eng.*, vol. 144, p. 04018021, 2018.
- [20] Q. Kang, R. Dewil, J. Degrève, J. Baeyens, and H. Zhang, "Energy analysis of a particle suspension solar combined cycle power plant," *Energy Conversion and Management*, vol. 163, pp. 292-303, 2018.
- [21] F. Yilmaz, M. Ozturk, and R. Selbas, "Development and performance analysis of a new solar tower and high temperature steam electrolyzer hybrid integrated plant," *International Journal of Hydrogen Energy*, 2019.
- [22] R. Ferreira, N. J. van Rensburg, and A. Nel, "A study into the efficiency of embedded solar photovoltaic cells in double roman shaped roof tiles," in *2018 5th International Conference on Renewable Energy: Generation and Applications (ICREGA)*, 2018, pp. 301-304.
- [23] N. El Gharbi, H. Derbal, S. Bouaichaoui, and N. Said, "A comparative study between parabolic trough collector and linear Fresnel reflector technologies," *Energy Procedia*, vol. 6, pp. 565-572, 2011.
- [24] D. Mills, "Advances in solar thermal electricity technology," *Solar energy*, vol. 76, pp. 19-31, 2004.
- [25] K. Lovegrove, G. Burgess, and J. Pye, "A new 500 m² paraboloidal dish solar concentrator," *Solar Energy*, vol. 85, pp. 620-626, 2011.
- [26] J. Coventry and C. Andraka, "Dish systems for CSP," *Solar Energy*, vol. 152, pp. 140-170, 2017.
- [27] P. H. Shaikh, F. Shaikh, and M. Mirani, "Solar energy: Topographical asset for Pakistan," *Applied Solar Energy*, vol. 49, pp. 49-53, 2013.
- [28] S. C. Stokler S, "Solar Resource Mapping for Pakistan: solar modelling report.



- ESMAP," *Renewable Energy Resource Mapping Initiative*. Washington, DC: World Bank Group, 2015.
- [29] W. B. G. International Finance Corporation, "A Solar Developer's Guide to Pakistan,," Jan 2016.
- [30] S. Adnan, A. Hayat Khan, S. Haider, and R. Mahmood, "Solar energy potential in Pakistan," *Journal of Renewable and Sustainable Energy*, vol. 4, p. 032701, 2012.
- [31] J. Spelling, A. Gallo, M. Romero, and J. González-Aguilar, "A high-efficiency solar thermal power plant using a dense particle suspension as the heat transfer fluid," *Energy Procedia*, vol. 69, pp. 1160-1170, 2015.
- [32] A. Fernández-García, E. Zarza, L. Valenzuela, and M. Pérez, "Parabolic-trough solar collectors and their applications," *Renewable and Sustainable Energy Reviews*, vol. 14, pp. 1695-1721, 2010.
- [33] U. Herrmann, B. Kelly, and H. Price, "Two-tank molten salt storage for parabolic trough solar power plants," *Energy*, vol. 29, pp. 883-893, 2004.
- [34] S. Odeh, G. Morrison, and M. Behnia, "Modelling of parabolic trough direct steam generation solar collectors," *Solar energy*, vol. 62, pp. 395-406, 1998.
- [35] D. Laing, W.-D. Steinmann, R. Tamme, and C. Richter, "Solid media thermal storage for parabolic trough power plants," *Solar energy*, vol. 80, pp. 1283-1289, 2006.
- [36] J. E. Pacheco, S. K. Showalter, and W. J. Kolb, "Development of a molten-salt thermocline thermal storage system for parabolic trough plants," *J. Sol. Energy Eng.*, vol. 124, pp. 153-159, 2002.
- [37] H. Michels and R. Pitz-Paal, "Cascaded latent heat storage for parabolic trough solar power plants," *Solar Energy*, vol. 81, pp. 829-837, 2007.
- [38] A. Farr and R. Gee, "The SkyTrough™ Parabolic Trough Solar Collector," in *ASME 2009 3rd International Conference on Energy Sustainability collocated with the Heat Transfer and InterPACK09 Conferences*, 2009, pp. 573-580.
- [39] P. technology. (11/22/2019). *The Andasol Solar Power Station Project*. Available: <https://www.power-technology.com/projects/andasolsolarpower/>



Collaborating Sharing Decentralized Solar Energy System in Pakistan

Syed Muhammad Kashif Shah¹, Tanzeel-ur-Rashid²

1- Department of Mechanical Engineering

2- University of Engineering and Technology Taxila, Pakistan

Corresponding Author: Email: Syed.kashif@uettaxila.edu.pk

Abstract:

This study signifies the need of a smart Integrated decentralized solar energy system in Pakistan. Since, outlook of energy is highly dominated by its power sector, policy measures must be adopted to ensure its penetration in system of any country. After Industrial, housing sector is the major energy consuming sector. In summer and peak load hours, this sector suffers high energy shortfall causing energy crisis. Currently, the whole country is driven through power supplied from the National Grid. The goal of this study is to assess energy generation through a smart Integrated decentralized solar energy system in the power hub of a commercial area in Taxila, Pakistan. Model Development involves a hypothetical model built on LabVIEW which allows user interface a way to intermingle by the source code. It permits the user to transformation of the values sent to the source code and see the information that the source code calculates. The proposed system is collaborative sharing integrate decentralized solar energy system. A system that credits sunlight-based energy framework proprietors for the power they add to different buildings due to collaborative sharing mechanism at Rs.10 per kWh. This low-cost electricity is available at your doorstep that you can share according to the collaborative sharing basis that will not range any certain variable.

Keywords: Decentralized Solar Systems, Collaborative Electricity Sharing, Solar View Electricity Model

1. Introduction

During the recent development in energy sector, petroleum products have driven all energy-based advancements. Since, the coal-period appearance, the world's interest for power kept on heightening and has kept on doing as such till date. Reports of International Energy Agency (IEA) confirm that during the following couple of decades the social and mechanical advancement of Global world will prompt a huge development in its power request. More noteworthy than the absolute current interest in the United States of America and Japan taken together [1]. Besides, the dispersion of new power based advancements, for example, electrical vehicles, will build the power request in industrialized locales, for example, Europe and United States which have prompted a general multiplication of power request [2]. Now the utilization of regular energy assets is over and over addressed due to its various hurtful ramifications on the general public and condition [3]. The dependable and prudent availability of these assets have turned into a reason for worry for some nations around the globe.

Furthermore, statistics suggest that a huge part of our emissions originate from coal-based technologies. Hence, this study identifies the major challenges in adoption of renewable energy

systems in Pakistan through a Decentralized Solar System. The overall energy deficiency has clearly upset the budgetary viewpoints, society, progression of the nations, and circumstances through ozone exhausting substances (GHGs) and by grabbing carbon credits. The creating enthusiasm of power over the world is being future and recorded to be exponential. Nonattendance of advantage with out of date framework system, ecological variation, increasing fuel costs, has come about inefficient and dynamically flimsy electrical structure.

1.1 Petroleum Decline

Rising energy request is thumping weight on petroleum derivative inventory and now oil investigation to "eccentric" oil assets. Changing after petroleum derivatives to renewable likewise offers considerable advantages, for example, autonomy from world market non-renewable energy source costs and the production of a great many innovative green employments. It may likewise give energy to two thousand million individuals right now without energy access. The changeover from the fossil-driven based energy sources to the sustainable power sources (SPS) is being tended to all-inclusive as per huge targets [4].



1.2 Climate Change Threat

The hazard of regular changes the most outrageous fundamental natural test being experienced by the globe since the start of the 21st time. It has critical repercussions for the world's social and financial predictable quality, its normal assets and expressly, the way wherein we produce our energy [5]. To avoid the most heart breaking impacts of climatic change, the overall temperature increase must be kept as far underneath 2°C as could be normal the situation being what it is. The essential ozone hurting substance is carbon dioxide (CO₂) made by using oil-based goods for energy and transport. In the event that rising temperatures are to be kept inside estimable breaking points, by then we have to all around reduction of our GHG transmissions [6].

1.3 Security of Supplies

Access to the two supplies and budgetary soundness is presently at the highest point of the energy approach motivation. Quickly fluctuating oil costs are lined to a mix of numerous occasions, anyway one explanation behind these value variances is that provisions of every single demonstrated asset of non-renewable energy sources are getting to be rare and progressively costly to create [7]. Some 'non-traditional' assets, for example, shale oil have turned out to be financial, with obliterating ramifications for the neighbourhood condition. Price decrease in only the previous two years have altered the financial aspects of renewable. In a general sense, particularly wind and sun powered photovoltaic (PV) alongside the normal highlights like, emanation of practically no GHG and for all intents and purposes endless fuel.

1.4 Decentralized Solar System

Decentralized system is opposite to centralized system in many regards. It does not require grid stations, sub-stations, transmission lines etc. It refers to smaller energy systems that produce energy on-site or near-site. The consumer often owns the system and directly receives the financial benefits of the system. In many locations, excess electricity which is not used by the owner can be sold to the local service and distributed for more widespread use. As it does not need transmission lines over long distances, therefore transmission losses are negligible. There are also no voltage losses or less voltage losses. Hence, it is more efficient than centralize solar power systems. The

end user is not completely dependent on Grid stations. Check and balance of the energy demand is done by the owner themselves [8][9][10][11].

1.5 Centralized System

Centralized systems are like traditional grid systems, which require transmission lines, distribution system, sub stations etc. It is the source of large power production and distribution to users via Grid station. It is mainly employed for the transmission to the long distances. Centralized solar power system is a large-scale system which requires large land scale and it is highly depend on the geographical location of the country. This system requires huge capital investment. Although it is beneficial, but the main issues are transmission losses due to long distances and its high cost.

There is a lot of potential available in Pakistan in the field of decentralized solar power systems and collaborating sharing mechanism of power. Several problems also exist such as political preference towards a more centralized system in favour of political power; however, the decentralized systems can be made part of the national grid as well as costs regarding the implementation of the system in rural areas in terms of affordability. However, currently no assessment has been performed using data sets of Pakistan. Hence, a large research room is available in this area. The next section of the study discusses the development of model on LabVIEW and the methodology adopted for performing this research. Further, the study will discuss the results obtained from this model and what policy measures can be adopted to promote its interpretation.

2. Methodology and Data Collection

2.1 Case Study Approach

The model is developed for the city of Taxila, Pakistan. The system is installed on roof tops and is analysed using various resources. The experimental data collection is from the installed four solar panels on the experimental bases to study the generation and consumption at the other end. As per the field model study and their energy consumption requirements the proposed model of sustainable green energy shows a tremendous output of saving energy. There recorded energy consumption analysis of WPADA and SOLAR ENERGY. Solar energy gives highlights of brilliant offer loads of preference and future viewpoints. Mono crystalline PV solar panel consumes sunlight as a source of energy to produce power. A mono crystalline photovoltaic (PV) module is a blend of



photovoltaic sun-based cells accessible in various voltages and wattages. It is established of a variety of a photovoltaic system that produces and supplies sun-based power in business and nearby areas. It has modules that involve wafer-based crystal-like silicon compartments or wobbly film cells [12][13][14].

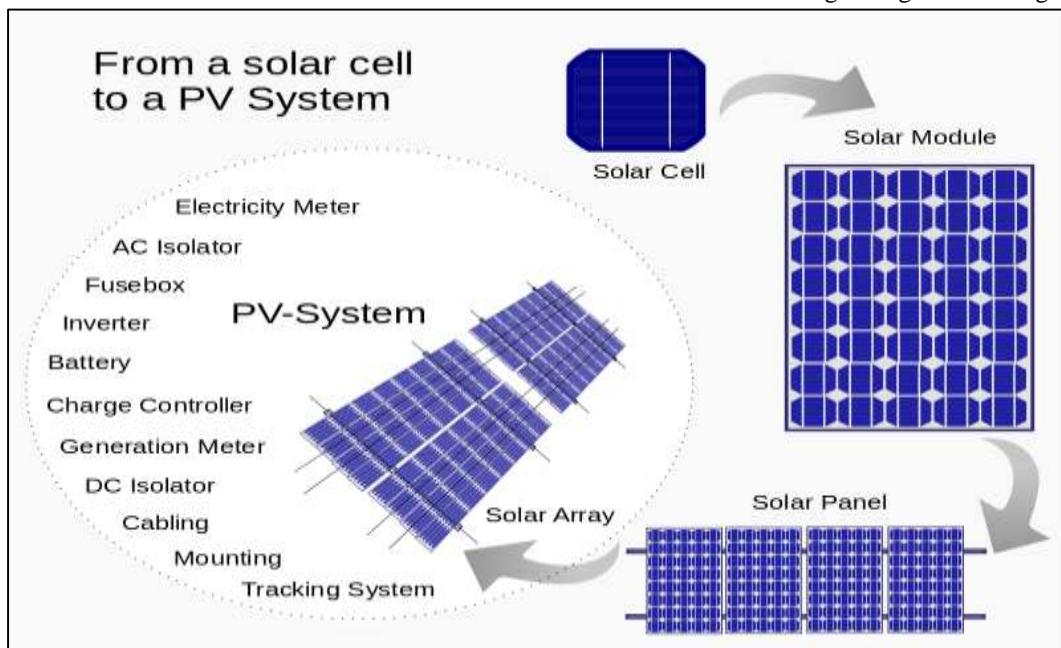
The cells are associated electrically in arrangement, to each other to an ideal voltage, and after that in parallel to expand ampere. The voltage and amperage of the module are increased to make the wattage of the module.

A PV connection box (ensure connections and give wellbeing hindrances) is connected to the back of the solar panel and it is its produce interface. Generally, PV modules use MC4 connector's sort to encourage simple weatherproof connections with the framework. Module connections are made in arrangement to accomplish an ideal produce voltage or in parallel to give an ideal current ability (amperes) of solar panel. The directing wires that take the current off the modules are estimated by the limit. Sidestep Diodes are utilized remotely for halfway module sharing to boost the yield. Sun powered boards additionally utilize metal casings comprising of racking segments, sections, reflector shapes, and troughs to more readily bolster the board structure.

these 4 house buildings after the data collection. This gathered data was recorded and monitored in the next process. Furthermore, we inspected the behaviour of almost 1 year data. On the basis of the behaviour of the inspected data, I examined the performance of my system according to the Global Horizontal Irradiance (GHI). By using the SAM model and LabVIEW generated the hypothetical model for the project and scanned the result outcome from the data.

So, this entire description regarding the collection of data, recording monitoring and analysis of data, I have explained all the major processing regarding my project of Decentralized Solar Energy System every one of the components can be utilized by the willing of the buyer. It relies upon the heaps whether it will control for both day and night or likewise in capricious circumstances. The present innovation has been progressed to the point that numerous devices and gadgets have been imagined that can keep running by sun powered legitimately. On the off chance that a buyer possesses those advances, he/she needn't bother with additional energy to run them for quite a while. Subsequently, the loads can be wiped out, and energy can be spared.

The capacity of this framework isn't unique in relation to the brought together sunlight-based



2.2 Model Development

This model will be integrated to perform the research. Data was collected of 4 house buildings which has been selected earlier to run the proposed system. The solar systems have been implanted on

energy framework. Every one of the components can be utilized by willing of buyer. It relies on the heap it will control for both day and night additionally in capricious conditions. A smaller than usual coordinated framework alludes to a lot



of power age and energy stockpiling. Frameworks are interconnected to the dispersion arrange that provisions power to a restricted gathering of clients. Smaller than expected coordinated frameworks are bigger in size than miniaturized scale. The kinds of burden that are served my smaller scale are typically private or are extremely little business while scaled down incorporated framework can serve huge business and little industrial burden.

3. Results and Discussion

This section provides the results of model Smart Integrated De-Centralized Solar Energy System. The process is done based on collaborative sharing system of individuals where each of them would share the electricity load. This collaborative sharing model is highly recommendable to dig out maximum benefits out of solar energy. The leading prospect of this project is the collaborative sharing of the energy where the surplus light of each house would be travelled to the houses with less light comparatively. This could be rated as the foremost emerging business model as well.

3.1 Decentralized Integrated System

This system has worked on the principle of collaborative sharing mechanism as the buildings are integrated with each other. Due to integration, there will be no wastage of electricity. These buildings share the extra amount of electricity with each other that will be recorded by our Decentralized Solar Energy System. In this way there is maximum usage of solar electricity.

3.2 Good Business Model:

Due to maximum usage of energy and cost minimization this system is a good individual and industrial business model. Similarly, it has maximum efficiency and the minimum lifetime of 25 years when the load is 80%.

3.3 Surplus power Generation and utilization:

Our system has efficiently recorded the power generation and utilization by all the building. Similarly, if any building has surplus power it will

also show in our record. The following figure shows the complete data including power generation, utilization and Surplus power.



3.4 Data Recording and monitoring

There are energy meters attached with each home in entire building and an energy meter overall for a building. These meters calculate records of energy used and an overall meter calculates the energy produces utilized and surplus power. Similarly, there is also a record unit shared by a building to another building. Due to integrated system the surplus power being shared between all of the buildings depending upon their requirements and is recorded by our system. Smart integrated decentralization is a business model its billing mechanism that credits solar energy system owners for the electricity they add to the other buildings due to collaborative sharing mechanism. For example, on the off chance that a private client has a PV framework on their rooftop, it might create more power than the home uses during sunlight hours.

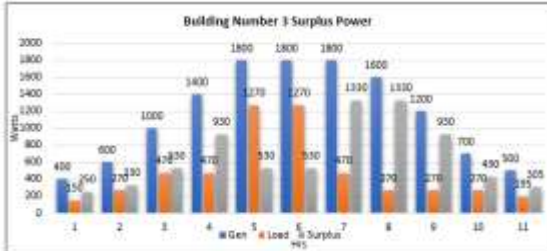
Installing 1000 Watts (250 Watt x 4 pcs) Solar Panels (A1 Brand) by applying the power factor of $(1.5 * 1000) = 1500$ Watts (250 Watt x 6 pcs will generate consumers an average of 4,000 Watts per day, this equals to savings of 4 electricity WAPDA units per day.



Table 1 Collaborative sharing Electricity billing Monthly basis

Collaborating sharing Electricity billings Monthly basis								
Sr.#	Buildings	Electricity Generation (kWh)	Electricity Consumed (kWh)	Required Electricity (kWh)	Surplus Electricity (kWh)	Shared Electricity (kWh)	Remaining Surplus Electricity (kWh)	Total Bill Units*10=RS PKR
1	B1	266	138		128		16	
2	B2	245	357	112		B1 shared 112 units to B2		1,120
3	B3	354	454	100		B4 shared 100 units to B3		1000
4	B4	225	100		125		25	

3.5 Collaborating sharing Electricity billings Monthly basis



In this table above, explained the process through which the consumers will utilize the electricity on collaborative sharing basis. The building 1 is generating 266 kWh and consuming 138 kWh with the surplus electricity of 128 kWh. If we look at the remaining surplus electricity, its reading is 16 kWh. Coming towards the 2nd building, it is generating 245 kWh power, its electricity consumption is 357 kWh and required electricity is 112 kWh. As the building 2 has less power generation in comparison to building 1, the electricity load of building 2 is greater than its generation, so required 112 kWh. Building 1 will share 112 units with building 2. The total bill will be paid by building 2 at the end of the month that is calculated Rs.1120 according to the fixed per unit rate of Rs.10. building 3 is generating 354 kWh, its electricity consumption is 454 kWh and required electricity is 100 kWh which is not enough for building 3 so it will fulfill its need from

building 4 by sharing 100 kWh. Whereas, building 4 generates 225 kWh units and its consumption is 100 kWh with the surplus light of 125 kWh. Remaining surplus would be 25 kWh and the total bill will be paid by building 3 that is calculated to Rs.1000.

4. Discussion and Conclusion

In this study, the work has been performed on Smart Integrated De-Centralized Solar Energy System. The process done is collaborative sharing on the basis of need of the individuals where each of them would share the load of the energy. Furthermore, I have collected field data for this study from the area of Taxila. Our main focus was collecting the data of electricity unit consumption of all the houses in that area. After gathering the field data, I started comparison among the unit consumers monthly and yearly for 2018 and 2019. After this field study data also calculating the unit's prices of WAPDA with comparison of our system. The Arduino Mega 2560 Micro-controller has been used in this project. This micro controller is used for this system for data monitoring and data recording and working efficiently for surplus light and shared to other buildings. The leading prospect of this project is the collaborative sharing of the energy where the surplus light of each house would be travelled to the houses with less light



comparatively. This could be rated as the foremost emerging business model as well.

The generation of kWh from this decentralized Integrated Solar Energy System and the working process of the system are listed below:

- The basic reason and working process is to read out the power generated then deliver this information to the controller
- All that process will resume after judging, monitoring and specifying the data.
- There are some relay switches that deal with function of monitoring the data inflow and outflow on the meter.
- The relay switches are attached to the controller that will turn on and off after monitoring wherever the power is required.
- After that, the energy will be travelled to the house where there would be a need of extra units through these relay switches.

Integrated De-Centralized Solar Energy System will offer cheaper and fixed electricity rates than regular market rates offered by WAPDA to the layman that will create a massive change in the electricity bills. The power will be generated and utilized by all the buildings. Similarly, if any building has surplus power that will also be shown in our record and it will be shared to the required house that will have less electricity generation. Due to maximum usage of energy and cost minimization this system is a good industrial business model.

More power could be used through solar panels means maximum efficiency of solar energy would be utilized. The distribution of energy through Decentralization would be very effective and cause decrease in electricity bill as well.

5. Future Recommendations:

There is a lot of potential available in Pakistan in the field of decentralized solar power systems and collaborating sharing mechanism of power. Several problems also exist such as political preference towards a more centralized system in favour of political power, however the decentralized systems can be made part of the national grid as well as costs regarding the implementation of the system in rural areas in terms of affordability.

- Smart integrated Decentralized solar power systems should be initiated in Pakistan.

- Develop this collaborating sharing mechanism of system in Pakistan.

REFERENCES

- [1] M. Kamran, "Current status and future success of renewable energy in Pakistan," *Renew. Sustain. Energy Rev.*, vol. 82, no. October 2017, pp. 609–617, 2018.
- [2] R. Aziz and M. B. Ahmad, "SPECIAL REPORT: Pakistan's Power Crisis - The Way Forward," pp. 1–18, 2015.
- [3] M. W. A., "ECO-FRIENDLY ENERGY IN PAKISTAN."
- [4] HDIP, *Pakistan Energy Yearbook*. 2018.
- [5] Safiya Aftab, "Pakistan's energy crisis: causes, consequences and possible remedies," no. January, pp. 1–4, 2014.
- [6] M. Arshad Javaid, S. Hussain, Z. Arshad, Ma. Arshad, and M. Idrees, "Electrical Energy Crisis in Pakistan and Their Possible Solutions," *Int. J. Basic Appl. Sci. IJBAS-IJENS*, vol. 11, no. October, pp. 5–38, 2011.
- [7] IEA, "Tracking Clean Energy Progress," IEA17, 2017.
- [8] K. Saeed, "Pakistan's Power Crisis: Challenges and the Way Forward," *Q. Criterion Mag.*, vol. 8, no. 4, 2013.
- [9] A. N. Khan, T. Begum, and M. Sher, "Energy Crisis in Pakistan: Causes and Consequences," *Abasyn J. Soc. Sci.*, vol. 4, no. 2, pp. 341–363, 2010.
- [10] G. Das, M. Aslam, H. Rahman, R. Samoo, N. Hussain, and K. Harijan, "Overcoming electricity crisis in Pakistan: A review of sustainable electricity options," *Renew. Sustain. Energy Rev.*, vol. 72, no. November 2016, pp. 734–745, 2017.
- [11] R. Shabbir and M. Taneez, "Rural and Urban Household Demand Analysis for Electricity in Pakistan," no. January 2013, 2014.
- [12] "USE OF SOLAR PHOTOVOLTAIC POWERED FANS."
- [13] "Pakistan Economic Survey," 2016.
- [14] P. B. of Statistics, "Census 2017," 2017.



Analysis of Wind Energy Potential of Southern Punjab using Measured Data

Arslan Ahmad¹, Usama Bin Saeed¹, Ammara Kanwal¹, Zia ul Rehman Tahir¹, Muhammad Asim¹, Hafiz Ameer Hamza¹, Naeem ullah Khan¹, Muhammad Zeeshan Jamil¹ and Muhammad Abdullah¹

1-Department of Mechanical Engineering, University of Engineering and Technology, Lahore,

*Corresponding author: ziartahir@uet.edu.pk

Abstract

Pakistan needs an indigenous source of energy for power production to make it independent of fossil fuels. Renewable technologies especially wind is a good solution to this issue. This study aims to examine the wind potential and to select the most economical and efficient turbine for Bahawalpur, Punjab, Pakistan. Wind speed of 10-minutes averaged-measured data at 20, 40, 60 and 80 m height is obtained from the mast installed by the World Bank in the area under study. Distribution frequency of wind speed, power density and wind potential are calculated. After a review, 10 turbines are selected and the net capacity factor, annual energy production and the levelized cost of electricity is computed. It is concluded that site under consideration belongs to wind class IV with annual mean wind speed of 5.15 ms^{-1} and annual wind power density of 134.88 Wm^2 at 80 m height. It is also concluded that, even under these conditions the Gamesa G136-4.5 MW wind turbine can produce 17.02 GWh annually with net capacity factor of 43.17% at 4.76 US cents/KWh. This study is useful for the future development of the wind farm at Bahawalpur, Punjab, Pakistan.

Key Words: Renewable energy, Wind energy, Wind Turbines, Capacity Factor

1 Introduction

Pakistan is dependent on fossil fuels (20% on petroleum and 34% on natural gas) for power production which is imparting bad impacts on its economy due to constantly increasing prices of fuels [1]. These impacts have forced the policymakers of Pakistan to make a change in energy policy. The best solution to solve this problem is to invest in Renewable Energy technologies [2]. In these technologies, wind is a good sustainable option [3, 4]. Pakistan is blessed with great wind potential as assessed by the Pakistan Meteorology Department (PMD) in 2002. Pakistan has 346 GW of wind energy potential above-mentioned out of which only 120 GW is feasible. Pakistan has 33000 MW installed capacity, while the installed wind potential is only 1.8 GW installed. Hence, wind energy's share in the total power production of the country is about 5.5% [1]. The use of wind energy for power production is increasing exponentially day by day. The installation of a wind farm requires accurate and reliable data of wind speed. Because minor deviation in wind speed has cubic effect on wind potential. For this purpose, World Bank in collaboration with Alternative Energy Development Board (AEDB), has installed 12 masts at different locations in Pakistan. One of the masts had been installed in Bahawalpur, Punjab, which was commissioned in 2016 [5]. This paper uses the wind data provided by this mast to find the wind potential and to select the most suitable turbine for the annual energy production at this site so that

annual energy production (AEP) can be enhanced and energy cost can be decreased for wind turbines.

This study leads to analyze the wind power density (WPD), AEP, capacity factor (CF) and the levelized cost of electricity (LCOE). Then different turbines have been selected and compared to get the best turbine in the area under study [6]. This method has been used in literature for the same purpose at different locations. Irfan et al. [7] calculated the wind potential for Keti Bandar, Pakistan by calculating the above-mentioned parameters. Similarly, Teimourian et al. [8] assessed wind potential at Southeastern province of Iran.

In this study, assessment of wind potential and turbine selection has been made at Bahawalpur, Punjab. The wind data measured at 20, 40, 60 and 80 m height for 2-years (2016-2018) was obtained from the mast at the location under study installed by the World Bank. WPD, AEP and CF are calculated. After that, different turbines are selected based on the CF and cut-in speed. Finally, economic assessment is performed to understand whether they are economically feasible or not.

2 Wind Data

The World Bank and Alternative Energy Development Board, Pakistan, in collaboration with each other installed a wind measuring mast at Bahawalpur, Punjab Pakistan. The design and installation of this mast is according to International Electrotechnical Commission (IEC) standards.



The wind mast was installed in Bahawalpur situated in the South-East of Punjab. The geographical location of the site is 29.326° N and 71.815° E. This location is land with flat terrain and is wide open with no obstruction in the surroundings of wind mast. The sampling rate of the data measurement was 1 Hz, the data provided by the acquisition system was averaged over 10-minute duration. To measure the wind speed, five anemometers were installed on the mast at heights of 20, 40, 60 and 80 m. Two wind vanes were installed at heights of 58.5 and 78.5 m to measure the direction of wind [5]. The data for the two-year duration from 1st September 2016 to 1st September 2018 is used for this study.

3 Methodology

3.1 Wind Speed Frequency Distribution

Determination of the wind frequency distribution for the wind energy potential of any location is imperative. Several Probability Density Functions (PDF) such as Beta, Gamma, Gaussian, Weibull, lognormal and Rayleigh distribution have been used in various previous studies. Wind performance is greatly dependent on PDFs to accurately analyze the wind speed data [9]. Most commonly used PDF is Weibull distribution because it is very simple, accurate and most importantly it provides a good fit to the measured data [10]. There are two parameters of Weibull distribution (shape and scale factor) which can be measured by different methods.

3.2 Wind Power Density and Wind Energy

WPD uses mean wind speed to find the wind potential at a specific site. WPD indicates dependence of wind power on air density and frequency distribution of wind speed. The wind potential is considered to be better explained by WPD as compared to wind speed since it shows the strength of winds in all over the time period at the specific site. It can be calculated by Eq. (1) [11].

$$WPD_{obs} = \frac{1}{2N} \rho \sum_{i=1}^N u_i^3 \quad (1)$$

3.5 Selection of Turbines for Analysis

3.3 Net Capacity Factor and Energy Output

The important factor which affects the performance of a wind turbine is its CF. Basically, it shows how much power is being produced out of the maximum energy which can be produced. Hence, it is defined as the ratio of mean maximum possible output power and rated power of the turbine over a period of time (2 years) (Eq. (3)) [10, 12]. The gross power output of a turbine is calculated using wind speed at the required height, the power curve of a specific turbine and air density. The net capacity factor is the ratio of net average output power over a certain period of time to the power when it is operated at its rated speed (Eq. (4)). The net power (P_{net}) can be calculated using the overall loss factor ($f_{overall}$) from gross power output (P_{out}) as in Eq. (2).

$$P_{net} = (1 - f_{overall}) \times P_r \quad (2)$$

$$CF = \frac{P_{out}}{P_r} \quad (3)$$

$$NCF = \frac{P_{net}}{P_r} \quad (4)$$

The AEP can be calculated by multiplying net power output of the turbine with the hours in a year, i.e. 8760 hours for non-leap years. Hence, AEP depends upon net power which further depends upon the wind speed. It can be calculated using Eq. (5) [13].

$$E_{ann} = P_{net} \times 8760 \quad (5)$$

3.4 Levelized Cost of Electricity

Economic feasibility in this study is performed by computing LCOE using Eq. (6). It represents the average cost per unit of electricity that would be required to recover the initial capital investment (I_i), maintenance and operational cost (M_i), transportation and grid connection cost (T_i) in the supposed period of time (T) using interest rate (r) [14].

$$LCOE = \frac{\sum_{t=0}^T (I_i + T_i + M_i) / (1+r)^t}{\sum_{t=0}^T E_t / (1+r)^t} \quad (6)$$

Table. 1 Characteristics of Selected Turbines

Turbine	P (MW)	Hub Height (m)	Rotor Dia. (m)	Cut-in speed (m/s)	Rated speed (m/s)	Cut-out speed
Gamesa G136-4.5 MW (120m)	5.0	120	136	1.00	10.0	28
REpower MM100 60Hz (120m)	2.0	100	100	3.00	11.0	22
Windtec FC 2000-Sinoma 50.2 (120m)	2.0	100	103	3.00	10.0	20
Windtec DD 3000-125 (120m)	3.0	110	125	2.75	10.3	25
Windtec DD 3000-140 (120m)	3.0	110	140	3.00	10.0	20
Goldwind GW 140/3.0 (120m)	3.0	120	140	2.50	10.5	21



Fuhrländer Wind technology LLC (120m)	3.0	120	120	3.00	12.0	17
LTW104 2000 (120m)	2.0	143	104	3.00	12.0	14
SG.2500.131DD (120m)	2.5	120	131	2.50	10.0	21
SG.2700.116DD (120m)	2.7	100	116	3.00	10.5	21

To find the most effective and economical turbine at the area under study, 300 turbines were reviewed on the basis of their capacity factors, cut-in, and cut-out speeds and LCOE. Out of these turbines, 10 are selected which have capacity factor more than 20% and cut in speed less than or equal to 3 ms^{-1} . The details of these turbines are shown in Table 1. The rated power, hub height, diameter, rated wind speed and cut-in wind speed ranges from 2.0 to 5.0 MW, 110 to 143 m, 100 to 140 m, 10 to 12 ms^{-1} and 1 to 3 ms^{-1} respectively.

4 Results

4.1 Wind Speed Characteristics

For the site under study, monthly mean wind speed for 2-years data at 80 m height is shown in Fig. 1. It ranges from 5.96 ms^{-1} to 3.72 ms^{-1} while the annual mean wind speed is 5.15 ms^{-1} . The maximum mean wind speed is observed in June while the minimum mean wind speed is observed in the month of November. The overall trend shows that the monthly mean wind speed increases from January to June, then decreases from June to December with some exceptions. It has been

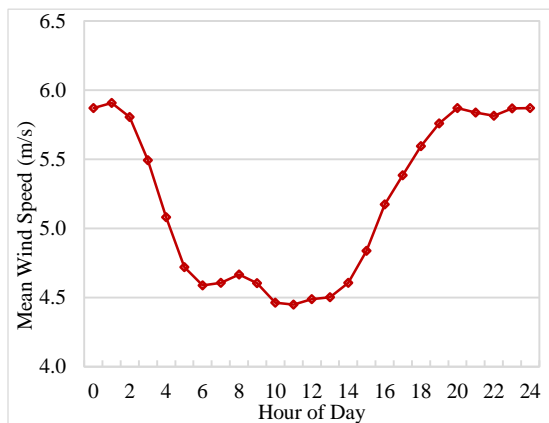


Fig. 1 Monthly mean wind speed

seen that the monthly mean wind speed is maximum in Summer season while it is minimum in Winter season. For the future wind power production, if a turbine is installed at that location, then it will give maximum power output in Summer season. The increase in the monthly mean wind speed from December to January is because the temperature is low in these months due to thermal convection causes momentum of the upper air transmitted to the lower layer [15].

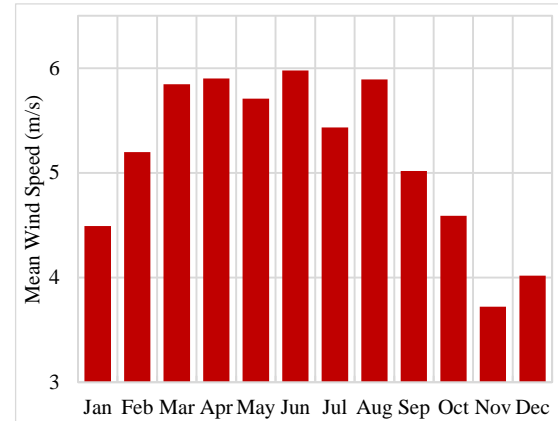


Fig. 2 Diurnal mean wind speed

Fig. 2 shows the average daily wind speed profile (diurnal mean wind speed) of 2-years data. As diurnal indicates the hour of the day in whole year which has the most suitable wind speed. It has been observed that 12 am to 12 pm are windy hours of the day while for remaining time it was constant. It is shown that wind speed increases after 12 pm and keep on increasing till 7 pm with a value of 5.87 ms^{-1} then it decreases to 5.81 ms^{-1} at 9 pm after that it increases to a maximum value of 5.91 ms^{-1} at 12 am. After this time, it slows down till 12 pm. Overall it is observed that for whole period, wind speed is consistent in day time and it has an increasing trend for evening as shown in Fig. 2. So, if a turbine is installed at the studied site, it will give maximum power output in the day time.

4.2 Weibull Probability Density Function

In order to determine the inconsistency of wind speed, Weibull PDF was used [10]. The mean annual wind speed frequencies and the corresponding best fit Weibull line is shown in Fig. 3. It is observed that the most frequent wind speed is 5.82 ms^{-1} as indicated by the peak of the frequency distribution curve. It is observed that Weibull curve has a good fit to the measured data of wind. The Weibull shape (a) and scale (k) factors are calculated and their values are 2.18 and 5.82 ms^{-1} respectively.

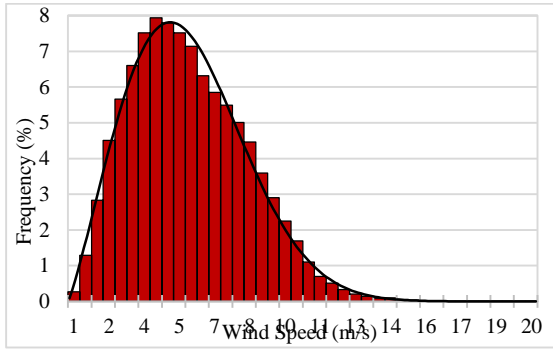


Fig. 3 Weibull Probability Density Function and best-fit line

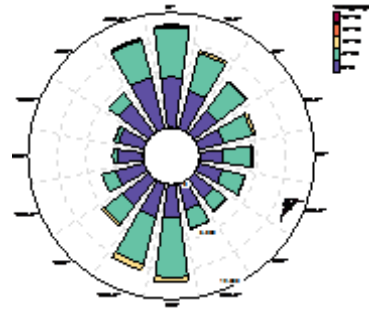


Fig. 4. Wind Rose

4.3 Wind Rose

Wind rose is also an important factor for the assessment of wind potential and to install a wind turbine at given site. The wind rose diagram is commonly used to access dominating wind direction at a specific site. The wind rose diagram was plotted in terms of wind direction frequency for 16 sections and each covering an angle of 22.5°. So, the distribution of the wind speed in different directions at 80 m height is shown as a polar diagram Fig. 4. This diagram is divided into 16 parts so each part corresponds to an angle of 22.5°. It is observed that the dominating wind speed was in North and South direction. After that the highest frequency of wind direction is observed in West of the South. The least frequency of the wind direction is observed in West direction

4.4 Wind Power Density

Wind power density (WPD) is calculated by mean wind speed, and it is an important factor to determine the wind potential at given site. For the site under consideration, WPD is shown in Fig. 5, it is observed that WPD ranges from 207.58 Wm^{-2} to 56.12 Wm^{-2} . The maximum WPD is observed in June while the minimum in November. The overall trend of graph showed that the WPD decreases from the maximum value in June to the minimum value in November then again it increases from November to May with some exceptions.

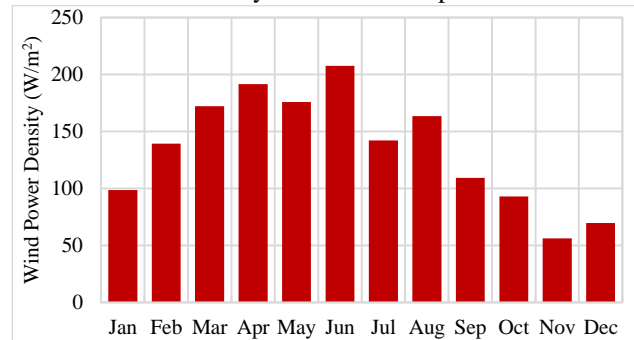


Fig. 5 Monthly mean Wind Power Density

4.5 Performance assessment of selected turbines

Table. 2 Annual CF and Energy Output of Selected Turbines

Turbine	Net CF (%)	AEP (GWh)	LCOE US cent/KWh
Gamesa G136-4.5 MW	43.17	17.02	4.76
Windtec FC 2000-Sinoma 50.2	23.13	4.05	8.88
Windtec DD 3000-140	28.02	7.36	7.33
Windtec DD 3000-125	24.03	6.32	8.55
REpower MM100 60Hz	24.27	3.83	9.41
Goldwind GW 140/3.0	31.7	8.33	6.48
Fuhrländer Wind technology LLC	25.02	6.58	8.21
SG.2700.116DD	21.95	5.19	9.36
SG.2500.131DD	30.68	6.72	6.70
LTW104 2000	26.71	4.68	7.69



As described above 10 turbines were selected for performance analysis. The evaluation of CF and AEP for selected turbines was based on Weibull probability distribution function. It can be seen that the most effective parameter in the analysis of wind turbine performance is CF which has a direct effect on the cost of electricity generated. The exponent power law approximation is used to find the wind speed at the desired hub height. Table 2 shows CF and AEP for the selected turbines. It is observed that Gamesa G136-4.5 MW turbine has the maximum CF (43.17%) at 120 m hub height. The minimum CF (21.95%) is observed for SG.2700.116DD turbine at 120 m hub height. Wind turbine Gamesa G136-4.5 MW has cut-in speed of 1 ms^{-1} while SG.2700.116DD has 3 ms^{-1} due to which Gamesa G136-4.5 MW shows maximum CF. After Gamesa G136-4.5 MW, highest CF (31.7%) is shown by Goldwind GW 140/3.0.

AEP for selected turbines is also present in the Table 2. It is shown that 17.02 GWh is the maximum AEP for Gamesa G136-4.5 MW and 4.05 GWh is the minimum AEP for Windtec FC 2000-Sinoma 50.2. It is because prior wind turbine has more CF as compared to the latter one. It is also shown that after Gamesa G136-4.5 MW, good AEP is shown by Goldwind GW 140/3.0, which is 8.33 GWh. So, Gamesa G136-4.5 MW is the best turbine on the basis of CF and AEP.

Economic assessment of all selected wind turbines is performed by calculating LCOE, which is shown in Table 2. The values of LCOE range from 4.76 to 9.41 US cents per KWh. According to the cost analysis, the Gamesa G136-4.5 MW turbine is the most economical wind turbine with the minimum value of 4.76 US cents per KWh. The maximum value (9.41 US cents per KWh) of LCOE is achieved by the RE-power MM100 60Hz turbine. The value of LCOE for Goldwind GW 140/3.0 is 6.48 US cents per KWh which is also reasonable.

From these results, it can be concluded that the most efficient and economical turbine, is Gamesa G136-4.5 MW because it shows maximum CF, AEP and minimum LCOE. The second-best choice is Goldwind GW 140/3.0.

5 Discussion

It is observed that the annual mean wind speed at Bahawalpur is 5.15 ms^{-1} . According to IEC standards for wind speed, this speed comes in class-IV which

indicates that wind at this site is low [16]. Also, annual WPD at the specified site is 134.88 Wm^{-2} which shows that wind potential at this site is not so good. Even in these conditions when a turbine like Gamesa G136-4.5 MW has cut-in speed of 1 ms^{-1} and hub height of 120 m is installed at this location, it can produce 17.02 GWh annually with net CF of 43.17%. As mentioned earlier, the LCOE for this turbine is 4.76 US cent/KWh, which is also economical. The second-best turbine which can produce 8.33 GWh annually with CF of 31.7% is Goldwind GW 140/3.0. This turbine can produce electricity at 6.48 US cent/KWh. Since the winds at Bahawalpur are strong in day-time so if turbines are installed at this location, they can meet the desired power production in day-time while in night time other power sources should be considered. In this way dependence on non-sustainable sources for power production can be reduced.

Conclusion

In this study the wind energy potential at Bahawalpur site is analyzed and turbine model suitable for this location is suggested. The wind energy potential at this site is not very good relative to other sites in the world where the wind energy potential is very good. So, the purpose of this study is to suggest wind turbine models for the sites where the wind potential is not so good. The wind data for this site for 2 years was measured at 10 min interval for 20, 40, 60 and 80 m heights and the feasibility of the turbines at this site is investigated. It is concluded that wind for Bahawalpur comes

under wind class-IV (as criteria developed by IEC) since monthly mean wind speed ranges from 5.96 ms^{-1} to 3.72 ms^{-1} and annual mean wind speed is 5.15 ms^{-1} . Also, in the evening, there is more wind speed as compared to the morning or night. The most frequent wind speed in the 2-year time period is in between $3\text{-}4 \text{ ms}^{-1}$ and the most frequent wind direction is North and South. Monthly WPD ranges from 207.58 to 56.12 Wm^{-2} and annual WPD is 134.88 Wm^{-2} . The comparison of 10 different selected turbines is done and it is concluded that due to the low value of cut in speed of 1 m/s , low value of LCOE (4.76 LCOE/kwh), a high value of CF 43.17 and consequently a high value of rated power (5MW), Gamesa G136-4.5 MW is the best choice for this site (Bahawalpur, Pakistan) and similarly for the sites where it is supposed that the wind energy potential is not very good.

REFERENCES

1. National Electric Power Regulatory Authority, *State of Industry Report 2018*. 2018.

2. Tahir, Z.u.R., et al., *Comparison of Reanalysis, Analysis and Forecast datasets with measured wind data for a Wind Power Project in Jhimpir, Pakistan*. Journal of Physics: Conference Series, 2018. **1102**: p. 012004.



3. Ritter, M. and L. Deckert, *Site assessment, turbine selection, and local feed-in tariffs through the wind energy index*. Applied Energy, 2017. **185**: p. 1087-1099.
4. Tahir, Z.u.R., et al., *Evaluation of ERA-Interim and NCEP-CFSR Reanalysis Datasets against in-situ Measured Wind Speed Data for Keti Bandar Port, Pakistan*. Journal of Physics: Conference Series, 2018. **1102**: p. 012001.
5. The World Bank, *Wind Resource Mapping in Pakistan, Site Installation Report: All Masts*. 2017.
6. Fazelpour, F., E. Markarian, and N. Soltani, *Wind energy potential and economic assessment of four locations in Sistan and Balouchestan province in Iran*. Renewable Energy, 2017. **109**: p. 646-667.
7. Ullah, I., Q.-u.-Z. Chaudhry, and A.J. Chipperfield, *An evaluation of wind energy potential at Kati Bandar, Pakistan*. Renewable and Sustainable Energy Reviews, 2010. **14**(2): p. 856-861.
8. Teimourian, A., et al., *Assessment of wind energy potential in the southeastern province of Iran*. Energy Sources, Part A: Recovery, Utilization, and Environmental Effects, 2019: p. 1-15.
9. Ucar, A. and F. Balo, *Assessment of wind power potential for turbine installation in coastal areas of Turkey*. Renewable and Sustainable Energy Reviews, 2010. **14**(7): p. 1901-1912.
10. Allouhi, A., et al., *Evaluation of wind energy potential in Morocco's coastal regions*. Renewable and Sustainable Energy Reviews, 2017. **72**: p. 311-324.
11. Shu, Z.R., Q.S. Li, and P.W. Chan, *Statistical analysis of wind characteristics and wind energy potential in Hong Kong*. Energy Conversion and Management, 2015. **101**: p. 644-657.
12. Wang, J., J. Hu, and K. Ma, *Wind speed probability distribution estimation and wind energy assessment*. Renewable and Sustainable Energy Reviews, 2016. **60**: p. 881-899.
13. Manwell, J.F., J.G. McGowan, and A.L. Rogers, *Wind Energy Explained: Theory, Design and Application*. 2010: Wiley.
14. Bahrami, A., et al., *Technical and economic analysis of wind energy potential in Uzbekistan*. Journal of Cleaner Production, 2019. **223**: p. 801-814.
15. Fyrippis, I., P.J. Axaopoulos, and G. Panayiotou, *Wind energy potential assessment in Naxos Island, Greece*. Applied Energy, 2010. **87**(2): p. 577-586.
16. LM Wind Power. *IEC wind classes*. 27/10/2019]; Available from: <https://www.lmwindpower.com/>.



Energy saving potential of evaporative cooling systems compared to traditional air conditioners

Hadeed Ashraf¹, Shazia Noor^{1,2}, Muhammad Sultan^{1,3}, * Zahid M. Khan¹

¹Department of Agricultural Engineering, Bahauddin Zakariya University, Multan 60800, Pakistan

²Department of Mechanical Engineering, Bahauddin Zakariya University, Multan 60800, Pakistan

³Adaptive AgroTech Consultancy International, 401 Brittany Rd, Seaside, CA 93955, USA

*Corresponding Author's Email: muhammadsultan@bzu.edu.pk

Abstract

Practitioners are more interested in the outcome results of cooling systems than the minute particulars of the processes going underneath. In this study, power saving potential of evaporative cooling (EC) systems as compared to traditional vapor compression air conditioner (VCAC) is highlighted. Cost effectiveness of direct evaporative cooler (DEC), indirect evaporative cooler (IEC) and M-cycle evaporative cooler (MEC) has been compared against 1-ton VCAC in this study. DEC, IEC and MEC systems were tested under the design conditions of Multan, Pakistan for a year. The systems' performance is investigated in terms of wet-bulb effectiveness (WBE) for DEC and IEC system and in terms of dew-point effectiveness (DPE) for MEC system. The results indicate that average WBE in case of DEC and IEC system is 0.85-0.95 and 0.56-0.65, respectively. However, the MEC system indicated a DPE of 0.48-0.52. EC's performance increased with rising temperature up to a certain limit where traditional VCACs struggle to deliver. The experimentally developed EC systems have the potential to be applicable to various human and non-human applications. Therefore, ECs are efficiently noticeable green energy future alternative to VCAC with a low carbon footprint.

Keywords: Evaporative cooling; M-cycle; air conditioning; energy saving

1. Introduction

Drastic changes in climate, specifically in temperature, have left the population of the world in proliferated discomfort. During these stressful temperate conditions, more energy is being consumed to bring the temperature down to human thermal comfort zone by using conventional vapor compression air conditioning (VCAC) systems. Aside from power plants and vehicles that devour an enormous amount of petroleum derivatives and produce huge amount of CO₂, VCACs are another critical source of Greenhouse Gas (GHG) emission. Such GHG emissions ordinarily have a Global Warming Potential (GWP) equal to tons of CO₂ [1], [2]. HVACs have been proved to be harmful to the environment and economically impractical. Evaporative cooling (EC) systems have been proved to be effective for heating, ventilation and air conditioning (HVAC) purposes as compared to the VCACs. Along these lines, there is a dire need to create novel green energy air conditioning frameworks, going for a manageable low carbon footprint future.

Evaporative cooling (EC) systems exchange heat and mass merely with working medium fluid as water and air blowers. EC systems have been well known in modern industrial applications for a couple of decades. Nevertheless, traditional evaporative coolers including direct evaporative cooler (DEC) and

indirect evaporative cooler (IEC) have the working threshold of the working medium fluid's wet bulb (WB) temperature, restricting their further application in industrial and residential sectors [3]. Lately, M-cycle evaporative cooling (MEC) or dew point evaporative cooling has arisen as a progressive cooling technology. It allows the working medium fluid air to be cooled below its WB temperature, up to its dew point (DP) temperature, hence the name. This innovation has introduced the MEC as an auspicious auxiliary for VCACs, which appeals research attention from different researchers around the globe. Figures 1-3 illustrate the schematic working principle and psychrometric representation of a typical MEC, DEC and IEC, respectively. For instance, Jradi et al. [4] numerically and experimentally investigated a

cross-flow MEC system. The authors presented a wet-bulb effectiveness (ϵ_{wb}) of 112% and a dew point effectiveness (ϵ_{dp}) of 78%. Duan et al. [5] designed and developed a

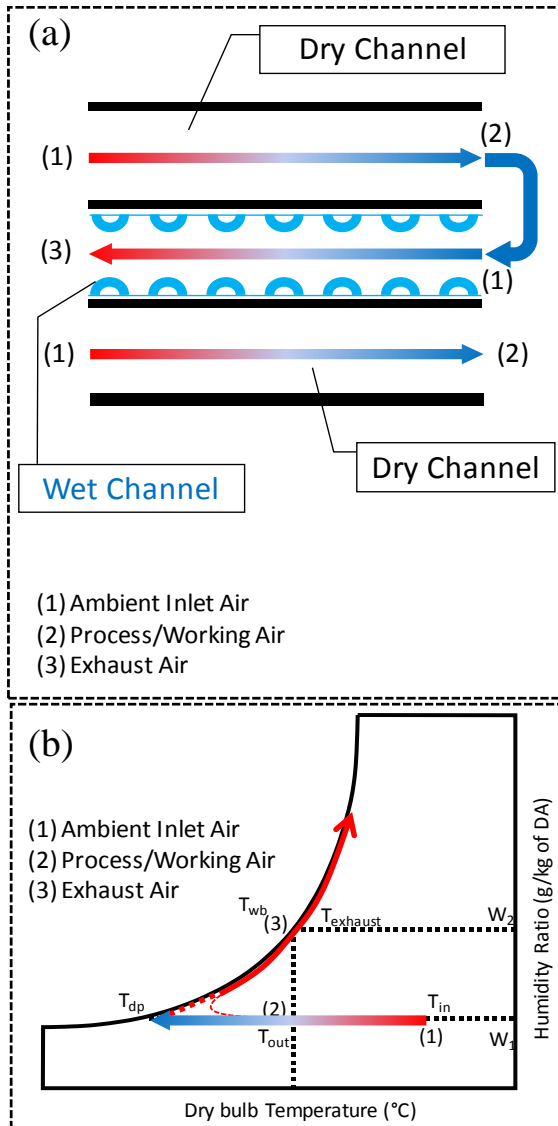


Fig. 1. A typical Maisotsenko-cycle based evaporative cooling (MEC) system: (a) schematic diagram, and (b) psychrometric representation of the cooling cycle

regenerative evaporative cooler (REC) with aluminum heat transfer plate and internal surface coated with porous fiber for increased wettability. Counter flow polygonal sheets with triangular guide vanes produced a ϵ_{wb} ranging from 0.55 to 1.06 with energy efficiency ratio (EER) varying from 2.8 to 15.5 under different boundary conditions for REC with coefficient of performance (COP) ranging from 2.8 to 15.5. Xu et al. [6] experimentally investigated the performance of a super dew

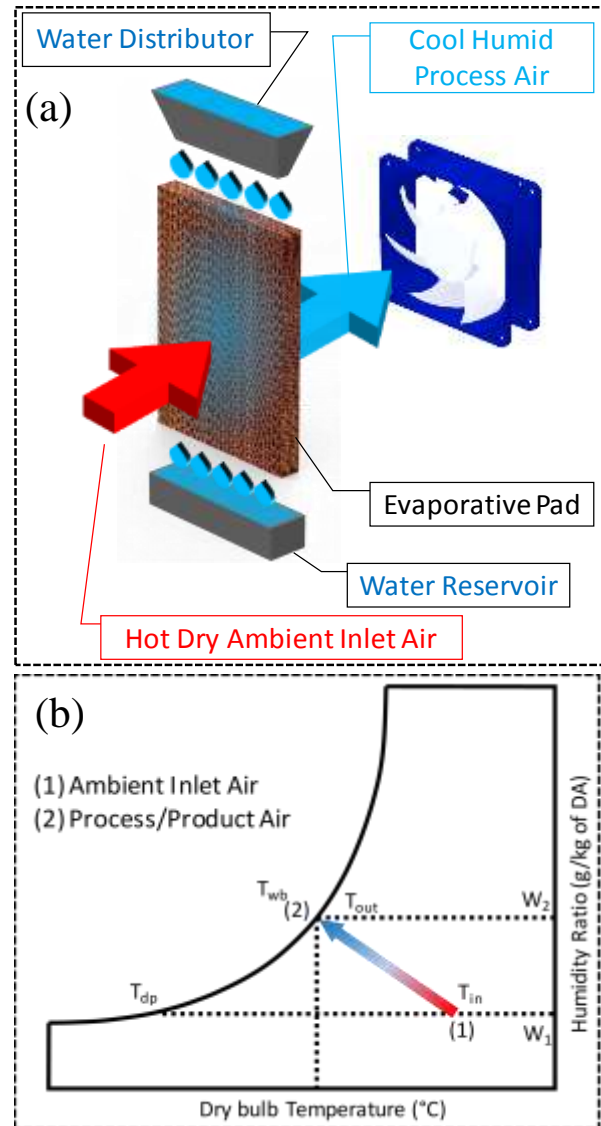


Fig. 2. A typical direct evaporative cooling (DEC) system: (a) schematic diagram, and (b) psychrometric representation of the cooling cycle

point evaporative cooler with a ϵ_{wb} of 112% to 128% and ϵ_{dp} of 67% to 76% with working air ratio of 0.364 and a significant increase in COP ranging 52.5. Bruno [7] investigated two counterflow dewpoint evaporative coolers in both commercial and residential applications. In application, the author found the system's average ϵ_{wb} to be 106% while the average ϵ_{dp} was 65%. EER was measured ranging 7.2-

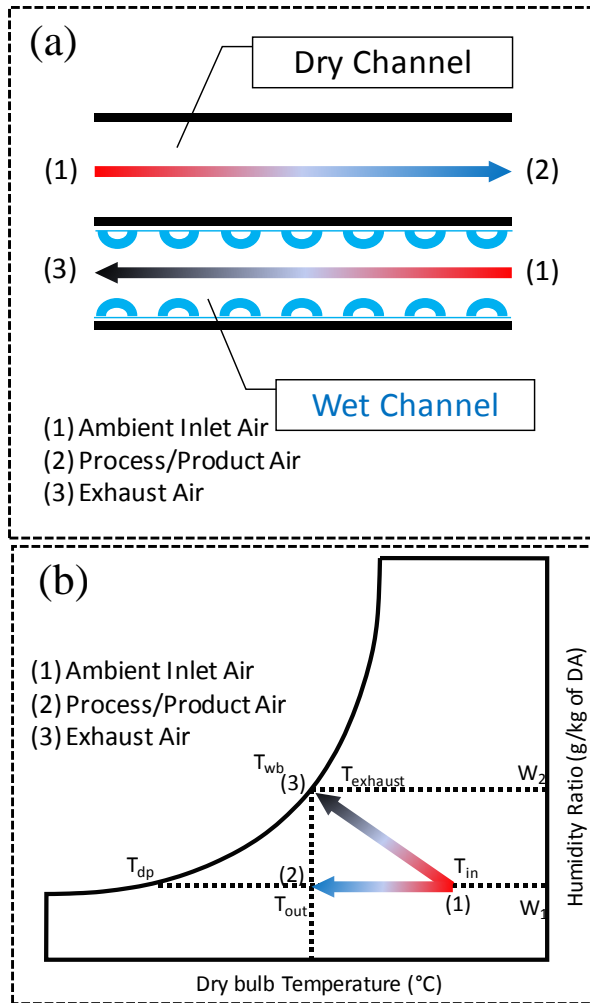


Fig. 3. A typical indirect evaporative cooling (IEC) system: (a) schematic diagram, and (b) psychrometric representation of the cooling cycle

11.5. In residential application, average ϵ_{wb} was 124%, average ϵ_{dp} was 75% and EER was ranging from 4.9 to 11.8. Woods et al. [8] investigated a counterflow dew point evaporative cooler coupled with a liquid desiccant dehumidifier which reduced the humidity level of the input air, subsequently enhancing the cooling potential of the cooler. Results showed that system was able to reduce humidity ratio from 14.6 to 8.4 g/kg while ambient air temperature 44.0°C was reduced to a drastic value of 15.0°C . Researchers also conducted abundant theoretical researches. Cui et al. [9] created a numerical model for indirect evaporative heat exchanger using modified log mean temperature difference (LMTD) and compared results with experimental data of counterflow regenerative indirect evaporative heat exchanger and crossflow indirect evaporative heat exchanger with a discrepancy of 8%. Pandelidis and Anisimov et al. [10], [11] numerically analyzed a modified effectiveness-number of transfer units (ϵ -NTU) method and researched heat and mass transfer processes in selected evaporative heat exchangers for

dew point evaporative coolers. Authors concluded that inlet air conditions and geometry of channel arrangement were the main driving factors of performance for M-cycle EC system. Zhu et al. [12] developed and validated a numerical model of dew point evaporative cooler using data driven artificial neural networking (ANN) technique. Impact of inlet air temperature, relative humidity, flow velocity of inlet air and extracted air ratio was investigated. It was suggested that model performed best when extracted air ratio was ranging between 0.3-0.36. Moreover, Pakari et al. [13] created a response surface methodology (RSM) using central composite design (CCD) matrix – a regression analysis technique, to determine the factors impacting the outlet temperature (T_{out}), ϵ_{wb} and outlet relative humidity (RH_{out}). The authors found the average discrepancy in case of numerical vs. regression results to be $\pm 4\%$ and incase of experimental vs. regression results, to be $\pm 10\%$. The author analyzed the feasibility of counterflow dew point evaporative cooler in Riyadh, Doha and Sur. Wan et al. [14], [15] compared two counterflow dew point evaporative coolers under different ambient conditions to develop key dimensionless parameters impacting T_{out} of product air. Mahmood, M. H. et al. [16] reviewed M-cycle applications in various sectors including air conditioning. Mahmood, M. H. [17] studied agricultural food processing using energy efficient desiccant based air conditioning. Sultan et al. [18] studied evaporative cooling assisted desiccant based air conditioning system for animal application in Pakistan. Sultan et al. [19] investigated solar-chimney supported passive air conditioning evaporative cooling based system for agricultural and livestock applications. The objective of this study is to determine energy saving potential of evaporative cooling (EC) systems under design conditions of Multan, Pakistan. In this study, the cost savings of DEC, IEC and MEC systems were calculated against 1-ton ideal VCAC. Design parameters are dry bulb temperature (T_{db}), wet bulb

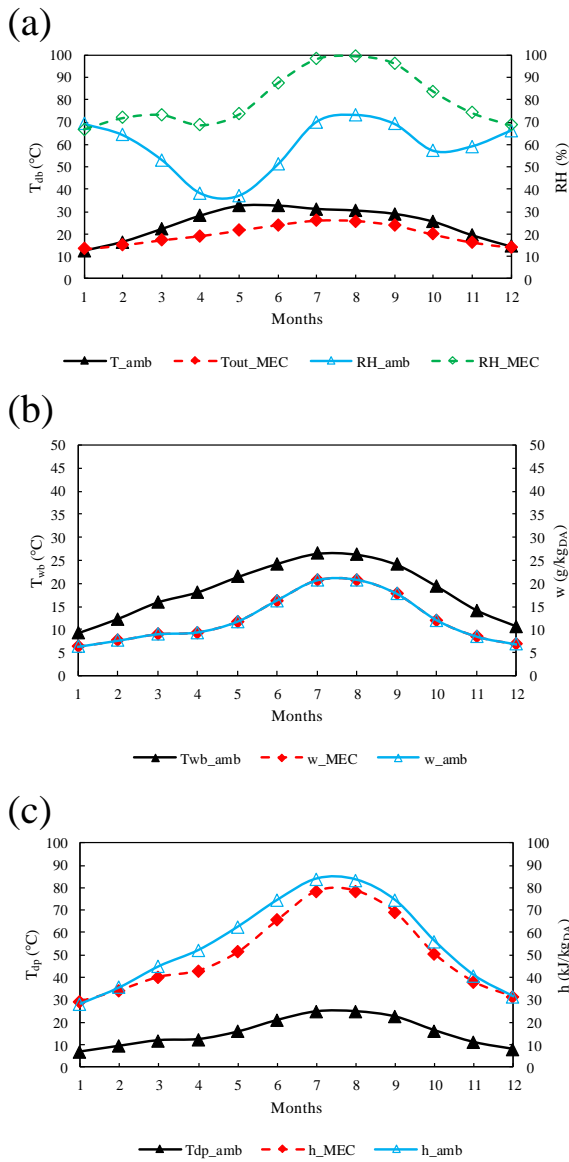


Fig. 4. Profile of experimental results for MEC system: (a) dry-bulb temperature and relative humidity, (b) wet-bulb temperature and humidity ratio, (c) enthalpy and dew-point temperature

temperature (T_{wb}), dewpoint temperature (T_{dp}), enthalpy (h), humidity ratio (w) and relative humidity (RH).

2. Methodology

2.1 Design conditions

Annual ambient climate data was

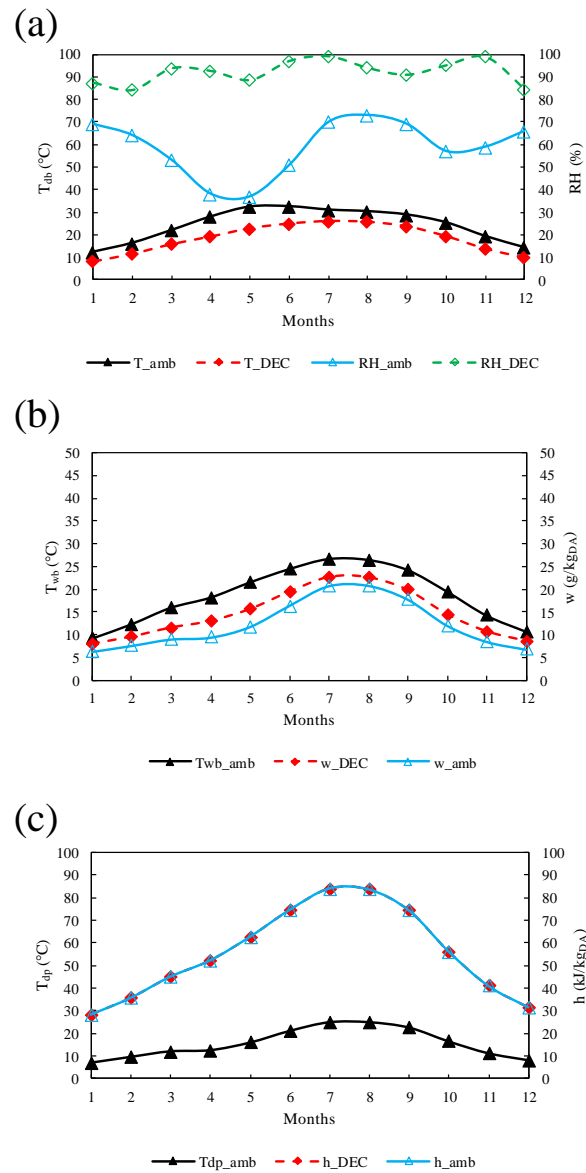


Fig. 5. Profile of experimental results for DEC system: (a) dry-bulb temperature and relative humidity, (b) wet-bulb temperature and humidity ratio, (c) enthalpy and dew-point temperature

obtained using sensors installed at Department of Agricultural Engineering, Bahauddin Zakariya University, Multan. Experimental EC systems were operated for a year and daily average T_{out} , w , h , V_{in} , V_{out} and RH were recorded for each of three systems. Systems' performance was analyzed based on dewpoint effectiveness (DPE) for MEC and wet-bulb effectiveness (WBE) in case of DEC and IEC. Results are shown and discussed in 3

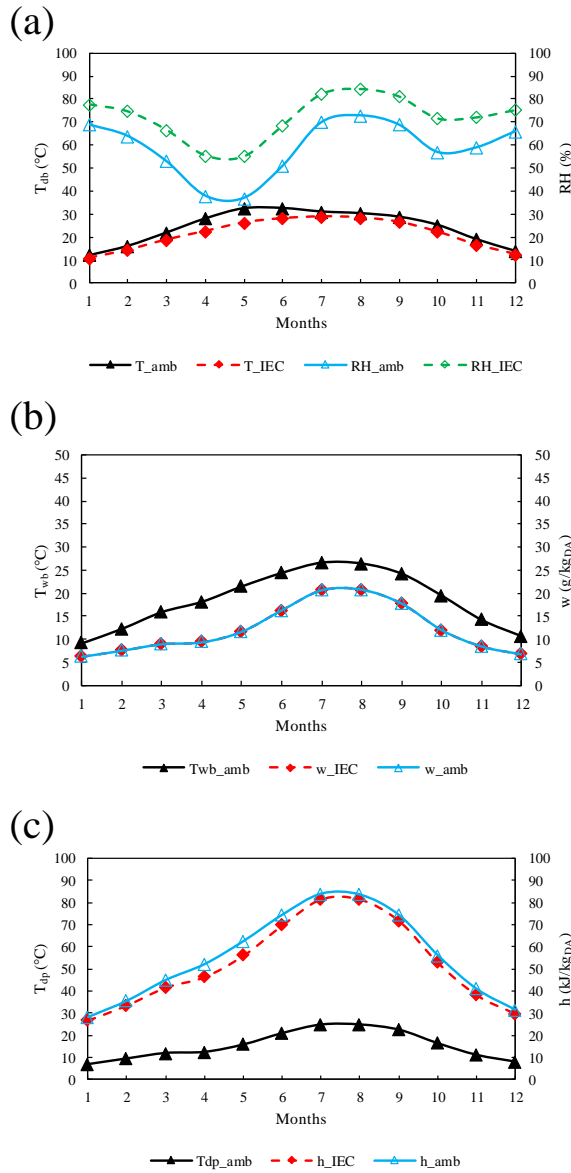


Fig. 6. Profile of experimental results for IEC system: (a) dry-bulb temperature and relative humidity, (b) wet-bulb temperature and humidity ratio, (c) enthalpy and dew-point temperature

$$\epsilon_{dp} = \frac{T_{in} - T_{out}}{T_{in} - T_{dp}} \quad (1)$$

$$\epsilon_{wb} = \frac{T_{in} - T_{out}}{T_{in} - T_{wb}} \quad (2)$$

where ϵ_{dp} represents dewpoint effectiveness, ϵ_{wb} represents wet-bulb effectiveness, T_{in} and T_{out} represent temperature of the inlet ambient air (°C) and

temperature of the outlet processed air from the system (°C), respectively, T_{dp} and T_{wb} represent dewpoint temperature (°C) and wet-bulb temperature (°C), respectively.

2.2 Specifications of system

In case of IEC and MEC, total effective area was 0.1032 m² while in case of DEC, total effective area was 0.0871 m². V_{in} for MEC and IEC varied between 4-5 ± 0.1 m/s while V_{out} ranged 2-3 ± 0.1 m/s. V_{in} in case of DEC, varied from 2-3 m/s whereas V_{out} was ranging between 1-2 m/s using 80 mm 12V DC fan.

$$Q_{sens} = m \cdot c_p (\Delta T) \quad (3)$$

$$Q_{latent} = m \cdot h_{fg} (\Delta T) \quad (4)$$

$$Q_{total} = Q_{sens} + Q_{latent} \quad (5)$$

$$\alpha = Q_{total} \cdot \mu \cdot \phi_{\mu} \quad (6)$$

where, Q_{sens} is the sensible energy of the system in kW, Q_{latent} is the latent energy of the system in kW, m is the mass flow rate in m³/s, c_p is the specific heat capacity of air (1.006 kJ/kg.°C), ΔT is the difference in T_{out} and T_{in} in °C, h_{fg} is the latent heat of evaporation in kJ/kg (2260 kJ/kg_{DA}), α is the cost/month (PKR), μ is the daily working hours of the systems (hours) i.e., 8 hours, and ϕ_{μ} is the cost per unit of energy (PKR) i.e., 15 PKR.

3. Results and discussion

Research study area, Multan, exists in a hot and dry zone. Average monthly temperature peaks at 33-35 °C in June. November, December, January and February are considered winter months. While May, June, July and August are summer months. Temperature in these months is relatively higher as compared to other months. **Error! Reference source not found.**(a) represents change in dry-bulb temperature T_{db} °C throughout the year showing a peak of 32.4 °C in May against a maximum temperature reduction down to 21.4 °C and ambient RH being 37% and MEC RH_{out} being 73.4% indicates that the performance of MEC is highly dependent on ambient air conditions. **Error! Reference source not found.**(b) represents variations in T_{wb} which peaks at 26.5 °C in July, w_{in} and w_{out} remain

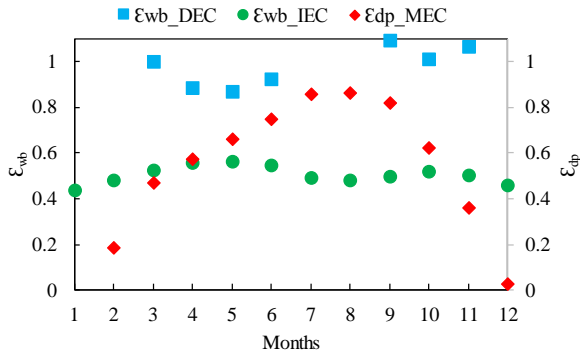


Fig. 7. Profile of experimentally resulted dew-point effectiveness (MEC) and wet-bulb effectiveness (DEC, IEC)

same throughout the experiment indicating no change in humidity ratio, adiabatically (M-Cycle being an advanced indirect evaporative cooler, no moisture being added to the system). **Error! Reference source not found.**(c) represents T_{dp} of the ambient inlet air and reduces enthalpy h_{in} (62.5 kJ/kgDA) to h_{out} (51.2 kJ/kgDA) of the system. Because w remains constant, change in enthalpy is only due to change in sensible temperature. **Error! Reference source not found.**(a) represents change in dry-bulb temperature T_{db} °C throughout the year showing a peak of 32.4 °C in May against a maximum temperature reduction down to 22.8 °C and ambient RH being 37% and DEC RH_{out} being 88.7% indicates that the performance of DEC is also dependent on ambient air conditions, DEC causes discomfort in July and August due to excess ambient air RH caused by rainfall (monsoon season). **Error! Reference source not found.**(b) represents variations in T_{wb} which peaks at 26.5 °C in July, DEC system increases w_{in} (20.6 g/kgDA)

ambient inlet air peaking at 24.9 °C in July, the enthalpies of the system as well as the ambient conditions remain constant, DEC being an isenthalpic process system. **Error! Reference source not found.**(a), represents change in dry-bulb temperature T_{db} °C throughout the year showing a peak of 32.4 °C in May against a maximum temperature reduction down to 26.1 °C and ambient RH being 37% and IEC RH_{out} being 55.1% indicates that the performance of IEC is also dependent on ambient air conditions, IEC causes very less change in RH relative to other systems. **Error! Reference source not found.**(b) represents variations in T_{wb} which peaks at 26.5 °C in July, w_{in} and w_{out} remain same throughout the experiment indicating no change in humidity ratio, adiabatically, similar to MEC. **Error! Reference source not found.**(c) represents T_{dp} of the ambient inlet air and reduces enthalpy h_{in} (62.5 kJ/kgDA) to h_{out} (56.1 kJ/kgDA) of the system. **Error! Reference source not found.** represents dew-point effectiveness ϵ_{dp} of MEC and wet-bulb effectiveness ϵ_{wb} of DEC and IEC. DEC has average ϵ_{wb} of 0.85-0.95 peaking in September, but DEC cannot be used in this month due to relatively higher RH (discomfort for human) and in case of IEC, average ϵ_{wb} of 0.56-0.65 was observed whereas ϵ_{dp} of MEC was observed to be average 0.48-0.52 throughout the year.

$$\sigma_{\epsilon_{wb}} = \pm \sqrt{\left(\frac{\delta \epsilon_{wb}}{\delta T_{out}} \cdot \sigma T_{out}\right)^2 + \left(\frac{\delta \epsilon_{wb}}{\delta T_{wb}} \cdot \sigma T_{wb}\right)^2} \quad (7)$$

$$\sigma_{\epsilon_{dp}} = \pm \sqrt{\left(\frac{\delta \epsilon_{dp}}{\delta T_{out}} \cdot \sigma T_{out}\right)^2 + \left(\frac{\delta \epsilon_{dp}}{\delta T_{dp}} \cdot \sigma T_{dp}\right)^2} \quad (8)$$

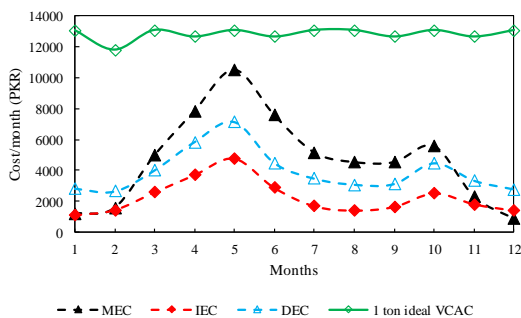


Fig. 8. Comparison of cost analysis of MEC, IEC and DEC compared to conventional 1-ton ideal vapor compression air conditioner

to w_{out} (22.6 g/kgDA) in the month of July. **Error! Reference source not found.**(c) represents T_{dp} of the

where, $\sigma_{\epsilon_{wb}}$ is the total experimental uncertainty of wet-bulb effectiveness, σT_{out} , σT_{wb} are the instrument uncertainties i.e., ± 1 °C. $\sigma_{\epsilon_{wb}}$ in MEC, DEC & IEC is ± 0.092 , ± 0.084 and ± 0.093 , respectively. $\sigma_{\epsilon_{dp}}$ is ± 0.14 in MEC.

Fig. 8 represents cost comparison of MEC, IEC, DEC against traditional 1-ton ideal VCAC. On an average, MEC system when compared to 1-ton VCAC can potentially save 8100 PKR/year, 8800 PKR/year in case of DEC, and 10600 PKR/year in case of IEC.

4. Conclusions

Results represented in 3 indicate that evaporative cooling (EC) systems perform better, economically, saving approximately 8100 PKR/year



in case of MEC, 8800 PKR/year in case of DEC and 10600 PKR/year in case of IEC compared to a 1-ton traditional vapor compression air conditioner working continuously at 3.52 kW (equals 1-ton of refrigeration) for office timings of government building, 8 hours a day. Therefore, evaporative cooling systems are efficiently noticeable green energy alternative with zero to no greenhouse gas emissions making it an economically and environmentally suitable alternative for traditional vapor compression air conditioners.

Acknowledgements

The study is financially supported by Bahauddin Zakariya University, Multan under research promotion grant titled “Development and performance evaluation of prototypes of direct and indirect evaporative cooling-based air-conditioning systems”.

Conflict of interest

The authors declare no conflict of interest.

REFERENCES

- [1] A. Handbook, “ASHRAE handbook—fundamentals,” *Atlanta, GA*, 2009.
- [2] J. Lin, S. M. Huang, R. Wang, and K. Jon Chua, “On the in-depth scaling and dimensional analysis of a cross-flow membrane liquid desiccant dehumidifier,” *Appl. Energy*, vol. 250, pp. 786–800, 2019.
- [3] Z. Duan *et al.*, “Indirect evaporative cooling: Past, present and future potentials,” *Renew. Sustain. Energy Rev.*, vol. 16, no. 9, pp. 6823–6850, 2012.
- [4] M. Jradi and S. Riffat, “Experimental and numerical investigation of a dew-point cooling system for thermal comfort in buildings,” *Appl. Energy*, vol. 132, pp. 524–535, Nov. 2014.
- [5] Z. Duan, C. Zhan, X. Zhao, and X. Dong, “Experimental study of a counter-flow regenerative evaporative cooler,” *Build. Environ.*, vol. 104, pp. 47–58, 2016.
- [6] P. Xu, X. Ma, X. Zhao, and K. Fancey, “Experimental investigation of a super performance dew point air cooler,” *Appl. Energy*, vol. 203, pp. 761–777, 2017.
- [7] F. Bruno, “On-site experimental testing of a novel dew point evaporative cooler,” *Energy Build.*, vol. 43, no. 12, pp. 3475–3483, 2011.
- [8] J. Woods and E. Kozubal, “A desiccant-enhanced evaporative air conditioner: Numerical model and experiments,” *Energy Convers. Manag.*, vol. 65, pp. 208–220, 2013.
- [9] X. Cui, K. J. Chua, M. R. Islam, and W. M. Yang, “Fundamental formulation of a modified LMTD method to study indirect evaporative heat exchangers,” *Energy Convers. Manag.*, vol. 88, pp. 372–381, 2014.
- [10] D. Pandelidis and S. Anisimov, “Numerical analysis of the heat and mass transfer processes in selected M-Cycle heat exchangers for the dew point evaporative cooling,” *Energy Convers. Manag.*, vol. 90, pp. 62–83, 2015.
- [11] S. Anisimov, D. Pandelidis, and J. Danielewicz, “Numerical analysis of selected evaporative exchangers with the Maisotsenko cycle,” *Energy Convers. Manag.*, vol. 88, pp. 426–441, 2014.
- [12] G. Zhu, T.-T. Chow, and C. K. Lee, “Performance analysis of counter-flow regenerative heat and mass exchanger for indirect evaporative cooling based on data-driven model,” *Energy Build.*, vol. 155, pp. 503–512, 2017.
- [13] A. Pakari and S. Ghani, “Regression models for performance prediction of counter flow dew point evaporative cooling systems,” *Energy Convers. Manag.*, vol. 185, no. November 2018, pp. 562–573, 2019.
- [14] Y. Wan, J. Lin, K. J. Chua, and C. Ren, “Similarity analysis and comparative study on the performance of counter-flow dew point evaporative coolers with experimental validation,” *Energy Convers. Manag.*, vol. 169, pp. 97–110, 2018.
- [15] Y. Wan, J. Lin, K. J. Chua, and C. Ren, “A new method for prediction and analysis of heat and mass transfer in the counter-flow dew point evaporative cooler under diverse climatic, operating and geometric conditions,” *Int. J. Heat Mass Transf.*, vol. 127, pp. 1147–1160, 2018.
- [16] M. H. Mahmood, M. Sultan, T. Miyazaki, S. Koyama, and V. S. Maisotsenko, “Overview of the Maisotsenko cycle – A way towards dew point evaporative cooling,” *Renewable and Sustainable Energy Reviews*, vol. 66. Elsevier, pp. 537–555, 2016.
- [17] M. H. Mahmood, M. Sultan, and T. Miyazaki, “Experimental evaluation of desiccant dehumidification and air-conditioning system for energy-efficient storage of dried fruits,” *Build. Serv. Eng. Res. Technol.*, p. 0143624419893660, Dec. 2019.
- [18] M. S. Hassan Niaz *et al.*, “STUDY ON EVAPORATIVE COOLING ASSISTED DESICCANT AIR-CONDITIONING SYSTEM FOR LIVESTOCK APPLICATION IN PAKISTAN,” 2019.
- [19] M. Sultan, T. Miyazaki, M. Mahmood, and Z. Mahmood Khan, “Solar assisted evaporative cooling based passive air-conditioning system for agricultural and livestock applications,” *J. Eng. Sci. Technol.*, vol. 13, pp. 693–703, Mar.



Passive Cooling based Thermal Management System of Lithium-ion Batteries employing Copper foam/Paraffin Composite

Muhammad Ramzan¹, Abid Hussain^{1*}

Mechanical Engineering Department, University of Engineering and Technology Taxila, Pakistan

Corresponding Author*: abid.hussain@uettaxila.edu.pk

Abstract

An efficient thermal management system is important to maintain high powered lithium ion battery pack within permissible temperature range for transmission of Electric Vehicles (EVs) and Hybrid Electric Vehicles (EVs). Present research work focuses on designing of thermal management system of Panasonic NCR 18650B lithium ion battery pack by employing copper foam with phase change material (PCM). A compact structure comprising of lithium ion battery cells and copper foam/PCM composite was designed and investigated experimentally. Thermal performance of the system was evaluated at different discharge rates and compared with two different cooling modes: cooling by employing pure PCM and by natural air convection mode. The results reveal that natural air as a cooling source for thermal management of lithium ion batteries cannot ensure safety requirements for the battery pack. The application of pure PCM can reduce the battery surface temperature dramatically and maintain temperature in suitable range due to heat absorption during the phase transition of PCM. Copper foam is perceived to be more effective in reducing the battery surface temperature. It was found that Copper foam saturated with PCM reduced the surface temperature by 34% as compared to natural air and 25% as compared to pure paraffin at 2C discharge rate. Furthermore, temperature is more uniform inside the battery pack by employing copper foam/PCM composite at 1.5C discharge rate.

Keywords: Thermal management, copper foam, phase change materials, lithium ion batteries

1. Introduction

Lithium ion batteries broadly used in the applications of electric vehicles (EV) and hybrid electric vehicles (HEV) due to higher energy density and power density. Literature shows that the conventional operating temperature for lithium ion batteries is in the range of 20-50 °C and temperature gradient between cells should be less than 5 °C [1]. In recent years, passive type thermal management system for lithium ion battery pack taking significant place in present research filed. Passive cooling of lithium ion batteries includes the utilization of phase change materials (PCM) due to extensive heat storage capacity of PCM having high value of latent heat. Differently, pure paraffin (PCM) has low value of thermal conductivity. Number of materials having high value of thermal conductivity are infiltrated into PCM to increase thermal conductivity [2–5]. By employing these type of composites for lithium ion battery thermal management, heat storage efficiency will be increased and temperature uniformity inside the battery pack will be improved significantly [6]. The effective approach for enhancement of thermal conductivity is the application of metal foams. Metal foams have characteristics like good stiffness, high porosity and excellent thermo-physical and mechanical properties. Many researchers discussed thermal management of lithium ion battery by employing metal foams. Lafdi et al [7]. experimentally evaluated for heat transfer profile by employing metal foam/PCM composite. They measured thermal conductivity of the composite by varying metal foam geometry. They proved

that large pore size metal foam shows more temperature reduction due to maximum heat transfer through convection. Zhonghao Rao et al [8]. studied thermal management of LiFePO₄ batteries by the application of PCMs. Their results demonstrated that low melting range less than 45 °C of PCM is more effective for heat removal through system, when desired extreme temperature is less than 50 °C. Wang et al [9]. perform experimentation on thermal management by utilizing aluminum foam/ PCM composite. Results shows that thermal conductivity enhancement of pure paraffin is 218% and the 11.7 °C drop in temperature at discharge rate of 2C by employing aluminum foam. Li et al [10]. performed experimental study on lithium ion battery of 10Ah capacity employing copper foam. They compared their results with pure paraffin and natural air cooling. Results shows 29% temperature reduction as compared to natural air convection and 12% temperature reduction as compared to pure paraffin under 1C discharge rate. Mancin et al [11]. performed experimental study on phase transition of paraffin wax by the application of copper foam inside a rectangular box by providing various heating loads. Their results prove that the temperature gradient is minimum by using copper foam/paraffin composite. Qu et al [12]. Performed simulation on 2D transient model of square type lithium ion batteries by the application of copper foam/ paraffin composite. Results reveal that surface temperature is reduce to 17 °C and 30 °C at 1C and 3C discharge rates respectively. Furthermore, many researchers also research on expanded graphite/ paraffin composite for passive thermal management of lithium ion



batteries Mills and Al Hallaj carried out simulation study on lithium ion battery pack which are utilized in a laptop by the application of expanded graphite. They proved that expanded graphite/paraffin composite could improve PCM thermal conductivity which results in temperature reduction of battery pack [13]. Fathabadi perform a study on thermal management by hybrid method of cooling through the application of expanded graphite with paraffin wax. Their results revealed that battery temperature goes to 70 °C i.e. safety limit for battery pack by employing natural convection cooling and the hybrid mode of cooling will maintain battery temperature up to 60 °C [14].

From literature review, studies investigating thermal management of lithium ion batteries by employing metal foam/PCM composite have been inadequate. Furthermore, comparison of temperature uniformity and effect of different discharge rates on temperature rise of battery pack is rarely mentioned in the literature. In this study, a passive thermal management system for commercial type Panasonic NCR 18650B lithium ion batteries integrated with copper foam/paraffin composite is developed and investigated experimentally. Results are compared with two other cooling modes: natural air and pure PCM cooling. Moreover, effect of temperature uniformity on battery pack are also studied.

2. Experimental Design

2.1 Preparation of copper foam/paraffin composite

Commercial paraffin (RT-42) is utilized as the organic PCM. Thermo-physical characteristics of PCM are shown in Table 1, given by businessperson. Copper foam geometrical properties includes: 0.97 porosity and 30PPI pore density. Copper foam thermal conductivity is 398 [W/(m.K)] taken from [15]. Composite was made through infiltration of paraffin within copper foam pores by the application of hot water bath. Images of copper foam before and after infiltration are shown in Figure 1. Copper foam/PCM composite effective thermal conductivity is calculated by using following relation [16].

$$k_e = A[\varepsilon_b k_{pcm} + k_f(1 - \varepsilon_b)] + \frac{1-A}{\varepsilon_b/k_{pcm} + (1-\varepsilon_b)/k_f} \quad (1)$$

Where k_e metal foam composite effective thermal conductivity, A represent correlation coefficient, k_f and k_{pcm} represent thermal conductivity of foam and PCM thermal conductivity respectively and ε_b show foam bulk porosity. In this study, value of k_f is 398 [W/(m.K)] and ε_b value is 0.97. The value of correlation coefficient A should be 0.35 according to Bhattacharya et al.[16]. Eq. (1) is effective when metal foam porosity is in range of 0.905 - 0.978 and pore density is in range of 5-40 PPI. Since pore density and porosity of proposed metal foam is in acceptable range so effective thermal conductivity is 4.37 [W/(m.K)] from Eq. (1)

Table 1: Paraffin Specifications for this Study

Parameters	Value
Melting Temperature	38-41 °C
Thermal conductivity	0.2 W/m.K

Note: Thermo-physical characteristics of PCM given by businessperson

Table 2: Properties of Cells utilized

Cell type	Panasonic NCR 18650
Cell capacity	3.4 Ah
Operating voltage	3.0-4.2 V

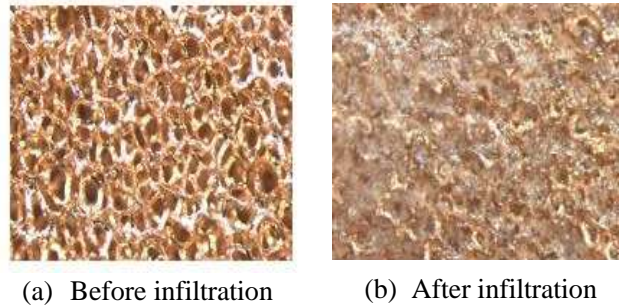


Figure 1. Images of Copper foam before and after Infiltration process

2.2 Construction of Battery pack

Commercial Panasonic NCR 18650B battery cells of cylindrical shape having a capacity of 3.4 Ah are used for experimentation. Battery pack comprises on six cells in series connection having nominal capacity more than 90%. First of all, every cell is tested at its maximum capacity and charging and discharging of cells are done at 0.5 C rate. Cell details are shown in Table 2. Cells are joined in series to rule out the overcharging and maintaining voltage in the battery pack a security circuit introduced. Schematic representation of experimental setup is shown in Figure 2.

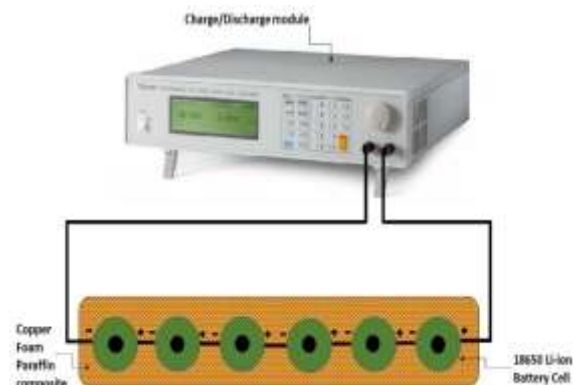


Figure 2. Schematic representation of battery pack enclosed by Copper foam saturated with Paraffin



2.3 Battery pack testing

Evolution of battery pack is carried out by using three approaches including (1) Natural air cooling (2) using pure PCM (3) Copper foam saturated with PCM. Surface temperature of battery is measured by using thermocouples of T-type having 0.1 °C accuracy.

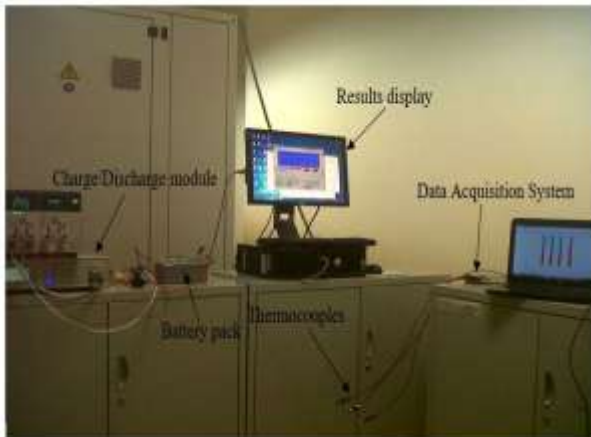


Figure 3. Image of Experimental setup

First thermocouple is attached to positive terminal of first cell and two thermocouples is inserted in between of third cell and fifth cell. An extra thermocouple of T-type is applied for measuring ambient temperature. Ambient temperature is controlled thermostatically to 25 °C. Charging of battery is done at constant 0.5C charge rate at 1.7A during galvanostatic approach, during potentiostatic battery is charged at 100 mA by applying 4.2 V cut off voltage to each cell. Then battery stay on rest until its temperature decreases and reach to ambient temperature. Discharging starts first at the rate of 0.5C (1.7 A) then at 2C (6.8 A) till voltage decrease to 3.0 V on each cell. Battery again stay on rest position until its temperature decreases and reach to ambient temperature. In this way charging cycle and discharging cycle is completed. Figure 3. shows experimental arrangement.

3. Results and Discussion

3.1 Temperature profile of Lithium ion battery pack at 0.5C by employing Natural air

A complete charge - discharge cycle was carried employing natural air as source of cooling. Maximum rise in temperature took place at the mid of battery pack so cell number 3 was selected and connected with T-type thermocouple. Temperature response of cell number 3 are shown in Figure is shown in Figure 4 at 0.5C discharge rate. The highest temperature after charging of battery pack ($t < 80$ min) is 36 °C recorded. when discharging ($200 \text{ min} < t < 295$ min) temperature rises and goes to 35.5 °C. This sudden increase in temperature is because of low natural air convection and also due to air suppression inside the battery pack because of

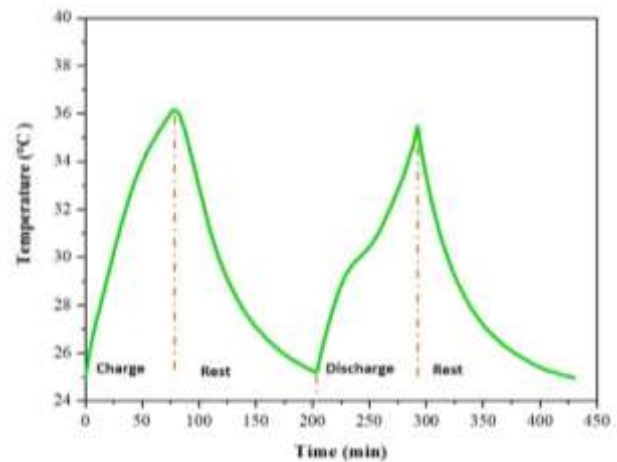


Figure 4. Battery Temperature profile by employing Natural air at 0.5C

because of compact design of battery pack. This increase in temperature suggest that thermal management structure or system for lithium ion battery pack is necessary specifically when battery is operating at severe conditions.

3.2 Temperature profile of Lithium ion battery pack at 0.5C by employing pure Paraffin

Again at 0.5C discharge rate battery pack temperature profile after employing pure paraffin is shown in Figure 5.

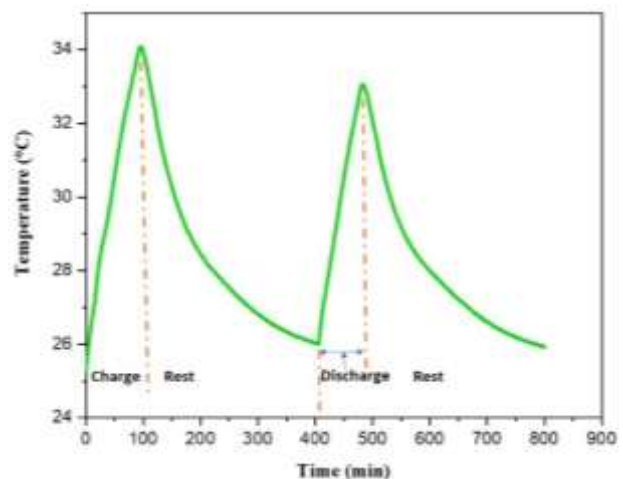


Figure 5. Battery Temperature profile by employing pure paraffin at 0.5C

Maximum temperature after charging stage ($t < 105$ min) is 34 °C. This temperature reduction is due to heat dissipation of battery pack through conduction of paraffin. During discharging stage ($402 \text{ min} < t < 495$ min) of battery pack temperature goes to 33 °C, almost 7% temperature drop when compared with natural air cooling. It is evident from temperature profile that maximum temperature rise is below the PCM melting temperature (38-41°C). Therefore, only conduction of paraffin is utilized.



3.3 Temperature profile of Lithium ion battery pack at 0.5C by employing Copper foam/paraffin composite

By employing copper foam/paraffin composite battery pack temperature profile at 0.5C discharge rate is shown

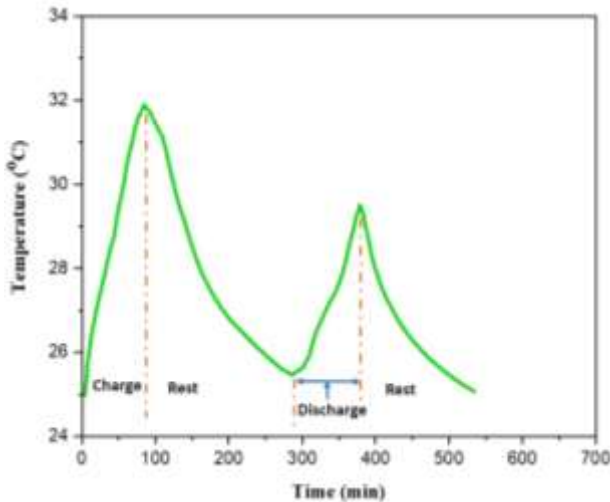


Figure 6. Battery Temperature profile by employing Copper foam/Paraffin Composite at 0.5C

in Figure 6. These results refer copper foam having 30PPI pore density and 0.97 porosity. In the charging process ($t < 95$ min) temperature rise is 31.85 °C. During discharging stage ($290 \text{ min} < t < 375$ min) temperature goes to 29.5 °C, almost 10.5% and 17% as compared to pure paraffin and natural air convection. Since PCM is not melted therefore heat transfer through conduction is prominent. The present temperature reduction reveal that copper foam plays a key role to enhance paraffin thermal conductivity. High thermal conductivity of copper foam enhances rate of heat transfer and extra heat will be dissipated from system which leads to reducing the surface temperature of the battery pack.

3.4 Sensible Heat effect

Again the battery was discharged at 2C (6.8 A) to check the sensible heat effect on all three cooling modes. Battery pack temperature profile for three cooling modes at 2C discharge rate as demonstrated in Figure 7.

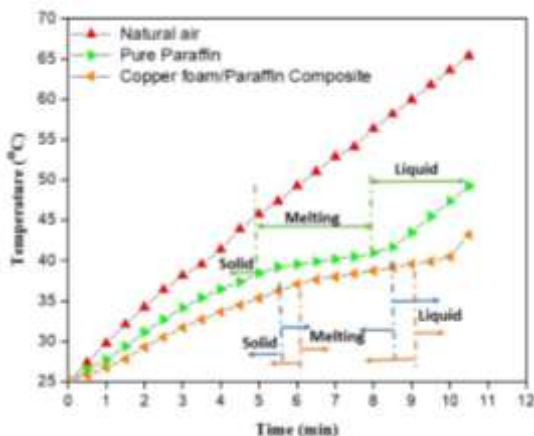


Figure 7. Battery Temperature profile by employing

Copper foam/Paraffin Composite at 2C

It is evident that for natural air cooling temperature increases to 65.42 °C that can damage the battery pack. When paraffin is utilized 24.7% temperature reduction was noticed. By utilizing copper foam/paraffin composite temperature goes to 43 °C which is 34.27% lower when compared with natural air cooling. This temperature reduction is due to thermal conductivity enhancement of paraffin which leads to increase in heat transfer rate that eventually reduce battery pack surface temperature therefore, we can conclude that copper foam/paraffin composite is a suitable choice as thermal management source for lithium ion batteries.

3.5 Temperature Uniformity

The uniformity of temperature in the battery pack is necessary to obtain suitable battery performance by increasing utilization of battery capacity. At 1.5C discharge conditions temperature uniformity between cell 1 and cell 3 was analyzed using cooling processes: cooling with copper foam/ paraffin composite and also natural air cooling. By employing natural air cooling a 3 °C temperature variation was obtained as shown in Figure 8.

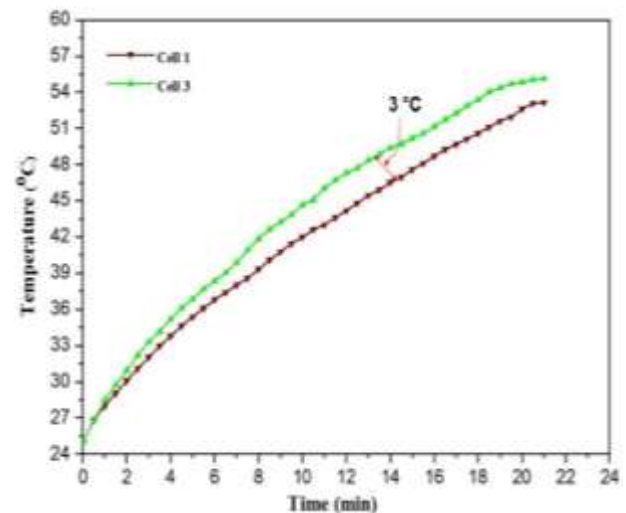


Figure 8. Temperature Uniformity using Natural Air at 1.5C

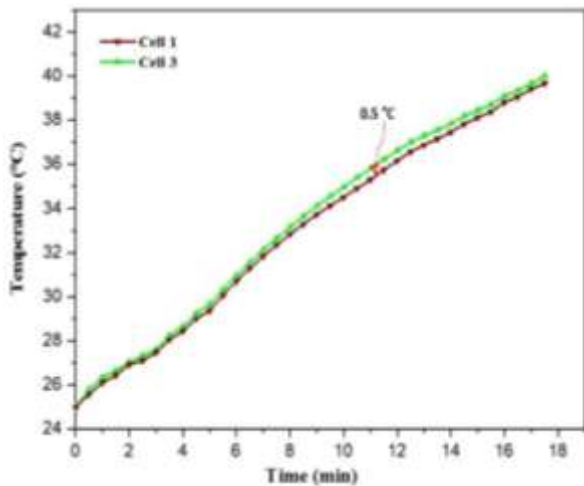


Figure 9. Temperature Uniformity using Copper foam/Paraffin Composite 1.5C

This temperature variation is greatly minimized to 0.5 °C when copper foam/paraffin composite is applied shown in Figure 9. This small variation in temperature among cell 1 and cell 3 represent heat is uniformly conducted through the metal foam/paraffin composite and also prove that paraffin is uniformly infiltrated within the metal foam pores.

4. Conclusion

The experimental investigation was carried out on lithium ion batteries thermal management system by employing copper foam/paraffin composite. Investigation results reveal that by the application of copper foam/paraffin composite 34% temperature reduction by comparing with natural air and 25% temperature reduction compared to paraffin on discharging rate of 2C. Furthermore, at 1.5C discharge rate temperature variation between cell 1 and cell 3 using natural air is 3 °C and this temperature difference reduced to 0.5 °C when utilizing copper foam/paraffin composite. This shows that temperature is more uniform inside a battery pack by employing copper foam/paraffin composite. Therefore, we can conclude that copper foam/paraffin composite is a good applicant for lithium ion batteries thermal management.

REFERENCES

- [1] Z. Ling *et al.*, "Experimental and numerical investigation of the application of phase change materials in a simulative power batteries thermal management system," *Appl. Energy*, vol. 121, pp. 104–113, 2014.
- [2] A. Sari and A. Karaipekli, "Thermal conductivity and latent heat thermal energy storage characteristics of paraffin/expanded graphite composite as phase change material," *Appl. Therm. Eng.*, vol. 27, no. 8–9, pp. 1271–1277, 2007.
- [3] X. Py, R. Olives, and S. Mauran, "Paraffin/porous-graphite-matrix composite as a high and constant power thermal storage material," *Int. J. Heat Mass Transf.*, vol. 44, no. 14, pp. 2727–2737, 2001.
- [4] D. Zhou and C. Y. Zhao, "Experimental investigations on heat transfer in phase change materials (PCMs) embedded in porous materials," *Appl. Therm. Eng.*, vol. 31, no. 5, pp. 970–977, 2011.
- [5] H. T. Cui, "Experimental investigation on the heat charging process by paraffin filled with high porosity copper foam," *Appl. Therm. Eng.*, vol. 39, pp. 26–28, 2012.
- [6] Z. Rao and S. Wang, "A review of power battery thermal energy management," *Renew. Sustain. Energy Rev.*, vol. 15, no. 9, pp. 4554–4571, 2011.
- [7] K. Lafdi, O. Mesalhy, and S. Shaikh, "Experimental study on the influence of foam porosity and pore size on the melting of phase change materials," *J. Appl. Phys.*, vol. 102, no. 8, 2007.
- [8] Z. Rao, S. Wang, and G. Zhang, "Simulation and experiment of thermal energy management with phase change material for ageing LiFePO₄ power battery," *Energy Convers. Manag.*, vol. 52, no. 12, pp. 3408–3414, 2011.
- [9] Z. Wang, Z. Zhang, L. Jia, and L. Yang, "Paraffin and paraffin/aluminum foam composite phase change material heat storage experimental study based on thermal management of Li-ion battery," *Appl. Therm. Eng.*, vol. 78, pp. 428–436, 2015.
- [10] W. Q. Li, Z. G. Qu, Y. L. He, and Y. B. Tao, "Experimental study of a passive thermal management system for high-powered lithium ion batteries using porous metal foam saturated with phase change materials," vol. 255, 2014.
- [11] S. Mancin, A. Diani, L. Doretto, K. Hooman, and L. Rossetto, "Experimental analysis of phase change phenomenon of paraffin waxes embedded in copper foams," *Int. J. Therm. Sci.*, vol. 90, pp. 79–89, 2015.
- [12] Z. G. Qu, W. Q. Li, and W. Q. Tao, "Numerical model of the passive thermal management system for high-power lithium ion battery by using porous metal foam saturated with phase change material," *Int. J. Hydrogen Energy*, vol. 39, no. 8, pp. 3904–3913, 2014.
- [13] A. Mills and S. Al-Hallaj, "Simulation of passive thermal management system for lithium-ion battery packs," *J. Power Sources*, vol. 141, no. 2, pp. 307–315, 2005.
- [14] H. Fathabadi, "High thermal performance lithium-ion battery pack including hybrid active-passive thermal management system for using in hybrid/electric vehicles," *Energy*, vol. 70, pp. 529–538, 2014.
- [15] X. Xiao, P. Zhang, and M. Li, "Preparation and thermal characterization of paraffin/metal foam composite phase change material," *Appl. Energy*,



Selection and Characterization of PV Cell Material for Thermophotovoltaic Application

Zertasha Shoukat¹, Mohsina Asif¹, Khujista Nadeem¹, Aqsa Shabbir², Rabia Nazir³, Muhammad Farooq⁴, Ali H. Kazim^{1*}

1- Department of Mechanical Engineering, University of Engineering and Technology, Lahore

2- Department of Electrical Engineering, Lahore College for Women University, Lahore

3- Department of Electrical Engineering, University of Engineering and Technology, Lahore

4- Department of Mechanical Engineering, University of Engineering and Technology, New Campus, Sheikhpura

*Corresponding author's email: ali.h.kazim@uet.edu.pk

Abstract:

The main objective of this paper is to compare different photovoltaic (PV) cell materials' characteristics and to model an efficient thermophotovoltaic (TPV) system that can produce electrical energy using radiations from a radiator. Choosing an optimum material for the TPV cells is a big challenge. In this paper, different materials of TPV cells, based on their bandgap energies, are compared on a Planck distribution curve using a fixed emitter temperature and then with different emitter temperatures. For high emitter temperatures (such as 1750K), InGaAs (0.74eV) is selected based on its band gap energy and low thermalization losses. The study, by assisting in the selection of an optimum PV cell material, aims to contribute to the development of an efficient TPV system that has the prospect of being a favorable sustainable solution to the current world's energy crisis.

Key words: Thermophotovoltaic, InGaAs, Planck Distributions, photon recycling, renewable energy

1. Introduction

Access to sufficient energy can help raise incomes and reduce poverty which would ultimately accelerate a country's rate of economic and human development [1, 2]. The energy demand of Pakistan has drastically increased in recent years due to the rapid growth in population and expansion of the industrial setup in Pakistan [3-5]. Currently, Pakistan relies on fossil fuels, a non-renewable energy source, to meet almost 60% of its energy demands [6]. A possible solution to this energy crisis is the use of Thermophotovoltaic (TPV) devices.

TPV devices convert radiation from a heated radiator or emitter to electricity [7]. TPV is most widely used in conjunction with concentrated solar power [8, 9] to heat a local emitter to a temperature mostly lower than 2500 K. A thermal energy storage (TES) can be used to maintain a constant emitter temperature even in the absence of sunlight. TPV systems have the potential to surpass the conversion efficiencies of solar PV cells because TPV systems can incorporate filters in front of the emitter to suppress the emission of very low energy photons, place reflectors behind the PV cell to recycle low energy photons which re-heat the emitter, use high emissivity emitters, and place PV cells in close proximity to source [10]. Moreover, the

selection of the most suitable PV cell material, dealt in this paper, is another key consideration in achieving high performance of TPV systems. To the best of our knowledge, this is the foremost study to compare the bandgap energies of up to 8 PV cell materials on a Planck distribution curve.

2. Literature Review

There has been a significant effort to study and minimize losses in a TPV cell because as established by Harder and Warfrel [11], TPV cells have a greater potential to considerably reduce conventional losses as compared to Solar PV cells. Louwen et al have concluded that as more research and development related to a technology is conducted, it becomes cheaper to further enhance the installed capacity by additional watts of power [12]. Solar cells' efficiency under AM0 solar spectrum is limited to 30% when minimum recombination losses occur in the cells [13]. While the theoretical maximum limit of the efficiency of TPV cell with concentrated sunlight is 85.4% [14], it was found that with realistic losses and geometric considerations but with concentrated light maximum efficiency can be up to 60%. In radiative recombination, an electron and hole recombine to produce a photon, whereas non-radiative recombination leads to heat dissipation by phonon



generation or energy transfer to another electron (Auger recombination) [15]. Practical losses, which can be minimized by improving the design and fabrication of TPV cells, have been observed to significantly affect a cell's performance [9]. Through the quantification of an Auger coefficient C and Auger current [16], it has been found that this type of non-radiative recombination decreases with an increase in the bandgap of PV cell. Iles and Chu [17] concluded that the optimum bandgap of a PV cell material can be found by matching it with the peak wavelength of radiations from emitter. It has also been recorded by Tuley and Nicholas [18], that it is difficult for a very low bandgap material ($E_g < 0.6\text{eV}$) to achieve a power output corresponding to the thermodynamic limit of TPV cells [19] due to a large amount of suppression in Auger recombination required. Tuley and Nicholas have also concluded that for high-temperature sources ($\geq 1800\text{K}$), series resistance can be minimized if a higher bandgap (0.7-0.8 eV) TPV cell is used.

3. General characteristics of a PV cell

The main objective of a TPV system is to fulfil the need of electrical energy with less production cost and high efficiency. In this aspect, PV has the benefit of being flexible, non-polluting and reliable. PV has the ability to make it possible to avoid the installation of generators [20]. Filters are used in PV module, in front of emitters, to increase the efficiency of a TPV cycle. Photon recycling is another way to achieve higher efficiency of TPV cell. This can be done by using reflectors on front or back side of PV cell. Another way of increasing efficiency is using multijunction or tandem cells because it increases the chances of the absorption of useful photons by having more than one band gap energy [21].

4. Mathematical Modelling

According to Planck's distribution law, the radiation intensity, emitted by any emitter or black body, is a function of temperature (T in Kelvin), emissivity (ϵ), and wavelength (λ in μm). Radiation intensity increases with an increase in temperature, thus when the emitter temperature increases, the peak intensity moves towards shorter wavelength [22]. The following function can be used to find out total radiation J emitted in $\text{W/m}^2\text{-sr}/\mu\text{m}$ for any wavelength range [23]:

$$E(\lambda, T) = \int_{\lambda_1}^{\lambda_2} \frac{C_1}{\lambda^5 \left[\exp\left(\frac{C_2}{\lambda T}\right) - 1 \right]} d\lambda \quad (1)$$

Where $C_1 = 3.742 \times 10^8 \text{ W/m}^2\mu\text{m}^{-4}$ and $C_2 = 1.4388 \times 10^4 \text{ K}\mu\text{m}$

According to the Stefan Boltzmann law, total radiant heat power for an infinite wavelength range, emitted from a perfect blackbody surface with $\epsilon = 1$ is proportional to the fourth power of its absolute temperature:

$$E_b = \int_0^\infty \frac{C_1}{\lambda^5 \left[\exp\left(\frac{C_2}{\lambda T}\right) - 1 \right]} d\lambda = \sigma T^4 \quad (2)$$

Stefan Boltzmann Constant $= \sigma = 5.7705 \times 10^{-8} \text{ W/m}^2 \text{ K}^4$. Eq. (2) also results in total area under Planck distribution.

A PV cell will convert photons that have a wavelength equal to or shorter than the wavelength corresponding to the bandgap wavelength λ_g of its material, found using Eq. 3:

$$E_g = \frac{hc}{\lambda_g} \quad (3)$$

Where E_g is the bandgap energy of the PV cell material in Joules, h is Planck's constant ($6.62607004 \times 10^{-34} \text{ m}^2\text{kg/s}$) and c is the speed of light ($2.998 \times 10^8 \text{ m/s}$).

Power intensity above the bandgap of cell i.e. area under the graph with energy greater than the bandgap energy of PV cell or wavelength shorter than the wavelength bandgap is calculated using the following formula:

$$E_{b(0 \rightarrow \lambda_g)} = \int_0^{\lambda_g} \frac{C_1}{\lambda^5 \left[\exp\left(\frac{C_2}{\lambda T}\right) - 1 \right]} d\lambda \quad (4)$$

The wavelength where the spectral intensity is maximum λ_p is found from Wein Displacement Rule:

$$\lambda_p T = 2898 \mu\text{mK} \quad (5)$$

The percentage of emitted power above bandgap $\eta_{E > E_g}$ is found by [24]:

$$\eta_{E > E_g} = \frac{E_{b(0 \rightarrow \lambda_g)}}{E_b} \times 100\% \quad (6)$$

Photon flux (ϕ) or number of photons/ m^2s with energy more than bandgap energy is found by:

$$\phi = \frac{E_{b(0 \rightarrow \lambda_g)}}{\int_{\lambda_g}^0 \frac{hc}{\lambda} d\lambda} \quad (7)$$



If each photon is assumed to produce one conductive electron, the maximum theoretical current density $J_{ph,max}$ (A/m^2) for a particular photon flux can be calculated by:

$$J_{ph,max} = \phi \times q \quad (8)$$

Where q is the charge of one electron i.e. 1.6×10^{19} Coulombs.

5. PV Cell Materials Used for Comparison

The materials that are to be compared on a Planck distribution (Figure 1) based on their bandgap wavelength at 300K are tabulated in Table. 1. The material investigated are Copper Gallium Selenide (CGS), Cadmium Telluride (CdTe), Silicon (Si), Copper Indium Selenide (CIS), Indium Gallium Arsenide (InGaAs), Gallium Antimonide (GaSb), Germanium (Ge), Indium Gallium Arsenide Antimonide (InGaAsSb). The band gap and wavelength have been enlisted.

Table 1 Bandgap energy (E_g in eV) and Bandgap wavelength (λ_g in μm) of various PV cell materials at 300K [25].

Materials	Bandgap energy, E_g (eV)	Bandgap Wavelength, λ_g (μm)
Copper Gallium Selenide (CGS)	1.70	0.729
Cadmium Telluride (CdTe)	1.50	0.827
Silicon (Si)	1.12	1.107
Copper Indium Selenide (CIS)	1.00	1.240
Indium Gallium Arsenide (InGaAs)	0.74	1.676
Gallium Antimonide (GaSb)	0.72	1.722
Germanium (Ge)	0.66	1.878
Indium Gallium Arsenide Antimonide (InGaAsSb)	0.55	2.254

6. Results and Discussion

Eight different materials used to manufacture PV cells are compared on a Planck Distribution curve for the fixed blackbody in Figure.1. The emitter temperature is 1750K, as used in [9] with λ_p of $1.656 \mu m$. Each vertical line represents the bandgap wavelength associated with the cell material (Table 1). It has been assumed that the TPV cells are water cooled and their temperature stays maintained at 300 K.

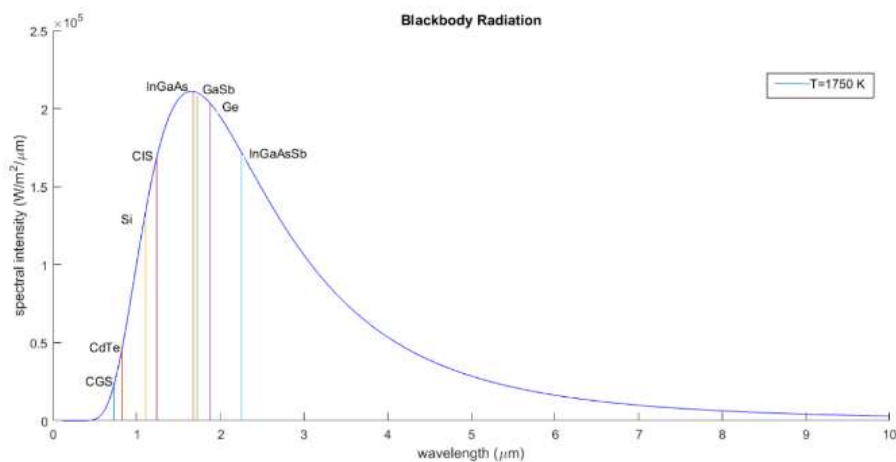


Figure 1 Graph of Spectral Intensity ($W/m^2/\mu m$) against Wavelength (μm) showing a comparison of bandgap wavelengths, $\lambda_g(\mu m)$ of 8 PV materials for a blackbody emitter at a temperature of 1750 K. CGS (blue , $\lambda_g=0.73 \mu m$), CdTe (orange , $\lambda_g=0.83 \mu m$), Si (yellow , $\lambda_g=1.11 \mu m$), CIS (indigo , $\lambda_g=1.24 \mu m$), InGaAs (red , $\lambda_g=1.68 \mu m$), GaSb (green , $\lambda_g=1.72 \mu m$), Ge (purple , $\lambda_g=1.88 \mu m$), InGaAsSb (sky blue , $\lambda_g=2.254 \mu m$).



The emitter should emit sufficient radiations with energy higher than a PV cell's bandgap energy (or photons with a wavelength shorter than bandgap wavelength). For a particular vertical line of a PV cell the useful portion of radiations is the area under the graph, to the left of the vertical line. Materials with a higher bandgap energy e.g. CGS (1.7 eV) and CdTe (1.5 eV) require a very large amount of incident energy for the promotion of electrons from valence band to the conduction band, moreover, the portion of useful emitted photons for them is very small compared to the total radiation emitted by the emitter. Therefore, CGS and CdTe are not recommended for TPV applications. For Si (1.12 eV) and CIS (1 eV) better proportions of above bandgap energies are yielded. While InGaAsSb (0.55 eV) has the smallest bandgap energy, longest bandgap wavelength, and highest above-bandgap proportion of photons; it has a

smaller power intensity at λ_g . Unlike InGaAsSb, the InGaAs (0.74 eV), GaSb (0.72 eV) and Ge (0.66 eV) cells provide an optimum between peak power intensity and high proportion of useful photons. Therefore, as suggested by Tuley and Nicholas [18], the most preferred PV cell material for a high temperature emitter has $E_g > 0.6\text{eV}$.

In order to further investigate the effect of changing temperature and the relation between high power density and λ_g , Figure 2 was plotted, where for the brevity purpose, 4 PV cell materials of distinct bandgap energy ranges were selected from Table 1. As temperature increases, the spectral intensity increases. Also, it was found that out of the 4 materials InGaAs λ_g corresponded most closely to λ_p especially for high temperature sources such as 1600 K, 1800K, 2000K.

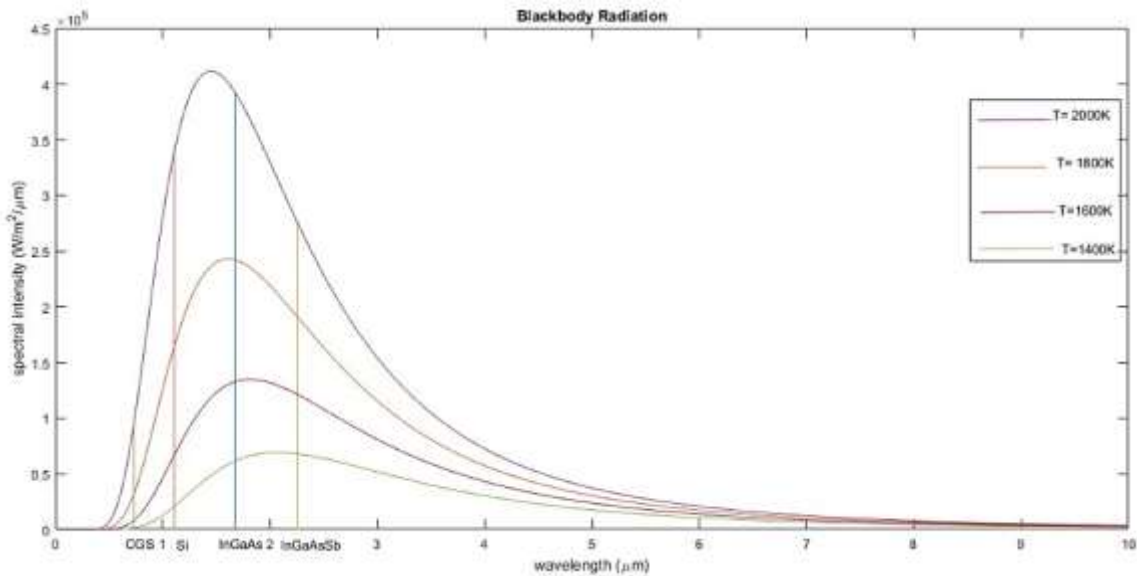


Figure 2 Planck Distribution for different emitter temperatures (green $T=1400\text{K}$, violet $T=1600\text{K}$, red $T=1800\text{K}$, purple $T=2000\text{K}$) and PV cells with different bandgap wavelengths, CGS (blue, $\lambda_g=0.73\ \mu\text{m}$), Si (red, $\lambda_g=1.11\ \mu\text{m}$), InGaAs (blue, $\lambda_g=1.68\ \mu\text{m}$) InGaAsSb (yellow, $\lambda_g=2.254\ \mu\text{m}$).

Therefore, if the emitter temperature is 1750K, the bandgap of InGaAs ($E_g=0.74\text{eV}$, $\lambda_g=1.68\ \mu\text{m}$) corresponds closely to high/peak power intensity (at $\lambda_p=1.66\ \mu\text{m}$), and has a small Auger recombination rate [18] and series resistance [19]. Figure 3 shows the emitted power that is above bandgap energy of InGaAs.

For an InGaAs cell, at an emitter temperature of 1750K, 13.689 W/cm² is the intensity of the useful

photons that have energy greater than bandgap energy of InGaAs emitted by the emitter, found by using Eq. 4 or finding the shaded area of Figure 3. The total emitted power intensity is found by Eq. 3.

Total emitted power intensity is calculated to be 54.052 W/cm². The percentage of emitted power with energy more than the bandgap energy of the cell is 25.298%. The photon flux calculated by Eq. 6 is determined to be 5.548×10^{38} photons/m²s.

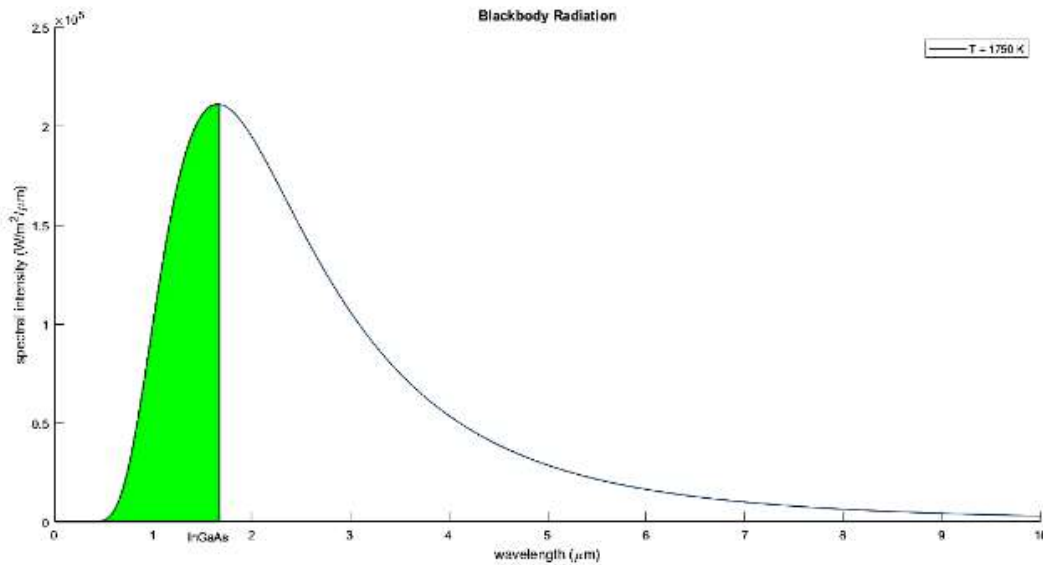


Figure 3 Emitter power by an emitter at 1750K that is above bandgap of InGaAs ($\lambda_g=1.68 \mu\text{m}$) cell is represented by the green shaded area.

7. Conclusion

In this paper, 8 different commonly available PV Cell materials (CGS, CdTe, Si, CIS, InGaAs, GaSb, Ge, and InGaAsSb) were compared on a Planck Distribution curve for TPV applications using an average emitter temperature of 1750K. CGS, CdTe, Si, and CIS, with $E_g \geq 1\text{eV}$ proved to be unfavorable due to the small above-bandgap photon flux. It has been shown that PV cells with low bandgap energy, e.g. InGaAsSb $E_g=0.55\text{eV}$, may have a high above-bandgap photon flux but have high thermalization losses and high non-radiative recombination rates (Auger current). The empirical relation of [16] can be used to show that at 0.55 eV, the Auger current coefficient is significantly high $3.28 \times 10^{-29} \text{cm}^6\text{s}^{-1}$. When selecting a PV cell material for TPV applications, it is important to match the peak wavelength at that particular emitter temperature to the bandgap wavelength of the cell. InGaAs ($E_g=0.74\text{eV}$) and GaSb ($E_g=0.72\text{eV}$) correspond most closely to peak wavelengths at high emitter temperatures. While both cells show favorable performance, GaSb cells are difficult to produce in series [26]. InGaAs cells demonstrate an intensity of $13.689 \text{W}/\text{cm}^2$ above bandgap and the percentage of emitted power with energy more than the bandgap energy of the cell being 25.298%. InGaAs cells when grown on reusable InP substrate would also make the TPV system more cost-effective [9].

Moreover, the problem of low performance for cell structures with a lattice mismatch to the substrate can be overcome by graded mismatched layers, a technology which has also been successfully demonstrated for InGaAs cells [25, 27]. This comparative study will prove helpful when selecting a PV cell for thermophotovoltaic applications with concentrated solar power plants, a clean and renewable source of electrical energy as opposed to fossil fuels. There exist many potential considerations and improvement avenues, such as the performance of different PV cells with the integration of photon recycling. The study alongside establishing InGaAs as a suitable choice for TPV, will also assist development in this arena.

REFERENCES

1. Cabraal, R.A., D.F. Barnes, and S.G. Agarwal, *Productive uses of energy for rural development*. Annual Review of environment and Resources, 2005. **30**.
2. Khandker, S.R., D.F. Barnes, and H.A. Samad, *Are the energy poor also income poor? Evidence from India*. Energy policy, 2012. **47**: p. 1-12.
3. Komal, R. and F. Abbas, *Linking financial development, economic growth and energy consumption in Pakistan*. Renewable and Sustainable Energy Reviews, 2015. **44**: p. 211-220.
4. NTDC, *Power system statistics Pakistan 2017-18*, National Transmission & Despatch Company, Editor. 2018.



5. Shah, S.A.A. and Y.A. Solangi, *A sustainable solution for electricity crisis in Pakistan: opportunities, barriers, and policy implications for 100% renewable energy*. Environmental Science and Pollution Research, 2019: p. 1-17.
6. Asif, M., *Sustainable energy options for Pakistan*. Renewable and Sustainable Energy Reviews, 2009. **13**(4): p. 903-909.
7. Bierman, D.M., et al., *Enhanced photovoltaic energy conversion using thermally based spectral shaping*. Nature Energy, 2016. **1**(6): p. 16068.
8. Swanson, R.M., *A proposed thermophotovoltaic solar energy conversion system*. Proceedings of the IEEE, 1979. **67**(3): p. 446-447.
9. Seyf, H.R. and A. Henry, *Thermophotovoltaics: a potential pathway to high efficiency concentrated solar power*. Energy & Environmental Science, 2016. **9**(8): p. 2654-2665.
10. Chubb, D., *Fundamentals of Thermophotovoltaic Energy Conversion*. 2007: Elsevier Science.
11. Harder, N.-P. and P. Würfel, *Theoretical limits of thermophotovoltaic solar energy conversion*. Semiconductor Science and Technology, 2003. **18**(5): p. S151.
12. Louwen, A., et al., *Life-cycle greenhouse gas emissions and energy payback time of current and prospective silicon heterojunction solar cell designs*. Progress in Photovoltaics: Research and Applications, 2015. **23**(10): p. 1406-1428.
13. Shockley, W. and H.J. Queisser, *Detailed balance limit of efficiency of p-n junction solar cells*. Journal of applied physics, 1961. **32**(3): p. 510-519.
14. De Vos, A., *Endoreversible thermoeconomics*. Energy conversion and management, 1995. **36**(1): p. 1-5.
15. Pelant, I. and J. Valenta, *Luminescence spectroscopy of semiconductors*. 2012: Oxford University Press.
16. Massé, N., A. Adams, and S. Sweeney, *Experimental determination of the band gap dependence of Auger recombination in In Ga As/ In P multiple quantum well lasers at room temperature*. Applied physics letters, 2007. **90**(16): p. 161113.
17. Iles, P. and C. Chu. *Design and fabrication of thermophotovoltaic cells*. in *Proceedings of 1994 IEEE 1st World Conference on Photovoltaic Energy Conversion-WCPEC (A Joint Conference of PVSC, PVSEC and PSEC)*. 1994. IEEE.
18. Tuley, R. and R. Nicholas, *Band gap dependent thermophotovoltaic device performance using the InGaAs and InGaAsP material system*. Journal of Applied Physics, 2010. **108**(8): p. 084516.
19. Cody, G.D. *Theoretical maximum efficiencies for thermophotovoltaic devices*. in *AIP Conference Proceedings*. 1999. AIP.
20. M. Belhadj, K.B., Abdelfatah Nasri, Benlaria Ismail, *Design and modeling of optical reflectors for a PV panel adapted by MPPT control*. November 2019.
21. Bauer, T., *Thermophotovoltaics Basic Principles and Critical Aspects of System Design*. 2011.
22. unknown. *Optotherm Support, Emissivity in the Infrared, Planck's Blackbody Distribution Law*. 2016; Available from: <https://www.optotherm.com/infrared-planck.htm>.
23. Bergman, T.L., et al., *Fundamentals of Heat and Mass Transfer*. 2011: Wiley.
24. Fraas, L., J. Avery, and H. Huang, *Thermophotovoltaic furnace-generator for the home using low bandgap GaSb cells*. Semiconductor Science and Technology, 2003. **18**(5): p. S247.
25. Bauer, T., *Thermophotovoltaics: basic principles and critical aspects of system design*. 2011: Springer Science & Business Media.
26. Mattarolo, G., *Development and modelling of a thermophotovoltaic system*. Vol. 8. 2007: kassel university press GmbH.
27. Andreev, V. *An overview of TPV cell technologies*. in *AIP Conference Proceedings*. 2003. AIP.



Modeling and Optimization of Solar Absorption Cooling System for Cold Storages in Pakistan

Musannif Shah¹, Adeel javed¹, Hamid Ikram¹

1. US-Pakistan Centre for Advanced Studies in Energy, National University of Sciences and Technology (NUST) Islamabad, Pakistan,
*Email: shah.musannif3@gmail.com

Abstract:

Cold storages are widely practiced methods for bulk handling of perishable fruits and vegetables. Conventional Cold storages are considered a major consumer of electricity. Generally, vapor compression cooling systems are installed to achieve the required cooling conditions in conventional cold storages. Due to the energy crisis and load shedding in Pakistan, cold storages are not able to achieve the required cooling in particular time-span to the food items. The solar energy can be efficiently capitalized to fulfill the cooling requirements of the cold storages while using the thermal operating cooling systems. This work aims at developing a model of solar absorption cooling (SAC) system for cold banana storage located in Peshawar at a necessary temperature of 15 °C using a TRNSYS dynamic modeling method. Furthermore, several energy conservation measures have been simulated for cold storage building design (building envelop, insulations, etc.) to explore developments in reducing cooling load and power consumption. Results revealed that actual cold storage with an operating time of 9 hours a day has a maximum cooling load of 69270 kJ/h which reduced to 65200 kJ/h after applying energy conservation measures. A simulation model that contains Evacuated tube collectors (ETC), storage tank, absorption chiller, and the building was developed. Results depict that the absorption system of rated capacity 60,000 kJ/h is required to achieve the required storage conditions. The study also reveals that to increase the reliability of the system, an optimized model containing a 35 m² collector area, a storage tank of 1.5 m³ volume is required to provide effective cooling.

Key words: Cold Storage; Absorption cooling system; Solar collectors; TRNSYS

1. Introduction

Increased energy demand and depleting fossil fuels have led to reduced natural resources. Extensive use of fossil fuels which releases greenhouse gases has adverse

effects on the environment [1]. Refrigeration is an energy-consuming process and approximately 1% of the global green house gases (GHG) emissions are caused by refrigeration process. The size of cold storage ranges from a small store of volume 10-20 m³ to large warehouses containing thousands of cubic meters. It contributes to a major electrical consumer in the commercial building sector. On average, the refrigerated facilities consume about 25 kWh of electricity and 9200 Btu/ft² per year. The function of the cold storage is to maintain the exact temperature for the storing product and to preserve the food quality [2]. A study conducted by foster showed that the specific energy consumption for chilled storages is 55.8 KWh/m³ per year, and for frozen storages is 69.4 KWh/m³ per year [3]. An investigation on multi-floor large scale refrigerated warehouses was carried out in China and a rough estimate of the specific energy consumption of 73-91.3 KWh/m³ per year was calculated [4].

The refrigeration system needs to be designed to provide the maximum refrigeration requirement.

Mainly, the peak demands occur in a few hours of the year otherwise the systems operate at the lower capacities [5]. Designing a refrigeration system for a building based on maximum cooling load results in increasing the initial cost of the system [6]. The refrigeration system is based on two cycles, vapor compression, and vapor absorption. Vapor compression is a widely used system and is known as conventional systems. It has higher COPs, lesser weights, and smaller sizes than the other systems. The major disadvantage is the utilization of CFCs and HCFCs in the vapor compression cycle, thus the release of harmful refrigerants to the environment and causing the depletion of the ozone layer [7,8]. On the other hand, the absorption system uses clean, free and renewable solar energy as an alternative to reduce the electrical demand and to meet the cooling load of a building.[9,10]. Besides, the working fluid for the absorption systems is water, methanol, etc. which are environmentally friendly and have no or less impact on the depletion of ozone layers [8].

In this study advance, renewable energy software TRNSYS 17 is used to develop a simulation model of a SAC system, which is being used by researchers to study new energy concepts in renewable energy. There had been a detailed experimental and theoretical research on solar absorption air conditioning. Islam did a detail study on simulation



and modeling of a SAC system for Abu Dhabi weather conditions [11]. A simulation-based study using TRNSYS was done by Balghouthi to select and optimize different components of a SAC system for Tunisia conditions [12]. A simulation and optimization analysis of a LiBr/H₂O SAC system was done by Assilzadeh. In the study, ETC were used to heat water. It was concluded that to get uninterrupted operation and to improve the reliability of operation of the system, a hot water storage tank of 0.8 m³ is necessary. For the climate conditions of Malaysia, an optimum system of 3.5 kW requires solar collectors of area 35 m² [13]. Florides modeled and optimized a SAC system for residential buildings for Cyprus using TRNSYS [14].

2. Research Methodology

The steps followed for modeling of a solar cooling system for cold storages are shown in Fig. 1. Following is the detail description of each step.

- i. Existed cold storage building was modeled in TRNSYS supported Sketchup (Google Sketchup) as shown in Fig. 2.
- ii. Weather data for a location was imported from the TRNSYS library as a TMY file. Weather file consists of annual solar beam and diffused radiations, ambient wet bulb and dry bulb temperature, relative humidity (RH) and wind velocity etc.
- iii. The maximum cooling load demand is calculated for an existing cold storage building to estimate the size of the cooling system.
- iv. Energy conservation measures are applied to investigate the reduction in the maximum cooling load demand of a building. Energy conservation measures consist of increasing insulation thickness and applying steel cladding for thermal insulation.
- v. Selection of suitable components from the TRNSYS library to model a solar cooling system.
- vi. Optimization of system components to avoid oversizing components and reduce the initial cost of the system.

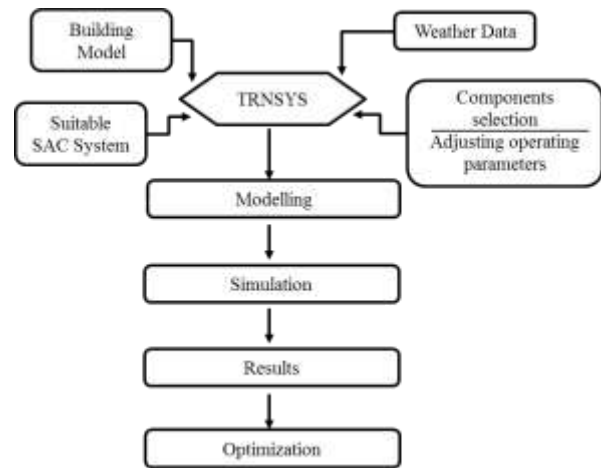


Figure 1: Technical approach to the study

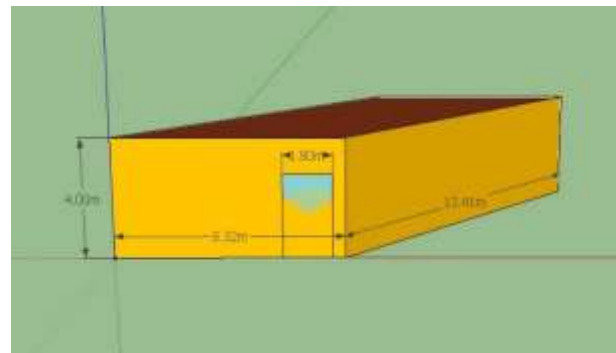


Figure 2: TRNSYS model of cold storage building

2.1 System Description

A complete Solar assisted absorption cooling system model is shown in Fig. 3. Solar absorption cooling complete model consists of 3 loops: hot water loop, chilled water loop and cooling water loop.

Hot water loop: It consists of ETC which receives solar energy from sunlight. The fluid in this loop is which absorbs energy from the collector which results in rising its temperature. The hot water from the collectors goes into a thermally insulated stratified hot water storage tank and then circulates back to collectors via a constant speed pump. A stratified storage tank is used for continuous supply of hot water and to increase reliability of the system. Hot water from the storage tank then passes through the boiler which works as an auxiliary heater. It only heats water when it is below its setpoint temperature. Hot water

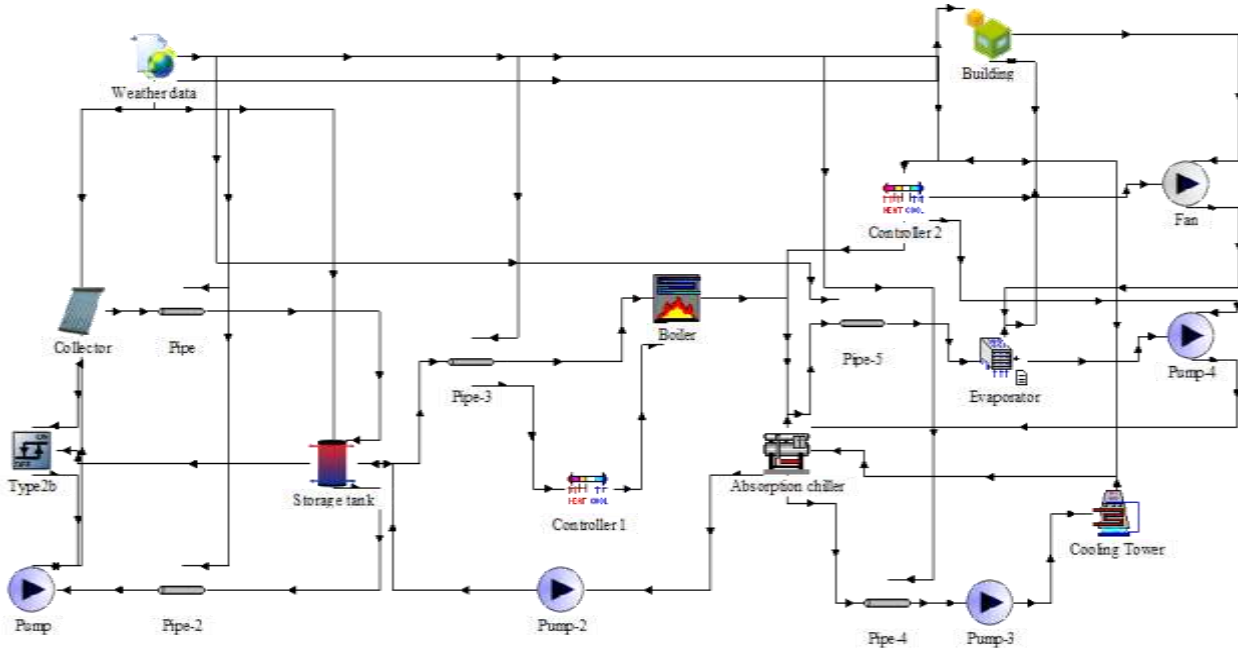


Figure 3: Model of SAC system in TRNSYS studio

returns to the storage tank after being passed through the generator of the absorption chiller.

Cooling water loop: It consists of a pump and a closed-circuit cooling tower. The cooling water which circulates in this loop removes heat from absorber and condenser (Q_a and Q_c) and rejects it to the atmosphere as shown in Fig. 3.

Chilled water loop: It consists of an evaporator, pump, fan and a thermostat controller. Chilled water from the absorption chiller enters the cooling coil where it absorbs heat from conditioned space and returns to chiller via a pump as shown in Fig. 3. Thermostat gives control signal to single speed fan which circulates air from conditioned space through cooling coil.

Following is the mathematical description of important components of the SAC system.

2.2 Evacuated tube collector

A TRNSYS Type 71 ETC is used in modeling the system. The efficiency of an ETC can be determined by Eq. 1.

$$\eta = a_0 - a_1 \frac{(\Delta T)}{I_T} - a_2 \frac{(\Delta T)^2}{I_T} \quad (1)$$

where, a_0 is collector optimal efficiency, a_1 and a_2 are first and second-order heat loss coefficients respectively. ΔT is equal to $(T_i - T_a)$, which is the difference between inlet temperature of working fluid (water) and the ambient temperature respectively, and I_T is the incident radiations on collector aperture.

Table 1: Parameters of collectors

Parameter	Description	Value
Type of collector	ETC	
C_p	Specific heat of fluid (kJ/kg K)	4.190
η	Efficiency mood	1 ($T_i - T_{amb}$)
m_{test}	Flow rate at tested condition ($kg/h m^2$)	3
a_0	Intercept efficiency	0.7
a_1	Negative of the first-order coefficient ($kJ/h m^2 K$)	10
a_2	Negative of the second-order coefficient ($kJ/h m^2 K^2$)	.03

The thermal efficiency of the ETC is defined by parameters a_0 , a_1 and a_2 values of these parameters are given in Table. 1.

2.3 Absorption chiller

Hot water fired single effect Lithium Bromide (LiBr- H_2O) absorption chiller (Type 107) is used in modeling of the system.

The performance indices are calculated as follow:

The coefficient of performance (COP) of the system is given in Eq. 2.

$$COP = \frac{Q_{chw}}{Q_{hw} + Q_{aux}} \quad (2)$$

where, Q_{chw} is the energy removed from the chilled water stream, Q_{hw} is the energy removed from hot



water stream and Q_{aux} is the energy consumed by various electrical components such as pumps. The COP of single-effect absorption chiller ranges between 0.5–0.8 and for double-effect absorption chiller, it ranges between 1.1–1.4[15]. Most of the researchers use single-effect absorption chillers due to their low initial, operation and maintenance costs [16].

The solar fraction (SF) is the fraction of total cooling load that is met by solar energy. It can be calculated by Eq.3.

$$SF = \frac{Q_{coll}}{Q_{coll} + Q_{aux\ heat}} \quad (3)$$

where, Q_{coll} is the energy delivered to hot water stream by solar collector array and $Q_{aux\ heat}$ is the energy delivered to the hot water stream from an auxiliary heater boiler.

2.4 Actual Building Description

The selected cold storage is located in Peshawar, Pakistan. The building has a floor area of 111.57 m² and four external walls of height 4 m. It has a single door on the south side wall of the building with an area of 4.5 m². The walls of cold storage buildings are made of 0.200 m thick common bricks layer with a 0.012 plaster layer on the inner side. The roof is made of 0.10 m thick heavyweight concrete along with a layer of 0.10 m common bricks. The walls and roof are thermally insulated with polystyrene material of thickness 0.025 m. The floor is made of 0.130 m heavyweight concrete.

2.5 Modification in the Building

In the modification of building the thickness of insulation material was increased to 0.051 m and a thin sheet of steel of thickness 0.005 m was used for cladding the inside walls and roof of a building.

2.6 Heat gains

Building cooling load was based on building envelope and internal heat gains. Gains were set according to ISO7730 standard with 8 persons, heavy work and lifting (470W), artificial lightning with a heat gain of 10 W/m² and a miscellaneous radiative power load of banana (178266 kJ/hr) with a schedule of 8 am to 5 pm daily.

2.7 Initial Component sizing

To obtain a baseline for simulation, initial sizing of system components was done as shown in Table. 2. To reduce the initial cost of installation, sizing of chiller is done about 5% less than the maximum cooling demand because maximum load only occurs for one day in a whole year and for the rest of the year it operates on part load.[5]

Table 2: Initial component sizing

Component	Size
Absorption chiller	60000 kJ/hr
Solar collector area	35 m ²
Hot water Storage tank	2.5 m ³
Slope of Collector	30 ⁰

3. Results and Discussions

Fig. 4. shows monthly average ambient temperature and percentage relative humidity for Peshawar, Pakistan. it is evident from the figure that ambient temperature is maximum in the month of June whereas, percent relative humidity is minimum in this month. Fig. 5. shows monthly radiation data for Peshawar including both beam and diffuse radiations. It is evident that total solar radiations are maximum in May and June having values of 1043 kJ/hr m² and 1089 kJ/hr m² respectively. It shows the potential of renewable solar energy available when cooling requirements are maximum.

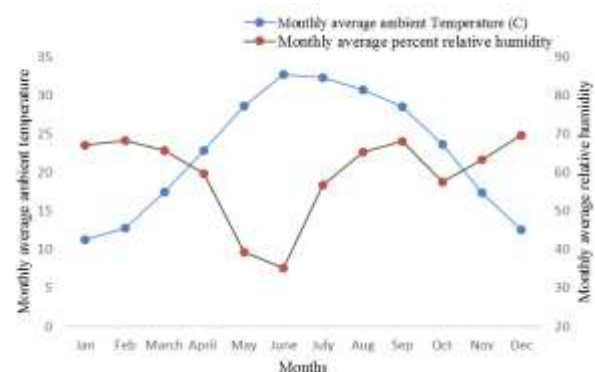


Figure 4: Monthly average ambient temperature and percentage relative humidity for Peshawar

Hourly cooling load demand of the actual building and modified building was calculated by maintaining storage temperature at 15 °C as shown in Fig. 6. and Fig. 7. respectively. Calculating maximum cooling load is essential for the estimation of the size of SAC system. Investigating the figures reveals that the maximum cooling load demand of actual building occurs in the month of July which is about 69270 kJ/hr. After applying the energy conservation measures there was 5.87% decrease in cooling load. The maximum cooling load demand of modified building reduces to 65200 kJ/hr. Fig. 8. shows a comparison of the monthly average cooling load of an existing and modified building. It is evident that there



is an enormous decrease in cooling load demand for summer.

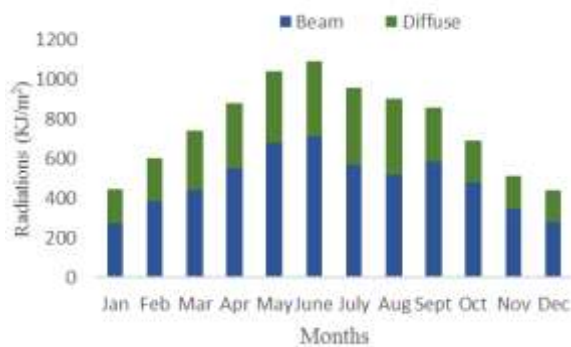


Figure 5: Average monthly beam and diffuse radiations for Peshawar

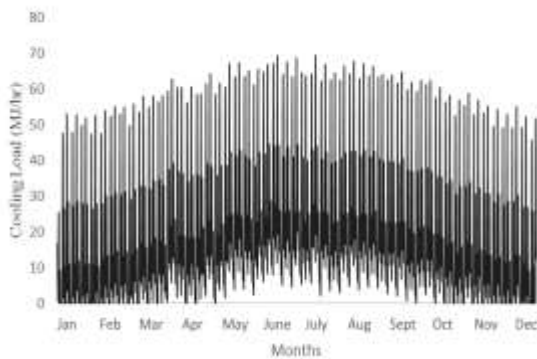


Figure 6: Hourly cooling load for actual building

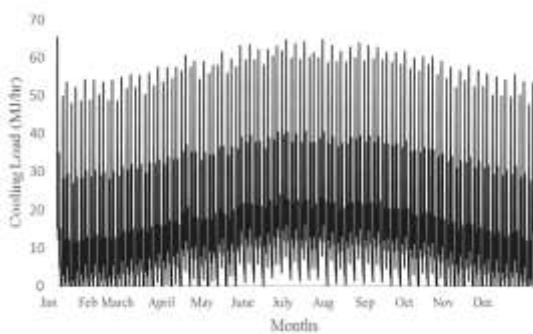


Figure 7: hourly cooling load for modified building

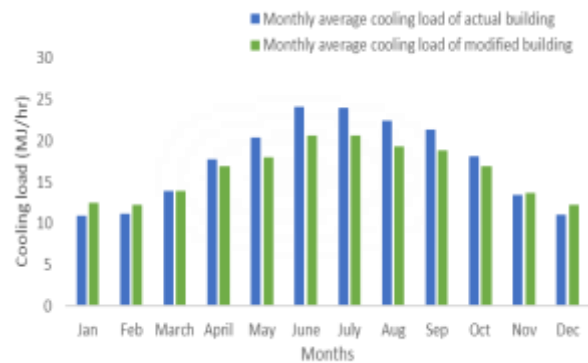


Figure 8: Monthly average cooling load of actual and modified building

3.1 Optimization of the System Components

The system optimization was done to determine the volume of hot water storage tank and area of solar collector at which the system attains the highest annually solar fraction without oversizing to minimize the capital cost of the system. For this purpose, the system component simulation model was run several times to get required results. Fig. 9. shows annual solar heat gain as a function of storage tank volume. As seen from the figure by increasing tank volume from 0.5 m³ to 5 m³ the solar heat gain first begins to increase and reaches a maximum value of 2694 MJ at tank volume of 1.5 m³. By further increasing volume, solar heat gain reduces therefore it is appropriate to use 1.5 m³ volume storage tank.

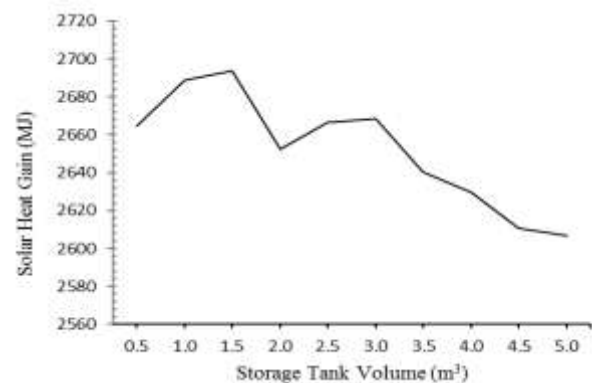


Figure 9: Effect of volume of storage tank on solar heat gain

Fig.10. shows a relation of solar fraction with the collector area. As the collector area increases solar fraction also increases up to 35 m². But if we further increase area, the slope of the graph gets decreasing and rise in the solar fraction is comparatively less, therefore, the optimize solar collector area is 35 m².

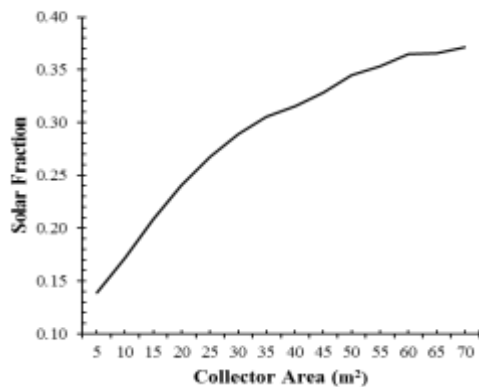


Figure 10: Variation of solar fraction with collector area

4. Conclusion

Modeling and optimization of solar assisted absorption cooling system for cold storage in Peshawar, Pakistan has been carried out. Results from simulations reveal that after applying modification and energy conservation measures to cold storage building the maximum cooling load reduced from 69270 kJ/h to 65200 kJ/h. The optimization analysis conducted for the system sizing reveals that an evacuated tube collector array of 35 m² area and 1.5 m³ hot water storage tank are appropriate to use so that to minimize the initial cost and increase the reliability of the system.

REFERENCES:

- [1] K. P. Amber, R. Ahmad, M. W. Aslam, A. Kousar, M. Usman, and M. S. Khan, "Intelligent techniques for forecasting electricity consumption of buildings," *Energy*, vol. 157, pp. 886–893, 2018.
- [2] J. A. Evans *et al.*, "Specific energy consumption values for various refrigerated food cold stores," *Energy Build.*, vol. 74, no. 2014, pp. 141–151, 2020.
- [3] J. A. Evans *et al.*, "Assessment of methods to reduce the energy consumption of food cold stores," *Appl. Therm. Eng.*, vol. 62, no. 2, pp. 697–705, 2014.
- [4] F. Tian, "An agri-food supply chain traceability system for China based on RFID & blockchain technology," *2016 13th Int. Conf. Serv. Syst. Serv. Manag. ICSSSM 2016*, 2016.
- [5] K. Street and L. E. Gb, "Ep 1 492 748 b1 (12)," vol. 1, no. 19, pp. 1–10, 2010.
- [6] H. Chen, T. Ngoc, W. Yang, C. Tan, and Y. Li, "Progress in electrical energy storage system: A critical review," *Prog. Nat. Sci.*, vol. 19, no. 3, pp. 291–312, 2009.
- [7] J. P. Praene, O. Marc, F. Lucas, and F. Miranville, "Simulation and experimental investigation of solar absorption cooling system in Reunion Island," *Appl. Energy*, vol. 88, no. 3, pp. 831–839, 2011.
- [8] K. Habib, B. Choudhury, P. Kumar, and B. Baran, "Study on a solar heat driven dual-mode adsorption chiller," *Energy*, vol. 63, pp. 133–141, 2013.
- [9] C. Sanjuan, S. Soutullo, and M. R. Heras, "Optimization of a solar cooling system with interior energy storage," *Sol. Energy*, vol. 84, no. 7, pp. 1244–1254, 2010.
- [10] X. Garcá, "Solar absorption cooling in Spain: Perspectives and outcomes from the simulation of recent installations ' a Casals *," vol. 31, pp. 1371–1389, 2006.
- [11] A. Al-Alili, M. D. Islam, I. Kubo, Y. Hwang, and R. Radermacher, "Modeling of a solar powered absorption cycle for Abu Dhabi," *Appl. Energy*, vol. 93, pp. 160–167, 2012.
- [12] M. Balghouthi, M. H. Chahbani, and A. Guizani, "Feasibility of solar absorption air conditioning in Tunisia," *Build. Environ.*, vol. 43, no. 9, pp. 1459–1470, 2008.
- [13] F. Assilzadeh, S. A. Kalogirou, Y. Ali, and K. Sopian, "Simulation and optimization of a LiBr solar absorption cooling system with evacuated tube collectors," *Renew. Energy*, vol. 30, no. 8, pp. 1143–1159, 2005.
- [14] G. A. Florides, S. A. Kalogirou, S. A. Tassou, and L. C. Wrobel, "Modelling, simulation and warming impact assessment of a domestic-size absorption solar cooling system," *Appl. Therm. Eng.*, vol. 22, no. 12, pp. 1313–1325, 2002.
- [15] U. Eicker and D. Pietruschka, "Design and performance of solar powered absorption cooling systems in office buildings," vol. 41, pp. 81–91, 2009.
- [16] Y. Hang, L. Du, M. Qu, and S. Peeta, "Multi-objective optimization of integrated solar absorption cooling and heating systems for medium-sized of fi ce buildings," *Renew. Energy*, vol. 52, pp. 67–78, 2013.



Experimental study on the thermal management of electronics using phase change material integrated metallic foam and heat pipe

Muhammad Aamer Hayat¹, Hafiz Muhammad Ali^{1,*}

1- Mechanical Engineering Department, University of Engineering and Technology, Taxila, Pakistan

* Corresponding Author: h.m.ali@uettaxila.edu.pk

Abstract

Phase change materials (PCMs) are widely used for the thermal management of electronic devices, but they have very low heat transfer rate due to its extremely low thermal conductivity which hinders its practical applications; therefore it is important to improve their thermal conductivity, PCM thermal conductivity can be improved by integrating it with high thermal conductive materials. In this study heat pipe (HP) and copper foam are integrated with PCM (RT-64) to examine the cooling performance of heat sink. Different heat sink configurations are investigated at two different heat fluxes 2 & 3 kW/m² for the same charging and discharging time of 6000 seconds to determine the best cooling arrangement. Results depicted that; the base temperature of heat sink increased with the increasing heat flux. At both heat fluxes, hybrid cooling (PCM-Cu Foam-HP) showed the best performance compared to other combinations. At heat flux of 2 and 3 kW/m² hybrid system with cooling fan reduces the base temperature by 38% and 39% respectively, as compared to empty heat sink. Setpoint temperature analysis also showed that hybrid cooling with fan is the best configuration.

Keywords: Thermal management, Phase change material, Heat pipe, Metal foam

1. Introduction

For the lifetime and performance of an electronic components thermal management plays an important role and 55% of microcircuits breakdown due to thermal reasons. The sizes of electronic components are decreasing, and power levels are increasing with the improvement in the technology [1]. If this heat generation cannot be controlled, then it may damage the electronic chip and diminish the performance of the appliance. A research conducted by defence department of US which showed that breakdown rate of electronic components increases as temperature rises above 75°C [2].

Recent advances in technology require high precision compact devices. Therefore, electronic control systems were implemented into the machines by the manufacturer. Over the past few decades, researchers worked on various thermal management methods for electronic devices such as the use of extended surfaces, phase-changing materials coupled with porous media and extended surfaces[3–5]. As examined by Kandasamy et al. [6] in 2008, heat sinks based on phase change material (PCM) showed incredible thermal performance. Subsequently, Yang et al. [7] conducted the three-dimensional heat transfer study for electronic cooling of the heat sink based on n-eicosane PCM. Results revealed the electronic system's more reliable operating temperature. Mahmoud et al. [8] investigated the thermal performance of heat sink using different PCMs. It was found that PCM with low melting temperature showed best performance in term of lowering the temperature of heat sink for longer duration. There are different

forms of PCMs, the most common are eutetic, organic and inorganic PCMs. Because of its abundance and low cost, organic PCMs are mainly used in electronic appliance cooling [9]. Though, because of the extremely low thermal conductivity of phase change materials, the rate of heat transfer is very low. So by using nanoparticles [10], carbon nanotubes [11], fins [12], heat pipe (HP) [13], and porous materials/foam [14], the rate of heat transfer in PCMs can be improved.

Allen et al. [15] used heat pipe/metal foil and heat pipe/metal foam configuration to examine the comparative efficacy, charging and discharging rates of PCM (n-octadecane). Results showed that the pore density (or foil thickness) of the foam for fixed porosity has a negligible effect on efficacy, while the most valuable variable was porosity. Measured efficacy was 0.957 and 0.870 respectively for HP/foil/PCM and HP/foam/PCM. Allen et al. [16] investigated six different configurations to evaluate the influence of melting and solidification of the phase change material in the cylinder enclosure. Results showed that the combined effect of HP with foils or foam result in much higher rates of melting and solidification compared to nano-enhanced system.

Above techniques have certainly provided promising results but have failed to provide satisfactory results for compact devices needing a large heat transfer. In current research authors addressed the problem by developing hybrid system, this hybrid system has excellent thermophysical properties that allow it to be



used in heat transfer devices in order to reduce its scale, cost and make it lighter and more efficient.

A lot of research had been conducted for the thermal management of electronic devices but using this hybrid system (HP-Foam-PCM) has not been studied yet. In this research paper, RT-64 with melting temperature of (63-65) $^{\circ}$ C is selected as PCM for low heat producing electronic components. Different heat sink configurations are investigated to determine the optimized configuration under heat load 2 and 3 kW/m 2 . Then conclusions will be drawn for the best heat sink configuration with optimal performance.

2. Methodology

The experimental method is adopted throughout to achieve the research objective. Different heat sinks configurations are investigated under different power inputs to evaluate its performance for proper cooling of electronic components.

3. Experimental setup

Experimental setup consists of six gravity assisted copper heat pipes with water as heat transfer fluid

(Condenser section of heat pipe has two cooling towers and an aluminium heat sink is also attached at the evaporator part of the heat pipe), Copper foam (Porosity 93% and Pore density 40PPI), data acquisition system, DC power supply, insulation block (thermal conductivity = 0.09 W/mK) and thermocouples. A 100 x 100 mm 2 silicone rubber plate heater of square shape is adhered to the sink base to mimic heat input. The plate heater facilitates in heat transferring due to which temperature change speedily in confined areas. Silicone rubber heaters are thin and lightweight. DC power supply provides heat flux to the plate heater which is attached at the base of sink. Power input given from the power supply ranges from 20W-30W selected on the basis of operating power input in mostly portable electronic devices. Temperature at different points of designed heat sink is measured with K-type thermocouples. Data Acquisition system (Agilent 34972A), to which thermocouples are inserted and connected to laptop record the sink temperature in each 5 seconds interval. Figure 2 and 3 shows the schematic and actual experimental setup respectively.

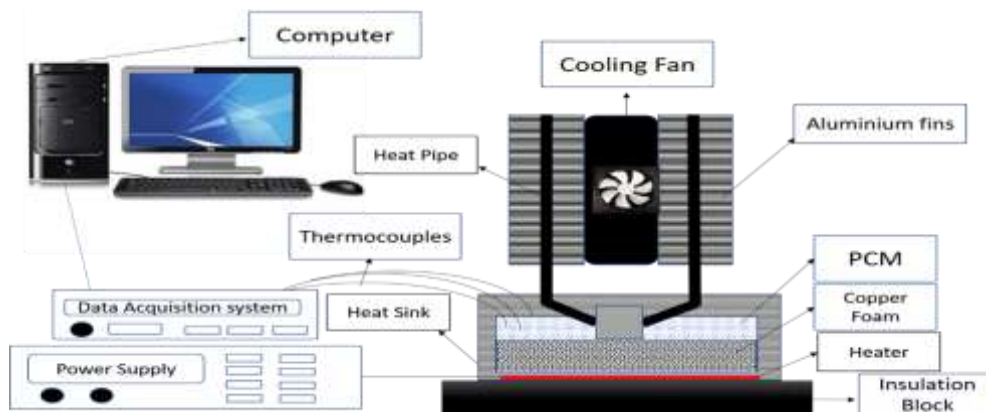


Figure 1 Schematic of experimental setup.



Figure 2 Actual experimental Setup.



4. Results and Discussions

Thermal behaviour of heat sinks, using RT-64 as PCM are investigated at two different heat fluxes for same charging and discharging time (6000Seconds). At heat flux of 2 kW/m² and 3 kW/m², base temperature of eight different configurations i.e. empty sink, sink within copper foam, HP w/o fan, HP with cooling fan, PCM only, PCM/copper foam composite, hybrid cooling(PCM-Cu Foam-HP) w/o fan and hybrid cooling with the fan are represented by C1, C2, C3, C4, C5, C6, C7 and C8 respectively, are shown in Figure 4 and 5. Empty sink (C1) is the reference case all configurations are compared with respect to it.

From figure 4 and 5 results revealed that, at heat flux of 2 kW/m² heat pipe cooling is superior to PCM cooling due to its ability to maintain the desired operating temperature but heat flux of 3 kW/m² PCM and PCM/copper foam composite has better reduction in heat sink base temperature than heat pipe because at higher heating load HP overheats. For heat flux of 2 kW/m², maximum temperature reduction with respect to empty heat sink (C1) are 3.8%, 22.2%, 25%, 14%, 18.9%, 30.3% and 38% for C2, C3, C4, C5, C6, C7 and C8 respectively. Similarly, at heat flux of 3kW/m² temperature reductions are 2.9%, 19.1%, 20.8%, 25%, 27.3%, 33.2% and 39% for C2, C3, C4, C5, C6, C7 and C8 respectively. At both heat fluxes hybrid cooling with fan (C8) is found to be extremely efficient because it provided stability to the base temperature for long term running condition of the microprocessor.

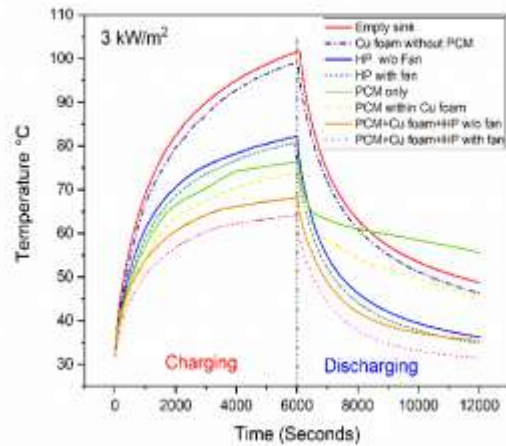


Figure 4 Behaviour of different configurations of the heat sink at 3 kW/m².

4.1 Analysis of Setpoint Temperature

Two setpoint temperatures (SPT) are analyzed to find the most effective combination, depending upon electronic component heat generation. Two setpoint temperatures with respect to time are selected for both charging and discharging to evaluate the performance of heat sink.

4.1.1 Charging Process

The setpoint temperature analysis during charging process at heat flux of 2 and 3 kW/m² are showed in Figure 6 and 7 respectively.

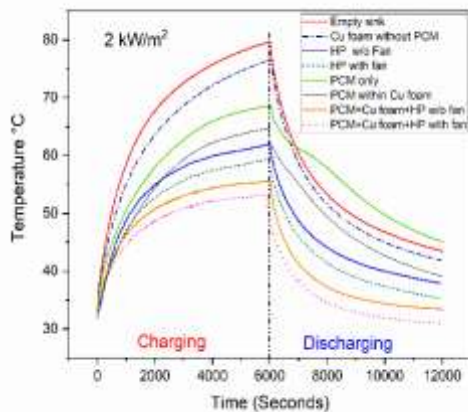


Figure 3 Behaviour of different configurations of the heat sink at 2 kW/m².

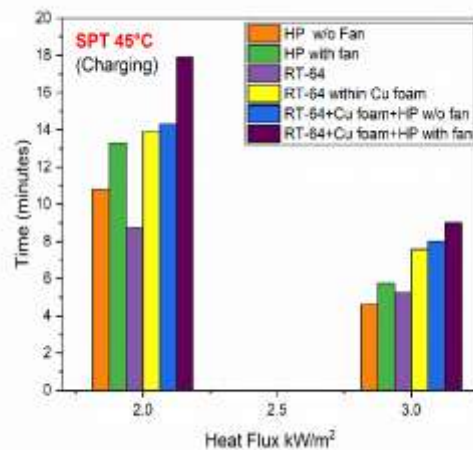


Figure 5 Comparison of operational time of different cooling methods at different heat fluxes for various composites at SPT 45°C.

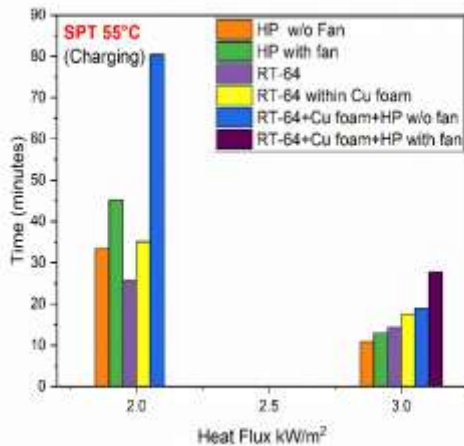


Figure 6 Comparison of operational time of different cooling methods at different heat fluxes for various composites at SPT 55°C.

In figure 6, hybrid system with cooling fan showed best performance because it took maximum time to reach the SPT while PCM took minimum time to reach the SPT that's why PCM exhibited least performance than other configurations at heat flux of 2 kW/m², at heat flux of 3 kW/m² again hybrid system with cooling fan showed best performance but in this case heat pipe without fan showed least performance that is due to overheating of heat pipe at higher heat fluxes. Figure 7 showed the SPT graph at 55°C, at heat flux of 2 kW/m² hybrid cooling with fan doesn't reach the temperature of 55°C and showed best performance and similarly at heat flux of 3 kW/m² hybrid system with cooling fan showed good results than other cooling systems.

4.1.2 Discharging Process

To examine the cooling proficiency of heat sink for discharging (cooling) process, two SPT are selected for investigation. Similar to charging (heating) process, hybrid cooling by RT-64 with fan is observed to be the most effective of all composites for cooling process at setpoint temperature 45°C and 55°C as shown in figure 8 and 9 respectively. At both setpoint temperatures, HP with fan behaved far better than RT-64/copper foam composite due to extra thermophysical properties of heat pipe.

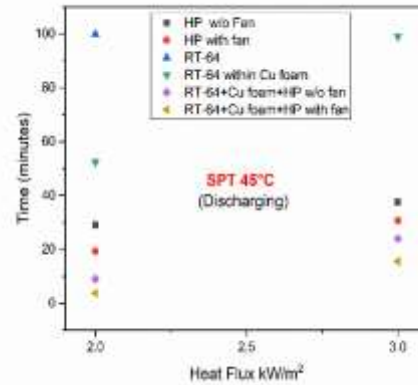


Figure 7 Discharging time comparison for different composites at various heating loads at SPT 45°C.

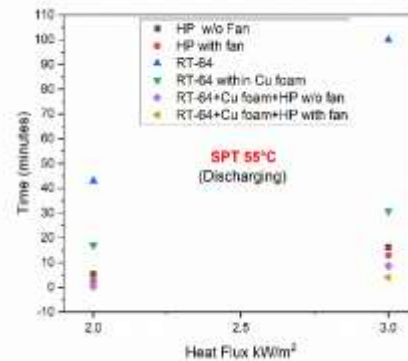


Figure 8 Discharging time comparison for different composites at various heating loads at SPT 55°C.

5. Conclusion

An experimental study is performed to investigate the thermal behaviour of different configurations of the heat sink using metal foam, heat pipe and PCM (RT-64HC) at two different heat fluxes 2 and 3 kW/m². From this experimental analysis, the following conclusions can be drawn:

- The addition of PCM in the heat sink lowered the temperature of the base by 14% and 25% at 2 and 3 kW/m² respectively as compared to empty heat sink, due to its high latent heat storage capacity.
- At lower heat flux (2kW/m²), heat pipe with and without cooling fan reduced the base temperature by 22.2% and 25% respectively and showed good performance than PCM only (14%) and PCM/copper foam composite (18.9%) cooling due to extra thermophysical properties of heat pipe.
- At higher heat flux 3 kW/m², PCM and PCM foam composite showed good cooling performance than heat pipe



because at higher heat fluxes heat pipe overheats.

- Overall, hybrid cooling with fan is the most effective cooling system it reduces the base temperature by 38% and 39% at heat flux of 2 and 3 kW/m² respectively, as compared to empty heat sink.
- For both charging and discharging, hybrid cooling system with fan is considered to best composite at all setpoint temperatures.

There has been a lot of research conducted to find the most effective thermal management method, but limitations of every technique opens the door for unending research activity. For further enhancement of thermal conductivity nanoparticles can also be used along with heat pipe and metal foam.

REFERENCES

- [1] H. Yin, X. Gao, J. Ding, Z. Zhang, Experimental research on heat transfer mechanism of heat sink with composite phase change materials, *Energy Convers. Manag.* 49 (2008) 1740–1746.
- [2] Military Handbook: Reliability Prediction of Electronic Equipment: MIL-HDBK-217F: 2 December 1991, Department of Defense, USA, (n.d.).
- [3] S.A. Nada, W.G. Alshaer, Comprehensive parametric study of using carbon foam structures saturated with PCMs in thermal management of electronic systems, *Energy Convers. Manag.* 105 (2015) 93–102.
- [4] A. Farzanehnia, M. Khatibi, M. Sardarabadi, M. Passandideh-Fard, Experimental investigation of multiwall carbon nanotube/paraffin based heat sink for electronic device thermal management, *Energy Convers. Manag.* 179 (2019) 314–325.
- [5] H.M. Ali, Experimental investigation on paraffin wax integrated with copper foam based heat sinks for electronic components thermal cooling, *Int. Commun. Heat Mass Transf.* 98 (2018) 155–162.
- [6] R. Kandasamy, X.-Q. Wang, A.S. Mujumdar, Transient cooling of electronics using phase change material (PCM)-based heat sinks, *Appl. Therm. Eng.* 28 (2008) 1047–1057.
- [7] Y.-T. Yang, Y.-H. Wang, Numerical simulation of three-dimensional transient cooling application on a portable electronic device using phase change material, *Int. J. Therm. Sci.* 51 (2012) 155–162.
- [8] S. Mahmoud, A. Tang, C. Toh, A.-D. Raya, S.L. Soo, Experimental investigation of inserts configurations and PCM type on the thermal performance of PCM based heat sinks, *Appl. Energy.* 112 (2013) 1349–1356.
- [9] X.-H. Yang, S.-C. Tan, Y.-J. Ding, L. Wang, J. Liu, Y.-X. Zhou, Experimental and numerical investigation of low melting point metal based PCM heat sink with internal fins, *Int. Commun. Heat Mass Transf.* 87 (2017) 118–124.
- [10] M. Alimohammadi, Y. Aghli, E.S. Alavi, M. Sardarabadi, M. Passandideh-Fard, Experimental investigation of the effects of using nano/phase change materials (NPCM) as coolant of electronic chipsets, under free and forced convection, *Appl. Therm. Eng.* 111 (2017) 271–279.
- [11] C. Kinkelin, S. Lips, F. Lefevre, U. Soupremanien, V. Remondiere, J. Dijon, H. Le Poche, E. Ollier, M. Zegaoui, N. Rolland, Experimental study of a hybrid CNT/PCM structure for the transient thermal management of electronics, in: *International Conference on Heat Transfer, Fluid Mechanics and Thermodynamics*, 2015.
- [12] H.M. Ali, A. Arshad, M. Jabbar, P.G. Verdin, Thermal management of electronics devices with PCMs filled pin-fin heat sinks: a comparison, *Int. J. Heat Mass Transf.* 117 (2018) 1199–1204.
- [13] J. Qu, Z. Ke, A. Zuo, Z. Rao, Experimental investigation on thermal performance of phase change material coupled with three-dimensional oscillating heat pipe (PCM/3D-OHP) for thermal management application, *Int. J. Heat Mass Transf.* 129 (2019) 773–782.
- [14] H.M. Ali, Experimental study on the thermal behavior of RT-35HC paraffin within copper and Iron-Nickel open cell foams: Energy storage for thermal management of electronics, *Int. J. Heat Mass Transf.* 146 (2020) 118852.
- [15] M.J. Allen, T.L. Bergman, A. Faghri, N. Sharifi, Robust heat transfer enhancement during melting and solidification of a phase change material using a combined heat pipe-metal foam or foil configuration, *J. Heat Transfer.* 137 (2015) 102301.
- [16] M.J. Allen, N. Sharifi, A. Faghri, T.L. Bergman, Effect of inclination angle during melting and solidification of a phase change material using a combined heat pipe-metal foam or foil configuration, *Int. J. Heat Mass Transf.* 80 (2015) 767–780.



Evaluation of Eight Reflected Solar Radiations Models to find Daily Optimum Tilt Angle for Lahore

Muhammad Hamza Faisal¹, Arsalan Naveed¹, Huzaiifa Maqsood¹, Zia ul Rahman Tahir^{1*}, Muhammad Asim¹, Bilal Mahmood¹, Zeeshan Arif¹, Muzammil Aslam¹ and Saiqa Hafeez¹

¹Department of Mechanical Engineering, University of Engineering and Technology, Lahore,

*Corresponding Author: ziartahir@uet.edu.pk

Abstract

Global trend is shifting towards utilizing renewable energy for production of electricity. Sun is a sustainable resource for electricity generation, but the problem lies with the efficiency of PV modules, however, efficiency can be enhanced by proper orientation based on optimum tilt angle and correct selection of sky model for a certain location. In this dissertation, methodology was described for calculation of daily total radiations based on different sky models and optimum daily tilt angle for maximum values of solar radiations. The sky models were evaluated and compared to select the most suitable one for Lahore site. The results obtained showed that summer season had maximum average solar radiations up to 280 W/m² and similarly, the winter season showed minimum average solar radiations equal to 105 W/m² for the year 2016. The isotropic and anisotropic models showed variable results depending upon sky conditions. In conclusion, Reindl model (anisotropic) is selected based on maximum average solar radiations values equal to 206.5 W/m² and 194.4 W/m² for daily tilt angle and annual tilt (latitude) angle during the whole year leading to maximum energy yield of PV modules. Optimum tilt angle is concluded to be varying between 0° and 65° degrees for Lahore. This research will help to evaluate other sky models for different locations and provide awareness to consumers to operate the PV modules at optimum conditions of maximum solar radiations and corresponding tilt angles to enhance their efficiency.

Key Words: Optimum Tilt Angle, Reflected Solar Radiations, Sky Models

1. Introduction

The fossil fuels are on the verge of becoming extinct in the coming years so there is a need to utilize renewable energy resources to meet the energy requirements. Sun is the primary source of all renewable resources and provides a sustainable source of energy. The amount of energy received from the Sun over the year is enough to provide electricity to the whole world. Pakistan has very high potential for solar energy because of its geographic location and climatic conditions [1]. The different technologies developed to convert this solar energy into electrical energy include photovoltaic cells, solar thermal and concentrated solar power [2]. Photovoltaic cells grouped together to form PV modules are responsible for converting solar energy into electrical energy thus by installing them at a large scale and maintaining them for efficient performance by optimizing different factors can be the answer to our problems.

The performance of the solar collector or panel is judged upon the solar radiations perceived by it. By changing the orientation, the amount of radiations falling on the PV module surface also become

variable [3]. The optimum orientation also regarded as optimum tilt angle is different for different locations and the day of the year. Khorasanizadeh et al. [4] has reported increase in energy as 23%, 22%, and 14% by changing the tilt angle monthly, seasonal and semi-yearly respectively. Now after providing optimum tilt to the PV module, depending upon the geography and climatic conditions of the location, total radiations incident on it are calculated. Total solar radiations (H_T) are calculated from beam (H_B), reflected (H_R) and diffused (H_D) components of radiations coming from the Sun. For the calculation of beam radiations, required parameters include direct normal irradiance (DNI) which is measured and ratio of average daily beam radiation incident on an inclined surface to horizontal surface (R_b) calculated using sunset hour angle, tilt angle and location coordinates. The calculation for reflected component is straightforward using H_g and the ground albedo (ρ) which is taken as 0.2 [5] and this value is widely accepted. The measured data for daily global radiations incident on a horizontal surface (H_g) is easily available for different locations. The long-term datasets for solar radiations are available from certain organizations such as The United States National



Centers for Environmental Prediction (NCEP), The European Centre for Medium-Range Weather Forecasts (ECMWF) and The Japan Meteorological Agency (JMA) [6]. Now, the problem lies with the calculation of diffused component of radiations because the measured data for diffused horizontal irradiance is not easily available and diffuse factor (R_d) is calculated from a specific sky model. The sky model does not affect the values of beam and reflected components and accounts only for the diffused components. These models directly provide with the diffused component of radiations on a tilted surface. The modelling technique behind these models is divided as isotropic and anisotropic. The minimum error in statistical analysis is desirable for best model selection of based on sky conditions such as sky being clear sky, intermediate sky (semi-cloudy) and cloudy sky [7]. Thus, same sky model cannot be used for all the locations. A variety of sky models are available which make use of extra-terrestrial radiations, daily global radiations on horizontal surface and tilt angle to provide mean daily total solar radiations (H_T). The tilt angle is varied daily, monthly, seasonal and semi-yearly between 0° and 90° degrees. A mechanical system or a solar tracker for the adjustment of daily tilt angle is to be designed to keep it at optimum value. This study is aimed at providing the optimum tilt angle on daily basis for maximum total incident radiations and a qualitative as well as quantitative comparison of some of the widely accepted isotropic and anisotropic sky models for Lahore site

2. Methodology

The mean daily total solar radiations (H_T) were classified as a mixture of beam (H_B), diffused (H_D) and reflected (H_R) radiations on an inclined surface as mentioned in Eq. (1).

$$H_T = H_B + H_D + H_R \quad (1)$$

here, H_B is solar radiations coming from the Sun to Earth without facing any obstacle or scattering in a straight path, H_D is solar radiations received after being scattered by molecules or suspensions in the atmosphere from all over the sky and H_R determines the amount of radiations reflected from the ground.

For all designs, the technique of calculating beam radiations on tilted surfaces is same. The only distinction is the approach by which component of diffuse radiations is determined.

The daily beam radiations (H_B) on inclined surface were expressed in Eq. (2) as a product of incident beam radiations on a horizontal surface on daily basis

(H_b) and ratio of average daily beam radiation incident on an inclined surface to horizontal surface (R_b).

$$H_B = H_b R_b \quad (2)$$

The ratio of average daily beam radiation incident on an inclined surface to horizontal surface (R_b) was described in terms of sunrise hour angle on horizontal surface (ω_s), sunrise hour angle on tilted surface (ω'_s), and latitude (ϕ) of the location in the northern hemisphere sloped towards equator in Eq. (3)

$$R_b = \frac{\cos(\phi - \beta) \cos \delta \sin \omega'_s + \sin(\phi - \beta) \sin \delta \omega'_s (\pi/180)}{\cos \phi \cos \delta \sin \omega_s + \sin \phi \sin \delta \omega_s (\pi/180)} \quad (3)$$

Sunrise hour angle on horizontal surface (ω_s) and sunrise hour angle on tilted surface (ω'_s) were obtained from Eq. (4) and Eq. (5) respectively.

$$\omega_s = \cos^{-1}(-\tan \phi \tan \delta) \quad (4)$$

$$\omega'_s = \min[\cos^{-1}(-\tan \phi \tan \delta)] \quad (5)$$

In Eq. (6), the daily sky-diffused radiations (H_D) on inclined surface were expressed in term of diffused horizontal radiations (H_d) and diffuse factor (R_d):

$$H_D = H_d R_d \quad (6)$$

R_d depends on the selection of sky models as it is a relation between daily diffused radiations on a tilted and horizontal surface [8]. The mathematical sky models have been described in Eq. (8) to Eq. (15).

The daily ground reflected radiations (H_R) on inclined surface were calculated from Eq. (7) in term of global horizontal radiations (H_g), tilt angle (β) and ground albedo or ground reflectivity (ρ):

$$H_R = H_g \rho \text{Error!} \quad (7)$$

3. Different Sky Models

Sky models determine the quantitative measure of incident radiations falling on a PV modules surface depending upon the atmospheric conditions. They are further divided as isotropic models and anisotropic models.

3.1 Isotropic Models

Isotropic models are based on the condition that saturation of radiations is constant over the sky and only isotropic part of radiations is considered.



3.1.1 Koronakis Model

Koronakis model [9] was proposed in 1986 with certain correction to improve its accuracy for calculating results of locations in Northern Hemisphere. It is an improved version of Liu and Jordan model by a particular mathematical factor as described in Eq. (8).

$$R_d = \frac{2 + \cos \beta}{3} \quad (8)$$

3.1.2 Tian Model

Tian model [10] shown in Eq. (9) estimates total slope radiations segregating global radiations. The pragmatic method of addressing the relationship between total incident solar radiations and atmospheric traits is an appreciable aspect of the Tian model.

$$R_d = 1 - \frac{\beta}{180} \quad (9)$$

3.1.3 Badescu Model

The Badescu model [11] mentioned in Eq. (10) defines zenith and azimuth angle based on 3D theory as an improvement of Liu and Jordan model that uses 2D theory to define zenith angle only.

$$R_d = \frac{(3 + \cos 2\beta)}{4} \quad (10)$$

3.1.4 Lui and Jordan Model

Lui and Jordan model [12] is the simplest isotropic model. It provides good approximation for empirical data of completely cloudy skies as written in Eq. (11). Lui and Jordan model relates the ratio between daily total radiations and the daily extra-terrestrial radiations insolation on a surface with sky cloudiness index. But, the validity of this model decreases as the skies become clear and amount of cloudiness decreases.

$$R_d = \frac{1 + \cos \beta}{2} \quad (11)$$

3.2 Anisotropic Models

The anisotropic models are the improved methods which help in analysing the diffused part of solar radiations in more detail. The anisotropic models assume the anisotropy of the diffuse sky radiations in the circumsolar region (sky near the solar disc) plus and isotopically distributed diffuse component from the rest of the sky dome.

3.2.1 Skartveit and Olseth Model

Skartveit and Olseth model [13] uses data of average monthly radiations to calculate beam and diffused

components on tilted surface by using Eq. (12). It provides us with best results no matter if you use constant, isotropic or seasonally varying albedo.

$$R_d = \frac{H_b}{H_o} R_b + \Omega \cos \beta + \left(1 - \frac{H_b}{H_o} - \Omega\right) \left(\frac{1 + \cos \beta}{2}\right) \quad (12)$$

where, $\Omega = \left\{ \max \left[0, \left(0.3 - 2 \frac{H_b}{H_o}\right) \right] \right\}$ and H_o is the extra-terrestrial radiations.

3.2.2 Hay Model

The Hay and Davies model [14] was proposed to treat diffused isotropic and circumsolar parts of radiations while neglecting horizon brightening. Hay model uses anisotropy index $\left(\frac{H_b}{H_o}\right)$ as seen in Eq. (13). Hay model acts as a Liu and Jordan Model for zero anisotropy index.

$$R_d = \frac{H_b}{H_o} R_b + \left(1 - \frac{H_b}{H_o}\right) \left(\frac{1 + \cos \beta}{2}\right) \quad (13)$$

3.2.3 Reindl Model

Reindl et al. Model [15] as described in Eq. (14) considers the circumsolar radiations and horizontal brightening along with the isotropic radiations. Circumsolar radiations (radiations seemed to be originated from region around the sun and scattered due to aerosols) and horizontal brightening (the increase in diffused radiations around the horizon due to multiple reflections and scattering) occur in clear skies only thus they are not considered by Lui and Jordan model for cloudy skies.

$$R_d = \frac{H_b}{H_o} R_b + \left(1 - \frac{H_b}{H_o}\right) \left(\frac{1 + \cos \beta}{2}\right) \left(1 + \sqrt{\frac{H_b}{H_g}} \sin^3 \left(\frac{\beta}{2}\right)\right) \quad (14)$$

3.2.4 Steven and Unsworth model

Steven and Unsworth model [16] is interpreted mathematically in Eq. (15). Now in Eq. (15) the value of a proposed constant (b) can be taken as 0, 1.23 and 2, however, with the change in value of " b " the percentage error changes. It comes out to be 20% for zero and 5% for two as compared to results obtained by using 1.23.

$$R_d = \cos \left(\frac{\beta}{2}\right)^2 + \frac{2b}{(3+2b)\pi} \left(\sin \beta - \beta \cos \beta - \pi \sin \left(\frac{\beta}{2}\right)^2 \right) \quad (15)$$

4. Results and Discussion

For Lahore site, solar data from 1st January 2016 to 31st December 2016 as obtained from Energy Sector Management Assistance Program (ESMAP) of the World Bank is used. The data for year 2016 was



complete and there were no gaps in the data. This data was easily available and comprehensive as compared to the succeeding years that's why analysis was performed on this data.

The formulae (Eq. (1) to Eq. (7)) mentioned in the methodology were used to compute results for total radiations (H_T) by changing the tilt angle from zero to ninety degrees and keeping the ground albedo as 0.2. The selected sky models were utilized to get maximum total incident radiations corresponding to optimum tilt angles on daily basis.

In Fig. 1, time series for daily total solar radiations (H_T) is drawn for Liu and Jordan model as shown below. The annual maximum average value of total solar radiations, against daily optimization of tilt angle, obtained were equal to 199.8 W/m^2 .

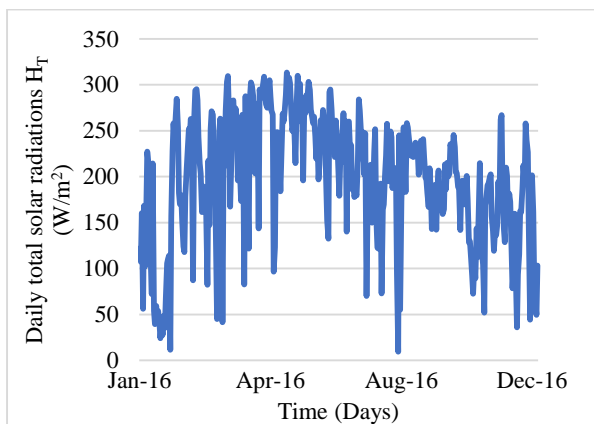


Fig.1 Time series of daily total solar radiations for Liu and Jordan model

In Fig. 2, time series for daily total solar radiations (H_T) is drawn for Koronakis model as shown below. The annual maximum average value of total solar radiations, against daily optimization of tilt angle, obtained were equal to 201.3 W/m^2 .

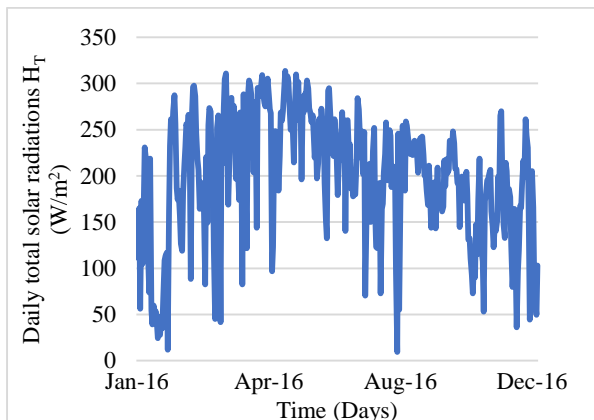


Fig. 2 Time series of daily total solar radiations for Koronakis model

Time series for daily total solar radiations (H_T) is drawn for Badescu model as shown below in Fig. 3. The annual maximum average value of total solar radiations, against daily optimization of tilt angle, obtained were equal to 197.3 W/m^2

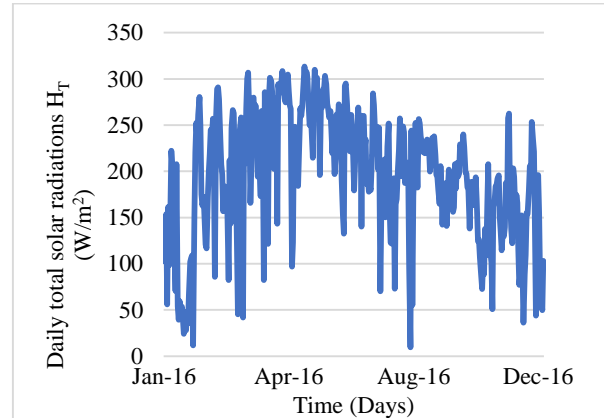


Fig. 3 Time series of daily total solar radiations for Badescu model

Time series for daily total solar radiations (H_T) is drawn for Tian model as shown below in Fig. 4. The annual maximum average value of total solar radiations, against daily optimization of tilt angle, obtained were equal to 196.1 W/m^2 .

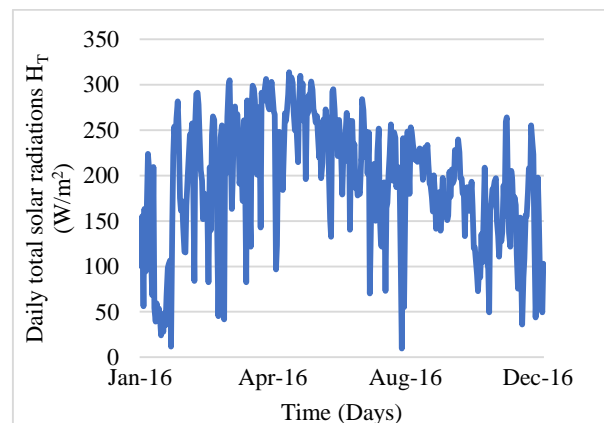


Fig. 4 Time series of daily total solar radiations for Tian model

Time series for daily total solar radiations (H_T) is drawn for Reindl model as shown below in Fig. 5. The annual maximum average value of total solar radiations, against daily optimization of tilt angle, obtained were equal to 206.5 W/m^2 .

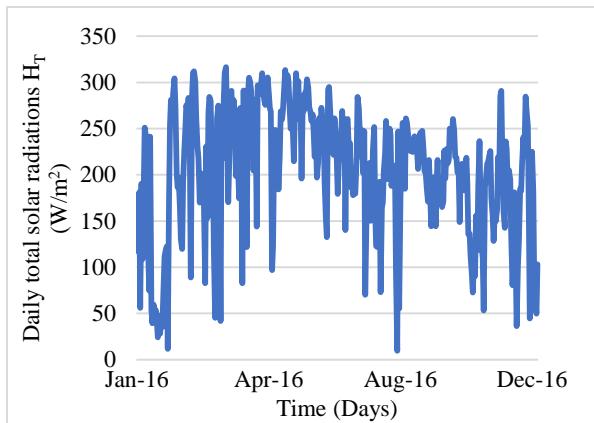


Fig. 5 Time series of daily total solar radiations for Reindl model

Time series for daily total solar radiations (H_T) is drawn for Skartveit and Olseth model as shown below in Fig. 6. The annual maximum average value of total solar radiations, against daily optimization of tilt angle, obtained were equal to 205.7 W/m^2 .

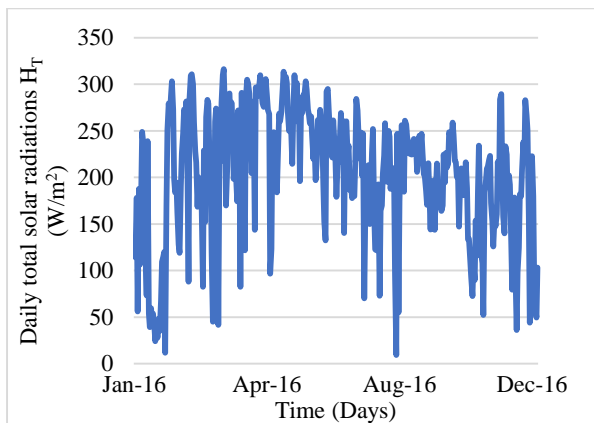


Fig. 6 Time series of daily total solar radiations for Skartveit and Olseth model

Time series for daily total solar radiations (H_T) is drawn for Steven and Unsworth model as shown below in Fig. 7. The annual maximum average value of total solar radiations, against daily optimization of tilt angle, obtained were equal to 198.6 W/m^2 .

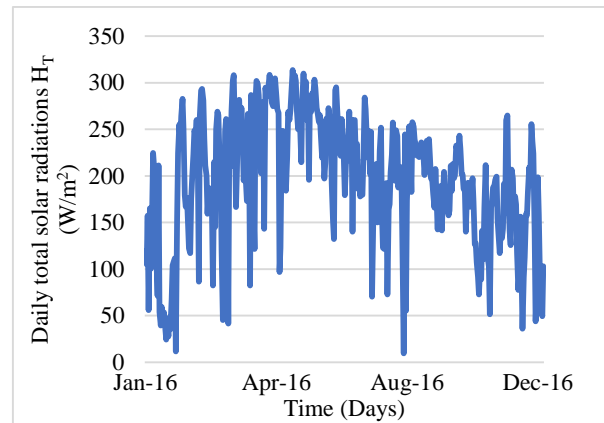


Fig. 7 Time series of daily total solar radiations for Steven and Unsworth model

Time series for daily total solar radiations (H_T) is drawn for Hay model in Fig. 8. The annual maximum average value of total solar radiations, against daily optimization of tilt angle, obtained were equal to 205.8 W/m^2 .

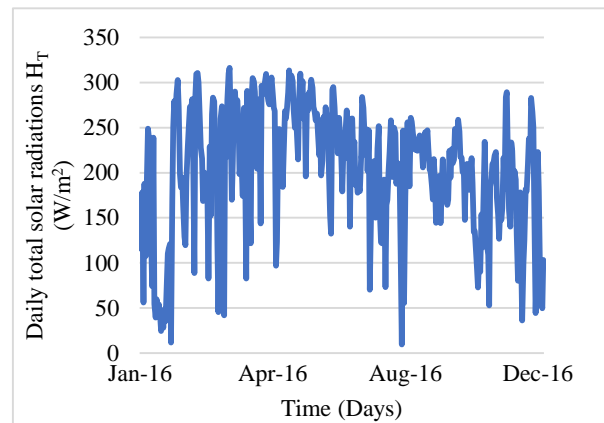


Fig. 8 Time series of total solar radiations daily total solar radiations for Hay model

The comparison was made between the different isotropic and anisotropic sky models as shown in Fig. 9. Fig. 9 describes the variation in mean total solar radiations for whole year falling on the PV module according to zero degrees, latitude tilt and daily tilt angle optimization. Different models gave different values for H_T . In Fig. 9, the symbols mentioned on the independent axis represent different parameters such as H_T -Zero represents the maximum average value of total solar radiations on a horizontal module surface or at zero degrees' tilt, H_T -Lat represents the maximum average value of total solar radiations on latitude tilt or fixed annual tilt and H_T -Max represents the maximum average value of total solar radiations on daily tilt angle optimization of a solar module. In Fig. 9, H_{T1} , H_{T2} , H_{T3} , H_{T4} , H_{T5} , H_{T6} , H_{T7} and H_{T8} represent Liu and Jordan model, Koronakis model, Badescu model, Tian model, Reindl model, Skartveit



and Olseth model, Steven and Unsworth model and Hay model respectively. The worst results were obtained for Tian Model with maximum average solar radiations equal to 180 W/m² and 196.1 W/m² for latitude tilt and daily tilt angle respectively. The best results (shaded as red in Fig. 9) were obtained for Reindl model as maximum average solar radiations value equal to 194.4 W/m² and 206.5 W/m² latitude tilt and daily tilt angle respectively. As shown in the Fig. 9, the values of H_T were higher by varying tilt angle on daily basis as compared to latitude tilt.

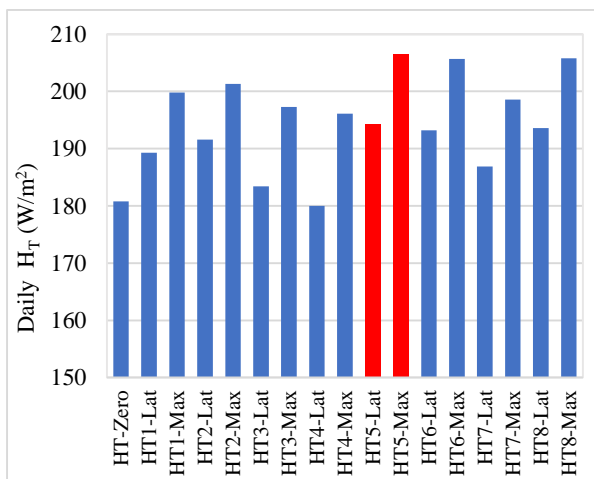


Fig. 9: Comparison of reflected solar radiation sky models based on H_T values for horizontal, latitude and daily tilt angle

The variation of optimum tilt angle on the daily basis for the complete year was also plotted in Fig. 10. It was seen to be non-uniform.

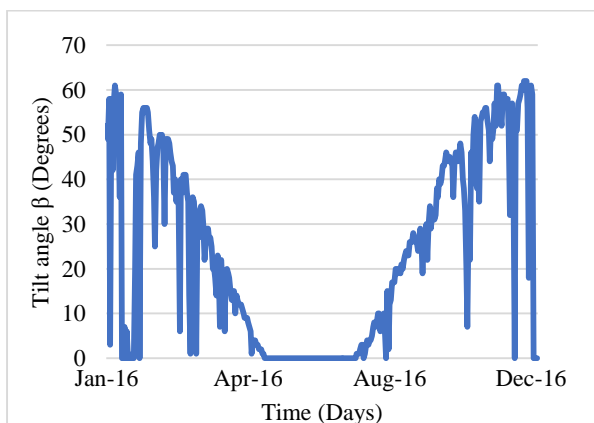


Fig.10 Optimum tilt angle variation on daily basis for a year

It was observed in Fig. 10 that from January to May, the optimum angle varied between 63 degrees to zero degrees. It remained approximately zero for the spring and summer season. Then, it showed an increasing

trend from zero to 63 degrees for autumn and winter season.

5. Conclusion

The optimum tilt angle for maximum total solar radiations to strike the surface of a PV module changes for each day of the year, thus, maximum efficiency can only be achieved if the module is tilted at this angle on daily basis. This can be validated by the results obtained after comparison of models for latitude and daily tilt angle optimization. Reindl model gives us the best results for both latitude and daily tilt angle orientation with maximum values for solar radiations falling on the PV module surface equal to 194.4 W/m² and 206.5 W/m² respectively. For this purpose, a design of mechanical system such as a gear mechanism to be fixed with the mounting of PV module could be proposed or a solar tracker could be installed for optimum orientation. The optimum tilt angle is to be varied between 0° to 65° degrees for Lahore. This research will help to evaluate other sky models for different locations and provide awareness to consumers to operate the PV modules at optimum conditions of maximum solar radiations and corresponding tilt angles to enhance their efficiency.

REFERENCES

- [1] Tahir, Z.u.R., et al., *The evaluation of reanalysis and analysis products of solar radiation for Sindh province, Pakistan*. Renewable Energy, 2020. **145**: p. 347-362.
- [2] Tahir, Z.R. and M. Asim, *Surface measured solar radiation data and solar energy resource assessment of Pakistan: A review*. Renewable and Sustainable Energy Reviews, 2018. **81**: p. 2839-2861.
- [3] Khan, J. and M.H. Arsalan, *Solar power technologies for sustainable electricity generation – A review*. Renewable and Sustainable Energy Reviews, 2016. **55**: p. 414-425.
- [4] Khorasanizadeh, H. and K. Mohammadi, *Diffuse solar radiation on a horizontal surface: Reviewing and categorizing the empirical models*. Renewable and Sustainable Energy Reviews, 2016. **53**: p. 338-362.
- [5] Despotovic, M. and V. Nedic, *Comparison of optimum tilt angles of solar collectors determined at yearly, seasonal and monthly levels*. Energy Conversion and Management, 2015. **97**: p. 121-131.



- [6] Tahir, Z.u.R., et al., *Evaluation of NCEP-Products (NCEP-NCAR, NCEP-DOE, NCEP-FNL, NCEP-GFS) of Solar Radiation for Karachi, Pakistan*. 2018. 1-12.
- [7] Noorian, A.M., I. Moradi, and G.A. Kamali, *Evaluation of 12 models to estimate hourly diffuse irradiation on inclined surfaces*. Renewable Energy, 2008. **33**(6): p. 1406-1412.
- [8] Benghanem, M., *Optimization of tilt angle for solar panel: Case study for Madinah, Saudi Arabia*. Applied Energy, 2011. **88**(4): p. 1427-1433.
- [9] Koronakis, P.S., *On the choice of the angle of tilt for south facing solar collectors in the Athens basin area*. Solar Energy, 1986. **36**(3): p. 217-225.
- [10] Tian, Y.Q., et al., *Estimating solar radiation on slopes of arbitrary aspect*. Agricultural and Forest Meteorology, 2001. **109**(1): p. 67-74.
- [11] Danandeh, M.A. and S.M. Mousavi G, *Solar irradiance estimation models and optimum tilt angle approaches: A comparative study*. Renewable and Sustainable Energy Reviews, 2018. **92**: p. 319-330.
- [12] Klucher, T.M., *Evaluation of models to predict insolation on tilted surfaces*. Solar Energy, 1979. **23**(2): p. 111-114.
- [13] Skartveit, A. and J. Asle Olseth, *Modelling slope irradiance at high latitudes*. Solar Energy, 1986. **36**(4): p. 333-344.
- [14] Hay, J.E., *Calculation of monthly mean solar radiation for horizontal and inclined surfaces*. Solar Energy, 1979. **23**(4): p. 301-307.
- [15] Shukla, K.N., S. Rangnekar, and K. Sudhakar, *Comparative study of isotropic and anisotropic sky models to estimate solar radiation incident on tilted surface: A case study for Bhopal, India*. Energy Reports, 2015. **1**: p. 96-103.
- [16] Steven, M. and M.H. Unsworth, *The angular distribution and interception of diffuse solar radiation below overcast skies*. Quarterly Journal of the Royal Meteorological Society, 1980. **106**: p. 57-61.



Assessment of Relative Humidity, Temperature, Carbon Dioxide & Particulate Materials in Labs

Tahir Nawaz^{1*}, Muhammad Bilal Sajid¹

1- US Pakistan Centers for Advanced Studies in Energy, NUST, Islamabad

*Email: tahirizhar125@gmail.com

Abstract:

Commonly, individuals spend their time inside dwellings, this makes the indoor environment of great health concern to the occupants because most of the poor-quality air is inhaled inside dwellings. Worldwide, indoor air pollutants cause the foremost vital indoor air quality challenges attributable to the number of people it affects, different types of pollutants involved, and the acuteness of the risks involved. Besides, in educational buildings especially in laboratories, the indoor environment can be much different than any other area of the institute because different processes are going on there. This study was carried out to investigate different parameters affecting the quality of the built environment and thermal comfort along with particulate materials in three laboratories of an educational building with a centralized ventilation system and split system. CO₂, temperature, relative humidity, and particulate materials were measured during the weekdays. The Extech-CO210 CO₂ data logger was used in the sampling of CO₂ and comfort parameters while Fluke 985 particle counter was used for measuring particles of different sizes. Also, measurements were compared against ASHRAE 55, 62.1 and US EPA standards for the minimum required performance. All parameters were observed to be within the limits of required standards except for the temperature in all studied spaces and particle mass concentrations for size less than 10 μ m.

Keywords: CO₂ concentration, RH, Thermal Comfort, Educational Building, Indoor Air Quality, PM10, PM2.5

1. Introduction:

Mostly, people spend their time indoor, around 90% of their daily lives in built environments like inside offices, schools, college, commercial, industrial buildings or inside their houses. Previously conducted studies suggest that the pollutants present in the indoor air are far more than that of the outside atmosphere [1]-[2]. Also, IAQ is strongly controlled by both outdoor and indoor contamination sources which need to be properly controlled [3]. According to the World Health Organization, more deaths occur due to indoor pollution than outdoor pollution [4]. Moreover, indoor air quality (IAQ) and thermal comfort can also influence the productivity, concentration, performance, and well-being of an occupant [3], [5].

Around the world, the IAQ is assessed by CO₂ levels as CO₂ is usually considered as a substitute for ventilation quality assessment because CO₂ levels above a certain concentration shows poor ventilation in the building which indicates the possibility of build-up of higher concentrations of other indoor pollutants which can have negative impact on human health [6]-[7]. Besides CO₂, temperature and relative humidity, solid suspended particles are also of great health risk in the built environment [8]. Particulate materials are one of the causes of asthma, rhinitis, allergic disease

[9] and can be carcinogenic in nature. PMs are suspended solid particles in the air, mainly sourced by construction, industrial processes, combustion processes in engines and other utility instruments like stoves, etc. and dust produced by vehicles [10].

Many researchers studied IAQ in past and investigated IAQ of different types of buildings such as museums, residential buildings, old age community centers, offices, health care centers and, academic buildings [11]-[15]. As students and teachers spend the majority of their time in Academic institutes after homes make them one of the most important built environment to be studied [3], [5], [12].

This study aimed to assess the indoor concentrations of CO₂ along with indoor temperature, relative humidity and particulate materials (PM) in three labs of an academic building present in Islamabad. Data were gathered during the occupational hours of the labs. ASHRAE 55, ASHRAE 62.1 and US EPA standards were used to check the quality of the built environment.

2. Methodology:

2.1 Measurement location:

This study was carried out to assess the quality of the built environment by measuring CO₂, temperature, relative humidity and particulate materials of different sizes of a newly built building of USPCAS-E. Three labs were selected and labeled as SL, FL & CL. A prior survey to the site was conducted to know about the activities and different factors that can affect the parameters being monitored. All three were different purpose labs. Among them, one lab CL was centralized HVAC, while the other 2 were equipped with a split system. SL was on the first floor, FL on the second floor and CL was on the third floor.

2.2 Instruments and sampling:

Indoor concentrations of CO₂ along with indoor temperature and relative humidity were monitored during the month of June 2019. Extech CO210 data logger was used during this study Fluke 985 particle counter was used to study the airborne particle concentrations in the built environment. Specification of these instruments is given in table 1 and 2.

Continuous measurements were taken for 2 to 3 days for CO₂ and thermal comfort parameters while airborne particles were sampled for 90 minutes during weekdays. The sampling data was logged for a period of 1 minute for all parameters. The sampling period was during the official working hrs. Mean 15-minutes average values of the comfort parameters and CO₂ are presented for comparison.

3. Results and Discussions:

The set of data collected for all three labs is presented in a mean graphical form to show its behavior for each lab as well as to compare the parameters. The mass concentrations of all six sizes for 3 labs are presented on box charts for comparison.

Table 1: Specification of Extech CO 210

Sr.no	Specification	Range
1	CO ₂	0-9999 PPM
2	Resolution	1 PPM
3	Temperature	-10 to 60 °C
4	Resolution	0.1°C
5	Humidity	0.1 to 99.9%
6	Resolution	0.1%
7	Datalogging	Up to 5333 points for each parameter

Table 2: Specification fluke 985 particle counter

Sr.no	Specification	Range
1	Particle-Size range	0.3, 0.5, 1.0, 2.0, 5.0, 10.0) μ m
2	Channels	6
3	Flow rate	2.83 liter/min
4	Data storage	10000 points

3.1 Variation of Carbon Dioxide:

Figure 1 shows the CO₂ distribution of the labs with time during the sampling period. Among the three labs, the fossil fuel lab was found to be having higher CO₂ levels as compared to the computer and solar lab. Though the CO₂ concentrations were measured different in all three labs, still CO₂ was found to be within the limits defined by ASHRAE 62.1 standard, which is below 1000ppm. The maximum and minimum values of carbon dioxide recorded were 814, 932 & 645 ppm max and 382, 405 & 530 ppm min for the computer lab, fossil fuel lab and solar lab respectively.

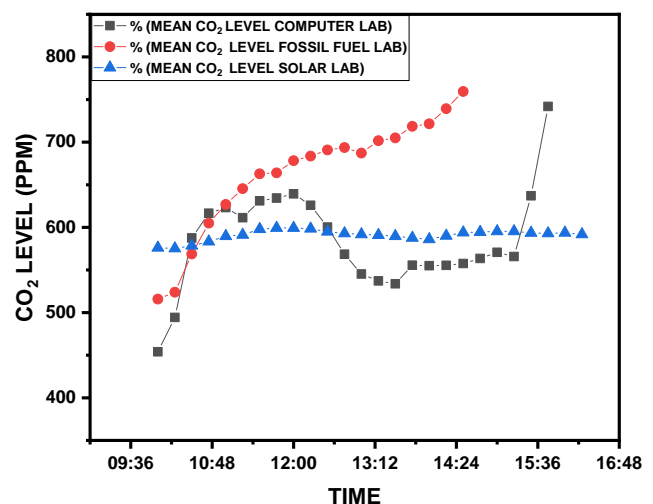


Figure 1: CO₂ profile of all three labs

3.2 Relative Humidity:

Figures 2 represents the relative humidity behavior of the monitored laboratories with time. The relative humidity of solar and computer fuel lab was observed in the range of 40-45 % for most of the monitoring duration while fossil fuel had relative humidity a little higher than the other two labs. This may be because of the processes involving water in the laboratory. The maximum values recorded was 64.9%, 63% & 49% respectively in computer lab, fossil fuel lab & solar lab. While the lowest reading measured in the computer lab was 37.3% and 35% for the other labs.

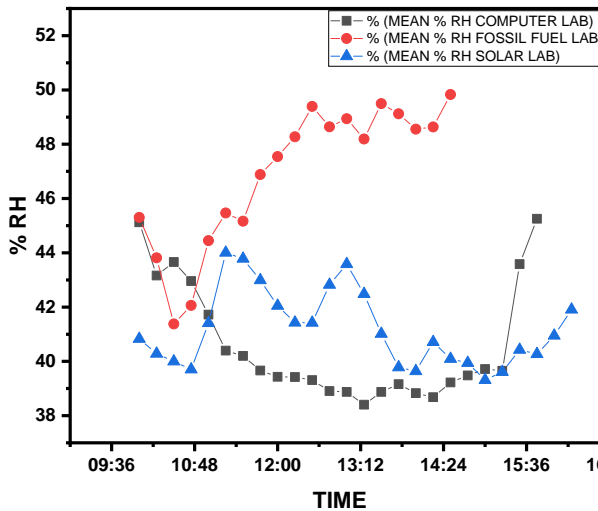


Figure 2: %RH profile of all three labs

3.3 Temperature:

Figure 3 shows a mean 15-minute average graph of the temperature of the monitored laboratories. The temperature profile computer lab is significantly higher than the other two tested locations. The main reason for this behavior was found to be the presence of high-performance computers which were performing continuous simulation and were releasing heat into the built space. The maximum values recorded were 32.6°C, 31.9°C & 30°C for computer lab, fossil fuel lab and solar lab respectively while, lower temperature recorded was 26.1°C, 24.9°C & 25°C respectively for computer, fossil fuel, and solar lab.

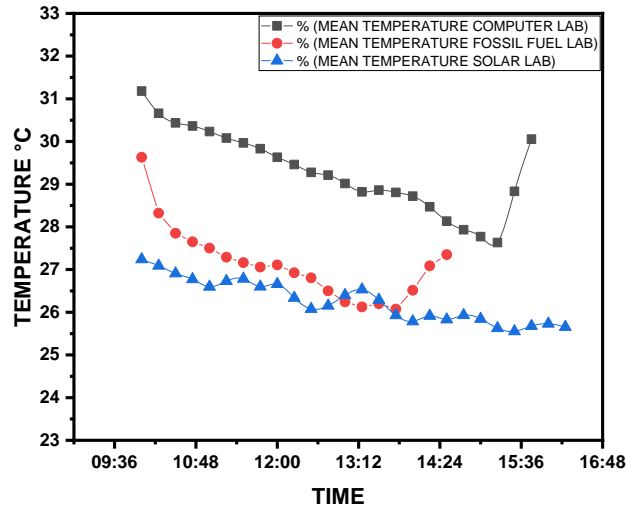


Figure 3: Temperature profile of labs

As compared to the computer lab, the fossil fuel and solar lab had temperatures at the lower level but were still above the ASHRAE 55 standard guideline for thermal comfort. The fossil and solar lab's temperature lies between 25°C-28°C for most of the time during measurement. The mean temperature for all tested areas was above the standard value of 25°C. This is mainly because of our university's rule or setting the thermostat of the air-conditioning devices at 26°C.

3.4 Particulates matter:

Six different sizes of solid suspended particles were measured in the selected built environment for the study. Figure 4-9, each chart shows the distribution of the mass concentration of the particles of the same size in different studied areas.

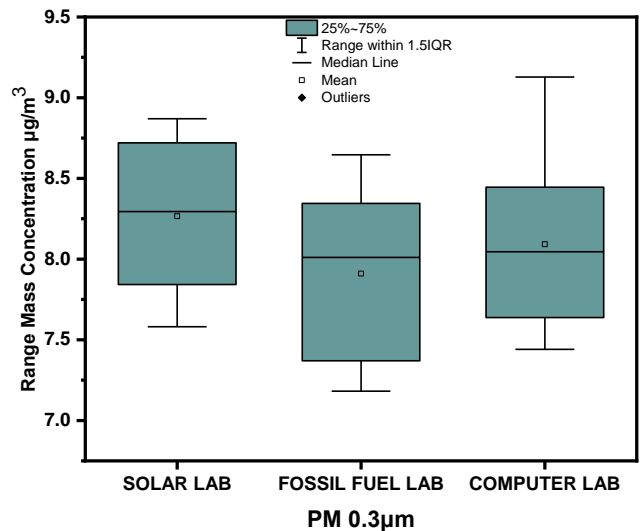


Figure 4: PM 0.3µm distribution in labs

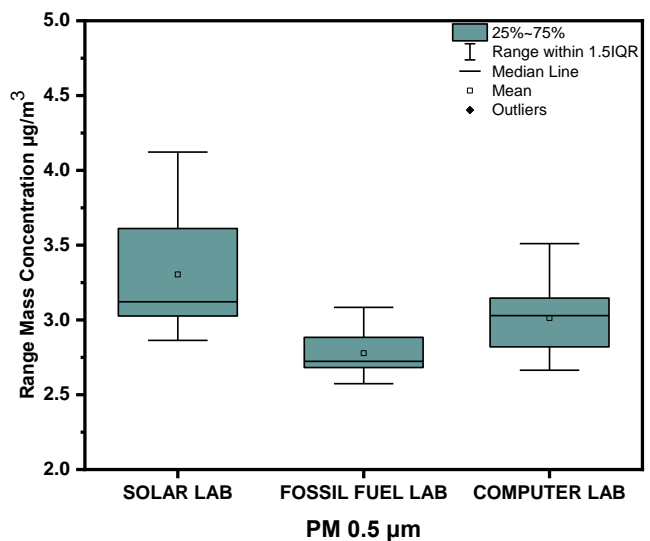


Figure 5: PM 0.5µm distribution in labs

The highest mass concentration of 0.3 μm and 0.5 μm particles were observed in a solar lab where for most of the time, a mass concentration between 7.5 $\mu\text{g}/\text{m}^3$ and 9 $\mu\text{g}/\text{m}^3$ for 0.3 μm and between 3 $\mu\text{g}/\text{m}^3$ and 4 $\mu\text{g}/\text{m}^3$ for 0.5 μm were observed. While mass concentration in the other two was just below for the other 2 studied areas for 0.3 μm and was lowest for in fossil lab for 0.5 μm .

The PM 1 μm and 2 μm mass concentrations were also the highest in the solar lab as compared to the other two studied labs. The mass concentration of all the labs for 1 μm and 2 μm were below 10 $\mu\text{g}/\text{m}^3$ for all three labs.

The mass concentration of 5 μm and 10 μm was the highest among all other particle sizes. Solar lab with PM10 as high as 335 $\mu\text{g}/\text{m}^3$ was recorded. The PM5 was also recorded with as high as 169 $\mu\text{g}/\text{m}^3$. The mass concentration in the computer lab and fossil lab was below 50 $\mu\text{g}/\text{m}^3$. Table.3 shows mean, minimum, maximum and std. deviation of the recorded mass concentrations of six sizes.

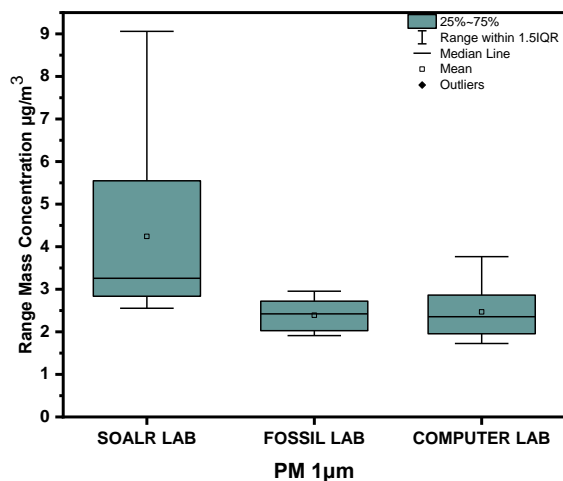


Figure 6: PM 1 μm distribution in labs

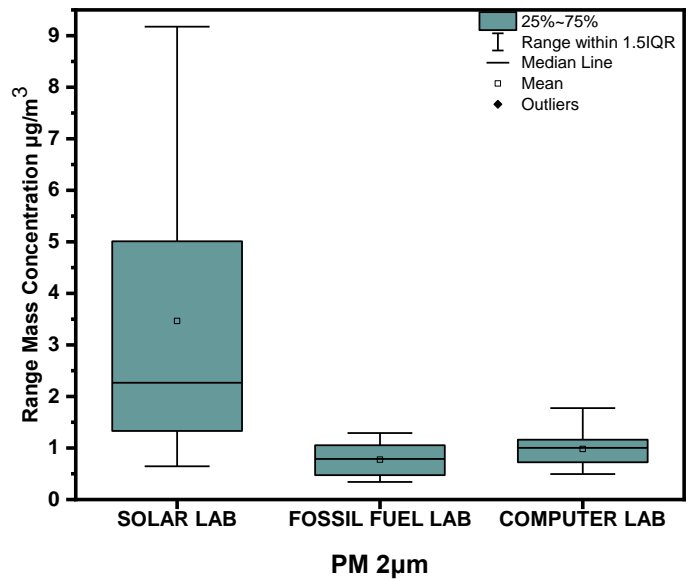


Figure 7: PM 2 μm distribution in labs

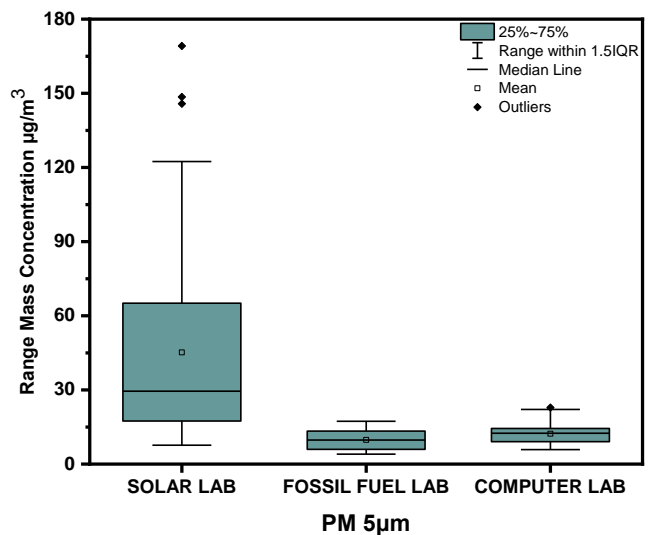


Figure 8: PM 5 μm distribution in labs

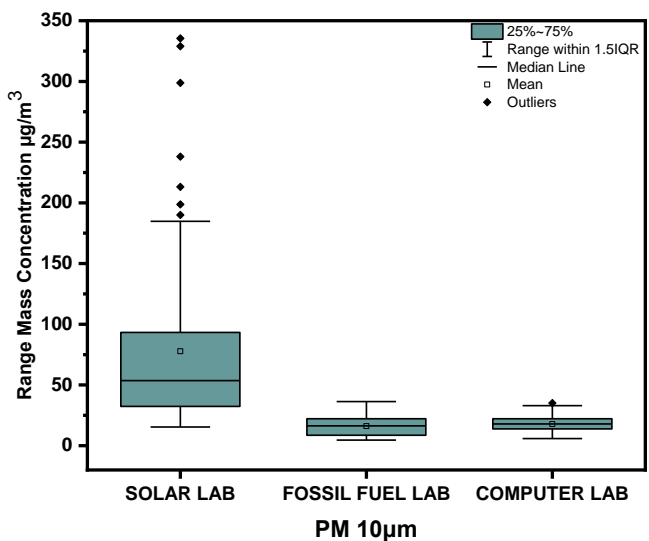


Figure 9: PM 10 μm distribution in labs

3.5 Safety Measures:

Till now, many mitigation techniques have been developed to counter the problems posed by indoor air pollutants. These techniques may require the involvement of the building management and staff along with educating the occupants on the causes of the indoor air pollutants.

Many problems can attribute to the poor indoor air quality, some examples of problems and solution are presented here:

Low air ventilation rate, poor distribution of ventilation, outdoor diffusion of pollutants, problems in HVAC, the lab equipment are the source of the contaminations, building material, and combustion processes in the occupied space.

According to US EPA, to counter such problems, for example, 1) source control by relocating contaminant producing equipment near to air exhaust, choose products with better safety, proper storage of contaminants producing materials, cleaning and disinfecting for micro-organism removal, 2) through measures related to ventilation by increasing the air supply and improving air distribution, avoid recirculation of the air, and maintain pressure differential to block the path of contaminant diffusion, 3) through air cleaning by particulate filtration, electrostatic precipitation, gas sorption, 4) exposure control by scheduling the contaminant producing activities to non-occupant hrs, etc. are few of the remedies to maintain good IAQ [16].

Table 3: Descriptive statistics of PM

PM 10 μ m					
Lab	Number of samples	Min (μ g/m ³)	Max (μ g/m ³)	Mean (μ g/m ³)	Std. Deviation
Solar Lab	90	4.6201	335.4223	72.967432	69.4197259
Fossil Fuel Lab		4.6201	36.3451	16.126005	7.8789266
Computer Lab		5.8522	35.1131	17.844012	6.6542657
PM 5 μ m					
Solar Lab	90	7.6232	169.1357	45.187549	36.4236699
Fossil Fuel Lab		5.8522	22.8697	12.284443	4.3366270

Computer Lab		4.0041	17.3255	9.804539	3.9124451
PM 2 μ m					
Solar Lab	90	.6456	12.5619	3.464435	2.7134587
Fossil Fuel Lab		.4953	1.7741	.980565	.3384511
Computer Lab		.3425	1.2912	.773145	.2952540
PM 1 μ m					
Solar Lab	90	2.5543	9.0592	4.243247	1.7043706
Fossil Fuel Lab		1.9115	2.9547	2.388535	.3309090
Computer Lab		1.7261	3.7660	2.467173	.5975701
PM 0.5 μ m					
Solar Lab	90	2.8631	4.1225	3.304141	.3514111
Fossil Fuel Lab		2.5742	3.0838	2.777282	.1279075
Computer Lab		2.6636	3.5099	3.012501	.2224972
PM 0.3 μ m					
Solar Lab	90	7.5809	8.8700	8.265608	.4531830
Fossil Fuel Lab		7.1818	8.6463	7.910159	.5046534
Computer Lab		7.4406	9.1280	8.092198	.5039062

4. Conclusion:

Indoor air quality and thermal comfort were assessed by measuring CO₂, temperature & relative humidity in 3 different laboratories with different ventilation systems. The results show that the IAQ not only depends on the number of occupants and outdoor conditions but also affected by different processes going on inside the occupied space. The overall CO₂ level was found to be under 1000ppm which is

considered very good according to ASHRAE 62.1 standard. It may be attributed to very low occupancy in FL & SL labs usually less than 10. The relative humidity was also found to be within the limits of ASHRAE 62.1 standard and valued under 65% all the time. The in and out of occupants, as well as the running equipment and water taps, contributed to the variation in RH. The temperature, on the other hand, was slightly higher for the lab CL than the other 2 labs. The main contributors to these higher values of temperature in CL were around 40 computers in which approximately half are simulation hardware and run 24/7. The other 2 labs also had a temperature higher than the allowed ASHRAE 55 standard, because there are also different machines running at relatively higher temperatures. The common factor which affected the temperature collectively is the university's policy of not allowing to set the thermostat below 26°C. In a bigger picture, the IAQ of the labs was found very good, of course, except for temperature. The particulate materials of size less than 2.5µm were found to be within limits of most of the standards like ASHRAE, US EPA and NAAQS, etc. which states that mass concentration of particles of size less than 2.5µm should be below 65 µg/m³ for 24 hrs average. On the other hand, PM10 particles' mass concentration was observed to be higher than the guidelines specified by the ASHRAE and US EPA, etc. which defines PM10 to be less than 150 µg/m³ for a 24hr average. The solar lab on few occasions exceeds this limit for both PM10 and PM5 particles. The reason solar lab having higher mass concentrations than the other labs could be explained by the fact that some pieces of equipment were under installation.

REFERENCES:

- [1] A. Datta, R. Suresh, A. Gupta, D. Singh, and P. Kulshrestha, "Indoor air quality of non-residential urban buildings in Delhi, India," *Int. J. Sustain. Built Environ.*, vol. 6, no. 2, pp. 412–420, 2017.
- [2] "Indoor air quality — European Environment Agency." [Online]. Available: <https://www.eea.europa.eu/signals/signals-2013/articles/indoor-air-quality>. [Accessed: 10-Jul-2019].
- [3] A. Asif, M. Zeeshan, and M. Jahanzaib, "Indoor temperature, relative humidity and CO₂ levels assessment in academic buildings with different heating, ventilation and air-conditioning systems," *Build. Environ.*, vol. 133, no. August 2017, pp. 83–90, 2018.
- [4] P. Kumar *et al.*, "Real-time sensors for indoor air monitoring and challenges ahead in deploying them to urban buildings," *Sci. Total Environ.*, vol. 560–561, pp. 150–159, Aug. 2016.
- [5] K. K. Kalimeri *et al.*, "Indoor air quality investigation of the school environment and estimated health risks: Two-season measurements in primary schools in Kozani, Greece," *Atmos. Pollut. Res.*, vol. 7, no. 6, pp. 1128–1142, Nov. 2016.
- [6] Z. T. Ai, C. M. Mak, D. J. Cui, and P. Xue, "Ventilation of air-conditioned residential buildings: A case study in Hong Kong," *Energy Build.*, vol. 127, pp. 116–127, Sep. 2016.
- [7] K. Gładyszewska-Fiedoruk, "Analysis of stack ventilation system effectiveness in an average kindergarten in north-eastern Poland," *Energy Build.*, vol. 43, no. 9, pp. 2488–2493, Sep. 2011.
- [8] W. Ji and B. Zhao, "Contribution of outdoor-originating particles, indoor-emitted particles and indoor secondary organic aerosol (SOA) to residential indoor PM_{2.5} concentration: A model-based estimation," *Build. Environ.*, vol. 90, pp. 196–205, 2015.
- [9] D. Norbäck, C. Lu, Y. Zhang, B. Li, Z. Zhao, and C. Huang, "Sources of indoor particulate matter (PM_{2.5}) and outdoor air pollution in China in relation to asthma, wheeze, rhinitis and eczema among pre-school children: Synergistic effects between antibiotics use and PM₁₀ and second hand smoke," *Environ. Int.*, vol. 125, no. February, pp. 252–260, 2019.
- [10] A. E. Ite, C. O. Ogunkunle, C. O. Obadimu, E. R. Asuaiko, and U. J. Ibok, "Particulate Matter and Staff Exposure in an Air-Conditioned Office in Akwa Ibom State University – Nigeria," *J. Atmos. Pollut.*, vol. 5, no. 1, pp. 24–32, 2017.
- [11] D. Mumovic *et al.*, "Winter indoor air quality, thermal comfort and acoustic performance of newly built secondary schools in England," *Build. Environ.*, vol. 44, no. 7, pp. 1466–1477, 2009.
- [12] "Indoor Air Quality Service in Phoenix - Air-Zona Air Conditioning." [Online]. Available: <https://www.air-zona.net/indoor-air-quality-phoenix/>. [Accessed: 17-Jul-2019].
- [13] S. Hasheminassab, N. Daher, M. M. Shafer, J. J. Schauer, R. J. Delfino, and C. Sioutas, "Chemical characterization and source apportionment of indoor and outdoor fine particulate matter (PM_{2.5}) in retirement communities of the Los Angeles Basin," *Sci. Total Environ.*, vol. 490, pp. 528–537, 2014.
- [14] D. Mickaël *et al.*, "Indoor air quality and comfort in seven newly built, energy-efficient houses in France," *Build. Environ.*, vol. 72, pp. 173–187, 2014.
- [15] M. Stranger, S. S. Potgieter-Vermaak, and R. Van Grieken, "Particulate matter and gaseous pollutants in residences in Antwerp, Belgium," *Sci. Total Environ.*, vol. 407, no. 3, pp. 1182–1192, 2009.
- [16] I. A. I. R. Problems, "Mitigating IAQ Problems," pp. 81–104.



Analysis of Temperature Distribution and Phase Change Time Inside Iron-Nickel Foam Infiltrated with Paraffin

Muhammad Mehboob¹, Abid Hussain^{1,*}

¹-Department of Mechanical Engineering, University of Engineering and Technology Taxila, Pakistan

*Corresponding Author: abid.hussain@uettaxila.edu.pk

Abstract

Thermal performance of phase change materials (PCMs) has a great importance in efficient thermal energy storage system (TESS). Pure PCMs have high heat absorption capacity and latent heat. In this study temperature distribution inside the pure paraffin, pure iron-nickel foam and Iron-nickel foam/paraffin PCM composite is experimentally compared along the X-axis. Heat flux of 1000 W/m² is supplied through flexible heater (100 mm × 100 × 1.3 mm) at bottom of the paraffin, pure iron-nickel foam and iron-nickel foam/paraffin wax composite. Phase change time of paraffin and iron-nickel foam/paraffin wax composite is also investigated. Experimental results show that new Iron-Nickel foam/paraffin PCM composite has improved the effective thermal efficiency that lowered the maximum temperature difference by 50%. Phase transition time of pure paraffin has increased by 16.67% more than that of composite PCM during the thermal storage process. In case of paraffin temperature difference is 4 °C while in pure iron-nickel foam it is 2 °C during heat process.

Key words: Heat Flux, Pure Paraffin, Iron-Nickel foam, Thermal storage.

1. Introduction

Different phase change materials are categorized into two principle sets organic and inorganic by their compositions or two groups are by melting temperature (low temperature PCMs and high temperature PCMs). Organic PCMs have low super cooling and non-corrosive, while inorganic PCMs have large latent heat. Low temperature PCMs (below 200 °C) are used in buildings and waste heat recovery system (WHRS). High temperature PCMs, due to large latent heat, are utilized in solar power plants (SPPs) and high thermal energy storage system (TESS)[1–4].

Metal foams are most emerging and popular materials used in thermal energy storage, having cellular construction of solid metal. These are of closed cell as well as open cell foams interconnected together. Due to open cells, high porosity, light weight and large surface area to volume ratio, used in thermal storage [5–7].

In order to enhance the thermal storage properties like heat absorption, heat extraction during melting and solidification process by adding the PCMs in metal foams (high thermal conductive)[8-9]. Thermal conductivity of metal foam is higher than that of pure PCM. For thermal enhancement PCM is impregnated in metal foams. There are various metal foams are used with different PCMs for thermal enhancement like copper foam, nickel foam and aluminum foam[10–15].

2. Experimental Setup

Heat cavity with complete measurement of 100 mm x 100 mm x 26 mm is utilized to perform the experimental analysis. Aluminum heat sink insulated with thickness of 3 mm plexiglass to make sure the one-



Figure 1. Experimental setup

dimensional heat flow. Flexible silicon heating pad pasted in little grooved sink bottom on external side with dimensions 100 mm x 100 mm x 1.3 mm. Despite of the fact that thermal conduction of glue is 9 W/mK

and thickness of the glue paste is less than 0.1 mm where, thermal resistance of paste is insignificant accordant $R = x/kA$. Flexible heating pad is used as heat generating element. High scaled 5-K-type (-50 °C to 1350 °C) thermocouples positioned at different places of heat sink to measure temperature distribution. Data acquisition (USB-34972A) is utilized to measure and scan the thermocouple's reading with time interval of 5 sec. The required



input power of 10 W is supplied to heating element through power supply (A M10-QD & QR series) using the respective voltages according Ohm's law. The experimental actual and schematic setup with

thermocouples positioning is shown as in fig. 1 and fig. 2 respectively.

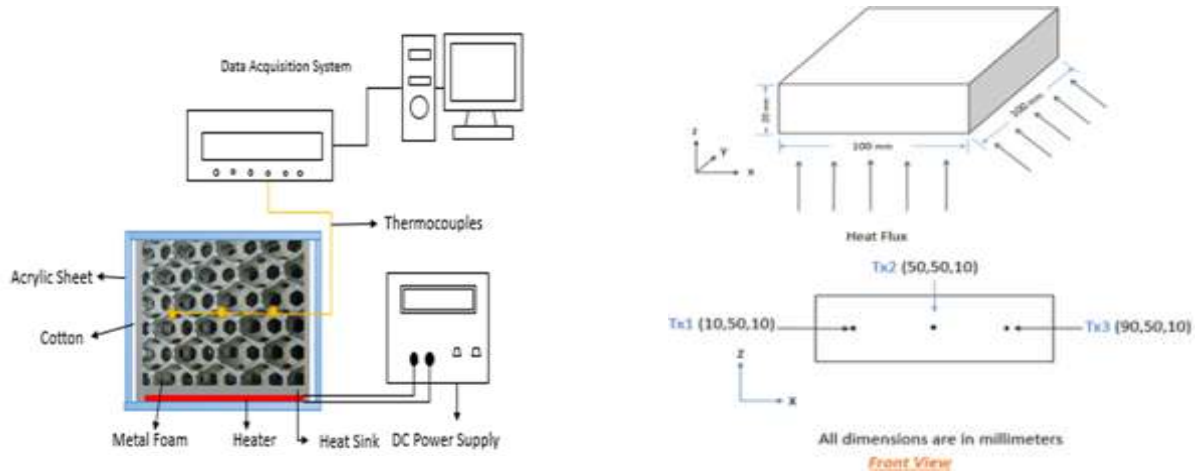


Figure 2. Schematic view of experimental setup and thermocouple positioning.

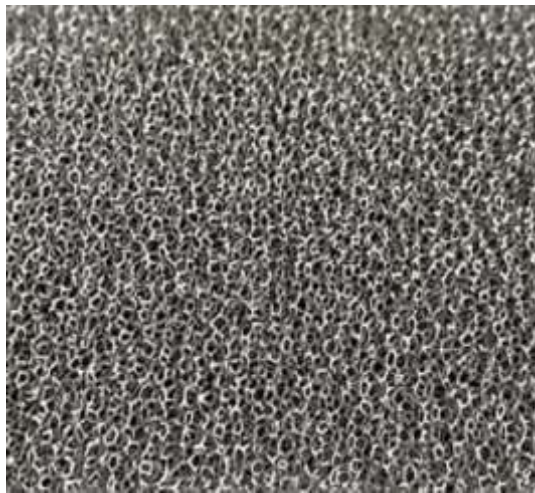
2.1 Materials

Paraffin have very importance due to thermal storage properties like temperature distribution and latent heat. To investigate the internal storage properties of metal foam, first cut the required metal and PCM. To infiltrate the paraffin by heating it and immersed the metal foam in melted PCM. Gradually cooldown the paraffin till solidification. The characteristics properties of paraffin wax and iron-nickel foam are shown in table 1 and table 2

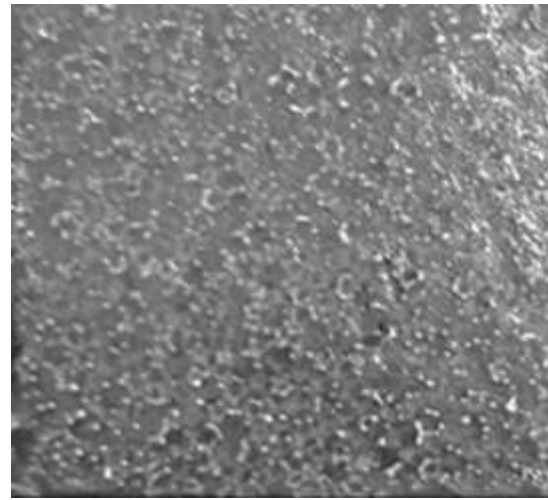
respectively. Thermocouples are positioned at heat sink bottom, 10 mm, 50 mm and 90 mm via length and at middle of metal foam via thickness as shown in figure 2. The actual image of iron-nickel foam and iron-nickel foam PCM composite is shown in fig. 3 (i) and (ii) respectively.

Table 1. Characteristics properties of PCM

Characteristics properties	High operating point	Congeaing point	Melting range	Heat capacity	Density @15 °C	Thermal conductivity
Common values	72 °C	42-38 °C	38-42 °C	2000 J/kg. K	880-900 kg/m ³	0.15-0.3 W/mK



(i)



(ii)

Figure 3. Pure iron-nickel foam (i) and Iron-nickel foam PCM composite (ii).

Table 2. Characteristic properties of Iron-Nickel foam.

Thermal Conductivity (W/m. K)	Density (Kg/m ³)	Porosity (%)	Pore density PPI	Specific heat (kJ/kg. K)
83	273	97	35	0.426

3. Result and Discussion

In present experimental work, heat flux of 1000 W/m² is supplied along the Z-direction to analyze the thermal storage properties of composite as well as pure PCM and pure iron-nickel foam. Different thermocouples placed at different dimensions (10 mm, 50 mm, 90 mm) along the X-axis to investigate the thermal storage properties as thermocouples position is shown in fig. 2. The ambient temperature for current study is 30 °C fixed. There are three specimens 1) Pure paraffin, 2) Pure Iron-Nickel foam, 3) Iron-Nickel foam/Paraffin composite are investigated and compared.

3.1 Thermal storage analysis

3.1.1 Temperature profile of pure paraffin

With the same heat transition/flux of 1000 W/m², in XY plane where Z=10 mm takes example, the temperature is most extreme/maximum at mid and lowered at sides. The maximum temperature variation at various positions is 4 °C along axis. Paraffin started to melt from 38 °C. During the phase change range inner temperature remained constant and sensible heating took 3246 sec (54 min) before melting started along X-axis. During the phase transition temperature uniformly distributed. Pure

PCM has more transition time due to low thermal conductivity as shown in fig. 4.

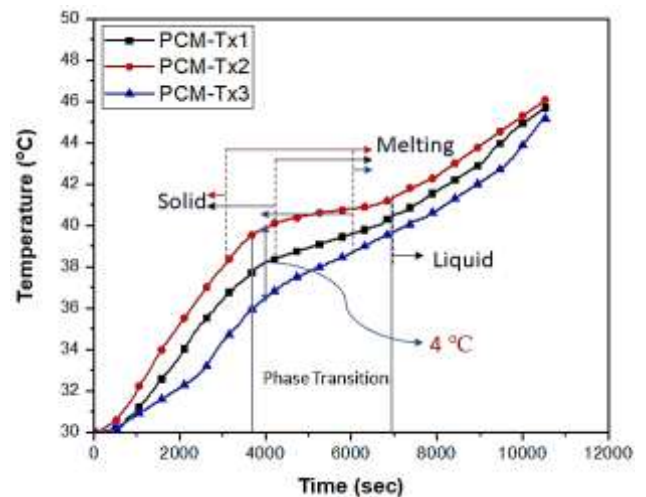


Figure 4. Temperature profile of pure paraffin

3.1.2 Temperature profile of pure Iron-Nickel

In this case also same heat flux of 1000 W/m² is supplied to analyze thermal flow along X-axis at different positions. Temperature is uniformly distributed from start and at the top it observed to be decreased at middle position. During the heat process, the greatest/extreme temperature difference



at various points is observed to be 2 °C. Due to high thermal conductivity of pure iron-nickel foam, it got stability in short time (3500 sec) during the thermal process as shown in fig. 5.

3.1.3 Temperature profile of Iron-Nickel foam/paraffin PCM composite.

The same constant heating process of 1000 W/m² was repeated for Iron-Nickel foam/PCM composite to analyze the heat flow along X-axis. During the heat process at various point, the maximum temperature difference is observed to be 2 °C. The maximum temperature distribution at center is higher as compared to that of sides. Due to variation of density of solid and molten pure paraffin during thermal storage process it moved upward to the surface as shown in fig. 6. So, the molten pure paraffin with high temperature move toward the surface and that's why temperature at center position is raised. The design of iron-nickel foam limited convection of pure paraffin (PCM) and conduction of heat become main way of thermal process during the thermal storage process.

Compared the temperature profile of pure paraffin with iron-nickel foam/paraffin PCM composite in thermal collection process. Pure paraffin due to low thermal conductivity have large phase transition time (54 min) as compared to that of composite PCM (45 min). In the melting process, pure paraffin moves up to upper surface. Due to volume expansion and without restriction of iron-nickel foam large quantity of paraffin collected at surface. At the same heat flux (1000 W/m²), the extreme temperature variation in paraffin wax is 4 °C, while in iron-nickel foam PCM composite is 2 °C. hence by addition of paraffin in iron-nickel foam it lowered the 50% maximum temperature difference.

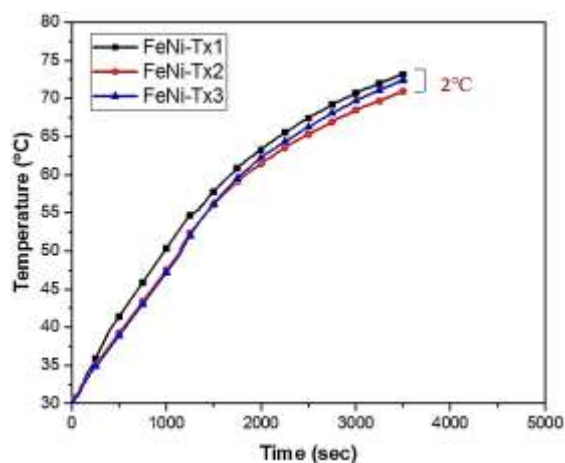


Figure 5. Temperature profile of pure Iron-Nickel foam

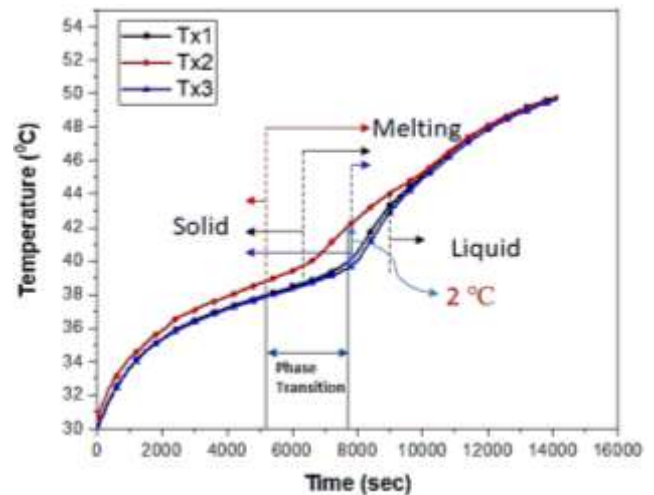


Figure 6. Temperature profile of Iron-Nickel foam/Paraffin composite.

4. Conclusion

In this present experimental study, thermal storage properties of iron-nickel foam saturated with phase change material is analyzed and compared three specimens which are pure paraffin, pure iron-nickel foam and iron-nickel foam/paraffin composite at heat flux of 1000 W/m². It is also checked the temperature uniformity along X-direction.

- According to present experimental study, the phase transition time of pure paraffin is 16.67% more as compared to that of iron-nickel foam/paraffin PCM composite.
- The addition of pure paraffin with iron-nickel foam lowered the maximum temperature difference of 50% and also increased the melting time compared to pure paraffin PCM during the thermal storage process.
- Experimental results prove that there is more temperature uniformity in iron-nickel foam/ paraffin PCM composite, especially at beginning and upper part as compared to that of paraffin and pure iron-nickel foam.

REFERENCES

- [1] B. Zalba, J. M. Marín, L. F. Cabeza, and H. Mehling, *Review on thermal energy storage with phase change: Materials, heat transfer analysis and applications*, vol. 23, no. 3. 2003.
- [2] X. Py, R. Olives, and S. Mauran, "Paraffin/porous-graphite-matrix composite as a high and constant power thermal storage material," *Int. J. Heat Mass Transf.*, vol. 44, no. 14, pp. 2727–2737, 2001.



- [3] Z. Zhang, J. Cheng, and X. He, "International Journal of Heat and Mass Transfer Numerical simulation of flow and heat transfer in composite PCM on the basis of two different models of open-cell metal foam skeletons," *Int. J. Heat Mass Transf.*, vol. 112, pp. 959–971, 2017.
- [4] P. Royo, L. Acevedo, V. J. Ferreira, T. García-Armingol, A. M. López-Sabirón, and G. Ferreira, "High-temperature PCM-based thermal energy storage for industrial furnaces installed in energy-intensive industries," *Energy*, vol. 173, pp. 1030–1040, 2019.
- [5] S. Hong and D. R. Herling, "Open-cell aluminum foams filled with phase change materials as compact heat sinks," vol. 55, pp. 887–890, 2006.
- [6] H. T. Cui, "Experimental investigation on the heat charging process by paraffin filled with high porosity copper foam," *Appl. Therm. Eng.*, vol. 39, pp. 26–28, 2012.
- [7] "et al.," no. September, p. 97104113, 1997.
- [8] W. Q. Li, Z. G. Qu, Y. L. He, and W. Q. Tao, "Experimental and numerical studies on melting phase change heat transfer in open-cell metallic foams filled with paraffin," vol. 37, pp. 1–9, 2012.
- [9] H. Zheng, C. Wang, Q. Liu, Z. Tian, and X. Fan, "Thermal performance of copper foam/paraffin composite phase change material," *Energy Convers. Manag.*, vol. 157, no. September 2017, pp. 372–381, 2018.
- [10] A. Hussain, C. Y. Tso, and C. Y. H. Chao, "Experimental investigation of a passive thermal management system for high-powered lithium ion batteries using nickel foam-paraffin composite," *Energy*, vol. 115, pp. 209–218, 2016.
- [11] T. X. Li, D. L. Wu, F. He, and R. Z. Wang, "International Journal of Heat and Mass Transfer Experimental investigation on copper foam / hydrated salt composite phase change material for thermal energy storage," vol. 115, pp. 148–157, 2017.
- [12] T. ur Rehman, H. M. Ali, A. Saieed, W. Pao, and M. Ali, "Copper foam/PCMs based heat sinks: An experimental study for electronic cooling systems," *Int. J. Heat Mass Transf.*, vol. 127, pp. 381–393, 2018.
- [13] Z. Wang, Z. Zhang, L. Jia, and L. Yang, "Paraffin and paraffin/aluminum foam composite phase change material heat storage experimental study based on thermal management of Li-ion battery," *Appl. Therm. Eng.*, vol. 78, pp. 428–436, 2015.
- [14] X. Xiao, P. Zhang, and M. Li, "Preparation and thermal characterization of paraffin/metal foam composite phase change material," vol. 112, pp. 1357–1366, 2013.
- [15] C. Wang, T. Lin, N. Li, and H. Zheng, "Heat transfer enhancement of phase change composite material : Copper foam / paraffin," vol. 96, pp. 960–965, 2016.



Improvement in Generation Economics by the Application of Selected Thermal Power Plant Repowering Strategies in Pakistan – A Case Study

Ahmad Jamil¹, Adeel Javed¹

1- Thermal Energy Engineering Department, US-Pakistan Center for Advanced Studies in Energy, National University of Sciences and Technology, Sector H-12, Islamabad, Pakistan

*Email: ahmadjamil472@gmail.com, adeeljaved@uspcase.nust.edu.pk

Abstract:

Repowering of thermal power plants is an important engineering strategy used to upgrade old power plants to modern standards. Thermal power generation plays a key role in the global energy market and is the backbone of Pakistan's energy mix. The paper presents three old thermal power plants of Pakistan as case studies with repowering strategies applied to highlight the improvement in generation economics. More than 50% reduction in fuel costs have been observed, making repowering of the selected power plants a feasible option. The study aims to pave way for further analyses on repowering of thermal power plants in Pakistan as thermal power generation will remain a key player in the energy mix for decades to come.

Keywords: Energy, Repowering, Energy Policy, Generation Economics, Thermal Power Plants

1. Introduction

Thermal power generation still retains its importance amidst the growing global trend of renewable energy generation technologies. This is mainly due to the base load operation and stability advantages of thermal power plants over the intermittency issues of the renewable generation technologies. The International Energy Agency's World Energy Outlook 2018 predicts the growth of renewables in the power generation from 25% to 41% in 2040 [1]. Thermal power generation will need to adapt to the changing market with reduced emissions, faster start-up and shutdowns, increased ramping rates and flexibility in operations [2].

Pakistan plans to modify its energy mix in the coming decades, following the global trend of increasing renewable power generation, while at the same time exploiting its indigenous coal resource. Thermal power generation will play a significant role in the decades to come. Till 2025, Pakistan is set to retire 1,477 MW of its gas and oil based thermal power generation units while adding new 7,230 MW coal-based power plants [3]. Figure 1(a) compares the energy mix of Pakistan in 2018 versus the one planned for 2025 while 1 (b) shows the addition and retirement of thermal power plants. The share of coal in the energy mix is forecasted to grow to 18.5% by 2025 and majority

of these plants are local lignite coal based like the upcoming TEL 330 MW Mine Mouth Lignite Fired Project at Thar Block-II, Thal Nova 330 MW Mine Mouth Lignite Fired Power Project and the 1320 MW SSRL Mine Mouth Power Plant in Thar Block-I [4,5].

The types of fuels utilized in the thermal power generation of Pakistan's energy sector are broadly coal, gas and oil. The coal used is of two types; imported and indigenous. Gas fuel is either natural gas or (Regasified Liquid Natural Gas) RLNG. The types of oil consumed by power plants for power generation are Furnace Oil (FO) and High-Speed Diesel (HSD). All these fuels are also utilized in a mixed fuel configuration based on their availability. The major thermal generation technologies that are employed are the boiler based Steam Turbines (STs), Combined Cycle Piston Engines (CCPEs) and Combined Cycle Gas Turbines (CCGTs) [6]. Pakistan imports the high-grade coal used, most of its FO and all of its RLNG. Pakistan has stable reserves of natural gas; the demand and supply gap is being met by RLNG, which is comparatively cheaper to import than oil [7].

The conversion efficiencies of most of the major thermal power plants of Pakistan are summarized in Fig. 2. The efficiency used is the



gross generation efficiency, and in case of unavailability, the efficiency on net export to the NTDC has been used. In the case of the value for 2016-17 being unavailable, the efficiency for the previous year has been used. For the case of the three GE 9HA class CCGT power plants that were recently setup, the efficiency assumed is 60% from the manufacturer's factsheet [8]. For the two recent 1320 MW imported coal power plants, their efficiencies have been taken from their generation licenses. Both power plants have a 42% gross generation efficiency listed [9], [10]. The new CCGT RLNG based power plants installed at Bhikki, Haveli Bahadur Shah and Balloki that add 3600 MW to the national grid of Pakistan and are operating on the new GE 9HA-class technology, delivering efficiencies of more than 60% mark, rank the highest. They are followed by a cluster over 50%. The major combined cycle configurations lie between 40-50%, which is low compared to the latest technologies. Two CCGTs lie close to 30% which shows deteriorated performance. STs rank lower, with the most efficiency being close to 40% and the major chunk being close to 30%. Older STs have lower than 30% efficiency showing high deterioration in efficiency.

In typically less developed countries such as Pakistan, restricted resources, lack of skills, pressure to keep the power plant online because of power shortages, and, in some cases, having to burn particularly difficult fuels can be the factors that can cause the performance decline to be greater compared to more developed countries. With over half of the country's power needs being dependent on fossil fuels, it is imperative that the older power

plants, which remain a part of the energy mix for the upcoming years be upgraded and kept streamlined with the modern technological advancements. The deteriorating efficiency of older thermal power plants and the rising cost of importing fossil fuels, in consideration with the above presented data makes a strong case for thermal power plant repowering.

Repowering of thermal power plants involves engineering strategies in order to (a) increase generation economics and plant life, (b) enhance maintenance and operability of the plant, (c) reduce emissions, (d) ensure energy security, and (e) resolve site related issues from local to national level. These involve modification or replacement of obsolete technologies with current state of the art equipment while retaining the maximum number of old usable components [11].

Repowering is a broad term that includes all sorts of component upgrades, fuel conversions, generation technology conversion, retrofitting, methods such as hot wind box repowering, feed water heating, waste heat recovery, integrating gasification and concentrated solar power to turn conventional power plants into hybrid ones and complete replacement of the power plant with a modern one.

The paper focuses on the potential benefits on the generation economics of old thermal power plants close to retirement, with the application of selected repowering strategies to 3 power plants selected as case studies; highlighting the prospect and importance of developing the concept of thermal power plant repowering in Pakistan.

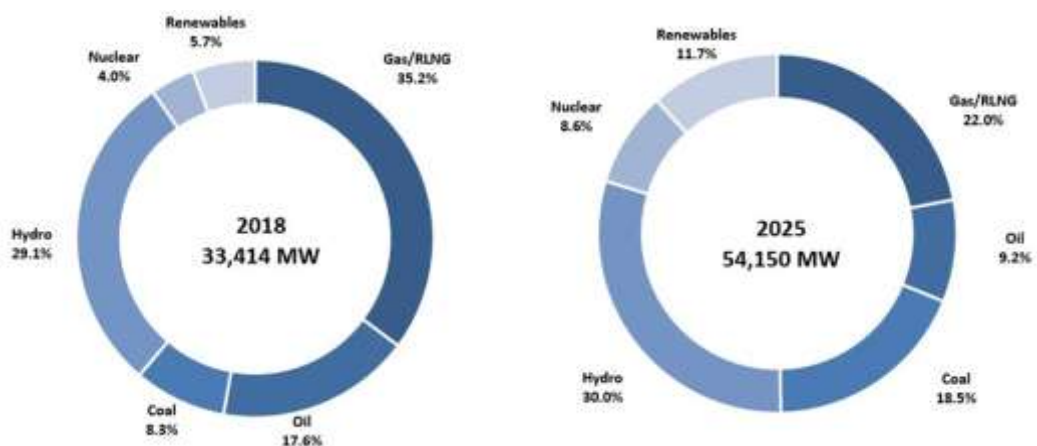


Figure 1 (a): Energy mix of Pakistan, 2018 vs. 2025 [6]

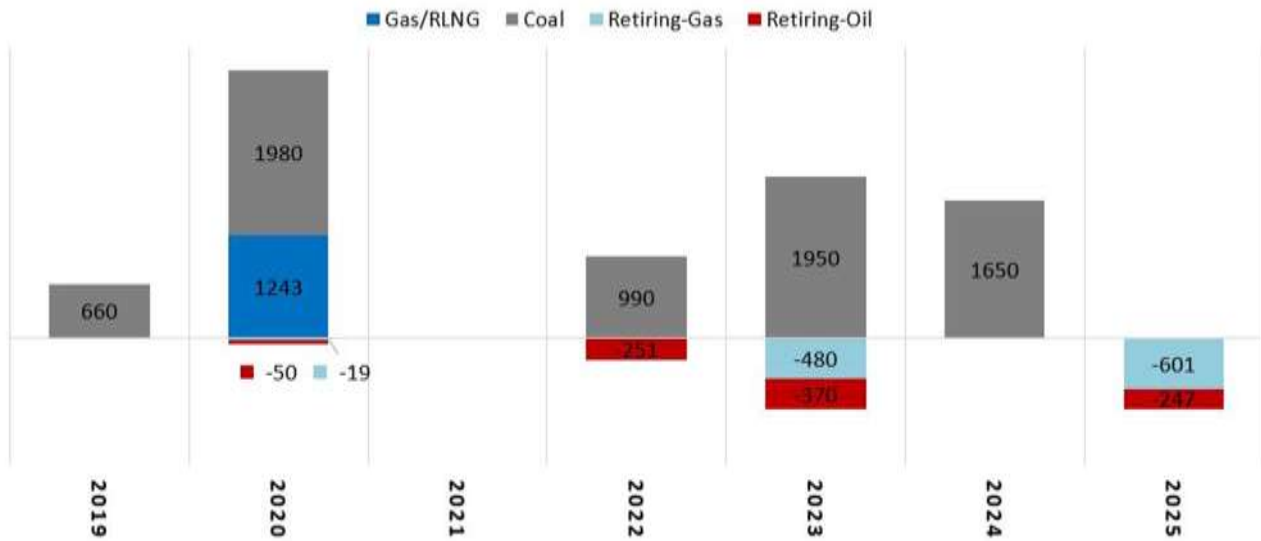


Figure 1 (b): Addition and retirement of thermal power plants till 2025 [3]

2. Methodology

Thermal repowering encompasses a wide range of strategies and techniques to improve power plants. This includes all upgrades, retrofits, installation of new equipment and even decommissioning of the entire power plant to install a new and more advanced power plant at the same site. The three repowering strategies selected for this analysis are Heat Recovery Repowering, Site Repowering and Fuel Conversion.

2.1 Heat Recovery Repowering:

This strategy involves converting the old ST based power plant into a CCGT power plant while retaining the maximum possible equipment from the older plant. The old boiler is replaced with a GT and a Heat Recovery Steam Generator (HRSG). The ST of the old power plant is retained, and its performance is optimized to match the new GT. The ST, heat rejection systems (condenser and cooling tower) and switchyard must be usable with minimum repair/upgrades or without major redesign/retrofitting to a capacity above or below their rating [12]. This option incurs comparatively less capital costs, as compared to Site Repowering.

2.2 Site Repowering:

This type of repowering is also termed as complete repowering and involves decommissioning all the older power plant equipment and the installation of

a new CCGT power plant at the same site instead [12]. The option incurs the most capital costs out of all the options.

2.3 Fuel Conversion:

Fuel Conversion of a power plant impacts generation economics, efficiency and emissions. The type of fuel to convert to is a multi-variable decision. In the context of the Pakistani energy market, a conversion of ST based power plants from FO to coal is proposed, considering the recent exploitation of the country's indigenous coal resource. Using coal in a power plant meant for oil or gas combustion can be done by erecting a new pulverized coal boiler next to the oil/gas fired boiler. This way there is little outage time and the power plant can have a dual fuel capability. Coal handling equipment like soot blowers, ash removal system, storage and pollution control technologies will have to be installed [13].

A review of literature shows that Site and Heat Recovery Repowering can bring an overall increase of more than 15% in thermal efficiency as the latest CCGT power plants can achieve an overall thermal efficiency close to 60% [14]. The GE 9HA class can achieve more than 63% efficiency [8]. Heat Recovery Repowering can increase the power output of a power plant by 200% and reduce the heat rate by 30% [15]. The Dutch experience with repowering using Heat Recovery Repowering



shows an efficiency increase of 12% and the new repowered power plant having 50-80% reduced emissions. The approximate outage time required is 12-18 months [16]. The Bandar Abbas Steam Power Plant is a 30-year-old power plant in Iran. One of its 4 320 MW units was simulated for Heat Recovery Repowering with different feed water heater arrangements. Efficiency was increased from 38.7% to between 50-55% for the cases simulated [17].

Three power plants that selected for analysis are TPS Muzaffar Garh, KAPCO and Pak Gen Power. The Pak Gen Power plant is a FO based power plant of an installed capacity of 365 MW commission in 1998. The power plant has 1 ST and an efficiency of 36.29% recorded during 2016-17 [6]. The company recently applied with the government regulatory bodies for a coal conversion for its power plant with the same efficiency as stated above. The benefits of generation economics of Fuel Conversion will be analysed on it.

Thermal Power Station or TPS Muzaffargarh is dual fuel-based ST power plant in Muzaffar Garh Pakistan under the Northern Power Generation Company Limited (GENCO III). It consists of 6 units with a combined installed capacity of 1350 MW. The 6 units are STs in the following configurations 3 x 210 MW, 2 x 200 MW, 1 x 320 MW. It runs primarily on FO, but also utilizes natural gas and RLNG. In 2018 the units generated by the power plant were 3413.62 GWh out of which 32336.4 GWh were by FO, 54.2 by natural gas & 123 by RLNG. Being an old power plant and

running on FO, the plant has a deteriorated efficiency of 29.76% recorded for the year 2016-17 [6], [18], [19]. A site repowering option is feasible for this power plant, converting this into a CCGT with the 60% and higher efficiency plants such as the HA class by GE.

Kot Addu Power Company Limited or KAPCO is Pakistan's largest CCGT power plant with an installed capacity of 1343 MW, divided into 3 energy blocks. The energy block 1 is the most efficient with an installed capacity of 332 MW and an efficiency of 48%. The energy block 2 is divided into 2 sub blocks, A and B having installed capacities of 279 and 479 MW respectively. Energy block 3 is the least efficient, having an installed capacity of 253 MW and an efficiency of 41%. It is the oldest energy block having 2 GTs of Fiat. The power plant has a 2x1 configuration, having a total of 5 such configurations. Energy block 3 and 2 (A) are coupled together. Each GT of energy block 3 is coupled with a GT of energy block 2 (A) in the 2x1 configuration. The primary fuels of the power plant are FO and natural gas, but it can run on HSD as well. Figure 2 shows a simplified schematic diagram of the power plants energy blocks. A heat recovery repowering is suggested for the 532 MW combined energy blocks 1 and 2 (A), with the HA class GTs by GE in the CCGT configuration. The 4 GTs and their corresponding 2 STs and 2 HRSGs will be decommissioned and a HA class GT with a customized HRSG and new ST will be installed. The older system's combined efficiency of 43% will be increased to 60% or higher.

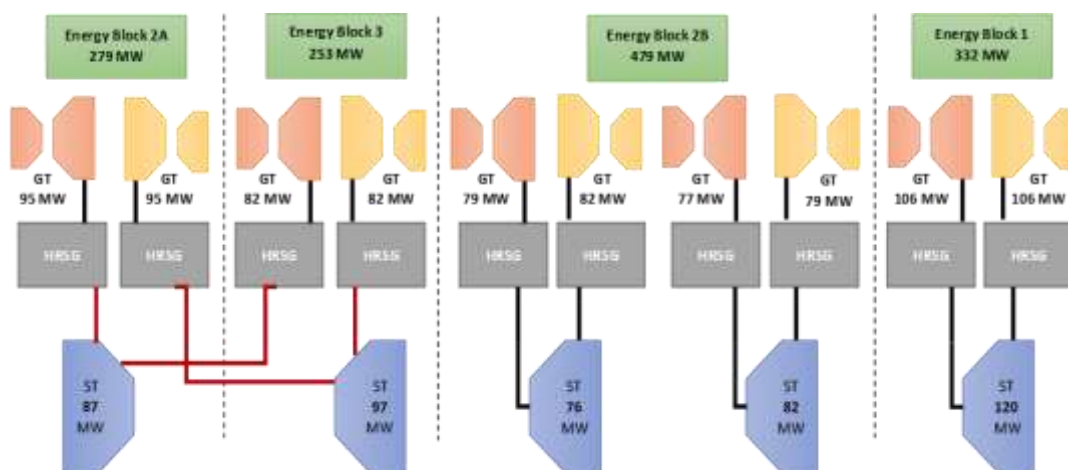


Figure 2: A simplified schematic of the layout of the KAPCO CCGT power plant



3. Fuel Cost Analysis of Selected Power Plants

The benefits on generation economics have been calculated and compared by comparing the fuel costs of the older systems with new repowered systems. Table 1 shows the specifics of the fuels used in the selected power plants. The fuel prices have been converted into PKR/kWh for the analysis. Equation (1) will be used to calculate the fuel costs.

$$\text{Fuel Cost} = \frac{\text{Price (PKR/kWh)}}{\text{Power Plant Efficiency}} \quad (1)$$

Table 1: Specifics of the fuels used in the power plants under analysis

Fuel	Calorific Value	Price	Price (PKR/kWh)
Imported FO Ex-Zot	9520 kcal/kg (Assumed) [20]	72,800 PKR/ton [21]	6.5796
RLNG	-	9.9012 USD/MM BTU [22]	5.3419
Imported Coal	25555.98 BTU/kg [23]	126.06 USD/ton [23]	2.6612
Indigenous Coal	22046 BTU/kg [23]	103.17 USD/ton [23]	2.5248

1 BTU = 0.000293071 kWh
1 kcal = 0.00116222 kWh
1 MMBTU = 293.07107 kWh
1 USD = 158.1182 PKR [24]

3.1 TPS Muzaffar Garh:

Using Eq. (1), the fuel cost of the older system running on FO and an efficiency of 29.76% is 22.109 PKR/kWh. When repowered by the Site Repowering using the latest GE HA Class CCGT and converting it to RLNG, the new fuel cost for an assumed efficiency of 60% is 8.903 PKR/kWh.

3.2 KAPCO Energy Blocks 3 and 2 (A):

Using Eq. (1) the fuel cost for 43% efficient older system running on FO, the fuel cost is 15.301 PKR/kWh. The repowered system by Heat Recovery Repowering will have a fuel cost of 8.903 PKR/kWh for 60% assumed efficiency.

3.3 Pak Gen Power:

Using Eq. (1), the fuel cost for the older 36.29% system is 18.130 PKR/kWh. Assuming the efficiency increases to 39% from the new boiler, the new fuel costs for imported and indigenous coals are 6.823 PKR/kWh and 6.47 PKR/kWh respectively. The slight efficiency increment is taken from the standard efficiency set in the licence agreement of the latest coal power plants [23].

4. Results and Discussions

The summarized results of the improvement in the generation economics are shown in Table 2. The results highlight a significant reduction in fuel costs of the repowered systems and an increase in efficiency from the conversion of ST power plants to the latest CCGT ones. The efficiencies are increased by more than 30% for TPS Muzaffargarh and more than 17% for KAPCO Energy Blocks. The fuel costs are reduced by 59.74 %, 41.83%, 62.36% and 64.31% for TPS Muzaffargarh, KAPCO Energy Blocks 3 and 2 (A), Pak Gen Power (Imported Coal) and Pak Gen Power (Indigenous Coal). Repowering would shift major fuel consumption from FO to RLNG for the CCGT plants and on coal for the ST plants. The exploitation of local coal, although providing better generation economics, leads to increased emissions. Whether or not repowering is done, is a multivariable decision that needs to account the payback period, value of reduction in fuel costs over environmental concerns and the choice of imported fuel. The power plant site also has significant value as thermal power plants require large amounts of water and must be close to a water body. Older power plants in Pakistan have been located keeping this in view. Whether the site needs to be re-used for power generation is also a key deciding factor. All these factors must be included when calculating the total potential economic benefit from the fuel cost reductions achieved from repowering, before a decision is taken. However, Site and Heat Recovery Repowering remain an attractive option for the deteriorating GENCOs like TPS Muzaffargarh.



Table 2: Summary of the case of the case studies

Case	Current Efficiency	Current Fuel Type	Current Fuel Cost	Repowering Option	New Fuel Type	New Fuel Cost	Improved Efficiency	Difference of Fuel Cost
TPS Muzaffargarh	29.76%	FO (Major), RLNG (Minor), Natural Gas (Minor)	PKR 22.109/kWh	Heat Recovery/Site Repowering	RLNG	PKR 8.9/kWh	>=60%	PKR 13.209/kWh
KAPCO Energy Blocks 3 and 2(A)	43%	FO (Major), HSD (Minor), Natural Gas (Minor)	PKR 15.301/kWh	Heat Recovery	RLNG	PKR 8.9/kWh	>=60%	PKR 6.401/kWh
Pak Gen. Power	36.29%	FO	PKR 18.13/kWh	Coal Conversion and Boiler Upgrade	Coal (Local and Imported)	PKR 6.823/kWh (Imported), PKR 6.47/kWh (Local)	>=39%	PKR 11.307/kWh (Imported), PKR 11.66/kWh (Local)

5. Conclusions

Repowering of thermal power plants is a challenging engineering task, that varies from case to case. Every power plant presents its unique set of challenges that must be overcome. Repowering of old thermal power plants shows great potential just from a fuel cost analysis. Among the strategies analysed from a fuel cost point of view, the conversion of old FO based ST power plants to coal shows the greatest reduction in fuel costs. Coal conversion of old FO based ST power plants offers the following potential benefits; 1) Comparatively more reduced fuel costs than the other two repowering strategies, 2) Energy security due to utilization of indigenous coal, 3) Improved efficiencies by retrofitting with the latest boiler technologies 4) Reduced outage time during repowering as compared to Heat Recovery and Site Repowering, 5) Comparatively less capital costs. However, as CCGTs represent one of the most efficient conversion technologies, higher efficiencies of more than 50% cannot be achieved

by coal conversion. Pollution caused by coal usage is also an important deciding variable when considering repowering. The latest CCGTs have reduced NO_x production and emissions.

Further detailed economic, environmental and policy-based analyses are recommended to make a complete decision and better decision on choosing an appropriate repowering strategy. Pakistan's thermal power plants will be the backbone of the energy market for the foreseeable future and coal power plant repowering will also gain importance as the exploitation of indigenous coal increases. Further studies are recommended with other retiring power plants to make the case for repowering stronger.

REFERENCES

- [1] "World Energy Outlook 2018 - Electricity," 2018. [Online]. Available: <https://www.iea.org/weo2018/electricity/>. [Accessed: 10-Jan-2019].



- [2] N. Honkasalo, "The future role for thermal generation," *Power Engineering International*, 2015. [Online]. Available: <https://www.powerengineeringint.com/2015/05/22/the-future-role-for-thermal-generation/>. [Accessed: 15-Nov-2019].
- [3] Power System Planning - National Transmission and Distribution Company (NTDC) Pakistan, "Indicative Generation Capacity Expansion Plan 2018-40," 2019.
- [4] "CPEC-Energy Priority Projects," *China-Pakistan Economic Corridor (CPEC) Official Website*. [Online]. Available: <http://cpec.gov.pk/energy>. [Accessed: 26-Jun-2019].
- [5] "Thar coal plant begins pumping power into national grid," *Dawn*, 19-Mar-2019.
- [6] National Electric Power Regulatory Authority (NEPRA) Pakistan, "State of Industry Report 2017," 2017.
- [7] M. Ghuman, "Replacing inefficient power plants, converting to LNG: detailed plan to be submitted to PM," *Business Recorder*, Islamabad, 31-Oct-2017.
- [8] General Electric, "9HA Power Plants." 2018.
- [9] National Electric Power Regulatory Authority (NEPRA) Pakistan, "Determination of the Authority in the matter of Generation Licence Application of Huaneng Shandong Ruyi (Pakistan) Energy (Pvt.) Limited (HSRPEPL)." 2015.
- [10] National Electric Power Regulatory Authority (NEPRA) Pakistan, "Determination of the Authority in the matter of Generation Licence Application of PQEPCP." 2015.
- [11] P. F. Mathieu, "Repowering Options for Existing Power Plants," in *Thermodynamic Optimization of Complex Energy Systems*, 2012, pp. 251–260.
- [12] S. C. Gülen, "Repowering Revisited," *Power Engineering*, 2015. [Online]. Available: <https://www.power-eng.com/articles/print/volume-119/issue-11/features/repowering-revisited.html>. [Accessed: 26-Dec-2018].
- [13] A. F. Havington, "Use of Coal in Boilers Designed for Oil or Gas," in *The Space Congress*, 1982, pp. 21–23.
- [14] D. Robb, "CCGT: Breaking the 60 per cent efficiency barrier," *Power Engineering International*, 2010. [Online]. Available: <https://www.powerengineeringint.com/articles/print/volume-18/issue-3/features/ccgt-breaking-the-60-per-cent-efficiency-barrier.html>. [Accessed: 23-Feb-2019].
- [15] H. G. Stoll, R. W. Smith, and L. O. Tomlinson, "GER-3644D - Performance and Economic Considerations of Repowering Steam Power Plants." GE Power Generation.
- [16] P. J. Ploumen and J. J. Veenema, "Dutch Experience With Hot Windbox Repowering," in *International Gas Turbine and Aeroengine Congress and Exhibition*, 1996, pp. 1–8.
- [17] S. Nikbakht Naserabad, A. Mehrpanahi, and G. Ahmadi, "Multi-objective optimization of feed-water heater arrangement options in a steam power plant repowering," *J. Clean. Prod.*, vol. 220, pp. 253–270, 2019.
- [18] "Licenses GENCOs - Thermal," *NEPRA*. [Online]. Available: https://nepra.org.pk/lic_gencos.htm. [Accessed: 26-Jun-2019].
- [19] Hydrocarbon Development Institute of Pakistan - Ministry of Energy (Petroleum Division), "Pakistan Energy Yearbook," 2018.
- [20] "Fuel Calorific Values," *CNG Europe*. [Online]. Available: <http://cngeurope.com/fuel-calorific-values/>. [Accessed: 26-Jun-2019].
- [21] "High Sulphur Furnace Oil (HSFO)," *Pakistan State Oil*, 2019. [Online]. Available: <https://psopk.com/en/product-and-services/product-prices/hsfo>. [Accessed: 26-Jun-2019].
- [22] Oil and Gas Regulatory Authority (OGRA) Pakistan, "Determination of Regasified Liquefied Natural Gas (RLNG) Weighted Average Sale Provisional Price For the Month of June 2019 Dated 12 June 2019." 2019.
- [23] National Electric Power Regulatory Authority (NEPRA) Pakistan, "Decision of National Electric Power Regulatory Authority in the matter of Application of Lucky Electric Power Company Limited (LEPCL) for Unconditional Acceptance of Upfront Coal Tariff for 660 MW Coal Power Plant." 2016.
- [24] State Bank of Pakistan, "Exchange Rates for Mark to Market Revaluation by Authorized Dealers in Foreign Exchange (3-Jun-19)." 2019.



Comparing the performance of wet-bulb and dew-point evaporative cooling systems

Hafiz S. Ullah¹, Hafiz M.U. Raza¹, Khawar Shahzad¹, Muhammad Sultan^{1,2,*}, Muhammad H. Mahmood, Zahid M. Khan¹

¹Department of Agricultural Engineering, Bahauddin Zakariya University, Multan 60800, Pakistan

²Adaptive AgroTech Consultancy International, 401 Brittany Rd, Seaside, CA 93955, USA

*Corresponding Author's Email: muhammadsultan@bzu.edu.pk

Abstract

The present study investigates the performance of wet-bulb and dew-point evaporative cooling systems for climatic conditions of Multan Pakistan. In the present era, low cost and energy efficient air-conditioning system is need of the hour for thermal comfort of humans and nonhumans. Vapor compression air conditioning (VCAC) system is generally opted for and consumes large amount of primary energy and be the major source in global warming. Wet-bulb and Dew-point evaporative cooling systems such as direct, indirect, and Maisotsenko evaporative cooling systems have been studied in this study to minimize the energy consumption and reduce global warming potential. The features and importance of each system are discussed with the help of schematic and psychrometric representations. Results conclude that the systems perform better in hot and dry climatic conditions but their performance is limited in hot and humid conditions.

Keywords: Evaporative cooling, wet-bulb, dew-point, Pakistan.

1. Introduction

The deficiency of energy and increasing environmental pollution is the serious problem in the world. In this century, the pure and fresh energy is necessary for humans as well as nonhumans [1]. The consumption of energy is increased with the increase of world population and on the other hand, the energy producing systems are unable to produce clean and sufficient amount of energy [1], [2]. Globally, the usage of energy in building sector is nearly about 90% Of market share and most of the energy is consumed in heating ,cooling and the ventilation process [2], [3]. Also, the cooling degree demand will rise in future across the globe. The existing energy producing technologies are harmful for the environment. Heating ventilation air conditioning (HVAC) system are widely used for cooling in building sector, shopping malls and offices [4]. This system consume large amount of energy because this system is based on the vapor compression cycles which are involved in global warming and cause the depletion of ozone layer [5]–[7]. To reduce the energy consumption and to control the global warming potential, evaporative cooling systems are designed and recommended.

The term ‘air conditioning’ means control of temperature and humidity in a control environment [8]. Evaporative cooling systems are energy efficiency air conditioning systems. The objective of this study is to explain the working principles of DEC, IEC and MEC systems and their performance evaluation for the different conditions of Multan.

2. Evaporative cooling systems

Evaporative cooling technologies are classified into three types names are direct evaporative cooling (DEC), indirect evaporative cooling (IEC), and Maisotsenko evaporative cooling (MEC) systems. These systems are extensively studied for advanced applications in China [9].

2.1 Direct evaporative cooling

The direct evaporative cooling is the simplest method to cool the temperature of ambient air. To understand the process of DEC system, the schematic and psychrometric representation of DEC system is shown in figure 1. In this process, ambient air is brought in direct contact with water stream and as a result, temperature of product air is decreased and humidity is increased simultaneously [10]. From the above description, it has been clear that the direct evaporative cooling system is valid for hot and dry regions.

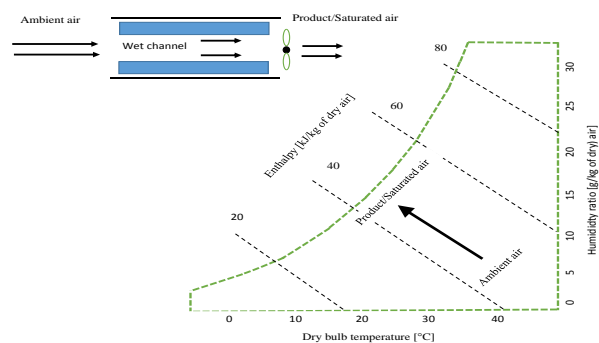


Figure 1 Schematic and psychrometric diagram of DEC system.



This system consists of fan and wetted porous medium. the porous medium may be the cellhouse paper or jute or fiber that's have water holding capacity. The effectiveness of direct evaporative cooling is 70-90% [4] and there is no heat exchanger used. The sensible heat is converted to the latent heat.

$$(T_{out})_{db} \geq (T_{in})_{wb} \quad (1)$$

$$RH_{out} > RH_{in} \quad (2)$$

$$\omega_{out} > \omega_{in} \quad (3)$$

$$h_{out} = h_{in} \quad (4)$$

$$\varepsilon_{wb} = \frac{T_{in} - T_{out}}{T_{in} - T_{wb}} \quad (5)$$

ε shows the effectiveness, T_{in} , T_{out} , T_{wb} represents the inlet, outlet and wet bulb temperatures of air respectively. The h_{out} and h_{in} represents the outlet and inlet enthalpy w_{in} and w_{out} represent inlet and outlet humidity, RH represents the relative humidity.

2.2 Indirect evaporative cooling

In the indirect evaporative cooling system, the temperature of the ambient air is decreased without much increase in moisture. In this system, the humidity ratio of working and process air remains same because this system works on the principle of sensible cooling [7] [2]. This system consists of two types of channel dry and wet channels [3]. The product air passes from dry channel and working air passes through wet channel. The inlet and outlet condition of IEC [2],

$$(T_{out})_{db} \geq (T_{in})_{wb} \quad (6)$$

$$RH_{out} > RH_{in} \quad (7)$$

$$\omega_{out} = \omega_{in} \quad (8)$$

$$h_{out} < h_{in} \quad (9)$$

$$\varepsilon_{wb} = \frac{T_{in} - T_{out}}{T_{in} - T_{wb}} \quad (10)$$

The wet-bulb effectiveness range of IEC system is between 45-65%.

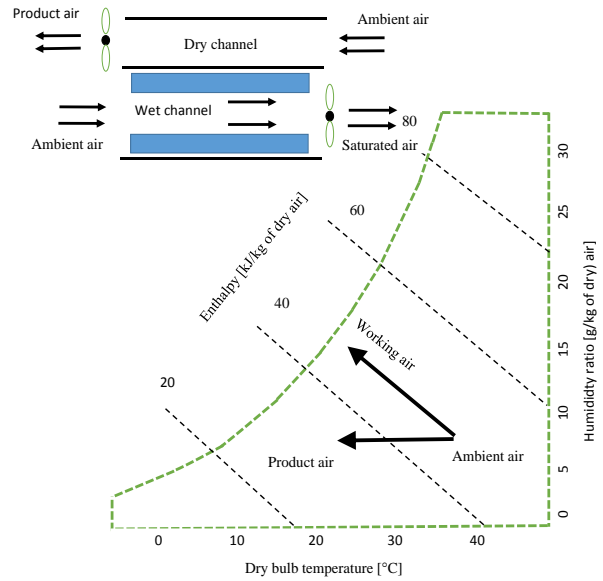


Figure 2 Schematic and psychrometric diagram of IEC system.

2.3 The Maisotsenko Cycle (M-Cycle)

The Maisotsenko Cycle (M-Cycle) is a thermodynamic conception which captures energy from the air by utilizing the psychrometric renewable energy available from the latent heat of water evaporating into the air [3] It can be used as cooler as well as humidifier [2],[4]. The system consists of one wet channel and two dry channels. the wet channel is sandwiched between dry channels the ambient air enter into the dry channel and becomes cool because of heat transfer from wet to dry channel then this air pass through wet channels in which the evaporation process occur by spraying water on it and by absorbing the heat the air becomes warm and humid.

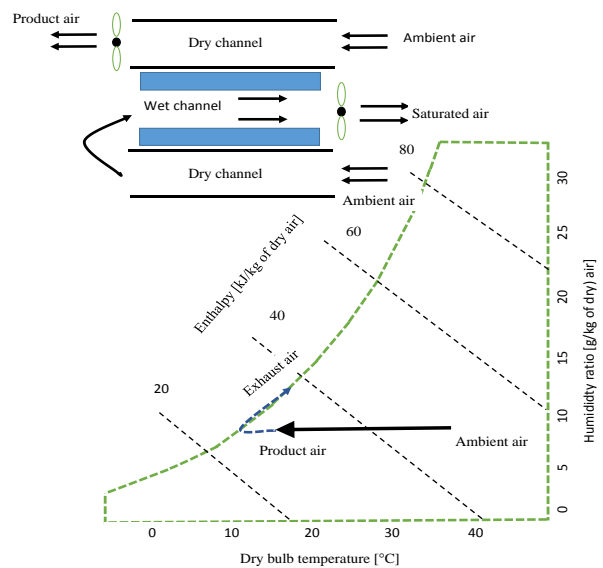


Figure 3 Schematic and psychrometric diagram of MEC system.



The inlet and outlet condition of MEC are,

$$(T_{in})_{dp} \leq (T_{out})_{db} \leq (T_{in})_{wb} \quad (11)$$

$$RH_{out} > RH_{in} \quad (12)$$

$$\omega_{out} = \omega_{in} \quad (13)$$

$$h_{out} < h_{in} \quad (14)$$

$$\varepsilon_{dp} = \frac{T_{in} - T_{out}}{T_{in} - T_{dp}} \quad (15)$$

3. Results and discussion

The present study investigates the performance of the developed evaporative cooling systems for different climatic conditions of Multan, Pakistan.

Figure 4 shows the variation in temperature of ambient air and the product air of developed evaporative cooling systems. From this figure, it is noticed that DEC and MEC systems perform better as compared to the IEC system.

Figure 5 represents the relative humidity (RH) comparison of evaporative cooling systems for different ambient air-conditions. It shows that

$$\sigma\varepsilon_{wb} = \pm \sqrt{\left(\frac{\delta\varepsilon_{wb}}{\delta T_{out}} \cdot \sigma T_{out}\right)^2 + \left(\frac{\delta\varepsilon_{wb}}{\delta T_{wb}} \cdot \sigma T_{wb}\right)^2} \quad (16)$$

$$\sigma\varepsilon_{dp} = \pm \sqrt{\left(\frac{\delta\varepsilon_{dp}}{\delta T_{out}} \cdot \sigma T_{out}\right)^2 + \left(\frac{\delta\varepsilon_{dp}}{\delta T_{dp}} \cdot \sigma T_{dp}\right)^2} \quad (17)$$

where, $\sigma\varepsilon_{dp}$ represents the total dew-point effectiveness' uncertainty of the experiment. i.e., ± 0.0832 in case of MEC. $\sigma\varepsilon_{wb}$ represents the total wet-bulb effectiveness' uncertainty of the experiment. i.e., ± 0.0748 in case of MEC, ± 0.0743 in case of DEC, and ± 0.0794 in case of IEC.,

the RH of the system is increased when the temperature is decreased.

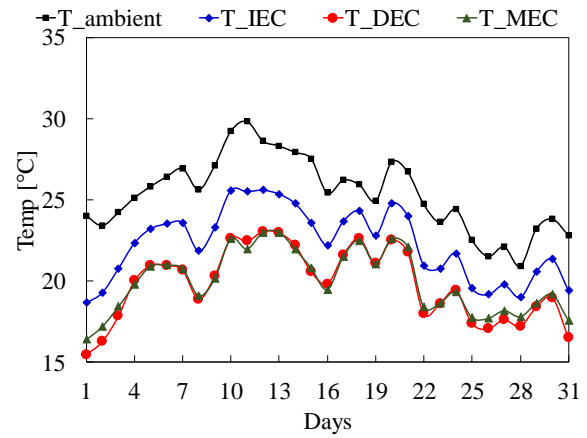


Figure 4 Temperature (T) comparison of evaporative cooling systems for different ambient air-conditions.

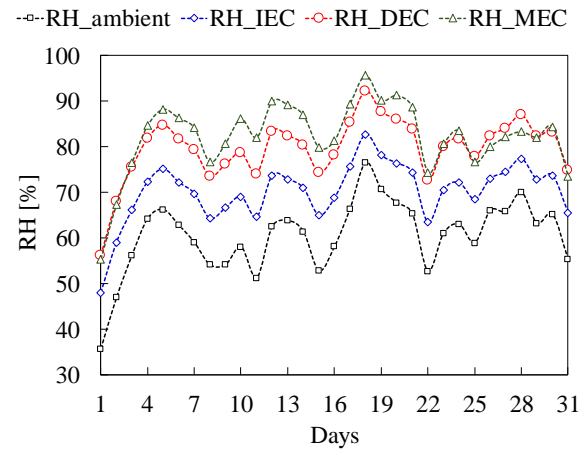


Figure 5 Relative humidity (RH) comparison of evaporative cooling systems for different ambient air-conditions.

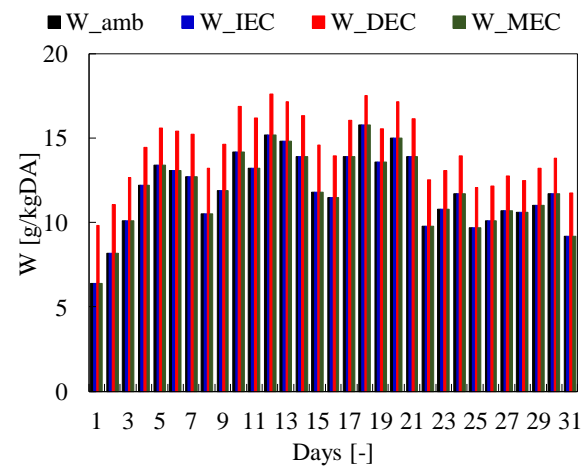


Figure 6 Humidity ratio (W) comparison of evaporative cooling systems for different ambient air-conditions.

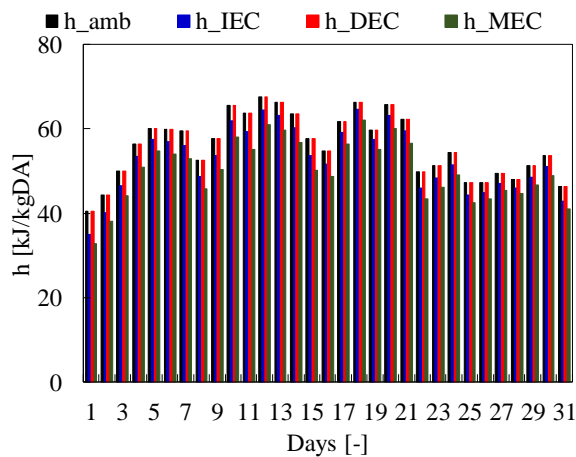


Figure 7 Enthalpy (h) comparison of evaporative cooling systems for different ambient air-conditions.

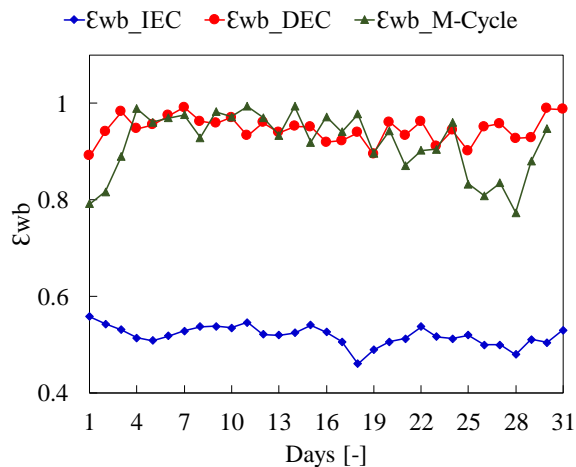


Figure 8 Wet-bulb effectiveness of DEC, IEC and dew-point effectiveness of MEC system.

Figure 6 and 7 shows the variation in humidity ratio (W) and enthalpy (h) of ambient air for evaporative cooling systems under different ambient air-conditions.

Figure 8 represents the wet-bulb effectiveness of DEC, IEC and MEC system. It is clear that the effectiveness of DEC and MEC system is comparatively high as compared to IEC system.

4. Conclusion

In this study three types of energy efficient air conditioning system have been studied. The performance of the systems is evaluated in terms of wet-bulb and dew-point effectiveness for climatic condition of Multan. The objectives to investigate the energy efficient and environment friendly air conditioning system is completed with certain findings that suggest DEC, IEC, and MEC systems as an alternative to VCAC. The limitation of these systems is their mechanism that imparts ambient air with much of the

humidity to cope up with the hot and dry weather. In case of hot and humid regions, successful studies have been conducted to develop hybrid evaporative cooling systems i.e. desiccant based evaporative cooling systems. This paper altogether encompasses the scientific principles of evaporative cooling systems and investigates their performance in hot and dry conditions. Furthermore, evaporative cooling systems are suitable for storage of vegetables and fruits for short term storage to increase their shelf life. Hybrid evaporative cooling systems coupled with thermally driven air conditioning systems can also be applied for greenhouse technique and animal shelters. And, the way to future ventures into hybrid combination of these systems is opened for future research.

Acknowledgements

The study is financially supported by Bahauddin Zakariya University, Multan under research promotion grant titled “Development and performance evaluation of prototypes of direct and indirect evaporative cooling-based air-conditioning systems”.

Conflict of interest

The authors declare no conflict of interest.

REFERENCES

- [1] M. Sultan, T. Miyazaki, S. Koyama, and Z. M. Khan, “Performance evaluation of hydrophilic organic polymer sorbents for desiccant air-conditioning applications,” *Adsorpt. Sci. Technol.*, vol. 36, no. 1–2, pp. 311–326, Feb. 2018, doi: 10.1177/0263617417692338.
- [2] M. Sultan and T. Miyazaki, “Energy-Efficient Air-Conditioning Systems for Nonhuman Applications,” *Refrigeration*, Aug. 2017, doi: 10.5772/intechopen.68865.
- [3] M. H. Mahmood, M. Sultan, T. Miyazaki, S. Koyama, and V. S. Maisotsenko, “Overview of the Maisotsenko cycle – A way towards dew point evaporative cooling,” *Renew. Sustain. Energy Rev.*, vol. 66, pp. 537–555, Dec. 2016, doi: 10.1016/j.rser.2016.08.022.
- [4] M. Sultan, H. Niaz, and T. Miyazaki, “Investigation of Desiccant and Evaporative Cooling Systems for Animal Air-Conditioning,” in *Refrigeration and Air-Conditioning [Working Title]*, IntechOpen, 2019.
- [5] P. M. Cuce and S. Riffat, “A state of the art review of evaporative cooling systems for building applications,” *Renew. Sustain. Energy Rev.*, vol. 54, pp. 1240–1249, Feb. 2016, doi: 10.1016/j.rser.2015.10.066.
- [6] O. Khalid, M. Ali, N. A. Sheikh, H. M. Ali, and M. Shehryar, “Experimental analysis of an improved Maisotsenko cycle design under low velocity conditions,” *Appl. Therm. Eng.*, vol. 95, pp. 288–295, Feb. 2016, doi: 10.1016/j.applthermaleng.2015.11.030.



- [7] M. W. Shahzad, M. Burhan, D. Ybyraiymkul, S. J. Oh, and K. C. Ng, "An improved indirect evaporative cooler experimental investigation," *Appl. Energy*, vol. 256, p. 113934, Dec. 2019, doi: 10.1016/j.apenergy.2019.113934.
- [8] M. Sultan, I. I. El-Sharkawy, T. Miyazaki, B. B. Saha, and S. Koyama, "An overview of solid desiccant dehumidification and air conditioning systems," *Renew. Sustain. Energy Rev.*, vol. 46, pp. 16–29, Jun. 2015, doi: 10.1016/j.rser.2015.02.038.
- [9] Y. M. Xuan, F. Xiao, X. F. Niu, X. Huang, and S. W. Wang, "Research and application of evaporative cooling in China: A review (I) – Research," *Renew. Sustain. Energy Rev.*, vol. 16, no. 5, pp. 3535–3546, Jun. 2012, doi: 10.1016/j.rser.2012.01.052.
- [10] A. Sharma and H. Darokar, "Two Stage Indirect/Direct Evaporative Cooling," vol. 7, no. 1, p. 6, 2018.



Experimental evaluation of desiccant dehumidification unit for air conditioning applications

Muhammad Ishaq¹, Akash Siddique¹, Hafiz M.U. Raza¹, Muhammad Sultan^{1,2,*}, Zahid M. Khan¹, Muhammad H. Mahmood¹

1- Department of Agricultural Engineering, Bahauddin Zakariya University, Multan 60800, Pakistan² Adaptive

2- AgroTech Consultancy International, 401 Brittany Rd, Seaside, CA 93955, USA

*Corresponding Author's Email: muhammadsultan@bzu.edu.pk

Abstract:

The air conditioning system is always given importance by human beings for thermal comfort. Not only human beings but also non-humans and industrial processes need an air conditioning system. For this purpose, different air conditioning systems have been developed i.e. Conventional vapor-compression based air conditioning (VCAC) and Desiccant based air conditioning (DAC). Conventional vapor-based air conditioning systems (VCAC) are not reasonable due to more utilization of energy and their harmful impact on the environment. Some cooling systems are water-based, and their performance is better in hot and dry conditions but not equally feasible in a hot and humid climate. In this regard, we need the technology which is not water dependent Desiccant air conditioning (DAC) is a promising technology in order to achieve the required load for air conditioning. In this study, the lab-scale model dehumidification unit has been used to check its performance. Temperature and relative humidity are the factors that influence the adsorption uptake of different materials. Silica gel is used as a desiccant material in the unit. In the present study working principle of desiccant air conditioning (DAC) system is highlighted. Different analysis has been made by using temperature and relative humidity to measure other parameters like humidity ratio, wet bulb temperature, enthalpy, dew point temperature and isosteric heat of adsorption. The feasibility of a desiccant air conditioning system has been investigated. The ambient air temperature was 33°C and the airflow rate was 0.10 kg/s. The data of ambient air and supply air have been represented on graphs, different parameters like enthalpy, the mass of supply air, isosteric heat of adsorption, and equivalent heat of adsorption have been analyzed.

Keywords: Desiccant, dehumidification, air-conditioning; performance evaluation, experiments.

1. Introduction

High humidity may cause problems for human thermal comfort as well as for different industrial processes. Additional moisture from the air can be removed by using mechanical refrigeration and desiccant dehumidification system. The mechanical refrigeration system reduces moisture by cooling the air below its dew point. The environmentally approachable adsorption cooling (AC) systems are an attractive substitute to the outdated vapor-compression cooling systems because they are categorized by their low working and repair costs, and easy to control [1]. Different sorts of AC systems like heating ventilating and air-conditioning (HVAC), direct evaporative cooling (DEC), indirect evaporative cooling (IEC) and desiccant air conditioning (DAC) are being used. These systems have been used for different applications i.e. agriculture products storage and industrial processes air

conditioning. In these methods, a satisfactory atmospheric condition is created for every product according to its features and local weather limitations [2].

Agricultural products (fruits and vegetables) when harvested behave like living things and perform the process of respiration, transpiration and ripening processes and contained moisture contents about (60-95%) [1][3]. The biological actions in agricultural products relate to water motion. A high level of water activity results in more deterioration of products due to the growth of microbes. Fresh agricultural products contain more moisture content and are highly affected by bacteria [3][4]. The basic purpose is to regulate the temperature and relative humidity to reduce these effects. Desiccant cooling consists of dehumidification of the ambient air by passing through the desiccant unit and then drying the air to the desired indoor-



temperature. A desiccant cooling system, therefore, contains mainly three components, namely the regeneration temperature source, the material for

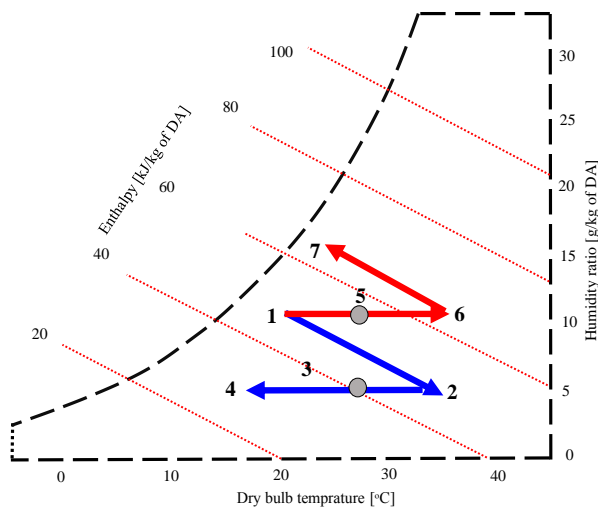
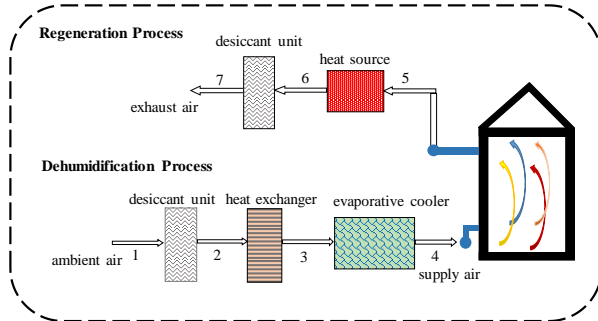


Figure 1 Schematic (above) and psychrometric (below) representation of the desiccant air-conditioning system.

dehumidification (silica gel), and the cooling unit [5].

The schematic of the is shown in figure 1 which shows the system with dehumidification and regeneration processes and equations used for the performance evaluation of the desiccant unit are given [6][7]. The desiccant dehumidification system can be used as an alternative against traditional systems in hot and humid conditions. The weak points of conventional systems are that they consume more energy and produce harmful gases like chlorofluorocarbon (CFC). These gases are the root cause of the depletion of the ozone layer and affect the environment [8][9]. Desiccant unit performance is measured in inlet and outlet. By using these two parameters

correlation has been developed. Feasibility has checked for various conditions. Two cycles (regeneration and dehumidification) are investigated. After passing some time the dehumidification process gets slow down due to saturation of desiccant material and regeneration should be done [10]. Desiccant material is regenerated in the temperature range of 65-70 °C. In the purposed system, silica gel is used as a desiccant material because it has a high adsorption uptake rate and easily available in the local market.

2. Research methodology

From the experimental setup, only air dehumidification data has been collected to check the performance of the DAC system. It consists of two cycles: the regeneration cycle and the dehumidification cycle. Ambient air (1) enters for dehumidification in the desiccant unit and exits (2). Heat exchanger and evaporative coolers are used to further cool down the ambient air. Dew point, enthalpy and humidity ratio can be calculated by using the given relationships

$$T_{dp} = T - \left(\frac{100-RH}{5}\right) \quad (1)$$

$$h = 1.006T + X(2501 + 1.86T) \quad (2)$$

$$q_{eq} = m(h_{out} - h_{in}) \quad (3)$$

$$X = 0.62 \frac{p_v}{p_{atm} - p_v} \quad (4)$$

$$\Delta X = X_{in} - X_{out} \quad (5)$$

where, T, RH, X, represents the temperature, relative humidity, and humidity ratio. q_{eq} , m and h represent the isosteric heat of adsorption, mass flow rate and enthalpy.

3. Results and discussion

The open cycle desiccant unit was evaluated for the performance of the system. The experimental system basically works in two cycles, namely, the regeneration cycle and the dehumidification cycle in the same process. i.e. 60min for regeneration and 60min for dehumidification. Desiccant based systems can easily achieve the required conditions of



temperature and relative humidity. The desiccant regeneration cycle was experimentally set up at ($T=50^{\circ}\text{C}$, $\text{RH}=16\%$) and the experimental setup is shown in Figure 1. Airstreams were dehumidified at [33°C , 45.5%].

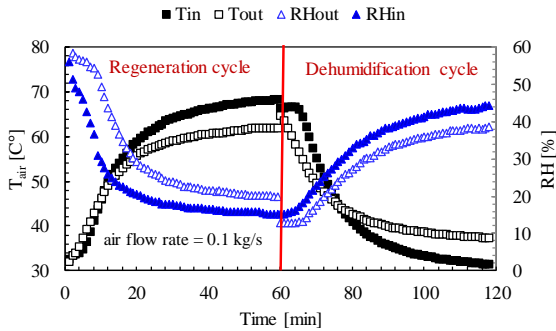


Figure 2. Experimental profile of desiccant dehumidification unit at regeneration temperature (i.e. 70°C) and cycle time (i.e. 60:60 min).

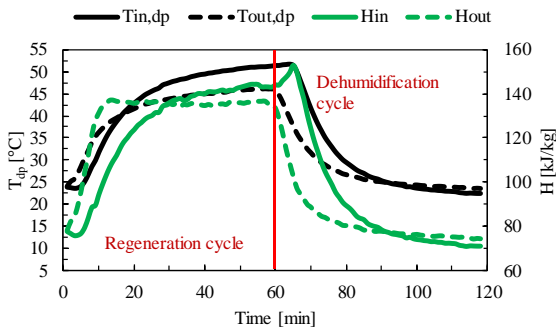


Figure 3 Obtained experimental profile for dewpoint temperature and enthalpy.

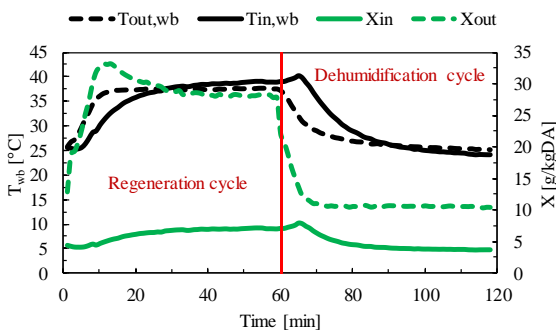


Figure 4. Obtained experimental profile for dewpoint temperature and humidity ratio.

The cycle time was chosen 60:60 for the desiccant unit. Figure 2 reveals that with the passage of time amount of humidity ratio gets

reduced and we need regeneration of air being used in the desiccant unit. It is found that the enthalpy of dehumidified air is higher than the heat of condensation/vaporization. When regeneration temperature increases then the temperature of supply air also increases, and relative humidity of supply air decreases as shown in Figure 2. Difference between temperatures and relative humidities at regeneration and dehumidification show potential for air dehumidification.

Figure 3 shows the relationship between time, dew point temperature and enthalpy, during the regeneration cycle it goes on the increase at specific points and during the dehumidification cycle. it goes to decrease at a specific level and then becomes constant. Figure 4 shows the experimental profile for dewpoint temperature and humidity ratio.

Figure 5 illustrates that the equivalent heat of adsorption increases and then it becomes constant. It shows the potential for dehumidification of air and the maximum amount that it can adsorb. The given figure reveals that with the passage of time amount of humidity ratio get decreases during the dehumidification cycle.

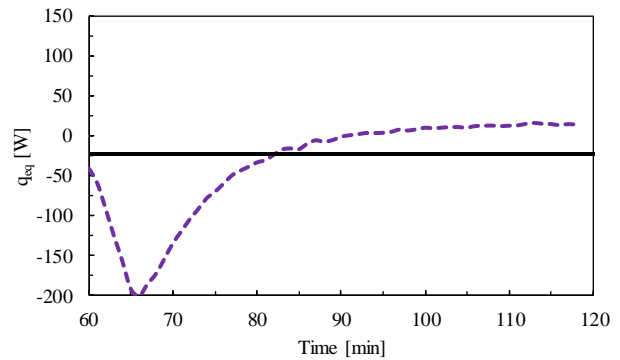


Figure 5 Profile of heat of adsorption at regeneration 70°C .

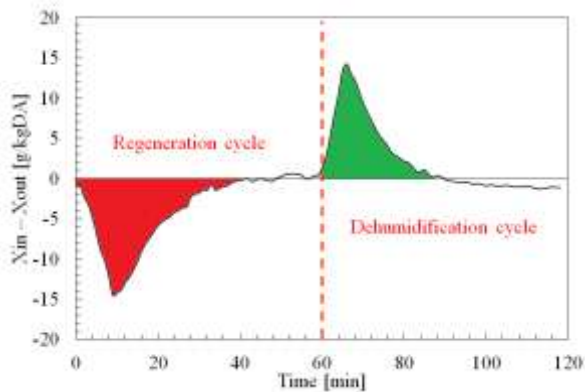


Figure 6. Amount of moisture removal during regeneration and dehumidification cycles.

Figure 6 demonstrates the amount of moisture removal during regeneration and dehumidification cycles of DAC. The amount of moisture removal seems higher than moisture adsorption on silica-gel surface. This difference may be due to uncertainty in measuring experimental data and the important associated factors for measuring experimental data are the instrument limitations, ambient conditions, data recordings, and experiment procedure. The cycle time was selected 60 minutes for this study to check the comprehensive performance of dehumidification and regeneration cycles.

4. Conclusions

Energy-efficient and approachable AC system is the need of this era. Desiccant based air conditioning system can be the best option for this purpose. In this study, silica gel has been used in a lab-scale desiccant unit. Silica gel adsorbs the moisture to a higher extent and is locally available. The desiccant unit gives the temperature and humidity ratio values at inlet and outlet conditions during the regeneration and dehumidification process and it can achieve the conditions of temperature and relative humidity. By using temperature and relative humidity other factors are calculated easily and their control is associated with temperature and humidity. From all the above experiments and discussions, it can be concluded that the DAC system is the best option for air conditioning due to energy-saving and easy to handle. This system has no environmental effect. Desiccant air

conditioning system can be used for many applications according to their requirements.

Acknowledgments

The study is financially supported by Bahauddin Zakariya University, Multan under research promotion grant titled “Development and performance evaluation of prototypes of direct and indirect evaporative cooling-based air-conditioning systems”.

Conflict of interest

The authors declare no conflict of interest.

REFERENCES

- [1] M. H. Mahmood, M. Sultan, and T. Miyazaki, “Solid desiccant dehumidification-based air-conditioning system for agricultural storage application: Theory and experiments,” *Proc. Inst. Mech. Eng. Part J. Power Energy*, p. 0957650919869503, Aug. 2019.
- [2] M. Sultan, M. H. Mahmood, T. Miyazaki, S. Koyama, and Z. M. Khan, “close and open cycle adsorption kinetics: development of correlation for desiccant air-conditioning,” vol. 35, no. 1, p. 9, 2016.
- [3] M. H. Mahmood, M. Sultan, and T. Miyazaki, “Significance of Temperature and Humidity Control for Agricultural Products Storage: Overview of Conventional and Advanced Options,” *Int. J. Food Eng.*, vol. 15, no. 10, Oct. 2019.
- [4] M. H. Mahmood, M. Sultan, T. Miyazaki, and S. Koyama, “Desiccant Air-Conditioning System for Storage of Fruits and Vegetables: Pakistan Preview,” *Evergreen*, vol. 3, no. 1, pp. 12–17, Mar. 2016.
- [5] M. Sultan, T. Miyazaki, and S. Koyama, “Optimization of adsorption isotherm types for desiccant air-conditioning applications,” *Renew. Energy*, vol. 121, pp. 441–450, Jun. 2018.
- [6] S. Jribi *et al.*, “A224 Experimental adsorption isotherms and adsorption cooling cycle performance of organic polymer sorbent-water pair,” p. 3.
- [7] M. Sultan, T. Miyazaki, S. Koyama, and Z. M. Khan, “Performance evaluation of hydrophilic organic polymer sorbents for desiccant air-



- conditioning applications,” *Adsorpt. Sci. Technol.*, vol. 36, no. 1–2, pp. 311–326, Feb. 2018.
- [8] O. Khalid, M. Ali, N. A. Sheikh, H. M. Ali, and M. Shehryar, “Experimental analysis of an improved Maisotsenko cycle design under low velocity conditions,” *Appl. Therm. Eng.*, vol. 95, pp. 288–295, Feb. 2016.
- [9] M. H. Mahmood, M. Sultan, T. Miyazaki, S. Koyama, and V. S. Maisotsenko, “Overview of the Maisotsenko cycle – A way towards dew point evaporative cooling,” *Renew. Sustain. Energy Rev.*, vol. 66, pp. 537–555, Dec. 2016.
- [10] K. Daou, R. Wang, and Z. Xia, “Desiccant cooling air conditioning: a review,” *Renew. Sustain. Energy Rev.*, vol. 10, no. 2, pp. 55–77, Apr. 2006.



Techno-Economic Analysis of Conventional & Variable Refrigeration Flow (VRF) for Hot Climatic Condition of Lahore

Haider Latif¹, Muhammad Asim², Hafiz Muhammad Waqas Badar³, Muhammad Farooq⁴, Yasir Rashid⁵

1. Mechanical Engineering Department, UET Lahore, Pakistan, haiderlatif@uet.edu.pk
2. Mechanical Engineering Department, UET Lahore, Pakistan, masim381@uet.edu.pk
3. Al-Khwarizmi Institute of Computer Science, UET Lahore, Pakistan, wagas.badar@kics.edu.pk
4. Mechanical Engineering Department, UET New Campus Lahore, Pakistan, enr.farooq@uet.edu.pk
5. Chair of Building Physics, BGU Department, TU Munich, Germany, yasir.rashid@ibp-extern.fraunhofer.de

Abstract

Affordable energy plays a key role in economic growth but the rate at which energy is being utilized in buildings has disturbed the whole world in various ways. The traditional HVAC systems installed in commercial & residential buildings with their several subunits consume energy in a huge amount. Thus, the optimization of energy usage in conventional HVAC applications is essential in terms of both technical & economic perspectives. In this paper, Variable Refrigerant Flow (VRF) solution has been proposed by developing a simulated model to cut both the total cost & energy consumption for a complex structured auditorium building with a total covered area of 7012m². Actual data measured from the centralized chiller equipment already installed in the building is compared with the modelled VRF's data in terms of electricity consumption, operational, owning & maintenance costs. Considering the local climatic conditions of the region, the VRF system is more energy efficient and around 23% more profitable than conventional chiller system already installed in the chosen building, proving VRF technology to be the acme of comfort, offering more economical & high energy performance.

Key Words: Techno-Economic Analysis; Energy Efficiency; HVAC; Optimization; Variable Refrigerant Flow

1. Introduction

World is facing the multiple contemporary challenges linked with energy and economic ultimatums, which needs to be contested through more energy efficient and rewarding technologies. Hence, the need is to bring such innovative & clean energy technologies towards the highest practical levels for the sake of forthcoming generations [1]. World Energy Outlook sheds light on the rise in energy demand with 65% of global growth rate in just a coming decade [2]. Most of such concerns over this growing demand have turned the world towards taking concrete steps to eliminate & replace devices that have caused energy wastage particularly in buildings. Furthermore, both commercial & residential buildings contribute up to 40% of total energy consumption. According to IEA's, 30% of total energy use around the globe in addition with half of the entire world's electricity consumption is through buildings, particularly designed without appropriate energy codes [3]. Thus, this demand could rise up to 30% by the mid of this century.

. As the energy demand is going to be increased three times in next decades & the electrical energy consumed by HVAC systems used around the world account for 10% of world's total electricity consumption. [4]. Being severely hit by climate change and with hot weather conditions prevailing in this region, there is need of promoting more economical technologies.

As HVAC systems are one of the key sources of energy consumption and are considered one of the most

expensive products installed especially in commercial buildings. Thus, chiller systems that are usually considered as traditional systems have been most often used on commercial scale that consume up to half of the total building's electricity [5]. This research focuses on most essential need of reducing building's energy consumption along with cost by providing more economically just and energy efficient system by keeping the comfort level same [6, 7].

One of such effective HVAC technology for buildings includes Variable Refrigerant Flow (VRF) systems that have been adopted and practiced on several scales around the world [8]. Binding all energy and financial crisis together, considering conventional HVAC systems installed in buildings as primary source of these consumption, VRF can be considered as a technology of huge potential to cut both the electricity and cost deficiencies on a decent scale. Various studies have been made on these non-water-based systems to make them suitable on different scales, thus, replacing those traditional chiller systems being practiced for the previous decades. Liu et al. analyzed electricity consumption of VRF systems with centralized models based on building energy management and regulating approach [9]. Further researches also carried out that kept digging more towards advancements in VRF akin to HVAC industry [10-13]. Aiming to replace many of such conventional systems by VRF models include several studies that involve comparative assessments. Lee et al. focused on the performance of VRF & Roof top Unit (RTU) by observing



changes in operating parameters [14]. Park et al. simulated VRF & dedicated outside air system (DOAS) systems & developed model to study & compare level of comfort of both systems [15]. Kim et al. extended the same research further & adopted more strategies to lower down energy wastage by combining both DOAS & VRF systems [16]. Xinqioa et al. in 2016 investigated the performances of two HVAC systems (VRF & VAV) adopting simulation approach [17]. Diagnosing problems from conventional chiller systems & their replacement with the latest VRF model through comparative results seems to be the solution in Pakistan [18-20]. This paper gives complete comparative analysis of both the systems through VRF modeling on a selected building already installed with traditional centralized Chiller system by using Duct-Sizer, Selection tool & sizing program.

In this paper, centralized chiller system of the university's auditorium building is investigated from the perspectives of energy and cost and alternative VRF system is proposed thorough modelling.

2. Site Selection

The site chosen for the study is located in Lahore, heartland of Pakistan. The selected location is representative of hot, dry summer condition with monsoon season as humid for Pakistan. The climate of the site is typical representation of major population of Pakistan.

The selected building is a social auditorium complex located in a public sector university in Lahore with a seating capacity of 2500 people.

Auditorium complex as shown in Figure 1 & 2. Building has a total covered area of 7012m² and is already installed with screw chiller and other indoor units. Other building information including constructional details are mentioned Table 1 below.

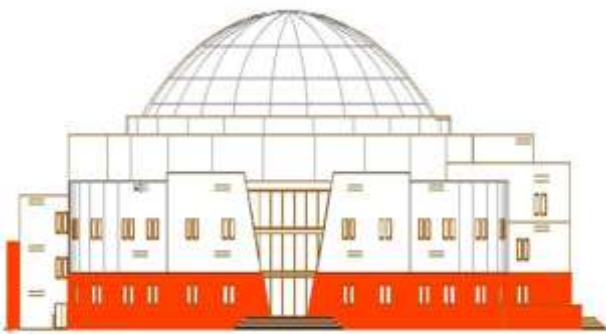


Figure 1: Architecture Elevated View



Figure 2: Actual Photograph

Table 1: Brief description of the building

Section	Details
Purpose	Social & Academic
Location	Lahore (32° Latitude, 24° Longitude, 702 Ft Elevation)
Operational Hours	University Hours Mon-Fri, 6 hr/day
Building Age	5 ½ years
Roof	Exposed with 120×120 Inches spherical dome. Height 75ft. (U Value= 0.30 BTU/hr/ft ² /F)
External Walls	9" Common Brick, 0.75" Insulation (U Value= 0.298 BTU/hr/ft ² /F)
Glass	0.24" Single glazed glass (U Value= 1.141 BTU/hr/ft ² /F)

3. Modeling & Simulation

Net load calculations are calculated through sizing software Hourly Analysis Program (HAP) & architectural drawings provided, by considering building structural & HVAC design parameters tailored according to Pakistan's local building energy codes [21]. Taking RH 50% & conditioned area 6410 m² with three core thermal zones, other design parameters are taken as:

Table 2: Design Parameters

Parameters	Values
Summer Design	115 F
Summer Constant WB	83 F
Winter Design DB	33 F
Coincident WB	30 F
Atm. Clearance No.	0.9
Thermostat Temperature	75 F
Wattage	10000 Watts

The total net coil load of the entire complex through sizing came out to be 423 tons or 5076 MBH keeping 10% safety factor according to the local climate conditions.



3.1. Conventional Chiller System: The Present Case

Auditorium Complex is currently installed with central chilled water system using electrically operated two operational & other standby water-cooled screw chiller systems each with the capacity of 215TRs. Such systems usually require plant rooms as shown in Figure 4 & a distributed duct network towards the indoor units.

Centralized HVAC system operating in building included cooling towers along with condensing water pumps & indoor units linked up with chillers in the plant room shown above. Furthermore, quantity of units installed along with their load capacity & energy consumptions in the chosen building is shown in Table 3.

Table 3: Chiller & other Equipments Unit Consumptions

Equipment	Code	Qty	Demand Load (Tn)	Standby Load (Tn)	Electricity Consumption (kW)
Chiller	CH-1	1	215	-	172
	CH-2	1	215	-	172
	CH-3 (Stand-by)	1	-	215	172
Colling Tower	CT-1	1	-	-	25.4
Chilled Pumps	CHP-1	1	-	-	22
	CHP-2	1	-	-	22
	CHP-3 (Stand-by)	1	-	22	22
	CHSP-1	1	-	-	22
	CHSP-2	1	-	-	22
	CHSP-3 (Stand-by)	1	-	22	22
	Condenser Pumps	CP-1	1	-	-
CP-2		1	-	-	22
CP-3 (Stand-by)		1	-	22	22
Total					739.4 kW

Refrigerant i.e. brine floats all over in auditorium via ducts & copper pipes to AHUs & FCUs technologies

which further consume huge amount of building's electricity. A detail of unit quantities & energy usage is shown in Table 4.

Table 4: Chiller System Indoor Unit Consumptions

Equipment	Code	Qty	Demand Load (Tons)	Electricity Consumption (kW)
Fan Coil Units	FCU-1	10	1.52	2.3
	FCU-2	15	1.66	3.75
	FCU-3	2	2.79	0.84
	FCU-4	3	3.36	1.5
	FCU-5	4	3.67	2.2
	FCU-6	2	3.35	1
	FCU-7	2	5.7	1.72
Mini Air Handling Units	MAHU-1	2	3	1.02
	MAHU-2	2	3.75	1.14
	MAHU-3	9	4.61	7.02
	MAHU-4	7	7	8.33
	MAHU-5	1	11.28	2
	MAHU-6	3	5.1	2.61
	MAHU-7	5	5.7	4.85
	MAHU-8	3	7.46	3.81
	MAHU-9	2	8.6	2.94
	MAHU-10	2	5.25	1.8
Air Handling Units	AHU-1	4	8.75	6
	AHU-2	2	12.1	4
	AHU-3	3	20.14	10.29
Ventilation Fans	EF/SF	Lot	15	15
	Total			84.12

Tables 3-4 show the total electric load that is required to run chiller & its subunits. Hence total electricity consumption is given as:



$$\sum_{In} 739.4 + \sum_{Out} 84.12 = \sum 823.52 \text{ kW} \quad (1)$$

With 10% safety factor we have 905.9 kW of electricity required to run HVAC chiller system which is already fitted in the selected building

outdoor units are connected via ducts to Ducted Indoor Units (DIU), designed on TOSHIBA Selection tool software with entering DB & WB temperatures taken as 76.2 F & 66.7 F respectively.

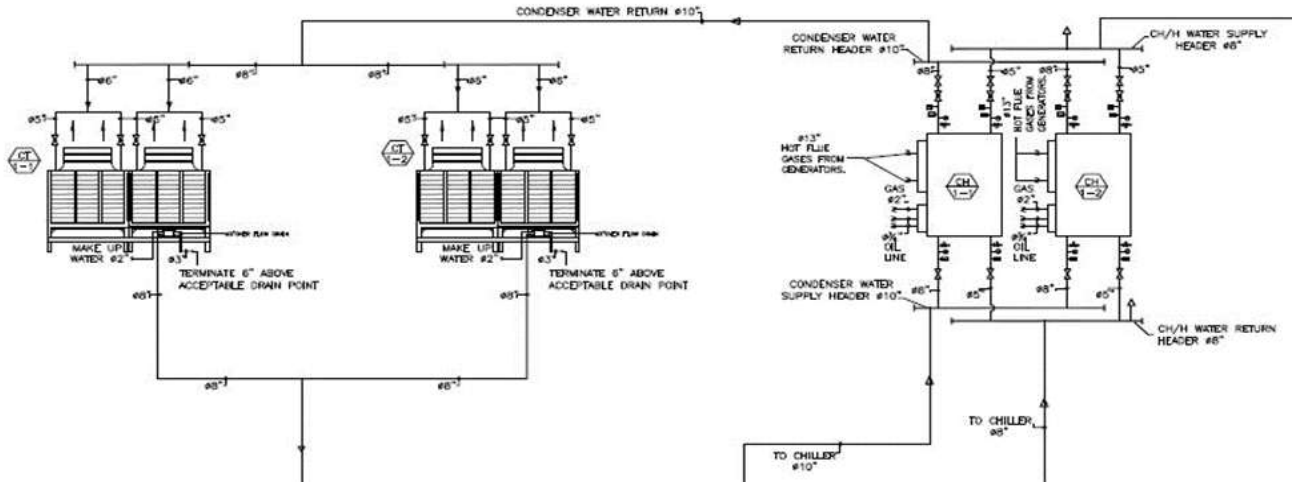


Figure 3: Plant Room Drawing of the Chiller System Installed

3.2. VRF Modeling

VRF usually consists of single outdoor Condensing Unit (CU) with multiple indoors & refrigerant in the form of liquid gas is variably distributed across the evaporators (indoor units) via tree like structures. Considering same load calculations for the auditorium, tree diagrams schematic diagrams are drawn by selecting leaders on architectural drawing.

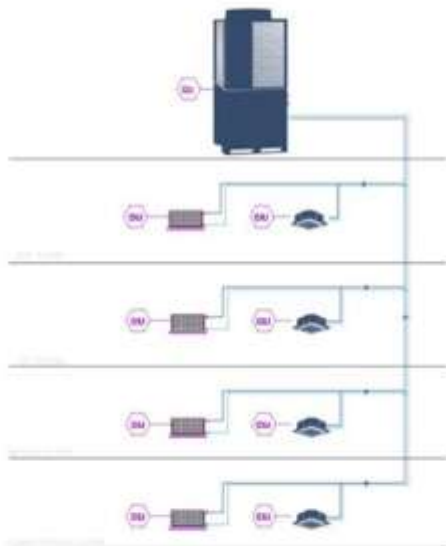


Figure 4: VRF System Tree Diagram A

Working VRF cycles with single condensing unit designed according their load capacities are shown in the tree diagrams above. The trees originating from the

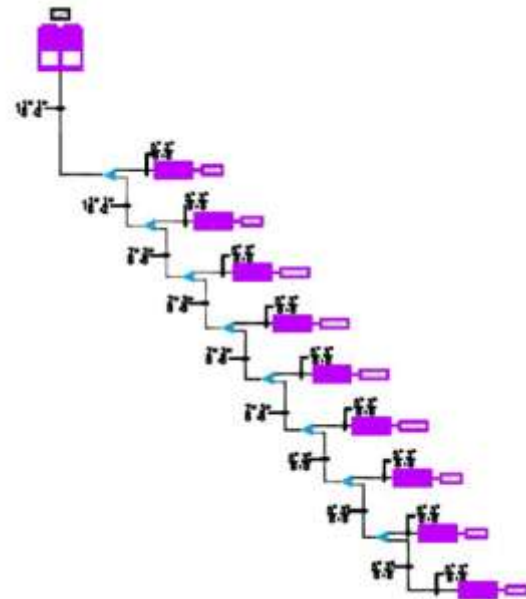


Figure 5: VRF System Tree Diagram B

Quantities along with load capacities & electricity consumption for both indoors & outdoors for the building are listed in the Table 5.

Table 5: VRF System Unit Consumption

Equipment	Code	Qty	Load per Unit	Total Load (Tons)	Total Electrical Load (kW)
Cond	CU-1	1	51.5	51.5	61.8



	CU-2	1	66.5	66.5	79.8
	CU-3	1	32.85	32.85	39.42
	CU-4	1	33.44	33.44	40.128
	CU-5	1	67	67	80.4
	CU-6	1	58.91	58.91	70.692
	CU-7	1	39.24	39.24	47.088
	CU-8	1	36.77	36.77	44.124
	CU-9	1	41.49	41.49	49.788
Ducted Type Indoor Units	DIU-1 (S-1)	7	1.52	10.64	1.596
	DIU-2 (S-2)	15	1.66	24.90	3.735
	DIU-3 (S-3)	2	2.79	5.58	0.837
	DIU-1	3	3	9	1.35
	DIU-2	6	3.75	22.5	3.375
	DIU-3	18	4.61	82.98	12.447
	DIU-4	4	5.1	20.4	3.06
	DIU-5	2	5.25	10.5	1.57
	DIU-6	11	5.7	62.7	9.405
DIU-7	20	7	140	21	
DIU-8	3	7.5	22.7	3.375	
DIU-9	2	8	16	2.4	

Ventilation	EF/S	Lot	15
	F		
Fans		Total	592.395

Load per unit with their total electricity consumption tells that 592.36 kW of load is required to run the VRF system modeled on the chosen building that is of same capacity. With 10% safety factor total electrical load turns out to be 651.634 kW.

Table 5 above clearly shows that 93 DIUs with 9 outdoor condensing units with varying capacities are required to model auditorium complex with VRF system. The complete VRF modeled design of the selected complex is shown in the above Figure 6. The above model is made on convocation hall architecture drawings where ducted units as indoors are connected from outdoors placed on roof of the building.

It is evident from both the cases that non-water based VRF consumes far less electrical energy than that centralized chiller equipment by keeping the system's net load same.

4. Conventional HVAC & VRF Economic Perspective

HVAC system is considered one of the most expensive products used in buildings. Therefore economical & more affordable HVAC solutions play key factor in reducing building's total spending. Hence operational, owning & maintenance cost comparisons of both HVAC systems are made as follows.

4.1. Operational Price

Air conditioning systems of any sort work in full swing during peak summers & their operational price is set according to per unit cost set by electric power regulatory authorities. As chosen auditorium complex is situated in a public sector institution with six working hours & HVAC system operates in summers from May till September. Table 6 shows the electricity consumption in kilo-Watt hours with electricity unit price taken as 0.13 USD/unit. [LESCO].



Table 6: Annual Operational Costs of Chiller & VRF system

System	Net Load (kW)	Total Power Consumption (kWh)	Yearly Operational Cost (USD)
Chiller System	905.9	597894	77726
VRF System	651.634	430,078	55,910

*2018 Electricity tariff= 0.13 USD/unit.

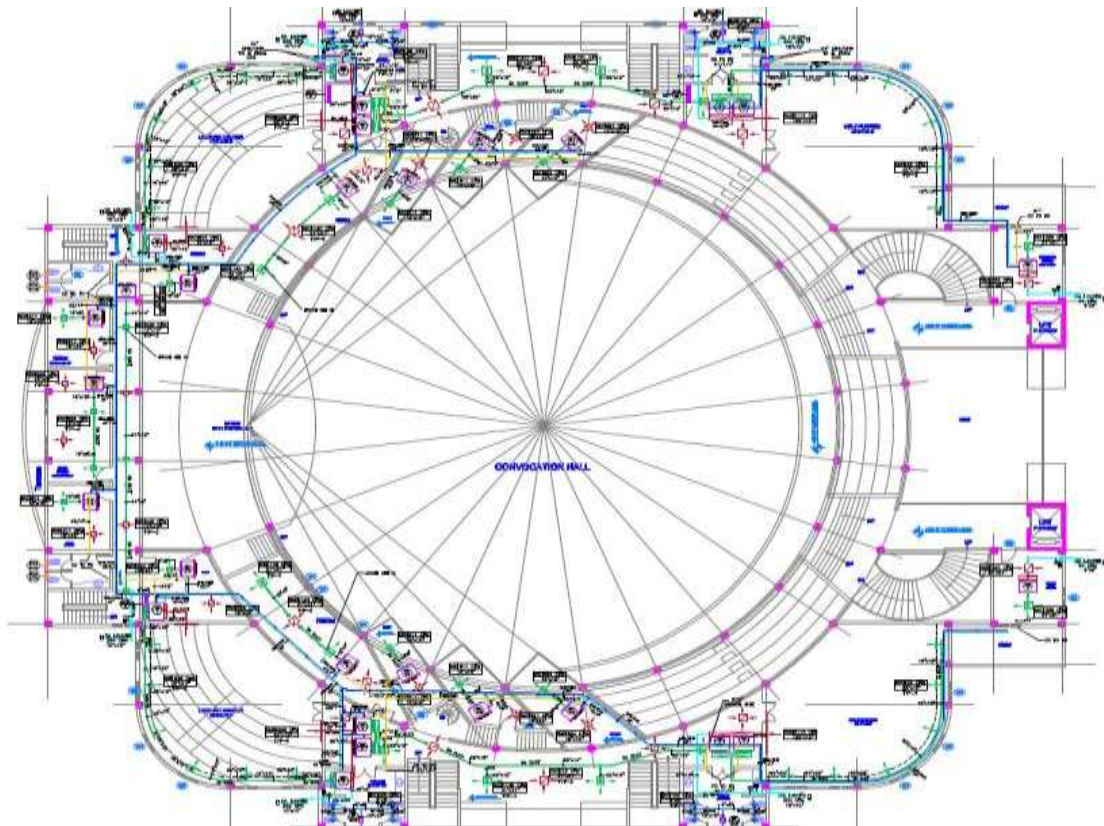


Figure 6: Complete VRF Model of Auditorium

Table 6 clearly states that up to 167816 kWh of electric power can be saved by replacing with VRF technology with building in use for 22 days a month. Thus, annual operational cost of VRF looks more reasonable than already system installed.

4.2. Initial Owning Cost

Building installed with centralized screw chiller system have initial owning price that includes both purchasing & installation costs. Total bill of quantities of the HVAC system already installed in auditorium was taken from Buildings & Works Department of the institution.

Table 7: Initial Owning Cost of VRF System Designed

Components of Chiller System	Total Cost (USD)
3 No. Electrically Operated Screw Chillers (Cap. 215 Tons each)	280744
Air Handling Equipment	145210
Fan Coil Units	86445



Pumps & Auxiliary Equipment	55420
Cooling Tower	9061
Installation of Equipment, Ductwork with Accessories, Pipe work with accessories, Fans, Valves, Auto-Control Works, Duct & Pipe Installations including other miscellaneous works.	67940
Total Owning Cost	644820

Table 8: Initial Owning Cost of VRF system designed

	CU-9 (41.49)	1	22321	22321
	DIU-1s (1.52)	7	646	4520
	DIU-2s (1.66)	15	408	6112
	DIU-3s (2.79)	2	692	1384
	DIU-1 (3) (3.75)	3	816	2448
	DIU-2 (3.75)	6	945	5670
	DIU-3 (4.61)	18	1146	20640
Ducted Indoor Units	DIU-4 (5.1)	4	1275	5100
	DIU-5 (5.25)	2	1373	2747
	DIU-6 (5.7)	11	1416	15583
	DIU-7 (7)	20	1595	31916
	DIU-8 (7.5)	3	1736	5208
	DIU-9 (8)	2	1946	3892
Supply & Installation of Duct & pipe works including their accessories, gauges, diffusers, dampers & ventilation fans	-	-	-	86790
Total Owning Cost				400318

Equipment	Code & Capacity (Tons)	Quantity	Unit Price (USD)	Total Cost (USD)
Condensing Units	CU-1	1	22900	22900
	CU-2	1	27683	27683
	CU-3	1	19901	19901
	CU-4	1	20009	20009
	CU-5	1	28229	28229
	CU-6	1	25141	25141
	CU-7	1	21288	21288
	CU-8	1	29845	29845
	CU-9	1	22288	22288
	CU-10	1	29845	29845

The VRF system modelled on building requires both indoor & outdoors cost estimations along with installation costs. Hence, prices of VRF equipments according to their capacities are taken from renowned suppliers of HVAC in Pakistan as shown in Table 8.



4.3. Maintenance Cost

Maintenance is essential need for all buildings that are exposed to public & are fitted with complex systems of HVAC. Cost of the maintenance of any system has a direct link with its age & type of technology building is installed with. Tables 7-9 show the maintenance & cost details required for the two systems.

Table 7: Maintenance Cost of Chiller System

Material	Qty	Total Cost (USD)	Yearly Maintenance
Chiller	3	870	1 time/year
Chilled & Condensing Pumps	6	1280	2 times/year
Cooling Tower	1	260	1 time/year
AHUs	9	1810	2 times/year
Mini-AHUs	36	2612	2 times/year
FCUs	38	3770	2 times/year
Calibration of controls, Anti-freezing, leak-test, Water Treatment	-	2450	1 time/year
Total			13052

Table 8: Maintenance Cost of VRF System

Job	Quantity of Indoors	Quantity of Outdoors	Yearly Maintenance	Total Cost (USD)
Inspection, testing, adjusting, Gas Charging, commissioning, air balancing & filter cleaning	93	9	1 time/year	7805

Both the Tables state that maintenance requirement for both the technologies & their total costs clearly shows VRF system is more applicable in regard of maintenance & inspection costs.

5. Results & Discussion

The calculated analysis clearly shows that electrical energy required by chiller system installed in the building is significantly higher compared to VRF system due to

energy saving potential of its outdoor & indoor units. Thus, system already installed in the building have around 17% more energy usage than non-water based VRF system modelled. This analysis seemed to be true everywhere where same climate conditions are considered. Furthermore, the operational, owning & maintenance costs with VRF system savings is summarized for comparison in Table 9.

The above total cost shows that VRF system is found to have around 23% more profit than conventional chiller system. It can be seen that annual cost savings of VRF system is mainly due to the differences in electricity consumption and lower maintenance cost.

Table 9: Comparison of the Operating, Owning & Maintenance Cost of Conventional & VRF Systems

	Conventional Chiller System (USD)	Variable Refrigerant Flow System (USD)
Operational Costs	77726	55,910
Initial Owning Costs	644820	400318
Maintenance Costs	13052	7805
Total	735598	464033

As a result, this costly traditional system needs to be replaced with more technological & affordable VRF systems in the near future.

6. Conclusion

Comparative approach is adopted for the two systems to highlight the advancements made in HVAC industry for the sake of reduction in substantial energy consumption & system's total cost on a large scale. The performance of a traditional chiller system already installed was evaluated & compared with the Variable Refrigerant Flow (VRF) model. Both systems are meant to provide comfort but VRF system found to be more applicable for the usage with a greater energy & cost saving potential. Further the VRF operation proved to be around 23% more economical than non-water-based system with comprehensively less owning cost & exemption of plant room. Also assembling & maintenance operations of VRF are more convenient than conventional fitted technologies with a less requirement of operational staff for continuous monitoring. This study will be true anywhere over the globe if same climate conditions are considered. Keeping leakages & other failures aside, it can be clearly seen that



VRF system provides the best solution for the energy wastage in buildings at a very low expense. Hence the future demands conventional HVAC systems to be replaced with more technological VRF on a commercial scale.

REFERENCE

1. Agency, I.E., *Energy Technology Perspectives 2017*. 2017.
2. Birol, F., *World energy outlook. Paris: International Energy Agency*. 2008: p. 23 (4): 329.
3. Pérez-Lombard, L., J. Ortiz, and C. Pout, *A review on buildings energy consumption information*. Energy and Buildings, 2008. **40**(3): p. 394-398.
4. Kessides, I.N., *Chaos in power: Pakistan's electricity crisis*. Energy Policy, 2013. **55**: p. 271-285.
5. Goetzler, W., M. Guernsey, and J. Young, *Research & development roadmap for emerging HVAC technologies*. 2014, US Department of Energy, Building Technologies Office Google Scholar.
6. Cheng, X. and X. Liang, *Analyses and optimizations of thermodynamic performance of an air conditioning system for room heating*. Energy and Buildings, 2013. **67**: p. 387-391.
7. Wang, Z., et al., *Analysis of energy efficiency retrofit schemes for heating, ventilating and air-conditioning systems in existing office buildings based on the modified bin method*. Energy Conversion and Management, 2014. **77**: p. 233-242.
8. Deru, M.a.P.T., *Source Energy and Emission Factors for Energy Use in Buildings (Revised)*. 2007, National Renewable Energy Lab.(NREL), Golden, CO (United States).
9. Liu, C., et al., *Operational electricity consumption analyze of VRF air conditioning system and centralized air conditioning system based on building energy monitoring and management system*. Procedia Engineering, 2015: p. 121: p. 1856-1863.
10. Jain, N., et al., *Partially decentralized control of large-scale variable-refrigerant-flow systems in buildings*. Journal of Process Control, 2014. **24**(6): p. 798-819.
11. Shah, A., et al., *Optimization of Buildings Energy Consumption by Designing Sliding Mode Control for Multizone VAV Air Conditioning Systems*. Energies, 2018. **11**(11).
12. Yun, G.Y., J.H. Lee, and I. Kim, *Dynamic target high pressure control of a VRF system for heating energy savings*. Applied Thermal Engineering, 2017. **113**: p. 1386-1395.
13. Zhai, Z. and J. Rivas, *Promoting variable refrigerant flow system with a simple design and analysis tool*. Journal of Building Engineering, 2018. **15**: p. 218-228.
14. Lee, J.H., P. Im, and Y.-h. Song, *Field test and simulation evaluation of variable refrigerant flow systems performance*. Energy and Buildings, 2018. **158**: p. 1161-1169.
15. Park, D.Y., G. Yun, and K.S. Kim, *Experimental evaluation and simulation of a variable refrigerant-flow (VRF) air-conditioning system with outdoor air processing unit*. Energy and Buildings, 2017. **146**: p. 122-140.
16. Yu, X., et al., *Comparative study of the cooling energy performance of variable refrigerant flow systems and variable air volume systems in office buildings*. Applied Energy, 2016. **183**: p. 725-736.
17. Kim, W., S.W. Jeon, and Y. Kim, *Model-based multi-objective optimal control of a VRF (variable refrigerant flow) combined system with DOAS (dedicated outdoor air system) using genetic algorithm under heating conditions*. Energy, 2016. **107**: p. 196-204.
18. Brotzu, A., et al., *Pipeline Corrosion Failure in an Absorption Chiller*. Procedia Engineering, 2015. **109**: p. 43-54.
19. Kim, N.-K., M.-H. Shim, and D. Won, *Building Energy Management Strategy Using an HVAC System and Energy Storage System*. Energies, 2018. **11**(10).
20. Zhang, R. and T. Hong, *Modeling of HVAC operational faults in building performance simulation*. Applied Energy, 2017. **202**: p. 178-188.
21. Iwaro, J. and A. Mwashia, *A review of building energy regulation and policy for energy conservation in developing countries*. Energy Policy, 2010. **38**(12): p. 7744-7755.



Life cycle assessment of Solar Assisted Geothermal Heat Pump for the Residential buildings in Pakistan

Ali Farooq^{1*} & Dr. Tauseef A. Khan²

1. Dept. of Mechanical Engineering, UET Lahore

2. Dept. of Mechanical Engineering, UET Lahore

* enr.alifarooq@outlook.com

Abstract:

This article examines the environmental implications of solar assisted geothermal heat pump in residential buildings of Pakistan for domestic heating and hot water production through life cycle assessment methodology. Simapro was used takingecoinvent for life cycle inventory and IMPACT 2002+ for life cycle impact analysis. Production of 1 kWh energy for space heating requirement and production of hot water at 43°C is selected as a functional unit for this system. Results indicated that the operational phase was the largest contributor towards all impact categories i.e. carcinogenic, Ozone layer depletion, Ionizing radiation, Aquatic, Eco toxicity except mineral extraction throughout the life cycle of solar assisted geothermal heat pump system. A comparison of operation phases between solar assisted geothermal heat pump and conventional geothermal heat pump and solar assisted air heat pump was also made with life cycle assessment methodology. The result indicated that operation phase of solar assisted geothermal heat pump was producing least environmental impacts among the three systems compared.

Keywords: Solar assisted geothermal heat pump, Life cycle assessment, Residential buildings, Impact analysis

1. Introduction

Global warming is among the largest environmental impacts due to availability of higher rates of greenhouse gases. In the previous century the average global temperature has increased by 0.74°C and set to increase further by 1.1°C and 2.4°C in low and high emission scenario by the end of this century respectively.[1] Pakistan stands 7th in the list of top 10 most affected countries according to Climate Risk Index 2018.[2] Overall losses of about \$3816 Million Annually with the death rate of 0.33/0.1 Million inhabitants. It is, therefore, need of the time to move towards the energy sources with less environmental impacts. Residential sector consumes up to 45% of total energy utilization worldwide mostly for air conditioning purposes. In Pakistan the residential sector consumes electricity double then the Industrial sector, 5 times that of agriculture and 7 times to the commercial utilization. The energy mix of Pakistan with thermal (Oil, Coal & Gas) as the major contributor is shown in fig 2.[3],[4] Thermal resources utilized for energy production are not only depleting but also creating hazardous environmental effects. It is therefore need of the time to introduce more energy efficient and clean ways of air conditioning. It is also necessary to find out environmental effects of conventional and latest technologies throughout their life time for decision making. There is no study

available regarding the use of geothermal heat pumps for heating & cooling purposes in Pakistan & associated environmental issues in the literature.

Geothermal heat pumps

Geothermal energy is a cleaner and safer form of energy. Geothermal heat pumps provide a viable solution for space cooling & heating in both in commercial and residential buildings.[5][6] Unlike ambient air, the temperature in several feet down from the ground surface remains almost constant throughout the year. A geothermal heat pump utilizes this low-grade energy for heating or transfers heat to the ground in cooling applications.[7][8] The Coefficient of performance (COP) and Seasonal performance factor (SPF) of geothermal heat pumps are larger as compared to air source heat pump systems. The main parts of the geothermal heat pump are:

- I. Ground heat Collector
- II. Heat Pump
- III. Distribution System

The two main types of geothermal heat pumps are open loop geothermal heat pumps and closed loop geothermal heat pumps. In open loop, the water is taken from the ground level transfers/receives heat



from the system and return back to the ground. The closed loop is further divided into three basic types 1) Horizontal 2) Vertical 3) Pound/Lake.[9] In horizontal systems the ground loop heat exchangers are buried horizontally with lower depths. The vertical system is preferred where space limitation is present. The vertical system has cost issues with the increase in the depth of ground heat exchangers. The length of the ground loop can be significantly reduced by integrating geothermal heat pump with other energy sources i.e. Solar thermal energy system.[10]. The most significant thing in the system designing is the length of the ground loop.[11] An oversized system will increase the installation cost & undersized will not be able to fulfil the energy requirement of the system. In pound/Lake systems the heat exchanger is buried in water.

Life cycle assessment methodology (LCA)

Life cycle assessment is a methodology for assessing processes, products, systems consisting of extraction of raw materials, manufacturing, processing, transportation systems required for distribution of products, utilization along with maintenance & recycling during their life cycle for evaluation of Environmental impacts. LCA is based on ISO14040 & defined as a method for assessment of the environmental aspects and potential impacts allied with a product or a process with creating an inventory system of all related inputs and outputs of the system; analyzing the potential environmental effects; and on these bases ,interpretation of the results of the inventory analysis and impact assessment phase. [1][12]

Goal & Scoped Definition:

The goal definition & scope identification is the first step in LCA study in which objects of the study are defined. According to ISO 14040 this phase of LCA study considers the product system, applications, functions, function units, boundaries of the study, impact categories selected, limitations and audience as well. The figure illustrates the life cycle assessment methodology.[13]

Life cycle Inventory Analysis (LCI)

Life cycle inventory analysis is the 2nd step in any LCA study. Input detailed data is collected and calculated in this phase. In flows and out flows including energy requirements, raw material, atmospheric and water emissions, solid wastes are quantified in this step. The LCI analysis is based on the nature and quantities of resources from nature including energy, water ,etc. the materials used in the production of the product, the ways of transportation, the utilization method during its life time, and

methods for its final disposing as shown in table 1 & 2 & fig1 .[14]

Life Cycle Impact Assessment (LCIA)

In this step the results of LCI phase are interpreted and transformed into impact indicators. As per recommendations of ISO 14042 the impacts are classified and divided in different categories as per their nature with characterization as essential step and Normalization and weighting as optional steps. Fig 2 shows the graphical representation of LCIA methodology explaining the modeling of a substance emissions from midpoint damage categories to endpoint damage categories.[15]

Interpretation of Results.

The last step of Life cycle assessment is interpretation in which the results are deducted and conclusions are made for utilization of this study in different decision making policies.

A brief literature review is being presented here:

According to the recommendation, professional Simulation software should be employed for the accurate determination of the length requirement of geothermal heat Pump.[16]. Xiang Li Developed a mathematical model for building energy for analyzing global warming and carbon emissions, It was analyzed that operation phase was responsible for 86-94% carbon emissions.[17]. Arat and Arslan used ANN model for the optimum design of geothermal heat pump by using back propagation learning algorithm.[18]. Han studied performance of ground source heat pump (GSHP) in Ohio USA, COP for

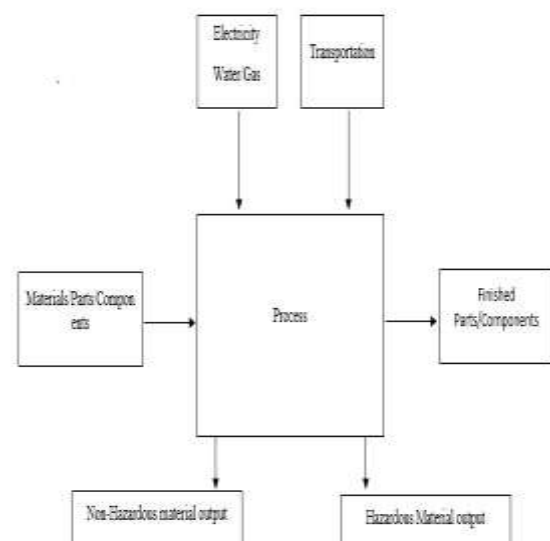


Figure 1: Mapping of the inputs and outputs of the system in the LCI phase

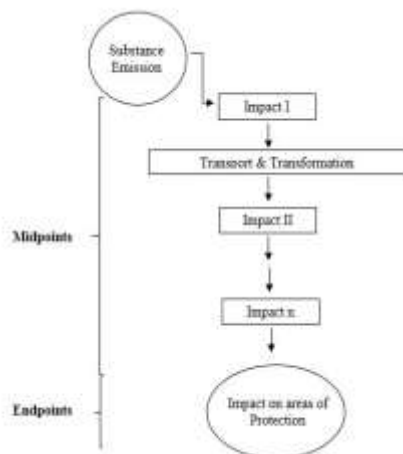


Figure 2: Schematic representation of LCIA step

the service life found to be in Between 3 & 4.[6] Air source heat pump and ground source heat pump with energy used and greenhouse gas emissions were compared with life cycle approach. Amount of Electricity utilized was the largest contributor towards environmental Impacts. Sustainability study with the help of LCA revealed that Ground source heat pump (GSHP) can reduce the energy utilization up to 40%.[19]. Comparison of GSHP with conventional diesel boiler for Nursery School in Galicia (Spain) showed that GSHP has 54.3% CO₂ emissions savings. An LCA study was employed for 40 residential houses in France. This study showed that embodied impacts are the major contributor to environmental impacts.[20]. C. Naldi analyzed seasonal performance factor of air source heat pump for heating applications using bin method that produced results comparable with dynamic hourly simulation results[21] A. Safa studied air source heat pump with two-stage variable capacity using TRNSYS simulations. In cooling applications the COP varied from 4.7 to 5.7 as the outdoor temperature changed between 33°C to 16°C. While in heating case, the COP varied from 1.79 to 5 as the outdoor temperature varies between -19°C to 9°C.[22] Abel studied air source heat pumps water heaters for residential buildings in the Australian climate for identification of key performance parameters. The assessment indicated that energy performance is dependent on COP and site-specific electricity tariff. [23] Liu investigated the feasibility and performance of Hybrid ground source heat Pump (HGSHP) in the cold area of Shenyang. It was observed that HGSHP system with boiler as auxiliary heat source can lower the conventional energy utilization.[24] Residential buildings in the Northern Areas of Pakistan are heating dominant. Solar Assisted geothermal heat pump for the residential building for the heating

purpose could be a good choice replacing the conventional systems being used (Wood, Electric heaters). The current study discusses the environmental impacts of the solar assisted geothermal heat pump (SAGHP), geothermal heat pump (GHP) and solar assisted heat pump (SAHP) only.

2. Methodology:

The life cycle assessment (LCA) methodology is utilized for environmental impacts of the system under study. Hourly analysis program HAP was utilized for heat load calculations. Polysun was utilized for system simulations and Simapro 8.4 for system model for LCA study. Ecoinvent 3.3, USLCI and values from literature & local manufacturers were used for life cycle inventory analysis. Impact 2002+ & IPCC GWP 100a were utilized for life cycle impact analysis.

Table 1: Detail of transportation utilization during LCA study.

Sr.	Type of carriage	Mood of travelling	No. of km
1	Material	Transport Truck <10ton	450
2	Machinery	Transport Truck >20ton	160
3	Staff	Passenger Car	160

System description

A residential building located in Pakistan (33E, 73N) with a floor area of 103m² with the occupation of 3 people is utilized as a system in this study. The average outdoor temperature is 14°C annually [25]. Building concrete was used for construction. The U values used for the heat load calculations were 0.213 & 0.161-0.213 for roof & walls respectively [6], [13]. Peak load for heating was determined as 14.6 kW for which the system is designed. The soil properties of Murree changes with the change in altitude (from 500m to 3000m). The soil type below the ground surface is mostly sandstone or limestone type [26]. Some values for this soil type are given as: Density: 2402-7608 kg/m³, Thermal Conductivity: 2.07-3.46 Wm⁻¹k⁻¹ & Diffusivity: 0.7-4.2.

2.1. Simulation with polysun

Solar assisted geothermal heat pump (SAGHP) system consisted of 3 flat Plate collectors of 7.6 m² gross area. The length of the ground loop was determined as 157m. 32mm double U type single ground loop was utilized. The seasonal performance factor of the system resulted in 6.4. Amount of solar



energy obtained was 6394 kWh/year. Energy obtained from geothermal source for SAGHP was 16492 kWh/year. The additional electricity requirement for this system was 3967 kWh/year. In GHP system increased ground loop length of 266m. Seasonal performance factor decreased to 4.6 and additional electricity demand raised to 6083 kWh/year. In SAHP flat plate collectors with the Overall area of 7.6 m² were employed. The seasonal performance factor decreased to 3.5. In the absence of geothermal energy, the electricity demand increases to 7600 kWh/year. From the simulation results, it was obvious that the SAGHP was the optimum solution for the area under study. Therefore, it was utilized as a reference system for comparison in this study.

Life cycle assessment (lca) methodology

LCA study of any system consists of four phases including goal & Scope definition, Life Cycle Inventory Analysis, Life Cycle Impact Analysis and Interpretation of results. [13],[27].

2.3.1. Goal & scope definition:

The goal of this study is the life cycle assessment of SAGHP for residential buildings in Pakistan. The scope of the study is life cycle assessment from cradle to grave. The total life of the system is 20 years for which the system is designed. The functional unit is assumed to provide 1kWh of energy for residential heating purpose and for hot water production with a set temperature of 43°C.

2.3.2. Life cycle inventory analysis (lci)

For inventory analysis, Ecoinvent, and USLCI data basis were utilized. The areas where appropriate data were not available, Literature and local manufacturers were consulted. For life cycle inventory analysis a complete link between all the inputs from nature (Raw materials etc.) from the techno sphere (extraction of raw materials, Processing, Production, Electricity requirement & Transport etc.) with the output to nature, air, Land, and water [28]. Table 1 contains the details of all distances and mode of travelling. Table 2 contains the detail of the materials used for the geothermal heat pump of 10KW capacity, solar collectors, underfloor heating system and refrigerant. The manufacturing plant was assumed to be located in Lahore. Sale point at Rawalpindi. The operation phase for 20 years consumes electricity 79344kWh, 121661kWh & 153909 KWh for SAGHP, geothermal heat pump without solar assistance & Solar Assisted geothermal heat pump without geothermal energy respectively.

Life cycle impact analysis (lcia)

LCI in life cycle assessment is followed by LCIA. This part of LCA analyzes significance of potential environmental impacts resulted from LCI flow results. In the current study IMPACT, 2002+ and IPCC GWP 100a were employed. Characterization is considered as the last step in the LCIA as per ISO 14044. Weighting and normalizing may be required as per goal & Scope definitions.

Interpretation of the results

This is the last step of LCA. In this phase all the results from LCI and LCIA are summarized, the conclusions are made and the suggestions are provided to the respective audience. The results of the current study are given in the next section.

3. Results and Discussions:

3.1. Results for the full system

I. Fig 3 & Table 3 shows the characterization results of our reference system using IMPACT 2002+ of geothermal heat pump system (including heat pump, under floor heating system, refrigerant, backfill, heat collector and all relevant transport utilization), Solar thermal system (including solar collector, storage tank, support and all transport utilization) and Operation Phase. It is obvious that the operational phase is the largest contributor to environmental impacts with the exception in the Mineral extraction where Heat Pump contributes the maximum in all 15 midpoint impact categories. From Carcinogens to Mineral extraction for geothermal Heat pump system, solar thermal system and operation phase. Fig 6 shows the normalization results form for each category.

II. After the normalization process, the end results (Damage category) showed that the operational phase dominates in all four damage categories i.e. Human Health, Ecosystem quality, Climate change & resources. The overall system has the least impacts on ecosystem quality. Heat pump system has the largest impacts on ecosystem quality. Overall maximum impacts were found in the category of resources. The results of the normalization categories are shown in fig 4.

III. In a geothermal heat pump, Heat collector has the largest Impacts as compared to other portions of the complete system. Manifold has also significant Impacts on aquatic eutrophication & Mineral extraction.



Table 2: Detail of all material utilization during LCA study

Name of the part	Material utilized	Quantity (kg)	Name of the part	Material utilized	Quantity (kg)	
Heat Pump	Low Alloyed Steel	20	Solar collector	Galvanized Steel	0.5	
	Reinforced Steel	75		Glass	0.15	
	Copper	22		Copper	0.12	
	Elastomer	10		SS	0.089	
	PVC	1		Al	0.05	
	Polyester Oil	1.7		Glycol	0.013	
Refrigerant	R134a	3.09		Insulation	0.6	
	Losses MFG& assembly 3%	0.0927		Brass	0.05	
Under Floor Heating System	Sand	4500		Storage Tank	G Steel	173.6
	Cement	900			Glass	
	Al	126	Copper		30.8	
	LDPE ¹	101	SS		73.5	
	Polystyrene	66	Al			
Heat Collector	HDPE ¹ Vertical Heat Collector	183.1	Glycol			
	LDPE	4.7	Insulation		16.8	
	Ethylene Glycol VCH	100.2	Brass		0.35	
Manifold	Brass	6.6	Support		G Steel	10
Back Fill	Bentonite	19.1			Glass	
Others (Heat Pump)	Reinforced Steel	3.8		Copper	3	
Other (Solar System)	Copper	0.46		SS	0.5	
	LDPE	0.8		Al	1.8	
	Card Board	3	Insulation	2		

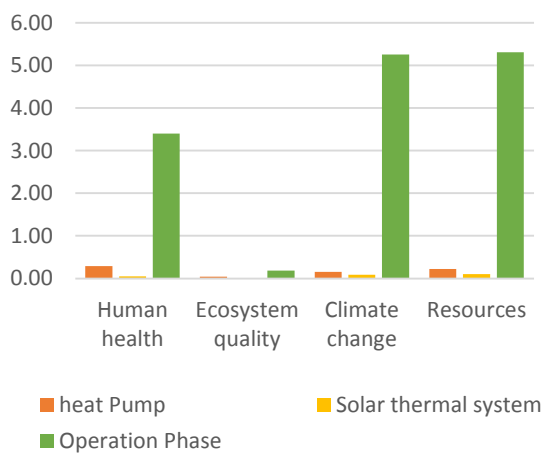


Figure 3: Normalization results of the system using IMPACT 2002+ (operation phase of solar assisted geothermal heat pump for 20 years)

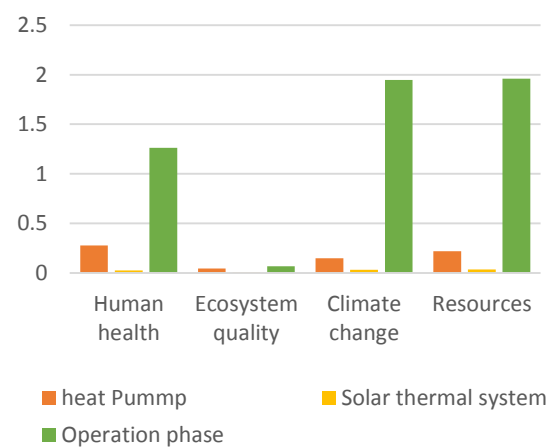


Figure 4: Damage category results of the system using IMPACT 2002+ (operation phase of solar assisted geothermal heat pump for 20 years)



Table 3: Characterization profile of solar assisted geothermal heat pump system

	Impact Category	Unit	Total	Heat Pump	Solar thermal System	Operation Phase
1	Carcinogens	kg C2H3Cl _{eq}	897	112	12.5	772
2	Non-Carcinogens	kg C2H3Cl _{eq}	3.33 ^{^3}	137	15.9	3.17 ^{^3}
3	Respiratory inorganics	kgPM2.5 _{eq}	20.8	1.92	0.419	18.5
4	Ionizing radiation	Bq C-14 _{eq}	3.29 ^{^5}	4.37 ^{^3}	1.81 ^{^3}	3.22 ^{^5}
5	Ozone layer depletion	kg CFC-11 _{eq}	0.0602	0.027	1.05 ^{^-5}	0.0332
6	Respiratory organics	kg C2H4 _{eq}	19.4	0.659	0.304	18.5
7	Aquatic ecotoxicity	kg TEG water	1.97 ^{^7}	1.64 ^{^5}	8.71 ^{^4}	1.95 ^{^7}
8	Terrestrial Eco toxicity	kg TEG soil	1.98 ^{^5}	6.87 ^{^4}	1.07 ^{^4}	1.18 ^{^5}
9	Terrestrial acid	kg SO2 _{eq}	591	35.5	11.2	544
10	Land occupation	m ² org.arable	38.4	6.77	1.18	30.4
11	Aquatic acidification	kg SO ₂ _{eq}	150	9.74	2.67	137
12	Aquatic eutrophication	kg PO ₄ lim	1.45	0.616	0.083	0.746
13	Global warming	kg CO ₂ _{eq}	5.44 ^{^4}	1.51 ^{^3}	892	5.2 ^{^4}
14	Non-renewable energy	MJ primary	8.55 ^{^5}	3.38 ^{^4}	1.49 ^{^4}	8.07 ^{^5}
15	Mineral extraction	MJ surplus	542	346	159	37

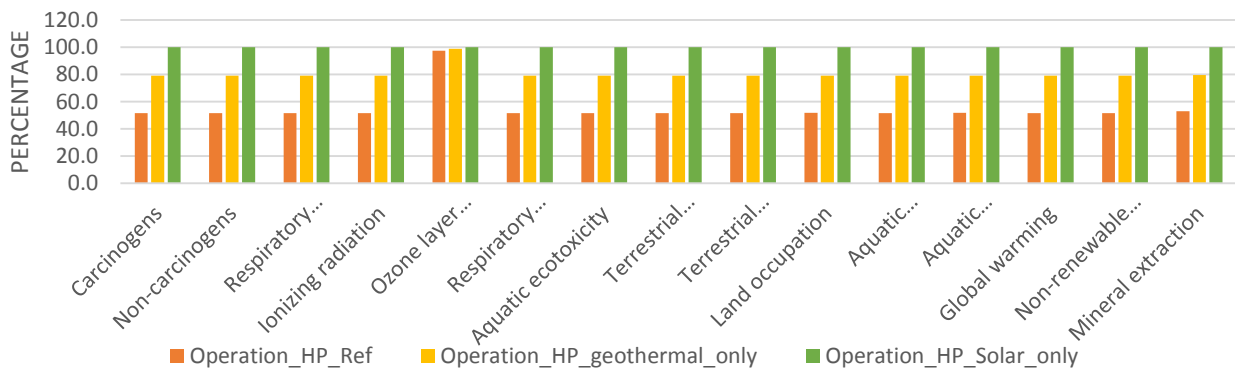


Figure 5: Characterization results using IMPACT 2002+ for SAGHP (Operation_HP_Ref), SAHP(Operation_HP_Solar_only) & GHP (Operation_HP_geothermal_Only) systems for operation phase of 20 years

In Damage assessment, heat collector has larger impacts

IV. In Solar thermal system, solar storage contributes the largest in all categories of Characterization, Damage assessment, Normalization & Single Source score as compared to solar collector & support.

V. Electricity from oil contributes the largest impacts in mid-term category characterization and end categories i.e. ecosystem, human health, climate change & resources.

Comparison of the operation phase for 20 years

As the operation phase is the largest contributor to environmental effects. Therefore only operation phase

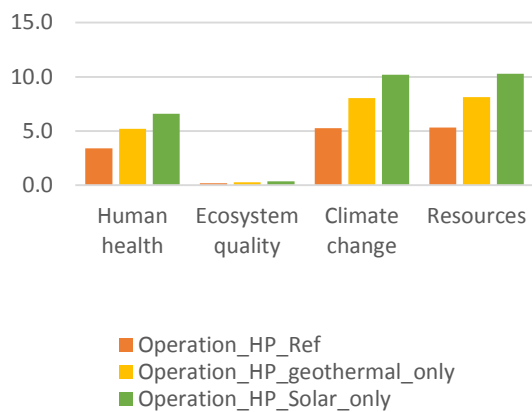


Figure 6: Damage assessment results using IMPACT 2002+ for SAGHP (Operation_HP_Ref), SAHP(Operation_HP_Solar_only) & GHP

is analyzed for finding out the potential impact for the operation phase for 20 years.

- I. Fig 5 & fig 6 shows characterization & damage category results respectively of operation phase using IMPACT 2002+ for SAGHP, GHP & SAHP. It is clear that SAGHP has the least impacts on the environment as compared to the other two systems in all impact categories

4. Conclusions:

1. Solar assisted geothermal heat pump system was analyzed using IMPACT 2002+. Results indicated that operation phase was the largest contributor in all midpoint impact categories except mineral extraction as compared to geothermal heat pump system (Heat Pump, Refrigerant, Under Floor Heating System, Heat Collector, Manifold & Others) & solar thermal system(Solar collector, Storage Tank, Support & others) .
2. Damage categories also indicated that the operation phase has the highest impact in all 4 categories i.e. human health, eco system quality, climate change and resources.
3. Operation phase being the largest contributor was compared with the operation phases of geothermal heat pump system and solar assisted heat pump system. Results indicated that solar assisted geothermal heat pump was least contributor among the three system compared.

REFERENCES:

- [1] M. M. Khasreen, P. F. G. Banfill, and G. F. Menzies, "Life-Cycle Assessment and the Environmental Impact of Buildings: A Review," no. i, pp. 674–701, 2009.
- [2] S. Kreft, D. Eckstein, L. Dorsch, and L. Fischer, "GLOBAL CLIMATE RISK INDEX 2016 Who Suffers Most From Extreme Weather Events ? Weather-related Loss Events in 2014 and 1995 to 2014," Berlin, 2016.
- [3] Ministry of Finance, "CHapter 14 Energy, Pakistan Economic Survey 2016-2017," 2016.
- [4] M. of Finance, "Energy , Pakistan Economic Survey 2015-2016," 2016.
- [5] M. H. Dickson, *Geothermal Energy utilization & technology*. Paris, France: UNESCO, 2003.
- [6] ASHRAE, *ASHRAE Handbook - HVAC Applications*. 2011.
- [7] A. J. Pertzborn, G. Nellis, and S. Klein, "Research on Ground Source Heat Pump Design," *Int. Refrig. Air Cond. Conf.*, 2010.
- [8] S. K. Wang, *Handbook of Air Conditioning and Refrigeration*, 2nd ed. McGraw-Hill, 2000.
- [9] A. G. Heat, H. Geothermal, and H. Pumps, "Guide to Geothermal Heat Pumps."
- [10] F. Busato, R. Lazzarin, and M. Noro, "Ground or solar source heat pump systems for space heating : Which is better ? Energetic assessment based on a case history," *Energy Build.*, vol. 102, pp. 347–356, 2015.
- [11] A. D. Chiasson, "Advances in Modeling of Ground-Source Heat Advances in Modeling of Ground-Source Heat," no. December 1999, p. 155, 1992.
- [12] G. Sonnemann and M. Schuhmacher, *LIFE-CYCLE AND RISK ASSESSMENT FOR INDUSTRIAL Library of Congress Cataloging-in-Publication Data* .
- [13] International Organization for Standardization, "ISO 14040-Environmental management - Life Cycle Assessment - Principles and Framework," *Int. Organ. Stand.*, vol. 3, p. 20, 2006.
- [14] Marry Ann Cunanan, "Life Cycle Assessment:Principals & Practise," US enviornmental Protection Agency, Ohio, 2006.
- [15] U. De Lleida, L. C. Analysis, and L. C. Impact, "An overview on Life Cycle Impact Assessment (LCIA) methodologies : State of the art," 2011.



- [16] J. W. Lund, "Design of Closed-Loop Geothermal Heat Exchangers in the U . S .," *Europe*, pp. 1–13, 2001.
- [17] L. Xiang-li, R. Zhi-yong, and D. Lin, "An investigation on life-cycle energy consumption and carbon emissions of building space heating and cooling systems," *Renew. Energy*, vol. 84, pp. 124–129, 2015.
- [18] H. Arat and O. Arslan, "Optimization of district heating system aided by geothermal heat pump : A novel multistage with multilevel ANN modelling," *Appl. Therm. Eng.*, vol. 111, pp. 608–623, 2017.
- [19] B. Huang and V. Mauerhofer, "Life cycle sustainability assessment of ground source heat pump in Shanghai , China," *J. Clean. Prod.*, vol. 119, pp. 207–214, 2016.
- [20] S. Lasvaux *et al.*, "Towards guidance values for the environmental performance of buildings : application to the statistical analysis of 40 low-energy single family houses ' LCA in France," *Int J Life Cycle Assess*, pp. 657–674, 2017.
- [21] C. N. Din *et al.*, "Comparison between hourly simulation and bin-method for the seasonal performance evaluation of electric air-source heat pumps for heating," pp. 255–262, 2014.
- [22] A. A. Safa, A. S. Fung, and R. Kumar, "Performance of two-stage variable capacity air source heat pump : Field performance results and TRNSYS simulation," *Energy Build.*, vol. 94, pp. 80–90, 2015.
- [23] A. S. Vieira, R. A. Stewart, and C. D. Beal, "Air source heat pump water heaters in residential buildings in Australia: Identification of key performance parameters," *Energy Build.*, vol. 91, pp. 148–162, 2015.
- [24] Z. Liu, W. Xu, X. Zhai, C. Qian, and X. Chen, "Feasibility and performance study of the hybrid ground-source heat pump system for one office building in Chinese heating dominated areas," *Renew. Energy*, vol. 101, pp. 1131–1140, 2017.
- [25] "Climate & Weather Averages in Murree, Pakistan." [Online]. Available: <https://www.timeanddate.com/weather/pakistan/murree/climate>. [Accessed: 31-Jan-2018].
- [26] S. Ellis, D. M. Taylor, and K. R. Masood, "Soil formation and erosion in the Murree Hills, northeast Pakistan," *Catena*, vol. 22, no. 1, pp. 69–78, 1994.
- [27] The International Standards Organisation, "Environmental management — Life cycle assessment — Requirements and guidelines," *Iso 14044*, vol. 2006, no. 7, pp. 652–668, 2006.
- [28] B. Greening and A. Azapagic, "Domestic heat pumps: Life cycle environmental impacts and potential implications for the UK," *Energy*, vol. 39, no. 1, pp. 205–217, 2012.



Experimental Investigation on Effect of YSZ Coated Piston Crown on the Performance of a Petrol Engine

*Hafiz Liaqat Ali, Muhammad Tahir Hassan, Farrukh Arsalan Siddiqui, Syed Asad Raza Gardezi, Muhammad Farooq Zaman, Muhammad Sanwal and Muhammad Jaon Haider

Department of Mechanical Engineering, University College of Engineering & Technology, BZU Multan, Pakistan

*Corresponding Author: Email: liaqatali@bzu.edu.pk

Abstract:

In an internal combustion (IC) engine only one third of fuel's energy is used as power output while two-third of the energy is discarded to the atmosphere through combustion chamber walls, exhaust valves, cylinder liners, cylinder head and through piston crown. The core objective of this study is to reduce this energy loss through the piston crown. In this regard ceramic thermal barrier coating (TBC) is used to drop energy loss as well as fuel consumption which will eventually enhance the thermal efficiency of an IC engine. It is an experimental investigation of a single cylinder, spark ignition (SI) engine to analyze the effect of ceramic TBC on its performance. The piston crown was layered through Yttria Stabilized Zirconia (YSZ) as top coat and NiCrAl as bond coat by using the Plasma Spray Technique (PST). YSZ ceramic was used for TBC because of its appropriate physical properties such as low thermal conductivity, maximum Poisson ratio, high coefficient of thermal expansion and stable phase structure against high temperature. The results were obtained on the baseline engine and Low Heat Rejection engine (LHR) which was layered with thickness of 300 μm . The results reflect that the Indicated Thermal Efficiency (ITE) of the LHR engine was improved by 5-10% over the conventional engine and Volumetric Efficiency (VE) and Specific Fuel Consumption (SFC) were reduced by 3-9% and 2-4% respectively. The Exhaust Gas Temperature (EGT) of ceramic coated engine was increased up to 31 $^{\circ}\text{C}$ over the uncoated engine. The findings are applicable for optimized performance of the IC Engine at bench and commercial scales.

Keywords: Petrol Engine; Thermal barrier coating (TBC); Yttria Stabilized Zirconia (YSZ); Low Heat Rejection (LHR) Engine

1. Introduction and background

Engine is a major part of automotive industry and plays a significant role in transport and agricultural industry. The increasing fuel demand along with the limited resources of fossil fuels and heat losses in engine requires an improved insulation system to minimize thermal losses and to enhance its efficiency. Many researchers worked on engine material to improve engine performance, they introduced metallic coatings which are sustainable under high temperature and pressure. Now trend is to enhance engine performance and ability using advanced material and better cooling system with different operating conditions. Introduction of ceramic coatings has brought a revolution in automobiles industry [1]. Fig. 1 displays the energy balance between a conventional and ceramic coated diesel engine.

Many researchers used metallic coating technique that is sustainable under high temperature and pressure for the improvement in engine performance. Recently, using advanced materials and better cooling systems with different operating conditions has become an interesting and effective trend of research for the enhancement of engine performance. Ceramic coating is one of the most emerging and revolutionary area of research in the automobile industry. Literature shows

that these techniques improve various engine's parameters

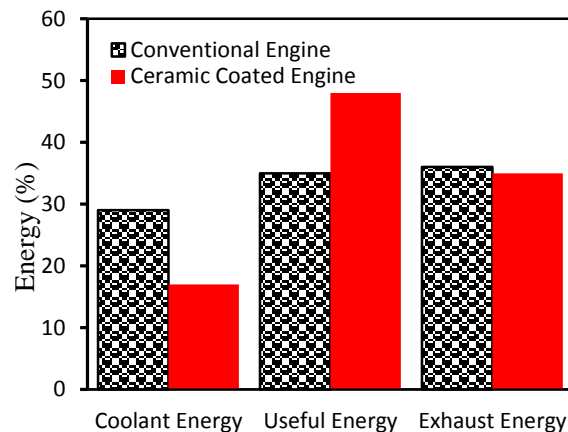


Figure 1: Conventional and ceramic coated diesel engine energy balance diagram [2].

such as fuel utilization and brake thermal efficiency (BTE) whereas reducing exhaust emissions [3]. Yttria stabilized zirconia (YSZ) on piston head provided insulation and helped in attaining adiabatic condition. In an investigation by Assanis et al. [4], it was concluded that for 1 mm thick coating, BTE was enhanced by 6% but for 0.5 mm coating BTE increased up to 10% compared with conventional



engine. Exhaust gas temperature (EGT) was enhanced by 10°C for 1 mm coating compared with 0.5 mm coated engine and baseline engine. VE decreased as the ceramic coating is increased. In an experimental study by Suresh Kumar Rupangudi et al. [5], the piston of a diesel engine was layered with Titanium dioxide by atmospheric PST. Results reflected that Brake specific fuel consumption (BSFC) decreased, BTE increased up to 3% and ITE improved by 3% with respect to conventional engine. Mechanical efficiency (ME) of coated piston is increased by 2% when estimated with baseline engine.

Experiments were carried out with different loads, velocity and injection timing for both coated and baseline engine. It was concluded that piston head coating was more efficient than the cylinder crown coating in developing thermal efficiency (TE), brake power (BP), indicated power (IP) and VE. Piston head coated engine had less fuel consumption than baseline engine [6]. Effect of TBC was investigated on the execution, combustion as well as exhaust emission characteristics compared with conventional engine. Thermally insulated piston had high TE, ME and BP compared with baseline engine. Test results showed that BTE was increased with ZrO₂-Al₂O₃ coated piston compared with uncoated piston engine [7]. Experimental examination of the influence of TBC on spark ignition engine was investigated. Piston, liner, head, ports and valves were used in TBC coated engines. Results showed an increase in 18% BP and 10% reduction in SFC. Moreover, ceramic coated engine did not produce any knock in the engine [8].

The performance analysis and emission of TBC engine with YSZ coating in combustion chamber was studied by Gosai et al. [9] and compared with baseline engine. Results show that BSFC is decreased while TE is increased. In a similar study by Büyükkaya et al. performed experimental analysis by using a 6-cylinder DI turbocharged diesel engine. Piston crown was layered with 0.150 mm of NiCrAl as a bond coat and 0.350 mm of MgZrO₃ as a top coat. The outcome showed a 1-8% reduction in BSFC, 65 °C rise in EGT, for the LHR engine with turbocharger over baseline engine [10].

The thermal barrier coating of Al₂O₃-TiO₂ and ZrO₂-Y₂O₃ with NiCrAl bond coat affected the temperature and stress distribution on the piston crown. Increased temperature because of the coated surface increased engine performance by approximately 8% [11]. ZrO₂-Y₂O₃ coating increases the engine performance, reduces pollution and rises fatigue life of the engine [12]. The thin coating of ceramic material to the aluminum alloy piston reduces the thermal waste of energy and increases efficiency. TBC of ceramic decreases consumption around 4.12%, increases BTE up to 12% while SFC decreases around 2.65% along with substantial decrease in emissions [13,14]. Having

an open literature review, it is revealed that coating of ceramic materials on engines decreases SFC, increases TE and improve emission characteristics. Many researchers [15,16,17] works on the diesel engine to reduce the heat losses, while on a gasoline engine still much work is to be done.

This is an experimental study carried out on a 4-stroke, overhead valve (OHV), inclined cylinder with 25 degrees, horizontal shaft, single cylinder, petrol engine using a coating of YSZ to reduce heat losses, to increase thermal efficiency and to minimize harmful exhaust gases compared to the conventional engine.

2. Coating material

Zirconium dioxide (Zirconia, ZrO₂) with 8% by weight of Yttrium Oxide (Y₂O₃) which known as YSZ which was used as TBC material in this study. The properties of YSZ and NiCrAl are specified in Table 1 below.

Table 1: Properties of YSZ and NiCrAl [18, 26].

Properties	YSZ	NiCrAl
Density (g/cm ³)	6.40	7.87
Thermal expansion 10 ⁻⁶ (1/°C)	11	12
Modulus of Elasticity (GPa)	40	90
Hardness (GPa)	14	3.11
Poisson's Ratio	0.30	0.27
Thermal Conductivity (W/mk)	2.10-2.20	16.10
Melting Point (°C)	2800	1400
Specific heat (J/ kg°C)	545	764

Furthermore, ZrO₂ can be found in three crystalline forms such as cubic, tetragonal and monolithic. The stable temperature for monolithic is about 1170 °C and for tetragonal it is about 2379 °C whereas for cubic temperature it is above 2379 °C. Zirconia stabilized with yttria (Y₂O₃) provides the finest and improved properties than zirconia through Mg (OH)₂ and CaO. Zirconia naturally occurs in monoclinic crystalline form. Zirconia dioxide is the ceramic material which adopts monoclinic structure at room temperature and changes to tetragonal and cubic at high temperature. Due to change in crystal structure from monoclinic to cubic volume changes, and are highly stressed when cooled from high temperature due to which cracks are developed. The tetragonal and cubic forms are stabilized when zirconia reacts with other oxides. Zirconia is always useful in stabilized state. On heating zirconia, it goes to a new state. If some amount of yttria is added, it goes back to the original form. Melting point of Yttria is about 2410 °C. Yttria cannot be melted easily and is stable at room temperature.



3. Coating process

Thermal coating techniques are of different types such as physical vapor deposition method, Plasma spray method, chemical deposition method and plasma arc method. Herein plasma spray technique (PST) was used for coating the piston crown. Plasma spray coating is a method in which heated molten materials are sprayed onto the surface. The coating materials, their thicknesses and specifications of Plasma spray coating are shown in the Table 2 and Table 3, respectively. The core objective in PST was to create a thin layer that has great shield over additional uncovered surfaces. PST schematic diagram is shown in Fig. 2.

The coated piston produced by this technique is shown along with conventional piston in the Fig. 3.

Table 2: Thickness of sprayed coatings

Coating process	Plasma spray Technique (PST)
Top coat TBC material	YSZ
Top coat thickness	200 μm
Bond coat material	NiCrAl
Bond coat thickness	100 μm

Table 3: Specifications of Plasma spray coating

Coating parameters	Specifications
Thermal spray gun type	3 MB plasma spray gun
Spraying distance (in)	3 to 5
Nozzle type	GH
Pressure of hydrogen gas (PSI)	45-50
Organ gas pressure (PSI)	100–110
Hydrogen flow rate (LPM)	10–20
Organ gas flow rate (LPM)	85–95
Powder feed rate (g/min)	40–45

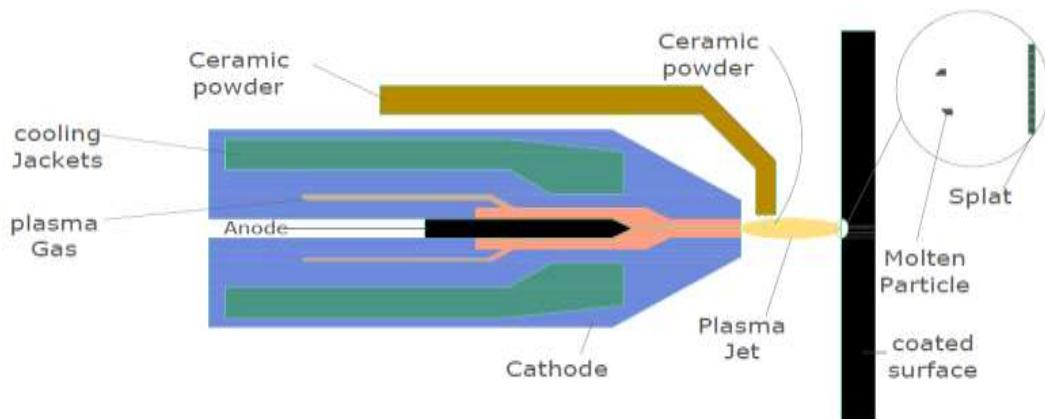


Figure 2: Plasm Spray Technique (PST)



Figure 3: Illustration of (a) YSZ coated piston (b) and Conventional piston



4. Experimental setup and procedure

In this experiment a single-cylinder, OHV petrol engine was used with a bore of 68 mm and stroke length 45 mm. The engine is studied at 3.5 kW (4.8 HP) and 3600 r/min. Other parameters of the engine are revealed in Table 4 below. A dynamometer was used to monitor the power output. Engine set-up shown in Fig. 4 was established to measure the various parameters such as cooling water temperature, engine speed, air and EGT, fuel consumption and load etc. For the process in the experiment, the engine was kept on 3600 (r/min) with the coated and uncoated piston.

Performance analysis was carried out on the engine using uncoated and coated piston with various speeds then placed at a fixed load. Experiments were performed at four levels of speed such as 2000, 2500, 3000 and 3500 r/min and various parameters such as air fuel ratio, mechanical efficiency (ME), BSFC, ITE, EGT and break thermal efficiency (BTE) were noted for all four levels of speed. Results obtained through these experiments were analyzed carefully and various graphs were plotted among engine's performance parameters to highlight the difference.

Table 4: Engine characteristics

Compression Ratio	9.0:1
Dimension (H x W x L) mm	346 x 362 x 312
Displacement (cm ³)	163
Starter	Recoil
Dry Weight (Kg)	15.1
Maximum net torque Nm (kgfm) / (rev/min)	10.3 (1.05) / 2500
Continued rated Power kW (H.P) / (rev/min)	2.5 (3.4) / 3000
KW (H.P) / (rev/min)	2.9 (3.9) / 3600
Fuel Tank Capacity (Liter)	3.1
Engine Type	Four-stroke single cylinder OVH petrol ENG.
Net Power KW (H.P) / (rev/min)	3.6 (.8) / 3600
Bore x Stroke (mm)	68 x 45
Engine Oil Capacity (Liter)	0.6

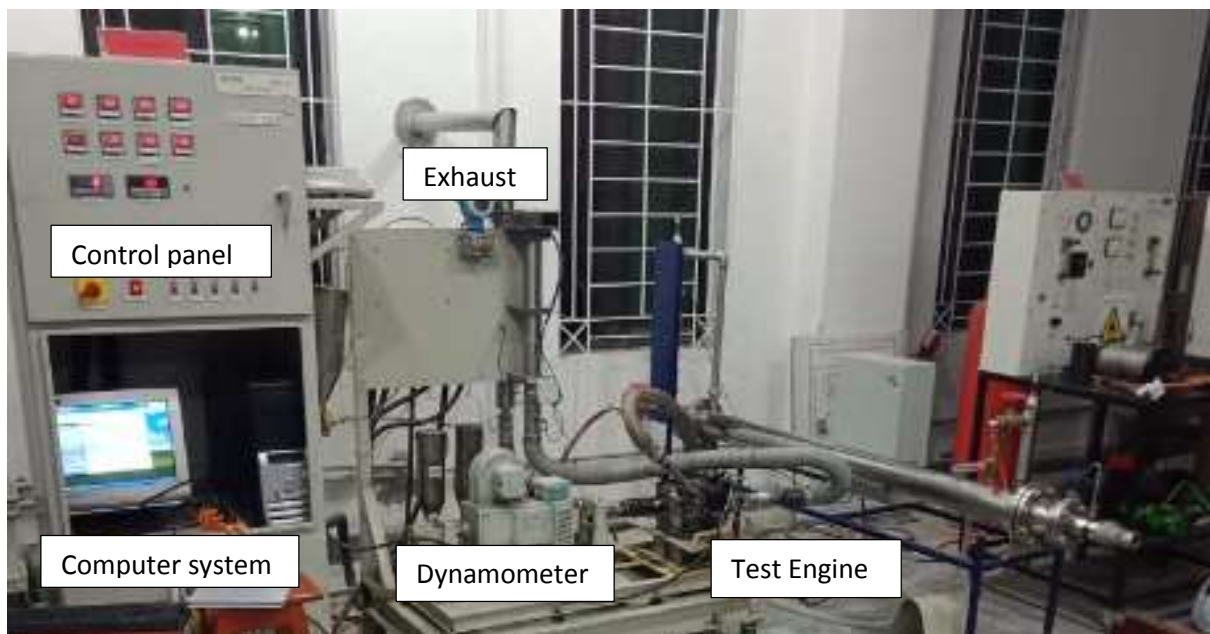


Figure 4: Engine Test Bed (MODEL: THO3)



5. Results and discussion

5.1 Brake specific fuel consumption

The BSFC is a quantity of fuel required to produce one watt of power. It was measured from the amount of fuel consumed to the power generated at output shaft. A comparison of BSFC for conventional and modified engine is revealed in Fig. 5. Results reflect that the BSFC of both uncoated and modified engine decreases with the increase in brake power however, its value is less in the case of modified engine (having TBC of the Yttria-Stabilized Zirconia) than the conventional engine (without coating). The BSFC was improved 2-4% in LHR engine over the conventional engine. It is because of the reduction in heat loss, temperature and heat energy is increased in the combustion chamber of coated engine. Due to high temperatures, an improved combustion process takes place in the chamber that reduces fuel combustion and harmful exhaust gases. The results obtained were similar to another investigation with different coating materials by Ali et al. [19] and Sivakumar et al. [20] improved BSFC by up to 9.1% and 28.29%, respectively.

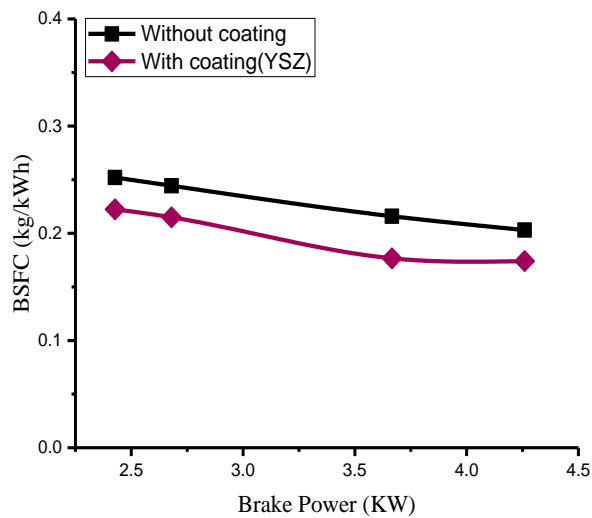


Figure 5: Comparison of Brake power with BSFC

5.2 Brake thermal efficiency

It is a ratio of power generated at the shaft to the fuel energy consumed per second. The variations in results of BTE with different engine powers of the conventional engine and modified engine are given in Fig. 6. BTE of modified engine increases to 7.5% at 3000 r/min engine speed as compared to the typical engine due to the TBC of the Yttria Stabilized Zirconia on piston crown. This is because the zirconia coating of the piston head reduces heat loss due to which higher temperature is available in the chamber, which aids proper combustion and reduces fuel consumption.

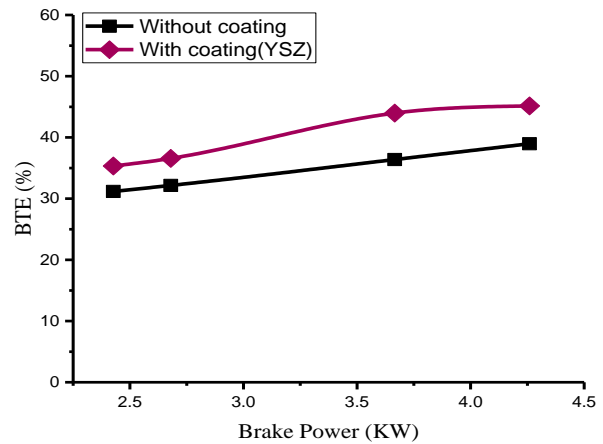


Figure 6: Comparison of Brake power with BTE

5.3 Indicated thermal efficiency

It is the ratio of the power generated due to the fuel combustion in the chamber to the energy of fuel released due to combustion. The results reported and variation of indicated thermal efficiency (ITE) for the conventional and LHR engine is shown in the Fig. 7. The ITE of the coated piston increases to 9.6% at 3000 r/min engine speed as compared to the typical engine. This is because the coated engine reduces heat loss and provides better combustion efficiency as compared with the uncoated engine. In addition, fuel consumption in the case of coated piston engine decreases due to better combustion.

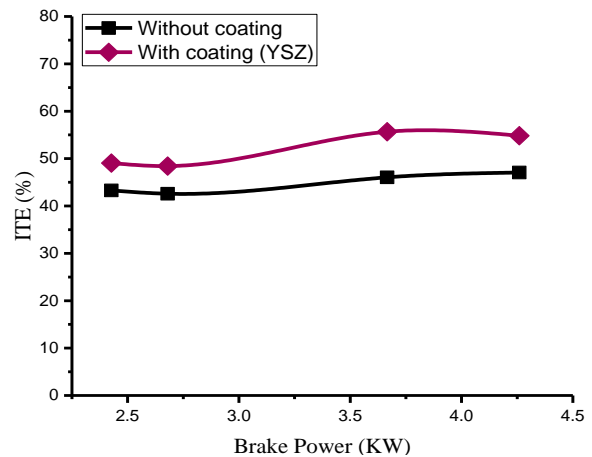


Figure 7: Comparison of Brake power with ITE

5.4 Mechanical efficiency

It is the ratio of break power to the indicated power. The dissimilarity in the mechanical efficiency (ME) at different output powers of coated and baseline engines are shown in Fig. 8. Mechanical efficiency rises with increase in the



brake power of engine. It may be noted that mechanical efficiency of modified engine is 4 to 10% above the conventional engine at various engine speed.

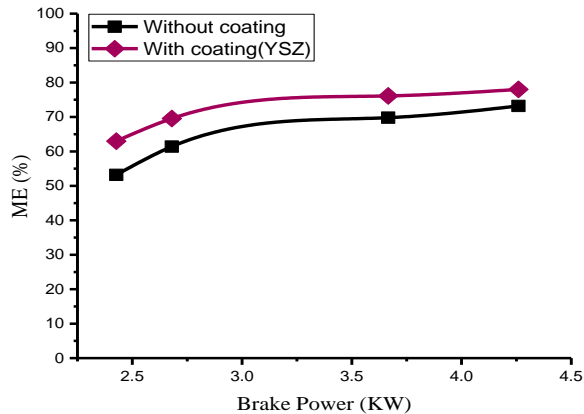


Figure 8: Comparison of Brake power with ME

5.5 Volumetric efficiency

It is ratio of the volume of mixture (air and fuel) which is introduced at normal air pressure to the swept volume. A comparison of volumetric efficiency (VE) of conventional and coated engine is shown in Fig. 9. It may be noted that VE decreases with the increase in engine power for both engines. Overall, VE is low (3 to 9%) in case of coated engine over the standard engine.

A low value of volumetric efficiency (VE) in case of coated engine indicates that less heat is lost and higher temperature is achieved in combustion chamber that reduces the density of inlet air. These results are comparable with some similar studies such as Chan et al. [21], Miyairi et al. [22] as well as Suzuki et al [23].

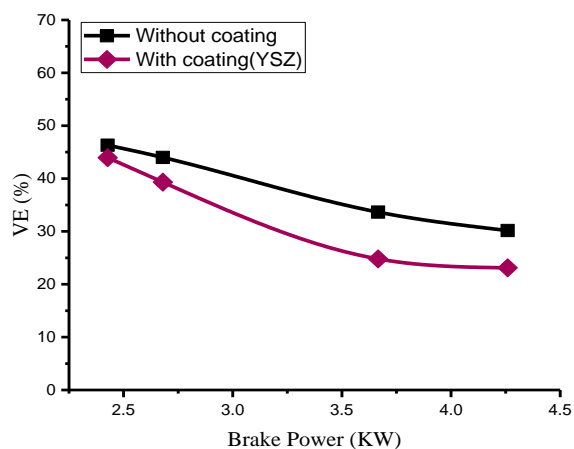


Figure 9: Comparison of Brake power with VE

5.6 Exhaust gas temperature

A Part of heat energy which is not converted to useful work is extracted from the combustion chamber as an exhaust of engine. Fig.10 shows a

comparison of exhaust gas temperature between coated and conventional engines at various power outputs. It can be seen that the EGT of LHR engine is 11-31°C higher than the conventional engine. This heat can further be recovered by using turbocharger to enhance engine's power and efficiency. Furthermore, similar results were found by the researchers such as Morel et al. [24], Sudhakar et al. [25].

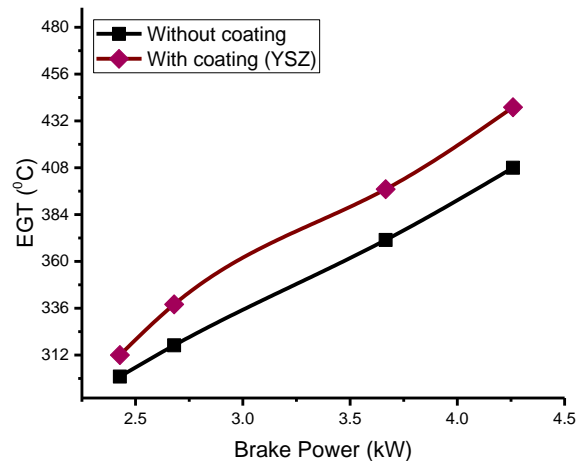


Figure 10: Comparison of Brake power with EGT

6. Conclusion

Conventional engine is modified with TBC of YSZ on piston crown by use of plasma spray coating method. We conclude the following results from this experimental investigation.

- i) Performance analysis of the modified engine is better as compared to uncoated engine. BSFC of coated engine is 2-4% lower than the uncoated engine.
- ii) TE of coated engine is improved by 4-8% as compared to uncoated engine.
- iii) The ITE of modified engine is increase up to 10% compared with the uncoated engine.
- iv) The ME of modified engine increases from 4% to 10%. Meanwhile the volumetric efficiency of modified engine is reduced by 3% to 9% compared with the uncoated engine.
- v) The EGT of the modified engine increased by 11-31 °C compared with uncoated engine and by the turbocharger we can use heat energy of exhaust again.
- vi) The heat energy released from the fuel in TBC engine is higher as associated to that of without coated engine.
- vii) Due to improved combustion process, exhaust of harmful gases is reduced in case of coated engine which can help to reduce carbon foot print and environmental degradation.



REFERENCES

- [1] Jaichandar, S., & Tamilporai, P. (2004, Mar.). The status of experimental investigations on low heat rejection engines (No. 2004-01-1453). SAE Technical Paper.
- [2] Büyükkaya, E. (1994). Ceramic Coating Application and Performance Analysis in a Diesel Engine. Post-Graduate Thesis.
- [3] Jaichandar, S., & Tamilporai, P. (2003, Mar.). Low heat rejection engines—an overview (No. 2003-01-0405). SAE Technical Paper.
- [4] Assanis, D. N., Wiese, K., Schwarz, E., & Bryzik, W. (1991, Feb.). The effects of ceramic coatings on diesel engine performance and exhaust emissions (No. 910460). SAE Technical Paper.
- [5] Rupangudi, S. K., Ramesh, C. S., Veerabhadhrappa, K., & Rohit V, R. (2014.). Study of Effect of Coating of Piston on the Performance of a Diesel Engine. SAE Int. Journal of Materials and Manufacturing, 7(3), 633-637.
- [6] Afify, E. M., & Klett, D. E. (1996, Feb.). The effect of selective insulation on the performance, combustion, and NO emissions of a DI diesel engine (No. 960505). SAE Technical Paper.
- [7] Ramu, P., & Saravanan, C. G. (2009, Apr.). Effect of ZrO₂-Al₂O₃ and SiC coating on diesel engine to study the combustion and emission characteristics (No. 2009-01-1435). SAE Technical Paper.
- [8] Assanis, D. N., & Mathur, T. (1990). The effect of thin ceramic coatings on spark-ignition engine performance. SAE Trans., 981-990.
- [9] Gosai, D. C., & Nagarsheth, H. J. (2014, Jan.). Performance and exhaust emission studies of an adiabatic engine with optimum cooling. Procedia Technology, 14, 413-421.
- [10] Büyükkaya, E., Engin, T., & Cerit, M. (2006, Jun.). Effects of thermal barrier coating on gas emissions and performance of a LHR engine with different injection timings and valve adjustments. Energy conversion and management, 47(9-10), 1298-1310.
- [11] Muthusamy, J., Venkadesan, G., & Krishnavel, U. (2016, Nov.). Experimental Investigation of Thermal Barrier (8ysz-Tio 2-Al₂O₃) Coated Piston Used in Direct Injection Compression Ignition Engine. Thermal Science, 20.
- [12] Chan, S. H., & Khor, K. A. (2000, Feb.). The effect of thermal barrier coated piston crown on engine characteristics. Journal of Materials Engineering and Performance, 9(1), 103-109.
- [13] Lin, C. Y., Chu, L. W., & Ker, M. D. (2012, Jan.). ESD protection design for 60-GHz LNA with inductor-triggered SCR in 65-nm CMOS process. IEEE Trans. on Microwave Theory and Techniques, 60(3), 714-723.
- [14] Modi, R. S., & Modi, M. A. IC Engine Performance Using Ceramic Coated Piston.
- [15] KR, V. K., & Sundareswaran, V. (2011, Oct.). The Effect of thermal barrier coatings on diesel engine performance of PZT loaded cyanate modified epoxy coated combustion chamber. JJMIE, 5(5).
- [16] Kamo, R., Mavinahally, N. S., Kamo, L., Bryzik, W., & Schwartz, E. E. (1999, Jan.). Injection characteristics that improve performance of ceramic coated diesel engines. SAE trans., 1476-1482.
- [17] Caputo, S., Millo, F., Cifali, G., & Pesce, F. C. (2017, Oct.). Numerical investigation on the effects of different thermal insulation strategies for a passenger car diesel engine. SAE Int. Journal of Engines, 10(4), 2154-2165.
- [18] Xu, H., & Guo, H. (Eds.). (2011). Thermal barrier coatings (pp. 193-197). Woodhead Pub Limited.
- [19] Ali, H. L., Li, F., Wang, Z., & Shuai, S. (2018, Sept.). Effect of Ceramic Coated Pistons on the Performance of a Compressed Natural Gas Engine. In IOP Conference Series: Materials Science and Engineering (Vol. 417, No. 1, p. 012021). IOP Publishing.
- [20] Sivakumar, G., & Kumar, S. S. (2014, Dec.). Investigation on effect of Yttria Stabilized Zirconia coated piston crown on performance and emission characteristics of a diesel engine. Alexandria engineering journal, 53(4), 787-794.
- [21] Chan, S. H., & Khor, K. A. (2000, Feb.). The effect of thermal barrier coated piston crown on engine characteristics. Journal of Materials Engineering and Performance, 9(1), 103-109.
- [22] Miyairi, Y., Matsuhisa, T., Ozawa, T., Oikawa, H., & Nakashima, N. (1989, Jan.). Selective heat insulation of combustion chamber walls for a DI diesel engine with monolithic ceramics. SAE Trans., 117-130.



- [23] Suzuki, T., Tsujita, M., Mori, Y., & Suzuki, T. (1986, Sept.). An observation of combustion phenomenon on heat insulated turbo-charged and inter-cooled DI diesel engines (No. 861187). SAE Technical Paper.
- [24] Morel, T., Keribar, R., Blumberg, P. N., & Fort, E. F. (1986, Jan.). Examination of key issues in low heat rejection engines. SAE trans., 398-414.
- [25] Kosaka, H., Wakisaka, Y., Nomura, Y., Hotta, Y., Koike, M., Nakakita, K., & Kawaguchi, A. (2013, May). Concept of “temperature swing heat insulation” in combustion chamber walls, and appropriate thermo-physical properties for heat insulation coat. SAE Int. Journal of Engines, 6(1), 142-149.
- [26] Buyukkaya, E., & Cerit, M. (2007, Nov.). Thermal analysis of a ceramic coating diesel engine piston using 3-D finite element method. Surface and coatings technology, 202(2), 398-402.



Experimental Investigation of Passive Cooling Techniques to Reduce Cooling Load in Residential Building in Lahore

Muhammad Asim¹, Ahmed Zohaib Zaidi¹, Muhammad Sajid Kamran¹

¹ – Department of Mechanical Engineering, University of Engineering & Technology, Lahore

Corresponding author's email: ahmedzz1993@gmail.com

Abstract:

Existing residential buildings consume considerable amount of energy specifically during summers in developing countries like Pakistan. This is mainly due to excessive usage of air-conditioners to maintain thermal comfort. However, there exists considerable potential to reduce building cooling load using passive cooling techniques. The study aims to reduce cooling load and improving thermal comfort of test room in existing residential building. Heat gain components of test room were analyzed to take an informed decision for reduction in cooling load. South wall partitioning, natural ventilation, green net and paint on roof were applied to test room in May and June. Hygro-thermal data, recorded using HTC-2A digital meters, was compared with adjacent room taken as reference. Test room cooling load was reduced by 24.4 %. Drop in average temperature and average relative humidity difference between the test and reference room was found to be 0.8 °C and 1.9% respectively. Passive cooling techniques not only reduce cooling load but also improve thermal comfort in existing residential buildings. An initial retrofitting cost may be more beneficial in the long run both in terms of finance and comfort.

Keywords: Passive cooling, shading, building retrofitting, cooling load reduction, thermal comfort

1. Introduction

Human activities, particularly energy use, are causing climate change on Earth. This alarming situation has brought 196 global parties together, The Paris Agreement, with the aim to develop sustainable development goals [1] and Nationally Determined Contributions [2]. According to [3], the developing world is being severely affected by climate change. With four major energy-consuming sectors i.e. industry, transport, agriculture and buildings [4], the building sector is the second largest energy-consuming sector [5]. Yet it is still the biggest sector where there is abundant potential to achieve energy efficiency [6]. And for societal needs, improvements in efficient use of energy must be sought [7].

Considering this state of affairs, [8] propose environmental quality management (EQM) passive measures in order to reduce building energy consumption. [9] report that about 50% of building energy is consumed by HVAC systems. For a single dwelling, air-conditioning requires more than 50% of electricity in developing countries [10]. [11], based on simulation results, proves that reduction in

both initial and operating cost of HVAC can be achieved through passive means. According to [12], existing buildings may be retrofitted to deliver economic and environmental benefits.

In this regard, [13] achieved up to 49% of energy savings for skin-load dominated building i.e. residential buildings using optimization. [14] and [15] point out that thermal insulation applied on the inside is more energy efficient as compared to the outside. Moreover, [16] conclude that tiled roof construction with a reflective top surface provides the best thermal performance during summer. [17] studies different walls and roof modifications and report significant differences in hygro-thermal performance of these structures. [18] varied wall and roof insulation thickness, window orientation and window to wall ratio and showed that peak cooling load could be reduced by 50%. [19] analyzed the effect of different types of insulations, green infrastructures and phase change materials in 22 building prototypes in order to quantify energy savings in Spain. [20] reviewed passive solar technologies and asserted that passive strategies though added small cost initially but were more cost effective in the long run. [21] simulated twenty



building models in different climatic conditions and found that fly ash brick with grey glass window might reduce cooling load in buildings in India. [22] explored monthly cooling potential of five different cities in India using evaporative cooling, nocturnal radiative cooling and PCM strategies. Significant energy efficiency can be achieved using passive cooling techniques according to their research. [23] found that solar reflectance of cool mortars is significantly higher as compared to existing ones in old building envelopes. They led to 3.6% reduction in cooling demand which can be further improved to 8.6% by using cool clay tiles. [24] also investigated passive cooling features including air cavities in the structures, high thermal mass and induced ventilation to improve thermal comfort in eight buildings in India and found them comfortable most of the time. [25] tested natural ventilation, shading, double glazing and green roofing techniques for energy efficiency and reported that total annual energy consumption of a residential building may be reduced by up to 23.6% in Dubai.

However, literature has rarely included, to our knowledge, studies regarding the variations in cooling load due to the application of different passive techniques. Furthermore, a combined effect of two or more passive techniques is seldom evaluated which may reduce the cooling load even more [19]. Also, research work pertaining to passive cooling methods requires further investigation particularly for South Asian region.

In the effort to mitigate the energy crises and/or sweltering weather conditions, we conducted experiments based on cooling load potential on two rooms located on the first floor of a residential building. The present work aims to reduce cooling load of a residential building which could, in turn, reduce electricity expenses. It also intends to improve thermal comfort for people living in hot and humid climate

2. Methodology

A two-story residential building was selected. It was located in Falcon Complex, Gulberg-3, Lahore, Pakistan. The building was a semi-detached house. The area occupied by the building was 3812 square feet. Exposed area of East, West, North and South walls of the building were 640, 560, 620 and 620 square feet respectively. The front side of the building was facing towards the South, the rear side was facing northwards.

2.1 Characteristics of selected building

Two of its rooms on the first floor were part of current study. One room was selected as test room in which different passive cooling techniques were applied. The room adjacent to it was made reference in which no changes were made. Temperature, humidity and cooling load for both rooms were analyzed. Table no. 1 shows the particulars of both of these rooms.

Table 1. Physical characteristics of rooms

Building	Test room operational characteristics	Reference room operational characteristics
Location	Westside	Eastside
Type	Bedroom	Living room
Dimensions	14' x 12'6"	14' x 18'3"
Average ceiling height	10'	10'
Operation	24 hours	24 hours
Floor area	175 sq. ft.	255.5 sq. ft.
Doors	1.5 in. plywood (U = 0.47)	1.5 in. plywood (U = 0.47)
Wall material/layers	9-inch thick double brick (U = 0.384)	9-inch thick double brick (U = 0.384)
Net area of East wall	0 (partitioned)	124.5 sq. ft.
Net area of West wall	136.5 sq. ft.	0 (partitioned)
Net area of North wall	0 (partitioned)	0 (partitioned)
Net area of South wall	92 sq. ft.	148 sq. ft.
Glass	5 mm single glass	5 mm single glass



GLF value of glass	EWNS: 47,47,23,31	EWNS: 47,47,23,31
Gross area of windows	30 sq. ft.	42 sq. ft.
Shades of windows	Yes	Yes
Lighting wattage	97 W	97 W
Equipment wattage	145 W	660 W
Occupancy	3 people	6 people
Roof material	5-inch RCC (U = 0.213)	5-inch RCC (U = 0.213)
Area of roof	175 sq. ft.	255.5 sq. ft.
Infiltration rate	0.7 ACH	0.7 ACH
Floor type	Above conditioned space	Above conditioned space
Wall partitions	East and North walls	West and North walls

2.2 Cooling load calculations

Cooling load calculations were performed according to the procedure given in [26]. In this procedure, only sensible load were calculated. Allowance was added at the end for latent loads. Lighting loads were considered negligible.

1. Cooling load for walls, roof, ceiling and floor were calculated using equation (1)

$$Q = U \times A \times CLTD \quad (1)$$

Where

Q is sensible cooling load (BTU/hr.), U is overall heat transfer coefficient (BTU/hr-ft²-F), A is area (ft²) and CLTD is cooling load temperature difference (F).

2. Heat gain through windows was calculated using equation (2)

$$Q = A \times GLF \quad (2)$$

where

Q is sensible cooling load due to heat gain through glass (BTU/hr.), A is area of glass (ft²), and GLF is glass load factor (BTU/hr-ft²). GLF accounts for both radiation and conduction through glass.

3. Cooling load due to people and appliances

The sensible heat gain per person was assumed to be an average of 255 BTU/hr. If the number of people is not known prior to calculations, it is assumed to be twice the number of bedrooms.

4. Infiltration and ventilation

The quantity of air infiltrating into the room was found using the equation (3)

$$CFM = ACH \times \frac{V}{60} \quad (3)$$

where

CFM is air infiltration rate into room (cubic feet per minute), ACH is number of air changes per hour and V is the volume of room (ft³).

If the infiltration air is expected to be less than 0.5 ACH, indoor air quality may be unsatisfactory. In this case, some outdoor air has to be introduced into the room.

Subsequently, heat gain due to air infiltration into the room was found using equation (4).

$$Q = 1.1 \times CFM \times TC \quad (4)$$

where

Q is sensible cooling load due to infiltrating air (BTU/hr.) and TC is temperature change between inside and outdoor air (F).

5. Room, building and air conditioning equipment load

The sensible cooling load for each room (RSCL) was found by adding up each of the room's cooling load components described above.

Building sensible cooling load (BSCL), as shown in equation (5), was found by adding sensible cooling load for each room.



$$BSCL = \sum_{\text{room}} RSCL \quad (5)$$

Equipment sensible cooling load (ESCL) was found by adding building sensible cooling load and the duct heat gains and leakages as shown in equation (6). Duct gain is 5% of the RSCL and, likewise, leakage was 5% of RSCL.

$$ESCL = BSCL + \text{duct heat gains} + \text{duct leakage} \quad (6)$$

Latent Cooling Load was found by multiplying BSCL with an approximate latent factor (LF) which was assumed to be 1.25 in our case.

The equipment total load, based on which air conditioning unit is selected, was found from the following equation (7)

$$Q_T = Q_S \times LF \quad (7)$$

where

Q_T is equipment total cooling load (BTU/hr.), Q_S is equipment sensible cooling load (BTU/hr.) and LF is latent factor.

Table 2. Cooling load in two rooms

Heat gain through	Reference room cooling load (BTU/hr.)	Test room cooling load initially (BTU/hr.)	Test room cooling load finally (BTU/hr.)
East wall	1084.4	0	0
West wall	0	1188.9	969.15
North wall	0	0	0
South wall	928.138	576.4	0
Roof	2612.23	1789.2	528.99
Floor	1658.2	1135.7	1135.75
East partition	0	523.1	523.123
West partition	523.123	0	0
North partition	682.167	467.5	467.553
South partition	0	0	352.581
Door	177.66	177.66	177.66
East window	660	0	0
West window	0	0	690
North window	0	0	0
South window	1140	1140	0
Infiltration	393.47	269.5	269.5
People	1350	675	675
Appliances	1800	900	900
Room sensible cooling load	13009.4	8843.65	6929.31
Equipment cooling load	17887.9	12160	9197.8

3. Experimental setup

Two HTC-2A sensors which display dry bulb temperature and relative humidity along with time were placed both in test and reference rooms. Indoor temperature range of the sensors is -10°C to $+50^{\circ}\text{C}$, temperature measurement accuracy is $\pm 1^{\circ}\text{C}$ and temperature resolution is $\pm 0.1^{\circ}\text{C}$. Likewise,

humidity range is 10% to 99% RH, humidity measuring accuracy is $\pm 5\%$ RH and humidity resolution is 1%. One of these sensors was placed in the test room near West wall at 2 feet height and the other was placed near West wall of reference room at the same height.



Data was recorded for both the rooms at 8:00, 12:00, 15:00 and 20:00 hours for a period of four days for each techniques in the months of May and June. Figure No. 1 shows picture of the sensor used. The residential building façade and rooftop before applying passive measures are shown in figure 2.



Figure 1. Temperature sensor



Figure 2. Residential building; (a) façade, b) roof top

For cooling load reduction, the south wall of the test room which was previously exposed to sun, as shown in figure 3, was partitioned with the construction of a new room. It is 12 x 17 ft² in dimensions. Window on the South wall was replaced with the one on the West wall. The second technique that was applied on the test room was shading on the

roof using green netting of 95% shade as shown in figure 3b. The third technique was application of white enamel paint on the roof surface to make the surface more reflective as shown in figure 3c. Temperature humidity data was recorded with natural ventilation during the night through the West wall window.



Figure 3. Experimental setup; (a) South wall shading, b) Green netting on roof, c) enamel paint on roof



4. Results and Discussions

Existing residential buildings have been constructed without keeping in mind the lifetime energy consumption cost of the building in hot and humid climatic conditions. Both theoretical and experimental results provide sufficient evidence that cooling load can be reduced and human thermal comfort can be improved by using passive cooling strategies.

4.1 Cooling load reduction

Building cooling load is the sum of all latent and sensible sub loads which have been calculated and depicted in Table no. 2. The South

wall which was exposed to direct sunlight has been shaded by constructing a room in front of it. This shading of exposed wall resulted in a reduction in cooling load by 224 Btu/hr. Similarly, single glass South window if replaced with window at West wall having double glass may reduce the cooling load by 440 Btu/hr. Moreover, the addition of shading at the roof may reduce cooling load by 1260 Btu/hr. due to reduction in cooling load temperature difference. Previously, total equipment cooling load for the test room was 12160 Btu/hr. and after application of proposed changes, it is reduced to 9197.8 Btu/hr. This amounts to a 24.4% reduction of the test room cooling load. Figure 4 shows bar chart of reduction in cooling load for test room.

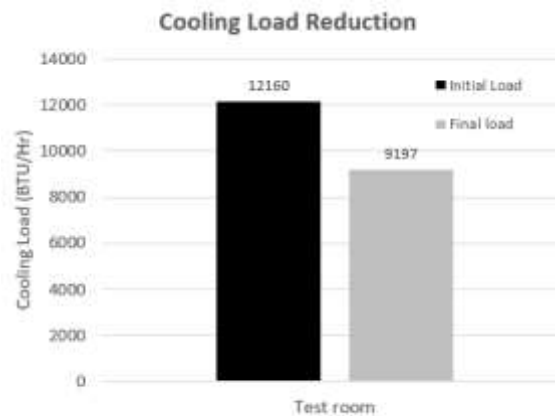


Figure 4. Cooling load reduction before and after passive cooling techniques

4.2 Temperature and humidity

Human thermal comfort can be improved using passive cooling strategies. The temperature and humidity data of both the test and reference rooms was collected before applying any changes to the test room. It revealed that the test room was 0.1 °C warmer and 1.1% more humid on average as compared to the reference room. Same data was gathered and analyzed after application of each passive measure. After shading the South wall, test room was observed to be 0.3 °C cooler and 3% more humid as compared to the reference room. South

wall shading with natural ventilation resulted in 0.57 °C drop in temperature and 2.3% hike in humidity of test room as compared to the reference room. With South wall shaded and green netting (95% shade) on the rooftop, average temperature and humidity change were recorded to be 0.35 °C and 1.6% more humid respectively. With South wall shaded and white enamel paint applied on the roof's surface rendered the temperature of the test room drop by 0.8 °C and humidity rise by 1.9% in comparison with the reference room. More details have been provided in Table no. 3.



Table 3. Temperature and humidity difference

No.	Passive cooling methods	Maximum temperature difference °C	Average temperature difference °C	Maximum humidity difference %	Average humidity difference %
1	Without changes	-0.3	-0.1	-6%	-1.1%
2	With south wall shaded	0.5	0.32	-6%	-3.4%
3	With south wall shaded and natural ventilation through west wall	1.1	0.57	-5%	-2.3%
5	South wall shading, green netting & natural ventilation	-0.6	-0.35	-5%	-1.6%
9	South wall shaded, ventilation, enamel paint and natural ventilation	1.5	0.8	-5%	-1.9%

Negative sign indicates that test room is warmer and more humid as compared to the reference room.

5. Conclusions

The cooling load of existing residential buildings which are located in regions having hot and humid climate can be significantly reduced. It may in turn reduce electricity consumption. Moreover, human thermal comfort can be improved by a few passive cooling strategies without investing additional energy.

REFERENCES

- [1] UNFCCC. The Paris Agreement. 2015 May 2019]; Available from: <https://unfccc.int/process-and-meetings/the-paris-agreement/what-is-the-paris-agreement>.
- [2] UNFCCC. Nationally Determined Contributions (NDCs). 2015 May 2019]; Available from: <https://unfccc.int/process/the-paris-agreement/nationally-determined-contributions/ndc-registry>.
- [3] UNFCCC, UN Climate Change Annual Report 2017.
- [4] Andrysek, J., et al., Mobility function of a prosthetic knee joint with an automatic stance phase lock. *Prosthetics and orthotics international*, 2011. 35(2): p. 163-170.
- [5] Brunner, S., AR5 Climate Change 2014: Mitigation of Climate Change. 2014, IPCC.
- [6] IEA, World Energy Investment 2019. 2019, International Energy Agency.
- [7] Thorsell, T. and M. Bomberg, Integrated Methodology for Evaluation of Energy Performance of Building Enclosures: Part II — Examples of Application to Residential Walls. *Journal of Building Physics*, 2008. 32(1): p. 49-65.
- [8] Bomberg, M., M. Furtak, and D. Yarbrough, Buildings with environmental quality management: Part 1: Designing multifunctional construction materials. *Journal of Building Physics*, 2017. 41(3): p. 193-208.
- [9] Pérez-Lombard, L., J. Ortiz, and C. Pout, A review on buildings energy consumption information. *Energy and Buildings*, 2008. 40(3): p. 394-398.
- [10] Hamdy, M., A. Hasan, and K. Siren, Applying a multi-objective optimization approach for Design of low-emission cost-effective dwellings. *Building and Environment*, 2011. 46(1): p. 109-123.
- [11] Al-Homoud, M.S., The Effectiveness of Thermal Insulation in Different Types of Buildings in Hot Climates. *Journal of Thermal Envelope and Building Science*, 2004. 27(3): p. 235-247.
- [12] IPCC. AR5 Climate Change 2014. 2014 May 2019]; Available from: https://www.ipcc.ch/site/assets/uploads/2018/02/ipcc_wg3_ar5_technical-summary.pdf.



- [13] Al-Homoud, M.S., A Systematic Approach for the Thermal Design Optimization of Building Envelopes. *Journal of Building Physics*, 2005. 29(2): p. 95-119.
- [14] Al-Sanea, S.A. and M.F. Zedan, Effect of Insulation Location on Initial Transient Thermal Response of Building Walls. *Journal of Thermal Envelope and Building Science*, 2001. 24(4): p. 275-300.
- [15] Zhang, X. and F. Cheng, Comparative assessment of external and internal thermal insulation for energy conservation of intermittently air-conditioned buildings. *Journal of Building Physics*, 2018. 42(4): p. 568-584.
- [16] De With, G., N. Cherry, and J. Haig, Thermal Benefits of Tiled Roofs with Above-sheathing Ventilation. *Journal of Building Physics*, 2009. 33(2): p. 171-194.
- [17] Radon, J., et al., Experimental and theoretical study on hygrothermal long-term performance of outer assemblies in lightweight passive house. *Journal of Building Physics*, 2017. 41(4): p. 299-320.
- [18] Sharma, L., K. Kishan Lal, and D. Rakshit, Evaluation of impact of passive design measures with energy saving potential through estimation of shading control for visual comfort. *Journal of Building Physics*, 2017. 42(3): p. 220-238.
- [19] De Gracia, A., et al., Experimental set-up for testing active and passive systems for energy savings in buildings – Lessons learnt. *Renewable and Sustainable Energy Reviews*, 2018. 82: p. 1014-1026.
- [20] Chan, H.-Y., S.B. Riffat, and J. Zhu, Review of passive solar heating and cooling technologies. *Renewable and Sustainable Energy Reviews*, 2010. 14(2): p. 781-789.
- [21] Kirankumar, G., S. Saboor, and T.P. Ashok Babu, Investigation of Different Window and Wall Materials for Solar Passive Building Design. *Procedia Technology*, 2016. 24: p. 523-530.
- [22] Panchabikesan, K., K. Vellaisamy, and V. Ramalingam, Passive cooling potential in buildings under various climatic conditions in India. *Renewable and Sustainable Energy Reviews*, 2017. 78: p. 1236-1252.
- [23] Rosso, F., et al., Smart cool mortar for passive cooling of historical and existing buildings: experimental analysis and dynamic simulation. *Energy Procedia*, 2017. 134: p. 536-544.
- [24] Leo Samuel, D.G., et al., Thermal comfort in traditional buildings composed of local and modern construction materials. *International Journal of Sustainable Built Environment*, 2017. 6(2): p. 463-475.
- [25] Taleb, H.M., Using passive cooling strategies to improve thermal performance and reduce energy consumption of residential buildings in U.A.E. buildings. *Frontiers of Architectural Research*, 2014. 3(2): p. 154-165.
- [26] Pita, E.G., *Air Conditioning Principles and Systems: An Energy Approach*. 4 ed. 2001, New Jersey: Prentice Hill. 544.



Deformation of neutrally buoyant droplet with clean and particle covered interface under an electric field

Muhammad Salman Abbasi^{1,2*}, Haroon Farooq³ and Hassan Ali¹

1- Mechanical Engineering Department RCET, University of Engineering and Technology, Lahore, Pakistan

2- School of Mechanical Engineering, Sungkyunkwan University, Suwon, Gyeonggi-do 16419, South Korea

3- Electrical Engineering Department RCET, University of Engineering and Technology, Lahore, Pakistan

*Email: m.salman@uet.edu.pk

Abstract

Electrohydrodynamic deformation of single leaky dielectric droplet with clean and particle covered interface, immersed in another immiscible leaky dielectric liquid is explored. Here, the electrohydrodynamic deformation have been demonstrated numerically and experimentally under moderate and strong electric fields. Numerical method involves the coupling of Navier Stokes equation with level set equation and governing equations of leaky dielectric theory. The simulation model developed for clean interface droplet is then extended to a capsule model for densely particle covered droplet. Experiments were conducted using various combination of immiscible oils and electric field strengths $\sim 10^5$ V/m are applied using high voltage supplier and images obtained were processed using image processing tool (MATLAB). Results showed that particle free droplet can undergo prolate (deformation along the applied electric field) or oblate deformation (deformation that is perpendicular to the electric field direction) of the droplet interface. A good agreement was observed with simulation and experimental results. The developed simulation model was then extended by considering a particle mono layer surrounding the droplet interface. It was then tested to predict the deformation of particle covered droplets under a range of electric capillary number (ratio of electric to capillary stresses acting at the interface). The results obtained were then compared with theory and experimental findings. It is shown that the proposed simulation model can serve as a tool to predict the deformation/distortion of both the particle free and the densely particle covered droplets.

Keywords: Electro-hydrodynamics, leaky dielectric theory, Particle covered droplet, Simulation

1. Introduction

The electric field effects on droplets and emulsions provide a versatile avenue for exploring the underlying fluid dynamic mechanisms and instabilities [1-8]. It has wide applications ranging from targeted drug delivery [9], particle synthesis [10], electrohydrodynamic atomization [11], particle manipulation [12] and producing unique colloidal assemblies [13]. The major stimulating force in these processes is the electric shear stresses that are generated due to the build-up of free electric charges at the interfaces that produce the

interfacial flows [2].

Taylor *et al.* [6] found the deformation of particle free leaky dielectric droplet immersed in another leaky di-electric liquid and this theory is now famously called leaky di-electric theory. Later, experimental investigations showed that the deformation predicted by Taylor matched well in low deformation regime but deviated at larger deformations. Different authors reported that the deformations predicted by numerical simulations matched well with the experimental results even at larger deformations [2, 3, 14]. Taylor theory is also

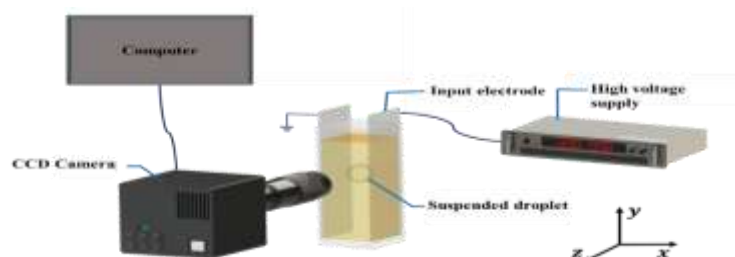


Figure 1. Experimental setup used for measuring droplet distortion under an applied electric field strength



invalid for the case of droplets with particles entrapped at the interface [3].

Ha and Yang [15] developed a theoretical model with in the small deformation limit with an aim to predict the deformation of the densely particle covered droplets. A recent model [16] has shown that the droplet coated with particles behaves like a capsule i.e. it is enclosed by an elastic membrane. Though, the theoretical models available can predict the deformation of either particle free or particle covered droplets, separately. They still are not valid for both the cases, simultaneously. Therefore, a versatile model is required that is applicable to both the particle free and the densely particle covered droplets.

In this paper, a numerical simulation model is developed as a consolidated model that can predict the deformation of both the particle free and the particle covered droplets. Here, we used COMSOL Multiphysics for the implementation of various equations governing the problem. We also perform experiments using the basic experimental facility and compared the experimental results with the theory and the simulation results.

2. Materials and methods

2.1 Experimental

The experimental setup for observing the droplet deformation is as shown in Fig. 2 and consists of a cuvette cell (acrylic with dimensions: 20.7mm × 20.7mm × 50mm) whose opposite sides were embedded with copper electrodes (0.35 mm thickness) and was filled with a leaky dielectric liquid (Liquid 1: Silicone oil or Castor oil). A single droplet (Liquid 2: Castor oil or silicone oil) was dispensed in the cuvette by using the micro-pipette. The high DC voltage was applied by the high voltage facility [1]. The dynamics of the droplet under electric field were observed using camera [1] and videos were recorded at 30 frame per second (fps). The recorded videos were then processed to get high quality images. An in-house code was developed on the plate-form of MATLAB for the image processing and the subsequent data acquisition. The obtained data was then represented in the form of the deformation (D) of the droplet. The physical properties of the liquids used in the study are summarized in Table. 1.

Table 1. Physical properties of tested liquids

Liquid	Mass Density (kg/m ³)	Dynamic Viscosity (Pa.s)	Electrical Conductivity (S/m)	Dielectric Constant
Castor Oil	961	0.78	3e -11	4.7
Silicone Oil	970	0.97	0.87e-13	3.2

2.2 Simulation Method

The electrohydrodynamic problem was solved using finite element method by coupling Navier Stokes equation with the governing equations of the electro-quasi-statics' theory. The interface

between the two liquids was tracked by using conservative form of the level set equation.

Leaky dielectric fluids behave differently as compared to dielectric fluids under high electric field. A small amount of charge is accumulated at the interface which is not present in perfect dielectrics. The deformation D is calculated as



$$D = \frac{P - W}{P + W} \quad (1)$$

where P and W are the dimensions of the distorted droplet in the parallel and

perpendicular directions with respect to the applied electric field.

The electric capillary number is defined as the ratio of electric to capillary stress, acting on the interface of the droplet of radius r .

$$Ca_e = \varepsilon_2 E_o^2 r / \gamma \quad (2)$$

ε_2 is the liquid permittivity at the outside of droplet and E_o is the external electric field. γ is the surface tension between liquid-liquid interface. The 2-phase laminar flow problem under high electric field is formulated by coupling the Navier-Stokes equation with level set equation and governing equation of electric field.

$$\rho \left(\frac{\partial \vec{v}}{\partial t} + (\vec{v} \cdot \nabla) \vec{v} \right) = -\nabla p + \mu \nabla^2 \vec{v} + \vec{f}_{st} + \vec{f}_e \quad (3)$$

$$\nabla \cdot \vec{v} = 0 \quad (4)$$

$$\frac{\partial \phi}{\partial t} + \nabla \cdot (\vec{v} \phi) = \alpha \nabla \cdot \left(\psi \nabla \phi - \phi (1 - \phi) \frac{\nabla \phi}{|\nabla \phi|} \right) \quad (5)$$

The governing equation of the electric field for leaky dielectric fluid is given as

$$\nabla \cdot (\sigma \vec{E}) = 0 \quad (6)$$

where the electric field is calculated as

$$\vec{E} = -\nabla V \quad (7)$$

and V is voltage applied to electrode.

The properties across the interface change as

$$\rho = \rho_2 + \phi(\rho_2 - \rho_1) \quad (8)$$

$$\mu = \mu_2 + \phi(\mu_2 - \mu_1) \quad (9)$$

The total electric force is given as

$$F_e = \nabla \cdot \sigma_M \quad (10)$$

where $\sigma_M = \varepsilon(\vec{E}\vec{E} - E^2 I/2)$ is the Maxwell stress tensor.

Taylor's theory [6] for predicting small deformations of leaky dielectric drops is given as

$$D = \frac{9}{16} Ca_e \left[\frac{R^2 - 2S + 1}{(2+R)^2} + \frac{3}{5} \frac{R - S}{(2+R)^2} \left(\frac{2+3\Gamma}{1+\Gamma} \right) \right] \quad (11)$$

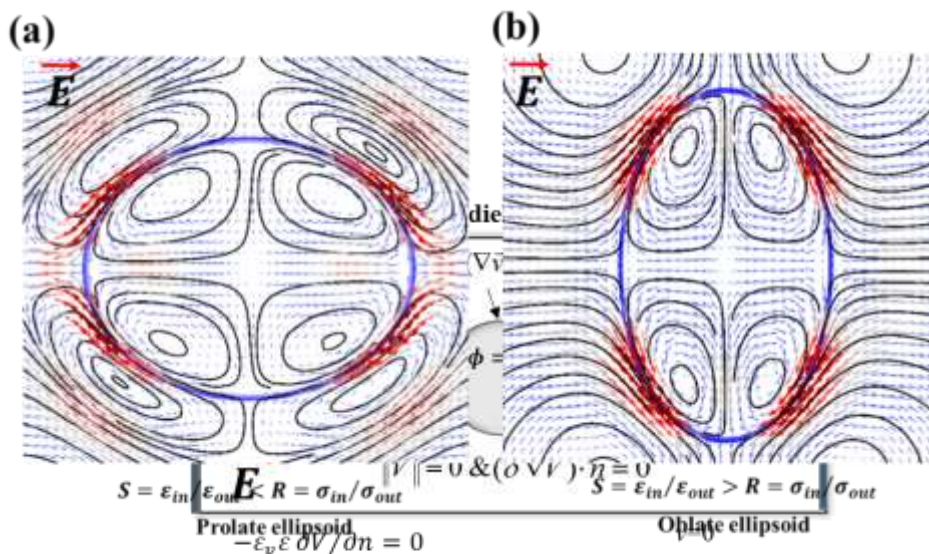


Figure 3. Simulation results pertaining to the distortion of particle free droplet under an applied electric field. (a) the droplet deforms prolate; the flow is from the equator towards the droplet poles. (b) the droplet deforms oblate; the flow is from the poles towards the droplet equator. Here, S is the permittivity ratio, whereas R is the conductivity ratio between the droplet and the ambient liquid.

subscript "i" and "j" are used to denote the liquid component at the inside and outside of the droplet, respectively.

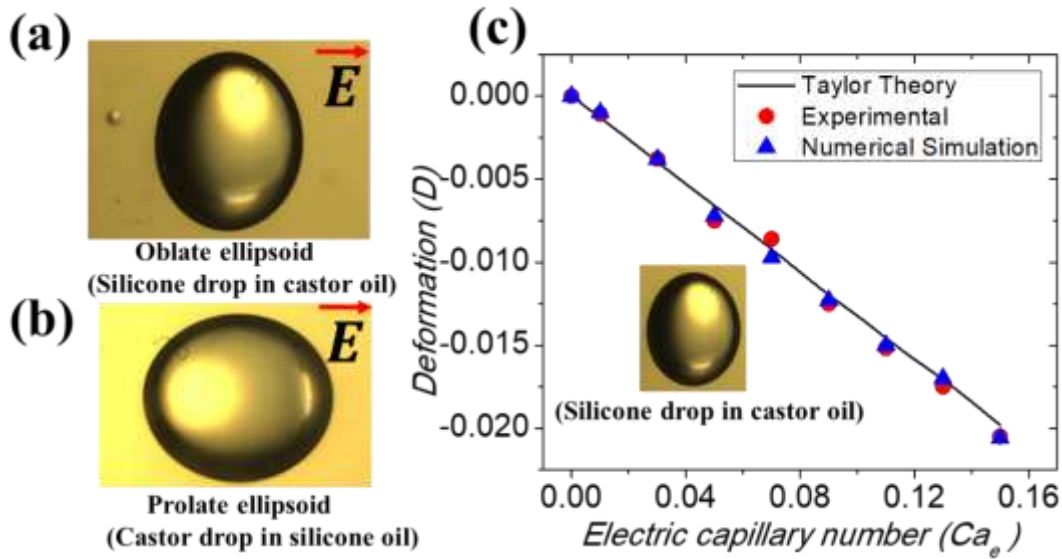


Figure 4. Experimental results for the particle free droplet deformation. (a) Oblate deformation, (b) Prolate deformation, (c) Comparison with simulation results and Taylor's theory [6].

where $\Gamma = \mu_1/\mu_2$ is the viscosity ratio.

The particle monolayer developed at the droplet interface can be modelled as an incompressible material, called the capsule model and the deformation is given as [17]

$$D_{eq} = Ca_s \left\{ \frac{27[(1+R)^2 - 4/S]}{32(2+R)^2} \right\} \quad (12)$$

3. Results and Discussions

In this paper, the dynamics of neutrally buoyant droplet suspended in immiscible liquid subjected to electric field is studied. A simulation model was developed to understand the deformation dynamics of the particle free droplet, which was then extended to predict the deformation of a particle covered droplet. Experiments were performed at different electric capillary number using silicone oil and castor oil. The simulation results were then validated with the experimental findings.

A particle free droplet was observed to show prolate (deformation that is aligned to the direction of applied electric field) or oblate deformation (deformation that was perpendicular to the electric field direction) under electric field. This is as shown in Fig. 3. When the permittivity ratio (S) was less than the conductivity ratio (R), the droplet

deformed prolate. In this case the flow was directed from the equator towards to the poles. Conversely, when the $S > R$, the droplet deformed oblate and the flow direction was now reversed i.e. from the poles towards the equator of the droplet.

Experiments were performed with different immiscible liquids (refer to Table. 1) as shown in Fig. 4. It can be seen from Fig. 4(a) and Fig. 4(b) that a silicone droplet in a castor oil shows oblate deformation whereas a castor droplet in silicone oil shows the prolate deformation. We continued to perform experiments on silicone droplet in castor oil under a wide range of electric capillary number and measured the deformation using MATLAB image processing tool. The results were plotted as shown in Fig.4(c). The extent of droplet deformation increased with an increase in the electric capillary number. Experimental results were then compared with the simulation results and the Taylor's theory. A good agreement was obtained.

It was reported by Ouriemi *et.al.* [17] that if a particle covered droplet or an armoured droplet with $S > R$ is subjected to electric field, it behaves differently compared with a particle free droplet. Here, only the droplets with high particle concentrations were considered. For such droplets, a mono layer of closely packed particles covered the entire interface. Such capsules deform more compared to the droplets with clean interfaces under electric field. This is due to the

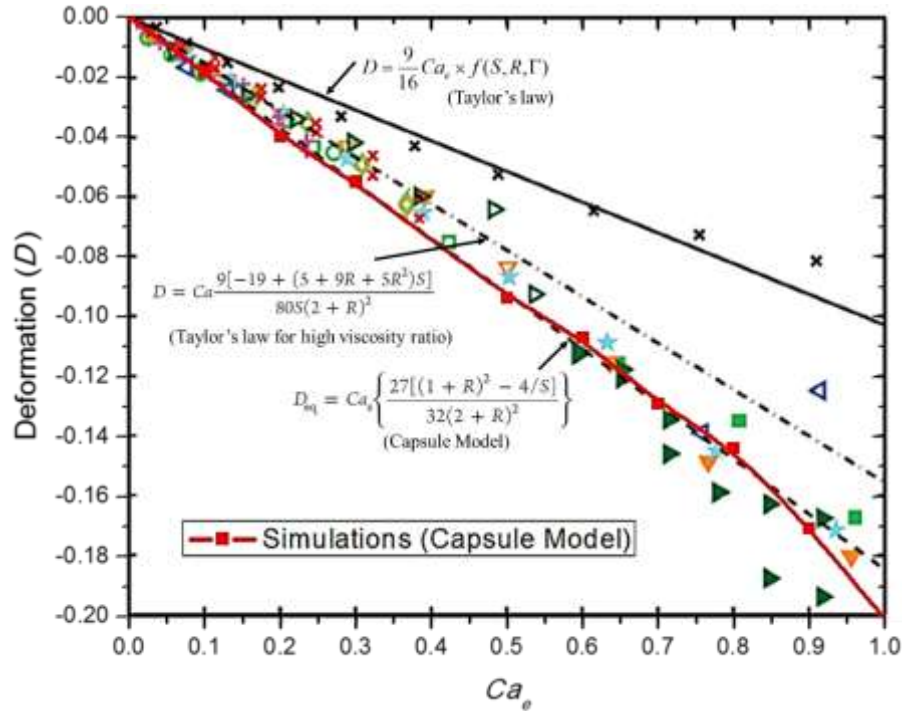


Figure 5. Simulation results pertain to the deformation of particle covered droplet under an electric field. The results are compared against experimental findings and capsule model. The black solid, dot dashed, and dashed lines represent the theoretical models. The experimental data are adopted from [17] for particle free (cross symbols) and densely particle covered droplets (other symbols). The red line with filled rectangular symbols is obtained from our simulation model.

interface/surface modification owing to the entrapped particles. The deformation of such droplets can no longer be predicted by the Taylor's theory. This effect is incorporated in the simulation model in terms of change in the electric capillary number such as

$$Ca_s = \frac{\epsilon_2 E_0^2 r}{G} = Ca_e \frac{\gamma}{G} \quad (13)$$

where, G is the elastic shear Modulus. The value of G for densely packed particle at the emulsion interface can be taken as 1.43 times the interfacial tension (γ) for a particle free interface [18].

We performed extensive simulations to predict the deformation of particle covered droplet using simulation model at different electric capillary number and results are plotted in Fig. 5. The simulation results are also compared with capsule model and experimental results for densely particle covered droplet from another researcher [17]. A good agreement can also be observed between our simulation model and capsule model. Thus, our simulation model predicted the deformation for both the cases effectively.

4. Conclusions

Here, we have developed a simulation model to predict the dynamics of neutrally buoyant particle free droplet that was then extended to particle covered droplet under an electric field. Experiments were performed using a cuvette cell and high electric field was generated. Deformation is measured by an in-house code developed using MATLAB image processing tool. The experimental results for particle free and particle covered droplets were then compared with the theory and our simulation results. Our simulation model emerged as a consolidated model and effectively predicted the deformation for both the cases.

Acknowledgments

The authors thank Professor. Jinkee Lee for his guidance and support.

Conflict of interest

The authors declare no conflict of interest.



REFERENCES

- [1] Abbasi, M.S., et al., *Multimodal breakup of a double emulsion droplet under an electric field*. *Soft matter*, 2019. **15**(10): p. 2292-2300.
- [2] Abbasi, M.S., et al., *Electrohydrodynamic behavior and interface instability of double emulsion droplets under high electric field*. *Journal of Electrostatics*, 2017. **85**: p. 11-22.
- [3] Abbasi, M.S., et al., *Mono-emulsion droplet stretching under direct current electric field*. *Soft matter*, 2019. **15**(11): p. 2328-2335.
- [4] Melcher, J. and G. Taylor, *Electrohydrodynamics: a review of the role of interfacial shear stresses*. *Annual review of fluid mechanics*, 1969. **1**(1): p. 111-146.
- [5] Taylor, G., *Disintegration of water drops in an electric field*. *Proceedings of the Royal Society of London. Series A. Mathematical and Physical Sciences*, 1964. **280**(1382): p. 383-397.
- [6] Taylor, G., *Studies in electrohydrodynamics. I. The circulation produced in a drop by electrical field*. *Proceedings of the Royal Society of London. Series A. Mathematical and Physical Sciences*, 1966. **291**(1425): p. 159-166.
- [7] Tomar, G., et al., *Influence of electric field on saturated film boiling*. *Physics of Fluids*, 2009. **21**(3): p. 032107.
- [8] Torza, S., R. Cox, and S. Mason, *Electrohydrodynamic deformation and bursts of liquid drops*. *Phil. Trans. R. Soc. Lond. A*, 1971. **269**(1198): p. 295-319.
- [9] Lakshmanan, S., et al., *Physical energy for drug delivery; poration, concentration and activation*. *Advanced Drug Delivery Reviews*, 2014. **71**: p. 98-114.
- [10] Chen, C.-H., et al., *Janus Particles Templated from Double Emulsion Droplets Generated Using Microfluidics*. *Langmuir*, 2009. **25**(8): p. 4320-4323.
- [11] Xie, J., et al., *Electrohydrodynamic atomization: A two-decade effort to produce and process micro-/nanoparticulate materials*. *Chemical engineering science*, 2015. **125**: p. 32-57.
- [12] Ahn, K., et al., *Dielectrophoretic manipulation of drops for high-speed microfluidic sorting devices*. *Applied Physics Letters*, 2006. **88**(2): p. 024104.
- [13] Dommersnes, P., et al., *Active structuring of colloidal armour on liquid drops*. *Nature communications*, 2013. **4**: p. 2066.
- [14] Benteitis, N. and S. Krause, *Droplet deformation in dc electric fields: the extended leaky dielectric model*. *Langmuir*, 2005. **21**(14): p. 6194-6209.
- [15] Ha, J.-W. and S.-M. Yang, *Electrohydrodynamic effects on the deformation and orientation of a liquid capsule in a linear flow*. *Physics of Fluids*, 2000. **12**(7): p. 1671-1684.
- [16] Erni, P., et al., *Interfacial viscoelasticity controls buckling, wrinkling and arrest in emulsion drops undergoing mass transfer*. *Soft Matter*, 2012. **8**(26): p. 6958-6967.
- [17] Ouriemi, M. and P.M. Vlahovska, *Electrohydrodynamic deformation and rotation of a particle-coated drop*. *Langmuir*, 2015. **31**(23): p. 6298-6305.
- [18] Vella, D., P. Aussillous, and L. Mahadevan, *Elasticity of an interfacial particle raft*. *EPL (Europhysics Letters)*, 2004. **68**(2): p. 212.



Effect of CTAB on stability, thermal conductivity and viscosity of 2D h-BN based nanofluids

Syed Nadeem Abbas Shah^{1,2*}, Syed Shahabuddin^{3*} and Mohd Faizul Mohd Sabri^{1*}

¹ Department of Mechanical Engineering, University of Malaya, 50603, Kuala Lumpur Malaysia

² Department of Mechanical Engineering, University of Engineering and Technology Lahore, Pakistan

³ Department of Science, School of Technology, Pandit Deendayal Petroleum University Gujarat, India

*Correspondence: engr.nadeem@uet.edu.pk; syedshahab.hyd@gmail.com; faizul@um.edu.my

Abstract

The shelf stability of nanofluids is crucial for thermal conductivity and viscosity. Surfactant are widely used as dispersing agents to improve the stability of nanofluids. Herein, the h-BN/EG based nanofluids (NFs) were prepared using two-step method at a constant volume concentration of h-BN (0.05%) and by varying the CTAB surfactant concentration from 0.05% to 1%. The nanofluids were characterized with various techniques such as zeta-sizer, particle size analyzer, thermal property analyzer and viscometer. The zeta potential values appeared between -8.8 to 12.8 mV which did not cross the threshold limit (± 30 mV) when CTAB was added to pristine NF. Consequently, the mean particle size was observed in a range of 699-1551.5 nm, reflecting the agglomeration state of colloids. However, the polydispersity index (PDI) was promising, sufficiently below 30%. Thus, the colloids could be regarded as monodisperse. In addition, the maximum thermal conductivity of NFs achieved to be 3.4% at 40°C. While the viscosity of NFs reduced up to 6.6% with minimum CTAB volume fraction (0.05 %) at an ambient temperature. The findings of present work clearly revealed the nascent of CTAB surfactant to lower the viscosity of nanofluids which could be exploited to mitigate the flow resistance with less pumping input requirements. Conversely, less stable state of NFs showed minor increment in thermal conductivity. Thus a trade-off exist among stability, thermal conductivity and viscosity due to integration of CTAB with h-BN/EG NFs.

Keywords: Zeta Potential; Particle size; Surfactant; Thermal conductivity; Viscosity.

1. Introduction

Recently, the heat transfer field has become an emerging area of research owing to growing needs of energy, miniaturizing of devices and sustainability requirements. Heat is a form of energy, generally it travels due to the temperature gradient between two bodies. Predominantly, the heat transport takes place with three modes such as conduction, convection, and radiations. Regarding convective heat transport, apart from the geometrical and boundary conditions variations of heat exchanging devices, the efficiency of flow thermal systems (FTSs) also depends on the flow and transport properties of heat transfer fluids (HTFs) [1].

Since the development of NFs, a new class of engineered HTFs, many scientists and engineers have shown keen interest to work on commercializing them. For instance, NFs have been integrated as coolant for thermal management of photovoltaics modules [2–6], advanced hypersonic aircrafts [7,8], polymer electrolyte membrane fuel cells [9], CPU cooling [10,11], very-large-scale integrated circuits [12] and electric vehicles battery pack cooling [13,14]. There are many commercial technologies which are primary stake holders to exploit the NFs potential, for example solar energy technologies to improve efficiency of solar collectors and receiver cavities [15,16], active solar distillation systems [17], NFs integrated steam power plants [18] and heat pipes for thermal management applications [13,19]. Recently combined heat and power (CHP) systems have also

shown substantial thermal efficiency improvement with NFs [20]. Thus the NFs have been widely studied and explored for heat transport and energy conversion processes.

As stated above, the NFs can tailor the energy conversion processes by improving heat transfer rates. However, the dispersed phase (NPs) within continuous phase (base fluid) can transform the flow behaviour as well as heat transport due to strong structured network formations as a results of co-particles and solid-liquid interactions. The co-particles interactions could also lead to coagulations which then causes flocculation and eventually phase out of the continuous phase of the two phase suspension. Therefore the remarkable thermal transport properties of NFs might deteriorate. Conversely, the dispersed phase may also give rise to the zero-shear viscosity (storage/low shear rate) leading to high pumping power (PP) to initiate the HTF flow. On the other hand, once the flow got maintained at desired rate, the NFs might have high apparent viscosity (high shear rate) as compared to corresponding base fluid. In both cases, the NFs would require higher PP which might decrease the FTSs efficiency and under extreme operational conditions the heat transport augmentation produced from NFs use might off-set.

As many studies have highlighted the increase in pressure drop due to incorporation of NFs. As a double-tube heat exchanger (HX), shot peened



double-tube HX, horizontal tube, plate HX and micro-channel heat sinks have demonstrated a great amount of pressure drop with NFs [10,21–24]. The pressure drop is a function of HTF viscosity, density, and Reynold's number (Re). Mainly such increment in pressure drop attribute to the enhancement in the apparent viscosity of NFs as compared to base fluid. However, density also becomes the crucial factor in determining the PP once the particles loading are very high such that they increase it substantially [10]. Whereas for small concentrations of particles loadings, the density of NFs remains practical constant. But in order to overcome the viscous effects of NFs, more flow rates and PP is desirable to maintain the flow conditions [25]. Thus, thermal conductivity improvement is not the sole decisive factor as far as FTS performance is concerned. Here it is noteworthy that the reduction in viscosity of HTF along with thermal conductivity improvement can significantly contribute to improve the FTSs overall performance. As, literature has not much focused on this aspect of the HTF which remained un-explored, yet.

In the literature the 2D materials have shown increment in thermal conductivity as well as improved antifriction capabilities. Among many, hexagonal boron nitride (h-BN) is receiving much consideration owing its astonishing mechanical, optical, thermal, antifriction, electronic, catalytic, and insulating (dielectric) properties [26]. Thus, the use of h-BN base nanofluids could also mitigate the rate of electrochemical corrosion in flow channels along with improved thermo-physical properties.

In view of aforementioned summary on NFs, to address the thermo-hydraulic challenges of NFs applications in terms of developing new NFs formulations, the present research have investigated the role of CTAB surfactant on stability, thermal conductivity and viscosity of h-BN/EG nanofluids.

The pristine h-BN nanofluids have been evaluated for stability with varying volume concentrations from 0.025-0.5% (in our previous work under production process). Among them, 0.05 vol% found to have maximum zeta potential (-34 mV) therefore, it was considered for further evaluation in the presence of CTAB.

2. Experimental

2.1 Materials

The 2D h-BN N70 nanoparticles (NPs) with an average particle size of 70nm, hexagonal crystal structure, chemical formula (hBN), coefficient of friction 0.15-0.7, thermal conductivity 33.5 (W/m.K), density 2.3 (g/cm³), purity 99% and white colour was purchased from lower friction (M.K Impex, Canada).

The cetyltrimethylammonium bromide (CTAB) with chemical formula (C₁₉H₄₂BrN), molecular weight 364.45 g/mol and density 0.5 (g/cm³) was purchased from Fisher scientific UK. Ethylene glycol (EG) with chemical formula (CH₂OH)₂, molecular weight 62.07 g/mol and density 1.11 (g/cm³) was purchased form Sigma Aldrich.

2.2 Nanofluids Preparation

Two-step scheme was followed to produce nanofluids. The calculated weight of nanoparticles (h-BN) and CTAB corresponding to desired volume concentration was dispersed into 50ml of ethylene glycol (EG). The volume concentration of h-BN was kept constant to 0.05% whereas CTAB varied (0.05%,0.5%,1%). To break aggregates the suspension was subjected to magnetic stirring for 15 minutes (40 °C, 250 rpm). Subsequently, to homogenize the colloidal dispersion bath sonication used for 90 minutes.

2.3 Nanofluids characterizations

The electrophoretic and dynamic light scattering techniques were used in order to estimate the stability and particle size distribution of NFs at 25°C, respectively, using litesizer500 (Anton Paar). To dilute the concentrated samples, supernatant liquid was utilized throughout the investigation. A table top centrifuge (Anton Paar) was used (5000rpm for 3minutes) to get supernatant from parent sample (s).

Thermal property analyzer (KD2, Decagon devices Inc., Pullman Washington, USA) was employed to record thermal conductivity data on NFs in a temperature of 25°C-50°C. Before taking measurements, the sample (s) were retained at targeted temperatures for 15 minutes to achieve thermal equilibrium.

The SV-10 sine wave vibro viscometer was employed to measure dynamic viscosity (measurement range 0.3-10000 mPa.s, A&D instruments ltd) at 25°C (±1°C) [27].

Three measurements of all tests were carried out and average value had been used for analysis. A view of experimental protocol employed to execute present work is shown in **Figure 1**.

Moreover, the KD2 showed error less than 2% for DIW and EG at targeted temperatures. While the viscometer calibration showed maximum error of ~3.2% for DIW.



Figure 1. A view of experimental setup

3 Results and Discussion

3.1 Zeta Potential and Particle Size Analysis

Figure 2 represents the variation of mean zeta potential and mean particle size with the volume concentration of CTAB surfactant. As can be observed, with addition of CTAB, firstly the zeta potential reduced from -34 mV to -8.8 mV at 0.05 vol% CTAB. Subsequently, by increasing the CTAB concentration up to 1 vol%, the inversion from negative to positive in mean zeta potential (-8.8 mV to 12.8 mV) was observed. Such inversion is possible due to positive charged hydrophilic head group of CTAB. So the increase in CTAB concentration neutralize the negative surface charge on h-BN and develop positive surface charge to produce steric hindrance. However, to consider well stable colloidal dispersions there must be sufficient surface charge on dispersed phase. Thus a universally accepted value of mean zeta potential is ± 30 mV that can keep colloids apart for longer time. But, in the present work, an interesting feature was observed as with CTAB addition zeta potential decreased as compared to

pristine NFs. Consequently, CTAB could not be used for long term dispersion of h-BN/EG NFs.

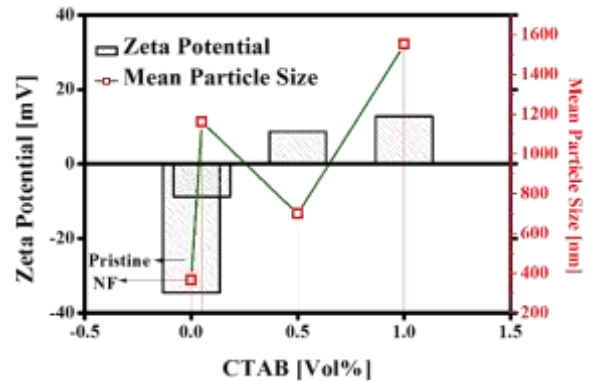


Figure 2 Zeta potential and mean particle size as a function of CTAB concentration

On the other hand, owing to the physical interactions among NPs and CTAB molecules, variation in particle size was obvious. As shown in Figure 2, the mean particles size of pristine NFs varied and maximum size was observed at 1 vol% of CTAB. Likewise to mean zeta potential, mean particle size also showed similar trend. Thus a promising correlation exist between these two parameters.

As the pristine NFs got zeta potential of ~ -34 mV with correspond mean particle size of ~ 365 nm. Comparing this with CTAB contained NFs, it could be postulated as the zeta potential decreased the mean particle size increased. The increased particle size attributed to the CTAB adsorption as well as agglomeration state.

3.2 Thermal Conductivity Analysis

Figure 3 shows the mean thermal conductivity of base fluid (EG) and NFs as a function of temperature (25°C - 50°C) and CTAB concentration (0.05-1 vol%). Interestingly, the thermal conductivity enhancement was not consistent with CTAB concentration. At a temperature of 25°C , NF with 0.05 vol% CTAB showed better enhancement on top of base fluid (EG). However, subsequent temperature sweep from 30°C - 40°C results of thermal conducted revealed the NF with 1 vol% was superior to other formulations. Here the results were deviating from stability evaluation. As at this particular CTAB concentration, the mean particle size was large. So the Brownian motion should be less effective compare to small size formulations. Thus to elucidate the exact reason for enhancement might need some fundamental study at molecular level. But the noteworthy point was that the stability analysis was carried out at 25°C . And it was expected that at 40°C for NF with 1 vol% of CTAB the large size agglomerates break-down into smaller leading to improved heat conduction in nano layering and due to Brownian motion [28].



However at 50°C, all the CTAB contained NFs thermal conductivity dropped down even below EG. Therefore, this temperature may be regarded as the critical limit beyond which the adsorbed CTAB molecules degrade and results in sedimentation (inset Figure 3).

Furthermore, in our previously accepted work, the pristine NF (0.05 vol %) have shown thermal conductivity enhancement in a range 0.26-3.67% (detail not given here). For comparison purpose, at a particular operating temperature of 40°C, the enhancement was ~3.4%. Whereas in the present work, the thermal conductivity enhancement was still ~3.4% even with 1 vol% CTAB addition as dispersant. So, as a results of these findings, it could be deduced that the CTAB has not much altered the thermal conductivity of corresponding pristine NF.

In addition, the trend of thermal conductivity was compared with our previous results. For pristine NF, the thermal conductivity was quite constant throughout the targeted temperatures range (25°C-50°C). But in the present work, with 1 vol% of CTAB, the thermal conductivity increased up to 40°C, subsequently an abrupt drop down appeared. So, here the best working temperature for 1 vol% CTAB was found to be 40°C.

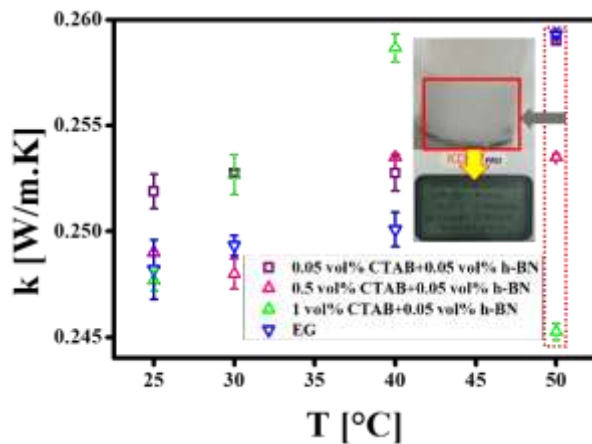


Figure 3 Thermal conductivity as a function of temperature and CTAB concentration.

3.3 Viscosity Analysis

The flow architecture of heat transfer fluids (HTF) is also a vital parameter which decides about momentum transfer and heat diffusion. Mainly to maintain the flow of HTF an external driving force is applied known as pumping power (PP). Therefore the analysis HTF viscosity could provide an up-front understanding about process design.

Figure 4 depicts the variation of viscosity as a function of CTAB concentration at ambient conditions (25±1°C). The mean viscosity of base fluid (EG) found to be more as compared to base fluid

combination with CTAB and NFs with CTAB. The decrease in the viscosity of CTAB contained base fluid and NFs could be attributed to interfacial tension lowering capability of surfactants. Due to decrease in the tension, the contact angle of NFs might also decrease which results in better surface contact/adhesion behaviour. Consequently, it can also improve the phase change heat transfer processes [29].

The maximum decrease in the viscosity was found to be ~6.7% for NF with 0.05 vol% CTAB when compared with base fluid (EG). Successively, by increasing CTAB concentration the reduction was observed to be around 6.1% and 4.6% for NF with 0.5 and 1 vol% CTAB. So it can be concluded, in case of CTAB contained NFs, the critical micelle concentration was 0.05 vol% CTAB. Therefore, any concentration of CTAB beyond 0.05% shall result in more resistance to flow as compared to former for stable colloids.

The possible mechanisms for such reduce viscosity could be assigned to lubrication effect of sheet like morphology of 2D h-BN as well as analogous micelles which reduced the contact among various fluid layers. Also, the h-BN possessed high surface due to sheet like morphology so attained high surface energy. The addition of CTAB reduced it to lower side which also could minimize the flow resistance leading to reduced viscosity. However, the detailed flow and storage behaviour of NFs could not be analysed owing to limitation of viscometer capabilities. Therefore, an extension of present work is still needed to employee advance rheometer to study in depth control shear flow, temperature sweep and storage behaviour.

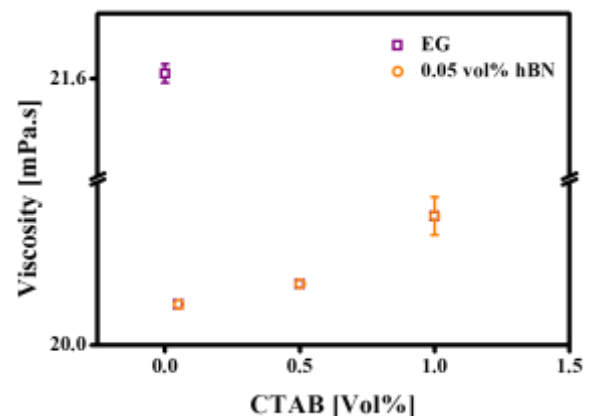


Figure 4 Viscosity of EG and NFs as a function of CTAB volume concentration.

The increase in colloid size due to CTAB addition is an obvious phenomenon due to adsorption. Subsequent, such adsorption assists in steric hindrance effect. The instability of colloids is a temporal phenomenon which also depends on temperature.



Though, the viscosity has been measured at laboratory conditions as mentioned in the methodology section using the vibro viscometer. Secondly, measurements were carried out immediately (as prepared) after sample (s) preparations. The vibro viscometer results had shown an upfront information about the potential of surfactant to reduce viscosity as it has the capability to minimize the solid-liquid interfacial tension. On the other hand, the temporal study of viscosity has not been performed in the present work so it cannot be correlated with the stability over time. Thus the results at laboratory conditions are rational and could be verified. Moreover, it has also been suggested in the conclusion section that to probe rheological behavior a sophisticated temperature control measuring system (rheometer) would be employed as an extension of the present work. By doing so, one can draw final conclusion based on the oscillation and rotational measurements.

As far as literature consistency is concerned, Gum Arabic surfactant has been reported to have 25.7% increment in thermal conductivity of CNT/EG-water nanofluids as compared to CTAB and PVP [2]. Also, the authors show that samples with higher values of zeta potential are not necessarily to yield higher thermal conductivity as Gum Arabic induce very less value (-6.09mV) as compared to CTAB (23.4mV) and PVP (9.37mV). Thus it shows a trade-off among measured thermo-physical properties of nanofluids. Based on similar analogy, the viscosity measurement results could be inferred as rational. In addition, a recent study has also shown the potential of SDS surfactant to reduce the viscosity of aqueous based TiO₂ nanofluids [3]. Furthermore, large number of studies on nanofluids have shown considerable variations in thermos-physical properties even for same kind of nanomaterials due to one another reason. Therefore, the intriguing behavior of the nanofluids is possible. To probe such behaviors molecular dynamic simulations could be fair tool as far as physical mechanism is concerned. Finally, this particular field has lot of room for debate.

In the present work, addition of CTAB reduced the surface charge of colloids as compared to the pristine h-BN/EG nanofluids. Simultaneously, it reduced the viscosity on the expense of stability. Furthermore the reduction in viscosity corresponding to the maximum thermal conductivity enhancement was ~4.6% whereas the maximum viscosity reduction achieved to be ~6.6% on the expense of both stability and thermal conductivity.

The desirable combinations of nanofluids must have better colloidal dispersion, storage stability, ease of re-dispersion, reduced viscosity, and enhanced thermal conductivity such that the performance index of thermal system maintained at an optimum level.

4 Conclusions

The current research has focused on the role of CTAB volume concentrations (0.05%, 0.5%, and 1%) on h-BN/EG nanofluids stability, thermal conductivity and viscosity for constant volume fraction of h-BN (0.05%) NPs. The findings of present work are enumerated as follows:

- 1) The CTAB contained NFs formulations have shown reduction in mean zeta potential and increase in particle size with increasing concentration. Thus, regarding stability, CTAB could not be appealing choice for h-BN/EG based NFs.
- 2) The maximum thermal conductivity enhancement (~3.4%) was observed for NF with 1 vol% CTAB at an operating temperature of 40°C.
- 3) The inclusion of CTAB revealed the reduced viscosity of NFs. A maximum reduction (6.7%) was seen at CMC (0.05 vol %) beyond which the viscosity still remained less than base fluid but with decreasing trend.
- 4) Comparison among investigated properties of NFs suggested that a trade-off exist among stability, thermal conductivity, and viscosity for 2D-hBN/EG NFs.
- 5) Being two-phase system, the nanofluids flow behavior could not be simply investigated with the viscometer. As, there is possibility the liquid part of the two-phase system can dissipate mechanical input (PP) known as viscous dissipation. While the solid particles can store some energy to break the inter-particles as well as solid-liquid interactions. Therefore a sophisticated measuring system (rheometer) should be employed to simulate two-phase system (nanofluids).

5 Acknowledgement

The authors acknowledge the financial support from University of Engineering and Technology Lahore, Pakistan under faculty development program and department of Mechanical Engineering, University of Malaya for research facilities.

REFERENCES

- [1] M. Zaboli, S.S.M. Ajarostaghi, M. Noorbakhsh, M.A. Delavar, Effects of geometrical and operational parameters on heat transfer and fluid flow of three various water based nanofluids in a shell and coil tube heat exchanger, SN Appl. Sci. 1 (2019) 1–17. doi:10.1007/s42452-019-1431-2.
- [2] A. Hassan, A. Wahab, M.A. Qasim, M.M. Janjua, M.A. Ali, H.M. Ali, T.R. Jadoon, E. Ali, A. Raza, N. Javaid, Thermal management and uniform temperature regulation of photovoltaic modules using hybrid phase



- change materials-nanofluids system, *Renew. Energy*. 145 (2020) 282–293. doi:10.1016/j.renene.2019.05.130.
- [3] Y. Wang, Y. Gao, Q. Huang, G. Hu, L. Zhou, Experimental study of active phase change cooling technique based on porous media for photovoltaic thermal management and efficiency enhancement, *Energy Convers. Manag.* 199 (2019) 111990. doi:10.1016/j.enconman.2019.111990.
- [4] M. Sangeetha, S. Manigandan, M.T. Chaichan, V. Kumar, Progress of MWCNT, Al₂O₃, and CuO with water in enhancing the photovoltaic thermal system, *Int. J. Energy Res.* (2019) 1–12. doi:10.1002/er.4905.
- [5] E. Bellos, C. Tzivanidis, N. Nikolaou, Investigation and optimization of a solar assisted heat pump driven by nanofluid-based hybrid PV, *Energy Convers. Manag.* 198 (2019) 111831. doi:10.1016/j.enconman.2019.111831.
- [6] S. Alous, M. Kayfeci, A. Uysal, Experimental investigations of using MWCNTs and graphene nanoplatelets water-based nanofluids as coolants in PVT systems, *Appl. Therm. Eng.* 162 (2019) 114265. doi:10.1016/j.applthermaleng.2019.114265.
- [7] X. Wu, X. Chen, S. Jin, G. He, Y. Guo, W. Fang, Highly stable macroinitiator/platinum/hydrocarbon nanofluids for efficient thermal management in hypersonic aircraft from synergistic catalysis, *Energy Convers. Manag.* 198 (2019). doi:10.1016/j.enconman.2019.111797.
- [8] X. Wu, D. Ye, S. Jin, G. He, Y. Guo, W. Fang, Cracking of platinum/hydrocarbon nanofluids with hyperbranched polymer as stabilizer and initiator, *Fuel*. 255 (2019) 115782. doi:10.1016/j.fuel.2019.115782.
- [9] I.A. Zakaria, W.A.N.W. Mohamed, M.B. Zailan, W.H. Azmi, Experimental analysis of SiO₂-Distilled water nanofluids in a Polymer Electrolyte Membrane fuel cell parallel channel cooling plate, *Int. J. Hydrogen Energy*. 44 (2019) 25850–25862. doi:10.1016/j.ijhydene.2019.07.255.
- [10] A. Alfaryjat, L. Miron, H. Pop, V. Apostol, M.F. Stefanescu, A. Dobrovicescu, Experimental investigation of thermal and pressure performance in computer cooling systems using different types of nanofluids, *Nanomaterials*. 9 (2019). doi:10.3390/nano9091231.
- [11] M. Neyestani, M. Nazari, M.M. Shahmardan, M. Sharifpur, M. Ashouri, J.P. Meyer, Thermal characteristics of CPU cooling by using a novel porous heat sink and nanofluids, *J. Therm. Anal. Calorim.* 138 (2019) 805–817. doi:10.1007/s10973-019-08256-y.
- [12] P.C. Mukesh Kumar, C.M. Arun Kumar, Numerical evaluation of cooling performances of semiconductor using CuO/water nanofluids, *Heliyon*. 5 (2019) e02227. doi:10.1016/j.heliyon.2019.e02227.
- [13] J. Smith, R. Singh, M. Hinterberger, M. Mochizuki, Battery thermal management system for electric vehicle using heat pipes, *Int. J. Therm. Sci.* 134 (2018) 517–529. doi:10.1016/j.ijthermalsci.2018.08.022.
- [14] R.D. Jilte, R. Kumar, M.H. Ahmadi, Cooling performance of nanofluid submerged vs. nanofluid circulated battery thermal management systems, *J. Clean. Prod.* 240 (2019) 118131. doi:10.1016/j.jclepro.2019.118131.
- [15] M.E. Zayed, J. Zhao, Y. Du, A.E. Kabeel, S.M. Shalaby, Factors affecting the thermal performance of the flat plate solar collector using nanofluids: A review, *Sol. Energy*. 182 (2019) 382–396. doi:10.1016/j.solener.2019.02.054.
- [16] R. Loni, E. Askari Asli-Areh, B. Ghobadian, A.B. Kasaeian, S. Gorjian, G. Najafi, E. Bellos, Research and review study of solar dish concentrators with different nanofluids and different shapes of cavity receiver: Experimental tests, *Renew. Energy*. 145 (2020) 783–804. doi:10.1016/j.renene.2019.06.056.
- [17] M. Muraleedharan, H. Singh, M. Udayakumar, S. Suresh, Modified active solar distillation system employing directly absorbing Therminol 55–Al₂O₃ nano heat transfer fluid and Fresnel lens concentrator, *Desalination*. 457 (2019) 32–38. doi:10.1016/j.desal.2019.01.024.
- [18] M.S. Khan, M. Abid, T.A.H. Ratlamwala, Energy, Exergy and Economic Feasibility Analyses of a 60 MW Conventional Steam Power Plant Integrated with Parabolic Trough Solar Collectors Using Nanofluids, *Iran. J. Sci. Technol. Trans. Mech. Eng.* 3456789 (2018). doi:10.1007/s40997-018-0149-x.
- [19] H. Sardarabadi, S. Zeinali Heris, A. Ahmadvand, M. Passandideh-Fard,



- Experimental investigation of a novel type of two-phase closed thermosyphon filled with functionalized carbon nanotubes/water nanofluids for electronic cooling application, *Energy Convers. Manag.* 188 (2019) 321–332. doi:10.1016/j.enconman.2019.03.070.
- [20] A. Kazemi-Beydokhti, M. Farrokhi, E. Menna, Carbon nanotube nanofluid for the efficiency improvement in a CHP system: simulation and experimental investigation, *J. Therm. Anal. Calorim.* 7 (2019). doi:10.1007/s10973-019-08857-7.
- [21] A. Bhattad, J. Sarkar, P. Ghosh, Experimentation on effect of particle ratio on hydrothermal performance of plate heat exchanger using hybrid nanofluid, *Appl. Therm. Eng.* 162 (2019) 114309. doi:10.1016/j.applthermaleng.2019.114309.
- [22] O. Keklikcioglu, T. Dagdevir, V. Ozceyhan, Heat transfer and pressure drop investigation of graphene nanoplatelet-water and titanium dioxide-water nanofluids in a horizontal tube, *Appl. Therm. Eng.* 162 (2019) 114256. doi:10.1016/j.applthermaleng.2019.114256.
- [23] G.K. Poongavanam, B. Kumar, S. Duraisamy, K. Panchabikesan, V. Ramalingam, Heat transfer and pressure drop performance of solar glycol/activated carbon based nanofluids in shot peened double pipe heat exchanger, *Renew. Energy.* 140 (2019) 580–591. doi:10.1016/j.renene.2019.03.059.
- [24] X. Tao, C.A. Infante Ferreira, Heat transfer and frictional pressure drop during condensation in plate heat exchangers: Assessment of correlations and a new method, *Int. J. Heat Mass Transf.* 135 (2019) 996–1012. doi:10.1016/j.ijheatmasstransfer.2019.01.132.
- [25] A.E. Kabeel, T. Abou El Maaty, Y. El Samadony, The effect of using nano-particles on corrugated plate heat exchanger performance, *Appl. Therm. Eng.* 52 (2013) 221–229. doi:10.1016/j.applthermaleng.2012.11.027.
- [26] Z.Q. Wang, T.Y. Lü, H.Q. Wang, Y.P. Feng, J.C. Zheng, Review of borophene and its potential applications, *Front. Phys.* 14 (2019) 1–45. doi:10.1007/s11467-019-0884-5.
- [27] I. Carrillo-Berdugo, D. Zorrilla, J. Sánchez-Márquez, T. Aguilar, J.J. Gallardo, R. Gómez-Villarejo, R. Alcántara, C. Fernández-Lorenzo, J. Navas, Interface-inspired formulation and molecular-level perspectives on heat conduction and energy storage of nanofluids, *Sci. Rep.* 9 (2019) 1–13. doi:10.1038/s41598-019-44054-0.
- [28] O.A. Hussein, K. Habib, R. Saidur, A.S. Muhsan, S. Shahabuddin, O.A. Alawi, The influence of covalent and non-covalent functionalization of GNP based nanofluids on its thermophysical, rheological and suspension stability, *RSC Adv.* 9 (2019) 38576–38589. doi:10.1039/c9ra07811h.
- [29] M. Hernaiz, V. Alonso, P. Estellé, Z. Wu, B. Sundén, L. Doretto, S. Mancin, N. Çobanoğlu, Z.H. Karadeniz, N. Garmendia, M. Lasheras-Zubiate, L. Hernández López, R. Mondragón, R. Martínez-Cuenca, S. Barison, A. Kujawska, A. Turgut, A. Amigo, G. Huminic, A. Huminic, M.R. Kalus, K.G. Schroth, M.H. Buschmann, The contact angle of nanofluids as thermophysical property, *J. Colloid Interface Sci.* 547 (2019) 393–406. doi:10.1016/j.jcis.2019.04.007.



Thermal Characterization of Graphene coated Copper Foam Saturated with Phase Change Material

Ali Hasan¹, Abid Hussain^{1,*}

¹Department of Mechanical Engineering, University of Engineering and Technology Taxila, Pakistan

*Corresponding Author: abid.hussain@uettaxila.edu.pk

Abstract:

Thermal characteristics of a composite phase change material (PCM) are investigated for the purpose of designing a better thermal management system by using graphene coated copper (GcC) foam saturated with paraffin wax (Rubitherm-42). The objective of this study is to investigate the phase change temperature profile for melting and freezing process, specific heat capacity, latent heat and heat transfer rate. These thermo-physical properties are investigated by using differential scanning calorimeter (DSC). The composite PCM is prepared by coating a layer of graphene on copper metal foam substrate through chemical vapor deposition (CVD) process and then infiltrated with PCM. The phase change behavior of GcC/PCM shows shift in temperature with 38 °C and 42 °C as extrapolated onset and peak temperatures respectively. The specific and latent heat of GcC/PCM are measured as 1.984 J/g. °C and 2.107 J/g. Furthermore, these thermal Properties of GcC/PCM composite are compared with pure PCM and copper foam/PCM composite.

Keywords: Copper foam, Graphene coated copper foam, Phase change material, Differential scanning calorimeter, Chemical vapor deposition

1. Introduction

In the past few years a great attention of society has been converted towards renewable energy sources due to fossil fuels depletion and their environmental impacts [1]. Solar energy is a suitable candidate as an alternate substitute of fossil fuels due to its easy availability, environmental friendly nature and low price characteristics [2-3]. Here an efficient energy storage device is required for the purpose of storing excess solar energy during day time and for the smooth and longer operation of electric vehicles (EV) and other portable electronic devices. Lithium ion batteries (LIB) appeared as a suitable candidate for energy storage purpose with longer life span, stable charge/discharge cycles, and low weight to volume ratio with high densities of energy and power [4]. Similarly, the lithium ion batteries also have a severer disadvantage of overheating during continuous charging/discharging cycles, which not only affects its storage capacity, performance and also working life cycle [5]. The desirable working temperature range for better performance of LIB is 25-55 °C as reported in [6].

Two different modes of cooling like active and passive are used in thermal management systems of LIBs. Where the passive mode of thermal management system is preferable over active mode due to its high efficiency, simplicity, compactness, less initial and maintenance cost with prolonged working life.

Three different types of PCM like organic, inorganic and eutectic are used in most of thermal systems

designed for batteries. Among these, organic PCMs are preferred for passive thermal management systems due to their non-poisonous, non-explosive, non-corrosive behavior with large latent heat, large specific heat capacity, low volume expansion/contraction with temperature change and low cost. On the other hand organic PCMs are affected by their lower values of thermal conductivity 0.1-0.3 W/m.K [7]. For higher heat transfer rate, enhancement in PCM's thermal conductivity is needed for better thermal management systems.

In previous studies, different types of PCM based composites with metallic additives like nano-particles, chips and foams were designed and tested for enhancement in heat transfer rate and other thermal properties. Researchers used nano-particles based nano-fluids and encapsulated composite PCM's in thermal management systems for indoor and outdoor applications. The enhancement in heat transfer rate for betterment in thermal management system is achieved by using additives with high thermal conductivity e.g. nano-particles (metallic, carbon) based, expanded graphite, encapsulation of PCM's and metallic foams. Further, due to low density and better dispersion than metallic nano-particles, carbon based nano-particles showed better performance and stability [8-9]. S. Mettawee et al. [10] conducted an experiment with composite of aluminum powder/PCM with 80µm particle size using a compact setup with solar collectors. Charging/discharging process carried out by absorbing/releasing solar energy through PCM to cold



water flowing inside pipes with flow rate of 9-20.4 kg/h. He founds that by using this composite PCM, charging/discharging time reduced by 60% with enhanced heat gain value. Average value of coefficient of heat transfer increased compared to pure PCM and mean daily efficiency increased from 32% to 54.8% and 82% to 94% for pure paraffin and composite PCM respectively.

X. Xiao et al. [11] performed studies numerically and experimentally for the purpose of investigation of latent thermal energy storage of shell-tube arrangement for charging/discharging using composite of expanded graphite EG with paraffin as PCM under 7, 10 % wt. of EG and water in cylindrical tank used as heat transfer fluid. The results indicate that the time required for charging/discharging has a direct relation with flow rate and initial temperature of heat transfer fluid. S. Khedache et al. [12] prepared and investigated thermal reliability and properties of a novel composite material (red brick, EG, paraffin) with ability to sustain PCM up to 40 wt. %. From results, he concluded that composite with mass fraction of EG and PCM of 60:40 as most suitable due to its enhanced conductivity with a very little effects on latent heat.

In thermal characteristics enhancement, metallic foam can perform better than metallic nano-particles due to their high stiffness, high specific strength, low density, large surface area, excellent mechanical and thermo-physical properties. Different researchers employed metal foams in PCM to study thermal properties of composite PCMs. X. Xiao et al. [13] prepared composite of carbon foam/paraffin for investigation of thermo-physic properties. Thermal effusivity of composite PCM increased and fruitful for enhancement in heat transfer rate. A. Hussain et al. [14] designed nickel foam/paraffin composite and investigated for thermal management of LIB. Due to enhanced thermal properties, composite PCM was able to maintain battery pack within desired operating range compared to natural air and pure PCM. With decreasing pore density and porosity of metal foam, the surface temperature of battery pack become smooth and uniform. A. Hussain et al. [15] designed thermal management system using graphene coated nickel GcN foam saturated with paraffin for stressed conditions. The results showed that the thermal conductivity of composite PCM with graphene coating and without graphene coating increased by 23 and 6 times respectively and during charging/discharging process battery pack temperature remained within desired temperature range.

H. T. Cui et al. [16] designed, manufactured, tested and analyzed a composite of paraffin and copper metal foam through charging process and compared with pure

paraffin. The heat transfer rate was enhanced by about 36% resulting faster melting of PCM, shorten time required for charging purposes and reducing the difference between PCM and wall temperature. Z. N. Meng et al. [17] analyzed thermal energy storage performance during charging/discharging process on the basis of latent heat by using copper foam/paraffin composite with fraction of 91.45 % vol. of PCM, in tube-in-tank arrangement and compared with 3D modeling. The temperature was uniformly distributed in composite PCM due to enhanced thermal conductivity and showed maximum ability of heat transfer. Charging/discharging time decreased by increasing speed and temperature difference between composite PCM and heat transfer fluid. P. Goli et al [18]. investigated heat transfer enhancement by using graphene/paraffin composite for batteries thermal management system. He found that heat transfer rate with composite PCM much was much greater than PCM with same of latent heat. He also observed that battery pack temperature limited to 16 °C with composite PCM compared to 37 °C at 5A discharge current.

In literature review, studies have been carried out on designing and investigation of thermal management systems based on composites of nano-fluids, expanded graphite and metal foams with PCM. In these systems, the nickel foam enhanced heat transfer rate of paraffin only six times and the thermo-mechanical properties (such as tensile strength and compressive strength) of composite becomes weaker at elevated temperatures. Other effective thermal properties like specific heat capacity and latent heat of PCMs are also greatly compromised.

Here, graphene coated copper metal foam infiltrated with paraffin wax is reported as a novel composite for LIB thermal management systems due to better thermo-mechanical properties of GcC foam and much higher thermal conductivity of graphene 2000-3000 W/m.K.

This study is performed with basic objective of enhancement in heat transfer rate along with other thermal properties e.g. Latent heat and specific heat capacity. These thermal properties of GcC/PCM composite are compared with pure paraffin and copper foam/PCM composite.

2. Experimental Design

2.1 Preparation of graphene coating on copper foam

The sample of graphene coated metal foam/PCM is prepared by using copper foam with porosity (ϵ) and pore density (ω) of 0.95, 12.7 PPI respectively under dimensions of 50 mm, 20mm, 1.7 mm as length, width



and height . Direct deposition of graphene is achieved on copper metal foam through chemical vapor deposition (CVD) technique to overcome thermal contact resistance between single layer of graphene and metal skeleton of copper foam. CVD, being gas phase deposition process, results in uniform deposition of graphene. For rapid heating/cooling rates, a tube type furnace along with a sliding type reaction chamber is used.

The CVD process started with washing and cleaning of copper metal foam with dilute hydrochloric acid (HCL) solution for removal of previously present oxides and organic compounds type impurities on metal skeleton and then dried with nitrogen based blower. The furnace chamber was purged for 10 minutes (min) with argon (Ar) gas at 250 standard cubic centimeter per minute (sccm) to flash out previously present gases like oxygen and nitrogen in chamber. Then the heating process of furnace started with switching ON the furnace under the same flow rate of Ar gas. The heating process was continued until the furnace temperature reached 1050°C. At that moment, the copper metal foam was introduced into the furnace under hydrogen (H₂) gas with flow rate of 15 sccm. The copper metal foam was annealed for 20 min to increase its ductility and decrease hardness. Here arrived the final stage of graphene coating and started with the introduction of methane (CH₄) based carbon precursor in gas phase at a flow rate of 15 sccm, with a composition of (500 ppm diluted in Ar) for 40 min. Then the sample was rapidly cooled to room temperature under Ar based inert atmosphere by simply switching OFF the furnace.

Carbon precursor, Experimental techniques and conditions were kept same during samples preparation to maintain quality and ensure uniform number of graphene layers on copper metal substrate.

To assure graphene smooth growth on copper foam, Raman-spectrum was conducted. The two peaks of raman-spectrum and their band ratios confirm single layer of graphene on copper metal foam shown in Figure 1.

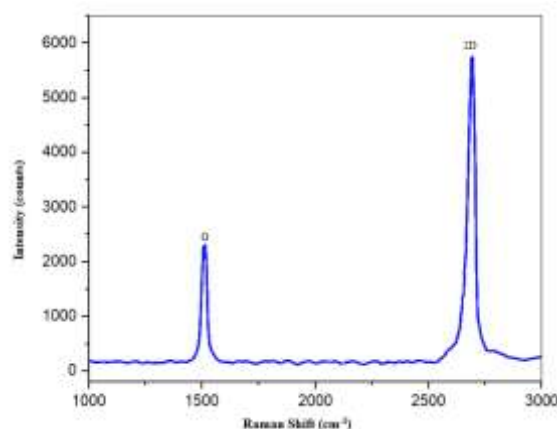


Figure 1. Raman-Spectrum of graphene coated copper metal foam

2.2 Infiltration of PCM into graphene coated copper foam

Commercial paraffin (RT-42) used as PCM with melting temperature range of 38-41 °C and thermal conductivity 0.19W/m.K was supplied by Chinese company, Ruhr Energy Technology Co. Ltd. The thermal characteristics of pure PCM provided by the company were verified and enlisted in table 1. The infiltration process of PCM into GcC metal foam was carried out by cutting the metal foam and paraffin wax with dimensions of 50 mm x 20mm x 1.7 mm. Then the paraffin wax, placed in stainless steel container, was heated through hot water bath maintained at 100°C for 60 min. Hot water bath based heat source was used for uniform and smooth melting of paraffin wax. The GcC metal foam was placed in stainless steel container and supported through wire mesh. When the PCM melted completely, then the GcC foam dipped in liquid PCM was suspended for few minutes to achieve maximum paraffin infiltration. The cooling process of molten PCM with metal foam was performed by placing the stainless steel container in cooled water bath maintained at 25°C for about 100 min. After the composite of paraffin wax was completely solidified, container was externally heated for 10 min for easy removal of paraffin wax/metal foam composite from container. Then the composite of paraffin wax was removed carefully from container and extra paraffin wax attached to composite faces was separated without damaging the composite PCM.



Table 1: Thermo-physical properties of PCM (RT-42)

Parameters	Value
Thermal conductivity	0.19 W/m.K
Density	Solid state 880 kg/m ³ , Liquid state 760 kg/m ³
Specific heat capacity	2.3 J/kg.K
Melting temperature range	38-41 °C

Note: These parameters are provided by the company and also verified in this study

2.3 Specific heat measurement

The specific heat capacity of graphene coated copper metal foam saturated with paraffin wax was determined by using differential scanning calorimetry based DSC (Q1000) apparatus. Experimentation was carried out by maintaining constant mass of sample in the range of 2.3-2.7 mg under nitrogen based environment. Sample sealing assembly containing the mass of composite PCM in a standard aluminum sample pan was placed in a furnace along with an empty aluminum sample pan as a reference. The empty sample aluminum pan was placed in furnace to remove pan effects. Then the sample was set to heating and cooling cycles at the rate of 2 °C/min between 5 °C and 60 °C under 50 ml/min nitrogen flow atmosphere. Temperature of sample was brought to 5 °C and then sample was set to isothermal segment of 3 min to achieve its thermal equilibrium stage. Then the heating cycle starts with the sample heating from 5 °C to 60 °C, followed by a 3 min isothermal stage for isothermal equilibrium. Similarly the cooling cycle starts from 60 °C and ends at 5 °C with same rate of cooling as for heating cycle. Then the specific heat capacity of samples was determined by using following relation reported in [15].

$$c_p = \frac{E_{sample} - E_{base\ line}}{M_{sample} \cdot dT/dt \cdot E} \quad (1)$$

Where, on left side c_p is the specific heat capacity of the test specimens and on right side E_{sample} and $E_{base\ line}$ is the sensitivity of DSC with sample and without sample respectively, M_{sample} is the mass of sample in mg, dT/dt is the heating/cooling rate in °C/min, and E is the overall sensitivity of DSC. DSC sensitivity is measured on the basis of tests with standard materials (e.g. platinum, aluminum) and without sample base line tests. DSC sensitivity is determined by following relation

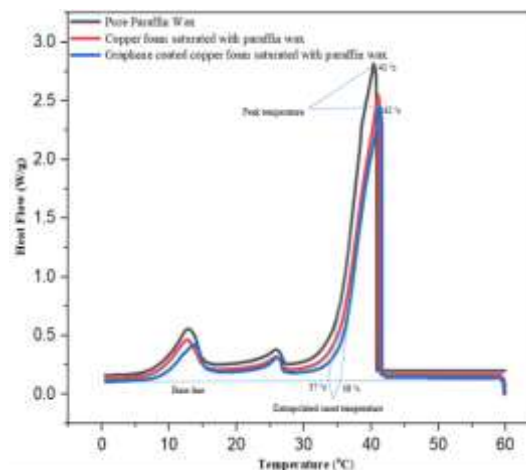
$$E = \frac{E_{sample} - E_{base\ line}}{M_{standard} \cdot dT/dt \cdot c_{p,standard}} \quad (2)$$

Where, $c_{p,standard}$ denotes the specific heat capacity of standard material as described above.

3. Results and Discussions

3.1 Phase change behavior of GcC/PCM composite

A shift in phase change temperature of graphene coated copper foam saturated with phase change material is noted in its melting/freezing phase change behavior. The melting and freezing curves of pure PCM, copper foam and graphene coated copper foam saturated with PCM are shown in Fig.8 and Fig.9 respectively. Where the positive and negative heat flows indicate the melting and freezing processes respectively and the small peak adjacent to main peak and main peak itself indicate solid-solid and solid-liquid phase change of pure PCM and composites of copper and GcC foam with PCM. During melting process, the GcC/PCM composite, compared to pure and copper foam/PCM composite, shows a shift in extrapolated onset and peak temperature towards higher with values of 38 °C and 42 °C respectively shown in figure 2(a). On the other hand, in case of freezing process the extrapolated onset and peak temperatures of GcC/PCM composite shows decrease in their respective values. During melting/freezing process, the shift in extrapolated onset and peak temperatures of graphene coated copper foam saturated with PCM as compared to pure PCM and copper foam/PCM composite, are due to the existence of good compatibility and metal foam skeleton firm interaction at pores level with solid as well as liquid state PCM shown in figure 2(b).



(a)

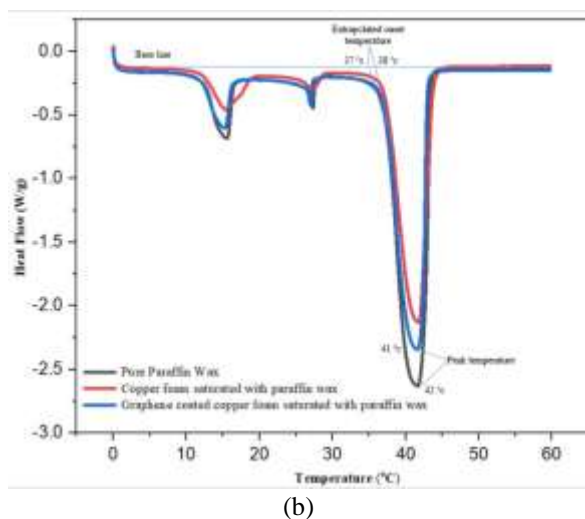


Figure 2. DSC phase change behavior of pure paraffin, copper foam/PCM and graphene coated copper foam/PCM composite for (a) melting (b) freezing process

Shift in temperature of GcC/PCM is best described by the Clapeyron Clausius equation, which works between two states of a specimen [19]. Where m and n indicate two states i.e. 1 and 2.

$$\ln \frac{T_2}{T_1} = \frac{\Delta_1^2 V}{\Delta_1^2 H} (P_2 - P_1) \quad (3)$$

The phase change temperatures of two states in melting and freezing process are represented by T_1 and T_2 and this change in temperature causes change in volume of PCM and is represented by $\Delta_1^2 V$. The enthalpy change is represented by $\Delta_1^2 H$ with P_1 and P_2 as the ambient pressures of state 1 and state 2.

During melting process, due to large amount of heat absorption by PCM as latent heat, the enthalpy of PCM will increase $\Delta_1^2 H > 0$). As molten form of PCM has less density compared to its solid form, the expansion in PCM volume takes place ($\Delta_1^2 V > 0$) in the range of 5-10%. Due to this expansion, the molten PCM has to face restriction effect by metal foam skeleton and causes enhancement in ambient pressure of composite PCM ($P_2 > P_1$). This ambient pressure increment is the cause of shift in extrapolated onset and peak temperatures of composite PCM towards enhanced temperature.

During freezing process, enthalpy and temperature of composite PCM decrease ($\Delta_1^2 H < 0$) due to negative heat flow, which results in solidification of molten PCM. As PCM density in solid state is higher than its molten state,

so the volume of the composite PCM also decreases during freezing process ($\Delta_1^2 V < 0$). Due to this decrease in volume, the ambient pressure of state P_2 decrease as compared to state P_1 , ($P_1 > P_2$), which results in shifting of composite PCM temperature towards lower compared to pure and copper foam/PCM composite.

3.2 Specific heat capacity of GcC/PCM composite

The specific heat capacity of pure PCM and composite PCM's of GcC foam, copper foam are shown in Figure 3. These values are measured at room temperature during heating cycle. Where the specific heat value for pure PCM is 3.106 J/g.°C along with 1.616 J/g.°C and 1.984 J/g.°C for copper foam/PCM and GcC/PCM composites respectively.

This decrement in specific heat values of composite PCM's compared to pure PCM, are due to less specific heats of graphene coated layer and metal skeleton of copper foam along with less mass fraction of paraffin in composite PCM's.

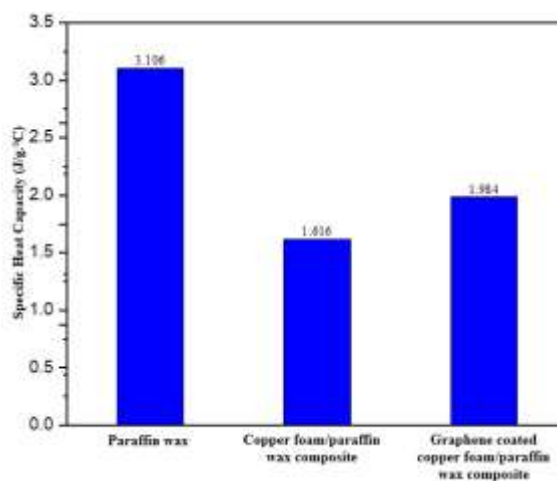


Figure 3. Specific heat capacity of paraffin wax, copper foam saturated with paraffin wax, graphene coated copper foam saturated with paraffin wax at room temperature

3.3 Latent heat of GcC/PCM composite

The latent heat of composite of GcC/PCM is calculated by numerical integration of the area under main peak of DSC melting/freezing curve. Where the latent heat value comes as 4.729 J/g, 2.037 J/g, 2.107 J/g, for pure PCM, copper foam/PCM and GcC/PCM composites respectively in Figure 4. This decrement in latent heat of composite PCM is firstly due to the presence of metal skeleton in composite PCM, which cannot take part in melting/freezing process along with paraffin and



secondly due to the formation of small cavities within the composite during infiltration, due to enhanced thermal conductivity of composite PCM resulting in rapid cooling.

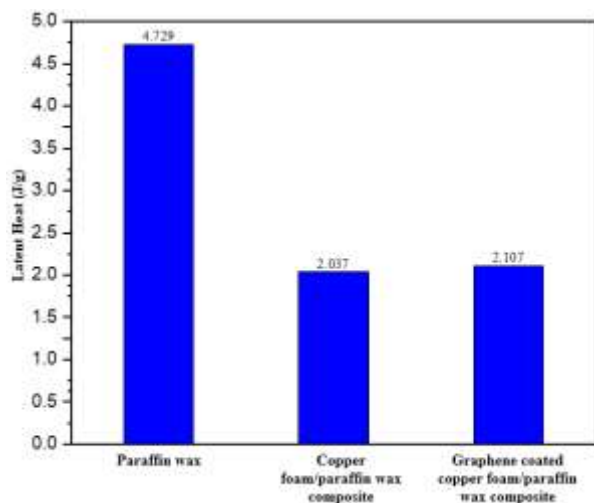


Figure 4. Latent heat of pure paraffin wax, copper foam saturated with paraffin wax, graphene coated copper foam saturated with paraffin wax at room temperature

4. Conclusion

This study was conducted for betterment in thermal management system of high power density LIB's using GcC metal foam saturated with PCM. The sample was prepared by single layer coating of graphene on copper metal foam substrate through CVD process followed by the infiltration of paraffin wax. Then the thermo-physical properties of GcC/PCM composite are investigated and compared with paraffin wax and copper foam saturated with paraffin wax. During melting and freezing cycles, the composite of GcC/PCM showed an increased and decreased melting temperature compared to pure PCM and composite of copper foam/PCM, due to better interaction of GcC foam's pores with solid and liquid paraffin wax. Furthermore, the heat transfer rate increased many times by using composite PCM of GcC with high specific and latent heat values compared to copper foam/paraffin composite.

REFERENCES

[1] F. A. Boyaghchi and M. Chavoshi, "Multi-criteria optimization of a micro solar-geothermal CCHP system applying water/CuO nanofluid based on exergy, exergoeconomic and exergoenvironmental concepts," *Appl. Therm. Eng.*, vol. 112, pp. 660–675, 2017.

[2] S. Suman, M. K. Khan, and M. Pathak,

"Performance enhancement of solar collectors - A review," *Renew. Sustain. Energy Rev.*, vol. 49, pp. 192–210, 2015.

[3] A. Wahab, A. Hassan, M. A. Qasim, H. M. Ali, H. Babar, and M. U. Sajid, "Solar energy systems – Potential of nanofluids," *J. Mol. Liq.*, vol. 289, 2019.

[4] W. Chen, J. Liang, Z. Yang, and G. Li, "A review of lithium-ion battery for electric vehicle applications and beyond," *Energy Procedia*, vol. 158, pp. 4363–4368, 2019.

[5] R. Spotnitz and J. Franklin, "Abuse behavior of high-power, lithium-ion cells," *J. Power Sources*, vol. 113, no. 1, pp. 81–100, 2003.

[6] A. Väyrynen and J. Salminen, "Lithium ion battery production," *J. Chem. Thermodyn.*, vol. 46, pp. 80–85, 2012.

[7] Z. Rao and S. Wang, "A review of power battery thermal energy management," *Renew. Sustain. Energy Rev.*, vol. 15, no. 9, pp. 4554–4571, 2011.

[8] Z. A. Qureshi, H. M. Ali, and S. Khushnood, "Recent advances on thermal conductivity enhancement of phase change materials for energy storage system: A review," *Int. J. Heat Mass Transf.*, vol. 127, pp. 838–856, 2018.

[9] X. Zhao *et al.*, "A review on heat enhancement in thermal energy conversion and management using Field Synergy Principle," *Appl. Energy*, vol. 257, no. October 2019, p. 113995, 2020.

[10] E. B. S. Mettawee and G. M. R. Assassa, "Thermal conductivity enhancement in a latent heat storage system," *Sol. Energy*, vol. 81, no. 7, pp. 839–845, 2007.

[11] X. Xiao and P. Zhang, "Numerical and experimental study of heat transfer characteristics of a shell-tube latent heat storage system: Part I - Charging process," *Energy*, vol. 79, no. C, pp. 337–350, 2015.

[12] S. Khedache, S. Makhlof, D. Djefel, G. Lefebvre, and L. Royon, "Preparation and thermal characterization of composite 'paraffin/Red Brick' as a novel form-stable of phase change material for thermal energy storage," *Int. J. Hydrogen Energy*, vol. 40, no. 39, pp. 13771–13776, 2015.

[13] X. Xiao and P. Zhang, "Morphologies and thermal characterization of paraffin/carbon foam composite phase change material," *Sol. Energy Mater. Sol. Cells*, vol. 117, pp. 451–461, 2013.

[14] A. Hussain, C. Y. Tso, and C. Y. H. Chao, "Experimental investigation of a passive thermal management system for high-powered



- lithium ion batteries using nickel foam-paraffin composite,” *Energy*, vol. 115, pp. 209–218, 2016.
- [15] A. Hussain, I. H. Abidi, C. Y. Tso, K. C. Chan, Z. Luo, and C. Y. H. Chao, “Thermal management of lithium ion batteries using graphene coated nickel foam saturated with phase change materials,” *Int. J. Therm. Sci.*, vol. 124, no. September 2017, pp. 23–35, 2018.
- [16] H. T. Cui, “Experimental investigation on the heat charging process by paraffin filled with high porosity copper foam,” *Appl. Therm. Eng.*, vol. 39, pp. 26–28, 2012.
- [17] Z. N. Meng and P. Zhang, “Experimental and numerical investigation of a tube-in-tank latent thermal energy storage unit using composite PCM,” *Appl. Energy*, vol. 190, pp. 524–539, 2017.
- [18] P. Goli, S. Legedza, A. Dhar, R. Salgado, J. Renteria, and A. A. Balandin, “Graphene-enhanced hybrid phase change materials for thermal management of Li-ion batteries,” *J. Power Sources*, vol. 248, pp. 37–43, 2014.
- [19] X. Xiao, P. Zhang, and M. Li, “Preparation and thermal characterization of paraffin/metal foam composite phase change material,” *Appl. Energy*, vol. 112, pp. 1357–1366, 2013.



Thermal Conductivity Measurement of Graphene Coated Metal Foam Saturated with Phase Change Material

Awais Ahmed¹, Abid Hussain^{1,*}, Ali Hasan¹,

¹-Department of Mechanical Engineering, University of Engineering and Technology Taxila, Pakistan

*Corresponding Author: abid.hussain@uettaxila.edu.pk

Abstract:

Phase change materials (PCMs) have large amount of latent heat and ability of maintaining uniform temperature through phase change process which makes them suitable material for thermal energy storage and utilization of waste heat. PCMs used have a problem of low thermal conduction which slows down the energy transfer process. Low thermal conductivity decreases the heat transfer rate and minimizes the energy storage efficiency of the system. In the current work the heat transfer rate of paraffin was investigated by using graphene coated copper (GcC) foam. The copper was coated with graphene through chemical vapor deposition. The paraffin was infiltrated into the coated metal foam by the infiltration process. Raman spectroscopy showed the smooth layer of coating on copper foam. Laser flash method was used to measure the thermal conductivity of composite PCM. Porosity effects of metal foam were seen on the thermal conductivity of the composite PCM. Thermal conductivity and porosity of metal foam have inverse relation with each other. Maximum thermal conductivity of 8.6(W/m.K) was seen at porosity of 0.90.

Keywords: Paraffin wax; Thermal conductivity; Graphene coated copper foam; Laser flash technique, Raman spectroscopy

1. Introduction

Passive thermal management comprising of phase change material has attracted great attention in recent time as it is efficient, compact lightweight. Phase change materials (PCM) have a wide range of application which includes cooling of electronic devices, renewable thermal energy storage and improvement of energy efficiency [1]. Phase change materials can absorb, retain and release massive quantity of heat while maintaining the temperature uniformity during the phase change process as they possess a huge amount of latent heat energy [2]. The phase transition process of PCM during melting or solidification takes place nearly at a constant temperature during latent heat storage. PCM has some additional advantage over other storage materials of being noncorrosive, non-poisonous and low volume expansion [3]. However, the low thermal conduction of the PCM severely disrupts its efficiency of energy storage and limits its usage in engineering applications [4]. Different techniques are reported in the literature to improve the low heat conductivity of PCM. Goli et al. [5] investigated the effect of thermal conductivity on paraffin by the addition of graphene. The enhancement of 225 times in thermal conductivity was seen. Kizile et al. [6] Experimentally studied the thermal conduction of paraffin by making a composite of paraffin and graphite. The thermal conductivity value increased to 17 W/ (m.K). Lafdi et al. [7] did an experimental study to evaluate the melting temperature of paraffin in an aluminum metal foam. They also studied the impact of pore size and porosity on heat transfer enhancement. They found that with higher porosity and larger pore size, the temperature reached

quickly to steady state as compared to metal foam with low porosity and low pore size.

Zhang et al. [8] carried out experiment to investigate the thermal conduction along with the thermal capacity and thermal diffusivity. He used different porosity of copper foam and used a transient plane source method for thermal conduction measurement. Improvement of thermal conduction was seen by 25 times in comparison with the pure paraffin. Wang et al. [9] prepared a merged PCM by blending aluminum powder into polyethylene and silica gel. The thermal conductivity was enhanced from 0.3847 W/ (m.K) to 0.7661 W/ (m.K) by the addition of 5–30 wt. % of b-aluminum nitride respectively. Cui et al. [10] worked on the phase change material made of soy wax. They found that the thermal conductivity of soy wax (0.324) was enhanced by adding carbon nanotube and carbon nanofiber. The 10% addition by weight of CNF and CNTs increased the thermal conductivity of soy wax by 0.469 and 0.403 respectively. The CNF was better distributed in soy wax which increased the thermal conductivity comprehensively. Tian et al. [11] formed a composite PCM by the combination of eutectic ternary carbonate salt with the magnesium particle. There was no comprehensive change in the melting temperature of the Composite PCM relative to pure carbonate salt. The effective thermal conductivity was enhanced by 145 % by the addition of 2 wt% of magnesium.

The heat transfer enhancement has a great impact on the thermal properties of PCM. Rapid heat transfer effects the heat-storing and release rate [12]. Hence



it is very important to enhance the low thermal conductivity of the PCM composite. Different approaches used by researchers were focused on using metal foam, using nanoparticles and enclosing PCM. However, the coating of the highly conductive material on metal foam is rarely been focused. In current work, different porosity of copper foam was coated with graphene and infiltrated with paraffin. Effect of varying porosity was seen on the thermal conductivity.

2. Material Preparation

2.1 Preparation for graphene coating on metal foams

Graphene coating on copper foam was accomplished by using tube furnace with sliding chamber through chemical vapor deposition at 1100 °C in presence of argon gas. Copper foam with pore size 0.5mm and porosity of 0.95 was washed through dilute hydrochloric acid solution and introduced in furnace for graphene coating. Gas phase carbon precursor is introduced in furnace for uniform graphene coating. After coating furnace was switched OFF and allowed copper foam to cool down to room temperature. The figure 1 and figure 2 shows the optical image of copper foam before coating and after coating, respectively.



Figure 1. Optical image of Copper foam before coating



Figure 2. Optical image of Copper foam after graphene coating

2.2 Raman Spectrum

The smoothness of graphene coating was analyzed using Raman Spectroscopy on graphene coated

copper metal foams. The Raman spectrum was achieved by using the micro-Raman spectroscopy for monitoring and assuring the smooth growth of graphene on copper metal foam coating process. Where the two peaks of Raman spectra indicate graphene growth shown in figure 3. The smoothness and uniformity of graphene distribution in coating process of copper metal foam substrate was checked by acquiring Raman spectra for 10 random points. The features indicated by these patterns points out towards uniform distribution of graphene due to gas phase deposition of carbon atoms in deposition process. These patterns are also indicating a single layer of graphene coating on copper metal substrate based on band ratios of G and 2D as ($G/2D < 1$). The graphene single layer thickness on copper metal foam substrate is in the range of (0.1-0.5) nm, also this thickness is used for estimation of graphene coated mass on copper metal foam. Whereas the mass fraction of graphene in graphene coated copper metal foam was found by the mass of copper metal substrate after coating with graphene minus the mass of copper metal substrate before graphene coating divided by the mass of copper metal substrate after graphene coating.

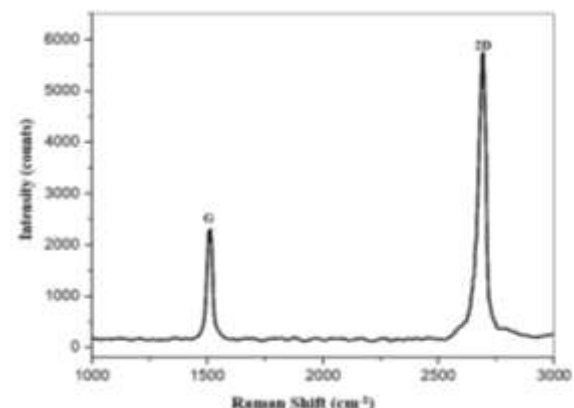


Figure 3. Raman Shift

2.3 Infiltration of Paraffin wax into copper and graphene coated copper (GcC) foam

In this study the paraffin wax was used was Rubitherm-42 with a melting temperature range and thermal conductivity of (38-41) °C and (0.2W/mK) respectively [13], provided by Ruhr Technology China. The thermal properties of materials are listed below.

Table 1. Thermal Properties [14]

Material	Thermal conductivity W/mK
Copper	398
Graphene	3000
Paraffin (38-41°C)	0.2



The composite PCM is prepared by infiltration of molten paraffin wax into graphene coated copper foam. The dimension of metal foam used in the experiment was 50 mm x 20mm x 1.7 mm. The paraffin was placed in metal container and heated uniformly through heater until the wax was melted completely. The graphene coated copper foam was lowered in the metal container through the wire mesh for infiltration of molten paraffin wax. When the paraffin was completely infiltrated inside the metal foam, the heat source was removed and left the wax to solidify. Metal container was then gently heated to separate the saturated coated metal foam paraffin composite from the container.

2.4 Infiltration Ratio

To find the infiltration ratio the sample was weighted using the electronic mass balance (JM10002) with precision of 0.01 g provided by Zhejiang Ltd China. The mass reading was taken before and after the infiltration of the paraffin. Bulk porosity of the metal foam was found by the following equation [15].

$$\varepsilon_b = 1 - \frac{m_{f_0}}{\rho_{sk}V_t} \quad (1)$$

In the above equation the ε_b is the bulk porosity of metal foam. V_t is the volume of the metal foam, ρ_{sk} represent the density of the metal skeleton and m_{f_0} represents the mass of metal foam. Following equation was then utilized to find the infiltration ratio [15].

$$\alpha = \frac{m_{actual}}{m_{ideal}} = \frac{\Delta m_i}{\varepsilon_b \rho_{pcm} V_t} \quad (2)$$



Figure 4. Laser Flash Method

Where ρ_{pcm} is represent the density of PCM when it is in solid form. Δm_i is the difference in masses of metal foam before and after the infiltration. The α is dimensionless parameter and represents the actual value of paraffin wax infiltrated into the metal foam

as compare to the ideal mass which could be infiltrated. If the value is 100% it implies that all the paraffin has infiltrated into the metal foam and all the pores are filled with the paraffin.

2.5 Thermal conductivity Measurement

Thermal conductivity of copper foam coated with graphene and saturated with paraffin wax along with copper foam and graphene coated copper foam was measured indirectly by thermal diffusivity, defined as heat transmission rate by conduction during changing specimen temperature with passage of time and denoted by (α). Where diffusivity is measured by using apparatus designed based on laser flash technique at 25 °C. The apparatus consist of metal rod with an inside electric heater for heating purpose and temperature of metal rod is constantly maintained by 35°C throughout the experiment and infrared radiator (IR detector) of (FLIR SC660) type is used for temperature measurement without any physical contact with apparatus or sample material. The samples of composite of graphene coated copper foam with paraffin wax with dimensions of (50 mm × 20mm × 1.7 mm) is tightly attached with metal rod along length through thermal tape (thermal interface material) to overcome interface resistance between metal rod and test samples. During experiment, sample temperature for each specimen is recorded by IR detector (FLIR SC660) from top to bottom at 5mm, 25mm and 45mm. The working temperature range of IR detector was from -40°C to 1500 °C. It has temperature sensitivity of 0.05°C and accuracy of ±1°C. The experiment was repeated 6 times to ensure the accuracy of the results. The thermal diffusivity is measured by using following relation [16].

$$\alpha = \frac{1.38 d^2}{\pi^2 t^{1/2}} \quad (3)$$

Where on left side, there is α in (m²/s) and on side d denotes sample length in (m) and $t^{1/2}$ as time in (seconds) for half maximum temperature on rare side of specimens. This value of time for half maximum temperature on rare side is the main parameter for thermal diffusivity measurement.

By using thermal diffusivity value from above equation, thermal conductivity for each specimen is determined through following equation [16].

$$\kappa = \alpha \rho c \quad (4)$$

Where, on left side κ denotes thermal conductivity in (W/ m k) and on right side, c denotes specific heat capacity in (j/g k) of respective specimen determined through calorimeter (DSC Q1000) determined in above section with ρ as density in (kg/m³). The density of respective specimen is determined by mass/volume relation. Where the



mass is determined by using the electronic mass balance (JM10002) with precision of 0.01 g provided by Zhejiang Ltd China and volume by ($L \times W \times H$) mm relation for each specimen.

3. Result and Discussion

Raman spectrum was conducted for assuring smoothness and uniform coating of graphene layer on copper metal skeleton. The two peaks of Raman spectrum at $1500 \text{ (cm}^{-1}\text{)}$ and $2650 \text{ (cm}^{-1}\text{)}$ confirms uniform deposition of graphene and bands ratio <1 confirms single layer coating shown in figure 3.

The graph in figure 5 shows the relation between the porosity and the thermal conductivity of GcC foam paraffin composite. The result shows that the effective thermal conductivity of the GcC foam decreased as the porosity of the foam was increased. Maximum thermal conductivity was seen at porosity of 0.90 which was 8.6 W/(m.K) while minimum thermal conductivity of 3 W/ (m.K) was seen at porosity of 0.980. The thermal conductivity was enhanced by 286.6% as porosity was varied from 0.98 to 0.90.

The graph in figure 6 shows that the pore density and pore size have inverse relation. As the pore density was increased, the porosity decreased.

The graph shows the inverse relation between the pore density (PPI) and infiltration ratio. As the pore density increased, the infiltration ratio of the paraffin decreased. Maximum infiltration ratio of 90 % was achieved. 100% infiltration ratio cannot be achieved due to the slight difference in the solidification rates of PCM. The solidification of the paraffin on the outer side of the metal foam starts early as compare to the inner side of the metal foam. There is also slight difference in the density of the paraffin when it in solid form as compare to paraffin that is in liquid form. When the PCM cools down this density difference causes the shrinkage of PCM and small cavity is formed on the inner side of PCM which does not allow complete infiltration of PCM in metal foam.

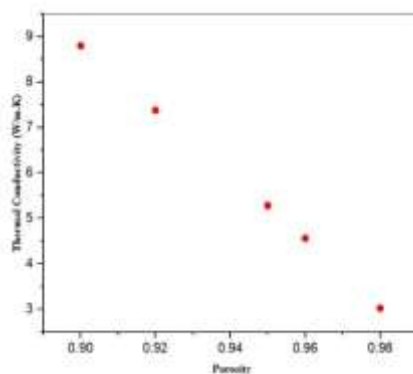


Figure 5. Comparison between porosity and thermal conductivity

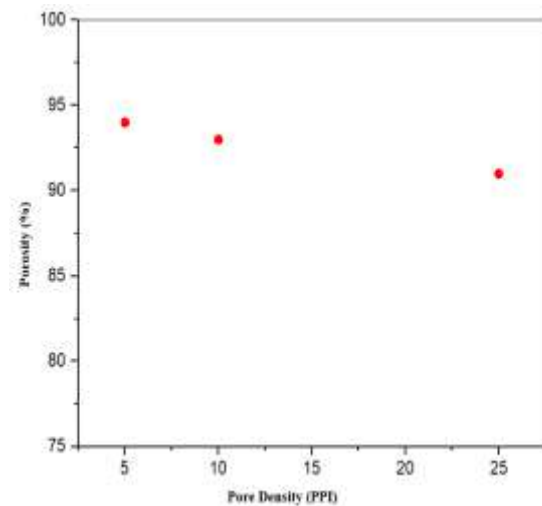


Figure 6. Comparison between pore density and porosity

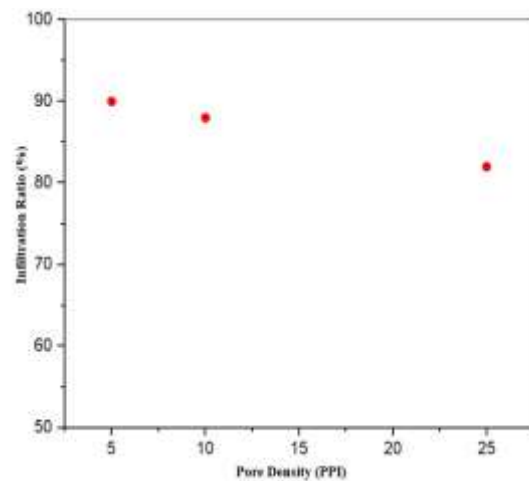


Figure 7. Comparison between pore density and infiltration ratio

4. Conclusion

The effective thermal conductivity of GcC foam was found at different porosity. The GcC foam was filled with paraffin. Chemical vapor deposition technique was used to coat the copper metal foam. The graphene coating layer was about 1-2nm on the metal foam. Raman spectroscopy was used to measure the smoothness of the graphene coating layer on the copper foam. The thermal conductivity of the GcC foam was found using the laser flash technique. Following outcomes are mentioned below.

- The thermal conductivity was highest at the porosity of 0.9 and decreased gradually as the porosity increases with all above cases.
- The effective thermal conductivity of the graphene coated metal foam was increases significantly as compare to the pure paraffin.



The thermal conductivity of the paraffin was enhanced by 44 times.

REFERENCE

- [1] H. Eslamnezhad and A. B. Rahimi, "Enhance heat transfer for phase-change materials in triplex tube heat exchanger with selected arrangements of fins," *Appl. Therm. Eng.*, 2016.
- [2] Z. Khan, Z. Khan, and A. Ghafoor, "A review of performance enhancement of PCM based latent heat storage system within the context of materials , thermal stability and compatibility," *Energy Convers. Manag.*, vol. 115, pp. 132–158, 2016.
- [3] W. Wu, X. Yang, G. Zhang, K. Chen, and S. Wang, "Experimental investigation on the thermal performance of heat pipe-assisted phase change material based battery thermal management system," *Energy Convers. Manag.*, vol. 138, pp. 486–492, 2017.
- [4] S. Shi *et al.*, "Non-steady experimental investigation on an integrated thermal management system for power battery with phase change materials," *Energy Convers. Manag.*, vol. 138, pp. 84–96, 2017.
- [5] P. Goli, H. Ning, X. Li, C. Y. Lu, K. S. Novoselov, and A. A. Balandin, "Thermal Properties of Graphene – Copper – Graphene Heterogeneous Films," 2014.
- [6] R. Kizilel, R. Sabbah, J. R. Selman, and S. Al-hallaj, "An alternative cooling system to enhance the safety of Li-ion battery packs," vol. 194, pp. 1105–1112, 2009.
- [7] K. Lafdi, O. Mesalhy, and S. Shaikh, "Experimental study on the influence of foam porosity and pore size on the melting of phase change materials," vol. 083549, 2007.
- [8] Z. Wang, Z. Zhang, L. Jia, and L. Yang, "Paraf fi n and paraf fi n / aluminum foam composite phase change material heat storage experimental study based on thermal management of Li-ion battery," *Appl. Therm. Eng.*, vol. 78, pp. 428–436, 2015.
- [9] W. Wang, X. Yang, Y. Fang, J. Ding, and J. Yan, "Enhanced thermal conductivity and thermal performance of form-stable composite phase change materials by using b -Aluminum nitride," *Appl. Energy*, vol. 86, no. 7–8, pp. 1196–1200, 2009.
- [10] Y. Cui, C. Liu, S. Hu, and X. Yu, "Solar Energy Materials & Solar Cells The experimental exploration of carbon nanofiber and carbon nanotube additives on thermal behavior of phase change materials," *Sol. Energy Mater. Sol. Cells*, vol. 95, no. 4, pp. 1208–1212, 2011.
- [11] H. Tian, L. Du, X. Wei, S. Deng, W. Wang, and J. Ding, "Enhanced thermal conductivity of ternary carbonate salt phase change material with Mg particles for solar thermal energy storage," *Appl. Energy*, vol. 204, pp. 525–530, 2017.
- [12] H. Zheng and C. Wang, "Numerical and Experimental Studies on the Heat Transfer Performance of Copper Foam Filled with Paraffin," 2017.
- [13] A. Hussain, C. Y. Tso, and C. Y. H. Chao, "Experimental investigation of a passive thermal management system for high-powered lithium ion batteries using nickel foam-paraf fi n composite," *Energy*, vol. 115, pp. 209–218, 2016.
- [14] K. C. Chan, C. Y. Tso, A. Hussain, and C. Y. H. Chao, "A theoretical model for the effective thermal conductivity of graphene coated metal foams," *Appl. Therm. Eng.*, vol. 161, no. July, p. 114112, 2019.
- [15] X. Hu, F. Zhu, and X. Gong, "Experimental and numerical study on the thermal behavior of phase change material in fi ltrated in low porosity metal foam," *J. Energy Storage*, vol. 26, no. July, p. 101005, 2019.
- [16] T. Lian *et al.*, "Rapid thermal conductivity measurement of porous thermal insulation material by laser flash method," *Adv. Powder Technol.*, vol. 27, no. 3, pp. 882–885, 2016.



Optimization of the number of vanes of a centrifugal pump to improve hydraulic efficiency for calcium chloride solution

Hafiz Ahmad Hassan¹, Awais Ali², Muhammad Farooq³

1. ahmad1011478@gmail.com
2. awaisalirafiq@gmail.com
3. Engr.farooq@uet.edu.pk

Abstract

This paper focuses on the effect of changing the number of blades/vanes of a centrifugal pump on the hydraulic performance for a 37% calcium chloride solution at a temperature of 55°C. The analysis was done using computational fluid dynamics (CFD). A single parameter i.e. the number of vanes was altered whereas, the rest of the parameters e.g. the volume flow rate, fluid density and rotational speed were kept constant. Commercial code ANSYS 15.0 was used to design a centrifugal pump and ANSYS CFX Solver was used to run the simulations. Calcium chloride solution properties were incorporated into ANSYS CFX manually. *K-epsilon* (*k-ε*) turbulence model was used for the simulations. As the effect of number of blades on the pump's performance is a complicated phenomenon, therefore, different number of blades were used to predict maximum outlet head. The simulations showed that changing the number of vanes changes the outlet pressure or head accordingly.

Key Words: Centrifugal pump, Hydraulic efficiency, Impeller, Blade number, CFD.

1. Introduction

Due to its numerous applications, ranging from industry to household, the yearly production of calcium chloride will reach to about 3.4 million tons in 2019 according to Independent Commodity Intelligence Services, United Kingdom. Whether it is produced as a solution or a solid, centrifugal pumps are used to transfer its solution from one location to another during the process. Therefore, attention should be paid towards optimizing the centrifugal pump, used for calcium chloride solution, for minimum energy consumption.

Centrifugal pump is a widely used mechanical device which imparts centrifugal force to the fluid by means of a rotating impeller. The mechanical energy of the pump is converted into the hydrodynamic energy of the fluid. As compared to gear pumps, centrifugal pumps are more vigorous and wear resistant and should be preferred if they meet the head and flow requirements for viscous fluids [1]. But, as the viscosity of the liquid changes, the results obtained change as well [2-6]. Using a viscous fluid increases both the lubrication and frictional losses. Though the former is beneficial, the latter reduces the hydraulic efficiency [7]. Therefore, performance of the pump depends a great deal on viscosity and hence, optimization of pump is inevitable for a fluid of specific viscosity. The researchers focus mainly on two performance parameters of centrifugal pumps which are cavitation performance and hydraulic performance [8, 9].

Most of the research has now been converted to numerical simulations i.e. computational fluid dynamics (CFD) and the results obtained from CFD are compared with experimental setups [10-14]. Two of the most widely used software for the CFD simulations are ANSYS CFX and OpenFOAM [15, 16].

Different researchers vary a chosen design parameter while keeping other parameters constant. At first, a combination of design parameters is made. After that, simulations are run using either of the above mentioned software. After a number of iterations, the results are compared and a combination is chosen for optimum pump efficiency. The impeller design parameters e.g. number of blades have significant effect on hydraulic efficiency of pump. If the number of blades is lower than the optimum number, then losses will increase due to the presence of a secondary flow whereas, if the number of blades is too high, frictional losses will increase due to the increasing number of impeller channels [17].

By changing the inlet and outlet angles of impeller, the shape and thinness of blades can significantly improve the hydraulic performance of the pump [18]. By reducing the gap between impeller neck ring and casing wear ring, the entry of liquid into the inlet of the pump can be made smoother and hence, efficiency can be improved [19]. Even though the hub and shroud blade angle variation has a major effect on cavitation, its



impact on hydraulic performance is negligible except for the shroud blade angle for high discharge flow rate [20]. Meridional shape of hub and shroud can also be altered to achieve optimization of pump performance. It reduces the frictional losses, improves velocity distribution and makes streamlines more smooth in the path of fluid and can increase the efficiency up to 6.1% [21]. Clearance between shroud and impeller casing is also an important optimization factor. By moving the impeller axially, significant changes in pump performance and hydraulic efficiency can be witnessed. As the clearance between the impeller and shroud increases, the efficiency of pump decreases [22].

Impeller trimming is also a famous technique to improve pump performance. For volute casings, generally the impeller is cut to smaller diameters. Other than that trailing edge is reworked [23-25]. Another perspective is to optimize the impeller for reducing vibrations caused by the fluid. Vibrations can damage the pump and affect its performance [26]. The shape of volute can also be varied to minimize the hydraulic forces acting on the impeller due to interaction between impeller and volute. For a slope volute the pressure pulsations are relatively lower than a spiral volute [27-29]. Many researchers have done a lot of work to improve the efficiency of a centrifugal pump, but none of the research has been carried out using calcium chloride solution as the fluid. As the viscosity of the fluid changes, the behavior of the pump changes accordingly. Therefore, the optimized parameters used to design a pump for a mundane liquid like water will not be the same for calcium chloride.

Given the wide range of applications of centrifugal pump in calcium chloride manufacturing, it is necessary to optimize its design to achieve maximum hydraulic efficiency. Number of vanes of the impeller will be optimized to gain maximum efficiency. With higher efficiency, energy consumption will be significantly improved.

2. Methodology

The following fig. 1 shows the approach taken to carry the research. Number of vanes used in industry are mostly 6. But in current study random numbers starting from 4 to 11 will be used for a simple research model and end results will be compared.

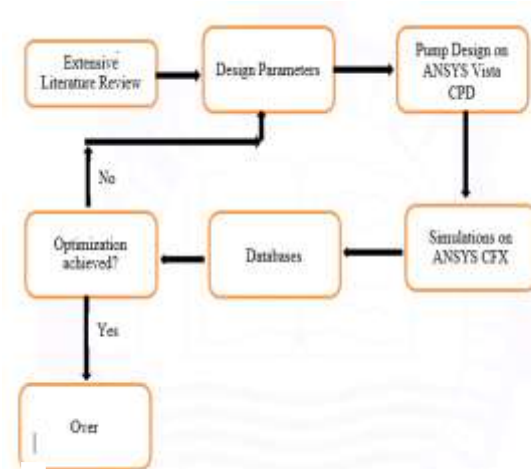


Fig. 1 Research methodology for the optimized number of blades

Commercial code ANSYS 15.0 was used to design the pump and run simulations.

i. ANSYS Vista Centrifugal Pump Design (CPD)

Blade geometry was generated using ANSYS Vista CPD and BladeGen. The parameters were collected from Ittehad Chemicals Limited (Kala Shah Kaku) which include volume flow rate = 15m^3 , head = 18m, speed = 2900rpm, density = 1350kg/m^3 .

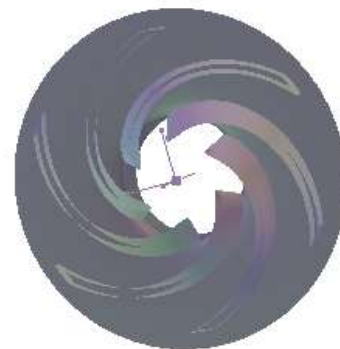


Fig. 2 Impeller generated in BladeGen

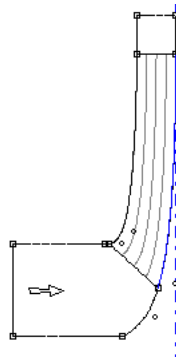


Fig. 3 Meridional flow path in BladeGen

ii. Mesh Generation

The most important phase of CFD analysis i.e. mesh generation was done on TurboGrid and Mesh modules. The mesh for volute was generated in Mesh whereas, that for the rotating parts and fluid was created in TurboGrid which is a specially designed module of ANSYS dedicated to turbomachinery. In the TurboGrid module, the mesh method was changed to target passage mesh size and a mesh was generated. To make the model mesh independent, mesh was chosen from coarse to medium to fine until unchanged results were achieved.

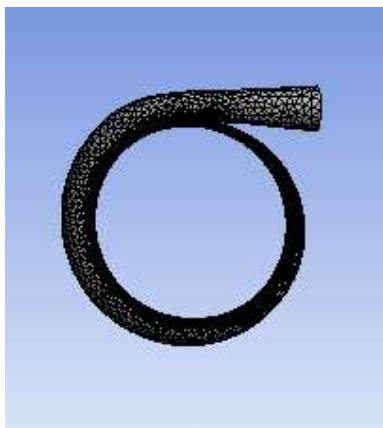


Fig. 4 Mesh generation in Mesh

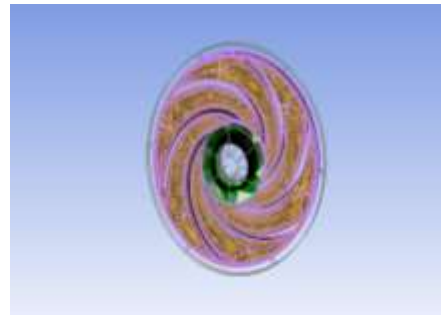


Fig. 5 Mesh generation in TurboGrid

Table 1 Mesh Data

Nodes	
Rotating Part	61054
Stationary Part	55522
Elements	
Rotating Part	52026
Stationary Part	158088

iii. Setup and Solution

After the mesh was generated, ANSYS Analysis system CFX was used to setup the solution and run simulations. In turbomode of the setup phase, the fluid properties for calcium chloride were manually entered as given by the table 2.

Table 2 Properties of 37% Calcium Chloride

Molecular weight	255.102 kg/kmol
Dynamic viscosity	4 cp
Density	1350 kg/m ³
Specific heat at constant pressure	2300 g/kj
Reference temperature	55°C

Rotating and stationary components were assigned to volute and impeller respectively. Steady state analysis type was chosen. K-Epsilon turbulence model was selected Maximum iterations were set to 500 unless the solution does not converge, in which case the solution was run again from previous solution data. For



convergence criteria, an RMS value of 10^{-4} was selected for residual target. After the setup, solution was run in platform message passing interface (MPI) local parallel mode.

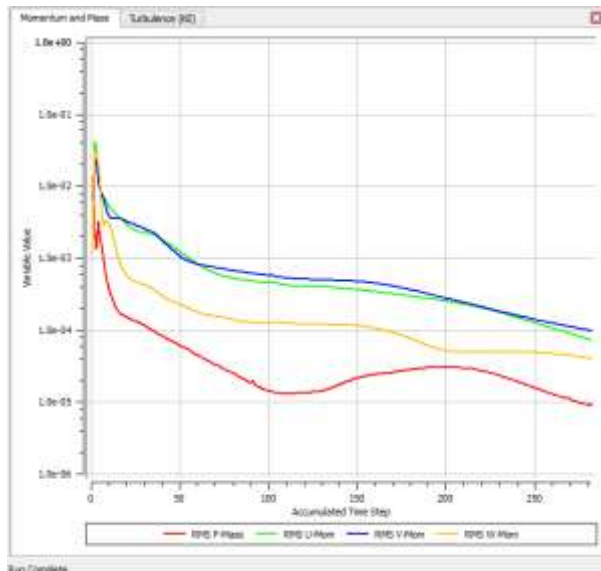


Fig. 6 Simulations in CFX solver

3. Results and Discussion

According to the simulations, the maximum head is achieved with 4 blades and minimum with 11 blades. There is no obvious relation between number of vanes and the head. Highest head can be observed at 4 number of vanes. The head first decreases from 4 blades to 6 blades and 8 blades but then increases for 10 blades. After that it decreases suddenly for 11 number of blades. A graphical representation of the results achieved is shown in fig. 7:



Fig. 7 Graphical representation of results

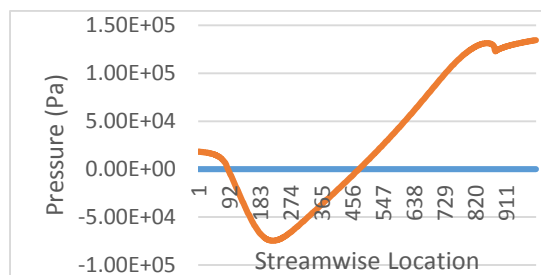


Fig. 8 Inlet to outlet pressure with 11 vanes



Fig. 9 Inlet to outlet pressure with 10 vanes



Fig. 10 Inlet to outlet pressure with 8 vanes

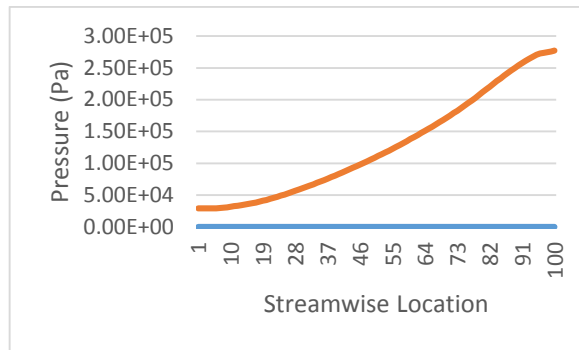


Fig. 11 Inlet to outlet pressure with 6 vanes

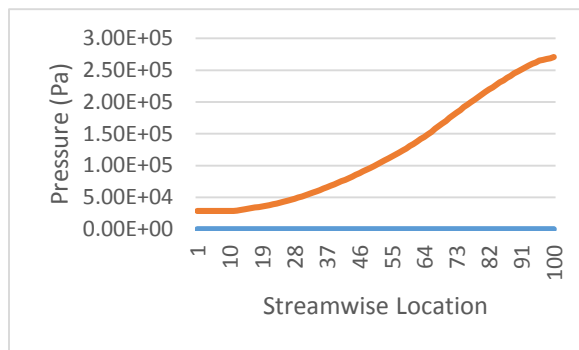


Fig. 12 Inlet to outlet pressure with 4 vanes

4. Conclusions

It can be concluded that there is no explicit trend for different number of blades and pump performance. The effect of the number of vanes on the performance of a centrifugal pump is complex and a lot of attention should be paid on the subject because the difference in outlet head is quite noticeable for varied number of blades. For a different set of pump parameters, the results may differ from the current investigation. Therefore, for a given set of pump parameters, the optimum number of blades should be chosen using simulations for the best design. An optimum design leads to better efficiency and, in turn, less electricity consumption. A comprehensive theoretical studies of the effect of blades on the pressure can also be conducted in terms of turbulence, frictional losses, velocity at circumference of impeller and passage losses etc.

REFERENCES

1. Olimstad, G., M. Osvoll, and P.H.E. Finstad, *Very Low Specific Speed Centrifugal Pump—Hydraulic Design and Physical Limitations*. Journal of Fluids Engineering, 2018. 140(7).
2. Morrison, G., et al., *Development of Modified Affinity Law for Centrifugal Pump to predict the effect of Viscosity*. Journal of Energy Resources Technology, 2018. 140(9): p. 092005.
3. Patil, A. and G. Morrison, *Affinity law modified to predict the pump head performance for different viscosities using the Morrison number*. Journal of Fluids Engineering, 2019. 141(2): p. 021203.
4. Morrison, G., et al. *Evaluation of effect of viscosity on an electrical submersible pump*. in *ASME 2017 Fluids Engineering Division Summer Meeting*. 2017. American Society of Mechanical Engineers Digital Collection.
5. Li, W.-G., *Effects of viscosity on turbine mode performance and flow of a low specific speed centrifugal pump*. Applied Mathematical Modelling, 2016. 40(2): p. 904-926.
6. Derakhshan, S. and M. Bashiri, *Investigation of an efficient shape optimization procedure for centrifugal pump impeller using eagle strategy algorithm and ANN (case study: slurry flow)*. Structural and Multidisciplinary Optimization, 2018. 58(2): p. 459-473.
7. Abazariyan, S., R. Rafee, and S. Derakhshan, *Experimental study of viscosity effects on a pump as turbine performance*. Renewable energy, 2018. 127: p. 539-547.
8. Pei, J., et al., *Cavitation optimization for a centrifugal pump impeller by using orthogonal design of experiment*. Chinese Journal of Mechanical Engineering, 2017. 30(1): p. 103-109.
9. Pei, J., et al., *Optimization on the impeller of a low-specific-speed centrifugal pump for hydraulic performance improvement*. Chinese Journal of Mechanical Engineering, 2016. 29(5): p. 992-1002.
10. Shim, H.-S. and K.-Y. Kim, *Evaluation of Rotor–Stator Interface Models for the Prediction of the Hydraulic and Suction*



- Performance of a Centrifugal Pump*. Journal of Fluids Engineering, 2019. 141(11).
11. Shim, H.-S., K.-Y. Kim, and Y.-S. Choi, *Three-Objective Optimization of a Centrifugal Pump to Reduce Flow Recirculation and Cavitation*. Journal of Fluids Engineering, 2018. 140(9).
 12. Bellary, S.A.I., et al., *Application of computational fluid dynamics and surrogate-coupled evolutionary computing to enhance centrifugal-pump performance*. Engineering Applications of Computational Fluid Mechanics, 2016. 10(1): p. 171-181.
 13. Limbach, P. and R. Skoda, *Numerical and Experimental Analysis of Cavitating Flow in a Low Specific Speed Centrifugal Pump With Different Surface Roughness*. Journal of Fluids Engineering, 2017. 139(10).
 14. Shim, H.-S., et al., *Three-objective optimization of a centrifugal pump with double volute to minimize radial thrust at off-design conditions*. Proceedings of the Institution of Mechanical Engineers, Part A: Journal of Power and Energy, 2016. 230(6): p. 598-615.
 15. De Donno, R., et al., *Shape optimization of the ERCOFTAC centrifugal pump impeller using open-source software*. Optimization and Engineering, 2019: p. 1-25.
 16. Wang, W., et al., *Application of different surrogate models on the optimization of centrifugal pump*. Journal of Mechanical Science and Technology, 2016. 30(2): p. 567-574.
 17. Elyamin, G.R.A., et al., *Effect of impeller blades number on the performance of a centrifugal pump*. Alexandria Engineering Journal, 2019. 58(1): p. 39-48.
 18. Yousefi, H., et al., *Numerical simulation for obtaining optimal impeller's blade parameters of a centrifugal pump for high-viscosity fluid pumping*. Sustainable Energy Technologies and Assessments, 2019. 34: p. 16-26.
 19. Matlakala, M., et al., *Impact of Design Parameters on the Performance of Centrifugal Pumps*. Procedia Manufacturing, 2019. 35: p. 197-206.
 20. Dönmez, A.H., Z. Yumurtacı, and L. Kavurmacıoğlu, *The effect of inlet blade angle variation on cavitation performance of a centrifugal pump: a parametric study*. Journal of Fluids Engineering, 2019. 141(2): p. 021101.
 21. Pei, J., W. Wang, and S. Yuan, *Multi-point optimization on meridional shape of a centrifugal pump impeller for performance improvement*. Journal of Mechanical Science and Technology, 2016. 30(11): p. 4949-4960.
 22. Lei, C., et al., *Effect of Axial Clearance on the Efficiency of a Shrouded Centrifugal Pump*. Journal of Fluids Engineering, 2015. 137(7).
 23. Detert Oude Weme, D.G.J., et al., *Prediction of the Effect of Impeller Trimming on the Hydraulic Performance of Low Specific-Speed Centrifugal Pumps*. Journal of Fluids Engineering, 2018. 140(8).
 24. Qu, X. and L. Wang, *Effects of impeller trimming methods on performances of centrifugal pump*. Journal of Energy Engineering, 2016. 142(4): p. 04016008.
 25. Wang, K., et al., *Effects of impeller trim on performance of two-stage self-priming centrifugal pump*. Advances in Mechanical Engineering, 2017. 9(2): p. 1687814017692493.
 26. Qian, B., et al., *Optimization of a Centrifugal Impeller on Blade Thickness Distribution to Reduce Hydro-Induced Vibration*. Journal of Fluids Engineering, 2019. 142(2).
 27. Zhang, N., et al., *Experimental and numerical analysis of unsteady pressure pulsation in a centrifugal pump with slope volute*. Journal of Mechanical Science and Technology, 2015. 29(10): p. 4231-4238.
 28. Zhang, N., et al., *Experimental Investigation on Unsteady Pressure Pulsation in a Centrifugal Pump With Special Slope Volute*. Journal of Fluids Engineering, 2015. 137(6).
 29. Alemi, H., et al., *Effects of Volute Curvature on Performance of a Low Specific-Speed Centrifugal Pump at Design and Off-Design Conditions*. Journal of Turbomachinery, 2015. 137(4).



Design and Performance Analysis of 500kW Solar Power Electric Vehicle Charging Station

Rauf Ahmad¹, Hafiz Liaqat Ali¹, Muhammad Tahir Hassan^{1*}, Farrukh Arslan Siddiqui¹, Usama Bin Mehboob¹, Muzammil Asif¹, Muhammad Jaon Haider¹, Muhammad Mustahson Awasi², Muftooh Ur Rehman Siddiqi¹

1- Department of Mechanical Engineering, UCET, BZU Multan.

2 - Department of Mechanical Engineering, CECOS University, Peshawar.

*Corresponding Author's Email: tahirqureshi@bzu.edu.pk

Abstract

Electric Vehicles are having great importance because of no emissions, maintainance cost and running cost. In today's world of renewable energy, the technology has been developed in such a way that it can harness solar energy. Significant research is being done to charge electric vehicles through solar energy. In this paper, the economic, environmental and sensitivity analysis of a 500kW PV system installed in Multan, Pakistan is carried out. The annual average energy yield is found to be 730 MWh. The plant's average annual predicted energy yield is estimated as 827 MWh. Around 20.3% system losses are because of different factors like irradiance, ohmic wiring, module quality, temperature, and inverter. The data shows that maximum energy is generated during the months of March, April and September while, in December, it is minimum. A careful cost comparison between gas and electric vehicles shows a notable savings of almost \$509/vehicle/year as fuel cost and taxes in case electric vehicles charging from solar energy system with a pay-back period of 12 years. Emissions of carbondioxide gases are reduced by 2360 kg/vehicle/year. The results show that solar vehicle charging system in Pakistan can be a highly feasible project which can help to meet the future environmental challenges in the country.

Key words: Electric vehicle, Emissions, Sensitivity, Grid Connection, Annual Yield

1 Introduction

The total consumption of electricity in Pakistan is 95.90 TWh per year. This constitutes to 436 kWh energy consumption per capita. On regular basis, almost 140 million people living in Pakistan either suffer load shedding of more than 12 hours duration or don't have access to electricity[1].

In 2015, 195 countries including Pakistan presented a draft called as "Intended Nationally Determined Contributions (INDCs)". In Pakistan, a large amount of emissions is because of vehicles on the road and so to reduce these emissions, the concept of electric vehicles should be adopted at a faster rate. In Pakistan Intended Nationally Determined Contributions, Pakistan has committed to reduce emissions of transportations by 8% [2].

1.1 Solar Energy in Pakistan

In Pakistan, on horizontal surface, falling of the typical global irradiation is of almost 195 to 255 watts/m²/day. This all constitutes to 1.9 to 2.3 MWh/m²/year and sunshine hours of almost 1,500 to 3,000. In a year, the sun shines at its best for almost 180 to 295 days in almost every region of Pakistan. It has yearly mean sunshine duration of 8 to 8.5 hours / day with day-to-day global insulation of 5.2 to 5.5 kWh/m²/day. In this region, the availability for day-to-day global radiation is of 23MJ/m². Fig. 1 shows Pakistan's solar radiation map which depicts that land area of Pakistan has solar radiation at almost all sites [3].

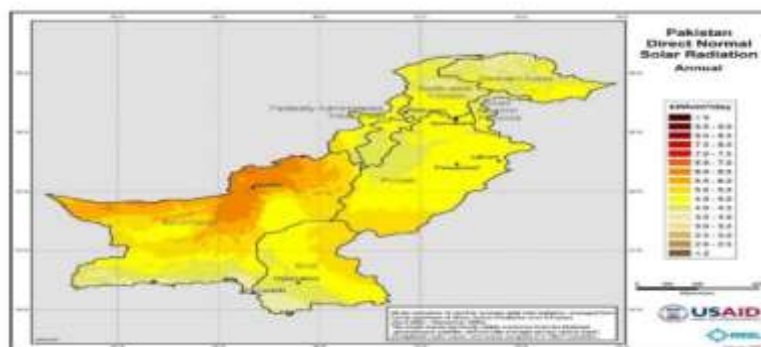


Figure 1: Map of Pakistan showing solar radiation [4]



1.2 Production of Energy in Pakistan

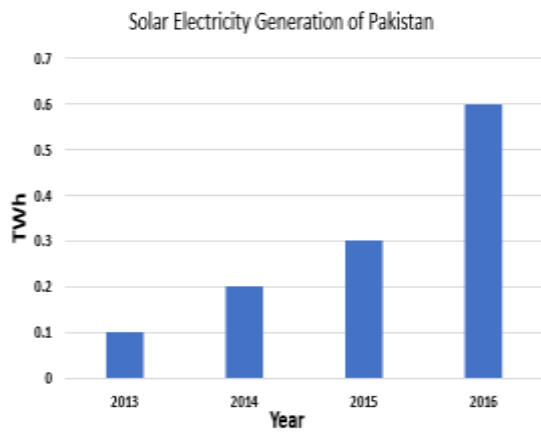


Figure 2: Solar Electricity Generation [5]

Fig. 3 shows the energy sources of Pakistan which clearly shows that only 3% of total energy is being produced through renewable energy sources.

Electricity Fuel Mix of Pakistan

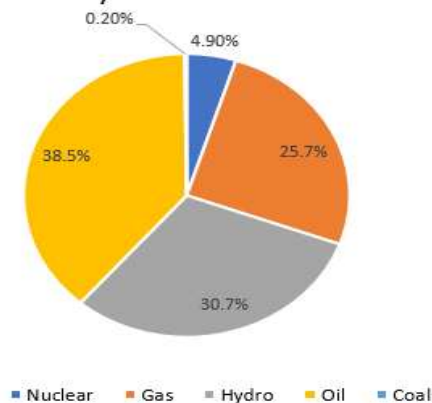


Figure 3: Electricity Mix of Pakistan 2014 [6]

1.3 Importance of Electric Vehicles

In 2017, worldwide sales of EVs have been increased by 54% that seems to be a good approach of achieving Sustainable Development Scenario-2015 and rising to 0.9% in 2020 and 14% in 2030 [7]. Government of Pakistan has given almost 16% relief from custom duty on EV's charging stations and 15% relief from regulatory duty on EVs.

Table 1 shows that for EVs, there are no motor taxes and vehicle purchase taxes per year. Besides, CO₂ emissions in fuel cars are much where there are no CO₂ emissions in case of EVs. According to a rough idea, about 2360 kg of CO₂ emissions can be reduced per year by an electric vehicle. This factor contributes towards a better and healthy environment.

Table 1: Comparison of Taxes and CO₂ Emissions from Vehicles [8]

Properties	Fuel Car	Grid Charged	Solar Charged
Motor Taxes/year	\$13.00	0\$	0\$
Vehicle Purchase tax	\$685.00	0\$	0\$
Tax Benefit (PV, EV)	No	Yes	Yes
CO ₂ emission (g/km)	166	0	0
CO ₂ emission for 20000 km (kg/year)	2360	0	0

Usage of Renewable Energy

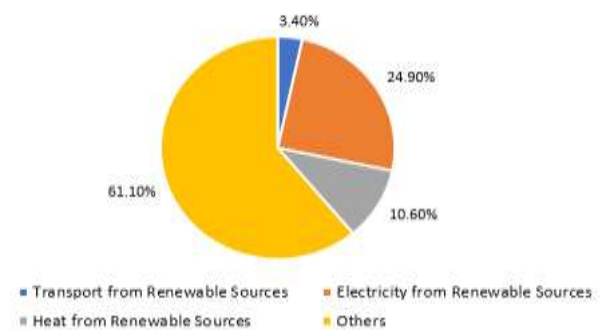


Figure 4: Usage of Renewable Energy [9]

As compared to engine vehicles, electric vehicles promise for a noise free and clean environment as they emit little or no emissions. These electric vehicles can be charged using EV-PV charger. Table 2 shows that initial cost of EV is much high as compared to the fuel car but the running cost of EV is very low as compared to the fuel cars.

Table 2: usage of fuel, grid and solar charged car [10].

Properties	Fuel car	Grid charged	Solar charged
Annual distance (km)	20,000	20,000	20,000
Fuel price (\$/L or \$/kWh)	0.74	0.13	0.068
Fuel use per 100 km (L or kWh)	5	17	17
Fuel/year (L or kWh)	1,000	3,400	3,400
Fuel costs/ year	\$740.00	\$442.00	\$231.20
Saving/year for 1 car	\$0.00	\$298.00	\$509.00
Saving/year for 4 cars	\$0.00	\$1,192.00	\$2,036.00



Savings for 10 years for 4 cars	\$0.00	\$11,920.00	\$20,360.00
Extra Investment for 4 EV	\$0.00	\$4,752.00	\$4,752.00
Total benefit 10 years 4 cars	\$0.00	\$7,168.00	\$15,608.00

of the types of solar charging stations are: Users can have 80% or even more of their charging at home. In a single-family home, as the electricity rates are of residential cheap rates, charging can be done in garage of homes and this is much economical method [11]. Parked charging station is the profitable scheme which has cost or without cost open with the corporation of the holder of the parking location. Fast public charging stations are located at relaxation point or at recreation stops to go to larger distance places such as tours or world journey. Many researchers [8, 12-20] have contributed in the study of PV-solar charging stations, and their contribution is revealed in Table 3.

1.4 Solar charging stations

In solar station of charging, solar energy is supplied to electric vehicles or to charge batteries. Some

Table 2: Summary of work related to PV-solar charging station

Author Name	Contribution	Year
Mouli et al. [8]	The use of electric vehicle PV system contributed towards less or no emission and is very economical	2016
Mouh et al. [12]	The perfect storage size of solar station can reduce the 25% battery from grid and he best solar angle was 28°	2016
Hung et al. [13]	They studied about increasing solar capacity by reduction in various energy losses	2016
Fatahabadi et al. [14]	They studied that grid connected plant can give enough electricity for peak loads from wind and solar both.	2017
Seyezhai et al. [15]	They describe the importance of sun-oriented energy usage in vehicles and gives consideration of different vehicle applications	2016
Khanghah et al. [16]	They discussed on a modern way of using solar charging stations and the use of power garage.	2017
Ashqui et al. [17]	They describe the use of external battery for the storage of solar power for night usage.	2017
Lee et al. [18]	They describe that by converting parking shed into charging station vehicles can be charged during parking	2016
Zeman et al. [19]	The feasibility of integrating a local storage to the EV-PV charger is evaluated	2016
Bhatti et al. [20]	They studied different techniques for the utilizing energy and concluded that Heuristic rule is good for energy management	2016

2 Methodology

Methodology used is based on seven major steps that are described below:

- i) Design of the solar PV modules array.
- ii) Design of system backup through batteries
- iii) Estimation of annual yield
- iv) Estimation of the number of vehicles charging per day per month and annually
- v) System design for AC grid connection as backup / excess transmission.
- vi) System optimum performance and sensitivity analysis
- vii) Cost analysis of the PV system

2.1 Design of Solar PV System

In the 500kW PV system, polycrystalline PV module of 320 W are used. Total panels require for 500 kW system are 1560. These panels are arranged in 104 strings with 15 panels in each string for maximum

output. Panels are tilted at angle of 30°. Total area covered by the panels is 3092 m² and total area required to arrange panels is 5770 m².

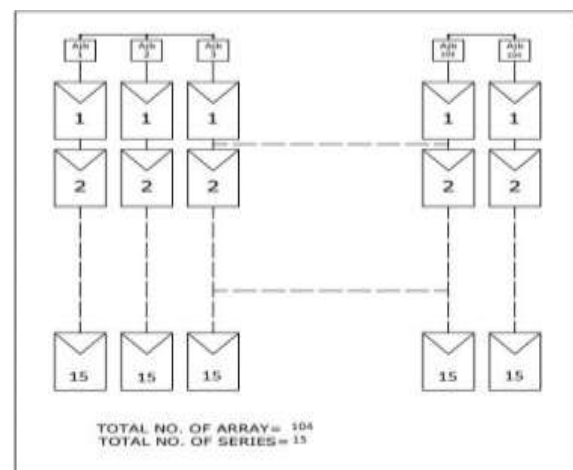


Figure 5: Design of PV Module Array [3]



The main features of the panel are given below:

Table 4: VOLTEC Solar Panel Characteristics [10]

Characteristics	Specifications	Characteristics	Specifications
Dimensions and weight	1980 x 998 x 42mm (± 1 mm) / 26 kg	Electric safety	Class II
Type of cells	Multi-crystalline or Monocrystalline	Maximum system voltage (V)	1000 V
Dimensions and no. of cells / panel	156 x 156 mm/72 cells	Maximum reverse current IRM	15 A
Solar glass	Tempered glass, thickness 4 mm	Peak Power Watts (Wp)	320
Connectors and wiring	MC4-Cable length: 2 x 1.10 m	Efficiency (%)	16.2

In 500kW solar system, invertors of 10kW are used. Total invertors required for our project are 49.

Table 5: Invertor Characteristics [21]

Characteristics	Specifications	Characteristics	Specifications
Maximum no of DC connections	2	MPP voltage range	340-800 VDC
Maximum Efficiency (%)	94.9	Max input voltage	900 VDC
Euro Efficiency (%)	93.1	Max open circuit voltage	850 VDC
Invertor Dimensions W x H x D mm	600 x 1481 x 600	AC current harmonics at rated power	<3%

2.2 Design of system backup through batteries

Backup is required for night time and for cloudy days. This project requires batteries for 10% backup of the total energy output. Vanadium redox batteries with rated power of 25kW are used. Number of batteries needed for this project are 8. Some other specifications are as follows.

Table 6: Vanadium Redox Battery Specifications [22]

Characteristics	Specifications	Characteristics	Specifications
Rated Voltage	125V	Rated Energy Efficiency	72%
Rated Current	200A	Maximum Power	100kW
Rated Power	25kW	Limited Charge Voltage	160V

2.3 Estimation of Annual yield

The annual yield obtained from PVsyst program according to local conditions of Multan shows that annual yield of 500kW PV system is 827 MWh per year at 30° tilt. The actual annual yield calculated for 500kW system is as follow.

Table 7: Actual Annual Yield Calculation

500kW PV System	Calculation	Annual Yield (MWh)
Annual Yield	40 * 50 * 365	730

2.4 Estimation of the number of vehicles charged

Five different electric vehicles are selected and number of full charges per day, per month and annually are calculated. Annual yield is calculated manually for these calculations because software gives us maximum possible output under optimum conditions. The results obtained are described in Table 8.

Table 8: No of Vehicles Charged by PV energy 730 MWh [8]

EV	Battery Size (kWh)	kWh/100 km	Full Charge s/ day	Full Charges/ month	Full charge s/ year
Leaf	24	12	83	2534	30416
Chevrolet Spark	18.4	17	108	3579	42942
Tesla Model S	75	20.5	26	811	9733
Mitsubishi MiEV	16	12.5	125	3802	45625
Ford Fusion	7.6	22.5	263	8004	96052



These vehicles can save a huge amount of fossil fuel and cause zero pollution with zero emission of CO₂.

2.5 System design for grid connection

The system required a grid connection because of two factors. First one is when sun shines in summer, excess power is generated that can be transmitted to grid and secondly when the solar energy is unavailable then grid provides power to run appliances and system. This design is used to meet the short-term peak demand without drawing any energy from the grid.

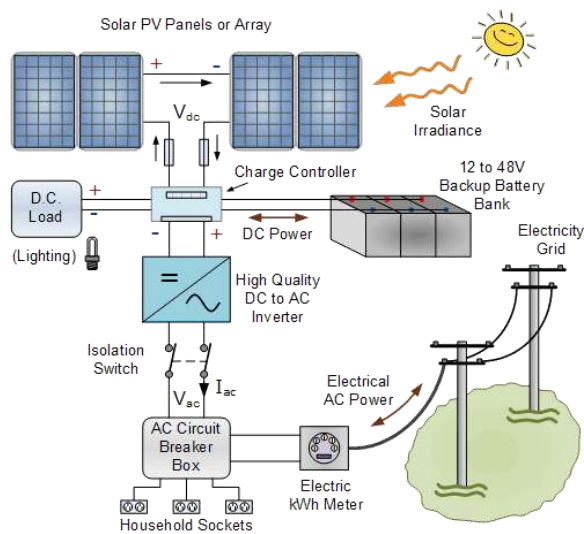


Figure 6: PV System with Grid Connection [23]

Table 10: Cost Analysis by PVsyst

Investment			
PV Modules (320Wp)	1560 units	143 US\$ / unit	223080 US\$
Supports / Integration		24 US\$ / module	37183 US\$
Inverters (10.0kW ac)	49 units	1487 US\$ / unit	72863 US \$
Settings, wiring			37183 US\$
Battery			80000 US\$
Gross Investment			450309 US\$
Financing			
Gross Investment (without tax)			450309 US\$
Taxes on Investment	Rate 10.0 %		45031 US\$
Gross Investment (including tax)			495340 US\$
Net Investment (all tax included)			495340 US\$
Annuities	(Loan 5 % over 15 year)		47722 US\$ / year
Annual running cost: maintenance			10000 US\$ / year
Total Yearly cost			57722 US\$ / year
Energy cost			
Produced Energy			827 MWh / year
Cost of produced energy			0.07 US\$ / kWh

2.6 System optimum performance and sensitivity analysis

In this analysis many simulations are performed at different tilt angle of the module. The output of the system is analyzed at every angle. Month for which the output yield is maximum is noted for every tilt angle. Results are given below.

Table 9: System Performance & Sensitivity Analysis

Tilt Angle (Degree)	Maximum Annual Yield (MWh)	Month with Maximum Output (MWh)
26	825	April-74.02
27	826	April-74.15
28	826	April-73.88
29	827	March-73.72
30	827	March-73.74
32	825	March-73.70

Overall annual yield is maximum for 29- and 30-degree tilt angle. So, modules in this project will be tilted at 30°.

2.7 Cost analysis of the PV system

Total cost of 500kW system is as follow. If loan from bank is taken at 10% interest rate, then total payable amount is called net investment. Running cost is the annual cost in terms of cleaning of solar panels and wages of the workers.



3 Results and Discussion

The totally yearly effective energy at the panel output was the 880.43 MWh and the energy transmitted to the grid 826.89 MWh. These variations are calculated through PVsyst software as shown in Table 11.

Table 11: Balances and main results

Month	E-Array MWh	E-Grid MWh	Month	E-Array MWh	E-Grid MWh
January	67.29	63.37	July	73.08	68.41
February	66.60	62.59	August	72.74	68.12
March	78.45	73.74	September	78.29	73.51
April	78.31	73.54	October	75.79	71.33
May	77.11	72.32	November	73.69	69.36
June	72.58	68.01	December	66.51	62.59
Year				880.43	826.89

E-Array is the energy output of the PV system and E-Grid is the energy transmitted to the grid after losses. The performance ratio ranges between 76% and 85% and with an average value of 79.8% as shown in Fig 7. These values are also estimated by PVsyst program.

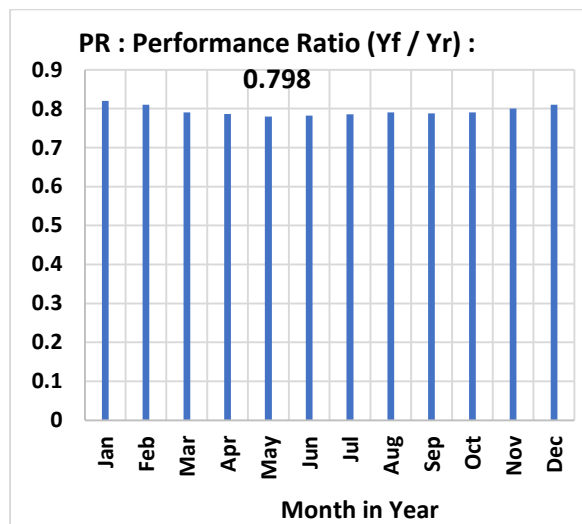


Figure 7: Performance Ratio of PV Module

The normalized production without loss ranges 4.3 kWh/kWp/day (December) to 6.4 kWh /kWp/ day (April) and with considered all losses then the normalized production is 3.9kWh/kWp/day (December) to 4.8 kWh/ kWp/day(April). The yearly produced useful output is 4.54 kWh/ kWp/ day as shown in Fig. 8.

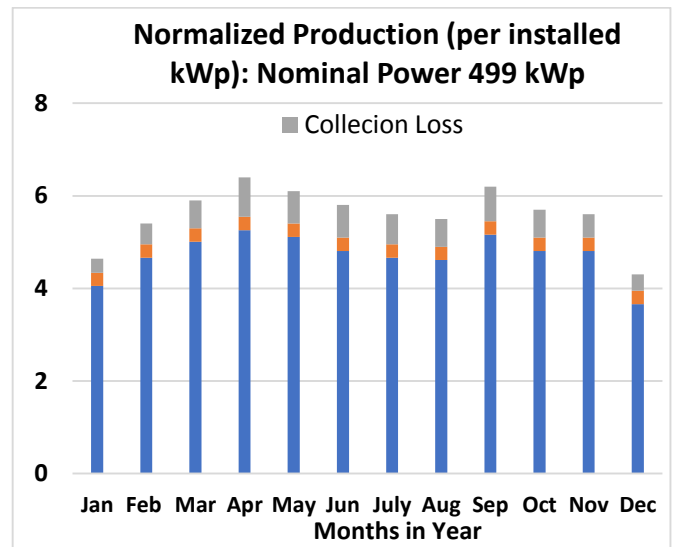


Figure 8: Normalized Production

The comparison between Global Irradiation when panel is horizontal and when it is tilted at 30° is shown in Fig. 9.

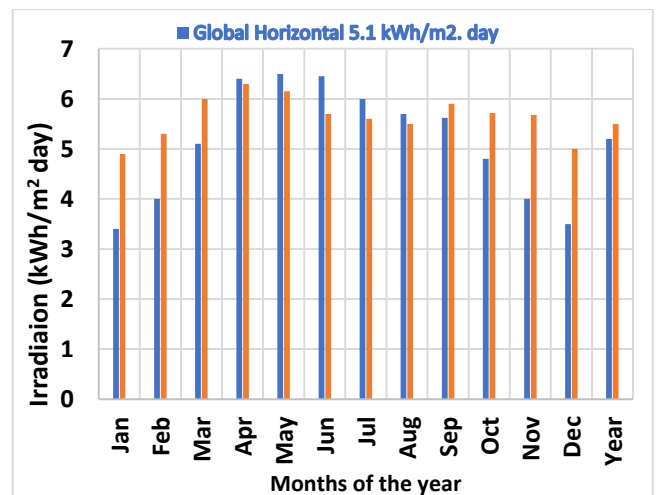


Figure 9: Comparison of horizontal and Tilted plane

Table 12: Losses Range in PV Module

Losses	Range (%)
Losses due to irradiations	-0.2
Loss due to temperature	-11.2
Losses due to module quality	+0.7
Losses due to array mismatch	+1
Losses due to ohmic wiring	-1.1
Losses due to inverter conversion (AC to DC)	+6.1



The global horizontal radiations are maximum in summer month like April to Sep and minimum in winter month like Oct to Feb. System losses including the ambient temperature, wiring, irradiance, module quality, arrays mismatch and inverter losses are calculated through PVsyst software are summarized in Table 12.

4 Conclusion

The economic benefits, sensitivity analysis and CO₂ emission reduction of a 500kW solar powered EV charging station in Multan (Pakistan) have been analyzed in this paper. An electric vehicle can save up to \$509 annually. Vehicle purchase tax and annual car taxes are also zero for an electric vehicle which are \$685 and \$13 respectively for a gasoline vehicle. CO₂ emissions can be reduced on an average of 166 gm /km/vehicle. This results in annual CO₂ emission reduction of 2360 kg /year/vehicle. Solar energy can be the most feasible and cost effective way of charging an EV in Pakistan. PV modules were adjusted at different tilt angles and saw that maximum annual yield was produced at 30⁰. The electricity price from PV System is \$0.7/kWh, which is less than the current grid price of \$0.13/kWh. Using a 500kW PV System, 730 MWh/year is produced. This provide annual charging capability for 30416 completely charged Nissan Leaf, 42942 full charged Chevrolet Spark and 9733 full charged Tesla Model S. The dual benefit of lower fuel price and no emissions make EV charging from PV System, both economic and environmental friendly.

By keeping PV module at tilt angle 30⁰, the total yearly effective energy at the output produced was 880.43MWh but the energy transmitted to grid was 826.89MWh only. Electric vehicles can be charged at low energy cost. Total energy produced is estimated 827 MWh/year using PVsyst software. By selling this energy at the rate 0.07 \$/kWh, revenue generated will be 57890\$ per year which is more than yearly cost with a payback period of 12 years only.

For future study, the authors recommend finding a way for fast charging to minimize the charging and waiting time for vehicles. The high charging capacity is also a challenge. More Research and innovation in technology are required to find a way to store large amount of solar energy for long period of time.

REFERENCES

- [1]. Anwar, J., Analysis of energy security, environmental emission and fuel import costs under energy import reduction targets: A case of Pakistan. *Renewable and Sustainable Energy Reviews*, 2016. 65: p. 1065-1078.
- [2]. Lin, B. and I. Ahmad, Analysis of energy related carbon dioxide emission and reduction potential in Pakistan. *Journal of cleaner production*, 2017. 143: p. 278-287.
- [3]. Sharma, V. and S. Chandel, Performance analysis of a 190 kWp grid interactive solar photovoltaic power plant in India. *Energy*, 2013. 55: p. 476-485.
- [4]. Sheikh, M.A., Renewable energy resource potential in Pakistan. *Renewable and Sustainable Energy Reviews*, 2009. 13(9): p. 2696-2702.
- [5]. Khalil, H.B. and S.J.H. Zaidi, Energy crisis and potential of solar energy in Pakistan. *Renewable and Sustainable Energy Reviews*, 2014. 31: p. 194-201.
- [6]. Valasai, G.D., et al., Overcoming electricity crisis in Pakistan: A review of sustainable electricity options. *Renewable and Sustainable Energy Reviews*, 2017. 72: p. 734-745.
- [7]. Fulton, L., et al., Technology roadmap: Electric and plug-in hybrid electric vehicles. 2009: OECD/IEA.
- [8]. Mouli, G.R.C., et al. Economic and CO₂ Emission Benefits of a Solar Powered Electric Vehicle Charging Station for Workplaces in the Netherlands. in 2016 IEEE Transportation Electrification Conference and Expo (ITEC). 2016.
- [9]. Pata, U.K., Renewable energy consumption, urbanization, financial development, income and CO₂ emissions in Turkey: Testing EKC hypothesis with structural breaks. *Journal of Cleaner Production*, 2018. 187: p. 770-779.
- [10]. Mouli, G.R.C., et al. Economic and CO₂ emission benefits of a solar powered electric vehicle charging station for workplaces in the Netherlands. in 2016 IEEE Transportation Electrification Conference and Expo (ITEC). 2016. IEEE.
- [11]. Wu, T., et al., Setting up charging electric stations within residential communities in current China: Gaming of government agencies and property management companies. *Energy Policy*, 2015. 77: p. 216-226.
- [12]. Mouli, G.C., P. Bauer, and M. Zeman, System design for a solar powered electric vehicle charging station for workplaces. *Applied Energy*, 2016. 168: p. 434-443.
- [13]. Hung, D.Q., Z.Y. Dong, and H. Trinh, Determining the size of PHEV charging stations powered by commercial grid-integrated PV



- systems considering reactive power support. *Applied Energy*, 2016. 183: p. 160-169.
- [14]. Fathabadi, H., Novel grid-connected solar/wind powered electric vehicle charging station with vehicle-to-grid technology. *Energy*, 2017. 132: p. 1-11.
- [15]. Sankar, B. and R. Seyezhai, Simulation and Implementation of Solar Powered Electric Vehicle. Vol. 07. 2016. 643-661.
- [16]. Khanghah, B.Y., et al. Combined solar charging stations and energy storage units allocation for electric vehicles by considering uncertainties. in 2017 IEEE International Conference on Environment and Electrical Engineering and 2017 IEEE Industrial and Commercial Power Systems Europe (EEEIC / I&CPS Europe). 2017.
- [17]. Ashique, R.H., et al., Integrated photovoltaic-grid dc fast charging system for electric vehicle: A review of the architecture and control. Vol. 69. 2016.
- [18]. Lee, S., et al. Shared solar-powered EV charging stations: Feasibility and benefits. in 2016 Seventh International Green and Sustainable Computing Conference (IGSC). 2016.
- [19]. Chandra Mouli, G.R., P. Bauer, and M. Zeman, System design for a solar powered electric vehicle charging station for workplaces. *Applied Energy*, 2016. 168: p. 434-443.
- [20]. Bhatti, A.R., et al., Electric vehicles charging using photovoltaic: Status and technological review. *Renewable and Sustainable Energy Reviews*, 2016. 54: p. 34-47.
- [21]. Sreenath, B., et al., Analysis of Output DC Current Injection in 100kW grid connected VACON 8000 Solar inverter.
- [22]. Fathima, A., et al., Intelligence-based battery management and economic analysis of an optimized dual-Vanadium Redox Battery (VRB) for a Wind-PV HYBRID SYSTEM. *Energies*, 2018. 11(10): p. 2785.
- [23]. Ferdous, S.M., et al., Energy Efficiency Constraints in Photovoltaic Power Generation Systems. Vol. 3. 2018. 41-47.



Effect of using nano-lubricant on COP of Vapor Compression System: An Experimental Study

Saif Ullah Khalid¹ *, Muhammad Saleem Khan²

1-Mechanical Engineering Department, University of Engineering and Technology, 47050 Taxila, Pakistan

2-Metallurgy and Materials Engineering Department, University of Engineering and Technology, 47050 Taxila, Pakistan

*Corresponding author: saifullahkhalid425@gmail.com

Abstract

The concept of nanotechnology in vapor compression system is very novel and much familiar to the modern researchers due to its high output orientation. In this research Al_2O_3 nano particles were added in polyol-ester (POE) oil to form a nano-lubricant. Nano-lubricant was used inside compressor instead of simple lubricant. R134a was used as refrigerant. 1.5% wt to vol concentration of nanoparticles in POE oil proved itself best for enhancing thermal performance characteristics. Due to adding nanoparticles in base lubricant thermal conductivity and viscosity were increased while compressor work and wear were reduced. At different ambient temperatures experiments were conducted. Coefficient of performance (COP) of vapor compression system increased from 6.4% to 3.91% due to use of nano-lubricant. The increase in COP was observed higher at low ambient temperatures, as ambient temperature increased the difference in COP of POE and nano-lubricant decreased. COP increased 6.4% at ambient temperature $34^\circ C$ while it increased 3.91% at $37^\circ C$. No significant change in pressure was observed due to using nano-lubricant.

Key words: Nano-lubricant, Coefficient of performance, Thermal performance, Refrigerant, Nanoparticles.

1. Introduction

The sole expected outcomes of research, in different prospects of a refrigeration systems is to get high COP, while keeping in view environment friendly factor. In this regard many novel areas have been explored like introducing new refrigerants, altering properties of lube oils, redesigning components of a refrigeration system etc.

There is much diversity in refrigerants being used in modern refrigeration systems. The properties of refrigerant directly impact the energy consumption and refrigeration effect produced. A refrigerant having higher thermal conductivity would result in greater heat transfer in evaporator as well as in condenser section, hence decreasing temperature difference between inside and outside the system, so increasing refrigeration effect and COP [1]. The utilization of high thermal conductivity edge is not limited to the selection of a best refrigerant, but it is spread up to preparation of a refrigerant possessing desired properties. Use of nanotechnology has got much abundance in refrigeration industry nowadays. Using nanofluids in refrigeration systems is a new frontier to augment COP. Nano-refrigerants have high thermal conductivity and viscosity than base refrigerants but lower specific heat [2]-[3] and their use decreases work of compression required by decreasing irreversible friction loss, which is 15-20 % in case of compressor [4]. The decrease in work of compression can also be achieved by using

nanoparticles in compressor oil, this would also enhance thermal conductivity of refrigerant, both these

techniques increase COP [5]. The nano-lubricants have higher thermal conductivity and viscosity and good antifriction and anti-wear properties but lower surface tension compared to base lubricants, these thermo physical properties effect work of compression [6]. With increase in temperature viscosity and thermal conductivity of nano-lubricants decreases in a non-Newtonian manner [7]. The addition of nanoparticles does not affect solubility of refrigerant in lubricant [8]. So nano-refrigerant and nano-lubricants are very interesting aspects in modern refrigeration systems, much research has been carried out in this area and still there is more need to explore [9].

J. Gill et al [10] performed detailed analysis on thermal performance characteristics of domestic refrigerator by using R134a and LPG as refrigerants, mineral oil (MO) and polyol-ester oil (POE) as lubricants and mineral oil based TiO_2 , Al_2O_3 and SiO_2 nano-lubricants. It was concluded that lowest irreversibility, highest COP and lower compressor discharge temperature was obtained by using nano-lubricant. Using LPG refrigerant and TiO_2 -MO (0.2g/L TiO_2) nano-lubricant 56.3% higher COP was obtained compared to R134a/POE combination.

Vipin Nair and Co researchers [11], investigated effect of using polyalkylene Glycol (PAG) based Al_2O_3 nano-



lubricant on COP of vapor compression system. 6.5% increase in COP was observed compared to simple PAG/ R134a and compressor exit temperature was observed much lower ensuring long compressor life.

Deokar et al [12], showed experimentally that thermal conductivity of nano-lubricants increases with increasing nanoparticles concentration in base lubricant. They used Al_2O_3 and ZnO nanoparticles in POE oil. They studied the heat transfer enhancement and pressure drop in a 9.5mm micro fin tube, with 20% wt concentration of Al_2O_3 in POE oil and R410A refrigerant, 15-40% enhancement in heat transfer coefficient was obtained with no significant drop in pressure.

Pico et al [13] studied the effects of adding nano particles in POE oil and using it in combination with R410A refrigerant. They used 0.1% and 0.5% by mass diamond-based POE nano-lubricant. The results were very interesting, addition of nanoparticles increased COP while compressor and oil sump temperatures were reduced.

R134a is most widely used refrigerant in domestic refrigerators [14] and compatible lubricant with this refrigerant is POE [15]. Therefore, there is need to explore thermal performance of domestic refrigerator having R134a refrigerant with POE based nano-lubricant.

In this paper authors presented experimental work to check effect of POE oil based Al_2O_3 nano-lubricant on thermal performance characteristics of vapor compression system. It was a preliminary investigation for checking behaviour of POE based nano-lubricant.

2. Methodology

Out of many refrigerants being used today R134a (tetrafluoroethane $\text{CF}_3\text{CH}_2\text{F}$) was selected as refrigerant for experimentation because it is non-toxic, non-flammable, non-corrosive and above all environment friendly. It is replacement of R12 CFC and has boiling point -26.5°C . The base lube oil is polyol-ester POE. The outcome is different for different combinations of refrigerants and lube-oil. The POE oil and R134a is commonly used combination in small refrigeration systems. POE oil is inexpensive and easily available.

The type, size and shape of nanoparticles specially effects experimental outcomes [16]-[17], therefore selection of nanoparticles type and size is very critical parameter. Al_2O_3 nanoparticles having spherical shape and nominal diameter 20nm and density 0.26 g/cm^3 were selected. With increase in size of nanoparticles sedimentation and capillary blockage increases while dispersibility decreases. With much decrease in size

coagulation and agglomeration increases. The optimum recommended size is 10nm to 50nm. Other reasons of selecting Al_2O_3 nanoparticles is their low price, hazardous to environment quality and high polarity. Lube oil is also polar therefore polarity of nanoparticles assists in dispersibility and long-term stability of nanofluid.

Nano-lubricant was prepared by sonication process in an ultrasonic oscillator model (Branson 5510). The two step nanofluid preparation method was used. Long term stable and homogeneous mixture was very necessary in this experiment therefore sonication was done for 12 hours. As a result of sonication, a stable mixture was obtained, stability of nano-lubricant was about 8 days. 1.5% vol by mass nano-lubricant was prepared, 6.375 grams of Al_2O_3 nanoparticles were mixed with 425ml of POE.

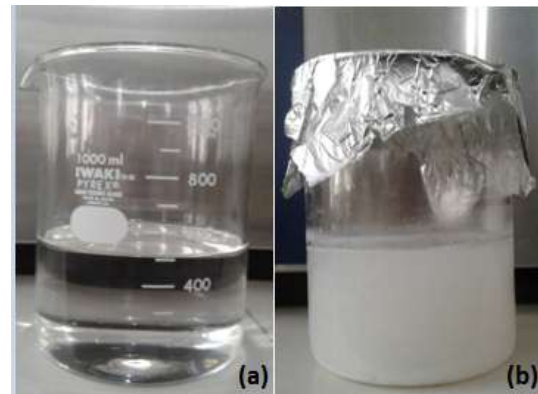


Fig 1: (a) POE Oil (b) Al_2O_3 /POE nano-lubricant

3. Experimental Setup

Experimental setup consists of a domestic refrigerator in which at four different locations pressure gauges and thermocouples were attached. Pressure gauges used were mechanical bourdon gauges and k-type thermocouples were used. A pressure gauge and a thermocouple were attached in between each two components of vapor compression system that is compressor, condenser, expansion valve and evaporator. The thermocouples were attached to data acquisition system (model number LXI 34972A), which was attached to a PC. An electric heater was used for controlling room temperature. A domestic refrigerator was used in experiment. A schematic is given below:

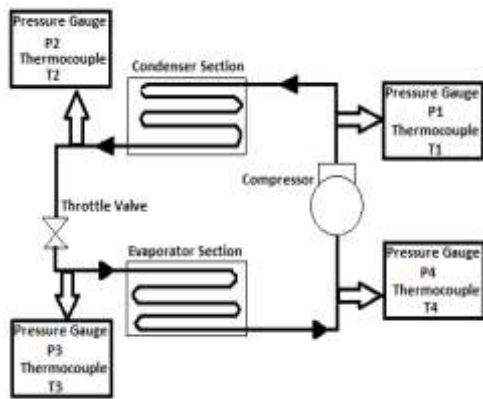


Fig 2: Experimental setup schematic

4. Results and Discussion

Initially experiments were performed on R134a/POE based system. Results were saved at different ambient temperatures. The ambient temperature was varied through an electric heater. Then system was charged with R134a/ nano-lubricant and experiments were repeated at various room temperatures. Comparison of results gives significance of using nano-lubricants. The condenser temperature increases with increasing ambient temperature, the increase is even more rapid while using nano-lubricant compared to POE oil. The temperature was lower in case of nano-lubricant because it has higher thermal conductivity hence good ability to dissipate heat. While using POE oil, condenser temperature was observed 2.6% higher than that with nano-lubricant and it was 1.9% higher at ambient temperature 37°C. The difference decreases as ambient temperature increases.

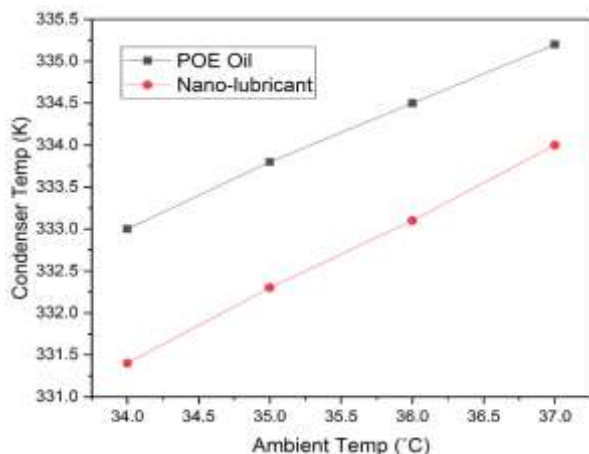


Fig 3: Comparison of condenser temperature while using POE oil and Nano-lubricant

Variation in evaporator temperature was also observed with variation in ambient temperature. The decrease in evaporator temperature was faster when nano-lubricants

were used, compared to POE oil. The relative difference was highest at lowest ambient temperature of 34°C and it was observed 62%. Compressor work increases due to increase in condenser temperature or decrease in evaporator temperature and refrigeration effect decreases with decrease in evaporator temperature. No significant change in working pressures was observed by using nano-lubricant instead of POE oil.

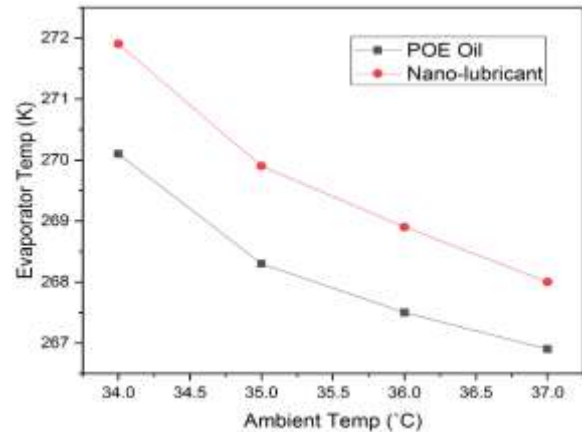


Fig 4: Comparison of evaporator temperature while using POE oil and Nano-lubricant

COP is function of condenser and evaporator temperatures. COP decreases with increase in compressor work (due to increasing condenser temperature and decreasing evaporator temperature) and decrease in refrigeration effect (due to decrease in evaporator temperature). Nano-lubricant has higher thermal conductivity compared to base POE oil, therefore compressor work is lower in case of nano-lubricant. By using nano-lubricants COP was observed 6.4% higher than using simple POE oil at ambient temperature 34°C and difference was 5.6%, 4.9% and 3.91% at 35°C, 36°C and 37°C respectively.

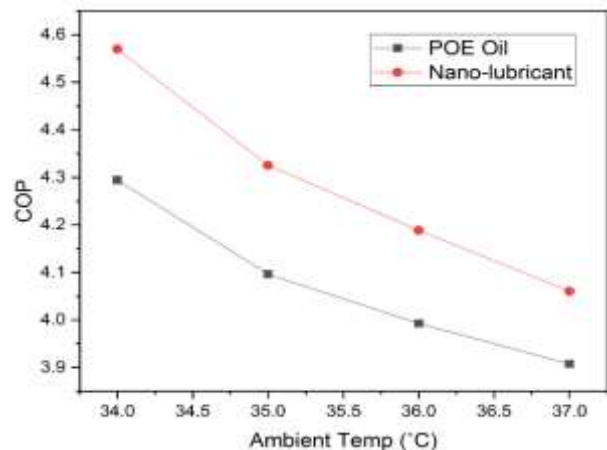


Fig 5: Comparison of COP while using POE oil and Nano-lubricant



5. Conclusion

Use of nano-lubricant compared to simple lubricant in compressor was observed highly significant. Use of nano-lubricant increases COP of system. Nano-lubricants reduces work of compression, irreversible friction work and wear therefore results in increasing compressor life. The results were even more significant at lower ambient temperatures. As ambient temperature increases the relative advantage of using nano-lubricant decreases. Nano-lubricant possesses special properties like high thermal conductivity and high viscosity

compared to base fluid, which are main source of thermal performance augmentation. No significant change in working pressure was observed by using nano-lubricant.

Acknowledgements

The authors acknowledge the work of previous researchers and pioneers, which was used as source of guidance and reference. The authors also acknowledge support of PEL refrigerator service center Rawalpindi.

REFERENCES

- [1] A. Bhattad, J. Sarkar, and P. Ghosh, "Improving the performance of refrigeration systems by using nano fluids : A comprehensive review," *Renew. Sustain. Energy Rev.*, vol. 82, no. August 2016, pp. 3656–3669, 2018.
- [2] W. Jiang, G. Ding, and H. Peng, "International Journal of Thermal Sciences Measurement and model on thermal conductivities of carbon nanotube nanorefrigerants," *Int. J. Therm. Sci.*, vol. 48, no. 6, pp. 1108–1115, 2009.
- [3] R. S. Anand, C. P. Jawahar, A. B. Solomon, J. Suresh, J. C. Jacob, and M. M. Tharakan, "Materials Today : Proceedings Heat transfer properties of HFE and R134a based Al₂O₃ nano refrigerant in thermosyphon for enhancing the heat transfer," *Mater. Today Proc.*, no. xxxx, 2019.
- [4] S. Yang, X. Cui, Y. Zhou, and C. Chen, "Study on the effect of graphene nanosheets refrigerant oil on domestic refrigerator performance Étude sur l'effet des huiles frigorigènes à nanofeuilles de graphène sur les performances d'un réfrigérateur domestique," *Int. J. Refrig.*, vol. 110, pp. 187–195, 2020.
- [5] S. S. Sanukrishna and M. J. Prakash, "Thermal and rheological characteristics of refrigerant compressor oil with alumina nanoparticles — An experimental investigation," *Powder Technol.*, vol. 339, pp. 119–129, 2018.
- [6] A. V Melnyk, "A complex investigation of the nanofluids R600 a -mineral oil-AL₂O₃ and R600 a -mineral oil-TiO₂. Thermophysical properties Une étude complexe des propriétés thermophysiques des nanofluides R600a-huile minérale-Al₂O₃ et R600a-huile," *Int. J. Refrig.*, vol. 74, pp. 488–504, 2017.
- [7] S. S. Sanukrishna, S. Vishnu, T. S. Krishnakumar, and M. J. Prakash, "Effect of oxide nanoparticles on the thermal, rheological and tribological behaviours of refrigerant compressor oil : An experimental investigation Étude expérimentale sur l'effet des nanoparticules d'oxyde sur le comportement thermique, rhéologique et tribologique de l'huile du compresseur frigorifique," *Int. J. Refrig.*, vol. 90, pp. 32–45, 2018.
- [8] S. Bobbo, L. Fedele, M. Fabrizio, S. Barison, S. Battiston, and C. Pagura, "Influence of nanoparticles dispersion in POE oils on lubricity and R134a solubility Influence de la dispersion des nanoparticules dans les huiles et la solubilité," *Int. J. Refrig.*, vol. 33, no. 6, pp. 1180–1186, 2010.
- [9] M. Z. Sharif, W. H. Azmi, R. Mamat, and A. I. M. Shaiful, "Mechanism for improvement in refrigeration system performance by using nanorefrigerants and nanolubricants – A review," *Int. Commun. Heat Mass Transf.*, vol. 92, no. February, pp. 56–63, 2018.
- [10] J. Gill, J. Singh, O. S. Ohunakin, and D. S. Adelekan, "Energetic and exergetic analysis of a domestic refrigerator system with LPG as a replacement for R134a refrigerant, using POE lubricant and mineral oil based TiO₂, SiO₂ and Al₂O₃ -lubricants Analyse énergétique et exergetique d'un réfrigérateur domestique fonctionnant avec du GPL en remplacement du R134a, utilisant du lubrifiant POE et des lubrifiants à base d'huiles minérales TiO₂, SiO₂ et Al₂O₃," *Int. J. Refrig.*, vol. 91, pp. 122–135, 2018.
- [11] V. Nair, A. D. Parekh, and P. R. Tailor, "Highlights :," *Int. J. Refrig.*, 2019.
- [12] P. S. Deokar and L. Cremaschi, "Effect of Nanoparticles Aspect Ratio on the Two Phase Flow Boiling Heat Transfer Coefficient and Pressure Drop of Refrigerant and Nanolubricants Mixtures in a 9.5 mm Micro-fin Tube.," 2016.
- [13] D. Fernando, M. Pico, L. Ribeiro, P. S.



- Schneider, E. Pedone, and B. Filho, "Department of Mechanical Engineering , Federal University of Rio Grande do Sul US CR," *Int. J. Refrig.*, 2018.
- [14] C. Aprea, A. Greco, A. Maiorino, C. Masselli, and A. Metallo, "HFO1234ze as drop-in replacement for R134a in domestic refrigerators : an environmental impact analysis," *Energy Procedia*, vol. 101, no. September, pp. 964–971, 2016.
- [15] K. Górny, A. Stachowiak, and P. Tyczewski, "Lubricity evaluation of oil – refrigerant mixtures with R134a and R290 Évaluation de la lubricité des mélanges d ' huile et des frigorigènes R134a et R290," *Int. J. Refrig.*, vol. 69, pp. 261–271, 2016.
- [16] H. Reza, M. Reza, M. Goodarzi, and M. Dahari, "Particle size and type effects on heat transfer enhancement of Ferro-nano fluids in a pulsating heat pipe," *Powder Technol.*, vol. 301, pp. 1218–1226, 2016.
- [17] H. J. Kim, S. H. Lee, S. Bin Kim, and S. P. Jang, "The effect of nanoparticle shape on the thermal resistance of a flat-plate heat pipe using acetone-based Al₂O₃ nanofluids," *Int. J. Heat Mass Transf.*, vol. 92, pp. 572–577, 2016.



Fossil fuel based Carbon footprint of Pakistan and its role towards sustainable development

Muhammad Wajid Saleem^{1*}, Muhammad Hanzla Tahir^{1*}, Muhammad Wajid Ashfaq¹

1- Mechanical Engineering Department, University of Engineering & Technology, Lahore.

*Corresponding authors wajidsaleem@uet.edu.pk & 2019msres03@student.uet.edu.pk

Abstract

Climate change is becoming dangerous due to increase in Green House Gas (GHG) emissions. Carbon dioxide (CO₂) is one of the major gasses among these emissions. There are many techniques available to analyze these emissions. Carbon footprint analysis is one of them. In this study, carbon footprint analysis based on annual fossil fuel consumptions of Pakistan is being done. CO₂ emissions are calculated to be 137 million metric tonnes which is approximately 0.695 metric ton per capita for year 2017. Although these emissions are very low as compared to 25 other selected countries but the rate of these emissions is increasing rapidly. Hence proper attention is required to cope with these emissions to avoid any negative impact on environment.

Keywords: GHG emissions, Health issues, Fossil fuels, Carbon footprint, Sustainable-development.

1. Introduction:

Climate change has become the most serious concern of the entire world within the past few decades as the significant amount of carbon dioxide is released to the atmosphere resulting a lot of health related issues such as anthropogenic, headaches, dizziness, restlessness, a tingling or pins or needles feeling, difficulty breathing, sweating, tiredness, increased heart rate, elevated blood pressure, coma, asphyxia, and convulsions diseases[1].

Pakistan is one of the highly defenseless country regarding the effects of climate change[2]. CO₂ emission from the consumption of fossil fuels is usually considered as the major factor of climate change, so our main concern is to count down the emissions caused by fossil fuels in Pakistan in term of carbon footprint.

Carbon footprint is actually a technique by using which any of the organization can estimate their own contribution to global climate change. This help them plan better to mitigate the GHG emissions[3].

It is the amount of CO₂ emissions allied with all the actions of a person or an entity like a building, cooperation, country etc. it consists of all the direct radiations caused by a fossil fuel combustion in heating, cooking, manufacturing and transportation etc. as well as those emissions caused due to electricity generation. This technique is also often

include the emissions of other GHG emissions like methane, nitrous oxide and CFCs[4].

According to the European Environment Agency report, there are different secretarial perceptions, explaining the ideas and procedures for three unlike air emission accounting perceptions, which are based on Production, Territorial and Consumption.

The territorial perspective reflects emissions that are free to the atmosphere inside a country's limits and authority. This outlook links to the legally preserved practice used by independent states under international conventions like, UN Framework Convention on Climate Change.

The European Environment Agency report clarifies how the production perspective offers different insights, showing emissions resulting from the economic activities of a country's occupants and the businesses registered in the country.

The third method described in the report delivers a depletion perspective. This studies emissions related with goods and services, assigning them to the country where they are consumed, irrespective of where production of these goods and services result in emissions[5].

Sustainability is effectively warning global climate change to safe stages in long term is expected to involve linking climate change policies to sustainable development strategies for both developing and industrialized republics.

An examination of connections among climate change and sustainable development from a developing country viewpoint requisite jump by considering native and provincial conditions and



policy backgrounds. He recognized issues and approaches related to a growing government for lecturing climate change, here we have given various nationwide and region wide circumstances and significances for sustainable development containing economic outlines, political comforts, institutions and capacities. Here we have some summarized points to evaluate sustainable energy[6].

- Expanding an agenda for intellectual about climate change inside the wider framework of sustainable development.
- Discovering why rising states should pay attention about climate change;
- Finding and manipulating interactions for a policies and addressing tradeoffs.
- Consolidation institutions to address climate change in a combined way crosswise and inside the institutions leading the worldwide environment, diagonally to national departments, also across subdivisions and at different levels of government.
- Covering the global system to address climate change.

The crucial factors having impacts on sustainable development and their inter-dependencies. They mentioned that the sustainable development as the union of energy and resources sustainability, economic sustainability, environmental sustainability, and social sustainability, and debated their correlations as given in a figure.1 [7].

Actually our major concern is to achieve sustainability by mitigating CO₂ emissions, so according to this paper we have an idea, if we make a successful relationship among energy and resource sustainability, means to say if we shift towards renewable energy resources then our dependence on fossil fuel decreases as the result emissions will be less and we will achieve a sustainable system. Secondly, if we shift towards renewable our economic sustainability will also be achieved, like wise environmental sustainability is also achieved if we consume our indigenous source of energy, means to say non-conventional sources like solar, wind, biomass and hydro etc.



Figure 1 Sustainable development and its interdependent components [7].

To mitigate the effects of carbon dioxide initially we have to make a comprehensive overview of CO₂ emissions by conventional fuels by implementing statistical analysis to find out carbon footprint of Pakistan based on fossil fuel consumption annually per capita. A lot of researchers have done a great job but they have not yet calculated fossil fuel consumption per capita involving majors like Coal, Natural Gas and Oil for Pakistan. In which we have to calculate CO₂ emissions inside Pakistan territory by using data available at International Energy Agency[8].

We will do this case study according to given direction, Section.2 will be a methodology, Section.3 will reflect the Results and discussions, Section.4 will covers the conclusion while final Section.5 shows all the available references for this case study.

2. Methodology:

The estimation of carbon footprint involves certain key steps. The first step is to set up a boundary. For our study we decided to calculate the CO₂ emissions in Pakistan. We decided to use the guidelines provided by IPCC in 2006.[9] According to those guide lines carbon emissions are divided into three tiers. Tier 1 includes the direct emissions of the system. Tier 2 is more related to the indirect emissions which are somehow linked to the system. These includes the emissions due to electricity consumption which is being transported to the system via grid station. Tier 3 also focusses on indirect emissions but in encompasses emissions due to transportation of goods which is linked to the system.[10]



In our study, we decided to the formula being provided by IPCC 2006 guidelines. It is described as:

$$E_{GHG, fuel\ type} = FC_{fuel\ type} \times EF_{GHG, fuel\ type} \quad E.1$$

Here,

$E_{GHG, fuel\ type}$ = Green House Gas emissions, *tonne CO₂e*

$FC_{fuel\ type}$ = Fuel Consumption, *TJ*

$EF_{GHG, fuel\ type}$ = Country specific emission factor of selected fuel, *tonne CO₂e/GJ*

To utilize this formula we have to collect the required data first. For our approach we have decided to calculate the CO₂ emissions by fossil fuel consumption in Pakistan. We categorized these fossil fuels as; Coal, Petroleum and Natural Gas.

2.1- Fuel Consumption Data:

The data of the consumption of these fossil fuels was obtained from International Energy Agency website. These consumptions can be seen in figures 2, 3 and 4.

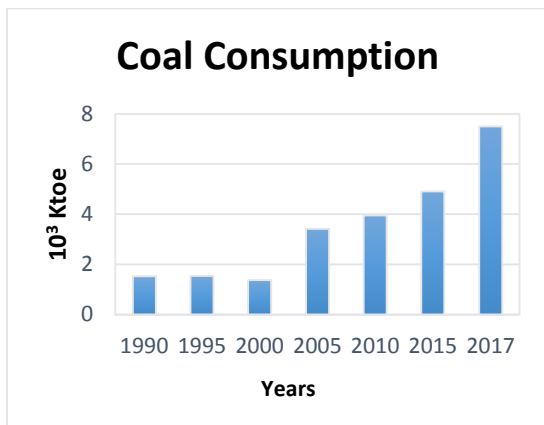


Figure 2 Coal Consumption in Pakistan till 2017 [11]

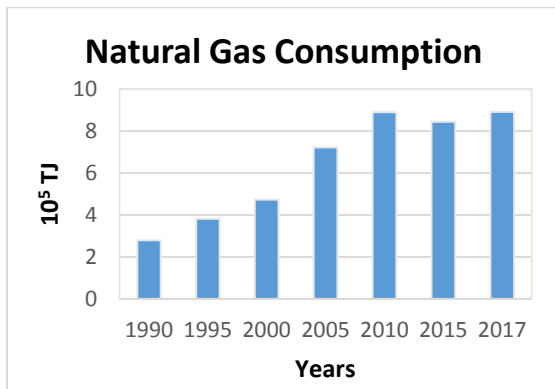


Figure 3 Natural gas consumption in Pakistan till 2017 [12]

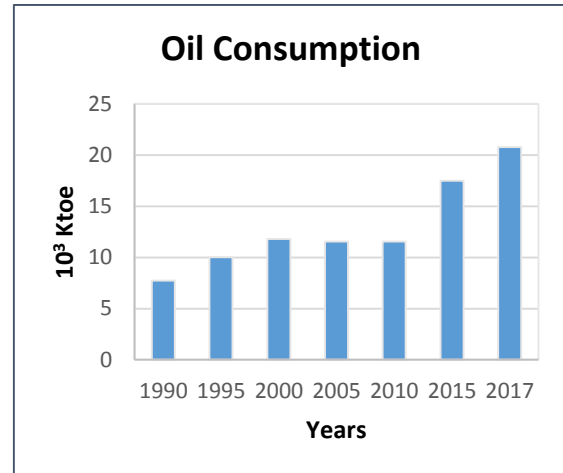


Figure 4 Oil consumption in Pakistan till 2017 [13]

2.2- Emission Factor Data:

The emission factors for coal, petroleum and natural gas for Pakistan were obtained from different authentic research papers and verified through authentic websites. The emission factor table is given below:

Table 1 Emission factors of coal, petroleum and natural gas [14]

Fuel Type	Emission factors, EF	Unit
Coal	0.094	<i>tonnes CO₂e/ GJ</i>
Petroleum	0.072	<i>tonnes CO₂e/ GJ</i>
Natural Gas	0.0503	<i>tonnes CO₂e/ GJ</i>

2.3- Calculation of CO₂ Emissions:

Using the above mentioned collected data, we used equation 1 to find the CO₂ emissions of respective fuel type. The CO₂ emissions for coal, petroleum and natural gas were found to be, 29.5, 62.6 and 44.9 million tonnes of CO₂e respectively. The sum of these emissions will be 137 million tonnes of CO₂e. A sector wise break down of CO₂ emissions with respect to each selected fuel type is also calculated. The results are shown in figure 7.



2.4- Per Capita Carbon Footprint:

In order to calculate the per capita carbon footprint of Pakistan we have divide the above mentioned emissions with the population of Pakistan during 2017. According to Google live population monitoring data, the overall population of Pakistan during 2017 was about 197 million. Hence the per capita emissions of Pakistan are 0.695 tonnes CO_{2e} per capita. (See figure 6).

2.5- Comparison of Pakistan's CF with other countries:

Lastly, the per capita emissions of Pakistan were compared with 25 selected countries throughout the world. Their emission data was collected from World Energy Outlook & International Energy Agency data base [8], [11], [12] & [13].

3. Results and discussions:

The sector wise CO₂ emissions of Pakistan for year 2017 are shown in figure 7. In case of natural gas, it can be seen that major contributors of CO₂ emissions are industrial, transport and residential sectors. The same trend can be seen for oil but this time transport sector accounts for 80% of CO₂ emissions. In case of coal, it was found that industrial sector accounts for 100% CO₂ emissions for year 2017.

According to the results of comparison made between selected countries, the per capita emissions of Pakistan are found to be very less (See figure 8,9). One can say that the impact of Pakistan in climate change is very low. Although the situation is not alarming yet but it does not mean that we don't have to do anything regarding sustainable development. It will be very wise for us to take some serious steps towards sustainable development.

As we can see in figure 5 that CO₂ emissions are rapidly increasing each year. It means that the situation is going to be extremely alarming in near future. Therefore, it's an hour of need to review our climate change policies. The possible solution is to start focusing on renewable energy resources and make suitable policies to utilize these resources more effectively. Pakistan has to invest a major amount of its budget on the import of fossil fuels. About 60 percent of power generation in Pakistan is done using fossil fuel based power plants. In other words, it relies greatly on these fossil fuels to meet its energy demand. If we start shifting from fossil fuels towards renewables, our dependency on other countries will be reduced to a great extent.

Furthermore, the dependency of energy demand on fossil fuels is greatly influencing on our future generation. There is a possibility that these resources will deplete one day. Hence, Government of Pakistan should start focusing on renewables for the betterment of our future generation. This will not only make us independent in meeting energy demands but also will reduce GHGs to large extent. Hence our environment will be more clean and safe for the inhabitation of our future generation.

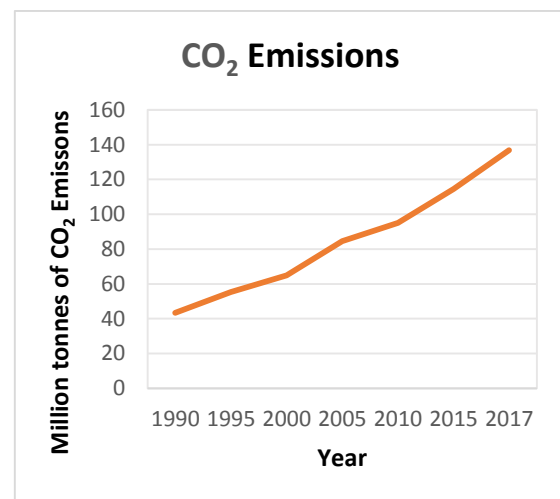


Figure 5 CO₂ emissions in Pakistan till 2017

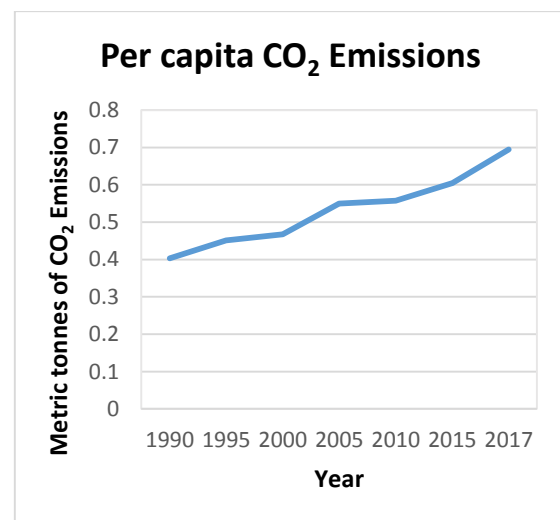


Figure 6 Per Capita CO₂ Emissions in Pakistan till 2017

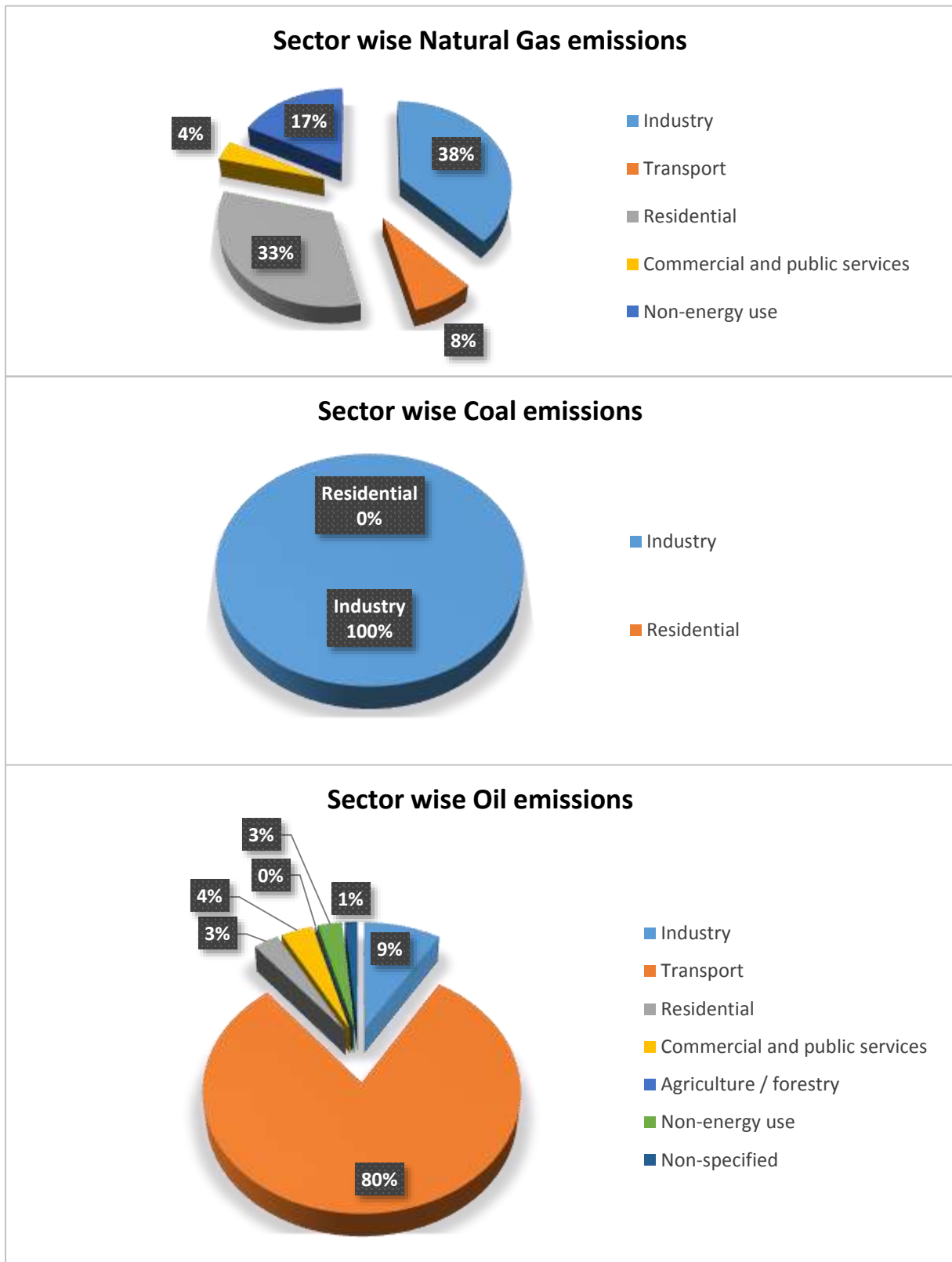


Figure 7. Sector wise CO₂ emissions of fossil fuels in Pakistan for year 2017.

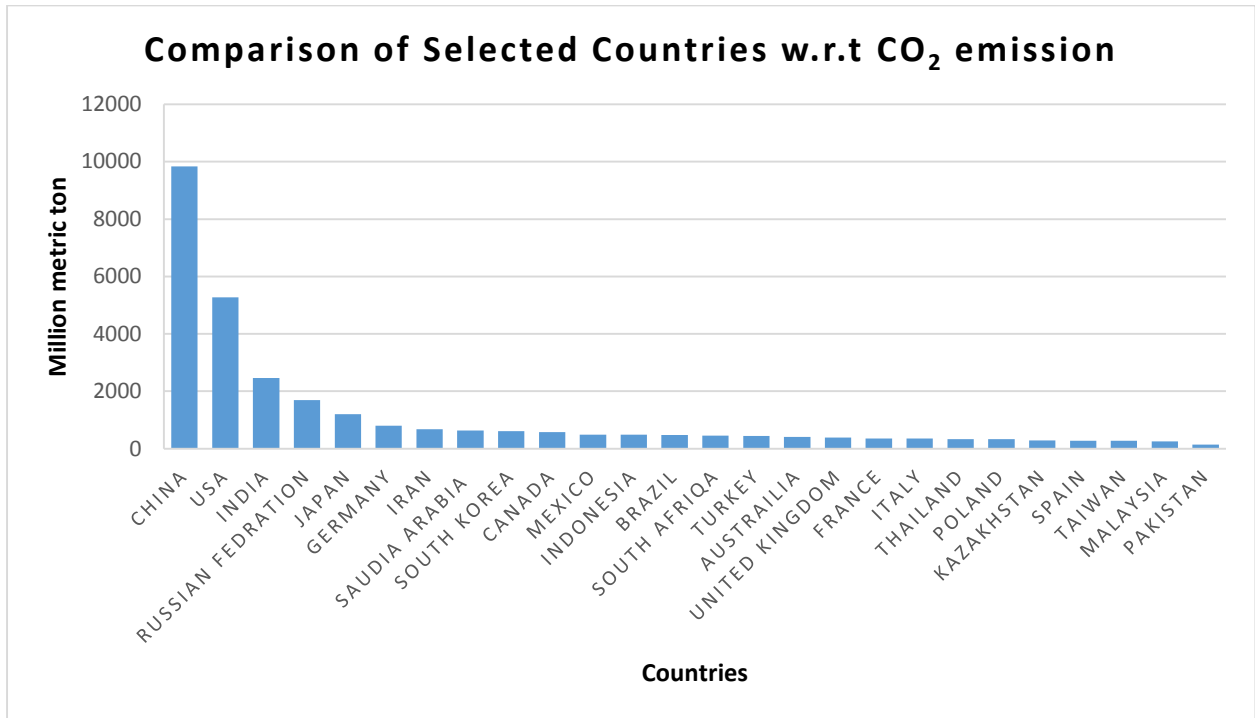


Figure 8 Comparison of CO₂ emissions in selected countries. It can be clearly seen that Pakistan has the lowest emissions as compared to other countries.

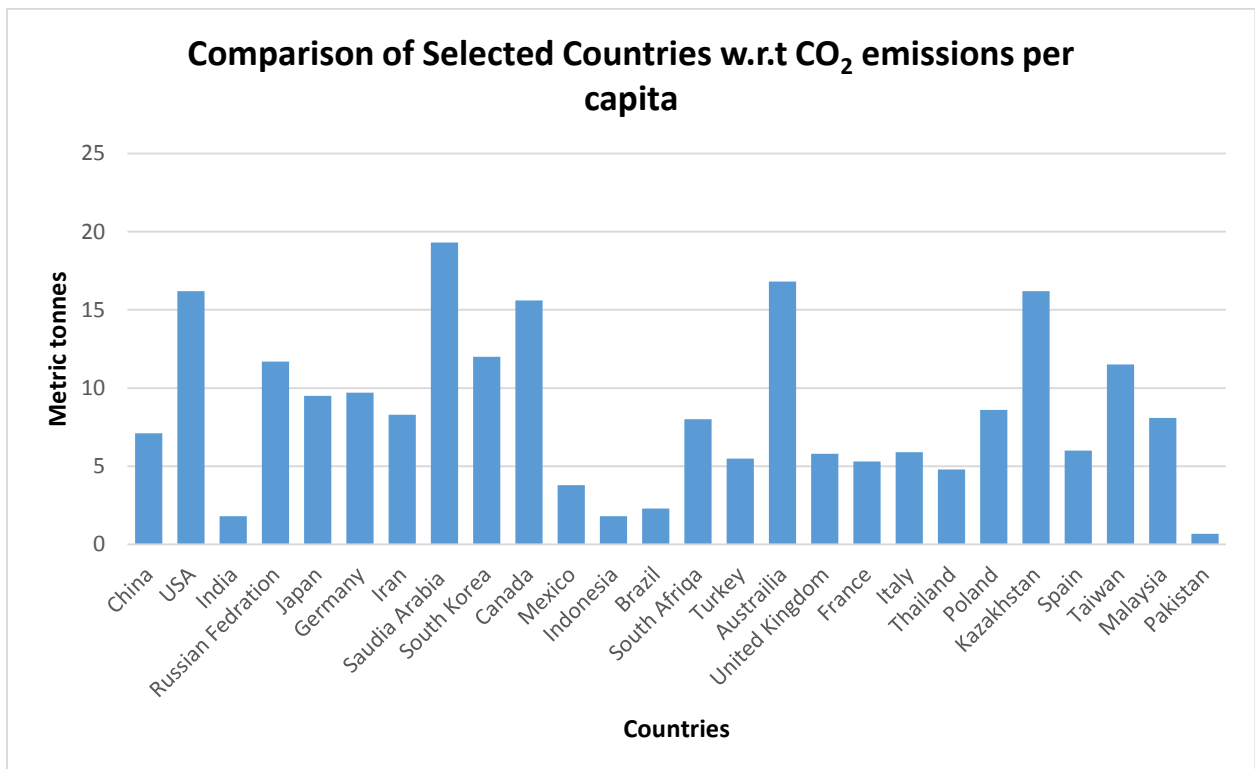


Figure 9 Comparison of Per Capita CO₂ emissions in selected countries. Pakistan has the lowest per capita CO₂ emissions.



4. Conclusion:

Carbon footprint analysis is used to measure the overall GHGs emissions which are linked directly and indirectly with our concerned system. This analysis can be considered as one of the initial steps that need to be done when someone is planning to move towards sustainability. Carbon footprint analysis can be used by individuals, companies, industries or even it can be applied nationwide. One can find the carbon emissions because of his actions and can compare it with the international standards. It can be used by countries to check their contributions in global GHGs emissions and furthermore planning their policies accordingly.

The study disclosed that although the emissions of the Pakistan are very low as compared to other countries but it is increasing to a great extent each year. So it is an hour of need that Government of Pakistan should take some serious steps to encounter this rapid increase in emissions. Government should invest in research and development regarding climate change studies. Air quality should be monitored regularly and strict actions should be taken against those individuals who are not following environmental standards. Another possible solution could be to utilize renewable energy resources to meet the energy demand of the country.

The research gap that we found during our study is that, there is no mathematical model available to calculate the carbon footprint of Pakistan. There is no authentic data available for the emissions factors of various fuels that are being consumed in Pakistan. So an extensive study can be done regarding above mentioned research gap.

REFERENCES:

- [1] D. R. Brooks and W. A. Boeger, "Climate change and emerging infectious diseases: Evolutionary complexity in action," *Curr. Opin. Syst. Biol.*, vol. 13, no. November 2018, pp. 75–81, 2019.
- [2] M. Abid, J. Schilling, J. Scheffran, and F. Zulfqar, "Climate change vulnerability, adaptation and risk perceptions at farm level in Punjab, Pakistan," *Sci. Total Environ.*, vol. 547, pp. 447–460, 2016.
- [3] G. P. Hammond and S. M. Seth, "Carbon and environmental footprinting of global biofuel production," *Appl. Energy*, vol. 112, no. December 1997, pp. 547–559, 2013.
- [4] F. Martins, C. Felgueiras, M. Smitkova, and N. Caetano, "Analysis of fossil fuel energy consumption and environmental impacts in european countries," *Energies*, vol. 12, no. 6, pp. 1–11, 2019.
- [5] E. E. A. (EEA), *European Union CO2 emissions: different accounting perspectives*, no. 20. 2013.
- [6] J.-C. & K. N. Hourcade, *Planetary Economics. (Energy, climate change and the three domains of sustainable development)*. 2014.
- [7] A. Midilli, I. Dincer, and M. Ay, "Green energy strategies for sustainable development," *Energy Policy*, vol. 34, no. 18, pp. 3623–3633, 2006.
- [8] International Energy Agency, "IEA Climate change report." [Online]. Available: <https://www.iea.org/reports/global-energy-co2-status-report-2018>. [Accessed: 08-Dec-2019].
- [9] IPCC, "Volumen 2. Energy. Chapter 6. Reference Approach. IPCC Guidelines for National Greenhouse Gas Inventories.," *IPCC Guidel. Natl. Greenh. Gas Invent.*, vol. 2, no. 6, pp. 1–14, 2006.
- [10] I. Yousuf, A. R. Ghumman, H. N. Hashmi, and M. A. Kamal, "Carbon emissions from power sector in Pakistan and opportunities to mitigate those," *Renew. Sustain. Energy Rev.*, vol. 34, pp. 71–77, 2014.
- [11] International Energy Agency, "Coal Consumption in Pakistan till 2017." [Online]. Available: <https://www.iea.org/fuels-and-technologies/coal>. [Accessed: 10-Dec-2019].
- [12] International Energy Agency, "Gas consumption by Pakistan till 2017." [Online]. Available: <https://www.iea.org/fuels-and-technologies/gas>. [Accessed: 10-Dec-2019].
- [13] International Energy Agency, "Oil consumption by Pakistan till 2017." [Online]. Available: <https://www.iea.org/fuels-and-technologies/oil>. [Accessed: 10-Dec-2019].
- [14] Intergovernmental Panel on Climate Change, "Volume 2 Annex 1," *2006 IPCC Guidel. Natl. Greenh. Gas Invent.*, pp. 1–19, 2006.



Investigation Regarding Thermal Management of Electric Heater Using Different Geometry Configurations

Saad Saeed Minhas¹, Abid Hussain^{1,*}

¹Department of Mechanical Engineering, University of Engineering and Technology Taxila, Pakistan

*Corresponding Author: abid.hussain@uettaxila.edu.pk

Abstract:

Advancement in technology and emphasis on portability are making devices compact. Compactness is attained by the closed packing of electronic components. Each electronic component generates heat during operation which leads to temperature rise in the device. Temperature is known to have a significant impact on the performance, life cycle, reliability and safety of the equipment. For thermal management, the application of heat sinks with natural convection is not enough to control the temperatures within limits. So, it is important to have an efficient cooling mechanism within a device to keep the temperatures in control. The objective is to study active cooling mode in closely packed devices with three different airflow configurations namely axial, reverse and crossflow configuration. Moreover, the effect of velocity on the flow configurations was also examined. The analysis was performed on graphical trends and discussed with explanations. Consequently, conclusions were drawn from them and are found in good agreement with existing literature and scientific knowledge.

Keywords: Thermal management, Electric heater, Geometric configuration, Active cooling, Velocity effects

1. Introduction

Modern equipment designing emphasis on compactness and portability. Compactness requires a close arrangement of complex circuitry in a confined space and is achieved at a cost of excess heat generation and performance degradation. Upon energizing the circuit there is a protentional drop across each resistive element that appears in the form of temperature rise in the system. To limit the temperature below an acceptable level for improved life and better performance, a cooling system is provided [1]. The type of cooling system used depends on number of factors. Passive cooling has its temperature limitations, but it does not require additional power. Contrary to that active cooling methods are efficient but need additional draw of energy from the source. In the current research, forced convection is used to study the cooling of the heater element. The hybrid system integrates phase change material (PCM) as passive cooling and forced convection as an active cooling technique. Phase change material (PCM) is known to have high heat storage capacity but its downside is that it has low thermal conductivity. Hence air cooling is applied to compensate for low thermal conductivity.

Forced convection cooling of electronic devices was studied by Durgam et al. [2]. He used three different substrates glass/epoxy FR4, Bakelite, single-sided copper-clad board at heat flux of 1000 and 2000 W/m² at an air velocity of 1m/s. Experimental result shows the maximum temperature excess of 11.6 °C and 24.2 °C at 1000 and 2000 W/m² for FR4. Nelson et al. [3] modelled the lithium-ion (Li-ion) batteries for thermal properties. He used air forced convection cooling to control the temperature of lithium-ion batteries. From experimentation, he concluded that air cooling is efficient till a certain limit after that it

would be difficult to control the temperature with air cooling. Khattak et al. [4] studied the influence of different flow regimes over the heat sink and concluded that heat transfer largely depends on the flow regime. Continuing his work Li et al. [5] introduced turbulence in test section to enhance the heat transfer. Li et al. [5] & Kim et al. [6] in their research concluded the effect of spacing on different design parameters like fin height, fin width, number of fins and flow velocity as Reynolds number.

Sabbah et al [7] studied the thermal conductivity of PCM. He analyzed the results of combining a high-conductivity graphite matrix to improve paraffin thermal conductivity. He found that the paraffin-graphite matrix thermal conductivity has enhanced to 17 W/(m. K). It has been found out that hybrid PCM in natural and high thermal environment promotes a uniform temperature for lithium-ion batteries. Li et al. [8] studied copper foam paraffin wax. The study determined the performance of the heat generation in 10 Ah Li-ion battery pack. For a discharge rate of 1 C, a comparative study was carried out between two control cases. First with air natural convection and second with porous metal foam saturated with PCM. In air convection, the surface temperature exceeds the safe temperature limit of 65 °C while in metal foam PCM surface temperature peaks at 42 °C which lies within safe operating limits. To enhance the thermal conductivity of PCM Hussain et al [9]. studied the effect of nickel foam paraffin composite. Heat generation in 3.4 Ah lithium-ion battery pack is studied experimentally. They observed a decrease in battery surface temperature by 31% and 24% compared to air convection and paraffin mode respectively under 2 C discharge charge. Hussain et al [10]. studied the lithium-ion batteries thermal management by using graphene covered nickel foam

saturated with PCM. The results show that battery temperature decreases about 17% after the use of graphene as compared with nickel foam saturated PCM at the discharge rate of 1.7 A compared to nickel foam.

2. Experimental setup

In order to perform the research, experimental equipment is set up in the laboratory. The experimental setup consists of power supply, data acquisition system, thermocouples, fan, cavity, electric heater and PCM. An electric heater is used to mimic the heat generation in electronics. In Figure 1. The pictographic view of setup used in the laboratory is shown

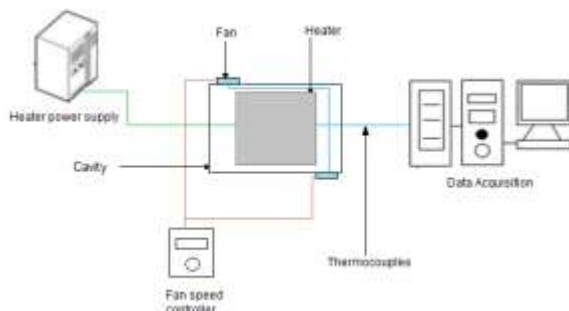


Figure 1. Schematic diagram of an experimental setup

Cavity used in the experiment is made from Plexi sheet. Dimensions of the cavity are 120 x 120 x 60 mm. Silicon rubber heater is mounted with clamps inside the cavity. The heater has a dimension of 100 x 100 mm. Heater maximum rated input is 50 W. Variable power supply unit of maximum 50 W is used to power the heater. The main property to be measured is temperature. For that three high precision thermocouples T_1 , T_2 , T_3 are used to measure the temperature of entering air in cavity, leaving air form cavity and temperature of cavity respectively. This analog data from thermocouples is converted to digital and is recorded by the data acquisition system made by Agilent 34972A through a laptop. Fan-made by Foxconn having dimensions of 40 x 40 mm is used for active cooling mode.

2.1 Air flow configuration

The rate at which heat is transferred from the body is critically dependent on the airflow configuration. The rate of heat transfer is more in turbulent flow as compared to the laminar flow [11]. Three different airflow configurations namely axial, cross and reverse flow configurations are compared experimentally. In axial flow configuration, both the air inlet and outlets are in line. In crossflow configuration air enters the cavity at one side and leaves the cavity at other side while in reverse flow configuration, air enters and exits from the same side after circulation in cavity and carrying the heat.

These airflow configurations are shown in figures 2, 3 and 4 respectively.

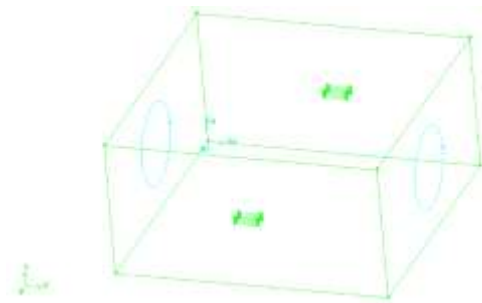


Figure 2. Axial flow configuration

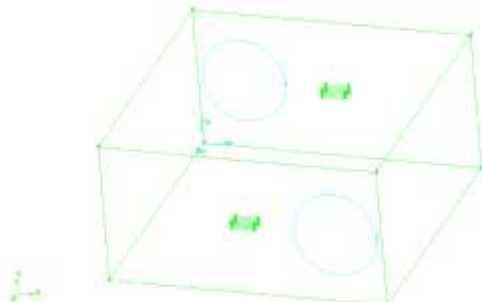


Figure 3. Cross flow configuration

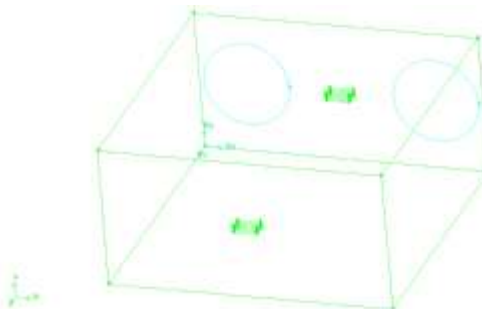


Figure 4. Reverse flow configuration

3. Results and discussions

Extensive experimentation was carried out in the laboratory. Data obtained from the data logger was analyzed and a comparative study was performed between different flow configurations. Factor defined to measure the effectiveness was the maximum temperature (T_{max}) attained during experimentation. Figure 5 shows the comparison of flow configuration. In graph green curve represents the T_{max} in the cavity for axial flow, the blue curve shows the T_{max} in the cavity for reverse flow while the curve in orange shows the T_{max} in cooling mode for cross flow configuration. In axial flow configuration, T_{max} rises to 73 °C. Which exceeds the safe operating temperature for electronic devices. While the T_{max} for reverse flow rises to 64 °C similarly the T_{max} in cross flow configuration is recorded as 54 °C.

Figure 5 shows a comparison of the above mentioned three configurations. From the data, it is

obvious that the maximum drop in temperature was achieved in cross flow which is because of the geometry configuration symmetry. Intermediate temperatures were observed in reverse flow configurations. As the air inlet and outlet are on the same side of the cavity, due to which the entering air does not completely travel in the cavity before leaving and creates a blind spot in the cavity which causes a temperature rise in cavity. For the case of axial flow configuration, a minimum temperature drop of all three configurations was obtained. This behaviour is due to the fact that air inlet and outlet in the cavity are inline and air entering cavity does not circulates and stay for enough time in cavity to carry out heat transfer and leave cavity without exchanging heat.

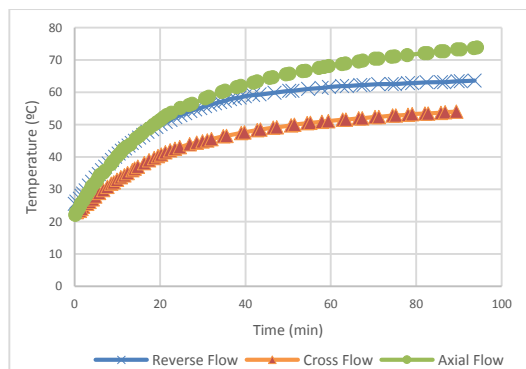


Figure 5. Comparison of temperature profiles for flow configurations

Another variable studied was the effect of velocity. Experiments were performed at three different velocities. Velocities considered under study were 1 m/s, 3 m/s and 5 m/s. At these velocities, the temperature was recorded as shown in figure 6. From the graph, it is evident that the maximum heat loss was obtained with 5 m/s velocity and lowest heat loss with 1 m/s while heat loss is intermediate for 3 m/s velocity configuration. Experimental results show the temperature plot of these velocities follows the same curve initially. With time and difference in heat transfer rate at velocities 1 m/s, 3 m/s and 5 m/s. The curves show different heat transfer rate and this behaviour is due to the fact that velocity of 5 m/s has more capacity to remove heat than 3 m/s. Similarly, in a comparison between 3 m/s and 1 m/s, heat loss obtained is greater in case of 3 m/s than 1 m/s velocity setting.

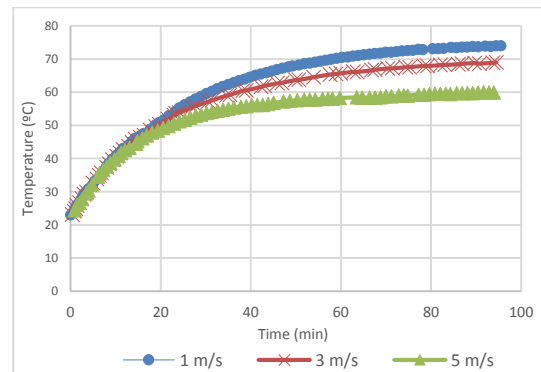


Figure 6. Comparison of T_{max} at air velocities of 1 m/s, 3 m/s and 5 m/s

4. Conclusion

This research aims at finding the best configuration to dissipate the heat for the compact devices which have various heat generating elements crammed closely in an enclosure.

Different geometry configurations comparison gives the result as cross flow is the most efficient geometry configuration. The maximum temperature drop was achieved in this configuration. This means that while designing the compact equipment a cross flow geometry configuration should be used for the effective thermal management of the equipment.

In reverse and axial flow geometry models temperature drop achieved was below the acceptable limit and if used in designing of commercial equipment, it will lead to the problem of thermal throttling which compromises the performance, reliability and safety of the equipment.

Another consideration under study was the effect of velocity. Three velocities 1 m/s, 3 m/s and 5 m/s were tested and concluded that maximum heat loss was obtained at a velocity of 5 m/s. A direct proportional relation is found between temperature drop and air velocity. The research suggested that cross flow geometry configuration along with 5 m/s velocity is recommended for effective thermal management of equipment.

The results obtained from this research will contribute to both academia and industry for obtaining effective thermal management in equipment. Application area includes cooling in smart devices, laptops, lithium-ion batteries in electric vehicles, electrical panels, servers and many more. With the addition of this knowledge, the behaviour of heat transfer in compact devices is better understood and the designer can optimize his design to obtain the required level of heat transfer.

REFERENCES

- [1] M.M. Mohamed, Air cooling characteristics of a uniform square modules array for electronic device heat sink, *Appl. Therm. Eng.* 26 (2006) 486–493. <https://doi.org/10.1016/j.applthermaleng.2005.07.013>.
- [2] F. Convection, C. Of, S. Heat, I.N.A.H. Channel, IHMTC2017-09-0178 FORCED CONVECTION COOLING OF SQUARE HEAT SOURCES, (2017) 2–9.
- [3] P. Nelson, D. Dees, K. Amine, G. Henriksen, Modeling thermal management of lithium-ion PNGV batteries, *J. Power Sources.* 110 (2002) 349–356. [https://doi.org/10.1016/S0378-7753\(02\)00197-0](https://doi.org/10.1016/S0378-7753(02)00197-0).
- [4] Z. Khattak, H.M. Ali, Air cooled heat sink geometries subjected to forced flow: A critical review, *Int. J. Heat Mass Transf.* 130 (2019) 141–161. <https://doi.org/10.1016/j.ijheatmasstransfer.2018.08.048>.
- [5] D.K. Kim, S.J. Kim, J.K. Bae, Comparison of thermal performances of plate-fin and pin-fin heat sinks subject to an impinging flow, *Int. J. Heat Mass Transf.* 52 (2009) 3510–3517. <https://doi.org/10.1016/j.ijheatmasstransfer.2009.02.041>.
- [6] H.Y. Li, S.M. Chao, G.L. Tsai, Thermal performance measurement of heat sinks with confined impinging jet by infrared thermography, *Int. J. Heat Mass Transf.* 48 (2005) 5386–5394. <https://doi.org/10.1016/j.ijheatmasstransfer.2005.07.007>.
- [7] R. Kizilel, R. Sabbah, J.R. Selman, S. Al-Hallaj, An alternative cooling system to enhance the safety of Li-ion battery packs, *J. Power Sources.* 194 (2009) 1105–1112. <https://doi.org/10.1016/j.jpowsour.2009.06.074>.
- [8] W.Q. Li, Z.G. Qu, Y.L. He, Y.B. Tao, Experimental study of a passive thermal management system for high-powered lithium ion batteries using porous metal foam saturated with phase change materials, *J. Power Sources.* 255 (2014) 9–15. <https://doi.org/10.1016/j.jpowsour.2014.01.006>.
- [9] A. Hussain, C.Y. Tso, C.Y.H. Chao, Experimental investigation of a passive thermal management system for high-powered lithium ion batteries using nickel foam-paraffin composite, *Energy.* 115 (2016) 209–218. <https://doi.org/10.1016/j.energy.2016.09.008>.
- [10] A. Hussain, I.H. Abidi, C.Y. Tso, K.C. Chan, Z. Luo, C.Y.H. Chao, Thermal management of lithium ion batteries using graphene coated nickel foam saturated with phase change materials, *Int. J. Therm. Sci.* 124 (2018) 23–35. <https://doi.org/10.1016/j.ijthermalsci.2017.09.019>.
- [11] P. Deb, G. Biswas, N.K. Mitra, Heat transfer and flow structure in laminar and turbulent flows in a rectangular channel with longitudinal vortices, *Int. J. Heat Mass Transf.* 38 (1995) 2427–2444. [https://doi.org/10.1016/0017-9310\(94\)00357-2](https://doi.org/10.1016/0017-9310(94)00357-2).



Recent advances in the use of phase change and silica aerogel based materials for energy applications in buildings

Biwole P. H.*^{1,2}, Nocentini K.² and Achard P.²

1- University Clermont Auvergne, CNRS, SIGMA Clermont, Institut Pascal, F-63000 Clermont–Ferrand, France

2- MINES ParisTech, MINES Paris Tech, PSL Research University, PERSEE - Center for Processes, Renewable Energies and Energy Systems, CS 10207, 06 904 Sophia Antipolis, France

*Corresponding author email address: pascal.biwole@uca.fr

Abstract:

Phase change and silica aerogel based materials for thermal energy storage and thermal insulation have attracted a lot of attention as promising materials to reduce the energy consumption and carbon footprint of the building sector. Here, we present two prototypes of innovative building envelopes integrating such materials. The first one is a recently patented fibrous insulating material impregnated with silica aerogel, while the second envelope is a translucent solar wall providing, concurrently, storage and restitution of heat, super thermal-acoustic insulation and daylighting to the interior environment. The used methodology is both experimental and numerical. The complex modeling of the heat and mass transfers through the materials is detailed. Life cycle assessment and economic analysis are also presented. Results show that while phase change and silica aerogel based materials can dramatically increase the energy performance of buildings, their dissemination in the building sector is still hampered by high initial investment costs. Therefore, their implementation is economically feasible where energy prices for heating and cooling are relatively high, making the initial capital cost lower than the expected savings.

Keywords: low energy buildings, phase change materials, silica aerogels, numerical simulation, experimentation

1. Introduction

There is a global concern related to energy consumption in the built environment, as one of the major contributors to greenhouse gas emissions, responsible for climate change and its associated impacts. According to the International Energy Agency statistics, buildings currently represent 30–35% of the world's total primary energy supply, 20–25% of the global CO₂eq emissions, and about half of the world's electricity consumption. If no action is taken to develop energy efficiency in buildings, the sector's energy need is predicted to augment by 50% in 2050. A significant proportion of the energy consumption in buildings is used for indoor air cooling and heating purposes. Therefore, a solution to achieve the goal of reducing energy consumption in buildings is to improve the energy performance of its envelope, which governs the heat exchanges between the outside and the indoor environment; and to promote renewable-energy-based HVAC systems. Along with building optimal orientation, this is the baseline of so-called net zero or net positive energy buildings approaches. Among the materials that can increase the thermal performance of the building envelope, phase change materials (PCMs) and silica aerogels based materials have attracted a lot of attention of both the academic and the industry communities. PCMs store or release heat during their

reversible solid – liquid or liquid – gas or even solid - solid cycles. Due to their high latent heat, those materials have been extensively developed and used to enhance the thermal inertia and delay the heat release in various applications including buildings. Numerous studies have shown that the integration of PCMs in the building envelope can significantly improve the energy performance of the building and save up to 80% of heating energy in winter, as the material captures the heat of the sun, melts, then restitutes the heat to the building by re-solidifying. However, one of the encountered problems is the high risk of summer overheating when the material can no longer de-stock the stored heat and remains in its liquid state. From the numerical simulation viewpoint, it is still challenging to capture the behavior of such materials due to the temperature dependence of their thermophysical properties and to the complex and sometimes un-deterministic phenomena occurring during phase change, such as supercooling. Because of this, numerical simulation often requires extended computational resources for a limited actual simulated time, typically a few hours, whereas the analysis of building energy behavior is usually conducted on a yearly basis.

Silica aerogels are highly insulating (thermal conductivity $\lambda \sim 0.015 \text{ W}\cdot\text{m}^{-1}\cdot\text{K}^{-1}$) transparent materials with high porosity and pore size less than 1 μm . They have been searched for integration in



buildings wallboards, as external coating to suppress thermal bridges in retrofitting cases and to enhance the thermal insulation of windows glazing. They can be used alone, or integrated into a mortar, or in a fibrous material to cope with their low mechanical resistance. The prediction of the hygro-thermal properties of silica-aerogel based materials poses the problem of understanding and modeling the heat and mass transfers in their nanoporous structure, with high volumes of empty (98 to 99%). For aerogels in monolithic or powdery form, the transfer of heat is done via solid conduction through the skeleton, gas conduction through the open pores and radiation between pore walls. The convective heat transfers within the pores are usually neglected because of the small pore size. When used associated with a mortar or a fibrous material, the correlations used to estimate the bulk properties are all based on simplifying assumptions, such as the orientation of all the fibers in the same direction, perpendicular to the heat flow. Predicting those composite materials effective properties such as the bulk thermal conductivity as a function of the fiber or mortar volume fraction is still an open challenge.

The current paper presents two innovative building envelopes integrated with phase change material and silica-aerogel based materials. The first wall includes is a recently patented fibrous insulating material impregnated with silica aerogel, while the second envelop is a translucent superinsulated latent heat storage wall, combining powdery silica aerogel and PCM. An experimental and numerical study of each wall thermal and energy behavior is presented, as well as an economic analysis.

2. Fibrous insulating material impregnated with silica aerogel

2.1. Preparation of the aerogel blanket

Initially, a fibrous network made materials such as PET (Polyethylene terephthalate) or glass, is impregnated by pre-hydrolyzed TEOS (Tetraethoxysilane) precursors. A silica organogel is obtained by the in situ gelation of the precursor, and the organogel is made hydrophobic by silylation with HMDSO (Hexamethyldisiloxane) in an acid medium. This last step prevents any modifications of the structure in case of capillary condensation, which would lead to the degradation of mechanical and thermal properties. The silylation reaction substitutes hydrolyzable groups such as silanol and ethoxy groups by non-hydrolyzable groups and allows the silica gel to reopen its pore during the last stage of drying due to the repulsion of the graft groups and elasticity of the solid network (spring back effect).

Finally, the composite obtained containing the fibrous network and the hydrophobic silica gel is dried by fixed frequency electromagnetic wave at 50 °C for 50 min. This process is described in Fig. 1. Fibers take the form of an un-woven mat with fiber diameter around 10 μm and a length of a few millimeters. The volume fraction of fibers is in the range 1% to 5 % in order to limit the increase of the solid thermal conductivity by the fibers themselves and to strengthen the aerogel. Fig. 2 shows the Scanning Electron Microscopy (SEM) photos of a PET mat impregnated with silica aerogel before and after impregnation. The analysis of the microstructure shows that the aerogel and fiber phases are well interpenetrated [1].

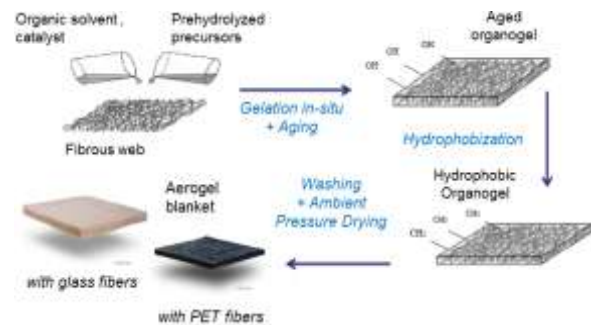


Fig. 1. Steps of the aerogel blanket preparation.

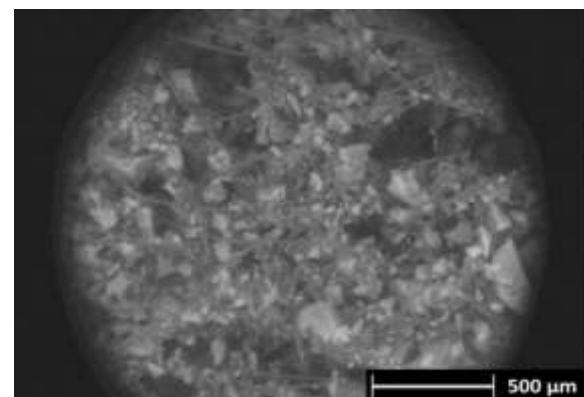
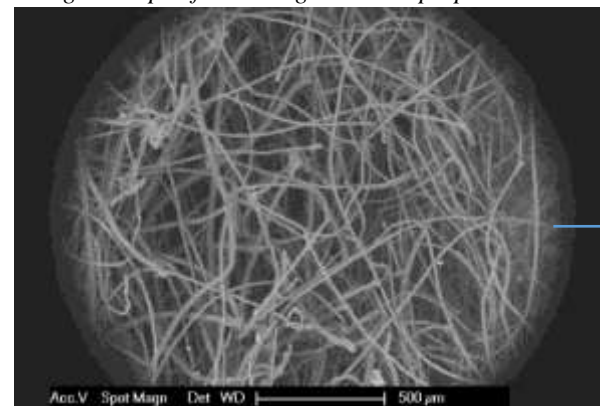


Fig. 2. SEM photo of a PET mat impregnated with silica aerogel (left: before, right: after).



2.2. Effective thermal conductivity

The effective thermal conductivity of the aerogel blanket was calculated as the sum of the solid conductivity through the aerogel skeleton and the fibers, the gaseous conductivity through the pores and the cracks, and the radiative conductivity between the pores. The solid conductivity $\lambda_{S/P}$ was estimated using a series/parallel heat transfer model which considers that only a fraction A of the fibers is parallel to the heat flux:

$$\lambda_{S/P} = A\lambda_P + (1-A)\lambda_S \quad (1)$$

where λ_P the parallel conductivity and λ_S the series conductivity. The gaseous conductivity λ_{cg} was calculated based on the Knudsen tri-modal model as the sum of the gaseous conductivity through the mesopores (pore size 2-50 nm), through the macropores (pore size > 5 nm) and through the internal cracks of the blanket:

$$\lambda_{cg} = \frac{F \cdot \phi_{meso} \cdot \lambda_{g,0}}{1 + 2 \cdot \beta \cdot \frac{l(P)}{D_{meso}}} + \frac{\phi_{macro} \cdot \lambda_{g,0}}{1 + 2 \cdot \beta \cdot \frac{l(P)}{D_{macro}}} + \frac{\phi_{fissures} \cdot \lambda_{g,0}}{1 + 2 \cdot \beta \cdot \frac{l(P)}{D_{fissures}}} \quad (2)$$

where ϕ is the heat flux, F is a factor representing the coupling between the gaseous and solid conduction (F=2.5), D is the mean diameter of the pores, beta is a constant of value taken between 1.5 and 3, $\lambda_{g,0}$ is the air thermal conductivity in a non-confined space, $l(P)$ is the pressure dependent mean free path of the air molecules. The radiative conductivity was estimated using the Rosseland approximation:

$$\lambda_r = \frac{16 \sigma n^2 T_r^3}{3 \rho e_R(T)} \quad (3)$$

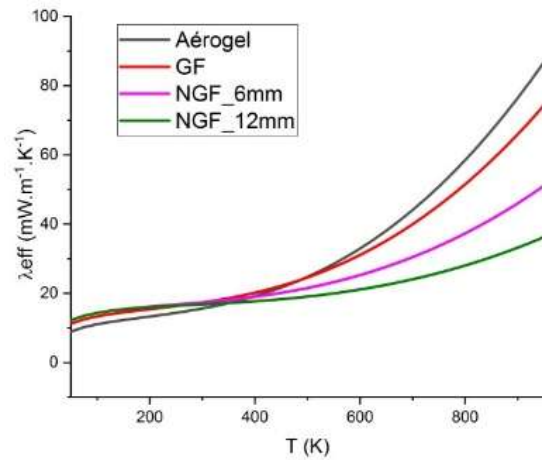
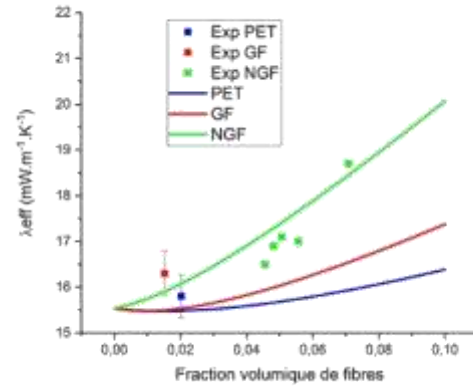
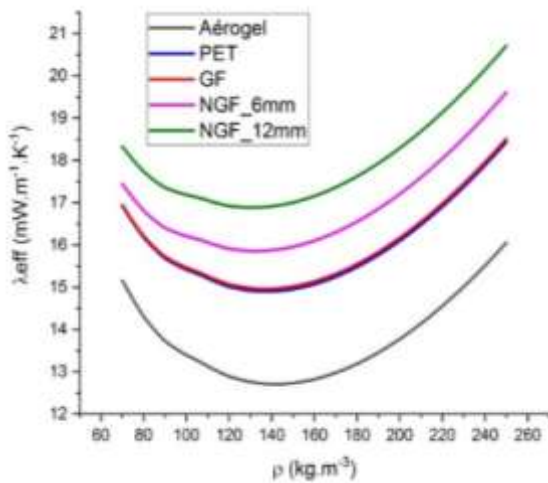


Fig. 3 aerogel blankets bulk thermal conductivity versus temperature ($\rho = 110 \text{ kg/m}^3$, $fv < 5\%$), bulk density ($T=300\text{K}$, $fv < 5\%$) and fiber volume fraction ($\rho = 110 \text{ kg/m}^3$, $fv < 5\%$).

where σ the Stephan-Boltzmann constant, n is the refraction index of the blanket, T the temperature, ρ the bulk density of the blanket and $e_R(T)$ is the temperature dependent extinction coefficient derived from experimental FTIR measurements ($e_R = 28$ for pure silica aerogel, 71 for glass fibers and 54 for PET fibers). Based on the above formulas, Fig. 3 shows the evolution of different aerogel blankets bulk thermal conductivity versus temperature, bulk density and fiber volume fraction.

2.3. Experimental assessment of the thermal behavior

A Needle Glass Fiber (NGF) aerogel blanket was used as an internal thermal insulation (ITI) system on the south wall of a test building in Sophia Antipolis, France, as shown in Fig. 4. The local climate is rated as warm Mediterranean (Csa) by the Köppen-Geiger classification. The outdoor and indoor air temperatures, the internal and external surface temperatures, the surface heat fluxes and the solar radiation were monitored. As a result, the measured



wall U-Value of $0.33 \text{ W}\cdot\text{m}^{-2}\cdot\text{K}^{-1}$ confirmed the previous correlation used for thermal conductivity. It was also shown that in free floating mode (i.e. without any HVAC system on), the building was able to maintain a room temperature 7°C degrees above the outdoor temperature in winter, while the overheating remained limited to 27°C in summer (Fig. 4).

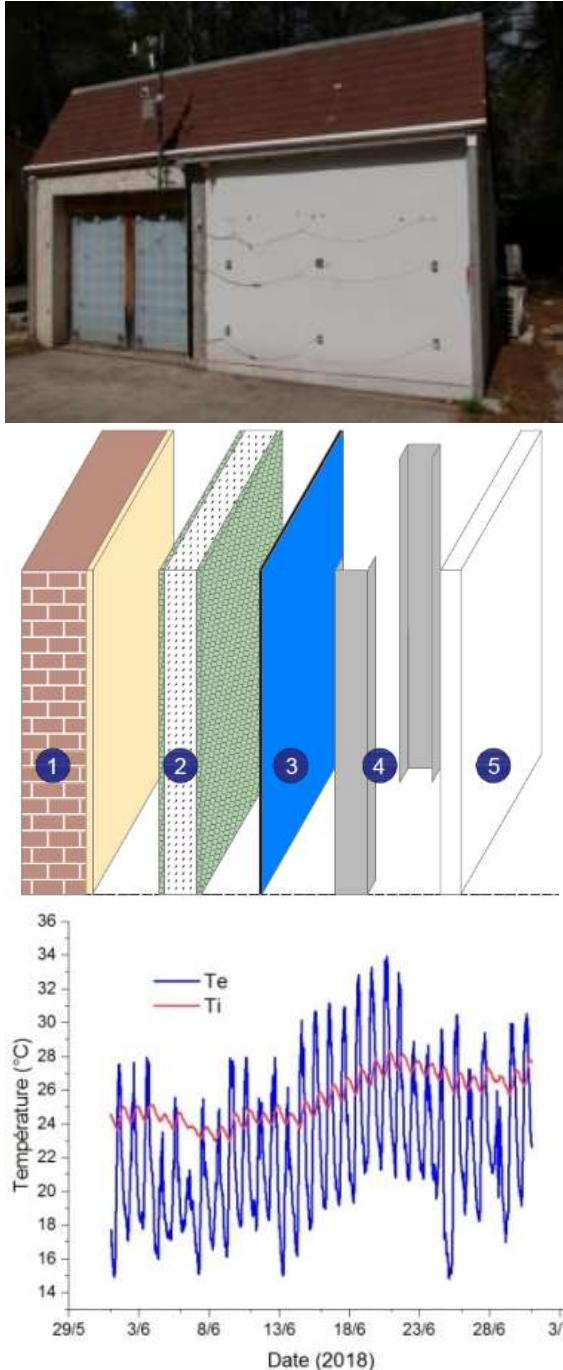


Fig. 4. Test building (left); wall structure (center):
 1-Concrete, 2- NGF aerogel blanket (25mm)
 between two polyethylene layers, 3- vapor barrier,
 4- air layer, 5- plywood; Outdoor and indoor air
 temperatures (right).

2.4. Whole building energy behavior

The retrofitting of an office building of floor area 500m^2 , with 20% window to wall ratio was simulated using real living scenarios under different climates using the whole building energy simulation software Energy Plus. The baseline walls were composed of 2.5 cm of external coating, 20 cm of concrete and 1.5 cm of internal plasterboard. The retrofitted walls included an NGF aerogel blanket set as an ITI system. The heating and cooling loads were computed for the European cities of Nice (Mediterranean climate with hot summers), Stockholm (humid and cold continental climate), Brussels (oceanic climate with mild summers) and Valencia (semi-arid dry and cold climate). As shown on Fig. 5, 1cm of aerogel blanket allowed reducing the heating load by 25% in Valencia and Brussels, while 3cm allowed a reduction up to 50% in Nice. The cooling load was reduced by 30% using 5 cm of blanket in Nice.

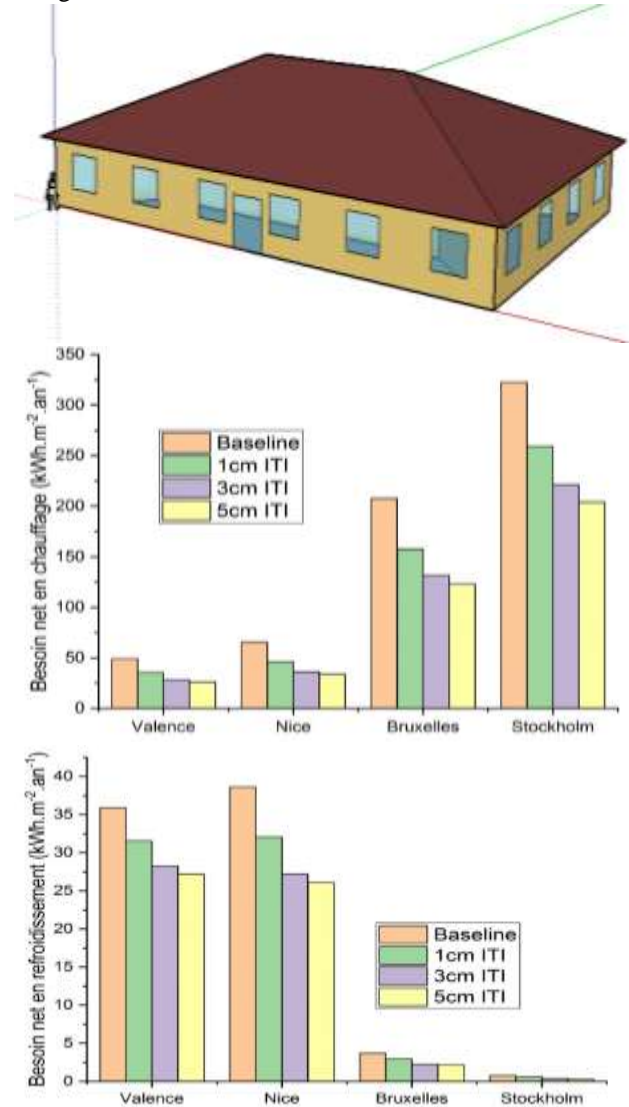


Fig. 5. Simulated building layout (left); Annual
 heating load (center); Annual cooling load (right)



2.5. Economic analysis

To assess the financial profitability of the innovative insulation, the annual energy gains from using the insulation were compared with the cost of installing the insulation. The calculations were made using a 1D numerical model developed on the software Comsol Multiphysics, for an average temperature gradient of 10°C and a heating period of 242 days. The efficiency of the heating installation was taken as 90%. The simulations were carried out on cases of interior and exterior renovation, for different baseline walls made of stone, hollow brick, filled brick and cinderblock. The price of insulation C_i per square meter was calculated as:

$$C_i = (a + be) \quad (4)$$

where a and b are constants depending on the nature of the insulating material, its coating, the labor cost, and e represents the thickness of the insulation. For the simulations, $a = 30 \text{ €/m}^2$ and $be = 20 \text{ €/m}^2$ per centimeter of insulation.

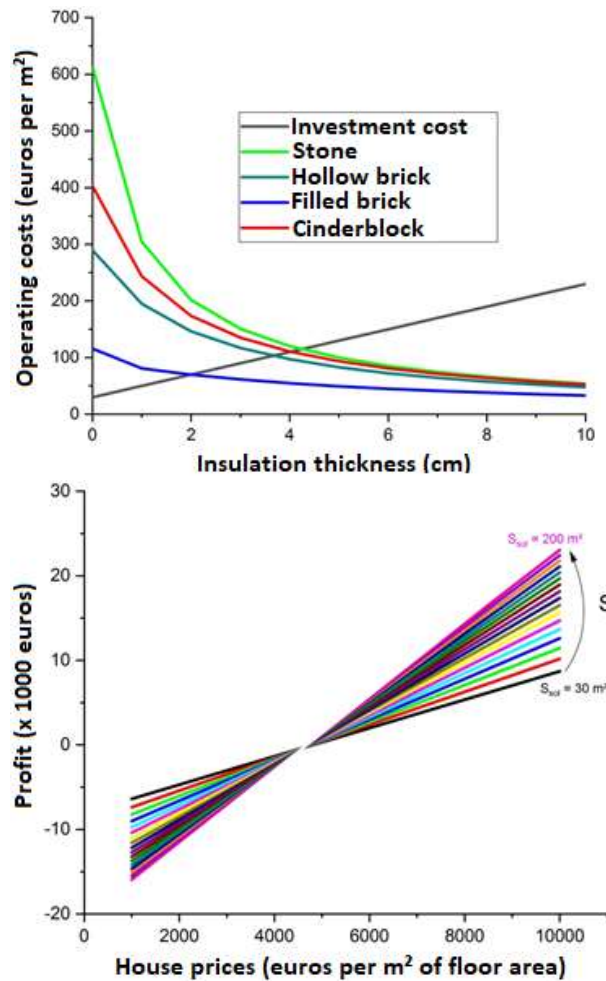


Fig. 6. Operating and investment costs related to the ITI using NGF blanket, per m^2 of surface to be insulated (left); Benefit made after the renovation using an NGF blanket instead of a conventional insulation material (right).

Depending on the period of operation envisaged for the building, the optimal economic thickness of insulation is determined as the thickness which minimizes both the investment and operating costs. Fig. 6 shows the building operating cost over 10 years as a function of the thickness of the NGF blanket, used as an ITI system. The economic thickness is found at the intersection of the operating curves and the investment curve. For the calculation of the operating cost, the price per kWh was taken 0.13 € per kWh. It was found that for walls with low thermal conductivity such as hollow bricks, a thickness of 4 cm NGF blanket insulation minimizes the total costs whereas for walls with a higher conductivity such as filled bricks, the optimal economic thickness is only 2 cm. Therefore, the first centimeters of insulation are the most important ones. Even though aerogel blankets are currently about 250 times more expensive than conventional insulating materials, the advantage of super-insulation is to preserve more living space when renovating a building from the inside. Fig. 6 also shows the total cost difference when using the NGF blanket or a conventional insulation material, during an ITI renovation, as a function of the price per square meter of floor space. The conventional insulation chosen for the calculation is a glass wool of thermal conductivity 0.032 W/(m.K), with a price of 30.8 €/m² per centimeter of insulation. It is found that from 4600 €/m², the use of aerogel blankets becomes more profitable than conventional insulation materials. It is the case in big cities like Paris, London or Berne (houses price ~10 000 €/m²).

3. Translucent super insulated latent heat storage wall

3.1. Wall description

The innovative passive solar wall presents a double layer design, as shown on Fig. 7. The inner layer is composed of glass bricks of dimension 19 cm x 19 cm x 5 cm filled with a eutectic PCM. This layer is mainly designed to provide radiation absorption, energy storage, and daylighting (see Fig. 7, right) The outer layer is composed of a 4 cm gap formed between the bricks and a 0.8 cm-large glass pane, filled with silica aerogel granulates. This layer is highly translucent and provides super-insulation. A wood frame maintains the system as a prefabricated assembly. The wall is hereafter referred to as TIM-PCM wall for Transparent Insulation Material –PCM wall. The thermophysical properties of the TIM-PCM wall are provided in Table 1.



3.2. Experimental assessment of the thermal behavior

The TIM-PCM wall was installed in the abovementioned test building. The building comprises three rooms: one south-east oriented room equipped with the silica aerogel blanket wall, one south-west oriented room equipped with the south facing TIM-PCM wall, and one north oriented room used for data acquisition. Each room is thermally insulated from each other. The indoor air dry bulb temperature in the TIM-PCM room, the PCM temperature, the outdoor air temperature as well as the solar radiation

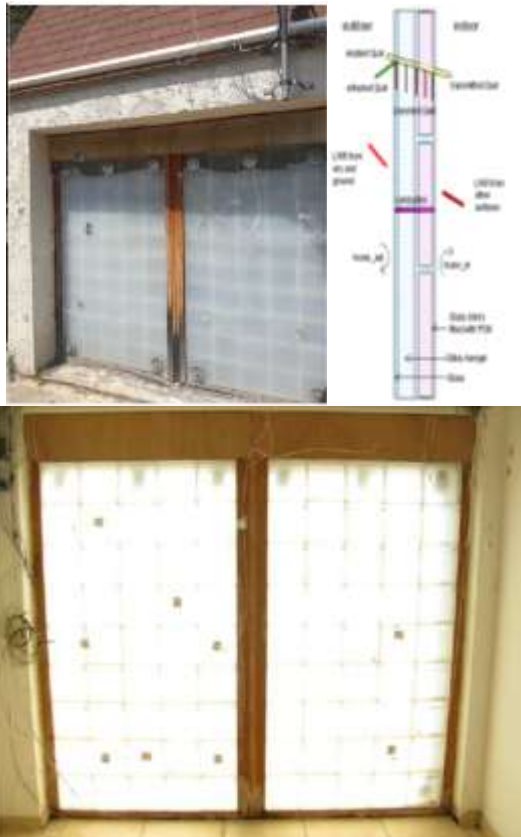


Fig. 7. TIM-PCM wall from outside (left); Layout of the TIM-PCM wall; TIM-PCM wall from inside (right).

were monitored. The TIM-PCM wall proved to be very effective in winter. Especially in cold sunny days, the PCM absorbed solar radiation, melted, then released the stored heat to the building at night by re-solidifying (see Fig. 8). During the whole winter season, the TIM-PCM room was able to maintain an 8°C average air temperature difference with outdoor air without using any heating system. However, in summertime, an overheating problem was encountered as the PCM remained in its liquid state due to high solar gains and high outdoor

temperatures, and it was unable to release the stored heat at night.

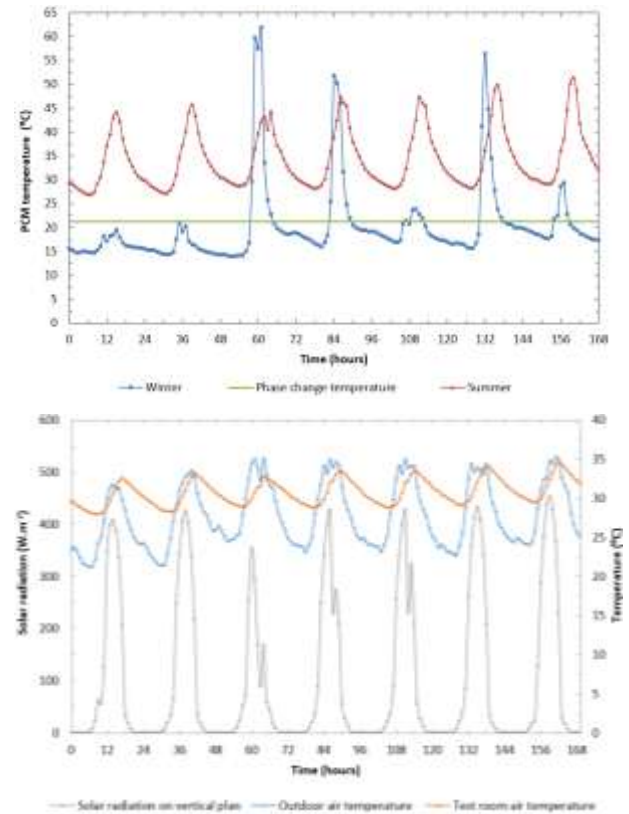


Fig. 8. Temperatures and solar radiation for seven consecutive days in summer (Jul 30 - Aug 5, 2017) (left). PCM temperatures for seven consecutive days in summer (Jul 30 - Aug 5, 2017) and winter (Jan 27 - Feb 2, 2017).

3.3. Simplified numerical model

A numerical model of the TIM-PCM wall was set up to evaluate different solutions to avoid the overheating problem. To avoid lengthy computational time, an innovative simplified model was developed in MATLAB, in order to predict the thermal behavior of the TIM-PCM wall on an annual basis. The unsteady energy equation for PCM regions is given as:

$$\rho C_p \frac{\partial T}{\partial t} = \frac{\partial}{\partial x} \left(k \frac{\partial T}{\partial x} \right) - \rho L_H \frac{\partial f_l}{\partial t} + \phi_{sol} \quad (5)$$

where ϕ_{sol} (W/m²) is the absorbed solar radiation in the layer, L_H is the latent heat of fusion (J/kg) and f_l is the liquid fraction. To solve the phase change problem a fixed-grid modified enthalpy method is used. The convection in the liquid PCM is accounted for by using the enhanced thermal conductivity approach together with the scaling theory [2]. The convection effect is only considered in the upper part of the PCM layer of height z_1 and width z_2 , while the zone $(z_2, H) - (z_1, z_2)$ is controlled by conduction.



Therefore, an average enhanced conductivity for liquid nodes is used in the one-dimensional model expressed by:

$$k_{enh,p} = \frac{k_l[(z_2.H)-(z_1.z_2)]+k_l.Nu_{z_1}(z_1.z_2)}{z_2.H} \quad (6)$$

where $k_{enh,p}$ is the liquid enhanced conductivity for the liquid PCM node p , H is the height of the glass brick filled with PCM and Nu_z is the Nusselt number correlation given by Berkovsky and Polevikov [3]. A one-dimensional unsteady energy equation was used for glazing and insulation layers and a heat balance taking into account convection, conduction and radiation was used on the surfaces in contact with the outdoor or indoor environments. The simplified model ran at least 75 time faster than CFD models dedicated to PCM thermal behavior. Comparing the results to those of CFD model, the difference found was less than 6%, in terms of the average liquid fraction, and less than 14% in terms of the position of the melting front. The TIM-PCM wall MATLAB model was then linked to the whole building energy simulation program TRNSYS, using TRNSYS Type 155. TRNSYS allowed taking into account the building geometry, the local weather data and to simulate different technical solutions to avoid the summer overheating problem. More details on the simplified model can be found in [4, 5].

3.1. Whole building energy behavior

Based on the numerical model, different scenarios were tested to solve the summer overheating problem. The scenarios are presented in Table 2. As shown in Fig. 9, the use of shading devices such as overhangs and blinds effectively reduced the indoor air temperature by six degrees, thus allowing thermal comfort, even though the PCM always remained in

liquid state. The indoor temperature could be further decreased when applying night ventilation.

3.2. Life cycle and economic analysis

The optimum TIM-PCM wall area was evaluated economically through life-cycle cost and payback period analysis. The solar wall was compared to a conventional double glazing window, set in the south wall of an office building in different climates: Barentsburg (polar), Kiruna (continental subarctic), Dras (continental), Toronto (humid continental), Paris (oceanic) and Sacramento (Mediterranean). For each location, the life cycle cost (LCC) and the payback period was calculated. The LCC is defined as:

$$LCC = IC + PWF.EC \quad (7)$$

where IC is the initial cost for implementing the considered wall (materials prices + installation + labor cost), EC is the annual energy cost required to maintain indoor comfort within the office building for the selected operating features and PWF is the present worth factor. The payback period is calculated as the ratio of the total initial cost by the energy savings cost including annual lighting savings cost in cities where its value is influential. More details on the definition of each term can be found in [5].

The results show that the incorporation of the TIM-PCM wall, on the south orientation, is more efficient than the use of a double-glazed on the same orientation in all considered climates. In polar and subarctic climates, the application of the TIM-PCM wall has a high economic value and the investment appears to be attractive, the payback period being 10.5 years and 7.8 years respectively. In Dras, the use of the wall is found infeasible economically due to low energy prices and high discount rates. At current prices, the TIM-PCM wall investment in Sacramento and Toronto does not offer economic benefits. Fig. 10 shows that in Paris, the wall is more cost effective than a double-glazed window, in terms of minimum life-cycle cost and payback period.

Table 1. Thermophysical properties of the PCM, the granulate silica aerogel and the glass layer.

Phase change material	Property	value	Properties/Materials	Silica aerogel	glass
Solid thermal conductivity	k_s (W/m.K)	0.182	Thickness (cm)	4	0.8
Liquid thermal conductivity	k_l (W/m.K)	0.182	k (W/m.K)	0.018 (at 25°C)	1
Latent heat of fusion	L_H (J/kg)	152000	C_p (J/kg.K)	1500	840
Solid specific heat	C_{ps} (J/kg.K)	1670	ρ (kg/m ³)	100	2700
Liquid specific heat	C_{pl} (J/kg.K)	2090	Solar transmittivity	57	80
Solid density	ρ_s (kg/m ³)	960	Solar absorptivity	10	12
Liquid density	ρ_l (kg/m ³)	884	Particle size	0.5-4.0 mm	-
Melting temperature	T_m (°C)	21.3	Pore diameter	20 nm	-
Thermal diffusivity	α (m ² /s)	$9,85.10^{-8}$	Porosity	> 90%	-



kinematic viscosity	ν (m ² /s)	11.10 ⁻⁶	Surface area	600-800 m ² g ⁻¹	-
Thermal expansion coefficient	β (1/K)	3.1.10 ⁻³			

Table 2. Simulated scenarios

Cases	Shading scenario
Case 1	No overhang and no external blinds (base case)
Case 2	Overhang of projection 1 m
Case 3	Venetian External Blinds with rotatable slat and a slat angle of 45 degrees /reduction factor 0.25
Case 4	Exterior Venetian Blinds with rotatable slat at 0-degree, silver color, reduction factor 0.069
Case 5	Overhang 1 m + blind 45° (case 2 + case 3)
Case 6	Overhang 1 m + blind 0° (case 2 + case 4)

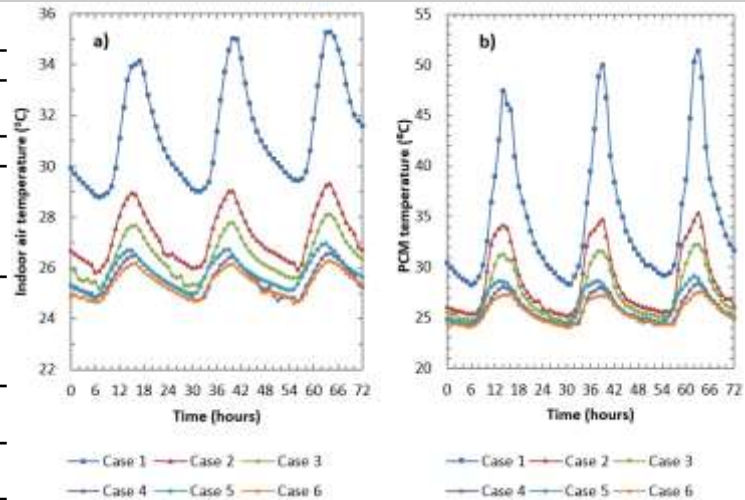


Fig. 9. (a) Indoor test room air temperature and (b) PCM temperature in summer (August 3-5, 2018)

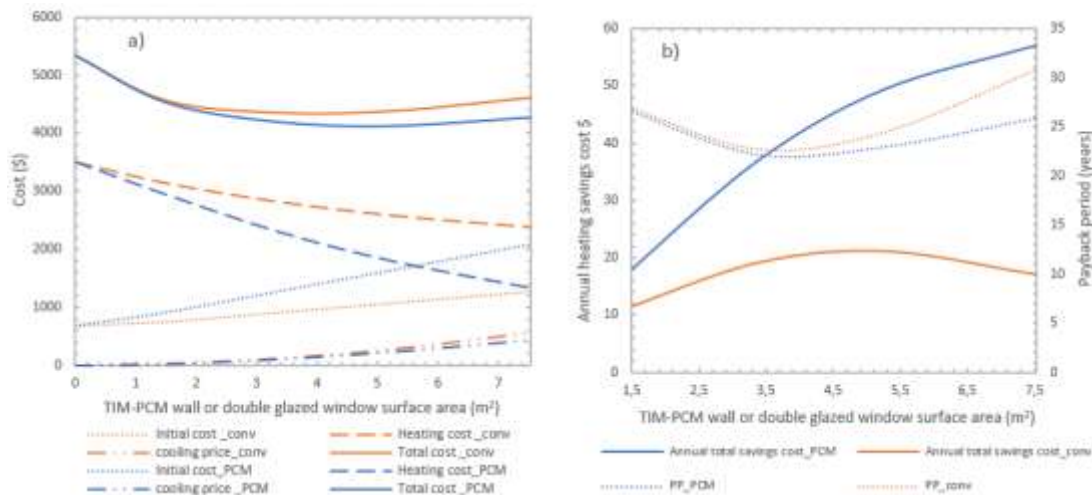


Fig. 10. (a) Life cycle cost and (b) payback period for a TIM-PCM wall and a double glazed window for Paris.

4. Conclusions

In the present paper, we presented the energy savings, thermal comfort, and economic analysis from using two innovative building envelopes integrating silica aerogels and PCMs. The methodology was both experimental and numerical. It was found that in all considered climates the proposed walls can provide huge energy savings while preserving thermal comfort. The best candidates for applying such systems are found where energy prices for heating (natural gas in our study) are relatively high, making the initial capital cost relatively insignificant compared to the heating and cooling savings cost.

REFERENCES

[1] Nocentini K., Achard P., Biwole P.H., Hygro-thermal properties of silica aerogel blankets dried 9, pp.1274 - 1291.

using microwave heating for building thermal insulation. Energy and Buildings, 2018, 158, pp.14 - 22.

[2] Jany P. and Bejan A., "Scaling theory of melting with natural convection in an enclosure," Int. J. Heat Mass Transf., 1988, vol. 31, no. 6, pp. 1221 - 1235.

[3] Bejan A., Convection heat transfer, Fourth edition. Hoboken, New Jersey: Wiley, 2013.

[4] Souayfane F., Biwole P.H., Fardoun F., Thermal behavior of a translucent superinsulated latent heat energy storage wall in summertime. Applied Energy, 2018, 217, pp. 390 - 408.

[5] Souayfane F., Biwole P.H., Fardoun F., Achard P., Energy performance and economic analysis of a TIM-PCM wall under different climates. Energy, 2019, 16



A Novel Nanocomposite Photocatalyst for Hydrogen Production

Nuray Güy¹, Keziban Atacan², Mahmut Özacar^{1,2}

¹ Sakarya University, Science&Arts Faculty, Department of Chemistry, 54187 Sakarya, Turkey.

² Sakarya University, Biomedical, Magnetic, Semiconductor Materials Application and Research Center (BIMAS-RC), 54187 Sakarya, Turkey.

Abstract:

The growing demand for energy has led to strong research to grow a clean and renewable energy source. Hydrogen stands out as one of the most perfect fuels thanks to its excellent energy conversion performance and zero carbon emissions. Photoelectrochemical (PEC) water splitting is a sustainable energy production technique that converts solar energy to hydrogen in the form of fuel. Semiconductors such as ZnO, TiO₂, WO₃, and BiVO₄ have an important role in the conversion of solar energy into the hydrogen via the PEC water splitting. But, they exhibit low PEC activity owing to their wide band gap energy which restricts the absorption of the visible light. Some methods such as noble metal doping, surface photosensitization and combining with narrow band semiconductors were applied to develop the photocatalytic performance. Coupling of TiO₂ with other semiconductors such as Bi₂O₃-TiO₂, g-C₃N₄-TiO₂, CdS-TiO₂, CuFe₂O₄-TiO₂ has exhibited to increase the photoelectrochemical efficiency by hindering the recombination of charge carrier. NiFe₂O₄ as a magnetic oxide semiconductor, is one of the co-catalysts due to its low cost and visible light response for photocatalysis and PEC water splitting. In this work, NiFe₂O₄/Ag/TiO₂ ternary nanocomposite was prepared for the PEC water splitting under visible light. Compared the PEC water splitting performance of NiFe₂O₄/Ag/TiO₂ with the pure TiO₂, NiFe₂O₄ and Ag/TiO₂, the ternary nanocomposite displayed the great activity. The superior activity of NiFe₂O₄/Ag/TiO₂ is related to its more visible light absorption and influential interfacial electron flow thanks to the synergetic interactions of Ag nanoparticles and TiO₂ and NiFe₂O₄. In conclusion, this work demonstrates that NiFe₂O₄/Ag/TiO₂ nanocomposite is effective in PEC water splitting applications.

Keywords: PEC water splitting, Ag doping, NiFe₂O₄.

1. Introduction

Continuous increase in the energy need in the world and the use of fossil fuels to meet this need increased the greenhouse gases in the atmosphere and caused other environmental problems. Both efforts to meet energy needs and solutions to environmental problems, researches were focused on the development of clean, environmentally friendly and renewable new energy sources [1,2]. Among the renewable energy sources, because hydrogen is a versatile clean fuel with high energy conversion efficiency and zero carbon emissions, it makes it the most ideal new generation energy source that has been researched in the hydrogen production and storage [3,4]. Photoelectrochemical (PEC) water splitting, which is one of several renewable energy production methods, is a good energy generation way for the production of hydrogen from water, which directly converts solar energy into clean and renewable energy [5,6].

Hitherto, various metal oxide photocatalysts such as ZnO, TiO₂, SnO₂, WO₃, BiVO₄, Fe₂O₃ and β-Bi₂O₃ have been extensively investigated for hydrogen production

by PEC water splitting [7]. Among these semiconductors, the TiO₂ is one of the mostly used photocatalysts for PEC water splitting due to its facile synthesis, non toxicity, low cost, good chemical stability, abundance in nature and excellent photoactivity [8]. But, the PEC hydrogen production efficiency of bare TiO₂ photoanodes is very limited owing to its wide band gap of ~3.18 eV and rapid electron-hole pair recombination [2]. In order to overcome increase photocatalytic activity of TiO₂ and shifting its light absorption from UV to visible region, many attempts, such as metal or non-metal doping, preparation nanocomposites of TiO₂ with a narrow band gap metal oxide or ferrites, surface sensitization with different quantum dots and formation of defects or oxygen vacancies on TiO₂ surface were carried out [9,10]. Also, many studies have shown that the fabrication of a composite of TiO₂ with noble metal nanoparticles, such as silver, gold and palladium, has highly efficient photocatalytic performance under visible-light because of the surface plasmon resonance (SPR) of Ag⁰, Au⁰ or Pd⁰ nanoparticles [11,12]. Furthermore, spinel ferrites were widely used in photocatalysis as co-catalysts due to their narrow



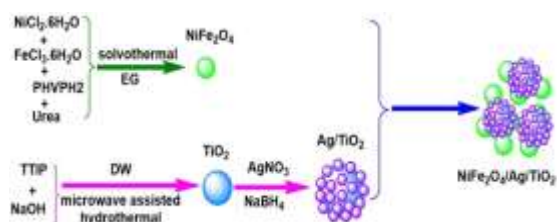
band gap, low cost, good photochemical stability and band gap located the visible spectrum [13]. When NiFe_2O_4 is used alone, it has low efficiency for hydrogen production by PEC water splitting due to the rapid recombination of charge carriers. Therefore, NiFe_2O_4 was utilized as composite photocatalysts fabricated with semiconductors such as TiO_2 , SnO_2 , ZnO or WO_3 in hydrogen production.

In this work, NiFe_2O_4 , TiO_2 , Ag/TiO_2 and $\text{NiFe}_2\text{O}_4/\text{Ag/TiO}_2$ photocatalysts for the PEC hydrogen production were successfully synthesized. Their crystal and morphological structures and optical properties were systematically characterized. The hydrogen production performance of these photocatalysts were evaluated under visible light through PEC water splitting. It was seen that the photocatalytic hydrogen production efficiency of $\text{NiFe}_2\text{O}_4/\text{Ag/TiO}_2$ increased compared to that of bare TiO_2 , NiFe_2O_4 and Ag/TiO_2 .

2. Materials and Methods

2.1. Synthesis of NiFe_2O_4 , TiO_2 , Ag/TiO_2 and $\text{Ag-NiFe}_2\text{O}_4/\text{TiO}_2$

Synthesis procedure of NiFe_2O_4 , TiO_2 , Ag/TiO_2 and $\text{NiFe}_2\text{O}_4/\text{Ag/TiO}_2$ nanocomposites were exhibited in Scheme 1. NiFe_2O_4 MNPs were prepared by the solvothermal method using Atacan et al [14]. For synthesis of TiO_2 nanoparticles, Çakar et al. synthesis procedure were used [15]. The borohydride reduction method was used for Ag doping on TiO_2 nanoparticles.



Scheme 1. The synthesis of NiFe_2O_4 , TiO_2 , Ag/TiO_2 and $\text{NiFe}_2\text{O}_4/\text{Ag/TiO}_2$ are shown schematically.

2.2. Synthesis of NiFe_2O_4 , TiO_2 , Ag/TiO_2 and $\text{Ag-NiFe}_2\text{O}_4/\text{TiO}_2$

The PEC characterizations were examined with a potentiostat/galvanostat to determine the hydrogen production using a three-electrode electrochemical cell

system. NiFe_2O_4 , TiO_2 , Ag/TiO_2 and $\text{NiFe}_2\text{O}_4/\text{Ag/TiO}_2$ onto ITO substrates as working electrodes, Ag/AgCl (saturated 0.3 M KCl) as reference and Pt wire as counter electrode were used, respectively [14]. 0.5 M of Na_2SO_4 aqueous solution was used as the electrolyte. A 500 W Xenon (Xe) lamp was used as the visible light source. An apparatus similar to that used by Kezban et al. was used for hydrogen gas production.

2.3. Characterization

The crystal phase was investigated by X-ray diffraction (XRD, PANalytical, Empyrean, Netherlands) with $\text{Cu K}\alpha$ ($\lambda = 1.54 \text{ \AA}$). The morphologies of the products were analyzed using a Philips XL30 SFEG scanning electron microscopy (SEM). The diffuse reflectance spectra (DRS) of the products were measured by using a Shimadzu UV-2600 UV-Vis spectrophotometer. Fourier transform infrared spectroscopy (FTIR) was analyzed with Perkin Elmer Spectrum Two FTIR spectrophotometer. In the preparation of ITO surfaces, platinum wire, and Ag/AgCl were used as working electrodes, counter electrode, and reference electrode, respectively [1]. The PEC measurements of the products were detected by the CHI 660C electrochemical workstation with a typical three electrode system.

3. Results and Discussions

The crystal structure and phase of the photocatalysts were analyzed by XRD patterns. The results are displayed in Figure 1. As can be seen in Figure 1., the diffraction peaks of NiFe_2O_4 verify that the NiFe_2O_4 had a crystal planes of the cubic spinel structure (ICSD no. 98-018-2237) [3]. TiO_2 has diffraction peaks at 25.3° , 37.8° , 48.0° , 53.9° , 55.1° , 62.7° , 69.7° , 75.6° and 83.0° , attributing to the (101), (004), (200), (105), (211), (204), (220), (215) and (303) reflections of anatase phase of TiO_2 (ICDS: 98-015-4601) [16]. For $\text{NiFe}_2\text{O}_4/\text{Ag/TiO}_2$ ternary nanocomposite, observed the diffraction peaks are well matched to crystal planes of anatase phase of TiO_2 and cubic spinel structure NiFe_2O_4 . Furthermore, in the XRD pattern of $\text{NiFe}_2\text{O}_4/\text{Ag/TiO}_2$, the diffraction peaks indicated with “#” corresponded with the (111), and (200) crystalline planes of metallic Ag.

FTIR spectra of NiFe_2O_4 , TiO_2 , Ag/TiO_2 and $\text{NiFe}_2\text{O}_4/\text{Ag/TiO}_2$ showed in Figure 2 in the range of $400\text{--}4000 \text{ cm}^{-1}$. The typical FTIR measurements for the prepared NiFe_2O_4 exhibit two absorption peaks in the range of 429 cm^{-1} and 554 cm^{-1} which assigned to the stretching vibrations of the metal-oxygen bond (Zn-O and Fe-O) at the tetrahedral sites octahedral

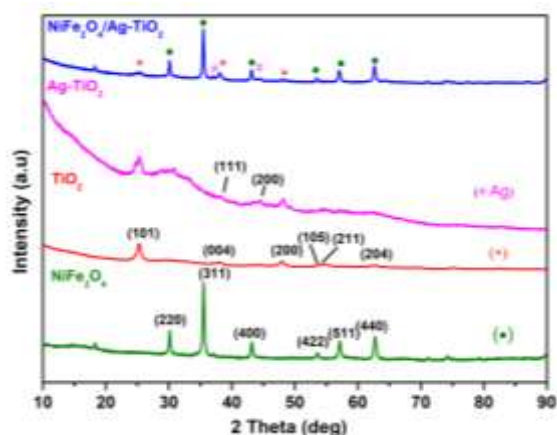


Figure 1. XRD patterns of samples

sites in spinel ferrite, respectively [17]. FTIR spectra of NiFe_2O_4 , TiO_2 , Ag/TiO_2 and $\text{NiFe}_2\text{O}_4/\text{Ag}/\text{TiO}_2$ showed in Figure 2 in the range of $400\text{--}4000\text{ cm}^{-1}$. The typical FTIR measurements for the prepared NiFe_2O_4 exhibit two absorption peaks in the range of 429 cm^{-1} and 554 cm^{-1} which assigned to the stretching vibrations of the metal-oxygen bond (Zn-O and Fe-O) at the tetrahedral sites octahedral sites in spinel ferrite, respectively [17]. For TiO_2 , a broad band below 1000 cm^{-1} was monitored at the spectra of both TiO_2 and Ag/TiO_2 , which can be corresponds to the bending and stretching vibrations of Ti-O-Ti bonds [18]. In the FTIR of $\text{NiFe}_2\text{O}_4/\text{Ag}/\text{TiO}_2$, the characteristic absorption peaks exhibit the curve of interactions between NiFe_2O_4 and Ag/TiO_2 .

Figure 3 shows SEM photographs of NiFe_2O_4 , Ag/TiO_2 and $\text{NiFe}_2\text{O}_4/\text{Ag}/\text{TiO}_2$. As seen from the images of SEM, the particles were generally agglomerated structures due to their magnetic properties [19]. The Ag/TiO_2 showed a regular rough spherical morphology in Figure 3 (b). The results obtained are supported by SEM images of reported studies [20].

The light absorption features of products were analyzed by UV-Vis diffuse reflectance spectroscopy (DRS) and Kubelka-Munk function, as illustrated in Figure 4. From in Figure 4, it is seen that only TiO_2 has a strong absorption in the UV spectrum owing to its large band gap energy. With doping Ag nanoparticles, band gap energy of TiO_2 shifts to the visible region. Due to the narrow band gap energy of NiFe_2O_4 , NiFe_2O_4 and $\text{NiFe}_2\text{O}_4/\text{Ag}/\text{TiO}_2$ nanocomposite also display absorption in the visible region, such as Ag/TiO_2 . The detected band gap energies of NiFe_2O_4 , TiO_2 , Ag/TiO_2

and $\text{NiFe}_2\text{O}_4/\text{Ag}/\text{TiO}_2$ are 1.60, 3.22, 2.98 and 1.68 eV, respectively. As a result, with doping Ag nanoparticles

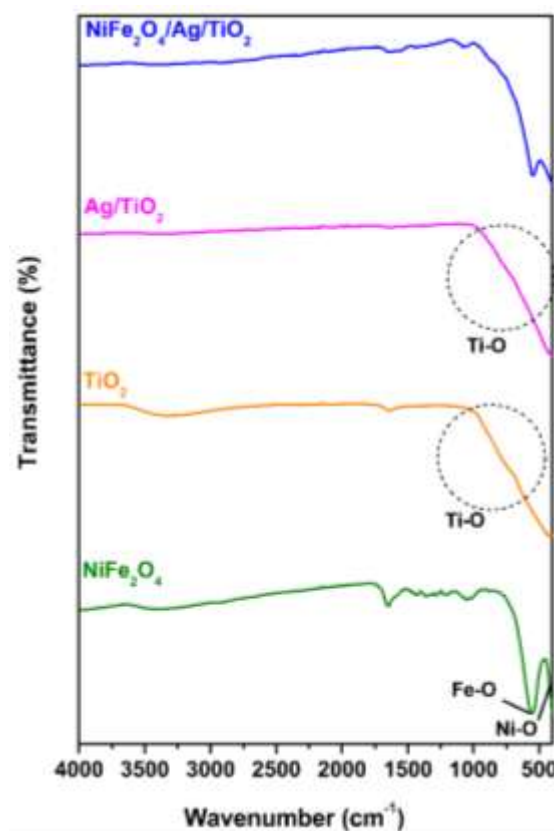


Figure 2. FTIR spectra of NiFe_2O_4 , TiO_2 , Ag/TiO_2 and $\text{NiFe}_2\text{O}_4/\text{Ag}/\text{TiO}_2$.

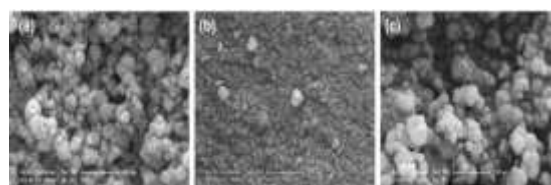


Figure 3. SEM images of NiFe_2O_4 (a), Ag/TiO_2 (b) and $\text{NiFe}_2\text{O}_4/\text{Ag}/\text{TiO}_2$ (c).

to the surface of TiO_2 and then combining with NiFe_2O_4 , the visible light absorption capability of TiO_2 was increased.

The photoelectrochemical (PEC) hydrogen production efficiency of the photocatalysts were investigated under visible light using a 300W Xenon lamp. The H_2 yields of NiFe_2O_4 , TiO_2 , Ag/TiO_2 and $\text{NiFe}_2\text{O}_4/\text{Ag}/\text{TiO}_2$ surfaces are illustrated in Fig. X. The PEC hydrogen production rate of NiFe_2O_4 , TiO_2 , Ag/TiO_2 and $\text{NiFe}_2\text{O}_4/\text{Ag}/\text{TiO}_2$ nanocomposites were measured to be 240.5, 6756.2, 26364.8 and 41453.6 μmol , respectively.



As seen in Figure 5, NiFe₂O₄/Ag/TiO₂ ternary nanocomposites have the highest PEC H₂ evolution efficiency. Based on the results of PEC H₂ evolution, it can be said that this is due to the formation of heterojunction structure of NiFe₂O₄ and TiO₂, the synergistic effect of Ag nanoparticles, and the delaying of recombination of photogenerated charge carriers [21].

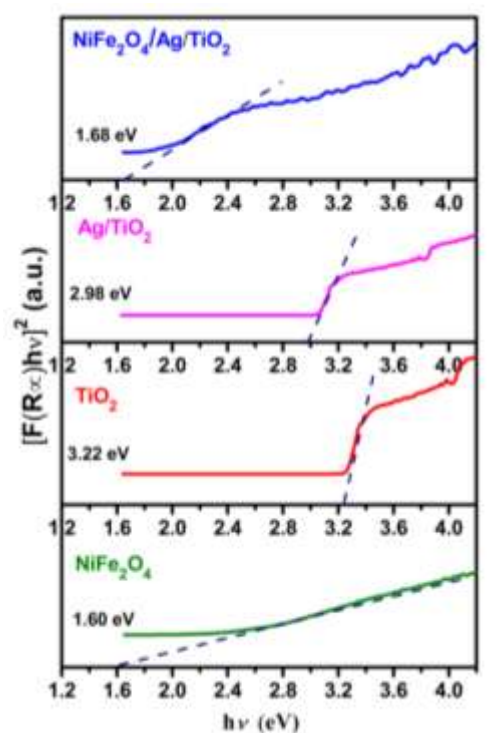


Figure 4. The band gap energies of samples.

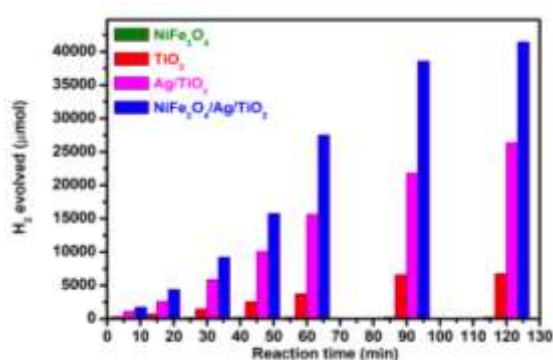


Figure 5. H₂ evolution by photoelectrochemical water splitting of the samples.

4. Conclusions

Ag metallic nanoparticles behave like electron traps that capture photoelectrons, improve interface charge transfer, and hinder recombination of photo excited

charge carriers. The ternary NiFe₂O₄/Ag/TiO₂ nanocomposites demonstrated several benefits such as stability, low-cost, simplicity and fast separation efficiency compared with other photocatalysts. This work provides insight on the improvement of photocatalysts for the production of hydrogen in energy applications.

REFERENCES

- [1] Yang H, Yan J, Lu Z, Cheng X, Tang Y. Photocatalytic activity evaluation of tetragonal CuFe₂O₄ nanoparticles for the H₂ evolution under visible light irradiation, *J. Alloys Compd.* 476 (2009) 715–719.
- [2] Hafeez H, Kumar, Lakhera SK, Karthik P, Anpo M, Neppolian B. Facile construction of ternary CuFe₂O₄-TiO₂ nanocomposite supported reduced graphene oxide (rGO) photocatalysts for the efficient hydrogen production, *Appl. Surf. Sci.* 449 (2018) 772–779.
- [3] Holladay, J.D., Hu, J., King, D.L., Wang, Y. An overview of hydrogen production technologies, *Catal. Today* 139 (2009) 244-260.
- [4] Sawant, S.Y., Munusamy, K., Somani, R.S., John, M., Newalkar, B.L., Bajaj, H.C. Precursor suitability and pilot scale production of super activated carbon for greenhouse gas adsorption and fuel gas storage, *Chem. Eng. J.* 315 (2017) 415-425.
- [5] Yang, W., Oh, Y., Kim, J., Jeong, M.J., Park, J.H., Moon, J. Molecular chemistry-controlled hybrid ink-derived efficient Cu₂ZnSnS₄ photocathodes for photoelectrochemical water splitting, *ACS Energy Lett.* 1 (2016) 1127-1136.
- [6] Masudy-Panah, S., Siavash Moakhar, R., Chua, C.S., Tan, H.R., Wong, T.I., Chi, D., Dalapati, G.K., Nanocrystal engineering of sputter-grown CuO photocathode for visible-light-driven electrochemical water splitting, *ACS Appl. Mater. Interfaces* 8 (2016) 1206-1213.
- [7] Park, J., Deshmukh, P.R., Sohn, Y., Gyu, W. ZnO-TiO₂ core-shell nanowires decorated with Au nanoparticles for plasmon-enhanced photoelectrochemical water splitting, *J. Alloys Compd.* 787 (2019) 1310-1319.
- [8] Kalathil, S., Khan, M.M., Ansari, S.A., Lee, J., Cho, M.H. Band gap narrowing of titanium dioxide



- (TiO₂) nanocrystals by electrochemically active biofilms and their visible light activity, *Nanoscale* 5 (2013) 6323–6326.
- [9] Khan, M.M., Ansari, S.A., Lee, J., Cho, M.H. Highly visible light active Ag@TiO₂ nanocomposites synthesized using an electrochemically active biofilm: A novel biogenic approach, *Nanoscale* 5 (2013) 4427–4435.
- [10] Chen, Z., Fang, L., Dong, W., Zheng, F., Shen, M., Wang, J. Inverse opal structured Ag/TiO₂ plasmonic photocatalyst prepared by pulsed current deposition and its enhanced visible light photocatalytic activity, *J. Mater.Chem. A2* (2014) 824–832.
- [11] Ding, D., Liu, K., He, S., Gao, C., Yin, Y. Ligand-exchange assisted formation of Au/TiO₂ schottky contact for visible-light photocatalysis, *Nano Lett.* 14 (2014) 6731–6736.
- [12] Su, C., Liu, L., Zhang, M., Zhang, Y., Shao, C. Fabrication of Ag/TiO₂ nanoheterostructures with visible light photocatalytic function via a solvothermal approach, *CrystEngComm* 14 (2012) 3989–3999.
- [13] Güy, N., Özacar, M. Visible light-induced degradation of indigo carmine over ZnFe₂O₄/Tannin/ZnO: Role of tannin as a modifier and its degradation mechanism. *Int. J. Hydrogen Energy* 43 (2018) 8779–8793.
- [14] Atacan, K., Topaloğlu, B., Özacar, M. General New CuFe₂O₄/amorphous manganese oxide nanocomposites used as photocatalysts in photoelectrochemical water splitting, *Appl. Catal. A – Gen.* 564 (2018) 33–42.
- [15] Ünlü, B., Çakar, S., Özacar, M. The effects of metal doped TiO₂ and dithizone-metal complexes on DSSCs performance, *Solar Energy* 166 (2018) 441–449.
- [16] Atacan, K., Güy, N., Çakar, S., Özacar, M. Efficiency of glucose oxidase immobilized on tannin modified NiFe₂O₄ nanoparticles on decolorization of dye in the Fenton and photo-biocatalytic processes, *J. Photochem. Photobiol. A: Chem.* 382 (2019) 111935
- [17] Zhou, T., Zhang, G., Yang, H., Zhang, H., Suo, R., Xie, Y., Liu, G. Fabrication of Ag₃PO₄/GO/NiFe₂O₄ composites with highly efficient and stable visible-light-driven photocatalytic degradation of rhodamine B, *RSC Adv.* 8 (2018) 28179–28188.
- [18] Zhang, L., Ni, C., Jiu, H., Xie, C., Yan, J., Qi, G. One-pot synthesis of Ag-TiO₂/reduced graphene oxide nanocomposite for high performance of adsorption and photocatalysis, *Ceram. Int.* 43 (2017) 5450–5456.
- [19] Haija, M.A., Abu-Hani, A.F.S., Hamdan, N., Stephen, S., Ayesh, A.I. Characterization of H₂S gas sensor based on CuFe₂O₄ nanoparticles, *J. Alloys Compd.* 690 (2017) 461–468.
- [20] Zhao, Y., Huang, Z., Chang, W., Wei, C., Feng, X., Ma, L., Qi, X., Li, Z. Microwave-assisted solvothermal synthesis of hierarchical TiO₂ microspheres for efficient electro-field-assisted-photocatalytic removal of tributyltin in tannery wastewater, *Chemosphere* 179 (2017) 75–83.
- [21] Gadelhak, Y., El Rouby, W.M.A., Farghali, A.A. Au-decorated 3D/1D titanium dioxide flower-like/rod bilayers for photoelectrochemical water oxidation, *Electrochim. Acta* 306 (2019) 185–197.



Hybrid Piezo-Pyroelectric Energy Scavenging by High β -phase Poly(Vinylidene fluoride) Membrane

IA Fadzallah¹, NS Sabran¹, NV Toan², T Ono³, SM Said⁴, MFM Sabri^{1*}

1-Department of Mechanical Engineering, Faculty of Engineering, University of Malaya, 50603 Kuala Lumpur, Malaysia

2- Microsystem Integration Center (μ SIC), Tohoku University, 980-0845 Sendai, Japan

3- Graduate School of Engineering, Tohoku University, 980-0845 Sendai, Japan

4- Department of Electrical Engineering, Faculty of Engineering, University of Malaya, 50603 Kuala Lumpur, Malaysia

*Corresponding author - Email: faizul@um.edu.my

Abstract:-

This article reports a novel work on the fabrication of microarrays of electrospun Poly(vinylidene fluoride) (PVDF) membrane for MEMS applications. Micropatterning of PVDF membrane is an essential step in fabrication process in order for the sample to be integrated in microelectromechanical systems. The high β -phase fraction of PVDF membranes was successfully synthesized by one step electrospinning technique. A new fabrication process for micropatterning of electrospun PVDF membrane is being proposed using dry reactive ion etching. Oxygen plasma was chosen as the feeding gas in investigation for high etching rate in PVDF microstructure fabrication process. Micropatterning dimensions of 200/500/200 μm with the height of over 50 μm and etching rate of 2 $\mu\text{m}/\text{min}$ were achieved in this work. Details of the fabrication process are discussed. High etching rate of patterning process with the selected parameters can be achieved on the electrospun PVDF membranes. This work has demonstrated successful micropatterning and integration of PVDF membrane into MEMS, thus open the possibilities for various application such as for sensing and actuators utilizing polymer membranes.

1. Introduction

Poly(Vinylidene Fluoride) (PVDF) is polymer that is flexible, lightweight, inexpensive and is available commercially in various thickness. It has high resistivity towards most chemicals, oxidants and intense ultraviolet light. PVDF exhibits five conformations; α , β , γ , δ , ϵ . From these conformations, the most influential and typical are those of α - and β -phases. The network of α -phase comprises of two chains that have TGTG' conformation (T = Trans, G=gauche⁻, and G'=gauche⁺) where the axis of the chain and the dipole components are antiparallel, thus neutralizing each other. The naturally occurred α -phase is categorized as nonpolar and non-piezoelectric. In contrast, the chain axis in β -phase PVDF and the dipole components are parallel since its conformation is all trans (TTTT), hence results in greatest spontaneous polarization. In addition, this type of conformation displaying pronounced ferroelectric and piezoelectric properties [1]. Various methods have been explored in order to produce β -phase PVDF, such as poling, mechanical

stretching, and electrospinning. In the poling process, the reorientation of molecular dipoles within the polymer bulk medium occurred through the application of a high electric field at an elevated temperature. In order to sustain the orientation state of the molecular dipoles, the temperature of the material is cooled down in the presence of the electric field [2]. Whereas in the mechanical stretching technique, the polymer will be stretched at elevated temperature which will result in polarity reorientation [3].

A high β -phase content PVDF membrane can be produced using the electrospinning process, where a high voltage is used to create an electrically charged jet of polymer solution out of the nozzle. The electric field encourages dipole alignment of its molecules, hence resulting in β -phase occurrence in PVDF which contributes to its piezoelectric property [4]. Thus, self-polarized PVDF membrane which eliminates a need for the post treatment process can be synthesized in a one step process [5,6]. To simplify the process of dipole alignment in electrospinning, as seen in Fig. 1, the β -phase will



be produced from α -phase as a high potential was applied.

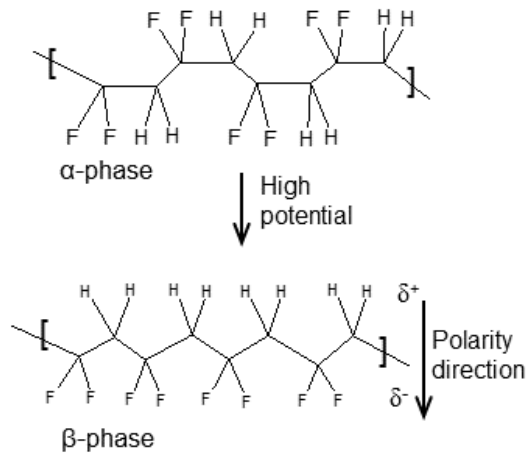


Fig. 1. The change of polarity in PVDF along the polymeric chain with potential applied.

The motivation of this work is to develop a process for fabrication of microarrays directly onto flexible electrospun β -phase (PVDF) membrane that will be useful for many applications such as thermal and tactile sensors and flexible energy harvesters. To the best of the authors' knowledge, micropatterning of electrospun PVDF membrane has yet to be explored. In this work, β -phase PVDF membranes were synthesized by electrospinning. The electrospinning technique was chosen due to its one step process in producing a highly β -phase content membrane, compared to the conventional process where the fabrication of the membrane requires a few separate processes and can be quite elaborate. The β -phase fraction of the electrospun PVDF membrane will be examined using Fourier transform infrared spectrometer and x-ray diffraction. Next, dry reactive ion etching utilizing oxygen plasma with particular process conditions have been chosen to investigate the micropatterning process on electrospun PVDF membrane.

2. Methodology

A. Electrospinning of PVDF membrane

The PVDF solution was prepared by dissolution of PVDF powder (Aldrich; $M_w = 534000$ g/mol) in a solvent mixture of N,N-dimethylformamide (Sigma-Aldrich) and acetone (Sigma-Aldrich). All chemicals were used as purchased. The solvent was mixed in a ratio of 7:3 (DMF:acetone) prior to use.

The PVDF solution was stirred overnight at 60°C to ensure homogeneity. Aluminium foil was used as a collector during the electrospinning process. The flow rate of PVDF solution is controlled at 4 mL/hour onto the aluminium foil with the drum rotating at a speed of 750 rpm. The tip-to-collector distance was fixed at 10 cm and the applied voltage was set at 12 kV. All of the collected PVDF membranes have thickness in the range of 50 – 70 μm .

B. PVDF membrane patterning

The PVDF membrane was fixed on a holder with the stencil mask covering the top part. The sample was exposed to oxygen plasma in dry RIE machine (Canon-ANELVA L-201D) for a specific time. The flow rate of oxygen gas was 20 sccm, process pressure was 5 Pa and RF power was 100 W. After the etching process, the depth of the etching part was measured with a contact type step meter (Kosaka Laboratory Ltd.) in order to determine the etching rate.

3. Results and Discussions

A. Morphology and β -phase characterization of electrospun PVDF membrane

Fourier transform infrared (FTIR) spectroscopy has been utilized to characterize the different crystalline phases. The FTIR patterns of PVDF originates from oscillations of large parts of the skeleton and/or attached functional groups. The fraction of β -phase can be calculated using the following equation [7,8]:

$$F(\beta) = \frac{A_\beta}{\left(\frac{K_\beta}{K_\alpha}\right)A_\alpha + A_\beta} \quad (1)$$

Where $F(\beta)$ is the β -phase fraction PVDF; A_β and A_α are the absorption peaks of α -phase at 763 cm^{-1} and β -phase peak at 840 cm^{-1} respectively; K_α denotes the absorption coefficient of α -phase peak at $763\text{ cm}^{-1} = 6.1 \times 10^4\text{ cm}^2\text{ mol}^{-1}$; K_β denotes the absorption coefficient of β -phase peak at $840\text{ cm}^{-1} = 7.7 \times 10^4\text{ cm}^2\text{ mol}^{-1}$.

From (1), we can estimate the fraction of β -phase PVDF by extracting the spectra specifically on the characteristic peaks of α -phase and β -phase in the range of 763 cm^{-1} and 840 cm^{-1} respectively as shown in Fig. 2. In the characteristic peak of α -phase (Fig.2a), the $F(\beta)$ was calculated to be 22% and the



amount increased to 81% in the characteristic peak of β -phase (Fig.2b).

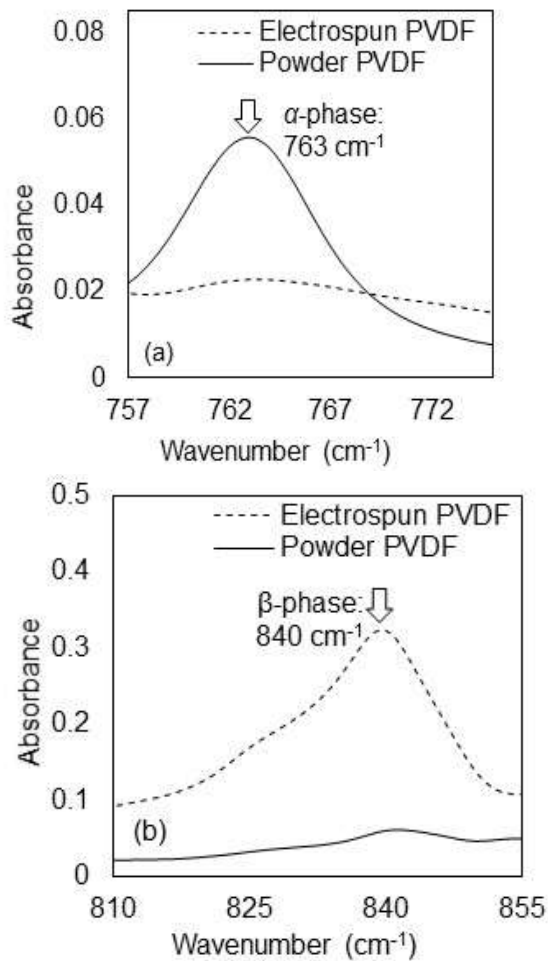


Fig. 2. Spectra extracted in the range of characteristic peak of; (a) α -phase and (b) β -phase

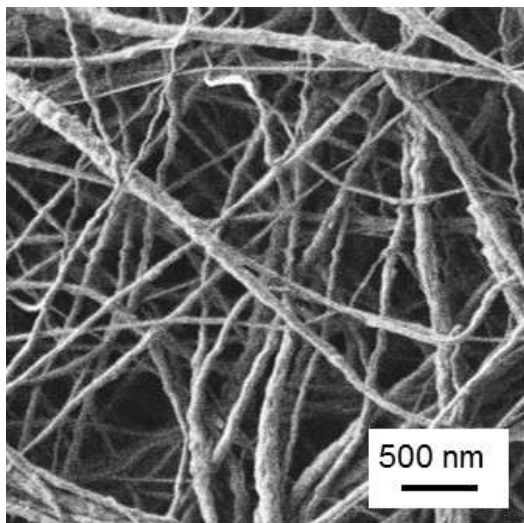


Fig. 3. SEM image of PVDF nanofiber

This shows that electrospinning process has successfully increased the β -phase fraction which contribute to its piezoelectricity. This can be done without further treatment i.e. poling, hence the electrospun PVDF membrane is expected to be used in application where the β -phase is crucial such as in energy harvesting device and sensors. The electrospinning process results in randomly oriented of PVDF nanofibers which can be seen SEM image as in Fig. 3 with the average diameter in the range of 90 – 230 nm.

The dimension of 200/500/200 μm width/length/ditch with height of over 50 μm were realized using the setup as shown in Fig. 4 (a). The etching rate of the process was calculated to be 2 $\mu\text{m}/\text{min}$. Hence, the micropatterning of electrospun PVDF membrane into microarrays were successfully done which can be seen in Fig. 4 (b).

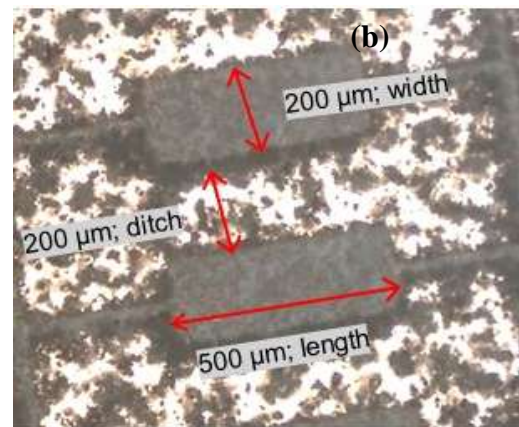
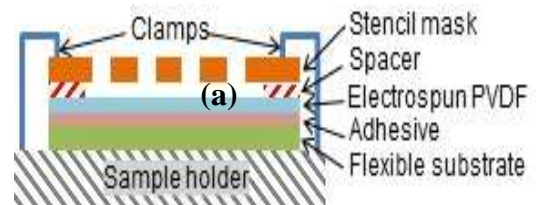


Fig. 4. (a) Sample setup of micropatterning process, (b) Image of the PVDF microarrays

The etching rate of PVDF microstructures in this work is higher than other reported values in the previous work by Han et al., (2012) and Miki et. al.,(2015) [9,10]. They claimed their etching rates to be 12.8 $\mu\text{m}/\text{hr}$ and 5.2 $\mu\text{m}/\text{hr}$ respectively. However, the long exposure etching time at high temperature might affect the d_{33} value thus a better process condition is needed in order to obtain a higher etching rate. The speed of the etching was improved in this work due to the morphology of the sample. In



the previous works they used conventional membrane which has a very little porosity, hence they are different compared to the one that was used in this work. The electrospun sample in this work has a different morphology where the fibers were randomly arranged and thus the membrane has higher porosity. The higher porosity thus results in higher etching rate which was reported to be 2 $\mu\text{m}/\text{min}$ in this work. In the current work, PVDF arrays were successfully fabricated with the process condition 100 W of RF-power, 20 sccm of O_2 gas-flow and 5 Pa of pressure with 35 mins of etching time.

4. Conclusions

This paper reported a relatively simple and easy micropatterning and integration process. The PVDF membrane with high β -phase fraction of 81 % was successfully synthesized by one step process using electrospinning. The study of surface morphology on the electrospun PVDF membrane shows good size of nanofibers with diameter ranging from 90 - 230 nm. The developed process using reactive ion etching with specific conditions were successfully implemented on electrospun PVDF membranes. Micrograph result indicated that the micropatterning process with reactive ion etching were successfully executed on the electrospun PVDF membrane, of array dimension of 200/500 μm length/width. This work presented the possibilities of micropatterning on the electrospun PVDF membrane for integration into MEMS and micro devices.

Acknowledgements

This work was supported by Postgraduate Research Fund (PPP), University of Malaya, PG119-2016A. Part of this work has been done in Graduate School of Engineering, Tohoku University, Japan and supported by Japan Student Services Organization (JASSO) Scholarship. Fadzallah would like to express heartfelt gratitude towards Ministry of Education of Malaysia for MyBrain Scholarship awarded.

REFERENCES

- [1] R. Khajavi and M. Abbasipour, "Piezoelectric PVDF Polymeric Films and Fibers: Polymorphisms, Measurements, and Applications," in *Industrial Applications for Intelligent Polymers and Coatings*, 2nd ed., vol. 3, M. Hosseini, and A. S. H. Makhlof, Ed. Switzerland: Springer International Publishing, 2016, pp. 313-336.
- [2] K. S. Ramadan, D. Sameoto and S. Evoy. (2014). A review of piezoelectric polymers as functional materials for electromechanical transducers. *Smart Mater. Struct.* 23(033001), pp. 1-26.
- [3] F. Wang, X. Zhao, and J. Li. (2015). PVDF energy-harvesting devices: Film preparation, electric poling, energy-harvesting efficiency. Presented at IEEE Conference on Electrical Insulation and Dielectric Phenomena (CEIDP).
- [4] D. Sengupta, A. G. P. Kottapalli, S. H. Chen, J. M. Miao, C. Y. Kwok, M. S. Triantafyllou, M. Asadnia. (2017, October). Characterization of single polyvinylidene fluoride (PVDF) nanofiber for flow sensing applications. *AIP Advances*. 7(10), 105205.
- [5] Ju, B.-J., Oh, J.-H., Yun, C., & Park, C. H. (2018). Development of a superhydrophobic electrospun poly(vinylidene fluoride) web via plasma etching and water immersion for energy harvesting applications. *Rsc Advances*, 8(50), 28825-28835.
- [6] Ghafari, E., & Lu, N. (2019). Self-polarized electrospun polyvinylidene fluoride (PVDF) nanofiber for sensing applications. *Composites Part B: Engineering*, 160, 1-9.
- [7] Q. Guo, M. Baqeri, M. M. Abolhasani, A. Oroumei, M. Naebe, and M. R. Mozdianfar. (2015, April). Influence of processing conditions on polymorphic behavior, crystallinity, and morphology of electrospun poly(vinylidene fluoride) nanofibers. *J. Appl. Polym. Sci.* 132(30), 42304.
- [8] E. Kabir, M. Khatun, L. Nasrin, M. J. Raihan and M. Rahman (2017, March). Pure β -phase formation in polyvinylidene fluoride (PVDF)-carbon nanotube composites. *J. Phys. D Appl. Phys.* 50, 163002.
- [9] H. Han, Y. Nakagawa, Y. Takai, K. Kikuchi, S. Tsuchitani, and Y. Kosimoto. (2012, July). Microstructure fabrication on a β -phase PVDF film by wet and dry etching technology. *J. Micromech. Microeng.* 22, 085030.
- [10] H. Miki, G. Matsui, M. Kanda, and S. Tsuchitani. (2015, February). Fabrication of microstructure array directly on β -phase poly(vinylidene fluoride) thin film by O_2 reactive ion etching. *J. Micro*
- [11] *mech. Microeng.* 25, 035026.



Numerical Study of Subcooling Effect on Single Bubble Growth by Using Volume of Fluid Model

Zeeshan Ahmad Khan^{1*}, Majid Ali¹

1- US-Pakistan Center for Advanced Studies in Energy (USPCAS-E) National University of Sciences and Technology Islamabad Pakistan

*Email: zakmt293@gmail.com

Abstract

Nucleate boiling phenomenon is heat transfer mechanism which is found in many engineering applications such as processing, chemical, nuclear and electronics industry. The basic physics associated with this phenomenon cannot be revealed with the proposed mechanistic and empirical models. To explicate the phenomenon an alternative approach of numerical simulation is adopted in this study. Bubble growth is simulated in both superheated and subcooled domain through volume of fluid interface tracking (VOF) method. Phase change which occurs due to evaporation and condensation in bulk fluid is modelled through Lee's model at the interface between two phases. Energy and mass source terms due to phase change are incorporated in governing equations through additional subroutines written in C language. The simulation results of mass transfer due to phase change and effect of subcooling on bubble growth are investigated in detail. The results show that subcooling effect retards the motion of bubble growth by an amount of bubble cap which is present in subcooled region. The size of the bubble increases in both subcooled and superheated regions due to evaporation of liquid in superheated region.

Keywords: Subcooling, VOF Method, Mass Transfer, Evaporation, Condensation

1. Introduction

Large amount of heat in the form of latent energy is transferred in nucleate boiling making it an efficient heat transfer mechanism. The applications of nucleate boiling is found in many areas of engineering including nuclear, chemical and microelectronics cooling[1]–[3]. Though number of applications in many areas, the science of the phenomenon is not yet very clear and varies from one application to another also called by some researchers as an “insecure” science[4]. Insecure world is used to reveal the dependence of phenomenon on a wide range of parameters. These parameters include nucleation site density, evaporation from superheated liquid and microlayer, surface properties, heat flux and other system variables due to which a comprehensive model is not available[5]. Number of empirical and semi-empirical correlations have been proposed in last decades to predict the associated dynamics of bubble[6]–[7]. However, the correlations which are proposed, are limited to their own experimental findings and cannot predict the findings of other researchers with reasonable accuracy. Therefore, an alternative numerical modelling approach is needed to depict dynamics of nucleate boiling with wide range of parameters.

Phase change phenomenon is involved in nucleate boiling for which mass and energy transfer are modelled at interface between two phases. For this

purpose, interface tracking algorithms are needed to be adopted to track the interface between two phases. Level-Set, Volume of Fluid (VOF) and a combination of Level-Set and VOF which is Coupled Level Set Volume of Fluid (CLSVOF) are the common interface tracking methods in simulations[8]–[10]. These interface tracking methods are used by researcher to simulation nucleate boiling with their own devised phase change models. First numerical study on nucleate boiling was done by Son and Dhir[11] who used level set method with mass and energy balance at interface. Son et.al[12] followed model of Son and Dhir[11] to simulate vertical bubbles merger from a single nucleation site. Mukherjee and Dhir[13] also followed the model of Son and Dhir[11] to simulate lateral bubbles merger from different nucleating sites in pool boiling respectively. Numerical model of Mukherjee and Dhir[13] was further used for studying the impact of dynamic contact angle and hydrophilic surfaces on vapor bubble growth[14]–[15]. CLSVOF interface tracking method was used by Kong Ling et.al[16] for simulating nucleate boiling and merger of vapor bubbles. Heat flux was measured and compared with experimental correlations which showed good agreement. CLSVOF interface tracking method and phase change model was further used by K.Ling and W.Q.Tao [17] to study the effect of heat transfer coefficient in shallow liquid which showed an increase in heat transfer coefficient. Kunkelmann and Stephan[18] were the first who simulated



growth of spherical bubble by coupling VOF with phase change model of S. Hardt and F.Wondra [19]. More refinement of mesh and more bubble ebullition cycles were recommended to capture evaporation and validate the results with experiment respectively. The literature review shows, level set is mostly used by researchers for interface tracking with their own devised phase change models. Though it has been reported that level set method is not volume conservative and may lead to diffusion of mass in simulating phenomenon involving phase change [20].

This study focuses on simulating nucleate boiling by coupling a phase change model with a conservative mass interface tracking method. To accomplish this, volume of fluid (VOF) method is used for the interface tracking and it is coupled with a phase change model to simulate nucleate boiling. A two-dimensional axi-symmetric geometry is considered for simulating nucleate boiling. The simulation results of mass transfer due to phase change and effect of subcooling on bubble growth are investigated.

2. Methodology

2.1 Governing Equations

Mass conservation equation solved during the simulation is given by equation (1)

$$\nabla \cdot (\rho \vec{v}) = S_m \quad (1)$$

In above equation S_m refers to the mass source term due to phase change. The volume fraction equation is solved only for the secondary phase. The secondary phase which is vapor in our case, the volume fraction equation is written as

$$\frac{\partial \alpha_v}{\partial t} + \nabla \cdot (\alpha_v \vec{v}) = \frac{\alpha_v}{\alpha} S_m \quad (2)$$

In equation (2) α_v and \vec{v} presents the volume fraction and velocity of the vapor phase. The volume fraction is sum of both phases and it must satisfy the following criterion of equation (3)

$$\alpha_l + \alpha_v = 1 \quad (3)$$

Both the phases share a same equation of momentum which is solved for both phases in the simulation and is given by equation (4)

$$\rho \frac{\partial \vec{v}}{\partial t} + \rho \nabla \cdot (\vec{v} \vec{v}) = -\nabla p + \nabla \cdot [\mu(\nabla \vec{v} + \nabla \vec{v}^T)] + \rho \vec{g} + \vec{F}_{cst} \quad (4)$$

\vec{F}_{cst} in equation(4) refers to the surface tension force at surface and it is modelled as volumetric force

through the continuum surface force model of Brackbill et.al[21]. The value of \vec{F}_{cst} is given for two phases and is given by equation (5)

$$\vec{F}_{cst} = \sigma \frac{\rho k \nabla \alpha_v}{0.5(\rho_l + \rho_v)} \quad (5)$$

In equation (5) σ presents surface tension coefficient and k represent the interface curvature which is further expressed in the form normal vector divergence which given by equation (7)

$$k = \nabla \cdot \hat{n} \quad (6)$$

$$\hat{n} = \frac{\nabla \alpha_v}{|\alpha_v|} \quad (7)$$

The equation of energy is modelled as

$$\frac{\partial}{\partial t} (\rho E) + \nabla \cdot [\vec{v}(\rho E + p)] = \nabla \cdot (k \nabla T) + S_e \quad (8)$$

Where S_e refers to the source of energy due to phase change. The values of other variables such as density, viscosity and thermal conductivity in each cell of a domain are based upon their volume fraction. Equation (9) presents a general expression for them in terms of ϕ which can be replaced by density, viscosity, and thermal conductivity.

$$\phi = \alpha_l \phi + \alpha_v \phi \quad (9)$$

2.2 Phase Change Model

In equation (1) and equation (8) S_m and S_e refers to mass and energy sources due to phase change and are incorporated in governing equations to model the energy and mass transfer. The phase change model of lee[22] is used to calculate these source terms of mass and energy. The model adds these terms based upon the volume fraction of a cell and its temperature. If a cell contains both vapor and liquid phases with temperature exceeding saturation temperature of the liquid. Evaporation of liquid would take place in the cell for which mass source term is given by equation (10)

$$\dot{m}_{lv} = \frac{\omega \rho_l \alpha_l (T_{cell} - T_{sat})}{T_{sat}} \quad 10$$

Similarly, if a cell temperature is less than the saturation temperature of the liquid, condensation of vapor would take place. The source term for condensation is given by equation (11)

$$\dot{m}_{vl} = \frac{\omega \rho_v \alpha_v (T_{cell} - T_{sat})}{T_{sat}} \quad 11$$



where T_{cell} is the temperature of a cell containing an interface while α and ρ represents volume fraction and density of respective phases with subscripts l and v stands for liquid and vapor. ω is a relaxation parameter for controlling the rate of mass transfer between phases. The value ω should be taken as such so that, the temperature in region containing interface remain near saturation temperature of fluid. For this purpose, the value of ω taken here is 100/s. The energy source e due to phase change process is evaluated through equation (12)

$$e = h_{lv} * \dot{m} \quad 12$$

3. Simulation Procedure

3.1 Computational Domain

A 2-dimensional axi-symmetric domain is considered to perform the simulation. The length of the domain is 2mm and 4mm in height. The imposed boundary conditions include constant surface temperature at bottom, pressure outlet at top of the domain, axi-symmetric conditions on left side and no flux conditions on right side as shown in Figure 1. To save the computational time, nucleation from the surface and development of thermal boundary layer processes are bypassed. To perform these processes, an initial bubble of radius of 0.1mm is placed in the domain, while a thermal boundary

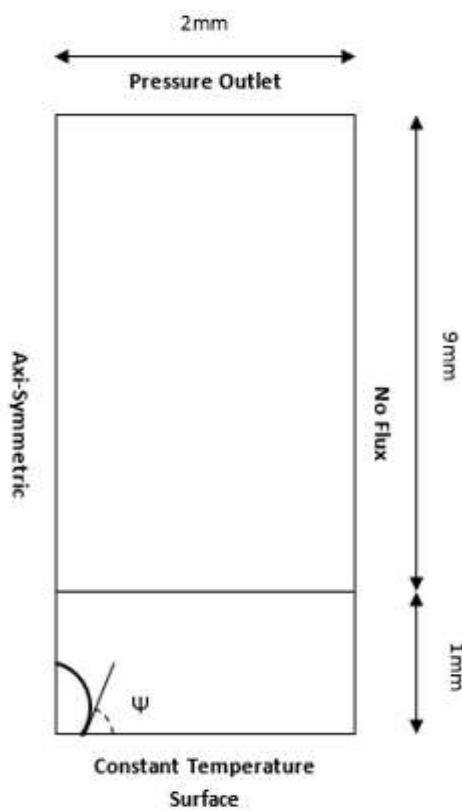


Figure 1 Illustration of Simulation Domain

layer is patched in domain. The temperature of thermal boundary layer varies linearly from 395K at 0mm to 353K at 1mm. The region above 1mm height is kept at subcooled temperature of 353K. The contact angle of the bubble with the wall Ψ considered here is 70° . A brief summary of simulation conditions is given in Table 1.

3.2 Working Fluid

The working fluid used in this simulation is water at atmospheric condition. The properties of water are given in Table 1 as shown below

Table 1 Properties of Working Fluids

Properties	Liquid	Vapor
Density (kg/m ³)	958.37	0.59759
Dynamic Viscosity (μPa-s)	281.67	12.231
Surface Tension (N/m)	0.005891	-
Thermal Conductivity (W/mK)	0.677	0.02458
Enthalpy (KJ/KgK)	419.06	2675.5
Specific Heat (KJ/KgK)	4.2156	2.0799
Latent Heat (KJ/Kg)	2256	-

3.3 UDF Implementations and Phase Change

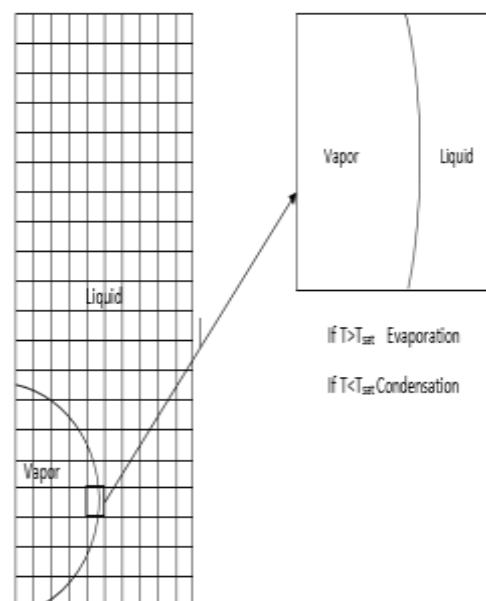


Figure 2 Interface Tracking and Phase Change



The rate of mass and energy transfer due to evaporation and condensation between the two phases needs to be modelled at the interface. To track the interface between the two phases, additional user-defined functions (UDFs) are written in C language. For the computational domain show in Figure 2, the UDFs first loop through all the cells

through c-loop. During looping the UDFs retrieve volume fraction of both phases in cells. For a cell which possess vapor phase volume fraction (α_v) between 0 and 1 is considered as an interfacial cell as shown on right side of Figure 2. Based upon temperature and volume fraction of the cell containing interface mass and energy source terms due to evaporation and condensation are calculated from equation (10), (11) and (12) and are implemented in governing equations.

3.4 Solver Settings

Fluent 16.0 is used to solve the governing equations of mass, momentum, and energy. Pressure and velocity are coupled with the PISO algorithm. The second-order upwind scheme is used for discretizing momentum and energy equations, while Geo-reconstruct scheme is used for reconstruction of interface. Transient simulation is performed with variable time steps by using courant number. Courant number is a dimensionless quantity refers to information wave traversed in a time step through a given cell element and is mentioned in equation (13). A constant value of courant number 0.25 is considered for simulation. Based upon this value the smallest time taken for a cell in overall domain is considered as time step. Convergence criterion is set to $1e-8$ for energy equation while for all other equations it is set to be $1e-4$.

$$Co = u \frac{\Delta t}{\Delta x} \quad 13$$

4. Results and Discussions

4.1 Grid Independence Test

At initial stage, the domain is discretized with a structured grid having a coarse element size of $14 \mu\text{m}$. The grid is further refined with a continuous decrease in an element size up to $8 \mu\text{m}$ as shown in Table 2. The growth of the bubble is observed both in a lateral and vertical directions. Figure 3 shows the contours of the bubble that are drawn at time $t=10\text{ms}$. It is observed that the results of grid c and d are very close to each other. Though the grid d has large number of cells than grid c which will require more time and computational resources. Therefore,

grid c is selected for further simulation to save computational time and resources.

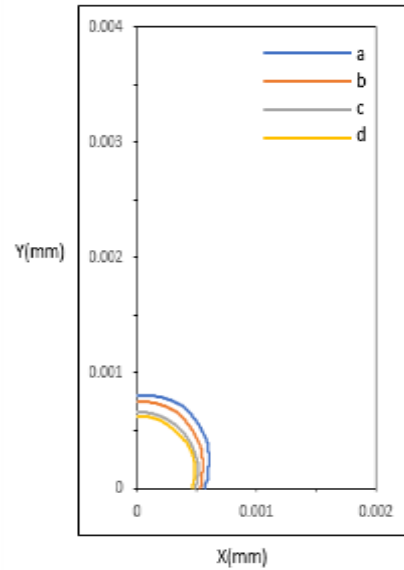


Figure 3 Contours of Bubble Growth at Time ($t = 10\text{ms}$)

Table 2 Element Size Distribution for Grid Independency

Grid	Element Size(μm)	Cells Amount	x-(mm)	y-(mm)
a	14	40044	0.57	0.79
b	12	54780	0.534	0.749
c	10	79401	0.495	0.661
d	8	124251	0.468	0.628

4.2 Mass Transfer

The contours of mass transfer for the bubble growth period is show in Figure 4. The region of the domain considered has a height of 0.7mm and a width of 1.0mm . At time $t=0\text{ms}$, bubble completely lies in superheated liquid due to which evaporation occurs at interface of the bubble. The rate of evaporation depends on the temperature distribution at the interface in domain. At initial stages, maximum rate of evaporation is observed, and the growth of vapor bubble occurs abruptly. As the bubble grows in vertical direction its upper portion proceed towards region near saturation temperature. This leads to a decrease in rate of evaporation which is observed at time $t=2\text{ms}$ and continues up to time $t= 5\text{ms}$. After time $t=5\text{ms}$ the bubble crosses the saturated temperature region of 373K and enters the subcooled region. Condensation starts take place at



the interface of the bubble when, time $t=6\text{ms}$. The rate of condensation is minimum at initial stage due to presence of small portion of the bubble interface in subcooled region. As the growth of bubble size continues, the rate of condensation also increases in subcooled region. The condensation halts the growth of bubble but still the size of bubble increases. It is due to presence of the major bubble interface portion in superheated region as compared to subcooled region. As a result of which more evaporation occurs at interface as compared to condensation.

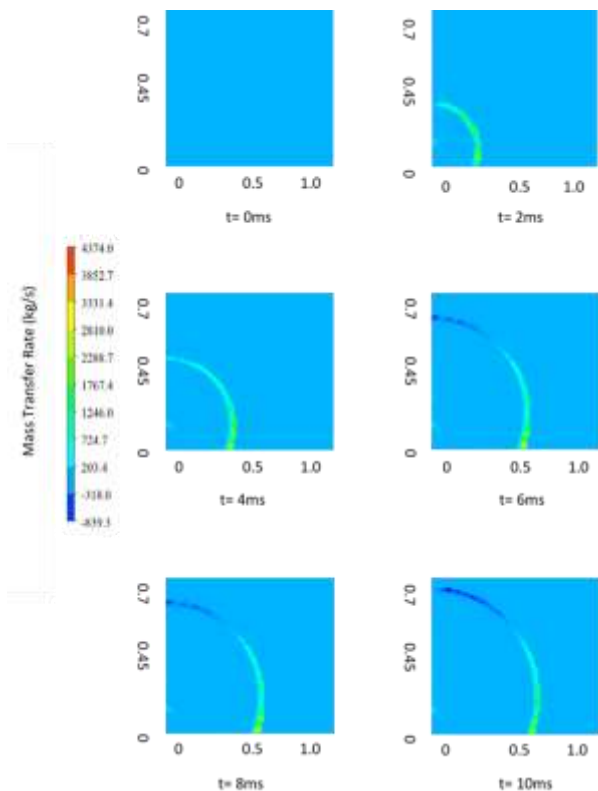


Figure 4 Contours of Bubble Growth

5. Conclusions

Numerical simulation of bubble growth and the impact of subcooling on bubble growth is studied. Continuous tracking of the interface is performed through the volume of fluid (VOF) model, and mass and energy transfer are evaluated based on the local temperature. The following conclusions are drawn from this study as,

- The growth rate and size of the bubble are affected by the local temperature at interface due to which mass is added or removed from the bubble in the form of evaporation and condensation respectively.

- The subcooling effect retards the motion of bubble growth in both vertical and lateral direction and this retardation depends on the portion of the bubble cap which is present in the subcooled regions.
- Increase of bubble size in the domain which contains both superheated and subcooled regions occur due to evaporation from the superheated liquid.

Acknowledgment

The author greatly acknowledges the support of the US-Pakistan (USPCAS-E) Center for Advanced Studies in Energy for the completion of this research.

REFERENCES

- [1] N. Cheng, Y. Guo, and C. Peng, "A numerical simulation of single bubble growth in subcooled boiling water," *Ann. Nucl. Energy*, vol. 124, pp. 179–186, 2019.
- [2] N. A. Patankar, "Supernucleating surfaces for nucleate boiling and dropwise condensation heat transfer," pp. 1613–1620, 2010.
- [3] I. Mudawar, "Assessment of High-Heat-Flux Thermal," vol. 24, no. 2, pp. 122–141, 2001.
- [4] J. M. S. Jabardo, "NUCLEATE BOILING HEAT TRANSFER," no. May, pp. 3–7, 2004.
- [5] V. K. Dhir, "BOILING HEAT TRANSFER," *J. Am. Soc. Nav. Eng.*, vol. 67, no. 2, pp. 457–466, 2009.
- [6] J. Kim, "Review of nucleate pool boiling bubble heat transfer mechanisms," *International Journal of Multiphase Flow*, vol. 35, no. 12. Elsevier Ltd, pp. 1067–1076, 2009.
- [7] R. L. Mohanty and M. K. Das, "A critical review on bubble dynamics parameters influencing boiling heat transfer," *Renewable and Sustainable Energy Reviews*, vol. 78, no. April. Elsevier Ltd, pp. 466–494, 2017.
- [8] S. Osher and J. A. Sethian, "Fronts propagating with curvature-dependent speed: Algorithms based on Hamilton-Jacobi formulations," *J. Comput. Phys.*, vol. 79, no. 1, pp. 12–49, 1988.



- [9] C. W. Hirt and B. D. Nichols, “Volume of fluid (VOF) method for the dynamics of free boundaries,” *J. Comput. Phys.*, vol. 39, no. 5, pp. 201–225, 1981.
- [10] D. L. Sun and W. Q. Tao, “A coupled volume-of-fluid and level set (VOSET) method for computing incompressible two-phase flows,” *Int. J. Heat Mass Transf.*, vol. 53, no. 4, pp. 645–655, 2010.
- [11] G. Son, V. K. Dhir, and N. Ramanujapu, “Dynamics and Heat Transfer Associated With a Single Bubble During Nucleate Boiling on a Horizontal Surface,” *J. Heat Transfer*, vol. 121, no. 3, p. 623, 2008.
- [12] G. Son, N. Ramanujapu, and V. K. Dhir, “Numerical Simulation of Bubble Merger Process on a Single Nucleation Site During Pool Nucleate Boiling,” *J. Heat Transfer*, vol. 124, no. 1, p. 51, 2002.
- [13] A. Mukherjee and V. K. Dhir, “Study of Lateral Merger of Vapor Bubbles During Nucleate Pool Boiling,” *J. Heat Transfer*, vol. 126, no. 6, p. 1023, 2004.
- [14] A. Mukherjee and S. G. Kandlikar, “Numerical study of single bubbles with dynamic contact angle during nucleate pool boiling,” *Int. J. Heat Mass Transf.*, vol. 50, no. 1–2, pp. 127–138, 2007.
- [15] Y. Nam, E. Aktinol, V. K. Dhir, and Y. S. Ju, “Single bubble dynamics on a superhydrophilic surface with artificial nucleation sites,” *Int. J. Heat Mass Transf.*, vol. 54, no. 7–8, pp. 1572–1577, 2011.
- [16] K. Ling, Z. Y. Li, and W. Q. Tao, “A direct numerical simulation for nucleate boiling by the VOSET method,” *Numer. Heat Transf. Part A Appl.*, vol. 65, no. 10, pp. 949–971, 2014.
- [17] K. Ling and W. Q. Tao, “Numerical simulation of nucleate boiling in shallow liquid,” *Comput. Fluids*, vol. 164, pp. 35–40, 2018.
- [18] C. Kunkelmann and P. Stephan, “CFD simulation of boiling flows using the volume-of-fluid method within OpenFOAM,” *Numer. Heat Transf. Part A Appl.*, vol. 56, no. 8, pp. 631–646, 2009.
- [19] S. Hardt and F. Wondra, “Evaporation model for interfacial flows based on a continuum-field representation of the source terms,” *J. Comput. Phys.*, vol. 227, no. 11, pp. 5871–5895, 2008.
- [20] E. Olsson, G. Kreiss, and S. Zahedi, “A conservative level set method for two phase flow II,” *J. Comput. Phys.*, vol. 225, no. 1, pp. 785–807, 2007.
- [21] J. U. Brackbill and D. B. Kothe, “ScienceDirect - Journal of Computational Physics : A continuum method for modeling surface tension*1,” *J. Comput. Phys.*, vol. 335354, 1992.
- [22] W. H. Lee, “A Pressure Iteration Scheme for Two-Phase Modeling,” 1979.
- [23] I. Perez-Raya and S. G. Kandlikar, “Numerical models to simulate heat and mass transfer at sharp interfaces in nucleate boiling,” *Numer. Heat Transf. Part A Appl.*, vol. 74, no. 10, pp. 1583–1610, 2018.



Design and Simulation of a Scale Model Thermo-Acoustic System for Refrigeration Applications

Muhammad Mahmood Aslam Bhutta¹, Muhammad Farooq², Sajid Kamran¹, Syed Muhammad Sohail Rehman³,
Syed Murawat Abbas Naqvi⁴

1- Assistant Professor, Department of Mechanical Engineering UET Lahore

2- Assistant Professor, Department of Mechanical Engineering, KSK Campus, UET Lahore

3- Department of Mechanical Engineering UET Lahore

4- Department of Mechanical Engineering School of Engineering & Technology Imperial College of
Business Studies Lahore, Pakistan.

Corresponding author: drbhutta@uet.edu.pk

ABSTRACT

The advent of new technologies is going on to revolutionize this world. Today it is a great need to convert different sources of energy in to heat energy in order to take some benefits. Sound is also a source of energy, and this energy can be converted into heat energy with the use of thermoacoustic. Thermoacoustic cooling devices use the thermoacoustic principle to move heat using sound. They consist of a standing wave tube in which a stack of fractional wavelength creates a temperature gradient across the stack, facilitating heat flow. These devices are simple in design and it is not harmful for environment. In this study, the design and analysis of a thermoacoustic system for refrigeration application operating on $\lambda/2$ & $\lambda/4$ standing wave is thoroughly established, and fabrication of the system for $\lambda/2$ standing wave is illustrated. The performance of the device was then tested and analyzed. It has been revealed by the numerical study that, position of stack and stack length in the resonator have a great importance for knowing about the performance of thermoacoustic device. The numerical study has shown that the stack length and the position of the stack in the resonator have a significant impact on the overall performance of the thermoacoustic device. In the fabrication of the system for $\lambda/2$ standing wave, air at standard temperature and pressure is employed as the working gas. The acoustic power source was a 15 W speaker operating at a frequency of 121 Hz. Based on a numerical study, the stack length was set equal to 7.1 cm with its center located from 70 cm long resonator tube to the driver-end at a distance of 21.5 cm. 30 K of temperature difference was set between the two ends of the stack. The 3D modeling of the design of a thermoacoustic system for refrigeration application operating on $\lambda/4$ standing wave is ready to fabricate. In the design, preliminary results of DELTA EC Simulation and MATLAB Computation have shown that a temperature difference of as high as 40 K could be achieved across the stack. Both ends were equipped with heat exchangers in order to exploit the effect of pumping the heat. Water at ambient temperature was chosen as the fluid for the heat exchangers to facilitate heat transfer to or from the stack. The maximum coefficient of performance (COP) of this device could be 3.5.

Key Words: Thermoacoustic, Refrigeration applications, Stack, Resonator, DELTA EC, Coefficient of performance

1. INTRODUCTION

In order to transfer heat from one place to another place using a sound medium, Thermoacoustic device can be used in order to convert sound energy into heat energy. Thermoacoustic, in term of refrigeration applications, operates by manipulating the temperature difference across the acoustic wave. In this chapter, a brief history about the research in the field of thermoacoustic is explained along with its basic principle and application.

Different parameters, which design the thermoacoustic refrigeration were described [1]. The performance parameters (heat flow and power) depend upon the stack and boundary layer. The experiments were done on the design of

thermoacoustic refrigeration which involved the conversion of sound into heat energy performed and the algorithm parameters were achieved [2]. The stack length is the main parameters on which heat produced and efficiency. The design procedure for thermoacoustic refrigerators were established which were driven by acoustic waves [3]. A simplified, small scale acoustically driven model was used in the development of design procedure, in which the position and length of the stack was varied in order to optimize the total power flow and its consumption in the model stack. A comprehensive design was made such that a designer can easily optimize the length and position of stack according to its need and parameters. In addition to this the geometric parameters such that the stack thickness and its cross sectional area can also be determined. The buffer and resonator for the thermos-acoustically driven



refrigerator were designed as an intention to develop the ozone friendly refrigeration system [4]. The modeling was done using CATIA software and the process simulation was carried out on MATLAB. The acoustically driven refrigerator were tested as a function of temperature difference attained at the either ends of stack placed in the resonator at two different positions in which helium was used as a working fluid. The system carried out the temperature difference of 160C [5]. The whole experimentation was carried out using the twin energy supplier. The boundary layer estimation were used in order to carry out the design optimization of sound driven refrigeration cycle using quarter wavelength short stack. The process simulation and optimized COP of the system was carried out using the Delta-EC simulation software [6]. The effect of geometry and material of resonator tube were studied out on the performance of sound driven refrigerator mainly dealing with COP. The resonance tube length is elongated to compensate for some effects that occur in the resonance tube, especially when the stack is placed in the resonance tube [7]. A sound driven refrigeration system driven by the exhaust gasses temperature from an internal combustion engine were designed and fabricated [8]. This system utilizes the temperature of IC engine which produce a large temperature difference across the stack, which increases the performance of refrigeration system.

2. EXPERIMENTAL SET-UP

Thermoacoustic refrigerators are systems which use sound to generate cooling power. They consist mainly of a loudspeaker attached to an acoustic resonator (tube) filled with a gas. In the resonator, a stack consisting of a number of parallel plates and two heat exchangers, are installed, as shown in figure 1.

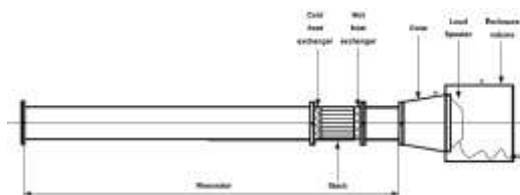


Figure 1: Schematic Diagram Of Thermoacoustic Refrigeration

The purpose of the resonator in a TAR is to contain the working fluid and to cause it to have a desired natural frequency. Resonators are generally either half or quarter wavelength resonators. Quarter wavelength resonators are made with tubes by sealing one end and making the length approximately one quarter of the desired resonant frequency wavelength. The open end of the tube is simulated by attaching a large volume to the end.

This large volume creates the boundary condition of zero pressure at the end. Quarter wavelength facilitates miniaturization of the model. The resonator is needed to interface with the speaker and stack cross sections. Finally, it should be easy to manufacture. A simple tube can be used as the resonator. It makes calculation of the resonator natural frequency easy. Stack is the most sensitive part of the refrigerator, as small changes in stack dimensions can lead to huge changes in performance. It consists of large number of closely spaced surfaces aligned parallel to the length of the resonating tube. The stack material and thickness are important design considerations. A material that has a low thermal conductivity is desired because heat conducting across the stack works against the refrigerator. However, the material must also have a heat capacity much larger than the heat capacity of the working fluid so that sustained temperature gradient may be created. Loud speaker is an electrical transducer that produces sound to an electrical input single. It is powered by the electrical generation. The magnetic coil in speaker produces the required frequency. Commercial high-control speakers regularly have vast distances across; there is a lessening cone between the speaker and the resonator. Cooling of the cone's external surface may likewise permit the utilization of a hot warmth exchanger with a low blockage part, which does not hinder the stack. The planner needs to restrict the cone edge to a little esteem to keep away from limit layer detachment in the swaying stream since stream division produces whirlpools, along these lines changing a portion of the dynamic vitality of the stream into warmth. In any case, restricted work has been done on limit layer stream detachment in swaying streams at low Reynolds numbers. A more drawn out cone appreciates littler cone edge and bigger warmth exchange surface zone yet positions the stack more distant from the speaker, which must be assessed against the extreme imperatives influencing the stack position. Diminishing the cone length enhances the execution, demonstrating that the imperative on the stack position is more essential than that on the cone point.

3. RESULTS AND DISCUSSIONS

The performance calculations are done as function of the normalized stack length L_{sn} , for different normalized stack positions x_n . The normalized position $x_n = 0$, corresponds to the driver position (pressure antinode). In all cases the COP shows a maximum. For each stack length there is an optimal stack position. As the normalized length of the stack increases, the performance peak shifts to larger stack positions, while the performance decreases.



The performance of setup depends upon different parameters distance between stack center wave generator and stack length. Figure 2 represents stack center position and power produced. The parameters stack center position and power produced has inversely related with different stack length. When stack position is lesser, power generation will be maximum due to presence of node while power minimum with increment of position. The maximum power produced with stack length of 0.089 at 0 m stack position and minimum with 0.038. After certain decrement in power on increasing in length because absence of the node position, again increasing in power.

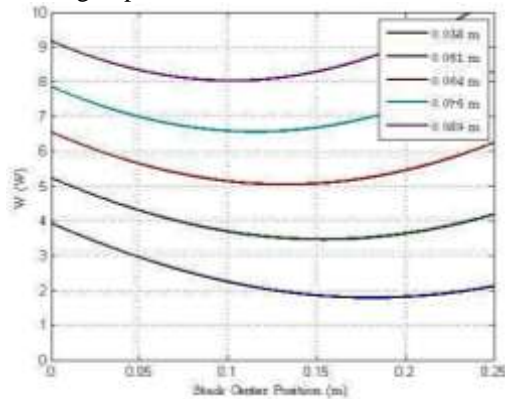


Figure 2: Acoustic Power Consumption V/S Center Stack Position.

The wave generator produce the wave of quarter wave length consists of one node and antinode. Figure 3 clearly shows heat generated maximum at middle of the stack of length due to presence of antinode in the middle. Higher the length of the stack, maximum the heat generated. Stack with length 0.089, produce maximum heat in comparison with all lower length values of the stack.

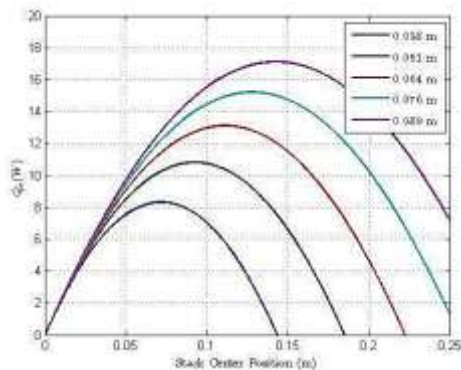


Figure 3: Cooling Power Consumption V/S Center Stack Position.

The COP depends upon the work input and heat generated shown in figure 4 .The coefficient of performance of Thermoacoustic is maximum with lower stack length because work output is lower than the heat generated on same length. the COP,

maximum with stack length is 0.038, is above than 3 while stack having a length higher is 0.076 having lower performance parameter. In figure 4 the COP peak, the cooling force, and the acoustic force, spotted at the peak position, are placed as the parts of the stack length. The cooling and acoustic force build as while COP finishes as ability of the stack length and hence, an ability of the standardized stack length position. Considering the above comments and for down to earth causes, a stack focus position of $x_n = 246$ mm is decided. To attain ideal performance, it requires a stack length of $L_{sn} = 0.114$ m. Under these conditions the dimensionless cooling force is $Q_{cn} = 0.0004077$ watts. Since the optimal cooling force is 10 watt, it requires a cross sectional area $A = 0.0083$ meter square. This means a range of $r = 0.0514$ m for a round and hollow resonator. 3.18 watt acoustic force (COP=3.1397) is used to pump 10 watt of heat.

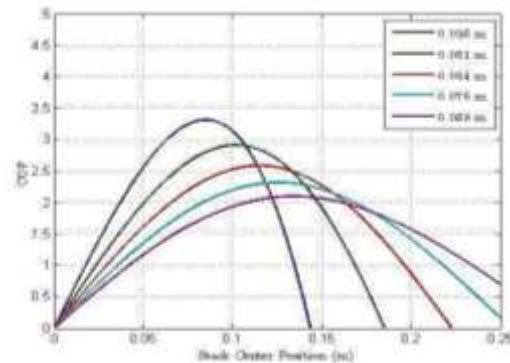


Figure 4: Cop V/S Stack Center Position

4. CONCLUSIONS

The principle of Thermo-acoustic devices based on the principle of energy conversion and have no bad effect on environment. The performance of system depend upon the stack position and its length. The system with the shorter stack length gave the maximum cooling effect produced at the maximum pressure anti-node. The power loss reduced by optimized the geometry of the tube. The parameters stack center position and power produced has inversely related with different stack length. The maximum power produced with stack length of 0.089 at 0 m stack position and minimum with 0.038m.

REFERENCES

- [1] Putnam AA and Dennis WR, 1956, "Survey of organ-pipe oscillations in combustionsystems", J AcoustSoc Am, 28 (2).
- [2] Higgins B, 1802 and Nicholson's J 1, p. 130.



- [3] Feldman KT, Jr., 1968, "Review of the literature on Rijke thermoacoustic phenomena", *J Sound Vibrations* 7 (1).
- [4] Bisio G and Rubatto G, 1999, "Sondhauss and Rijke oscillations - thermodynamic analysis, possible applications and analogies", *Energy* 24.
- [5] Rijke PL, 1859, "Notiz über eine neue Art, die in einer an beiden enden offenen Röhre enthaltene Luft in Schwingungen zu versetzen", *Ann Phys* 107 (6).
- [6] Sondhauss C, 1850, "Ueber die Schallschwingungen der Luft in erhitzten Glasröhren und in gedeckten Pfeifen von ungleicher Weite" - *Ann Phys Chem* 79.
- [7] Feldman KT, Jr., 1968, "Review of the literature on Sondhauss thermoacoustic phenomena", *J Sound Vib* 7 (1).
- [8] R.L. Carter, M. White and A.M. Steele, "Private communication of Atomic International Division of North American Aviation Inc.", (1962).
- [9] Taconis KW, Beenakker JJM, Nier AOC, Aldrich LT, 1949, "Measurements concerning the vapor-liquid equilibrium of solutions of He^3 in He^4 below 2.19°K ", *Physica* 15 (8-9).
- [10] Kramers HA, 1949, "Vibrations of a gas column", *Physica* 15 (11-12).
- [11] Rott N, 1969, "Damped and thermally driven acoustic oscillations in wide and narrow tubes", *Z angew Math Phys* 20.
- [12] Rott N, 1973, "Thermally driven acoustic oscillations. Part II: stability limit for helium", *Z angew Math Phys* 24.
- [13] Rott N, 1975, "Thermally driven acoustic oscillations. Part III: second-order heat flux", *Z angew Math Phys* 26.
- [14] Rott N, 1976, "Thermally driven acoustic oscillations. Part IV: tubes with variable cross-section", *Z angew Math Phys* 27.
- [15] Rott N, 1983, "Thermally driven acoustic oscillations. Part VI: excitation and power", *Z angew Math Phys* 34.



Experimental Analysis of Alternative Hydrocarbons for R134a by a Vapor Compression Cycle Based System

Muhammad Mahmood Aslam Bhutta¹, Nasir Hayat¹, Muhammad Farooq², Sajid Kamran¹, Syed Muhammad Sohail Rehman¹, Muhammad Umair Mirza³

1- Department of Mechanical Engineering UET Lahore, Pakistan

2- Department of Mechanical Engineering, New Campus, UET Lahore, Pakistan

3- Department of Mechanical Engineering School of Engineering & Technology Imperial College of Business Studies Lahore, Pakistan.

Corresponding Author: drbhutta@uet.edu.pk

Abstract:

Researchers made improvements in refrigeration systems and number of researchers has been working to reduce the environmental impact to improve energy efficiency and reduce emissions. This analysis was done on refrigerants (R290, R600a, R1270) in a medium sized system incorporating vapor compression cycle. The outcomes were also obtained for R134a refrigerant and were compared with other fluids. It was investigated that the performance achieved by R600a was slightly higher than the rest of the COPs obtained by R290, R1270 and R134a. For this, the evaporating temperature range was noticed as -30°C -10°C . Moreover, on the same evaporating temperature range -30°C -10°C evaporating pressure, Compressor discharge temperature, Temperature profile inside the cabin, Refrigeration effect, mass flow rate, Coefficient of performance, Compressor power and refrigerant type were also studied. It was noticed that instead of using R134a, hydrocarbons refrigerants were more efficient and should be used.

Keywords: Refrigerants; Alternative refrigerants; R290; R600a; R1270

1. Introduction

Ozone depletion potential (ODP) and global warming potential (GWP) due to refrigerants CFCs is the basis of development of new refrigerants. Hydro carbon refrigerants (HC) and hydrofluoro carbon (HFC) have been chosen for use in several industrial and domestic applications with zero ODP, alternatives to refrigerants CFCs and HFCs. DAMANSKI et al. in 2006 [1] concluded that the high-pressure refrigerants conquer the thermodynamics disadvantages related to their low critical temperature and had higher COP than the R130a and R600a with low pressure. MURTADHA et al. in 2008 [2] gave a result that the compressor used with R12 showed that the hydrocarbon mixture (R290/R600) at 61% mass fraction of R290 showed 3 to 4% increment in the energy efficiency and also indicated faster cooling rate as compared with R12. MOHANRAJ et al. in 2009 [3] made an experimental investigation and concluded that the HC mixture (R290/R600) had lower values of energy consumption, on time ratio and pull down time by about 11.1%, 13.2% and 11.6% respectively, with 3.25-3.6% higher coefficient of performance (COP). ALMEIDA et al. in 2010 [4] concluded that the HC decrease the level of pressures on the condenser and evaporator along with smaller compression tasks necessary in the system.

ZAKARIA et al. in 2011 [5] made the possibility of using liquefied petroleum gas in house hold refrigeration systems and explained the effects of performance analysis such as refrigerant type, degree of sub cooling and super heating on the refrigerating effect, coefficient of performance and volumetric refrigeration capacity. BASKARAN et al. in 2012 [6] made the performance comparison of eco-friendly refrigerants used in vapor compression refrigeration system. RASTI et al. in 2013 [8] enhanced the Energy efficiency of a house hold refrigerator using R436a and R600a as substitute refrigerants to R134a and made the calculations that total energy destruction of the domestic refrigerator with HFC type compressor for R134a, R436a and R600a are 0.0389, 0.0471 and 0.0301 respectively and for R600a and R436A with HC type compressor 0.0292, 0.0472 respectively. PERIYASAMY et al. in 2014 [10] made an Experimental study by using HC mixture in a vapor compression refrigeration system and R-12 refrigerant. Qureshi et al. in 2014 [11] did the comparative analysis of COP using R134a & R600a refrigerant in domestic refrigerator at steady state condition and stated that COP of R600a is greater than R134a. YADAV et al. in 2015 [12] made an experimental analysis of liquid line heat exchanger in vapor compression refrigeration by



using R134a & R404a. Authors performed simulation analysis of vapor compression cycle, hydrocarbon refrigerants such as R290 and R600a were considered as a refrigerants. The results were compared with the refrigerants such as R134a, R12 for different condenser and evaporator temperatures. It was concluded that R134a and R12 are halogenated compounds which are harmful for the environment. Among the hydrocarbons the mixture of R290 and R600a with 50% concentration has optimum performance, better COP and heat transfer. In domestic and industrial refrigeration systems the mixture of R290 & R600a can be used as alternate refrigerant instead of R12 and R134a. [13].

In this research paper, a comparison is made between different refrigerants with an objective of getting improved performance in sense of coefficient of performance, compressor power, evaporating pressure, compressor discharge temperature, temperature profile inside the cabin, refrigeration effect, mass flow rate etc. Goal of the study and investigation is to choose a refrigerant which not only optimize the performance of VCC but also fulfill the environmental conditions set by Kyoto and Montreal Protocol. Data has been collected through experimentation on medium size vapor compression cycle and assessed in tabulated and graphical form. Different mathematical equations governing the VCC, psychometric chart, pressure-enthalpy curve, refrigerants property tables are used to interpret the experimental results.

During the study hydrofluoric refrigerants such as R134A and R 404A were taken as refrigerants, different performance measures were analyzed. The results were compared with halogenated refrigerants like as R134A and R404A for different temperatures. From the results it was also concluded that the successful use of this mixed refrigerant of HFC R134A and R 404A refrigerants in domestic refrigerator.[14]. An energy and exergy analysis were performed using R152 A, R290, R600, R600A, R123 and R717 refrigerants. The results indicated that these alternative refrigerants had high efficiency and COP than R134A for evaporative temperature. It was found that R600 was suitable replacement than the other refrigerants, and other parameters like COP, superheating, PTR and RE etc. were also investigated for different temperatures [15]. A theoretical study on vapor compression refrigeration system with refrigerant mixtures based on HFC134a, HFC152a, HFC32, HC290, HC1270, HC600, and HC600a was conducted.

The results showed that all the alternative refrigerants have slightly lower COP than CFC12, CFC22. And it was also concluded that the COP and refrigeration efficiency increases, with increasing evaporating temperature for a constant condensing temperature [16].

A theoretical study was conducted to investigate the performance of hydrocarbon refrigerants as alternative to R22 in Vapor compression system. From the results it was obtained that specific volume and Vapor pressure of R290 and R1270 was very close to the R22. R1270 are better than that of R22, which perform better as refrigerants in heat pump systems. COP of all the refrigerant was in the range of 3.10–3.51. It was also observed that thermodynamic properties of R290 and R1270 matched those of R22 [17]. An experimental study was conducted to investigate the performance parameters for refrigeration system using different hydrocarbon blends and compared with R-134a.

From the results it was observed that system performance was 14% increase in COP, reduction percentage in freezing compartment temperature was 12% and 6% increase in the refrigeration effect was noticed. A possible improvement in refrigeration system performance can be obtained when hydrocarbon blends used as refrigerants [18]. A performance analysis on vapour compression refrigeration system with different refrigerants was performed, and results were compared with R134a. Through experiments it was analyzed that the alternative refrigerants RE170, R152A and R600A have higher COP than R134A for condensation and evaporating temperature. Refrigerant RE170 was found to be the most suitable alternative among other refrigerants [19].

This research provides substantial understanding of refrigerant characteristics and their effect on performance of vapor compression cycle. Outcomes thus obtained are encouraging enough for a novel research aspirant to pursue in the said field of study and research in future.

2. Experimental Setup

The performance analyses performed on medium scale refrigeration system setup with different working fluids. Different refrigerants were charge in the system using following conditions.

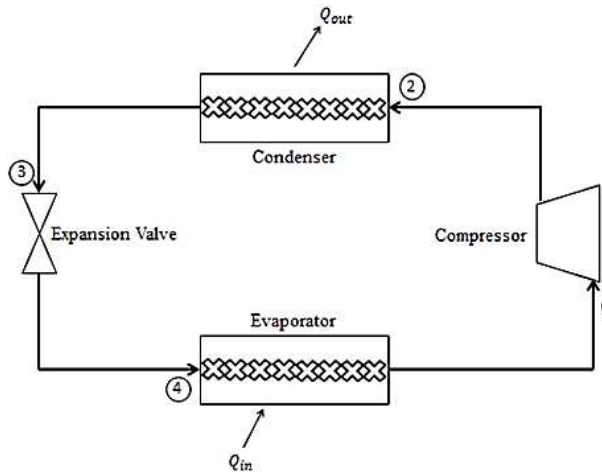


Fig 1: Schematic diagram of vapor compression cycle

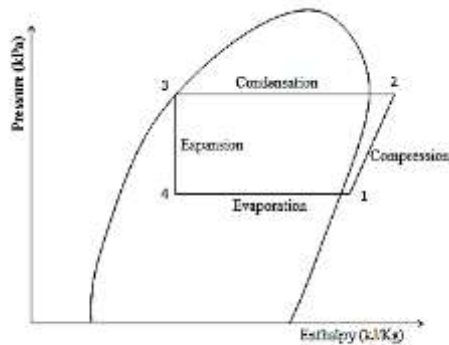
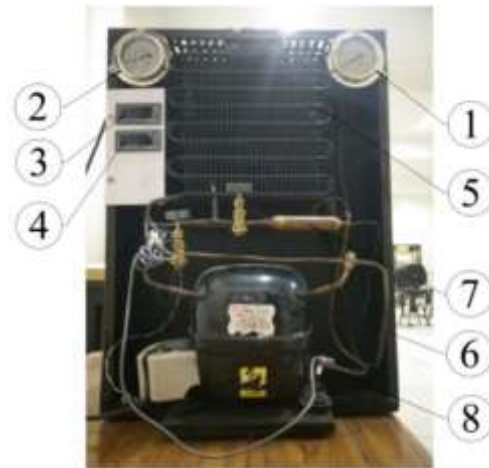


Fig 2: P-h diagram of vapor compression cycle

1. First locate outlet valve through which working fluids can be removed from refrigerator.
2. Then the system is evacuated using the vacuum pump with a purpose of removing the moisture and the gases captured during the exhaust.
3. A mass flow measuring device is connected to compressor and cylinder to fill system. Filling process is performed slowly at the beginning and then at the given rate. Amount of the fluid filled in the system is volume conscious as the relation between pressure and volume can be affected by the overfilling.



(a)



(b)

Fig 3: Experimental Setup: (a): (1) Compressor Discharge Pressure gauge, (2) Condensing gauge, (3) Temperature gauge (4) Mass flow rate gauge (5) Condenser (6) Reciprocating Compressor (7) Capillary Tube (8) Thermocouple (b): (9) Evaporator (10) Evaporating temperature regulator

Reciprocating compressor of 70 W was used for compression in the system. Using the design calculations for the length of evaporator and condenser using R134a, it was calculated as 6.09m and 13.7m respectively.

As alternative different hydrocarbons refrigerants (R290, R600a, and R1270) were used and their performance analysis was done with R134a. Some important specifications of used hydrocarbon refrigerants and R134a are summarized in table 1.



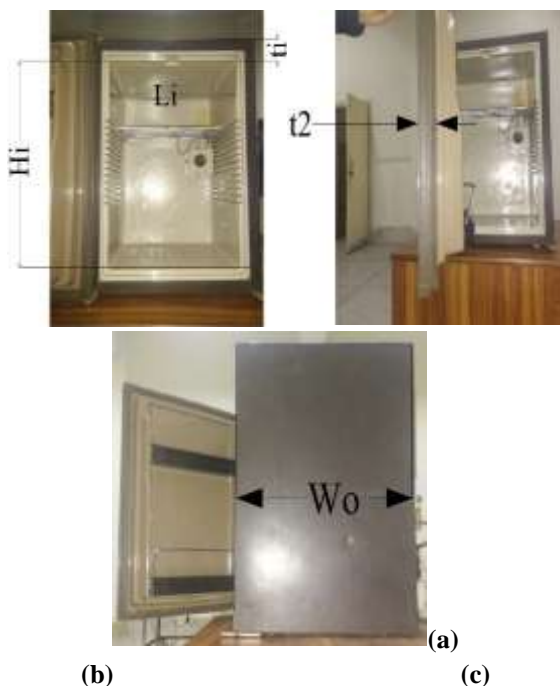
Table 1: Properties of Hydrocarbon Refrigerants [5]

Properties	Hydrocarbon Refrigerants			R134a
	R1270	R290	R600a	
Chemical Formula	CH_3CHCH_2	$\text{CH}_3\text{CH}_2\text{CH}_3$	$(\text{CH}_3)_2\text{CHCHF}_3$	CH_2FCF_3
Molecular Pressure (gmol^{-1})	42.09	44.9	58.12	102.03
Critical Temperature ($^{\circ}\text{C}$)	91.8	96.67	134.98	101.1
Critical Pressure (MPa)	4.42	4.24	3.66	4.067
Boiling Point ($^{\circ}\text{C}$)	-47.5	-42.2	-11.80	-26.15
Freezing Point ($^{\circ}\text{C}$)	-185	-189.4	-145	-96.7
GWP	00	00	00	00
ODP	08	08	08	1300
Latent Heat of Vaporization (KJkg^{-1})	441	425.6	366.5	215
Specific Volume (m^3kg^{-1})	0.00449	0.00454	0.004526	0.001810

As the ODP (Ozone Layer Depletion) of hydrocarbon refrigerants are far less than that of R134a, so they can be used as an alternative of R134a, keeping the other analysis parameter comparable with that of R134a.

The complete dimensions of the refrigerator cabin are shown in Fig.4.

Fig 4: Cabin views with dimensions, (a) H_i = Inside cabin height = 463 mm, L_i = Inside cabin length = 317 mm, t_i = Cabin wall thickness = 35 mm, (b) t_2 = Door thickness = 35 mm (+35mm of gasket) = 70 mm, (c) W_o = Outside cabin width = 423.5 mm



3. Results and Discussions

Different experiments were done for the performance and experimental analysis of medium size vapor compression cycle incorporating different various naturally occurring HC refrigerants and were compared with that of R134a. Evaporating temperature was taken as the varied parameter and flowing performance parameters were calculated.



Table 2: Calculations of Total Thermal Losses of the Cabin

Calculation	K (Wm ⁻¹ k ⁻¹)	A (m ²)	ΔT (K)	Piece(s)	Thermal losses (kcalh ⁻¹)
Refrigerator door area	0.033	0.1471	40	1	0.554
Refrigerator side area	0.033	0.1206	40	2	0.909
Refrigerator back area	0.033	0.1471	55	1	0.762
Refrigerator door gasket	0.08	0.02148	35	1	6.0144
Refrigerator Floor	0.033	0.0826	40	1	0.312
Refrigerator roof	0.033	0.0826	50	1	0.389
Total losses					8.9 kcalh⁻¹

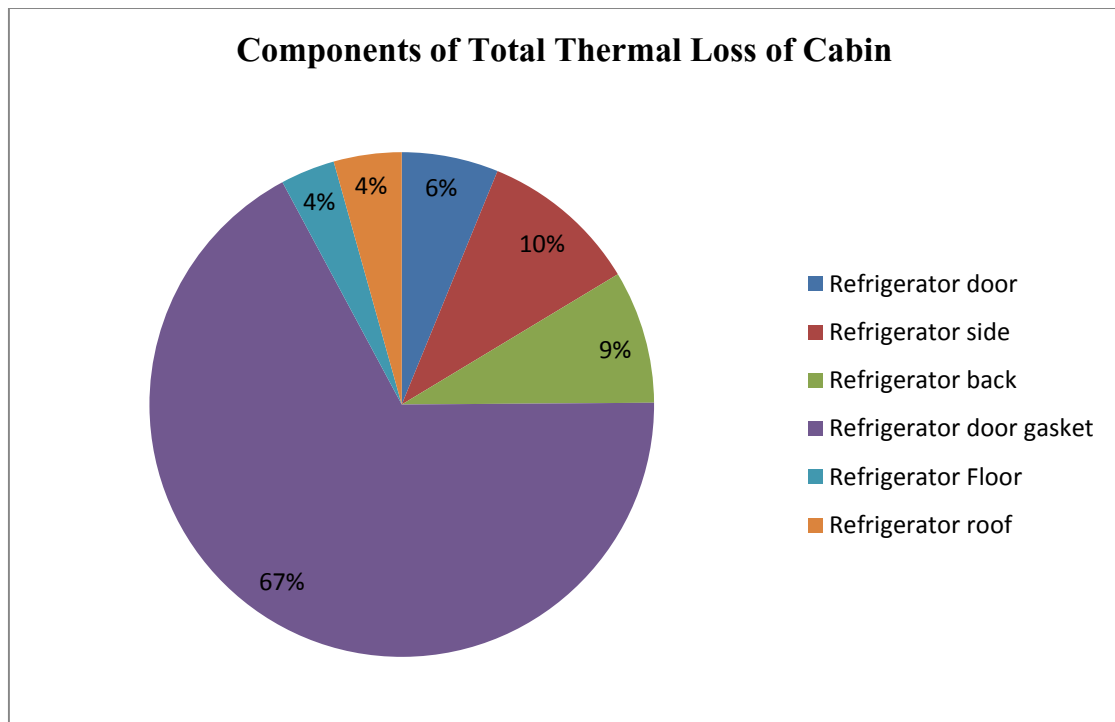


Fig 5: Different components of total thermal loss of cabin

3.1 Mass Flow Rate

Rate of mass flow for the refrigerant can be calculated by using following expression [4]

$$W_{in(Compressor)} = m_{ref} \times (h_2 - h_1) \quad (Eq-----1)$$

Where;

- Win = Work input to compressor (kW)
- m_{ref} = Rate Mass flow of refrigerant (kgs⁻¹)
- h₁ = Specific enthalpy of refrigerant at inlet of compressor (kJkg⁻¹)
- h₂ = Specific enthalpy of refrigerant at exit of compressor (kJkg⁻¹)



Enthalpy values at the exit of each component (evaporator, Condenser, Compressor and Capillary tube), were determined by using the Mollier diagram of

vapor compression cycle for each refrigerant. Fig.6 shows the trend of mass flow rates of the refrigerants used against evaporating temperatures T_{evap} .

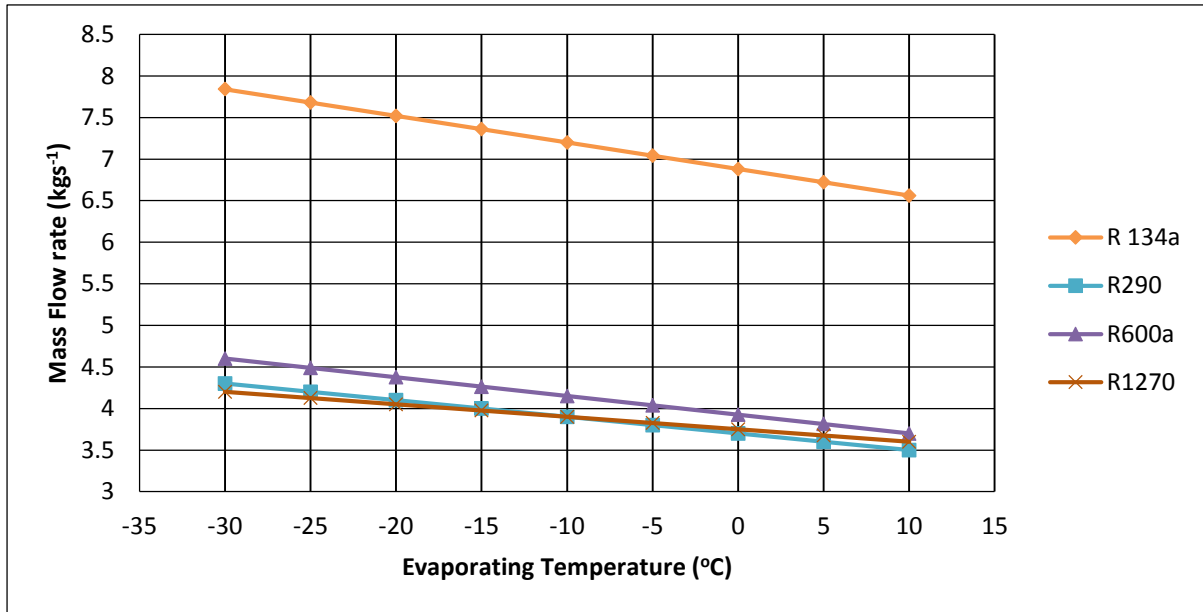


Fig 6: Mass Flow Rate Variation with Evaporating Temperature

It is evident from the above plot that R134a possesses more flow rate rather than other refrigerants used at given evaporating temperature.

3.2 Compressor Power

The Compressor power can be calculated as follows [4];

$$P_{comp} = \frac{n}{n-1} P_1 V_1 \left(\frac{P_2}{P_1} \right)^{\frac{n-1}{n}} - 1$$

(Eq-----2)

Where;

P_{comp} = Compressor power (W)

n = Polytropic Index = 1.25

P_1 = Suction Pressure (Pa)

V_1 = Volume of refrigerant before compression

P_2 = Discharge Pressure

Fig.7 depicts the change in compressor work input against the temperature of evaporator using different refrigerants. It is evident from the figure that R134a needs more compressor work against an evaporating temperature.

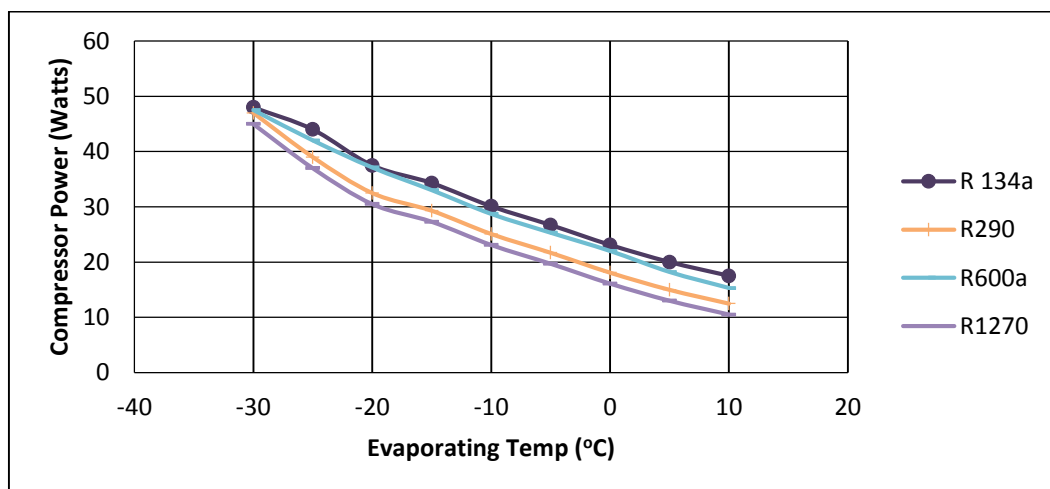


Fig 7: Compressor Input Power with Evaporating Temperature



3.3 Heat absorbed in evaporator (Q_e) can be calculated as [3]:

$$Q_e = m_{ref} \times (h_1 - h_4) \quad \text{(Eq-----3)}$$

Where;

Q_e = Heat removed in condenser (kW)

m_{ref} = Mass flow per second of refrigerant (kgs^{-1})

h_1 = Specific enthalpy of refrigerant at stage 1 (kJkg^{-1})

h_4 = Specific enthalpy of refrigerant at stage 4 (kJkg^{-1})

Refrigerant effect is the desired parameter attained by using compression cycle from the equation Eq.3. Fig.8 shows the variation in refrigerant effect with respect to evaporating temperature using different refrigerants. It is evident from the figure that R134a attains lower refrigerant effect than that of other refrigerants used due to higher compressor work and higher condenser temperature.

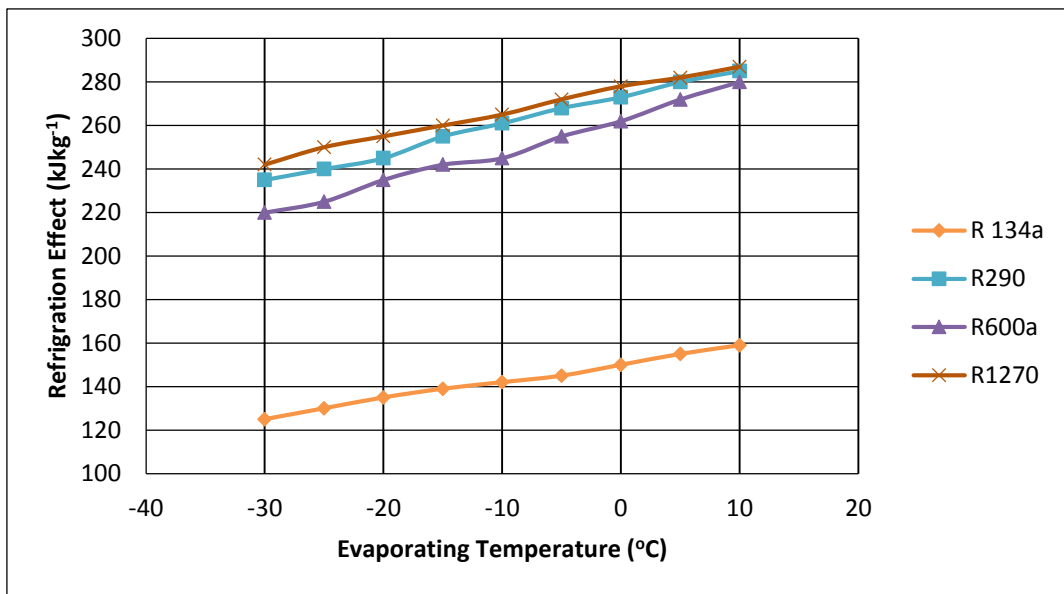


Fig 8: Refrigeration effect with evaporating Temperature

3.4 Coefficient of Performance (C.O.P)

COP is utilized to measure the execution of refrigeration cycles. The image utilized for coefficient of performance is "COP". Much the same as the efficiency of power cycles, the COP is characterized as the proportion of the useful refrigeration or cooling effect achieved and the required power of compressor. In fact it is different from the efficiency because it is by and large more than 1. No doubt, exceptionally odd to talk about efficiency more prominent than 1. In this way, rather, we call it the coefficient of performance. In a refrigeration cycle, the desired yield is heat

absorbed in evaporator (Q_e), in light of the fact that the objective is to expel heat from the evaporator and the required information is the work data. Coefficient of performance was computed as [5]:

$$C.O.P = \frac{\text{heat absorbed in evaporator}}{\text{work input by compressor}} \quad \text{(Eq----- 4)}$$

Fig.8 shows the variation in COP with respect to evaporating temperature using different refrigerants. It is evident from the figure that R134a attains lesser COP than that of other refrigerants used due to higher compressor work.

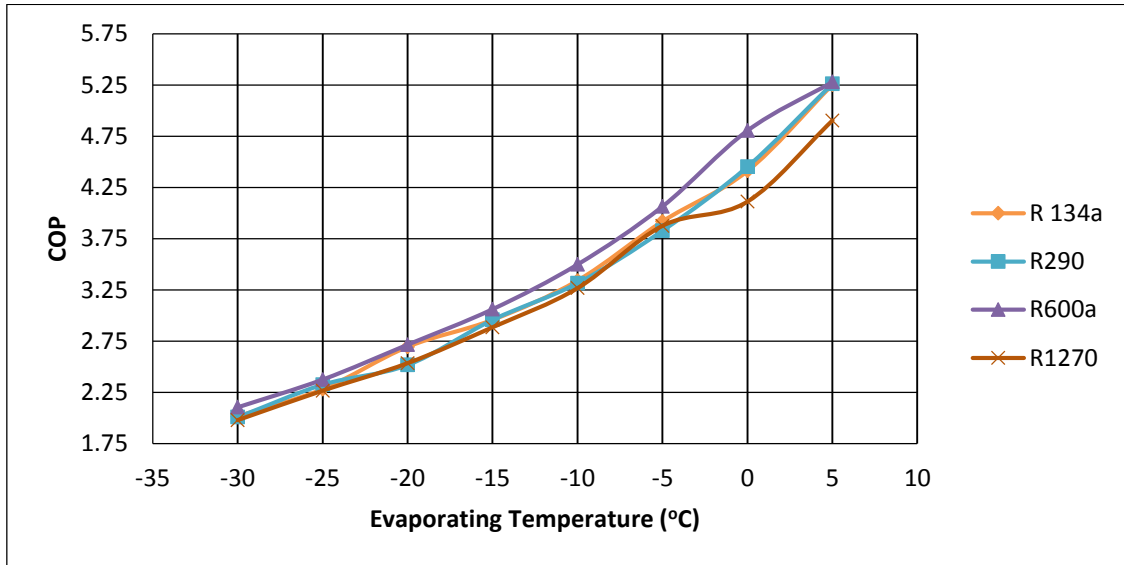


Fig 9: Variation in COP with Evaporating Temperature

3.5 Pressure Ratio with Evaporating Temperature

Pressure ratio can be defined as the ratio between condenser outlet pressures to the evaporator outlet pressure. Fig.10 represents the variation in pressure

ratio against evaporating temperature using different refrigerants. It is evident from the figure that R134a attains higher pressure ratio than that of other refrigerants used due to higher compressor work.

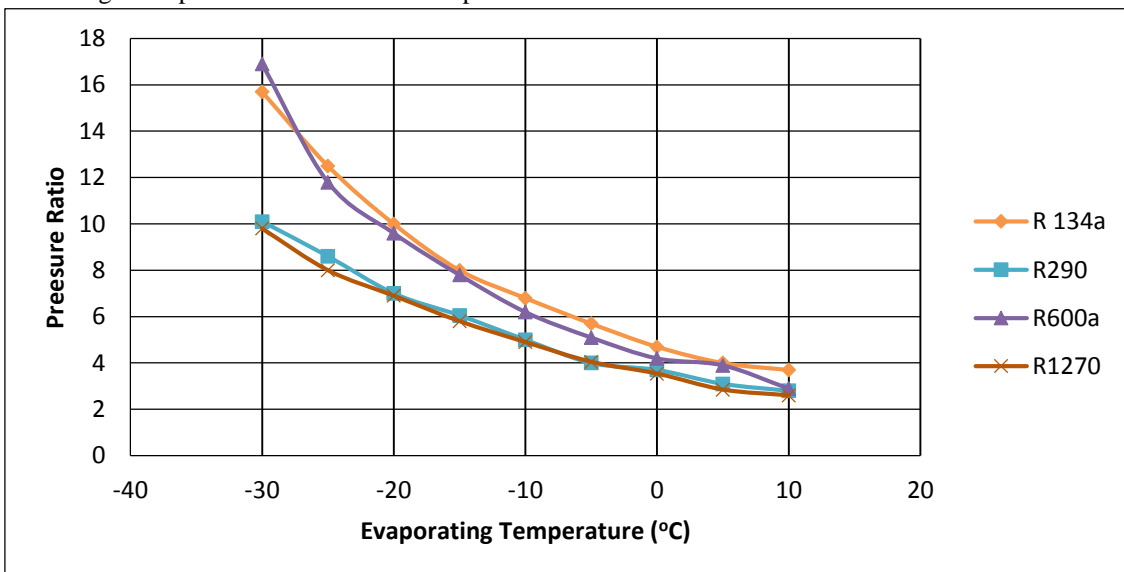


Fig 10: Pressure Ratio with Evaporating Temperature

3.6 Temperature Profile with Respect to Time

Temperature inside the cabin was measured at different time intervals (1 min to 70 min) and it was noticed that R134a gives higher temperature values than other refrigerants used due to its less refrigeration effect

(Fig.11). Temperature gauges installed in the setup was used for the display readings of the temperature measured at different points using thermocouples. The temperature profile of cabin using different refrigerants and their comparison are compiled in fig.11.

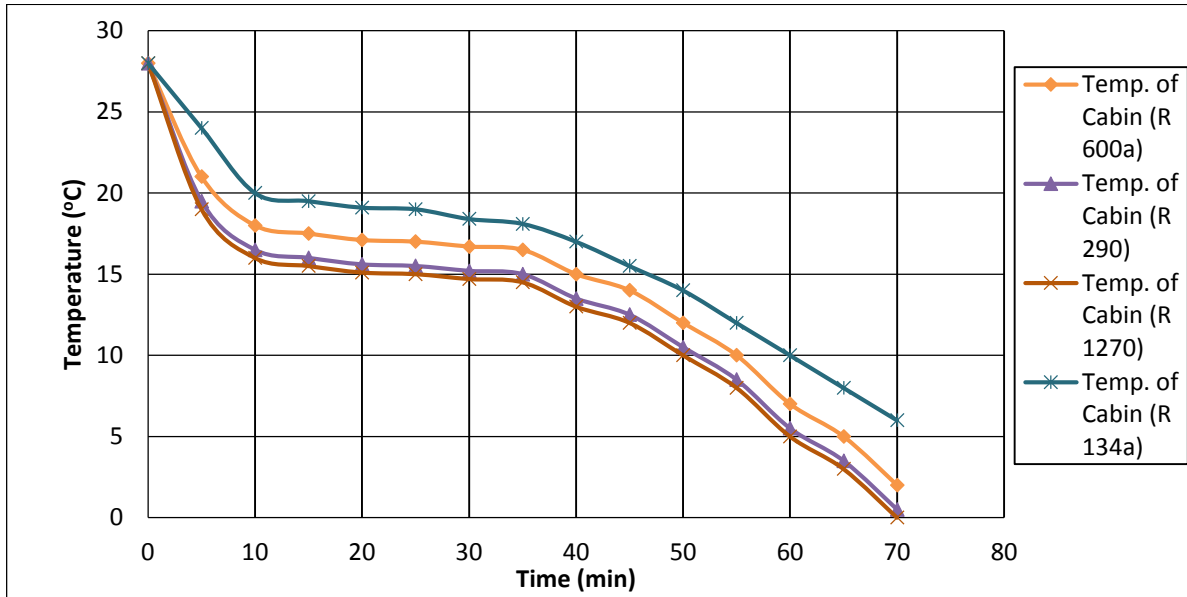


Fig 11: Temperature profile of the cabin with respect to time

3.7 Evaporating Pressure with Evaporative Temperature

Evaporating pressure defines the duty of compressor. Higher the pressure, lesser work load would be on the compressor. Fig.12 shows the variation in evaporating pressure with respect to evaporating temperature using different refrigerants. It is evident from the figure that

R600a evaporating pressure is closely comparable to R134a which proves it a better alternative of R134a.

Evaporating pressure was determined by the pressure gauge installed at the outlet of the evaporator. Different readings were taken at different evaporative temperature.

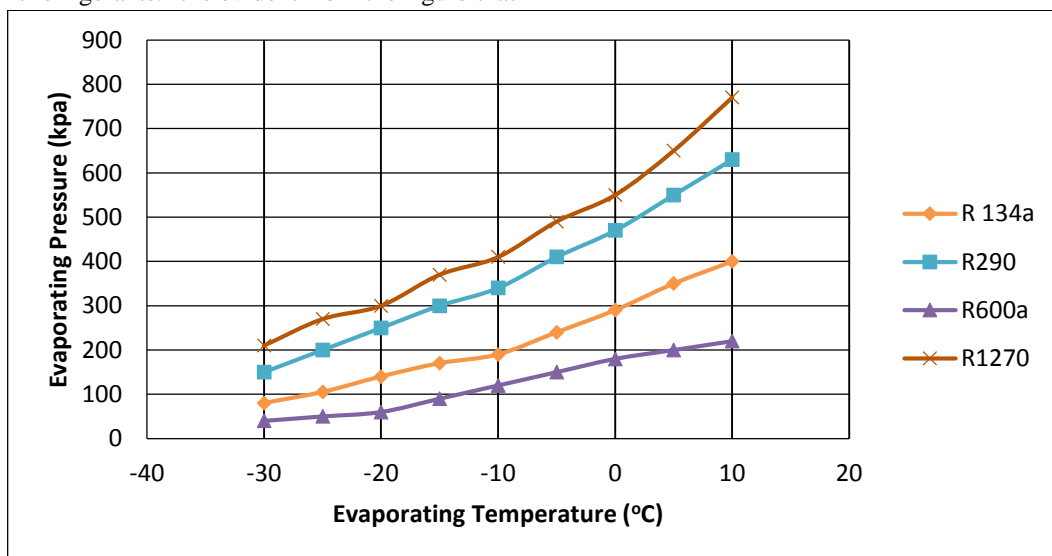


Fig 12: Evaporative pressure with evaporating Temperature

3.8 Discharge Temperature with Evaporative Temperature

The compressor discharge temperatures were calculated at different evaporating temperatures. The compiled data of discharge temperature is depicted in

Fig.13. The graph given below represents that as the evaporating temperature increases, correspondingly the discharge temperature decreases. In addition to it, R600a gives the lowest temperature at discharge with respect to that of other refrigerants used.

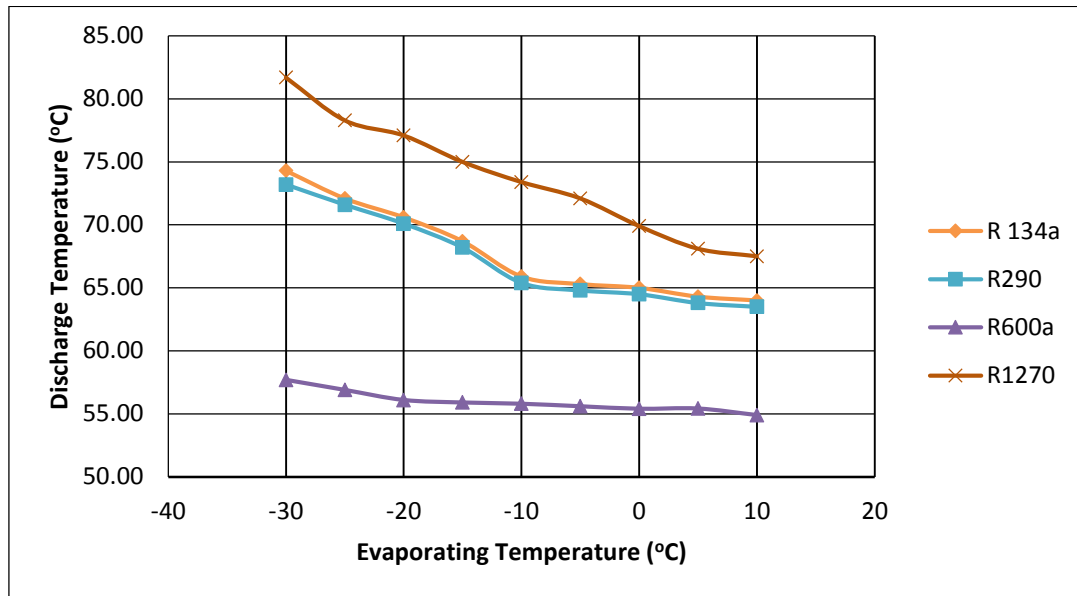


Fig 13: Discharge Temperature with Evaporative Temperature

4. Acknowledgments

We are thankful to the management of National Fertilizer Corporation (NFC) Faisalabad who has permitted us to collect data and to work in the laboratories. And also a special thanks to the Lab Staff for their cooperation.

5. Conclusions

A comprehensive experimental practice of environment friendly and cheap refrigerants (R290, R1270, and R600a) was investigated theoretically as alternative to R134A in a medium size vapor compression refrigeration system at varying range of evaporating temperature. From the results achieved, we can make the following conclusions based on the experimental analysis:

- The mass flow rate of the refrigerant was investigated varying inversely proportional to evaporating temperature. At a fixed evaporating temperature the rate of mass flow for R134a was found greater than the other refrigerants used.
- Compressor input power was needed higher while using R134a at a fixed evaporating temperature due to its higher mass flow rate in compare with other refrigerants used.
- The refrigeration effect was found to be slightly direct to the evaporating temperature and R134a effect was found to be less to that of other refrigerant's effect due to higher discharge temperature.
- Performance coefficient (COP) varies directly as the evaporating temperature and it was found that COP of R600a was highest amongst all i.e. 5.25 due to less compressor input power.
- The behavior of pressure ratio was found inversely to the evaporating temperature and it was found that R134a gives higher pressure ratio due to the higher discharge temperature which founds to be direct to the pressure ratio.
- Temperature profiles were drawn against different time intervals of 70 min and it was noticed that R1270 gives the lowest temperature values with respect to time.
- The evaporating pressure was noticed to be direct with the evaporating temperature and it was noticed that evaporating pressure of R600a was lowest due to higher refrigeration effect.
- Discharge temperature effects inversely to the evaporating temperature and it was noticed that R600a shows lesser trend of evaporating pressure due to lesser discharge temperature.



REFERENCES:

- [1] Piotr. A. Yashar. D.D.,” Comparable Performance Evaluation of HC and HFC Refrigerant in an Optimized System”, 7th Iir Gustav Lorentzen Conference on Natural Working Fluids, Trondheim, Norway, May 28-31, 2006.
- [2] Murtadha. T. K., Hussain S.H, “Domestic Refrigerator Energy Testing With Alternative Refrigerants”, Journal of Kerbala University, Volume 6, Issue 2, Pages 111-116, 2008.
- [3] Mohanraj. M., Jayaraj.S., Muraleedharan. C., Chandrasekar P., "Experimental Investigation of R290/R600A Mixture as an Alternative to R134A in a Domestic Refrigerator". International Journal of Thermal Sciences, Volume 48.Issue 5, Pages 1036-1042, 2009.
- [4] Almeida M. G. Barrosab C. R. F, and, Fontes F. A. O,” Thermodynamic and Thermo Physical Assessment of Hydrocarbons Application in Household Refrigerant”, Journal of Thermal Engineering, Volume 9, Issue 2, Pages 19-27, 2010.
- [5] Zakaria Z. and Shahrum. Z. “The Possibility of Using Liquefied Petroleum Gas in Domestic Refrigeration Systems”, International Journal of Research and Reviews in Applied Sciences Volume 9, Issue 3, Pages 347-354, 2011.
- [6] Baskaran. A, Koshy. P.M., “A Performance Comparison of Vapor Compression Refrigeration System Using Eco-Friendly Refrigerants of Low Global Warming Potential”, International Journal of Scientific and Research Publications, Volume 2, Issue 9, 2012.
- [7] Baskaran. A., Mathews P.K, “A Performance Comparison of Vapor Compression Refrigeration System using Various Alternative Refrigerants”, International Journal of Scientific and Research Publications, Volume 3 Issue 10, 2012.
- [8] Rasti.M., Aghamiri. S.F., Hatamipour. M.S. "Energy Efficiency Enhancement of a Domestic Refrigerator Using R436A and R600A as Alternative Refrigerants to R134A". International Journal of Thermal Sciences Volume 74, Pages 86-94, 2013.
- [9] Srinivas. P., Chandra P.R, Kumar.M.R., and Reddy N.Y. “Experimental Investigation of LP Gas Refrigerant in a Domestic Refrigerator”, Journal of Mechanical Engineering Research and Technology, Volume 2, Issue1, Pages 470-476,2014,
- [10] Periyasamy. S, Saravanan.M. “Experimental Studies on A Vapor Compression Refrigeration System Using Hydrocarbon Mixture and R-12 Refrigerant” International Journal of Engineering Research &Technology Volume 3, Issue 5, Pages1070-1073, 2014.
- [11] Qureshi M.A. and Bhatt. S, “Experimental Studies on A Vapor Compression Refrigeration System Using Hydrocarbon Mixture and R-12 Refrigerant”, International Journal of Science and Research Volume 3 Issue 2, Pages 935- 939, 2014.
- [12] Yadav G. M, Rajendraprasad P., Veeresh G.,” Experimental Analysis of Vapor Compression Refrigeration System with Liquid Line Section Line Heat Exchanger by Using R134a and R404a”, International Journal of Scientific Research and Management Studies, Volume 1 Issue 12, Pages 382-395, 2015.
- [13] Thangavel.P.,Somasundaram. D.P, Sivakumar.T. Kumar. C.S, Vetriselvan. G, “Simulation Analysis of Compression Refrigeration Cycle with Different Refrigerants” International Journal of Engineering and Innovative Technology, Volume 2, Issue 10, April 2013.
- [14] Subash.V, “performance Analysis of Vapour Compression Refrigeration System using Mixed Refrigerants of R134A and R404A” International Journal of Research in Mechanical Engineering, Volume 03, Issue 03, 2016.
- [15] Gond R.K.,Chaudhary Khan R.P.,M.A, Gaurav Jain.G “Performance and exergy analysis of vapour compression refrigeration system using various alternative of R134a” International Research Journal of Engineering and Technology, Volume 03 Issue: 05, 2016.
- [16] Dalkilic, A.S., Wongwises. S. “A performance comparison of vapour-compression refrigeration system using various alternative refrigerants” International Communications in Heat and Mass Transfer, Volume 37, pages 1340–1349, 2010.
- [17] Bolaji, B.O and Huan.Z., “Comparative Analysis of The Performance of Hydrocarbon Refrigerants With R22 in a Sub-Cooling Heat



Exchanger Refrigeration System. *Journal of Power and Energy*, Volume 226 issue 7 pages 882–891, 2012.

[18] Hamad.A.J, “Performance Investigation of Vapor Compression Refrigeration System with Integrated Mechanical Sub-cooling Circuit using Hydrocarbon Blends” *Diyala Journal of Engineering Sciences*, Vol 09, issue 01, pages 1-17, 2016.

[19] Baskaran A., Mathews P.K., “A Performance Comparison of Vapour Compression Refrigeration System using Eco Friendly Refrigerants of Low Global Warming Potential” *International Journal of Scientific and Research Publications*, Volume 2, Issue 9, 2012.

[20] Samaneh Daviran, “A comparative study on the performance of HFO-1234yf and HFC-134a as an alternative in automotive air conditioning systems” *Journal of Applied Thermal Engineering*, Volume 110, Pages 1091-1100, 2017.

[21] Saleh S. Baakeem, Jamel Orfi, Abdullah Alabdulkarem, “Optimization of a multistage vapor-compression refrigeration system for various refrigerants” *Journal of Applied Thermal Engineering*, Volume 136, Pages 84-96, 2018.

[22] Naeem Abas, Ali Raza Kalair, Nasrullah Khan, “Natural and synthetic refrigerants, global warming: A review” *Renewable and Sustainable Energy Reviews*, Volume 90, Pages 557-569, 2018.

[23] Kashif Nawaz, Bo Shen, Ahmed Elatar, “R290 (propane) and R600a (isobutane) as natural refrigerants for residential heat pump water heaters” *Applied Thermal Engineering*, Volume 127, Pages 870-883, 2018.



INVESTIGATION AND DESIGN OF ARCHEMEDES SCREW TURBINE FOR RUN OF THE RIVE SCENARIO

Ahmad Naveed^{1*}, Umair Ashraf¹, Muhammad Farooq¹, Warda Ijaz¹, Mahnoor Amir¹, Zara Saqib¹

¹ Mechanical Engineering Department, University of Engineering & Technology, Lahore, Pakistan

*ahmadnaveed@uet.edu.pk

ABSTRACT:

Hydropower from very low head (VLH) is an area in which head vary from 1 to 10 m generally. A significant, but unused, potential both in rivers and in irrigation canal systems is available in Pakistan. The basic idea of this research is to investigate and to design a portable small turbine that can be used in rivers, canals and in hilly areas where small head is available. This small portable hydlye turbine would help to generate a small amount of electricity. Hydlye power is an abundant source of energy in Pakistan but most of the sites with small head are not exploring energy because the technologies to convert energy form these low potential sites is not mature enough locally. In Northern hilly areas of Pakistan, the rivers have flow at very high velocity and energy can be harnessed in small amount if some suitable convertor is developed. In this research a general description of all small hydro power turbines has been made and potential of micro hydro turbine in Pakistan has been made. A turbine working on reverse principle of Archimedes Screw (has been used for uplifting water) has been investigated in portable size and variation of power and expected efficiency for range of dependent parameters has been determined.

Key Words: Archimedes turbine, Hydro Power, Screw.

1. INTRODUCTION:

One of the oldest hydraulic machine that is still in use is Archimedes screw. For many years, its function was only to uplift water from lower level to higher level and it was used as a pump but now a day in modern era the same machine is operating as a turbine to produce electricity. Archimedes invented this machine in 212B.C. [1] To modify and to keep the device design up to date a roman researcher named Vitruvius did a thorough investigation of this mechanism in his book De architecture. [2] Although the device is oldest but till now its complete working theory has not been described in published data. Due to this reason the use of this devise depends completely upon the skills of design engineer. Data published up till now describes the empirical design of the machine and energy optimization in accordance to the volume flow rate,

velocity of flowing water, head available etc. It has been observed that the efficiency of the device depends mainly upon the leakage losses according to Negal-1968 (book on Archimedean Screw). [3]. Such screw type generators have high efficiency ranging from 80 to 85%. Efficiency varies by varying radius of the screw and by changing the flow water. So, this turbine is a good replacement of other low head hydropower turbines [4][5][6][7][8]. Maximum diameter of screw is limited to 4 meter because larger than this diameter produces large fatigue weldment stresses along with fabrication and maintenance issues [5]. Archimedes turbine is environment friendly because it gives safe passage to the fish and many other species. Even it can allow to python bags, forest grass and garbage etc. so it avoids from choking due to large gap between the blade turns [9]. Efficiency of screw is mainly



dependent upon water flow rate, geometrical parameters, and inclination angle. Inclination angle is directly proportional to the efficiency and inversely proportional to the flow rate [10]. The lowest Archimedes screws are of 1 m diameter and have capacity to pass flow of 250 L/s and the largest screw is of diameter 5 meters having flow capacity of around 14 m³/s. More screws can be installed in parallel arrangement if more flow is available. In terms of power output, the very smallest Archimedean screws can produce as little as 5 kW, and the largest 500 kW. [11]. Pakistan is a country that has vast potential of hydro power. In northern areas of Pakistan rivers are flowing with very high velocity. Tourists from all over the world come to see and enjoy the nature in these areas. Mostly tourists choose some suitable place on river sides for camping as well. Small amount of energy can be harnessed from these high speeds flowing waters to fulfill the basic needs of lightening and mobile charging etc. for these tourists. So, in this research an Archimedes power screw is investigated and designed on small scale to produce electricity from the kinetic energy of water. We summarized the variation of power and expected efficiency of small hydro power turbines working on reverse Archimedes principle.

2. DESIGN OF ARCHIMEDES SCREW TURBINE:

The geometry of an Archimedes screw is governed by certain external parameters (its outer radius, length, and slope) and certain internal parameters (its inner radius, number of blades, and the pitch of the blades). The external parameters are usually determined by the location of the screw and flow rate of water. The internal parameters, however, are free to be chosen to optimize the performance of the screw.

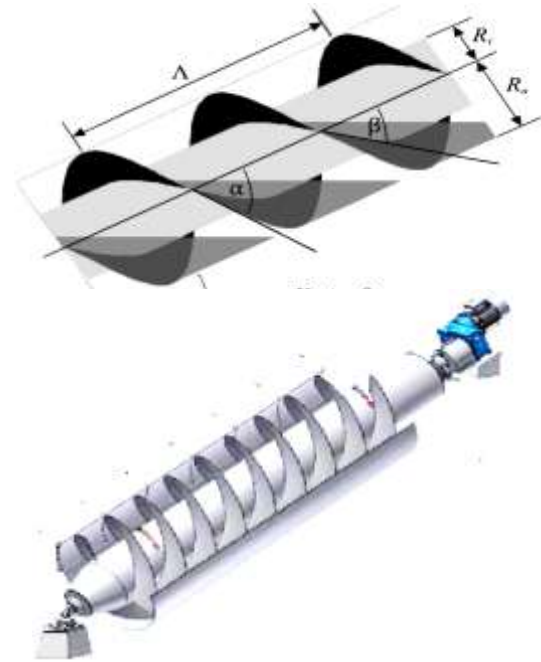


Figure 1: Archimedes Screw reversed pump or turbine [1]

Archimedes screw has high efficiency as compared to other micro hydro power technologies. Along with the flow rate geometrical parameters have direct influence on the power output and efficiency, so designer selection depending upon the site for installation is much important.

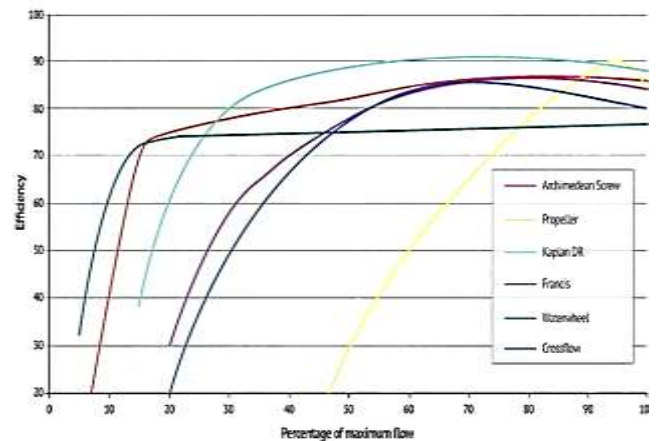


Fig 2: Turbine efficiency comparison [12]

Table 1 gives optimum values of various factors to calculate other parameters like inner and outer radius, power input to the screw, volume of water in one cycle of the screw (m³/revolution), power output etc.

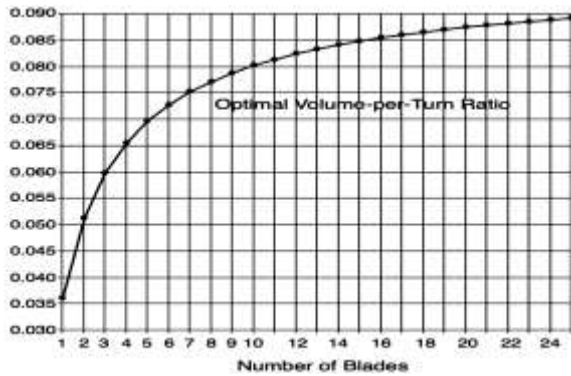


Table 1 : Optimal Ratio Parameter values of Archimedes Screw [1]

N	ρ^*	λ^*	v^*	$\lambda^*v(N, \rho^*, \lambda^*)$
1	0.5358	0.1285	0.2811	0.0361
2	0.5369	0.1863	0.2747	0.0512
3	0.5357	0.2217	0.2697	0.0598
4	0.5353	0.2456	0.2667	0.0655
5	0.5352	0.263	0.2647	0.0696
6	0.5353	0.2763	0.2631	0.0727
7	0.5354	0.2869	0.2619	0.0752
8	0.5354	0.2957	0.2609	0.0771
9	0.5356	0.3029	0.2601	0.0788
10	0.5356	0.3092	0.2592	0.0802

Figure 3: Optimal Ratio Parameters of Archimedes Screw & Number of blades [1]

Fig. 3 gives variation of different optimum parameters corresponding to the number of blades of the screw. We are to design this screw on small basis so it may be easy to carry and it should be portable. So, calculations are made here for single blade screw to find other optimum parameters using these figures and tables.

3. DESIGNING OF SCREW:

For single blade with screw inclination less than 30° , length of screw 50cm and outer radius of 10cm remaining parameters are calculated for range of velocity of flowing water. Formulae to calculate various parameters are given in the table 2.

Table 2: Geometrical parameter calculations

Model	Comments
$R_i = \rho^*R_o$	Inner radius of the screw
$p = 2.4^*R_o$	Optimum value of pitch for inclination angle less than 30°
$Q = (v^*)(\text{Total area of screw})(\text{Velocity})$	flow rate for selected parameters
$C = 0.0045(2R_o)^{0.5}$	Clearance between trough and the screw
$H_1 = V_1^2/2^*g$	Velocity head
$P_i = \rho g Q_1 H_1$	Input Power to turbine
$N_{\text{speed}} = 60^*Q/V_T$	Rotating speed of screw
$V_T^* = 2\pi^2 R_o^3 \lambda^* v(N, \rho^*, \lambda^*)/K$	V_T = volume of water in one cycle of the screw ($m^3/\text{revolution}$)
$\eta = [1 - 0.01125^*D_o^2/Q] / [(2^*rps + 60)/(2^*rps + 120)]$	Efficiency of the turbine
$P_o = \eta^* \text{input power}$	Power output
$T = P_o^*60/2\pi N_{\text{speed}}$	Torque generated
$\text{Tan}\alpha = 2\pi R_o/p$	α the angle that the sinusoidal curve defining the outer edge of a blade makes with axis of the screw
$\text{Tan}\beta = 2\pi R_i/p$	β is the angle that the sinusoidal curve defining the inner edge of a blade makes with axis of the screw.
$P_e = \eta_{GB} \eta_{DS} \eta_{Gen} P_o$	electrical power from produced torque
$\text{Max rpm} = 53/D_o^{2/3}$	Maximum allowable rpm

4. RESULTS & DISCUSSION:

Calculations are made only to harness the velocity head. So, it is run of the river scheme and uses only kinetic energy.

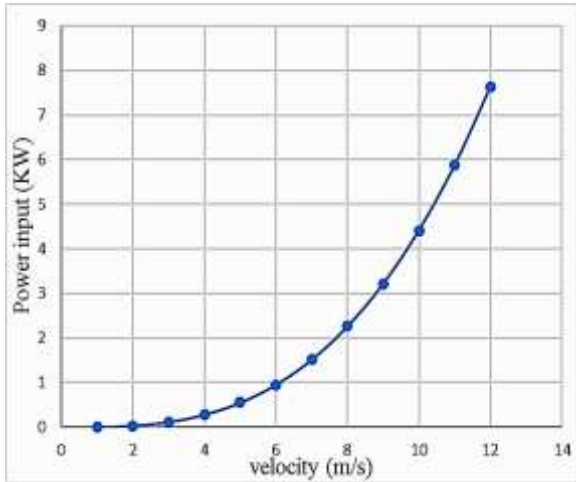


Fig. 4: Power Input vs velocity of flowing water

If water fall or slope is available, then it is assumed to be very small so can be neglected. Fig. 4 gives variation of power input corresponding to the velocity change of flowing water. It gives exponential increase in power input with increase in velocity.

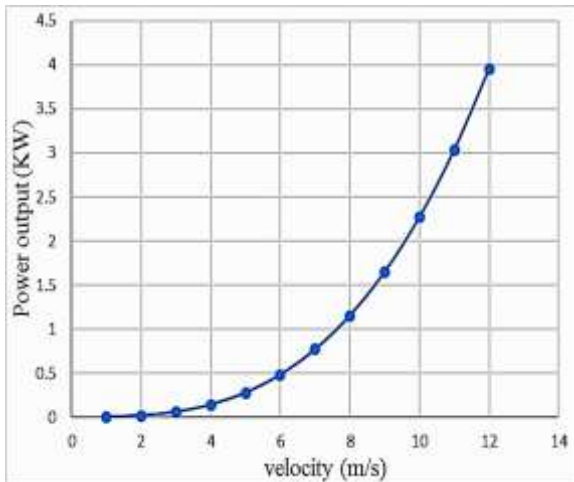


Fig. 5: Power output vs velocity of flowing water
Fig. 5 shows that power output also increases as the velocity of water or in other words flow rate increases.

Power input increases with the increase in velocity. But higher velocity increases the rpm that has its limit of 155 rpm. So, flowing velocity above this is not recommended. In actual the flowing velocity of water would be much smaller than this value

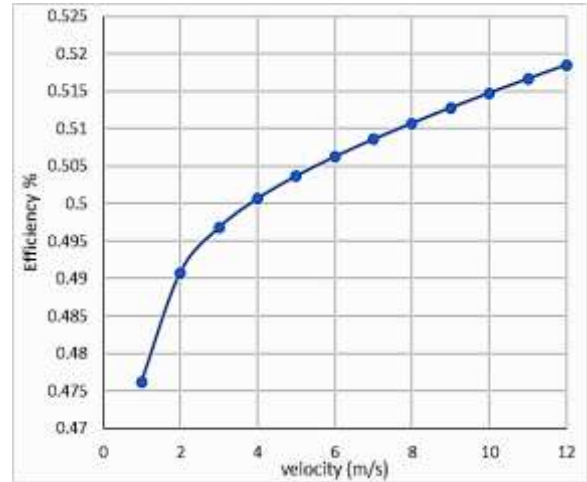


Fig. 6: Efficiency vs velocity of flowing water

Fig. 6 gives variation of efficiency with respect to the velocity of flowing water. It can be seen that the velocity increases abruptly in the beginning the rate of increase in velocity decreases but still towards increase as the velocity increases. Due to limitations of the rpm the velocity of water cannot be increased too much so efficiency of this model will be approximately 50%.

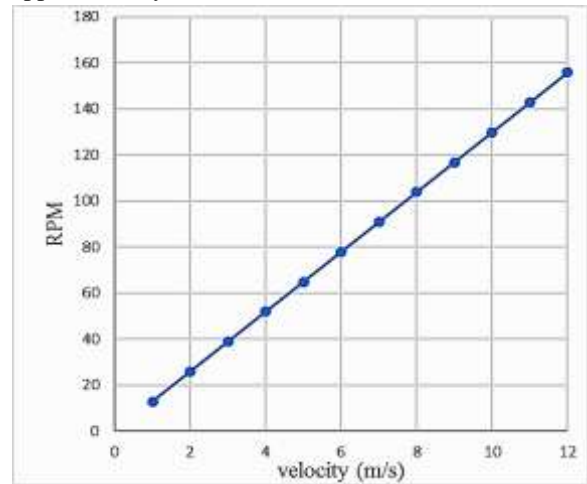


Fig. 7: RPM vs velocity of flowing water

Fig. 7 gives increase in rpm with increase in the velocity of water. As given in Table 2 (Max rpm to be less than $53/D_o^{2/3}$) rpm cannot be increased beyond limitations so velocity in the model is assumed to be less than 10 m/s.

Fig. 8 gives relation between torque and velocity. Torque increase with increase in velocity so larger the flow rate or the velocity of water would be more it would produce torque.

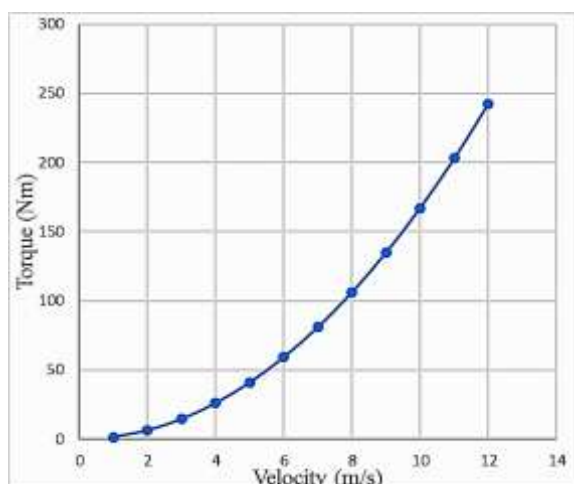


Fig. 8: Torque vs velocity of flowing water

If above calculations are made for two number of blades, then it has been observed that flow rate of water decreases with slight decrease in Mechanical Power. RPM of screw decreases. Torque generated increases slightly and efficiency of screw decreases a little bit.

5. CONCLUSION:

In this paper a model of Archimedes Screw for power production on very small scale has been presented. It has been found that this technique can be applied on sites where the velocity of the flowing water is high enough like in Northerns Areas of Pakistan. For different flow rate values results are determined and are found close to the results obtained in related research work [10]. Depending upon the site location and slope of water if available the designer can modify the geometrical parameters. If reasonable velocity of water is available, then this technique can produce small amount of energy. It has been observed that efficiency of turbine largely depends upon the geometry of screw and inflow water rate.

REFERENCE

- [1] Rorres, C. "The turn of the screw: Optimal design of the Archimedean screw" (2000) *J. Hydr. Engng.* 126(1), 72–80
- [2] "The Water Screw" *De Architectura*, Book X Chapter VI Vitruvius (first century B.C.). Diagram and Translation by Morris Hicky Morgan in Vitruvius: "The Ten Books on Architecture", Harvard University Press, Cambridge, 1914. Republished by Dover, New York, 1960, 295–297.
- [3] Nagel, G. (1968). "Archimedean screw pump handbook". Ritz- Atro Pumpwerksbau GMBH Roding, Nu'rnberg, Germany.
- [4] Brada, K. "Wasserkraftschnecke ermöglicht Stromerzeugung über Kleinkraftwerke" [Hydraulic screw generates electricity from micro hydropower stations]. <http://www.maschinenmarkt.vogel.de/index.cfm?pid=5156 &pk=303> Maschinenmarkt Würzburg, Mitteilung (1999) 14, 52–56. [in German].
- [5] Brada, K., Radlik, K.-A. Water screw motor for micropower plant. 6th Intl. Symp. "Heat exchange and renewable energy sources", (1996) 43–52, W. Nowak, ed. Wydaw Politechniki Szczecińskiej, Szczecin, Poland.
- [6] Hellmann, H.D. "Gutachten zur Wirkungsgradbestimmung einer Wasserkraftschnecke Fabrikat Ritz-Atro" [Report on determination of hydraulic screw efficiency manufactured by Ritz-Atro Ltd.] (2003) Fachbereich Maschinenbau und Verfahrenstechnik, Technical University, Kaiserslautern, Germany (http://www.ritz-atro.de/2006/downloads/Wasserkraft_GB.pdf) [in German].
- [7] D. M. Nurnberg, C Rorres, "Analytical Model for water inflow of an Archimedean screw using in hydro power generation" *J. Hydraul. Eng.* (2013) V-139 page 213-220
- [8] G. MÜLLER & J. SENIOR, "Simplified theory of Archimedean screws" *J HR V-47 No. 5* (2009) 666–669
- [9] Fishtek Consulting Ltd. Mann Power Consulting, "Fish Monitoring and Live Fish Trials Archimedes Screw Turbine, River Dart", Unit 3D Betton Way Moretonhampstead, Devon.
- [10] Ali Raza, Muhammad Saleem Mian, Yasir Saleem "Modeling of Archimedes Turbine for Low



Head Hydro Power Plant in Simulink MATLAB”
(IJERT) V-2 No. 7 (2013) ISSN: 2278-0181

[11] Alkistis Stergiopoulou & Efrosini Kalkani
“Investigating the hydrodynamic behavior of
innovative Archimedean hydropower turbines”
IJRRAS 17 (1) November 2013
Volumes/Vol17Issue1/IJRRAS_17_1_10

[12] Santos, Daryl, and Sunil Chhabra. "An Analysis
of Archimedes Screw Design Parameters and their
Influence on Dispensing Quality for Electronics
Assembly Applications." State University of New
York at Binghamton.



DESIGN AND STRESS ANALYSIS TRACK



Ti-HA Biocomposite Produced By Powder Metallurgy

Görkem Kahraman^a, Eren Yılmaz^b, Fehim Fındık^{a,b}

^aMetallurgy & Materials Engineering Department, Faculty of Technology, Sakarya Applied Sciences University, Sakarya, Turkey, E-mail: findik@sakarya.edu.tr

^bBiomedical, Magnetic and Semiconductor Materials Application & Research Center, Sakarya University, Sakarya, Turkey, E-mail: erenyilmaz@sakarya.edu.tr

Abstract:

In this study, titanium (Ti) - hydroxyapatite (HA) biocomposites sintered at 800 ° C and 1200 ° C in argon atmosphere and pure Ti sample were produced for comparison under the same conditions. The effects of the addition of hydroxyapatite into titanium on microstructure, phase content, surface wettability and corrosion behavior of titanium were investigated. While the density decreased with increasing sintering temperature, the density approached the bone with the addition of HA. Sintered titanium contains α -Ti and titanium oxide phases. The Ti-10HA composite contains α -Ti, titanium oxide and hydroxyapatite phases as well as hydroxyapatite decomposition phases depending on the sintering temperature. Furthermore, the water contact angle was reduced from about 71 ° to 30 ° by the addition of HA into the Ti. In addition, the mechanical properties and corrosion resistance of Ti-Ha biocomposite were found to be lower compared to pure titanium.

Keywords: Titanium, hydroxyapatite, biocomposite, powder metallurgy

1. Introduction

Ti and its alloys are widely used in implant applications such as knee, hip, tooth root due to its superior corrosion resistance, non-toxic, low density, high mechanical properties. In medical implant applications, it is desirable that the implant material is non-toxic and has physical properties as well as properties that permit bone cell growth in the body. Although metal-based implants are advantageous in terms of mechanical properties and corrosion resistance, they have low biocompatibility in stimulating natural bone growth. Metallic implants also have a high elastic modulus relative to bone. As a result, the surrounding bone cannot transmit tension to the tissue, resulting in bone dissolution and loosening around the implant [1].

In metallic implants, hydroxyapatite, which resembles the structure of bone and stimulates natural tissue growth, is widely used as a coating material to increase biocompatibility. However, HA cannot be used in carrier implant applications alone because of its low mechanical properties and brittle bone. The combination of HA and Ti materials provides excellent mechanical and biological properties [2]. In recent years, studies on Ti-HA composites have increased for implant applications [3-5]. Han and friends fabricated functionally graded materials of titanium/hydroxyapatite (Ti/HA) by selective laser melting. They examined the phases formed in this study and observed that the addition of HA increased the brittleness [6]. Sedighi and his colleagues conducted a dental study consisting of Ti / HA composite. They conducted microstructure and

hardness investigations. Although the addition of HA increased the hardness to a certain rate, the addition of more than 30% by volume of HA reduced the hardness due to the increase in porosity [7]. Gabriella M. Penarrieta-Juanito and colleagues have focused on the bio-properties of Ti-HA biocomposites. Compared to the Ti6Al4V alloy, surface wettability and cell viability improved with composite production [8].

The aim of this study is to produce Ti-HA composite as a medical implant composite and to perform characterization studies. The effects of sintering temperatures on microstructure, phase content and mechanical properties were investigated. Better sintering ability was obtained at 1200 ° C sinter temperature. Therefore, corrosion behavior and surface wettability of sintered samples at this temperature were investigated.

2. Experimental

2.1. Materials and Methods

Elemental powders were used as starting materials. Ti powder, 45 μ m in size and irregular shape morphology, was obtained from Alfa Aesar. HA powder is 5 μ m in size, provided from Sigma Aldrich. These powders were weighed in suitable compositions and then mixed in the turbula mixer for 2 hours. Then, uniaxial pressing was applied at 45 MPa. Finally, sintering was carried out at 800 ° C (Ti800, Ti10HA800) and 1200 ° C (Ti1200, Ti10HA1200) in Ar atmosphere for 2 hours to increase the density and obtain the final product.



2.2. Characterization

The size and density changes of the samples after pressing and sintering were measured. After sintering, samples were prepared metallographically and etched with Kroll solution. Microstructure images were examined by scanning electron microscopy (SEM, Jeol JSM 6060LV), phase contents were determined by X-ray diffraction analysis (XRD, Rigaku D / Max 2200). Temperature-dependent phase changes of Ti-10HA composite were interpreted by thermogravimetric analysis (TGA) and differential thermal analysis (DTA). Water contact angle measurements were performed to determine the surface wettability of the samples. The mechanical properties of the samples were determined by nanoindentation tests (maximum load 20mN). In addition, potentiodynamic polarization technique was used to determine the corrosion behavior of the samples. For electrochemical corrosion tests, the surface of each sample was first polished. 1 cm² surface areas of the samples were exposed to electrolyte. Simulated body fluid (SBF, 7.4 pH) was prepared as electrolyte. The test sample, platinum wire and saturated calomel electrode was used as working electrode, counter electrode and reference electrode, respectively. Open circuit potentials (OCP) were recorded for 1800 s after each sample was immersed in SBF. Then potentiodynamic polarization tests were started. Potentiodynamic polarization tests were carried out by Gammry potentiostat in the range of -2V to +1.5V at a scanning speed of 5mV / s.

3. Results and Discussion

3.1. Density and mechanical properties

After sintering, the samples were successfully produced without any deformation. After pressing Ti and Ti-10HA density was measured as 2-2.15 g / cm³, densities increased after sintering (table 1). The Ti-10HA has a relative density of about 59%, while Ti has about 91% of its relative density by sintering at 1200 ° C. Addition of Ti to HA, reduction of density and sinterability. In this study, it is thought that the theoretical density of HA (3.16 g / cm³) is lower than Ti (4.506 g / cm³), and its low electrical and thermal conductivity affects neck formation during HA sintering [9]. Another reason why the relative densities in the sintered samples is low is that the selected press pressure is low. In addition, the density value approached the bone (cortical bone density 1.8 g / cm³) with the addition of HA [10]. The effect of HA in reducing the density of Ti-HA composites is consistent with the literature [11]. In addition, the increase in porosity with the addition of HA provides an advantage for osseointegration and mechanical clamping of new bone tissue on the surface after implantation.

Mechanical properties of the biocomposites are given in Table 1. The addition of HA to titanium and the change in sintering temperatures affected the mechanical properties. In general, mechanical properties decreased with the addition of HA and approached bone values. The addition of HA with low thermal and electrical conductivity can be considered to affect neck formation and thermal expansion differences between Ti and HA are another cause. In addition, the decomposition of HA and insufficient condensation caused by the reaction between HA and other particles also reduced mechanical properties.

Table 1. Density values and mechanical properties of Ti and Ti-10HA samples at different sintering temperatures

Samples	Density (g/cm ³)	Hardness (MPa)	Elastic Modulus (GPa)
Ti800	2,51±5	5448±50	83±4
Ti1200	4,11±6	6917±40	129±5
Ti10HA800	2,31±2	4076±35	48.5±4
Ti10HA1200	2,54±2	5383±45	80±3

3.2. Microstructure and phase composition

As stated in the literature, dehydroxylation of HA begins at about 900 ° C in the air and at about 850 ° C in the anhydrous atmosphere. It has been reported that pure hydroxyapatite can remain stable up to 1200 ° C in an argon atmosphere [2]. However, in HA / Ti composites, Ti ions react with the dried water of HA to obtain titanium oxide, accelerating dehydroxylation and decomposition of HA at about 800 ° C. According to XRD analysis, α-Ti and TiO₂ phases were determined in sintered titanium samples. In the Ti-10HA composite sintered at 800 ° C, HA and tricalcium phosphate, the decomposition phase, were observed. In the Ti-10HA sample sintered at 1200 ° C, Ti₃P, CaTiO₃ phases were formed as a result of various reactions with increasing temperature (figure 1). In the literature, findings consistent with these results have been determined and it is reported that calcium titanate phase can be stable above 1000 ° C. The formation of these phases is explained by the following reactions.

Possible reactions during the sintering of Ti-10 HA composite at 1200 ° C are given in equations 1-4 [9]. In the first stage of sintering, according to equation 1, HA loses a hydroxyl chain. H₂O reacts with titanium and forms titanium oxide (equation 2). HA



then reacts with titanium oxide to form tricalcium phosphate (TCP) and calcium titanate (equation 3). Furthermore, as given in equation 4, Ti reacts with P. These reactions confirmed the XRD results.

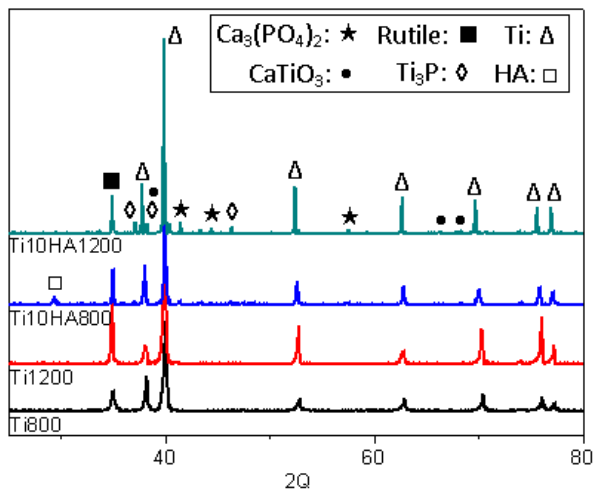
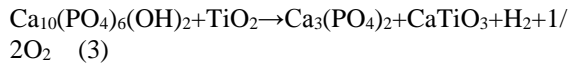
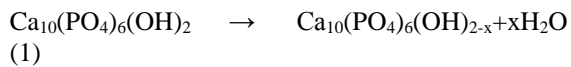


Figure 1. XRD patterns of Ti and Ti-10HA composite sintered at different temperatures

Figure 2 shows SEM images of Ti and Ti-10HA samples sintered at 1200 ° C. Since sintering temperature differences did not cause significant changes on microstructure, images of sintered samples at 1200 ° C were given. At elevation to sintering temperature, the Ti- α phase is converted to the Ti- β phase above 882 ° C [12], then, during slow cooling to room temperature in the furnace, the β phase is converted to the α phase. The microstructure of the sintered Ti in Figure 2a appears to be composed of a single phase (single color), according to the literature review, this phase is thought to be α phase [13]. Metallographic preparation of Ti-10HA composite is difficult due to the brittle properties of HA, the phases formed between the Ti particles during polishing can be partially separated. This may be the reason why the phosphorus content of the Ti-10HA sample sintered at 1200 ° C is lower than expected in the EDS analysis. According to SEM investigations in Figure 3, the tricalcium phosphate ($\text{Ca}_3(\text{PO}_4)_2$) phase may be surrounding the titanium particles. Furthermore, phosphorus diffusion to Ti particles during sintering can lead to the formation of the Ti_xP_y phase. As shown in the image of Ti-10HA at 10000x magnification in Figure 3.a, two different morphologies were observed. The region 1

is rich in titanium, the P content is high and the Ca content is low, which region is thought to have the Ti_xP_y phase. In the region 2 between these particles, the Ca and O contents are increased, indicating the region dominated by the tricalcium phosphate and calcium titanate phase (Figure 3b-c). In addition, the presence of oxygen may come from the HA and titanium oxide phases. SEM examinations confirm the results of XRD analysis.

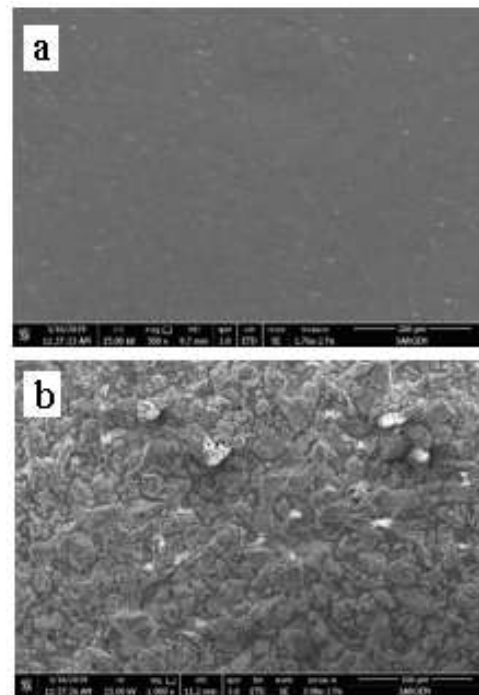


Figure 2. Microstructure images of a) Ti and b) Ti-10HA samples sintered at 1200 ° C

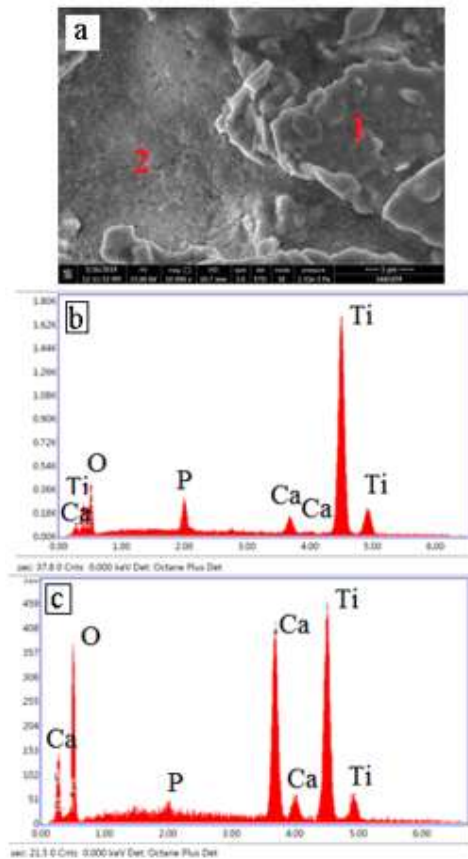


Figure 3. a) SEM image of a 1200 ° C sintered Ti-10HA sample, b)EDS analysis of region 1 and c) EDS analysis of region 2

Figure 4 shows the thermal analysis results of the Ti-10HA composite. Peaks observed up to 800 ° C are mainly due to titanium oxidation caused by air remaining in the environment. Oxidation is also shown in Figure 4b by temperature-dependent weight gain in TGA analysis. During thermal analysis, the air was replaced by a high purity argon flow since the equipment was unable to perform a vacuum. It is unlikely that air will disappear completely in this procedure. At about 440 ° C, rutile begins to nucleate, and then the oxide film consists of anatase and rutile substrates. The peak at 800 ° C indicates that the anatase converted to rutile, the only stable oxide above 730 ° C, is no longer stable, and in the previous thermal analysis studies of Ti-HA composites, peaks above 800 ° C are associated with HA. decomposition. In Figure 4a, the exothermic peak at about 1100 ° C shows that HA is converted to TCP-TCP. In summary, the thermal analysis findings confirmed the results of the XRD analysis. Tricalcium phosphate formation is a precursor to the formation of Ti_3P_2 and $CaTiO_3$ phases at temperatures above 1000 ° C and 1000 ° C.

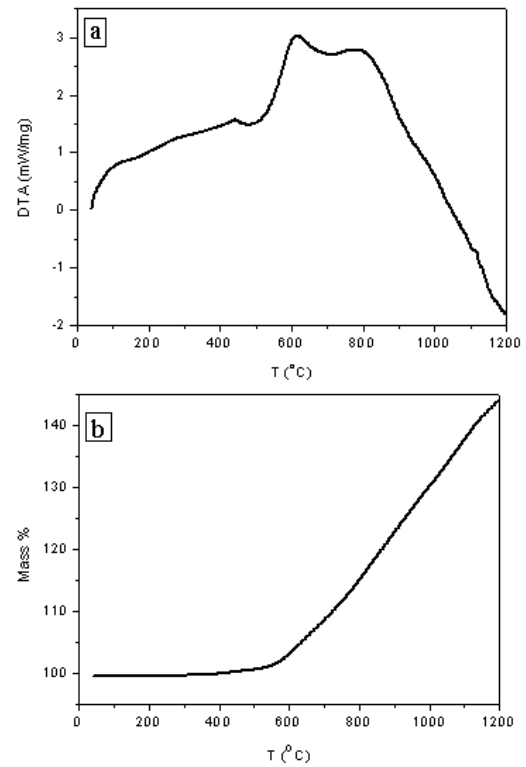


Figure 4. DTA and TGA curves of Ti-10HA composition

3.3. Corrosion behavior and surface wettability

Figure 5 shows the changes in potentiodynamic polarization behavior of Ti-10HA composite and titanium in SBF. For each sample, passivation occurred after corrosion occurred in the anodic active site. The addition of HA to Ti reduced the corrosion resistance. As the HA content increased, the surface area exposed to electrolysis increased due to the increase in porosity and became more susceptible to corrosion. Oxide layers formed on porous surfaces are unstable. As shown in Figure 5, the addition of HA increased the corrosion current density (I_{corr}) while reducing the corrosion potential (E_{corr}). In particular, an increase in corrosion current density means a decrease in polarization resistance. Figure 6 shows the water contact angle of samples of Ti and Ti-10HA sintered to 1200 ° C. The contact angle decreased from 71° to 30° with the addition of 10% by weight. HA to Ti. The reason for the development of wettability is the hydroxyl groups in the HA content. Surface energy increased with decreasing contact angle. In implant applications, high surface wettability is desirable for protein and bone cell adhesion and proliferation [14]. In summary, the combination of titanium with HA provides advantages in this respect in implant applications.

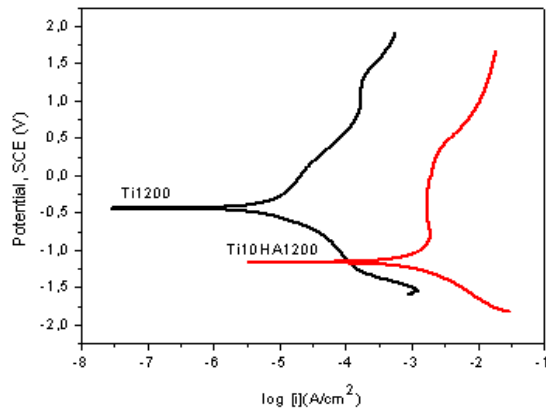


Figure 5. Potentiodynamic polarization curves of Ti and Ti-10HA composite sintered at 1200 ° C

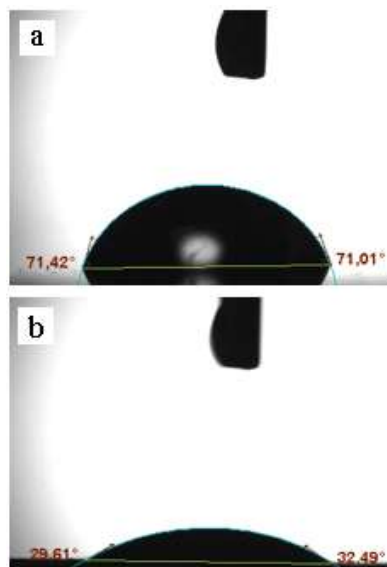


Figure 6. Contact angle measurements of a) Ti, b) Ti-10HA composite sintered at 1200 ° C

4. Result

Ti and Ti-10HA biocomposites have been successfully produced by conventional powder metallurgy. Depending on the sintering temperature, Ti phase as well as HA decomposition phases were determined. The addition of HA to the Ti reduced its sinterability, increased the amount of porosity, and reduced the density to approximate the density of the cortical bone. Due to these effects, addition of HA also reduced the mechanical properties to values compatible with bone. Furthermore, with the addition of HA to titanium, the surface changed from hydrophobic to hydrophilic. This is important for the success of the implant. However, the addition of HA decreased the corrosion resistance by increasing the amount of porosity. In the future study, it is planned to investigate the bio properties of these composites such as cell culture, apatite formation ability. In

addition, it is aimed to start functional grade composite studies for implant production of these composites.

Acknowledgements

Thanks to SUBU and BIMAS-RC due to provision of laboratory facilities and SAU due to partial financial support within international bilateral Mevlana project (Project Number: MEV-2018-644) between Pakistan and Turkey.

REFERENCES

- [1] Yılmaz, E., Gökçe, A., Findik, F., Gülsoy, H., Powder metallurgy processing of Ti-Nb based biomedical alloys, *Acta Phys Pol A.*, Vol 134, 278-280, 2018.
- [2] Arifin, A., Sulong, A.B., Muhamad, N., Syarif, J., Ramli, M.I., Material processing of hydroxyapatite and titanium alloy (HA/Ti) composite as implant materials using powder metallurgy: A review, *Mater Des.*, Vol 55, 165-175, 2014.
- [3] Ye, H., Liu, X.Y., Hong, H., Characterization of sintered titanium/hydroxyapatite biocomposite using FTIR spectroscopy, *J. Mater. Med.*, Vol 20, 843-850, 2009.
- [4] Zhang, L., He, Z.Y., Zhang, Y.Q., Jiang, Y.H., Zhou, R., Enhanced in vitro bioactivity of porous NiTi-HA composites with interconnected pore characteristics prepared by spark plasma sintering, *Mater Des.*, Vol 101, 170-180, 2016.
- [5] Cheng, Y., Wang, X., Xu, L., Liu, Z., Do Woo, K., Tribological behavior study on Ti-Nb-Sn/hydroxyapatite composites in simulated body fluid solution, *J Mech Behav Biomed Mater.*, Vol 10, 97-107, 2012.
- [6] Han, C., Li, Y., Wang, Q., Cai, D., Wei, Q., Yang, L., Wen, S., Liu, J., Shi, Y., Titanium/hydroxyapatite (Ti/HA) gradient materials with quasi-continuous ratios fabricated by SLM: Material interface and fracture toughness, *Materials and Design*, vol 141, 256-266, 2018.
- [7] Sedighi, M., Omidi, N., Jabbari, A.H., Experimental investigation of FGM dental implant properties made from Ti/HA composite, *Mechanics of Composite Structures*, vol 4, 233-237, 2017.
- [8] Penarrieta-Juanito, G.M., Costa, M., Cruz, M., Miranda, G., Henriques, B., Joana, M., Magini, R., Mata, A., Carames, J., Silva, F., Souza, J.C.M., Bioactivity of novel functionally structured titanium-ceramic composites in contact with human osteoblasts, *Society For Biomaterials*, vol7, 1923-1931, 2018.
- [9] He, Y.H., Zhang, Y.Q., Jiang, Y.H., Zhou, R., Effect of HA (hydroxyapatite) content on the microstructure, mechanical and corrosion properties of $(Ti-10Nb-10Zr-xHA)$ biocomposites



- synthesized by sparkle plasma sintering, *Vacuum*, Vol 131, 176-180, 2016.
- [10] Yılmaz, E., Gökçe A., Findik, F., Gülsoy, H., İyibilgin, O., Mechanical properties and electrochemical behavior of porous Ti-Nb biomaterials, *J Mech Behav Biomed Mater.*, Vol 87, 59-67, 2018.
- [11] Zhang, L., He, Z.Y., Zhang, Y.Q., Jiang, Y.H., Zhou, R., Rapidly sintering of interconnected porous Ti-HA biocomposite with high strength and enhanced bioactivity, *Mater Sci Eng C.*, Vol 67, 104-114, 2016.
- [12] Yılmaz, E., Gökçe A., Findik, F., Gülsoy, H., Characterization of biomedical Ti16Nb-(0-4)Sn alloys produced by powder injection molding, *Vacuum*, Vol 142, 164-174, 2017.
- [13] Yılmaz, E., Gökçe A., Findik, F., Gülsoy, H., Metallurgical properties and biomimetic HA deposition performance of Ti-Nb PIM alloys, *J Alloys Compd*, Vol 746, 301-313, 2018.
- [14] Yılmaz, E., Çakıroğlu, B., Gökçe, A., Findik, F., Gülsoy, H., Gülsoy, H., Mutlu, Ö., Özacar, M., Novel hydroxyapatite/graphene oxide/collagen bioactive composite coating on Ti16Nb alloys by electrodeposition, *Mater Sci Eng C*, Vol 101, 292-305, 2019.



Experimental Study on Heat Storage Properties Comparison of Paraffin/Metal foams Phase Change Material Composites

W. Ahmed¹, A. Hussain¹ *

¹- Department of Mechanical Engineering, University of Engineering and Technology Taxila, Pakistan

* Corresponding Author: abid.hussain@uettaxila.edu.pk

Abstract

Heat storage properties of phase change materials (PCMs) are essential characteristics which perform a key role in thermal heat energy storage systems. Thermal properties of PCMs can be improved by developing metal foam/PCM composites. Addition of metal foam in PCMs has significant effect on the thermal performance of PCMs. In this paper, the heat storage properties of three different materials were experimentally examined. The behavior of paraffin in metal foams (copper and iron-nickel)/paraffin composites with respect to pure paraffin at a constant heat flux was studied. Paraffin was infiltrated into copper and iron-nickel foams to develop composite materials which resulted in enhancing heat storage rate of the paraffin. A comparative analysis is made on heat storage properties of paraffin in copper and iron-nickel foams/paraffin composites. Inner temperature distribution during the phase transition process is experimentally considered. This comparison indicates that temperature uniformity in Copper foam/paraffin composite is better than iron-nickel foam/paraffin composite and pure paraffin at the same heat flux. Experimental results show that when heat flux is 1000 W/m^2 , the heat storage time for copper foam/paraffin composite is 20.63% to that of iron-nickel foam/paraffin composite.

Keywords: heat storage capacity; paraffin/metal foam composite; temperature uniformity; heat storage rate; phase transition process

1. Introduction

Phase change materials (PCMs) are broadly used in thermal controlling and thermal energy storage systems owing to their excellent heat storage capacity. This feature of PCMs is utilized in different applications and is profoundly publicized. However, PCMs are characterized as bad thermal conductors. Therefore, PCMs composites were developed using many techniques by addition of different thermal conductivity promoters constituents in PCMs [1]. Conversely, by improving the heat absorbing efficiency and thermal conductivity, the heat storage capacity of PCMs is contracted. Heat transfer efficiency improvement in PCMs composites challenge certain amount of heat storage capability. Hence, it is essential to investigate experimentally the heat storage properties of PCMs which are infiltrated in different metal foams.

The usage of PCM composites has brought great improvement in thermal energy management by limiting the temperature rise. Thermal management is indispensable for thermal safety and optimal performance of power batteries. The nature of chemical reactions taking place with in battery, performance competence of power and energy, material characteristics and life cycle are impacted to large extent by operational temperature range [2]. In passive thermal management systems of batteries by using PCMs composites has substantial cooling influence on limiting the temperature rise. Abid et al. [3] studied the thermal performance and management of battery pack using PCMs/graphene coated nickel

(GcN) foam PCM composite. This kind of PCM composite could be utilized in controlling the temperature rise. The thermal heat is dissipated in discharging process. There was 23 times better improved thermal conductivity of the GcN PCM composite compared to that of pure paraffin. However, at the same time there was diminution in specific heat capacity of the composite by an amount of 34%. The addition of Fe_3O_4 nanoparticles in PCM has enhanced the thermal conductivity by 48% [4]. The process of PCM infiltration in aluminum foam was studied. It was found that the foam with 70% porosity, after melting of PCM infiltration was performed, 80% pores of foam were filled. The reason was due to PCM shrinkage after solidification [5]. The present research work summarized that the inner temperature distribution within composites largely effects the phase transition rate during the charging process of PCMs. For current research study, paraffin Rubitherm (RT-42) has been selected. It is nontoxic, noncorrosive, stable and possess high latent energy.

Rehman et al. [6] studied the behavior of heat sink at different heat fluxes with different PCMs. They observed the operational time for heat sink without PCMs and with PCMs composites. Different PCMs/composites were investigated by changing heat fluxes from 800 W/m^2 to 2400 W/m^2 . They pointed that as the power provided increased, there was reduction in maximum temperature across the heat sink. Copper foam/PCMs composites were least proficient at 2400 W/m^2 based on the performance of aluminum heat cavity. Another similar study by Rehman et al. [7] found that increasing the porosity of



copper has negative effect on the thermal conductivity of the PCM composite. Furthermore, the study revealed that increasing the PCMs volume fraction decreased the base temperature of heat cavity. Since copper foam is characterized among high conductive materials, presence of copper increased the heat transfer rate with in composites. When copper foam is embedded in PCMs, the melting time of PCM reduced and there was 36% increase in heat transfer rate [8]. Heat storage properties of paraffin mixtures can be improved when nanoparticles of Al_2O_3 are encapsulated in paraffin by direct-synthesis method [9]. Metal filler and carbon based filler materials both added in PCMs largely improve the thermal conductivity. However, carbon additives show excellent stability compared to metal based PCMs composites [10]. R. Baby et al. [11] studied the behavior of copper foam/PCM based heat sink. They found that orientation does not influence the rate of heat transfer.

The better the heat transfer efficiency of the composite, less time would be consumed for phase transition of the PCMs during the melting process. Therefore, it is very essential to investigate the phase transition time of PCMs and inner temperature distribution with in the composites. These properties define the heat storage possessions of PCMs and are prerequisite to investigate in different directions. However, most of the previous study was focused on improving thermal management by limiting the rise in surface temperature of batteries. Moreover a lot of research carried out on improving the thermal conductivity and enhancement of heat absorbing efficiency of PCMs. In this paper, the comparative analysis has been made on heat storage properties of paraffin infiltrated in copper and iron-nickel foams and without infiltration.

2. Theoretic active thermal conductivity of the PCM composite

The operative thermal conductivity of the composite mainly depends upon the process through which the PCMs/metal foam composite were developed. When PCMs are in parallel with the different samples of conductive material, thermal conductivity for this particular case is maximum [12]. This is given as by Eq. 1.

$$\lambda_{max} = (1 - \varepsilon)\lambda_{Cu} + \lambda_{PCM} \quad (1)$$

Minimum thermal conductivity can be also found by following eq. 2. When PCMs are placed in adjacent layers alternatively with conductive metals [12].

$$\lambda_{min} = \frac{\lambda_{Cu} \lambda_{PCM}}{\varepsilon \lambda_{Cu} + (1 - \varepsilon)\lambda_{PCM}} \quad (2)$$

3. Materials and methods

3.1 Metal foam/paraffin composite development

Paraffin was first heated and melted into liquid form. This liquefied paraffin was of infiltrated in two metal foams separately to develop two different paraffin composites under same conditions. After infiltration, both composites were kept for 24 hours for homogenous solidification. One of such composite was iron-nickel/paraffin composite and other was copper foam/paraffin composite. Two metal foams (copper and iron-nickel) having porosity 97 and 30 PPI pore density were used. The dimensions of both metal foams were equally 100 mm x 100 mm x 20 mm.

3.2 Experimental setup configuration

For current research experiment, an experimental setup is developed to analyze and compare the heat storage properties of PCMs infiltrated in various metal foams. This special apparatus is also used to give measurements of temperature for analysis of temperature uniformity along the different directions and at various pints inside PCM/metal foam composite. A M10-QD & QR series adjustable power supply is used to provide constant heat flux for the purpose of investigating the heat storage properties of metal foam/PCM composite. A square type (100 mm x 100 mm) silicon based rubber plate heater (SRFG-202/10-P-220V) is used to provide constant and control heat exchange at the base of the heat sink. K-type thermocouples (OMEGA Eng.) produce voltage signals that are converted by data acquisition system to get the temperature measurement. A typical aluminum based heat sink is designed for this research purpose. A square type heat sink 100 mm x 100 mm is developed. The depth of the heat sink is 30 mm deep inside, made by aluminum metal (Al-6061T2) which is light weight and has low density as compared to copper. Data acquisition system is used for collecting and documenting information coming of some ongoing phenomenon /process.it comprises of built-in products mainly sensors to record temperature.

4. Results and discussions

An experimental study was carried out at heat flux of 1000 W/m² for copper foam/paraffin composite and iron-nickel foam/paraffin composite with respect to pure paraffin. Temperature uniformity with in paraffin infiltrated in metal foams and without infiltration in metal foams was experimentally studied. Similarly melting range of paraffin/metal foam composites and pure paraffin with respect to time and temperature was compared and discussed. Heat storage time was also compared for copper and iron metal foam/paraffin composites to analyze the heat transferal process with in the composites.



4.1 Heat storage experiment for copper foam/paraffin composite

Constant heat was provided at the rate of 10 W or constant heat flux of 1000 W/m² from the bottom of heat sink. It was found that Copper foam/PCM composite started melting after 32 or 33 minutes of constant heating and continued until 113 minutes to 116 minutes. The temperature curve shows excellent temperature uniformity as shown in fig. 6. It means heat flows uniformly within the composite for the case of Copper foam/PCM composite. Moreover, first 32 minutes of heating, heat was absorbed by the composite as sensible heating due to which temperature of the composite raised from 30 °C to 37 °C. Then latent heat process was compromised for 84 minutes during which complete phase transition of PCM within composite occurred.

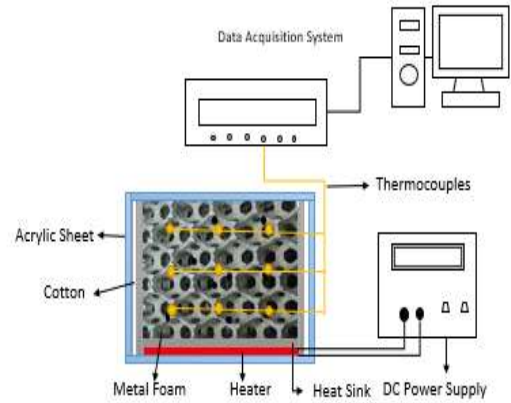


Figure 1. Heat flow direction and Thermocouple position



Figure 3. Copper foam/paraffin composite

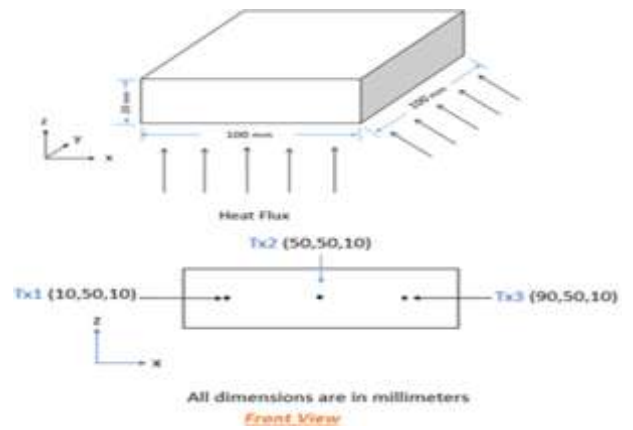


Figure 2. Experimental setup



Figure 4. Iron-nickel foam/paraffin composite

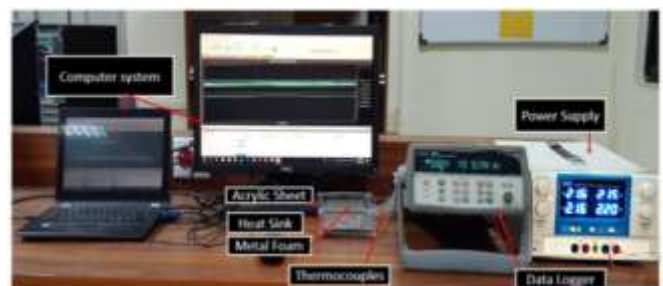


Figure 5. Schematic view of the experimental setup

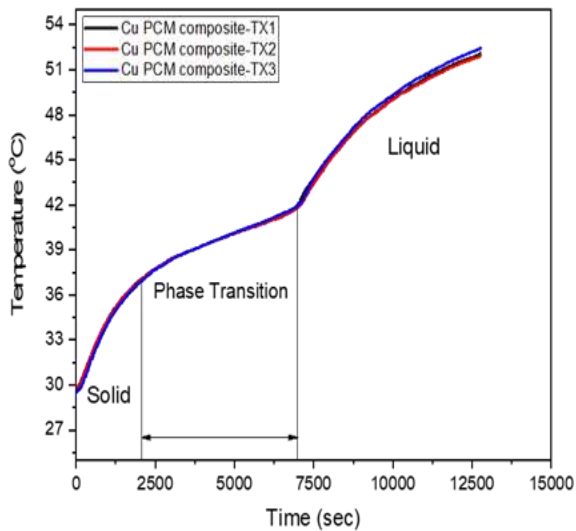


Figure 6. Temperature profile for copper foam/paraffin composite

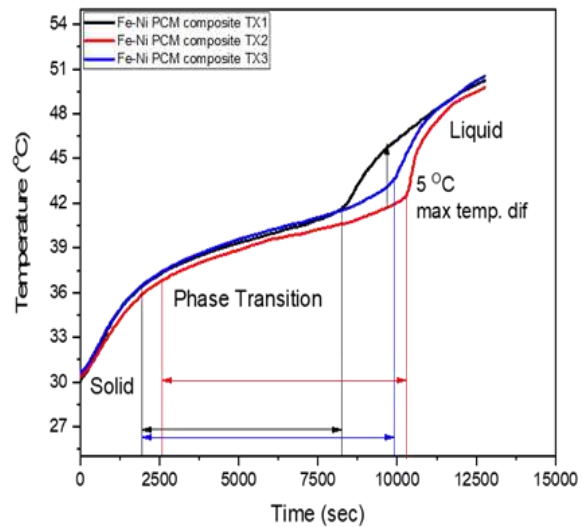


Figure 7. Temperature profile for pure paraffin

uniformity decreased as time went by till the completion of the melting process.

4.3 Heat storage experiment for unpolluted paraffin

The same charging process is carried out for paraffin. The melting process in this case starts after 60 minutes of uniform heat flux. The reason behind this slow heat transfer is the poor thermal conductivity of paraffin. Temperature is not uniform with in pure paraffin as shown in fig. 8.

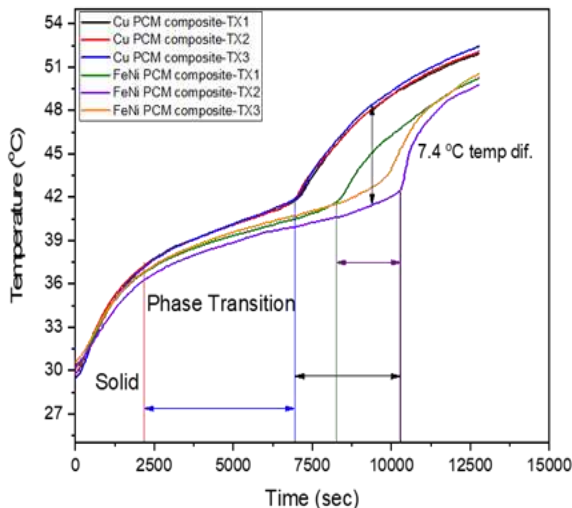


Figure 8. Temperature profile for iron-nickel foam/paraffin composite

4.2 Heat storage experiment for iron-nickel foam/paraffin composite

During the sensible heating, temperature of the composite was increased from 30 to 37 °C. For an average time of 40 minutes of sensible heating, paraffin in the composite started to melt. Phase change process continued for fastest melting of paraffin took time of 105 minutes. The heat absorbed is called latent heat during this process. The melting temperature range for iron-nickel composite is not uniform as in case of the copper foam composite. The maximum temperature difference that was observed with in iron-nickel

foam/paraffin composite was 5 °C as in fig. 7. As the phase change process started, temperature

4.4 Comparison of heat storage properties of metal foam/paraffin composite

For the case of copper foam/paraffin composite, paraffin infiltrated in copper foam took nearly 80 minutes for complete melting into liquid phase. However in case of iron-nickel/paraffin composite the minimum time taken by paraffin for complete melting was 101 minutes. In other words, for the same operating conditions, paraffin in the copper foam/paraffin composite melts 2% faster than iron-nickel foam/paraffin composite with respect to total time consumed. For the case of iron-nickel/paraffin composite, paraffin in the center of the composite takes almost 33 minutes more time for complete phase transition. The maximum temperature difference that has been occurred between the composites was 7.4 °C which was found at 167 minutes of constant heating as shown in fig. 9. This could also be described as at 10 W power of constant heating there was 18% more temperature rise in copper foam composites compared to iron-nickel composite.



5. Conclusions

Heat storage properties of paraffin infiltrated in various metal foams are investigated and analyzed. Temperature curves for copper foam/paraffin composite are more uniform as associated to iron-nickel foam/paraffin composite due to fact that copper has the high thermal conductivity and much better tendency for heat transfer. The effect infiltrating the paraffin in metal foam composites is that it limits the natural convection of the paraffin in the composite when paraffin starts melting. Metal foams hinders the natural convections of paraffin. However presence of the metal foam increases conductance heat transfer

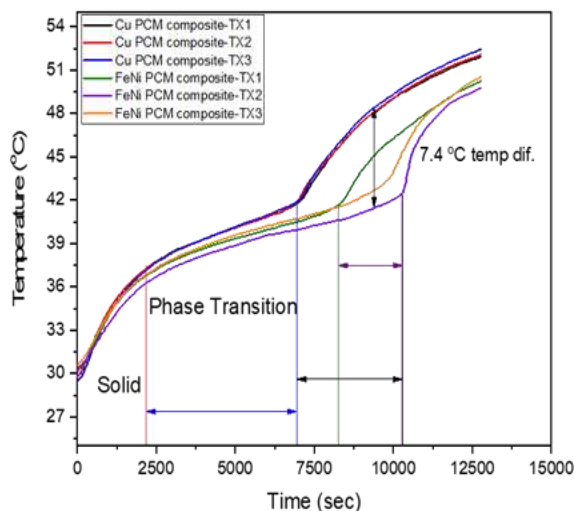


Figure 9. Comparison of heat storage properties of paraffin infiltrated in metal foams

within composite that results in increase in thermal conductivity. As a result it enhances heat transfer rate in the paraffin. Temperature curves for copper foam/paraffin are more uniform and almost uniformly heat is distributed throughout the composite with respect to iron-nickel foam/paraffin composites. This could be described as due to fact that thermal conductivity and other thermal characteristics of copper are better than iron-nickel. The results can be summarized as under

- The temperature curves show that the actual thermal conductivity of copper foam/paraffin composite is greater than iron-nickel/paraffin composite and takes minimum time for phase transition of paraffin at 1000 W/m².
- The experimental results indicate that for the same operating conditions, paraffin infiltrated in the copper foam melts 21% faster than iron-nickel foam/paraffin composite with respect to total time

consumed during the complete phase change.

- The maximum temperature difference that has been occurred between the composites is 7.4 °C which is found at 167 minutes of constant heating. This could be concluded that at 10 W power of constant heating there is 18% more temperature rise in copper foam/paraffin composites compared to iron-nickel foam/paraffin composite.

This experimental study needs numerical analysis to investigate the heat distribution within the composite structure at various points in all three directions when the natural convection of the liquefied paraffin is suppressed due to the presence of metal foam.

REFERENCES

- [1] L. Liu, D. Su, Y. Tang, and G. Fang, "Thermal conductivity enhancement of phase change materials for thermal energy storage: A review," *Renew. Sustain. Energy Rev.*, vol. 62, pp. 305–317, 2016.
- [2] Z. Wang, Z. Zhang, L. Jia, and L. Yang, "Paraffin and paraffin/aluminum foam composite phase change material heat storage experimental study based on thermal management of Li-ion battery," *Appl. Therm. Eng.*, vol. 78, pp. 428–436, 2015.
- [3] A. Hussain, I. H. Abidi, C. Y. Tso, K. C. Chan, and Z. Luo, "Thermal management of lithium ion batteries using graphene coated nickel foam saturated with phase change materials International Journal of Thermal Sciences Thermal management of lithium ion batteries using graphene coated nickel foam saturated with phas," *Int. J. Therm. Sci.*, vol. 124, no. October, pp. 23–35, 2017.
- [4] N. Şahan, M. Fois, and H. Paksoy, "Improving thermal conductivity phase change materials - A study of paraffin nanomagnetite composites," *Sol. Energy Mater. Sol. Cells*, vol. 137, pp. 61–67, 2015.
- [5] S. E. E. Profile, "Closed Cell Aluminium Foams with Phase Change Material," no. August, 2017.
- [6] T.- Rehman, H. Muhammad, A. Saieed, W. Pao, and M. Ali, "International Journal of Heat and Mass Transfer Copper foam / PCMs based heat sinks: An experimental study for electronic cooling systems," *Int. J.*



- Heat Mass Transf.*, vol. 127, pp. 381–393, 2018.
- [7] T.- Rehman, “Experimental investigation on paraffin wax integrated with copper foam based heat sinks for electronic components thermal cooling,” vol. 98, pp. 155–162, 2018.
- [8] H. T. Cui, “Experimental investigation on the heat charging process by paraffin filled with high porosity copper foam,” *Appl. Therm. Eng.*, vol. 39, pp. 26–28, 2012.
- [9] A. Babapoor and G. Karimi, “Thermal properties measurement and heat storage analysis of paraffinanoparticles composites phase change material: Comparison and optimization,” *Appl. Therm. Eng.*, vol. 90, pp. 945–951, 2015.
- [10] Y. Lin, Y. Jia, G. Alva, and G. Fang, “Review on thermal conductivity enhancement, thermal properties and applications of phase change materials in thermal energy storage,” *Renew. Sustain. Energy Rev.*, vol. 82, no. May 2017, pp. 2730–2742, 2018.
- [11] R. Baby and C. Balaji, “Experimental investigations on thermal performance enhancement and effect of orientation on porous matrix filled PCM based heat sink,” *Int. Commun. Heat Mass Transf.*, 2013.
- [12] A. Bhattacharya, V. V Calmidi, and R. L. Mahajan, “Thermophysical properties of high porosity metal foams,” vol. 45, no. December 2000, 2002.



Evaluation of Stability and Rheological Behavior of TiO₂-H₂O Nanofluid

Muhammad Assad Khan^{1*}, Majid Ali¹, Waqas Ahmad¹

1- US Pakistan center for advanced studies in energy NUST Islamabad Pakistan

* Corresponding Author: assadkhan948@gmail.com

Abstract:

Nanofluid is the suspension of nanomaterials in the conventional fluid. The nanofluid possesses interesting thermal properties and features due to which it has the potential for different applications. The current study deals with the synthesis of titanium dioxide nanoparticles and fabrication of water-based titanium dioxide nanofluid along with cetyl trimethyl ammonium bromide surfactant using sonication for stability enhancement. The nanoparticles are prepared by the chemical method. The nanoparticles are characterized using the scanning electron microscope, energy-dispersive X-ray spectroscopy, and X-ray diffractometer. Stability is important in the practical application of the nanofluid. Nanofluid stability is evaluated using photo capturing and UV-Vis spectroscopy. The rheological behavior of water-based titanium dioxide nanofluid is evaluated with temperature (30 °C, 40 °C, 60 °C and 80 °C), particle loadings (0.01vol%, 0.02vol%, 0.03vol %) and shear rate (50 s⁻¹, 100 s⁻¹, 150s⁻¹, 200 s⁻¹, 245s⁻¹). The characterization confirmed the formation of nanoparticles. The nanofluid is found to be stable for almost 408 hours. The nanofluid viscosity increases as the shear rate and particle loading are increased while it decreases with the rise of temperature. The highest viscosity was observed for 0.03vol% at 245 s⁻¹ shear rate and 30 °C.

Keywords: Titanium dioxide nanoparticles, nanofluid, viscosity, UV-Vis spectroscopy, CTAB

1. Introduction

researchers have attempted to lower the size of the heat exchanging systems by improving the heat exchange surfaces with fins etc. and by improving the properties of the heat exchanging fluids to increase its thermal conductivity. The nanotechnology developments have led researchers to prepare different types of nanomaterials which can be suspended in the fluids such as ethylene glycol, engine oil, and water. Choi in 1995 developed a fluid containing nanomaterials suspended in a fluid known as nanofluid, which possessed improved thermal properties compared to e has three main phases brookite, anatase and rutile. Brookite is not stable while the anatase phase possesses better properties compared to the rutile phase of titanium dioxide [14].

In recent past scientists have developed different techniques for the synthesis of different types of nanoparticles. Mahshid et al prepared titanium dioxide °C. Smaller size particles are formed in acidic solution while size increases as the pH of the solution raised [15]. Oliveira et al. used the sol-gel method for the preparation of titanium dioxide nanoparticles [16].

The fabrication of nanofluid is not simply nanoparticles addition to the base fluid. It requires special treatment so that the particles do not

In past researchers have tried to enhance the performance of the heat exchange systems for various applications. The conventional fluid and offered stability for a long period of time[1]. Nanofluid possesses better thermal conductivity and therefore has better ability for heat transport in various applications such as electronic devices cooling [2][3], solar heating system[4]–[7], engine cooling system[8]–[13], etc.

Researchers have focused on titanium dioxide because of its good dispensability in solvents, excellent chemical stability, non-toxicity, and its resistance to organic erosions. Titanium dioxide

nanofluid using hydrolysis and peptization method. They varied the pH value and calcination temperature of the solution during the preparation of nanoparticles. The results showed that as the calcination temperature is lowered size of the particles also decreases. Anatase phase is formed below 600 °C while the transformation of phase to rutile takes place above 600

agglomerate or settle down to the bottom and the particles are well dispersed so that stable nanofluid is produced. The main difficulty faced in the practical application of the nanofluid is the low stability of the nanofluid. The stability of the nanofluid can be enhanced by ultra-sonication, the surfactant addition or their combination. The pH of the solution



maintained at a certain value can also improve the stability but then the application of the nanofluid will be restricted [17].

The most commonly used surfactants for stability enhancement are oleic acid (OA), sodium dodecyl sulfate (SDS), cetyl trimethyl ammonium bromide (CTAB), polyvinyl alcohol (PVA), polyvinyl pyrrolidone (PVP), sodium dodecyl-benzene sulfonate (SDBS) and acetic acid (AA). The surfactant reduces the agglomeration of particles by electrostatic repulsion or static hindrance performed by the molecules. Das et al. prepared water-based nanofluid along with different surfactants such as SDS, CTAB, acetic acid, and SDBS. They evaluated the stability of the nanofluid using zeta potential and found that the nanofluid with CTAB and SDS were stable for more than 24 hours. The nanofluid having a CTAB surfactant showed better stability than nanofluid containing other surfactants [18]. Ghadimi et al. fabricated water-based nanofluid with SDS surfactant. According to their results, the nanofluid prepared using 3-hour bath sonication showed better stability compared to nanofluid prepared using 15minute horn sonication. The nanofluid was observed to be stable for more than one year [19].

The viscosity is an important property since it provides information about the pumping power requirement and pressure drop in the system. The viscosity of the nanofluid depends on particle loading, temperature, particle size, particle shape, and shear rate. Turgut et al. fabricated nanofluid containing water and TiO₂ and measured its viscosity in the range of 15 °C to 55 °C and 0.2vol% to 3vol%. They concluded that the nanofluid becomes more viscous as the particle loadings are raised and less viscous as the temperature of the sample is raised [20]. Das et al. experimental results confirmed the direct relation of viscosity with particle loading and shear rate while inverse relation with the temperature of the sample [21][22]. Teng et al. found that by raising the temperature from 10°C to 40°C for TiO₂ nanofluid at 0.5 wt% the increase of 8.2% to 16% was observed in relative viscosity [23].

In this article, titanium dioxide nanoparticles are prepared using the wet chemical method. The prepared nanoparticles are characterized by energy-dispersive X-ray spectroscopy, scanning electron microscopy, and X-ray diffraction. The nanofluid is fabricated using titanium dioxide nanoparticles, water, and cetyl trimethyl ammonium bromide by the two-step method. The stability of the nanofluid is evaluated using a photo capturing of sedimentation

and UV-Vis spectroscopy. The nanofluid viscosity is measured using Brookfield viscometer and its variation is studied for different temperatures, shear rate, and particle loading.

2. Experimental Section

2.1 Preparation and characterization of nanoparticles

Titanium dioxide nanoparticles were prepared using titanium tetra isopropoxide (sigma Aldrich 97%), ethanol (Merck 99%) and hydrogen peroxide (BDH laboratory 35%). 1mol of titanium isopropoxide was added to 1mol ethanol along with few drops of hydrogen peroxide. The solution was adjusted to 100ml using ethanol. The solution was kept at a stirring rate of 400rpm.

The solution was heated at 200 °C along with stirring at 200rpm. The solution was heated until the solution starts decreasing and a small amount of a highly viscous solution is left. The solution was dried in an oven at 100°C for 18hours. The solution was completely dried before the calcination process. The powder kept in china dish was placed in the furnace for 3 hours at 600 °C for the calcination process. TiO₂ particles were obtained after the calcination process.

The phase, crystallite size, and purity of the particles were measured using Bruker D8 advanced x-ray diffractometer. The sample was studied for angle (2θ) kept in the range of 10° to 80°. The sample is kept in the sample holder and is exposed to the x-ray beam. The X-rays are diffracted by the crystals which are detected and map the lattice pattern, which enables us to analyses the shape obtained from the diffracted x-rays. The particle crystallite size is calculated using Debye-Scherrer's equation [24].

$$p = \frac{C\lambda_x}{\beta \cos\theta} \quad (1)$$

where λ_x is X-ray radiation wavelength (Cu $\lambda = 0.15406\text{nm}$), p is crystallite size, C is equal to 0.94, θ is the angle of diffraction, and β is the width of line at half maximum height for peaks. The elemental composition and surface morphology of the nanoparticles are evaluated using TESAN VEGA3 Scanning Electron Microscope. The sample was prepared using the aurum coating.

2.2 Preparation of nanofluid

The preparation of stable nanofluid requires special treatment. The stability can be improved by using sonicator, surfactant, pH value or combination of all



these. The behavior of nanofluid is studied at lower concentrations only such as at 0.01vol%, 0.02vol% and 0.03vol% concentration of nanoparticles added to distilled water along with 0.1g CTAB surfactant and the mixture is sonicated for 1 hour using probe sonicator for the mixing and suspending the particles in the fluid. The surfactant is used during the fabrication process to lower the rate of agglomeration in the nanofluid which results in the formation of stable nanofluid. The mass of nanoparticles and surfactant is measured using the digital balance. The particle loadings in volume percentage can be calculated using the equation.

$$\phi = \left[\frac{\left(\frac{m_n}{\rho_n} \right)}{\left(\frac{m_n}{\rho_n} + \frac{m_{nf}}{\rho_{nf}} \right)} \right] \times 100 \quad (2)$$

where ρ_n is TiO_2 nanoparticles density, m_n is the mass of the titanium dioxide nanoparticles, m_{nf} is the mass of the fluid and ρ_{nf} is the density of the fluid.

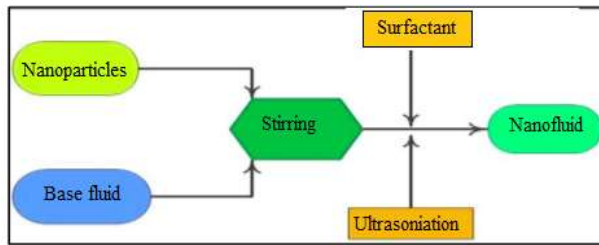


Figure 1. nanofluid preparation process

2.3 Nanofluid stability

The stability of the nanofluid can be observed using photo capturing, UV-Vis spectroscopy and zeta potential. In this study, the stability of water-based titanium dioxide nanofluid is measured using photo capturing and UV-Vis spectroscopy. The images can show the settling down of the particles with time while in UV-Vis the light ray is passed through the sample and standard fluid whose results are compared and we get the value of the difference between their absorbance. The more the particles are suspended in the fluid the higher will be the value of absorbance and the more stable will be the nanofluid.

2.4 Viscosity of nanofluid

The viscosity of titanium dioxide nanofluid for particle loading concentration of 0.01vol%, 0.02vol% and 0.03vol% along with 0.1g CTAB is measured using Brookfield viscometer DV2T. Viscosity is important to be known for the practical application of the nanofluid. Brookfield viscometer DV2T uses a

spring to measure the torque needed to rotate the spindle. A magnetic rotor lightweight floats in a tube filled with fluid and rotates at a constant speed. The rotor is driven by the viscous force of the fluid. This leads to equilibrium rotor speed which is recorded as fluids viscosity. A spindle (S18, having a range of measuring viscosity from 1 cP to 2000 cP) is attached to the viscometer and is inserted in the tank containing 16ml of the sample solution. The viscosity variation with temperature is measured at temperatures of 30 °C, 40 °C, 60 °C and 80 °C for all concentrations 0.01vol%, 0.02vol% and 0.03vol% at a shear rate of 100s^{-1} . The nanofluid behavior for all concentration is also inspected at different shear rate of 50s^{-1} , 100s^{-1} , 150s^{-1} , 200s^{-1} , 245s^{-1} and constant temperature of 30 °C.

Table 1. Particles amount in nanofluid fabrication

Concentration (vol%)	Water(ml) ($\pm 0.1\text{ml}$)	Mass(g) ($\pm 0.001\text{g}$)
0.01	70	0.0264
0.02	70	0.0528
0.03	70	0.0792

3. Results and discussions

3.1 X-ray diffraction

The XRD testing is used for the determination of purity, crystallite size and phase of the particles. The pattern obtained for XRD testing is shown in Figure 4. The (101) peaks show the formation of the anatase phase of TiO_2 (Pdf#1166), well-matched with the literature [25]. The results confirm that the pure anatase phase of titanium dioxide nanoparticles is synthesized as only the peaks of the anatase phase are present in the pattern. The crystallite size calculated by Scherer's equation is around $24 \pm 0.3\text{nm}$.

3.2 Scanning electron microscopy and energy-dispersive x-ray spectroscopy

The SEM and EDS testing were performed for the inspection of surface morphology, the particle diameter, and the elemental composition of the particles. Figure 2 is the SEM images of TiO_2



nanoparticles which shows that spherical shape titanium dioxide nanoparticles are formed. It can also be observed the nanoparticles are well agglomerated with each other and the average diameter of the particles is around 50nm.

The EDS results shown in Figure 3 confirms the presence of only titanium, oxygen in the sample. Although a small amount of aurum is also detected this is because aurum is used during sample preparation for SEM and EDS testing.

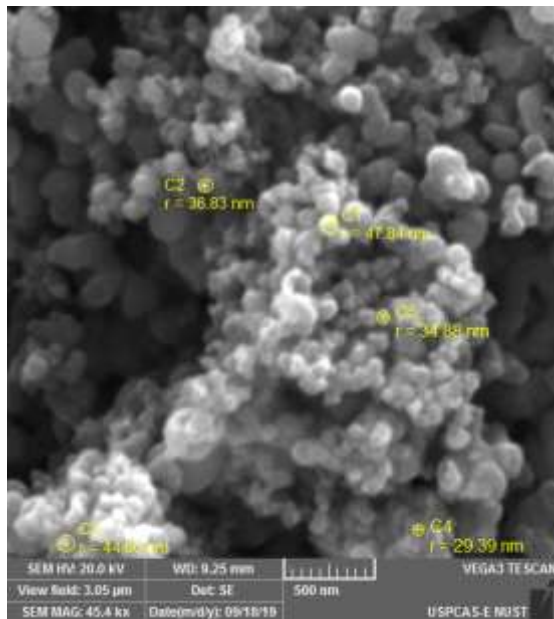


Figure 2. SEM image of TiO₂ nanoparticles

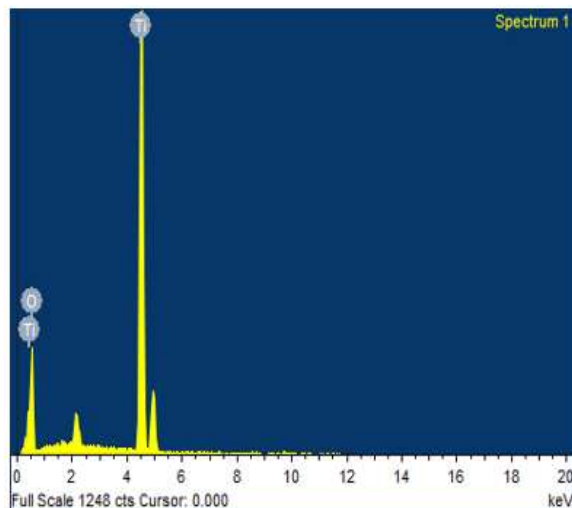


Figure 3. EDS spectra of TiO₂ nanoparticles

3.3 Stability of nanofluid

The fabrication of stable nanofluid is important for practical application. Figure 5 shows the UV-Vis spectroscopy result of nanofluid. According to the results, the nanofluid is stable for almost 408 hours. The more the nanoparticles are suspended in the nanofluid the higher will be the absorbance and hence the more stable will be the nanofluid. It can be seen in the image that the absorbance of the nanofluid is at high value till day 17 which shows that the nanofluid is stable for 17 days. The absorbance decreases with time rapidly and it becomes close to zero after 20 days which shows that all the particles which were suspended have now settled down to the bottom of the fluid and the fluid is no longer stable. UV-Vis spectroscopy technique for stability evaluation is used by Jiang et al. [26].

The sedimentation photo capturing technique for stability evaluation is also used by Fedele et al. and they found that the TiO₂ based nanofluid was stable for 5 days [27]. Figure 6 shows the photo capturing of the nanofluid on different days. It can be observed in the images that the nanofluid contains enough amount of suspended particles till day 17 that it can be considered stable which confirms the UV-Vis results while at day 20 all the particles have settled down to the bottom of fluid.

3.4 Viscosity of nanofluid

The determination of viscosity is important because it determines the pumping power requirement for the fluid. The viscosity of the nanofluid is expected to be higher than that of the base fluid and therefore can result in more power requirement and in some cases may even decrease the rate of heat transfer, therefore its determination is necessary for practical applications of the nanofluid. The results are shown in

Figure 9. According to the results, the viscosity of the nanofluid decreases as the temperature of the sample is raised for all concentrations of the nanofluid. Researchers have observed a similar trend in the viscosity of nanofluid [18], [21].

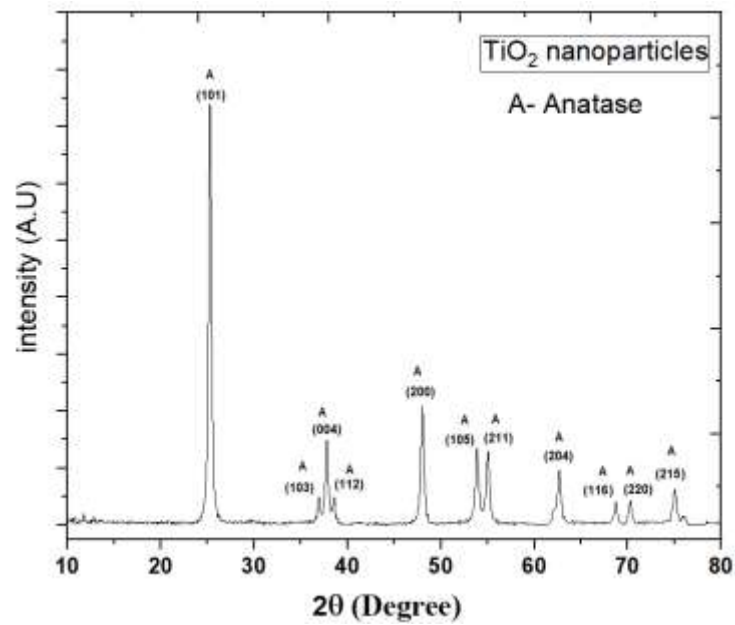


Figure 4. XRD pattern of TiO_2 nanoparticle

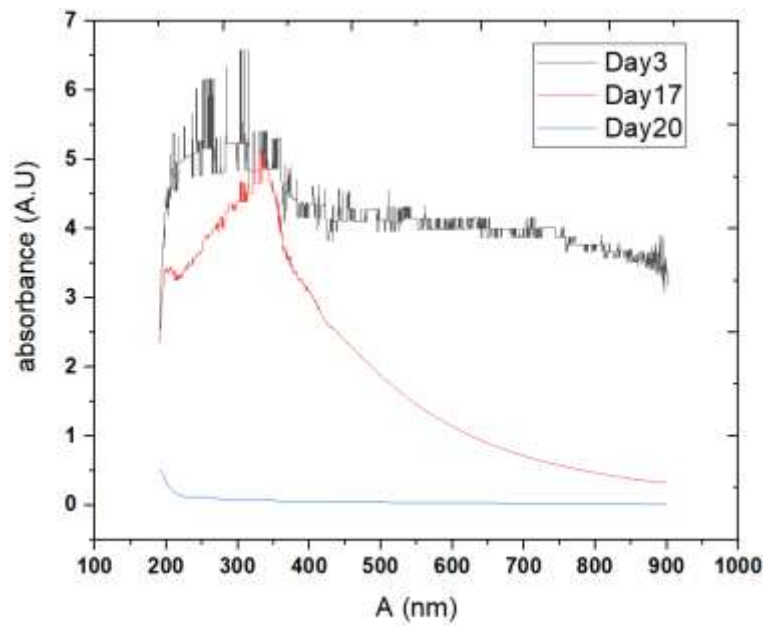


Figure 5. UV-Vis absorbance spectra of TiO_2 -water nanofluid sample

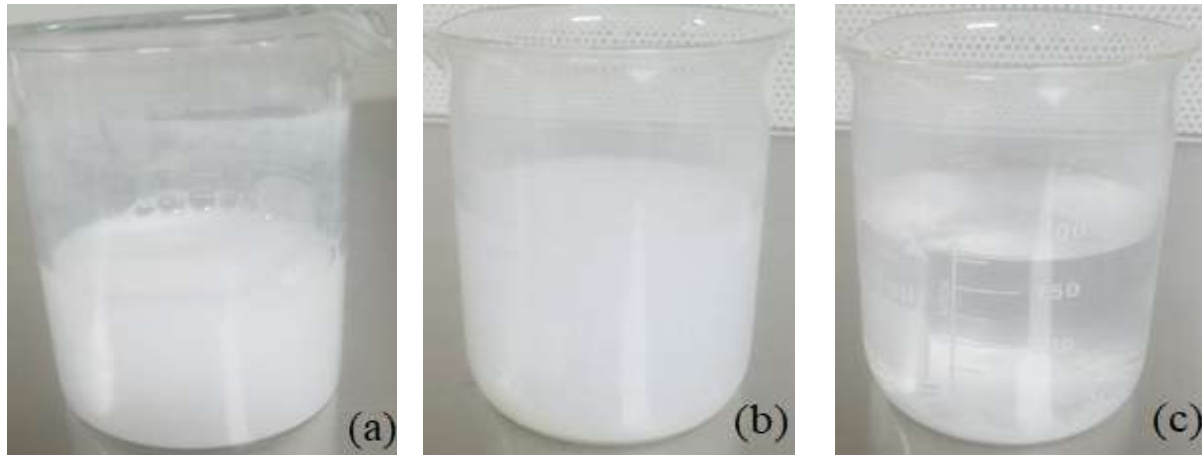


Figure 6. Nanofluid images (a) Day1 (b) Day 17 (c) Day20

The variation of viscosity is also evaluated with the number of particle loadings and is represented in Figure 7. The shear rate is kept constant at 100s^{-1} . The results show that the viscosity of the nanofluid increases with the number of particle loadings at a constant shear rate. Das et al. observed a similar trend in the viscosity of nanofluid [21]. The Utomo et al. experimental results for lower concentration up to 0.03vol% show that the enhancement is observed to be 120% compared to 140% enhancement in the current

study which is higher due to the presence of 0.1g of CTAB surfactant [28].

The shear rate applied to the sample also changes the viscosity of the sample. The variation of viscosity with the shear rate is represented in Figure 8. It is observed that the nanofluid viscosity increases with the shear rate of the sample at a constant temperature of $30\text{ }^{\circ}\text{C}$.

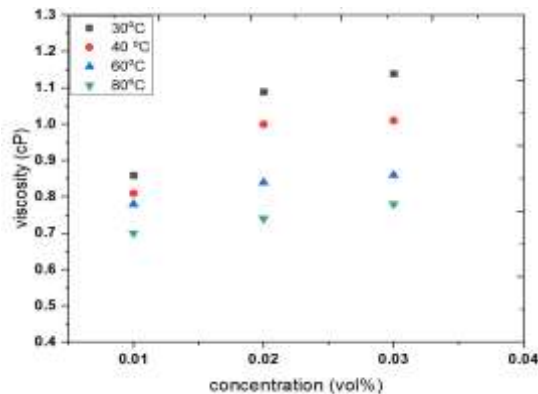


Figure 7. Viscosity variation with concentration at a shear rate of 100 s^{-1}

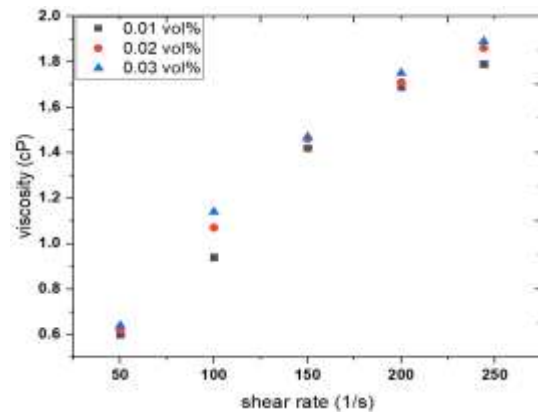


Figure 8. Viscosity variation with a shear rate at $30\text{ }^{\circ}\text{C}$.

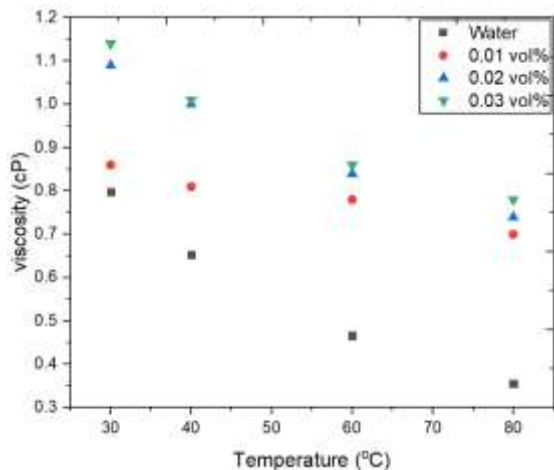


Figure 9. Viscosity variation with the temperature at a shear rate of 100 s^{-1}

4. Conclusions

In the current study, titanium dioxide nanoparticles were prepared using the wet chemical method. The XRD, SEM and EDS characterization confirmed the formation of spherical shape anatase phase titanium dioxide nanoparticles. The stability of the nanofluid is found to be around 408 hours confirmed by the results of both UV-Vis spectroscopy and sedimentation photo capturing which is good compared to many of the recently published literature. The viscosity of the nanofluid is found to be increasing with particle loadings and shear rate while it decreases as the temperature of the sample is raised. The highest viscosity is found for the concentration of 0.03vol% at a shear rate of 245s^{-1} and a temperature of $30\text{ }^{\circ}\text{C}$.

REFERENCES

- [1] S. U. S. Choi and J. A. Eastman, "ENHANCING THERMAL CONDUCTIVITY OF FLUIDS WITH NANOPARTICLES *," 1995.
- [2] A. Ijam and R. Saidur, "Nanofluid as a coolant for electronic devices (cooling of electronic devices)," *Appl. Therm. Eng.*, vol. 32, pp. 76–82, 2012.
- [3] A. M. Siddiqui, W. Arshad, H. M. Ali, M. Ali, and M. A. Nasir, "Evaluation of nanofluids performance for a simulated microprocessor," *Therm. Sci.*, vol. 21, no. 5, pp. 2227–2236, 2017.
- [4] T. Youse, F. Veysi, E. Shojaeizadeh, and S. Zinadini, "An experimental investigation on the effect of $\text{Al}_2\text{O}_3\text{-H}_2\text{O}$ nanofluid on the efficiency of flat-plate solar collectors," vol. 39, pp. 293–298, 2012.
- [5] A. Kasaeian, A. T. Eshghi, and M. Sameti, "A review on the applications of nanofluids in solar energy systems," *Renew. Sustain. Energy Rev.*, vol. 43, pp. 584–598, 2015.
- [6] R. Saidur, T. C. Meng, Z. Said, M. Hasanuzzaman, and A. Kamyar, "International Journal of Heat and Mass Transfer Evaluation of the effect of nanofluid-based absorbers on a direct solar collector," *Int. J. Heat Mass Transf.*, vol. 55, no. 21–22, pp. 5899–5907, 2012.
- [7] Z. Said *et al.*, "Performance enhancement of a Flat Plate Solar collector using TiO_2 nanofluid and Polyethylene Glycol dispersant," *J. Clean. Prod.*, 2015.
- [8] N. A. Che Sidik, M. N. A. Witri Mohd Yazid, and R. Mamat, "Recent advancement of nanofluids in engine cooling system," *Renew. Sustain. Energy Rev.*, vol. 75, no. October 2016, pp. 137–144, 2017.
- [9] H. M. Ali, M. D. Azhar, M. Saleem, Q. S. Saeed, and A. Saeed, "Heat transfer enhancement of car radiator using aqua-based magnesium oxide nanofluids," *Therm. Sci.*, vol. 19, no. 6, pp. 2039–2048, 2015.
- [10] H. M. Nieh, T. P. Teng, and C. C. Yu, "Enhanced heat dissipation of a radiator using oxide nano-coolant," *Int. J. Therm. Sci.*, vol. 77, pp. 252–261, 2014.
- [11] S. A. Ahmed, M. Ozkaymak, A. Sözen, T. Menlik, and A. Fahed, "Improving car radiator performance by using $\text{TiO}_2\text{-water}$ nanofluid," *Eng. Sci. Technol. an Int. J.*, vol. 21, no. 5, pp. 996–1005, 2018.
- [12] H. M. Ali, M. U. Sajid, and A. Arshad, "Heat Transfer Applications of TiO_2 Nanofluids," *Appl. Titan. Dioxide*, 2017.
- [13] K. Y. Leong, R. Saidur, S. N. Kazi, and A. H. Mamun, "Performance investigation of an automotive car radiator operated with nano fluid-based coolants (nanofluid as a coolant in a radiator)," *Appl. Therm. Eng.*, vol. 30, no. 17–18, pp. 2685–2692, 2010.
- [14] N. Kaewgabkam, N. Jaitanong, and S. Narksitipan, "Preparation and Characterization of Cement- TiO_2 Composites," vol. 804, pp. 133–136, 2015.
- [15] S. Mahata, S. S. Mahato, M. M. Nandi, and B. Mondal, "Synthesis of TiO_2 nanoparticles by hydrolysis and peptization of titanium isopropoxide solution," *AIP Conf. Proc.*, vol. 1461, no. 1, pp. 225–228, 2011.



- [16] L. Raquel, A. Christine, A. Silva, N. Oliveira, and E. P. Bandarra, "International Journal of Heat and Mass Transfer Thermophysical properties of TiO₂-PVA / water nanofluids," vol. 115, pp. 795–808, 2017.
- [17] M. Vakili, A. Mohebbi, and H. Hashemipour, "Experimental study on convective heat transfer of TiO₂ nanofluids," *Heat Mass Transf. und Stoffuebertragung*, vol. 49, no. 8, pp. 1159–1165, 2013.
- [18] P. K. Das, A. K. Mallik, R. Ganguly, and A. K. Santra, "Stability and thermophysical measurements of TiO₂ (anatase) nanofluids with different surfactants," *J. Mol. Liq.*, vol. 254, pp. 98–107, 2018.
- [19] A. Ghadimi and I. H. Metselaar, "The influence of surfactant and ultrasonic processing on the improvement of stability, thermal conductivity and viscosity of titania nanofluid," *Exp. Therm. Fluid Sci.*, vol. 51, pp. 1–9, 2013.
- [20] H. P. S. C. S. S. Tavman, "of Water-Based TiO₂ Nanofluids," pp. 1213–1226, 2009.
- [21] P. K. Das, A. K. Mallik, R. Ganguly, and A. K. Santra, "Synthesis and characterization of TiO₂-water nanofluids with different surfactants," *Int. Commun. Heat Mass Transf.*, vol. 75, pp. 341–348, 2016.
- [22] S. K. Das, S. U. S. Choi, and H. E. Patel, "Heat transfer in nanofluids - A review," *Heat Transf. Eng.*, vol. 27, no. 10, pp. 3–19, 2006.
- [23] T. P. Teng, Y. H. Hung, C. S. Jwo, C. C. Chen, and L. Y. Jeng, "Pressure drop of TiO₂ nanofluid in circular pipes," *Particuology*, vol. 9, no. 5, pp. 486–491, 2011.
- [24] P. S. Determination, "No Title," vol. 56, pp. 978–982, 1939.
- [25] P. Srinivasu, S. P. Singh, A. Islam, and L. Han, "Novel Approach for the Synthesis of Nanocrystalline Anatase Titania and Their Photovoltaic Application," vol. 2011, 2011.
- [26] L. Jiang, L. Gao, and J. Sun, "Production of aqueous colloidal dispersions of carbon nanotubes," vol. 260, pp. 89–94, 2003.
- [27] L. Fedele, L. Colla, S. Bobbo, S. Barison, and F. Agresti, "Experimental stability analysis of different water-based nanofluids," pp. 1–8, 2011.
- [28] A. T. Utomo, H. Poth, P. T. Robbins, and A. W. Pacek, "International Journal of Heat and Mass Transfer Experimental and theoretical studies of thermal conductivity, viscosity and heat transfer coefficient of titania and alumina nanofluids," *Int. J. Heat Mass Transf.*, vol. 55, no. 25–26, pp. 7772–7781, 2012.



Analysis of South Asian Electric Vehicle's Policies and Recommendations for Electric Vehicle's Policy for Pakistan

Zain Ul Hassan^{1*}, Naseer Ahmad¹, Awais Ahmad Khan¹

¹-Department of Mechanical Engineering, University of Engineering & Technology, Lahore

*Corresponding Author: 2019msame9@student.uet.edu.pk

Abstract:

With pollution damaging climate all around the world, focus is inclined towards clean energy and that pushed investors and manufacturer towards the launch of electric vehicles (EVs) in market in recent years. Starting from developed countries and spreading toward developing countries EVs has now become hot topic. Pakistan has recently approved the EVs policy drafted by Ministry of Climate Change and Ministry of Industries. Now with the approval of EVs Policy 2019 along with Auto Development Policy (ADP) 2016-2021 doubts has been removed from investors and manufacturers minds. The objective of this study was to investigate engineering and social challenges that exists in Pakistan regarding electric vehicles and an analysis was done on EVs policy and ADP in contrast with policies in other south Asian countries that rank near to Pakistan in overall development index. After analyzing some critical challenges were discovered regarding engineering point of view and some loop holes were found in policies, upon which some improvement recommendations were suggested in this paper.

Keywords: Electric Vehicles in Pakistan, Electric Vehicle Policy 2019, Automobile Development Policy 2016-2021, Infrastructure for EVs in Pakistan

1 Introduction

The world is excelling in technology at very fast pace[1]. With the rapid change of technology, the existence of species including humans is under severe threat as climate is being destroyed drastically[2]. Core cause of extinction for species will be rise in global temperature by 1.5°C to 2°C[3].

Many develop countries are struggling to fight back climate change by introducing environment friendly policies especially renewable energy systems (RES) to replace fossil fuel (FF) energy systems [4]. Many developed European and American Countries are planning to introduce electric and alternate fuel-based transportation systems as transportation is one of the leading causes of climate change[5, 6]. Among them many countries are planning to completely ban FF Vehicles [7].

Pakistan is amongst ten countries most affected by climate change[8]. Economically we are second most affected country[3, 8]. The melting of glaciers in Himalayas to the smog problem of our cities gives us a strong indicator that climate change impacts millions of lives and if continue unabated it will impact millions of more lives [3].

The Government of Pakistan is committed to curb emissions to mitigate and adapt to the harmful effects of climate change[9]. Therefore, the Government of Pakistan has approved mandated minimum penetration targets for Electric Vehicles[9]. An Electric Vehicle policy is being developed to ensure

meeting the penetration numbers set forth[9]. We hope that this approval of this policy will begin an era of clean air in the country[2].

1.1 Electric Vehicles the healers of mother nature

Electric Vehicles (EVs) have potential to solve critical challenges faced by Pakistan [8]. In Pakistan transport sector is the leading factor in deteriorating the climatic conditions[10]. 43% of the airborne emissions in Punjab are from transport sector[2]. With the anticipated rise in Fossil Fuel Vehicles (FFVs), the problem of air pollution is only going to get worse[3]. EVs do not emit any pollutants so their introduction will limit emissions to a large extent[11, 12].

1.2 Oil import and trade deficit in Pakistan

Rising trade deficit is one of the major factors towards stagnant economic growth in Pakistan[13]. EVs will substantially limit the bill for oil import which is the largest import commodity in Pakistan[9]. Moreover, EVs have a potential to set up a whole new industry in Pakistan, creating numerous green businesses and employment opportunities and ameliorating the overall socio-economic situation of the country[9].

Cost a core hindrance for public acceptance to EVs

The capital cost of EVs is still high due to high battery costs[14]. However, according to various forecasts the battery prices are falling rapidly[15]. According to



Bloomberg New Energy Finance the cost of EVs will be at par with FFVs by 2022[16]. Similarly, McKinsey estimates the total cost of ownership of small EVs and buses to be at par with their FFV counterparts by 2020 and cost ownership of all types of EVs to be at par with their FFVs counterparts by 2025[7, 17]. International Energy Agency (IEA) forecasts around 250 million EVs on road by 2030, excluding two and three wheelers[18].

1.3 Right time to launch EVs in Pakistan

It is important for Pakistan to tap into this market on priority. Not only will it solve the problems of emissions and surging oil import bill but also it will be an excellent opportunity for exports[19]. Moreover, EVs are an excellent flexible load for the national electric grid[19]. With right planning, EVs will use the electricity in off-peak hours and reduce the burden of idle capacity payments on the national exchequer[20].

1.4 World Readiness Index for Electric Vehicles

Table 1 shows Norway plans to ban sale of all FFVs by 2025, Netherlands plans to ban such sales by 2030, while France and UK plan to do the same by 2040[7].

Table 1: Global Consideration for Ban of FFV

Country	Years to Ban FFV
Norway	2025
Netherland	2030
Israel	2030
India	2030
Germany	2030
Ireland	2030
Scotland	2032
UK	2040
France	2040

2 Scope of this Paper

This paper covers all electric vehicles that are not covered by the Auto Development Policy 2016-21 of Pakistan. The policy recommendations and subsequent recommended incentives are related to all-battery operated vehicles that do not contain internal combustion engine and are run solely through the available on-board battery charge.

2.1 EVs penetration recommendations

Globally, EVs are steadily capturing the automobile industry[21]. EVs are being particularly promoted in view of the global commitments to bring down Green House Gas (GHG) emissions as vehicular emissions are one of the major causes of GHGs[22].

For a country to introduce and sustain EVs and its infrastructure, it is important to determine penetration targets of EVs[23]. Table 2 mentions proposed minimum EVs penetration targets along with expected penetration time frame.

Electric Vehicles bring in a number of benefits to the economy[24]. Table 2 provides a conservative estimate of benefits to the country with the EV penetration targets mentioned earlier. This include benefits of fuel savings which can directly result in reduced fuel import bill and also reduce other associated socio-economic costs[25, 26]. EVs will also use the idle capacity available in the national electricity grid due to intra-day and seasonal variations. On one hand this will reduce the idle capacity payments and on the other hand this will generate extra revenue from using electricity that otherwise may not be sold altogether.

Table 2: Electric Vehicle Penetration Targets.

	Medium Term Targets (5 Years)	Long Term Targets (2030)	90% for 2040 (New Sales)
4 Wheelers	100,000	30%	
2/3 Wheelers	500,000	50%	
Buses	1000	50%	
Trucks	1000	30%	



Estimations of Data for Fig 1 is as following:
Carbon Management Cost for Pakistan = USD50/Metric Ton
Tailpipe Emission reductions = ±61%
Renewable Energy Sources Counted for Pakistan = ±45%

Cost of Electricity for Using EVs in Pakistan = PKR 15/KWh
Fuel Price Calculated for Petrol = 110/Liter
Fuel Price Calculated for Diesel = 125/ Liter
Total Saving in Earnings = Approx. 110 B /Year [Table 1]

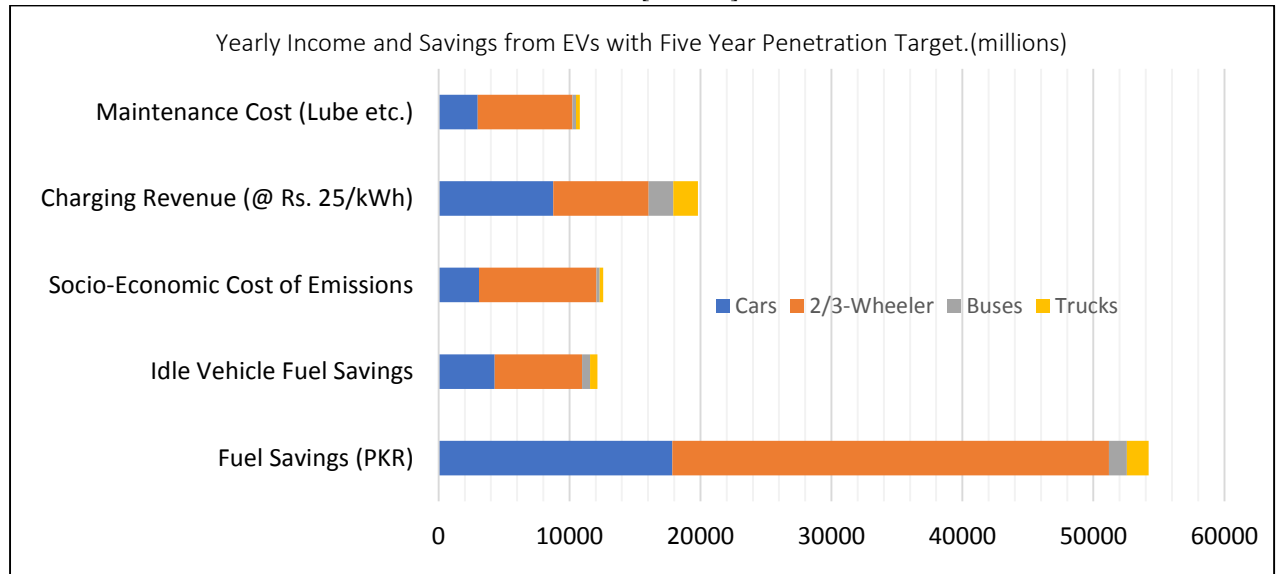


Figure 1. Yearly Income and Savings from EVs with Five Year Penetration Target.

3 5 Proposed phases to achieve foresaid targets

Table 3 shows the proposed plan for initial 5 years after policy in approved.

Table 3: (5 Years proposed plan for EVs Penetration)

Year 1	Year 2	Year 3	Year 4	Year 5
Public Awareness				
Market Development				
Subsidization for EVs Charging Infrastructure				
Subsidized Import of Parts and Tools for Repair				
Fuel Import Substitutions with EVs				
Local Adoption of EVs				

The initial years of EV penetration in Pakistan are not possible without governmental support[8]. EVs still costs much higher than their Fossil Fuel Vehicles (FFV) counterparts and governments around the world give subsidies, incentives and tax breaks for EV adoption amongst the masses[11]. These initial incentives, tax breaks and benefits will pay for itself with the savings in fuel import bill, reduction in emission related expenses, usage of idle electricity capacity and income from charging revenues[11, 21]. For example, with the target penetration of first five years the country will conservatively get around PKR 110 Billion yearly through savings and earnings [table 2].

3.1 Registration Recommendations for EVs

Currently there is no mechanism to register an all-electric vehicle in Pakistan[8]. The Government of Pakistan needs to establish a system based on other countries or following international standardized parameters along with the collaboration of relevant entities.

The following table provides categories of two-three wheelers and cars for their registration categorization



Table 4: Registration Categories EVs

Category	'Rated' Power of Electric Motor
1	0-7.5 KW
2	7.5-15 KW
3	15 KW – 50KW
4	50-60 KW
5	75-100 KW
6	100-150 KW
7	Above 150 KW

The Government can take the following proposed measures for categorizing the EVs in different segments based on rated motor power, that could be similar to FFV in terms of engine capacity:

1. The categorization of registration shall be based on their 'rated' electric motor.
2. Distinct registration plate color and design will be allocated to EVs.

3.2 Charging Infrastructure Recommendations

In order to promote EVs in such a way that it penetrates the market, a minimum custom duty (MCD) on infrastructure should be allowed. Following measures should be taken to achieve targets:

1. Charging infrastructure in cities in every 2.5x2.5 Square Km area.
2. DC fast chargers shall be installed at 60km range along motorways and 30km range on highways.
3. Private charging station shall opt swappable battery facilities.
4. Electric Distribution Company (DISCO) shall made to support fast charging.
5. Existing CNG and Fuel Stations shall be encouraged to establish charging infrastructure

3.3 Core Objectives to Consider

The objectives of the upcoming EV policy can includes:

1. Mitigate climate change through a reduction in emissions from transport sector.
2. Create a pivot to industrial growth in Pakistan and encourage auto and related industry to move towards local EV manufacturing
3. Forge links with the global EV value chain for export potential of EVs and their parts.
4. Meet the objective of generating employment through Green Economy initiatives.
5. Reduce oil import bill.
6. Use electricity in off-peak times for useful purposes.
7. Develop affiliated industry such as battery manufacturing, charging infrastructure, etc.

3.4 Incentive Recommendations

There are four segments of EVs including 2/3 wheelers, cars, buses and trucks which require different policy incentives as national and international markets are at various stages of development for each of the respective segment.

In Table 5, some recommendations have been listed for 4 segments under electric vehicles.

In table 6, some recommendations are suggested for auxiliary systems that potentially support the successful penetration of electric vehicles in country.



Table 5: Recommended incentives for 4 segments of EVs (Cars, Scooter, Rickshaws, Buses and Trucks)

Cars (Light 4 Wheelers)	2/3 Wheel Vehicles	Buses	Light Trucks
All existing incentives under ADP 2016-2021 shall remain intact.			
EVs Manufactured Locally to be sold at Minimum GST.		Government should purchase 100 E-Buses & 100 Light Trucks for introducing E Bus in country	
For few initial years no registration fees and token tax should be imposed for all 4 segments of EVs			
EVs Specific Components for all 4 segments should be allowed to be import at MCD for initial years			
Distinct incentives for EVs as compare to FFV		Encourage manufacturers to setup plants for Buses and Trucks through some Government to Government Contracts	
Incentives should be given for training of repair and maintenance for Cars	Low Speed 4-Wheeler should be allowed under the same category as for 2/3 Wheel	Locally manufactured buses and trucks should be allowed to be sold at minimum GST	
Used and CKD EVs should be allowed to be imported with relaxed MCD for initial years	A special provision for swappable battery for 3-Wheeler should be introduced	Rapid Bus Transit projects should be converted to electric buses on priority bases	Charging infrastructure for trucks should be allowed to installed along CPEC, Motorways & Highways
State Bank of Pakistan should allow buying all EVs except 2/3-wheeler with cost effective financing schemes			

Table 6: Incentives for Auxiliary Support Systems for EVs Penetration in Country

Incentives of Setting up EV Manufacturing Units	Incentives for EV Components and Modules Manufacturing	Incentives for Charging Infrastructure and Battery Swapping Stations
Uphold the incentives from Auto Development Policy 2016-21 for the 3 above mentioned segments & Greenfield Investment to all sectors should be ensures at all levels		
Existing Automotive Manufacturer and Assemblers should be allowed to use their plants under the auspices of Greenfield investment regulation of prevailing ADP 2016-21.	All components used only in International Standard (WP.29) EVs, other than locally manufactured should be allowed to be imported at MCD and Minimum GST.	Level 2 Chargers and their relative components should be allowed and MCD and Minimum GST for few initial years.



The State Bank should allow lower financing rates for EV manufacturing plants setup under Long Term Financing Facility (LTFF).	Individual components of batteries, motors, and electronics etc. should be allowed at import MCS and Sold at Minimum GST.	Entities offering public Level-2 charging should be pushed to show the installation cost of the charging facility as Corporate Social Responsibility (CSR) contribution.
A policy should be approved for land allotment for initial decade to setup Manufacturing Units with lease agreements and easy finances.	Components for conversion Kits should be allowed to import at MCD and Minimum GST for few initial years.	All Level-3 DC fast chargers and its associated infrastructure should be allowed to be imported at MCD and Minimum GST should be applicable.
A policy should be framed to evolve incentives for export of charging infrastructure and EV's from Pakistan to ensure that Pakistan's growing market.	Establishment of recycling and refurbishment plants to ensure proper recycling and/or disposal of batteries and other electronic waste.	All modules and components of Level-3 DC & beyond fast chargers Should be allowed at MCD and minimum GST.

4. Conclusions

Center for EVs Regulations

The government can establish a Center for EVs to jumpstart the EV penetration in the country & work towards developing EVs related industry.

EVs Model Cities and Economic Zones

Lahore and Islamabad can be designated as model cities to jump-start 'Green Rickshaw' and 'Green Taxi' schemes respectively. EV related greenfield projects including those for charging infrastructure may use existing Special economic zones.

Projected decrease in Fossil Fuel Import

It is expected that with the penetration of electric vehicles in country there will be significant drop in oil imports, hence therefore reduction in import bill. Figure 2 presents an estimated reduction in import fuel bill.

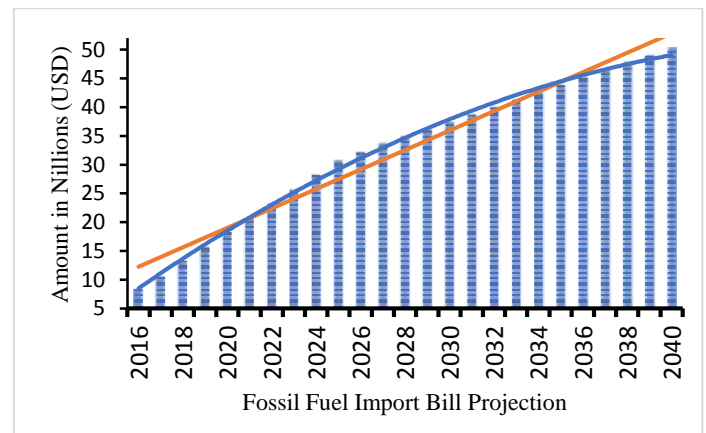


Figure 2. Projected Estimate of Reduction in Fuel Import Bill

Electricity Consumption at Idle Hours and Load on Grid

From the figure 3, it can be observed that during idle hours, a domestic home without EV utilizes peak energy 1.7KWh for 1 hours, while a house with EV utilizes approximately 2KWh for approximately 4 hours.

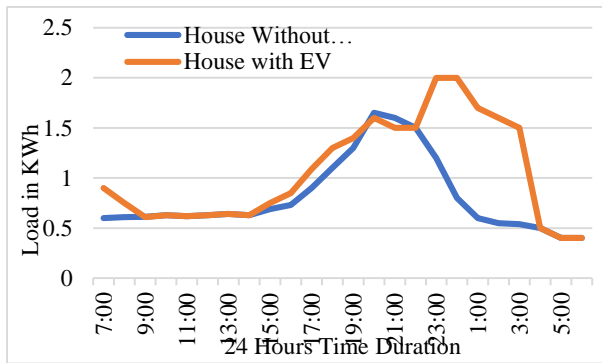


Figure 3. Estimated Utilizing of Idle Electricity comparison

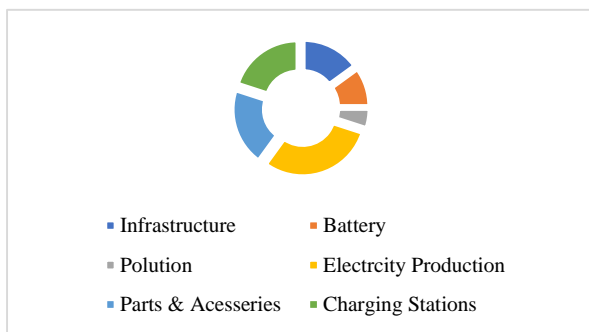


Figure 4. Potential Sectors that could be uplifted with EVs

There are many sectors in country that can potentially get a boom with the launch of EVs in country. Figure 4 depicts some major one of these industries that can be benefitted with EVs.

Potential decrease in Carbon Emission due to EVs

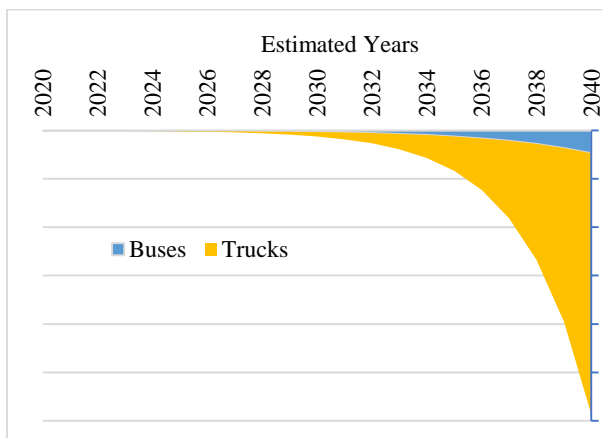


Figure 5. CO₂ Emissions Reduction by Electric Buses & Trucks

Figure 5, 6 and 7 shows the decrease in pollutants of tail pipes of buses & truck, 2/3 wheelers and cars respectively. This data is based on Table 2 estimated

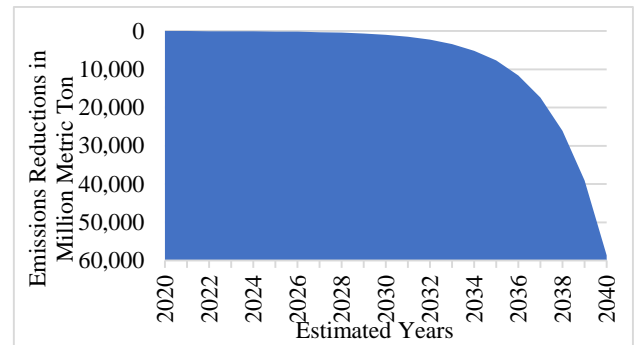


Figure 6. Reduction in Carbon Emissions due to 2/3 Wheelers

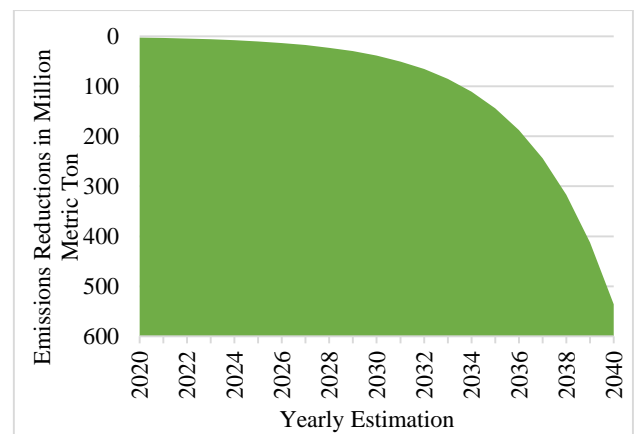


Figure 7. Reduction in Carbon Emissions due to E-Cars

projected penetration of vehicles for next 20 years with continuous increase per year. For the first 4 years the trends show less affective role, but once the vehicles will start replacing FFVs on large scale, the trend become prominent.

Finally, EVs can completely alter the whole automotive sector of country. The only need that left is a comprehensive policy for EVs that can seriously attract new ventures, existing manufacturers and general public towards utilizing the green clean energy. A policy initially oriented towards awareness and utilization of EVs with ease can bring long lasting effects. Once adapted the Government can modify the policy to make it more efficient for country and general public interests.

REFERENCES

1. Tulman, S. *How to Stay Relevant in Today's Fast-Paced Digital World*. [Website] 2015 January 22, 2015 [cited 2019 November 22, 2019]; 1:[1]. Available from: <https://www.business2community.com/business-innovation/stay-relevant-todays-fast-paced-digital-world-01133550>.



2. Thomas, C.D., et al., *Extinction risk from climate change*. Nature, 2004. **427**(6970): p. 145.
3. Myles Allen (UK), M.B.S., et. al., *Global Warming of 1.5°C*. 2018, Intergovernmental Panel on Climate Change: Intergovernmental Panel on Climate Change. p. 24.
4. Kiani, K. *New transport policy for sustainable mobility*. [Website] 2018 [cited 2019 Nvember 24]; Available from: <https://www.dawn.com/news/1414708>.
5. Kintner-Meyer, M., K. Schneider, and R.J.P.N.N.L. Pratt, *Impacts assessment of plug-in hybrid vehicles on electric utilities and regional US power grids, Part 1: Technical analysis*. 2007. **1**.
6. Pakistan, N.H.A., *Infrastrucutre Development for Transportation*. 2019, National Highways Authority, Pakistan: <http://nha.gov.pk/en>. p. 1.
7. Reuters, T. *Will electric vehicles really create a cleaner planet?* 2018 [cited 2019 November 25]; Available from: <https://www.thomsonreuters.com/en/reports/electric-vehicles.html>.
8. Arshad, N., *EV Report Pakistan by LUMS*. 2019, Lahore University of Management Sciences p. 70.
9. HUSSAIN, S., *Sector Profile Automotive and Auto-parts manufacturing*. 2019, Investment Board Pakistan: <https://invest.gov.pk/automobiles>. p. 26.
10. Hamilton, K. and S. Akbar, *Assessing the environmental co-benefits of climate change actions*. 2010, World Bank.
11. Agency, I.E., *Global EV Outlook 2019*. 2019, IEA: International Energy Agency.
12. Wu, Y. and L. Zhang, *Can the development of electric vehicles reduce the emission of air pollutants and greenhouse gases in developing countries?* Transportation Research Part D: Transport and Environment, 2017. **51**: p. 129-145.
13. Association, P.A.M., *Automotive Productions Statistics*. 2018, PAMA: PAMA Online Portal. p. 4.
14. Ashby, M.F., *Chapter 10 - Case Study: Electric Cars*, in *Materials and Sustainable Development*, M.F. Ashby, Editor. 2016, Butterworth-Heinemann: Boston. p. 151-166.
15. Tang, Y., et al., *Economic Analysis on Repurposed EV batteries in a Distributed PV System under Sharing Business Models*. Energy Procedia, 2019. **158**: p. 4304-4310.
16. Van Donkelaar, A., et al., *Global estimates of ambient fine particulate matter concentrations from satellite-based aerosol optical depth: development and application*. 2010. **118**(6): p. 847-855.
17. Ke, B.-R., C.-Y. Chung, and Y.-C. Chen, *Minimizing the costs of constructing an all plug-in electric bus transportation system: A case study in Penghu*. Applied Energy, 2016. **177**: p. 649-660.
18. Van de Graaf, T., *Obsolete or resurgent? The International Energy Agency in a changing global landscape*. Energy Policy, 2012. **48**: p. 233-241.
19. Shaukat, N., et al., *A survey on electric vehicle transportation within smart grid system*. Renewable and Sustainable Energy Reviews, 2018. **81**: p. 1329-1349.
20. Szinai, J.K., et al., *Reduced grid operating costs and renewable energy curtailment with electric vehicle charge management*. Energy Policy, 2019: p. 111051.
21. *\$52.5 bn electric vehicle (car) polymers market - global forecast to 2024*. Focus on Catalysts, 2019. **2019**(9): p. 2.
22. Ehrenberger, S.I., et al., *An international dialogue about electric vehicle deployment to bring energy and greenhouse gas benefits through 2030 on a well-to-wheels basis*. Transportation Research Part D: Transport and Environment, 2019. **74**: p. 245-254.
23. Noori, M. and O. Tatari, *Development of an agent-based model for regional market penetration projections of electric vehicles in the United States*. Energy, 2016. **96**: p. 215-230.
24. Glitman, K., D. Farnsworth, and J. Hildermeier, *The role of electric vehicles in a decarbonized economy: Supporting a reliable, affordable and efficient electric system*. The Electricity Journal, 2019. **32**(7): p. 106623.
25. Babones, S. *China Could Be The World's First All Electric Vehicle Ecosystem*. 2018 [cited 1; Available from: <https://www.forbes.com/sites/salvatorebabones/2018/03/06/china-could-be-the-worlds-first-all-electric-vehicle-ecosystem/>].



26. Siddique, A., *DEVELOPING THE PAK-CHINA ECONOMIC CORRIDOR TO FACILITATES INO - EUROPE TRADE*. 2017, All Pakistan Shipping Association: All Pakistan Shipping Association. p. 15.



Comparative Analysis of a Medium Concentrated Photovoltaic/Phase Change Material System with a Flat Plate Photovoltaic System

Arshmah Hasnain^{*1}, Jawad Sarwar¹, Ahmed E. Abbas², Konstantinos E. Kakosimos²

1- Department of Mechanical Engineering, University of Engineering & Technology, Lahore, Pakistan

2- Sustainable Energy & Clean Air Research Laboratory, Texas A&M University at Qatar, Doha, Qatar

* Corresponding author email: arshmahhasnain@gmail.com

Abstract:

In this work, a concentrated photovoltaic system has been analysed for one day of all months of a year. The system is thermally regulated by using phase change material, RT-47. A parabolic trough concentrator with concentration ratio of 25 has been used to concentrate sunlight onto CPV cell. Phase change material is contained in an aluminium container, on the bottom side of which photovoltaic cell is attached. A combined thermal, optical and electrical model is established and validated. Temperature regulation and electrical output are presented for four months of a year representing four seasons of winter, spring, summer and autumn. The results obtained by CPVPCM system are compared to non-concentrated PV system to check the effectiveness of CPVPCM system. It is reported that CPVPCM system is able to keep the temperature below 85 °C and excels the non-concentrated PV system for all months of a year with maximum increase of 25% of power production for the month of January.

Key Words: Medium Concentrated Photovoltaics, Finite Element Method, Thermal Regulation, Phase Change Material

1. Introduction

Concentrated photovoltaic technology has rendered conventional photovoltaic technology more efficient and cost-effective. A crystalline Si photovoltaic cell converts 21.2 – 27.6 % of incident energy to electricity [1] and the remaining portion is converted to heat which raises the temperature of the cell. Optical concentrators focus concentrated sunlight on to PV cells which can reduce the size and cost of PV cell. But adding concentrators have an added disadvantage that the increased irradiance tends to increase the temperature of cell beyond the safe operating temperature. The increased cell temperature reduces the efficiency and the life of PV cell [2]. It has been reported by Skoplaki et al. [3] that increasing temperature of PV module, reduces efficiency by an average $0.0045^{\circ}\text{C}^{-1}$. To keep the temperature of cell below the safe working temperature of 85 °C, various thermal regulation techniques are employed [2].

One such passive thermal regulation technique using phase change material was first proposed by Huang et al. [4]. Phase change materials can use excess heat for phase transition as latent heat of fusion and can maintain a constant phase transition temperature. A two-dimensional finite volume based conjugated heat transfer model was developed and validated by experiments for thermal analysis of PV/PCM system and it was shown that significant temperature moderation can be achieved by using PCM [4]. A detailed experimental investigation was carried by [5] to evaluate the effects of thermal conductivity of PCM and the containment for PCM on the thermal

regulation of the PV/PCM system. A maximum drop of 18 °C in temperature was observed for 30 min. Temperature drop of 10 °C for longest period of 5h was also observed with CaCl_2 . A transient one-dimensional energy balance model was developed by [6]. Polycrystalline Si cell was analysed for RT20, RT25 and RT28HC as PCM. The results indicated a maximum of 5% increase in efficiency of PV/PCM system.

A 2D numerical model was developed by [7]. It comprised of a thermal model for CPV module and thermo-fluid model for the phase change phenomenon of PCM. The system was analysed at three CR(s) (5, 10 and 20) and $\text{CaCl}_2 \cdot 6\text{H}_2\text{O}$ as PCM with varying thicknesses (50, 100 and 200 mm). It was found that temperature of PV module was maintained at 64 °C for 2 hours and an average temperature of 38 °C was maintained for 8.4 hours. A reflective conical concentrator with CR of 4 was analysed experimentally and $\text{CaCl}_2 \cdot 6\text{H}_2\text{O}$ used as PCM and enclosed in an aluminium container maintained a temperature difference of 57 °C [8]. A CPV/PCM system that can self-regulate its temperature was presented by [9]. Paraffin as PCM (melting range: 56-58 °C) was enclosed in aluminium container. Aluminium metal turnings (1mm wide) were embedded in the PCM for enhancing the thermal conductivity. The indoor experiment using 0.06 m thick PCM layer maintained 65-68°C temperature for 3h. In outdoor testing, V-trough concentrator with CR of 1.7 was employed. The temperature was maintained 64-65°C throughout the day. The system enhanced power gain by 55%. A 2D unsteady-state model for



CPV/PCM system has been analysed in COMSOL Multiphysics by [10]. The system comprised of OM-32 as PCM, Fresnel lens concentrator, multijunction PV module, Cu fins as heat sink and a cooling fan for removing heat from the heat sink. The system has been analysed for varying CR (3, 5, 8, 10) and varying PCM height (0.75, 1.5, 2.25 and 3mm). It is concluded that increasing PCM height maintains temperature of system for longer duration of time. As compared to CPV without PCM, enhancement of 22 and 27% have been observed for CR of 3 and 5 respectively. It was concluded that PCM can regulate the temperature of CPV/PCM system at higher concentration ratios.

Although optical concentrators can enhance the incident radiation and increase power output but most of the systems found in literature have been analysed for $CR < 10$ since concentrating sunlight can increase temperature beyond safe limits. In this work, a CPVPCM system is analysed for CR of 25. The CPVPCM system is solved for the weather circumstances of Doha, Qatar. Results of temperature variation and electrical output are compared to conventional non-concentrated PV system to check the effectiveness of proposed system.

2. Methodology

2.2. Physical Model

The physical model of the proposed design is presented in fig. 1. It consists of a single axis tracker and a non-ideal parabolic trough concentrator (concentration ratio of 25) that concentrates sunlight onto receiver. The receiver comprises a crystalline Si PV module separated by an aluminium container that houses phase change material RT-47 (phase change transition temperature of 41-48°C). CPV cell receives concentrated sunlight. The length of CPVPCM is 2.13m that makes 1m² footprint.

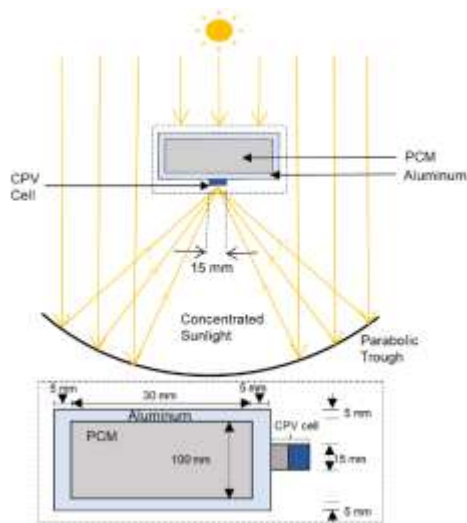


Figure 1. Schematic of CPVPCM system (not to scale)

The proposed design is analysed for one day of a month over the year and result is presented for four months that represent four seasons (winter, spring, summer and autumn) for Doha, Qatar (latitude:25.314779°N longitude:51.43978°E). Experimentally determined whether data is obtained from meteorological department, Qatar and the irradiance input is obtained by the model described in [11].

The CPVPCM system is solved for direct beam irradiance. Fig. 2 shows the variation of input parameters of irradiance and weather data for selected day of each month. Weather data comprises of ambient temperature and wind speed. The maximum ambient temperature analysed is 49°C for July while the mean maximum temperature recorded for period of 1962-2013 is 41.9°C [12]. So, the selected day for analysis can provide a better approximation of performance for the peak temperature days. For comparison of results, the flat plate PV system is considered at slope of ~25.3° with south orientation and is solved for global horizontal irradiance.

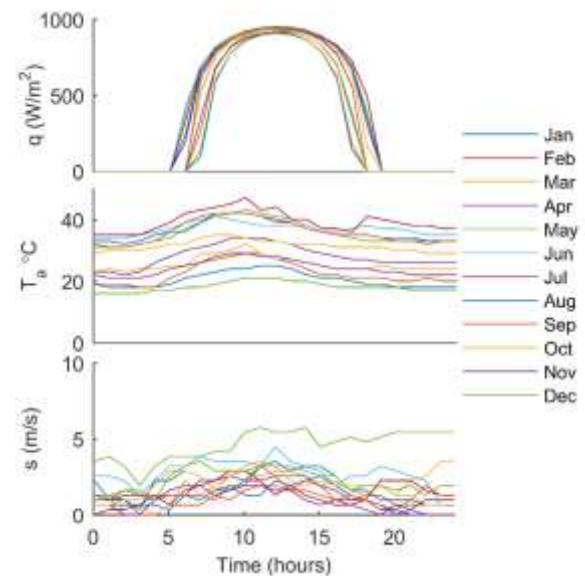


Figure 2. Variation of input parameters



2.2. Theoretical Model

A finite element model is developed. The electrical behaviour is evaluated using the five parameter model presented in [13]. It relates current and voltage to five parameters including reverse saturation diode current I_o , photocurrent I_{pv} , shunt resistance R_p , series resistance R_s and diode ideality α .

$$I = I_{pv} - I_o [\exp((V + R_s I)/V_t \alpha)] - (V + R_s I)/R_p$$

The reflection and absorption losses before it strikes the module are calculated using Fresnel equations. 2D differential heat equation is solved considering convection and radiation heat transfer at boundary. The simplified energy balance equation is given in Eq. 2

$$M\dot{T} + KT - q + (H + R)T = 0$$

Where M, K, q, H, R represent mass, conductivity, irradiance, convection and radiation matrices. The thermal, electrical and optical models are coupled using Eq. 3

$$\begin{aligned} q_{aol} &= (1 - \rho - \alpha)q_i \\ q_e &= [\eta_{ei-STC} + \mu(T - T_a)]q_{aol} \quad (3) \\ q &= q_{aol} - q_e \end{aligned}$$

Depending upon absorption α and reflection ρ the incident radiation q_i is converted to irradiance available after optical losses q_{aol} . The electrical conversion depends on temperature of module and is calculated using the rated electrical efficiency of module at standard test conditions η_{ei-STC} and temperature coefficient of power μ . The electrical conversion losses are accounted in q_e . Net irradiance is calculated as the difference of q_{aol} and q_e . Crank Nicholson method has been used for temporal discretization of both the CPVPCM and PV system. The detailed methodology is presented by the authors elsewhere [14]. Table 1 shows the material properties.

Table 1: Material properties

Thermal Properties					
Material	RT47	Aluminum	PV cell		
T_m (°C)	41 - 48	-	-		
H (kJ kg ⁻¹)	165	-	-		
K (W m ⁻¹ K ⁻¹)	0.2	211	125.4		
ρ (kg m ⁻³)	880	2675	2205		
C_o (kJ kg ⁻¹ K ⁻¹)	2 (solid, liquid)	0.9	0.8		
Electrical Properties					
I_{sc} (A)	V_{oc} (V)	I_{mp} (A)	V_{mp} (V)	K_I (%K ⁻¹)	K_V (%K ⁻¹)
8.21	32.9	7.61	26.3	0.0032	-0.1
Optical Properties					
	Refractive index	Extinction coefficient (m ⁻¹)	depth (m)		
PV	4	4710	5×10 ⁻⁴		
Number of Cells					
PV			CPV		
36			10		

2.3. Validation

To validate the developed model, simulated results of temperature are compared to experimental results obtained for PV and PVPCM systems presented in [15]. The systems were designed for polycrystalline cell and RT-42 was used as phase change material in the PVPCM system. The experimental results of the literature are compared with the simulation results. The details have been presented by authors elsewhere [14] and fig. 3 is presented for completeness. The standard deviation between the simulated and the experimental results is found to be <±3%. The reported cumulative uncertainty in the experiment is 5.26% which is comparable to the standard deviation between simulated and experimental results. So, the developed model represents the practical system very well.

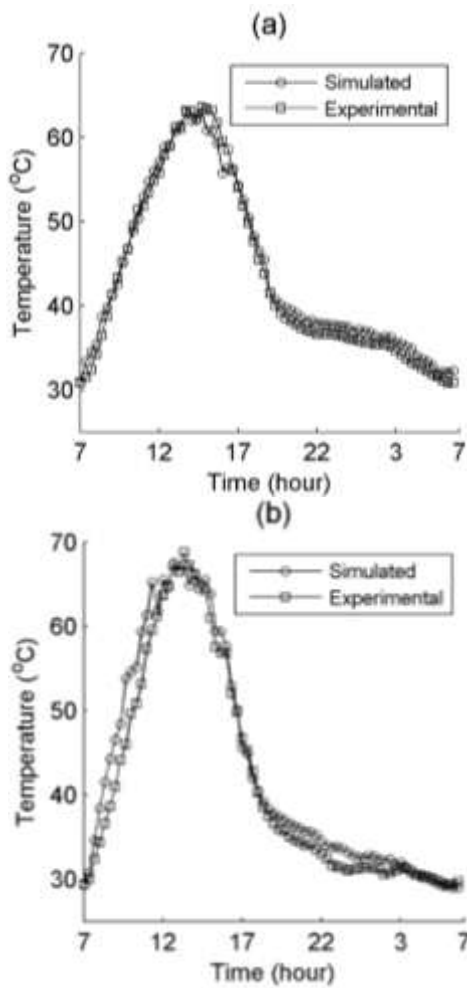


Figure 3. (a) Comparison of simulated result of PV temperature with experimental result of PVPCM system (b) Comparison of simulated result of PV temperature with experimental result of PV system

3. Results and Discussions

In order to determine the thermal regulation effects of phase change material on the concentrated photovoltaic system, temperature variation over a day for the selected months is shown in fig.4. The temperature of CPVPCM system stays higher than the conventional flat plate PV system because CPVPCM system receives concentrated sunlight. But the added phase change material thermally regulates the system and is able to keep the operating temperature below 85 °C for all months of a year.

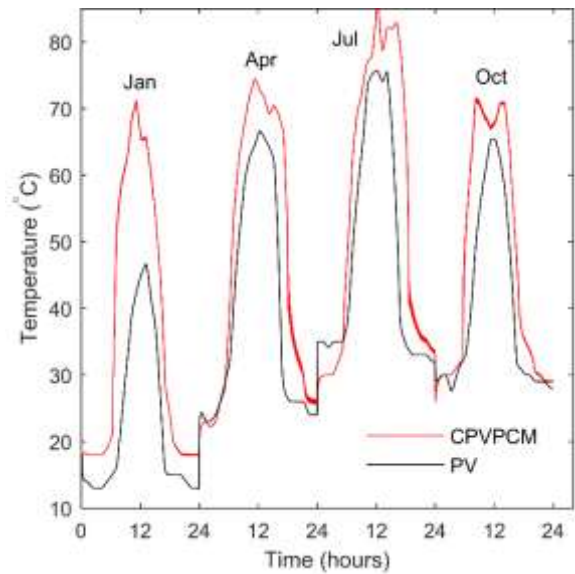


Figure 4. Temperature variation of CPVPCM and conventional PV system for one day of selected months.

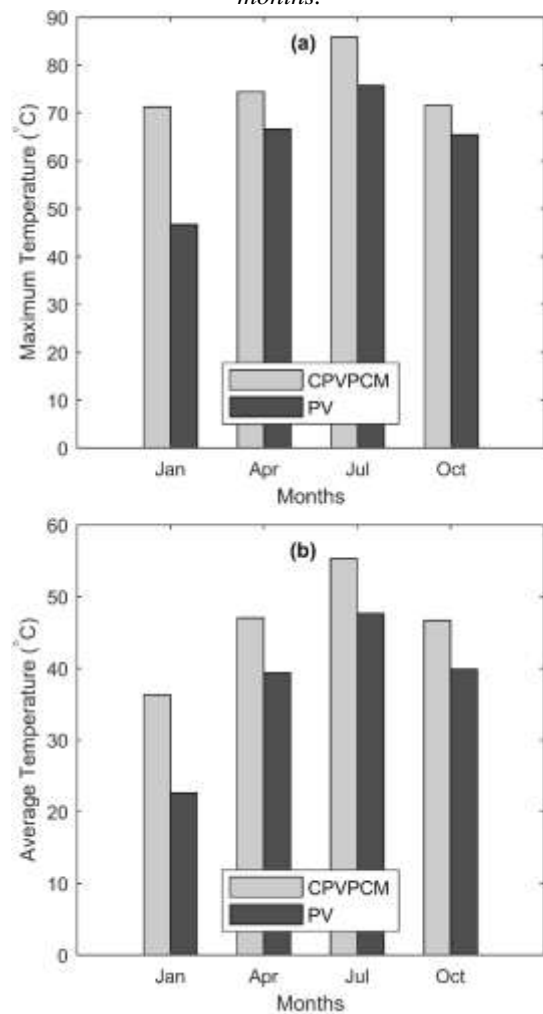


Figure 5. (a) Comparison of maximum temperatures of CPVPCM and conventional PV system (b) Comparison of average temperatures of CPVPCM and conventional PV system



The CPV cell temperature in CPVPCM system stays consistently higher than PV cell temperature in non-concentrated PV system. A maximum variation of 34.5% is observed for the month of January while for all other months, the variations stays below 11.8% as compared to PV system. The peak shifting has been observed in the CPV temperature profile which is due to the fact that phase change material tends to delay the effect of temperature rise.

The maximum and average temperatures of CPVPCM and conventional PV systems are given in fig. 5. Due to concentrated irradiance, the maximum and average temperatures of CPVPCM are greater than that of PV system. The maximum temperature varies in the range of 10 °C except for the month of January where the difference is 24.6 °C. The average temperature varies in the range of 8 °C for all months except for January where the difference is 13.6 °C.

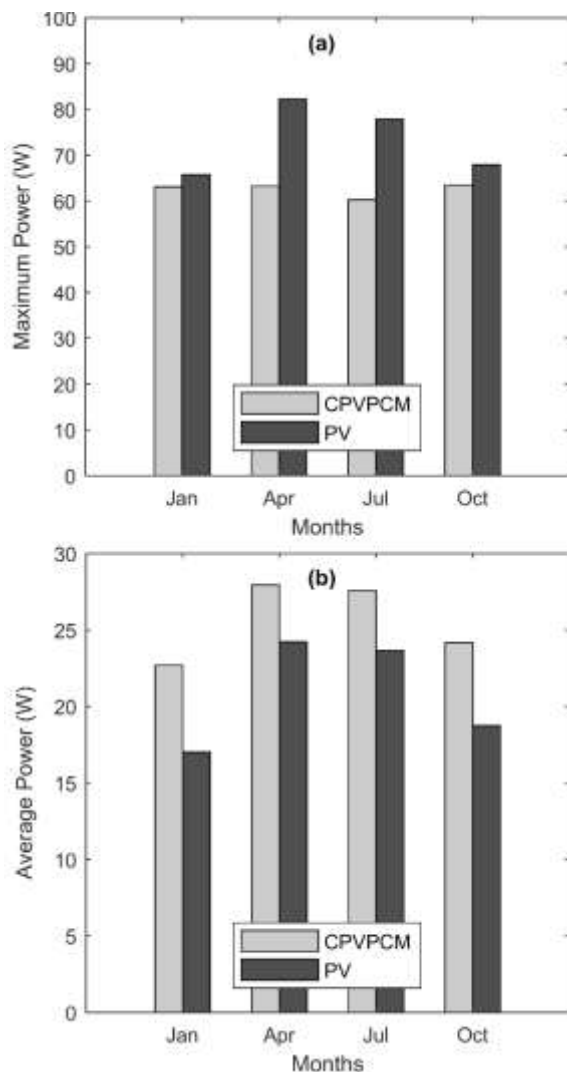


Figure 6. Maximum and average powers obtained from CPVPCM and PV system

The maximum and average powers obtained from CPVPCM system and PV systems are shown in fig.6. It can be seen that although the maximum power obtained from CPVPCM system is lower than conventional PV system but the average power of CPVPCM stays higher over the day for all months of a year. The maximum increase of 25% in power is obtained for the month of January. The consistency in higher average power shows that proposed design can consistently supply electrical power over the year.

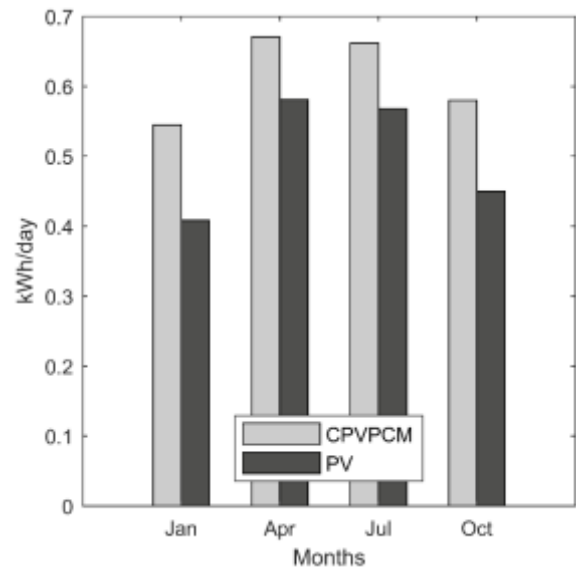


Figure 7. kWh/day obtained from CPVPCM and PV systems

To further analyse the CPVPCM system, kWh obtained over a day are plotted in fig. 7. The CPVPCM system is able to consistently deliver more units over the year as compared to the PV system. CPVPCM system excels for the month of January where it can deliver 25% more power than the conventional flat plate system.

Conclusions

Concentrated photovoltaic systems increase the power output by increasing the irradiance flux but the system should be thermally regulated against the increased temperature rise. Analysed CPV system that is thermally regulated with phase change material, delivers higher average power for all months of a year as compared to conventional PV system with a maximum rise of 25% in the power for the month of January.



REFERENCES

1. NREL *Best Research-Cell Efficiency Chart*. 2019 30/03/2019].
2. Hasan, A., J. Sarwar, and A.H. Shah, *Concentrated photovoltaic: A review of thermal aspects, challenges and opportunities*. Renewable and Sustainable Energy Reviews, 2018. **94**: p. 835-852.
3. Skoplaki, E. and J.A. Palyvos, *On the temperature dependence of photovoltaic module electrical performance: A review of efficiency/power correlations*. Solar Energy, 2009. **83**(5): p. 614-624.
4. Huang, M.J., P.C. Eames, and B. Norton, *Thermal regulation of building-integrated photovoltaics using phase change materials*. International Journal of Heat and Mass Transfer, 2004. **47**(12): p. 2715-2733.
5. Hasan, A., et al., *Evaluation of phase change materials for thermal regulation enhancement of building integrated photovoltaics*. Solar Energy, 2010. **84**(9): p. 1601-1612.
6. Kibria, M.A., et al., *Development of a thermal model for a hybrid photovoltaic module and phase change materials storage integrated in buildings*. Solar Energy, 2016. **124**: p. 114-123.
7. Emam, M., M. Ahmed, and S. Ookawara, *Performance Enhancement of Concentrated Photovoltaic System Using Phase-Change Material*. 2016(50220): p. V001T08A006.
8. Sarwar, J., et al., *Experimental Investigation Of Temperature Regulation Of Concentrated Photovoltaic Using Heat Spreading And Phase Change Material Cooling Method*. 2013.
9. Maiti, S., et al., *Self regulation of photovoltaic module temperature in V-trough using a metal-wax composite phase change matrix*. Solar Energy, 2011. **85**(9): p. 1805-1816.
10. Manikandan, S., et al., *Thermal management of low concentrated photovoltaic module with phase change material*. Journal of Cleaner Production, 2019. **219**: p. 359-367.
11. Bird, R.E. and R.L. Hulstrom, *Simplified clear sky model for direct and diffuse insolation on horizontal surfaces*. 1981, ; Solar Energy Research Inst., Golden, CO (USA). p. Medium: ED; Size: Pages: 46.
12. *Qatar Meteorology Department*. 2019 28/11/2019]; Available from: <https://qweather.gov.qa/CAA/ClimateNormals.aspx>.
13. Villalva, M.G., J.R. Gazoli, and E. Ruppert Filho, *Comprehensive approach to modeling and simulation of photovoltaic arrays*. IEEE Transactions on power electronics, 2009. **24**(5): p. 1198-1208.
14. *In review*. Thermal Science, 2019.
15. Hasan, A., et al., *Yearly energy performance of a photovoltaic-phase change material (PV-PCM) system in hot climate*. Solar Energy, 2017. **146**: p. 417-429.



Performance Analysis of Constant Current Process of Capacitive Deionization with CFD Flow Simulation and AI Optimization

Shahrose Imran¹, Muhammad Nouman Zafar¹, Hira Naveed¹, Muhammad Wajid Saleem^{1*}
¹ Department of Mechanical Engineering, University of Engineering and Technology, Lahore
*Corresponding Author: wajidsaleem@uet.edu.pk

Abstract:

Capacitive deionization (CDI) works like super-capacitor with two modes of operation i.e. constant current (CC) and constant voltage (CV), and several designs based on flow type and configuration of components. In this paper, a comparison is made for stability and life of system components of two types of CDI based on flow of feed solution, flow-by and flow-through, by calculating pressure and wall shear stress. The flow analysis makes flow-through CDI preferable to flow-by. Moreover, CC CDI is evaluated for effluent concentration, average energy consumption and salt adsorption rate (ASAR) against two fundamental operating variables: flowrate and applied current. The performance evaluation discloses the conflicts in behaviors of performance parameters with variation of operating conditions, therefore, to tradeoff between these parameters optimization of cell is done to get the optimum performance point.

Keywords: CFD; competitiveness and performance; optimization; Capacitive deionization

1. Introduction

In world's economic and energy efficiency corridor, capacitive deionization is a promising technology for purification of brackish water (1000-3500 mg/L) at subsidized cost [1, 2]. In this technique low salinity brackish water is purified by placing two electrodes in front of each other and giving them opposite charge by DC source. Instead of chemical reaction, ions from brackish water are adsorbed on electrodes of opposite charge forming electron double layers (EDL) [3]. This process is adsorption or purification phase of CDI [4]. After electrodes reach saturation, no more ions can be removed from feed solution, therefore, it is needed for the electrodes to be regenerated by either reversing the polarity or short circuiting. The electrodes release absorbed ions into feed solution therefore, this phase is called desorption or electrode regeneration. Energy can be recovered during desorption, that's why CDI is an energy efficient process due to its energy recovery property [5]. There are several classifications of CDI based on the electrode configuration, operational mode, electrode material etc. [6]

The two fundamental electrode configurations are "flow by" and "flow through" electrodes. In the first arrangement, water flows in the spacer channel between the two electrodes perpendicular to electric field [7]. Whereas, in the later configuration, water flows directly through the porous electrodes parallel to electric field [8]. With the development in configuration of electrodes in the CDI cell, its performance is improved by adjoining ion exchange membranes (IEM) to the electrode, this is called membrane capacitive deionization (MCDI) [9]. Moreover, advancements in the field of electrode

materials led to the exploitation of properties. Different materials were sorted out for electrodes to improve their salt adsorption property significantly [10]. Carbon aerogel as electrode material, was found to have large surface area, structural design stability and low resistivity [11].

CDI cell arrangement, which includes single pass and batch mode, makes the difference in the operation of desalination [12, 13]. The CDI cell assumes different characteristics when mode of electrical energy is changed. This lead to the constant voltage (CV) and constant current (CC) mode of CDI [14-16]. However, the selection of mode of operation solely depend on the target properties to be achieved [17].

Emphasizing on volume flow analysis, different performance functions have been evaluated on variable flowrates. Flow efficiency, ratio of salt removed from effluent relative to the amount of salt absorbed [18], has been investigated to determine its dependence on flowrate. The flow losses are avoided by increasing the flowrate or introducing a flushing process in desalination cyclic process [19]. Moreover, average salt adsorption rate (ASAR), amount of energy consumed, water and energy recoveries have been studied for responses to varying flow rates of feed solution [20, 21]. Effect of increasing feed solution flow rate on quality of purified water reported in the Ref. [22], is degenerative i.e. at higher flowrate effluent concentration increases. The effect of volume flow rate is premeditated and is being studied in the pretext of its effect on performance parameters solely. There is not much work on the stability and life of CDI system components based on different values of flow rate and CDI cell architectures. In this paper,



comparison of flow-by and flow-through CDI has been done, incorporating CDI components pressure and stress endurance.

2. Methodology

2.1 Materials, model and methods

The CDI cell design used in this paper is the same as outlined in the Refs. [23, 24]. A brief description regarding the cell design and architecture is delineated here. The CDI cell consisted of two porous electrodes made of carbon aerogel (density = 650 kgm⁻³, capacitance = 410 Fg⁻¹, porosity = 0.67, mass = 10.8 g, thickness = 362 μm), two ion exchange membranes (CEM and AEM) used in Flow-by design, composed of Polyvinyl alcohol (PVA, porosity = 0.85, permeability = 6.5 x 10⁻¹⁴ m², thickness (CEM, AEM) = 170, 140 μm), a spacer membrane placed between the electrodes in Flow-by CDI, with material composition of A-type glass fiber (density = 2440 kgm⁻³, porosity = 0.90, permeability = 1.5 x 10⁻¹² m², thickness = 250 μm). Brackish water used for one dimensional flow analysis of CDI cell, enters from an inlet (diameter = 2.25 cm²), passes through the spacer channel (5.6 x 4 cm²) and exits from the outlet at opposite end with same dimensions as inlet.

For flow analysis of CDI cell, two major indicators pertaining to the life and stability of porous structures; Pressure and Wall shear stress, are considered in the ANSYS Fluent. These two indicators are calculated at different flow rates of brackish water; 60 and 120 mL/min, as exploited in the Ref. [15], by turbulent model (k-epsilon) simulation. With similar boundary conditions and turbulent model, we compare the flow-by and flow-through CDI for the two indicators, we call electrodes stability indicators.

After the flow analysis and comparison of the two most frequent CDI cell designs, we evaluate the performance of CC CDI in terms of three performance parameters; effluent concentration, energy

consumption and average salt adsorption rate (ASAR). The variable operating conditions for this parameter based performance evaluation constituted of flow rate and applied current.

Performance evaluation of CC CDI cell begets conflicts among the different parameters for same operating conditions. In this situation, we have to make trade-offs and bargain for the most optimal overall performance of the system with reasonable compromises on parameters. This optimized performance is obtained by multi-objective optimization of CDI system subjected to operating variables constraints using the *goalattain* algorithm in MATLAB. We present the percentage change in the overall performance of the system by comparing the optimized system parameters with un-optimized ones.

2.2 Mathematical model

Capacitive deionization is a cyclic process with adsorption and desorption loops. The concentration of feed solution changes inside CDI cell with time, making it a transient system. This transient behavior needs to be incorporated in mathematical model of CDI system. In the Ref. [25], CDI model based on GCS-EDL model has been developed which is used in this paper.

The effluent concentration varies from maximum to minimum possible concentration depending upon a number of variables, following is the equation of effluent concentration during adsorption:

$$c_{eff} = c_{fd} - \frac{\varepsilon \times I}{z \times F \times \Psi} \times (1 - e^{-\Psi \times \frac{t_{ad}}{V_c}}) \quad (1)$$

Where, c_{fd} is feed concentration, ε is charge efficiency, I is applied current, z is charge, F is

Table 1: Numerical Values for parameters used in the evaluation

Parameters	Values	Parameters	Values
Ψ	60 mL/min	z	1 (+ or -)
V_c	0.0067658 L	V_{tar}	1.2 V
F	96485 C/m	I	1 A

Faraday constant, t_{ad} is the time for adsorption, Ψ is flowrate and V_c is cell volume.

Concentration for the desorption mode is given as:



$$c_{eff,d} = c_{fd} + \frac{\varepsilon \times I}{z \times F \times \varphi} \times \left(1 - e^{-\varphi \times \frac{t_{des}}{V_c}} \right) \quad (2)$$

The energy consumed by the CDI system for one liter of purified water delivered is a function of target voltage and flow rate of the feed solution. Energy consumption, a prime concern for competitiveness of desalination technologies, is modelled using basic capacitor equation for energy storage.

$$E = \frac{I \times V_{tar}}{2 \times \varphi} \quad (3)$$

The change in effluent concentration results from the adsorption of ions into the electrodes. The mathematical expression representing the adsorption of salt into the electrodes is given as;

$$G_{ion} = \varphi \times M_{salt} \int_1^{t_{ad}} (c_{fd} - c_{eff}) dt \quad (4)$$

Where, M_{salt} is molar mass of the salt, which is 58.45 g/mol, t_{cc} is the time for adsorption and it is given as;

$$t_{ad} = \frac{V_{tar}}{I}$$

The performance of CDI cell can also be evaluated by considering the rate of salt

adsorption as it varies throughout the cycle. Average salt adsorption rate (ASAR) meters the rate of adsorption.

$$ASAR = \frac{G_{ion}}{\text{cycles} \times m_{electrode} \times t_{cycle} \times M_{salt}} \quad (5)$$

Where, mass of electrodes ($m_{electrode}$) is 10.8 g, cycles are number of cycles and t_{cycle} is the cycle time which is the summation of adsorption and desorption times. Table 1, shows the numerical values for the parameters used in performance evaluation.

3. Flow Analysis of Electrodes

Flow analysis of CDI cell is performed to check the system components endurance during operation. Both designs of the cell i.e. flow-by and flow through are analyzed using ANSYS Fluent (**Error! Reference source not found.**). For the purpose of analysis, energy and k-epsilon models in ANSYS fluent are utilized. Energy model carries out the calculation to assess the impact of salt diffusion and viscous dissipation of fluid into the electrodes. K-epsilon model adds to the precision of calculation of energy model by analyzing the turbulent behavior of fluid and its effects on the electrodes.

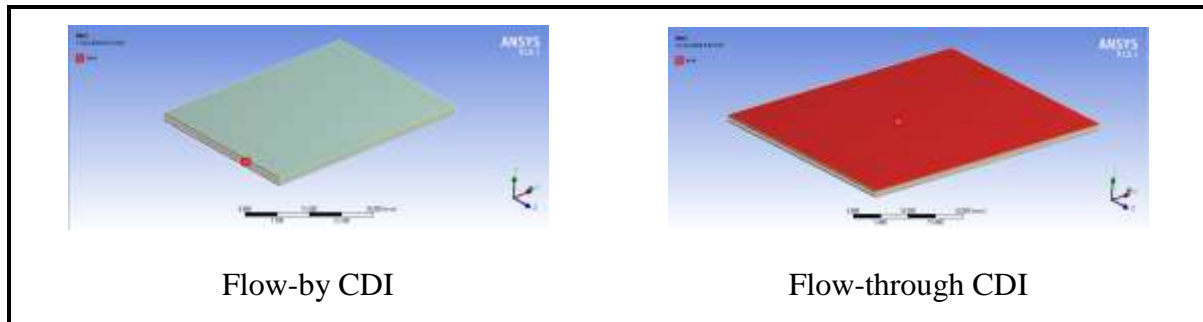


Figure 1. Inlet configurations for CDI systems. Outlet is at opposite to inlet in both cases.

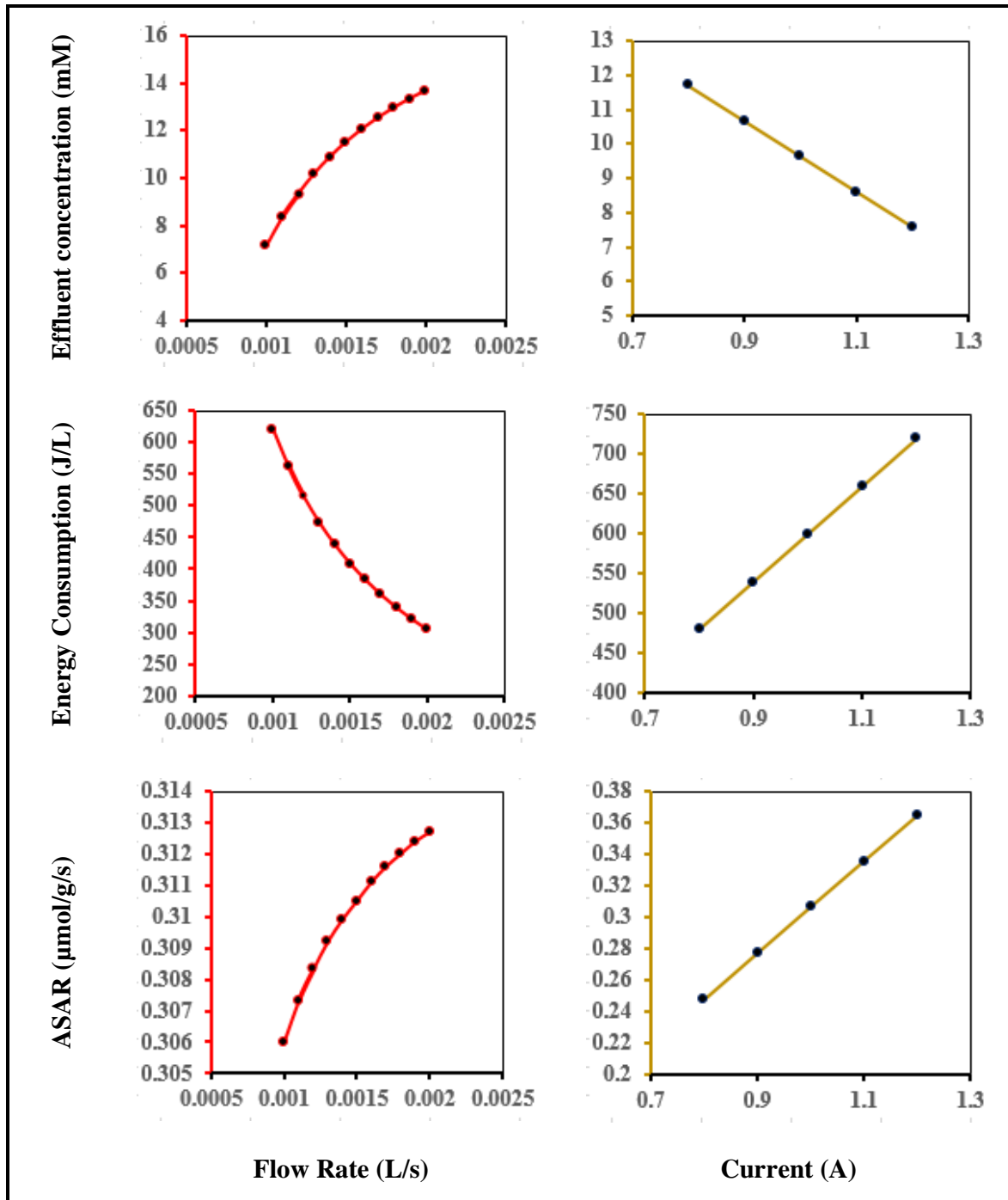


Figure 2. Parametric performance evaluation of CC CDI

Two outputs, namely, wall shear and pressure are obtained from ANSYS Fluent energy and k-epsilon model calculation at two flowrates i.e. 60 mL/min and 120 mL/min, as discussed later. (Fig. 3-Fig. 4). Modelling parameters for simulation in ANSYS Fluent are provided in the Table 2.

4. Performance Evaluation

The performance of CDI cell is evaluated against two fundamental operational parameters i.e. applied

current and flow rate. As evident from the Fig. 2, ASAR shows increment with increasing flowrate, the rationale to this accretion is increasing salt adsorption due to greater flux of ions on electrodes. Moreover, ASAR increases with applied current. The rate electron flux into the electrodes increases due to high current, which is balanced by increased rate of salt adsorption, therefore, increasing the ASAR.

Fig. 2 represents the decrease of energy with flowrate. The reason behind this behavior is more physical than



electrical or chemical. The turbulence of the fluid increases as we increase the flowrate, which leads to

self-deposition of ions while striking the electrodes. Therefore, the

Table 2: Modelling of System in ANSYS Fluent

Characteristics	Mesh Size		Boundary Conditions		Convergence	Solution Type
Value	Min Size (m)	1.00E-07	Velocity Inlet	8.8 m/s ⁻¹	10E-3	Steady
	Max face Size (m)	3.00E-04	Pressure Outlet	0 Pa		
	Max. Tet Size (m)	1.00E-03				

energy consumption decreases. However, energy consumption increases with applied current, for there is greater flow of electrons to the electrodes which produces stronger electric field potential. Therefore, greater amount of energy is stored between the electrodes at high current values.

Effluent concentration is intrinsic parameter to judge the performance of CDI cell. As shown in the Fig. 2, effluent concentration decreases with increase of current since salt adsorption increases (explained earlier). On the other hand, effluent concentration increases with flowrate, although amount of salt absorbed increases yet effluent concentration also increases because greater amount of salt was fed as influent, therefore proportion of the salt absorbed to the total salt fed decreases.

The trends of performance functions from Fig. 2 are quite conforming to that of mathematical model. The change of performance is exponential against flowrate and linear against current. It is mathematically justified since flow rate (Ψ) appears in the exponential component and current (I) in the linear component of Eqs. 1-6. Moreover, capacitor is a linear device therefore it has linear relation between current and voltage (ASAR, salt adsorption and energy storage). However, in the case of flowrate, the turbulence comes into effect making the system performance grow or decay exponentially.

5. Optimization

Different performance parameters of CDI system show contradictory responses to the same operating conditions i.e. flow rate and current in present case. This conflicting behavior of performance parameters

is evident from the performance evaluation section; summarized in Table 3. As evident from Table 3, at least one performance parameter demonstrates negative effect on system performance while others show positive behavior for in-situ operating condition. For example, increase in flow rate over same range has positive effect on energy consumption and ASAR but negative effect on water quality (Effluent concentration). Therefore, it is necessary to perform multi-objective performance optimization of CDI system to find optimum operating condition. In this paper, we use *fgoalattain* algorithm in MATLAB to optimize the objective functions of system performance (Effluent concentration, Energy consumption and ASAR) against operating variables ($d(1)$; Flow rate and $d(2)$; Current).

All the three objective functions have equal weight. The objective function of purified water concentration in terms of operating variables is as follows.

$$c_{eff}(d) = c_{fd} - \frac{\varepsilon * d(2)}{z * F * d(1)} * (1 - e^{-d(1) * \frac{V_{tar} * C}{d(2) * V_c}}) \quad (6)$$

The objective function of energy consumed for per liter of purified water delivered is given as follows.

$$E(d) = \frac{d(2) * V_{tar}}{2 * d(1)} \quad (7)$$



The average salt adsorption rate is expressed in terms of salt adsorbed (G_{ion}), therefore, it is a complicated objective function. The ASAR in terms of salt adsorbed is as follows.

$$ASAR(d) = \frac{G_{ion}(d)}{\text{cycles} * m * t_{ad}(d)} \quad (8)$$

Where,

The operating variables are subjected to the constraints of actual CDI system limitations. The bounds of flow rate are determined according to characteristics of the pump used to feed the brackish water into CDI cell. As mentioned in the Ref. [15, 26], flow rate is constrained to [40,120] mL/min and current is restrained to [0.8,1.2] A. Flow rate and current cannot be increased to very high values because former will worsen the water quality and latter will trigger the faradaic reactions at electrodes which will increase energy consumption due to water splitting.

The optimized and un-optimized performance parameters of CDI system are juxtaposed with percentage change to demonstrate the effectiveness of optimization technique. It will also give an insight into room for improvement in incumbent CDI system.

6. Results

6.1 Flow analysis

The pressure analysis of CDI flow-by and flow-through designs has been demonstrated at two selected flow rates of 60 mL/min and 120 mL/min in the Fig. 3. It is evident from the cursory view of this analysis that flow-by CDI endures higher gage pressure than flow-through CDI. It is attributable to the thinner contact region between brackish water and CDI systems at the inlets. The turbulent model calculations for pressure show that the pressure is maximum at the inlets of flow-by and flow-through CDI. The maximum values of pressure for flow-by and flow-through calculated are 136.1 kPa and 0.830 kPa respectively. The higher pressure at flow-by CDI inlet is due to the smaller area of contact (3.70 mm²) than at flow-through CDI inlet (22.5 mm²). Another important consideration for the stability and life of

CDI is its endurance to the wall shear stress which is exerted on the CDI system constituents i.e. electrodes, spacer and membranes, by the stream of brackish water.

In the Fig. 4, wall shear stress analysis of flow-by and flow-through CDI has been juxtaposed at preselected flow rates, 60 mL/min and 120 mL/min. The turbulence model calculations for the two flow rates for both CDI systems designates higher wall shear stress at flow-through CDI inlet as compared to flow-by CDI inlet. The values for higher and lower wall

$$G_{ion}(d) = d(1) * M_{salt} \int_1^{t_{ad}(d)} (c_{fd} - c_{eff}(d)) dt \quad (9)$$

shear stress are 197 Pa and 125 Pa respectively. The higher wall shear stress in flow through CDI is related to lower gage pressure at its inlet that begets high velocity at the water electrode interface [27].

6.2 Performance evaluation

The parametric performance evaluation of CC CDI system on range of flow rate and current has been performed. Performance parameters of CC CDI depicted tenable trends at different values of operating variables. Ostensibly, the increase in flow rate of brackish water affects the ASAR and energy consumption in positive manner while increase in current affects ASAR and effluent concentration in positive terms. Therefore, we can conclude quite reasonably that ASAR can be ameliorated either way i.e. increasing flow rate or current, depending on the desired tradeoff either in the favor of energy consumption or effluent concentration respectively.

6.3 Optimization

The performance optimization of CC CDI parameters using multi-objective optimization algorithm, *fgoalattain*, in MATLAB provided an insight into room for improvement within existing CC CDI system at available operating conditions. The results of optimization are represented in the Fig. 5, with comparison between optimized and un-optimized system parameters and their corresponding percentage changes.



Table 3. Response of performance parameters to the variable operating conditions. The positive (✓) and negative (✗) implications on the cell performance are indicated.

Operating variable	Performance Parameter		
	Effluent concentration (mM)	Energy consumption (J/L)	ASAR ($\mu\text{mol}/\text{g.s}$)
Flow rate (L/s)	✗	✓	✓
Current (A)	✓	✗	✓

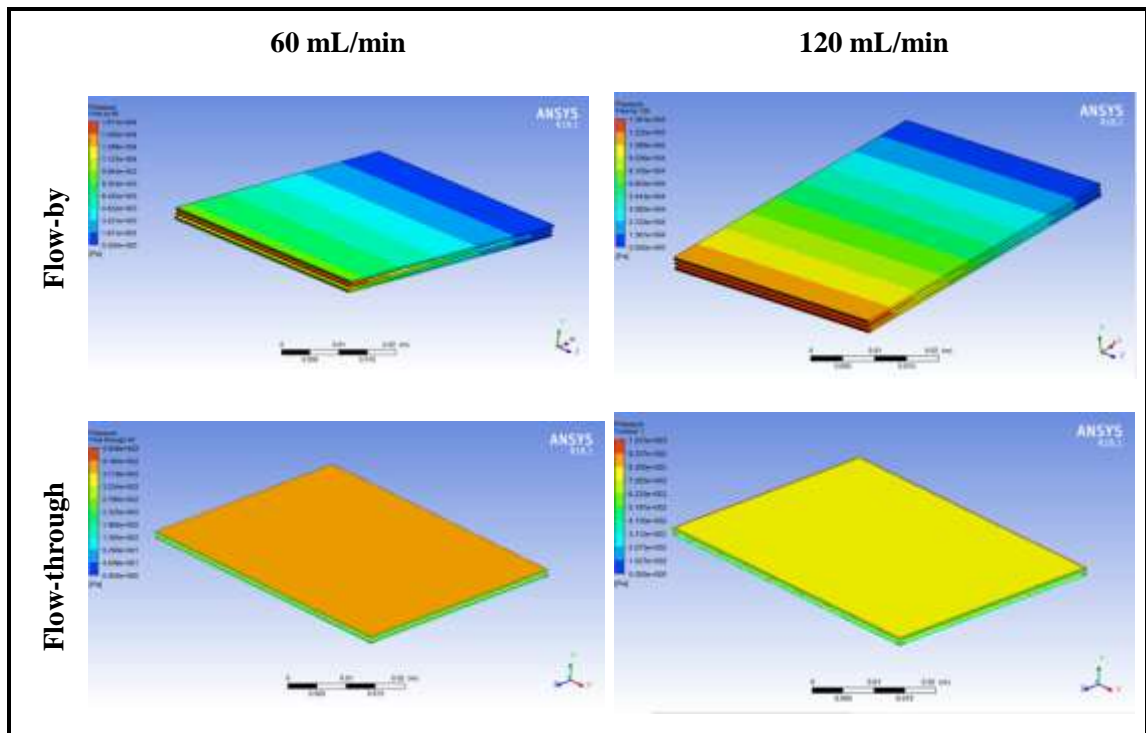


Fig.3. Pressure analysis and comparison of flow-by and flow-through CDI at different flow rates

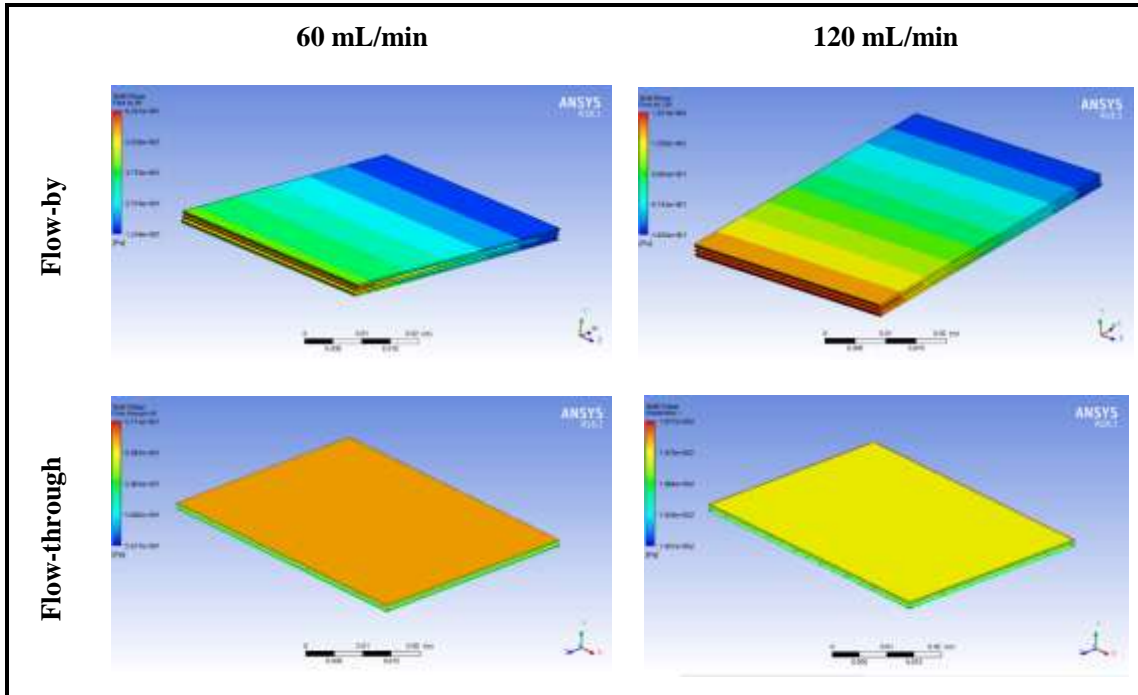


Figure 4. Wall Shear Stress analysis and comparison of flow-by and flow-through CDI at different flow rates

The negative percentage change does not mean deterioration in the performance of certain parameter but it is a useful result of optimization in case of energy consumed per liter of fresh water recovered and effluent concentration.

consumption. However, ASAR reduces by -16% which is a negative effect on CDI system performance at the cost of improved energy consumption and effluent concentration.

The most significant improvement in the performance of CC CDI system is projected to be -21% in energy

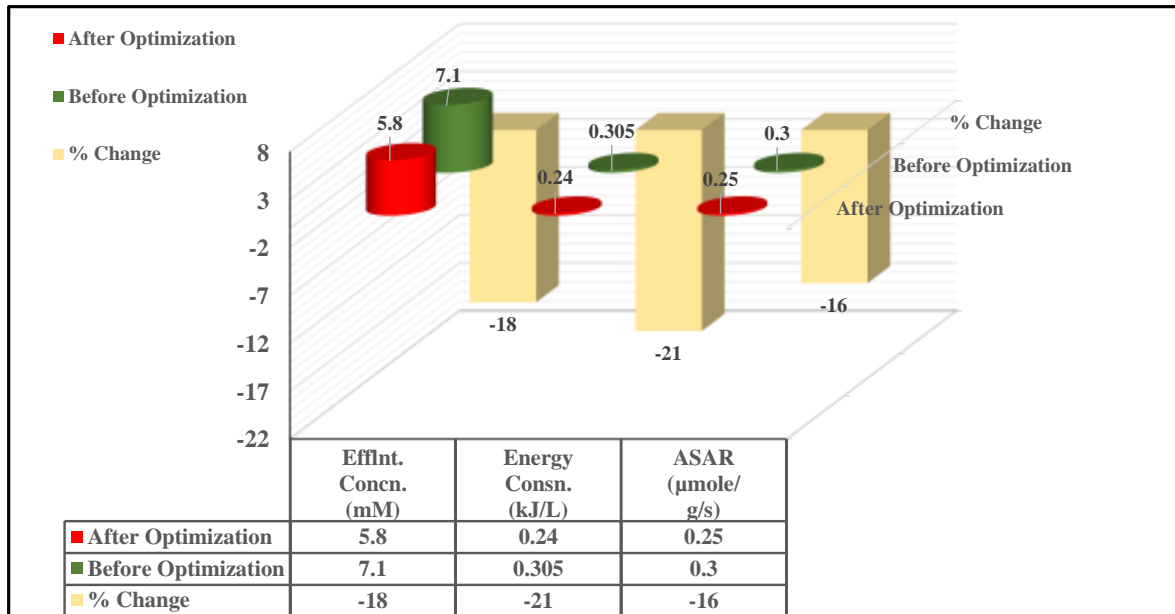


Figure 5. Optimized and unoptimized performance parameters for CC CDI system with percentage change



7. Conclusions

In this paper, three types of methodologies have been adopted for CDI system improvement, flow analysis, performance evaluation and optimization. Flow analysis gave the insight into prospects in stability of CDI system components. Performance evaluation gave the outlook of capabilities of incumbent CDI system used in this paper. However, optimization of CC process of CDI established its projections for performance improvement. From the flow analysis of flow-by and flow-through CDI systems, it has been established that flow-through CDI system is far better in terms of pressure endurance. Therefore, it should be preferred for long life and stability of the system. Performance evaluation reveals the conflicts in energy consumption and effluent concentration with increase in flow rate and current, with mutual desirable behavior of ASAR. Therefore, tradeoffs are to be made either in the favor of effluent concentration or energy consumption. Optimization of CDI system parameters with multi-objective optimization tool projects the room for improvement in energy consumption by 21%, effluent concentration by 18%. In this paper, we have systematically covered all the aspects related to CDI system life, operation and improvement.

REFERENCES

1. Oren, Y., *Capacitive deionization (CDI) for desalination and water treatment—past, present and future (a review)*. Desalination, 2008. **228**(1-3): p. 10-29.
2. Guide, S.M. *Measures of salinity*. 2007; Available from: http://www.salinitymanagement.org/Salinity%20Management%20Guide/ls/ls_3d.html.
3. Długołęcki, P. and A. van der Wal, *Energy Recovery in Membrane Capacitive Deionization*. Environmental Science & Technology, 2013. **47**(9): p. 4904-4910.
4. Andelman, M., *Flow Through Capacitor basics*. Separation and Purification Technology, 2011. **80**(2): p. 262-269.
5. Biesheuvel, P., B. Van Limpt, and A. Van der Wal, *Dynamic adsorption/desorption process model for capacitive deionization*. The journal of physical chemistry C, 2009. **113**(14): p. 5636-5640.
6. Porada, S., et al., *Review on the science and technology of water desalination by capacitive deionization*. Progress in materials science, 2013. **58**(8): p. 1388-1442.
7. Chang, L.M., X.Y. Duan, and W. Liu, *Preparation and electrosorption desalination performance of activated carbon electrode with titania*. Desalination, 2011. **270**(1-3): p. 285-290.
8. Suss, M.E., et al., *Capacitive desalination with flow-through electrodes*. Energy & Environmental Science, 2012. **5**(11): p. 9511-9519.
9. Kim, Y.-J. and J.-H. Choi, *Selective removal of nitrate ion using a novel composite carbon electrode in capacitive deionization*. Water research, 2012. **46**(18): p. 6033-6039.
10. Wang, G., et al., *Activated carbon nanofiber webs made by electrospinning for capacitive deionization*. Electrochimica Acta, 2012. **69**: p. 65-70.
11. Linneen, N., et al., *Application of the macrohomogeneous line model for the characterization of carbon aerogel electrodes in capacitive deionization*. Electrochimica Acta, 2019. **301**: p. 1-7.
12. Porada, S., et al., *Effect of electrode thickness variation on operation of capacitive deionization*. Electrochimica Acta, 2012. **75**: p. 148-156.
13. Tang, W., et al., *Fluoride and nitrate removal from brackish groundwaters by batch-mode capacitive deionization*. Water research, 2015. **84**: p. 342-349.
14. Avraham, E., et al., *Limitations of charge efficiency in capacitive deionization II. On the behavior of CDI cells comprising two activated carbon electrodes*. Journal of the Electrochemical Society, 2009. **156**(10): p. P157-P162.
15. Saleem, M.W. and W.-S. Kim, *Parameter-based performance evaluation and optimization of a capacitive deionization desalination process*. Desalination, 2018. **437**: p. 133-143.
16. Kang, J., et al., *Comparison of salt adsorption capacity and energy consumption between constant current and constant voltage operation in capacitive deionization*. Desalination, 2014. **352**: p. 52-57.
17. Wang, L. and S. Lin, *Membrane Capacitive Deionization with Constant Current vs Constant Voltage Charging: Which Is Better?* Environmental Science & Technology, 2018. **52**(7): p. 4051-4060.
18. Johnson, A. and J. Newman, *Desalting by means of porous carbon electrodes*. Journal of the Electrochemical Society, 1971. **118**(3): p. 510-517.
19. Hawks, S.A., et al., *Quantifying the flow efficiency in constant-current capacitive deionization*. Water research, 2018. **129**: p. 327-336.



20. Zhao, R., et al., *Optimization of salt adsorption rate in membrane capacitive deionization*. Water research, 2013. **47**(5): p. 1941-1952.
21. Zhao, R., et al., *Energy consumption in membrane capacitive deionization for different water recoveries and flow rates, and comparison with reverse osmosis*. Desalination, 2013. **330**: p. 35-41.
22. Jande, Y. and W.-S. Kim, *Predicting the lowest effluent concentration in capacitive deionization*. Separation and Purification Technology, 2013. **115**: p. 224-230.
23. Zhao, R., et al., *Optimization of salt adsorption rate in membrane capacitive deionization*. Water Research, 2013. **47**(5): p. 1941-1952.
24. Hawks, S.A., et al., *Quantifying the flow efficiency in constant-current capacitive deionization*. Water Res, 2018. **129**: p. 327-336.
25. Jande, Y.A.C. and W.S. Kim, *Desalination using capacitive deionization at constant current*. Desalination, 2013. **329**: p. 29-34.
26. Zhao, R., P.M. Biesheuvel, and A. van der Wal, *Energy consumption and constant current operation in membrane capacitive deionization*. Energy & Environmental Science, 2012. **5**(11): p. 9520-9527.
27. Katritsis, D., et al., *Wall Shear Stress: Theoretical Considerations and Methods of Measurement*. Progress in Cardiovascular Diseases, 2007. **49**(5): p. 307-329.



Derailment accidents due to SPAD in railways: Improving modeling and analysis of risks quantification

Qamar Mahboob¹, Awais Ahmad Khan¹, Ghulam Moeen Uddin¹, Attiq ur Rehman¹

¹-Department of Mechanical Engineering of UET Lahore.

*Corresponding Author: qamar.mahboob@uet.edu.pk

Abstract:

Modern railway systems are equipped with automatic signaling systems that are highly reliable, but safe train movement is still relying upon train driver who is reading and responding to caution and danger signals. The derailment accidents due to signal passed at danger (SPAD) by train drivers need to be modeled carefully. The classical ways of modeling risks in railway engineering systems are Fault Tree (FT) and Event Tree (ET). The causes of SPAD by drivers in are modeled by using FT. A risk model is constructed by combining the FT with the ET, for the accidents due to train derailment in British railways. This FT and ET based risk model for human error analysis in railway system has limitations. The Bayesian Networks (BN) modeling technique is probabilistic and represents the influences between the variables that are uncertain. An improved risk model will be obtained by mapping FT and ET into BN. The two methods of modeling risks will be compared with respect to the required modeling efforts, the information obtained from the analysis and the visualization of the model.

Keywords: safety risk model; dependence modelling; railway operation

1. Introduction

Drivers of trains have to follow signals in order to proceed further and switch railway lines. These signals ensure adequate distance between the trains and avoid collisions. Driver is not allowed to pass the signal on seeing the red light until it turns to green. But there are cases when drivers do not stop before the red light and passes the signal at danger, called SPAD (signal passed at danger). This SPAD could lead to a train derailment and a more dangerous situation could arise if there is an immediate conflict with another train. There may be several causes of the SPAD. The train driver may makes error in reading and responding the cautionary signals, faulty brakes, inadequate train speed, track alignment, and faulty signals are some of the causes of SPAD. The causes of SPAD related to drivers may be categorized into (1) misjudgments (2) misreading (3) disregarded and (4) miscommunication (Dhillon 2007). According to the data provided by (Ford 2001) 58% of SPAD caused by train drivers are "disregarded". He further divides disregarded SPAD: reaction to a caution signal (24%), check signal aspect (16%), signal location (7%), expecting signal clearance in advance (5%), and violating signals (6%). It implies that reaction to a caution signal (24%) is one of the main causes of SPAD. This paper presents an improved approach to model the derailment risks arising from reaction to a caution signal. Different methods have been proposed for modeling human errors in transportation. For example, (Whittingham 2004)

uses Human Reliability Event Tree (HRET) to analyze the errors caused by train drivers. The most common methods used for the purpose of modeling causes and consequences of undesired events called "Top Events" are Fault Tree (FT) and Event Tree (ET) methods. However, these methods have problems,

- in establishing the dependence among the events in the model,
- multistate representations of the events in the model,
- dynamic states of the system

Therefore, an alternative modeling approach called "Bayesian Networks (BN)" is proposed herein. BN methodology has recently been used for a number of applications in engineering risk analysis (Straub and Kiureghian 2010), (Mahboob 2014) (Mahboob and Zio 2018), and (Lampis und Andrews 2009). BN can give an improved solution to the problem of determining the risks arising from SPAD committed by train driver. As far as the knowledge of the authors, no much effort has been made to use BN in modeling human errors in railway transport. The risk model based on FT for SPAD due to human errors and the ET for derailment caused by this SPAD is constructed. The scope of this risk model is limited to the data of British railways. Then this risk model is mapped into BN in order to have an improved risk model for the problem. The advantages of BN methodology over FT and ET methodologies in analyzing the SPAD risks in relation to "reaction to a caution signal" are presented.



2. Problem Description

Modern railway systems are equipped with intelligent signaling systems that are highly reliable. They work in a way that if some fault occurs the signaling system reaches to a state at which the train movement is stopped. In spite of high reliable signaling systems, safe train movement is still relying upon train driver who is reading and responding to caution and danger signals. The total probability that a train driver will pass signal at danger is calculated by considering the ways of happening SPAD. For a driver to commit a SPAD he has to pass a series of caution signals. In our case, from British railways, a driver will have to pass double yellow, single yellow and red signals to commit SPAD, shown in Figure 1. It implies that there is a dependency between the signals, hence there exist 2^3 ways of dependence among the signals.

F_8 = driver acknowledges double yellow, ignores single yellow and stops red signal

The SPAD happens once the driver passes red signal. If the driver does not pass red signal (regardless of acknowledgement or ignorance on double yellow or single yellow signals) it is not treated as SPAD. Thus, failure dependence in the failure ways from $F_5 - F_8$ is not important as they will not lead to a SPAD. In this work, only the failure ways from $F_1 - F_4$ are considered for SPAD error analysis. The consequences of SPAD depend on operation and track conditions. The SPAD can lead to the train derailment, head on collision with another train, collision with track side installations, infrastructure and so on.

The classical ways of modeling the causes and

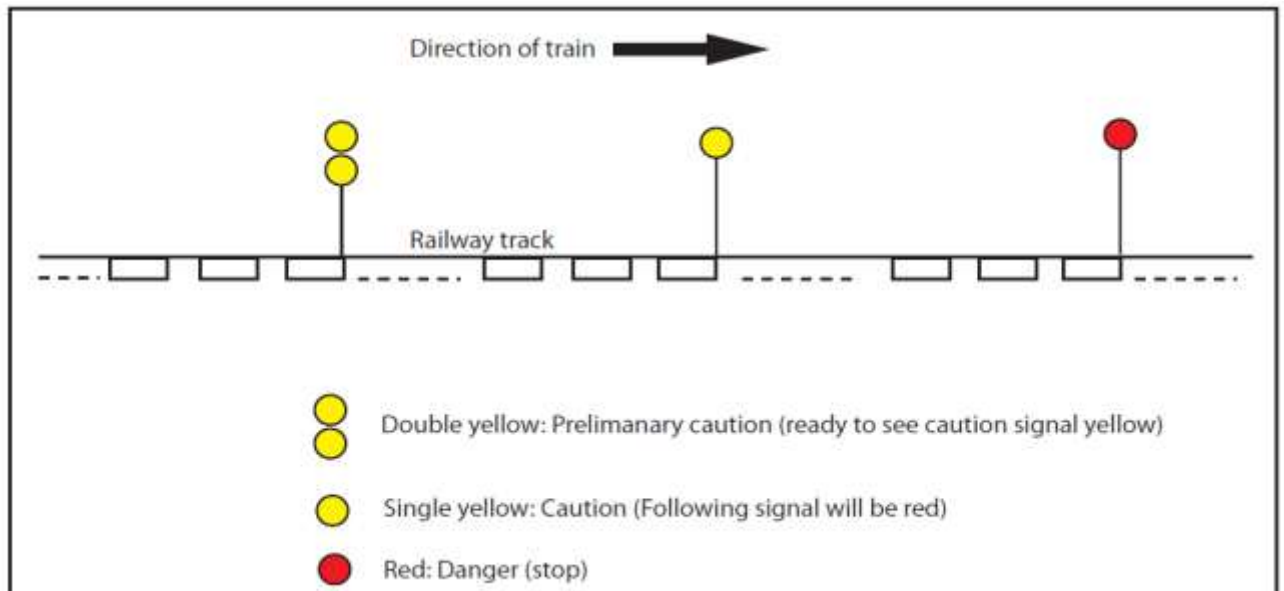


Figure 1. Scheme of cautionary and danger signals

F_1 = driver ignores double yellow and single yellow and passes red signals

F_2 = driver acknowledges double yellow, ignores single yellow and passes red signals

F_3 = driver acknowledges double and single yellow and passes red signals

F_4 = driver ignores double yellow, acknowledges single yellow and passes red signals

F_5 = driver acknowledges both double and single yellow signals and stops at red signal

F_6 = driver ignores double yellow and acknowledges single yellow and stops at red signals

F_7 = driver ignores double and single yellow and stops red signal

consequences are FT and ET methodologies. In FT methodology we usually consider that all basic events (that trigger the TE) are statistically independent. However, this is not usual in technical systems as there are statistical dependences among the basic events due to dependent failures. Statistical dependence among basic events means that happening of one failure will lead to an increased/decreased tendency for another component to fail. The dependence will be positive if the failure of component leads to an increased tendency for another component to fail, and vice versa. For example, the probability of SPAD will be high if the driver ignores double yellow. This probability of SPAD will be higher if driver continues to ignore next cautionary signal ‘single yellow’. It implies that there is dependence among the signals. If we neglect this dependence then the probability of the SPAD will be,



- Overestimated if the signals are connected in a series system
- Underestimated if the signals are connected in a parallel system

One limitation in FT analysis is that it treats the events as binary events (fail – success) and may therefore fail to address other states of system and its components. When we consider different types and quantities of failures and their effects on the whole system then performance ranking of the system and its components becomes important for making decisions on system safety, operation and maintenance. The system can't be classified as (1) working and (2) fail on the basis of evidence. For example, failure ways $F_5 - F_8$ do not lead to SPAD and system will work well, but failures are still. Especially, system becomes less reliable when driver ignores both double and single yellow (F_7). Therefore, there may be some other states e.g. safe and reliable, unsafe and reliable, unsafe and unreliable, and failed. In other words, multi-state failures connected with the SPAD will lead to the multi-state failure conditions of the railway system. If we want to introduce multi-states of the SPAD in the FT then we need copies of the FT. For example, one additional state of the SPAD will require one duplicate of the FT. Hence, number of duplicates is proportional to the additional states of the events in the FT, and analysis is made by combining all duplicates with an OR gate. In this way, eight FTs will be required for eight ways of failures; however, we will limit our analysis up to four ways. This duplication of the fault tree for the purpose of multi-states in the FT increases the number of possible network structures exponentially. It makes the visualization of the FT model complex and requires more computation efforts. Moreover, FT model has difficulties in analyzing systems with dynamic properties; it again refers to the multi-state representation of failures. The ET for the consequences of the train derailment due to SPAD has the same problems as mentioned for the FT. In this paper, we propose to address these limitations for the causes of SPAD due to reaction to a caution signal and the consequences of the train derailment due to SPAD.

3. Fault tree model for the causes of SPAD

The usual technique used for schematic representation of a technical system for the purpose of reliability and safety analysis is FTA (Fault Tree Analysis). It is a top-down approach which provides a logical framework for understanding the ways in which a system can fail. This is a deductive system analysis method in which we postulate the undesired event and try to find out the modes of system or its

components that contribute to it (Limnios 2007). An unwanted event, also called the Top Event (TE) is defined and the system is analyzed in the context of its design, operation, maintenance and safety requirements and environment to find all combinations of basic events that will lead to the occurrence of the Top Event (Stewart und Melchers 1997). The basic assumptions of the standard FTA techniques are (Xing und Amari 2008)

- events are binary events – meaning that working or failed;
- events are statistically independent;
- logical gates are used to represent the relationship between events and causes;
- TE is the root of Fault Tree.

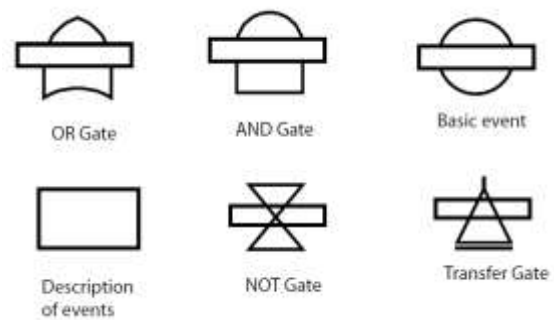
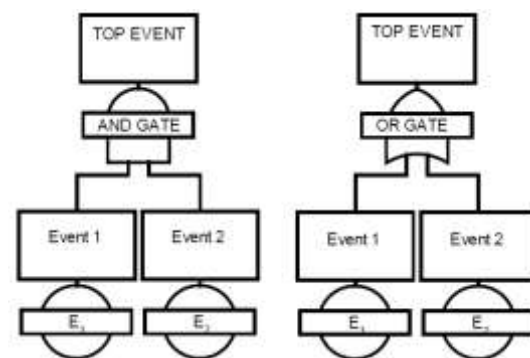


Figure 2. Description of symbols in the FT of SPAD



(a) Single AND gate (b) Single OR gate

Figure 3. Logical frameworks

The graphical symbols that show the relation among the events and the causes are called logical gates, shown in Figure 2 and description of each is given below.

OR gate: output is true if any one of the inputs is true

AND gate: output is true if all of the inputs are true

NOT gate: output is true if all inputs are NOT true

TRANSFER gate: repeats logic gate in the same FT



Basic event: a triggering event for hazard/TE, i.e. human error, basic machine component, environment etc.

Description of event: explains the events in the FT
The output from a logical gate is determined by the input states. The probability that the TE occurs for a single AND gate shown in Figure 3(a) is calculated as,

Suppose, $P_0(t) =$

$\Pr(\text{The Top Event occurs at time } t)$

$$p_i(t) = \Pr(\text{Basic event } i \text{ occurs at time } t)$$

Let $E_i(t)$ denote that the event E_i occurs at time t ,

and $p_i(t) = \Pr(E_i(t))$ for $i = 1, 2, \dots$

The Top Event probability is,

$$P_0(t) = \Pr(E_1(t) \cap E_2(t)) \quad (1)$$

In case we have m basic events that are statistically independent then Eq. (1) becomes,

$$P_0(t) = \prod_{j=1}^m p_j(t) \quad (2)$$

Now considering the single OR gate in Figure 3(b), the Probability that the TE occurs when the basic events are independent,

$$\begin{aligned} P_0(t) &= \Pr(E_1(t) \cup E_2(t)) \quad (3) \\ &= \Pr(E_1(t)) + \Pr(E_2(t)) - \Pr(E_1(t) \cap E_2(t)) \\ &= p_1(t) + p_2(t) - p_1(t) \cap p_2(t) \\ &= 1 - ((\overline{p_1(t)}) \cap (\overline{p_2(t)})) \end{aligned}$$

For m statistical independent events we get

$$P_0(t) = 1 - \prod_{j=1}^m (1 - p_j(t)) \quad (4)$$

Based on the ways and failure criteria described in Section 2 the fault tree for the four ways of SPAD ($F_1 - F_4$) is constructed and is shown in the lower part of the risk model in Figure 4. The mathematical representation of the FTA becomes,

$$\Pr(\text{SPAD}) = \Pr(F_1 \cup F_2 \cup F_3 \cup F_4) \quad (5)$$

$$= 1 - \Pr(\overline{F_1} \cap \overline{F_2} \cap \overline{F_3} \cap \overline{F_4}) \quad (6)$$

$$= 1 - \Pr(\overline{F_1}) \cdot \Pr(\overline{F_2}) \cdot \Pr(\overline{F_3}) \cdot \Pr(\overline{F_4}) \quad (7)$$

The probabilities of the basic events in the FT are taken from (Whittingham 2004) where HRET for the same problem of SPAD is constructed. These probabilities of the events are based on the study of SPAD carried out in 2001, for UK railways. However, this HRET only considers three scenarios (F_1 to F_3) therefore probabilities of the basic events for F_4 are interpolated. The total SPAD probability is the joint probability of a number of errors (made by the driver) in the FT. Based on the probabilities given in the Table 1 the total probability of SPAD (Top Event) is $8.0634E - 05$. It means that there is a possibility of an average one SPAD per driver if he encounters 12,402 red signals. This result is useful in making decision on the system safety.

4. EVENT TREE MODEL OF THE CONSEQUENCES

ET analysis is used to determine the consequences of the TE. The event scenarios produced by TE are drawn. A number of possible consequences may arise from an ET. These may include damage to the property, human life and economy. In ET all event scenarios are connected with an OR gate. Hence, the probability of the TE is calculated as shown in Eq (2).



Table 1. Probabilities of the basic events in the FTA of SPAD (Whittingham 2004)

Event name	Description	Probabilities (without dependence among signals)	Probabilities (with dependence among signals)
E_1	Driver ignores double yellow	0.0005	0.0005
E_2	Driver ignores single yellow given E_1	0.0005	0.1433
E_3	Driver passes red signal given E_1 and E_2	0.0005	0.5003
E_4	Driver ignores single yellow given \bar{E}_1	0.0001	0.0001
E_5	Driver passes red signal given E_4 and \bar{E}_1	0.0001	0.1429
E_6	Driver passes red signal given \bar{E}_1 and \bar{E}_4	0.00001	0.00001
E_7	Driver passes red signal given E_1 and \bar{E}_2	0.0479	0.0479

The ET for the consequences of train derailment was constructed by (Bearfield und Marsh 2005), based on the study carried out in 2001 for UK railways. The probabilities of the seven events and twelve consequences ($A_1 - A_{12}$) as a part of ET are shown in the upper part of risk model in Figure 4. The severity of consequences increases from A_1 to A_{12} . The consequences in Figure 4 only consider train derailment on open areas of track, therefore, no scenarios for the bridges, tunnels and others are considered. These derailment accidents on open track happen due to many TE and SPAD may be one of them. For example, when driver passes red signal at danger the derailment may occur due to,

- switches ahead not set for the train that has committed SPAD
- immediate conflict with another train or trains
- conflict with maintenance machinery and barriers

The consequences drawn in the ET for train derailment are combined with the causes of SPAD. When combination of ET and FT takes place it is called a safety risk model for a system (Sotera 2006) & (RS 2001).

5. FT and ET based Risk model for derailment accidents due to SPAD

Both the FT for the causes of the SPAD due to reaction to a caution signal and the ET for the consequences of the train derailment are constructed (1) for the same railway system and (2) in the same year. Hence, we combine both the FT and the ET in order to have a risk model for the specific causes and consequences. The risks model is shown in Figure 4. By combining the ET and FT of a system or subsystem the TE in the FT becomes the basic event of the ET. The TE is in the middle of the risk model. The causes of this SPAD are on the lower side of the TE and the consequences are on the upper side of the TE. There will be a change in the probabilities of the consequences ($A_1 - A_{12}$) with the change in the probabilities of the events in the FT and the ET. This risk model analyses the consequences of train derailment due to SPAD, result of the analysis is shown in Table 2. The limitations of the risk model are same as described for FT and ET. Hence, we propose BN methodology to address the limitations.

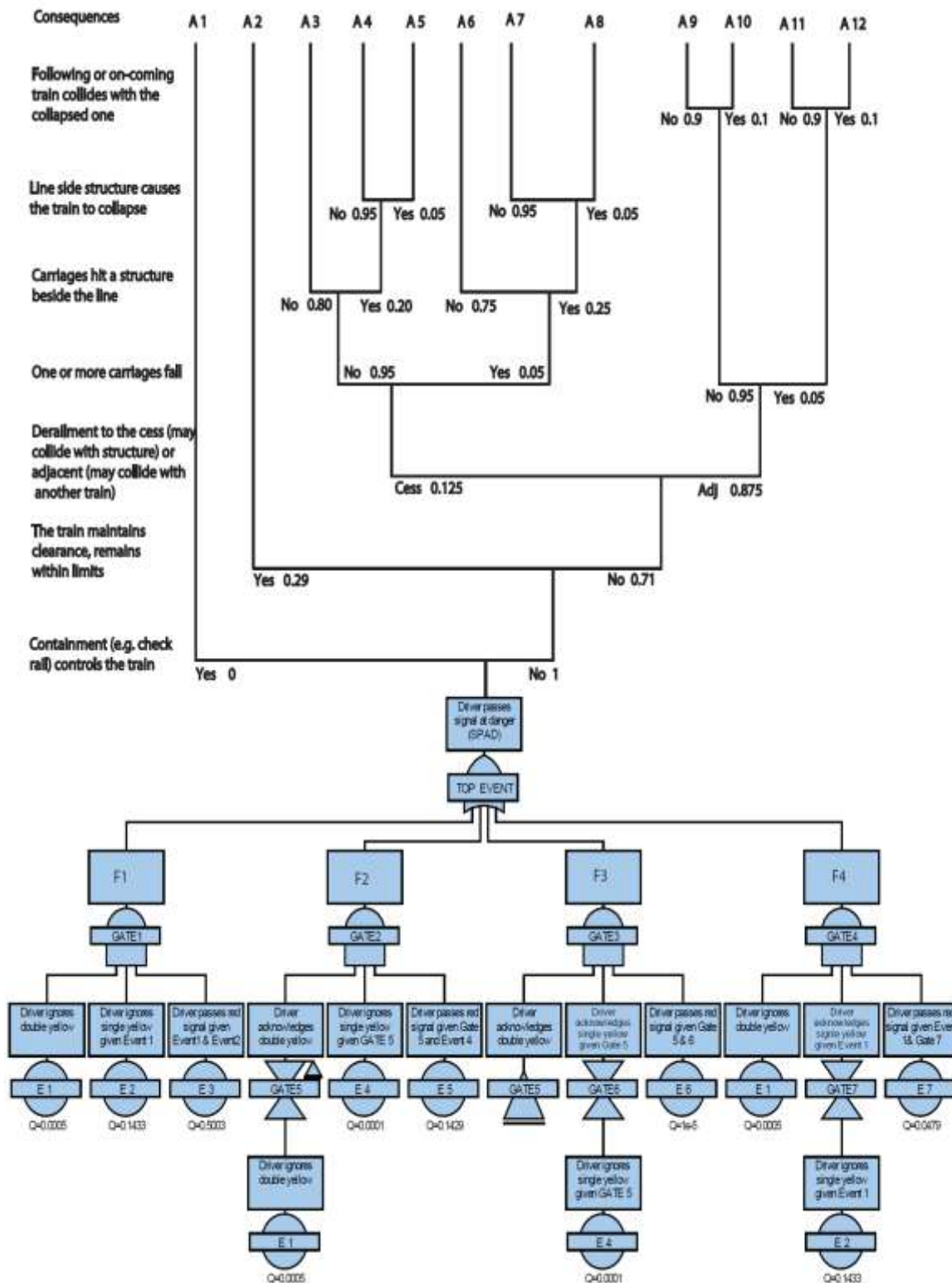


Figure 4. FT and ET based risk model for derailment accidents due to SPAD (Mahboob 2014)

6. Mapping of FT and ET based risk model into Bayesian Networks

BN is also called belief network, causal network, or influence diagram. The nodes in network are random variables and directed links between them

represent the causal relationship. The random variables represent a set of possible states of affairs, and a causal relation is used to determine how a change of certainty in one variable may change the certainty for other variables in the network. Each



node can be in various states; the number of states is selected by the risk analyst.

How elements of the causal network are dependent on each other and how information can flow in such a network is given by (Jensen und Nielsen 2007) and (Neapolitan 2003) and is explained below. If the state of the intermediate random variable is not known with certainty and evidence can be transmitted through a serial connection then it is called a serial connection. A serial connection is illustrated in Figure 5 (B). When this evidence can be transmitted through a diverging connection and the state of the common parent variable is not known with certainty it is called a diverging connection, shown in Figure 5 (D). Figure 5 (C) shows a converging connection in which evidence can be transmitted through a converging connection only if there is some information about the child variable or one of its descendants.

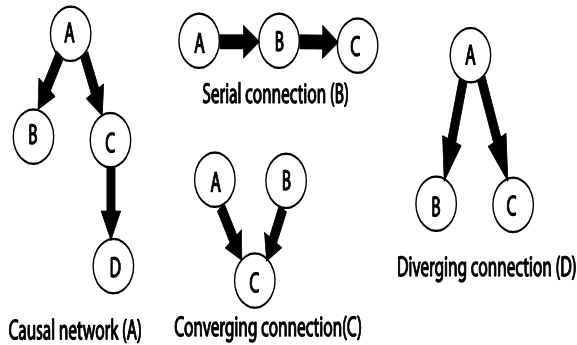


Figure 5. Types of connections in a BN

The random variables in the BN have a finite set of mutually exclusive states. A conditional probability table is attached with each random variable and each random variable is defined conditional on its parents. In Figure 5 (A) the nodes B and C are the children of A, which is parent of the formers. If variable A in Figure 5 has no parents, then the table reduces to the unconditional probability $\Pr(A)$. Prior probability $\Pr(A)$ must be specified because it is an integral part of reasoning about certainty. BNs are based on the d-separation properties of causal networks and directed links represent the dependence structure among the random variables.

Suppose we have a Bayesian network with random variables that are defined in a finite space $\mathbf{X} = [X_1, \dots, X_n]$. Each random variable X_i is independent of all other variables in the network if the values of the variables in its Markov blanket are known. Whereas, Markov blanket of variable X_i consist of its parents, its children and other parents of its children. The probability mass function (PMF) of each random variable is defined conditional on its parents, i.e., $p(x_1 | x_2, \dots, x_n)$ and the joint probability mass function $p(\mathbf{x})$ of a set of random variables \mathbf{X} is

derived by multiplying all dependent conditional probabilities.

$$p(\mathbf{x}) = p(x_1, x_2, \dots, x_n) \\ = p(x_1 | x_2, \dots, x_n) p(x_2 | x_3, \dots, x_n) \dots p(x_{n-1} | x_n) p(x_n)$$

The joint PMF for a BN can be generalized as,

$$p(\mathbf{x}) = p(x_1, \dots, x_n) = \prod_{i=1}^n p[x_i | pa(x_i)] \quad (8)$$

In the equation above, $pa(x_i)$ are set of realizations of the parents of variables X_i .

In a quantitative analysis, we must determine conditional probabilities for the states of events (random variables) given in the causal connections. To update these probabilities, we make use of the Bayes' rule. The new evidence on the variables can change the dependence among the variables in the BN.

Keeping in view the properties of the BN we transform the risk model into BN. For this, all the events in the risk model shown in Figure 4 are treated as random variables and the links among these variables are established as shown in Figure 6. The conditional probabilities for each variable in the BN are assigned.

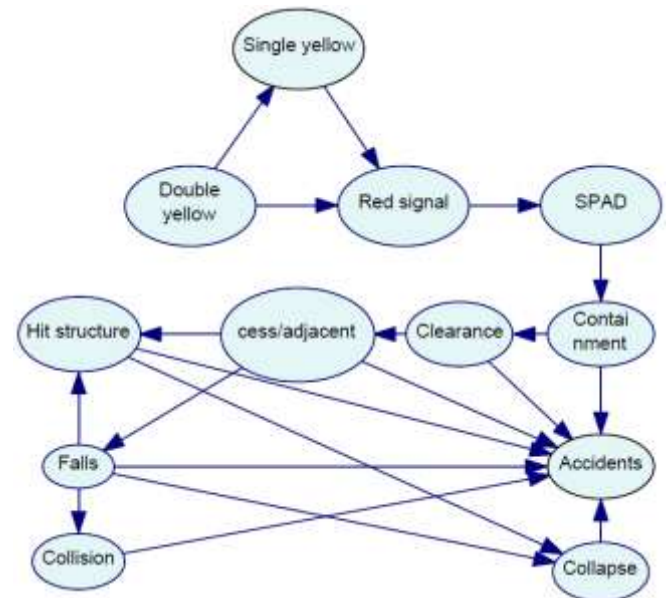


Figure 6. Bayesian Network based Risk Model for train derailment accidents due to SPAD

The two methods of modeling risks are compared with respect to the required modeling efforts, the



information obtained from the analysis and the visualization of the model.

7. RESULTS AND DISCUSSIONS

The results of the risk model are shown in Table 2 where derailment accidents are updated with the causes of SPAD due to driver's reaction to caution signal. The BN shown in Figure 6 has many advantages over FT and ET based safety risk model in Figure 4.

The BN risk model for the human error analysis for SPAD allows entering evidence. The probabilities in the BN are updated when new information is available. For example, when the driver acknowledges the single yellow after ignoring the double yellow, this information propagates through the BN and the probability of SPAD reaches to $3.0517202e - 005$. It means that the possibility of an average one SPAD per driver per year has reduced. In other words, an average one SPAD will be after encountering the 32,769 red signals. Consequently, the marginal probabilities of other variables in the BN are also updated. These results are useful in making more precise decisions concerning driver's training, replacement of signals, rolling stock, infrastructure and the safety of railway system.

- I. Information updating
- II. BN can well handle dependence among the
 - a. events in the risk model

The BN facilitates the complete and compact establishment of dependence among the signals without increasing the size of network exponentially, which is a big limitation in FT and ET methodologies. In the FT we need new logic gates or copies of FT for new dependences among the signals. However, the dependences among

Table 2. Probabilities of consequences for train derailment due to SPAD

<i>Deraulment Accidents</i>	<i>Probability with all causes of derailment</i>	<i>Probability with SPAD</i>	<i>Probability with SPAD after 5 years</i>
A1	0	0.9999	0.99891

A2	0.29	2.33e-05	0.000313
A3	0.06745	5.43e-06	7.287e-05
A4	0.016075	1.29e-06	1.730e-05
A5	0.000825	6.79e-08	9.109e-07
A6	0.003325	2.68e-07	3.595e-06
A7	0.001091	8.49e-08	1.138e-06
A8	5.54e-05	4.47e-09	5.993e-08
A9	0.531675	4.28e-05	0.000573
A10	0.050187	4.75e-06	6.376e-05
A11	0.027956	2.25e-06	3.020e-05
A12	0.00325	2.50e-07	3.356e-06

the signals with their states are managed in three nodes by the BN. In other words, the complete FT for SPAD is mapped into the part of the BN that consist of only three nodes. Similarly, the complete ET for the accidents due to train derailment is managed by the rest of nodes in the BN.

- III. Multistate representation of the events in the risk model

There are difficulties in analysis of a multi-state (non-binary) system by FT and ET. The size of FT and the ET is sometime difficult to manage when new states of the events are introduced in the risk model, and each state lead to a new cause or consequence of TE. BN has advantage to deal with the multi-states of the events in the BN. The four failure ways $F_1 - F_4$ involve different states (combination) of the signals in the FT. These states are managed by a considerably large FT than BN. Similarly, the same FT network will expand for the next $F_5 - F_8$ failures, whereas, BN manages them in the same network. Additionally, the node "Accidents" in the BN has all the twelve states of the consequences (A1 - A12) of the TE, whereas ET has 12 different branches for the same consequences.



IV. *Handles dynamic properties of the system and its components*

The learning towards recognition and acknowledgement of signals by the driver is a time taking phenomena. A driver travelling on a same route for many years will experience less SPAD than the drivers who are not travelling frequently on it. A young driver is more prone to SPAD than experienced. The SPAD as well as derailment accidents vary from one location to another depending upon the operation and infrastructure conditions. Therefore dynamic modeling is essential for the better analysis of risks. The FT and ET based risk model has complications in modeling the dynamic behavior of the system. A dynamic BN (DBN) consists of slices of BN connected by directed links (that represent time or space) in sequence. The structure and the conditional probability tables (CPT) for the BN model in each slice may be identical or different. For example, the condition state of the variable SPAD in each slice of BN may change due to lack of training for drivers and management control in the next slice. If this change is 0.1% in five years then the probability of SPAD will become 0.00108 after five years. In this case, driver has to face an average 926 red signals in order to experience one SPAD, new probabilities of the consequences are shown in Table 2. This example highlights the importance of dynamic modeling of the human errors in railway system which BN handles very well. Similarly, other variables in the BN can be modeled for different time and space steps.

V. *Modeling is flexible and easy*

BN modeling is flexible and easy in introducing/removing nodes and links among the nodes. The graphical representation of BN is easy to understand for a common man. It does not require knowledge of logic gates. Moreover, it can handle multiple TE, dependent components and systems in a compact way.

VI. *Combines systematic, factual and expert knowledge*

The FT analysis is mainly based on system knowledge; used for system design. The ways of system failure, based on design knowledge, are identified. Similarly, ET models an accident as a sequence of events that is mainly based on the system knowledge. Both the FT and ET do not explicitly represent the system state and its environment. The risk analysis of railway system becomes more challenging when its environment is changing from one location to another. Especially, the factual data; failures and repairs or reliability

data and the expert knowledge; learned from the history of the system by the maintenance engineers is neglected in the FT and ET based risk model. However, BN combines all three knowledge in order to have an improved risk analysis. In this way, a data of certain feature can be forced to include, if necessary. Because of this advantage, BN has potential to exploit all essential features of a problem. For example, reliability of a specific type of signal components or type of track may be included into the BN.

In contrary to the advantages, BN can only exploits the causal relations that are considered by its designer, not follow any pattern. Additionally, it requires the knowledge of Bayes theory. Due to lack of universal methods for constructing a network from (large amount of) data a BN considerably takes large efforts in its construction, especially when system is complex and more dependence among the system components is involved. In case of risk model for SPAD the expansion of BN depends on the choices of designer as which variables he wants to consider. Additionally, the computational time increases exponentially with respect to the number of random variables in the BN. The risk model for SPAD has small number of variables otherwise BN could be computationally demanding. Similarly, they have high memory demand for real-time applications and discretization of continuous random variables is also required. Future work should aim at extending the existing risk model for SPAD (1) by introducing other variables of interest in the SPAD risk model (2) to multiple causes of SPAD other than driver's reaction to a caution signal (3) other causes of derailments leading to accidents. The flexibility of the BN methodology allows these extensions. BN allows integrating the utility and decision nodes in the framework that further improves modeling. Furthermore, dynamic BN risk model for the presented framework and the proposed extensions are also part of future developments.

9. Conclusions

In this paper we have shown a combined usage of Fault Tree (FT) and Event Tree (ET) in order to model the consequences of train derailment caused by SPAD due to driver's reaction to a caution signal. FT provides a systematic way to identify the causes of Top Event (TE) whereas ET generates scenarios that could lead to different consequences. We have shown that the same risk model can be mapped into Bayesian Networks (BN), for an improved modeling of human error analysis for a railway system. We have compared both modeling techniques for special problem of SPAD. The dependence among the events, their multistate representations, concise visualization of large risk models, flexible and easy



way of modeling and better handling of dynamic states of the system are the advantages of BN framework. Keeping in view the advantages of BN methodology several extensions to the presented work can be made, risk and safety related issues can be better modeled in other areas of railway engineering systems.

REFERENCES

- [1]. Bearfield, G., and D. W. R, Marsh. "Generalising Event Trees using Bayesian Networks with a Case Study of Train Derailment." *24th International Conference on Computer Safety, Reliability and Security, SAFECOMP 2005*. LNCS 3688, 2005. 52-66.
- [2]. Dhillon, B.S. *Human Reliability and Error in Transportation Systems*. London: Springer, 2007.
- [3]. Ford, R. "Modern Railways." *The Forgotten Driver*, January 2001: 45-48.
- [4]. Jensen, Finn V., and Thomas D. Nielsen. *Bayesian Networks and Decision Graphs*. Berlin: Springer, 2007.
- [5]. Lampis, Mariapia., and John D. Andrews. "Bayesian Belief Networks for System Fault Diagnostics." *Quality and Reliability Engineering International*, 2009: 409-426.
- [6]. Limnios, Nikolaos. *Fault Trees*. London: ISTE Ltd, 2007.
- [7]. Mahboob, Q. *A Bayesian Network methodology for railway risk, safety and decision support*. Dresden: <https://nbn-resolving.org/urn:nbn:de:bsz:14-qucosa-138087>, 2014.
- [8]. Mahboob, Q., and E. Zio. *Handbook of RAMS in Railway Systems: Theory and Practice*. Boca Raton: CRC Press, 2018.
- [9]. Marsh, William., and George Bearfield. "Representing Parametrized Fault Trees Using Bayesian Networks." *SAFECOMP*. Heidelberg: Springer, 2007. 120-1333.
- [10]. NASA. *Fault Tree Handbook with Aerospace Applications*. Washington, DC: NASA Office of Safety and Mission Assurance, 2002.
- [11]. Neapolitan, Richard E. *Learning Bayesian Networks*. Illinois: Prentice Hall, 2003.
- [12]. RS, London. *Risk Profile Bulletin: Profile of Safety Risk on Railtrack PLC- Controlled Infrastructure. Issue 2*. London: RS, London, 2001.
- [13]. Sotera, Ltd. *Developing a location specific risk model for Irish rail*. 2006. <http://www.sotera.co.uk/pdf/Location%20specific%20risk%20model.pdf> (accessed February 9, 2010).
- [14]. Stewart, Mark G., and Robert E. Melchers. *Probabilistic Risk Assessment of Engineering Systems*. London: Chapman & Hall, 1997.
- [15]. Straub, D., and A. Der Kiureghian. "Bayesian Networks Enhanced with Structural Reliability Methods. Part B: Application." *Journal of Engineering Mechanics*, 2010: Trans. ASCE, in press.
- [16]. Whittingham, R.B. *The Blame Machine: Why Human Error Causes Accidents*. Oxford: Elsevier, 2004.
- [17]. Xing, Liudong, and Suprasad V. Amari. "Fault Tree Analysis." In *Handbook of Performability Engineering*, by Krishna B. Misra, 595-620. London: Springer, 2008.



Minimization of Warpage and Average Volumetric Shrinkage on a multi cavity Injection Molded Polymeric Nut using Taguchi Optimization Method

Bisma Ali¹*, Yasir Qayyum Gill¹

1- Department of Polymer and Process Engineering UET,

*Corresponding author: bismaali968@gmail.com

Abstract:

Injection molding of plastic is one of the most important polymer processing technique worldwide. But the quality and characteristics of the molded product depend upon various factors and processing conditions. The objective of this simulation was to determine the effect of average volumetric shrinkage and warpage on polymeric nut. Process parameters i.e. melt temperature, injection pressure and injection time were selected and their effects on average volumetric shrinkage and warpage on final part were analyzed. Taguchi design of experiment (DOE) was used for the generation of orthogonal arrays. Simulations were run according the arrays and average volumetric shrinkage and warpage were determined. S/N response was studied, and analysis of variance (ANOVA) was performed. It was observed that injection time has the most prominent effect on the volumetric shrinkage and warpage of the polymeric bolt.

Keywords: Taguchi DOE, Orthogonal Array, S/N ratio, ANOVA, multi Optimization

1. Introduction

Plastic injection molding is the most important molding process in polymeric industry. More than 70% of consumer products are made from plastic injection molding [1]. Injection molding has various advantages i.e. short cycle time, better mechanical properties, ease in process ability etc and they can be recycled[2]. Injection molding generally consist of four phases i.e. plasticizing phase, injection phase, packing phase and cooling phase. In plasticizing phase raw material mostly in pallets form is fed and heated to its melting temperature. During injection phase the melted polymer is injected into the cavity via sprue, runners and gate system. When filling is almost done packing phase starts to fill the remaining volume of the mold cavity to compensate for volumetric shrinkage during cooling phase. All the process parameters involved during processing have a significant effect on the final product dimension[3]. The dimensional stability of injection molded part depend on the material properties, process parameters, and mold design. The defects in dimensional stability results in shrinkage, warpage, sink marks, weld lines, meld lines etc. Among them volumetric shrinkage and warpage are most common[4]. Sometimes the formation of these defect is inevitable. In that case such parameters should be selected which has least effect on products dimensions. Packing pressure, packing time, injection pressure, in injection time and cooling time has a prominent effect on the shrinkage and warpage behavior[5]. In polymers, shrinkage is the most important parameter and it depend on the morphology of the polymer. Semi crystalline polymers shrink more than amorphous polymers because of the closely packed structure. Process parameter i.e. melt and mold temperature, holding time and pressure have a prominent effect on

shrinkage[3]. Shrinkage is related to reduction in volume of the product and it mainly depends on the materials properties. When the part is demolded a prominent shrinkage and reduction in volume is observed because chain get time to relax. This can be reduced by increasing the injection pressure during packing phase [6]. Warpage occur due to residual stresses in the molded part and these stresses are due to non-uniform shrinkage in the final product. This non-uniform shrinkage can be due to many reasons i.e. uneven pressure distribution, uneven cooling, mold design, processing conditions etc[7]. Warpage is more prominent in parts in which the area is larger than the part thickness[8]. To control warpage, initial process parameter is the critical step and require hit and trail and research[9]. Shrinkage and warpage also depend on the mold cavity, runner and mold design and the manufacturing process[8]. Warpage and sink marks can cause change in the final product design on cooling. In this study, melt temperature, injection pressure and injection time were selected because they have most prominent effect on the shrinkage and warpage.

2. Taguchi Method

Taguchi method is the most widely used optimization method for determining the performance and characteristic of various plastic part before running the actual molding process. This method provides the range of optimal values for the selected parameters. It is the most simple and effective approach and is used mostly in the designing of high quality and high performance parts[10].

Taguchi method is based on three phases i.e. planning, experimental and analysis. These phases include



formation of Orthogonal Array (OA), signal to noise (S/N) ratio and analysis of variance (ANOVA).

Orthogonal arrays provide the most suitable combinations for the selected parameters. This can reduce research and development cost by giving the optimal result of various parameters at different levels by running few simulations. In this method, the selection of range for the processing parameter is the most critical step. The design of orthogonal arrays and the response depend upon the selection of the processing conditions[11]. Most commonly L_9 and L_{18} OA are used. L_9 OA contain four processing parameters at three different levels[7]. Whereas, L_{18} OA study five parameters at three different levels[10].

Taguchi method also use signal to noise ratio for quality control and characteristics analysis. S/N ratio is classified into three stages i.e. smaller the better, nominal the best, larger the better. As in most plastic parts it is desired that response i.e. warpage, shrinkage, sink marks etc should be as low as possible. For this smaller the better is preferred. In the same way where high response is required i.e. tensile strength, flexural strength, hardness, tear strength etc, larger the better is the best choice for better quality and characteristics of final part. For process where intermediate properties are required nominal the best is the right choice[10]. Finally, ANOVA is used for the determination the percentage contribution of each factor on the response being studied[7].

3. Experimental details

3.1 Part selection

Polymeric nut was selected because of its wide range of applications in electrical insulations as polymers are insulators in nature. They are mainly used in house hold applications i.e. washing machines, automotive parts etc as a fitting material. Nuts are usually made of metals, but plastics nuts are now in demand because they are light in weight and show properties nearly equal to metals.

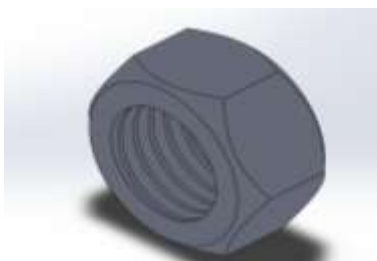


Figure 1. Plastic Bolt

3.2 Material Selection

Nylon (manufactured by A Schulman) also known as Polyamide was selected for the analysis. Nylon is the

most widely used plastic worldwide. Nylon is used because of its better wear properties, light weight, weather resistant, inert and non-toxic nature. Nylon can be used at high temperature. Due to its better heat stability, it can be retain it properties upto 185°C.

Table 1 Properties of PA [12]

Nylon(Polyamide)	Properties
Density	1.13 - 1.35 g/cm ³
Melting point	190-350°C
Mold temperature	30-50°C
Elongation at break	15-45%
Thermal expansion coefficient	80×10^{-6}
Tensile strength	90-185 N/mm ²
Glass transition temperature	45°C

4. Mold Flow Simulation

4.1. Selection of Orthogonal Array

In this study L_9 orthogonal array was preferred as there are three parameters and three levels. Complete analysis require $3^3=27$ experimental runs which involve high research and development cost[7]. These orthogonal arrays reduce the full factorial design to number of combinations at which simulation will give best results. Taguchi optimization can be performed using *Minitab Statistical software*. Melt temperature, injection pressure and injection time were the selected processing parameters. And their effect on the injection molded part was studied.

Table 2 Processing parameters and levels

Level	Melt temperature	Injection pressure	Injection time
1	230	70	3
2	240	80	4
3	250	90	5



Based upon these parameters and level, L_9 was most suitable orthogonal array which provide nine different combinations given in table 3. Running these combinations on *Moldflow Insight simulation software* will give the value of average volumetric shrinkage and warpage.

Table 3 Array formed using Minitab software

No. of trial	Melt temperature	Injection pressure	Injection time
1	230	70	3
2	230	80	4
3	230	90	5
4	240	70	4
5	240	80	5
6	240	90	3
7	250	70	5
9	250	80	3
10	250	90	4

On running the simulations, following values of average volumetric shrinkage and warpage were obtained given in table 4.

Table 4 Average volumetric shrinkage and warpage obtained after simulations

No. of trials	Average volumetric shrinkage	Warpage
1	6.23	0.195
2	9.08	0.188
3	6.20	0.195
4	6.27	0.195
5	5.87	0.186
6	6.78	0.207
7	7.09	0.215
8	7.16	0.216
9	7.17	0.216

5. Results & Discussion

5.1. S/N Response

Signal to noise ratio was used for quality characteristics. Here average volumetric shrinkage and warpage was selected so smaller the better was the right choice as minimum value of volumetric shrinkage and warpage was required[1]. The S/N response is given in table 5. S/N response can be mathematically calculated from formula given in equation 1.

$$S/N = -10 \log_{10}(\text{MSD}) \quad (1)$$

Where MSD is mean square deviation for the response parameter being studied.

MSD for smaller the better can be calculated from formula given in equation 2.

$$\text{MSD} = (y_1^2 + y_2^2 + y_3^2 \dots) / n \quad (2)$$

MSD for nominal the best can be calculated from formula given in equation 3.

$$\text{MSD} = ((y_1 - m)^2 - (y_2 - m)^2 + \dots) / n \quad (3)$$

MSD for larger the better can be calculated using equation 4.

$$\text{MSD} = (1/y_1^2 + 1/y_2^2 + 1/y_3^2 \dots) / n \quad (4)$$

y_1, y_2, y_3 and so on = experimental result from simulation

The S/N response for volumetric shrinkage and warpage is represented by S/N_A and S/N_B , respectively. The sum of signal to noise response for average volumetric shrinkage and warpage is given as S/N_{AB} in table 5.



Table 5 S/N response for average volumetric Shrinkage and Warpge

No. of trials	Melt temperature	Injecti on Pressure	Injection time	Average volumetric shrinkage	S/NA	Warpge	S/N _B	S/N _{AB}
1	230	70	3	6.230	-15.8898	0.1950	14.1993	-1.690
2	230	80	4	9.080	-19.1617	0.1880	14.5168	-4.644
3	230	90	5	6.202	-15.8506	0.1950	14.1993	-1.651
4	240	70	4	6.270	-15.9454	0.1947	14.2127	-1.732
5	240	80	5	5.873	-15.3772	0.1858	14.6191	-0.758
6	240	90	3	6.775	-16.6182	0.2068	13.6890	-2.929
7	250	70	5	7.094	-17.0178	0.2147	13.3634	-3.654
8	250	80	3	7.155	-17.0922	0.2156	13.3270	-3.765
9	250	90	4	7.165	-17.1043	0.2165	13.2908	-3.813

Main effect plots were generated for each response and combined response was studied. Main effects plots for average volumetric shrinkage, warpge and for both average volumetric shrinkage and warpge is given in figure 2,3 and 4 respectively.

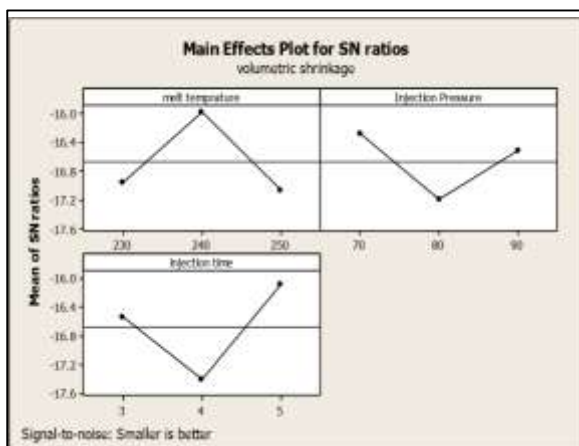


Figure 2. Main effect plots for average volumetric shrinkage

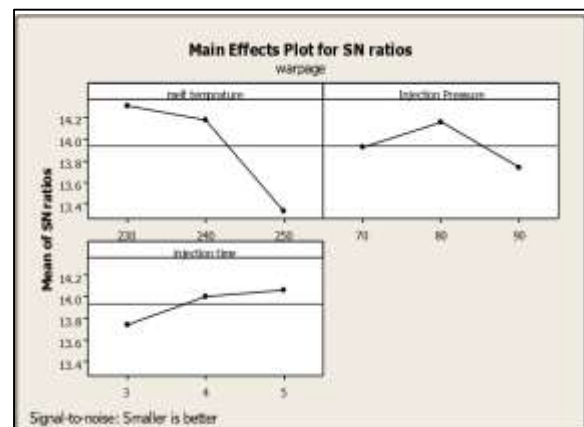


Figure 3. Main effects plots for warpge

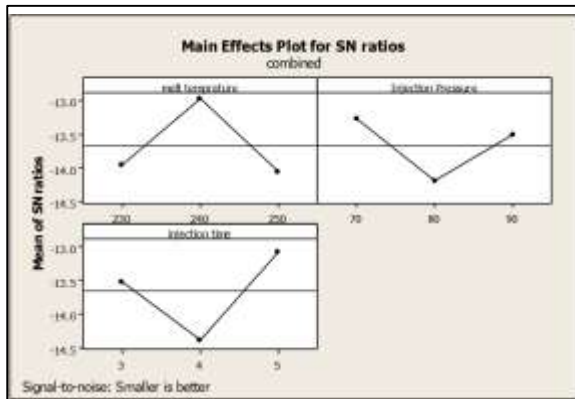


Figure 4. Main effect plots for combined response

5.2. Verification test

From the above graph for combined S/N response for Shrinkage and Warpage, the highest point on each graph will give the optimized level for melt temperature, injection pressure and injection time. The optimized level for melt temperature was 240°C, injection pressure was 70 MPa and injection time was 5 seconds. Another simulation was run with this combination of optimized array and this will give the optimum level of shrinkage and warpage in the polymeric nut.

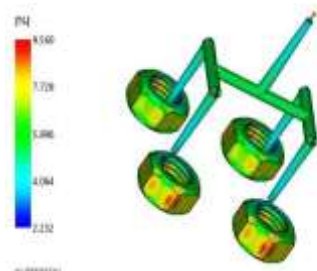


Figure 5. Volumetric shrinkage at optimum level

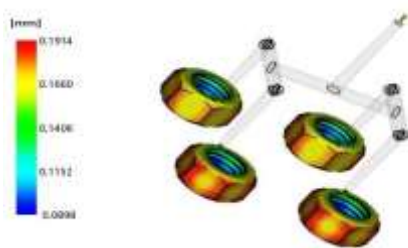


Figure 6. Warpage analysis at optimum level

After running the optimized simulation, the value of average volumetric shrinkage and warpage was determined. Response table was calculated for both warpage and volumetric shrinkage is given in table 6 and 7.

Table 6 S/N response table for warpage

level	Melt temperature	Injection pressure	Injection Time
1	14.31	13.92	13.74
2	14.17	14.15	14.01
3	13.33	13.73	14.08
Delta	0.98	0.43	0.32
Rank	1	2	3

Main effect plots were generated for each response and combined response was studied. Main effects plots for average volumetric shrinkage, warpage and for both average volumetric shrinkage and warpage is given in figure 2,3 and 4 respectively.

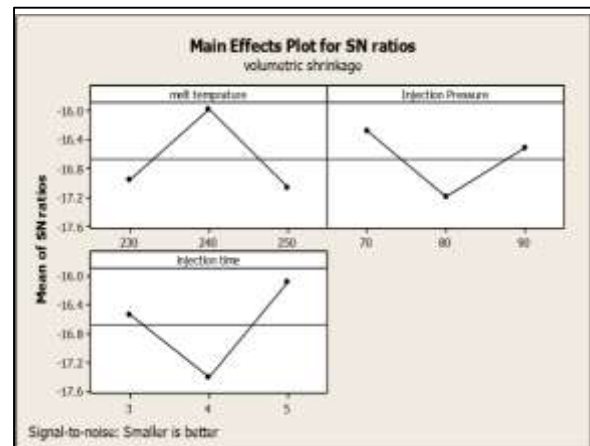


Figure 2. Main effect plots for average volumetric shrinkage

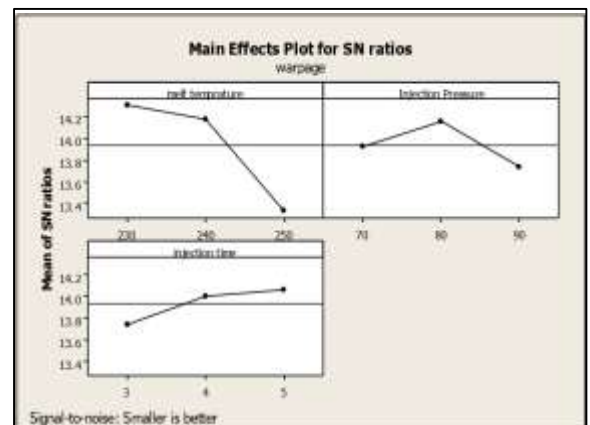


Figure 3. Main effects plots for warpage

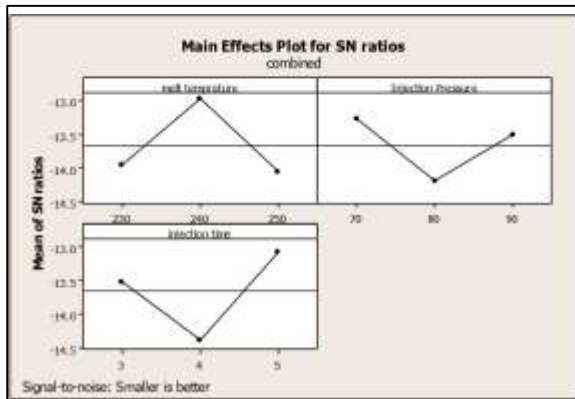


Figure 4. Main effect plots for combined response

5.3. Verification test

From the above graph for combined S/N response for Shrinkage and Warpage, the highest point on each graph will give the optimized level for melt temperature, injection pressure and injection time. The optimized level for melt temperature was 240°C, injection pressure was 70 MPa and injection time was 5 seconds. Another simulation was run with this combination of optimized array and this will give the optimum level of shrinkage and warpage in the polymeric nut.

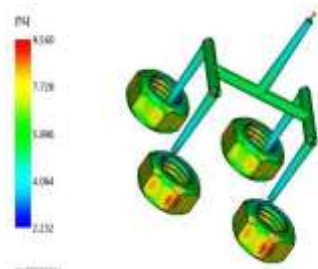


Figure 5. Volumetric shrinkage at optimum level

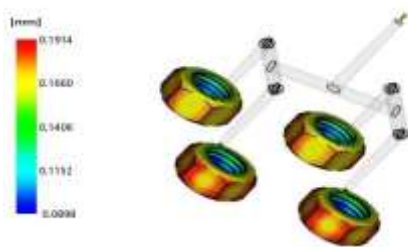


Figure 6. Warpage analysis at optimum level

After running the optimized simulation, the value of average volumetric shrinkage and warpage was determined. Response table was calculated for both warpage and volumetric shrinkage is given in table 6 and 7.

Table 6 S/N response table for warpage

level	Melt temperature	Injection pressure	Injection Time
1	14.31	13.92	13.74
2	14.17	14.15	14.01
3	13.33	13.73	14.08
Delta	0.98	0.43	0.32
Rank	1	2	3

Table 7. S/N Response table for average volumetric shrinkage

level	Melt temperature	Injection pressure	Injection Time
1	-16.97	-16.28	-16.53
2	-15.98	-17.21	-17.4
3	-17.07	-16.52	-16.08
Delta	1.09	0.93	1.32
Rank	2	3	1

5.4. Analysis of Variance (ANOVA)

Analysis of variance (ANOVA) was performed for the conformation of test parameters selected and the percentage contribution of each parameter was determined. ANOVA gave the degree of freedom, sequential square, adjusted square, %age contribution values and error given in table 9.

From table generated from ANOVA, percentage P factor was most important as it gives information about each factor contribution on the response being studied [10]. For calculation of P the formula was used given in equation 5 [13].

$$\%P = \frac{Seq SS}{SST} \times 100 \quad (5)$$



Table 8. ANOVA for Warpage

sources	DF	Seq SS	Adj SS	Adj MS	F	P	%P
Melt temperature	2	1.441	1.441	0.72	0.52	0.656	19.6831
Injection Pressure	2	1.165	1.165	0.583	0.42	0.702	15.91313
injection time	2	1.969	1.969	0.985	0.72	0.582	26.89523
ERROR	2	2.746	2.746	1.373			37.50854
TOTAL	8	7.321					62.49146

Table 9. ANOVA for average volumetric shrinkage

sources	DF	Seq SS	Adj SS	Adj MS	F	P	%P
Melt temperature	2	0.0009289	0.000929	0.000465	3.627	0.027	78.36173
Injection Pressure	2	0.0001393	0.000139	6.96E-05	5.44	0.155	11.75131
injection time	2	0.0000916	9.16E-05	4.58E-05	3.58	0.218	7.727349
ERROR	2	0.0000256	2.56E-05	1.28E-05			2.159609
TOTAL	8	0.0011854					97.84039

Table 10. ANOVA for both Average volumetric shrinkage and warpage

sources	DF	Seq SS	Adj SS	Adj MS	F	P	%P
Melt temperature	2	2.174	2.174	1.087	0.56	0.642	21.391
Injection Pressure	2	1.383	1.383	0.692	0.35	0.738	13.608
injection time	2	2.705	2.705	1.353	0.69	0.590	26.616
ERROR	2	3.900	3.900	1.950			38.385
TOTAL	8	10.163					61.615

The rank value from response table showed that which factor has the highest effect on the response being studied i.e. warpage and shrinkage. 1 being the highest parameter and 3 being the lowest. For shrinkage, melt temperature and for warpage, injection time has the highest effect and ranked as 1.

ANOVA showed the percentage contribution value for each parameter. Table 8 showed %P value i.e. which parameter has the most influence on the volumetric shrinking of polymeric bolt. From ANOVA results it was observed that injection time has most significant effect on the warpage i.e. 26.89%. As higher the injection time more material will enter the cavity and less void spaces will be available for the material to relax.

ANOVA was performed for volumetric shrinkage and the results are given in table 9. It was observed that melt temperature has the most prominent effect on the shrinkage of polymeric bolt i.e. 78.36%. The combined response of average volumetric shrinkage and warpage was also studied and given in table 10. It was concluded from the combined results that injection time has the most influence on the shrinkage and warpage of nylon nut.

6. Conclusion

It is concluded from the above experimental that for volumetric shrinkage the most significant effect is of melt temperature which can be seen from both ANOVA table S/N response table as it has the highest rank value. Similarly, for warpage the most significant parameter is injection time. When the combined effect of both warpage and volumetric shrinkage was studied, it showed optimum values of the responses at melt temperature 240°C, injection pressure 70MPa and injection time 5 seconds and the most significant effect was of melt temperature. However, there are various other parameters which effect shrinkage and warpage but in the study the effect of melt temperature, injection time and injection pressure was studied. And among these three parameters the highest contributing factors were determined. Moreover, the shrinkage and warpage values depends on material properties, mold and die design.

REFERENCES

- [1] T. Erzurumlu and B. Ozcelik, "Minimization of warpage and sink index in injection-molded thermoplastic parts using Taguchi optimization method," *Mater. Des.*, vol. 27, no. 10, pp. 853–861, 2006.



- [2] H. Oktem, "Materials & Design Application of Taguchi optimization technique in determining plastic injection molding process parameters for a thin-shell part," *Mater. Des.*, vol. 28, pp. 1271–1278, 2007.
- [3] E. Faison, "Shrinkage Behavior and Optimization of Injection Molded Parts Studied by the Taguchi Method," *Polym. Eng. Sci.*, vol. 41, no. 5, pp. 703–710, 2001.
- [4] D. Choi and Y. Im, "Prediction of shrinkage and warpage in consideration of residual stress in integrated simulation of injection molding," *Compos. Struct.*, vol. 47, no. 1999, pp. 655–665, 2000.
- [5] M. Altan, "Reducing shrinkage in injection moldings via the Taguchi , ANOVA and neural network methods," *Mater. Des.*, vol. 31, no. 1, pp. 599–604, 2010.
- [6] R. Sánchez, J. Aisa, A. Martinez, and D. Mercado, "On the relationship between cooling setup and warpage in injection molding," *Measurements*, vol. 45, pp. 1051–1056, 2012.
- [7] N. M. Mehat and S. Kamaruddin, "Multi-Response Optimization of Injection Moulding Processing Parameters Using the Taguchi Method," *Polym. Plast. Technol. Eng.*, vol. 50, no. 15, pp. 1519–1526, 2011.
- [8] E. Hakimian and A. B. Sulong, "Analysis of warpage and shrinkage properties of injection-molded micro gears polymer composites using numerical simulations assisted by the Taguchi method," *J. Mater.*, vol. 42, pp. 62–71, 2012.
- [9] W. Guo, L. Hua, H. Mao, and Z. Meng, "Prediction of warpage in plastic injection molding based on design of experiments ," *Springer*, vol. 26, no. 4, pp. 1133–1139, 2012.
- [10] Y. Wang, J. Kim, and J. Song, "Optimization of plastic injection molding process parameters for manufacturing [1] Y. Wang, J. Kim, and J. Song, 'Optimization of plastic injection molding process parameters for manufacturing a brake booster valve body,' 2014.a brake booster valve body," *Mater. Des.*, vol. 56, pp. 313–317, 2014.
- [11] R. Hussin, R. M. Saad, R. Hussin, M. Syedi, and I. Mohd, "An Optimization of Plastic Injection Molding Parameters Using Taguchi Optimization Method," *Res. Gate*, vol. 2, no. 5, pp. 75–80, 2012.
- [12] J. Shoemaker, "Moldflow Design Guide," *Moldflow Des. Guid.*, pp. I–XX, 2006.
- [13] S. H. Tang, Y. J. Tan, S. M. Sapuan, S. Sulaiman, N. Ismail, and R. Samin, "The use of Taguchi method in the design of plastic injection mould for reducing warpage," *J. Mater. Process. Technol.*, vol. 182, no. 1–3, pp. 418–426, 2007.



Sliding wear behavior of carbon fiber reinforced polyphenylene sulfide composites

Mehmet İskender ÖZSOY^{*}, Levent ESATOĞLU¹

¹- Department of Mechanical Engineering, Sakarya University, Sakarya 54187, Turkey

^{*}Corresponding Author : iozsoy@sakarya.edu.tr

Abstract:

In this study, sliding wear performance of polyphenylene sulfide polymer (PPS) and 40% and 50% weight ratio of chopped carbon fiber reinforced polyphenylene sulfide composites were investigated. In this context friction and wear tests were performed by pin-on-disc test arrangement. Test conditions are chosen as 50, 100, 200 N normal loads and 1, 2, 3 m/s sliding speeds. The counter face disc material is AISI 1040 steel. The results showed that adding fiber decreased the friction and wear rates. Furthermore increasing load decreased the friction coefficients of PPS and composites, however increasing speed increased the friction coefficients of PPS polymer but speed decreased the friction coefficients of fiber reinforced composites.

Keywords: Polyphenylene sulfide, carbon fiber, composite materials, sliding wear

1. Introduction

Polymer composites are widely used in industry such as automotive, aeronautical, sports equipment. Low weight, high strength, high mechanical performance properties make the composite materials advantageous than metals and ceramics [1,2]. Fiber reinforced polymers are used in sports and recreational equipment, filament-wound rocket motor bodies, pressure vessels and aircraft structural components [3-6]. Nowadays, several studies have been being studied about tribological area and reinforcements which added into the polymers are effective on friction and wear behaviors such as reinforcement type, reinforcement ratio and distribution of fibers on different sliding speeds and various loads [7-20, 22-29]. Myshkin et al. [7] investigated the wear properties of the PA6 polymer. They made the wear tests 0.5-1 m/s sliding speeds, 0-20 MPa normal loads and 1000 m sliding distance test conditions. They observed that the increasing load decreased the friction. They also stated that deformation and contact temperature play an important role on the polymer wear. Şahin et al. [8] studied the 42 wt% carbon fiber reinforced epoxy composites. Wear tests were carried out at 0.42 m/s speed, 90 and 160N load and 1000m sliding distance conditions. Although carbon fiber decreased the wear rate, it increased the friction coefficient. Bolvari et al. [9] carried out the pin-on-disc wear tests of 5-30 wt% carbon fiber reinforced PA66 composites and 5-30 wt% carbon fiber + 10 wt% PTFE reinforced PA66 composites. Test conditions were 30N normal load and 1 m/s speed. Minimum friction coefficient was obtained with 15 wt% carbon fiber + PA66 composite.

The polyphenylene sulfide (PPS) is a semi-crystalline thermoplastic polymer which shows resistance to heat at high temperatures. It is resistant against to fire, flammability and chemicals and has good electrical properties. Polyphenylene sulfide polymer is mostly used in the production of various parts of automotive such as electrical and electronic equipment, fuel systems, and transmission parts, heating and cooling systems. It is also used to make electricity equipment such as contactor, switch and motor components [21]. Researchers used fibers and fillers to improve the wear properties of PPS [22-29]. Ma et al. [22], studied the mechanical and tribological behavior of fiber reinforced polyphenylene sulfide composites. They stated that fibers improved the wear properties. Cho [23] investigated the friction and wear behavior of carbon fiber and CuO reinforced PPS composites. He determined that increasing sliding distance decreased friction coefficient and wear rate of the carbon fiber reinforced composites. Although kevlar and CuO reinforcements decreased the wear amount but also increased the friction coefficient. Luo et al. [24], studied the carbon fiber reinforced PPS/PTFE composites. It is found that adding carbon fiber reinforcements decreased the friction and wear. Kurt [25], investigated the friction and wear properties of the PAI and PAI composites, PEEK + 30wt% carbon fiber composites, PEEK + 30wt% glass fiber composites, PPS + 40% glass fiber composites, PSU + 20% glass fiber composites, PEI + 15wt% PTFE composites and PK and LCP polymers. He stated that increasing load decreased the friction coefficients and increasing sliding speed increased the friction coefficient. Hanmin et al. [26] studied the wear properties of 10-70 wt% carbon fiber reinforced PPS composites. Tests were made at 0.4 m/s sliding speed, 0-800N normal load and 1500 m



sliding distance. They found that increasing load decreased the friction coefficient, and increasing carbon fiber ratio decreased the wear rate and friction coefficient. Zhou et al. [27] studied the friction and wear properties of the 0-15 wt% carbon fiber reinforced PA6/PPS composites. Tests were performed at 500-1500 rpm speeds, 10-20 N normal loads and 1000 m sliding distance conditions. They determined that increasing load and sliding speed decreased the friction values and increased the wear rate. Zhao and Bahadur [28] investigated the wear properties of the NiS and PbSe filled PPS composites. While NiS fillers decreased the wear rate, PbSe filler increased it. Sinha et al. [29] investigated the wear properties of the 0-10 wt% CuO, ZnO, TiO₂ and SiC filled PPS composites. They stated that although CuO and TiO₂ fillers decreased the wear losses, ZnO and SiC fillers increased the wear.



Figure 1. Experimental configuration

As a result of the working conditions, design flexibility and high strength provided by fiber reinforced PPS composite applications, components in the automotive and aerospace industries are the starting point of this study. In literature studies, it is seen that there is not enough friction and wear studies related to Polyphenylene sulfide (PPS) polymer and composites and experiments with different load and speeds are not performed very much. In this study, effect of chopped carbon fiber (at the 40 and 50 wt% fiber ratios) content ratio on the friction and wear properties of carbon fiber reinforced polyphenylene sulfide composites were investigated. Also, different parameters such as according to fiber ratio, load and speed were investigated. In this context tribological tests were carried out by pin-on-disc test arrangement. Test conditions are chosen as 50, 100, 200 N loads and 1, 2, 3 m/s speeds. The counter face disc material is AISI 1040 steel.

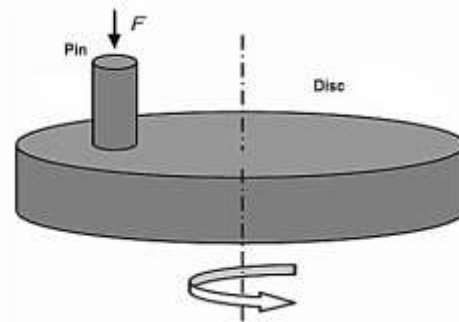


Figure 2. Schematic drawing of pin-on-disc test configuration

2. MATERIALS AND EXPERIMENTAL STUDIES

In this study, PPS polymer as the matrix and carbon fiber are used as the reinforcement. Specimens were obtained by extrusion and injection molding method as a pin shape. Experimental densities of produced composites are given in Table 1. Tribological behavior of materials tested with pin-on-disc test rig which shown in Figure 1. Tests were carried out according to ASTM G99 standard. Before and after each test, pins and steel disc were cleaned acetone and dried. The disc is 100 mm diameter and 5 mm thickness. Average surface roughness (Ra) of disc is 0.29 μm . Friction force was measured with a load cell sensor.

Table 1. Densities of composites

Composite specimen	Density (g/cm ³)
PPS+40CF	1.49
PPS+50CF	1.54



The friction coefficient values (μ) were obtained from the equipment that records the μ value by using Eq. (1).

$$\mu = F_F / F_N \quad (1)$$

where F_F is the frictional force and F_N is the load on the sample. Wear amount was calculated by weighing the pin before and after the tests to an accuracy of 1×10^{-4} g in a precision balance. Tests were performed at room temperature conditions and loads were 50, 100, 200 N and sliding speeds were 1, 2, 3 m/s. The specific wear rates of materials were calculated using Eq. (2).

$$= \frac{\text{Specific wear rate}}{\text{Wear loss}} \quad [\text{mm}^3 / \text{Nm}]$$

$$= \frac{\text{Density} \cdot \text{Load} \cdot \text{Sliding distance}}{\text{Wear loss}} \quad [\text{mm}^3 / \text{Nm}]$$

3. RESULTS AND DISCUSSIONS

Figure 2 shows the surface temperatures variation of pin specimens at 1 m/s sliding speed and 50 N load. Surface temperatures of pins were measured by infrared thermometer. It is seen from Figure 2 that surface temperatures started at 23-27°C and finished at 49-69°C ranges because of the frictional contact of pin and disc surfaces during the rubbing. The temperature differences were found to be 41.5°C for the PPS polymer, 28.9°C for 40 wt% fiber reinforced PPS composite and 25.5°C for 50 wt% fiber reinforced PPS composite. The temperatures of contact surfaces increased during the rubbing process. Increase trend of surface temperatures decreased as a result of increasing fiber ratio as it is seen in the figure.

Figure 3 shows the optical microscopy image of worn pin surface of PPS polymer at 1 m/s speed and 100 N load values. In the Figure 3, micro ploughings and partial peelings are seen. As a result of this temperature increase, particles detached from the soft pin surface and adhered again pin surface and it caused the increase of friction coefficient. Surface temperature increased with increasing sliding time. As a result of this, partial melting regions were occurred on the matrix.

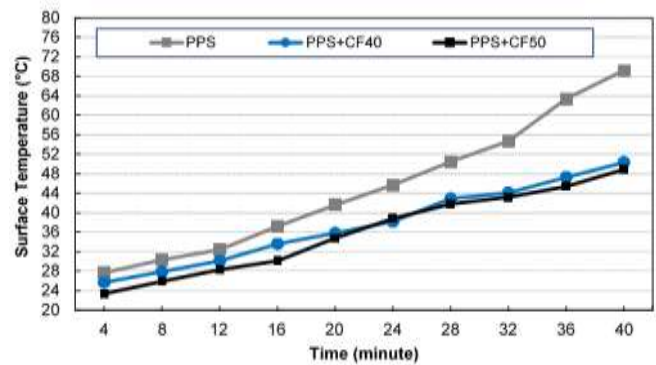


Figure 2. Surface temperatures of pin specimens (1 m/s and 50 N load condition)



Figure 3. Optical microscopy image of worn pin surface of PPS polymer at 1m/s sliding speed and 100 N applied load

Figures 4 and 5 show the variation of friction coefficients of PPS polymer and carbon fiber reinforced PPS composites with load and speed respectively. In Figure 4, while the PPS polymer has a maximum friction coefficient and the 50 wt% carbon fiber reinforced PPS composite has a minimum friction coefficient. Furthermore, increasing load decreased the friction coefficients of PPS polymer and fiber reinforced composites. These results are consistent with the literature [7,25,26]. According to increasing load from 50 N to 200N, friction coefficients are between the 0.344 and 0.4 for PPS polymer, 0.3 and 0.38 for 40 wt% fiber reinforced PPS composite and 0.26 and 0.36 for 50 wt% fiber reinforced PPS composite. In figure 5, increasing sliding speed decreased the friction coefficients except for PPS polymer. According to increasing speed from 1 m/s to 3 m/s, values of the friction coefficients are between the 0.38 and 0.45 for PPS polymer, 0.30 and 0.34 for 40 wt% fiber reinforced PPS composite and 0.29 and 0.33 for 50 wt% fiber reinforced PPS composite. Effect of speed on friction coefficient and wear behavior in polymers is considered with temperature effect. This



is related to the viscoelastic properties of the polymer [31,32]. When the temperature increase comes up the glass transition temperature of the polymer, the friction is dependent on the speed [33,34]. It is thought that increasing speed approaches the PPS polymer to the glass transition temperature and this situation could cause the increasing of friction coefficient of PPS polymer. Increasing fiber ratio decreased the contact temperatures of materials as shown in Figure 1 and so friction forces decreased as seen in Figures 3 and 4. Carbon fiber generates transfer film layer during the adhesive rubbing process and hence it decreased the friction and wear [9]. It is clear that from Figures 4 and 5, adding fiber decreased the friction of PPS polymer. The frictional force reduces due to the fact that the increase in the stiffness of the polymer by adding fibers reduce the deformation region of the polymer material during sliding [35].

Figures 6 and 7 show the wear rates of PPS and carbon fiber reinforced PPS composites according to load and speed respectively. Adding fibers decreased the wear rates of PPS polymer. It is seen in Figures 6 and 7, increasing load and sliding speed increased the specific wear rates of PPS polymer and fiber reinforced PPS composites. According to applied load from 50N to 200N, the values of specific wear rates are the range of 0.89 and 4.93 ($\text{mm}^3/\text{Nm}10^{-5}$) for PPS polymer, 0.66 and 1.28 ($\text{mm}^3/\text{Nm}10^{-5}$) for 40 wt% fiber reinforced PPS composites and 0.62 and 2.75 ($\text{mm}^3/\text{Nm}10^{-5}$) for 50 wt% fiber reinforced PPS composites (Figure 6). The added carbon fibers formed hardness and increased the load carrying capacity of the polymer [23,24].

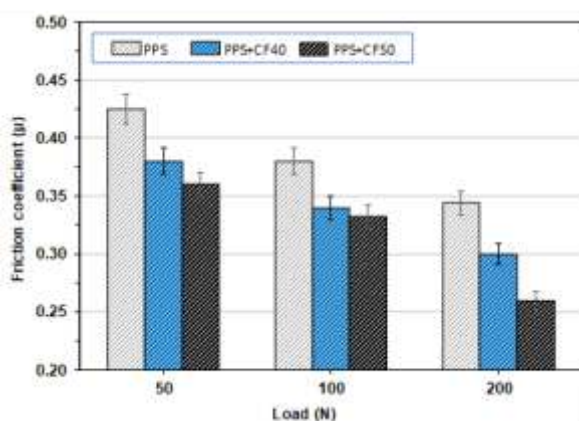


Figure 4. Variation of friction coefficients of PPS and PPS composites according to load (1 m/s speed)

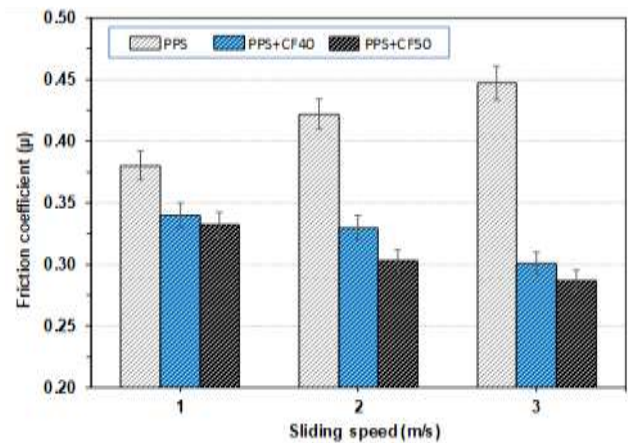


Figure 5. Friction coefficients of PPS and PPS composites according to speed (100N load).

It is seen in Figure 6, 50 wt% reinforced PPS composite shows the most distinct increase at the 200N load condition. This may result from the PPS matrix not having sufficient interfacial bonding at high fiber ratios and separation of the fibers in the case of high load.

In figure 7, according to sliding speed changing from 1 m/s to 3 m/s, the values of specific wear rates are the range of 1.33 and 2.77 for PPS polymer, 0.68 and 0.89 ($\text{mm}^3/\text{Nm}10^{-5}$) for 40 wt% fiber reinforced PPS composites and 0.64 and 1.2 ($\text{mm}^3/\text{Nm}10^{-5}$) for 50 wt% fiber reinforced PPS composites. As can be seen from Figure 7, PPS polymer shows the most noticeable wear increase trend. During the rubbing process contact temperatures are increased due to the frictional heating as is seen in Figure 1 and besides as a result of increasing speed increased the contact surface temperature. The wear and temperature increasing could soften the pin surface and caused the high material losses from the surface. The temperature increase due to friction, accelerated the transfer of the polymer to counterface [35]. Sliding surfaces cause the frictional heating and it is given by Eq (3).

$$q_{total} = \mu \cdot p \cdot U \quad (3)$$

Where, q_{total} is the rate of the heat generated per unit area contact, μ is the friction coefficient, p is the contact pressure and U is the relative velocity [30]. According to Eq. (3) increasing load and speed are increased the heat generation and this can soften the pin surfaces. Gahr [31] stated that increasing load increased the wear rate depending on thermal softening of polymer materials.

SEM images of composite samples after rubbing tests are shown in Figure 8 (1 m/s sliding speed and 100 N load condition). It is seen that fibers are



oriented towards the sliding directions. Wear marks have been formed due to contact on the surface. In Figure 8a and 8b fibers showed resistant to rubbing to prevent the matrix failure. Partial fiber breaks are seen at the some regions. In Fig. 8b, it is seen that fibers separated from the matrix. It is thought that PPS polymer softened by temperature increase due to effect of increasing speed and load so it made fibers debonding and break up the fibers at some regions. As the sliding time increases, the surface temperature is increased by the effect of the friction. As a result of softening of pin surface, damages were become more dominant.

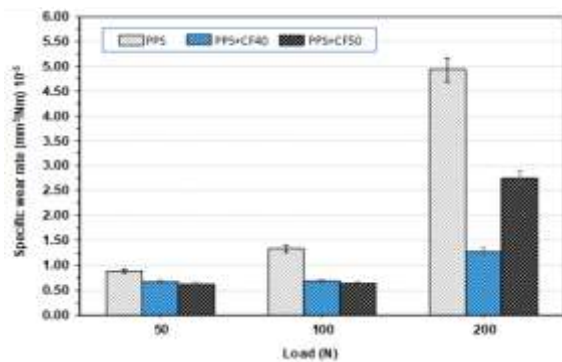


Figure 6. Specific wear rates of PPS and PPS composites according to load at (1 m/s speed).

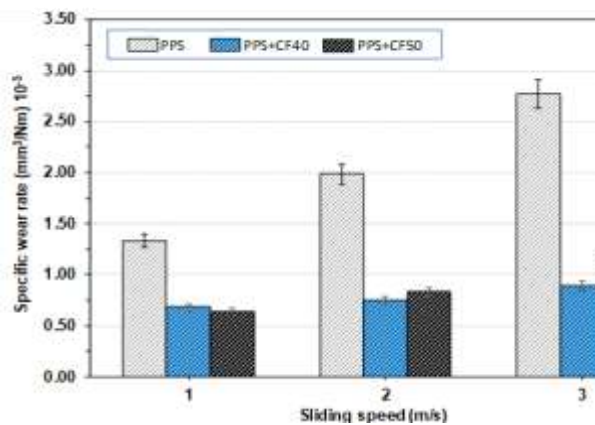


Figure 7. Specific wear rates of PPS PPS composites according to speed (100N load)

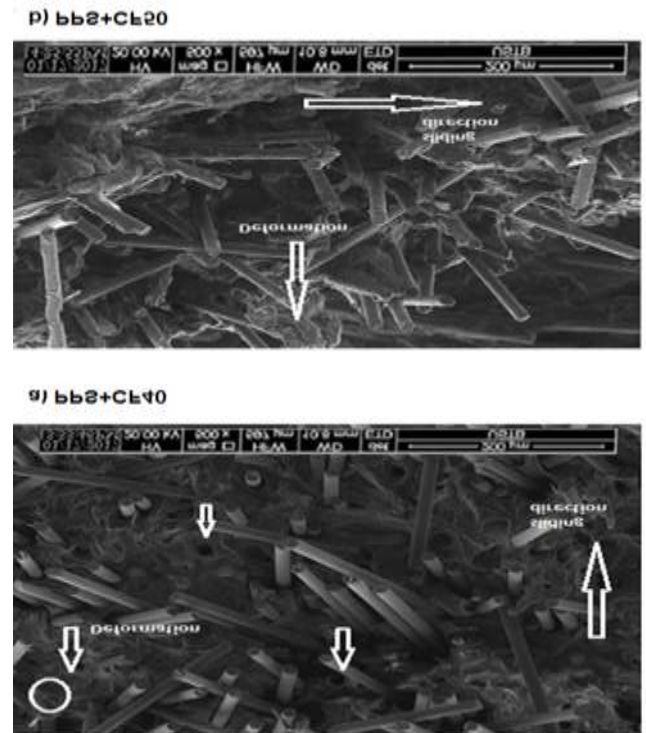


Figure 8. Scanning electron microscopy images of composite worn surfaces.

4. CONCLUSIONS

In this study, the influence of chopped carbon fiber content on the sliding wear performance of carbon fiber reinforced PPS composites was investigated. The results are listed from this below:
 Adding fiber into the PPS polymer were gained the friction and tribological properties.
 Increasing load decreased the friction coefficients of PPS polymer and carbon fiber reinforced PPS composites.
 Friction coefficients of PPS polymer increased with increasing sliding speed.
 Friction coefficients of PPS composites decreased with increasing speed.
 Increasing load and speed increased the wear rates of PPS polymer and carbon fiber reinforced PPS composites.
 Fiber breaks are seen at high fiber ratios at the SEM images.

Acknowledgments

This study is supported by Sakarya University Scientific Research Projects Coordination Unit. Project Number: 2017-50-01-083.



REFERENCES

- [1] J. Alen, A. Sanu, A Review on the Composite Materials used for Automotive Bumper in Passenger Vehicles, *International Journal of Engineering and Management Research*, vol.4 (4), pp. 98-101, 2014.
- [2] R. Wang, S. Zheng, Y.G. Zheng, *Polymer Matrix Composites and Technology*, Woodhead Publishing, 2011.
- [3] M. Masuelli, *Introduction of Fibre-Reinforced Polymers – Polymers and Composites: Concepts, Properties and Processes, Fiber Reinforced Polymers - The Technology Applied for Concrete Repair*, Publisher: InTech, Chapter: 1, pp. 3-40, 2013
- [4] R.A. Donald, P.F. Pradeep, J.W. Wendelin, *The Science and Engineering of Materials*, Cengage Learning, USA, 2010.
- [5] Y.A. Hüsnergül, *Polymer Composites; Properties, Performance and Applications*, Polymer science: research advances, practical applications and educational aspects, A. Méndez-Vilas; A. Solano, Eds.
- [6] N.G. Mccrum, C. Buckley, C.B. Bucknall, *Principles of polymer engineering*, Oxford University Press, 1997.
- [7] N.K. Myshkin, *Polymer Tribology: Current State and Applications*, *Tribology in Industry*, vol. 37(3), pp. 284-290, 2015.
- [8] Y. Sahin, Tribological behaviour of unidirectional carbon fibre reinforced epoxy composites, *Materials Science and Engineering*, vol.174, pp. 1-8, 2007.
- [9] A. Bolvari, S. Glenn, R. Jansen, C. Ellis, Wear and friction of aramid fiber and polytetrafluoroethylene filled composites, *Wear*, vol. 203-204, pp. 697- 702, 1997
- [10] L. Chang, K. Friedrich, Enhancement effect of nanoparticles on the sliding wear of short fiber-reinforced polymer composites: A critical discussion of wear mechanisms, *Tribology International*, vol.43 (12), pp. 2355–2364, 2010.
- [11] L. Chang, Z. Zhang, Tribological properties of epoxy nanocomposites: Part II. A combinative effect of short carbon fibre with nano-TiO₂, *Wear*, vol. 260 (7–8), pp. 869–878, 2006.
- [12] Q.B. Guo, M.Z. Rong, G.L. Jia, K.T. Lau, M.Q. Zhang, Sliding wear performance of nano-SiO₂/short carbon fiber/epoxy hybrid composites, *Wear*, vol. 266 (7–8), pp. 658–665, 2009.
- [13] N. Chand, A. Naik, S. Neogi, Three-body abrasive wear of short glass fiber polyester composite, *Wear*, vol. 242 (1–2), pp. 38–46, 2000.
- [14] N.S.M.E. Tayeb, A study on the potential of sugarcane fibers/polyester composite for tribological applications, *Wear*, vol. 265 (1–2), pp. 223–235, 2008.
- [15] J.Quinteliera, P.De Baetsa, P.Samyna, D.Van Hemelrijck, On the SEM features of glass–polyester composite system subjected to dry sliding wear, *Wear*, vol. 261 (7–8), pp. 703–714, 2006.
- [16] N.S.M. E. Tayeb, B.F. Yousif, Evaluation of glass fiber reinforced polyester composite for multi-pass abrasive wear applications, *Wear* 262 (9–10), pp. 1140–1151, 2007.
- [17] B. Suresha, K. Siddaramaiah, S. Seetharamu, P.S. Kumaran, Investigations on the influence of graphite filler on dry sliding wear and abrasive wear behaviour of carbon fabric reinforced epoxy composites, *Wear*, vol. 267 (9–10), pp. 1405–1414, 2009.
- [18] S. Kishore, P., S. Seetharamu, P. Thomas, M. Janardhana, A study on the effect of the type and content of filler in epoxy–glass composite system on the friction and slide wear characteristics, *Wear*, vol. 259, pp. 634–641, 2005.
- [19] S. Basavarajappa, S. Ellangovan, K. V. Arun, Studies on dry sliding wear behaviour of Graphite filled glass-epoxy composites, *Materials and Design*, vol. 30(7), pp. 2670 – 2675, 2009.
- [20] S.A.R. Hashmi, U.K. Dwivedi, N. Chand, Graphite modified cotton fiber reinforced polyester composites under sliding wear conditions, *Wear*, vol. 262(11–12), pp.1426–1432, 2007.
- [21] R.O. Ebewe, *Polymer science and technology*, CRC Press, Newyork, 2000.



- [22] M. Yuning, C. Peihong, C. Haiming, H. Ting, L. Xujun, L. Tongsheng, Mechanical and Tribological Properties of Self-Reinforced Polyphenylene Sulfide Composites, *Journal of Macromolecular Science, Part B Physics*, vol. 54(10), pp.1169–1182, 2015.
- [23] M.H. Cho, The role of transfer film and back transfer behavior on the tribological performance of polyphenylene sulfide in sliding, *Journal of Mechanical Science and Technology*, vol. 23, pp. 2291-2298, 2009.
- [24] L. Wei, L. Qi, L. Yi, Z. Shengtai, Z. Huawei, L. Mei, Enhanced mechanical and tribological properties in polyphenylene sulfide/polytetrafluoroethylene composites reinforced by short carbon fiber, *Composites Part B* vol. 91, pp. 579-588, 2016.
- [25] M. Kurt, Tribological behaviours of high performance Industrial Thermoplastics at elevated temperatures, Msc Thesis, Sakarya University, Institute of Natural Sciences, 2011.
- [26] Z. Hanmin, Friction and wear of poly(phenylene sulphide) and its carbon fiber composites: I Unlubricated, *Wear*, vol. 116(1), pp. 59-68, 1987.
- [27] S. Zhou, Z. Qiaoxin, W. Chaoqun, H. Jin, Effect of carbon fiber reinforcement on the mechanical and tribological properties of polyamide6/polyphenylene sulfide composites, *Materials and Design*, vol. 44, pp. 493-499, 2013.
- [28] Q. Zhao, S. Bahadur, The mechanism of filler action and the criterion of filler selection for reducing wear, *Wear*, vol. 225, pp. 660-668, 1999.
- [29] K. Sinha, *Tribology of Polymers and Their Composites-Environmental Effects*, Indian Institute of Technology Kanpur, 24-28, 2016.
- [30] Francis E. Kennedy, Frictional heating and contact temperatures, *Principles of Tribology, Modern Tribology Handbook, Volume-I*, Editor in chief Bharat Bhushan, CRC Press, USA 2001.
- [31] K.H.Z Gahr, *Microstructure and Wear of Materials*, Elsevier Science Publishing, New York, 1987.
- [32] K.C. Ludema, D. Tabor, The friction and visco-elastic properties of polymeric solids, *Wear*, vol. 9(5), pp. 329–348, 1966.
- [33] S.K. Sinha, B.J. Briscoe, *Polymer Tribology*, Imperial College Press, London, 2009.
- [34] G.V. Vinogradov, G.M. Bartenev, A.I. Elki, V.K. Mikhaylov, Effect of temperature on friction and adhesion of crystalline polymers, *Wear*, vol. 16(3), pp. 213–219, 1970.
- [35] A.C. Greco, R. Erck, O. Ajayi, G. Fenske, Effect of reinforcement morphology on high-speed sliding friction and wear of PEEK polymers, *Wear*, vol. 271 (9–10), pp. 2222–2229, 2011.



Comparison of Various Shapes of Internal Cut-outs in Gas Turbine Blades Using FEA Based Modal Analysis

Ahmed Naveed^{1*}, Sohail Afzal¹, Ahmed Aqeel¹, Haziq Sajjad¹ and Rafay Tariq¹

¹- Department of Mechanical Engineering, University of Engineering and Technology, Lahore, Pakistan

*Corresponding Author: ahmadnaveed@uet.edu.pk

Abstract:

Gas Turbine is the most critical element of a power plant. Gas turbines are high-speed rotating machines that often fail due to the resonance effect which is produced when the forcing frequency becomes equal to the natural frequency. This study presents the effect of the cut-outs on the natural frequency of a gas turbine blade. The study consists of the modelling of the model on SolidWorks and the modal analysis using Ansys Modal analysis module. The different cut out shapes are used in the analysis to find the optimum shape of the cut out by keeping the number of cut-outs and the volume of cut-outs constant. Three different geometric configurations are taken under consideration for the Modal Analysis. The results of the Modal Analysis are generated in the form of Graph and tabular data. MATLAB has been used for the generation MAC (Modal Assurance Criteria) plots from the tabular data. Modal Assurance Criteria (MAC) plots are used to monitor the change in mode shapes due to the cut-outs induced in the rotor. The Auto-MAC plots are used as an ideal model to differentiate the change produced due to the cut-outs. The effect of reduction of volume by the induction of cut-outs is also studied on the natural frequency and the mode shapes. The analysis is performed for the first 10 modes of vibration.

Keywords: Resonance, natural frequency, Ansys, Modal analysis, Modal Assurance Criteria, geometric cut-outs

1. Introduction

Durability, stability, strength, cost, and vibration are important parameters to be considered during blade designing. Out of the above-listed parameters, vibration reduction is important to enhance blade performance and 42% of blade failures are due to the vibrations induced in blade structure. The blade, an important part, of the rotating system i.e. turbine must tolerate most of the loads during operation, so its structural stability is very crucial. The stability and stiffness can be hardly calculate using purely classical theory, so the simulation of the blade is necessary because of the complex nature of blade and direct modelling done by using APDL of Ansys. So, for that purpose 1.2 MW horizontal axis wind turbine blade selected and direct modelling achieved by APDL Ansys and results obtained. (Chen, Wang et al. 2013)

It was distinguish and listed that the various failure mechanisms for gas turbine blades such as high cycle fatigue (HCF), thermo-mechanical fatigue (TMF), damage due to creep, erosion and wear, foreign object damage (FOD), domestic object damage (DOD) or clash/clang of compressor blades owing to surge) or a combination of above failure mechanisms. By inciting HCF 70% failure of bladed disks occurred due to mistuning. (Meher-Homji and Gabriles 1998) A blade modeled for parametric analysis using CREO and treated blade as a cantilever and do modal analysis for computing natural frequency. They created cut-outs like circle and

rectangle in blade geometry for comparative analysis and generated mode shapes and evaluated results for blade stability. (Vasant and Dhawale 2007)

Since failure is mainly due to vibration and vibration can be avoided in inducing structure by avoiding resonance phenomena so for that either U500 or IN 738 material had to be selected for blade design for Trans-Amadi power plant in Port Harcourt, Nigeria under operational frequency 85Hz. Under the same load conditions, FEM used to evaluate two-blade material natural frequencies. Results showed that both blade materials were dynamically stable but U500 had better mechanical properties and provide better and long service and selected that material. (Efe-Ononeme, Ikpe, et al. 2018)

It was made a deduction that changes in mode shapes cannot be easily quantified due to the involvement of the displacement at many points. To determine different mode shapes, they used Modal Assurance Criterion (MAC). The MAC gives a scalar constant which compares the modal vector with the reference modal vector concerning the degree of linearity (consistency). (Rehman, Worden, et al. 2016)

The failure analysis of the 9E GE gas turbine blade carried out by utilizing the non-linear FEA technique under operating conditions and at an excessive rotational speed. Stress concentration regions and variables affecting the service life of high pressure and high-Temperature turbine blade determined. By utilizing criterion of maximum tensile stress made a



deduction that cracks formation dangerous regions are located at lower fir-tree slot. (Mohamad, Abdelhussien, et al. 2016)

Mode shapes and first, two flap-wise natural frequencies of three small wind turbine blades of different materials were obtained by exploiting FEA. Fast Fourier transform analyser used for experimental vibration analysis. The 2 flap-wise natural frequency obtained from experiment and FEA compared and deduced that blade made of glass fibre reinforced plastic blade reinforced with aluminium sheet metal (small) strips is the best suitable material for the wind turbine. (Chandgude, Gadhave, et al. 2019)

The service life of a gas turbine is affected by induced vibration, hot gases entering the combustion chamber and other operational factors so by applying FEM suitable material selected under operational conditions. Cambridge engineering software (CES) utilized for material selection. The maximum service temperature, maximum Total Heat flux, maximum von-misses stress and total deformation values for different materials obtained experimentally as well as by applying FEA and results showed that U500 had satisfactory structural static results and IN 738 had better thermal characteristics and both materials best for blade manufacturing. (Ikpe, Efe-Ononeme, et al. 2018)

3 case studies presented in which they diagnosed the root causes of failure and vibration for the gas turbine. High amplitude has appeared to be one of the main causes of failure and it must be avoided. (Al Adawi, Rameshkumar, et al. 2016) The equations of motion are derived for the formulation of vibration of a typical gas turbine blade. The equations are transformed to form a matrix-eigen value form. The numerical results obtained after the solution of these equations are directly used to determine both static and operational frequencies of the blade. (Sinha, Turner, et al. 2011) Apart from the Modal Analysis, the various NDT damage detection techniques such as ultra-sonic, X-ray, thermal emission is used for monitoring the frequency as well. (Wu1a and Li 2014)

Modal shaping is defined as a technique in which the modes and shapes are altered through mass and stiffness matrix which makes them less responsive to the air-loads. (Walsh 1991) When the natural frequency of the turbine blade becomes coincident with the excitation frequency having a higher amplitude then resonance is generated. (Kalapala, Anjaneya, et al. 2017) For the general practice, the Finite Element Analysis is performed by using both static and dynamic methods and then the results were

compared with the experimental data. (Kalapala, Anjaneya, et al. 2017)

The Modal analysis of the blade also finds its application in the calculation of the RPM (rotation speed of the blade) so that the natural frequency should not overlap with operational frequency. (Kumar 2017) Considering the structure of the turbine blade, the axial dimension is much greater than the dimension along the cross-section. During the first mode for the vibration, the blade is considered as a cantilever beam which is rotating along the axis of the rotor. Two cases such as flapping and lapping arise in this case. (Mohan, Sarkar, et al. 2014) Campbell diagram is an efficient tool that relates the turbine speed with frequency. After performing the modal analysis on a 3D turbine blade, it can be used to analyse the resonance produced in the blade due to increasing RPMs. (Poursaeidi, Babaei, et al. 2012)

Weight is one of the most important factors regarding the design and performance of the turbine blade during its operation. It has been also observed that the generation of cut-outs in the turbine blades ultimately leads to a reduction in weight which increases its natural frequency. (Sahu and Patel 2015) If the resonance produced in the turbine blade is not damped by using a suitable damping mechanism then the periodic input energy, amplitude, and the stress grow it can lead to failure by the overstress or by the propagation of the fatigue crack. (Rajesh 2014)

In this study, modal analysis on the blade of gas turbine is performed. Two models are taken into consideration: one is the plain model whereas the other contains cut-outs of different shapes. The change in natural frequency is studied and Modal Assurance criteria plot are utilized to check any irregularities. The variation of natural frequency due to the shape of cut-out is investigated and the mode shapes are also studied.

2. Methodology

The modal analysis is method is generally used to determine the solution for the equation of motions. The method is known to be an effective tool for the reduction of partial differential equations to the ordinary differential equations.

The generalized equation of motion for any structure under the damped vibration is given by:

$$[M] \left\{ \frac{d^2x}{dt^2} \right\} + [C] \left\{ \frac{dx}{dt} \right\} + [K]\{x\} = [F] \dots(1)$$

In the above equation the overall mass matrix, damping coefficient matrix, stiffness matrix and the external excitation force are represented by [M], [C], [K] and [F] respectively. The acceleration, velocity



and the displacement are given by $\left\{\frac{d^2x}{dt^2}\right\}$, $\left\{\frac{dx}{dt}\right\}$ and $\{x\}$ respectively. Assume the system to be under free vibration without any excitation force. Then the above equation becomes:

$$[M] \left\{\frac{d^2x}{dt^2}\right\} + [K]\{x\} = 0 \dots\dots (2)$$

The above equation must be solved for the vibration analysis of the above equation. Some of the effective techniques to determine the eigenvalue and eigen vector are Power method, inverse iteration method and the Rayleigh Quotient method. (Purohit and Bhandari 2013) The frequencies are generally considered to be the eigenvalues which are determined by the Rayleigh Quotient method. (Inaudi 2016)

2.1. Mathematical modelling:

Initially a single blade (attached to the rotor) is analysed. The blade is generated by using a 3D CAD software. The modal analysis is initially employed on the plane geometry without making any reduction in the volume of the blade. Then three blades are generated with the different geometrical cut-outs (circular, square and triangular) along the depth of the blade. The number of cut-outs, depth and area of the cut out for all three shapes is kept constant. In this way three cut-outs are produced which result in the same volume reduction for all three blades. The distance between the centres of the three cut-outs remains the same as well. The geometry is then imported into the Ansys Workbench and a mapped face mesh is generated. In our study we have used aluminium alloy.

After the completion of the analysis, graphical and tabular results are generated. These results are imported in MATLAB to produce a MAC plot. The MAC compares the natural frequencies of the geometries for the all 6 modes. Finally, the results for the reference model are compared with each of the models with the geometric cut-outs.

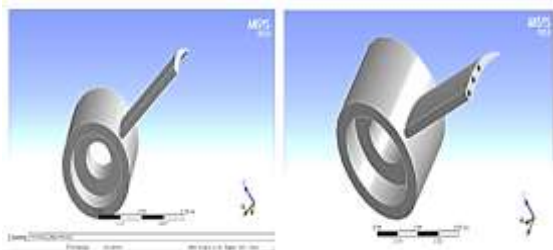


Figure 1. Reference Model and Circular Cut-out

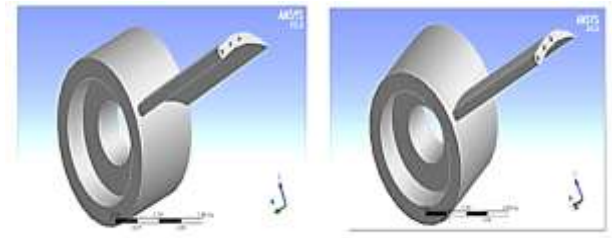


Figure 2: Triangular and Circular Cut-out

The material properties of Aluminium Alloy are shown below in table:

Table 1: Material Properties of Aluminum Alloy

Material properties	Values
Density	2770
Modulus of elasticity	7.7e10
Poisson's ratio	0.33

3. Analysis

The purpose of our analysis is the evaluation of the mode shapes and the natural frequencies for the different modes of vibration. One of the faces of the blade is fixed and then it is analysed for the 10 modes of vibration. The nodes are considered to be the points of maximum displacement, the displacement of the adjacent nodes is compared with each other. After solving the model, the graphical results and the tabular data appear at the bottom. The graph results the variation of frequency with the number of modes. The tabular data can be further used for the generation of the MAC plots.

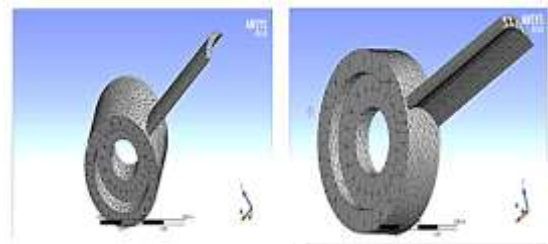


Figure 3: Mesh for the reference model and circular cut-out

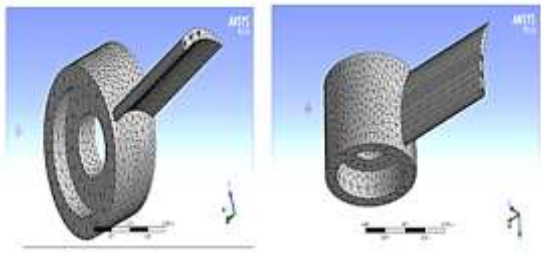


Figure 3: Mesh for the triangular and circular cut-out

3.1 Mesh Correspondence:

Mesh correspondence study is the determination of the size of the mesh element from which the further decrease causes no further change in the result. The purpose of this study is to find an optimum mesh size between the available computational power and the accuracy of the analysis. The smaller the mesh, the higher computational power is required. Mesh correspondence is dependent on the available computing power. Higher computational power may result in smaller mesh size and vice versa. The mesh correspondence study is given as follows:

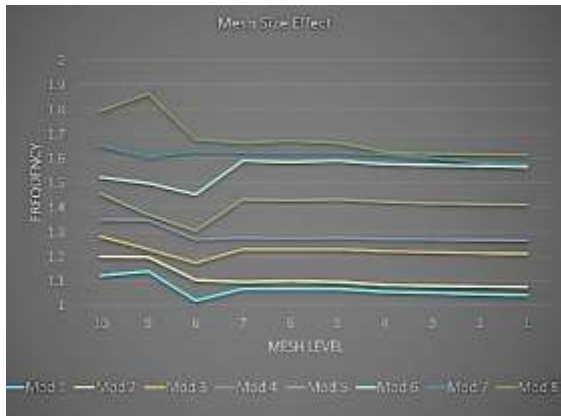


Figure 4: Results from the mesh correspondence study

4. Results:

4.1. Comparison between mode shapes:

1st mode of Vibration:

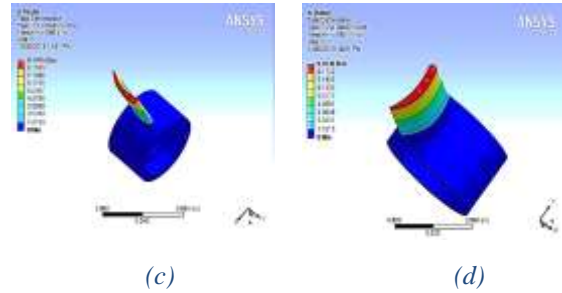
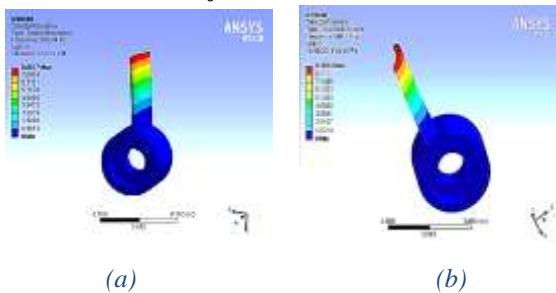


Figure 5: 1st mode of vibration for (a) Reference Model (b) Circular Cut-out (c) Triangular Cut-out (d) Square Cut-out

5th mode of Vibration:

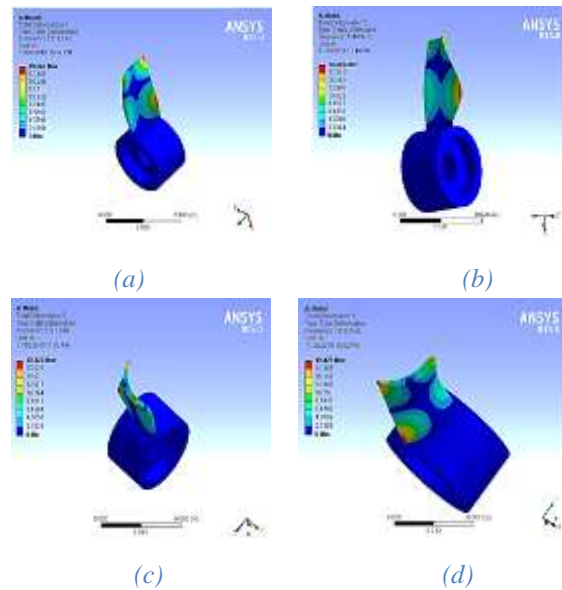
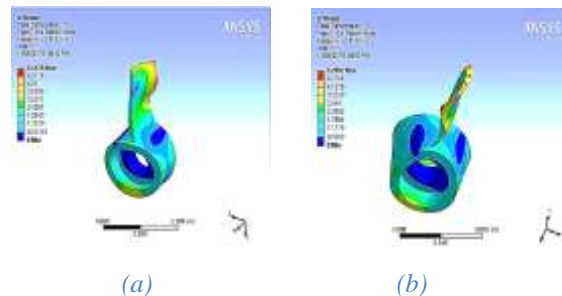


Figure 6: 5th mode of vibration for (a) Reference Model (b) Circular Cut-out (c) Triangular Cut-out (d) Square Cut-out

10th mode of Vibration:



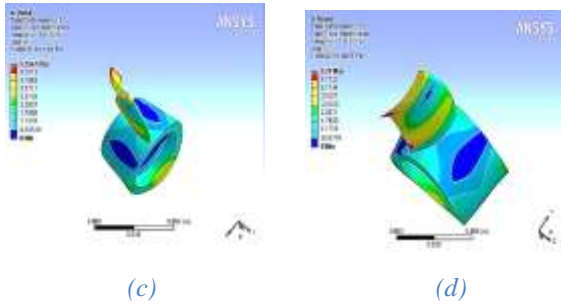


Figure 7: 10th mode of vibration for (a) Reference Model (b) Circular Cut-out (c) Triangular Cut-out (d) Square Cut-out

4.2 Change in natural frequency:

The results of the modal analysis for the first two modes of the four different models, simple and the three cut out models are presented by the following charts.

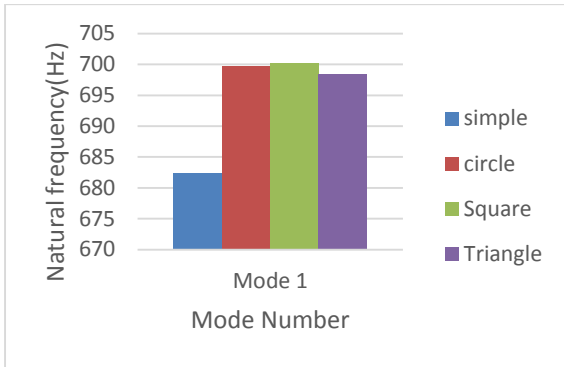


Figure 8: Natural frequencies of different models for the 1st mode

The highest natural frequency is for the first mode is shown by the square cut out model. The circular and triangular cut-out models have very small difference from the maximum frequency. There is a large difference of frequency between the cut-out models and the plain model.



Figure 9: Second Natural frequencies of different models

For the second mode, the circular cut out has the highest natural frequency. The square model has the second highest frequency where the triangular comes at the last for the cut-outs. The natural frequency of plain model has the least natural frequency.

4.2 MAC (Modal Assurance Criterion) plots:

The cut-out models are further compared with the simple model and the results are presented in the form of MAC plots as following:

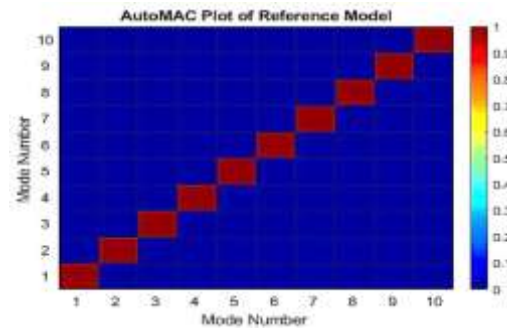


Figure 10: AutoMAC of Reference Model

4.2.1 Case 1: Circular Cut-out:

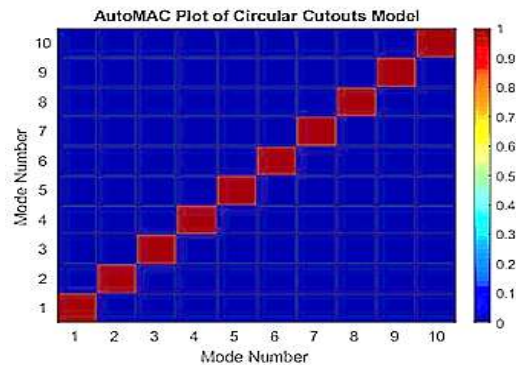


Figure 11: Mac-plot for the circular cut-out

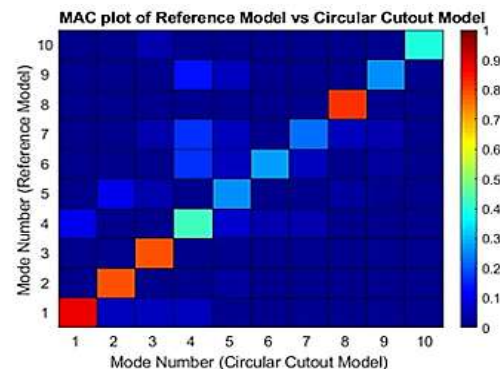


Figure 12: Comparison b/w Mac-plots of reference model and circular cut-out



4.2.2 Case 2: Triangular Cut-out:

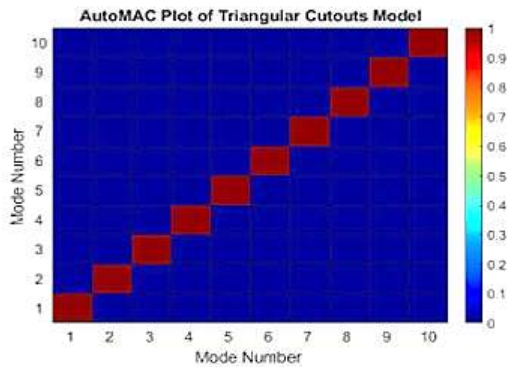


Figure 13: Auto-Mac for the triangular cut-out

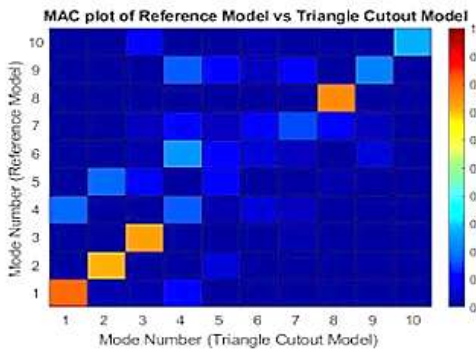


Figure 14: Comparison b/w Mac-plots of reference model and triangular cut-out

4.2.3 Case 3: Square Cut-out:

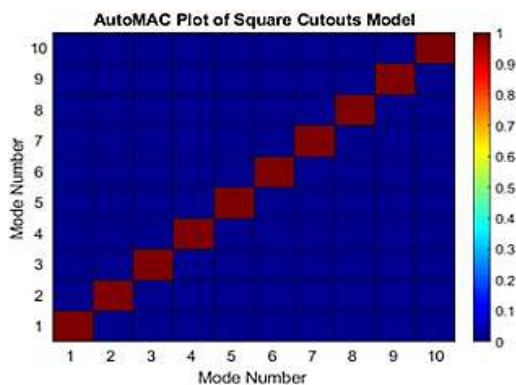


Figure 15: Auto-Mac for the square cut-out

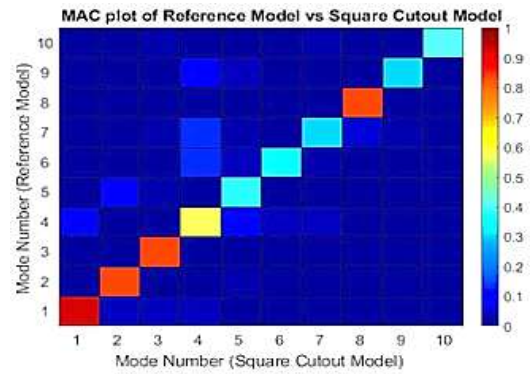


Figure 16: Comparison b/w Mac-plots of reference model and square cut-out

5. Conclusion

It can be concluded from the Modal Analysis that the natural frequency of a rotor increases when the cut-outs are introduced. The shape of cut-out, despite having the same volume, also has some effect on the natural frequency. The triangular cut-out yields the lowest natural frequency for both first and second modes. The circular and square cut-outs have comparable values of natural frequencies for the first and second mode. From the MAC plot, the maximum change in mode shape is observed in the triangular cut-out whereas the minimum change in the mode shape is observed in the circular cut-out. So, the model with the least change in the mode shapes (Circular cut-outs) will produce less fatigue and hence would enhance the life and reliability of the blisk.

References:

- [1]. Al Adawi, S. K. S., G. J. C. J. o. A. S. Rameshkumar and Technology (2016). "Vibration diagnosis approach for industrial gas turbine and failure analysis." 1-9.
- [2]. Chandgude, N., N. Gadhav, G. Taware and N. J. W. E. Patil (2019). "Investigation of stiffness of small wind turbine blade based on vibration analysis technique." 0309524X19849824.
- [3]. Chen, C., M. Wang and L. Zou (2013). Modal Analysis of Wind Turbine Blades Based on ANSYS Modeling. Advanced Materials Research, Trans Tech Publ.
- [4]. Efe-Ononeme, O. E., A. Ikpe, G. O. J. J. o. E. T. Ariavie and A. Sciences (2018). "Modal Analysis of Conventional Gas Turbine Blade



- Materials (Udimet 500 and IN738) For Industrial Applications." **3**(2): 119-133.
- [5]. Ikpe, A., O. Efe-Ononeme, G. J. I. J. O. E. Ariavie and A. Sciences (2018). "Thermo-Structural Analysis of First Stage Gas Turbine Rotor Blade Materials for Optimum Service Performance." **10**(2): 118-130.
- [6]. Inaudi, J. A. (2016). "RAYLEIGH QUOTIENT ALGORITHM FOR MODAL ANALYSIS OF STRUCTURAL MODELS."
- [7]. Kalapala, P., B. Anjaneya, M. J. I. J. o. S. Anandarao and E. Research (2017). "Material Optimization and Dynamic Approach for performance criteria in application to Gas Turbine Blade to overcome resonance." **8**(6): 189-196.
- [8]. Kumar, R. R. (2017). Static structural and modal analysis of gas turbine blade. IOP Conference Series: Materials Science and Engineering, IOP Publishing.
- [9]. Meher-Homji, C. B. and G. Gabriles (1998). Gas Turbine Blade Failures-Causes, Avoidance, And Troubleshooting. Proceedings of the 27th turbomachinery symposium, Texas A&M University. Turbomachinery Laboratories.
- [10]. Mohamad, B. A., A. J. I. J. o. M. E. Abdelhussien and Technology (2016). "Failure analysis of gas turbine blade using finite element analysis." **7**(3).
- [11]. Mohan, R., A. Sarkar and A. Sekhar (2014). Vibration analysis of a steam turbine blade. INTER-NOISE and NOISE-CON Congress and Conference Proceedings, Institute of Noise Control Engineering.
- [12]. Poursaeidi, E., A. Babaei, M. M. Arhani and M. J. E. F. A. Arablu (2012). "Effects of natural frequencies on the failure of R1 compressor blades." **25**: 304-315.
- [13]. Purohit, K. and M. J. E. J. Bhandari (2013). "Determination of Natural Frequency of Aerofoil Section Blades Using Finite Element Approach, Study of Effect of Aspect Ratio and Thickness on Natural Frequency." **17**(2): 51-62.
- [14]. Rajesh.M, T. S., Mohan Kumar.B (2014). "Finite Element Analysis and Vibration Aspects of Rotating Turbine Blade with Known Stress Concentration Factors " **4**(11).
- [15]. Rehman, A. U., K. Worden and J. A. J. S. Rongong (2016). "On crack detection in tuned and mistuned repeating structures using the modal assurance criterion." **52**(3): 175-185.
- [16]. Sahu, J. K. and B. Patel (2015). "International Journal Of Scientific Research And Education."
- [17]. Sinha, S. K., K. E. J. J. o. S. Turner and Vibration (2011). "Natural frequencies of a pre-twisted blade in a centrifugal force field." **330**(11): 2655-2681.
- [18]. Vasant, B. and A. Dhawale (2007). "Vibration Analysis of Isotropic and Orthotropic Turbine Blade Using ANSYS."
- [19]. Walsh, J. L. (1991). "Performance optimization of helicopter rotor blades."
- [20]. Wu1a, B. and Z. Li (2014). "Multiscale features and information extraction of online strain for long-span bridges."



Design and Fabrication of a Low Cost 3-Axes CNC Precision Router

Sarmad Ishaq^{1*}, Muhammad Ali Bhutto¹, Muhammad Shoaib Butt¹, Saad Ali¹, Khalid Rahman¹, Wasim Ahmed Khan¹

1- Faculty of Mechanical Engineering, Ghulam Ishaq Khan Institute of Engineering Sciences and Technology, sarmdishfaq94@gmail.com

Abstract:

Additive Manufacturing (AM) has been around in the global market for past few decades but the concept is still alien to most of the developing countries. Lack of precision, accuracy and expensive technology not available locally are the core issues encountered by emergent nations working on the novel technology. The focus of this paper is to design and fabricate a rigid and economical 3-Axis CNC Precision Router for the local industries of developing countries to compete with the ever-progressing world in using novel AM techniques for manufacturing purposes. This article reports the independent development of machine based on mechanical hardware, electronics and a proposed software system. It is also reported the necessity to achieve the precision of order of microns (10^{-6}) without increasing the capital by using locally available components for developing the required machine. The innovation in software for the designed system is comparable to any machine developed in modern world. The machine proposed here will be able to perform many of AM techniques such as spray forming by providing a routing mechanism for the printing head attached.

Key Words: Additive Manufacturing; Precision Router; Developing Nations; Accuracy; Precision

1. Introduction

Additive Manufacturing (AM) first commercial application dates back to 1987 with stereolithography from 3D Systems [1]. A relative new technology which uses material accumulation is considered as revolutionary in area of manufacturing in recent times [2]. AM technology is gaining increasing importance presently, becoming the core technology for the national strategic industry. The third industrial revolution is considered to be the amalgamation of digital information technology with new materials [3]. 3D printing has received extraordinary attention recently. Institution such as government, investors and media developed deep interest in additive manufacturing. In 2013, worldwide, AM products and services grew 34.9% to \$3.07 billion compared to growth in 2012 of 32.7% to \$2.275 billion [1]. AM has also received attention from developed countries in Europe and America. These nations have formulated development policies focused on investing in AM by increasing research and development in this novel technology[4].

Some application of AM includes automobiles, aerospace, printed sensors etc. Recently, application of AM technology in aircraft manufacturing and medical application have shown rapid progress [5].

AM technology can be divided into the following technologies according to the method and manufacturing mode: laminated object manufacturing, spray forming, materials extrusion molding, photosensitive polymer curing molding and laser powder sintering molding, etc. [6].

The developing economies of the world are still not deep into AM. The challenges faced by these countries' accounts to availability of AM experts, decrease in manufacturing job market etc. [7]. While in general the challenge faced in AM are the lack of thorough research on AM equipment, low manufacturing efficiency, high costs, and poor accuracy etc. [8]. It cannot be denied that progress is made in this area but to promote the wide spectrum of AM applications, technology upgrade and cost reduction needs to be considered.

In this regard the idea of a 'low cost' and 'accurate' machine named "3-Axis CNC Precision Router" is being proposed for AM methods and applications. The focus on cost and precision is to accommodate the local industries of third world countries to take advantage of this technology and challenge the global market to exploit its potential [9].

Accuracy and precision are extremely important parameters for AM equipments. Accuracy means to approximate measurement results to a reference



value whereas precision means the repeatability, or reproducibility, of the measurement. Accuracy and Precision are very pivotal in AM applications. For example, Drop on demand (DoD)-based machines apply print heads with nozzles placed at distances of about 40 μm . The diameter of a droplet is typically 100 $\mu\text{m} \pm 5\%$. Lack of precision occurs accidentally and is mainly due to the design of the AM machine [10].

The Precision Router is to be designed to keep the cost of fabrication as minimum as possible without effecting the precision and accuracy of the machine. The precision of the 3-axis CNC Precision Router depends on the rigidity of mechanical structure design, precision of rotating parts selection of motors, microcontroller and the process of fabrication [11]. There is a tendency for machine tools to misperform due to self-excited vibrations leading to precision errors and possible machine damage. The vibrations caused by the machine tools needs to be measured for improving the machine performance.

In this paper the mechanical hardware design and fabrication will be discussed. This will be followed by the proposed electronics scheme and software complying the ISO 6983-1:2009 standards. The techniques used in designing and fabrication of the Precision Router will be made as economical as possible without comprising the accuracy of the machine.

Design and Analysis of Mechanical Hardware

The flowchart in Figure 1 summarizes the design process adapted for the Precision Router.

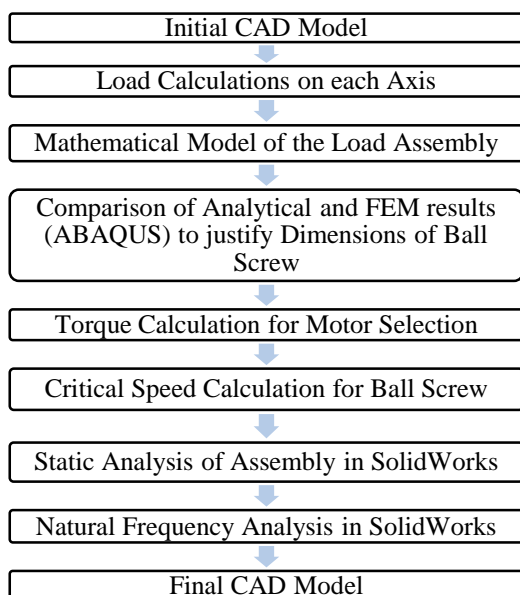


Fig. 1. Flow Chart of Design Process

Before evaluating loads for the critical axis, an initial 3D model of 3-Axes CNC Precision Router is modelled in SolidWorks 2016 as shown in Figure 2a. The machine is designed with three Cartesian axes, with 500 mm of length both X and Y axes and 100 mm of length Z axis. The material assumed is ASTM A36 Steel with density of 7850 kg/m³. The bed dimensions (X-Axis Table) as shown in Figure 2b is taken to be 250mm * 250mm *10mm. A safety factor of 1.5 is considered for all the three axes to make the design more mechanically sound. The loads evaluated at each axis are shown in Table 1.

Table 1. Load evaluation on each axis

	X-Axis	Y-Axis	Z-Axis
Calculated Load	54 N	78.5 N	19.6 N
Factor of Safety	1.5	1.5	1.5
Corrected Load	81 N	118 N	29.4 N

So, the critical load 'Fc' is on Y-Axis and is equaled to be 118 N.

The critical load will be used for the mathematical modeling and eventually finding the diameter of ball screws which is critical to the function of the CNC machine. Ball screws are used as elements of feed systems in today's highly accurate machine tools working [12]. A mathematical model of the ball screw is developed using beam theory as shown in Figure 3 [13]. The beam is considered as a simply supported beam with circular cross section and distributed load of 1180 N/m. Due to eccentricity of the Z-Axis mount as seen from Figure 2b a moment of 6.4 N-m is calculated to act on the Y-Axis which can be seen in Figure 3.

The following material parameters are considered for the ball screw:

- AISI 6150 alloy steel
- Density 7850 kg/m³
- Modulus of Elasticity 200 GPa
- Poisson Ratio 0.3
- Yield Strength 415 MPa

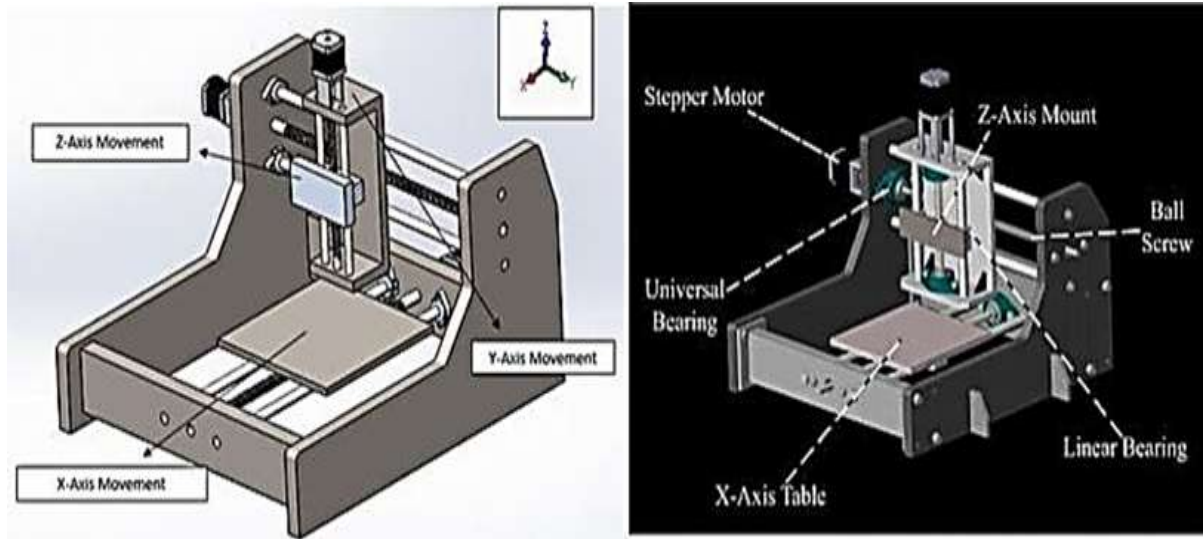


Fig. 2. a) Initial CAD Model of CNC Router. b) Final Design of CNC Router

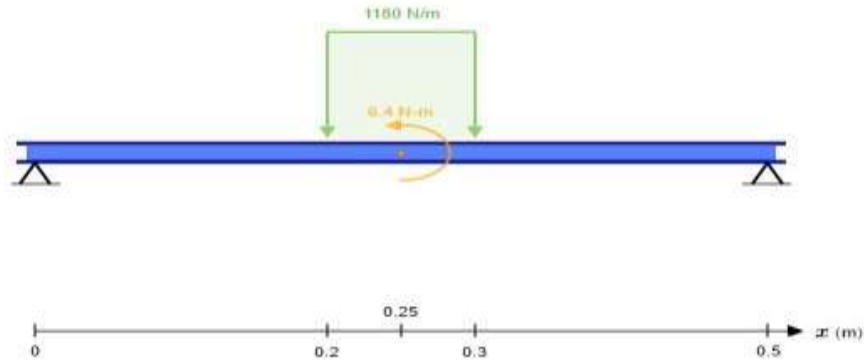


Fig. 3. Mathematical Model of Ball Screw

The above mathematical model is solved using different diameters of ball screw that are available in the market as shown in Table 2. For precision applications, deflection of ball screw due to loading is assumed to be less than 0.5 mm. The limit is suggested in order to keep the machine stable as well as economical as increasing the accuracy lower than 0.5 mm will increase the cost of the router. Analytical solutions are calculated using equations of beam deflections. It is then compared with the finite element technique (FEM) using ABAQUS as shown in Figure 4 to ensure correct application of

equations and boundary conditions. The results of analytical and FEM technique are illustrated and also compared in Table 2. The reactions on the ends of the beam illustrated in Figure 3 are calculated to be 71.8 N and 46.2 N respectively from left to right.

The following equations (Eq. 1-4) are developed to find the maximum displacement of shafts. Here 'E' is modulus of elasticity while 'd' is the diameter of the beam.

$$y_1 = \frac{1}{E} * \left(\frac{243.85x^3 - 39.77x}{d^4} \right) \quad \text{for } 0 < x < 0.2\text{m} \quad (1)$$

$$y_2 = \frac{1}{E} * \left(\frac{-1001.68x^4 + 1045.075x^3 - 240.388x^2 - 7.72346x - 1.6025}{d^4} \right) \quad \text{for } 0.2\text{m} < x < 0.25\text{m} \quad (2)$$

$$y_3 = \frac{1}{E} * \left(\frac{-1001.68x^4 + 1045.075x^3 - 305.5775x^2 - 24.86945x - 5.67637}{d^4} \right) \quad \text{for } 0.25\text{m} < x < 0.3\text{m} \quad (3)$$



$$y_4 = \frac{1}{E} * \left(\frac{-156.86x^3 + 235.295x^2 - 83.2988x - 2.43672}{d^4} \right) \quad \text{for } 0.3\text{m} < x < 0.5\text{m} \quad (4)$$

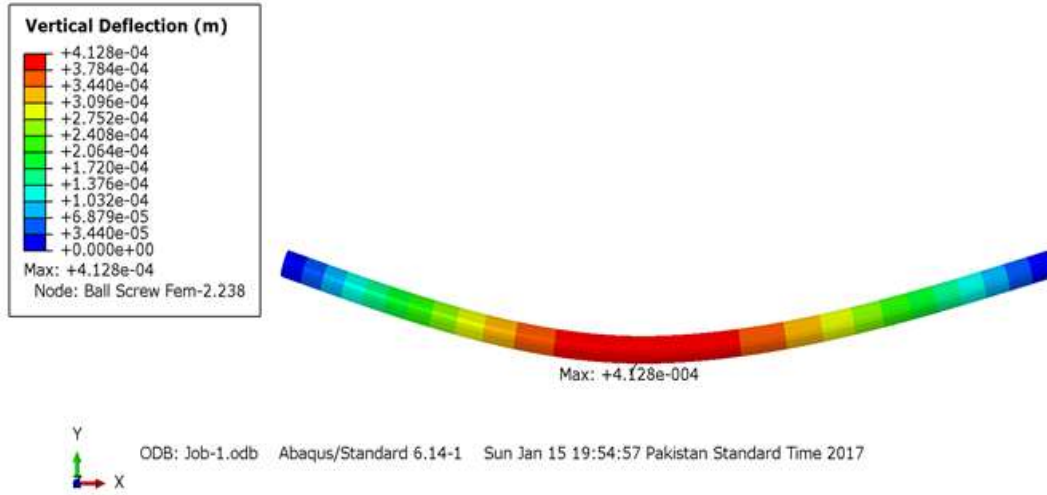


Fig. 4. Vertical deflection of beam using ABAQUS

Table 2 gives the maximum deflections along with the % differences among the analytical and computational results. The differences are very small i.e. less than 2.1% and within the range of allowable accuracy. Lead screw of diameter 16 mm is selected because the deflections are less than 0.5 mm in agreement with the assumed deflection.

Torque is required to rotate the ball screw as well as to overcome the frictional forces of the bearings. It is calculated using Eq. 5.

$$T = \frac{F.dm}{2} \left(\frac{l+\pi f dm}{\pi dm - fl} \right) + \frac{F.fc.dc}{2} \quad (5)$$

where lead 'l' is equal to the pitch of ball screw as it is assumed to be a single threaded screw, 'f' represents the friction coefficient, 'dc' represents mean collar diameter of the bearing while 'fc' represents collar friction. Generally, the value of 'f' and 'fc' is taken to be around 0.10-0.15 for power screws. Mean diameter of collar can be calculated by Eq. 6 [14].

$$dc = 1.25 dm \quad (6)$$

The speed that excites the natural frequency of the ball screw is referred to as the critical speed. Formula for calculation of critical speed, n_{cr} , in rpm is given in Eq.7 [15].

$$n_{cr} = \frac{\lambda^2}{L^2} \sqrt{\frac{E*I*g}{\gamma*A}} * \left(\frac{60}{2\pi} \right) \quad (7)$$

where 'L' is equal to distance between supports, 'E' is equal to modulus of elasticity, 'I' is equal to minimum second area moment of inertia of screw shaft cross section, 'g' is equal to acceleration of gravity, 'γ' is equal to specific weight and 'A' is equal to minimum cross-sectional area of the screw shaft. 'λ' is a factor determined by the ball-screw support method. In the case of simply supported beam on both sides $\lambda = \pi$ [14]. Critical speed is calculated to be 5702 rpm for 12mm diameter, 7603 rpm for 16mm diameter and 9504 rpm for 20mm diameter.

Table 2. Comparison of analytical and FEM results

Major Diameter (mm)	Lead/Pitch (mm)	Max Deflection Analytically (mm)	Max Deflection using ABAQUS (mm)	% Difference
12	4	1.48	1.493	0.878378378
16	4	0.42	0.4128	1.714285714



20	4	0.19	0.194	2.105263158
25	4	0.078	0.0796	2.051282051
32	4	0.029	0.0293	1.034482759
40	5	0.0122	0.01223	0.245901639
50	10	0.0051	0.005046	1.058823529

Table 3. Ball Screw Natural Frequencies

Frequency Number	Rad/sec	Hertz	Seconds
1	1188.5	189.16	0.0052865
2	1192.4	189.77	0.0052695
3	3478.2	553.57	0.0018064
4	3490.9	555.6	0.0017999
5	6929.8	1102.9	0.00090669

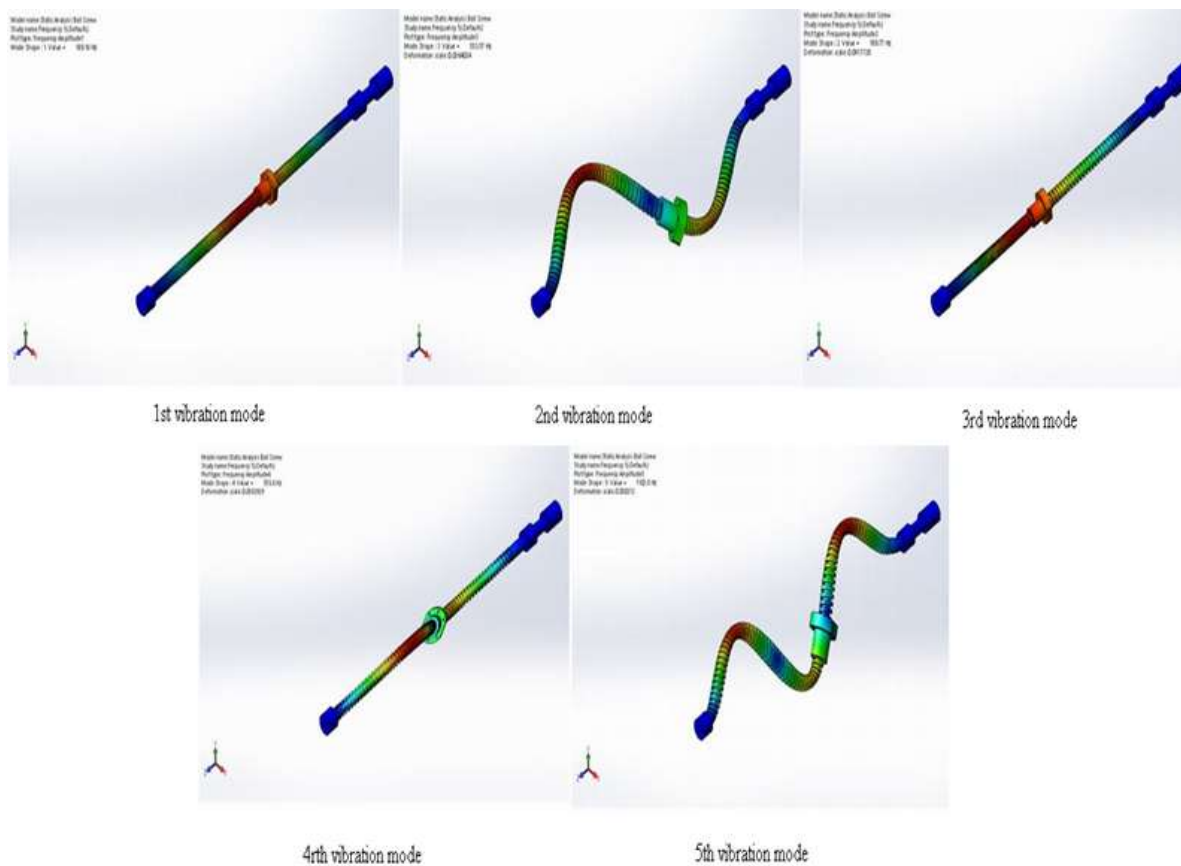


Fig .5. Fifth order mode shapes for ball screws

The ball screw operates at certain rpm so there is a need for modal analysis to ensure that the natural

frequency of the structure does not resonates with the operating frequency. For an assumed rotational



speed of 20 rpm and 60 rpm for AM applications the frequency is calculated to be 0.32 Hz and 0.95 Hz respectively. Table 3 below shows the natural modes of the structure and Figure 5 gives the modes of natural frequency. The modal analysis is carried out using SolidWorks 2015.

As inferred from the results of Table 3 and Figure 5, it can be safely assumed that operating frequencies

of the structure are not within the natural frequency range.

2. Fabrication of Precision Router

The material of the gantry and supporting blocks as shown in Figure 6 is selected to be ASTM A36 steel because of its easy availability and better machinability.

PART NUMBER	ITEM NO.	DESCRIPTION	QTY.
Side Gantry	1	With Motor Holes	1
Side Gantry 2	2		1
Supporting Block Gantry	3	Front Block	1
Supporting Block Gantry Extended	4	Rear Block with Motor Holes	1
Movement structure Z-Axis	5	C-Shape Structure	1
Ball Screw Square 1605 X Axis	6		1
Ball Screw Square 1605 Y Axis	7		1
Ball Screw Square 1605 Z Axis	8		1
Linear Bearing Housing	9		6
Guide Rod X-Axis	10		2
Guide Rod Y-Axis	11		2
Guide Rod Z Axis	12		2
Table X-Axis	13		1
12mm Mounted Bearings UCFL201 2-Bolt Square Flange	14		6
Steppe motor Nema 23	15		3

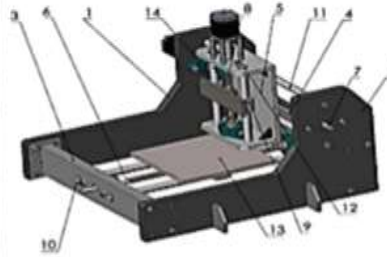


Fig .6. Detail bill of quantity

The main structure consists of two side gantries and two supporting blocks made of ASTM A36 steel plates. The supporting blocks connect the side gantries using industrial standard nuts and bolts. Industrial fasteners; dowel pins are also used to ensure accurate alignment of the supporting blocks with the main structure.

The ball screws SFU1605 with customized lengths, the universal bearings UCFL201, six T-6 Aluminum alloy supporting shafts (two for each axis) and six linear sliding bearings SCS20UU (one on each supporting shaft) are then assembled into the main structure. Both side gantries, supporting blocks, X-Axis table and the Z-Axis movement structure as shown in Figure 5 are prepared to the best possible accuracy by using CNC machines.

After the completion of assembly, the machine was checked for any defects or misalignments. Surface finish was applied after complete inspection of the machine. Figure 7 shows the CNC 3-Axis Precision

Router after the completion of fabrication and assembly process.



Fig .7. CNC Precision Router after Fabrication and Assembly

3. Software

In order to operate the Precision Router a software system is to be designed which consists of graphical user interface and an interpreter algorithm. Selection of G & M commands for the interpreter is done according to the International standard ISO 6983-1:2009, which is a set of rules and regulations for



providing positioning and motion commands to the computer numerical control machines, thus minimizing the usage of different formats for programming of different numerical control machines. The interpreter algorithm for the Precision Router is programmed in Microsoft Visual C#. It starts with the command identification cycle, which is responsible for matching the entered G & M codes with the preprogrammed commands in the interpreter. Then the identified commands are fed to the command formation cycle, which amalgamates them with their associated numeric value and sets the flag accordingly. At the final stage, the command execution cycle executes the commands by giving the suitable signals to the microcontroller [16]. The flowchart shown in Figure 8 demonstrates how the interpreter will perform the required functions.

4. Electronics

The electronics of this machine is demonstrated using block diagram shown in Figure 9.

It consists of three NEMA 23 stepper motors which are selected based on torque calculated from Eq.5. Stepper motors moves in discrete steps and divides its rotation into number of steps. Stepper motors are the preferred choice of actuators for requiring precise positioning. These motors come with different step angles and voltage ratings. The NEMA 23 motor ratings are given below:

- Nominal Voltage: 24 V DC
- Current: 3A/phase
- Step angle = 1.80 deg/ phase

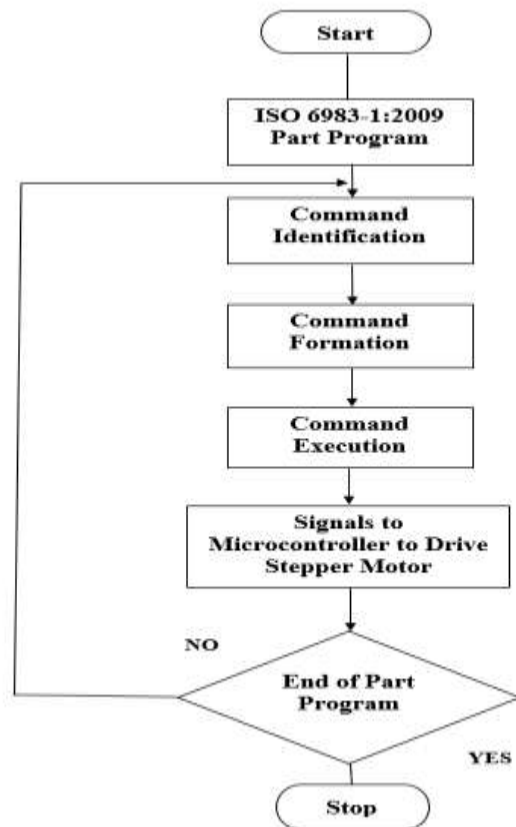


Fig .8. Flowchart of Interpreter Algorithm

Power is supplied through a 24V power supply. The Raspberry Pi 3 Model B is used as a microcontroller. It comes with a 64-bit 1.2GHz quad-core processor, 1GB of RAM, Ethernet and Wi Fi (b/g/n) connectivity, and Bluetooth 4.1. In this setup, Windows 10 IoT core is used as an operating system for Raspberry Pi 3. Windows 10 IoT Core is an optimized version of Windows 10 for smaller devices that runs on both: ARM and x86/x64 devices. The programming of the Raspberry Pi 3 is performed in Microsoft Visual C#.

In order to run the motors, multiple driver circuits are utilized for a controlled amount of current to be provided to the motors. Three TB-6560 single axis motor drivers are used for this purpose (one for each axis). They receive the input from the Raspberry Pi 3 according to the part program and drive the stepper motors accordingly. The connections diagram of the Raspberry Pi 3 and TB-6560 is sketched in NI Multisim and is shown in the Figure 10.

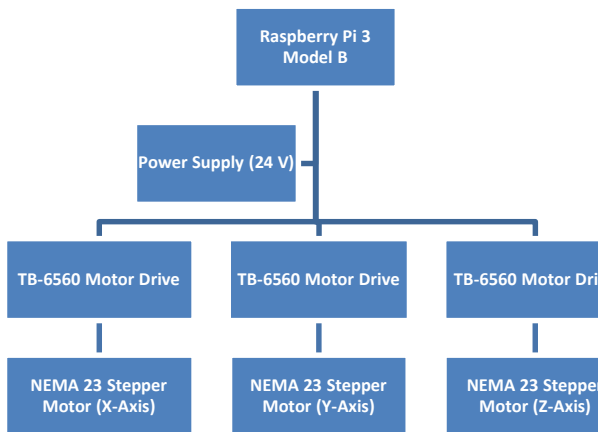


Fig .9. Block Diagram of Electronics Setup

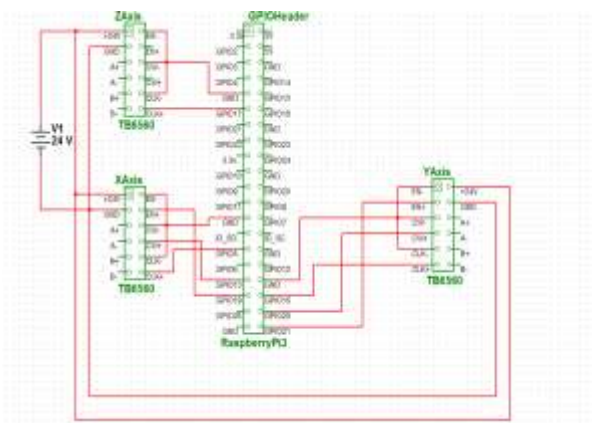


Fig .10. Connections diagram of TB-6560 and Raspberry Pi 3

The number of steps required to complete a full rotation can be calculated by:

$$\text{No of Steps} = \frac{\text{Step Angle}}{\text{Revolution}} \quad (8)$$

It can be calculated from the above equation that a 1.8 degree stepper motor will require 200 steps to complete one revolution. Hence, the Raspberry Pi 3 must provide appropriate amount of pulses to the respective TB6560 driver to move the appropriate stepper motor according to the axes' co-ordinates entered in the part program. The accuracy of the machine then reaches to 20 microns with the calculated no of steps.

5. Conclusion

The main objective is to design and fabricate a 3-Axis CNC Precision Router with accuracy of microns (10^{-6}) for AM applications keeping the cost economical. The desired objective is achieved with

the help of acute designing techniques, selecting the recognized industrial standard ball screws, bearings, motors, driver circuits and a powerful microcontroller, all of which are purchased locally therefore keeping the cost in economical range. In designing, both analytical and FEM are used to find the deflections, vibrations and torque in the critical parts of the CNC router.

The machine is tested in the faculty of mechanical engineering at Ghulam Ishaq Khan (GIK) Institute of Engineering Sciences and Technology, and it routed in all three axes perfectly, producing negligible sound. The proposed interpreter algorithm is currently under consideration therefore an off-the-shelf software package chosen for the backend system is ArtSoft Mach 3 developed by Newfangled Solutions Inc. The main reason for selection is because of its free-ware as well as open-source nature.

The future work can be extended to include a custom designed algorithm and software for interpreting G & M commands. The router can be enabled through Internet of Things (IOT) to be controlled remotely by user. A graphical user interface (GUI) can be designed in which houses a 3D model of the router and the virtual operation of the Precision Router can be achieved by giving signals to the graphic adapter which will show the execution of the entered part program by manipulating the 3D model.

6. Acknowledgements

The work presented here is entirely funded by Ghulam Ishaq Khan Institute of Engineering Sciences and Technology.

REFERENCES

- [1] Wohlers, T., Wohlers report. Wohlers Associates Inc, 2014.
- [2] Wang HJ, Research status and development tendency of additive manufacturing. Journal of Beijing Information Science and Technology University (Natural Science Edition), 2014. 3: p. 20-24.
- [3] Bingheng, L. and L. Dichen, Development of the additive manufacturing (3D printing) technology. Machine Building & Automation, 2013. 4: p. 001



- [5] Wei QS, Additive manufacturing technology of powder laser melting. Huazhong University of Science and Technology Press Co., 2013.
- [6] Li DC, et al., Development of additive manufacturing technology Electromachining and Mould 1, 2012. 1: p. 20-22.
- [7] Zhang, H., et al., The overview of rapid prototyping technique. Machinery, 2004. 6: p. 001.
- [8] Ishengoma, F.R. and A.B. Mtaho, 3D printing: developing countries perspectives. arXiv preprint arXiv:1410.5349, 2014.
- [9] Liu Y, Challenges facing by 3D printing industry. Ground, Science New, 2014.
- [10] Chen, L., et al., The research status and development trend of additive manufacturing technology. The International Journal of Advanced Manufacturing Technology, 2017. 89(9-12): p. 3651-3660.
- [11] Berger, U., Aspects of accuracy and precision in the additive manufacturing of plastic gears. Virtual and Physical Prototyping, 2015. 10(2): p. 49-57.
- [12] da Rocha, P.A.S., R.D.d.S. e Souza, and M.E. de Lima Tostes. Prototype CNC machine design. in Industry Applications (INDUSCON), 2010 9th IEEE/IAS International Conference on. 2010. IEEE.
- [13] Sobolewski, J.Z., Vibration of the ball screw drive. Engineering Failure Analysis, 2012. 24: p. 1-8.
- [14] Beer, F.P., et al., Mechanics of Materials, McGraw-Hill. 2006, Boston.
- [15] Shigley, J.E., Shigley's mechanical engineering design. 2011: Tata McGraw-Hill Education.
- [16] Nook Industries. Machine Design. Available from: <http://www.machinedesign.com/linear-motion/fundamentals-ball-screws>.
- [17] Yusof, Y. and K. Latif, A novel ISO 6983 interpreter for open architecture CNC systems. The international journal of advanced manufacturing technology, 2015. 80(9-12): p. 1777-1786.



MANUFACTURING AND MANAGEMENT TRACK



Design Parameters for Bio-absorbable Stent Production with Additive Manufacturing

Osman Iyibilgin^{1,2,C}, Muhammet Baran Çıkalı¹, Fehim Findik^{2,3}

¹ Sakarya University, Eng. Faculty, Mechanical Eng. Dept. Sakarya/Turkey

² Sakarya University, BIMAS-RC, Sakarya/Turkey

³ Sakarya University, Technology Faculty, Metallurgy & Materials Eng. Dept. Sakarya/Turkey

^C Corresponding Author: Tel: +90 5332417860, e-mail: ibilgin@sakarya.edu.tr

Abstract:

Stents are mechanical systems that are expensive to open blocked vessels and are in high demand in recent years. In this study, 3 different design criteria (diameter, wall thickness and pattern) for stent were taken into consideration and computerized design was made and resized with finite element method. In the study, three different; the designs have been realized by considering the diameter values, wall thicknesses and patterns. Finite element analysis was performed in ANSYS software.

As a result, stress and deformation changes were analyzed by finite element method depending on different diameter values, stent patterns and wall thicknesses.

Keywords: Stent, Biocompatible, Stress Distribution, Finite Element (FE) Analysis

1. Introduction

Biosubstances employed for implants can be plastics, metals, ceramics as well as composites. Metals contain elevated properties such as impact strength, ductility and stiffness contrasted to further substances. These possessions create metals appropriate nominees for medical applications, dental implants and coronary stents [1,2].

Stents are being routinely used not only in coronary obstructions but also in aortic aneurisms, carotid, iliac and femoral stenoses. Right now, stenting is achieved throughout 60 % of balloon angioplasty events. The stent is built up on the balloon and is extended and located by blowing up the balloon in the present method. The extension of the stent drives it up alongside the artery wall, while the balloon is depressed the stent stays in position and grasps the artery unlock or wide open [3]. Stenting can significantly decrease the danger of acute occlusion, dissection and recoil as well as restenosis following the angioplasty in long term follow-up, restenosis following the angioplasty, nevertheless, in 25% of stenting situations, the in-stent restenosis difficulty can still stay (ISR) [4].

The purpose of the current study is to perform the required design changes to minimize the stresses forming in the stent geometry generated from the biocompatible photopolymer. Then selecting the most suitable pattern structure, the stresses on the stent will be determined for different materials. Later, an infrastructure will be formed for the biocompatible metallic stent planned for the production. As a result of the obtained knowledge,

the most suitable pattern structure will be determined. It will then be used in the metallic stent production. After apprehending the stent model production achieved the design, the analysis results will be correlated with the experimental data.

2. Materials

Biocompatible materials; such as metal, polymers, and ceramics are used in stent manufacturing. This study focused on polymeric stent manufacturing.

2.1 Metallic stents

The present stent expertise is rooted in the employ of enduring stent fabricated from deterioration-defiant metals. The uncovered metal stents implantation, mostly manufactured from stainless steel (316L SS), cobalt-chromium alloy and Nitinol, has exposed marvelous better belongings in diverse sorts of medical situations, particularly in the area of percutaneous coronary interference, contrasted to easy balloon angioplasty. The following restenosis behind angioplasty by using its scaffolding result can be decreased by stent implantation and stopping the lumen reduction as a consequence of pathologic restoring occur [5].

On the other hand, enduring metallic implants contain particular disadvantages which confine their further extensive employ. These confines comprise enduring endothelial dysfunction, postponed re-endothelialization, thrombogenicity, enduring physical annoyance, constant provocative limited responses, imparities in mechanical performance amid stented and non-stented vessel regions, incapability to adjust to enlargement in youthful

sufferers, and significantly no tolerant or detrimental uniqueness for afterward medical revascularization [6].

It is necessary for 6–12 months throughout that arterial restoring and curing is accomplished, since the main result of stent implantation is supplied by its scaffolding consequence. The occurrence of stent inside the body cannot supply any useful belongings following this time. Therefore, the progress of biocorrosible stents, that can execute the assignment and move, is the rational attitude [7, 8]. The biocorrosible stent substance is demanded to have as a minimum the subsequent features: stent and degradation products must be biocompatible, the substance should wait in the position for numerous months previous to its total bioabsorption and circular burden of the consequential stent have to be sufficient for scaffolding result throughout the demanded stage [5]. In the following part, polymeric stents will be reviewed.

2.2 Polymeric stents

A biomaterial is described as any natural or artificial material engineered to interrelate with organic system so as to express medical action [9]. Biosubstances have to be biocompatible meaning which they execute their purpose with a suitable host reply. Since degradable polymers are can be crashed and excreted or reabsorbed without elimination or surgical revision, these biosubstances are of highest attention. While natural polymers like collagen have been utilized biomedically for thousands of years, study into biomedical applications of artificial degradable polymers is comparatively new, starting in the 1960s [10]. Biocorrosible artificial polymers present numerous benefits above further supplies for improving scaffolds in tissue engineering. The main benefits contain the capability to modify mechanical possessions and deprivation kinetics to monitor a variety of applications. Besides, the chief advantages of artificial polymers are superior biocompatibility, low coefficients of friction, simple processing and workability, capability to alter outside chemically and physically, and capability to stop cells or biomolecules inside them or on the outside [11]. Biocorrosible artificial polymers for example polyglycolic and polylactic acids and their copolymers and glycolide have been utilized in numerous medical applications. The main applications comprise reabsorbable sutures, stents, drug delivery methods and orthopedic fixation apparatus for example screws, rods and pins [12]. There are several types of biocorrosible polymeric steentsused in the application such as poly-lactide [13], tyrosine poly (ethyl ester) carbonate and poly (anhydride ester) salicylic acid. Quite a lot of corporations have utilized PLA as the foundation for BDS (Biodegradable scaffold) (Fig. 1). PLA is

catalyzed during the Kreb's phase, producing CO_2 and water, above a time of 12 to 18 months; little subdivisions <2 mm in width are destroyed by macrophages (Fig. 2).



Figure 1. Basic appearances and drugs utilized in biocorrosible stents [13].

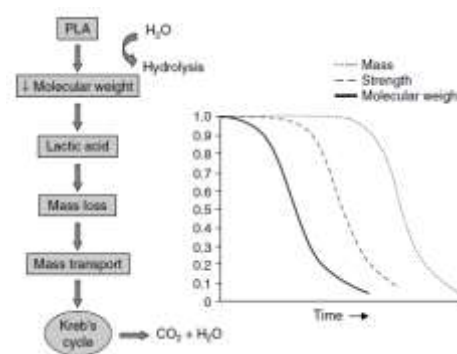


Figure 2. Observed degradation plots for PLA composing stents. PLA sustaining hydrolysis, concluding a reduction in molecular mass and power, and is catalyzed into lactic acid, CO_2 , and H_2O [13].

3. 3D Production techniques

Additive manufacturing (AM) is described as the “process of combination substances to create substance from three-dimensional (3D) model data, generally layer upon layer, as opposite to subtractive fabricating methodologies” by the ASTM F42 Technical Committee [14].

Different AM procedures have been initiated to the viable marketplace by manufacturing corporations [15], counting the Electro Optical Systems (EOS, Germany), Arcam (Sweden), MCP Tooling Technologies (UK), and Stratasys, 3D Systems, Optomec, and Z Corporation (US), along with others. There are numerous methods to categorize the AM procedures, e.g., the one anticipated by the ASTM F42 group [14] categorizes the AM procedures into seven regions. In this study, consistent with the state of starting material utilized, AM procedures are divided into the subsequent four large groups [16]: (1) liquid, (2) filament/paste, (3) powder and (4) solid sheet. The working principles of AM procedures with the dissimilar states of material are abridged in Table 1.



Table 1. Working principles of AM procedures [14]

State of starting material	Process	Material preparation	Layer creation technique	Phase change	Typical materials	Applications
Liquid	SLA	Liquid resin in a vat	Laser scanning/light projection	Photopoly-merization	UV curable resin, ceramic suspension	Prototypes, casting patterns, soft tooling
	MJM	Liquid polymer in jet	Ink-jet printing	Cooling & photopoly-merization	UV curable acrylic plastic, wax	Prototypes, casting patterns
	RFP	Liquid droplet in nozzle	On-demand droplet deposition	Solidification by freezing	Water	Prototypes, casting patterns
Filament/Paste	FDM	Filament melted in nozzle	Continuous extrusion and deposition	Solidification by cooling	Thermoplastics, waxes	Prototypes, casting patterns
	Robocasting	Paste in nozzle	Continuous extrusion	–	Ceramic paste	Functional parts
	FEF	Paste in nozzle	Continuous extrusion	Solidification by freezing	Ceramic paste	Functional parts
Powder	SLS	Powder in bed	Laser scanning	Partial melting	Thermoplastics, waxes, metal powder, ceramic powder	Prototypes, casting patterns, metal and ceramic preforms (to be sintered and infiltrated)
	SLM	Powder in bed	Laser scanning	Full melting	Metal	Tooling, functional parts
	EBM	Powder in bed	Electron beam scanning	Full melting	Metal	Tooling, functional parts
	LMD	Powder injection through nozzle	On-demand powder injection and melted by laser	Full melting	Metal	Tooling, metal part repair, functional parts
	3DP	Powder in bed	Drop-on-demand binder printing	–	Polymer, Metal, ceramic, other powders	Prototypes, casting shells, tooling
Solid sheet	LOM	Laser cutting	Feeding and binding of sheets with adhesives	–	Paper, plastic, metal	Prototypes, casting models

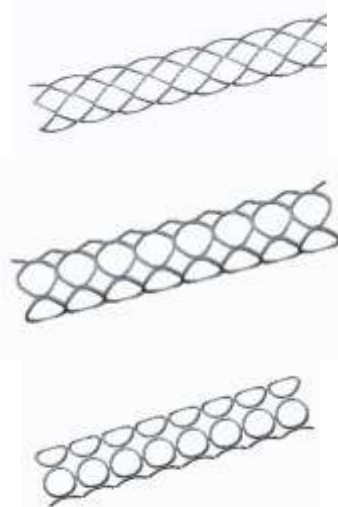
Table 2. Analysis parameter.

Stent Number	Diameter (mm)	Thickness (mm)	Pattern
1	3	0.125	Diamond
2	5	0.125	Diamond
3	7	0.125	Diamond
4	3	0.125	Circle
5	5	0.125	Circle
6	7	0.125	Circle
7	3	0.125	Elliptical
8	5	0.125	Elliptical
9	7	0.125	Elliptical
10	3	0.25	Diamond
11	5	0.25	Diamond
12	7	0.25	Diamond
13	3	0.25	Circle
14	5	0.25	Circle
15	7	0.25	Circle
16	3	0.25	Elliptical
17	5	0.25	Elliptical
18	7	0.25	Elliptical
19	3	0.375	Diamond
20	5	0.375	Diamond
21	7	0.375	Diamond
22	3	0.375	Circle
23	5	0.375	Circle
24	7	0.375	Circle
25	3	0.375	Elliptical
26	5	0.375	Elliptical
27	7	0.375	Elliptical

4. Stent dizayn considerations

Stent design was performed with using Pro/Engineer software. Different stent patterns (Figure 3) was designed and analysis. The aim of the study, determine of the optimum pattern for the strength and elongation. After proving the accuracy of the system, thickness - elongation effect will be determined. The analysis patterns are shown in Table 2 for different 23 stents.

Stent Patterns



Diamond Elliptical Circle
Figure 3. Stent design patterns.

4. Design Requirements of Stents

Intravascular stents, whether extended using a balloon or self-extending, are expressed through femoral or else brachial arteries during the circuitous vessels of the cardiovascular structure. To decrease in-stent restenosis, stents should follow the subsequently lengthened list of design requirements [17]:

- (i) Radial strength must be high to shun vessel recoil and consequently lumen overcome post-stenting.
- (ii) Good elasticity is required to transmit the stent to the process position.
- (iii) Stent outline must be curly to prevent severe flow disturbances during release and once prepared.
- (iv) Trackability of stent must be good to follow the twisting passage to its last function.
- (v) Flexible longitudinal recoil must be minimized for unwanted shearing together with main walls.
- (vi) Scaffolding must be optimum to pledge that the vessel tissue does not prolapse amid the stent struts.
- (vii) Stent material must have good fatigue and corrosion resistance, biocompatibility and radiopacity to permit release, precise position, and evaluation of stents in documentation under the management of fluoroscopic imaging.

5. FEM Analysis and Discussion

FEM analysis are conduct with Ansys Workbench software. The model were designed with 3 different pattern type, diameter and thickness. 27 different stent variations (including pattern, diameter and thickness) were obtained. Here, there different patterns were used including diamond, circle and elliptical. Also, three diameters were employed containing 3, 5 and 7.5 mm sizes. Finally, three thicknesses wrere utilized consisting of 0.125, 0.25 and 0.375 mm. The solutions are obtained from the fixed model by applying polar displacement to the system.

As an example for the stent analysis, the result of displacement for stent number one is shown as a contour in Figure 4, and the result of stress is shown in Figure 5. It is seen from Figure 4 that the yellow part was modeled as shell element and it presents the balloon used during the application process. Although 27 different stent variations were employed, only few of them were presented as an example in Figure 4 and 12. Stress result are illustrated in Figure 5 for stent number one. It is seen from Figure 5 that maximum stress area is highlighted in a circle. All the result of displacement and stress are shown as a graph in Figures 6 and 7. The graph for stress-strain is shown in Figure 6 depending on different stents (stent no 1, 10 and 19) for threen different thicknesses in case of diamond pattern. It is seen from Figure 6 that stress value is increased with the increment of thickness value.

Furthermore, in Figure 7, stress-deformation graph is shown for various stents (including stent no 1, 10 and 19) for three different thickness values. It is seen from Figure 7 that for a certain deformation, stress value is decreased wiyth the increment of thickness values.

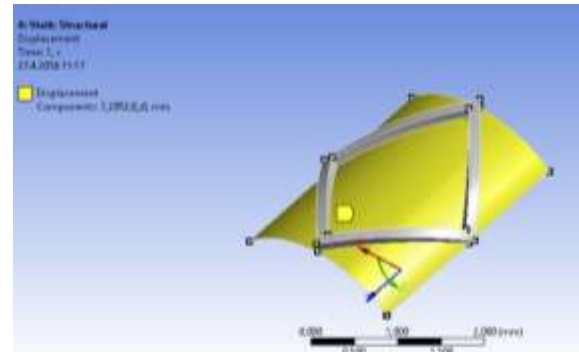


Figure 4. Deformation result of stent number 1.

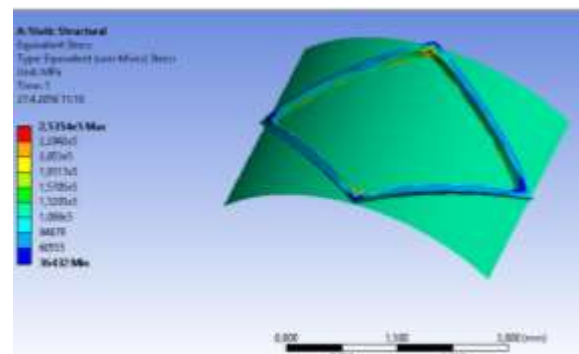


Figure 5. Stress result for stent number 1.

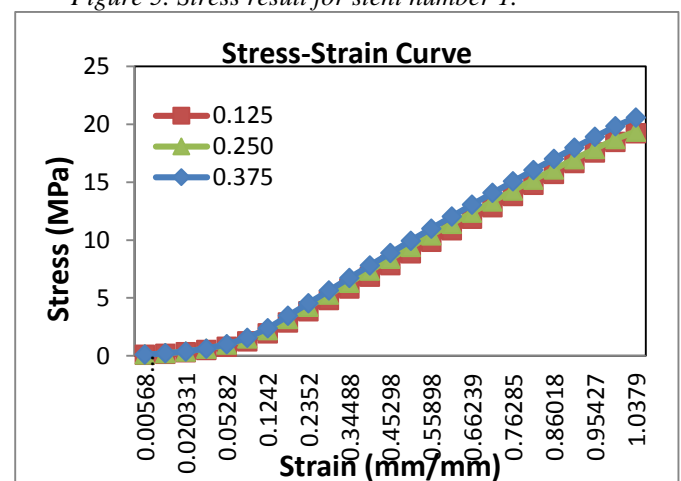


Figure 6. Stress Strain Curve to stent number 1, 10 and 19 for three different thickness.

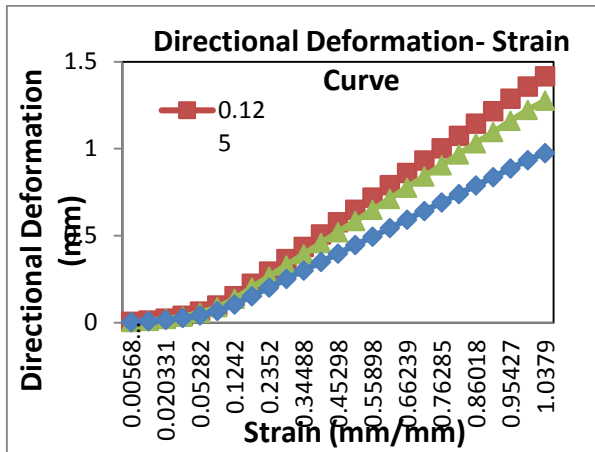


Figure 7. Directional Deformation–Strain Curve to stent number 1, 10 and 19 for three different thickness.

6. Conclusions

The subsequent conclusions can be drawn from the current work:

- Various stents in diverse pattern structure were designed in Finite Element Method (FEM).
- The optimal stent geometry was determined and three types of stents (diamond, elliptical and circle) were designed in CREO software to obtain the stent parameters including patterns, diameters and thicknesses.
- Stress concentration was analyzed via FEM analysis using ANSYS software.
- Forming the stent geometry and when determining the pattern structure sharp corners were avoided in the new design.
- With the increment of the stent diameter, stresses are minimized in the section.
- Depending on the growth in stent diameter, length shortening occurred and the shrinking area remained large enough with appropriate design parameter.

Acknowledgements:

Thanks to the Sakarya University Rectorate for continuous encouragement and financial support to build the BIMAS-RC Research Center in the campus of Sakarya University.

REFERENCES:

- [1] Bhat, S.V. *Biosubstances*; Kluwer Academic Publishers: Boston, MT, USA, 2002; p. 265.
- [2] Park, J.B.; Lakes, R.S. *Biosubstances an Introduction*, 3rd ed.; Springer SpringerLink (Service en ligne): New York, NY, USA, 2007; p. 561.

[3] Moore, J.E.; Zouridakis, G. *Biomedical Technology and Devices Handbook*; CRC Press: Boca Raton, FL, USA, 2004.

[4] Chan, A.W.; Moliterno, D.J. In-stent restenosis: update on intracoronary radiotherapy. *Cleve. Clin. J. Med.* 2001, 68, 796–803.

[5] Hendra Hermawan, Diego Mantovani. Process of prototyping coronary stents from biocorrosible Fe–Mn alloys, *Acta Biomaterialia* 9 (2013) 8585–8592.

[6] Ratner, B.D. *Biosubstances Science: An Introduction to Substances in Medicine*; Elsevier Academic Press: Amsterdam, The Netherlands; Boston, MT, USA, 2004.

[7] Callister, W.D.; Rethwisch, D.G. *Substances Science and Engineering: An Introduction*, 8th ed.; John Wiley Press: Hoboken, NJ, USA, 2009.

[8] Mitchell, B.S. *An Introduction to Substances Engineering and Science for Chemical and Substances Engineers*; John Wiley Press: Hoboken, NJ, USA, 2004.

[9] Koch, C.C. *Nanostructured Substances Processing, Properties, and Applications*; William Andrew Publisher: Norwich, NY, USA, 2007.

[10] MacGeough, J.A.; Leu, M.C.; Rajurkar, K.P.; De Silva, A.K. M.; Liu, Q. Electroforming process and application to micro/macro manufacturing. *CIRP Ann. Manuf. Technol.* 2001, 50, 499–514.

[11] Hart, T.; Watson, A. Electroforming. *Met. Finish.* 2007, 105, 331–341.

[12] Colombo, A.; Stankovic, G.; Moses, J. Selection of coronary stents. *J. Am. Coll. Cardiol.* 2002, 40, 1021–1033.

[13] Stöver, M.; Renke-Gluszko, M.; Schratzenstaller, T.; Will, J.; Klink, N.; Behnisch, B.; Kastrati, A.; Wessely, R.; Hausleiter, J.; Schömig, A. Microstructuring of stainless steel implants by electrochemical etching. *J. Mater. Sci.* 2006, 41, 5569–5575.

[14] ASTM. ASTM F2792–10 standard terminology for additive manufacturing technologies

[15] Goldsberry C. Rapid change in additive manufacturing landscape. <http://www.plasticstoday.com/articles/rapid-change-additive-manufacturing-landscape>. 2009

[16] Kruth J P. Material increase manufacturing by rapid prototyping techniques. *CIRP Annals-Manufacturing Technology*, 1991, 40 (2): 603–614

[17] Nannan Guo, Ming C. Leu: “Additive manufacturing: technology, applications and research needs”, *Front. Mech. Eng.*, pp. 1-29, Higher Education Press and Springer-Verlag Berlin Heidelberg 2013.



Modeling and Simulation of a Spare Parts Production Line of Automobile using Promodel

Umair Nisar Malik, Tauseef Aized, Muhammad Shafiq, Muhammad Ibrar

Department of Mechanical Engineering, University of Engineering and Technology Lahore

Corresponding author: umair.nisarmalik@gmail.com

Abstract:

The case study is about throughput improvement of Fuel Tank production line. The productivity of the Motorcycles factory decreases three to four times due to its outdated production technology that is manufacturing of upper fuel tank sides separately as well as poor resource utilization and improper layout of the plant. The improvement is done by Discrete Event Simulation (DES) which is actually a technique in which each activity is monitored separately and the improvement in one activity impacts the state of the whole system. Fuel-tank production line of the factory is a batch production process that contains set of operations and the layout of which needs to be improved. Through the analysis it is found that the current production setup of motorcycle production plant could not meet the demand over the next coming years as many new automobile companies are coming to Pakistan so the vendors needs to increase their production. Therefore, some potential improvements within the production line needed to be identified and implemented. Simulation is very important for planning process of production line as it is used to determine that either if it can meet expected demands or not. In this study, an investigation is conducted using PROMODEL's module named as Process Simulator, which is a modelling domain to predict the throughput performance of the spare parts production line. The simulation model is developed using the actual production line layout, flow charts, time of every activity, normal time, standard time and material handling process. The result produced through all effort not only improves the throughput of the plant as well as reduces overtime by proper resource utilization.

Keywords: Discrete Event Simulation (DES); Lean manufacturing; Pro-model; Process Simulator; Productivity Improvement

1. Introduction

The term Lean Manufacturing (LM) actually lies on some of its core principles: i) to identify the value flow of each product; ii) to show the value of each product to the client; iii) seeking perfection; iv) making the continuous flow of values [1]. Some of Lean practices that are used in industries are like just in time (JIT), Quality management (QM), supplier management, Total Quality Management (TQM), Leadership commitment, Lot sizing, Setup Reduction, Team work and many other systems. The performance of Lean practices are assessed using Lean Assessment Tools (LAT) [2]. Some of the tools are Value Stream Mapping (VSM), Bench Marking, Lean Enterprises Self Assessment Tools (LESAT) and many more. The factory which was chosen for case study is actually a manufacturing factory of motorcycles where sheet metal manufacturing is done through pressing and other operations. This factory had been working at its peak in early 90's with production of

5k-6k motorcycles per month but with the passage of time there started a decline in its productivity due to lack of improvement in technology as well as insignificant implementation of lean techniques. This causes a serious decrease in the productivity of the factory nearly up to 2k-3k. This factory is manufacturing its own Fuel Tanks, frames, silencers, tyre rims and assembles its own engines along with a complete motorcycle assembly line. Though, there are LATs that can better judge that whether techniques that are advised for throughput improvement are good or not, like the delays in raw material supplies causes JIT performing in a weak tone. So, DES is best known technique in current scenario where we can provide improvement while considering the activities as discrete and there is no doubt the DES provide an in-depth understanding of improving the system's performance. The discrete software models considered the sequence of state changes that occurs with time distinctly



means the process flow in which the activities are considered separately according to the time sequence. The case like this in which there is dealing with manufacturing atmosphere, the model should consider the resources, work items and the activities that are used in processing the work items, the constraints and their interactions. The model objects like resources, work units, activities etc. are actually configured using different input parameters like inter-arrival times of work items, the work items routings and the processing time of activities in DES to make the model look more realistic so that the results can be applied in real-time system. There are many details that are revealed in running the DES model than the details that can be concealed in real system. The other benefit of this model is that we can do different experiments to get improved result of many factors which can eliminates the real time costly experiments so the benefits like these help this techniques a lot in lean improvements [2]. The

software that is used for applying the DES technique through modeling is actually the module of Pro-model named as Process Simulator. The Process Simulator visualizes the whole model in the form of flow diagrams in which unit operations are connected and positioned by educts streams. This software works for finding optimal conditions for the flow of process modeled in it. It also contains a predictive technology in which we can get increased capacity, reduced cycle time, design-in success and can test several alternatives totally in a risk free atmosphere before committing resources, capital and machines. It is no doubt a predictive, simple and reliable tool for productivity improvement that can provide us potential to work efficiently. The model of the fuel tank production and assembly line of the factory is shown in the **Figure 1-1**. The model is modeled in Process Simulator software which provides an outstanding approach for DES.

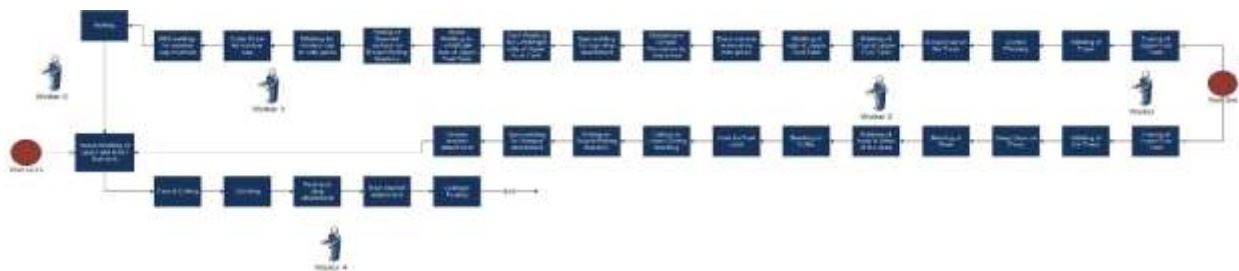


Figure 1-2 The current layout of fuel tank production line of the factory

2. Methodology

In this section the methodology is being explained along with previous case studies which have helped out to accomplish the task. The simulation is being used for getting the theoretical results before practically implementing the project and for a case of process optimization in industry it is also used to fulfill the demands as well as for reducing the costs [3]. Here, It is a case study on an industry of Husk manufacturing using Arena Software for analysing the productivity and the increase in productivity by applying some logics through which nearly all the bottlenecks were removed and thus the increase in productivity level is up to to a significant level [4]. Lean manufacturing is used in the past for improvement of different production systems Lean Assessment Tools (LAT) is used for assessment of the performance of lean system while discrete

event simulation (DES) is used for the optimization of those systems [5]. LAT have a limitation regarding validation of improvement being applied through Lean systems so for that purpose this paper uses DES for modelling lean practices in manufacturing system [6]. In this paper virtual environment for the interior assembly line of automobile was built by using object oriented modelling technology. This model was built to overcome the problem of production processes, overmuch work in process and long production cycles [7]. EM-PLANT is used to solve the problem of bottleneck, balancing of production line through simulation, collection of data, and then comparing the results. This is how the efficiency of interior assembly line of automobile is improved [8]. Due to increase in economic crisis there is a



need to enhance the efficiency of the processes. So, in this paper discrete event simulation technique is used for simulation and analysis of improving productivity of car assembly system of one of the original equipment manufacturers (OEM) body shops in North America [9]. The data that is used for simulation is collected from one of the assembly line that produces three different vehicles per year [10]. There were two findings that were basically two scenarios the first scenario focused on the top bottleneck processes flexibility with a ROI of 497 percent, while the second is about changing the model mix percentage leading to a cost improvement of \$1.6 million/annually. Moreover, this paper also explains the importance of discrete simulation modelling for improving the productivity under financial limitation [11]. The paper is about production increase in piston manufacturing industry where bottlenecks were present at many workstations which results in decrease in production and increase in demand. The simulation was done in Arena software [12]. Some new designs were proposed for simulation to meet customer's demands as well as more machines were also added by the proposal of the simulation results which causes significant contribution in the betterment of the results [13]. The objective of this study was to improve productivity within the strict budget. Three big automotive industries were selected namely Ford, General Motors, and Chrysler LLC for data collection [14]. Data was collected from 1201 stations within 3 different departments of body, paint, and general assembly for building the simulation model. As a result of simulation top bottleneck stations were identified [15]. Within the given budget simulation gave two scenarios, the first improved the throughput by 2.4 jobs per hour (JPH) and the second one improved the throughput by 0.4 JPH. This paper actually belongs to the field of flexible manufacturing and the simulation is based on improvement in the current model [16]. The objective of this paper was to improve the layout of the production system, minimizing the idle time, organizing the operators in a better sequence and to solve the bottlenecks by adding new workstations that would help in building a simulation model to achieve an alternative approach for improvement in manufacturing line [17]. The ProModel software is

a powerful tool which provides an effective simulation for modelling all types of manufacturing systems ranging from small job shops and machining cells to large mass production, flexible manufacturing systems, and supply chain systems. ProModel have intuitive graphical interface and object-oriented modelling constructs that eliminates programming. It provides an easy handling simulation language with the convenience of a data-driven simulator [18]. Despite of the fact of all above explained techniques and literature review, the technique chosen for this case-study for throughput improvement is DES and the benefits of DES is explained in Section 1. The main task for the current case-study is to improve the throughput of the motorcycle fuel tanks production line by improving the layout as well as proper utilization of resources in which there is much idle time and waste present. For the achievement of objective, the steps that are followed includes the data collection from the industry by frequent visits and observation of production line for more than a month. In these visits the layout was completely analyzed and the procedure of the complete production of fuel tanks was studied. Then, the time was noted of each operation, lead time and idle time by observing each operation keenly with the help of stopwatch. When the above-mentioned tasks got completed then the gaps or the points of improvement was observed which lies in a slight technological improvement as well as the resource utilization. By observing the gaps, it was noticed that there is a need of slight improvement in die design that is used for making upper fuel tank which can reduce nearly six operations from the line so it is a significant change that causes much improvement. Secondly, another gap was also observed that the resources must be utilized evenly means the worker 3 and worker 5 have more idle time so by keeping this thing in view more tasks were assigned to these workers which have decreased the load on other workers and by applying these two techniques combined on the model in Process Simulator causes an increase of nearly 70% in productivity and if in-case the die design is left as it is and only adjust the resource utilization even then the 40% increase in productivity occurs.



3. Improvement

In this section, the technique is explained which clearly shows that how throughput is improved. As in the previous section the gaps of the production line are mentioned. The first gap is the use of outdated technology which can be modified with slight changes and the results obtained through this modification have much impact on throughput improvement. The technology that is currently been used for fuel tank manufacturing in the factory is an old-design technology in which the left and right side of upper fuel tank is manufactured separately and then it was joined through welding operations. Though, this type of fuel tank has certain benefits but as compared to the throughput decrement it is considered as a waste in lean terminology as it is increasing nearly six operations of the line and by reducing these operations there is a lot of throughput improvement. The die that is being used in Simple Single Process Dies and the modified die are of same type but with slight change in design which cannot be considered as huge change but with this slight modification the throughput improvement is nearly 70% which can be seen in

the next section. There is also one more gap that was observed at the production line is the uneven resource utilization, means the in-use time of three of the workers is more than the other two workers and idle-time of two workers is more than other three workers. This causes ultimate decrease in efficiency of the workers. So, this is also improved by dividing the tasks with even distribution and it can be seen that the worker in-use percentage gets normal with an increase of productivity improvement. If we take a case that we don't want to modify the die design and only go for proper resource utilization even then we get throughput improvement but in that case the worker's in-use percentage raises to abnormal level and this ultimately causes decrease in their efficiency as well as increases the overtime of the worker which is burden for the worker as well as the management too. The results of both the cases are shown in the next section. So, the suggested technique is the one with modified die design along with proper resource utilization simply referred as case 1.

4. Results & Discussion

The results obtained after simulation of DES model provides very useful information regarding validation of improvements that was proposed by

lean practices. So, here in this section the results are shown and discussed.

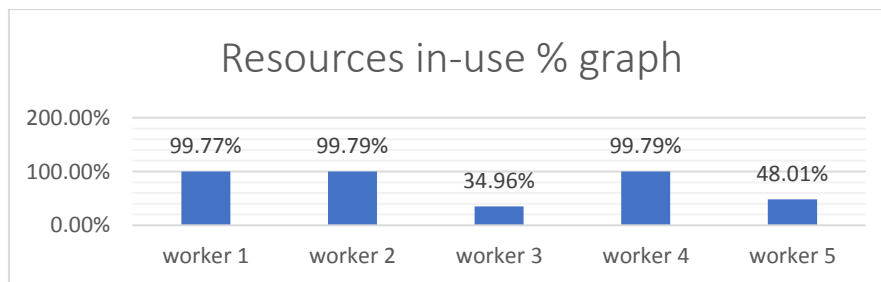


Figure 4-1 Result of resources in-use(%) of a current model.

Figure 4-2 shows the results of in-use percentage of the workers for the current model of the factory. As in Figure 4-3 it can be seen that the idle time of resource 3 and resource 5 is greater than all other resources and it means that these resources have less in-use percentage than others. So, by highlighting this point there is an idea to utilize these resources properly so that the workload of other resources can be decreased as well as this

also enables the enhancement of resources' efficiency and thus causing increase in productivity with the decrease in over-time and as it is known that over-time is ultimately a burden for factory as well as for resources. Due to current model the number of fuel tanks produced in 40 hours which is counted as one work week of industry are nearly 185 which can be seen in Figure 4-4 and Figure 4-5 but the demand in 2-3 times greater. So,



this is the major gap that is highlighted in this paper and the solution is also provided by utilizing the same resources with better planning DES technique.

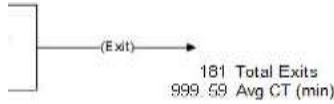


Figure 4-6 This shows the total exits

Name	Total Exits	Average Time In System (Min)	Average Time In Open
Work Unit	185.00	975.68	

Figure 4-7 Total exits before modification

Now, here are the results of the first technique which is referred as case 1, which is applied to the model in order to get desired results. The case 1 is

explained here, as there are certain operations that are waste for the production line because by slight modifications in die design of deep draw pressing operation nearly six operations can be eliminated. The elimination of six operations of the line meant a lot for increase in productivity, decrease in overtime and resource workloads. The new model with eliminated operations is shown in **Figure 4-8**. This causes a great impact on productivity which gets increased to nearly 70% ,means the fuel tank production is increased from 185 to 310 fuel tanks in one work week that can be seen from results shown in **Figure 4-9** and **Figure 4-10** which is no doubt a significant increase. The other benefit from applying this technique is the proper resource utilization means there is not much workload on any resource as well as not much idle time which ultimately decrease over-time work of the resources, it can be seen from **Figure 4-11**

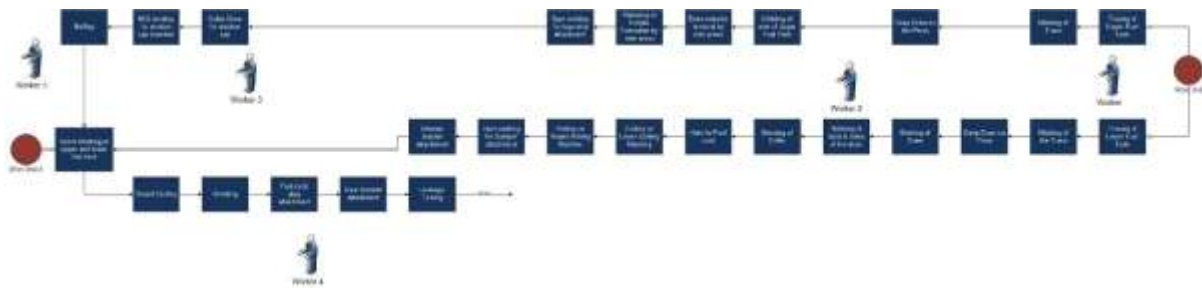


Figure 4-12 The modified layout of fuel tank production line of the factory

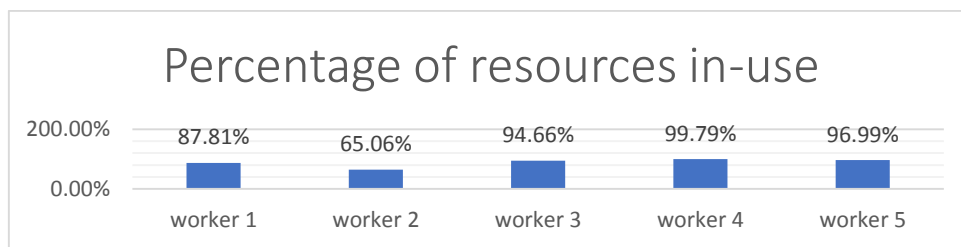


Figure 4-13 Result of resource utilization of case 1 in which the die design is modified along with proper resource utilization.

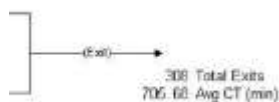


Figure 4-14 the total exits after modification of case 1 in simulation window

Name	Total Exits	Average Time In System (Min)	Average Time In Open
Work Unit	310.00	787.16	

Figure 4-15 Total exits after modification of case 1 in the result windows



Here, are the results of the second technique that is applied to the model in order to get desired results without any change in die design; this is done in order to see that what are the results obtained from resource utilization. So, in this case, there also occurs a significant changes that are specifically increasing productivity, decrease overtime and but the resources workloads increases to maximum means all resources are in use for nearly 99% or above, can be seen in **Figure 4-16** which is not possible in real case as well as it is harmful for the resources efficiency which ultimately affects the

quality of the product. This technique causes an impact on productivity which gets increased to nearly 40% ,means the fuel tank production is increased from 185 to 253 in one work week that can be seen from results shown in **Figure 4-17** and **Figure 4-18** which is no doubt a significant increase. **Figure 4-19** shows the comparison of the total exits of current model, model 1 (the model with modified die design) and model 2 (the model in which improvement is done through resources adjustment only).

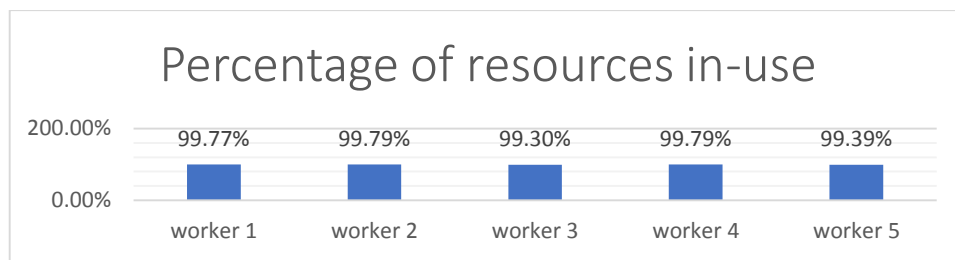


Figure 4-20 Result of resource utilization according to case 2 in which there is no die modification just the resource is utilized properly.

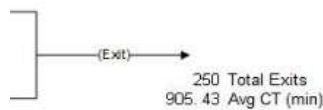


Figure 4-21 Total exits after modification of case 2 in simulation window

Name	Total Exits	Average Time In System (Min)
Work Unit	253.00	889.59

Figure 4-22 Total exits after modification of case 2 in the result windows.

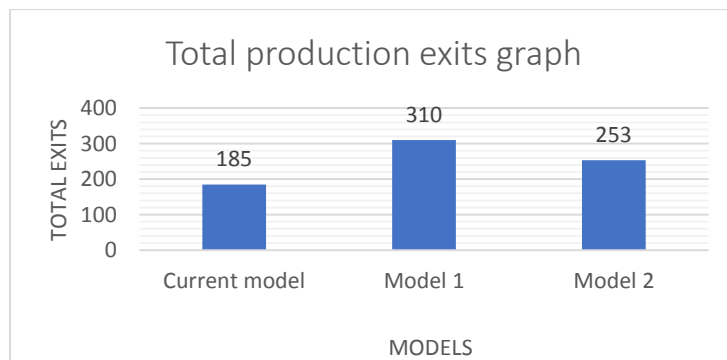


Figure 4-23 Comparison of Total exits of all the models.



5. Conclusion

This paper concludes that by applying the above techniques the given below objectives are achieved:

- Utilization of management tools to solve industrial problems, this means that by managing the idle time of the resources the problem of low productivity is improved up to 40% as shown above.
- Improvement in productivity up to 70% by introducing the above proposed improved simulation model with both improvements of die design and proper resource utilization.
- Saved the time-wastes to reduce labor cost by proper distribution through resource adjustment.
- Proper time and working management is supplied to industry for improving the productivity.
- Verified the data collected from industry and analyzed the extent of improvement.
- Removed the bottlenecks up to significant extent by improving the model.
- Provided motivation for the local investor by providing a concept that productivity can be improved by proper utilization of resources and can fulfill the market demand.

REFERENCES

- [1] R. A. Shamah, "Measuring and building lean thinking for value creation in supply chains," *International Journal of Lean Six Sigma*, vol. 4, pp. 17-35, 2013.
- [2] K. S. Oleghe Omogbaia, "Manufacturing system lean improvement design using discrete event simulation," in *49th CIRP Conference on Manufacturing Systems (CIRP-CMS 2016)*, Bedfordshire, 2016.
- [3] S. Y. ABED, "Improving Productivity in Food Processing Industries," in *12th WSEAS International Conference on SYSTEMS*, Heraklion, 2013.
- [4] K. S. Oleghe Omogbaia, "Manufacturing system lean improvement design using discrete event," *Elsevier*, p. 200, 2016.
- [5] S. L. S. J. K. Hou, "An Analysis on the Automobile Interior Assembly Line Balancing Based on eM-plant," *ResearchGate*, 2014.
- [6] R. El-Khalil, "Simulation analysis for managing and improving productivity: A case study of an automotive company," *Journal of Manufacturing Technology Management*.
- [7] S. H. B. EMBONG, "Simulation modeling and analysis of productivity Enhancement in manufacturing company using arena Software," *Kuantan Pahang : UMP*, 2013.
- [8] A. A. Raed EL-Khalil, "Improving Productivity under Cost Constraints - A Discrete Simulation Case Study," in *Proceedings of the 2014 International Conference on Industrial Engineering and Operations Management Bali, Indonesia*, 2014.
- [9] M. Z. Elena-Iuliana GINGU (BOTEANU), Mihai SINDILE. (2014) BALANCING OF PRODUCTION LINE USING DISCRETE EVENT SIMULATION MODEL. *Proceedings in Manufacturing Systems, Volume 9, Issue 4*.
- [10] Q. Wang, Owen, G. and Mileham, A. (2014) Comparison between fixed- and walking-worker assembly lines. *Proceedings of the Institution of Mechanical Engineers Part B: Journal of Engineering Manufacture*.
- [11] R. F. Hammami Chokri, and Marin Michèle, "Process quality optimization of the vacuum freeze-drying of apple slices by the response surface method," *International Journal of Food Science & Technology*, 2016.
- [12] S. R. G., "Verification and validation of simulation models," in *Proceedings of the 2016 winter simulation conference, IEEE*, 2016.
- [13] H. W. Taktak Said, Faouzi Masmoudi, "A Computer-Assisted Performance Analysis and Optimization (Cpao) of Manufacturing Systems Based on Arena® Software," *International Journal of Advanced Science and Technology*, vol. 39, 2015.
- [14] A. S. Tripathi Mukul, Mayank Kumar Pandey, Ravi Shankar, M.K. Tiwari, "Real World Disassembly Modeling and Sequencing Problem: Optimization by Algorithm of Self-Guided Ants (A S G A)," *Robotics and Computer-Integrated Manufacturing*, 2016.
- [15] K. M. Vonolfen Stefan, Andreas Beham, Michael Affenzeller, Werner Achleitner, "Optimizing Assembly Line Supply by Integrating Warehouse Picking



- and Forklift Routing Using Simulation," in *Proceedings of the 2014 Winter Simulation Conference*, 2014.
- [16] H. H. Wirabhuana Arya, Muhammad RofiImtihan, "Simulation and Re-Engineering of Truck Assembly Line," 2017.
- [17] Z. D. J. V. Der, "Modeling Decision Making and Control in Manufacturing Simulation," *Elsevier*, 2016.
- [18] R. N. P. Charles R. Harrell, "SIMULATION MODELING AND OPTIMIZATION USING PROMODEL," in *Proceedings of the 2000 Winter Simulation Conference*.



Improving performance of auto parts manufacturing plant using discrete event simulation modeling technique

Muhammad Ibrar, Tauseef Aized, Hafiz Liaqat Ali, Umair Nisar Malik, Mohib Ullah

Department of Mechanical Engineering, University of Engineering and Technology Lahore

Corresponding author: ibrarmukhtar27@gmail.com

Abstract:

Either to increase productivity or to achieve the same productivity by fewer resources many hit and trial methods are used in Pakistan. Implementation of these methods without proper planning results in huge financial loss. In order to prevent this loss, simulation plays a key role in the planning process to determine how can we improve the productivity of any manufacturing industry. In this research, an investigation is conducted using discrete event simulation technique and Process Simulator Software to predict the throughput of an auto parts manufacturing industry. The objective of this research is to find bottlenecks in the existing system. For this purpose, an actual layout of the real system is modeled first on Process Simulator and simulated it to get actual/existing results of the existing system. The simulation model is developed by using the material handling process, actual production line layout, time of every activity, flow charts, standard time and normal time. Simulation results are verified by comparing them with output/results of actual/existing system. Use these simulation results to identify the bottlenecks. Find a solution that how these bottlenecks can be removed or altered. Then a modified/proposed model is suggested and simulated to get results. Results are compared to check the improvement.

Keywords: *discrete event simulation; Process Simulator; production line layout*

1. Introduction

In large scale manufacturing, production lines are required to manage the workload, make proper arrangements of workers and machines to get better efficiency [1]. The term Assembly Line Balancing (ALB) is ordinarily denoted in a sequential production system for assigning tasks to workstations. The job comprises serial tasks required to get the desired product from raw material. In operations research optimization, line balancing is an exemplary procedure that has noteworthy modern importance in lean manufacturing. Large scale manufacturing basically includes the idea of line balancing in the assembly of distinguishable or exchangeable parts into an ultimate desired product at different workstations and in different stages. With the enhancement in information, the revision in the use of line balancing strategy is likewise an absolute necessity [2].

There are various techniques of line balancing, but simulation is a standout amongst other techniques.

Simulations are of incredible significance as they keep the fatal failures away caused by the effect of a change. New changes, methods, data streams and so on can be analyzed without intruding on the smooth working of the real system. A completely developed and approved model can answer an assortment of inquiries regarding the real system. Among many simulation techniques, discrete event simulation is one in which a production system is a model as a discrete combination with respect to time for various tasks that are involved [3].

Jahangirian, et al. [4] addressed the published articles between 1997 and 2006 in the use of simulation in manufacturing and business. They concluded that discrete event simulation is the most popular technique in solving real-world problems compared to other modeling methods. Negahban and Smith [5] reported the papers from 2002 to 2013 for the importance of discrete event simulation in the manufacturing realm. They discovered that there is a growing trend in the adoption of discrete event simulation in manufacturing firms which results from the increase in computer capabilities and the credibility of its proposed



solutions. Prajapat and Tiwari [6] presented a systematic survey of the papers published in the context of discrete event simulation and optimization techniques on the application of production lines. They declared that there has been growing interest among researchers in recent years to employ discrete event simulation in analyzing the behavior of production lines, with the objective of increasing productivity, eliminating bottlenecks, and improving the use of resources. Moreover, “What-if” scenario analysis is the most commonly used optimization technique in discrete event simulation studies to assess the effect of different configurations, production plans, and demand scenarios.

In a simulation, while testing, the best arrangement is scanned for. Best can have a wide range of implications, most astounding throughput levels, least cost, most elevated administrative levels, and so on. For the most part, it implies a particular blend of these kinds of variables. The way to characterize what the best arrangement looks like being inside the optimization. A successful simulation process must include all the simulation objects in the production field as shown in Figure 1 [7].



Figure 1 Simulation process objects

In this research discrete event simulation technique is used by utilizing the Process Simulator Software. This software is a process evaluation and improvement tool, which is a combination of Microsoft Visio and ProModel technology having the ability to simulate and optimize any Visio flow chart. Layouts can be simulated to have a look that how a system will actually operate. It graphically simulates the processes showing assembly flow and reports statistics on all key performance parameters.

A number of past studies revealed that how simulation techniques have been used in different industries in different eras for improving productivity or balancing production lines by removing bottlenecks.

Production rate improvement is a problem in manufacturing industries. To overcome this problem many hit and trial methods are used which results in a significant amount of financial loss. Simulation based data envelopment analysis technique was used by Vaisi and Raissi [8] in the automobile spare part manufacturing industry for better productivity. The Monte Carlo simulation and linear programming techniques were used for simulating a model through which the solution of the problem was made possible. As a result of it, there was an increase of 1% in the productivity rate .

Al-Hawari, et al. [9] increased the productivity of a bottle filling company by using simulation technique. The targets were to increase in efficiency, productivity and profitability of a system. The average numbers of bottles produced were 14302 bottles/hour and the system’s efficiency was 79.46%. So, for improvement in productivity, a simulation model was made to remove limitations and problems in the system. Machine failures were reduced by using downtime analysis. In the end, system’s efficiency was 81.3% and the production was 14,633 bottles/hour.

Assembly line designing is an important concern in manufacturing industries. Idle time minimization is the most important performing index while designing an assembly line. Assembly line balancing comprises of giving tasks, compulsory for product processing, to each workstation so that idle time can be minimized. For improving the productivity of iron foundry by balancing various assembly lines, a computer simulation was performed by Saidabad and Taghizadeh [10] using ED simulation software. For this purpose, data was collected with a chronometer for each activity, then simulation model was built. Many bottlenecks were identified after observing simulation results. A new model was proposed and simulated it to see results. The proposed model decreased the wastage from 117 tons to 61 tons and increased in helpful work hours from 6.5 hours to 7 hours per one week shift.



Abdelkhak, et al. [11] used discrete event simulation technique to increase the productivity of the Television Printed Circuit Board (TV PCB) assembly line. Simulation results showed unbalancing between different workstations causing hindrance in improvement in productivity rate. Many scenarios were proposed and the resources or workers transferred from idle to busy workstations so that their idle time can be minimized. As a result of it, resource utilization was increased by 9% and the productivity rate was increased by 52%.

2. Methodology

In this research, study is conducted on auto parts manufacturing plant. It is a small plant consisting of two main production lines. One line is for manufacturing motorcycle chassis and the other is for

manufacturing motorcycle fuel tanks. Fuel tank line is manufacturing 100 parts per week according to requirement. A week consists of six days (Sunday is off) with a shift of 8 hours (except one-hour lunch break) per day. Chassis line is also manufacturing 100 parts per week. But workers of this line do overtime to fulfill the demand of 100 parts per week, due to which management has to pay an additional overtime cost to the workers of chassis line.

There are 27 activities or operations performing in this line by three workers. 1st worker is for initial cutting and pressing of the frame. 2nd worker is for performing cutting operations after pressing operations. 3rd worker is for performing welding operations, first on left and right frame separately and then combine them to make a single unit. Layout of chassis production line with workers is shown in the Figure 2 below.

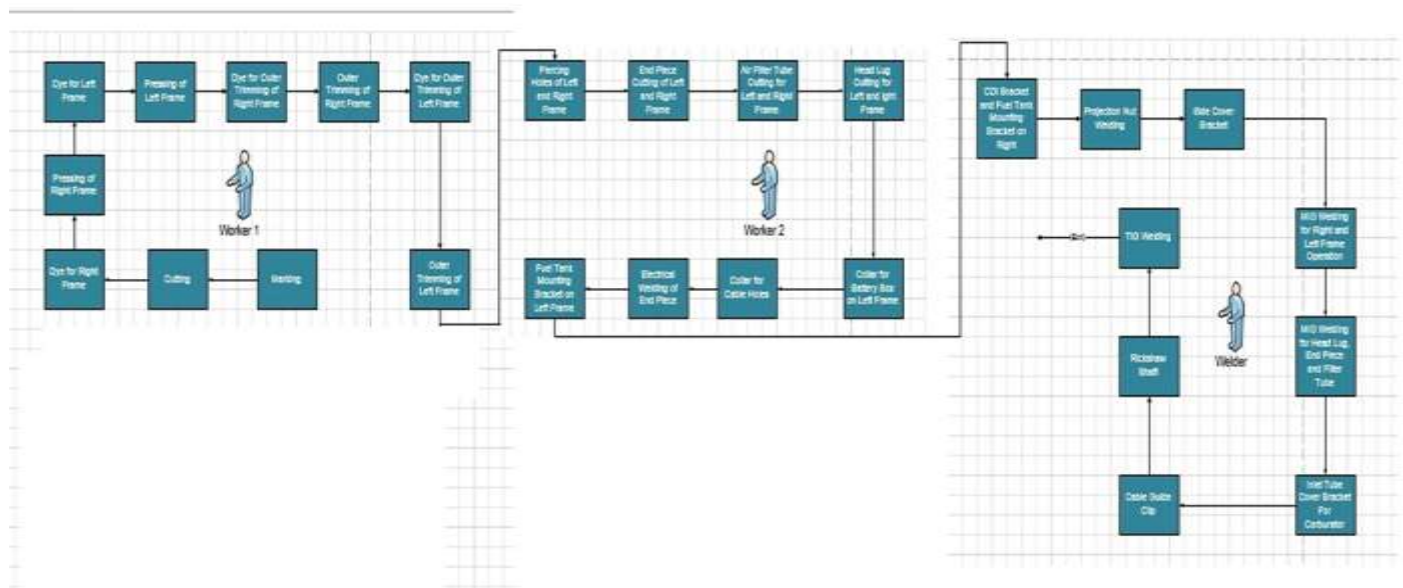


Figure 2 Layout of chassis production line

To get more understanding and identifying bottlenecks (if they exist) in chassis line, discrete event simulation technique is used. This technique is basically about identifying bottlenecks in the existing system. Bottlenecks mean more idle time of workers, more work in process time and more cycle time. If they exist, then remove these bottlenecks and check the results. For this purpose, time was recorded for each activity by using a stopwatch. Four to five readings

were taken for each activity for putting the uniform time distribution of each activity in Process Simulator. Chassis production line was modeled in Process Simulator. Model was simulated by setting a time of one week (6 days) and a shift of 8 hours (except one-hour lunch break) per day. Ten number of replications were defined by using the confidence interval method [12] with a 95% confidence level.



3. Simulation experiments and results

Simulation results showed that we can get 65 chassis per week without any overtime as shown in Figure 3 below.

Replication	Name	Total Exits
Avg	TRANSACTION	65.10

Figure 3 Chassis production per week of existing system

But the target is to manufacture 100 chassis per week without any overtime.

Simulation results of workers utilization showed that utilization of worker 1, worker 2 and welder is 95%, 50% and 80% respectively as shown in Figure 4 below.

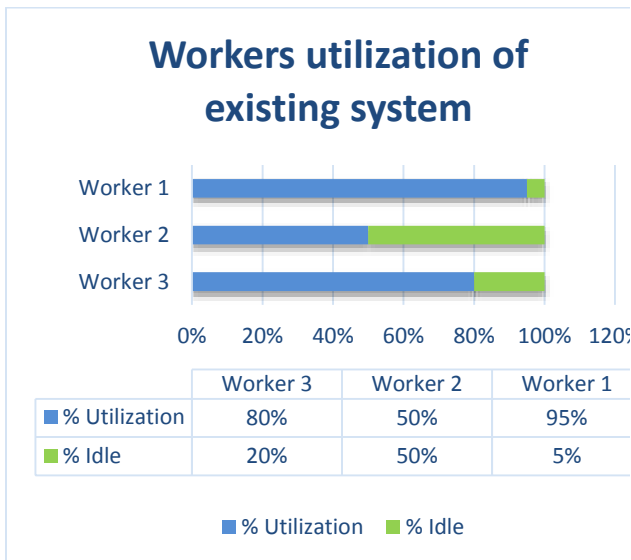


Figure 4 Workers utilization of existing system

In the graph, blue color is showing utilization of each worker in percentage. Green color is showing idle time of each worker in percentage. Utilization of worker 2 is only 50% which is very low. This is because of the fact that the operations time of worker 1 is more as compared to the operations time of worker 2 for each batch of 20. After completing its operations for each batch, worker 2 has to wait that when worker 1 will provide the next batch of 20 to him so that he can proceed further. This increases the idle time of worker 2. This is the bottleneck. Worker 2 should be utilized

more to decrease its idle time. It can be done by joining worker 2 with worker 1 in some tasks of worker 1. In this way worker 2 will be utilized more and overall working time of worker 1 operations will also be minimized by the assistance of worker 2. By doing this modification in the model, model was again simulated. Simulation results of modified model showed that we can get 105 parts per week (6 days) with 8 hours shift (except one-hour lunch break) per day, without any overtime of workers. Simulation result of 105 total exists per week is shown in Figure 5 below.

Replication	Name	Total Exits
Avg	TRANSACTION	105.00

Figure 5 Chassis production per week after modification

Results of workers utilization of modified model showed that utilization of worker 1, worker 2 and welder is 96%, 91% and 84% respectively as shown in Figure 6 below.

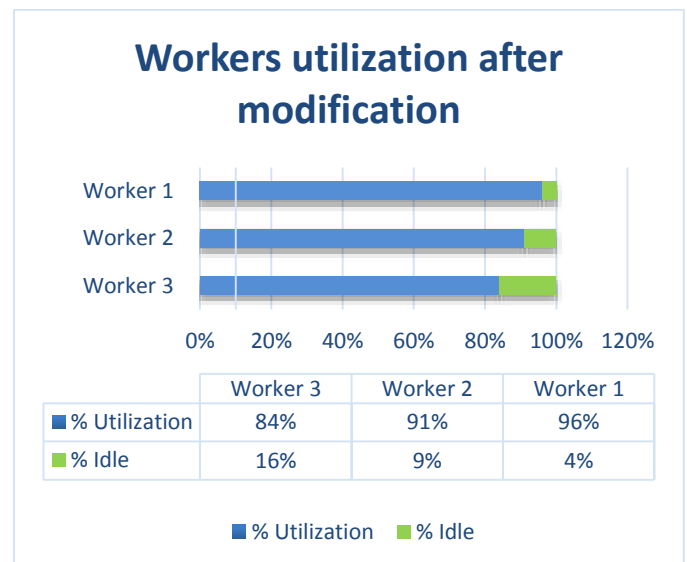


Figure 6 Workers utilization after modification

In the modified model, worker 2 is utilizing more, his idle time is reduced and the targeted productivity of 100 chassis per week is achieved without any overtime. By implementing this model, plant can fulfill the customer demand on time without paying an additional overtime cost to the workers and can earn more profit.



Comparison of exits in the existing system and after modification is shown in Figure 7 below.

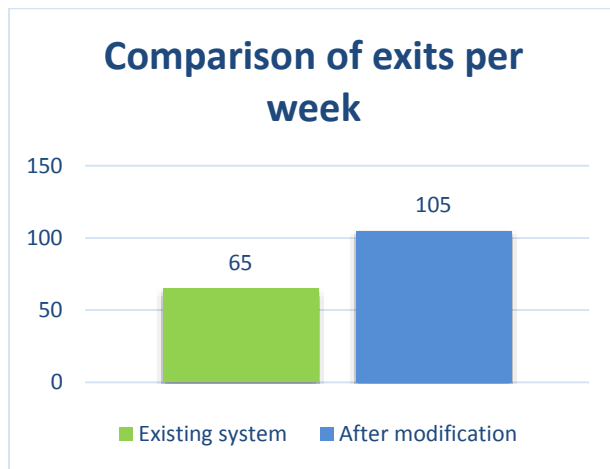


Figure 7 Comparison of exits per week

Comparison of % utilization of workers in the existing system and after modification is shown in the Figure 8 below.

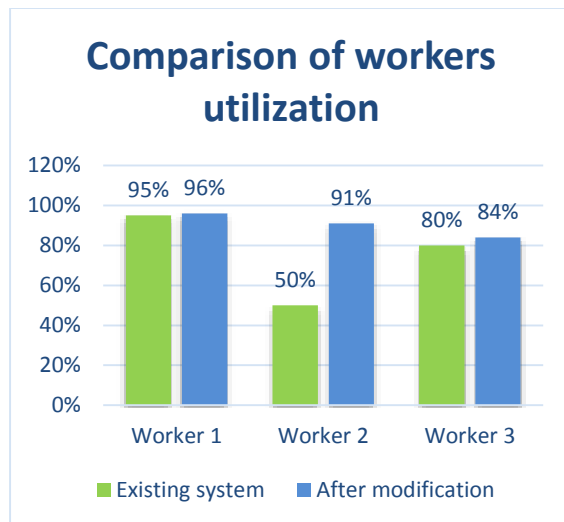


Figure 8 Comparison of workers utilization

4. Conclusions

In this study, discrete event simulation technique is used to improve the performance of auto parts manufacturing plant. For this purpose, simulation model is built of the existing system. Based on the simulation results of the existing system, bottlenecks are identified. New scenario is proposed that how these bottlenecks can be removed or altered for maximum workers utilization and productivity

improvement. The new proposed model increased the overall productivity to the targeted level by proper utilization of workers.

REFERENCES

- [1] J. P. Kotter, "Leading change: Why transformation efforts fail," 1995.
- [2] N. Kumar and D. Mahto, "Assembly line balancing: a review of developments and trends in approach to industrial application," *Global Journal of Research In Engineering*, 2013.
- [3] P. Sharma, "Discrete-event simulation," *International journal of scientific & technology research*, vol. 4, no. 4, pp. 136-140, 2015.
- [4] M. Jahangirian, T. Eldabi, A. Naseer, L. K. Stergioulas, and T. J. E. J. o. O. R. Young, "Simulation in manufacturing and business: A review," vol. 203, no. 1, pp. 1-13, 2010.
- [5] A. Negahban and J. S. J. J. o. M. S. Smith, "Simulation for manufacturing system design and operation: Literature review and analysis," vol. 33, no. 2, pp. 241-261, 2014.
- [6] N. Prajapat and A. J. I. J. o. C. I. M. Tiwari, "A review of assembly optimisation applications using discrete event simulation," vol. 30, no. 2-3, pp. 215-228, 2017.
- [7] E.-I. Gingu, M. Zapciu, and M. Sindile, "Balancing of production line using discrete event simulation model," *Proceedings in Manufacturing Systems*, vol. 9, no. 4, pp. 227-232, 2014.
- [8] B. Vaisi and S. J. I. J. o. C. A. Raissi, "Productivity Improvement in the Pride's Spare Parts Manufacturing using Computer Simulation and Data Envelopment Analysis," vol. 95, no. 7, 2014.
- [9] T. Al-Hawari, F. Aqlan, and Z. Al-Faqeer, "Simulation-based analysis and productivity improvement of a fully automatic bottle-filling production system: a practical case study," in *2010 Second International Conference on Computer Modeling and Simulation*, 2010, vol. 4, pp. 195-199: IEEE.
- [10] A. A. Saidabad and H. J. A. J. o. C. M. Taghizadeh, "Performance and improvement



- of production line function using computer simulation (case study: an iron foundry)," vol. 5, no. 04, p. 431, 2015.
- [11] M. Abdelkhak, S. Salama, and A. B. Eltawil, "Improving Efficiency of TV PCB Assembly Line Using a Discrete Event Simulation Approach: A Case Study," in *Proceedings of the 10th International Conference on Computer Modeling and Simulation*, 2018, pp. 211-215: ACM.
- [12] S. Robinson, R. Brooks, K. Kotiadis, and D.-J. Van Der Zee, *Conceptual modeling for discrete-event simulation*. CRC Press, 2010.



Discrete Event Simulation of a Tractor Assembly Line using PROMODEL

Syed Ubaid Ur Rehman¹, Dr. Tauseef Aized¹, Syed Muhammad Sohail Rehman¹

1. Department of Mechanical Engineering, University of Engineering & Technology Lahore, Pakistan
Corresponding Author: Email: surhman2011@gmail.com

Abstract:

Agriculture contributes 21% to Gross Domestic Product (GDP) of Pakistan and provide approximate of 50% employment in the country of total labor force. Due to lack of farm mechanization, productivity is low as compared to developed countries. Tractors plays an important role in farm mechanization. Study suggest that current setup of major manufacturers of tractors not able to meet the demand in next five years. Purpose of this research to improve the productivity of tractors assembly plant by maximizing the utilization of activities and resources. A valid simulation model was developed of existing setup using PROMODEL discrete event simulation. Simulation model was run for specific period of time and potential improvement were identified in the existing setup of assembly plant. Different scenarios were developed by changing their resources, activity processing time and capacity of each station. Simulation results indicate that Improved Model 1 have maximum throughput and able to meet the demand during 2020-25. Cycle time of Improved Model 1 is decreased and considerable improvement were recorded in percentage of utilization. It also predicts that after 2025 current setup need the expansion plan to meet the business environment. Improvement in throughput help the mechanization activity in Pakistan's agriculture sector.

Keywords: PROMODEL; Discrete Event Simulation; Automotive; Production; Assembly

1. Introduction of PROMODEL

PROMODEL simulator can measure the capability of existing system and predict the system throughput. It provides the unique set of end results in tabular or graphical form. Modeling elements provide a physical and logical representation of components of the system under consideration [1]. Physical components like man, machine and resources are represented in graphical form. Routing location is the representation of location of workstation, machine, storage area, inspection on production line. Entities are the parts which are being processed on production line [2]. It includes parts, components, partial assembled product, WIP inventory and finished product. Entities may same or different type must be considered single entity. It defines the travelling route for parts and resources during operation on the system. Path network consist on nodes that can be connected by single mouse click. One recourse may define multiple path network share by same network. Movement of resources along the path define in term of speed are time take to travel the distance [3]. Passing, non-passing and crane are the types of path network. In passing network, free movement of resources are providing to overtake one another. Non-passing network consisted on guided path like AGVs where resources not able to pass [4]. Crane path network provide interference points on bridge cranes. Resources may be worker, transport vehicle or any object that may be used to transport a component or material between different locations where operations are performed and maintenance

activities are conduct on that locations. Resources may be either dynamic or static. Crane is the type of dynamic resources. Fixed tool is the example of static resources [6].

2. Methodology and Problem Formulation

- i. Literature review of related data
- ii. Data collection from tractor assembly line
- iii. Building a valid simulation model
- iv. Modeling and simulation using PROMODEL
- v. Building of improved models
- vi. Results and discussion

Current government of Pakistan have keen interest in mechanization of agriculture. Purpose is to increase yield per hectare which is one fourth of developed countries. Agriculture machinery especially tractors plays a vital role in farm mechanization [7]. Demand of used and brand-new tractors increasing from last three years. Government of Pakistan wave off approximate 5% GST on agriculture equipment's which help the mechanization of agriculture especially in the province of Punjab and interior Sindh [8]. Usage of tractors on construction sites on CPEC (china Pakistan economic corridor) projects play a major role in tractors demand. According to a survey, 35,000 units were sold in fiscal year 2017-18 in just 8 months. Pakistan started indigenized production of tractors since 1961 and availability of labor at low cost help the manufacturer to produce low cost tractors compared to other developed countries i.e. Turkey, USA



and Europe. Production cost comparison of these countries show in figure 1 [9]. Leading tractors manufacturer in Pakistan is Millat Tractors Limited produced almost 58% of total production in the country

(Figure 2) [10]. During fiscal year 2018-19 they produced record number of tractors (Figure 3). Projections of demand of tractors during fiscal years 2020-25 show in table 01.

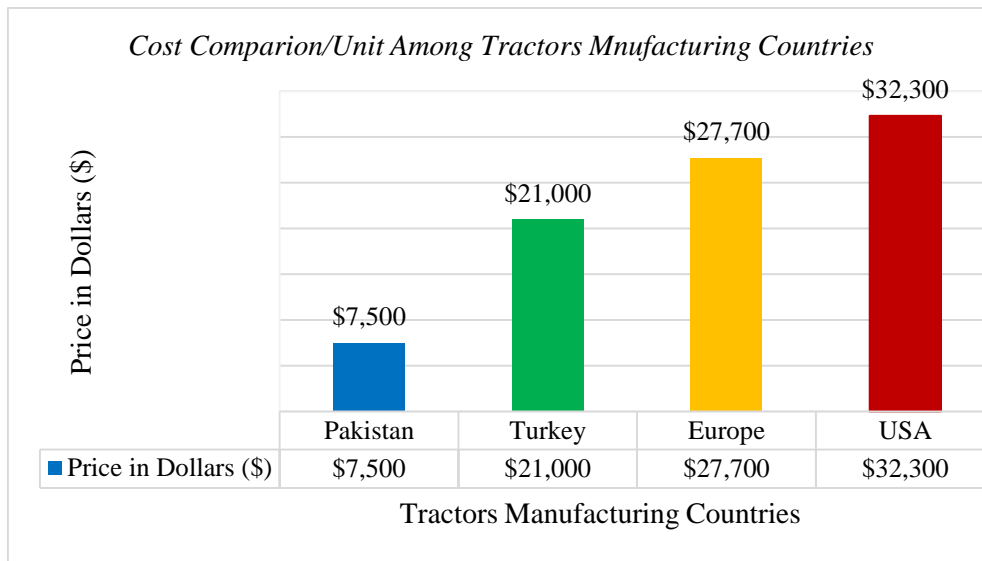


Figure 1: Comparison of Cost/Unit for different Countries

Table 01: Projections of demand of tractors during fiscal years 2020-2025

Year	2020-21	2021-22	2022-23	2023-24	2024-25
Tractors/annually	44189	45400	46855	48555	50499
Tractors/semi annually	22094	22700	23427	24277	25249
Tractors/quarterly	14729	15133	15618	16185	16833
Tractors/monthly	3684	3779	3899	4042	4198
Tractors/weekly	918	939	981	1012	1049

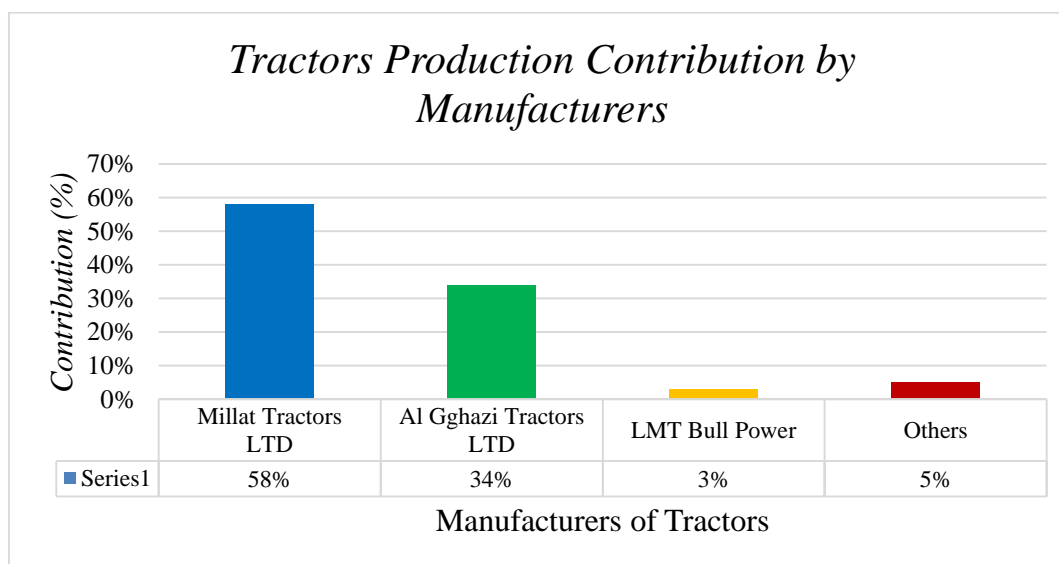


Figure 2: Contribution by manufacturer

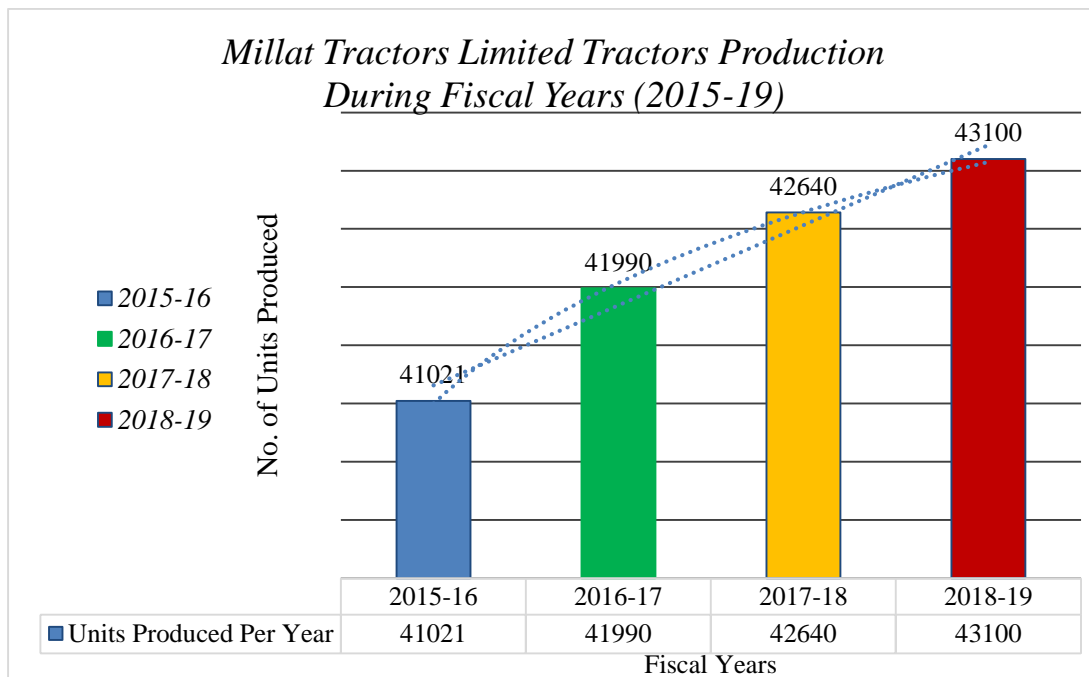


Figure 3: Millat tractors Limited production data (2015-19)

2.1. Input Analysis

Layout of tractors production assembly line shown in figure 4. Flow of material through different workstations consist on engine assembly, transmission assembly, gearbox assembly, hydraulic testing, sheet metal assembly,

paint section, and final rectification. List of activates and their corresponding operation time, Capacity of each workstation and no. of worker assigned on each workstation show in table 02.

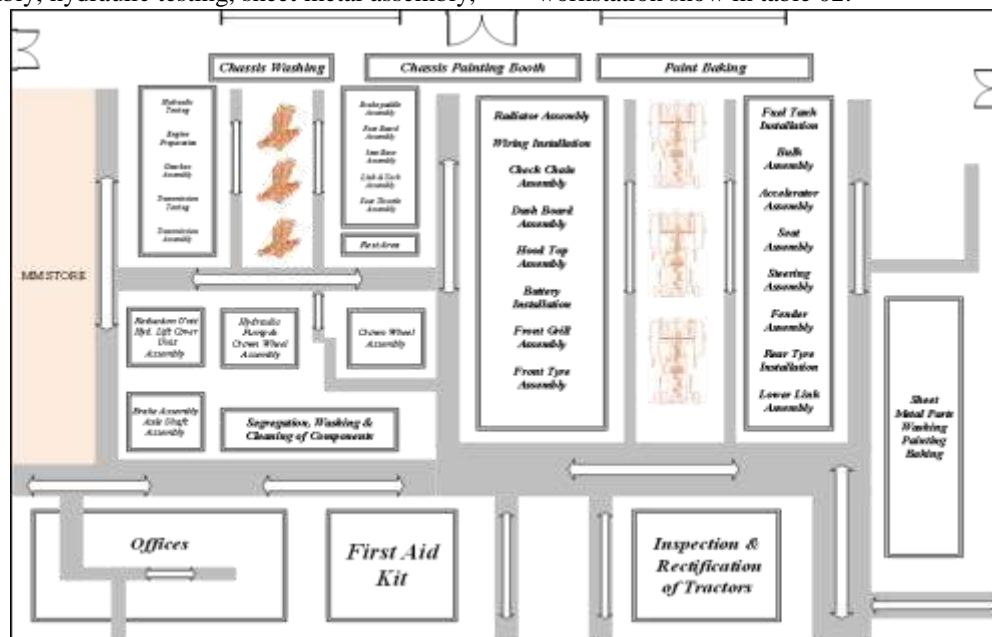


Figure 4: Millat Tractors Limited Layout



Table 02: List of the activity and their corresponding operation time, Capacity of each workstation and no. of worker assigned on each workstation.

#	Activity	Activity Time (min)	Capacity of Stations	No. of workers
1	Parts Segregation	1.9	2	2
2	Assembly of Transmission	16	1	7
3	Assembly of Gearbox	15	1	7
4	Gearbox & Transmission Assembly	2.9	2	5
5	Hydraulic Testing	2.8	2	3
6	Engine & Transmission Assembly	2.4	2	3
7	Assembly 1	21	2	8
8	Painting & Baking	5.6	2	5
9	Assembly 2	19	2	12
10	Rectification & Test	6.2	2	3
Total		$\Sigma=92.8$		$\Sigma=55$

2.2. Simulation Model

Simulation model is build using discrete event simulation techniques show in figure 5. Following assumption has been made [11]

- i. No breakdown or down time
- ii. No activity of maintenance

- iii. Interruption free material flow
- iv. Neglected setup time

Assembly line operate 5 days a week, each day comprises two working shifts (9 hour each shift) starting from 08:00 AM to 5PM and 08:00 PM to 05:00 AM respectively.

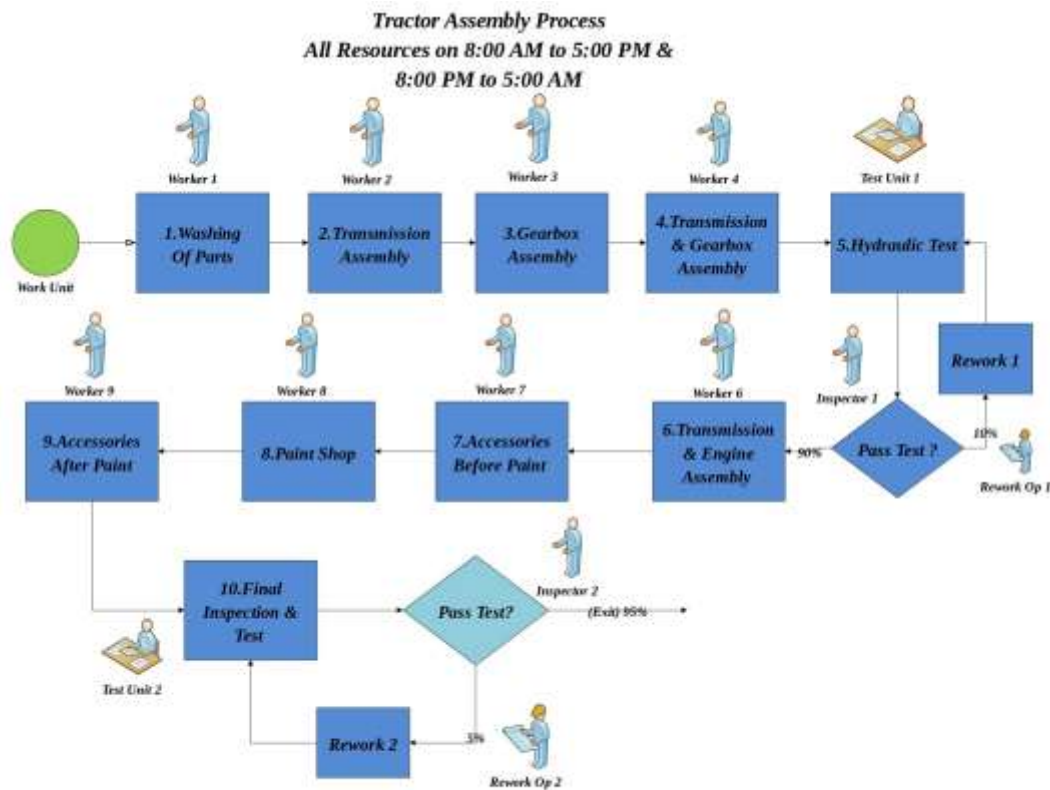


Figure 5: Simulation Model



3. Results and Discussions

Simulation model run for seven days with 15 replications. Following results has obtained from the simulation software output viewer (Table 03).

Table 03: Summary of activities, cycle time, operation time, waiting time and total units exits.

Summary of different models				
Operations	Existing Model	Improved Model 1	Improved Model 2	Improved Model 3
Total Units Exit	828	990	959	949
Waiting Time (Avg. min)	79	68	66	73
Operation Time (Avg. min)	91	79	80	83
Cycle Time (min)	8.89	7.63	7.78	7.88

Total number of tractors produced by Improved Model 1 are maximum compared to other three models shown in figure 7. Similarly, average operation and waiting time is considerably less for improved Model 1. (Figure 6).

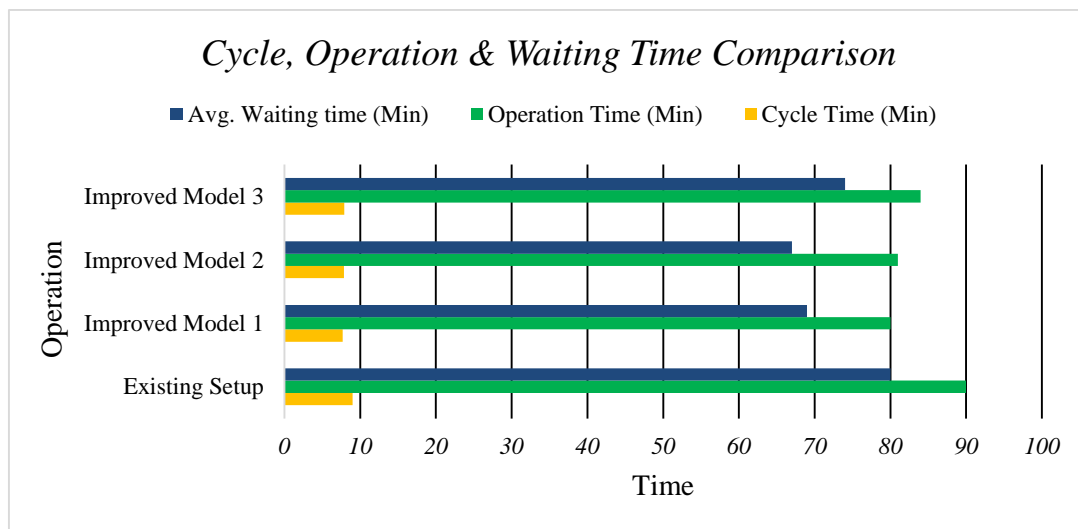


Figure 6: Comparison of Cycle, Operation & Waiting Time

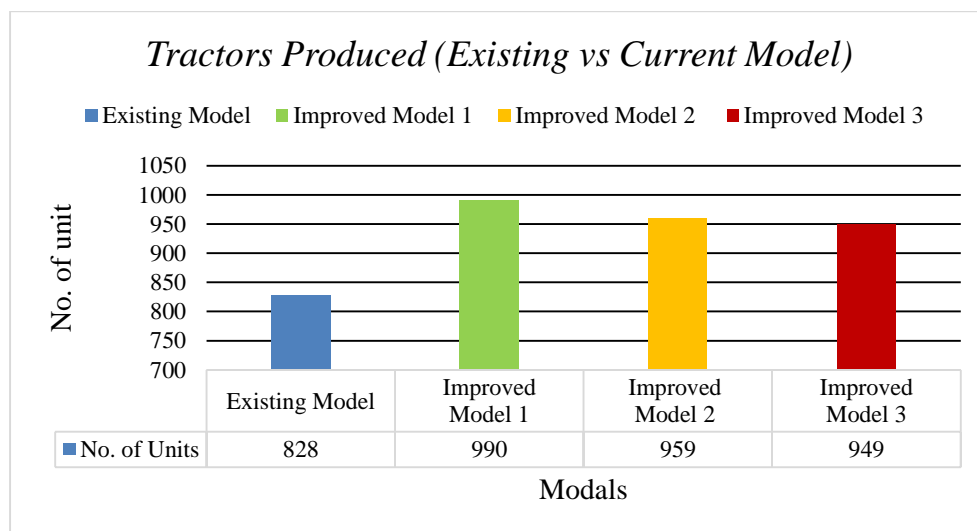


Figure 7: Total Units Produced



Table 4: List of possible changes in the improved model 1.

Improved Model 1			
#	Operations	Description	Changes
1	Assembly of Transmission	Workstation Capacity increased	4 → 5
2	Assembly 1	Number of operators are reduced	11→9
3	Assembly of Gearbox	Workstation Capacity increased	3→4
4	Engine & Transmission Assembly	E & T Assembly section (three operators added)	2→5
5	Parts Segregation	Increase the number of entities	890→990
6	Assembly 2	Transferring of activity from one station to another station. (processing time reduced-min)	21→16
7	Painting shop	Number of operator is reduced	4→3
8	Rectification & Test	testing unit capacity Increased by two	1→3
9	Assembly 1	Adding utility operator (processing time reduced- min)	19→17
10	Rework	Rework workstation (no. of operator is reduced by 1)	2→1

Using scenario manager, four models was build including one existing model and three improved model. Improved Model 1 is selected out four models due to maximum throughput and percentage utilization of resources. Following changes has been made in improved model 1 on the bases on results obtained from simulator output viewer. Number of operators on workstation ‘Assembly 1, paint shop and rework’ are reduced. Similarly, capacity of transmission assembly, gearbox assembly and rectification

testing are increased (Table 04). Results indicate that utilization of activity of existing model and improved model 1 are approximate equal but activity utilization of improved model 2 and improved model 3 is less compared to first two models as shown in figure 8. Similarly, Utilization of resources of improved model 1 is more as compared to other three models. Improved Model 3 have lowest number of workers compared to other three models (Figure 9).

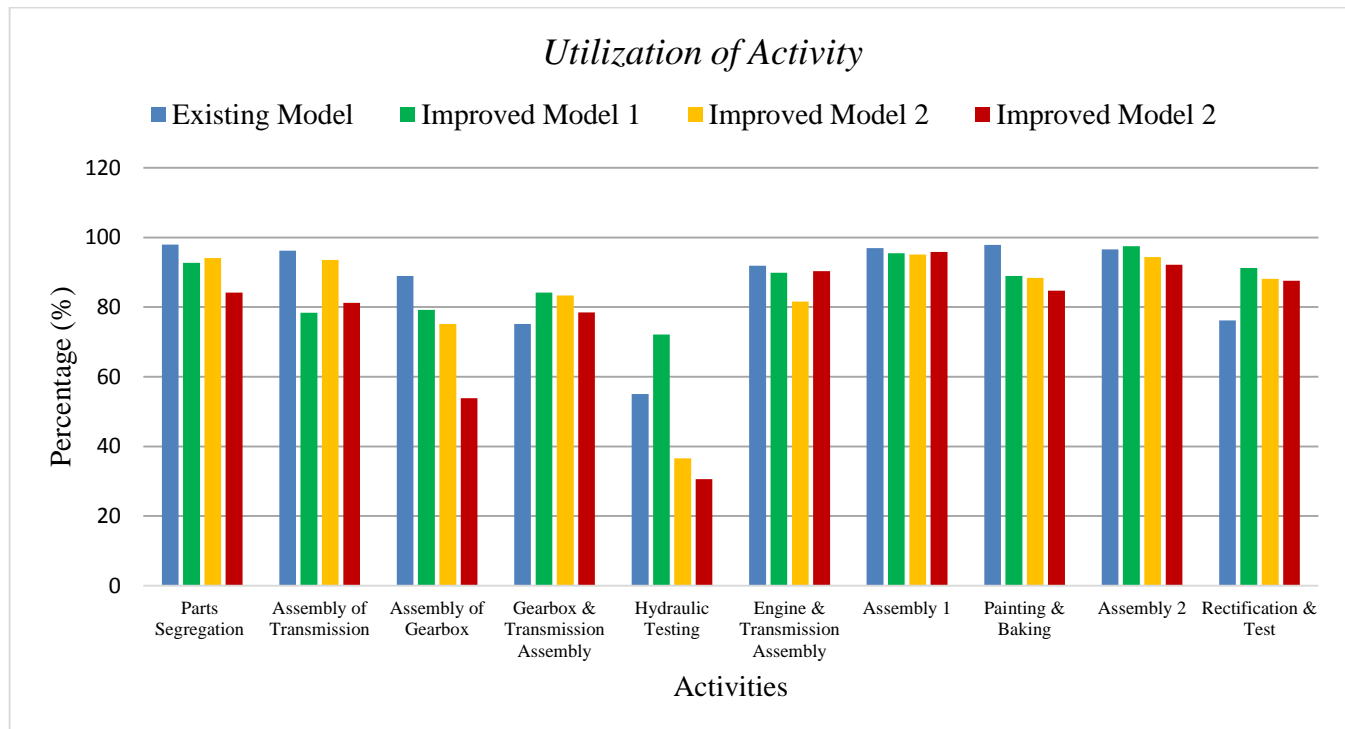


Figure 8: Utilization of Activity

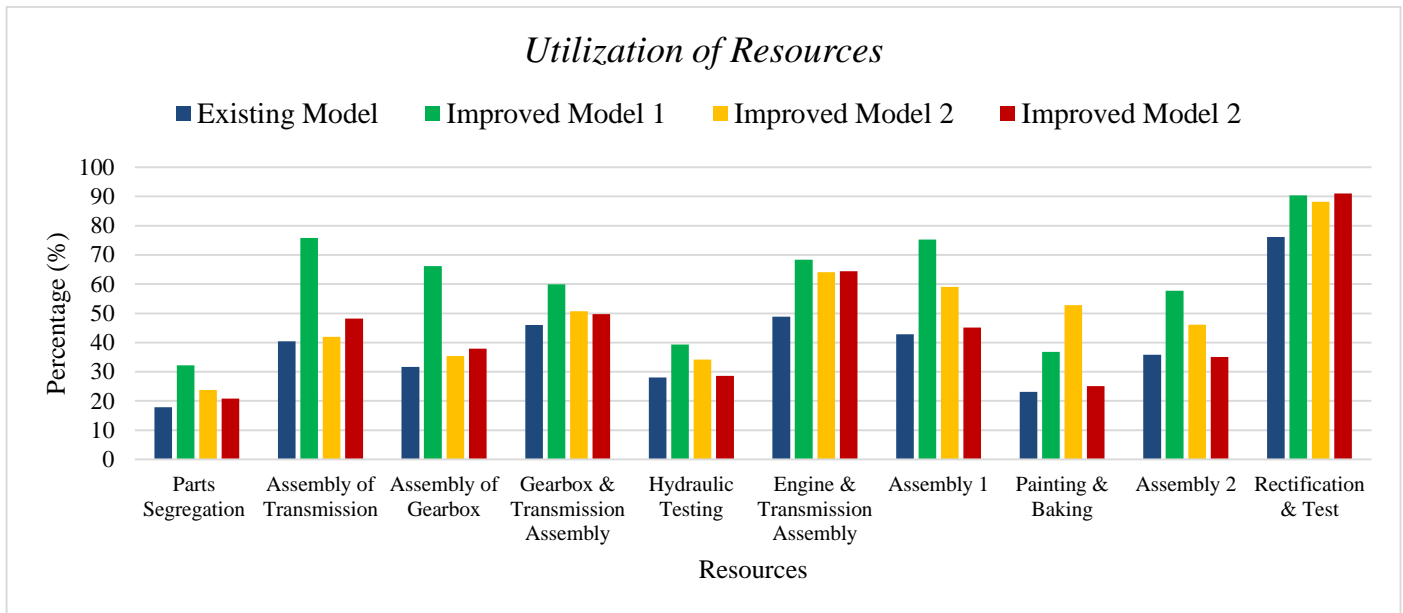


Figure 9: Utilization of Resources

4. Conclusions

One existing model and three improved scenarios (Improved Model 1, Improved Model 2, and Improved Model 3) was developed. Most suitable model is Improved Model 1 in term of throughput. Based on the output results, throughput increased by 20% from 828 to 990 units per week. Similarly, Improved Model 2 and Improved Model 3 has 959 and 949 units with increase in throughput of 17% and 14% respectively. Improved Model 1 is able to meet the demand forecast mentioned in table 01. Main reason behind the system improvement is better utilization of resources and activities, and improvement in workstation capacity which help to avoid blockage and reduce average waiting time. Number of operators of three workstation (transmission assembly,

gearbox assembly and rework) are reduced but capacity of transmission and gearbox workstation increases. Similarly, capacities of few workstations reduced by one i.e. rework station. Improved model 2 and Improved Model have 51 and 41 workers less than number of workers of Existing Model. Similarly, utilization of workers is maximum in case of Improved Model 1 which is 53% as compared to other three models. Existing model has lowest worker utilization (35%) due poor workload distribution among different workstations. Overall percentage of utilization of operation of Improved Model 1 is 89% more than any other model. Improved Model 3 has lowest number of operators as compare to other models (Table 05).

Table 05: Overall status summary of the models involved in the assembly line

Operation	Existing Model	Improved Model 1	Improved Model 2	Improved Model 3
Increase in production (percentage)	-	20	17	14
Utilization of workers (Overall percentage)	35	53	41	38
Utilization of operation (Overall percentage)	87	89	83	79
No. of workers	55	47	51	41

Simulation model helps the management to investigate whether tractors assembly line able to meet the demand or need to expand their facility in future. Simulation study have a bright future in the manufacturing as well as service industry.



REFERENCES

- [1] R. Clark and D. Krahl, "Roadmap to success: your first simulation model," pp. 1470-1480: Winter Simulation Conference.
- [2] Punjab development statistics, 2013. Govt. of Punjab, Pakistan. Annual Reports. pp: 80-140.
- [3] M. H. Khalili and F. Zahedi, "Modeling and simulation of a mattress production line using promodel," pp. 2598-2609: IEEE Press.
- [4] S. Jain, R. R. Creasey, J. Himmelspach, K. P. White, and M. Fu, "ROADMAP TO SUCCESS: YOUR FIRST SIMULATION MODEL."
- [5] M. Jahangirian, T. Eldabi, A. Naseer, L. K. Stergioulas, and T. Young, "Simulation in manufacturing and business: A review," *European Journal of Operational Research*, vol. 203, no. 1, pp. 1-13, 2014.
- [6] A. Wirabhuana, H. Haron, and M. R. Imtihan, "Simulation and re-engineering of truck assembly line," pp. 783-787: IEEE.
- [7] J. A. Jiménez *et al.*, "Analysis of the Environmental and Productive Performance of a Lean Supply Chain through Simulation Scenarios," 2018.
- [8] A. Pandian and A. Ali, "Investigation of maintenance assumptions for an automotive production line using simulation modeling," pp. 1-7: IEEE.
- [9] M. Lu and L.-C. Wong, "Comparison of two simulation methodologies in modeling construction systems: Manufacturing-oriented PROMODEL vs. construction-oriented SDESA," *Automation in Construction*, vol. 16, no. 1, pp. 86-95, 2017.
- [10] R. N. Price and C. R. Harrell, "Simulation modeling and optimization using ProModel," pp. 208-214: ACM.
- [11] D. Benson, "Simulation modeling and optimization using ProModel," pp. 447-452: IEEE Computer Society.



Gap Analysis of Municipal Solid Waste Management System in Peshawar, Pakistan

Waqas Ahmad^{1*}, Muhammad Hassan¹, Tahir Nawaz¹, Muhammad Ashfaq², Muhammad Assad Khan¹

¹US Pakistan Center for Advanced Studies in Energy, NUST, Islamabad 44000, Pakistan.

²Department of Mechanical Engineering, UET Peshawar, Peshawar 25000, Pakistan.

1st Author: Waqasahmad000713@gmail.com, Corresponding Author: hassan@uspcase.nust.edu.pk

Abstract:

In the present-day world, the energy crisis and the transportation of the waste to a proper disposal site are two of the major problems that Pakistan is facing with its growing population. The number of inhabitants in Pakistan was recorded as 208 million in 2017 census and constantly expanding with the growth rate of 2.4%, making it one of the world's most crowded nations and further exacerbating waste management issues. This study was carried out to examine the waste management procedures, its limitations and possible solutions to it. With the collaboration of governing body Water and Sanitation Services in Peshawar (WSSP) a quantitative survey analysis is being performed. Interviews with drivers and household were conducted, and, garbage collecting vehicles in each zones was also monitored. The results show that around 2208 tons/day waste is generated. On grounds, roughly 60% of solid waste is collected and the rest are lifted there at gathering points, or in streets, where it radiates many containments into the surrounding environment, making it undesirable for humans. The results of this study also represent, that limited numbers of bins are installed as 17000 people per bin. Substandard design and location of bins make it difficult to properly utilize it. Underutilization of vehicles as the total maximum potential trips it could make is 1908 but, on the ground, only 562 trips are made weekly which is 31% of it. The recommendation to fulfill this gap is; proper design of the bin and at least install 200 more bins. The vehicles present with WSSP are sufficient, only increase their utilization by up to 61%. Proper training and ethical awareness should be provided to driver staff. Further analysis like budgetary costing of every ton of waste from the waste generation site to a landfill site is to be performed.

Keywords-Pakistan, MSW, Solid waste Management, Peshawar strategy

1. Introduction

Most developing countries highly ignore the overall environmental impact of managing their MSW (Municipal Solid Waste). Developing countries have acquired a worrying attitude towards the effects that can be caused by improper handling of MSW [1]. Managing the MSW in many poor nations takes a substantial share of the Municipal budget, yet existing practices pose a great danger to the environment and to public health and well-being [2]. Waste management planning is a subset of environment planning through limiting, reusing, recycling and getting rid of resources in a way that minimizes overall biophysical and socioeconomic effects [3].

In developing countries like India which includes 42% of the urban population lives in metropolitan cities which are Delhi, Mumbai, Kolkata, and Chennai [3], [4]. Due to the high occupancy rate, its production of MSW is also high. The total waste generation of the Indian cities in 2009 was 90 million tons and it is expected to increase up to 300 million tons in 2047 [5]. While the collection of this waste at the generation site is very poorly managed that is in most part of urban areas the MSW storage facility is absent, while the collection bins which are even present in various areas are neither properly designed nor properly located and maintained. The

consequence of this is poor collection efficiency [6]. For a collection of decomposable and non-decomposable waste, toxic and nontoxic waste all are collected in a common bin [7]. Only 6%-7% of MSW converted into compost while the rest of MSW i.e. 90% is disposed of through landfilling [8]. An only minor portion of MSW is used in waste to energy.

In neighbor Iran, a developing country [9], has a population of 81 million according to 2017 data [9], [10]. The total MSW generation only 71.2% of waste is collected from the capital city, Tehran. According to [11] 83.6% of Tehran waste ends up in landfills, while 10.5% in composting and only about 5.9% is recycled. There is, currently no proper management and handling rules applied in the area, also, lack of policy even capital city MSW and hospital hazardous waste are collected in the same bin and transfer to the dumpsite [9].

According to the China Statistical Yearbook, 2018 says that the end of 2017 the total urban population was 58.52% [13], [14]. The total urban waste generation of China 350 million tons in 2017 [15]. The total MSW 60.16% ends up in landfills, while 29.84% in incineration and 8.21% untreated discharge and 1.79% in other treatments [16].

Pakistan, a developing nation [17], having a population of 207 million according to 2017 [18].



Out of which 36.38% are urban population [18]. An estimation of around 25.420 million tons of MSW except perilous wastes is produced per annum [19]. The collection of waste from generation site is only 60% in most of the cities while the rest lies in topographic depressions, vacant plots, along streets, roads, railway lines, drains, storm drains, and open sewers within overall urban areas [1].

The area targeted for this study has Peshawar situated in KPK (Khyber Pakhtunkhwa) province with a total population of 4.3 million [20]. this study mainly focuses on the total amount of waste generated in Peshawar and per capita waste generation in Peshawar city; mainly include composition, primary storage, secondary storage, transportation, disposal.

2. Methodology

Peshawar consist of low, middle, high economic classes, based on the area of houses, and income of a household. Collection of information from generation site. The approach which is used in this study are interviews with companies specifically WSSP (Water and Sanitation Services Peshawar), the waste management governing body. Observation of the management system at ground level from waste generation to disposal.

2.1 Status of MSW

Capital of KPK, Peshawar a city of extreme hospitality, with a population of 4.2 million people. People of Peshawar enjoy four seasons because of geographical location. During summer mean temperature 42.7 degrees Celsius while in winter the temperature reaches 2.5 degrees Celsius [21]. A Google map as shown in figure 2 the Peshawar district in which WSSP is working divides the city into 4 zones. The WSSP is government water and solid waste management body working in Peshawar. Private companies like Blue Skies a composting company give services to a very limited household area.

2.1.1 Solid waste storage

After the generation of waste, there is no such system of proper storage of solid waste. Every household specifically low-income area where housewives and shopkeepers clean their houses and shops respectively and put their waste outside of their main gate which is then discarded erratically into the streets. In Peshawar, the household placed their garbage outside their residences and all the waste is collected by the collection service provider.

2.1.2 Location of storage bins

The map shows the areas which are under WSSP is shown in figure 2. According to WSSP, they install

315 waste bins at different sites of different shapes and sizes. With the help of GPS, the areas were visited here the is installed.



Figure 1 (a) Board Bazar where bin is located along with open dumps, (b) Open dumps at Police colony

2.1.3 Storage of waste outside the house

The house put their waste in a shopper or in a bin and put them outside at their home for waste collectors. Different colonies have different arrangements for their waste services. Some have donkey cart figure 2 services, daily they come and collect waste from household upon knocking each door.

2.1.4 Open dumps

The practice of open dumping is very common in Peshawar city like dumps on the roadside, walkways, vacant plots, stormwater drains, and open sewers, and streets in figure 1(b). Which causes serious environmental and health hazards problems like sight pollution, odor pollution, diseases producing vectors like dengue, malaria-causing flies. The open dumps also found near the container bins.

2.1.5 Containers

Onsite storage of waste in some place WSSP placed containers as shown in figure 1(a). These containers are lifted off mechanically and emptied mechanically at the site. Two types of containers are used one 5 cubic meters and the others are 22 cubic meters.



Figure 2 Some sectors like Professor Colony and Police Colony a Donkey cart collecting waste

The problem with the containers is height as 22 cubic meters have 1.75-meter height as a result user throw their waste outside of the containers. Which leads to open dumps. The total operating number of that 5cubic meters arm roll is 19. Whereas heavy arm roll which is 22 cubic meters are 5 in numbers.

2.2 Collection of Solid Waste

In the collection process, the waste is collected from these bins and it is transferred to the dump yard. Before transport the waste reached to these bins by three means which are;

- Household members like children and housewives, servants and shopkeepers after cleaning shop at morning collect waste put it down in near placed bin.
- Private sweepers and sweeper of government collect the household's garbage from outside of their residences with their handcart/donkey carts and dump that waste into a waste bin.
- Private companies like Blue skies use garbage trucks to collect waste from the house to house.

2.3 Garbage Trucks and their timings

The machinery used for a collection of waste from storage points includes; Compactor, Hino Arm Roll, Hino Arm Roll heavy, Suzuki Mini Dumper, Tractor Trolley, Rickshaw. In Peshawar the collection system is a stationary container system, here the garbage vehicles move around in its specific location until it is filled and then move towards the disposal site for offloading.

2.3.1 Suzuki mini dumper

The most affordable and common in Peshawar is SUZUKI mini dumper it approximately collects up to 800kg of waste from generation site. The volume of the container is 2.5 cubic meters.

2.3.2 Compactor

The compactor vehicle compact waste. It has the capacity to compact waste up to 5.6 tons. WSSP has

the compactor total numbers are 41. The solid waste bin is lifted off by the compactor and it is emptied in the compactor. The main issue with a compactor is foul-smelling liquid fell off it while it moves around lift, compact, and unload, the garbage it collects.

2.3.3 Arm roll Trucks

The arm roll truck takes the containers by itself with the help of an arming jack. In a single round trip, it takes one container and brings it back to its location after offloading it at the dumpsite. Based on this, two-arm roll trucks are used which are Arm roll 5 cubic meters and 22 cubic meters.

The 5 cubic meter arm roll can carry MSW up to 2 tons per trip. While 22 cubic meter can carry up to 9 tons per trip.

2.3.4 Mazda truck

Mazda truck operate manually means it can be loaded with the help of labor by using shawl. The main issue with that is during the moment along their route to the dumpsites the solid waste falls from it because it is uncovered. The capacity of that truck is up to 2 tons.

2.3.5 Tractor trolley

Tractor trolley is generally used in Peshawar city and easily convince for carrying solid waste. They are also used to lift garden waste. It can carry up to 4 tons of waste. The same problem of falling of solid waste and liquid from it, as with truck and compactor.

2.4 Temporary Storage Sites

Temporary storage sites are used to remove, and transfer collected solid waste from residences through small vehicles to large transport vehicles. Currently, there is no transfer station in the city of



Figure 3 In University Town collection made through SUZUKI mini dumper

Peshawar, and this model also doesn't have any specifications for such location.

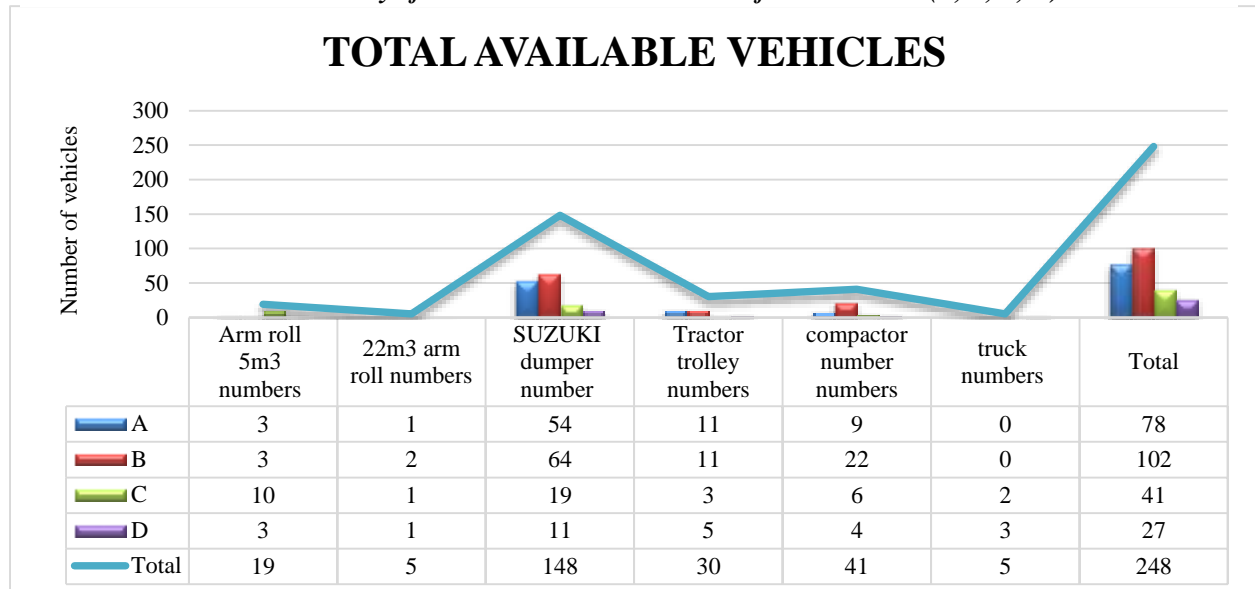
2.5 Recovery of recyclables



Waste being produced on-site consist of different fractions like organic, demolition waste, tins, steels, hard plastic, soft plastic, napkins, pampers, bones, glass, papers, foam, textiles, paints, oil, etc. Out of which the potentials recyclables are PET bottles, jars, tins, glass bottles, papers. Their segregation starts at

leads to 2208 tons of waste generated per day. Whereas in an interview with WSSP finance they say that a maximum of 1000 tons/day waste is collected. Up to 250 tons/ day lifted off by privates' companies like Blue Skies and Scavenger and Junk dealers.

Table 1 Summary of available vehicles with WSSP for each Zones (A, B, C, D)



the generation sources. Scavengers wander around in the streets and call for recyclable waste, they get it either free of cost or even pay some money for it. Scavengers sort out the materials placed in dustbins, skips and other pickup points. They also collect the recyclables from disposal sites. These materials then sold out to the junk dealers (Kabariys) in the market by these scavengers at low rates.

2.6 Solid waste disposal

Disposal of solid waste means landfilling. The landfill sites are not properly managed, but it involves open dumping at multiple unplanned locations inside and around the city. The official dumpsite currently decides by government and WSSP is 12 Km radius away from city zones the dumpsite name as Shamshatto dumpsite and Chowa Gujjar Gari site. The field survey shows that open dumping is carried out in the open empty plots of governments, back swamps, slum areas, and rivers. With the presence of an official dumpsite driver still disposes waste illegally in order to steal oil. This illegal dumping practices causes complex and serious environmental problems, and adversely affects public health.

3. Results and Discussions

3.1 Total waste generation

The total population of Peshawar city is 4.3 million. Which on average produces 0.4-0.8 kg/capita/day waste. If we take 0.5 kg/capita/day average, then it

While the rest lay there, that is 960 tons/day.

3.2 Result of vehicles availability

The total vehicles available with WSSP are present in table 1 in detail. It shows that the SUZUKI dumper number is high in each zone, where trucks and 22 cubic meter arm roll are minimal in number. It is a common observation that each zone not fully utilizing its vehicles. They use limit numbers of vehicles for waste collection while the rest stand there at the garage. Each zone trip detail to dump yard is present in the given tables.

There is no precise account of distances that each vehicle traveled because in most machines the speedometers are not working properly. This promotes the dumping of waste at dumpsites located closer to the collection sites other than specified disposal locations. This requires a GPS-based control system to be installed in the vehicles for tracking purposes. It is very uneconomical as well as inefficient to load and unload the vehicles manually in terms of time and effort. In areas with limited space for storage, it requires the more frequent collection of waste by smaller vehicles due to limited space is an uneconomical practice.



Table 2 Trips details of each vehicle in zone A for a week (WSSP Verified)

Zone A	Trips/Day 6/6/19	Trips/Day 7/6/19	Trips/Day 8/6/19	Trips/Day 10/6/19
Arm roll-11(5m ³)	3	2	2	4
Arm roll-15(5m ³)	5	1	5	4
Arm roll-8(5m ³)	0	2	4	5
Trolley 47	2	2	2	4
Arm roll(22m ³)	4	0	2	4
Comp.-79(7m ³)	0	0	1	0
Comp.-82(7m ³)	1	1	1	1
Comp.-85(7m ³)	1	1	1	2
Comp.-90(7m ³)	1	2	0	1
Comp.-91(7m ³)	1	1	1	1
Comp.-92(7m ³)	0	0	0	0
Comp.-94(7m ³)	1	1	0	2
Comp.-177(4m ³)	1	1	2	1
Comp.-180(4m ³)	1	1	0	1
Comp.-187(4m ³)	1	1	0	1
Trolley-76	2	1	2	1
Trolley-77	2	2	1	1
Trolley-1 messi	2	0	1	5
Dumper 3	1	2	1	2
Dumper4	2	1	0	2
Total	31	22	26	42

Table 3 Trips details of each vehicle in zone B for a week (WSSP Verified)

Zone B	Trips/Day 6/6/19	Trips/Day 7/6/19	Trips/Day 8/6/19	Trips/Day 10/6/19
Arm roll-large 1	2	3	4	4
Arm roll-large2	2	3	4	4
Comp.-01(4m ³)	2	1	2	0
Comp.-64(7m ³)	1	1	1	1
Comp.-65(7m ³)	2	1	2	2
Comp.-80(7m ³)	2	1	1	2
Comp.-84(7m ³)	2	1	1	1
Comp.-97(7m ³)	0	0	0	0
Comp.-98(7m ³)	1	1	1	1
Comp.-99(7m ³)	1	0	0	0
Comp.-156(7m ³)	0	0	0	0
Comp.-174(7m ³)	1	1	1	2
Comp.-175(4m ³)	2	1	2	2
Comp.-178(4m ³)	2	1	1	2
Comp.-181(4m ³)	0	0	0	0
Comp.-182(4m ³)	2	1	2	2
Comp.-183(4m ³)	1	1	0	0
Comp.-184(4m ³)	1	1	1	1
Comp.-185(4m ³)	2	1	1	2
Comp.-186(4m ³)	1	1	1	2
Comp.-188(4m ³)	1	2	0	2
Comp.-189(4m ³)	2	1	2	2
Comp.-190(4m ³)	2	1	0	0



Comp.-191(4m ³)	1	1	1	2
Comp.-193(4m ³)	2	2	1	2
Total	35	27	29	36
SUZUKI damper1	4	4	4	4
SUZUKI damper2	4	0	4	0
SUZUKI damper3	5	3	5	4
Trolley Messi4	5	5	5	6
Multi Loader	5	0	0	0
Arm roll large 1	3	0	0	0
Arm roll large 2	2	0	0	0
Arm roll 7	5	3	6	3
Arm roll 8	5	5	5	5
Arm roll 16	4	5	6	6
Trolley 44	0	0	0	0
Trolley 48	3	2	3	3
Trolley 45	0	0	3	0
Trolley 51	2	1	5	1
Trolley 52	3	1	0	3
Trolley 53	4	4	3	4
Trolley 54	0	0	0	2
Trolley 55	5	5	5	5
Trolley 56	0	0	0	0
Trolley 57	6	1	4	0
Truck 29	0	0	0	0
comp.52	1	0	1	1
Total	66	39	59	47

Table 4 Trips details of each vehicle in zone C for a week (WSSP Verified)

Zone C	Trips/Day 6/6/19	Trips/Day 7/6/19	Trips/Day 8/6/19	Trips/Day 10/6/19
Arm roll-1(5m ³)	6	3	5	5
Arm roll-2(5m ³)	0	0	0	0
Arm roll-6(5m ³)	3	3	5	5
Arm roll-8(5m ³)	5	5	4	6
Arm roll-10(5m ³)	2	1	0	2
Arm roll-12(5m ³)	3	1	1	0
Arm roll-13(5m ³)	6	0	2	0
Arm roll-14(5m ³)	0	0	0	0
Arm roll-17(5m ³)	4	1	3	5
Arm roll-20(5m ³)	1	1	0	0
Arm roll(22m ³)	2	1	2	0
Comp.-96(7m ³)	1	1	1	1
Comp.-86(7m ³)	1	1	1	1
Comp.-179(4m ³)	2	1	1	1
Comp.-03(4m ³)	1	1	0	0
Comp.-165(7m ³)	1	1	1	1
Comp.-93(7m ³)	1	1	0	1
Truck-06	0	0	0	0
Truck-10	2	1	2	2



Trolley-13	0	0	0	0
Trolley-46	0	0	0	0
Trolley-03	0	0	0	0
Multi loader(5m ³)	0	0	0	0
Total	41	23	28	30

Table 5 Trips details of each vehicle in zone D for a week (WSSP Verified)

Zone D	Trips/Day 6/6/19	Trips/Day 7/6/19	Trips/Day 8/6/19	Trips/Day 10/6/19
Arm roll-3(5m ³)	3	3	3	4
Arm roll-4(5m ³)	3	4	4	3
Arm roll-5(5m ³)	3	3	3	3
Arm roll2(22m ³)	2	2	2	2
Comp.-192(7m ³)	2	1	2	1
Comp.-02(7m ³)	2	1	2	1
Comp.-176(4m ³)	1	1	1	1
Comp.-95(4m ³)	1	1	2	1
Trolley-04	6	4	2	2
Trolley-37	1	2	1	1
Trolley-15	3	1	0	2
Trolley-57	3	2	3	2
Multi loader(5m ³)	2	0	1	2
Total	32	25	26	25

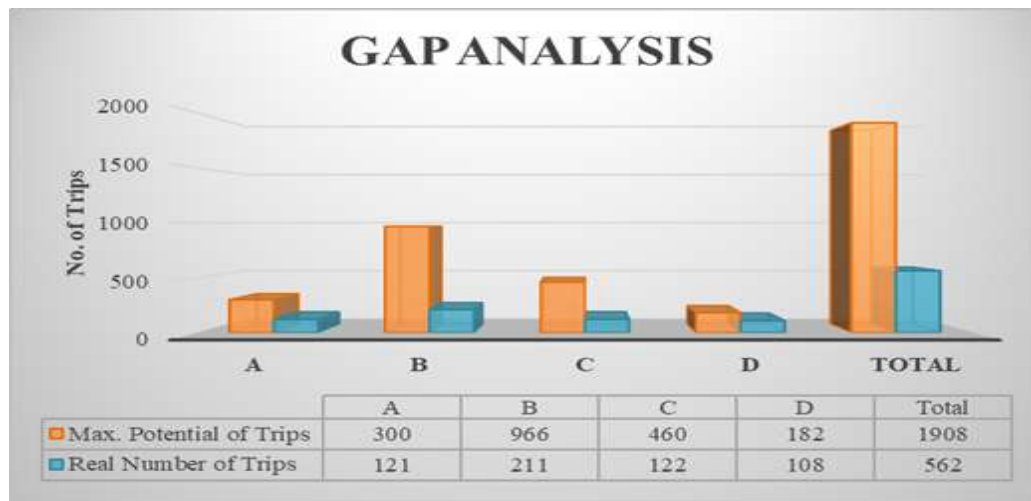


Figure 4 Gap analysis summary of four zones of Peshawar city

4. Conclusions

The primary collection that is from households and shops to bins is the main issue by looking at the map of bins installed, first, they are very few as compared to the population as 17000 people per bin. The most common practice as the distance of bin from household is more so people mostly placed their waste at the roadside or through it to empty plot nearby which more commonly seen in Professor colony and Board Bazar, Police colony, Town, etc. Improper location of bins is the cause of open dumps around the city. Second due limit resources with

WSSP in terms of staff due to which most of the vehicles are not running at full capacity. Also due to low wages of staff specifically drivers due to which most of the drivers found suspicious in stealing oil and dumping waste illegally at roadside or river or plots instead of dumping it in the dump yard. Such a list of drivers is given to WSSP but due to security issues, we are not authorized to publish it here. According to WSSP data, they collect 45%-55% of the total waste generated in Peshawar city while the rest 40%-50% left there and remain uncollected. If managed properly, the resources present is quite enough to carry and collect all the waste produced in



the city. According to analysis says if WSSP improves its management and increases its vehicle utilization up to 60% the whole waste collection problem of the city will be solved.

Public awareness is another issue as the public generally do not cooperate with the staff and are not entirely familiar with the health and social issues associated with solid waste management. The sanitary workers are also inexperienced or barely educated and untrained. Low salaries of workers are the main cause of illegal practices like selling recyclables, selling fuel issued for the vehicles and doing part-time private jobs during duty hours. The sanitary workers lack self-respect and social acceptability and are poorly motivated to perform their duty. The sanitary staff, compared to sanitary workers, is educated but neither trained nor motivated.

To improve the city waste management system training session should be conducted for sanitary workers and proper education should be given to them in order to perform their work in a better way. The minimum wages of the labor should be increase and ethical education to be provided through conducting seminars, conferences that motivate the drivers and labors to perform their work with honesty. City wise campaign to be conducted in which awareness is to be provided to the public regarding waste management by reducing, reusing and recycling.

Acknowledgments

The authors acknowledge the assistance of Sheraz Khan, Manager Finance at Head Office of Water and Sanitation Services Peshawar Khyber Pakhtunkhwa. The author also thanks, the site supervisors and drivers for their support.

REFERENCES

- [1] S. A. Batool and M. N. Chuadhry, "The impact of municipal solid waste treatment methods on greenhouse gas emissions in Lahore, Pakistan," *Waste Manag.*, vol. 29, no. 1, pp. 63–69, 2009.
- [2] R. Joshi and S. Ahmed, "Status and challenges of municipal solid waste management in India: A review," *Cogent Environ. Sci.*, vol. 2, no. 1, pp. 1–18, 2016.
- [3] S. Oduro-Appiah, K., Aidoo, D.O. and Graham, "Fee-based solid waste collection in economically developing countries: The case of Accra metropolis," *Int. J. Dev. Sustain.*, vol. 2, no. 2, pp. 629–639, 2013.
- [4] R. Ghosh and A. Kansal, "Urban Challenges in India and the Mission for a Sustainable Habitat," vol. 2, no. Vesilund 1982, pp. 281–304, 2014.
- [5] T. TERI, "Energy data directory and yearbook (teddy) 2001–2002," *Tata Energy Res. Institute, New Delhi, India*, 2002.
- [6] S. Saxena, R. K. Srivastava, and A. B. Samaddar, "Sustainable Waste Management Issues in India," vol. III, no. 1, 2010.
- [7] S. Rathi, "Alternative approaches for better municipal solid waste management in Mumbai, India.," *Waste Manag.*, vol. 26, no. 10, pp. 1192–1200, 2006.
- [8] R. Reddy, "Secured Landfills for Disposal of Municipal," vol. 1, no. 1, 2013.
- [9] P. F. Rupani, R. M. Delarestaghi, and H. Asadi, "Current Scenario of the Tehran Municipal Solid Waste Handling Rules towards Green Technology."
- [10] Iran Population, "Iran population," 2019. [Online]. Available: <https://www.worldometers.info/world-population/iran-population/>.
- [11] M. R. Alavi Moghadam, N. Mokhtarani, and B. Mokhtarani, "Municipal solid waste management in Rasht City, Iran.," *Waste Manag.*, vol. 29, no. 1, pp. 485–489, Jan. 2009.
- [12] P. Agency, "(Draft) Guideline for Solid Waste Management," *Pakistan Environ. Prot. Agency*, pp. 1–142, 2005.
- [13] B. Zhou, C. Sun, and H. Yi, "Solid waste disposal in Chinese cities: An evaluation of local performance," *Sustain.*, vol. 9, no. 12, pp. 1–20, 2017.
- [14] China, "China Statistaical Year Book 2018," 2018. [Online]. Available: <http://www.stats.gov.cn/tjsj/ndsj/2018/indexe h.htm>.
- [15] Y. Geng, Q. Zhu, and M. Haight, "An overview of municipal solid waste management in China.," *Waste Manag.*, vol. 27, no. 1, pp. 716–24, 2007.
- [16] M. M. Mian, X. Zeng, A. A. N. Bin Nasry, and S. M. Z. F. Al-Hamadani, "Municipal solid waste management in China: a comparative analysis," *J. Mater. Cycles Waste Manag.*, vol. 19, 2016.
- [17] Finance Division Government of Pakistan,



- “Pakistan Economic Survey,” 2019. September, pp. 3–5, 2015.
- [18] G. of P. M. of Statistics, “Population Census 2017.pdf,” 2017. [20] Pakistan Bureau of Statistics, “Population and household detail from block to district Level-Peshawar KPK,” 2017.
- [19] M. S. Korai, R. B. Mahar, M. A. Uqaili, and K. M. Brohi, “Assessment of Municipal Solid Waste Management Practices and Energy Recovery Potential in Pakistan,” *14th Int. Conf. Environ. Sci. Technol.*, no. [21] T. A. Khan and S. Ahmad, “Analysis of Climate Data of Khyber Pakhtunkhwa , Pakistan Analysis of Climate Data of Khyber Pakhtunkhwa , Pakistan,” no. May, 2018.



Process Improvement of Pet Bottle by Eliminating Bottlenecks

Eng. Daniyal Farooque¹, Shakeel Ahmed Shaikh², Sonia Irshad Marri³, Muhammad Saad Memon⁴,
Department of Industrial Engineering and Management, Mehran University of Engineering and Technology, Sindh,
Pakistan

Abstract:-

This paper elaborates in-depth analysis of steps involved in the PET bottles process and also highlight the issues and problems occurring during the process of PET bottles. During the manufacture process of PET Bottle various quality issue occur which lead to wastage in shape of product loss. For example Deformed Base, Poor Material Distribution, Stress Cracking and Crystallinity. Major causes of Product failure are due to variation in controlling parameter like temperature variation in oven and cooling parameter. This research therefore, focuses on product process optimization to reduce bottleneck and improve productivity and quality. Work study methods, Task Analysis and DPR (Daily progress report) were used to collect the data. The main output from this study is the task efficiency, which achieved through different remediation resulted in improved quality of PET bottle.

Keywords: Work study, Daily Progress Report, Task Analysis, Injection stretch blow Molding, PET bottle

1 Introduction

PET has been tremendously successful as material for flexible and rigid packaging and has grown to a commodity business in many sector.

“Think Process- Not Product “

PET (also abbreviated PETE) is short for polyethylene terephthalate, the chemical name for polyester. PET is a clear, strong, and lightweight plastic that is widely used for packaging foods and beverages, especially convenience-sized soft drinks, juices and water.

Polyethylene terephthalate (PET) bottles, which are usually produced by injection stretch blow molding (ISBM) are widely used for carbonated soft drinks (CSD). Nestle, Coca Cola, Pepsi, Jam e Shirin and other similar types of organization produce different sizes PET bottles that are being processed through number of steps. Approximately around 80 thousand PET bottles are being produced per shift by each company. This leads all other process to perform very fast in order to complete the requirement of production around 80,000 PET bottles per shift. However, during processes of PET bottles, number of bottlenecks / Wastes occur that create hurdles / obstacles in the processes (for examples process stoppage, temperature issues in Chiller and Oven, blowing pressure etc.) as well as in PET bottles (for example; Strangled Neck, KNIT Lines etc.) This research therefore, focuses on product process optimization to reduce bottleneck and improve productivity and quality.

1.1 Process of Pet Bottle

Injection blow-molding is a two-step process for producing completely finished plastic containers. the plastic is first molded into a "preform" using the injection molding process. These preforms are produced with the necks of the bottles. These preforms are packaged, and fed later (after cooling) into a reheat stretch blow molding machine. According to H Hosokoshiyama, J Chiba, Y Watanabe 2018” The method includes: a pre-blow-molding phase during which a fluid with a pre-blow-molding pressure is injected into the preform, and the rod is moved from its upper position to its lower position with a maximum travel speed of greater than or equal to 2.5 m/s” In the ISB (Injection stretch blow-molding) process, the preforms are heated then blown using high-pressure air into bottles using metal blow molds. The preform is always stretched with a core rod as part of the process.

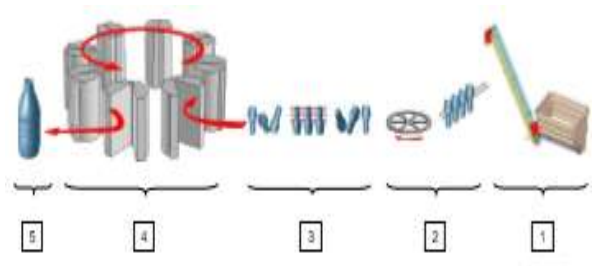


Figure 1: 5 steps process of PET bottle

1.2 Blow Molding

Blow molding is a specific manufacturing process by which hollow plastic parts are formed and can be joined



together. It is also used for forming glass bottles or other hollow shapes.

1.3 Injection stretch blow molding process

In injection stretch blow molding process, the plastic is first molded into a "preform" using the injection molding process. These preforms are produced with the necks of the bottles, including threads (the "finish") on one end. These preforms are packaged, and fed later (after cooling) into a reheat stretch blow molding machine. According to Rogers, Mike, and Anja Gottschalk. "Process for producing injection stretch blow molded polyolefin containers." In the ISB process, the preforms are heated (typically using infrared heaters) above their glass transition temperature, then blown using high-pressure air into bottles using metal blow molds. The preform is always stretched with a core rod as part of the process. According to Aoki, Shigeto. "Injection Mold for Injection Stretch Blow Molding Machine, Method for

Molding Preform, Preform, Method for Molding Container, and Container"

2 Methodology

Following Methods will be adopted to collect the Data;

- Work study methods (Time and work measurement)
- Task Analysis
- DPR (Daily progress report)

2.1 Work study methods (Time and work measurement)

Time and motion study is performed for each size of the PET Bottle i.e. 500 ml, 1 liter, 1.5 liter and 2.25 liter. Calculation of the total bottle in crates of each size in 8 hours, which shown in given table

Table 1: Total Bottle in crates in 8 hour

Size of PET Bottle	RP M	Nozzle	Bottle/ sec	Bottle/ min	Bottles/ hr.	Bottles/ 8 hr.	Bottle/ crates	Total bottles in crate in 8 hr.
500 ml	25	8	3.3333333	200	12000	96000	12	8000
1 litre	20	8	2.6666667	160	9600	76800	6	12800
1.5 litre	15	8	2	120	7200	57600	6	9600
2.25 litre	11	8	1.4666667	88	5280	42240	4	10560

2.2 Task Analysis

It is the process of breaking a skill down in to the smaller.

In-depth analysis of steps involved the processes of PET bottles using Task analysis approach

- The preforms in bulk are elevated
- Positioned at the machine infeed
- Preforms are introduced into the machine
- Preforms are heat conditioned
- Preforms are blown in a mold
- Finally, the finished articles

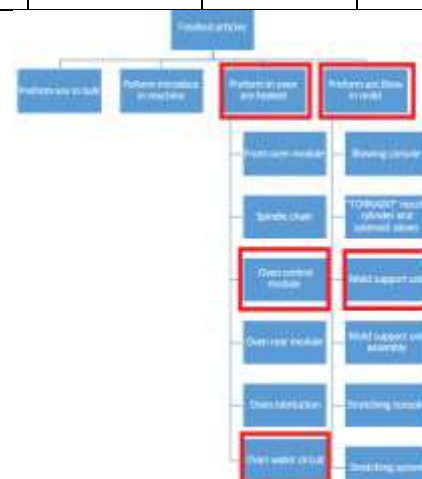


Figure 2: Pet Bottle of Process

2.3 DPR (Daily progress report)

Daily progress report is a vital tool that help to achieve daily target. Report is created for per shift in which every detail is highlighted that show actual achieve vs



plan target. Any bottleneck/issue that impact line efficiency or OEE (Overall Equipment Effectiveness) are noted in this DPR and action plan or CAPA (Corrective and Preventative actions) are developed accordingly that help to resolve reoccurring issue.

3 Analysis

3.1 Daily Production Report Of Long Neck Clear 500ml Shift A (01/08/2019)

DPR was collected to identify the defects during the process of PET bottles. Data were collected from 8.00 am till 4.00 pm at interval of 30 minutes to identify the defects and times loss occurred against the production demand per 30 minutes. Table shows failures, numbers of defects, time loss, resulting in less production against the required production demand.

Table 2: Daily Production Report of Long Neck Clear 500ML Shift A (01/08/2019)

Date	Shift	Daily Production Report				Bottle size	Prod
		No of Production	No of Defect	Failure Description	Time loss in term of Failure	Quantity loss in term of time	Production Demand 30 min
01/08/2019	A	80420	63	Cell C3 Obstruction	17	2680	8000
08:30 - 09:00		5356	0	Not Failure found	0	0	8000
09:00 - 09:30		5983	0	Not Failure found	0	0	8000
09:30 - 10:00		5830	0	Not Failure found	0	0	8000
10:00 - 10:30		5820	0	Not Failure found	0	0	8000
10:30 - 11:00		5812	0	Not Failure found	0	0	8000
11:00 - 11:30		5875	0	Not Failure found	0	0	8000
11:30 - 12:00		5870	0	Not Failure found	0	0	8000
12:00 - 12:30		5719	0	Cell C3 Obstruction	17	2680	8000
12:30 - 01:00		4762	0	Cell C3 Obstruction	6	1290	8000
01:00 - 01:30		5820	0	Not Failure found	0	0	8000
01:30 - 02:00		5879	0	Not Failure found	0	0	8000
02:00 - 02:30		5810	0	Not Failure found	0	0	8000
02:30 - 03:00		5820	0	Not Failure found	0	0	8000
03:00 - 03:30		5888	0	Not Failure found	0	0	8000
03:30 - 04:00		5872	0	Not Failure found	0	0	8000
Total		80420	63		69	13800	96000

Above table shows following details of failure description:

From 8:00 to 8:30 am, failure occurred that is oiling the Mold and Recipe Setting (CRISTALLINITY) which cause total 27 min loss time i.e. 22 min for mold oiling and remaining 05 min for Recipe Setting (CRISTALLINITY) that lead to 26 defects till recipe is set to use. It means out of 30 min, 27 min is lost time that resulting 5400 lost bottle and only 03 min is of good production time that help to make 450 good quality bottles. Actual schedule for 30 min production is 6000 bottle but due to time loss of 27 min, 5400 bottles are lost bottles due to time loss and only 450 bottles are those bottles that are produced in required time.

From 10:00 to 10:30 am, failure occurred that is Recipe setting (Poor Material Distribution) which cause total 3 min loss time for Recipe setting (Poor Material Distribution) that lead to 8 defects till recipe is set to

use. It means out of 30 min, 3 min is lost time that resulting 6000 lost bottle and only 27 min is of good production time that help to make 5230 good quality bottles. Actual schedule for 30 min production is 6000 bottle but due to time loss of 3 min, 6000 bottles are lost bottles due to time loss and only 5230 bottles are those bottles that are produced in required time.

From 01:00 to 01:30 pm, failure occurred that is Recipe setting (Poor Material Distribution) which cause total 4 min loss time for Recipe setting (Poor Material Distribution) that lead to 13 defects till recipe is set to use. It means out of 30 min, 4 min is lost time that resulting 800 lost bottle and only 26 min is of good production time that help to make 5100 good quality bottles. Actual schedule for 30 min production is 6000 bottle but due to time loss of 4 min, 800 bottles are lost bottles due to time loss and only 5100 bottles are those bottles that are produced in required time.

From 02:30 to 03:00 pm, failure occurred that is Recipe Setting (CRISTALLINITY) which cause total 3 min loss time for Recipe Setting (CRISTALLINITY) that lead to 16 defects till recipe is set to use. It means out of 30 min, 3 min is lost time that resulting 600 lost bottle and only 27 min is of good production time that help to make 5290 good quality bottles. Actual schedule for 30 min production is 6000 bottle but due to time loss of 3 min, 600 bottles are lost bottles due to time loss and only 5290 bottles are those bottles that are produced in required time.

3.2 Daily Production Report of Green 1.5ltr Shift A (01/10/2019)

DPR was collected to identify the defects during the process of PET bottles. Data were collected from 8.00 am till 4.00 pm at interval of 30 minutes to identify the defects and times loss occurred against the production demand per 30 minutes. Table shows failures, numbers of defects, time loss, resulting in less production against the required production demand.



Table 3: Daily Production Report of Green 1.5 LTR Shift A (01/10/2019)

Date		Daily Production Report				Bottle size	
Shift						Variety	Green
Time	No of Production	No of Defect	Failure Description	Time loss in term of failure	Quantity loss in term of time	Production Demand	30 min
08:00-08:30	411	0	Recipe setting (STRESS CRACKING)	26	3120	3600	3600
08:30-09:00	383	0	Cell C1 Obstructions	21	3000	3600	3600
09:00-09:30	1917	0	Not Failure found	0	0	3600	3600
09:30-10:00	3980	0	Not Failure found	0	0	3600	3600
10:00-10:30	3312	0	Not Failure found	0	0	3600	3600
10:30-11:00	3450	0	Not Failure found	0	0	3600	3600
11:00-12:00	2590	0	Not Failure found	0	0	3600	3600
12:00-12:30	3189	0	Not Failure found	0	0	3600	3600
12:30-01:00	3488	0	Not Failure found	0	0	3600	3600
01:00-01:30	1889	0	Cell C3 Obstructions	14	1888	3600	3600
01:30-02:00	3379	0	Not Failure found	0	0	3600	3600
02:00-02:30	3488	0	Not Failure found	0	0	3600	3600
02:30-03:00	345	0	Recipe setting (DEFORMED BASE)	7	3000	3600	3600
03:00-03:30	3449	0	Not Failure found	0	0	3600	3600
03:30-04:00	3112	0	Not Failure found	0	0	3600	3600
Total	46291	91		84	10080	57600	

Above table shows following details of failure description:

From 8:00 to 8:30 am, failure occurred that is Oiling the Mold and Recipe setting (STRESS CRACKING) which cause total 26 min loss time i.e. 22 min for mold oiling and remaining 04 min for Recipe setting (STRESS CRACKING) that lead to 17 defects till recipe is set to use. It means out of 30 min, 26 min is lost time that resulting 3120 lost bottle and only 04 min is of good production time that help to make 412 good quality bottles. Actual schedule for 30 min production is 3600 bottle but due to time loss of 26 min, 3120 bottles are lost bottles due to time loss and only 412 bottles are those bottles that are produced in required time.

From 11:00 to 11:30 am, failure occurred that is Recipe setting (Poor Material Distribution) which cause total 4 min loss time for Recipe setting (Poor Material Distribution) that lead to 24 defects till recipe is set to use. It means out of 30 min, 4 min is lost time that resulting 480 lost bottle and only 26 min is of good production time that help to make 3015 good quality bottles. Actual schedule for 30 min production is 3600 bottle but due to time loss of 4 min, 480 bottles are lost bottles due to time loss and only 3015 bottles are those bottles that are produced in required time.

From 02:30 to 03:00 pm, failure occurred that is Recipe setting (DEFORMED BASE) which cause total 7 min loss time for Recipe setting (DEFORMED BASE) that lead to 14 defects till recipe is set to use. It means out of 30 min, 7 min is lost time that resulting 840 lost bottle and only 23 min is of good production time that help to make 2678 good quality bottles. Actual schedule for 30 min production is 3600 bottle but due to time loss of

7 min, 840 bottles are lost bottles due to time loss and only 2678 bottles are those bottles that are produced in required time.

From 03:30 to 04:00 am, failure occurred that is Downstream Pressure Insufficient which cause total 8 min loss time for Downstream Pressure Insufficient that lead to 8 defects till recipe is set to use. It means out of 30 min, 8 min is lost time that resulting 960 lost bottle and only 22 min is of good production time that help to make 2450 good quality bottles. Actual schedule for 30 min production is 3600 bottle but due to time loss of 8 min, 960 bottles are lost bottles due to time loss and only 2450 bottles are those bottles that are produced in required time.

3.3 Daily Production Report Of Green 2.25 Ltr Shift B (01/11/2019)

DPR was collected to identify the defects during the process of PET bottles. Data were collected from 4.00 pm till 12.00 pm at interval of 30 minutes to identify the defects and times loss occurred against the production demand per 30 minutes. Table shows failures, numbers of defects, time loss, resulting in less production against the required production demand.

Table 4: Daily Production Report of Green 2.25 LTR Shift B (01/11/2019)

Date		Daily Production Report				Bottle size	
Shift						Variety	Green
Time	No of Production	No of Defect	Failure Description	Time loss in term of failure	Quantity loss in term of time	Production Demand	30 min
04:00-04:30	3590	0	Recipe setting (STRESS CRACKING)	06	3584	3600	3600
04:30-05:00	3590	0	Not Failure found	0	0	3600	3600
05:00-05:30	3583	0	Not Failure found	0	0	3600	3600
05:30-06:00	3585	0	Not Failure found	0	0	3600	3600
06:00-06:30	3588	0	Cell C1 Obstructions	27	3318	3600	3600
06:30-07:00	3580	0	Not Failure found	0	0	3600	3600
07:00-07:30	3580	0	Not Failure found	0	0	3600	3600
07:30-08:00	3580	0	Not Failure found	0	0	3600	3600
08:00-08:30	3570	0	Not Failure found	0	0	3600	3600
08:30-09:00	3585	0	Not Failure found	0	0	3600	3600
09:00-09:30	3585	0	Not Failure found	0	0	3600	3600
09:30-10:00	3590	0	Not Failure found	0	0	3600	3600
10:00-10:30	3582	0	Not Failure found	0	0	3600	3600
10:30-11:00	3570	0	Recipe setting (Poor Material Distribution)	04	3566	3600	3600
11:00-11:30	3575	0	Not Failure found	0	0	3600	3600
11:30-12:00	3580	0	Cell C3 Obstructions	14	3566	3600	3600
Total	36496	28		53	4664	42240	

Above table shows following details of failure description:

From 4:00 to 4:30 pm, failure occurred that is Recipe setting (STRESS CRACKING) which cause total 06 min loss time for Recipe setting (STRESS CRACKING) that lead to 15 defects till recipe is set to use. It means out of 30 min, 6 min is lost time that resulting 528 lost bottle and only 24 min is of good production time that help to make 1950 good quality bottles. Actual schedule for 30 min production is 2640



bottle but due to time loss of 06 min, 528 bottles are lost bottles due to time loss and only 1950 bottles are those bottles that are produced in required time.

From 10:30 to 11:00 pm, failure occurred that is Recipe setting (Poor Material Distribution) which cause total 6 min loss time for Recipe setting (Poor Material Distribution) that lead to 13 defects till recipe is set to use. It means out of 30 min, 6 min is lost time that resulting 528 lost bottle and only 24 min is of good production time that help to make 2100 good quality bottles. Actual schedule for 30 min production is 2640 bottle but due to time loss of 6 min, 528 bottles are lost bottles due to time loss and only 2100 bottles are those bottles that are produced in required time.

4 Result and Discussions

4.1 Result of Daily Production Report of Long Neck Clear 500ml Shift A (01/08/2019)

Defects that were identified through DPR data were mitigated with the help of recommended remedies that help to recover from time loss in effective way which leads to achieve production target on time. Below Table shows recommended remedies against each failure description as a guideline.

Table 5: Result Daily Production Report of Long neck Clear 500ML Shift A (01/08/2019)

Date	Shift	Daily Production Report						Bottle size	Yield	Long neck Clear
		No of Production	No of Defect	Failure Description	Time loss in term of failure	Quantity loss in term of time loss	Efficiency			
01/08/2019	A	80420	63	Oiling the mold Recipe setting (STESS CRACKING)	27	5400	73	Start up Machine Increase oven speed		
08:30 - 09:00		3506	0	Cell C3 Obstruction	03	2800	91.811553	Filter Machine		
09:00 - 09:30		3963	0	Not Failure found	0	0	99.746667	Smooth production		
09:30 - 10:00		4826	0	Not Failure found	0	0	97.146667	Smooth production		
10:00 - 10:30		528	1	Recipe setting (Poor Material Distribution)	06	600	87.166667	Reduce air delay time		
10:30 - 11:00		3382	0	Not Failure found	0	0	96.888889	Smooth production		
11:00 - 11:30		3970	0	Not Failure found	0	0	99.583333	Smooth production		
11:30 - 12:00		3876	0	Not Failure found	0	0	97.833333	Smooth production		
12:00 - 12:30		3219	0	Cell C3 Obstruction	13	2800	53.45	Labeling Machine		
12:30 - 01:00		4792	0	Cell C3 Obstruction	6	1200	79.266667	Packaging Machine		
01:00 - 01:30		3506	13	Recipe setting (Poor Material Distribution)	06	600	85	Reduce time pre-blow pressure		
01:30 - 02:00		3373	0	Not Failure found	0	0	97.883333	Smooth production		
02:00 - 02:30		3916	0	Not Failure found	0	0	98.2	Smooth production		
02:30 - 03:00		4206	16	Recipe setting (Poor Material Distribution)	06	600	88.166667	Adjust pre-blow timing		
03:00 - 03:30		3888	0	Not Failure found	0	0	98.133333	Smooth production		
03:30 - 04:00		3972	0	Not Failure found	0	0	97.886667	Smooth production		
Total		80420	63		69	13800	83.77			

From 8:00 to 8:30 am, failure occurred that is Oiling the Mold and Recipe Setting (CRISTALLINITY) was mitigated with Startup Machine and Increase oven speed as a recommended remedies that restrict the problem to only 27 min otherwise time loss could be greater than 27 min that help to achieve production target on time with good quality products.

From 10:00 to 10:30 am, failure occurred that is Recipe setting (Poor Material Distribution) was mitigated with Reduce air delay time as a recommended remedies that restrict the problem to only 30 min otherwise time loss could be greater than 3 min that help to achieve production target on time with good quality products.

From 1:00 to 1:30 pm, failure occurred that is Recipe setting (Poor Material Distribution) was mitigated Reduce time pre-blow pressure as a recommended remedies that restrict the problem to only 4 min otherwise time loss could be greater than 4 min that help to achieve production target on time with good quality products.

From 2:30 to 3:00 pm, failure occurred that is Recipe Setting (CRISTALLINITY) was mitigated with Adjust pre-blow timing as a recommended remedies that restrict the problem to only 3 min otherwise time loss could be greater than 3 min that help to achieve production target on time with good quality products.

4.2 Result of Daily Production Report Of Green 1.5ltr Shift A (01/10/2019)

Defects that were identified through DPR data were mitigated with the help of recommended remedies that help to recover from time loss in effective way which leads to achieve production target on time. Below Table shows recommended remedies against each failure description as a guideline.

Table 6: Result of Daily Production Report of Green 1.5 LTR Shift A (01/10/2019)

Date	Shift	Daily Production Report						Bottle size	Yield	Green
		No of Production	No of Defect	Failure Description	Time loss in term of failure	Quantity loss in term of time loss	Efficiency			
01/10/2019	A	46291	84	Oiling the mold Recipe setting (STESS CRACKING)	26	3120	80.4	Start up Machine Reduce air delay time		
08:30 - 09:00		2500	0	Cell C3 Obstruction	21	3000	18.111111	loading machine		
09:00 - 09:30		3247	0	Not Failure found	0	0	99.838889	Smooth production		
09:30 - 10:00		3580	0	Not Failure found	0	0	99.888889	Smooth production		
10:00 - 10:30		3312	0	Not Failure found	0	0	97.555556	Smooth production		
10:30 - 11:00		3400	0	Not Failure found	0	0	95.833333	Smooth production		
11:00 - 11:30		3506	1	Recipe setting (Poor Material Distribution)	06	600	83.75	Reduce air delay time		
11:30 - 12:00		3280	0	Not Failure found	0	0	98.888889	Smooth production		
12:00 - 12:30		3200	0	Not Failure found	0	0	99.666667	Smooth production		
12:30 - 01:00		3480	0	Not Failure found	0	0	96.666667	Smooth production		
01:00 - 01:30		3880	0	Cell C3 Obstruction	14	1680	51.5	loading machine		
01:30 - 02:00		3576	0	Not Failure found	0	0	99.416667	Smooth production		
02:00 - 02:30		3480	0	Not Failure found	0	0	96.666667	Smooth production		
02:30 - 03:00		3800	0	Recipe setting (Poor Material Distribution)	06	600	74.388889	Increase pre-blow delay		
03:00 - 03:30		3480	0	Not Failure found	0	0	96.361111	Smooth production		
03:30 - 04:00		3800	0	Not Failure found	0	0	88.055556	40 bar issue		
Total		46291	84		84	10080	80.4			

From 8:00 to 8:30 am, failure occurred that is Oiling the Mold and Recipe Setting (STESS CRACKING) was mitigated with Startup Machine and Reduce air delay time respectively as a recommended remedies that restrict the problem to only 26 min otherwise time loss could be greater than 26 min that help to achieve production target on time with good quality products.



From 11:00 to 11:30 am, failure occurred that is Recipe setting (Poor Material Distribution) was mitigated with Reduce air delay time as a recommended remedies that restrict the problem to only 4 min otherwise time loss could be greater than 4 min that help to achieve production target on time with good quality products.

From 02:30 to 03:30 pm, failure occurred that is Recipe setting (DEFORMED BASE) was mitigated with Decrease pre-blow delay as a recommended remedies that restrict the problem to only 7 min otherwise time loss could be greater than 7 min that help to achieve production target on time with good quality products.

From 03:30 to 04:00 pm, failure occurred that is Downstream Pressure Insufficient was mitigated with 40 Bar Issue as a recommended remedies that restrict the problem to only 8 min otherwise time loss could be greater than 8 min that help to achieve production target on time with good quality products.

4.3 Result of Daily Production Report of Green 2.25 Ltr Shift B (01/11/2019)

Defects that were identified through DPR data were mitigated with the help of recommended remedies that help to recover from time loss in effective way which leads to achieve production target on time. Below Table shows recommended remedies against each failure description as a guideline.

Table 7: Result of Daily Production Report of Green 2.25 LTR Shift B (01/11/2019)

Class	Shift	Time	No. of Production	% of Defect	Failure Description	Time loss in hrs	Quantity loss in terms of failure units of time loss	Efficiency %	Recommended remedies
04:00	01/11/2019	11:00	2149	0	Non Failure Issue	0	0	99.99999	Smooth production
05:00	01/11/2019	08:00	0	0	Non Failure Issue	0	0	99.99999	Smooth production
07:30	04/01/2019	06:12	0	0	Non Failure Issue	0	0	99.99999	Smooth production
08:00	08:30	2187	0	0	Non Failure Issue	0	0	99.99999	Smooth production
09:00	01/11/2019	08:00	0	0	Call CO Orientation	77	3788	99.99999	Package Machine Shift Start
07:00	07:30	2189	0	0	Non Failure Issue	0	0	99.99999	Smooth production
07:30	08:00	2149	0	0	Non Failure Issue	0	0	99.99999	Smooth production
08:00	08:30	2029	0	0	Non Failure Issue	0	0	99.99999	Smooth production
08:30	09:00	2192	0	0	Non Failure Issue	0	0	99.99999	Smooth production
09:00	09:30	2051	0	0	Non Failure Issue	0	0	99.99999	Smooth production
09:30	10:00	2139	0	0	Non Failure Issue	0	0	99.99999	Smooth production
10:00	10:30	2111	0	0	Non Failure Issue	0	0	99.99999	Smooth production
11:00	11:30	2120	0	0	Non Failure Issue	0	0	99.99999	Smooth production
11:30	12:00	2186	0	0	Call CO Orientation	16	1233	99.99999	Package Machine Shift Start
Total		36496	28			53	4664	96.4	

From 04:00 to 04:30 pm, failure occurred that is Recipe setting (STRESS CRACKING) was mitigated with Reduce air delay time as a recommended remedies that restrict the problem to only 6 min otherwise time loss could be greater than 6 min that help to achieve production target on time with good quality products.

From 10:30 to 11:00 am, failure occurred that is Recipe setting (Poor Material Distribution) was mitigated with Increase bottom zone heat as a recommended remedies that restrict the problem to only 6 min otherwise time loss could be greater than 6 min that help to achieve production target on time with good quality products.

5 Conclusion

This research therefore, focuses on product process optimization to reduce bottleneck and improve productivity and quality. The main output from this study focuses on task efficiency which achieved through different remediation to improve quality of PET bottle that are defined in below tables

There are following finding and Recommendation which are giving below

- Deformed Base,
- Poor Material Distribution,
- Stress Cracking,
- Cristallinity

5.1 Deformed Base

Description: Poor material distribution at the base of the bottle, the example above is of a deformed base at the gate area in the inside of the bottle.



Figure 3: Deformed Base

Table 8: Deformed Base

CAUSE	REMEDY
Poor material distribution	Adjust preform heating zones and temperature
Poor Stretch rod timing	Decrease pre-blow delay

5.2 Poor Material Distribution

Description: Too much resin material is forced up into the top shoulder area of the PET bottle (inside the neck)



Figure 4: Poor Material Distribution

Table 9: Poor Material Distribution

CAUSE	REMEDY
Too much delay in blow time	Reduce air delay time
Stretch rod too slow	Increase stretch rod speed
Preform incorrectly heated	Adjust zone heat in oven
Preforms too cold	Hotter preforms (conditioning) Increase oven temperature
Bases incorrectly heated	Increase bottom zone heat

5.3 Stress Cracking

Description: Chemical aggression / drying of the container base causing it to crack.



Figure 5: Stress Cracking

Table 10: Stress Cracking

CAUSE	REMEDY
Material Distribution	Adjust heating profile Reduce air delay time Reduce low air pressure
Heavy base contains a lot of un oriented material	Reduce preform temperature to reduce base weight if necessary

5.4 Crystallinity

Description: Material appears as opaque, or milky white in appearance



Figure 6: Crystallinity

Table 11: Crystallinity

CAUSE	REMEDY
Preforms too hot	Lower heating power / Increase oven speed
Wrong heating profile	Adjust heating lanes
Insufficient air flow	Adjust air baffles / Check exhaust fans
Insufficient oven cooling	Check water flow & water temperature
Too much pre-blow	Adjust pre-blow timing



Acknowledgement

After the Almighty, I would like to thank my parents; my mother Hajiyan kausar Farooque, father Haji Farooque Memon, brother Muzammil Fareed, sister, auntie and specially to my better half for all their prayers. Lastly to my Supervisor Dr Shakeel Ahmed Shaikh and Shahid Majeed for their support

REFERENCES

- [1] Aoki, Shigeto. "Injection Mold for Injection Stretch Blow Molding Machine, Method for Molding Preform, Preform, Method for Molding Container, and Container." U.S. Patent Application No. 15/564,583.
- [2] Demirel, B. (2017). Optimisation of mould surface temperature and bottle residence time in mould for the carbonated soft drink PET containers. *Polymer Testing*, 60, 220-228.
- [3] Hosokoshiyama, H., Chiba, J. and Watanabe, Y., Yoshino Kogyosho Co Ltd, 2018. Injection molding process of a preform for use in biaxial stretching and blow molding. U.S. Patent 9,862,157.
- [4] Joshi, R., Mody, R.D., Wheelwright, D. and Kerr, R., Coca-Cola Co, 2018. Carbonated beverage bottle bases and methods of making the same. U.S. Patent Application 15/536,930..
- [5] Laico, Donato. "Apparatus and method for optical inspection of parisons." U.S. Patent Application No. 15/562,607.
- [6] Moffitt, Ronald D., Yu Shi, and Jasmeet Kaur. "Refillable polymer bottle and method for improved caustic stress crack resistance." U.S. Patent Application No. 15/566,233.
- [7] Roa, Fortún Leza, and Miguel Ángel Caballero López. "Opaque single-layer bottle with light protection and production method thereof." U.S. Patent No. 9,994,383. 12 Jun. 2018.
- [8] Rogers, Mike, and Anja Gottschalk. "Process for producing injection stretch blow molded polyolefin containers." U.S. Patent Application No. 10/239,267.
- [9] Rogers, Mike, and Anja Gottschalk. "Process for producing injection stretch blow molded polyolefin containers." U.S. Patent Application No. 10/239,267.
- [10] Stoiber, Christian, et al. "Container treatment plant and a container treatment method for the treatment of containers capable of being filled with a product." U.S. Patent No. 9,546,011. 17 Jan. 2017..
- [11] Zhang, Keqiang. "Handle positioning apparatus outside mould for pre-inserted-handle bottle blow moulding machine, and method of use thereof." U.S. Patent No. 9,662,827. 30 May 2017



Investigating the Effects of Process Parameters of FDM using RSM

Muhammad Arslan^{1*}, Dr. Tauseef Aized², Muhammad Ahsaan ul Haq³

1. Student, Department of Mechanical Engineering UET Lahore.
2. Professor, Department of Mechanical Engineering UET Lahore.
3. Student, Department of Industrial Engineering UET Taxila.

Corresponding author: engrarslan.ahmad32@gmail.com

Abstract:

In this paper, the parametric analysis of the most effective and consistently utilized 3D printing process i.e. Fused Deposition Modeling (FDM) process was carried out. Element activation and deactivation tool in ANSYS was utilized to develop a Finite Element Analysis (FEA) model of the FDM process for the analysis of Residual stresses and Part Distortion on the basis of variation in critical input parameters of FDM process i.e. Filling speed, Layer Thickness, Extrusion Head Temperature, and Bed Temperature. To investigate the influence of Process parameters on Residual Stresses and Part Distortion Analysis of Variance (ANOVA) was employed in this study. The mathematical model to predict residual Stresses and Part Distortion was developed by using regression analysis. It was concluded from this parametric analysis that Layer Thickness has the highest influence on both Residual Stresses and Part Distortion while the other three parameters have less impact in comparison with the effect of Layer Thickness.

Keywords: Fused Deposition Modeling; Finite Element Analysis (FEA) Parametric Analysis; Residual Stresses; Part Distortion

I. INTRODUCTION

Fused Deposition Modeling (FDM) is one of the most efficient and commonly used additive manufacturing technology. The production of products with complex geometry and having multiple sub-parts by using a simple 3D printer is the main distinctive attribute of this modern manufacturing process and it is less expensive as compared to conventional manufacturing processes[1]. Multiple manufacturers are employing FDM for commercial usage for the production of different products. The main industries which are using FDM for mass production are aerospace, medical implants, food packaging, and electronics industries[2]. During the FDM process, the raw material is melted at a temperature higher than its melting point and it is extruded layer by layer through extrusion head which is known as a nozzle of FDM printer. This extrusion head travels along a specified path i.e. tool path defined by software which controls the fabrication process[3]. There are numerous materials that are used in the FDM process for the fabrication of different products. Pellets, Laminates, and wire are the main forms of Raw material available in the market. ABS (Acrylonitrile-Butadiene styrene), Polyamide, polyethylene, polypropylene and PLA (poly-lactic acid) are the most widely used materials for the FDM process. Moreover, PZT, Stainless Steel and Silicon Nitrate are also being used depending upon the requirements of the product [4]. Due to excellent tensile strength, bond formation between layers

and rigidity PLA is the most common material used in FDM[5]. The poor surface finish and lack dimensional accuracy due to thermal shrinkage and warping which aggravates quality of the FDM products badly[6]. The process parameters affect significantly the part distortion (due to accumulation of residual stresses) individually and in the combination with other parameters [7]. Multiple studies have been proposed by the different researcher to investigate the influence of critical process parameters on part distortion of various additive manufacturing processes. In Swayam Bikash et al [8] parametric investigation was carried out to examine the wear behavior of products manufactured by FDM. The effect of important process parameters i.e. Contour Number, Layer Thickness, Raster Angle, Air Gap, Raster Width on the wear of test specimen. The wear of FDM parts under the influence of critical process parameters was analyzed by using Analysis of Variance (ANOVA). Finally to predict the wear behavior of products manufactured by the FDM process a mathematical model was developed. Anthony A. et al. experimentally examined residual stresses and mechanical properties of the FDM process. Moreover, thermal expansion was also analyzed through experimentation. The experimental analysis revealed that thermal strain will increase up to 22% with the decrement in Layer thickness. In Omar Ahmed et al they developed an analytical model to analyze the temperature-dependent mechanical properties of PC-ABS Parts. The dynamic mechanical properties on the basis of variation in process parameters of the FDM process were investigated by using multilayer feed-forward



neural networks (MENN) and also by utilizing Response Surface Methodology (RSM). Finally, the analytical models were validated by comparing the results of RSM and MENNs with the experimental results.

For a particular problem in which a particular response is affected by more than one input factors RSM (which is a statistical and mathematical analysis technique) is utilized for the analysis of such kinds of problems [9]. A number of experimental designs for RSM are available. Based upon incomplete factorial design consisting of three levels 2nd order design are Box-Behnken designs (BBD) [10]. Box Behnken design is more efficient as compare to other experimental design as it reduces the number of experiments and also prevents a researcher from conducting the experiments at extreme values of input process parameters. Moreover, it enables us to develop the sequential designs, evaluate the non-linear models and lack of fit of the model can also be examined by using BBD [11].

In the current literature the research carried out on the analysis of Part distortion influenced by input parameters of the FDM process is very limited. The effect of four input parameters (in association with each other) on residual stresses and part distortion has not been examined in the previous research. In this research, a FEM model of the Fused Deposition Modeling process for the prediction of residual stresses and part distortion is developed by using a commercial software ANSYS. And Finally, RSM is utilized to investigate the effect of process parameters on part distortion and residual stresses.

2. FEA MODEL OF FUDED DEPOSITION MODELING PROCESS

The FEM model of the Fused Deposition Modeling process is developed with the help of commercial software ANSYS by using the element activation technique. To investigate the temperature distribution, residual stresses and distortion a coupled thermal structural analysis was employed in this particular study. The output of the thermal analysis was taken as input for structural analysis, and both of these analyses were performed step by step for each element of the simulation model. The residual stresses i.e. first principle stress were calculated from structural analysis while distortion was measured by taking the average of the deflections at four corners of the test specimen.

3. Governing Equations of the thermal Analysis

FDM is a layer by layer deposition process of hot molten material. First of all raw material is converted into liquid form from solid beads, pellets, etc by heating it at a high temperature and then it is extruded through extrusion head of 3D printer in a continuous fashion. Conduction,

convection, and radiation are the means of heat transfer from build material to its surroundings. The heat transfer because of phase change is also released to the control volume. The mechanism of thermal analysis can be described by the Eq.1.

$$\rho c_p \frac{\partial T}{\partial t} = \nabla(K\nabla T) + q \quad (1)$$

P denotes the density, c_p is the Symbol of Specific heat capacity. T is the notation of Temperature. While t and K are used to represent thermal time and thermal conductivity respectively. So $(\rho c_p \frac{\partial T}{\partial t})$ represents the change in thermal energy stored in the system. While Eq.2 represents q i.e. heat generated during the deposition process

$$\dot{q} = q_{\text{convection}} + q_{\text{radiation}} + q_{\text{phasechange}} \quad (2)$$

The following assumptions were made during the development of the FEA Model.

1. For a short interval of time feedstock can be considered as an element having a finite volume.
2. The travel speed of the nozzle is equal to the extrusion speed of Feedstock.
3. The temperature at which molten material is extruded from the nozzle is considered to be the initial temperature of the material in the FEA Model.
4. Convection was considered to be the main mean of heat transfer from the bottom layer of feedstock and the bed of the 3D printer.
5. The effect of radiation is neglected in this simulation process.

In assumption, 1 Extrusion melting technology was the basic principle that was taken into consideration. The Practical analysis of G-code played an important role in while making assumptions 2 and. Assumption 3 was made for precise simulation of the FDM process by taking the initial temperature of Material exactly the same extrusion temperature of feedstock during the actual fabrication process. The theory of thermal conductance is the benchmark of assumption 4 [12].

For FDM process where the convective heat transfer coefficient has a value greater than $60Wm^{-2}K$ the effect of radiation is neglected as described in assumption 5 [13].



4. FEA Model Description

Due to the extensive simulation, the time required to solve this model a small test specimen was used in this study. The dimensions of the test specimen are given as 40.23 mm length 1.18 mm thickness and 10.19 mm width. After meshing, the total number of nodes was 16600 nodes while the number of elements was 850 elements.

4.1.1 Boundary condition.

The coupled thermal structural analysis was performed by employing the following boundary conditions.

1. Each element was assigned an initial temperature equal to the temperature at which feedstock is extruded from the extrusion head.
2. The test specimen for this simulation analysis is of rectangular shape so the value of the convective heat transfer coefficient for this simulation analysis is $88 \text{ Wm}^{-2}\text{K}^{-1}$ [12].
3. The thermal contact resistance was assigned a value of $4257 \text{ Wm}^{-2}\text{K}^{-1}$ which was calculated by Gibbins[14].
4. In order to avoid any sort of displacement or movement in any direction, the bottom side of the model was fixed.

4.1.2 Properties of Material for FEA Model

PLA was used as the main material for the simulation analysis which is well-known thermoplastic used in the Fused Deposition Modeling process. Some properties of material were considered to vary with temperature changes due to the phase changes and successive heating and cooling including pressure and thermal conductivity, specific heat capacity was also considered to be temperature-dependent property. The density of the material which was considered to be constant i.e. it does not change with the variation in temperature. The properties of PLA are listed in Table I.

Property	Unit	Value
Temperature	(K)	298.15
Density	(Kg/m ³)	1145.2
E	(Mpa)	1280
Coldness	(1/K)	7.4×10^{-4}
Specific heat capacity	(J/K.mole)	94.69
Thermal conductivity	(W/mK)	0.111

Table I Properties of PLA

5. Parametric Analysis

The effect of Four process parameters on residual stresses and part distortion were analyzed through this model. This FEA Model and these parameters are defined below.

1. Filling speed

It the speed with which extrusion head of 3D printer travels along the tool path specified by software that controls the FDM printer[15].

2. Layer thickness

It is the thickness of a single-layer extruded by FDM printer depending upon the size of the extrusion head.

3. Extrusion Head temperature

The temperature of the Extrusion Head (nozzle) during the Fabrication process is called extrusion head temperature.

4. Bed Temperature

The absolute temperature of the platform during the FDM process is called Bed temperature [16].

The values of each process parameters used in this study are listed in Table II

Table II values of process Parameters

Process parameter	Notation	Unit	Level (-1)	Level (0)	Level (+1)
Filling speed	A	mms ⁻¹	70	90	110
Layer Thickness	B	mm	0.1	0.2	0.3
Extrusion Head Temperature	C	°C	210	225	240
Bed Temperature	D	°C	65	70	75

6. Experimental Design

The Design of the experiment was developed by using BOX-Behnken Design with four input parameters (A, B, C, and D) and two output parameters Residual Stresses and Part Distortion and is given by Table III.

7. RESULTS AND DISCUSSIONS

A. Mathematical Model

The Mathematical Model for both output parameters i.e. Residual Stresses and Distortion is developed by using regression analysis and the adequacy of model is checked by ANOVA.

1. Mathematical Model of Residual Stresses (RS)

A non-linear (quadratic) mathematical model of residual stresses is developed on the basis of fit summary of the output response. The effect of all four process parameters on Residual Stresses is represented by Table IV. The model is significant as R², Predicted R² and Adjusted R² all approaches to unity. The mathematical model of residual is given Eq.3.



$$RS = 2171.89 - 1578.17 \times A - 2846.76 \times B + 692.44 \times C - 496.64 \times D + 697.57 \times A \times B - 210.94 \times A \times C + 523.22 \times A \times D - 225.22 \times B \times C + 106.46 \times B \times D - 214.46 \times C \times D + 379.12 \times A^2 + 443.55 \times B^2 + 131.45 \times C^2 + 202.07 \times D^2 \quad (3)$$

2. Mathematical Model of Distortion (DT)

The mathematical model for distortion is also of quadratic nature and effects of process parameters are listed in table Table V. The Model for distortion is also significant because the values of R^2 predicted, R^2 and adjusted R^2 are almost equal to one. Eq.4 represents the mathematical model of part distortion.

$$DT = 0.59 - 0.63 \times A - 1.07 \times B + 0.21 \times C - 0.23 \times D + 0.57 \times A \times B - 0.089 \times A \times C + 0.23 \times A \times D - 0.22 \times B \times C + 0.24 \times B \times D - 0.056 \times C \times D + 0.20 \times A^2 + 0.47 \times B^2 + 0.027 \times C^2 + 0.10 \times D^2 \quad (4)$$

Table III Experimental Design

Sr. NO	Input Parameters			Output responses		
	Filling Speed mms ⁻¹	Layer Thickness mm	Extrusion Head Temperature °C	Bed Temperature °C	Residual Stresses Pa	Distortion mm
1	90	0.1	225	75	5117	1.83
2	110	0.2	240	70	1476	0.34
3	90	0.2	225	70	2229.86	0.61
4	90	0.3	225	65	271.20	0.04
5	70	0.2	225	75	3230.63	1.00
6	90	0.2	210	65	2103.45	0.62
7	70	0.1	225	70	8000	3.60
8	90	0.2	225	70	2209.55	0.62
9	90	0.3	240	70	353.83	0.05
10	110	0.1	225	70	3570.91	1.13
11	70	0.2	225	65	5403.91	1.96
12	90	0.2	225	70	2174.89	0.59
13	110	0.2	225	75	1154	0.22
14	90	0.1	210	70	4694.86	1.63
15	70	0.2	210	70	3433.14	1.14
16	90	0.3	210	70	-637.59	0.10
17	70	0.2	240	70	5209.92	1.75
18	90	0.2	240	75	2506.99	0.71
19	90	0.1	240	70	6587.14	2.47
20	90	0.2	240	65	3890.29	1.19
21	110	0.2	210	70	543	0.10
22	90	0.2	225	70	2037.14	0.53
23	70	0.3	225	70	1051.61	0.25
24	110	0.2	225	65	1234.40	0.29
25	110	0.3	225	70	-587.20	0.07
26	90	0.1	225	65	6228.57	2.78
27	90	0.2	225	70	2208	0.59
28	90	0.3	225	75	-414.51	0.06
29	90	0.2	210	75	1578	0.36



Table V ANOVA Table of Part Distortion

Source	Sum of Squares	df.	Mean Square	F Value	p-value Prob. > F	
Model	23.26	14	1.66	301.68	< 0.0001	significant
Filling Speed (A)	4.75	1	4.75	862.12	< 0.0001	
B-Layer Thickness (B)	13.80	1	13.80	2506.63	< 0.0001	
Extrusion Head Temperature (C)	0.55	1	0.55	99.05	< 0.0001	
Bed Temperature(D)	0.61	1	0.61	110.73	< 0.0001	
AB	1.31	1	1.31	237.86	< 0.0001	
AC	0.03	1	0.03	5.70	0.0316	
AD	0.20	1	0.20	36.81	< 0.0001	
BC	0.20	1	0.20	35.92	< 0.0001	
BD	0.24	1	0.24	42.96	< 0.0001	
CD	0.01	1	0.01	2.26	0.1549	
A ²	0.26	1	0.26	46.89	< 0.0001	
B ²	1.43	1	1.43	260.49	< 0.0001	
C ²	0.00	1	0.00	0.84	0.3757	
D ²	0.07	1	0.07	12.23	0.0036	
Residual	0.08	14	0.01			
Lack of Fit	0.07	10	0.01	5.07	0.0658	not significant
Pure Error	0.01	4	0.00			
Cor. Total	23.33	28				
Std. Dev.	0.07				R-Squared	1.00
Mean	0.92				Adj. R-Squared	0.99
C.V. %	8.08				Pred. R-Squared	0.98
PRESS	0.42				Adeq Precision	66.11

B. Response Surface Plots

The influence of critical input parameters on output

Table IV ANOVA Table of Residual Stresses

Source	Sum of Squares	df.	Mean Square	F Value	p-value Prob. > F	
Model	141399413.36	14	10099958.10	1071.27	< 0.0001	significant
Filling Speed (A)	29887626.95	1	29887626.95	3170.09	< 0.0001	
Layer Thickness (B)	97248648.24	1	97248648.24	10314.85	< 0.0001	
Extrusion Head Temperature (C)	5753713.45	1	5753713.45	610.28	< 0.0001	
Bed Temperature (D)	2959842.44	1	2959842.44	313.94	< 0.0001	
AB	1946407.65	1	1946407.65	206.45	< 0.0001	
AC	177989.97	1	177989.97	18.88	0.0007	
AD	1095036.67	1	1095036.67	116.15	< 0.0001	
BC	202889.76	1	202889.76	21.52	0.0004	
BD	45338.27	1	45338.27	4.81	0.0457	
CD	183972.37	1	183972.37	19.51	0.0006	
A ²	932293.20	1	932293.20	98.89	< 0.0001	
B ²	1276141.23	1	1276141.23	135.36	< 0.0001	
C ²	112086.94	1	112086.94	11.89	0.0039	
D ²	264845.71	1	264845.71	28.09	0.0001	
Residual	131992.28	14	9428.02			
Lack of Fit	107743.80	10	10774.38	1.78	0.3047	not significant
Pure Error	24248.49	4	6062.12			
Cor. Total	141531405.65	28				
Std. Dev.	97.10				R-Squared	1.00
Mean	2650.31				Adj. R-Squared	1.00
C.V. %	3.66				Pred. R-Squared	1.00
PRESS	658492.54				Adeq Precision	126.73



parameters is illustrated by the response surface plots given below.

1. Response surface plots of residual Stresses

The effect of input parameters on residual stresses is given by the following figures.

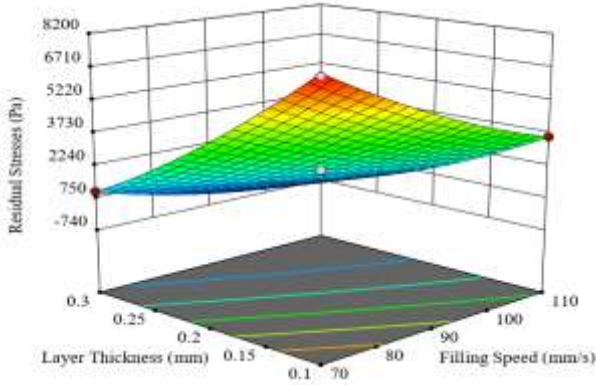


Figure 1 Response Surface plot of residual stresses between Layer thickness and Filling speed

Form Figure 2 it is clear that the relationship between Filling speed and residual stresses is nonlinear same is the case for layer thickness. Residual stresses diminish with the increment in filling speed and layer thickness and layer thickness has more effect than filling speed.

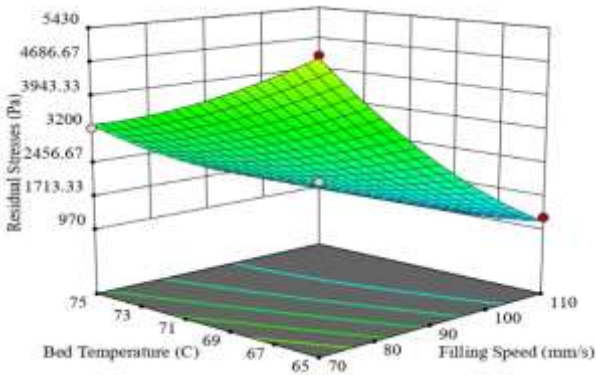


Figure 3 Response Surface plot of residual stresses between Extrusion Head Temperature and Layer Thickness

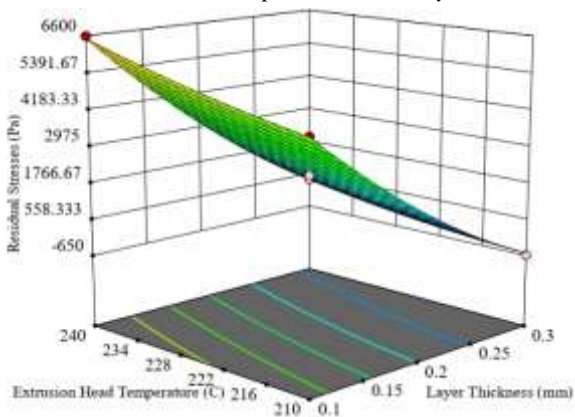


Figure 4 Response surface plot of Distortion between Layer thickness and Bed Temperature

Figure 1 illustrates the relationship bed temperature and filling speed with layer thickness. Residual stresses decrease with the enhancement in both filling speed of nozzle and bed temperature.

It is obvious from Figure 3 that greater the layer thickness less the residual stresses but Extrusion Head Temperature has the opposite effect. Moreover, the relationship is of a quadratic nature.

2. Response Surface Plots of part Distortion

The response surface plots of part distortion are given below.

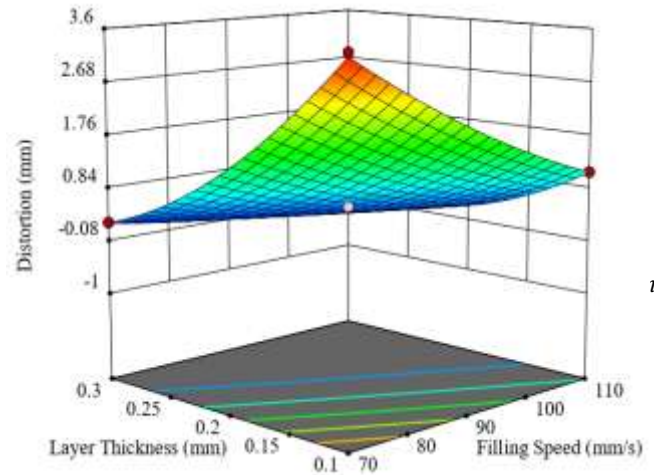


Figure 5 Response surface plot of distortion between Filling Speed and Layer Thickness.

Figure 5 reveals that increment in both layer thickness and Filling speed will result in less distortion of FDM parts. Also layer thickness has more effect than Filling Speed

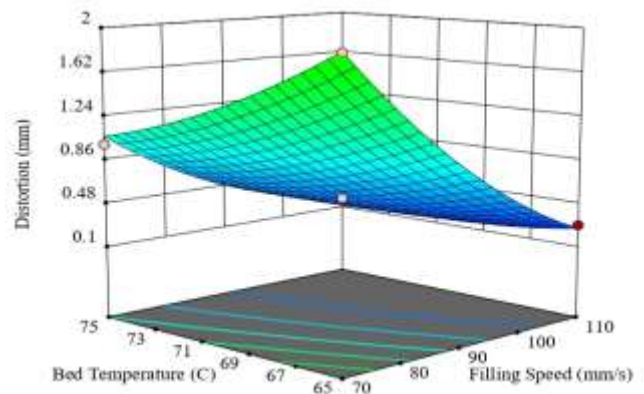
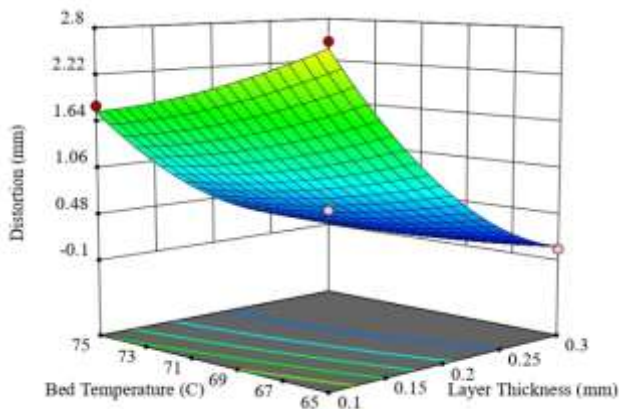


Figure 6 Response Surface plot of distortion between Filling speed and Bed Temperature

Figure 6 represents the behavior of distortion under the influence of Filling speed and bed temperature Higher values of Filling speed and Bed temperature will reduce the distortion .



It can be concluded from Figure 4 that High Bed Temperature will result in a low value of Distortion. But this decrement in distortion will not be linear but it will occur in a nonlinear manner. More the Layer thickness less will be the distortion and the relationship between layer thickness and part Distortion will also be quadratic as it is illustrated by the response surface plot. Because more layer thickness will result in fewer cycles of heating and cooling.

8. Conclusion

In this research an FEA Model of Fused Deposition Modeling process was developed by using element death and birth technique in ANSYS to investigate residual stresses and part distortion accrued during FDM process under the influence of Four input process parameters i.e. Filling Speed, Layer Thickness, Extrusion Head Temperature, and Bed Temperature. ANOVA was utilized to examine the individual and combined effect of four input parameters on residual stresses and Part Distortion. It was concluded from this analysis that Layer thickness is the most significant factor influencing both residual stresses and Part distortion. While the impact of the other three factors is also significant but it is less than the effect of Layer thickness. The findings of this research work can play an important role in obtaining the optimum process parameters of FDM process in order to enhance the process and product quality during commercial production of FDM Parts.

REFERENCES

- [1]. Gebhardt, A., *Understanding additive manufacturing*. 2011.
- [2]. Yan, Y., et al., *Rapid prototyping and manufacturing technology: principle, representative technics, applications, and development trends*. Tsinghua Science and Technology, 2009. **14**(S1): p. 1-12.
- [3]. Peng, A., X. Xiao, and R. Yue, *Process parameter optimization for fused deposition modeling using response surface methodology combined with fuzzy inference system*. The International Journal of Advanced Manufacturing Technology, 2014. **73**(1-4): p. 87-100.
- [4]. Novakova-Marcincinova, L. and I. Kuric, *Basic and advanced materials for fused deposition modeling rapid prototyping technology*. Manuf. and Ind. Eng, 2012. **11**(1): p. 24-27.
- [5]. Rodríguez-Panes, A., J. Claver, and A. Camacho, *The influence of manufacturing parameters on the mechanical behaviour of pla and abs pieces manufactured by fdm: a comparative analysis*. Materials, 2018. **11**(8): p. 1333.
- [6]. Turner, B.N. and S.A. Gold, *A review of melt extrusion additive manufacturing processes: II. Materials, dimensional accuracy, and surface roughness*. Rapid Prototyping Journal, 2015. **21**(3): p. 250-261.
- [7]. Noriega, A., et al., *Dimensional accuracy improvement of FDM square cross-section parts using artificial neural networks and an optimization algorithm*. The International Journal of Advanced Manufacturing Technology, 2013. **69**(9-12): p. 2301-2313.
- [8]. Mishra, S.B., R. Pattnaik, and S.S. Mahapatra, *Parametric analysis of wear behaviour on fused deposition modelling build parts*. International Journal of Productivity and Quality Management, 2017. **21**(3): p. 375-391.
- [9]. Montgomery, D.C., *Design and analysis of experiments*. 2017: John Wiley & sons.
- [10]. Box, G.E. and D.W. Behnken, *Some new three level designs for the study of quantitative variables*. Technometrics, 1960. **2**(4): p. 455-475.
- [11]. Ferreira, S.C., et al., *Box-Behnken design: an alternative for the optimization of analytical methods*. Analytica chimica acta, 2007. **597**(2): p. 179-186.
- [12]. Bergman, T.L., et al., *Fundamentals of heat and mass transfer*. 2011: John Wiley & Sons.
- [13]. Costa, S., F. Duarte, and J. Covas, *Thermal conditions affecting heat transfer in FDM/FFE: a contribution towards the numerical modelling of the process: This paper investigates convection, conduction and radiation phenomena in the filament deposition process*. Virtual and Physical Prototyping, 2015. **10**(1): p. 35-46.
- [14]. Gibbins, J., *Thermal Contact Resistance of Polymer Interfaces*. 2006, UWSpace.
- [15]. Wiedemann, B., K.-H. Dusel, and J. Eschl, *Investigation into the influence of material and process on part distortion*. Rapid Prototyping Journal, 1995. **1**(3): p. 17-22.
- [16]. Coogan, T.J. and D.O. Kazmer, *Bond and part strength in fused deposition modeling*. Rapid Prototyping Journal, 2017. **23**(2): p. 414-422.



(Industry paper)

Surgical Instruments Manufacturing Sector in Pakistan – Current Scenario, Issues and Recommendations

M.J. Afzal¹ and T.A. Khan¹

1. University of Engineering & Technology, Lahore, Pakistan, javedafzal569@gmail.com

Abstract:

There are three major sectors of Pakistan's economy; industry, agriculture and services. Surgical Instruments Manufacturing sector is one of the important sub-sectors of industry with its notable contribution to exports, GDP and employment. Industrial units of this sector are clustered in the city of Sialkot. This industry has its existence in Sialkot for almost a century and has shown gradual progression because of the business acumen of the industry owners, availability of the skilled workforce and networking of the industry owners with the international buyers. Manufacturing of surgical instruments involves a series of the mechanical operations and progressive technology. Although there have been different support interventions of the Government for development of the surgical instruments sector but it is still faced with a range of the challenges like access to technology, finance, HR, international markets and other related services. If these issues are overcome, Pakistan can capitalize the opportunities for export to existing markets as well as untapped markets, like the Middle Eastern, African and other neighboring countries. Therefore, further development and promotion of the surgical instruments industry can help the sector to contribute for the economy of Pakistan far more effectively.

Keywords: surgical instruments; cluster development; manufacturing process; export market

1. Introduction

Industry, agriculture and services are the main sectors of Pakistan's economy. Although there are number of subsectors within the industrial sector, but this paper is limited to the study and analysis of Surgical Instruments Manufacturing Sector. This sector involves a variety of the manufacturing processes and is one of the important sectors in Pakistan's economy from the point of view of its contribution to exports, GDP and employment etc. The state of the engineering industry in an economy shows the status of industrialization and economic stability, as it represents the capacity to add value to the products. The developed countries generally assign priority to the engineering industry. Surgical instruments manufacturing in Pakistan is part of Light Engineering Industry. Pakistan needs to capitalize on export of engineering goods as the other newly industrialized countries like Korea and Malaysia have done that. Pakistan can capitalize the opportunities for export of surgical instruments to the existing markets as well as to the untapped export markets, especially the Middle Eastern, African and other neighboring countries. According to Economic Survey of Pakistan, the economy of Pakistan witnessed a muted growth of 3.29 percent in the year 2018-19 and the sectoral growth was 1.4 percent for industry [1]. This shows an overall slow down of industrial sector in the country during the year 2018-19, if compared with the previous years.

Sialkot is part of the golden triangle along with the industrial cities of Gujranwala and Gujrat and is known for its surgical products and the other

products being manufactured there and exported. In Pakistan, almost 99% of the surgical instruments are produced in Sialkot [2]. This industrial cluster mainly consists of Small and Medium Enterprises (SMEs). Majority of the small enterprises generally supply their products to the medium or large size enterprises or sell to the traders and exporters. Besides maintaining the export of conventional surgical instruments, there is also a huge potential for the industry to focus on manufacturing of diversified products including the body implants and electro-medical equipment that are high value items. The SMEs do not have sufficient capacity to innovate, while the large firms have focus on the ongoing production and do not have time for trying innovative and high value products.

Surgical instruments manufacturing sector in Pakistan is faced with a variety of issues and challenges including policy, regulatory, access to finance, access to business development services (BDS), lack of infrastructure facilities, human resource development, limited R&D. The current situation requires resolving the issues through the appropriate forums and appropriate levels to realize the full potential of this sector for its contribution to economy, jobs and exports. The growth strategy for the surgical sector is through rapid development and promotion of this sector to increase its share in GDP as well as share in exports. Besides that, export led growth strategy for value added items needs to be adopted for boosting exports and for catering to the needs of local consumption. Further development and promotion of this sector would help for creating jobs



and economic prosperity.

2. Background

The Surgical instruments manufacturing industry in Pakistan was started in the early 1940s at Sialkot [3]. A wide range of medical, surgical and veterinary instruments are manufactured and mainly being exported. Sialkot has a history of almost a century of skilled craftsmanship in manufacturing the surgical instruments. This craftsmanship has played a vital role for the sustainability of this industry. The craftsmanship has been combined with modern equipment and technology to manufacture the surgical instruments of good quality, which are mainly exported. The industry makes specialized instruments that are used for surgery. The industry produces the surgical instruments in accordance with applicable / required international standards and specifications. Europe and America are the main export markets for Pakistan's surgical instruments.

The Surgical Instruments Manufacturing Sector in Pakistan started focus on mechanization from 1960's [2]. New technology was adopted quickly and gradually the production processes went through transition from handmade to machine-made instruments. Pakistan's surgical instruments sector with its improved marketing and through networking with major importing countries can capitalize by enhancing the base of the industry for product diversification more importantly to value added surgical instruments.

3. Overview

Surgical Instruments Manufacturing Sector of Pakistan at a glance is given in Table 1.

Table 1. Surgical instruments industry at a glance

Sr. No.	Description	Value
1	Total number of units	2,300 [4]
2	Employment	450,000 [5]
3	Contribution to GDP	0.42 % [6]
4	Export (2018)	\$ 385 Million [7]

The surgical instruments are the devices or tools that are used to perform surgical procedures including cutting, holding, grasping, retracting or suturing. Steel is the basic material used in production of surgical instruments along-with other materials including radium, titanium, chromium and molybdenum. Due to emerging requirements, the nature of surgical instruments has transformed to include computerized components. Thus, and the emergence of advanced technology has compelled the change in the design and manufacturing of surgical instruments.

The industry at Sialkot manufactures the

instruments that are used in the variety of braches of surgery. Surgical instruments are mainly used for; diagnostic, anesthesia, vaccination, suture, plaster, bone surgery, neurology, tracheotomy, cardiovascular, lung surgery, dermatology, ophthalmology, otology, rhinology, oral, tonsil, sterilization, urology, gynecology, obstetrics, intestinal, stomach rectum and others related procedures [3]. Developments in the medical field have implied application of new procedures for healthcare that enable the medical professionals to carry out complex surgical procedures more effectively with less health risk and ensuring speedy recovery of patients especially using electro-medical equipment, body implants and other high precision surgical instruments.

4. Analysis of Business Operations

The analysis of business operations of Pakistan's surgical instruments manufacturing sector is given below.

4.1 Value Chain

The value chain of Surgical Instruments Sector in Pakistan comprises of the following;

4.1.1. Inputs

- Export orders - product specifications, price, quantity, delivery time and destination.
- Equipment and material supply – Steels, chemicals, hardware, machinery and packaging.
- Infrastructure – Electricity, gas, roads, communication and logistics.
- HR – Graduates of universities, institutes of TEVTA, PVTC, PSDF and informal training through Ustad Shagird system.

4.1.2. Process

- Representation & facilitation – SIMAP, SCCI, TDAP, PCSIR, PSIC, SMEDA
- Firms – Tier 1 firms, tier 2 firms, tier 3 firms, vendors
- Mechanical operations – Heat treatment, forging, machining, polishing

4.1.3. Marketing

- Distributors – Institutional buyers, wholesalers, retailers
- Trading firms - Repackaging firms, wholesalers, retailers
- Direct export – Distributors, wholesalers, retailers

4.2. Raw Material

The surgical instruments being produced at Sialkot cluster are mainly produced through outsourced arrangement. The international brands / buyers outsource their production to the manufacturing firms of surgical instruments at Sialkot. The international buyers impose very



stringent quality standards for their ordered products. Most of the large firms use imported stainless steel as raw material along with other raw materials to produce surgical instruments. Whereas the small and medium companies use the mix of local and imported raw materials. There are the suppliers of the raw materials who operate in the cluster. General ingredients used in the production of surgical instruments include Stainless Steel, Titanium, Brass and Aluminium along with other inputs including emery powder, felt mops, gloss powder, electroplating polishes, grinding belts, trichloroethylene, satin finishing wheels, grinding wheels and emery grains [2].

4.3. Technology and Machinery

The machinery and technology used by the cluster for manufacturing of surgical instruments includes both the local as well as the imported machinery and equipment. The local industry is competing in the world market not only because of the unique products but also because of price competitiveness. The imported machinery in the cluster includes the machinery discarded by western companies. Importers of equipment import this machinery and supply to the local industry. There is dire need to support this sector by establishing and strengthening common facilities at Sialkot for technology level support. The local industry started adapting mechanization and new technology since 1960's. There was use of reverse engineering and the industry also started to produce certain equipment locally and subsequently the industry shifted to mechanical processes e.g. the industry shifted from manual forging to drop forging hammer. Surgical instruments sector need to capitalize by enhancing the technological capability to diversify its product portfolio to value added surgical instruments like body implants and electro medical equipment which are high value items. Additive manufacturing is a useful manufacturing technique for manufacturing patient specific appliances, thus increasing the comfort of the patient and is also cost effective [8].

4.4. Workforce

A vast majority of the workforce in the surgical instruments cluster Sialkot is semi-literate. However, this workforce is highly skilled due to which they produce complicated instruments with far more ease. There are training facilities at Sialkot offered by TEVTA and PVTC but the dilemma is that a very limited number of workers prefer for formal training. However at large manufacturing units, the formal technical training acquired by the workforce makes difference in designing, quality and productivity. The gap of demand and supply of trained workforce still prevails and there is shortage of skilled workforce in the surgical instrument industry at Sialkot. The shortage of skilled labor is in the fields of grinding, polishing, milling machine operators, lathe machine

operators and CNC machine programmers. Shortage of skilled workforce causes productivity and quality related issues. Business support organizations like PSIC, TEVTA and SMEDA are offering training and capacity building programs for the surgical instruments industry at Sialkot. Workforce involvement is instrumental for quality improvement. There are barriers for implementation of quality improvement initiatives. Lack of employee motivation to the quality program to adopt new practices is one such barrier. Employee attitude to quality practices is another barrier to implementation of quality program [9].

4.5. Compliance to National & International Standards and Certifications

The surgical instrument is intended to be used inside the human body therefore it must be manufactured according to the safety requirements of the medical devices law. Thus, it must be established through various tests according to international standards that the materials to be used and the manufacturing processes will not lead to any danger to the human during the use [10].

Quality is the main area of concern of the importers due to which the foreign buyers impose strict quality standards. The importers also have to comply with the requirements to ensure improvements in management, technology and labor. The production process at surgical instruments manufacturing cluster is in line with the requirements of supply orders from the international buyers. The supply of these surgical instruments is mainly aimed at export where as it is limited in the local market. Surgical instruments cluster at Sialkot took a variety of measures in order to ensure good quality of the products and to fulfil the requirements of importers. For export to US, it requires 'Good Manufacturing Practice (GMP) certification. The importers from Europe require the Pakistani exporters to have ISO 9002 certification. Certificate of Europe (CE) is another quality assurance certification required. Surgical instruments manufacturing industry of Sialkot has been following the international standards in conformance with WHO requirements. In the surgical instruments industry cluster at Sialkot, more than almost 300 of the firms are ISO 9002 certified and about 250 firms are certified for Good Manufacturing Practice (GMP) [2]. The local firms need to have more certifications for compliance to the requirements of international buyers. Environmental cost of surgical instruments manufacturing is also an important area of concern that needs to be improved. [11]

4.6. Production Process Flow

The production process flow of majority of the items comprises of a series of mechanical operations that are carried out by the highly skilled workforce. The process of making of generic surgical instruments



comprises of the mechanical operations including; die making, raw material shearing, forging, annealing, heat treatment, initial assembly, filing, machining, trimming, electro polishing, finishing, final assembling, testing, cleaning, tagging and packing [2]. In order to improve surface finish of the parts, both grinding (via mounted points) and vibratory tumbling can be used in meeting the requirements. [12]

4.7. Marketing, Sales & Distribution Channels

Marketing of surgical instruments by the industry at Sialkot is demand driven. There is limited sale of the surgical instruments in the local market. The main target of marketing of the surgical instruments is export market. Buyers from USA, UK, EU countries and Germany order the required designs of the surgical instruments. Because of no focus on branding, surgical instrument firms are still working as support organizations for the international brands. However, by registering their own logos, firms from this cluster may be able to create their own identity and export with brand identity. It will add value to the status of local industry. Some of the large firms in the cluster have their offices in importing countries including Germany to get orders from the importers. This practice helps in getting orders from export market. Contacts also help market the products. Most of the Pakistani producers focus on Germany because of its expertise in surgical instruments. Visits of local industrialists to other countries also help to introduce the products and explore new business opportunities. Trade fairs and exhibitions are also important source of marketing and participation of local industry representatives in the international exhibitions helps to develop new contacts in the international market and to explore new opportunities and new buyers of their products. Electronic media and other communication sources help to approach the international buyers and get orders for export. Most of the firms are exporting to international buyers through exporters and others, directly in the market. These firms also use brochures and social media channels for the marketing of the products.

4.8. Institutional Support

The following is the institutional support at Sialkot for Surgical Instruments Manufacturing Sector;

4.8.1. Metal Industries Development Centre (MIDC)

MIDC offers common facility services to the surgical instruments cluster.

4.8.2. Sialkot Material Testing Laboratory (SIMTEL)

SIMTEL was established in the year 2000 comprising of the three material testing labs; Spectro Lab, Metallographic Lab and Chemical Testing Lab.

4.8.3. Government Apprentices Training Centre Sialkot

This Centre offers technical training related with the surgical instruments industry.

4.8.4. SMEDA

SMEDA offers a range of business development services including business counseling, matchmaking, training and capacity building.

4.8.5. PSIC

PSIC also offers its services for development of the surgical instruments industry. More recently PSIC is supporting the industry through its Cluster Development Initiative (CDI).

5. Pakistan's Exports

Year-wise Pakistan's exports of Surgical Instruments are given in Figure 1. There is lack of focus on local brands therefore brand development is one of the potential areas for improvement. Despite lack of focus on branding, Pakistan is still performing reasonably in the export market as shown in Figure 1.

5.1. Main Export Items

Top three of the items of surgical instruments being exported by Pakistan are given in Table 2

Table 2. Top three of the items of surgical instruments being exported by Pakistan [7]

Sr. No.	HS Code	Product	Export 2018 (US \$ Million)
1	901890	Instruments and appliances used in medical or veterinary sciences	373.18
2	901849	Instruments and appliances, used in dental sciences	4.93
3	9032	Automatic regulating or controlling instruments and apparatus	1.90

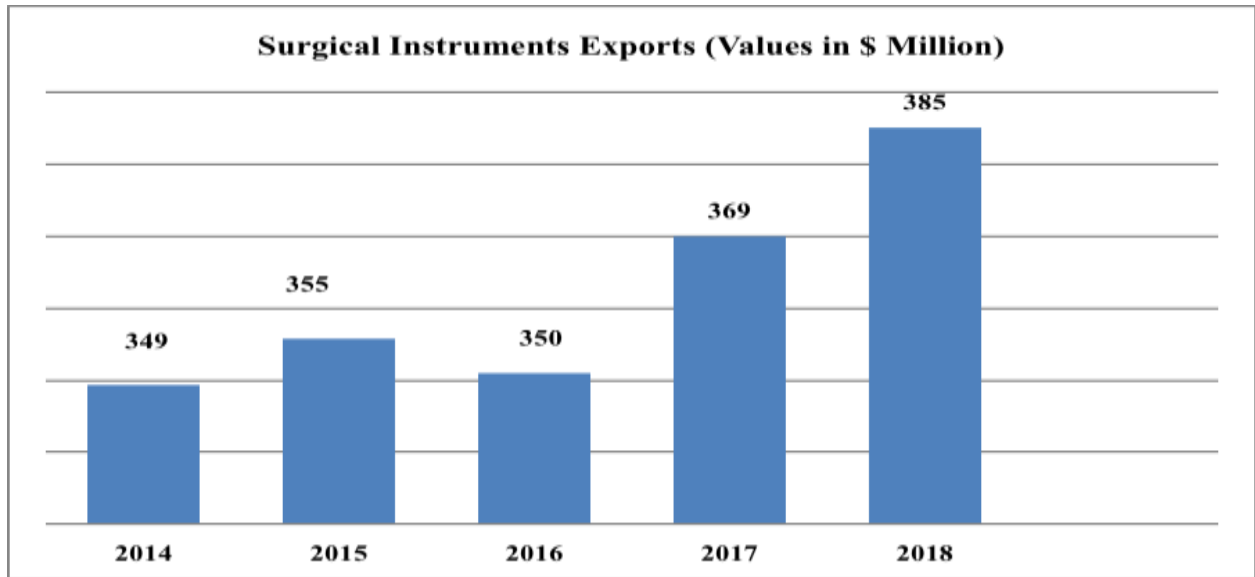


Figure 1. Year-wise Pakistan's exports of surgical instruments [7]

5.2. Pakistan's Share in Global Trade

Figure 2 depicts Pakistan's surgical instruments exports in 2018 to world's exports in US \$ Million for the same items that Pakistan exports. The %age share of Pakistan in the World exports for the same items that Pakistan exports is only 0.13% that is almost negligible and it shows the huge potential, Pakistan can capitalize by increasing its share in the world exports. However, if Pakistan's Surgical Instruments sector goes for serious efforts for pursuing product

diversification and tapping new markets, the increase in share of exports can be manifold.

6. Pakistan's Imports

Year wise trend of Pakistan's imports of Surgical Instruments are given in Figure 3. Gradual and consistent increase in the imports of surgical instruments by Pakistan is a matter of serious concern and therefore immediate steps need to be taken for import substitution.

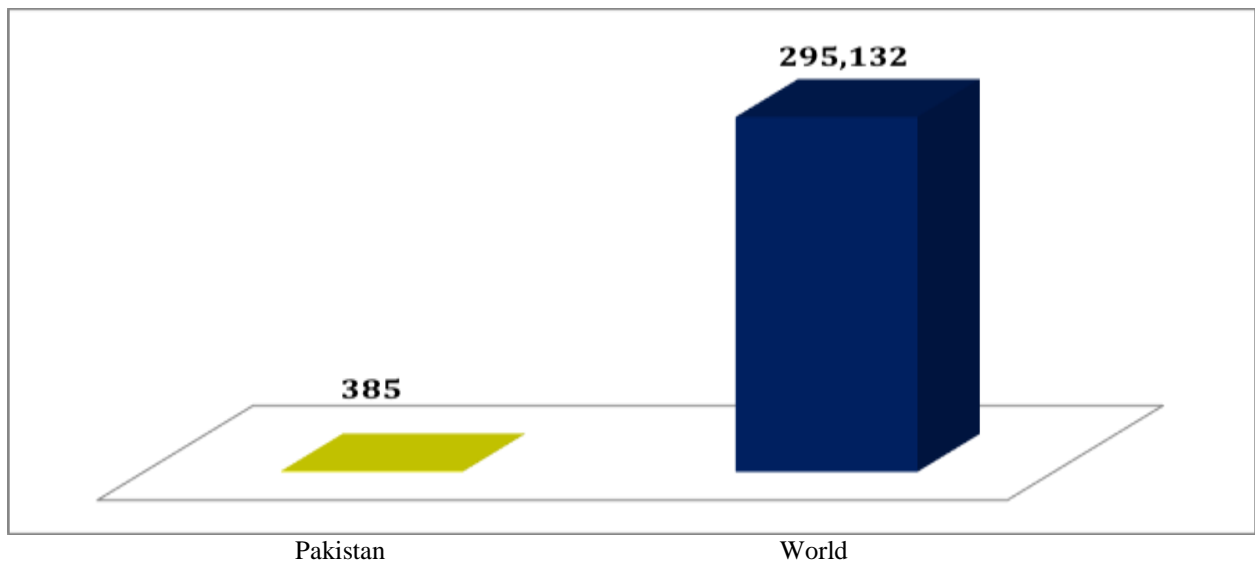


Figure 2. Pakistan's surgical instruments sector exports 2018 to world's exports in US \$ Million [7]

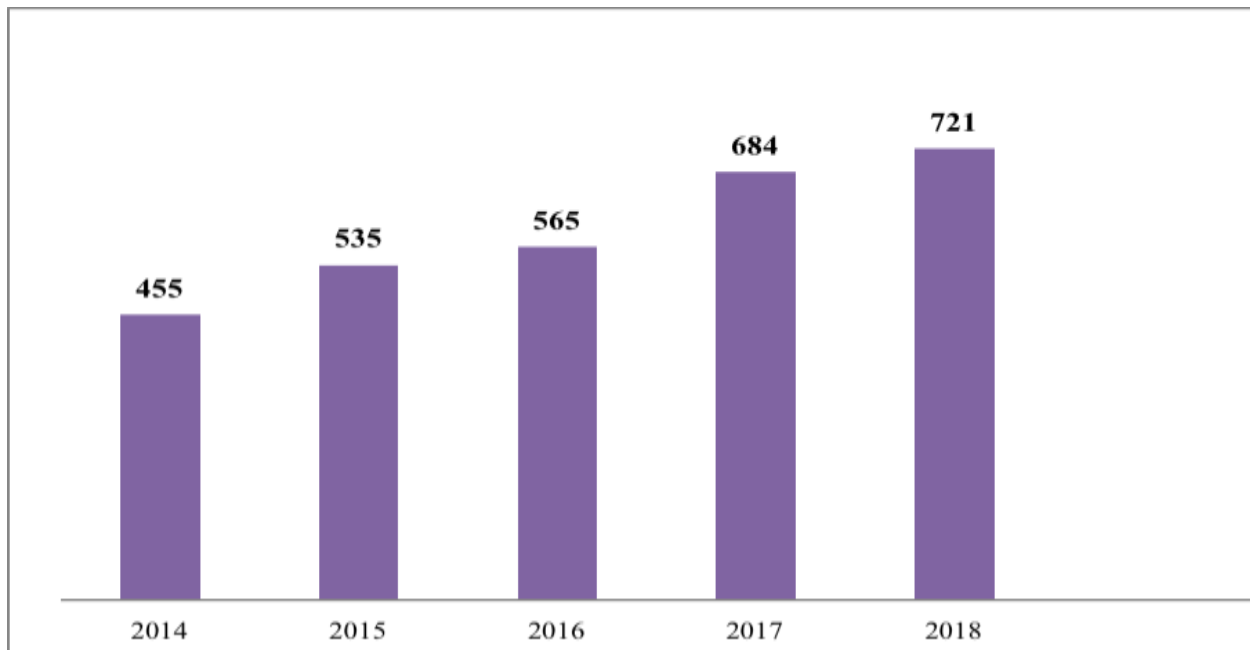


Figure 3. Pakistan's imports of surgical items in US \$ Million [7]

6.1. Main Import Items

Top three items of Pakistan's imports of surgical instruments in 2018 are given in Table 3.

7. SWOT Analysis

SWOT Analysis of Pakistan's surgical instruments manufacturing sector is given in Table 4. It shows the main areas of strengths, weaknesses, opportunities and threats for the surgical instruments industry in Pakistan.

8. Investment Opportunities

Surgical instruments manufacturing sector is one of the promising and prominent sectors in Pakistan's economy. This sector has shown quite an extent of resilience during the recent phase of

decline of overall exports of the country. As far as the investment opportunities in this sector are concerned, there is a significant potential of investment for expanding the scope of the conventional surgical products along with making investments for manufacturing of new and high value items like body implants and electromedical equipment that have huge potential for gains both in the domestic market as well as in the export market.

9. Issues

The sector is faced with a number of the issues and challenges that cause hindrance for growth. Main issues of Surgical Instruments Manufacturing sector in Pakistan are given in Table 5.

Table 3. Top three items of Pakistan's imports of surgical instruments in 2018 [7]

Sr. No.	HS Code	Description	Imports 2018 (US \$ Million)
1	9018	Instruments and appliances used in medical, surgical, dental or veterinary sciences	342.85
2	9027	Instruments for physical/chemical analysis; inst for viscosity, heat etc.	89.87
3	9022	Apparatus based on the use of X-rays/of alpha, beta/gamma radiations	73.55



Table 4. SWOT analysis of Pakistan's surgical instruments manufacturing sector [2]

<p>Strengths;</p> <ol style="list-style-type: none"> 1. Industry in place for over a century 2. Management staff 3. Workforce skills 4. Availability of raw materials 5. Linkage with export market 6. Presence in domestic market 7. Established sales channels 8. Affordable prices 	<p>Weaknesses;</p> <ol style="list-style-type: none"> 1. Energy shortage and cost of Energy 2. Rising prices of raw materials 3. Limited marketing effort 4. Limited quality control 5. Weak Complaint Resolution 6. Limited R&D initiatives 7. Lack of diversification 8. Limited capacity to meet high demand
<p>Opportunities;</p> <ol style="list-style-type: none"> 1. Linkages with suppliers & brands 2. Standardized items 3. Innovation in manufacturing 4. Effective marketing techniques 5. Brand development 6. Up-gradation of technology 7. Improved policy interventions 8. Changes in lifestyle patterns 	<p>Threats;</p> <ol style="list-style-type: none"> 1. Rising energy prices 2. Lack of availability of skilled workers 3. Regulatory and policy matters 4. Limited access to finance 5. Legal Issues 6. High duties and taxes 7. Limited technological upgrades 8. Easy entry for new entrants

Table 5. Main issues of surgical instruments manufacturing sector in Pakistan

Sr. No.	Major Category	Issues
1	Policy and Regulatory	Inadequate policy focus & weak implementation Inadequate policy focus and inadequate regulatory enforcement
2	Business Development Support	Low level of productivity Shortage of skilled workforce Limited training opportunities Inadequate wages for entry level workforce Inadequate product, standardization Lack of certifications; CE Marking, GMP, ISO 9002, ISO 13485 Lack of quality apparatus & use of non standard grade materials Limited product categories & range of product models Low level of technology Capital inadequacy for technology up-gradation Lacking integration with global supply chain Lack of focus on branding
3	Infrastructure and Strategic Initiatives	Lack of infrastructure facilities like testing etc. Inadequate & expensive power supply
4	Networking & Institutional Strengthening	Weak industry academia linkage Weak institutionalized R&D



10. Recommendations

Following are the proposed recommendations / interventions for development and promotion of Surgical Instruments Manufacturing in Pakistan;

- a. Developing product standards and transformation to international standards
- b. Developing technical regulations & enforcement mechanism
- c. Rationalization of tariffs – Inputs at zero rating
- d. Free Trade Agreements (FTAs) to accommodate interest of local industry
- e. Support for access to finance for machinery
- f. SME Export House
- g. Revitalizing TVET sector
- h. Vendor development programme
- i. Research for export markets
- j. Product development & diversification
 - i. Body implants
 - ii. Electromedical equipment
- k. Promotion of country image
- l. Consultancy support for branding, energy efficiency, quality & productivity
- m. Support for compliance to international standards
- n. Accredited testing & certification facilities in cluster
- o. Capacity building of existing CFCs & testing facilities
- p. Capacity building of PSIC, PNAC, PSQCA, PCSIR, SMEDA.
- q. Framework for institutionalized R&D with PPP

11. Conclusion

Pakistan's economy is faced with a number of challenges including the overall decline in Pakistan's exports for the last few years. In order for the economy to come out of this situation, export led growth of industry is the strategy that can take the country forward. Surgical Instruments Manufacturing sector being one of the promising sub-sectors in industry with its existence for over a century because of the business acumen of the industry entrepreneurs, skilled workforce, linkage the international buyers etc. This sector is operating at a level from where it can capitalize for further growth by addressing the issues being faced. This sector is faced with issues related with policy and regulatory matters, access to finance, access to technology, good quality HR, access to business development services and issues related with proper marketing approach etc. Given the current situation of the sector, there is need for developing product standards, technical regulations along with enforcement mechanism, rationalization of tariffs, FTAs to accommodate interest of the local industry, increasing access to finance and technology. Other proposed interventions include SME Export House, revitalizing TVET institutes in the area, vendor development, exploring new markets, product diversification; body implants and

electro-medical equipment, improving quality, productivity, compliance to international standards and certification, strengthening of CFCs along with a framework for R&D. Product diversification and focus on branding can be the game changer transformations for the sector. Thus, a strong Surgical Instruments Manufacturing sector can help contribute for Pakistan to regain the stability and growth in exports for the uplift of the economy.

REFERENCES

- [1] Pakistan Economic Survey 2018-19.
- [2] Diagnostic Study of Industrial and Handicrafts Clusters in Punjab (2016). *Punjab Small Industries Corporation*.
- [3] Pakistan Light Engineering Sector (2010). *Board of Investment, Govt. of Pakistan*.
- [4] Surgical & Medical Instruments Industry of Pakistan (n.d.). *Trade Development Authority of Pakistan*.
- [5] Policy For Technology Up-Gradation In Surgical Instruments and Pharmaceutical Sectors (n.d.). *Trade Related Technical Assistance Programme*.
- [6] The Sectoral Analysis of Surgical Instruments of Pakistan (n.d.). Pakistan Institute of Trade and Development.
- [7] ITC (n.d.). Trade statistics for international business development. Retrieved November 29, 2019, from <https://www.trademap.org>
- [8] Javaid, M., & Haleem, A. (2019). Journal of Oral Biology and Craniofacial Research Current status and applications of additive manufacturing in dentistry: A literature-based review. *Journal of Oral Biology and Craniofacial Research*, 9(3), 179–185.
- [9] Awan, U., Kraslawski, A., & Huiskonen, J. (2018). Understanding influential factors on implementing social sustainability Understanding influential factors on implementing social sustainability practices in Manufacturing Firms: An interpretive structural modelling (ISM). *Procedia Manufacturing*, 17, 1039–1048. <https://doi.org/10.1016/j.promfg.2018.10.082>
- [10] Coemert, S., Traeger, M. F., Graf, E. C., & Lueth, T. C. (2017). Suitability evaluation of various manufacturing technologies for the development of surgical snake-like manipulators from metals based on flexure hinges. *Procedia CIRP*, 65, 1–6.
- [11] Nadvi, K. (1999). Collective Efficiency and Collective Failure: The Response of the Sialkot Surgical Instrument Cluster to Global Quality Pressures. *World Development*, 27(9).
- [12] Nahata, S., & Ozdoganlar, O. B. (2019). Feasibility of Metal Additive Manufacturing for Fabricating Custom Surgical Instrumentation for Hip and Knee Implants. *Procedia Manufacturing*, 34, 772–779.



Impacts of Electric Vehicle's on Emissions & Economy for Developing Nations & Recommendations for Electric Vehicle's Policy for Pakistan

Zain Ul Hassan¹, Dr. Naseer Ahmad¹

¹Department of Mechanical Engineering, University of Engineering & Technology, Lahore,

Corresponding author 2019msame9@student.uet.edu.pk

Abstract:

With pollution damaging climate all around the world, focus is inclined towards clean energy and that pushed investors and manufacturer towards the launch of electric vehicles (EVs) in market in recent years. Starting from develop countries and spreading toward developing countries EVs has now become hot topic. Pakistan has recently approved the EVs policy drafted by Ministry of Climate Change and Ministry of Industries. Now with the approval of EVs Policy 2019 along with Auto Development Policy (ADP) 2016-2021 doubts has been removed from investors and manufacturers minds. The objective of this study was to investigate engineering and social challenges that exists in Pakistan regarding electric vehicles and an analysis was done on EVs policy and ADP in contrast with policies in other south Asian countries that rank near to Pakistan in overall development index. After analyzing some critical challenges were discovered regarding engineering point of view and some loop holes were found in policies, upon which some improvement recommendations were suggested in this paper.

Keywords: *Electric Vehicles in Pakistan; Electric Vehicle Policy 2019; Automobile Development Policy 2016-2021; Infrastructure for EVs in Pakistan*

1. Introduction

The world is excelling in technology at very fast pace[1]. With the rapid change of technology, the existence of species including humans is under severe threat as climate is being destroyed drastically[2]. Core cause of extinction for species will be rise in global temperature by 1.5°C to 2°C[3].

Many develop countries are struggling to fight back climate change by introducing environment friendly policies especially renewable energy systems (RES) to replace fossil fuel (FF) energy systems [4]. Many developed European and American Countries are planning to introduce electric and alternate fuel-based transportation systems as transportation is one of the leading causes of climate change[5, 6]. Among them many countries are planning to completely ban FF Vehicles [7].

Pakistan is amongst ten countries most affected by climate change[8]. Economically we are second most affected country[3, 8]. The melting of glaciers in Himalayas to the smog problem of our cities gives us a strong indicator that climate change impacts millions of lives and if continue unabated it will impact millions of more lives [3].

The Government of Pakistan is committed to curb emissions to mitigate and adapt to the harmful effects of climate change[9]. Therefore, the Government of

Pakistan has approved mandated minimum penetration targets for Electric Vehicles[9]. An Electric Vehicle policy is being developed to ensure meeting the penetration numbers set forth[9]. We hope that this approval of this policy will begin an era of clean air in the country[2].

Electric Vehicles the healers of mother nature

Electric Vehicles (EVs) have potential to solve critical challenges faced by Pakistan [8]. In Pakistan transport sector is the leading factor in deteriorating the climatic conditions[10]. 43% of the airborne emissions in Punjab are from transport sector[2]. With the anticipated rise in Fossil Fuel Vehicles (FFVs), the problem of air pollution is only going to get worse[3]. EVs do not emit any pollutants so their introduction will limit emissions to a large extent[11, 12].

Oil import and trade deficit in Pakistan

Rising trade deficit is one of the major factors towards stagnant economic growth in Pakistan[13]. EVs will substantially limit the bill for oil import which is the largest import commodity in Pakistan[9]. Moreover, EVs have a potential to set up a whole new industry in Pakistan, creating numerous green businesses and employment opportunities and ameliorating the overall socio-economic situation of the country[9].



Cost a core hinderance for public acceptance to EVs

The capital cost of EVs is still high due to high battery costs[14]. However, according to various forecasts the battery prices are falling rapidly[15]. According to Bloomberg New Energy Finance the cost of EVs will be at par with FFVs by 2022[16]. Similarly, McKinsey estimates the total cost of ownership of small EVs and buses to be at par with their FFV counterparts by 2020 and cost ownership of all types of EVs to be at par with their FFVs counterparts by 2025[7, 17]. International Energy Agency (IEA) forecasts around 250 million EVs on road by 2030, excluding two and three wheelers[18].

Right time to launch EVs in Pakistan

It is important for Pakistan to tap into this market on priority. Not only will it solve the problems of emissions and surging oil import bill but also it will be an excellent opportunity for exports[19]. Moreover, EVs are an excellent flexible load for the national electric grid[19]. With right planning, EVs will use the electricity in off-peak hours and reduce the burden of idle capacity payments on the national exchequer[20].

World Readiness Index for Electric Vehicles

Table 1 shows Norway plans to ban sale of all FFVs by 2025, Netherlands plans to ban such sales by 2030, while France and UK plan to do the same by 2040[7].

Table 1: Global Consideration for Ban of FFV

Country	Years to Ban FFV
Norway	2025
Netherland	2030
Israel	2030
India	2030
Germany	2030
Ireland	2030
Scotland	2032
UK	2040
France	2040
China	Actively Thinking to

2. Scope of this Paper

This paper covers all electric vehicles that are not covered by the Auto Development Policy 2016-21 of

Pakistan. The policy and subsequent incentives are related to all-battery operated vehicles that do not contain internal combustion engine and are run solely through the available on-board battery charge. Hence all recommendations in this paper are solely for all-electric vehicles.

3. EVs penetration recommendations

Globally, EVs are steadily capturing the automobile industry[21]. EVs are being particularly promoted in view of the global commitments to bring down Green House Gas (GHG) emissions as vehicular emissions are one of the major causes of GHGs[22].

For a country to introduce and sustain EVs and its infrastructure, it is important to determine penetration targets of EVs[23]. Table 1 mentions proposed minimum EVs penetration targets along with expected penetration time frame.

Electric Vehicles bring in a number of benefits to the economy[24]. Table 2 provides a conservative estimate of benefits to the country with the EV penetration targets mentioned earlier. This include benefits of fuel savings which can directly result in reduced fuel import bill and also reduce other associated socio-economic costs[25, 26]. EVs will also use the idle capacity available in the national electricity grid due to intra-day and seasonal variations. On one hand this will reduce the idle capacity payments and on the other hand this will generate extra revenue from using electricity that otherwise may not be sold altogether.

Table 2: Electric Vehicle Penetration Targets.

	Medium Term Targets (5 Years)	Long Term Targets (2030)	90% for 2040 (New Sales)
4 Wheelers	100,000	30%	
2/3 Wheelers	500,000	50%	
Buses	1000	50%	
Trucks	1000	30%	

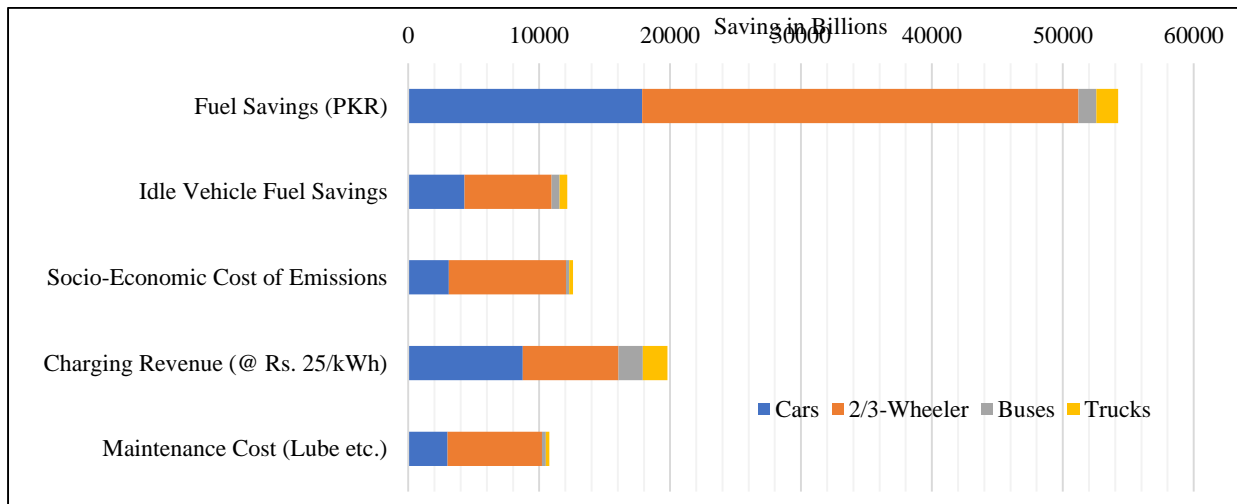


Fig 1: Yearly Income and Savings from EVs with Five Year Penetration Target.

Estimations of Data for Fig 1 is as following:

- Carbon Management Cost for Pakistan = USD50/Metric Ton
- Tailpipe Emission reductions = $\pm 61\%$
- Renewable Energy Sources Counted for Pakistan = $\pm 45\%$
- Cost of Electricity for Using EVs in Pakistan = PKR 15/KWh
- Fuel Price Calculated for Petrol = 110/Liter
- Fuel Price Calculated for Diesel = 125/ Liter
- Total Saving in Earnings = Approx. 110 B /Year [Table 1]

5 Proposed phases to achieve foresaid targets

Table 3 shows the proposed plan for initial 5 years after policy in approved.

Table 3: (5 Years proposed plan for EVs Penetration)

Year 1	Year 2	Year 3	Year 4	Year 5
Public Awareness				
Market Development				
Subsidization for EVs Charging Infrastructure				
Subsidized Import of Parts and Tools for Repair				
Fuel Import Substitutions with EVS				
Local Adoption of EVs				

The initial years of EV penetration in Pakistan are not possible without governmental support[8]. EVs still costs much higher than their Fossil Fuel

Vehicles (FFV) counterparts and governments around the world give subsidies, incentives and tax breaks for EV adoption amongst the masses[11]. These initial incentives, tax breaks and benefits will pay for itself with the savings in fuel import bill, reduction in emission related expenses, usage of idle electricity capacity and income from charging revenues[11, 21]. For example, with the target penetration of first five years the country will conservatively get around PKR 110 Billion yearly through savings and earnings [table 2].

3.1. Registration Recommendations for EVs

Currently there is no mechanism to register an all-electric vehicle in Pakistan[8]. The Government of Pakistan needs to establish a system based on other countries or following international standardized parameters along with the collaboration of relevant entities.

The following table provides categories of two-three wheelers and cars for their registration categorization

Table 4: Registration Categories EVs

Category	'Rated' Power of Electric Motor
1	0-7.5 KW
2	7.5-15 KW
3	15 KW – 50KW
4	50-60 KW
5	75-100 KW
6	100-150 KW
7	Above 150 KW



The Government can take the following proposed measures for categorizing the EVs in different segments based on rated motor power, that could be similar to FFV in terms of engine capacity:

1. The categorization of registration shall be based on their 'rated' electric motor.
2. Distinct registration plate color and design will be allocated to EVs.

3.2. *Charging Infrastructure Recommendations*

In order to promote EVs in such a way that it penetrates the market, a minimum custom duty (MCD) on infrastructure should be allowed. Following measures should be taken to achieve targets:

1. Charging infrastructure in cities in every 2.5x2.5 Square Km area.
2. DC fast chargers shall be installed at 60km range along motorways and 30km range on highways.
3. Private charging station shall opt swappable battery facilities.
4. Electric Distribution Company (DISCO) shall made to support fast charging.
5. Existing CNG and Fuel Stations shall be encouraged to establish charging infrastructure

3.3. *Core Objectives to Consider*

The objectives of the upcoming EV policy can includes:

1. Mitigate climate change through a reduction in emissions from transport sector.
2. Create a pivot to industrial growth in Pakistan and encourage auto and related industry to move towards local EV manufacturing
3. Forge links with the global EV value chain for export potential of EVs and their parts.
4. Meet the objective of generating employment through Green Economy initiatives.
5. Reduce oil import bill.
6. Use electricity in off-peak times for useful purposes.
7. Develop affiliated industry such as battery manufacturing, charging infrastructure, etc.

3.4. *Incentive Recommendations*

There are four segments of EVs including 2/3 wheelers, cars, buses and trucks which require different policy incentives as national and international markets are at various stages of development for each of the respective segment.

In Table 5, some recommendations have been listed for 4 segments under electric vehicles.

In table 6, some recommendations are suggested for auxiliary systems that potentially support the successful penetration of electric vehicles in country.

Table 5: Recommended incentives for 4 segments of EVs (Cars, Scooter, Rickshaws, Buses and Trucks)

Cars (Light 4 Wheelers)	2/3 Wheel Vehicles	Buses	Light Trucks
All existing incentives under ADP 2016-2021 shall remain intact.			
EVs Manufactured Locally to be sold at Minimum GST.		Government should purchase 100 E-Buses & 100 Light Trucks for introducing E Bus in country	
For few initial years no registration fees and token tax should be imposed for all 4 segments of EVs			
EVs Specific Components for all 4 segments should be allowed to be import at MCD for initial years			
Distinct incentives for EVs as compare to FFV		Encourage manufacturers to setup plants for Buses and Trucks through some Government to Government Contracts	
Incentives should be given for training of repair and maintenance for Cars	Low Speed 4-Wheeler should be allowed under the same category as for 2/3 Wheel	Locally manufactured buses and trucks should be allowed to be sold at minimum GST	



Used and CKD EVs should be allowed to be imported with relaxed MCD for initial years	A special provision for swappable battery for 3-Wheeler should be introduced	Rapid Bus Transit projects should be converted to electric buses on priority bases	Charging infrastructure for trucks should be allowed to installed along CPEC, Motorways & Highways
State Bank of Pakistan should allow buying all EVs except 2/3-wheeler with cost effective financing schemes			

Table 6: Incentives for Auxiliary Support Systems for EVs Penetration in Country

Incentives of Setting up EV Manufacturing Units	Incentives for EV Components and Modules Manufacturing	Incentives for Charging Infrastructure and Battery Swapping Stations
Uphold the incentives from Auto Development Policy 2016-21 for the 3 above mentioned segments & Greenfield Investment to all sectors should be ensures at all levels		
Existing Automotive Manufacturer and Assemblers should be allowed to use their plants under the auspices of Greenfield investment regulation of prevailing ADP 2016-21.	All components used only in International Standard (WP.29) EVs, other than locally manufactured should be allowed to be imported at MCD and Minimum GST.	Level 2 Chargers and their relative components should be allowed and MCD and Minimum GST for few initial years.
The State Bank should allow lower financing rates for EV manufacturing plants setup under Long Term Financing Facility (LTFF).	Individual components of batteries, motors, and electronics etc. should be allowed at import MCS and Sold at Minimum GST.	Entities offering public Level-2 charging should be pushed to show the installation cost of the charging facility as Corporate Social Responsibility (CSR) contribution.
A policy should be approved for land allotment for initial decade to setup Manufacturing Units with lease agreements and easy finances.	Components for conversion Kits should be allowed to import at MCD and Minimum GST for few initial years.	All Level-3 DC fast chargers and its associated infrastructure should be allowed to be imported at MCD and Minimum GST should be applicable.
A policy should be framed to evolve incentives for export of charging infrastructure and EV's from Pakistan to ensure that Pakistan's growing market.	Establishment of recycling and refurbishment plants to ensure proper recycling and/or disposal of batteries and other electronic waste.	All modules and components of Level-3 DC & beyond fast chargers Should be allowed at MCD and minimum GST.

4. Conclusions

Center for EVs Regulations

The government can establish a Center for EVs to jumpstart the EV penetration in the country & work towards developing EVs related industry.

EVs Model Cities and Economic Zones

Lahore and Islamabad can be designated as model cities to jump-start 'Green Rickshaw' and 'Green Taxi' schemes respectively. EV related greenfield projects including those for charging infrastructure may use existing Special economic zones.

Projected decrease in Fossil Fuel Import

It is expected that with the penetration of electric vehicles in country there will be significant drop in oil imports, hence therefore reduction in import bill. Figure 2 presents an estimated reduction in import fuel bill.

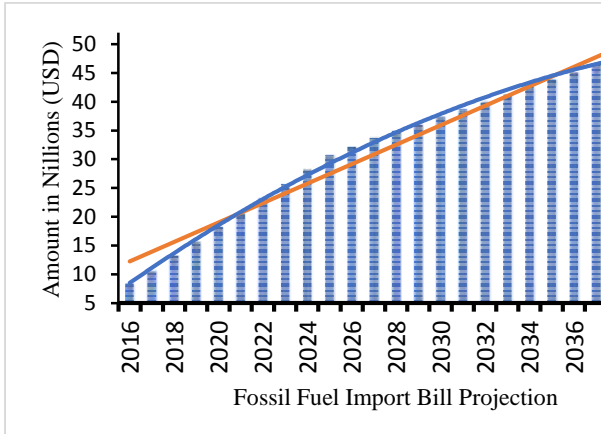


Figure 2: Projected Estimate of Reduction in Fuel Import Bill

Electricity Consumption at Idle Hours and Load on Grid

From the figure 3, it can be observed that during idle hours, a domestic home without EV utilizes peak energy 1.7KWh for 1 hours, while a house with EV utilizes approximately 2KWh for approximately 4 hours.

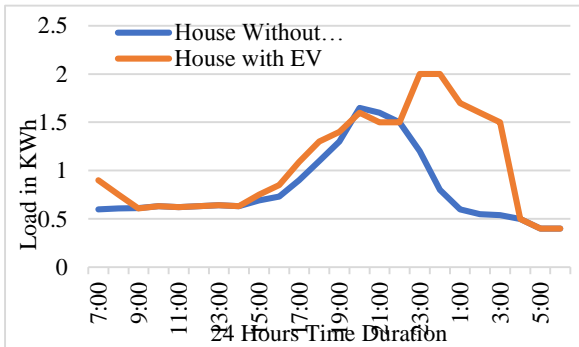


Figure 3: Estimated Utilizing of Idle Electricity comparison

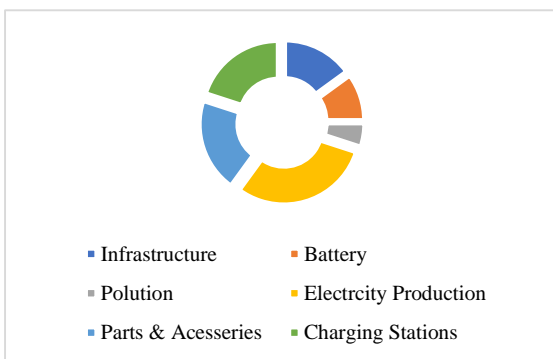


Figure 4: Potential Sectors that could be uplifted with EVs

There are many sectors in country that can potentially get a boom with the launch of EVs in country. Figure 4 depicts some major one of these industries that can be benefitted with EVs.

Potential decrease in Carbon Emission due to EVs

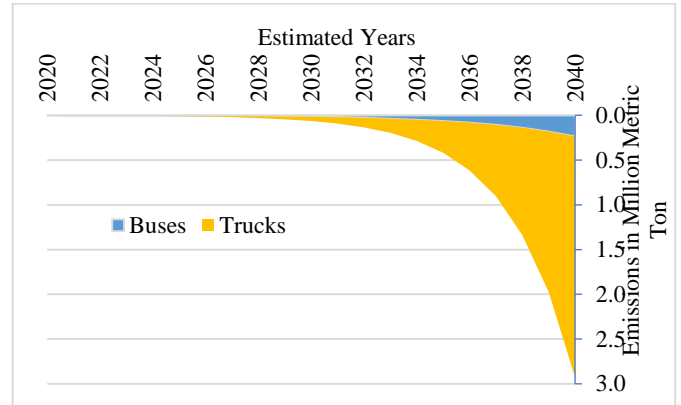


Figure 5: CO₂ Emissions Reduction by Electric Buses & Trucks

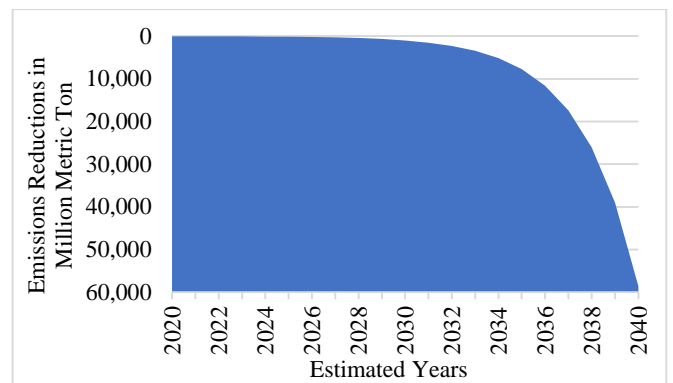


Figure 6: Reduction in Carbon Emissions due to 2/3 Wheelers

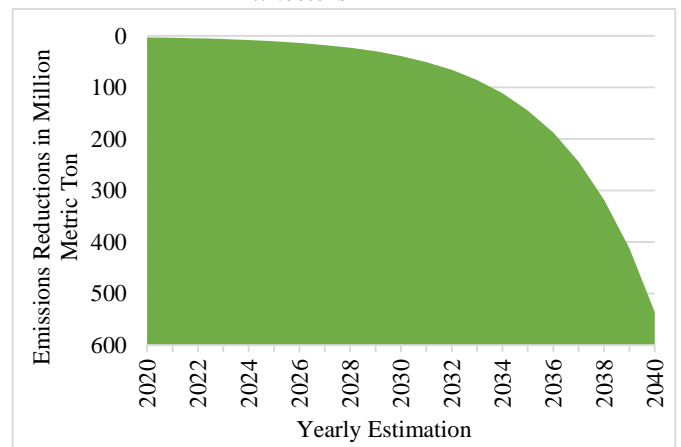


Figure 7: Reduction in Carbon Emissions due to E-Cars



Figure 5, 6 and 7 shows the decrease in pollutants of tail pipes of buses & truck, 2/3 wheelers and cars respectively. This data is based on Table 2 estimated projected penetration of vehicles for next 20 years with continuous increase per year. For the first 4 years the trends show less affective role, but once the vehicles will start replacing FFVs on large scale, the trend become prominent.

Finally, EVs can completely alter the whole automotive sector of country. The only need that left is a comprehensive policy for EVs that can seriously attract new ventures, existing manufacturers and general public towards utilizing the green clean energy. A policy initially oriented towards awareness and utilization of EVs with ease can bring long lasting effects. Once adapted the Government can modify the policy to make it more efficient for country and general public interests.

REFERENCES

- [1]. Tulman, S. *How to Stay Relevant in Today's Fast-Paced Digital World*. [Website] 2015 January 22, 2015 [cited 2019 November 22, 2019]; 1:[1]. Available from: <https://www.business2community.com/business-innovation/stay-relevant-todays-fast-paced-digital-world-01133550>.
- [2]. Thomas, C.D., et al., *Extinction risk from climate change*. Nature, 2004. **427**(6970): p. 145.
- [3]. Myles Allen (UK), M.B.S., et. al., *Global Warming of 1.5°C*. 2018, Intergovernmental Panel on Climate Change: Intergovernmental Panel on Climate Change. p. 24.
- [4]. Kiani, K. *New transport policy for sustainable mobility*. [Website] 2018 [cited 2019 Nvember 24]; Available from: <https://www.dawn.com/news/1414708>.
- [5]. Kintner-Meyer, M., K. Schneider, and R.J.P.N.N.L. Pratt, *Impacts assessment of plug-in hybrid vehicles on electric utilities and regional US power grids, Part 1: Technical analysis*. 2007. **1**.
- [6]. Pakistan, N.H.A., *Infrastrucutre Development for Transportation*. 2019, National Highways Authority, Pakistan: <http://nha.gov.pk/en>. p. 1.
- [7]. Reuters, T. *Will electric vehicles really create a cleaner planet?* 2018 [cited 2019 November 25]; Available from: <https://www.thomsonreuters.com/en/reports/electric-vehicles.html>.
- [8]. Arshad, N., *EV Report Pakistan by LUMS*. 2019, Lahore University of Management Sciences p. 70.
- [9]. HUSSAIN, S., *Sector Profile Automotive and Auto-parts manufacturing*. 2019, Investment Board Pakistan: <https://invest.gov.pk/automobiles>. p. 26.
- [10]. Hamilton, K. and S. Akbar, *Assessing the environmental co-benefits of climate change actions*. 2010, World Bank.
- [11]. Agency, I.E., *Global EV Outlook 2019*. 2019, IEA: International Energy Agency.
- [12]. Wu, Y. and L. Zhang, *Can the development of electric vehicles reduce the emission of air pollutants and greenhouse gases in developing countries?* Transportation Research Part D: Transport and Environment, 2017. **51**: p. 129-145.
- [13]. Association, P.A.M., *Automotive Productions Statistics*. 2018, PAMA: PAMA Online Portal. p. 4.
- [14]. 14. Ashby, M.F., *Chapter 10 - Case Study: Electric Cars*, in *Materials and Sustainable Development*, M.F. Ashby, Editor. 2016, Butterworth-Heinemann: Boston. p. 151-166.
- [15]. Tang, Y., et al., *Economic Analysis on Repurposed EV batteries in a Distributed PV System under Sharing Business Models*. Energy Procedia, 2019. **158**: p. 4304-4310.
- [16]. Van Donkelaar, A., et al., *Global estimates of ambient fine particulate matter concentrations from satellite-based aerosol optical depth: development and application*. 2010. **118**(6): p. 847-855.
- [17]. Ke, B.-R., C.-Y. Chung, and Y.-C. Chen, *Minimizing the costs of constructing an all plug-in electric bus transportation system: A case study in Penghu*. Applied Energy, 2016. **177**: p. 649-660.
- [18]. Van de Graaf, T., *Obsolete or resurgent? The International Energy Agency in a changing global landscape*. Energy Policy, 2012. **48**: p. 233-241.
- [19]. Shaukat, N., et al., *A survey on electric vehicle transportation within smart grid system*. Renewable and Sustainable Energy Reviews, 2018. **81**: p. 1329-1349.
- [20]. Szinai, J.K., et al., *Reduced grid operating costs and renewable energy curtailment with electric vehicle charge management*. Energy Policy, 2019: p. 111051.
- [21]. *\$52.5 bn electric vehicle (car) polymers market - global forecast to 2024*. Focus on Catalysts, 2019. **2019**(9): p. 2.
- [22]. Ehrenberger, S.I., et al., *An international dialogue about electric vehicle deployment to bring energy and greenhouse gas benefits through 2030 on a well-to-wheels basis*. Transportation Research Part



- D: Transport and Environment, 2019. **74**: p. 245-254.
- [23]. Noori, M. and O. Tatari, *Development of an agent-based model for regional market penetration projections of electric vehicles in the United States*. Energy, 2016. **96**: p. 215-230.
- [24]. Glitman, K., D. Farnsworth, and J. Hildermeier, *The role of electric vehicles in a decarbonized economy: Supporting a reliable, affordable and efficient electric system*. The Electricity Journal, 2019. **32**(7): p. 106623.
- [25]. Babones, S. *China Could Be The World's First All Electric Vehicle Ecosystem*. 2018 [cited 1; Available from: <https://www.forbes.com/sites/salvatorebabones/2018/03/06/china-could-be-the-worlds-first-all-electric-vehicle-ecosystem/>].
- [26]. Siddique, A., *DEVELOPING THE PAK-CHINA ECONOMIC CORRIDOR TO FACILITATES INO - EUROPE TRADE*. 2017, All Pakistan Shipping Association: All Pakistan Shipping Association. p. 15.



Analysis of Overall Equipment Effectiveness by Implementing TPM Strategy and Equipment Reliability Approach

Muhammad Faisal¹, Tauseef Aized², Syed Muhammad Sohail Rehman³
Department of Mechanical Engineering, University of Engineering and Technology Lahore

Corresponding author: tauseef.aized@uet.edu.pk

Abstract:

This research study focuses the implementation of Total Productive Maintenance in a production line of a ready-made garments (RMG) industry with the purpose of improving Overall equipment effectiveness of machines by reducing machine downtime losses and increasing the productivity. This study is carried out by following a comprehensive process flow and detailed data studies of equipment breakdown time. The methodology comprises of firstly mapping the existing situation of machines OEE by analyzing the current data to identify the critical machine, significant loss groups and the reason of that losses. Secondly to develop the process for applying analytical approach and TPM pillars for improving the OEE of critical machine and to reduce the significant production losses. This study is useful for both the manufacturing and academic perspective for making the analysis and improvement of equipment effectiveness. The tools used in this study are cause & effect diagram, Pareto chart and WWBLA and TPM pillars of autonomous maintenance and 5S. TPM implementation with the aim of changing organizational culture of maintenance policy by effective involvement of all the employees towards making improvement can bring the remarkable increase in system efficiency and productivity. After implementing the improvement policies and countermeasures obtained from the set of techniques, the Overall Equipment Effectiveness of the critical machine increased from 48% to 63% and the overall line effectiveness is increased from 62% to 73%. Also the equipment downtime losses were reduced by 22% as compared to previous breakdown losses while increasing the production of extra 67 pieces per day. The improved results of Overall Equipment Effectiveness after TPM implementation are capable enough to extend the TPM approach in other production lines.

Keywords: Total Productive Maintenance, Overall Equipment Effectiveness, Productivity, Autonomous Maintenance, Why-Why-Because Logical Analysis WWBLA

1. Introduction

Manufacturing industries in developed countries are more focused towards the product quality while maintaining the equipment efficiency, less breakdowns and reliability at same time [1]. Overall Equipment Effectiveness (OEE) performs a vital role for retaining production quality at higher equipment efficiency [2]. OEE is a method to control and monitor the process efficiency. It was developed in 1990 and accepted as management tool for better control over plant production facility [3]. The measuring parameters which effect in OEE calculation are Availability, Performance Efficiency and Quality Rating. These factors provide the equipment efficiency and assess the key production losses in manufacturing process [4]. The Overall

Equipment Effectiveness addresses six big downtime losses including breakdowns, setup and adjustments, idling & minor stoppages, reduced speed, process defects and reduced yield. These six big losses fall under the three parameters of OEE. The availability level is concerned with breakdown & setup losses when equipment is unable to run for production, performance efficiency are concerned with idling & minor stoppages and reduced speed when equipment is not running and quality parameter is concerned with product quality defects and rework and reduced yield losses [5]. The need of the time is to maximize the availability of production facilities. TPM is a distinctive Japanese approach which has developed for achieving the productive and reliable maintenance concepts. It was firstly developed by M/s Nippon Denso Co. which was a supplier of Toyota Motor Company, Japan in 1971. It works to gain the higher equipment effectiveness, reduced breakdowns [6, 7].



TPM use overall equipment effectiveness as a quantitative tool for assessing the production system performance. The success of TPM implementation system is measured by OEE matrix [8]. The OEE tool is broadly acknowledged as a quantitative tool for assessing the production system efficiency, productivity and quality [9]. The analyses of overall equipment effectiveness by the use of TPM pillars is done by different researchers in past. A lot of effectiveness methodologies were developed but the initial and most useful method was developed by *Nakajima* [7] in 1988 and mentioned TPM implementation as a core objective to enhance the machine efficiency. *Samat et. al.* [10] developed an equipment performance and reliability model for analysis of equipment performance and maintenance efficiency. This model is integrated with overall equipment effectiveness for assessing the machine efficiency based on maintenance performance. *Chong et. al.* [11] carried out the construction of maintenance Failure mode and effect analysis in order to enhance the OEE. This maintenance FMEA is based on structure analysis, function analysis, failure analysis, measure analysis and optimization phase. All the equipment potential failure and downtimes are studied under this maintenance FMEA to find and resolve the bottleneck equipment as a result. *Almeanazel* [12] carried out the studies on implementing TPM practices and focused the OEE by considering the six big losses related to quality, availability and speed. The results showed that the implementation of TPM practices eliminated the major waste, downtime losses.

Batumalay et. al. [13] investigates the implementation of OEE by checking the influence of principal TPM pillars, theoretical framework is devised and survey based analyses is done through SPSS statistical software. The results show that the TPM pillars of planned maintenance, quality maintenance and training & education of employees gives the substantial amount of benefits to attain the better OEE collectively. *Domingo et al.* [14] devised overall equipment effectiveness metric to address the lean and green manufacturing environment to work as a problem solving method. This study targets to major problems regarding OEE in lean and green manufacturing environment. A new parameter of environment is integrated with OEE to make it overall equipment environment effectiveness which

defines its compatibility with lean and green manufacturing. *Francesco et. al.* [15] presented the central limit theorem to analyze the stochastic nature of OEE. An approximated procedure is used in which OEE is considered as a stochastic random variable and its probability density function is created by making the combination (PDF) function and basic causes of waste. Since the OEE is used only as the deterministic tool and only provides static value of the process and not covering the real changeability in real time scenario. *Albert et. al.* [16] assessed that OEE is a basic requirement and fulfilling criteria for achieving improvement through TPM strategy. *Nakajima* [7] defined that OEE required standards are 90 percent of machine availability, 95 percent performance efficiency and 99 percent quality rating. An overall 85 percent of OEE value is acknowledged as a world-class performance standard. *Chong et. al.* [17] in another study analyzed the link between OEE and equipment throughput which result the strong positive linear relationship between OEE index and production throughput. So it can be easily identified that by knowing the throughput, the costs of production part can be calculated. *Huang et al.* [18] concluded that the OEE is widely accepted approach to enhance the productivity because it allows the analysis of root causes of production system and also provides the effective solutions. *Thun et. al.* [19] investigated the dynamic effects of TPM pillars by inter-relating the various aspects of manufacturing conditions and developed the fundamental approach to provide the most relevant and adaptive strategy between the relationship of different pillars of TPM. *Ahuja et. al.* [20] have analyzed the influence of TPM strategies for significant improvement in manufacturing system by involving the success factors of management leaderships, traditional maintenance techniques and developed the holistic approach of TPM initiatives that have direct implications for improving manufacturing performances in the Indian Industry.

a. TPM and its Pillars

TPM is an organized systematic approach which is based on 5S to achieve a complete housekeeping environment at the workplace. The 5S practices require strong commitment by the employees of that

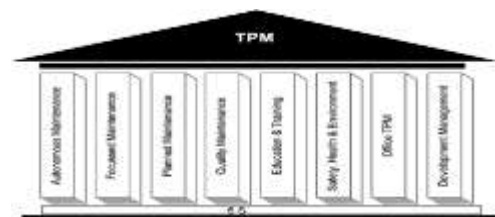


Figure 1 TPM Pillars



organization to maintain a clean, organized, standardized and disciplined workplace premises. These actions help the team to highlight the problems at first stage and then to identify the solution of these problems. 5S acts as a foundation before TPM implementation.

5S is a state of workplace environment which use the five Japanese words i.e. *seiri, seiton, seiso, seiketsu, and shitsuke* which means sort, set in order, shine, standardize and sustained. Ahmed, Ireland et. al. [21, 22]

TPM is considered as driving force and plays a vital role towards making improvement in the manufacturing organizations. Manufacturing at higher efficiency, quality and productivity with reduced costs is considered as the basic indicator of that organization performance [23]. The initiatives of TPM were endorsed and suggested by Japan Institute of Plant Maintenance (JIPM) which covers the eight pillared methodology to make plant improvement by resulting the significant enhancement in terms of labor and equipment productivity and reducing the plant maintenance costs, downtimes, losses and wastages. The essential TPM elements are comprised of eight pillars that include 5S as a base, autonomous maintenance; focused maintenance; planned maintenance; quality maintenance; education and training; office TPM; development management; and safety, health and environment [24].

b. Overall Equipment Effectiveness

Overall equipment effectiveness is a basic indicator to analyze that how effective the machine or equipment is working under the given manufacturing conditions. TPM aims to enhance the equipment effectiveness. OEE is a quantitative measure of analyzing the implementation of TPM strategies. The quantitative value of OEE is the product of equipment availability, performance efficiency and quality rate of products. The driving concept of OEE is to have a 'zero-waste' in the manufacturing system. Ljungberg et. al. [25]

The quantitative value of OEE can be calculated as below:

$$\begin{aligned}
 OEE & \quad (1) \\
 &= \text{Availability } (A) \\
 &\times \text{Performance Efficiency } (P) \\
 &\times \text{Quality Rate } (Q)
 \end{aligned}$$

Where, the three parameters can be evaluated mathematically through the following equations:

$$\begin{aligned}
 \text{Availability} \\
 &= \frac{\text{Actual Production Time } (T_{act})}{\text{Planned Production Time } (T_{plan})} \times 100 \quad (2)
 \end{aligned}$$

$$\begin{aligned}
 \text{Performance Efficiency} \quad (3) \\
 &= \frac{\text{Net Production Time } (T_{net})}{\text{Actual Production Time } (T_{act})} \times 100
 \end{aligned}$$

$$\begin{aligned}
 \text{Net Production Time } (T_{net}) \quad (4) \\
 &= T_c \times \alpha(\text{Actual Output})
 \end{aligned}$$

$$\begin{aligned}
 \text{Quality Rate} &= \frac{\text{Actual Output} - \text{Rejection}}{\text{Actual Output}} \quad (5) \\
 &\times 100
 \end{aligned}$$

OEE provides a systematic approach to maintain the production targets by implementing the practical management and technical rules in order to achieve optimized manufacturing results by maximizing the equipment availability, performance efficiency and quality rate.

2. Problem Statement

This study is conducted at a production line of garments manufacturing industry. The finishing operations of round neck T-shirts are being done at this line. This line contains three machines namely flat Lock (F/L), Single Needle Lock Stitch (SNLS) and Over-lock (O/L) machine. It is observed that the huge downtime losses, wide range of defects and hence less productivity and effectiveness of this line. Since last three to four months repetitive machine breakdowns and unwanted waiting time is causing to reduce the productivity and equipment effectiveness. The major causes of high machine downtimes need to be identified on priority that's why it was decided to form a task force to analyze the root causes of machine down time that lead to lower the equipment effectiveness.

3. Methodology

This study monitors the factors affecting on equipment effectiveness and performance of overall machine line by implementing the TPM strategy and

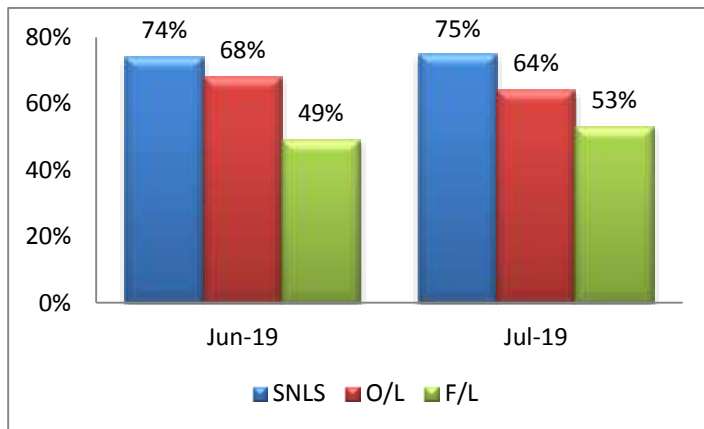


WWBLA analytical approach for reducing the losses. The detailed process include

- 1- Primary data collection of machines downtime and evaluation of OEE based on existing situation.
- 2- Identifying the bottleneck machine which has reduced OEE and causing higher breakdown losses.
- 3- Prioritizing the significant losses and their reasons by statistical tools.
- 4- TPM pillars implementation
- 5- Validation of results by collecting the data after improvement.

a. Data Collection

In the first step frequently occurring losses were identified by studying machine history data of the manufacturing plant. Hence the entire focus was to determine the overall machine breakdown and production downtime due to various machine maintenance or runtime problems, that is why total breakdown time of each machine was calculated for the selected period of time. Total breakdown was calculated and the average is taken to understand a general behavior of machine breakdown. Machine downtime for 20 days during the production runs was collected. The collected data clearly depicts that the breakdown time for the flat lock machine is higher as compare to other two machines in the same line. Furthermore, by reviewing and analyzing the previous two months data of individual machine OEE



Single Needle Lock Stitch M/C---- 688 minutes
Over-lock Machine ----898 minutes
Flat Lock Machine ---1952 minutes
Total Downtime --3538 minutes

The above data is collected during the general shift timings of 570 minutes from 8:30 AM to 6:00 PM including the breaks (planned downtime) of 90 minutes.

b. Critical Machine Identification and Initial OEE Calculation

Historical data of the manufacturing line showed that OEE value of flat lock machine was very low since last two months compared to general manufacturing scenario. Therefore compiled reports of each machine downtime and OEE for the last two months was also studied and compared with current month collected data. This is shown in fig-2 bar charts respectively. It was observed that the breakdown time of flat lock machine was very high and OEE value was very low as compared to other two machines. Therefore the F/L machine was considered as a critical machine to undertake for analysis and TPM implementation to gain the better OEE value of overall process. In M/C downtime comparison as per the total breakdown time of each machine 11292 minutes breakdown is occurred collectively which comprises almost 20 days of production based on the general shift timings

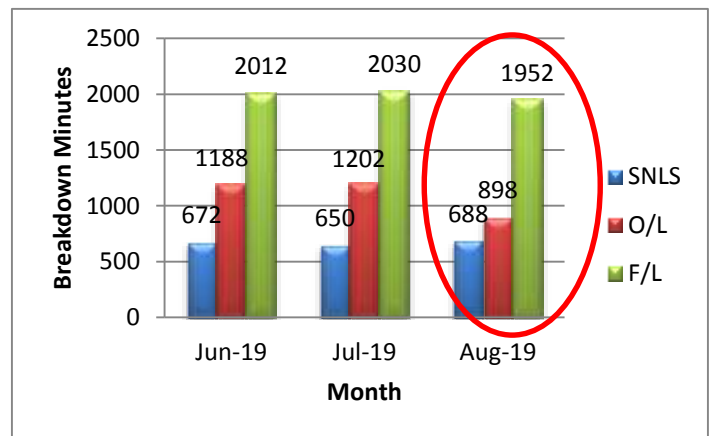


Figure 2 M/c downtime data and OEE comparison

and breakdown time, the flat lock sections were the major cause of less OEE and higher breakdown time. As per the collected data for the period of 20 days of Aug-19, each machine average downtime in minutes is as follows:

of 570 minutes per day. But the highest downtime loss at flat lock machine and individual calculation of losses for this machine is as follows:



Production Loss: It can be seen that the total of 5994 minutes loss was occurred at flat lock sections during the period of three months interval which contains $5994/570 =$ almost 11 days of production based on the general shift timings of 570 minutes per day.

Time Loss: The cycle time for to complete the operation of a single piece at flat lock machine is 1.90 minutes so the loss of 5994 minutes production for the period of three months means: $5994/1.90 =$ 3155 parts.

So it indicates that 3155 extra pieces can be produced if the machine was working without any kind of breakdowns. In *fig-3* the Pareto chart of machine breakdown is constructed. The 80% cumulative machine breakdown occurs in flat lock and over-lock machine. Out of this 80.6% the major portion of 55.2% of overall process breakdown is occurring in the flat lock machine. So it is also clear that from this Pareto analysis that the flat lock machine problems are the vital few of the overall downtime which carrying the major proportion for losses. In *table-1* data is accumulated and the overall equipment effectiveness of the individual machine is calculated based on the collected data for the month of Aug-19. The data is arranged as per the sequence of calculating OEE parameters. The calculated value of OEE is the average value of 20 days on the basis of Aug-19 data. The planned downtime, shift time, output target and the standard cycle time cycle time of each machine is same for each day whereas machine downtime i.e. T_{updt} , actual output α and rejection β is taken as the average of collected data in table-1.

The data of actual output and rejection of the each machine which is taken as the average value of 20 days for the month of Aug-19. Equations 1 to 5 are

used for evaluating the OEE for each machine. As per the combined calculated data of OEE in *table-1* for each machine, it can be seen clearly that the OEE value of flat-lock is 48% which is very less from other two machines which have 65% and 74% value of OEE for Over-lock and SNLS respectively. Whereas the OEE value of the whole line is 62%. It also gives a clear indication that Flat lock machine is critical machine which reducing the OEE of overall process. Comparing these OEE values with world-class standard which states 85% OEE as a benchmark gives also a clear indication for making the improvement.

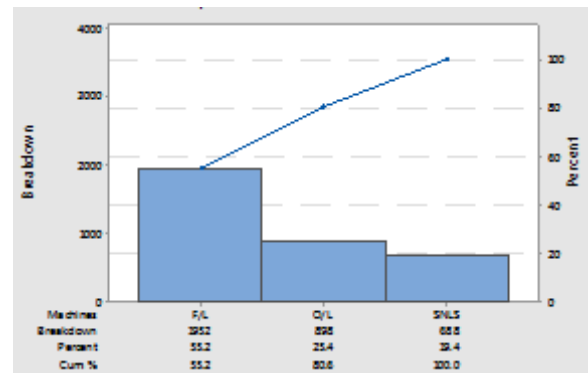


Figure 3 M/c downtime Pareto chart



Table 1 Initial OEE calculation

OEE for F/L Machine before TPM Implementation Aug-19			OEE for O/L Machine before TPM Implementation Aug-19			OEE for SNLS Machine before TPM Implementation Aug-19		
A	Shift Time (General)	570	A	Shift Time (General)	570	A	Shift Time (General)	570
B	Planned Downtime T_{pdt}	90	B	Planned Downtime T_{pdt}	90	B	Planned Downtime T_{pdt}	90
C	Running Time (A-B) T_{plan}	480	C	Running Time (A-B) T_{plan}	480	C	Running Time (A-B) T_{plan}	480
D	Running Time Losses T_{updt}	97.6	D	Running Time Losses T_{updt}	44.9	D	Running Time Losses T_{updt}	34.4
E	Operating Time (C-D) T_{act}	382.4	E	Operating Time (C-D) T_{act}	435.1	E	Operating Time (C-D) T_{act}	445.6
F	Availability $(E/C) \times 100$	79.67%	F	Availability $(E/C) \times 100$	90.65%	F	Availability $(E/C) \times 100$	92.83%
G	Cycle Time T_c	1.90	G	Cycle Time T_c	2.75	G	Cycle Time T_c	1.25
H	No. of M/C σ	1	H	No. of M/C σ	1	H	No. of M/C σ	1
I	Target/Capacity $(E \times H)/G$	201	I	Target/Capacity $(E \times H)/G$	158	I	Target/Capacity $(E \times H)/G$	356
J	Actual Output (α)	165	J	Actual Output (α)	132	J	Actual Output (α)	296
K	Net Production Time T_{net} $(G \times J)$	313.5	K	Net Production Time $T_{net} (G \times J)$	363	K	Net Production Time $T_{net} (G \times J)$	370
L	Performance $(K/E) \times 100$	81.98%	L	Performance $(K/E) \times 100$	83.43%	L	Performance $(K/E) \times 100$	83.03%
M	Rejection β	45	M	Rejection β	18	M	Rejection β	11
N	Quality $(J-M)/J \times 100$	72.73%	N	Quality $(J-M)/J \times 100$	86.36%	N	Quality $(J-M)/J \times 100$	96.28%
OEE	Availability \times Performance Efficiency \times Quality Rate	48%	OE E	Availability \times Performance Efficiency \times Quality Rate	65%	OE E	Availability \times Performance Efficiency \times Quality Rate	74%

c. Identification of Significant Losses and their Reasons

Based on the results of current data OEE, it is clear that machines are running below capacity due to various runtime losses. These losses need to identify on the basis of actual data with the reasons associated with these losses. For that purpose, machine downtime data of 10 days with the reasons of failure, loss category, and loss group was collected and categorized as per frequency of occurrence. The identified loss categories with loss groups are categorized (table-2)

and prioritized by using Pareto analysis in figure-4:

Table 2 M/c losses data (loss category and downtime)

Loss Group	Loss Category	Down Time (min)	Cumulative Percentage
Downtime Losses	Setup & Adjustment	1010	57%
	Equipment Failure	283	73%
Speed Losses	Idling & Minor Stoppages	260	88%
	Reduced Speed	84	93%
Losses due to defects	Defect Loss	74	97%
	Reduced Yield	54	100%
	Total	1765	

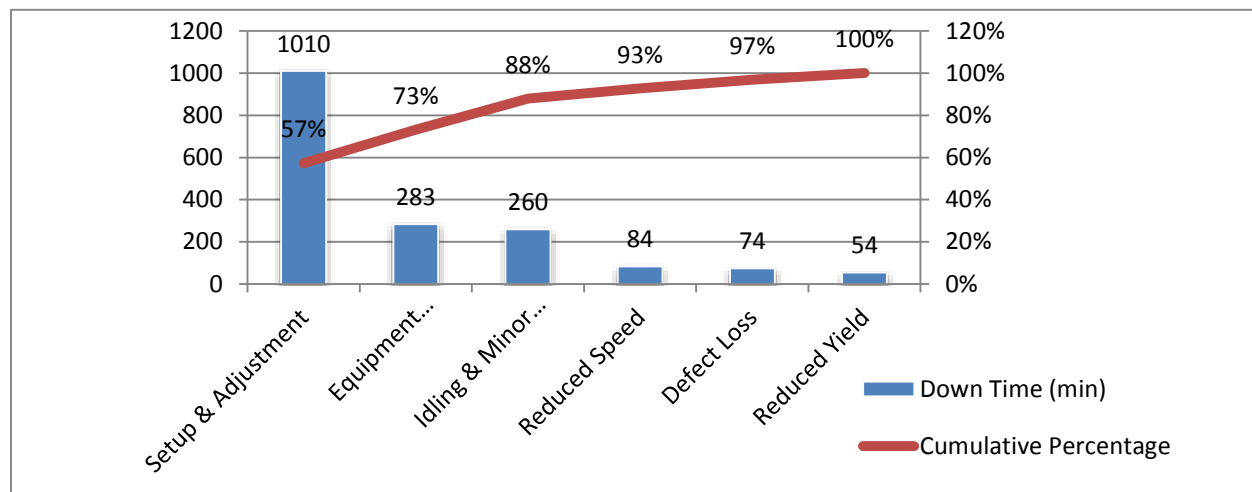


Figure 4 M/c losses Pareto chart (loss category wise)

Once the vital loss categories which contributing the major equipment downtime were identified and prioritized, Pareto analysis is done only for that reasons of machine downtime that are due to these prioritized loss categories which occupy the 88% of cumulative machine downtime highlighted in *table-2*. Pareto chart for vital few reasons is shown in *fig-5* which shows that 60% of the machine downtime is due to skip, open seam and broken stitch problem. These major reasons of higher machine downtime is from the Flat lock machine whose OEE value is also less. It also gives a clear indication that these major problems are the cause of low OEE of that machine. So these causes are identified as the major failure reasons which need to be addressed on priority basis.

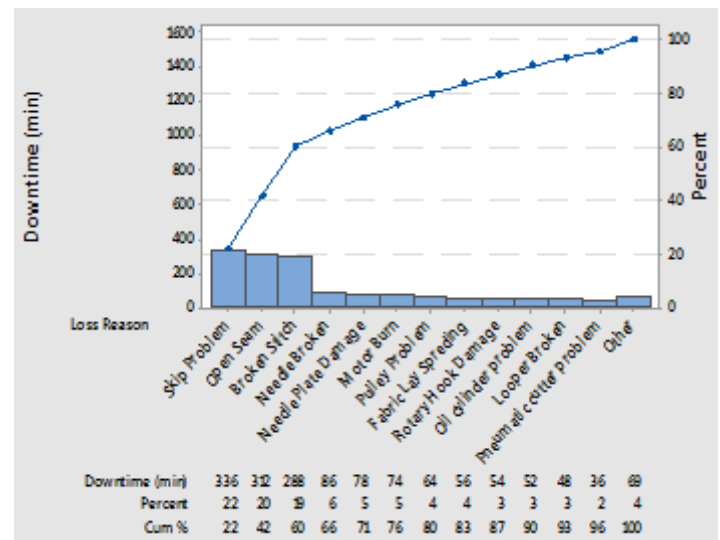


Figure 5 Pareto chart of major loss reasons

d. Cause & Effect Diagram of Critical Loss Group

The cause & effect diagram in *fig-6* shows the causes of the major loss category i.e. setup and adjustments failures. The given causes are the machine downtime loss reasons related to man, machine, material and methods. The problems related to material and methods shown in this diagram. As per the reasons related to improper method, the problem of absence of autonomous maintenance practice is observed. Whereas the problems related to machine causes i.e. skip, open seam and broken stitch are machine timing out, contact problem between the needle and looper and needle heat up due to uneven thread tension

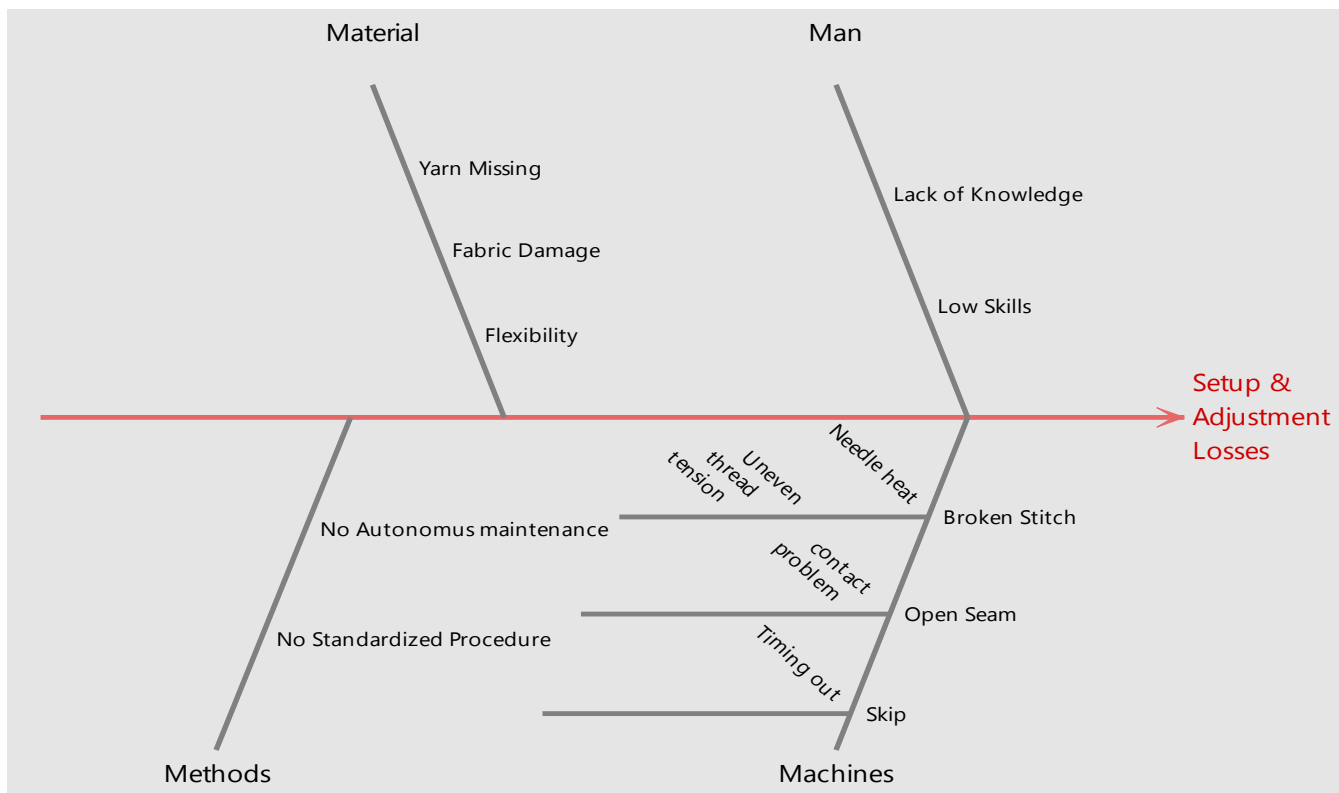


Figure 6 Cause & Effect diagram of significant loss

e. Improvement Policy

After finding and analyzing the reasons of critical downtime losses (highlighted in table-2) there was an immediate need of taking corrective action. That is why a systematic approach leading to enhance the OEE was developed by using analytical technique and TPM pillars. Formation of TPM team with the aim of increasing the system OEE and reducing breakdown was done at first stage. The team was comprised of production floor operators, supervisors and managers. Its motive was to introduce the TPM practices and activities in the selected production line at first step then to implement it across the production facilities throughout the company. The necessary education and training about TPM importance and significance of 5S for the operators and workers was done at first.

i. Losses Reduction by using Analytical Approach (WWBLA)

As stated above, we have selected the first three reasons of major loss groups data from table-2. These

causes are inhabiting 60% of total losses from major loss groups in the overall machine line.

The table-3 consists of the selected loss causes along with the M/C incurring these problems, cumulative percentages of these loss causes loss group and category in which these causes fall as per collected data.

Table 3 Selected reasons of major loss groups

Loss Group	Loss Category	M/C	Major Causes	Freq uency	Downt ime (min)	Cumul ative Percen tage
Downti me Losses	Setup & Adjust ment	F/L	Skip	43	336	22%
			Open Seam	34	312	42%
			Broken Stitch	29	288	60%



Table 4 Why-Why Because Logical Analysis
(WWBLA) worksheet

WWBLA Work Sheet for Setup & Adjustments Problems							
Problem	1st Factor for Problem	Verification	2nd Factor for Problem	Verification	3rd Factor for the Problem	Verification	Countermeasures
Skipping	1. Needle Timing out	G	1.1 Needle & Loper are not contact at same time	G	1.1.1 Needle Stitch Missed	NG	1.1.1 Needle Position Should be adjusted properly
	2. Loper Timing is Out	G	2.1 Needle & Loper are not contact at same time	NG			2.1 Loper Timing is Adjusted
Broken Stitch	1. High Thread Tension	G	1.1 Friction Generated in Thread	G	1.1.1 Heat produced in thread	NG	1.1 Silicon Lubricant should be used
	2. Needle Heat Up	G	2.2 High tension between thread and needle	NG			2.2 Thread Guide should be adjusted
Open Seam	1. Improper Fabric Handling	G	1.1 Uneven width of stitch produced	G	1.1.1 Open Seam produced	NG	1.1.1 Operator Training is required
	2. Fabric Slips from boat	G	2.1 Improper M/c boat used	NG			2.1 Proper Machine Boat is required
	3. Excess Vibration in machine	G	3.1 Fabric displaced from actual position	G	3.1.1 Open Seam produced	NG	3.1.1 Machine Placement or Maintenance is required

Here we have used WWBLA analysis to logically analyze the selected reasons of machine downtime with the aim to minimize these losses and to increase the OEE of related machines. WWBLA is an analytical approach used in TPM to systematically identify, analyze and reduce the losses. In this technique, a worksheet is used on which individual major problem of loss is considered separately on a sheet and a cause is identified for that problem which is called as *first factor*. Then verification of that identified factor to check whether its break down it into further root causes is possible or not. If it is possible then it is assigned with the alphabetical letter 'G' which stands for 'Go further'. Then further root cause is identified till all possible cause in which the main problem can be divided. When the final cause of the main problem is identified, it is assigned with the letters 'NG' which means not go further. The undertaken problem is mentioned on very left column of the sheet and the countermeasure of the each problem is on the very right column of the sheet. Between these columns, factors from first to last are written.

In *table-4* WWBLA worksheet is given for the main problems which are under the setup and adjustments category of equipment downtime losses. The main loss reasons under this category are skip, open seam and broken stitch which carry a cumulative loss percentage of 60%.

ii. *TPM Implementation and Remedial Actions*

The implementation of the countermeasures obtained from WWBLA analysis against each root cause was done by using the TPM pillars. As the major root causes reason is the operator skills issue and lack of routine maintenance operations. From the factors affecting due to the problems of skip, broken and open seam, many of those have the countermeasure of minor adjustments which are the part of autonomous maintenance. For that purpose, comprehensive training session for operators was arranged by the effective involvement of maintenance staff, production floor supervisors and top management to give them hands-on practice and



guidance for minor machine parts adjustments. For that purpose a tentative template for autonomous maintenance standards and activities was also implemented on the machines. Furthermore, arrangement of daily preventive maintenance schedule with the aim of proactive approach to reduce the maintenance time and cost during

production runs was adopted as an improvement strategy. Implementation of 5S practices of cleaning and shining checklists for each machine to avoid machine abnormalities was also implemented.

f. OEE Calculations after Adopting Remedial Actions

A substantial reduce in equipment downtime losses and increase in actual output was observed and noted after implementing the improvement policies i.e. countermeasures of WWBLA analysis, TPM pillars and preventive maintenance schedules. Detailed data of equipment downtime, actual production and rejection was collected after the remedial actions in next month Sep-19 for the 20-days production runs. Before that in the previous month data (Aug-19), maximum machines unplanned stoppage was 3538 minutes in 20 days. Now it was reduced to 2740 minutes in 20 days (Sep-19). Previously maximum rejected count was 1480 pieces in 20 days production but now it decreased to 1120 pieces. The actual output was also increased to 13200 pieces from 11860 in 20-days production. That means an extra 67 pieces per day production of 570 minutes shift was producing from this line. Whereas the increase in OEE value of critical machine i.e. F/L is 63% from 48%. The whole line OEE value is also improved from 62% to 73%. The final OEE for individual machine is calculated on the basis of improved data.

g. Comparison between Initial OEE and Final OEE

The comparison between initial and final OEE values of the individual machine and whole line is shown below in table-5:

Table 5 Initial & Final OEE Comparison

M/C	Initial OEE				Final OEE			
	A %	PE %	Q %	OE %	A %	PE %	Q %	OE %
F/L	79.7%	82.0%	72.7%	48%	84.38%	89.14%	83.68%	63%
O/L	90.7%	83.4%	86.4%	65%	92.7%	89.6%	89.7%	74%
SNLS	92.8%	83.0%	96.3%	74%	94.4%	89.7%	96.9%	82%
M/C Line OEE %	87.7%	82.8%	85.1%	62%	90.5%	89.5%	90.1%	73%

4. Results & Discussion

Implementing TPM techniques and approach as an improvement methodology brought the drastic change through improved results of equipment availability, efficiency and quality which can be seen in fig-7. The OEE value also gives the indication that how effective the equipment is being utilized to gain the higher productivity and reduced losses. After applying the improvement methodologies the OEE of critical machine and overall machine line is improved which can be seen

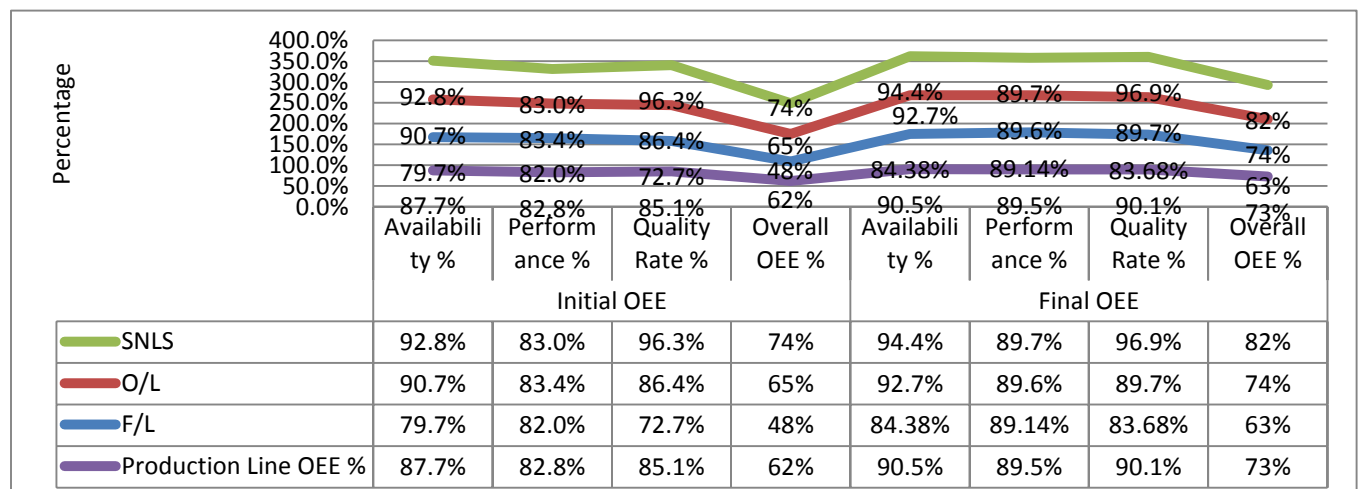


Figure 7 Line chart comparison of OEE parameters



Table 6 Production Line KPI comparison (based on 20-days production data)

KPI	Units	Before	After	% Improvement
M/c Unplanned Stoppages	Minute	3538	2740	-23%
Actual Output	Piece	11860	13200	11%
Rejection Count	Piece	1480	1120	-24%
Line OEE	Percentage	62%	73%	18%

through the results in *fig-7*. Not only the OEE is increased but the other production line KPIs also improved shown in *table-6*. The improvement policies of this study has more focus towards continuous improvement, standardizing the method and procedures, training of employees, and preventive plans for maintenance to avoid sudden breakdown.

5. Conclusion

A ready-made garments (RMG) industry is studied and analyzed for the implementation of TPM practices and techniques. Total productive maintenance techniques have the progressive impact of improving the equipment effectiveness in terms of reducing the breakdown losses and increasing the availability, performance and quality of products. By integrating all the equipment maintenance activities with total productive maintenance pillars, we can obtain the increased equipment effectiveness and productivity at reduced costs. Implementation of TPM activities like preventive maintenance schedule, 5S and autonomous maintenance provided the enhanced results of equipment effectiveness in this study. The autonomous maintenance activities involve the operators in routine maintenance activities to enhance their skills along-with maintenance department. Its purpose is to making the operator capable enough to resolve the minor issue of the machine so that to reduce the equipment downtime. Thus this study ends with the result that the TPM activities can bring tremendous results for improving the equipment effectiveness if applied completely in a true sense with the effective involvement of all the employees from top to bottom. In a nutshell, many further improvements can be achieved by using TPM techniques with its proper implementation, trainings and educating the employees to learn them its benefits for making continuous improvement.

REFERENCES

- [1] Becker, Juan M. Jauregui, Jesper Borst, and Abele van der Veen. "Improving the overall equipment effectiveness in high-mix-low-volume manufacturing environments." *CIRP Annals* 64, no. 1 (2015): 419-422.
- [2] Hegde, Harsha G., N. S. Mahesh, and Kishan Doss. "Overall Equipment Effectiveness Improvement by TPM and 5S Techniques in a CNC machine shop." *SaSTech* 8 (2009): 25-32.
- [3] Patel, Chetan & Deshpande, Vivek. (2016). A Review on Improvement in Overall Equipment Effectiveness. *International Journal for Research in Applied Science & Engineering Technology*. 4. 642-650
- [4] Sisodiya, P. S., M. Patel, and V. Bansod. "A literature review on overall equipment effectiveness." *International journal of research in aeronautical and mechanical engineering* 2, no. 2 (2014): 35-42.
- [5] Agustyadi, Tina Kanti, and Elizabeth A. Cudney. *Total Productive Maintenance: Strategies and Implementation Guide*. CRC Press, 2016
- [6] Bhadury, Bikas. "Management of productivity through TPM." *Productivity* 41, no. 2 (2000): 240-51
- [7] Nakajima, Seiichi. *TPM Development Program: Implementing Total Productive Maintenance*. Preventative Maintenance Series. Productivity press, 1989.
- [8] K-Y.Jeong, and D.T.Phillips, "Operational efficiency and effectiveness measurement", *International Journal of Operations & Production Management*, Vol. 21 No. 11, pp. 1404-16, 2001.
- [9] H.H.Samuel, P.D.John, J.Shi, and S.Qi, "Manufacturing system modeling for productivity improvement", *Journal of Manufacturing Systems*, Vol. 21 No. 4, pp. 249-60, 2002.
- [10] Abdul Samat, H., S. Kamaruddin, and I. Abdul Azid. "Integration of overall equipment effectiveness (OEE) and reliability method for measuring machine effectiveness." *South African Journal of Industrial Engineering* 23, no. 1 (2012): 92-113.
- [11] Chong, K. E., K. C. Ng, and Gerald Guan Gan Goh. "Improving Overall Equipment Effectiveness (OEE) through integration of Maintenance Failure Mode and Effect Analysis (maintenance-FMEA) in a semiconductor manufacturer: A case study." In 2015 *IEEE International Conference on Industrial Engineering and Engineering Management (IEEM)*, pp. 1427-1431. IEEE, 2015.
- [12] Almeanazel, Osama Taisir R. "Total productive maintenance review and overall equipment effectiveness measurement." *Jordan Journal of Mechanical and Industrial Engineering* 4, no. 4 (2010).
- [13] Batumalay, K., and A. S. Santhapparaj. "Overall Equipment Effectiveness (OEE) through Total



Productive Maintenance (TPM) practices—A study across the Malaysian industries." In 2009 International Conference for Technical Postgraduates (TECHPOS), pp. 1-5. IEEE, 2009.

[14] Domingo, Rosario, and Sergio Aguado. "Overall environmental equipment effectiveness as a metric of a lean and green manufacturing system." *Sustainability* 7, no. 7 (2015): 9031-9047.

[15] Francesco Zammori, Marcello Braglia, and M. Frosoline, "Stochastic overall equipment effectiveness," *International Journal of Production Research*, vol. 49, No. 21, pp. 6469-6490, November 2011.

[16] Albert H.C.Tsang & P.K.Chan, 2000 "TPM implementation in China: a case study", *International Journal of Quality & Reliability Management*, Vol 17 No.2, pp.144-157

[17] Chong, Kuan Eng, and Kam Choi Ng. "Relationship between overall equipment effectiveness, throughput and production part cost in semiconductor manufacturing industry." In 2016 IEEE International Conference on Industrial Engineering and Engineering Management (IEEM), pp. 75-79. IEEE, 2016.

[18] S. H. Huang, J. P. Dismukes, A. Mousalam, R. B. Razzak , and D. E. Robinson, "Manufacturing productivity improvement using effectiveness metrics and simulation analysis," *International Journal of Production Research*, vol. 41, pp. 513-527, 2003.

[19] Thun, Jörn-Henrick. "Maintaining preventive maintenance and maintenance prevention: analysing the dynamic implications of Total Productive Maintenance." *System Dynamics Review: The Journal of the System Dynamics Society* 22, no. 2 (2006): 163-179.

[20] Ahuja, I. P. S., and J. S. Khamba. "An evaluation of TPM initiatives in Indian industry for enhanced manufacturing performance." *International Journal of Quality & Reliability Management* 25, no. 2 (2008): 147-172.

[21] Ahmed, Shamsuddin, Masjuki Hj. Hassan, and Zahari Taha. "TPM can go beyond maintenance: excerpt from a case implementation." *Journal of Quality in Maintenance Engineering* 11, no. 1 (2005): 19-42.

[22] Ireland, Frank, and Barrie G. Dale. "A study of total productive maintenance implementation." *Journal of Quality in Maintenance Engineering* 7, no. 3 (2001): 183-192.

[23] Hayes, Robert H., and Steven C. Wheelwright. "Restoring our competitive edge: competing through manufacturing." (1984).

[24] Rodrigues, Marcelo, and Kazuo Hatakeyama. "Analysis of the fall of TPM in companies." *Journal of Materials Processing Technology* 179, no. 1-3 (2006): 276-279.

[25] Ljungberg, Örjan. "Measurement of overall equipment effectiveness as a basis for TPM activities." *International Journal of Operations & Production Management* 18, no. 5 (1998): 495-507.



Competitiveness Enhancement of SMEs by Integrating Lean and Corporate Social Responsibility (CSR) – A Case Study

Qasar Wasique Ahmad¹, Amjad Hussain¹, Amjad Mehmood¹, Muhammad Imran¹ and Fahad Noor²

1- Department of Industrial and Manufacturing Engineering, University of Engineering and Technology, Lahore, Pakistan

2- Department of Mechanical Engineering, University of Engineering and Technology, Lahore, Pakistan

*Corresponding Author: Q.W. Ahmad Email: waseek541@gmail.com

Abstract

Competitive enhancement of small and medium enterprises (SMEs) is possible by integrating lean and corporate social responsibility (CSR). Sustainable lean transformation and improvement in CSR compliance is generally a challenge due to lack of resources and employees' motivation in SMEs. This study proposes a 9-step methodology for SMEs to overcome the barriers to sustainable cultural change by enhancing stakeholders' participation and employing low cost interventions. The devised methodology is a participatory based cyclic approach for continuous improvement. Lessons learned from the implementation of this methodology serve as a guide for future use. A case study was conducted to validate this methodology using SA8000 as a guide for CSR compliance and different lean tools like TAKT time, assembly line balancing, Pareto analysis, root cause analysis, ECRS method to improve quality and productivity and organizational reputation. Key performance indicators (KPIs), to measure the intended competitive enhancement, were quantified at pre- and post-intervention stages. Low cost interventions suggested by stakeholder especially employees were implemented; and their effects were measured in terms of productivity, quality and CSR compliance improvement. Results of the case study show that these low-cost interventions reduced number of SA8000 non-conformances by 53%, defect rate by 60%. Further, 94%, 120% and 64% improvement were recorded in line balancing efficiency, value added time and average production per day respectively. It is concluded that low-cost interventions for lean implementation and CSR compliance improvement enhance organizational competitiveness of SMEs.

Key Words: Competitiveness; SMEs; Productivity; Quality; Lean Production; CSR

1. Introduction

In the modern era of globalization, each organization aspires to stay competitive but achieving this goal is a challenge. Small and medium enterprises (SMEs) are the backbone of economies as these provide 60% of the job opportunities globally [1]. So, many SMEs development initiatives has been witnessed worldwide because of their importance [2]. Economy of Pakistan is dependent on the performance of SMEs as these are contributing about 30% in GDP and 25% in the export revenue of Pakistan. SMEs are also employing 80% of Pakistan's non-agricultural labor and 25% of manufacturing value addition [3,4]. Leather sector of Pakistan is the second largest contributor to its export volume, but this sector experienced a negative growth of 6.83% during fiscal year 2017-18 and a growth of 0.97% in fiscal year 2018-19 mainly due to high production cost [5]. Among the products of leather sector, gloves have highest export value and most of the gloves manufacturing companies are SMEs [6]. Improving competitiveness of these SMEs can help this sector flourish.

Competitiveness can be defined as a group of five dimensions i.e. financial performance, quality, productivity, innovation and image of an organization [7]. SMEs have to improve their way of doing work, especially to reduce their cost of production because of competitive external environment [8]. SMEs can overcome this challenge by implementing systematic approaches to improve their performance like lean manufacturing, total quality management, and human resource management. Research literature shows that SMEs face several barriers to implementing these approaches like lack of top management commitment, disproportionate workload among workers, resistance to transform conventional business practices, lack of employees' participation and inadequate infrastructure [9]. Competitiveness of export-oriented organizations is also linked with their reputation and image in global market. This global image of an organization depends upon Corporate Social Responsibility (CSR) compliance as global customer is more aware of social and development related world issues [10-12]. The following



paragraphs discuss lean manufacturing and CSR in detail.

Lean manufacturing is a socio-technical system for improving organizational productivity and focuses on waste minimization and continuous improvement [9,13,14]. Implementation of appropriate blend of lean tools is found effective to enhance organizational productivity [15,16]. It is recommended that SMEs should focus on low cost interventions and should start their lean journey as a pilot project [17]. Commitment of top management and training of a team driving lean transformation is also essential so that result of the pilot project could be up-scaled to the organizational level [17-19].

Though the idea of CSR was put forward in 1950s [20] yet there is no consensus on its definition due to its wider scope [21,22]. However, its importance is well agreed and its compliance by an organization increases its sales globally as it improves organizational reputation and competitiveness [10,23,24]. Thus, CSR implementation not only contributes to social development but also assists in meeting the expectations of the stakeholders and society besides meeting the legal obligations [20,24,25]. Considering these benefits, all types of organizations are focusing on CSR [26]. SA8000 issued by Social Accountability International (SAI) is the most commonly used CSR standard. SA8000 standard certification not only improves working conditions and transparency among stakeholders but also improves reputation besides making supply chain better from CSR viewpoint [27,28].

It is evident from the above discussion that plethora of literature is available on lean manufacturing implementation as well as CSR compliance, but there is very little literature available on the combined implementation of lean manufacturing and CSR [12]. This study tries to fill this gap by developing an integrated methodology for implementing lean manufacturing and improving CSR compliance in SMEs. It will help them implementing and sustaining low cost interventions; hence enhancing their competitiveness.

2. Methodology

A nine-step methodology is devised for combined implementation of lean manufacturing and CSR. Proposed approach for implementation (Figure 1) is based on active participation of stakeholders especially top management and employees. Their involvement helps getting real time feedback throughout the process which enhances the sustainability of interventions. The process starts with problem identification by meetings with top management and employees as well as by studying available data from the organization. This identifies the possible areas for improvement process. Setting

the goals and key performance indicators (KPIs) provide the bases for assessment of existing work practices. This assessment against well-defined KPIs of lean and SA8000 audit provides diagnosis of current practices with reference to their feasibility in terms of ease of doing work, time and cost. Data collection against set KPIs of lean manufacturing and SA8000 and its analysis is done to measure the current performance of the system as well as its strengths and weaknesses. This provides a ground to develop intervention plans for encouraging good work practices and eradicating bad ones. Participation of stakeholders especially top management and employees is essential for this transformation process as results of data analysis are discussed with all these stakeholders at this stage and their participation is required in proposing potential interventions. Interventions plan is finalized in the light of these suggestions which develops ownership of employees which is essential for sustainable cultural change. The major strength of this methodology is involvement of all the stakeholders especially employees throughout the improvement process. Implementation of new initiatives is easier with higher employee involvement as it empowers the employees for learning and encourages them sharing innovative ideas [29-31]. Therefore, it is vital for problem-solving and bringing sustainable cultural change [32].

After finalizing the interventions plan, this plan is implemented. Data is collected at post-intervention stage against pre-defined KPIs of lean and SA8000 to measure the impact of interventions. Best practices and lessons learned are documented for future use. The cyclic process starts again with identification of

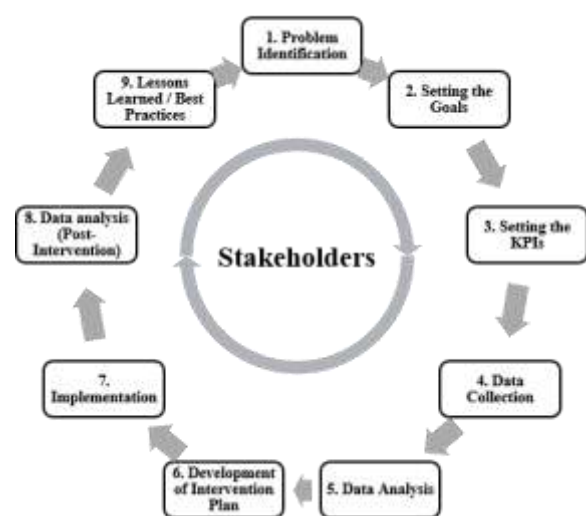


Figure 1 Framework for Integrated Lean Implementation and CSR Compliance Improvement



new problems and so on. Thus, following this integrated approach, better competitiveness can be achieved in terms of productivity, quality and CSR compliance.

3. Validation Case Study

To validate the proposed methodology of integrated implementation of lean manufacturing and CSR for SMEs, a case study was conducted in a leather gloves manufacturing organization having around 250 employees. The framework shown in figure 1 was followed for implementing lean manufacturing and CSR simultaneously. The case study was completed in one year. As discussed earlier, special attention was paid to the suggestions put forward by the employees as it increases the level of motivation of the employees and eases the process of sustainable cultural change. Below are the details and results of the case study.

3.1. Problem identification

As a first step, the researchers had a meeting with top management of the organization to share objectives

5. Increase in Average Production per Day
6. Improvement in CSR compliance per SA8000 criteria

3.3. Data Collection and Data Analysis

Existing work practices were measured against the set KPIs. CSR related practices were audited against SA8000 by certified auditors and total 38 non-conformances were identified (detailed results shown in table 1). Lean related practices were evaluated by using established lean tools e.g. time study, assembly line balancing, Pareto analyses and cause and effect diagram.

Gloves were being manufactured in three major steps: 1) Preparing Sub-Assembly 1; 2) Preparing Sub-Assembly 2 and 3) Joining Two Sub-Assemblies. Each step consisted of several activities. Time study was conducted to calculate the cycle time for every activity of the process and appropriate allowances were added to define standard time. This data was used to calculate line balancing efficiency. The values used to calculate line balancing are as

Table 1 SA8000 Audit Report at Pre-interventions stage (Number of Non-Conformances)

Sr. No.	Original Clause Requirement	Level of Non-conformance (Pre-Interventions)		
		Critical	Major	Minor
1	Laws and Regulations	0	0	1
2	Child Labor	0	0	1
3	Wages and Benefits	2	0	2
4	Hours of Work	1	1	0
5	Health and Safety	0	17	6
6	Freedom of Association and Collective Bargain	0	0	1
7	Environment	0	4	1
8	Monitoring and Compliance	0	1	0
Total		3	23	12

of the case study and constitute an interventions team responsible for the follow-up of the process. The interventions team consisted of people representing all departments and work groups of the organization. The interventions team identified problems by meetings with top management and employees. The team also analyzed available data from the different departments of the organization to identify problems. The major problems identified were related to productivity, quality and compliance to SA8000.

3.2. Setting the Goals and KPIs

The interventions team set the goals to improve productivity, quality and compliance to SA8000. The following KPIs were set to achieve the goals:

1. Reduction in Defect Rate
2. Improvement in Line Balancing Efficiency
3. Reduction in number of workers
4. Increase in Value Added Time

under:

- Start Time: 08:00 AM
- End Time: 05:00 PM
- Number of Breaks: 01
- Total Working hours per day: 08 hours
- Demand per Month: 6800 pieces
- Number of workers: 23

Figure 2 shows the line balancing graph for pre-intervention stage which clearly identifies bottleneck activities.

It was found from the previous data and observations that rework rate of gloves was 31% due to a number of causes. Pareto analysis was performed to investigate this issue and to identify major causes of defects (figure 3). Investigation found that two causes, 'broken stitches' and 'wrong position' were contributing 76% of total defects. So, these two causes were selected for further investigation. Root



Cause analysis revealed the following sub-causes of these major causes:

1. Unavailability of quality inspector
2. Not using OSM approach by Production supervisors
3. Helpers were not trained on use of trimming tools
4. Improper machine setting
5. Poor thread strength

KPIs set in Section 3.2 were measured and results are as under:

- Quality Defect Rate: 31%
- Line Balancing Efficiency: 34%
- Number of Workers: 23
- Value Added Time: 29%
- Average Production per Day: 47 Pairs
- Number of Non-conformances in SA8000: 38

3.4. Development of Interventions Plan

As Implementation framework is based on participatory approach, interventions team shared the findings with all the stakeholders. Stakeholders were requested to suggest low cost interventions which could be implemented by the SME. A Focus group discussion was conducted where representatives of all the stakeholders shared their ideas for improvement. Later these ideas were analyzed by a team of experts and the conclusion were shared with stakeholders so that they could learn about other ideas.

3.5. Implementation of Interventions Plan

To start with, SA8000 related low cost interventions were implemented e.g. training the workers about health, safety and ergonomic related issues, fixing guards on moving parts of the machines, floor markings, provision of Personal Protective

equipment and first aid box (pre- and post-intervention pictures are shown in figure 4).

Eliminate, Combine, Rearrange, Simplify (ECRS) method was used to improve the line balancing and reducing the number of workers form this assembly line. 23 activities were reduced to 15 and then further reduced to 9 activities. Improved results are shown in figure 5.

To improve quality, root causes identified through root cause analysis were eliminated by using proper countermeasures. Root causes and their corresponding countermeasures are shown in table 2.

3.6. Post-Interventions Assessment of KPIs and Lessons Learned

Post-intervention assessment was performed to measure effectiveness of interventions. KPIs set and measured at pre-interventions stage were measured again to see if there is some improvement and considerable improvement was found against all KPIs (table 3 & 4). Results of SA8000 audit at pre- and post-intervention stages show that there was 50% improvement in number of non-conformances. But there was not much emphasis on eliminating all non-conformances only critical non-conformances were fully addressed. It was observed that employees' participation and involvement throughout the process was very valuable and a good source to develop low cost interventions. Being part of the interventions process, employees showed their ownership to the process which helped which is very helpful to bring sustainable organizational cultural change. Work performance and investigation tools e.g. root cause analysis, ERCS, Pareto analysis as well as guidelines of SA8000 were found to be very useful. It is concluded that implementation lean and improvement in CSR compliance can be made easier by using the proposed methodology.

Pre-Interventions

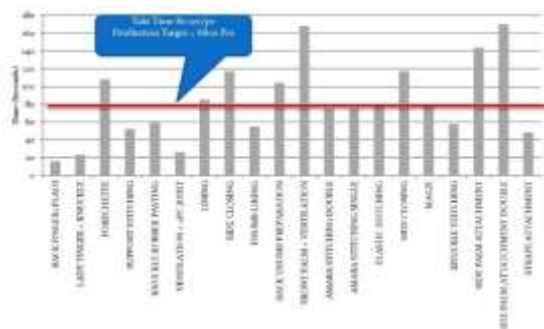


Figure 3 Line Balancing Graph (Pre-interventions)

Post-Interventions

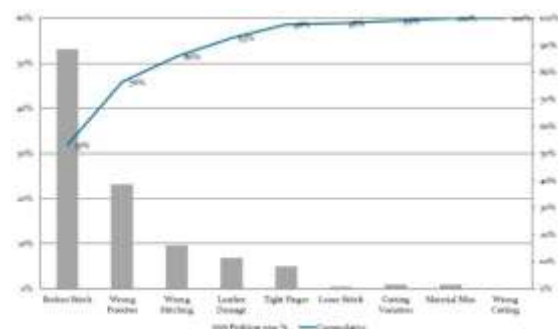


Figure 3 Pareto Analysis for Defects (Pre-Intervention)



(a) Machine without pulley guard



(b) Machine with pulley guard



(c) Floor Markings are Missing



(d) Floor Markings

Figure 4 Pre- and Post-Interventions Pictures



Figure 5 Line Balancing Graph (Post-Interventions)

Table 2 Root causes of defects and thier countermeasures

Root Causes	Countermeasures
Unavailability of quality inspector	Hiring of quality inspector
Production SV not using OSM approach	Placement of operators according to OSM
Helpers were not trained on use of trimming tools	Training of helper by operator
Improper machine setting	Setting machines per SOPs
Poor thread strength	Following procurement SOPs and pre-production inspection



Table 3 KPIs at Post-Interventions Stage

S. No.	KPI	Post-interventions value	Percentage Improvement
1	Quality Defect Rate	12%	60%
2	Line Balancing Efficiency	68%	94%
3	Number of Workers	13	76%
4	Value Added Time	64%	120%
5	Average Production per Day	77 Pairs	64%
6	Number of Non-Conformances in SA8000	19	50%

Table 4 SA8000 Audit Report at Post-interventions stage (Number of Non-Conformances)

Sr. No.	Original Clause Requirement	Level of Non-conformance (Pre-Interventions)			Percentage Improvement
		Critical	Major	Minor	
1	Laws and Regulations	0	0	1	0%
2	Child Labor	0	0	0	1000%
3	Wages and Benefits	0	0	2	50%
4	Hours of Work	0	0	0	100%
5	Health and Safety	0	7	3	57%
6	Freedom of Association and Collective Bargain	0	0	1	0%
7	Environment	0	4	0	20%
8	Monitoring and Compliance	0	0	0	10
Total		0	11	7	53%

4. Discussion

Implementation of lean leads to increased customer satisfaction through cost reduction and quality improvement. But most of the lean initiatives fail to bring sustainable cultural change because of lack of employee involvement fail [33-35]. Improvement in CSR compliance is linked with global competitiveness of the organizations and motivates the employees to participate [11,36]. Moreover, use of participatory approach also enhances employee participation and sustainable lean transformation can be achieved [32].

Results of SA8000 audit show 50% improvement in number of non-conformances. But only critical non-conformances were fully addressed. This result also confirms the findings of [10], that there is a need to spread awareness about CSR in Pakistani context. SMEs face lack of resources which was the major reason of non-conformances at post-interventions stage. For example, there were 4 major environmental issues and none of them was resolved because of high initial cost which the SME couldn't afford. Most of the other requirements of SA8000 were met by the organization such as child labor, issues related to hours of work.

In general results of this case study show that challenge of successful lean implementation can be

overcome by combining lean with CSR and using participatory approach. The proposed participatory based approach provides an effective way to utilize human resource at disposal to bring a sustainable cultural change in an organization. Employees' participation at every stage of the processes is beneficial for sustaining the intervention and developing new ideas for continuous improvement. This shows the potential of participatory approach to implement lean and improve CSR compliance for enhancing competitiveness of SMEs through continuously designing cost effective solutions.

Implementation of lean and compliance of CSR requires long term commitment of the top management as these are cultural transformations and take time to get embedded in the organizational culture. Cultural change also requires resources and time along with providing training and spreading awareness. This study is also a way forward for the managers and provides them an opportunity to learn from experience of involving the employees. Some common issues related to CSR compliance, quality and productivity improvement have been investigated and effectiveness of this methodology and interventions have been reported.

The findings of this research will help managers understand and appreciate the advantage of integration of lean and CSR. Based on results of this study, it is suggested that consideration of CSR in a lean environment will further enhance the



competitiveness of the organization. Specifically, managers can learn and understand the following lessons from this study:

- A participative approach to integrate lean and CSR influences organizational competitiveness positively.
- An integrated and participative approach provides a good organizational environment for continuous improvement.

5. Conclusion

Integration of lean and CSR is linked with organizational cultural change. Major challenges that are faced by SMEs related to employees' motivation and lack of resources. Employees can be motivated by using participatory approach to implement lean and improve CSR compliance. Low cost and easy to implement interventions can overcome the challenge of lack of resources. This study used a 9-step methodology based on the concept of continuous improvement and stakeholders' involvement to achieve sustainable cultural change. This methodology was validated by implementing it in an SME as a case study and very promising results were achieved. The CSR was gauged against the SA8000 by certified auditors at pre- and post-interventions stages. KPIs of lean were defect rate, line balancing efficiency, number of workers, value added time and average production per day. ECRS, root cause analysis, time study etc. were among the tools and techniques used to solve the problems. Suggestions given by stakeholders especially employees were implemented which motivated the employees and proved effective. Results indicate 53% reduction in number of non-conformances to SA8000, 60% reduction in defect rate, 94% improvement in line balancing efficiency, 120% increase in value added time and 64% increase in average production per day. It is concluded design and implementation of low-cost interventions based on participatory approach can significantly improve compliance to CSR and benefits of lean transformation which leads to improvement in competitiveness of SMEs.

6. Limitations and Future Directions

Scope of this case study was to implement lean and improve CSR in one production line of a leather gloves manufacturing organization due to resources and time constraint. In future this work may be extended to other sectors of manufacturing. Lesson learned like role of employees' involvement, participatory approach to implement lean and improve CSR simultaneously could be used in future research.

REFERENCES

- [1] Ali Shah Syed, A. G., Muneer Ahmadani, M., Shaikh, N., Muhammad Shaikh, F., & Anwar Ali Shah Syed, A. G. (2012). Impact Analysis of SMEs Sector in Economic Development of Pakistan: A Case of Sindh. *Journal of Asian Business Strategy*, 2(22), 44–53.
- [2] APO. (2017). *Productivity Databook 2017*. Retrieved from http://www.apo-tokyo.org/publications/wp-content/uploads/sites/5/APO-Productivity-Databook_2017.pdf
- [3] Veskaisri, K., Chan, P., & Pollard, D. (2007). Relationship Between Strategic Planning and SME Success: Empirical Evidence from Thailand California State University-Fullerton, California, USA California State University-Fullerton, California, USA. *Asia and Pacific DSI*, 1–13.
- [4] Khalique, M., Isa, A. H. M., & Shaari, J. A. N. (2011). Challenges for Pakistani SMEs in a Knowledge-Based Economy. *Indus Journal of Management & Social Science (IJMSS)*, 5(2), 74–80.
- [5] Finance Division Government of Pakistan. (2019). Pakistan Economic Survey 2018-2019.
- [6] Trade Development Authority Of Pakistan. (2016). Sectoral Competitiveness and Value Chain Analysis: Leather Gloves.
- [7] Vilanova, M., Lozano, J. M., & Arenas, D. (2009). Exploring the nature of the relationship between CSR and competitiveness. *Journal of Business Ethics*, 87(SUPPL. 1), 57–69. <https://doi.org/10.1007/s10551-008-9812-2>
- [8] Dahlgaard, J. J., Chen, C. K., Jang, J. Y., Banegas, L. A., & Dahlgaard-Park, S. M. (2013). Business excellence models: Limitations, reflections and further development. *Total Quality Management and Business Excellence*, 24(5–6), 519–538. <https://doi.org/10.1080/14783363.2012.756745>
- [9] Corbett, L. M., & Angell, L. C. (2011). Business excellence in New Zealand: Continuous improvement, learning, and change. *Total Quality Management and Business Excellence*, 22(7), 755–772. <https://doi.org/10.1080/14783363.2011.585782>
- [10] Hussain, A., Fahad Ali, S., Case, K., Masood, T., & Masood, M. (2017). Assessment of Corporate Social Responsibility (CSR) awareness and practices in manufacturing sector of Pakistan. *Advances in Transdisciplinary Engineering*, 6, 389–394. <https://doi.org/10.3233/978-1-61499-792-4-389>
- [11] Nyuur, R. B., Ofori, D. F., & Amponsah, M. M.



- (2019). Corporate social responsibility and competitive advantage: A developing country perspective. *Thunderbird International Business Review*, 61(4), 551–564. <https://doi.org/10.1002/tie.22065>
- [12] Machado, C. F., Bezerra, A., & Oliveira, B. F. (2017). Corporate Social Responsibility Role in SMEs: A Critical Way of Thinking in Green and Lean Management Arena. In C. Machado & J. P. Davim (Eds.), *Green and Lean Management* (pp. 207–220). <https://doi.org/10.1007/978-3-319-44909-8>
- [13] Hodge, G. L., Goforth Ross, K., Joines, J. A., & Thoney, K. (2011). Adapting lean manufacturing principles to the textile industry. *Production Planning and Control*, 22(3), 237–247. <https://doi.org/10.1080/09537287.2010.498577>
- [14] Manfredsson, P. (2016). Textile management enabled by lean thinking: a case study of textile SMEs. *Production Planning and Control*, 27(7–8), 541–549. <https://doi.org/10.1080/09537287.2016.1165299>
- [15] Sundar, R., Balaji, A. N., & Satheesh Kumar, R. M. (2014). A review on lean manufacturing implementation techniques. *Procedia Engineering*, 97, 1875–1885. <https://doi.org/10.1016/j.proeng.2014.12.341>
- [16] Rose, A. M. N., Deros, B. M., Rahman, M. N. A., & Nordin, N. (2011). Lean manufacturing best practices in SMEs. *International Conference on Industrial Engineering and Operation Management*, 1(1), 872–877.
- [17] Lee, C. Y. (1997). JIT adoption by small manufacturers in Korea. *Journal of Small Business Management*, 35(3), 98.
- [18] Nallusamy, S., & Adil Ahamed, M. A. (2017). Implementation of lean tools in an automotive industry for productivity enhancement - A case study. *International Journal of Engineering Research in Africa*, 29, 175–185. <https://doi.org/10.4028/www.scientific.net/JERA.29.175>
- [19] Scherrer-Rathje, M., Boyle, T. A., & Deflorin, P. (2009). Lean, take two! Reflections from the second attempt at lean implementation. *Business Horizons*, 52(1), 79–88.
- [20] Carroll, A. B. (2015). Evolution of a Definitional Construct. *Business & Society*, 38(3), 268–295.
- [21] Freeman, I., & Hasnaoui, A. (2011). The meaning of corporate social responsibility: The vision of four nations. *Journal of Business Ethics*, 100(3), 419–443. <https://doi.org/10.1007/s10551-010-0688-6>
- [22] Pérez, A., Martínez, P., & Rodríguez del Bosque, I. (2013). The development of a stakeholder-based scale for measuring corporate social responsibility in the banking industry. *Service Business*, 7(3), 459–481. <https://doi.org/10.1007/s11628-012-0171-9>
- [23] Mishra, S., & Suar, D. (2010). Does corporate social responsibility influence firm performance of Indian companies? In *Journal of Business Ethics* (Vol. 95). <https://doi.org/10.1007/s10551-010-0441-1>
- [24] Boulouta, I., & Pitelis, C. N. (2014). Who Needs CSR? The Impact of Corporate Social Responsibility on National Competitiveness. *Journal of Business Ethics*, 119(3), 349–364. <https://doi.org/10.1007/s10551-013-1633-2>
- [25] Panayiotou, N. A., Aravossis, K. G., & Moschou, P. (2009). A new methodology approach for measuring corporate social responsibility performance. *Water, Air, and Soil Pollution: Focus*, 9(1–2), 129–138. <https://doi.org/10.1007/s11267-008-9204-8>
- [26] Danilovic, M., Hensbergen, M., Hoveskog, M., & Zadayannaya, L. (2015). Exploring diffusion and dynamics of corporate social responsibility. *Corporate Social Responsibility and Environmental Management*, 22(3), 129–141. <https://doi.org/10.1002/csr.1326>
- [27] Gilbert, D. U., & Rasche, A. (2015). Discourse Ethics and Social Accountability: The Ethics of SA 8000. *Business Ethics Quarterly*, 17(2), 187–216.
- [28] Leipziger, D. (2017). *SA8000: The first decade: Implementation, influence, and impact*. Routledge.
- [29] Muduli, K., Govindan, K., Barve, A., Kannan, D., & Geng, Y. (2013). Role of behavioural factors in green supply chain management implementation in Indian mining industries. *Resources, Conservation and Recycling*, 76, 50–60. <https://doi.org/10.1016/j.resconrec.2013.03.006>
- [30] de Sousa Jabbour, A. B. L., de Oliveira Frascareli, F. C., & Jabbour, C. J. C. (2015). Green supply chain management and firms' performance: Understanding potential relationships and the role of green sourcing and some other green practices. *Resources, Conservation and Recycling*, 104, 366–374. <https://doi.org/10.1016/j.resconrec.2015.07.017>
- [31] Malviya, R. K., Kant, R., & Gupta, A. D. (2018). Evaluation and Selection of Sustainable Strategy for Green Supply Chain Management Implementation. *Business Strategy and the Environment*, 27(4), 475–502. <https://doi.org/10.1002/bse.2016>
- [32] Govindan, K., Muduli, K., Devika, K., & Barve, A. (2016). Investigation of the influential strength of factors on adoption of green supply chain management practices: An Indian mining scenario. *Resources, Conservation and Recycling*, 107, 185–194. <https://doi.org/10.1016/j.resconrec.2015.05.022>



- [33] Atkinson, P. (2010). 'Lean' is a Cultural Issue
Philip Atkinson addresses the key issues that relate to culture change. 35–41.
- [34] Bhasin, S. (2011). Measuring the Leanness of an organisation. *International Journal of Lean Six Sigma*, 2(1), 55–74.
<https://doi.org/10.1108/20401461111119459>
- [35] Bhasin, S. (2012). An appropriate change strategy for lean success. *Management Decision*, 50(3), 439–458.
<https://doi.org/10.1108/00251741211216223>
- [36] Farrukh, M., Sajid, M., Lee, J. W. C., & Shahzad, I. A. (2019). The perception of corporate social responsibility and employee engagement: Examining the underlying mechanism. *Corporate Social Responsibility and Environmental Management*.
<https://doi.org/10.1002/csr.1842>



Application of Total Productive Maintenance (TPM) Technique in Improved Productivity of Industrial Equipment: A case study from Pakistan

Hamid Minhas¹, Usman Ghani², Shar Noor³, Muhammad Usman⁴, and Zain Ul Hassan⁵

¹ Department of Industrial Engineering, University of Engineering and Technology, Peshawar, minhas.mech@gmail.com

² Department of Mechanical Engineering, University of Engineering and Technology, Peshawar, Jalozi, Campus, saharanoor@gmail.com

³ Department of Industrial Engineering, University of Engineering and Technology, Peshawar, usmanghani@uetpeshawar.edu.pk

⁴ Department of Mechanical Engineering, University of Engineering and Technology, Lahore, muhammadusman@uet.edu.pk

⁵ Department of Mechanical Engineering, University of Engineering and Technology, Lahore, zhassan.uet@gmail.com

Abstract:

One of the most important technical key performance indicators (KPIs) is the overall equipment effectiveness (OEE) which measures the productivity of any process to achieve set goals in manufacturing. Producing better quality and cost-effective products is a fundamental need to remain competitive in any consumer market. Thus, many techniques are developed to eliminate any wastage in manufacturing processes and produce economical products by enhancing OEE. Maximization of the efficiency of equipment i.e. to eliminate the losses impedes the improvement of efficiency. These losses are the real problems, therefore in this research, multiple factors have been analyzed which affect the productivity and Overall Equipment Efficiency (OEE). A case study of local industry has been discussed and reported for future industrial processes in perspective of maintenance while focusing on the causes of major losses and countermeasures to enhance performance, hence contributing to OEE improvement. This research will enable industries to understand the implementation procedures of TPM practices.

Key Words: Overall Equipment Efficiency (OEE); Productivity; Total Quality Management (TQM); Lean Manufacturing; Key Performance Indicators

1 Introduction

Producing better quality and cost-effective products is key to remain competitive globally. In this regard, tools like Total Quality Management (TQM) and Lean Manufacturing assist to eliminate any wastages in manufacturing processes and produce quality and economical products. There are various parameters which affect the productivity such as environment, methods, machines, personals, material and measurements but machines are mostly unpredictable resource that causes variability in overall production. So, the productivity of industrial machine equipment is directly linked with Overall Equipment Efficiency (OEE) which is very important indicator to achieve direct and sustained improvements in any industry. The OEE was the first time defined by the Japan Institute of Plant Maintenance resulted from a long-term evaluation of TPM [1]. It is basically a set of metrics to evaluate the effectiveness of any manufacturing process regarding the availability of resources, performance of each component, and

quality of the whole procedure [2]. The operation availability with respect to the total scheduled time is measured by the availability portion and corresponding losses are called availability losses [3]. Similarly, the process rate of the operation with regard to the standard speed is measured by the performance portion and losses involved are called speed losses which occur due to wasted performance [4]. Finally, the quality portion is basically the representation of total number of conformities in comparison to the total number of units produced when the effects of availability and performance are not considered. [5]. The application of OEE is not limited to any single-stage process but covers a whole plant production. Also, multiple specific parameters e.g. particular part number can be analyzed by OEE. However, it is not possible for any industry to achieve 100% OEE, therefore, many manufacturers set the target of 85% OEE [6].

Different processes in industries experience random breakdowns and maintenances issues which are the key areas that impact productivity



[7]. Industries like food processing, medicines processing, cloth making, tile making, wood making, and many other face similar problems. Among various industries, cigarette manufacturing, which is a high demand item production plant particularly in Pakistan is not working to desired productivity level, which is due to downtime and ill-planned maintenance procedures and processes. Plant maintenance is an important area in manufacturing where 15-60% of manufacturing cost is associated with different maintenance activities [8].

Primarily there are two main sections of a cigarette manufacturing factory. One is the making section and other is the packing section. Since, the making section has huge amount of raw material available with multiple machines for making process, the losses occurred in this section are not of major concern as it is not affecting the production rate. Huge amount of processed tobacco is readily available to be sent to packing section having limited machines running continuously. Therefore, any downtime in packing machine will have direct implication on the final packing stage of processed tobacco and cigarette. Hence, packing section is taken for improvements to reduce losses and increase the net production rate of factory. The current OEE of packing Cell is around 67 % and the production of this Cell is around 2 Billion sticks yearly. The processing accuracy is the main area where this industry lacks the implementation of TPM practices. Packing machines are vulnerable to breakdowns and because of that, the company is losing their desired productivity along with an increase in production cost.

A practical case study has been taken in this regard and concept of TPM is applied to see the improvement trend in a set of machines by reducing the losses during manufacturing processes. A detailed analysis is carried out with identification of root cause problems and their remedial solutions.

2 Literature Review

Researchers have worked on the improvement of industries by applying TPM techniques. A few of the relevant state of art knowledge background has been discussed in this section to benefit industries and academics in terms of measures of efficiency. The results may be useful to compare the OEE of this industry with others as it is based on an actual problem and will improve the efficiency of a set of machines thereby increasing the net production rate.

Gupta et al. studied the positive impact of improved OEE on the production and sale volume of the manufacturing industry. It helped the top management enhance the process capabilities and improve plant operational effectiveness. Almost all machines showed above 85% overall equipment efficiency [9]. Tenera et al. designed a model involving the DMAIC cycle and multiple statistical tools according to different project performance variables. This allowed management to address the problems systematically and develop necessary actions to implement the solutions for a long period of time [10]. Yousouf et al. focused on the implantation of lean six sigma to optimize the maintenance activities of any process. It is a quality improvement method involving statistical control of a manufacturing process by an organization [11]. Khaled et al. studied the optimization of transportations and solved the problem of routing straddle carriers in port container terminals [12].

2.1 Research Gap

As discussed, many researchers have used statistical tools to bring improvement in different industries. However, despite a number of studies on the implantation of TPM in the manufacturing industries, no detailed research is available for its impacts in Small and Medium Enterprises (SMEs), especially in Pakistan. Therefore, to implement TPM strategy in SMEs, a more systematic approach needs to be developed. Implementation of TPM is not a common practice in Industries of Pakistan. Therefore, very little research work is available related to a specific industry with regards to the optimum utilization of equipment. The cigarette manufacturing industry is a high revenue-generating industry all over the world as well in Pakistan, whereas its production is not optimum as per the requirements. The cost-effective way is to analyze the production processes on the lines of other industries and improve the existing machines instead of installing new machines in order to enhance the production rate. The focus of this research is to study the packing processes of the cigarette manufacturing industry and highlight the improvements by implementing TPM practices.

3 Methodology

Overall equipment effectiveness was improved by following the basic steps for the implantation of TPM to enhance productivity and improve machine performance. Six Sigma tools were used to analyze the collected data after its verification by the plant manager. Details of all the relevant machines and equipment were obtained at the beginning of the research process for the classification of different



parts according to their availability. Six Sigma methodology of Define, Measure, Analyze, Improve and Control known as “DMAIC” was implied to measure net operating rate losses on account of stoppages, determine improvement opportunities and develop a control strategy for the sustainability of determining factors in the ‘Improve Phase’. For this purpose, the machine cell of the processing plant was selected comprised of a set of different machines in a row.

The sources of stoppages in the machine are identified and categorized as per the nature of cause which affects the performance efficiency. A data collection and analysis plan was developed to measure the dispersion, determine current process capability, identify major variation and losses, and establish a relationship between variables.

3.1 Process Measurement

Process Measurement is carried out that entails total downtime and stoppage frequency of 60 days of the machine running. However, for analysis and improvement phases of priority areas, Simple Random Sampling is used to determine (randomly) 30 days of data for study purposes. After analyzing the data using box plots and Pareto analysis, data is further grouped and stratified in terms of stoppage frequency and corresponding downtime for each day. Stoppages with recurring values and significant stoppage time are considered for the analysis phase, while the rest is deemed insignificant. Henceforth, the stoppages which are identified that are major and impactful in the process from initial screening and their effects are analyzed to establish significance on Machine Performance Efficiency. From the results of the analysis, a dedicated improvement plan is made to reduce the stoppages and to improve the OEE.

4 Datatype and Chart Characteristics

S.No.	Detail	Measure	Type
Performance Efficiency	Actual Output / Potential Output	%	Discrete
Stoppages No. of Stops Downtime	Frequency of Minor Stops	Number of times Hr: Min	Continuous Continuous

	Stoppage Time	: Sec	us
Cycle Time	Item / min	No. of products	
Breakdowns	Over 1 hr. Equipment Failure	Hrs:Min	Continuous
Available Production Time	Loading – Breakdown Time	Hrs:Min	Continuous
Production Output	The yield of Good product	Volume in Millions	Continuous

The main focus is on the improvement of OEE of a machine by analyzing the factors involved in downtime losses. Thus six major losses have been described in the Table 4.1 below as a significant hurdle in the improvement of overall equipment efficiency.

4.1 Data Collection

The calculations of OEE highly depends on the accuracy of data which was corrected by comparing the collected data with the output of the product packing machine showing different parameters such as total product quantity both rejected and selected, loading and operation time and downtime losses. The calculations were performed in the MS Excel template. To investigate the different losses and their occurring trend, the data was filled up which helped in recognition of the possible causes of machine brake downtime based on past and present data.

4.2 Data Analysis

The first problem which identified was downtime losses because there was no procedure about machine setup, machine maintenance and operator inefficiency. The time analysis was performed to identify non-valued activities in the process which affect the OEE. Autonomous maintenance is proposed as a solution to this problem which enables operators to manage machine equipment independently. Various standards and checklist for setting, cleaning, inspection and lubrication were also added.



The second main reason for the downtime losses was equipment breakdown and minor stoppages. These were identified as shut down, equipment failure, process failure, and production adjustment. The solution to this problem is one of the pillars of TPM i.e. planned maintenance to achieve zero breakdowns and evaluate current performance.

Table 4.1: Six major losses

Six big losses category	OEE Loss Category	Event examples (Reason codes)	Remark
1) Equipment Failure (Breakdown)	Downtime Loss	<ul style="list-style-type: none"> • Tooling failures • Unplanned maintenance • General Breakdowns • Equipment failures 	The threshold between a breakdown (downtime loss) and shortstop (Speed loss) must be defined
2) Setup and Adjustments	Downtime Loss	<ul style="list-style-type: none"> • Setup / Changeover • Material shortage • Operator shortage • Major adjustments 	Setup / Changeover reduction is one major issue to increase efficiency
3) Minor Stops	Speed Loss	<ul style="list-style-type: none"> • Product flows • Short jams • Misfeeds • Blocked sensors • Blocked delivery • (Short) Checking / Cleaning 	“Short Stop” definition: <ul style="list-style-type: none"> • No maintenance required • Not exceeding certain time limit (typical 5 min)
4) Reduced Speed	Speed Loss	<ul style="list-style-type: none"> • Running not smooth • Below capacity • Wear • Inefficient operator 	Also includes speed reduction because of material shortage
5) Startup rejects	Quality Loss	<ul style="list-style-type: none"> • Scrap at startup • Damage in process • Expiration in process • Incorrect assembly 	All rejects or waste ejected during startup
6) Production rejects	Quality Loss	<ul style="list-style-type: none"> • Scrap in production • Rework • Damage in process • Incorrect assembly 	Rejects during production



Table 4.2: Data collection plan.

Measures	Define	Data Source & Location	Sample Size	How to collect data
Stoppage	Small or idling stops	Data acquisition system	60 days	Excel format
Cycle Time	Packs/m in In 20HL form	From machine IPC	Std.	Excel format
Breakdowns & major stops	Equipment failures. Over 15 min duration	Data folder	60 days	Excel format
Available Production Time	M/C loading Time Breakdown time	OEE calculation sheet	60 days	Excel format

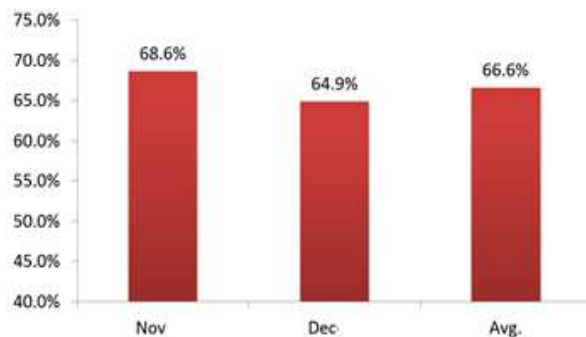


Figure 4.1: OEE of complete modules of the packing line

The current process performance of the module revealed that machines were operating on average of 66.6 % OEE. Performance in Nov is high and decreasing in next month. Hence, based on average OEE, the target in this case study is to improve Efficiency to 69% (2% increase).

4.2.1 Pareto Analysis

Based on the initial findings, a Pareto chart was developed to identify major stoppages in machine land 2:



Figure 4.2: Pareto Chart – Machine 1.

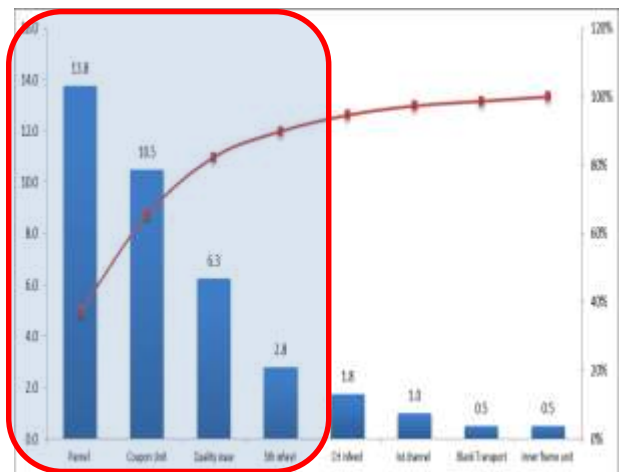


Figure 4.3: Pareto Chart – Machine 2.



Pareto analysis was performed which is a statistical technique in decision-making to select a limited number of tasks that produce a significant overall result. It uses the Pareto Principle (also known as the 80/20 rule) i.e. a majority of problems (80%) are produced by a few key causes (20%).

Based on the initial findings, a Pareto chart was developed to identify major stoppages in machine 1 and 2. For module 1, blank transport and Panel faults are the top contributors for downtimes and for module 2, Panel faults, coupon unit, and quality issues constitute the highest downtime.

4.2.2 Data Selection and Stratification

Data was further grouped and stratified in terms of stoppage frequency and corresponding downtime for each day. Stoppages with recurring values and significant stoppage time were considered for the analysis phase, while the rest were deemed insignificant. Henceforth, the stoppages were identified as major and impactful in the process from initial screening and their effects were analyzed to establish significance on Machine Performance Efficiency.

4.2.3 Descriptive Analysis

Entire readings in the last 2 months (data sheets are attached in appendix) were plotted, to generate a histogram indicating Std. Deviation, Mean Performance Efficiency, Skew-ness, and Kurtosis values.

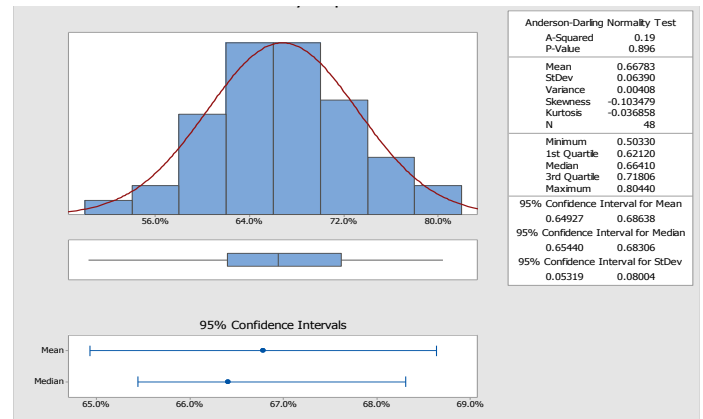


Figure 4.4: Machine's Histogram.

The spread of data and distribution curve in the histogram indicates comparatively negative skewness. High frequency of data is in the range between 62% to approx. 71.8%. Some outliers are below 50% efficiency. Standard Deviation of 6.3%. Negative Kurtosis indicates a non-peaked distribution. Process Capability – Normal Distribution Curve revealed the following results:

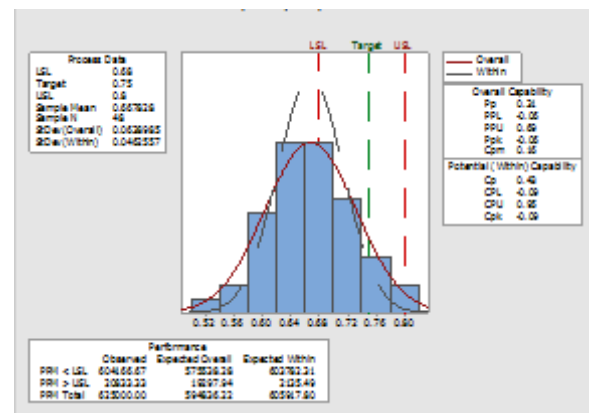


Figure 4.5: Cell 2 Process Capability

Baseline Cpk is negative at 0.09. Target is to improve Cpk levels through the identification of major impediments in stoppages. Analyze present process performance and develop action plans for the reduction of total downtime lost on account of these stoppages.



5 Improvement Phase

Improvements are made in the production plant by suggesting the formation of maintenance teams relevant to identical faults from stoppages data. The maintenance teams will form a maintenance program with respect to each machine. Each maintenance team will evaluate the time required and cost of maintenance which will increase the production cost as maintenance cost increases but overall production rate will increase thereby increasing the overall efficiency of equipment and reducing downtime.

The preventive Maintenance process flow is devised, comprising of different preventive maintenance activities. A detailed monthly maintenance plan is made for machines.

5.1 Monthly Maintenance Schedule

Table 5.1: Schedule of maintenance for 1st month.



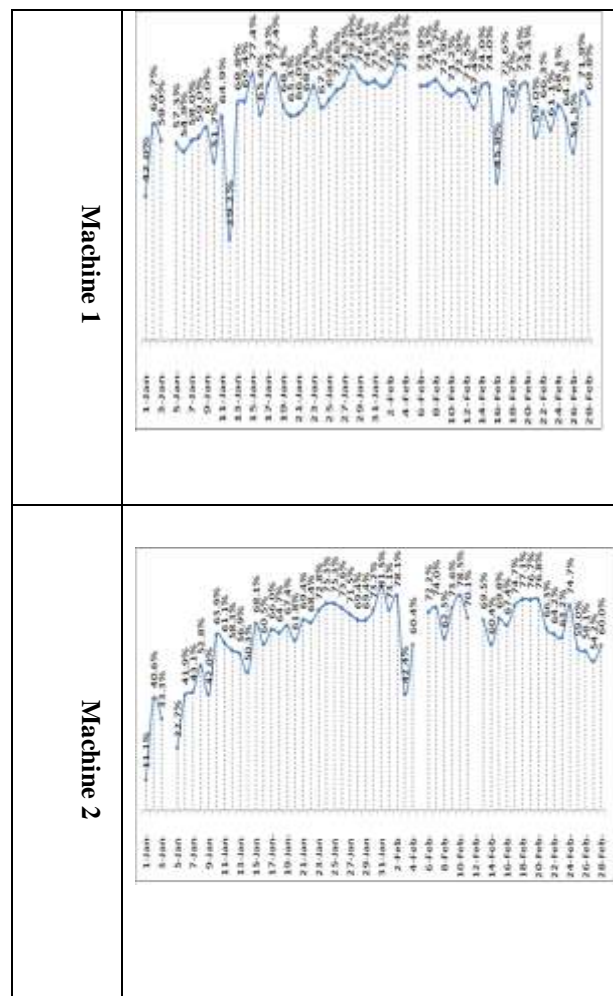
Table 5.2: Schedule of maintenance for 2nd month.



6 Result and Discussion

Improvement in OEE is observed after the implementation of maintenance regimes. OEE is

expected to increase from 6-8 % from this planned maintenance activity. Based on the implementation of the above-mentioned improvement plans, the results were observed over a span of 2 months. Since the focus of improvement was machine 1 and machine 2, individual OEE results are appended here first, followed by the results of the cell. From the results it can be clearly seen that both the modules show the improvement trend in the first half of the month, translating into increased OEE for the machines for the 2 months. Another comparison is shown here showing the improved OEE across the cell for the entire span of the project:



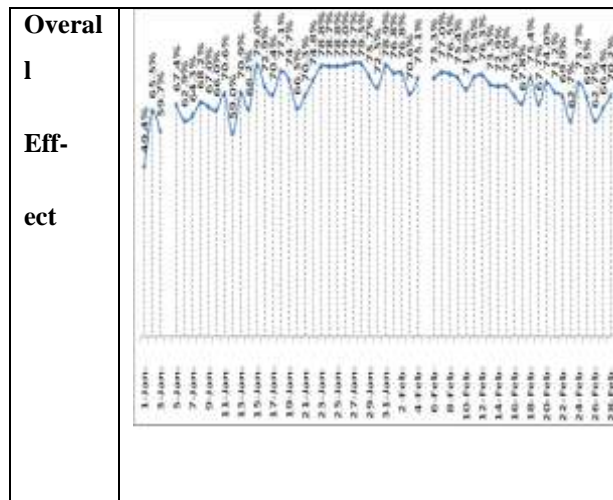


Figure 6.1: OEE results after improvements.

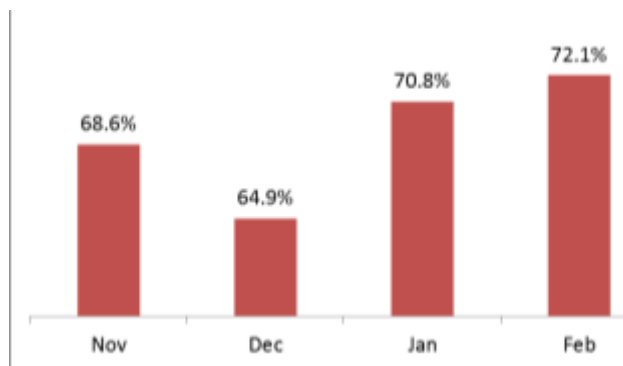


Figure 6.2: OEE across the machines set before and after improvements.

The implementation of TPM methodology for analysis and improvement has shown excellent results across the machines set.

7 Conclusion

Based on the results shown above, using the TPM methodology, performance can be significantly improved, through a systematic approach. The results may be useful to compare the OEE of this industry with other industries which was increased from 67% to 72%. OEE can also be improved by reducing process wastages therefore process can be modeled to improve OEE by reducing process wastages. Various digital techniques which include OEE dashboard and machine learning can also be employed to make smart decisions leading to the improvement of OEE.

It is recommended that the concept of DMAIC should be implemented in small medium enterprises gradually and latest techniques of TPM be implemented in industrial sector of Pakistan to compete with the rest of world in manufacturing sector.

REFERENCES

- [1] Nakamura T. Total productive maintenance. Encyclopedia of Statistics in Quality and Reliability. 2008 Mar 15;4.
- [2] Raguram R. Implementation of Overall Equipment Effectiveness (OEE). Middle-East Journal of Scientific Research. 2014;20(5):567-76.
- [3] Dal B, Tugwell P, Greatbanks R. Overall equipment effectiveness as a measure of operational improvement—a practical analysis. International Journal of Operations & Production Management. 2000 Dec 1;20(12):1488-502.
- [4] Sandengen OC, Estensen LA, Rødseth H, Schjøberg P. High Performance Manufacturing- An Innovative Contribution towards Industry 4.0. In6th International Workshop of Advanced Manufacturing and Automation 2016 Nov 10. Atlantis Press.
- [5] Vijayakumar SR, Gajendran S. Improvement of overall equipment effectiveness (OEE) in injection moulding process industry. IOSR J Mech Civil Eng. 2014;2(10):47-60.
- [6] McKone KE, Schroeder RG, Cua KO. The impact of total productive maintenance practices on manufacturing performance. Journal of operations management. 2001 Jan 1;19(1):39-58.
- [7] Lõun K, Riives J, Otto T. Evaluation of the operation expedience of technological resources in a manufacturing network. Estonian Journal of Engineering. 2011 Mar 1;17(1):51.
- [8] Muchiri P, Pintelon L. Performance measurement using overall equipment effectiveness (OEE): literature review and practical application discussion. International journal of production research. 2008 Jul 1;46(13):3517-35.
- [9] Gupta, Pardeep, and Sachit Vardhan. "Optimizing OEE, productivity and production cost for improving sales volume in an automobile industry through TPM: a case



study." *International Journal of Production Research* 54.10 (2016): 2976-2988.

[10] Alexandra Tenera, Luis Carneiro Pinto (2014). UNIDEMI, Mechanical, and Industrial Engineering Department, Caparica, 2829-516, Portugal vol.119, pp 912- 920.

[11] Ayadi Youssouf, Chaib Rachid (2014). Badji Mokhtar University, Annaba laboratory environment, and transport engineering. Mentouri University, Roumania, vol. 55 , pp 512 –518.

[12] Khaled Mili (2014). Higher Institute of Business Administration of Gafsa, Jemmel 5020, Tunisia vol.111, pp-1195-1205



Experimental Investigation of Test Samples' Mechanical Properties Produced from Pure Titanium with Binder Jet 3D Metal Printer

Osman İYİBİLGİN^{1,2}, Engin GEPEK²

¹Mechanical Engineering Department, Faculty of Engineering, Sakarya University, Sakarya, Turkey

²Biomedical, Magnetic and Semiconductor Materials Application & Research Center, Sakarya University, Sakarya, Turkey

¹Communication author, E-mail: ibilgin@sakarya.edu.tr, Tel: +90-264-295 7390

Abstract:

Polymer, ceramic and metal powders are used in production with Binder jet 3D printer. Samples are subjected to sintering after pre-bonding using adhesive. This heat treatment process significantly affects the mechanical properties and strength values of the sample. In this study, test specimens were fabricated via pure Ti powders and the effect of heat treatment processes on mechanical properties was experimentally investigated. Ti powders are preferred because they are biocompatible, have sufficient strength and a high weight strength ratio in porous structures in implant manufacturing. After the experimental work, it was detected that the surface hardness of the sample increased with increasing sintering temperature. The powder distribution was close to homogeneous in the SEM micrographs. In the conventional powder metallurgy method, strength problems due to the heterogeneous pore are overcome.

Keywords: Binder Jetting; Titanium; Metallic 3D Printer; Mechanical Properties.

1. Introduction

Porous Ti and Ti alloy materials are mostly used in biomedical applications due to their high biocompatibility, good corrosion resistance and mechanical properties close to human bone [1]. In addition, the porosity of piece provides better adhesion of bone structure to the surface. However, the hardness and wear resistance of Ti-based parts are low. In biomedical applications where high hardness and wear resistance are required, porous Ti pieces are reinforced by using TiN, TiC, SiC, B₄C and TiB compounds [2]. Additive Manufacturing, Traditional Powder Metallurgy and foaming method are frequently used in the production of porous Ti pieces [3]- [5].

Additive manufacturing (AM) is the process of producing the part modeled in CAD program in layers. In this method, the production of materials are named according to the method of aggregation (FDM), selective laser sintering (SLS), selective laser melting (SLM), electron beam melting (EBM) and adhesive layered manufacturing (Binder Jetting) [6] - [8]. The material used in production and the manufacturing technology have special benefits and drawbacks. The additive manufacturing method used for prototype

production is now being used in many industrial fields such as medical, aerospace, automotive and defense industries [9] - [11].

One of the additive manufacturing methods is the Binder Jetting method in which powder materials are combined with binders. In this method, unlike other additive production methods, the powder materials are combined with the help of binders and then sintered and heat treatment processes are applied. Binder Jetting method can be produced with various materials such as polymer, ceramic and metal powders. In this method, the production process consists of the modeling of the part in CAD program, production of the 3D printer, blowing of the binder, sintering and heat treatment stages.

In the conventional powder metallurgy method, powders are shaped in a single-axis press mold. After the sintering and annealing processes are applied to the press shaped samples, they become usable. In this method, cavity-forming materials are used to obtain porous structures. Carbamide (CO (NH₂)₂), ammonium hydrogen carbonate (NH₄HCO₃), sodium chloride (NaCl), starch, sucrose, polymethyl methacrylate (PMMA) and paraformaldehyde are the most commonly used gap formers [1], [12].



The melting temperature of Ti is 1670 °C and has a density of 4.51 g cm⁻³. The highest relative density and optimum mechanical properties were obtained in the sintered parts at 1200 C in the production of Ti parts in the range of 700 - 1350 °C by Spark Plasma Sintering method [13]. In the study of the production of porous Ti by Three-dimensional printing (3DP) method and the sintered in the range of 1200 to 1400 °C has been found that the

2. Material and Methods

2.1. Materials

The present investigation, titanium powders (Alfa Aesar, 42624) with 99.5% purity and average particle size of 19.37 μm were shaped by Binder Jetting method and Conventional Powder Metallurgy method and test samples were produced. The powder size distribution and SEM

mechanical properties of Ti parts increase depending on temperature [14]. In this study, porous Ti samples are sintered at 1200 to 1400 °C to compare the effect of sintering temperature of samples shaped by Binder Jetting and Powder Metallurgy methods. After sintering process, porosity morphology, porosity distribution, mechanical and structural properties of samples produced by both methods were studied.

image of Ti powder are shown in Figure 1. In the Binder Jetting method, a water-based binder is used to combine the powders. In the conventional powder metallurgy method, ammonium hydrogen carbonate (NH₄HCO₃) (Alfa Aesar stock no: 14249) was used as a void forming agent.

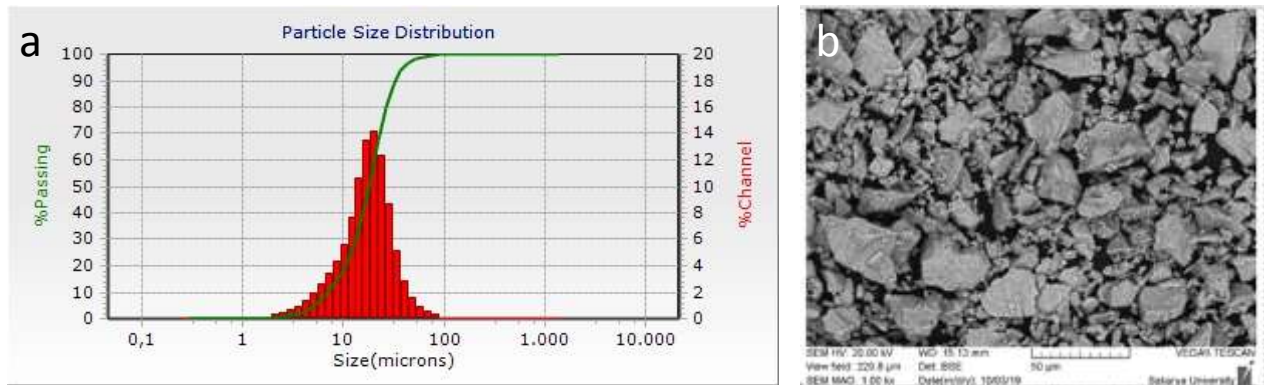


Figure 1. CP Ti powders a) Particle size distribution graph b) SEM image of powders

2.2. Binder Jetting

Ti test specimens are produced in Binder Jetting type printer, modeled in CAD (Solidworks) drawing program with 10 mm diameter and 15 mm height in accordance with standard printing tests. The production parameters of the material to be utilized in BJ printer first are entered into the system and production starts. In the first layer, powder material is sprinkled onto the production

2.3. Traditional Powder Metallurgy

Commercial Pure Ti test specimens were produced using a mold has same diameter and height with the Binder Jetting one. Ammonium hydrogen carbonate (NH₄HCO₃) (Alfa Aesar stock no: 14249) was used as a cavity builder to obtain porous structure in these samples. The shaping of the test samples took place in 2 steps. First, 50% by volume NH₄HCO₃ and 50% pure titanium powders were placed in high-density polyethylene

platform and a smooth and homogeneous distribution of the powders is ensured with the help of a roller. Binders are sprayed onto these powders to form the model and the first layer is completed. The second and subsequent layers, like the first layer, are firstly dispersed in a homogeneous manner and the production is completed by spraying the binder. After the production is completed, dusts which are not bonded with adhesive are cleaned and samples are obtained.

jars. The Turbula T2F was stirred in the agitator for 2 hours to mix the powders put into the jar homogeneously. The powder mixture was then compressed by applying a pressure of 200 MPa in the mold and the test specimens were observed. Compression pressure has been examined in previous studies and the minimum tensile and maximum compressive strength values have been selected [15]. The test specimens fabricated both methods are shown in Figure 2.

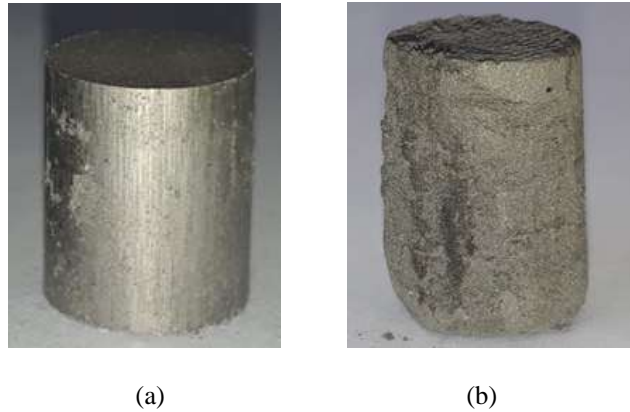


Figure 2. Test specimens a) Traditional Powder Metallurgy, b) Binder Jetting.

2.4. Sintering

Binder Jetting and press-shaped specimens have low strength. Test specimens are sintered to give strength. Pure Titanium samples were sintered in an atmosphere controlled furnace (PTF series, Proterm, USA) for 2 hours at 1200, 1300 and 1400 °C. In sintering process, the oven temperature is 5 °C / min. speed of 250 °C after waiting for 2 hours

at 5 °C / min. speed sintering temperature. After waiting for 2 hours at sintering temperature, the sintering process was completed by cooling at 5 °C / min. During the sintering process, the binders and void formers in the structure were removed by standing at 250 °C. The temperature-time graph for the sintering process at 1300 °C is shown in Figure 3.

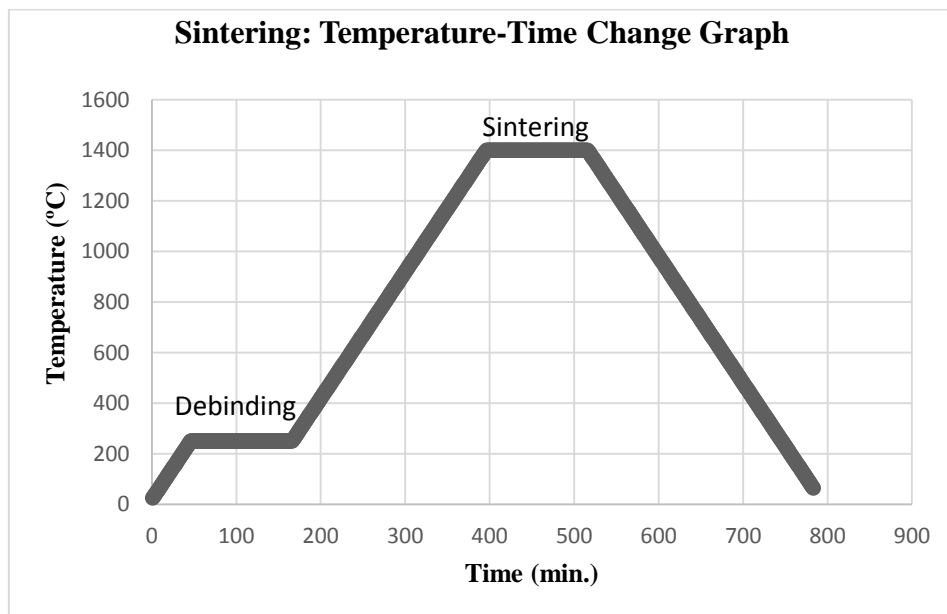


Figure 3. Temperature - Time change graph

2.5. Mechanical Tests and Characterizations

The density of the test samples after sintering process was calculated by Archimedes principle. In this method, the porosity ratio of each sample was calculated using Equation 3.2 (ρ : measured alloy

density, ρ_s : calculated theoretical density of titanium).

$$P = \frac{1-\rho}{\rho_s} \times 100 \quad (1)$$



Optical microscope (OM), scanning electron microscope (SEM) (Geol JSM 6060LV), SEM (IXRF 5000EDX) and X-ray diffraction (XRD) (XRD) (RIGAKU D / Max 2200) were utilized for observing the microstructure, composition, porosity and distribution of the samples.

Hardness measurements of the test specimens related to Binder Jetting and Conventional Powder Metallurgy method via Vickers (HV0.2) technique (Wilson 402 MVS) for each test samples were analyzed. The hardness level was calculated with the mean of the measurements. Zwick-Roell (Z50, USA) has conducted compression tests. For each sintering temperature, 2 compression tests have been performed to use in the center.

3. Results and Discussion

The theoretical density of pure titanium is 4.51 g / cm³. The density and porosity measurements of the test specimens produced by Binder Jetting and Conventional Powder Metallurgy method are

exhibited in Table 1 and Table 2. Meanwhile the gap forming and binder are used in production, the density values of Ti parts are lower than the theoretical values. The relative density of the parts formed by the Binder Jetting method varies between 74.73% and 89.97% depending upon the sintering temperature. The relative density of the parts formed by conventional Powder Metallurgy ranged from 60.75% to 66.55%. When density values are examined, the density of Ti pieces produced by both methods increases with increasing temperature. When the SEM images shown in Figure 4 and Figure 5 are studied, it is observed that the porosity size of the samples produced by the Binder Jetting method is smaller and more homogeneous. As the sintering temperature increases, it is realized that the porosity size of the specimens fabricated by both methods increases. It is possible owing to the increase in temperature and the convergence of the grains and cavities and then the merging.

Table 1. Density values of specimens sintered at several temperatures.

Sintering Temperature (°C)	Conventional Powder Metallurgy		Binder Jetting Method	
	d (g/cm ³)	d (%)	d (g/cm ³)	d (%)
1200	2,77	60,75	3,41	74,73
1300	2,99	65,54	3,89	85,23
1400	3,04	66,55	4,10	89,97

Table 2. Porosity values of sintered specimens at several temperatures.

Sintering Temperature (°C)	Porosity	
	Conventional Powder Metallurgy	Binder Jetting
1200	33,45	25,27
1300	34,46	14,77
1400	39,26	10,04

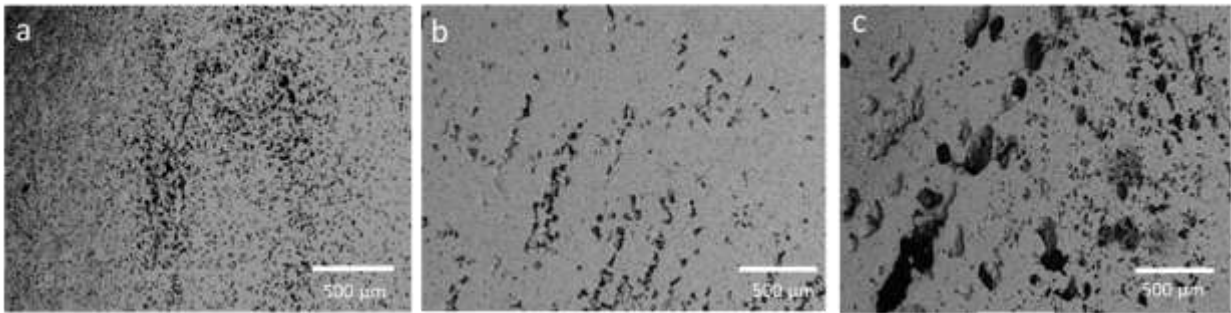


Figure 4. SEM images of test specimens produced by Binder Jetting Method a) 1200 °C b) 1300 °C c) 1400 °C

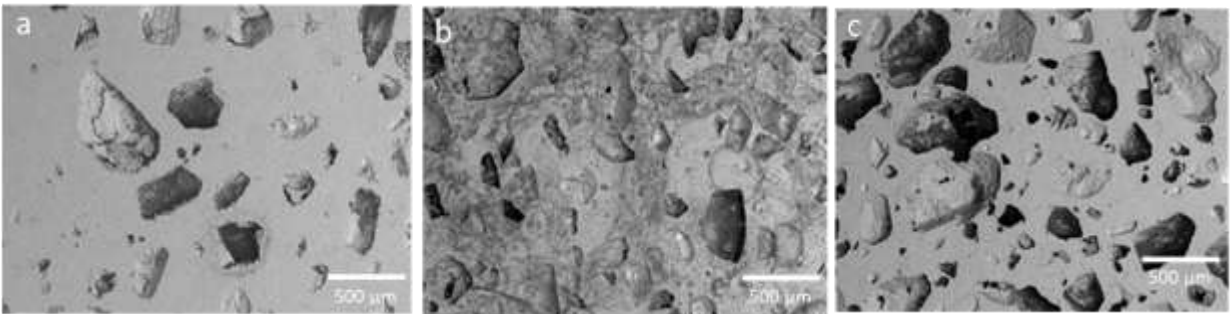


Figure 5. SEM images of test specimens produced by Conventional PM a) 1200 °C b) 1300 °C c) 1400 °C.

The hardness measurements of the specimens fabricated via both methods and sintered at various temperatures are illustrated in Figure 6. As the sintering temperature increases, it is observed that the hardness values of the specimens fabricated by both methods increase. The hardness value of Ti

parts varies depending on sintering temperature and the hardness of Ti parts increase as the sintering temperature raise from 1200 to 1400 °C [16]. It is thought that hardness increases with increasing density and grain size with increasing sintering temperature.

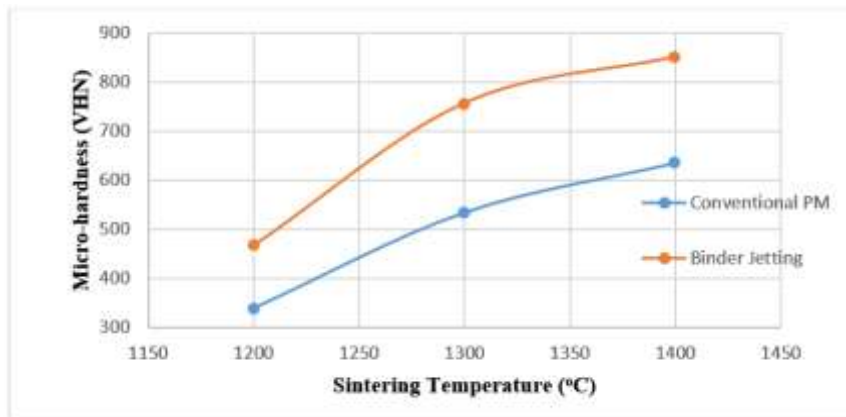


Figure 6. Vickers Micro-Hardness Values Graph.

Table 7 shows the compressive strength test result of Ti samples sintered at different temperatures. As seen in the table, the compressive strength increases with increasing sintering temperature. Sintering temperature increased from 329 MPa to 1025 MPa by increasing the sintering temperature from 1200 °C to 1400 °C. The compressive strength of the parts produced by conventional powder metallurgy increased from 248 MPa to 532

MPa. As the sintering temperature increases in the parts produced by both methods, compressive strength increases. Since the density of the samples produced by conventional powder metallurgy is lower, lower compressive strengths were obtained compared to the samples produced by Binder Jetting method. As a result, it has been found that compressive strength increases due to increase of sintering temperature and density.



Table 3. Compression Test Results

Method	Sintering Temperature (°C)	Yield Strength (MPa)	Ultimate Yield strength (MPa)	Strain (%)	Young modulus (GPa)
Binder Jetting	1200	329	384	5	4,39
	1300	651	685	2	4,95
	1400	1025	1085	4	5,63
Traditional Powder Metallurgy	1200	248	258	1	3,33
	1300	469	479	1	4,64
	1400	532	535	2	4,95

4. Conclusion

- Comparing SEM images of additive manufacturing and conventionally produced samples, it was seen that additive manufacturing samples had a more homogeneous structure.
- As the sintering temperature increases, a better thermal bonding is provided. As a result of this, less wear has been seen with the increase of the strength of the sample and the wear scar depth has decreased.- The abrasion resistance of the porous parts after sintering affects the pore size and shape.

REFERENCES

- [1] E. Yılmaz, A. Gökçe, F. Findik, H. O. Gulsoy, and O. İyibilgin, "Mechanical properties and electrochemical behavior of porous Ti-Nb biomaterials," *Journal of the Mechanical Behavior of Biomedical Materials*, vol. 87, no. May, pp. 59–67, 2018.
- [2] H. Attar *et al.*, "Mechanical behavior of porous commercially pure Ti and Ti-TiB composite materials manufactured by selective laser melting," *Materials Science and Engineering A*, vol. 625, pp. 350–356, 2015.
- [3] C. Domínguez-Trujillo *et al.*, "Bioactive coatings on porous titanium for biomedical applications," *Surface and Coatings Technology*, vol. 349, no. May, pp. 584–592, 2018.
- [4] Q. Han, C. Wang, H. Chen, X. Zhao, and J. Wang, "Porous Tantalum and Titanium in Orthopedics: A Review," *ACS Biomaterials Science and Engineering*, vol. 5, pp. 5798–5824, 2019.

Acknowledgement

Thanks to BIMAS-RC due to provision of laboratory facilities and Sakarya University due to financial support within the international bilateral Mevlana project (Project Number: MEV-2018-644) between Pakistan and Turkey. This study was supported by the Sakarya University Scientific Research Projects Foundation with projects numbered as 2017-50-01-044 and 2017-50-01-045.

- [5] X. Rao, C. L. Chu, and Y. Y. Zheng, "Phase composition, microstructure, and mechanical properties of porous Ti-Nb-Zr alloys prepared by a two-step foaming powder metallurgy method," *Journal of the Mechanical Behavior of Biomedical Materials*, vol. 34, pp. 27–36, 2014.
- [6] L. C. Hwa, S. Rajoo, A. M. Noor, N. Ahmad, and M. B. Uday, "Recent advances in 3D printing of porous ceramics: A review," *Current Opinion in Solid State and Materials Science*, vol. 21, no. 6, pp. 323–347, 2017.
- [7] L. Yuan, S. Ding, and C. Wen, "Additive manufacturing technology for porous metal implant applications and triple minimal surface structures: A review," *Bioactive Materials*, vol. 4, no. 1, pp. 56–70, 2019.
- [8] A. Mostafaei *et al.*, "Binder jetting: A review of process, materials, and methods," *Materials Science and Engineering C*, vol. 83, no. December 2018, pp. 781–801, 2019.
- [9] H. Kim, Y. Lin, and T. L. B. Tseng, "A review on quality control in additive manufacturing," *Rapid Prototyping*.



- [10] *Journal*, vol. 24, no. 3, pp. 645–669, 2018.
- [11] A. W. Gebisa and H. G. Lemu, “Investigating effects of Fused-deposition modeling (FDM) processing parameters on flexural properties of ULTEM 9085 using designed experiment,” *Materials*, vol. 11, no. 4, pp. 1–23, 2018.
- [12] B. Dutta, F. H. Froes, B. Dutta, and F. H. Froes, “Chapter 6 – Markets, Applications, and Costs,” in *Additive Manufacturing of Titanium Alloys*, 2016, pp. 61–73.
- [13] Y. H. Li, N. Chen, and H. L. Zhang, “Powder sintering and characterization of biomedical porous tin alloy,” *Digest Journal of Nanomaterials and Biostructures*, vol. 13, no. 2, pp. 491–498, 2018.
- [14] M. Shahedi Asl, A. Sabahi Namini, A. Motallebzadeh, and M. Azadbeh, “Effects of sintering temperature on microstructure and mechanical properties of spark plasma sintered titanium,” *Materials Chemistry and Physics*, vol. 203, pp. 266–273, 2018.
- [15] Y. Xiong, C. Qian, and J. Sun, “Fabrication of porous titanium implants by three-dimensional printing and sintering at different temperatures,” *Dental Materials Journal*, vol. 31, no. 5, pp. 815–820, 2012.
- [16] B. Arifvianto and J. Zhou, “Fabrication of metallic biomedical scaffolds with the space holder method: A review,” *Materials*, vol. 7, no. 5, pp. 3588–3622, 2014.
- [17] G. Gagg, E. Ghassemieh, and F. E. Wiria, “Effects of sintering temperature on morphology and mechanical characteristics of 3D printed porous titanium used as dental implant,” *Materials Science and Engineering C*, vol. 33, no. 7, pp. 3858–3864, 2013.



Influence of Plain and N₂ purging Conditions on Corrosion Mechanism correlated with Microstructures of Low Alloy Steel Multiphases Weldments

¹Kamran Ghafoor, ¹Riffat Asim Pasha⁺, ²Aneela Wakeel, ²Rizwan Ahmed Malik

¹Department of Mechanical Engineering, University of Engineering and Technology Taxila, Pakistan

²Department of Metallurgy and Materials Engineering, University of Engineering and Technology Taxila, Pakistan

Email: ⁺asim.pasha@uettaxila.edu.pk

Abstract:

The influence of plain and N₂ Purging conditions in plain water and 0.5 NaCl solutions of low alloy steel weldments have been investigated through electrochemical technique. Gas Tungsten arc welding (GTAW) as root / hot pass and submerged arc welding (SAW) as filling / capping was applied to SA 516 (grade 70) steels. To optimize effect of multipass welding cycles on Base Metal (BM), Heat Affected Zone (HAZ) and Weld Zone (WZ) NDT, tensile testing, micro-vicker hardness, optical microscopy, (XRD) X-ray diffraction and potentiodynamic polarization scan was carried out. The attempt is made to correlate the corrosion kinetics with microstructural change in tap water and 0.5 % NaCl solution in both plain and N₂ purging conditions. Due to microstructural changes in Heat affected Zone and Weld Zone the different corrosion behaviors obtained as compared to base metal.

Keywords: Boiler & Pressure vessel steel, Multipass GTAW Welding, HAZ, WZ, Corrosion and Microstructures

1. Introduction

Steels are known as most important materials for structural and other engineering applications owing to their strength, toughness and low-cost as compared to others. Due to variation in cyclic heating and cooling may alter the properties of steel in welding process. Low alloy steels are progressively used in most of the appliances like boiler and bridges, pressure vessels, wind turbine tower, gas pipe lines etc. In the following applications, it is necessary to form solid joints so welding is usually chosen to the other joining processes [1].

Among various arc welding techniques Submerged arc welding (SAW) process is thought to be the best in manufacturer industry owing to its numerous advantages like high production rates, economical, great quality of welds, automation and requiring least operator skill [2]. The mechanisms of welds in SAW are mainly affected by these factors: effect of environmental contamination [3][4][5], transferral of ingredients to or from slag [6][7][8] and dilution of weld pool [9][7][10].

The elevated heat input generates during welding is accompanying by higher temperatures that produces the weld-pool of molten metal. Chemical reactions can stimulate between molten metal and flux at high temperature. These thermal cycles and chemical reactions can cause of stresses, compositional changes and unwanted phase transformation which change the final microstructure and resultant properties of welded joints [11][12][13].

Generally failure of welded components in service is attributed to complex microstructural mechanism of weld zone and Heat Affected zone. This is because of morphologies of the constituents during weld deposit and compositional change. This morphology of microstructural change and compositional dependences of mechanical properties in steel weldments were studied by many researchers [14][15][16][17]. Only fewer literatures are available related to the corrosion behavior of low alloy steel weldments. The heating and cooling cycles induced by the arc in welding process may results in phase transformation in welding regions and influenced the corrosion behavior of material because electrochemical potential difference produced at weld metal sites [18][19][20].

In this research corrosion behavior of low alloy steel plates welded by two different welding processes Gas Tungsten Arc Welding (GTAW) at root / hot and Filling / Capping was done by Submerged Arc Welding was investigated. To evaluate corrosion mechanism different conditions like tap water, 0.5 % NaCl, tap water with Nitrogen (N₂) purging and 0.5 % NaCl with Nitrogen (N₂) purging were employed to Base Metal (BM), Heat Affected Zone (HAZ) as well as Weld Zone (WZ). The obtained results were associated with change in microstructure that developed during high thermal cycles of welding and quantitate phase analysis. The corrosion behavior was simulated by potentiodynamic polarization Tafel scan.



Table 1: welding parameters for GTAW and SAW

Welding Layers	Welding Process	Filler Metal		Shielding		Welding Position	Non Consumable Electrode
		Class	Dia. (mm)	Type	Flow Rate / Composition		
Root	GTAW	ER 70S2	2.5	Argon Gas	7 – 9 L/M	Vertical	(2.4mm) 2% TH
Hot	GTAW	ER 70S2	2.5	Argon Gas	7 – 9 L/M	Vertical	(2.4mm) 2% TH
Filling	SAW	EM 12K	3.2	Flux	F 7A2	Flat	-
Capping	SAW	EM 12K	3.2	Flux	F 7A2	Flat	-

Table 2: Radiography parameters

Parameters	Value
Welding Process	GTAW , SAW
Source	IR 192
Activity	16 CI
OFD (mm)	14
Sensitivity	< 2%
Technique	Double Wall Exposure
Film Type	D-4
Film Brand	AGFA
Reinforcement Thickness (mm)	2
Source Size	3x1.8
Screen	Pb
SOD (mm)	286
Density Range	2-4
Exposure Time	5 min
Reference standard	ASME V
Acceptance Standard	ASME Sec IX

2. Experimental

2.1. Base Material and welding process:

Base metal in this investigation was Low carbon steel ASTM A516 (Grade 70) used. Two plates of size (300x150x12) mm were cut from a sheet for welding.

In this research work V groove with 35° was prepared so the welding should be completed in number of passes to ensure full penetration. The V type butt joint was chosen with the root face of 1.5 – 2 mm and root opening of 3 mm. All the edges were thoroughly cleaned to avoid any contaminants i.e. dust, rust, scale and moisture.

After tacking the plates together the root and hot pass were applied by GTAW process. Similarly filling and capping were done by using submerge arc welding according to welding parameters mentioned in table 1. The specimens were not subjected to any pre or post weld heat treatment. GTAW processing was carefully done manually so that readings can be obtained at each welding cycle to calculating heat inputs. Most importantly in this work all the best welding practice used which is available in fabrication industry.

Joints were visually inspected after each welding cycle to ensure their quality and to maintain good geometrical consistency throughout welding beads.

2.2. Destructive and Non Destructive Testing:

Radiography was carried out using ASTM E 1032-12 to examine the quality of weld [21]. The parameters of radiography were mentioned in table 2. Results concluded that radiography was satisfactory.

Tensile test was carried out to inspect mechanical properties of welded plate by follow ASTM E-8M standard [22]. Tensile Test was conducted at a loading rate of 0.1 mm/sec using an Instron Universal Testing machine (Load Frame 5589). For welded plate three specimens were tested at room temperature with 48 % humidity and the mean values of the properties was reported.

Polished specimens were used for hardness measurements with Vickers Micro-hardness Tester. Transverse portions from Base Metal (BM), Heat Affected Zone (HAZ) and Weld Zone (WZ) were tested on the load of indentation 200 g for 15 seconds.



2.3. Sample preparation for metallography:

Transverse cross sectional Metallographic samples were cut with EDM wire cutting and prepared according to ASTM E-3 in order to determine the microstructural phase changes under optical microscopy. Grinding and polishing was done with 100, 220, 320, 400, 500, 1000, 1200 silicon carbide papers and diamond paste. Etching was carried out in 2 % Nital solution with exposure time of 15 s.

2.4. XRD analysis:

X-ray diffraction was performed on Weld Zone (WZ), Base Metal (BM), and Heat Affected Zone (HAZ) for qualitative phase analysis. The X-ray diffraction samples were obtained by EDM wire cutting. Joel X-ray diffractometer was used for XRD analysis.

2.5. Sample preparation for corrosion Analysis:

To investigate corrosion behavior of BM, WZ and HAZ the cross sectional surfaces towards welding of the specimens were selected. Each specimen was first ground from 100 to 1000 grit silicon carbide paper. After that distilled water was used to wash polished specimens and rinsed by using acetone for electrochemical testing. Before start of the test each specimen was soldered with copper wire covered with glass tube from the back and mounted in silica gel, leaving an exposed area of 1.6 cm².

2.6. Electrochemical measurements:

Potentiodynamic polarization was used in this research to obtain the parameters of corrosion kinetic for all the samples (Base Metal, Heat Affected Zone

and Weld Zone). The tests were performed in water consists of 269 ppm Total dissolved solids (TDS) and 15 ppm Chloride (cl) under tap water and 0.5 % NaCl as well as with plain and N₂ purging conditions. The Gamry Potentiostat (PC/750) equipment was used in this research. The electrochemical cell containing graphite rod and standard calomel electrode as counter electrode and reference electrode similarly. The potentiodynamic patterns were attained at a scanning rate of 1 mV/s (range of -250 - +250 mV) vs. Open Circuit Potential (OCP). Within the period of 10 s the OCP (Open Circuit Potential) was observed before the start of the electrochemical measurements.

3. Results and Discussion:

3.1. Base Metal Chemical Composition and weld parameters:

Base Metal (BM), Weld Metal (WM) and Filler Metal (FM) chemical compositions are given in table 3. From the result shown in table 3, carbon is present at different levels in base metal and filler metal hence the change in carbon content of the weld metal is ascribed to dilution of electrode which depends upon heat input. The reduction in carbon contents in weld metal will reduce the carbides formed similar findings were reported by Y-Yang [23].

The mechanical properties and microstructures of weldments can be altered by the function of heat input which is the energy transfer per unit length of weld. Heat input is typically calculated and reported in table 4 as follows:

$$H = [60 \times E \times I] / 1000 \times S$$

Where H = Heat Input (kJ/mm), E = Arc Voltage (Volts), I = Current (Amps) and S = Travel Speed (mm/min) [24][25][26][27].

Table 3: Chemical Composition of BM, WM and filler metal

Chemical Composition	C (wt %)	S (wt %)	P (wt %)	Si (wt %)	Mn (wt%)	Fe (wt %)
Base Metal	0.189	0.002	0.016	0.343	1.123	Balance
Weld Metal	0.12	0.0079	0.012	0.75	1.63	Balance
Filler Metal	0.08	0.011	0.012	0.47	1.48	Balance

Table4: Weld parameters and heat input

Welding Layers	Welding Process	Current		Volt Range	Range of Travel Speed (mm/min)	Heat Input (kj/mm)
		Polarity	Ampere			
Root	GTAW	DCEN	82-105	17 Max	60-80	1.33
Hot	GTAW	DCEN	90-118	18 Max	65-95	1.34
Filling	SAW	DCEP	450-510	31-33	350-450	2.24
Caping	SAW	DCEP	470-550	31-33	350-450	2.42



3.2. Tensile and hardness Properties:

Table 5 shows the vicker microhardness values and tensile properties. From the results it can be seen that the base metal has the lowest value of hardness as compare to weld interface, weld zone and heat affected zone. The tensile strength of the welded specimens was

more than the base metal which is evidence of quality weld.

3.3. Microstructures:

Figure 1 showing a polished and etched typical microstructure on different magnification of Base Metal. From the microstructure of BM it is clearly seen that it consist of primarily equiaxed polygonal ferrite (white) and perlite (Black) along with the rolling direction.

Table 5: Tensile and hardness values.

Yield strength (MPa)	UTS (MPa)	Elongation (%)	Microhardness at base metal (HV)	Microhardness at HAZ (HV)	Microhardness at Weld Interface (HV)	Microhardness at Weld zone (HV)
354.95	491.98	26.00	172	201	218	197

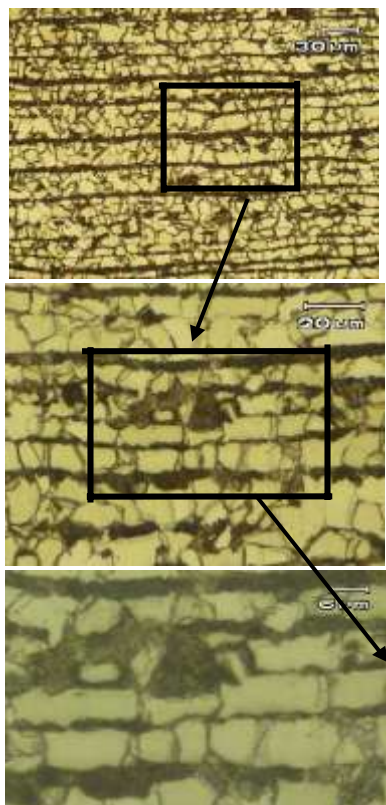


Figure 1: Typical optical Microstructures of the base metal showing polygonal ferrite and perlite.

Complex mixtures of microstructural constituents are produce as a result of welding. During welding process comparative proportion and

morphologies of complex constituents extremely influence on the weld deposit properties [20]. The main microstructural constituents identified in typical Weld Zone are proeutectoid ferrite on grain boundary, secondary Widmanstatten side plate ferrite having wedge shape and inter-granular acicular ferrite. As a result of welding Widmanstatten ferrite originated from the typical microstructure of upper bainite inside the grain, known as allotropic acicular ferrite and formed by para- equilibrium austenite grains transformation. The microstructure of Weld Zone is shown in figure 2. During cooling of low alloy steel weldments as austenite transformation Widmanstatten ferrite is the most common phase observed. [20][28][29][30].

To support the microstructural results, XRD quantitative phase analysis was carried out Table 6 shows the XRD results which indicate that there was no second phase present or if present that was below to the detection limit.



Figure 2: Micrograph showing weld zone.

Table 6: XRD Results

Specimen	Peak #	$2\theta^\circ$	d-Value (\AA)	(hkl)	Results
Base Metal, Weld Zone and HAZ	01	44.45	2.036	(110)	α -Fe Bcc
	02	64.75	1.438	(200)	α -Fe Bcc
	03	82.05	1.173	(211)	α -Fe Bcc



As the weld bead is covered with the granular flux so the cooling rate of HAZ was very rapid as compare to WZ. This rapid cooling of HAZ results in the transformation of austenite to Widmanstatten ferrite directly at the grain boundaries. Moreover internal structure was replaced by lower bainite and lath like arrangement of acicular ferrite with allotropic ferrite as shown in figure 3.



Figure 3: microstructure of HAZ.

Table 7: Potentiodynamic Polarisation parameters

Specimen	E_{oc} (mV)	E_{corr} (mV)	I_{corr} (μ A)	β_a (V decade)	β_c (V decade)	CR(Tafel) (mpy)
Plain water						
BM	-747.3	-750.0	5.320	86.60e-3	219.8e-3	1.520
HAZ	-678.2	-744.0	8.230	92.60e-3	269.7e-3	2.349
WZ	-719.5	-716.0	10.70	82.40e-3	318.6e-3	3.069
Plain water with N2 Purging						
BM	-746.5	-771.0	7.390	116.6e-3	211.7e-3	2.112
HAZ	-726.2	-792.0	10.00	195.5e-3	260.4e-3	2.860
WZ	-739.4	-785.0	16.00	414.4e-3	339.4e-3	4.571
Plain 0.5% NaCl Solution						
BM	-735.5	-781.0	9.360	76.70e-3	226.0e-3	2.673
HAZ	-737.7	-810.0	8.250	168.1e-3	133.4e-3	2.357
WZ	-721.3	-719.0	22.90	71.30e-3	382.2e-3	6.535
0.5% NaCl with N2 Purging						
BM	-704.6	-783.0	16.90	132.9e-3	110.1e-3	4.824
HAZ	-779.5	-801.0	19.20	188.1e-3	187.5e-3	5.483
WZ	-779.9	-795.0	23.30	396.2e-3	349.9e-3	7.108

3.4. Corrosion

Before the start of polarization scan (OCP) open circuit potential of base BM, HAZ and WZ was measured in both plain and N2 purging conditions. The trend of open circuit potential is shown in figure 4 which indicates that the HAZ and WZ are nobler (more positive) in plain water and plain salt solution as compared to the both purging conditions and the difference in OCP is attributed to the different chemical composition of filler wire.

Figure 5 represents the variation in corrosion potential E_{corr} . It can be seen from the figure that weld zone are more negative in N2 purging conditions as compare to the plain conditions. Similarly the potential of HAZ in 0.5 NaCl is more negative than the plain water.

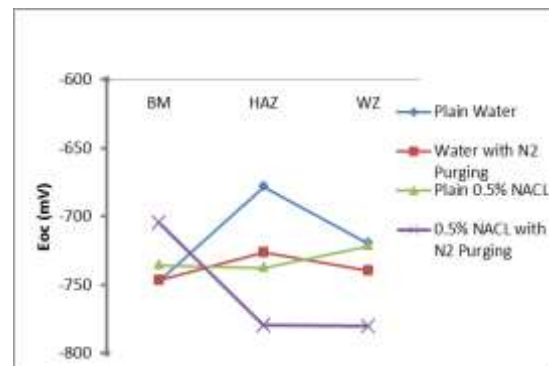


Figure 4: Open Circuit Potential (OCP) variations under different Condition

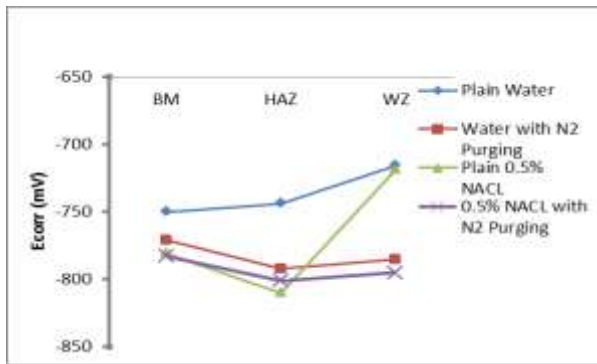


Figure 5: Corrosion potential variations under different conditions

The electrochemical behavior of BM, HAZ and WZ was evaluated separately in tap / ordinary water and 0.5 % NaCl solution in both plain and N₂ purging conditions. The potentiodynamic polarization curves of BM, HAZ and WZ in water under plain and N₂ purging conditions are given in figure 6. The potentiodynamic polarization curves of BM, HAZ and WZ in 0.5 % NaCl solution under plain and N₂ purging condition are given in figure 7. The potentiodynamic polarization parameters gathered from the curves are represented in table 7. From the observation of results it can be see that the corrosion potential of BM, HAZ and WZ in plain water is nobler than the corrosion potential of water with N₂ purging. Similar observations are recorded in plain 0.5 % NaCl solution with N₂ purging. Higher the value of β_c represents the diffusion controlled oxygen reduction reaction. Moreover except NaCl with N₂ purging conditions all the conditions suggesting that the corrosion current of HAZ is more than its base metal similar finding were reported in literature [31][32]. The variation in cathodic appearances among the BM, HAZ and WZ as in figure

6 and 7 may explain the local cathodic / anodic behavior of low alloy steel weldments.

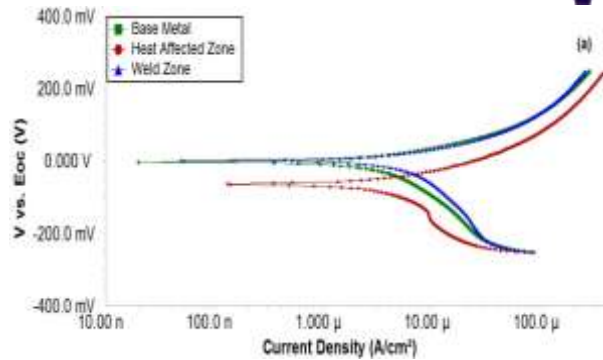


Figure6: Potentiodynamic Polarization Scan in water under (a) Plain (b) N₂ Purging conditions

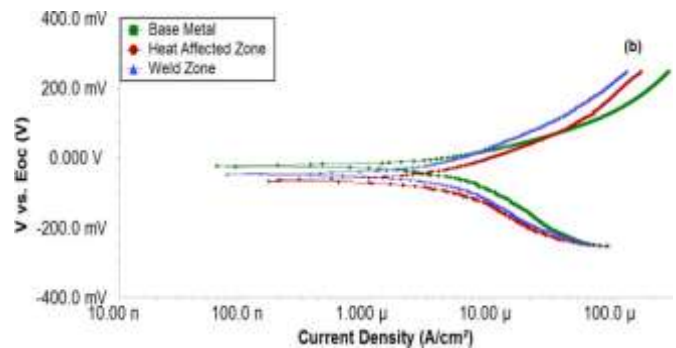


Figure7: Potentiodynamic Polarization Scan in 0.5 % NaCl solution in (a) Plain and (b) N₂ purging conditions



3.5. Influence of Microstructure on corrosion behavior:

From figure 1 the microstructure of base metal showing perlite relates to higher corrosion resistance. The coarsening of Widmanstatten ferrite in HAZ from base metal is one of the main reason of large corrosion current in plain water and 0.5 % NaCl solutions with both plain and N₂ purging conditions. The difference in microstructures will influenced the corrosion behavior and is still not well known specially between acicular ferrite and grain boundary ferrite of weld zone. The presence of acicular ferrite and grain boundary ferrite in WZ as shown in figure 2 indicates the grain boundary ferrite is more corrosion resistant than the acicular ferrite in such environments. The microstructure WZ comparatively higher volume of acicular ferrite which allied higher imperfection results in speed up the rate of localized oxygen reduction reaction. Similar phenomenon investigated by Her-Hsiung et al [32].

4. Conclusions

Joining of SA 516 grade 70 with GTAW as root/ hot pass and SAW as filling / capping can be done with overmatching strength level. The N₂ purging conditions both in water and saline environment accelerate corrosion damages. The base metal is more corrosion resistance than HAZ and HAZ is more corrosion resistance than WZ. The grain boundary ferrite and Widmanstatten side plate ferrite is more corrosion resistant than acicular ferrite. As a result the presence of acicular ferrite in weld zone shows higher corrosion rate in weld zone as compare to Base metal and Heat Affected Zone in water and 0.5 % NaCl solution both in plain and N₂ purging conditions.

REFERENCES

1. Bhadeshia H. D. K. H., 1985 Structural Steels for the 1980s. United Kingdom: University of Cambridge,.
2. Brien RLO, 1995 Welding handbook, 8th ed.: AWS,.
3. Coe F.R. Davis M.L.E., 1977 "The Chemistry of Submerged Arc Welding Fluxes," The Welding institute London, London, The Welding Institute Research Report 39/1977/M, May.
4. Eagar T.W., Chai C.S, 1982 "Slag metal reactions in binary CaF₂—metal oxide welding fluxes," Welding J, vol. 16, no. 7, pp. 229–232,.
5. . Eagar T.W, 1978 "Sources of weld metal oxygen contamination during submerged arc welding," Welding J, vol. 57, no. 3, pp. 76–80,.
6. S. Liu, D.L., Dallam C.B, 1990."Flux composition dependence of microstructure and toughness of submerged arc HSLA weldments," welding J, vol. 64, no. 5, pp. 140–151, 1985.
7. Indacochea J.E., Olson D.L, Burck P.A., "Effects of welding flux additions on 4340 steel weld metal composition," Welding J, vol. 3, pp. 115-122,
8. Eagar T.W, Mitra U. 1984, "Slag metal reactions during submerged arc welding of alloy steels," Metall. Trans, vol. 15 A, pp. 217–227,.
9. Bailey N., Davis M.L.E., April 1980 "How submerged arc flux composition influences element transfer," in International conference on Trends in steels and consumables for welding, The Welding Institute, London, , pp. 289–310.
10. Blander M., Indacochea J.E. June 1985.
- 11., "Chemical reactions during submerged arc welding with FeO– MnO–SiO₂ fluxes," Metallurgical Trans, vol. 16B, pp. 237–245,.
G. M. Evans and N. Bailey, Metallurgy of Basic Weld Metal. United Kingdom: Abington Publishing, Cambridge, 1999.
12. Colvin and G. Kraus S. W. Thompson, D. J. 1996 "Austenite Decomposition During Continuous Cooling of an HSLA-80 Plate Steel," Metallurgical and Materials Transaction, vol. 27A, no. 6, pp. 1557-1571,
13. Honeycombe R. W. K. and Bhadeshia H. K. D. H. 1996, Steels Microstructures and properties, 2nd ed. UK: Edward Arnold,.
14. Farrar R. A., Taylor L. G., and Harrison E. M., 01 January 1979.
15. "Effect of stress relieving on fracture properties of submerged-arc welds of C–Mn steels," Metals Technology, vol. 6, no. 1, pp. 380-390,
16. EVANS G. M., April 1982 "The Effect of Heat Input on the Microstructure and Properties of C-Mn All-Weld-Metal Deposits," WELDING RESEARCH SUPPLEMENT, vol. WRC Bulletin 274, pp. 125-132,.
17. Dallam C. B., 1 May 1985. "Flux compositional dependence of microstructure and toughness of submerged arc HSLA weldments," AMERICAN WELDING SOCIETY Welding journal , pp. 140 - 152,
18. BANGARU N. V. FAIRCHILD D. P., DECEMBER 1991 "A Study Concerning Intercritical HAZ Microstructure and Toughness in HSLA Steels," American Welding Society and the Welding Research Council, pp. 321 - 330,.
19. Gooch TG, 1982 "The effect of welding on corrosion. Process industry corrosion," NACE publication, pp. 739–55,.
20. Linnert GE, 1994 Welding metallurgy. Carbon and alloy steels, 1st ed. Florida, USA: AWS,.
21. Ahmad R., Khan I.H, Farahat Z., Deen K.M, jan 2010. "Microstructural study and electrochemical behavior of low alloy steel weldment," Materials & Design, vol. 31, pp. 3051–3055,
22. 2006, ASTM 1032-06 Standard Test Method for Radiographic Examination of Weldments, ASTM International.



23. ASTM, Standard Test Methods for Tension Testing of Metallic Materials E 8M , 2004, ASTM International, 100 Barr Harbor Drive, PO Box C700, West Conshohocken, PA 19428-2959, United States.
24. Yang Y, 2008."The Effect of Submerged Arc Welding Parameters on the Properties of Pressure Vessel and Wind Turbine Tower Steels," Canada, Saskatoon, MSc. Thesis
25. Pawan Kumar, April 2011 "Process Parameters Optimization of an Aluminium Alloy with Pulsed Gas Tungsten Arc Welding (GTAW) Using Gas Mixtures," Materials Sciences and Applications, vol. 2, pp. 251 - 257,.
26. 2010. ASME section IX 2010 boiler and pressure vessel code. New York, USA: ASME an international codes , Linnert G.E.,: American Welding Society, 1994, pp. 667 - 693.
27. Raouf A. H., Mehdi ., N. P, Gharibshahiyan R. E., 2011."The effect of microstructure on hardness and toughness of low carbon welded steel using inert gas welding," Material & Design, vol. 32, pp. 2042–2048,
28. Oguocha I. N. A. and Yannacopoulos S. , Amanie , March 2012. "Effect of submerged arc welding parameters on microstructure of SA516 steel weld metal," Canadian Metallurgical Quarterly, vol. 15, no. 1, pp. 48 - 57,
29. Natarajan S. , Kumaresh S.P. ,Babu, 13 May 2008 "Influence of heat input on high temperature weldment corrosion in submerged arc welded power plant carbon steel," Material & Design, vol. 29, pp. 1036–1042,.
30. Juan L.Y.W., 2003.
31. "Microstructure characterization in the weld metals of HQ130 + QJ63 high strength steels ," Bulletin of Materials Science, vol. 26, Luft H.B., Degeer D., Voruganti V.S., 1991 "Scanning Reference Electrode Technique for the Investigation of Preferential Corrosion of Weldments in Offshore Applications," Corrosion, vol. 47, no. 5, pp. 343-351,., no. 3, pp. 295-299,
32. Tsai W.T. , Huang H.H., 1994. "The Influences of Microstructure and Composition on the Electrochemical Behaviour of A516 Steel weldments," Corrosion science , vol. 36, no. 6, pp. 1027- 1038,



Development, up-gradation and maintenance of engineering laboratories for teaching and research in the universities of developing countries

Wasim Ahmad (wasim@giki.edu.pk)

Abstract:

Due to rapid change in technology, universities of developing countries are not able to maintain/develop state of the art laboratories due to high capital cost. Keeping in mind the financial constraints of these countries, the in-house development of computer numerical control (CNC) machines prototypes was carried out and presented in this work. Three CNC prototypes machines, CNC milling machine (MM), CNC turning machine (TM) and CNC engraving machine (EM) have been developed and tested. The development of CNC milling machine is presented in detail with mechanical, electronics, control and the software aspects. Similar procedure has been adopted for the development of CNC-turning and CNC-engraving machines, which are briefly discussed. The in-house developed prototypes machines have been added to other equipment already available in CNC training laboratory at Ghulam Ishaq Khan (GIK) Institute of Engineering Sciences and Technology. The proposed methodologies are now been used for teaching and research activities in low cost development of state of art technologies.

Key Words: Laboratory development; In-house development; Computer numerical control machines; ISO 6983-1:2009

1 Introduction

Additive Manufacturing (AM) first commercial In undergraduate and postgraduate engineering programs, laboratories play an important role [1]. Technology is changing at a rapid pace and it affects almost every part of our lives including engineering education [2]. Specifically, the electronics and computer part of the laboratory equipment has been affected due to this change. Almost every theoretical subject has a laboratory session [3-5]. Also, as the research activities accelerate the demand of engineering laboratories increases to produce accurate and timely results at a reduced cost. The ability to adopt new technologies is becoming a vital factor for the developing countries like Pakistan. However, the engineering institutes procure these laboratories by spending huge amount of their budget so that advance technologies can be taught to the students. Such equipments are expensive, difficult to import, and; difficult to maintain due to limited after sales services available. These equipments are essentially black box for engineering institutes of developing countries, where a graveyard of such machines can easily be found in the laboratories of these countries. It is therefore becoming imperative that for the teaching and research activities a development, up-gradation, and maintenance program is needed [6].

Similar conditions as mentioned above happened to the CNC laboratory at Faculty of Mechanical Engineering (FME) in GIK Institute. The CNC laboratory at FME was developed in 1996. Various CNC machines including milling (DENFORD, EMCO and Spectralight) and turning (DENFORD, EMCO and Spectralight) were imported at a huge cost to this laboratory. At that time all the machines were working smoothly, and the faculty was able to perform teaching and research activities. With the passage of time, as the technology changed the subject laboratory became outdated and, in many cases, non-functional without the support of overseas vendors. It was not feasible for the institute to again spend a huge amount and import new machines. Therefore, the in-house development in the subject laboratory has been started. The main objective of this development to design and fabricate new CNC prototypes which will be synchronized with the latest technology that will be used for research and teaching activities.

In this work, low cost CNC machines prototypes such as CNC Milling Machine (CNC-MM), CNC Turning Machine (CNC-TM) and CNC Engraving Machine (CNC-EM) have been developed which is an addition to the already present equipment in Computer Numerical Control (CNC) laboratory at Faculty of Mechanical Engineering (FME),



Ghulam Ishaq Khan (GIK) Institute of Engineering Sciences and Technology as shown in Figure 1.



Fig. 1. CNC laboratory in FME at GIK Institute of Engineering Sciences and Technology

2 CNC Milling Machine

The idea behind the development of low-cost CNC-MM is to full fill the demand of milling processes of CNC laboratory. The CNC-MM developed in this work is now used by the undergraduate students for the basic CNC experiments and for the milling of high density foam, wood or aluminum alloy parts. The development process of CNC-MM has been divided into three main domains; the mechanical domain, electronics & control domain and the software domain.

2.1 Mechanical domain

The design of the mechanical system is carried out in a way to attain the motion in three axis using power screws and guide rods. In each axis, a separate stepper motor is attached to generate motion in the respective direction in accordance with the control signal generated from microcontroller and transmitted through the electronic circuit. Hence, for the milling process to be carried out smoothly on the work piece, the speed and movement of the tool spindle attached to the end effector is controlled in each direction. The stepper motors are responsible to drive each axis. To select the appropriate stepper motors, torque calculation was performed. The torque required to rotate power screw is given as [7]:

$$T_r = \frac{F \cdot d_m}{2} \left(\frac{l + \pi f d_m}{\pi d_m - f l} \right) \quad (1)$$

Where T_r is the required torque, F is the load on power screw, d_m is the mean diameter of the power screw, l is the lead of power screw and f is the friction coefficient. The power screw is single threaded so lead l will be equal to the pitch of screw. A thrust bearing is installed to give support to the power screw. As cutting forces act in all directions so, axial forces will act on the power screw and on bearing. Torque required to overcome collar friction is as follows [7].

$$T_c = \frac{F \cdot f_c \cdot d_c}{2} \quad (2)$$

Where f_c is the collar friction, d_c is the mean collar diameter which can be calculated as [7]:

$$d_c = 1.25 d_m \quad (3)$$

So, the Total required torque has been calculated as:

$$T = \frac{F \cdot d_m}{2} \left(\frac{l + \pi f d_m}{\pi d_m - f l} \right) + \frac{F \cdot f_c \cdot d_c}{2} \quad (4)$$

The mechanical design of CNC-MM is shown in Figure 2. The same design has been fabricated in-house.

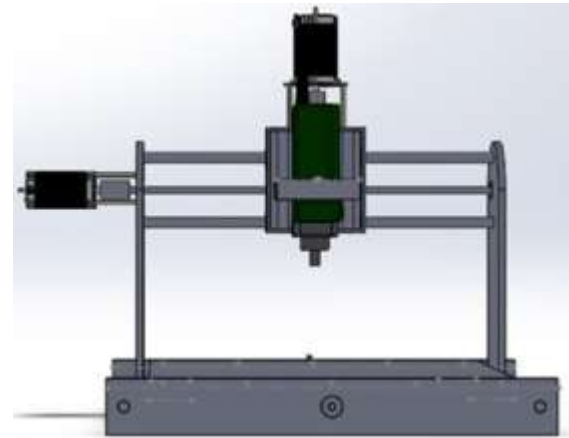


Fig. 2. CAD model of the developed CNC-MM

2.2 Structural Analysis

The structural analysis of the three major components bearing, guide ways and the side plates is performed using off-the-shelf software "ANSYS". The results include both the deformation and the Von Mises stress distribution over the critical components. For bearing both the maximum deformation and stress lies on the inner ring as the maximum load also applies in the radially outward direction. For the guide ways, the



maximum tensile stress lies at the bottom due to bending stresses, and the maximum deformation also lies at the bottom. Whereas the maximum compression stress lies at the top which is approximately equal in magnitude with the tensile one. The side plates, on the other hand, has maximum deformation at the bottom where it is attached to the base. The maximum stress, however, exists at the location where the guide ways passes through it. The maximum deformation and the stress distribution for the bearing, guide ways and side plate are shown in Figure 3.

2.3 Electronics and Control domain

Electronics and control system comprise of a computer, microcontroller (STM-32), stepper motor driver developed in-house, variable frequency drive (VFD) to control the speed of the spindle motor and a power supply. The power supply converts the AC voltage to DC and supplies the required voltages to the corresponding devices as per their requirements. Microcontroller board operates at 5 V whereas the stepper motor board operates at 12 V which are provided by the power supply. The stepper motor driver circuit receive the control signal from the STM-32 which generate the corresponding digital pulse signal for stepper motor and control the rotation of the stepper motor. Electro-mechanical equipment calibration was

performed for precise operation of CNC-MM. The spindle motor speed is controlled through VFD. The complete block diagram of the electronics and control domain is shown in Figure 4.

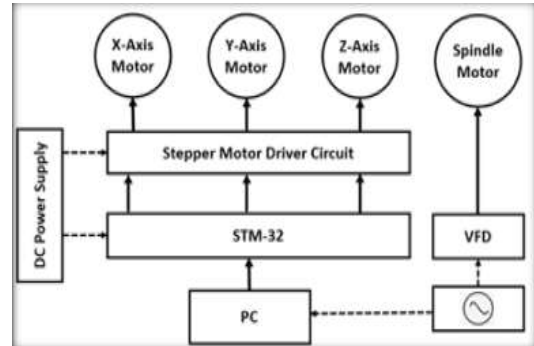


Fig .4. Block diagram of electronics and control system of CNC-MM

The stepper motor driver circuit is designed and fabricated in-house. The schematic diagram of circuit for single axis stepper motor driver is shown in Figure 5. Single axis stepper motor driver contains eight power MOSFETS, out of which Q1, Q2, Q7 and Q8 are P-channel whereas Q5, Q6, Q11 and Q12 are the N-channel. P-channel act as normally open contacts while N-channel operate as normally closed contacts. The four bipolar junction transistors Q3, Q4, Q9 and Q10 can switched on-off with a microcontroller signal through CIN MC1 and CIN MC2. The stepper motor wires are connected with the MC1 and MC2 connectors.

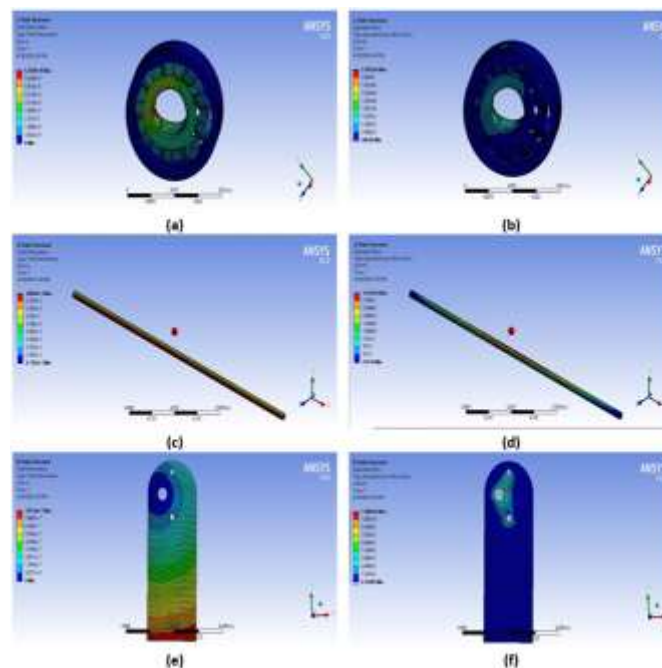


Fig .3. Finite element analysis (a) bearing deformation (b) bearing stress distribution (c) guide ways deformation (d) guide ways stress distribution (e) side plate deformation (f) side plate stress distribution

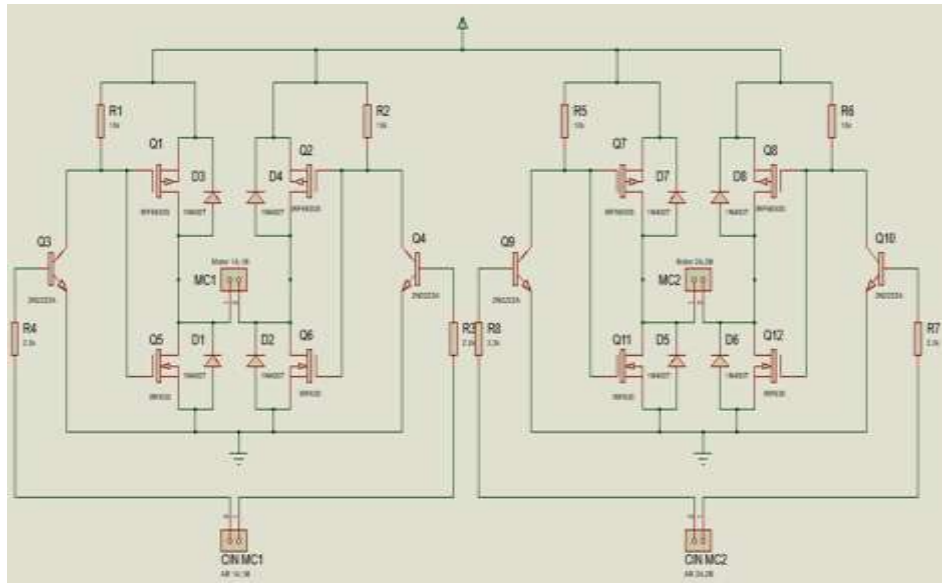


Fig .5. Schematic of one stepper motor driver circuit

Software domain

An interpreter as per ISO 6983-1:2009 standard has been developed that reads the selected G & M codes, interpret them and perform linear/circular interpolation [8-10]. The users will generate the G & M codes file through any CAD/CAM software which is then fed into the interpreter. The interpreter controls the machine tools according to the G & M codes. The developed interpreter is capable of performing linear and circular interpolation. The flow chart for the interpreter logic without error trapping is shown in Figure 6.

Finally, all the three domains developed for CNC-MM have been combined to build the complete CNC-MM. The developed CNC-MM has been shown in Figure 7.

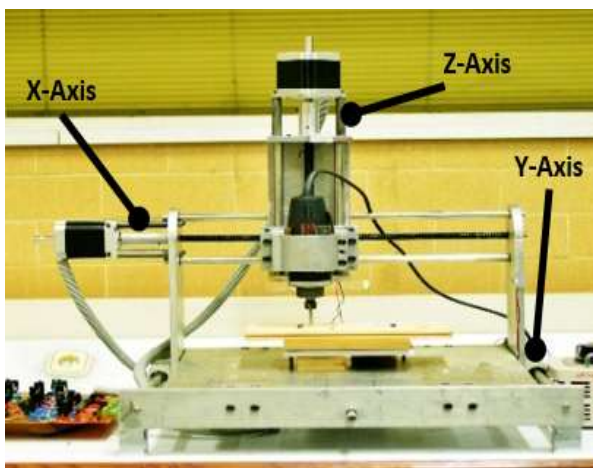
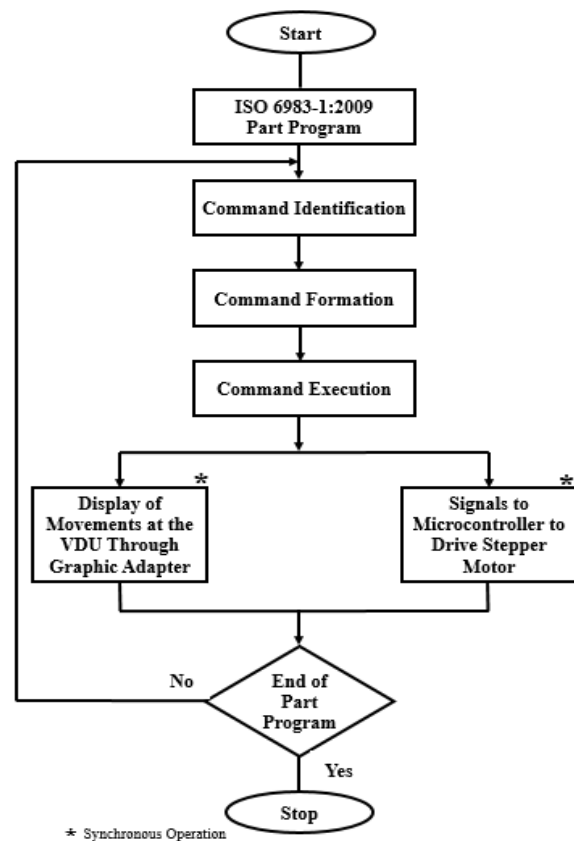


Fig .7. Developed CNC milling machine



* Synchronous Operation
Fig. 6. Flowchart for interpreter logic without error trapping

Testing

The developed CNC-MM has been tested successfully to mill on the wooden work piece. The developed part program (G & M code) are then fed



in to the interpreter developed for the CNC-MM machine. The code generated for the specific shape is shown in Figure 8 (a). The CNC-MM while engraving the specific shape is shown in the Figure 8 (b). The complete milled shape is shown in Figure 8 (c).

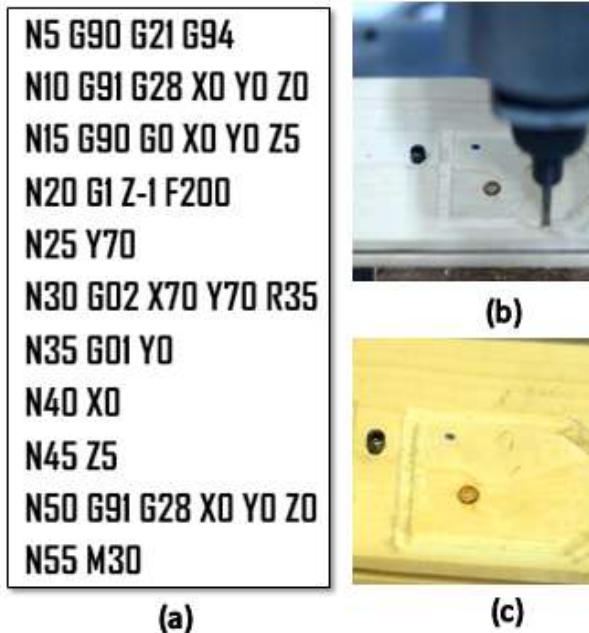


Fig .8. Testing of CNC-MM (a) CNC code for the complete circle (b) wooden work piece clamped in the machine (c) Final milled shape

3 CNC Turning Machine

Design and fabrication of CNC Turning Machine (CNC-TM) was also a part of the development of CNC laboratory. Like CNC-MM the CNC-TM developing process was divided into three domains. The electronics and control domain are the same as that of the CNC-EM machine including the microcontroller i.e. STM-32. In case of CNC-TM only two H-bridges and two stepper motors have been used for the X and Z axes. The interpreter developed for CNC-EM has been modified according to ISO 6983-1:2009 standard. Mechanical domain consists of two axes table; X-Axis Table and Z-Axis Table. Mild steel was procured to fabricate these two plates because it can damp the vibrations better than aluminium. The chuck is securely fixed with a mild steel shaft which is enclosed in mild steel circular housing for proper rotation of the shaft. Double row deep groove ball bearings were fixed in the housing to support the shaft rotating at high RPM. CAD model

and developed prototype of CNC-TM have been shown in Figure 9 (a) and (b) respectively.

4 CNC Engraving Machine

To complete the indigenous manufacturing setup in the CNC lab a CNC Engraving Machine (CNC-EM) has also been developed in-house. The design of CNC-EM is almost similar to the CNC-MM having three axes. The same electronics & control and software setup has been used in the CNC-EM. However, the mechanical system is not similar to the CNC-MM. The proper torque calculation has been done as in the CNC-MM case. Three steppers motors having high torque has been selected. The assembling of the mechanical system is carried out in such a manner that the movement in three axis direction is attained through power screw and guide rods. In each axis the desired motion and speed are achieved with stepper motors through the control signal produced and transmitted by the electronic circuit.

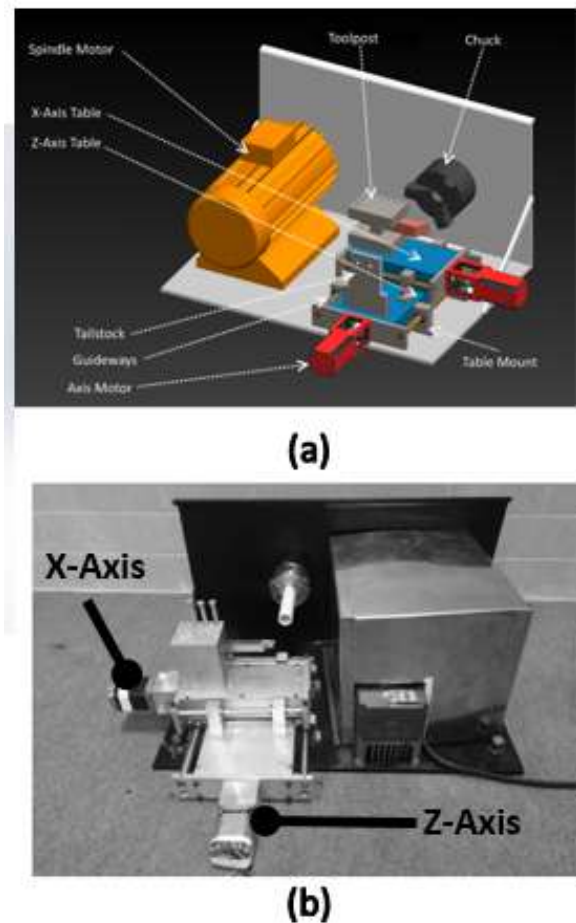


Fig .9. (a) CAD model CNC-TM (b) Develop prototype of CNC-TM

The rotational motion of the stepper motor is converted to linear motion through the power screw



rod and nut arrangement. The desired motion and speed in each direction was attained by controlling the speed and rotation of the stepper motor through the control signal. Hence, for the carving or cutting action to be carried out smoothly on the work piece, the speed and movement of the tool spindle attached to the end effector is controlled in each direction. The complete CAD model and the developed prototype have been shown in Figure 10 (a) and (b) respectively.

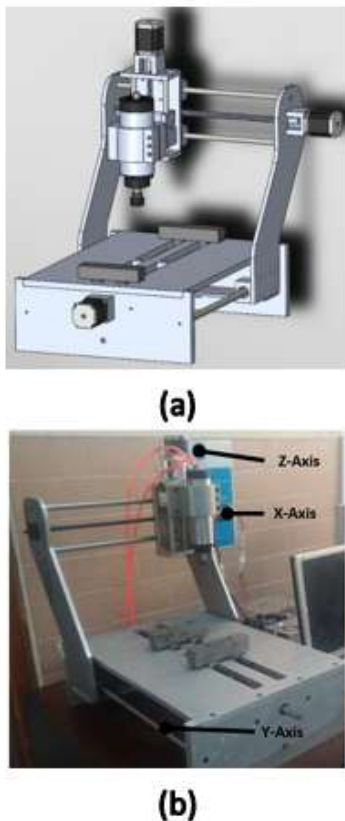


Fig .10. (a) CAD model CNC-EM (b) Develop prototype of CNC-EM

5 Conclusion

Indigenous development and up-gradation of engineering laboratory for teaching and research has been presented in this paper. Three prototypes of CNC machines have been successfully developed and tested. The development of CNC-MM has been discussed in detail i.e. the mechanical domain, electronics & control domain and the software domain. The CNC-MM interprets the G & M codes and executes it successfully through the interpreter developed specially for these machines. The CNC-TM and CNC-EM have also been developed and tested. The development process has been briefly discussed. The newly

developed machines have been added to the CNC laboratory present at the Ghulam Ishaq Khan (GIK) Institute. Since the design and development of these machines is carried out at the GIK Institute, it is very convenient to maintain these machines. The work carried out by the machine tool group at the Faculty of Mechanical Engineering at GIK Institute leads to the development of industrial scale machine. The working of these machines can be seen at the following links.

<https://youtu.be/8M7iXLebeUM>
<https://youtu.be/TQ-I298WAo0>
<https://youtu.be/Toiq8FMROFs>

6 Acknowledgements

The work presented in this paper is funded by the Ghulam Ishaq Khan Institute of engineering sciences and Technology.

REFERENCES

- [1] Khan, W.A., S.M.R. Al-Doussari, and A. Al-Kahtani, Establishment of engineering laboratories for undergraduate and postgraduate studies. *European journal of engineering education*, 2002. 27(4): p. 425-435.
- [2] Millson, M.R., S. Raj, and D. Wilemon, A survey of major approaches for accelerating new product development. *Journal of Product Innovation Management: AN INTERNATIONAL PUBLICATION OF THE PRODUCT DEVELOPMENT & MANAGEMENT ASSOCIATION*, 1992. 9(1): p. 53-69.
- [3] Dym, C.L., et al., Engineering design thinking, teaching, and learning. *Journal of engineering education*, 2005. 94(1): p. 103-120.
- [4] Brophy, S., et al., Advancing engineering education in P-12 classrooms. *Journal of Engineering Education*, 2008. 97(3): p. 369-387.
- [5] Wild, P., Physics or Technology? Technology or Physics? An experiment in curriculum development. *International Journal of Technology and Design Education*, 1991. 1(3): p. 171-175.
- [6] Upadhyaya, B., et al. Development of a Maintenance Engineering Laboratory. in *Proceedings of the 2002 American Society for Engineering Education Annual Conference & Exposition, Montreal, Canada*. 2002.



- [7] Shigley, J.E., Shigley's mechanical engineering design. 2011: Tata McGraw-Hill Education.
- [8] Absar Ahmad, H.A., Saifullah, Hamza Bilal, Wasim A. Khan, Design and Fabrication of Small-Scale CNC Engraving Machine in Faculty of Mechanical Engineering 2016, Ghulam Ishaq Khan Institute of Engineering Sciences and Technology.
- [9] Abubakar Rashid, M.H., Saad Bin Arshad, Zaryab Shahid, Wasim A. Khan, Design and Fabrication of Small Scale CNC Turning Machine in Faculty of Mechanical Engineering 2016, Ghulam Ishaq Khan Institute of Engineering Sciences and Technology
- [10] Adnan Moiz, F.T.S., Muhammad Annas Zakir, Muhammad Zarrar Shakeel, Wasim A. Khan, Design and Fabrication of a Small Scaled Milling Machine, in Faculty of Mechanical Engineering 2016, Ghulam Ishaq Khan Institute of Engineering Sciences and Technology



Functional Reverse Engineering of Machine Tools

Wasim Ahmed Khan

Faculty of Mechanical Engineering

GIK Institute of Engineering Sciences and Technology

Topi-23640, Khyber Pakhtunkhwa, Pakistan

E-mail: wasim@giki.edu.pk

Abstract:

The purpose of this talk is to persuade academia to develop capacity building in strategic and non-strategic machine tool technology, and machinery in other sectors. Strategic machines can produce non-strategic machines and any other discrete product. Nonstrategic machines directly or indirectly produce machines used in production of food, apparel and shelter.

Functional Reverse Engineering of Machine Tools and Equipment is meant for acquiring self-sufficiency in discrete manufacturing sector. The same process is applicable to other sectors as well. Functional reverse engineering is a redesign and manufacturing procedure that does not violate anybody's intellectual property rights and allows incorporation of innovative features making the discrete product under consideration more viable for the client.

Pakistan being one of the Next Eleven emerging markets, requires focus on more exports from the country and lessen the burden of imports. To achieve this and to move on to BRICS nations, the country has to have the capacity to develop machinery in sectors such as machine tools, construction, food processing and packaging, textile, automobiles, home appliances, energy, biomedical engineering etc. The Faculty of Mechanical Engineering at the GIK Institute is fully aware of this necessity and the Machine Tool Research Group at the GIK Institute has spent three years working in this area.

The responsibility of the group is to provide a general model for an enterprise of functional reverse engineering that can generate profit in less focused but advance areas of research and development in the country and share the model with peers working in other sectors.

The work is being done with the support of Directorate of Science and Technology, Department of Science and Technology, Government of Khyber Pakhtunkhwa and GIK Institute.

1. Introduction¹:

The economy of Pakistan is 26th largest in the world in terms of purchase power parity (PPP) and 40th when it comes to nominal gross domestic product. Pakistan has a population of more than 190 million (6th in the world), giving it a nominal GDP per capita of \$1,427, which ranks 133rd in the world. However, when calculating per capita income, Pakistan's undocumented economy is not taken into account which is 36% of its total economy. Pakistan is developing nation and is one of the eleven countries (Next Eleven) along with the BRICs (Brazil India Russia and China), which possesses the potential to become of the world's biggest economies in the 21st century. However, after years of instabilities due to war and social unrest, as of 2016, serious deficiencies in basic services such as urban

transportation; cross country railway transportation; and electric power generation had been developed. The economy is semi-industrialized, with centers of growth along the Indus River. Primary export commodities include textiles, leather goods, sports goods, chemicals and carpets/rugs. Pakistan has to increase the numbers and types of export goods and services and decrease the numbers and types of import commodities. Considering the growth in Higher Education Sector, Functional Reverse Engineering shall play an important role in developing and marketing new products in the areas of machine tools, agriculture, health, water resources development, mining, and; power sector [1].

Promoting enterprises of reverse engineering in the areas of machine tools, agriculture, health, water



resources development, mining and power sector is the basic goal of this scheme. A huge number of other products are also likely to emerge from these fields which can boast Khyber Pakhtunkhwa's economy.

Growth poles of Pakistan's economy are situated along the Indus River; the diversified economies of Karachi and major urban centers in the Punjab, coexisting with lesser developed areas in other parts of the country. The proposed project on functional reverse engineering has the potential to be a preliminary project which can set a healthy platform to change the economic tide of the country and bring Khyber Pakhtunkhwa at the forefront of this engineering revolution [2].

With the help of three types of organizations and their constituents this aim can be achieved. These organizations are: Engineering Education institutions, Research and Development Organizations, and Public and Private Engineering Enterprises. The team undertaking the proposed project has collaborations with all three types of organizations and their constituents. The proposed project will initially aim to establish a mechanism to identify the products in various sectors needing reverse engineering with the potential of sale in local and overseas market. This will yield several benefits, for example, increased manufacturing resulting in economic growth of Khyber Pakhtunkhwa, increased export in developing countries and, more job creation.

Moreover, to further ensure the sustainability of Khyber Pakhtunkhwa's economic activity indigenous expertise in areas of design, prototyping, manufacturing and assembly (Functional Reverse Engineering) will be developed. This will enable the availability of future Human Resources and create more jobs simultaneously.

Most importantly, the team possesses the expertise to transfer technology from academia to industry and training of students as well as engineers and practitioners from participating industry in various sectors identified above.

The province of Khyber Pakhtunkhwa has the 3rd largest economy in the country. Although the province accounts for 11.9% of the total population of Pakistan but its share in the total GDP of the nation comprises of only 10.5% which renders it as

the second poorest province after Baluchistan. The part of the economy that Khyber Pakhtunkhwa dominates is forestry, where its share has historically ranged from a low of 34.9% to a high of 81%, giving an average of 61.56%. Currently, Khyber Pakhtunkhwa accounts for 10% of Pakistan's GDP, 20% of Pakistan's mining output and since 1972, it has seen its economy grow in size by 3.6 times [3].

Agriculture remains important and the main cash crops include wheat, maize, tobacco, rice, sugar beets, as well as various fruits are grown in the province. Some manufacturing and high-tech investments in Peshawar and other industrial estates have helped improve job prospects for many locals, while trade in the province involves nearly every product. The bazaars in the province are renowned throughout Pakistan. Unemployment has been reduced due to establishment of industrial zones [4].

Numerous workshops throughout the province support the manufacture of small arms and weapons of various types. The province accounts for at least 78% of the marble production in Pakistan.

Products from manufacturing (Machine Tools), agriculture, health, water resources development, mining and power sectors are the prime target for Promoting Enterprises of Reverse Engineering Annual Development Program (2016-19). This range from development of machineries and tools, chemical and biological structures in technological sector to enterprise development in service sector in order to promote the outcome of development in technological sector.

2. Functional Reverse Engineering:

Functional Reverse Engineering is a redesign methodology. This means that it is a design process that is applied to an existing product, or at least to a prototype or a detailed concept. It is normally a process that uses a variety of techniques in the form of models, charts, diagrams, guidelines and normative theories to dissect and fully understand a product. Stated concisely, functional reverse engineering ".....initiates the redesign process, wherein a product is observed, disassembled, analyzed, and documented in terms of its functionality, form, physical principles, manufacturability and assemble-ability."



The most important factor in reverse engineering is functional reverse engineering that produces a design that is not an infringement of intellectual property rights. The functional reverse engineering relies upon following three step processes:

- I. Identifying the product or component that will be reverse engineered
- II. Observing or disassembling the information documenting how the original product works and mapping the physical model to function model
- III. Recreating a new product based on the function model generated by the reverse engineering in a modified version of the original one

Otto and Wood [5], Tang et al. [6] and Dieter and Schmidt [7] present methods of performing reverse engineering for machinery, tools and equipment in detail. Other references are also available for structuring and restructuring of chemical and biological products. Similarly, business models for service sectors may also be quoted.

3. Enterprises of Reverse Engineering:

As mentioned before, the primary aim of this scheme is the promotion of enterprises of reverse engineering in the areas of manufacturing, agriculture, health, water resources development, mining and power. A huge number of projects are likely to emerge from above mentioned fields. A list of projects in above mentioned areas on the basis of priority shall lead to a high impact from available ADP - Promoting Enterprises of Reverse engineering.

The core objectives of the proposed research project are:

- I. To establish a mechanism to identify the products in various sectors needing reverse engineering with the potential of sale in local and overseas market.
- II. To develop indigenous expertise in areas of design, prototyping, manufacturing and assembly (Functional Reverse Engineering).
- III. To carry out independent performance analysis of the developed products.
- IV. To transfer technology from academia to industry and training of students as well as

engineers and practitioners from participating industry in various sector identified above.

4. Results

Following URLs show the functionality of some of the developed products:

- I. Robot Arm

<https://drive.google.com/open?id=1Gdnpvmmq09IAdb30MOrUK650GllwYHZg>

- II. Milling Machine

<https://www.youtube.com/watch?v=8M7iXLebeUM&t=53s>

<https://drive.google.com/open?id=1v9RwHL5zm6ssoSijbCOynUfCkpZCvTJW>

- III. Turning Machine

<https://drive.google.com/open?id=1VBREYoQgyErpsqh-TJvtKnsOE-WiD4zW>

<https://drive.google.com/open?id=1h7lrY5abfjaBgMhPg3FR6Mw0tjUednV1>

- IV. Monitoring

<https://drive.google.com/open?id=1gc4rly3EhvRDqwTCOCGUdGeBDBHe43hq>

5. Conclusion:

It is envisaged that the promoting enterprises of functional reverse engineering is a viable scheme and more academic institution and technology sectors need to be involved. It is estimated that the developed machinery using this scheme reduces the cost of the product to less than 50% when compared to imported objects. Self-sufficiency, especially in manufacturing of discrete products at small to medium enterprises, is the key factor. It is also supplemented by an economic ecosystem that is self-dependent.

REFERENCES

- [1] <https://www.giki.edu.pk/ProfessionalEducation/Courses/DesignOfMachineTools>
- [2] <http://pakembnepal.org.pk/trade-and-economy/>



- [3] https://en.wikipedia.org/wiki/Economy_of_Khyber_Pakhtunkhwa
- [4] http://ps.wikipedia.org/wiki/پښتونخوا_ځيبر
- [5] Otto, K., & Wood, K. (1996, August). A reverse engineering and redesign methodology for product evolution. In Proceedings of the 1996 ASME Design Theory and Methodology Conference (Vol. 96).
- [6] Tang, D., Zhu, R., Chen, X., Zang, T., & Xu, R. (2010). Functional reverse engineering for re-creation design. In *Proceedings of the 6th CIRP-Sponsored International Conference on Digital Enterprise Technology* (pp. 185-195). Springer, Berlin, Heidelberg.
- [7] Dieter, G. E., Schmidt, L. C., & AZARM, S. (2009). Engineering design.



The relationship among working hours per shift, worker productivity and errors in locksmith work

Benjamin Durakovic^{1*}, Tauseef Aized Khan², Ramo Palalić¹

1 - International University of Sarajevo, Sarajevo, Bosnia

2 - University of Engineering and Technology, Lahore, Pakistan

*Corresponding author E-mail: bdurakovic@ius.edu.ba;

Abstract:

Various tests were carried out in the labour-intensive manufacturing industry to find the optimal number of working hours in the manufacturing process. The literature shows that productivity is variable from hour to hour, and that longer working hours are negatively correlated with productivity. Furthermore, it was observed that the relationship between errors and working hours is not well defined. The goal of this paper is to investigate the relationships among productivity, errors, and the number of working hours. To collect the data, a series of experiments have been conducted in the labour-intensive locksmith manufacturing processes, and statistical tools were used for analysis. It was observed that there is a significant and strong correlation between productivity and error rate, the impact of lunch break has a positive impact on productivity, the best productivity is observed up to six hours, and longer working hours have a negative impact on productivity.

Keywords: Productivity; errors; working hours; lunch break effect

1 Introduction

With the aim of increasing productivity and efficiency in manufacturing processes, various studies have been conducted since WWII. These studies were focused on the investigation of the issues that have an impact on productivity. Among others, a number of working hours has been investigated as well. Correlation between a number of hours and productivity has been investigated for decades with variable conclusions from industry to industry [1]. At the time, it was a common opinion that working more the output of the manufacturing will be better [2]. Longer working hours may provide better utilization of goods and may have a positive impact on productivity [3], or longer working hours may have a negative impact on productivity after a certain number of hours due to fatigue of workers [4]. As it can be a trigger to the increase of the human errors and accidents in the production systems, fatigue represents one of the key issues in the working environment [5]. It is usually defined as an enabler in executing a certain task, or leads to a low-performance execution with errors [6], and occurs as a reaction to working environment conditions. It appears in a form of physical weakness due to a prolonged activity during working hours or as a result of stress and emotional response to a demanding workload in the

form of mental weakness [7]. It can lead to lowering productivity and increasing error and injury rates. Moreover, the majority of studies prove that longer working hours have are harmful to a worker and company [8] and may increase injuries, up to 40% [9] [10]. To achieve better efficiency in the manufacturing process, a number of working hours should be taken into account. Productivity decreases with the increase of working overtime hours [11]. The happiness of workers is another important factor in achieving better productivity. The efficiency of the worker is increased if the worker more satisfied [12]. A negative correlation between working hours and happiness was found. The impact of the number of working hours on the error rate is not defined well in the literature. Errors rate depend on many factors such as machine, method, and environment [13]. The goal of this research is to investigate the impact of working hours on error rate. It is important to understand how the number of working hours affects productivity and error rate in locksmith manufacturing. Innovation in the manufacturing process help to improve the quality of output and reduce error rate [14]. Applying innovative continuous improvement initiatives such as lean manufacturing and six sigma [15] [16] initiatives helps to reduce all types of waste and improves customer satisfaction [17]. Therefore, this study examines this issue and attempts to determine



the impact of working hours on error rate and impact of the lunch break on productivity and error rate. To archive the goal of the study, the following *alternative hypotheses* were tested with $\alpha = 0.05$:

H1: Productivity per hour is significantly different for at least one hour;

H2: Error rate is significantly different for at least one hour;

H3: Lunch break is positively associated with productivity.

2 Methodology

As a case study, a locksmith manufacturing process from a Bosnian company has been studied. The manufacturing belongs to the labour-intensive industry in which the human factor has significant impact on the process output and error rate. The process output in terms of productivity and error rate per each hour was recorded and analysed. Statistical tools Analysis of Variance and *F*-test were used [18]. Analysis of variance is an important method for event-related potential in order to minimize type II error and type I error. It is also used to identify the events for any kind of enhancement [19]. ANOVA is used to test whether the mean production of all hours and provides the variations of the sample within the sample, and between the samples. The test statistics is calculated as follows:

$$F = \frac{\frac{SS_{between}}{K-1}}{\frac{SS_{within}}{K(n-1)}}$$

where; K is the number of samples, n is the size of each sample, $\bar{Y}_..$ is the grand mean which is mean of the sample means; \bar{Y}_i is the mean of the i -th sample; Y_{ij} is j -th variable of the i -th sample.

To get a significant result observed *F*-value has to be greater than its critical value F_{cr} . If this

requirement is met, post hoc pair-wise comparisons are performed to identify which hour significantly differs from the others. In this study, *Tukey's Honest Significant Difference* (Tukey's HSD) is employed. This method is capable of controlling the family-wise error rate at the specified significance level of 0.05 across any number of comparisons. The test statistic for Tukey's test for $H_1: \mu_i \neq \mu_{j'}$ for all pair-wise differences is given by

$$q_0 = \frac{\bar{x}_j - \bar{x}_{j'}}{SE} = \frac{\bar{x}_j - \bar{x}_{j'}}{\sqrt{\frac{s^2}{2} \left(\frac{1}{n_j} + \frac{1}{n_{j'}} \right)}}$$

where, $\bar{x}_j > \bar{x}_{j'}$; SE is standard error, s^2 is estimated variance of σ^2 from ANOVA, n_j , and $n_{j'}$ are sample sizes.

In this test as the first step, pair-wise differences $\bar{x}_j - \bar{x}_{j'}$ are computed first for all means. The critical value $q_{\alpha, v, k}$ is determined from critical value table for the Tukey q test, based on significance level α , the total number of compared means k , and the degrees of freedom due to error v , ($v = n - k$, where n is the total number of observations). In case $q_0 \geq q_{\alpha, v, k}$, a significant difference exists between compared means.

3 Results and Discussions

To get reliable results, recorded data from the manufacturing must obey to a normal distribution and the variance has to be equal. Values of skewness and kurtosis fall within the acceptable range and provided sufficient evidence that the data is normally distributed and parametric analysis can be used. Figure 1 shows the normal probability plot of residuals as well as residual distribution around fitted value.

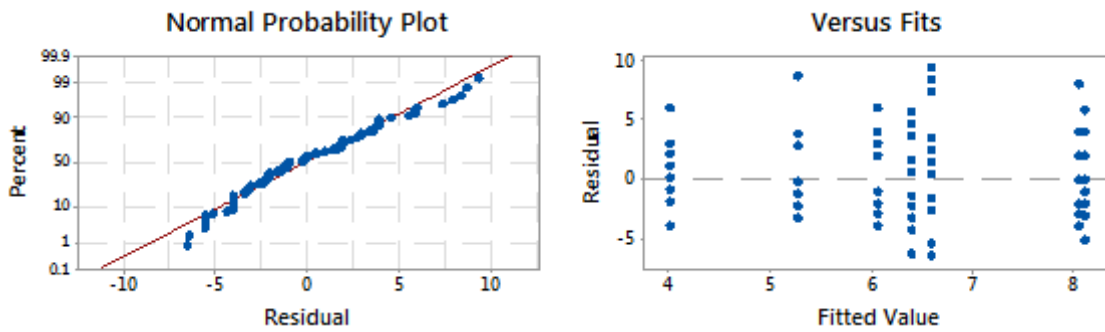


Figure 1. Residual plot for productive shift hours

It was observed that the variance has no trend to change along with fitted value, which is sufficient evidence to assume that the variance is equal. From a normal probability plot, it was observed that the residuals are grouped per along straight line with no extreme signs of an unusual pattern. This means that the data has a normal distribution tendency around the mean. Since this

Table 1.

Table 1. ANOVA results for hourly productivity

Source	DF	Adj SS	Adj MS	F-Value	P-Value
Between Hours	6	191.8	31.97	2.29	0.042
Error	97	1355.7	13.98		
Total	103	1547.5			

It is observed that calculated *P*-value is 0.042 indicating that at production rate is different for at least one hour. Therefore, null hypotheses is rejected and H1 is true, (H1: Productivity per hour is significantly different for at least one hour). Since

basic prerequisite is met, ANOVA and post hoc test can be used for this analysis.

3.1 Productivity Analysis

To theist hypothesis H1, and to check whether the hourly production rate is different for at least one hour, ANOVA test was performed with 95% confidence interval. The results are shown in

Table 2.

Table 2. Tukey pair-wise comparison results

Factor	Mean	Grouping
4th h	8.133	A
5th h	8.07	A B
6th h	6.6	A B
7th h	6.4	A B
2nd h	6.067	A B
1st h	5.267	A B
8th h	4	B

Mean values that do not share letter A are significantly different. Based on

Table 2, the 8th hour does not contain letter "A", it belongs to group B, which means the productivity in

ANOVA does not provide information which hour differs significantly from the others, post hoc Tukey Pair-wise comparisons were performed at 95% confidence interval. The results are shown in

the last hour is **significantly lower productivity** (*mean* = 4; the lowest) from the rest hours in the shift (significantly different from 2nd to 7th hour).



3.2 Error Rate Analysis

Everything that disturbs smooth flow of production (wrong part, packaging, hanging, displacement, improper handling of

tools/materials/machine etc.), and that was caused by human factor was considered as an error in this research. To goal of these analyses is to test hypothesis H2, which states "Error rate is significantly different for at least one hour". The results of ANOVA are shown in

Table 3.

Table 3. ANOVA results for error rate

Source	DF	Adj SS	Adj MS	F-Value	P-Value
Between Hours	6	80.76	13.46	3.94	0.001
Error	98	334.8	3.416		
Total	104	415.56			

Referring to

Table 3, it was observed that P-value is less than 0.05, indicating the that H2 hypothesis is true. To check which hour differs

significantly from the others, post hoc Tukey Pair-wise comparisons were performed at 95% confidence interval and the results are shown in

Table 4.

Table 2

Table 4. Tukey pair-wise comparison results

Factor	Mean	Grouping
5th h,e	3.4	A
6th h,e	3	A B
4th h,e	2.8	A B
7th h,e	2.4	A B
8th h,e	1.333	B
2nd h,e	1.267	B
1st h,e	1.067	B

Observing the data from

Table 4

Table 2, the hour that belong to the group B, are significantly different. The lowest error rate is observed in the 1st, 2nd and 8th hour.

3.3 Effect of the Break

Locksmithing manufacturing process was consisted of the following operations: taking measure, sawing, grinding, clamping, welding, weld grinding. Error due to human factor can

occur at any step of manufacturing process. As an error, it was considered all instances that disturb a smooth flow of the production. Productivity is defined as number units produced coming out at the from the process after each shift hour. Average productivity and average error trends are shown in Figure 2. Productivity and errors increase with the increase of working hour until the certain point and it started to decrease until the end of the last hour in



the shift. Lunch break was scheduled after the third hour.

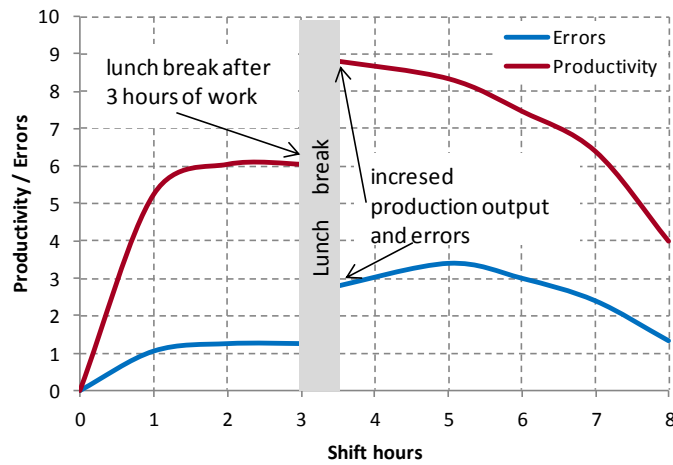


Figure 2. Average production rate per shift hour

As it was expected, productivity in the first hour is transient continuously growing and in the second hour reaches steady state continues up to the lunch break. The lunch break was for 30 minutes without any manufacturing activity during this period. It is important to mention that transient curve is not observed after the break even though productivity was equal to zero during the break. Moreover, after the lunch break productivity was rapidly increased reaching its maximum, and in the following hours started slightly to decrease. In the last two hours, productivity was rapidly decreasing.

Impact of break to the productivity is not well investigated in the literature and this study tries to detect its benefit to the productivity. Observing the Table 5.

previous diagram, it is found that the productivity after lunch break is increased as well as errors. Therefore, it was proved that lunch break has a positive impact on productivity. Comparing the production before and after brake, it was calculated that about 32% the production was increased. Excluding the first hour which represent transient state, it was observed that the best productivity is up to seven hours. Therefore, longer working hours have a negative impact on productivity due to fatigue. Similarly, error trend was following the productivity trend. With better productivity increase more error had been generated, which indicates mutual relationship between these two variables. To estimate this relationship correlation test was conducted and the results are shown in

Table 5. Correlation matrix

	Working Hours	Errors	Productivity
Shift Hours	1		
Errors	0.430207436	1	
Productivity	0.141126383	0.890797*	1

* Significant for two tail test significance level $\alpha = 0.05$, and degrees of freed $\nu = 14$, (critical value is 0.497)

There is strong relationship between productivity and error rate with Pearson

coefficient $r = 0.89$. This can be explained that errors more related to productivity than to number of working hours. Correlation between number of working hours and errors is moderate with Pearson correlation coefficient of 0.43. Overall, this led to the conclusion that reduced productivity is caused by reduced worker activities and that results of error



reduction. Based on the correlation result it was reasonable to test a linear regression model, in which error is considered as dependant variable

while Shift Hours and Productivity as independent variable. The results are shown in

Table 6.

Table 6. Linear regression results

	Coefficients	Standard Error	t Stat	P-value	Lower 95%	Upper 95%	Lower 95.0%	Upper 95.0%
Intercept	-0.510	0.435	-1.172	0.286	-1.576	0.555	-1.576	0.555
Shift Hours	0.116	0.070	1.663	0.147	-0.055	0.287	-0.055	0.287
Productivity	0.324	0.073	4.472	0.004*	0.147	0.502	0.147	0.502

* Significant variable, at $\alpha = 0.05$

As it was expected, it is confirmed again that there is significant positive relationship between productivity and error, which implies that errors are mainly produced due to activities

in product producing. The number of working hours are not major contributor to the error rate.

4 Conclusions

The best productivity was observed in the period from 2nd to 7th hour. Based on the results in

Table 2, it was observed that productivity at the end of the 8th hour is significantly lower. This proves H1 hypothesis, which states: "Productivity per hour is significantly different for at least one hour". The lowest rate of errors is associated with 1st, 2nd and 8th hour. These are period with significantly lower errors than the rest of the working shift. This proves H2 hypothesis which states: "Error rate is significantly different for at least one hour". In the literature, it was stated that worker fatigue is highly correlated with working hours, but this study found that errors have no

strong correlations with increased working hours. This imply that the errors are more generated due to of increased worker's activity than due to their fatigue, which is confirmed that strong and significant relationship exists between productivity and errors. In another word, higher productivity requires more activity in the production and consequently cases more error. Therefore, it was found that *lunch break has positive impact on productivity*, which is H3 proved. It would be worthful to conduct more detailed experiments with brakes and their positive impact to the productivity, such as investigation whether multiple breaks will produce better results in eight-hour shift.

REFERENCES

- Health at Work*, vol. 8, pp. 343-346, 2017.
- [1] R. A. Hart and P. G. Mcgregor, "The Returns To Labour Services In West German Manufacturing Industry," *European Economic Review*, vol. 32, pp. 947-963, 1988.
 - [2] J. Park, Y. Kim and B. Han, "Long Working Hours in Korea: Based on the 2014 Korean Working Conditions Survey," *Safety and*
 - [3] M. S. Feldstein, "Specification of the labour input in the aggregate production function.," *Review of Economic Studies*, vol. 34, no. 4, pp. 375-386, 1967.
 - [4] J. Pencavel, "The Productivity of Working Hours," vol. 125, no. 589, p. 2052-2076, 2015.
 - [5] Y.-H. Chang, H.-H. Yang and W.-J. Hsu, "Effects of work shifts on fatigue levels of air traffic controllers," *Journal of Air Transport*



- Management*, vol. 76, no. May, pp. 1-9, 2019.
- [6] A. Craig and R. Cooper, "Symptoms of acute and chronic fatigue," in *In Smith, AP, Jones, DM, editors. Handbook of human performance, 3: State and trait*, San Diego: CA, Academic Press Inc., 1992, p. 289–339.
- [7] H. Yoshitake, "Three characteristic patterns of subjective fatigue symptoms," *Ergonomics*, vol. 21, no. 3, p. 231–233, 1978.
- [8] P. NIE, S. OTTERBACH and A. SOUSA-POZA, "Long work hours and health in China," *China Economic Review*, vol. 33, pp. 212-229, 2015.
- [9] D.-M. Kang, S.-Y. Kim, Y.-J. Kim and J.-A. Kim, "Psychological Intervention for Post-traumatic Stress Disorder among Witnesses of a Fatal Industrial Accident in a Workers' Health Center," *Safety and Health at Work*, vol. 8, pp. 410-412, 2017.
- [10] J. Lee and Y.-K. Lee, "Can working hour reduction save workers?," *Labour Economics*, vol. 40, pp. 25-36, 2016.
- [11] R. Euwals and A. Van Soest, "Desired and actual labour supply of unmarried men and women in the Netherlands," *Labour Economics*, vol. 6, pp. 95-118, 1999.
- [12] M. Collewet, A. Grip, Koning and Jaap, "Conspicuous work: Peer working time, labour supply, and happiness," *Journal of Behavioral and Experimental Economics*, no. 10.1016/j.socec.2017.04.002, 2017.
- [13] B. Durakovic and H. Basic, "Continuous Quality Improvement in Textile Processing by Statistical Process Control Tools: A Case Study of Medium-Sized Company," *Periodicals of Engineering and Natural Sciences*, vol. 1, no. 1, pp. 39-46, 2013.
- [14] B. Durakovic, H. Basic and H. Muhic, "The Interrelationships between Quality Management Practices and Their Effects on Innovation Performances," in *Trends in The Development of Machinery and Associated Technology TMT 2014*, Budapest, 2014.
- [15] H. Bašić, B. Duraković and A. Softić, "Six Sigma Model Testing in Optimizing Medium-Sized Company Production Process," *Journal of Trends in the Development of Machinery and Associated Technology*, vol. 16, no. 1, pp. 103-106, 2012.
- [16] B. Durakovic and H. Bašić, "Textile Cutting Process Optimization Model Based On Six Sigma Methodology In a Medium-Sized Company," *Journal of Trends in The Development of Machinery and Associated Technology*, vol. 16, no. 1, pp. 107-110, 2012.
- [17] B. Durakovic, R. Demir, K. Abat and C. Emek, "Lean Manufacturing: Trends and Implementation Issues," *Periodicals of Engineering and Natural Sciences*, vol. 6, no. 1, pp. 130-143, 2018.
- [18] B. Durakovic, "Design of Experiments Application, Concepts, Examples: State of the Art," *Periodicals of Engineering and Natural Sciences*, vol. 5, no. 3, p. 421–439, 2017.
- [19] J. Dien, "best practices for repeated measures ANOVAs of ERP data; References, regional channels, and robust ANOVAs," *international journal of psychophysiology*, no. 10.1016/j.ijpsycho.2016.09.006, 2016.
- [20] S. K. C. NARAYANAN, "FATIGUE-RELATED MEDICAL CONDITIONS AFFECTING SEAFARERS: An exploratory case study of Indian seafarers," The Maritime Commons: Digital Repository of the World Maritime University. World Maritime University Dissertations, Malmö, Sweden, 18 September 2017.

Brief CVs

Benjamin Durakovic

Dr. Benjamin Durakovic is an Assistant Professor and program coordinator for Mechanical and Industrial Engineering at the Faculty of Engineering and Natural Sciences, International University of Sarajevo. His research interests include energy efficiency, design of experiments, and data analysis, lean topics. He has authored a book related to energy efficiency published by Springer Nature, authored/co-authored many research papers on the aforementioned topics and published in a variety of leading journals including Sustainable Cities and Society, the International Journal of Low-Carbon Technologies, and the Journal of Materials and



Environmental Science, Periodicals of Engineering and Natural Sciences. He teaches courses at both undergraduate and graduate levels, and has participated in more than 20 R&D innovation projects with Bosnian and US companies.

Ramo Palalić

Dr. Ramo Palalić is an Assistant Professor at the Economics and Management Department, Faculty of Business and Administration (FBA), International University of Sarajevo (IUS), Sarajevo, Bosnia and Herzegovina. His research interests include entrepreneurship, leadership, marketing, and

management. Dr. Palalić teaches in the above listed areas at undergraduate, graduate and post-graduate study cycles. He is a Coordinator of Leadership and Entrepreneurship Centre (LEC) at IUS. Apart from this, he is actively involved in business projects in the areas of entrepreneurial leadership and marketing management, in private and public organizations. He has authored and co-authored many articles and books in the above areas with internationally recognized publishers. Additionally, Dr. Palalić is serving as the reviewer/editor board member in several international journals.



Manufacturing of composite materials via 3D printers: Materials selection and process optimization

Osman İyibilgin^{a,b}, M. İskender Özsoy^a, Engin Gepek^b, Fehim Findik^{b,c,d}

^aMechanical Engineering Department, Faculty of Engineering, Sakarya University, Sakarya, Turkey

^bBiomedical, Magnetic and Semiconductor Materials Application & Research Center, Sakarya University, Sakarya, Turkey

^cMetallurgy & Materials Engineering Department, Faculty of Technology, Sakarya Applied Sciences University, Sakarya, Turkey

^dCommunication author, E-mail: findik@sakarya.edu.tr, Tel: +90-264-616 0260, Fax: +90-264-616 0221

Abstract

Three-dimensional printing (3DP), called alternating layered production, is an emerging technology for sequential layering to create numerous objects with numerous design flexibility. Research that spins 3DP to develop different high-performance materials is progressing exponentially at the young stage and around the world. The most extensive applications of 3DP technology are found in automobile, aerospace, construction, metal and alloy, electronics and biomedical fields. Recently, the opportunity to use fiber as reinforcement in the plastic resin of the 3D printed model has made a significant contribution to improving the mechanical performance of the 3D printed composites. In this review, with the introduction of the brief history of 3DP, the microstructural and mechanical properties, including the mechanism of embedding of different continuous fibers into different plastics and their predictive models, are critically reviewed. In addition, future research guidelines have been identified based on the limitations of existing technology.

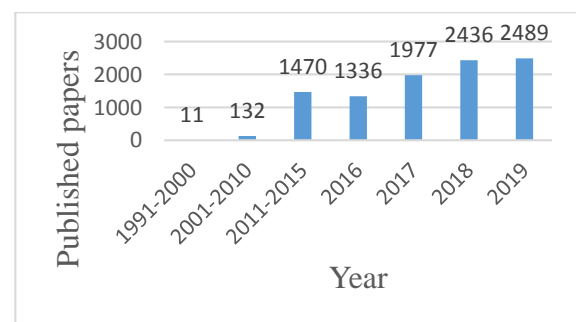
Keywords: 3d printer, composites, materials selection, microstructure, mechanical properties, process optimization

1. Introduction

Three-dimensional printing (3DP) is a term in material production and is the result of recent research for material scientists. It is estimated that this technology has shown significant growth over the last few years and will revolutionize the manufacturing industry to create a new generation of high performance materials [1,2]. Customization, rapid prototyping, automated production and flexibility in reducing complex geometries at relatively low cost and time during the design phase have encouraged and brought to the spotlight the remarkable advancement of 3DP.

In order to increase the performance of plastic composite, different reinforcement; for example, carbon black, platelets, chopped fibers, polymer fibrils, mixed with the thermoplastic matrix and then co-extruded during printing. The performance of these composites is strongly dependent on the fiber orientation in the plastic and fiber volume fraction (FVF). However, they still exhibit lower mechanical performance than conventional fiber reinforced composites. Therefore, in order to expand the application of 3D printed FMD technology to design high performance composites, it requires continuous fiber reinforced composite printing. The commercially available technology with this feature is known as continuous filament production (CFF) [3].

Exposure to exponential research over the last decade has resulted in numerous research articles and patents. Figure 1 illustrates the trend of scientific papers based on 3DP technology (a) and continuous fiber reinforced 3DP (b). In determining that published patents are used as keywords in the Web of science search engine, headings containing '3D printing * / additive * production *' are counted and reported in Figure 1. These findings are compiled to meticulously understand the scopes and limitations for the future research on demand. The flow of this article begins with the history of 3DP and the continuous fiber-reinforced composite manufacturing mechanism, followed by our recommendations for materials used, investigated properties, future appearance and future research.



a

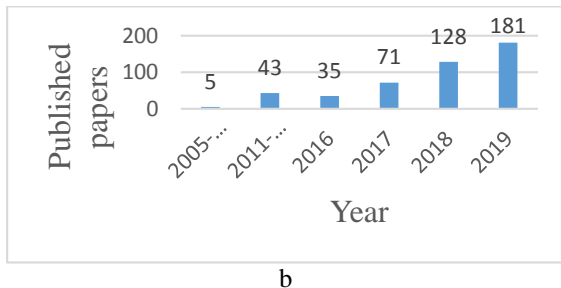


Fig. 1. An overview of the number of published papers regarding 3DP (a) and composite and 3DP (b) since their inceptions.

2. History

The history of 3DP is only a 40-year-old technology [3]. The revolutionary growth of research in science, engineering and technology has brought this innovation to mature level. During the important period of its history, 3D printers were unsuitable, but now the price has dropped tremendously from about \$ 20,000 (before 2009) to \$ 500-1000 [3]. In order to better understand the development of 3BP, this article covers the timeline-based history as well as significant developmental stages.

2.3. 1991–2000

In this decade, there have been many improvements that have emerged in addition to existing 3D printers, new printers, and new materials for these printers [4]. The first printers had significant technical limitations and flaws that restricted them for the bulk production of 3D objects. Therefore, research has been carried out to improve the technical performance of printers, which mainly include laminated object production, solid floor hardening, direct shell production and SLS and large-scale printing. During this decade, some new printers have also been developed, such as 3D wax printers, Z printers, and 3D metal printers. During this decade, several key developments have been seen for several astounding discoveries, including the most remarkable innovation, including 3D printed organ development, a bladder created from a patient's own cells, and the design of flexibility to print hard and soft materials with different aesthetics and functions.

2.4. 2001–2010

Functional flexibility, mass customization, precision, high resolution, personal home printers, user-friendliness, and easy accessibility along with the explosion of research to produce new materials with sophisticated product characteristics are key developments that have occurred over the course of this decade [5]. In 2001, Envisiontec launched Perfactory Machine, which can produce

exceptionally large parts at high speeds with precision and precision. In the following years, the metal powder and multicolor 3D melting commercial electron beam melting system was discovered by Z Corp printer. One of the groundbreaking ideas of the decade was the RepRap project, which brought the 3D printer with an easily accessible open source system and self-replicating nature at home [5]. Remarkably, the material developments in this decade were: 3D printed kidney, human blood vessel, 3D printed prostheses without first assembly, creation of consumer products, first garment (3D printed bikini), 3D printed films for 3D moving films, and 3D printed by first Chinese researcher's furniture. Another important event of this decade was the expiration of the patent of the FDM method, which expanded accessibility. Then thousands of stakeholders around the world began to use and experience technology easily. In addition, the growth of materials at that time and the widespread adoption of this technology by stakeholders followed the development of the first ASTM standard for additively manufactured products as quality and terminology reference [4].

2.5. 2011-to-date

The history of this period is often concerned with the cost-effectiveness of 3D printers and the ability to use this technology for first-class materials that come out for multi-dimensional purposes, ranging from personal products to industrial products such as food, toys, jewelery, automobiles, buildings, aircraft. clothing and fashion accessories, biomedical and robotics [6]. The cost of FDM 3D printers has decreased from five to four or even three between 2012 and 2013, which has increased the affordability of this technology [7]. Increasing research risks associated with this amazing technology include Urbee (first 3D printed car), Cornell University and NASA's 3D food printer, making vehicles on demand, 3D printed rocket fuel injector, moon space made by the European Space Agency (ESA), and 3D printed splint that caused lifesaving. President Obama has announced that he has granted a \$ 30 million research grant to the National Institute of Additional Production Innovation in Ohio to motivate AM and 3DP research in the United Nations Union State. As a result, many "wow" factors have not yet undergone 3DP technology [8].

3. Continuous filament fabrication

3.1 Mechanism

The basic working procedures for creating an object using 3DP technology are the same in all existing technologies and consist of three basic steps. 3D model creation, slicing and printing [9]. First, it



requires the development of a virtual 3D object using CAD software, which can create a comprehensive file format that is easily readable to the slicing software. Slicing software is designed to work on every 2D layer of an object's 3D model, processing and transmitting this information to the printer for printing to the physical structure [10]. Printing technology differs from one another, mainly due to the printing mechanism and the physical forms of the starting materials.

Figure 2 (a) shows a schematic representation of the continuous fiber production method using conventional 3D printers with modified print heads. Unlike shredded fiber reinforced composites, it has two separate materials for matrix / plastic / resin and reinforcing filament. The extrusion nozzle receives both thermoplastic polymer and continuous fibers, and continuous fibers are made to pass through the core of the nozzle. As a result, when the nozzle is heated, matrix infusion occurs and the molten thermoplastic material is deposited together with the reinforcing filament. The temperature of the nozzle is selected according to the thermal properties of the thermoplastic polymer. As soon as the material is deposited and reaches the print bed, it quickly solidifies and adheres to the previous layer. The print head is designed to move in 2D movements, ie in X-Y directions, and is responsible for the design of each layer according to the trajectory of the 3D CAD model transmitted with slicing software. The third movement up to a distance equal to the layer thickness along the Z direction is performed by the building platform after each platform is constructed; this continues until the structure is completed [11].

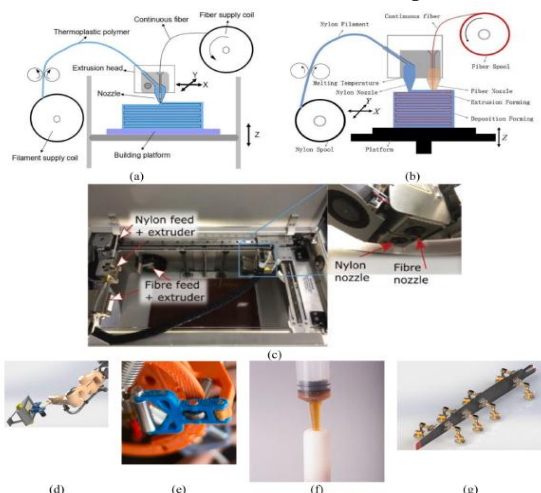


Fig. 2. Schematic representation of the FMD 3DP process using continuous filament with a printing head of single nozzle (a), reprinted with permission from (Emerald Publishing Ltd.) and dual nozzles (b), reprinted with permission from (Elsevier Ltd.), a close look of Markforged dual nozzle system (c) robotic printing head with coaxial extruder (d),

molding roller (e), capillary injection method (f) and printing head with multiple extruders (g) [11].

3.2 Factor affecting quality

The characteristics and properties of the printed parts depend on a number of factors, which can be divided into three main stages: preparation, printing and finishing. Goh et al. [12] provide definitions of terms contained in 3DP factors. Detailed production factors affecting the mechanical properties of the 3D printed composite in the FDM process Banjanin et al. [13]. Figure 3 compiles and classifies almost all possible factors related to the quality and performance of 3D printed composites found in the literature.

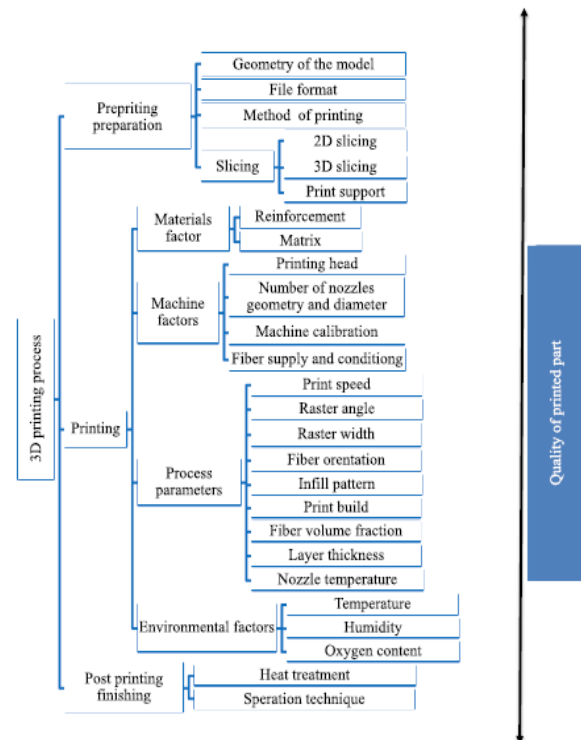


Fig. 3. List of preparatory, machine, process and environmental factors affecting quality of 3D printed composites [1].

Preparatory factors → (file format, slicing software)

Printing factors → (nozzle temperature, heating mechanism, diameter and geometry; moisture and electrical property; viscosity and rheology; print speed, raster angle, fiber orientation, infill patterns; ambient temperature and humidity)

Finishing factors → (print bed, special glue, support material, heat treatment, separation technique)

4. Materials



Obviously, the CFF comprises both the matrix and the reinforcement, whereas the reinforcing material is always a continuous fiber. The matrix holds the fibers firmly for long-term serviceability, and protects the fibers from corrosion, deterioration, abrasion, etc. It is a base material that protects from external forces. Furthermore, the role of the matrix material is very important in carrying the compression load of the composites. On the other hand, incorporation of the reinforcement into the plastic matrix synergistically improves the final properties of the composites in terms of their tensile, elastic and load bearing capacity. In the manufacture of a composite, the choice of matrix and reinforcement is physically (good adhesion), chemically (matrix and fiber should not chemically react) and thermally (similar thermal behavior; coefficient of thermal expansion) [14]. Materials and properties used for 3D printed CFF are summarized in Table 1.

Table 1 Materials used for continuous filament fabrication [1]

Materials	Properties				
	Density in g/cm ³	Diameter in μm (number of mono filaments, diameter)	Tensile modulus in GPa	Flexural modulus GPa	
Matrix	Onyx	1.2	1750	1.4	2.9
	Nylon	1.1	1750	0.94	0.84
	PLA	1.25	1750	2.02	2.392
	ABS	1.04	1750	0.998	1.9
	Epoxy	1.54	1750	3.5	
	PEEK	1.3	1750	3.6	
Continuous filament	Carbon	1.4/1.3	400 (1000, 10)	54	51
	Kevlar	1.2	300 (1000, 12)	27	26
	Fiberglass	1.5	300 (1000, 10)	21	22
	Jute	1.3-1.45	20-200	39.4	

In addition to polymer filament preparations, polymer processing factors such as melting temperature, viscosity, rheology and solidification are as important as the mechanical properties of the polymers and play an important role in the performance of a printing (mechanical properties, solubility and accuracy) section [15]. Fuenmayor et al. [16] and Rahim et al. [17] elaborated polymer preparation requirements and process-related considerations for the FDM 3DP system. Polymer filament preparations include polymer morphology, filament hardness, softness, brittleness, dimensional consistency, and appropriate winding on the reel. The desired polymer morphology for FDM / FFF is amorphous, so it can undergo rapid cooling and eventually helps to achieve better dimensional accuracy of the printed parts. In this regard, polyamides are preferred over other semi-crystalline and crystalline polymers because they have amorphous structures. Semi-crystalline polymers of low crystallinity (20-32%), such as PEEK, can also be used depending on the molecular structure and the structure of the cooling, since polymers with a high degree of crystallinity tend to cause part bending

after printing [21]. The diameter of the polymer filament (1.75 ± 0.1 mm) should be equal, coiled parallel to the spool to minimize the tension of the filament, and should not be brittle or too soft to prevent friction and prevent friction. The polymer filament must be rigid enough to maintain the extruded deposition rate as it exerts pressure on the fluidizer [16].

5. Conclusion

Embedding continuous fiber into the plastic resin of the 3D printed model is a very new and promising innovation to dictate a new generation of composites due to its significant contribution to the enhancement of mechanical properties such as tensile, bending, compression and impact. The most surprising credentials behind the widespread acceptance of this technology is the freedom to produce the equipment as required and the ability to create complex designs in minimized process steps. Significant improvements of up to several layers compared to non-reinforced composites can allow CFF composites to serve for high load carrying purposes. However, commercial application is very narrow due to the limited range of materials (matrix and reinforcement) to personalize the anisotropic behavior, poor interface bond, high porosity and composite properties as needed. Furthermore, the mechanical procedure of the 3DP device and the 3DP principle, meso and microstructural studies show poor mechanical performance compared to conventionally prepared composites. Furthermore, time, cost and scalability are of great concern. In fact, the CFF composite research is a new application or discovery stage that often underlines changing printing and processing parameters as well as reinforcement configurations, rather than replacing existing materials.

Acknowledgements

Thanks to SUBU and BIMAS-RC due to provision of laboratory facilities and SAU due to partial financial support within international bilateral Mevlana project (Project Number: MEV-2018-644) between Pakistan and Turkey.

REFERENCES

- [1]. Kabir SMF, Mathur K, Seyam AFM. A critical review on 3D printed continuous fiber-reinforced composites. *Composite Structures* 2020; 232: 111476.
- [2]. Goh GD, et al. Recent progress in additive manufacturing of fiber-reinforced polymer composite. *Adv Mater Technol* 2019; 4(1): 1800271
- [3]. Oztan C, et al. Microstructure and mechanical properties of three dimensional printed continuous fiber composites. *J Compos Mater* 2019; 53(2): 271–80.



- [4]. Practice P. Brief history of 3D printing technology – a timeline. 2019 [cited 2019 January 27]; Available from: <https://pixelpractice.nyc/history-3d-printing/>.
- [5]. Savini A, Savini G. A short history of 3D printing, a technological revolution just started. in History of High-Technologies and their Socio-Cultural Contexts Conference (HISTELCON), 2015 ICOHTEC/IEEE International. 2015. Tel Aviv, Israel IEEE.
- [6]. Wohlers T, Gornet T. History of additive manufacturing. Wohlers report. 24(2014): p. 118.
- [7]. Goldberg D. History of 3D printing: it's older than you are (that is, if you're under 30). Manufacturing 2018 [cited 2019 January 27]; Available from: <https://www.autodesk.com/redshift/history-of-3d-printing/>.
- [8]. Hickey S. Chuck Hull: the father of 3D printing who shaped technology, in The Guardian 2014, Guardian Media Group: Kings Place, London.
- [9]. Wang X, et al. 3D printing of polymer matrix composites: a review and prospective. Compos Part B Eng 2017; 110: 442–58.
- [10]. Bogue R. 3D printing: the dawn of a new era in manufacturing? Assembly Automation 2013; 33(4): 307–11.
- [11]. Yang C, et al. 3D printing for continuous fiber-reinforced thermoplastic composites: mechanism and performance. Rapid Prototyp J 2017; 23(1): 209–15.
- [12]. Goh G, et al. Process–structure–properties in polymer additive manufacturing via material extrusion: a review. Crit Rev Solid State Mater Sci 2019: 1–21.
- [13]. Banjanin B. et al. Production factors influencing mechanical and physical properties of FDM printed embossing dies. In: 9th International Symposium on Graphic Engineering and Design. 2018. Novi Sad, Serbia: University of Novi Sad.
- [14]. Fidan I, et al. The trends and challenges of fiber-reinforced additive manufacturing. Int J Adv Manuf Technol 2019: 1–18.
- [15]. Popescu D, et al. FDM process parameters influence over the mechanical properties of polymer specimens: a review. Polym Test 2018; 69: 157–66.
- [16]. Fuenmayor E, et al. Material considerations for fused-filament fabrication of solid dosage forms. Pharmaceutics 2018; 10(2): 44.
- [17]. Rahim TNAT, Abdullah AM, Md Akil H. Recent developments in fused deposition modeling-based 3D printing of polymers and their composites. Polym Rev 2019: 1–36.



MECHATRONICS AND CONTROL TRACK



Implementation of Impedance Control Schemes for Position and Force Tracking on Redundant Manipulator

Muhammad Bilal^{1*}, Mohsin Rizwan², Ali Raza² and Muhammad Ali³

1. Al-Khawarizmi Institute of Computer Science, University of Engineering and Technology (UET), Lahore Human Centered Robotics Lab (HCRL), National Center of Robotics and Automation (NCRA) Lahore, Pakistan
 2. Dept. of Mechatronics & Control Engineering, UET Lahore. HCRL, NCRA Lahore, Pakistan
 3. Dept. of Mechatronics & Control Engineering, UET Lahore
- * Corresponding Author: muhammad.bilal@kics.edu.pk

Abstract:

The aim of this research is to explore and implement the underlying concepts of torque-based and position-based impedance control schemes for force and position tracking during the physical interaction of the manipulator's end-effector with its environment. In this pursuit, the complete mathematical expressions for torque based impedance control (TBIC) and position based impedance control (PBIC) schemes are derived as well as complete kinematics and dynamics model of redundant 3R planar robot are presented. To ensure the convergence of the force error to zero in the unknown environment stiffness, a PBIC for force tracking is implemented on a 3R planar manipulator. Extensive simulation studies with a 3R redundant manipulator using full arm dynamics are performed on MATLAB/Simulink to validate the effectiveness of each scheme.

Key Words: Impedance control; Position Tracking; Force Tracking; Unknown Environment Stiffness

1. Introduction

Most tasks performed by robot manipulators require safe physical interaction between the manipulator's end-effector with its environment. Initially, the industrial robots are used to perform tasks where no energy exchange occurs between the manipulator's end-effector and its environment. The typical examples of industrial operations performed by the robots include scrapping, pushing, grinding, machining, deburring, polishing, twisting, cutting, etc. In the context of safe robotic interaction, two major control paradigms that have been proposed are 1) Hybrid position and force control and 2) Impedance control. In hybrid position and force control, the Cartesian space is separated into a position-controlled and force-controlled subspaces through a projection of a feedback signals. In hybrid position and force control, it is not possible to control the force and position along the same path apart from that there is no consideration for dynamic contact between the manipulator's end-effector and its environment, as a result, the force and position cannot be controlled accurately at operational space.

To resolve this issue, Hogan [1], [2] proposed *Impedance control* which is an integrated force control scheme suitable for safe physical interaction of manipulator's end-effector with its environment, apart from that, the desired position can be controlled accurately as compared to classical hybrid position and force control [3]. The purpose of the impedance control scheme is to control the relationship between the contact forces and the motion variables of the manipulator simultaneously so that the desired

manipulation task can be fulfilled [4]. The impedance control can be implemented in two major ways 1) Torque-based impedance control and 2) Position-based impedance control. In general, manipulators with TBIC have stable dynamic interaction with stiff environment but due to unmodeled robot dynamics and friction have less accuracy in free space [5]. On contrary to TBIC, PBIC provides high accuracy in free space and concentrates on force tracking applications [6]. For dealing with uncertain environment location and stiffness [7] as well as uncertain robot dynamic [8], neural network-based impedance [9], [10] and adaptive variable impedance control law [11] showed improved performance for desired force tracking compared to general impedance control law.

The review of relevant literature indicates to upgrade existing approaches from a practical standpoint as well as to see the effectiveness of each impedance control paradigms on redundant manipulator. In this context, authors upgraded and implemented the control paradigms on a redundant 3R planar robot, and additionally have also incorporated realistic motor parameters, I/O details, and cascaded servo-control scheme to ensure transparency. In order to further improve the transparency and reproducibility, complete derivations have been provided herein. It is important to highlight that authors have implemented both the TBIC and PBIC schemes. Within the position-based approach as well, the force tracking as well as position tracking options have been exhausted. Moreover, different experiments have been performed considering unknown environmental stiffness with both even and uneven



surfaces. This has enabled the authors to conclusively argue the effectiveness of one impedance control paradigm over the other considering the interaction with the environment.

The paper structure is organized as follows: Section II describes the fundamental concepts and mathematical modeling of each control paradigm. In section III, robot kinematics and dynamic model is presented. The simulation and results are discussed in section IV, followed by a conclusion in section V.

2. Background Concepts

2.1 Definition of Impedance Control

Impedance control law can be defined as a physical system that accepts motion input and returns the effort which means the force generated from the interaction between the robot end-effector and its environment. In mathematical form, the ratio of output effort to motion input is termed as impedance.

$$Z(s) = \frac{F(s)}{\dot{X}(s)} \quad (1)$$

By taking Laplace transform of effort (force) and motion input (velocity), following expression obtained

$$sZ(s) = \frac{F(s)}{X(s)} \quad (2)$$

$$F(s) = sZ(s) \cdot X(s) \quad (3)$$

If both position $X(s)$ and force $F(s)$ are controlled accurately, the manipulator can achieve remarkable performance. But these parameters cannot be controlled independently due to $sZ(s)$ factor as shown in (3). To overcome this problem, an approach is adopted to control the position $X(s)$ and applying the desired relation using $Z(s)$, as a result, $F(s)$ will be controlled indirectly by (3). To derive the mathematical model of the manipulator's end-effector with its environment during the contact process, the impedance relationship is represented by the mass-spring-damper system. The mathematical model of the mass-spring-damper system is

$$M\ddot{X} + B\dot{X} + KX = F(t) \quad (4)$$

By taking the Laplace transform, we get

$$Z(s) = \frac{X(s)}{F(s)} = Ms^2 + Bs + K \quad (5)$$

Where M , B , and K represents the system inertia, damping, and stiffness respectively. Where F and X are the actual contact force and displacement of the system respectively. Usually, the desired impedance

behavior can be represented by a differential equation as

$$M_d(\ddot{X} - \ddot{X}_r) + B_d(\dot{X} - \dot{X}_r) + K_d(X - X_r) = -F_{ext}(t) \quad (6)$$

$$M_d(\ddot{E}) + B_d(\dot{E}) + K_d(E) = -F_{ext}(t) \quad (7)$$

The terms M_d , B_d and K_d are diagonal matrices representing the desired inertia, damping, and stiffness parameters respectively. Where X_r is the desired position of the end-effector while X represents the actual position.

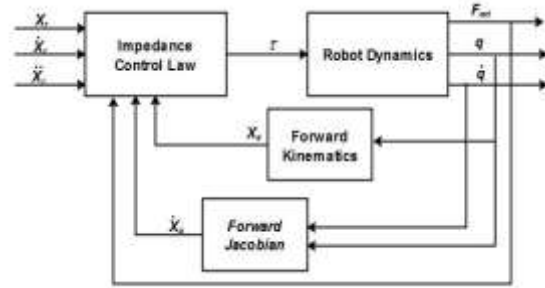


Fig. 1. Torque based impedance control block diagram

The impedance control paradigm is further classified based on the choice of the input signal to robot and feedback closure of various measurement signals such as position, velocity, and force.

2.2 Torque Based Impedance Control

A typical block diagram of a TBIC scheme is shown in Fig. 1. The required torque is calculated using the feedback force signal, actual end-effector position, and velocity along with reference input. In this case, the final torque value becomes the input to the robot's actuators. Generally, the TBIC law is suitable for all electrically actuated arms where motor torque is a basic control variable. Considering n degree of freedom (DOF) manipulator interacting with the environment, the equation of motion for n DOF manipulator in joint space can be represented as

$$H(q)\ddot{q} + C(q, \dot{q})\dot{q} + g(q) + f(\dot{q}) = \tau - J^T F_{ext} \quad (8)$$

Where q , \dot{q} , and \ddot{q} represent the joint's variable indicating position, velocity, and acceleration respectively. $H(q)$, $g(q)$, and $f(\dot{q})$ represent positive definite inertia matrix of order $n \times n$, gravitational forces of order $n \times 1$ and frictional forces of order $n \times 1$ respectively. Whereas $C(q, \dot{q})\dot{q}$ is the $n \times 1$ matrix represent Coriolis and centrifugal terms. Terms involving product of $q_i q_j$, where $i \neq j$ are referred to

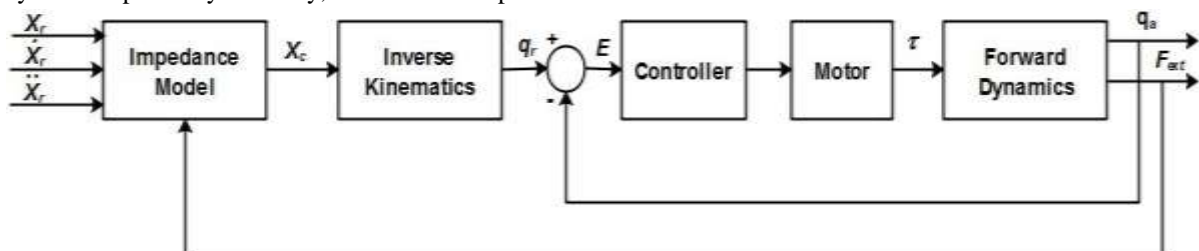


Fig. 2. Position-based impedance control (admittance control) for position tracking



as Coriolis terms while those involving q_i^2 referred to as centrifugal terms. J denotes the Jacobian matrix of order $6 \times n$ that relate the joint velocities to end-effector velocities. F_{ext} is an external force applied to manipulator's end-effector measured by a 6-dimensional force sensor mounted on wrist whereas τ represents $n \times 1$ joint torques. In the contact space, the manipulator's end-effector interface with its environment, it is suitable to represent robot dynamics in Cartesian space. The dynamics equation in task space can be represented as in [12]

$$H_x(x)\ddot{x} + C_x(x, \dot{x})\dot{x} + g_x(x) + f_x(\dot{x}) = J^{-T}\tau - F_{ext} \quad (9)$$

Where x representing the position and orientation of the manipulator's end-effector w.r.t reference frame, the following expressions are used to relate joint space with task space dynamics.

$$\begin{aligned} H_x &= J^{-T}HJ^{-1} \\ C_x(x, \dot{x}) &= J^{-T}(C - HJ^{-1}\dot{J})J^{-1} \\ g_x &= J^{-T}g \\ f_x(\dot{x}) &= J^{-T}f \end{aligned} \quad (10)$$

Where subscript x denotes terms in Cartesian space. Given the robot dynamics and impedance filter as shown in (9) and (6) respectively, the following expressions generate desired control torque $\tau = J^T F$ such that overall robot dynamics coincide with impedance filter (6). Equation (11) is modified to (12) which is in joint space form.

$$F = F_{ext} + C_x\dot{x} + g_x + f_x + H_x\{\ddot{x}_v - M_d^{-1}[B_d(\dot{x} - \dot{x}_v) + K_d(x - x_v) + F_{ext}] \quad (11)$$

$$\begin{aligned} \tau &= J^T \left\{ (JH^{-1}J^T)^{-1} \left[M_d^{-1} \left(K_d(x_d - T(\theta)) + B_d(\dot{x}_d - J\dot{\theta}) \right) + \ddot{x}_d + \right. \right. \\ & \left. \left. JH^{-1}(f + C\dot{\theta} + g) - J\dot{\theta} \right] + [I - (JH^{-1}J^T)^{-1}M_d^{-1}]F_{ext} \right\} \end{aligned} \quad (12)$$

Where $T(\theta)$ represents the forward kinematics operator that relates joint variables to end-effector pose.

2.3 Position Based Impedance Control for Position Tracking (Admittance Control)

Position based impedance control law (Admittance control) has an inner/outer loop arrangement as shown in Fig. 2. In this scenario, the force signal along with reference input is processed to calculate the position command for the outer loop. In the case of PBIC, the

manipulator is position-controlled and behaves like a mechanical impedance that accepts effort as an input and yield flow as an output. The PBIC is suitable for a practical approach to realize compliant physical interaction of position-controlled robots. The impedance model and PD controller for position control loop can be mathematically represented as

$$M_d(\ddot{X}_c - \ddot{X}_r) + B_d(\dot{X}_c - \dot{X}_r) + K_d(X_c - X_r) = -F_{ext}(t) \quad (13)$$

$$F = K_p(\theta_c - \theta) - K_d(\dot{\theta}) \quad (14)$$

Where X_c is commanded position while K_p and K_d are positive proportional and derivative gains. Whereas θ_c and θ are commanded joint variables and actual joint variable respectively. The admittance control law is mainly used for force tracking as compare to TBIC.

2.4 Position Based Impedance Control for Force Tracking

Most industrial robots successfully complete tasks with high accuracy in position control mode but are less accurate when operated in force control mode. It is difficult to achieve desired force tracking using a TBIC [13], therefore, PBIC is preferable over TBIC. The block diagram for PBIC for force tracking can be shown as in Fig. 3. A PBIC does not use joint torque explicitly and work on position mode. The servo driver position mode consists of three loops: the outer P position-loop, the middle PI velocity-loop, and the inner PI current-loop. When the servo driver worked on position mode, the servo driver receives a joint position as input and drives the joint to the commanded position. The torque mode implementation of impedance control requires the exact dynamic model of the robot, which is not possible in any physical scenario.

According to Fig. 3, X_r represents the reference position trajectory, X_c denote commanded position and X_m represents the actual trajectory followed by robot end-effector. In the position control mode, if the inner loop dynamics is fast compared to the outer loop, the commanded position will be equal to the actual position within no time, the change in a position due to the interaction force can be represented as

$$E = X_m - X_r = X_c - X_r \quad (15)$$

Now, the contact force F_e between the manipulator's end-effector and the environment stiffness K_e can be

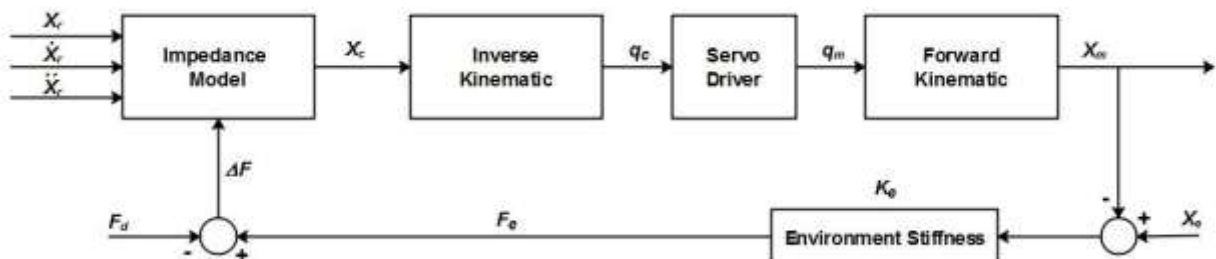


Fig. 3. Position-based impedance control for force tracking. Servo driver block denote cascaded motor control



written as

$$F_e = K_e(X_e - X_m) = K_e(X_e - X_c) \quad (16)$$

The force tracking error is $\Delta F = F_e - F_d$, where F_d is the desired contact force. The dynamical relationship between the position perturbation E and force tracking error ΔF can be mathematically expressed as

$$M \frac{d^2 E(t)}{dt^2} + B \frac{dE(t)}{dt} + K E(t) = \Delta F(t) \quad (17)$$

To modify reference position trajectory X_r , perturbation E is used to produce the commanded position as

$$X_c = X_r + E = X_r + \Delta F.K(s) \quad (18)$$

Where $K(s)$ is

$$K(s) = \frac{1}{ms^2 + bs + k} \quad (19)$$

For 1 DOF, the force tracking error Δf can be written as

$$\begin{aligned} \Delta f &= f_e - f_d = k_e(x_e - x_c) - f_d \\ &= k_e x_e - k_e(x_r + k(s) \Delta f) - f_d \end{aligned} \quad (20)$$

By substituting (19) into (20) gives

$$\begin{aligned} \Delta f(ms^2 + bs + k + k_e) \\ = (ms^2 + bs + k)[k_e(x_e - x_r) - f_d] \end{aligned} \quad (21)$$

The steady-state force error is given by

$$\Delta f_{ss} = \frac{k}{k + k_e} [k_e(x_e - x_r) - f_d] \quad (22)$$

The reference trajectory must be calculated according to (23) so that make steady-state force error converges to zero.

$$x_r = x_e - \frac{f_d}{k_e} \quad (23)$$

For desired force tracking f_d , environment stiffness k_e as well as environment location x_e must be known for reference trajectory computation. In practical scenarios, it's difficult to measure environment location and stiffness. Hence, the steady-state force error will be infinite because the reference trajectory not known accurately.

2.5 Position Based Impedance Control for Force Tracking in Unknown Environmental Stiffness

In the case of unknown environment stiffness, the computation of the reference trajectory is difficult as (23). Substituting $E = X_c - X_r$ and $\Delta F = F_e - F_d$ into (17) gives

$$F_e - F_d = M(\ddot{X}_c - \ddot{X}_r) + B(\dot{X}_c - \dot{X}_r) + K(X_c - X_r) \quad (24)$$

Due to unknown environment information, it is difficult to obtain accurate reference trajectory X_r . By replacing X_r with X_e yields

$$F_e - F_d = M(\ddot{X}_c - \ddot{X}_e) + B(\dot{X}_c - \dot{X}_e) + K(X_c - X_e) \quad (25)$$

where $E = X_c - X_e$.

Consider two cases for analyzing unknown environment stiffness. In the first case, by setting the desired force equal to zero, the robot end-effector will just come into contact with the environment. Equation (25) is always satisfied for any environment stiffness when $F_d = 0$. In the second case, by setting the desired force equal to a non-zero value, the robot end-effector will exert specific force on the environment which makes $X_c \neq X_e$, as a result, $\Delta F_{ss} \neq 0$. According to [6], by setting desired stiffness $K = 0$ in (25), the desired force tracking can be achieved when environment stiffness is unknown or dynamically changing. It can be mathematically represented as

$$\Delta F = M(\ddot{E}) + B(\dot{E}) + K(E) \quad (26)$$

In steady-state, differential terms become zero because no variation in system response. If we set stiffness $K = 0$, it yields $\Delta F_{ss} = 0$ for any environmental stiffness.

3. Kinematics and Dynamics of 3R Planar Robot

The robot kinematics deals with the relationship between the joint's variable and the robot's end-effector. The kinematic model is shown in Fig. 4. The forward kinematics of 3R planar robot is represented as

$$\begin{aligned} x &= l_1 \cos \theta_1 + l_2 \cos(\theta_1 + \theta_2) + l_3 \cos(\theta_1 \\ &\quad + \theta_2 + \theta_3) \\ y &= l_1 \sin \theta_1 + l_2 \sin(\theta_1 + \theta_2) + l_3 \sin(\theta_1 \\ &\quad + \theta_2 + \theta_3) \end{aligned} \quad (27)$$

Where l_1 , l_2 , and l_3 are 1st, 2nd and 3rd link lengths respectively. Whereas θ_1 , θ_2 , and θ_3 are 1st, 2nd and 3rd joint variables respectively. For given end-effector coordinates X , Y , the inverse kinematics of 3R planar robot can be represented as

$$\varphi = \tan^{-1} \left(\frac{Y}{X} \right) \quad (28)$$

$$X_2 = X - (l_3 * \cos \varphi) \quad (29)$$

$$Y_2 = Y - (l_3 * \sin \varphi)$$

$$A = \left(\frac{X_2^2 + Y_2^2 + l_1^2 - l_2^2}{2l_1 \sqrt{X_2^2 + Y_2^2}} \right) \quad (30)$$

$$B = \left(\frac{l_1^2 + l_2^2 - X_2^2 - Y_2^2}{2l_1 l_2} \right) \quad (31)$$

$$\theta_2 = \pi - \tan^{-1} \left(\frac{\sqrt{1 - B^2}}{B} \right) \quad (32)$$



$$\theta_1 = \tan^{-1}\left(\frac{Y_2}{X_2}\right) - \tan^{-1}\left(\frac{\sqrt{1-A^2}}{A}\right) \quad (33)$$

$$\theta_3 = \varphi - \theta_2 - \theta_1 \quad (34)$$

The robot dynamics deals with the relationship between joint torques/forces and joint acceleration. The equation of motion for 3R planar manipulator using Lagrange formulation can be expressed as

$$H(q)\ddot{q} + C(q, \dot{q})\dot{q} + G(q) = \tau \quad (35)$$

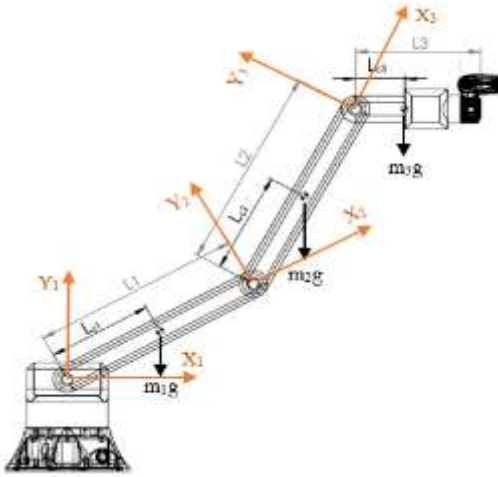


Fig. 4. Kinematics design of 3R planar robot

Where,

$$H = \begin{bmatrix} a & b & c \\ d & e & f \\ g & h & i \end{bmatrix}, C = \begin{bmatrix} j & k & l \\ m & n & o \\ p & q & r \end{bmatrix}, G = \begin{bmatrix} s \\ t \\ u \end{bmatrix}, \tau = \begin{bmatrix} \tau_1 \\ \tau_2 \\ \tau_3 \end{bmatrix}, q = \begin{bmatrix} \theta_1 \\ \theta_2 \\ \theta_3 \end{bmatrix}$$

$$\begin{aligned} a &= m_1 a_{c1} + I_1 + m_2 a_1^2 + m_2 a_{c2}^2 + I_2 + 2m_2 a_1 a_{c2} \cos \theta_2 + m_3 a_1^2 + m_3 a_2^2 + m_3 a_{c3}^2 + 2m_3 a_1 a_2 \cos \theta_2 + 2m_3 a_2 a_{c3} \cos \theta_3 + 2m_3 a_1 a_{c3} \cos(\theta_2 + \theta_3) + I_3 \\ b &= m_2 a_{c2}^2 + I_2 + m_2 a_1 a_{c2} \cos \theta_2 + m_3 a_2^2 + m_3 a_{c3}^2 + m_3 a_1 a_2 \cos \theta_2 + 2m_3 a_2 a_{c3} \cos \theta_3 + m_3 a_1 a_{c3} \cos(\theta_2 + \theta_3) + I_3 \\ c &= m_3 a_{c3}^2 + m_3 a_2 a_{c3} \cos \theta_3 - m_3 a_1 a_{c3} \cos(\theta_2 + \theta_3) + I_3 \\ d &= m_2 a_{c2}^2 + I_2 + m_2 a_1 a_{c2} \cos \theta_2 + m_3 a_2^2 + m_3 a_{c3}^2 + m_3 a_1 a_2 \cos \theta_2 + 2m_3 a_2 a_{c3} \cos \theta_3 + m_3 a_1 a_{c3} \cos(\theta_2 + \theta_3) + I_3 \\ e &= m_2 a_{c2}^2 + I_2 + m_3 a_2^2 + m_3 a_{c3}^2 + 2m_3 a_2 a_{c3} \cos \theta_3 + I_2 \end{aligned}$$

$$\begin{aligned} f &= m_3 a_{c3}^2 + m_3 a_2 a_{c3} \cos \theta_3 + I_3 \\ g &= m_3 a_{c3}^2 + m_3 a_2 a_{c3} \cos \theta_3 + m_3 a_1 a_{c3} \cos(\theta_2 + \theta_3) + I_3 \\ h &= m_3 a_{c3}^2 + m_3 a_2 a_{c3} \cos \theta_3 + I_3 \\ i &= m_3 a_{c3}^2 + I_3 \\ j &= -m_3 a_1 a_{c3} \sin(\theta_2 + \theta_3) \dot{\theta}_1 - m_3 a_1 a_2 \sin \theta_2 \dot{\theta}_2 - m_3 a_2 a_{c3} \sin \theta_3 \dot{\theta}_3 \\ k &= -m_2 a_1 a_{c2} \sin \theta_2 (\dot{\theta}_1 + \dot{\theta}_2) + m_3 a_1 a_2 \sin \theta_2 (\dot{\theta}_1 + \dot{\theta}_2) - m_3 a_1 a_{c3} \sin(\theta_2 + \theta_3) (\dot{\theta}_1 + \dot{\theta}_2) \\ l &= -m_3 a_2 a_{c3} \sin \theta_3 (\dot{\theta}_1 + \dot{\theta}_2) - m_3 a_2 a_{c3} \sin \theta_3 (\dot{\theta}_2 + \dot{\theta}_3) - m_3 a_1 a_{c3} \sin(\theta_2 + \theta_3) (\dot{\theta}_1 + \dot{\theta}_2) - m_3 a_1 a_{c3} \sin(\theta_2 + \theta_3) (\dot{\theta}_1 + \dot{\theta}_3) \\ m &= -m_2 a_1 a_{c2} \sin \theta_2 (\dot{\theta}_2) - m_3 a_1 a_2 \sin \theta_2 (\dot{\theta}_2) - m_3 a_2 a_{c3} \sin \theta_3 (\dot{\theta}_3) - m_3 a_1 a_{c3} \sin(\theta_2 + \theta_3) (\dot{\theta}_2 + \dot{\theta}_3) + m_2 a_1 a_{c2} \sin \theta_2 (\dot{\theta}_1 + \dot{\theta}_2) + m_3 a_1 a_2 \sin \theta_2 (\dot{\theta}_1 + \dot{\theta}_2) + m_3 a_1 a_{c3} \sin(\theta_2 + \theta_3) (\dot{\theta}_1 + \dot{\theta}_2) \\ n &= m_3 a_1 a_{c3} \sin(\theta_2 + \theta_3) \dot{\theta}_1 - m_2 a_1 a_{c2} \sin \theta_2 \dot{\theta}_1 \\ o &= -m_3 a_2 a_{c3} \sin \theta_3 (\dot{\theta}_1 + \dot{\theta}_2) - m_3 a_2 a_{c3} \sin \theta_3 (\dot{\theta}_2 + \dot{\theta}_3) + m_3 a_1 a_{c3} \sin(\theta_2 + \theta_3) (\dot{\theta}_1) \\ p &= -m_3 a_2 a_{c3} \sin \theta_3 \dot{\theta}_3 + m_3 a_2 a_{c3} \sin \theta_3 (\dot{\theta}_1 + \dot{\theta}_2) + m_3 a_1 a_{c3} \sin(\theta_2 + \theta_3) (\dot{\theta}_1) \\ q &= m_3 a_2 a_{c3} \sin \theta_3 (\dot{\theta}_1 + \dot{\theta}_2) - m_3 a_2 a_{c3} \sin \theta_3 (\dot{\theta}_3) \\ r &= m_3 a_1 a_{c3} \sin \theta_3 (\dot{\theta}_1 + \dot{\theta}_2) \\ s &= m_1 g a_{c1} \cos \theta_1 + m_2 g a_1 \cos \theta_1 + m_2 g a_{c2} \cos(\theta_1 + \theta_2) + m_3 g a_1 \cos \theta_1 + m_3 g a_2 \cos(\theta_1 + \theta_2) + m_3 g a_{c3} \cos(\theta_1 + \theta_2 + \theta_3) \\ t &= m_2 g a_{c2} \cos(\theta_1 + \theta_2) + m_3 g a_2 \cos(\theta_1 + \theta_2) + m_3 g a_{c3} \cos(\theta_1 + \theta_2 + \theta_3) \\ u &= m_3 g a_{c3} \cos(\theta_1 + \theta_2 + \theta_3) \end{aligned}$$

Where,

$$\begin{aligned} m_i &= \text{mass of link } i \\ a_i &= \text{length of } i^{\text{th}} \text{ link} \\ a_{ci} &= \text{distance from } i^{\text{th}} \text{ joint to COM of } i^{\text{th}} \text{ link} \\ I_i &= \text{inertia of link } i \\ \tau_i &= \text{torque of } i^{\text{th}} \text{ joint} \\ \theta_i &= i^{\text{th}} \text{ joint variable} \end{aligned}$$

4. Simulation and Results

In this section, the proposed impedance control schemes are implemented on the 3R planar robot to verify the proposed approaches and observe the results for multiple scenarios. A series of simulations are carried out on MATLAB/Simulink software. For a 3R planar robot, listed parameters are used $m_1 = I$



kg , $m_2 = 1 kg$, $m_3 = 1 kg$, $l_1 = 0.3 m$, $l_2 = 0.3 m$ and $l_3 = 0.2 m$. The Maxon Micro Drives DC motor M4870U with gear head ratio 17:1 is used for robot joint actuation. The selected motor parameters are Winding Resistance (R)=0.8 ohm, Rotor Inductance (L)=400 μH , Back-emf Constant (K_t)= 2.15 mV/rpm, Rotor Inertia (J) = 180 gcm^2 and Rotor damping (B)=3.5e-6 Nm/(rad/s). The motor nominal torque and rated speed are 42.68 mNm and 11,000 rpm respectively.

In the case of TBIC, two cases are considered for analyzing behavior. In the first case, damping values B_x , B_y are kept constant while stiffness parameter K_x , K_y are varied. Whereas K and B are diagonal matrices of order 3 by 3 and subscript denotes desired behavior along the Cartesian axis. The z -axis is omitted because of the planar redundant robot and has no effect on system response. The reference position is set to $X_r = 0.3 m$ and $Y_r = 0.1 m$ while desired inertia of required impedance is set to $M_x = M_y = 0.5 Ns^2/m$. A constant external force $F_x = F_y = 10 N$ is applied on the end-effector for a duration of 2 sec. As shown in Fig. 5, it is concluded that the robot becomes stiffer as the stiffness parameter increased. In the second case, the stiffness values K_x , K_y are kept constant and damping values B_x , B_y are varied from 10 Ns/m to 50 Ns/m. As shown in Fig. 6, the robot becomes less oscillatory as damping value increases. Overall, in the case of TBIC, the set value of the damping factor defines the end-effector oscillations while the stiffness adjusts the compliance of the robot along each axis.

In the case of PBIC for position tracking, the reference position is set to $X_r = 0.4 m$ and $Y_r = 0.2 m$. The impedance model parameters are selected as $M_x = M_y = 1 Ns^2/m$, $B_x = B_y = 25 Ns/m$ and $K_x = K_y = 150 N/m$. The PD controller parameters are set to $K_p = 7650$ and $K_d = 600$. As shown in Fig. 7, the external force of magnitude 10 N is applied along the x-axis for 5 to 7-sec interval. Whereas, the external force of magnitude 15 N is applied along the y-axis during 4 - 6-sec interval. The commanded position X_c and Y_c are updated according to external force while the reference position remains unchanged. The robot behavior against stiffness and damping parameters variation is the same as in torque based impedance control.

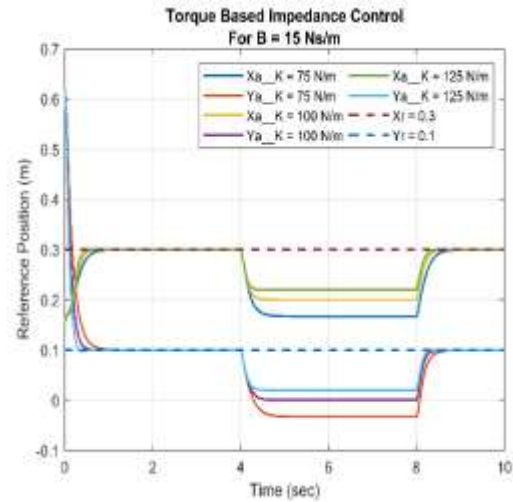


Fig. 5. Torque based impedance control for $B = 15 Ns/m$

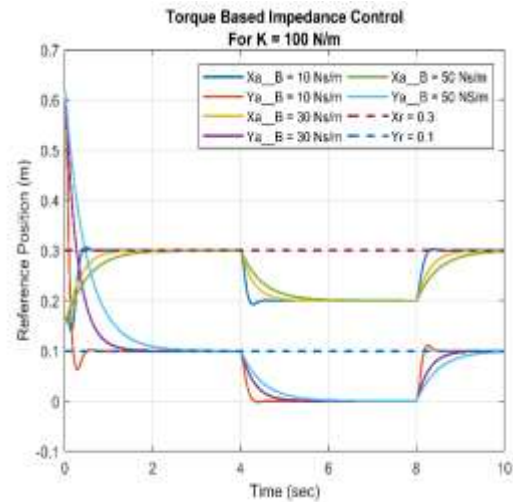


Fig. 6. Torque based impedance control for $K = 100 N/m$

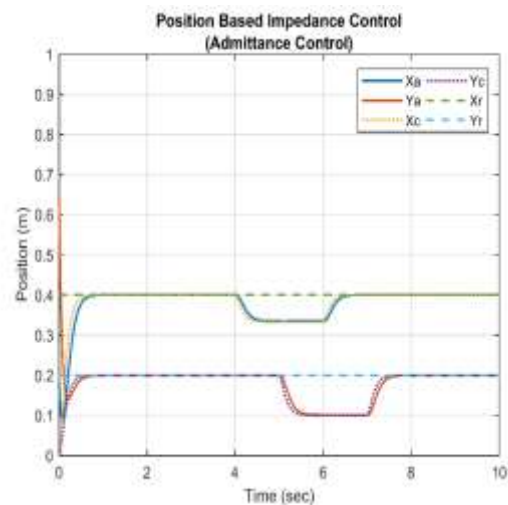


Fig. 7. Position-based impedance control for position tracking

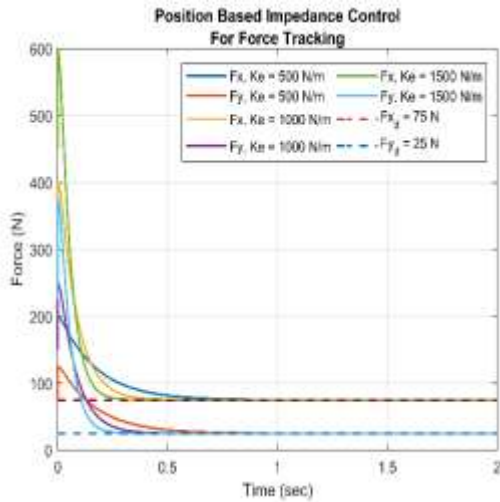


Fig. 8. Position based impedance control for force tracking

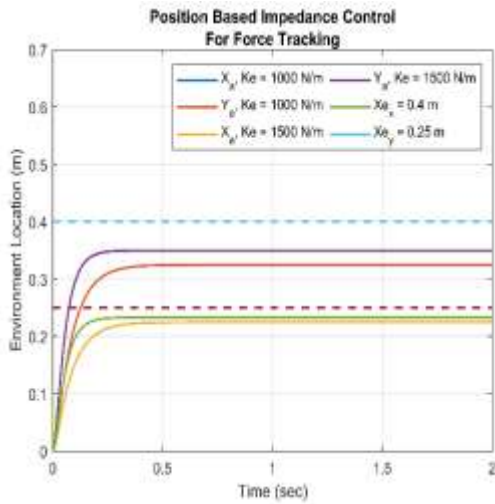


Fig. 9. Position based impedance control for force tracking

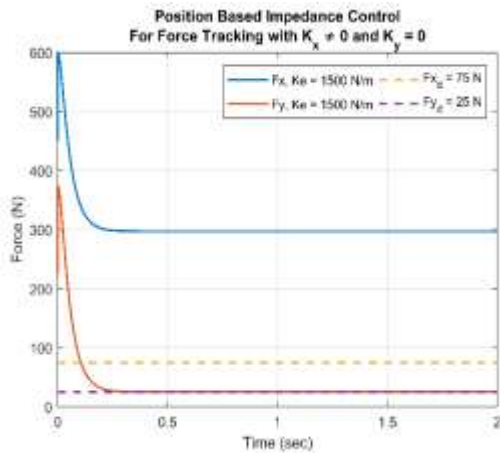


Fig. 10. Position based impedance control for force tracking, for $K_x \neq 0$

To verify the force tracking performance of the PBIC scheme against unknown environment stiffness, two

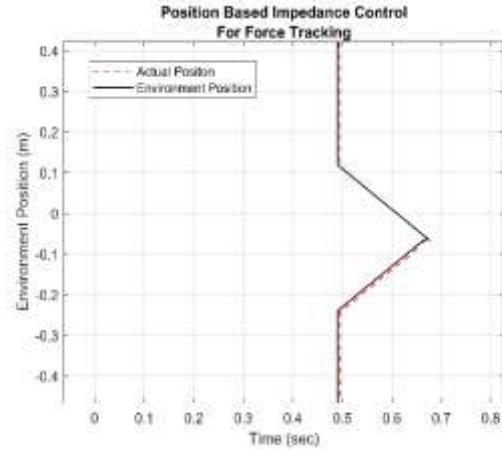


Fig. 11. Force tracking on un-even surface with variation in K_e

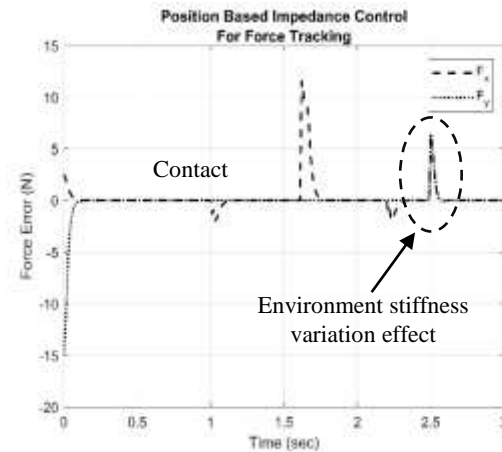


Fig. 12. Force tracking error with variation in K_e

cases are considered for validating the proposed approach. In the first case, the desired force of magnitude 75 N and 25 N along x and y-axis is selected respectively. By setting stiffness value $K_x = K_y = 0$ N/m and damping value $B_x = B_y = 90$ Ns/m, steady-state force error is zero for any environment stiffness as shown in Fig. 8. From Fig. 8, it's observed that the convergence rate is faster for stiffer environment. The environment location is set to $X_{ex} = 0.4$ m and $X_{ey} = 0.25$ m. The actual position of end-effector for different environment stiffness $K_e = 1000, 1500$ N/m is shown in Fig. 9. In the second case, we consider the non-zero value of desired stiffness along the x-axis and zero value of stiffness along the y-axis. From Fig. 10, it's observed that steady-state force error exists along the x-axis whereas force error is zero along the y-axis. To ensure the convergence of force error to zero when robot's end-effector interacted with rough surface, a simulation is performed on un-even surface with varying environment stiffness as shown in Fig. 11. The damping parameters are set to $B_x = B_y = 120$ Ns/m and desired Cartesian forces of magnitude 15 N

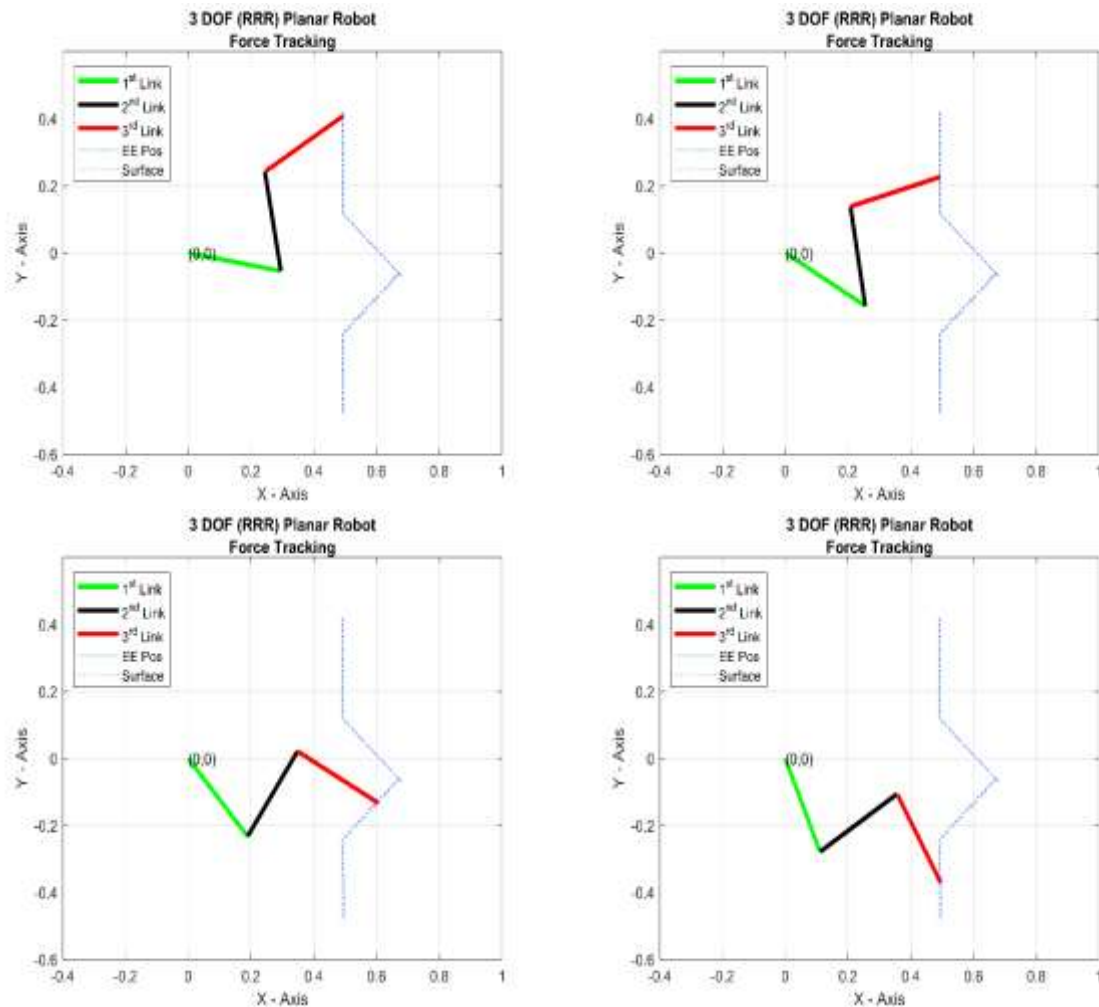


Fig. 13. Simulation snapshots for force tracking on un-even surface with varying environment stiffness

along each axis is selected. The environment stiffness is varied according to following profile

$$K_e = \begin{cases} 3500 \text{ N/m} & 0 < t \leq 2.5 \text{ s} \\ 5000 \text{ N/m} & 2.5 \text{ s} < t \leq 3 \text{ s} \end{cases}$$

The force tracking error profile is shown in Fig. 12, it is observed that as environment stiffness varied, as a result, overshoot indicates force error which converges to zero again. The snapshots of a MATLAB simulation are presented in Fig. 13.

5. Conclusion

In this paper, authors have derived and implemented the mathematical expressions of each impedance control paradigm, for redundant planar robots, and have also compared their effectiveness under different scenarios using MATLAB/Simulink. In addition to providing the complete mathematical model of the system, realistic parameters of a complete system are employed. In free space, it is exhibited that the effect of damping and stiffness on robot's behavior is consistent in both the paradigms: torque-based and position-based impedance control

law. The tuned PD controller parameters improved the system's transient response in the case of PBIC for position tracking. In the contact space, the system was able to track the desired force accurately on flat surface using constant PBIC law by setting desired stiffness to zero. It is also concluded that as the environment becomes stiffer, the desired force convergence rate is increased. In the case of complex surfaces with varying environment stiffness, the PBIC law is implemented on planar redundant robot to ensure convergence of force error to zero.

6. Future Work

Implementation of adaptive variable impedance control law on a redundant manipulator interacting physically with the unknown location and stiffness of the environment as well as exploiting redundancy resolution.

REFERENCES

- [1] N. Hogan, "Impedance Control: An Approach To Manipulation," pp. 304–313, 1984.



- [2] N. Hogan, "Impedance Control: An Approach to Manipulation: Part II — Implementation," no. June 1983, 1985.
- [3] J. J. Craig, "Hybrid Position / Force Control of Manipulators," vol. 102, no. June 1981, 1981.
- [4] P. Song, Y. Yu, and X. Zhang, "Impedance control of robots: An overview," *Proc. - 2017 2nd Int. Conf. Cybern. Robot. Control. CRC 2017*, vol. 2018-Janua, no. 1, pp. 51–55, 2017.
- [5] C. Ott, R. Mukherjee, and Y. Nakamura, "Unified impedance and admittance control," *Proc. - IEEE Int. Conf. Robot. Autom.*, pp. 554–561, 2010.
- [6] H. Seraji, "Force Tracking in Impedance Control," vol. 16, No.1, pp. 97–117, 1997.
- [7] S. Jung, T. C. Hsia, and R. G. Bonitz, "Force Tracking Impedance Control of Robot Manipulators Under Unknown Environment," vol. 12, no. 3, pp. 474–483, 2004.
- [8] S. Jung and T. C. Hsia, "Robust neural force control scheme under uncertainties in robot dynamics and unknown environment," *IEEE Trans. Ind. Electron.*, vol. 47, no. 2, pp. 403–412, 2000.
- [9] S. Jung and T. C. Hsia, "Neural Network Impedance Force Control of Robot Manipulator," vol. 45, no. 3, pp. 451–461, 1998.
- [10] Z. Yang, J. Peng, and Y. Liu, "Adaptive neural network force tracking impedance control for uncertain robotic manipulator based on nonlinear velocity observer," *Neurocomputing*, vol. 331, pp. 263–280, 2018.
- [11] D. Jinjun, G. Yahui, C. Ming, and D. Xianzhong, "Adaptive variable impedance control for dynamic contact force tracking in uncertain environment," *Rob. Auton. Syst.*, vol. 102, pp. 54–65, 2018.
- [12] W. Lu and Q. Meng, "Impedance Control with Adaptation for Robotic Manipulations." pp. 408–415, 1991.
- [13] P. Song, Y. Yu, and X. Zhang, "Impedance Control of Robots: An Overview," no. 1, 2017.



Design and Development of Sun Tracking System Using Programmable Logic Controller (PLC)

Hammad Farooq¹, Hafiz Muhammad Waqas Badar², Ahmad Hussain Safder³

1. Al-Khawarizmi Institute of Computer Science, UET Lahore, Pakistan, hammad.farooq@kics.edu.pk
2. Al-Khawarizmi Institute of Computer Science, UET Lahore, Pakistan, waqas.badar@kics.edu.pk
3. Al-Khawarizmi Institute of Computer Science, UET Lahore, Pakistan, ahmad.hussain@kics.edu.pk

Abstract:

This paper describes the calculation and implementation of the azimuth and zenith angles of the sun by using astronomical equations. Dual-axis electromechanical hardware is developed to track the sun on both axes. This tracking system is controlled using ON-OFF controller which is implemented in the programmable logic controller (PLC). A performance monitoring system is developed using human-machine interface (HMI), this system continuously monitors and log data at one sample per minute. It was observed that the tracking controller operated without a problem with a maximum error of 0.13° which is acceptable. Besides, when data attained from HMI was compared to MATLAB simulation of equations, it was seen that simulation and hardware results were approximately same.

Key Words: Sun tracking; PLC; ON-OFF controller

1. Introduction

Sun is the earth's closest star and the main source of energy for the earth. The solar radiations reaching the earth's surface might be harvested, stored and converted to other usable forms. To harvest the maximum energy from solar radiations, the collector's surface should be kept at a specific position, e.g. in case of solar panel, parabolic dish and parabolic trough, the surface should be perpendicular to sun rays. In the case of the heliostat, orientation angles for heliostat mirrors needs to be determined to focus rays on tower receiver. To harvest the maximum possible energy, solar angles and collector tracking angles are of vital importance to be computed.

Over the years, several researches have published in sun-tracking filed, which involve the sun's angle calculation. The main purpose of determining the sun position is to increase the amount of energy obtained from sun rays. G.C Lazaroiu, et al., investigated the obtained energy by using two solar panel system, one is fixed system and other one is sun tracking system and experimental results shows 12-20% increase in energy by using sun tracker [1]. A. Chaib, et al., have worked on the orientation of concentrated solar power system using heliostat, the program for daily, monthly and, the yearly position of the sun is developed in MATLAB and orientation of heliostat is done by using PLC [2]. L. Mounire, et al., have developed a solar tracking system for heliostat, java language is used to calculate and generate sun position according to geographical location[3]. H. Fathabadi has proposed an offline sensorless dual-axis solar tracker

that find sun position where maximum solar energy capture by using solar map equations [4]. X. Zhikun has designed a solar tracking system by using a photoelectric sensor which also employs perturbation and observation algorithm for accurately locating the position of the sun [5]. K Kumar, et al., have used the RTC module and microcontroller to implement sun-tracking equations for solar dish concentrator [6]. K Mao, et al., have presented a solar tracking system, using ARM controller to implement equation for sun position [7]. S.A.A Shufat, et al., have used an astronomical algorithm to find sun trajectory and stored constant data for a specific location for further use by parabolic dish to get orthogonal to sun radiations [8]. Hassan N. Muslim has proposed an algorithm to optimize solar tilt angle based on MATLAB software [9].

In this paper, a sun position tracking method is proposed. Astronomical equations were used and implemented in MATLAB and then in PLC for sun position calculation, which was used as a reference to control the position of receivers. The ON-OFF controller was used in PLC for sun tracking. The generated data sent to the HMI unit through serial communication. In HMI, these angle's data were store in USB as an excel sheet. Data from excel files were extracted and used in the MATLAB program for plotting PLC resultant graphs.

2. The Equations of Sun Position

The sun's visible movement, caused by the Earth's rotation around its axis, shifts the angle at which the earth will be struck by the primary



component of light. The sun appears to be moving across the sky from a fixed location on Earth. The sun's position depends on the location of a point on Earth, day time, and year time.

Earth revolves around the sun in an elliptic path tilted at 23.458°, but for calculations, earth is considered as static object and sun is considered as moving object. The angle between the line joining the center of the sun and the earth and its projection on the equatorial plane is called the solar declination angle (d) [10]. Value of declination can be calculated as [11].

$$d = 23.45 \sin \left[360 \frac{(284 + n)}{365} \right] \quad (1)$$

Where n is day of year

The angular time measurement is the angle of hour (ω). The Hour Angle transforms the local solar time (LST) into the number of degrees that the sun moves through the sky. It is calculated as follows.

$$\omega = 15 * (LST - 12) \quad (2)$$

LST can be found as:

$$LST = LT + \frac{TC}{60} \quad (3)$$

Where LT is local time, that is obtained using real time clock (RTC) and TC is time correction. TC depend on location on earth and can be calculated as [11].

$$TC = 4(\text{Longitude} - LST) + EoT \quad (4)$$

Where LSTM is local standard time meridian and determined by:

$$LSTM = 15 * \Delta T_{UTC} \quad (5)$$

Where ΔT_{UTC} is difference of local time from universal coordinate time.

Equation of Time (EoT) (in minutes) is an empirical formula that corrects the Earth's orbit's eccentricity and axial title of the Earth [11]:

$$EoT = 229.2 \begin{pmatrix} 0.000075 \\ +0.001868 \cos B \\ -0.032077 \sin B \\ -0.014615 \cos 2B \\ -0.04089 \sin 2B \end{pmatrix} \quad (6)$$

Where

$$B = (n - 1) \frac{360}{365} \quad (7)$$

Solar zenith angle (θ_z) which is a vertical angle between sun's rays and a line perpendicular to the horizontal plane through the point [11].

$$\theta_z = \cos^{-1} [\cos j \cos d \cos w + \sin d \sin \varphi] \quad (8)$$

Where Φ is latitude.

The azimuth angle (γ) is the compass direction from where the sunlight is coming. It is the angle between the projection of the line through the center of the sun to center of the earth and north-south direction. At solar noon, sun in the northern hemisphere is always directed south and in northern hemisphere is directed north [10, 12]. The sun rises exactly east and sets exactly west, regardless of the latitude, rendering the azimuth angle 90° at sunrise and 270 at sunset. Azimuth angle varies with latitude, hour angle, and declination angle, it can be calculated as follows [11]

$$g = \text{sign}(w) \left| \cos^{-1} \left[\frac{\cos \theta_z \sin \varphi - \sin d}{\sin \theta_z \cos \varphi} \right] \right| \quad (9)$$

To calculate daylight time, sunrise time and sunset time should be known and this would calculate with eq (10) and (11) for sunrise and sunset respectively.

$$\text{Sunrise} = 12 - \frac{1}{15} \cos^{-1} (-\tan \varphi \tan d) - \frac{TC}{60} \quad (10)$$

$$\text{Sunset} = 12 + \frac{1}{15} \cos^{-1} (-\tan \varphi \tan d) - \frac{TC}{60} \quad (11)$$

3. Hardware Setup

Figure 2 represents hardware setup. In this hardware, to move receiver in two axes, dual-axis slew drive was used. Slew drive has a gear ratio of 1:62 and to move into two directions, it contains two DC motors. The maximum voltages of these motors are 24 V DC. These motors provide a maximum speed of 3 rev/min and 33N.m torque after the gear ratio. These DC motors are geared motors, they have a gear ratio of 1:575. So, the total gear ratio provided by the slew drive is 1:35650. These motors have built-in magnetic pulse generator as speed encoder, which provides 2 pulses per revolution with two channels, channel A and channel B. To control the tracking process, Fatek FBs-44MNT2-AC PLC was used. This PLC has a built-in real-time clock. This PLC has 8 differential inputs from which 4 differential input were used to get motors speed from motor encoders, which provide differential output per channel. Four single-ended output were used to trigger the 4 relays, two relays per motor. Each motor was controlled by two double pole double



throw relays. The connection diagrams of the system shown in figure 1, both motors were wired according to this diagram.

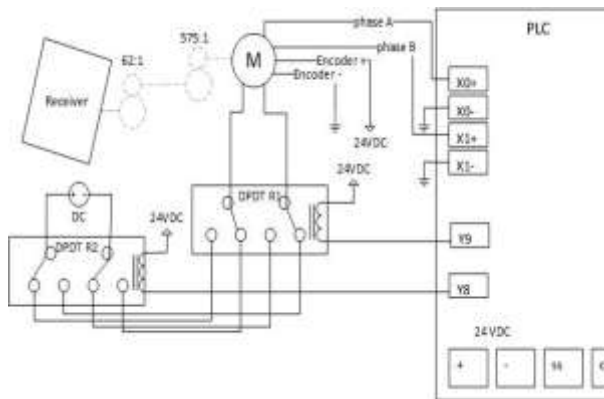


Figure 1: Connection diagram for both motors

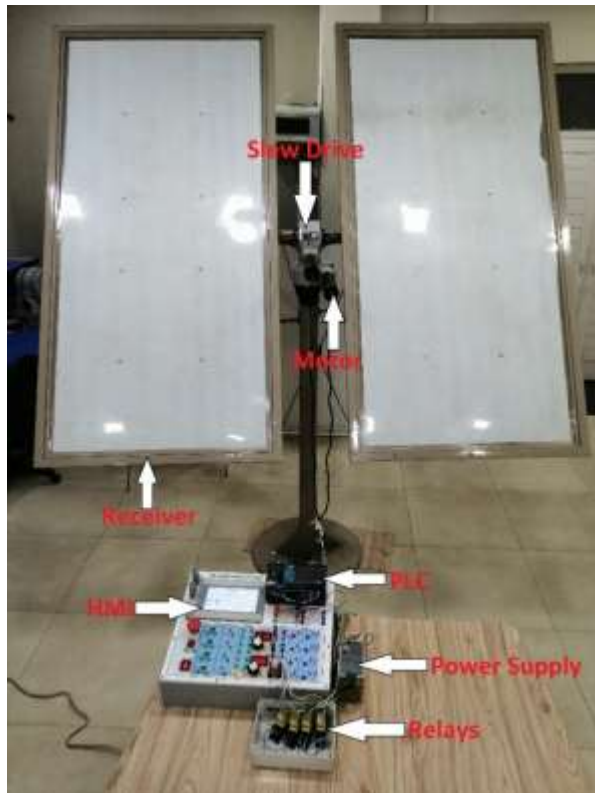


Figure 2: Hardware Setup

4. Implementation on PLC

The flow chart of the program for PLC, which was developed for the double-axis sun tracing system is shown in figure 3.

4.1 Initialization

At the initialization stage, the program first read latitude and longitude value from the PLC register

then it set all outputs to 0V. whenever the program starts from the initial stage, it read the receiver azimuth (P-Az) angle and receiver zenith angle (P-Zi), and convert it into corresponding counter value. As mentioned before encoder gives 2 pulses per revolution of the motor, so per revolution at slew drive output shaft give 71,300 pulses. As 1 revolution is 360° so, 1° at slew drive output give 198.05555 counts. Therefore, the current value of the counter is updated by multiplying the angle value by 198.05556. Fatek FBs PLC provides built-in 4 hardware high-speed counter (HHSC), which employed a special hardware circuit to count pulse value.

4.2 Time Correction

The second stage in the PLC program is time correction calculation. To calculate time correction, eq 4,5,6,7 were used in PLC. Day of the year was obtained with the help of Table 1 [11].

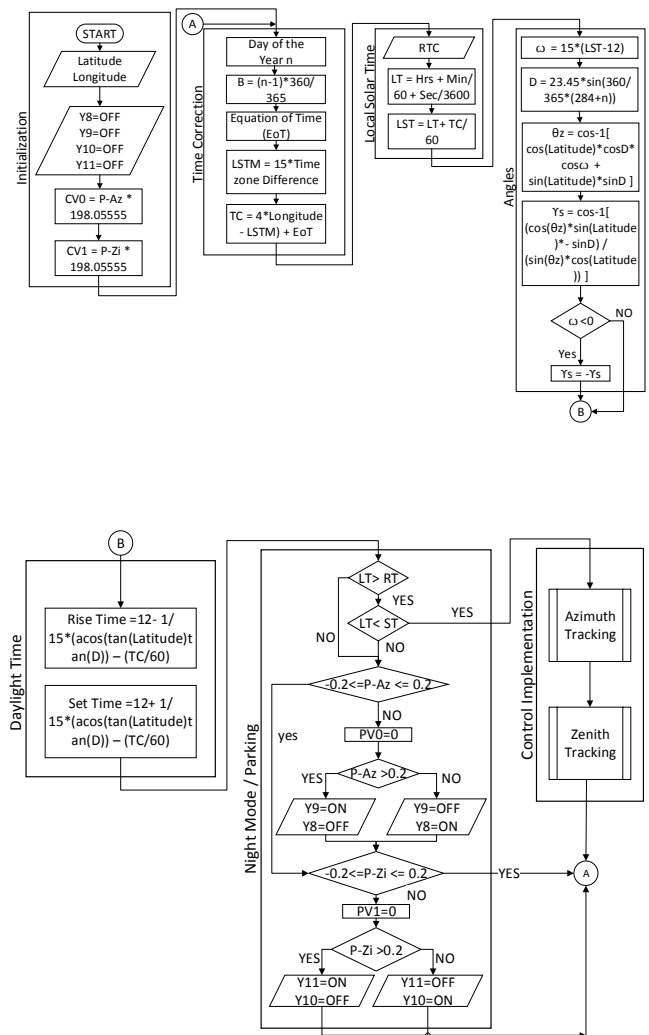


Figure 3: Flow chart of the PLC program



Table 1: Recommended average days for months

Month	n for ith day of Month
January	i
February	31+i
March	59+i
April	90+i
May	120+i
June	151+i
July	181+i
August	212+i
September	243+i
October	273+i
November	304+i
December	334+i

4.3 Local Solar Time

At the 3rd stage of the program, local solar time was calculated by using eq 3. Real-time clock module is used to get local time in an hour, minutes and, seconds. Minutes and seconds are converted into corresponding hour value by dividing it by 60 and 3600 respectively. similarly, time correction calculated in minutes, then converted to hours.

4.4 Angles Calculation

In the 4th stage of the program, different angles were calculated including Hour angle, declination angle, zenith angle and azimuth angle by using eq 2,1,8 and 9 respectively. As the azimuth angle makes zero angles at solar noon so, before noon, the sun makes angle from -90° towards 0° and afternoon it gives angle from 0° towards 90° but eq 9 gives only positive angle. As the sign of hour angle and azimuth must be same at the given time that's why the sign of azimuth angle was set according to hour angle's sign.

4.5 Daylight Time

Daylight time was calculated in 5th stage. Daylight was calculated in PLC using eq 10 and 11. Sunrise time and sunset time were used to make decision between tracking mode and night parking mode. If the local time is greater than sun rise time and less than sunset time then tracking mode will run otherwise program set the receiver position at parking.

4.6 Parking Mode

In this mode at every instruction cycle program will check if receiver's azimuth and zenith angle does

not lie in between -0.2° and $+0.2^\circ$, then program will reset the preset value (PV0) of PLC's HHSC0 and HHSC1 respectively and then it runs the motors in anti-clockwise direction if receiver's angle is greater than 0.2° or it runs motors in clockwise direction if receiver's angle is less than -0.2° . If the receiver's angle is in between -0.2° and 0.2° then program will keep the receiver's position as it is.

4.7 Interrupt Service Routine (ISR)

Interrupt Service Routine (ISR) was used in this program to stop motors. ISR will run when the program receives interrupt signal. As aforementioned about HHSC provided by Fatek PLC, it generates an interrupt signal whenever HHSC current value (CV) becomes equal to a preset value (PV) of HHSC. Another way round, PLC program has written in such a way that this interrupt signal generated whenever error between sun angle and receiver angle becomes zero. On receiving this signal, ISR runs. As we are using two encoders for dual-axis tracking system so, two HHSC counters are used, therefore, two interrupt signals are expected by PLC, one is from HHSC0 (for Azimuth position) and second one from HHSC1 (for Zenith position). HHSC0 counter has a higher priority than HHSC1. At the start of each ISR code, it reset output pins of PLC to stop the motor. Very next to this a Fatek block is used to immediately update output pins. immediate input/output instruction refresh outputs at the same time as it generated, to avoid scan time delay.

4.8 Tracking Program

If local time is greater than sunrise time and less than sunset time, then the program will run the sun-tracking program. ON/OFF controller was used to control the tracking as shown in figure 4. To control the oscillation of ON/OFF control, 0.056% of hysteresis was introduced. Another way round controller dead band is 0.2. At first sun azimuth tracking starts then zenith tracking comes into the picture. It can be possible that both motors are running at the same time. This would happen in the morning, at the start of tracking and in the evening during parking mode or when there is a large error between the sun angles and receiver angles. PLC ladder program turns ON motors according to error difference but the motor will turn OFF when an interrupt signal (zero error) is received by PLC from HHSC hardware circuitry. Flowchart for azimuth tracking and zenith tracking program is shown in figure 5 and 6 respectively.

At the start of the tracking program, initially error is calculated by subtracting receiver angle from sun angle. Then the error in degrees converted to



equivalent HHSC count value which is then added to the current counter value of HHSC, which is equivalent to the receiver angle as desired position of the receiver. This desired position's count value sets to HHSC preset value as a reference signal so, when HHSC current value becomes equal to its present value, resulting in zero error, an interrupt signal is generated to stop motors. As aforesaid, 0.056% hysteresis is used in this controller, that's why when the error is in between -0.2° to 0.2° , the motor will not run. If the error is greater than 0.2° , the motor will run in the clockwise direction and if the error is less than -0.2° , the motor will run in the anti-clockwise direction.

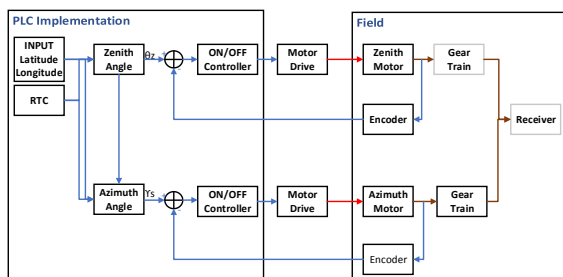


Figure 4: Control system block diagram

5. Results and Discussion

The experiment was conducted for Lahore city, which is located at latitude 31.5781 and longitude 74.3579. Firstly, the aforementioned astronomical equation for sun position was implemented in MATLAB and PLC then tracking code tested. We have chosen four typical days to implement aforementioned equation, those four days were 21 March (Day 80), 21 June (Day 172), 23 September (Day 266) and 22 December (Day 356). MATLAB simulation and PLC hardware results shown in figure 7 to 10. Results indicate that MATLAB simulated angles and PLC calculated angles have approximately the same values at any solar time. According to results, the zenith angle is approximately 90° at sunrise and fall to its minimum value at solar noon, when the sun is overhead, and the zenith value again rises to 90° at sunset.

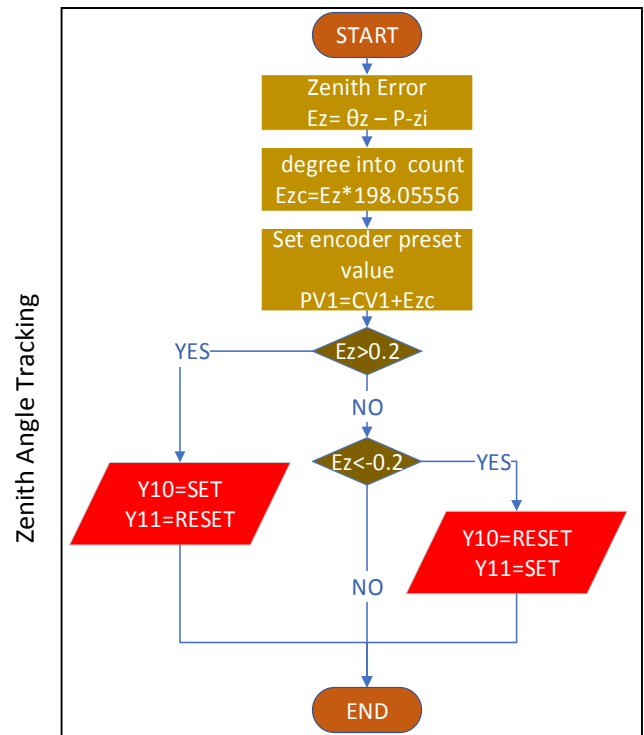


Figure 5: Flowchart for azimuth tracking

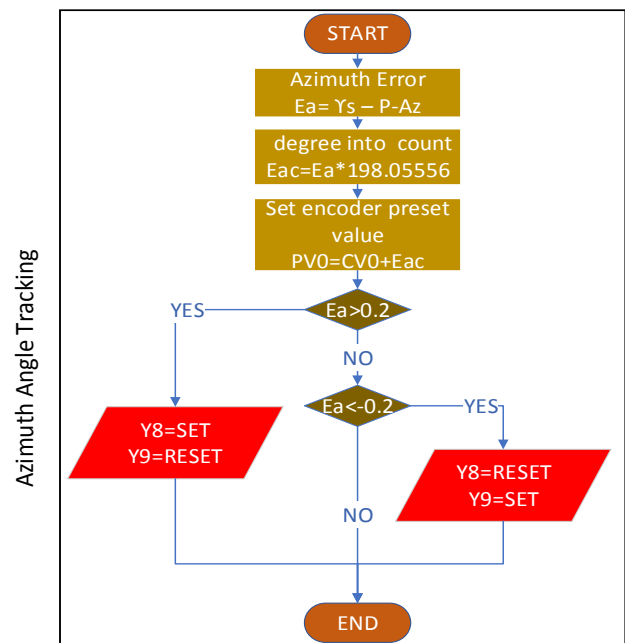


Figure 6: Flow chart for zenith tracking

The solar zenith angle reaches to its minimum value (8.143°) of the year on 21 June (Day 172) at solar noon, however, the maximum value is 55.02° on December 22 (Day 356) at solar noontime. The azimuth angle is the direction from which sunlight is coming. Azimuth angle faces toward the south in the northern hemisphere at solar noon at 0° .



The solar azimuth angle reaches to its maximum absolute value 117.8° of the year on 21 June (Day 172) at sunrise and sunset time. However, the minimum value is 62.15° on December 22 (Day 356) at sunrise and sunset time.

Sun tracking experiment was conducted on 5th July 2019. Tracking results are shown in figure 11 and 12. In those figures, the x-axis represents local solar time in an hour and the y-axis shows angle value. Figure 11 shows sun azimuth tracking from 4:54 A.M to 17:14. Tracking starts at time 4.908 hour (h), the sun's azimuth position is -117.8° and receiver position is -13.46° . At 4.992 h, sun azimuth position reached to -117.1° and receiver reached to -117° with the error of 0.1° .

Figure 12 shows sun zenith tracking from 4:54 A.M to 17:14. Tracking starts at time 4.908-hour (h), sun's zenith position is 91.06° and the receiver position is 4.908° . At 4.975 h, sun zenith reached to 90.31° and the receiver reached to 90.25° with the error of 0.06° .

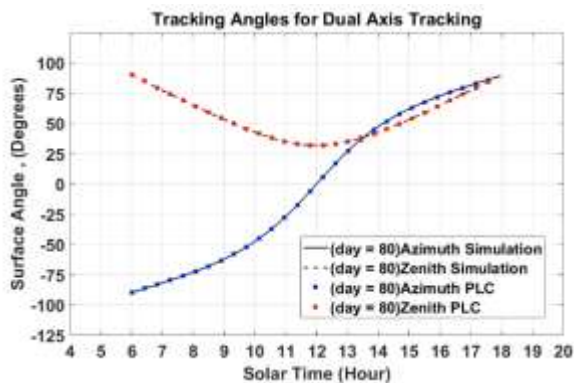


Figure 7: Day_80 simulated and practical results

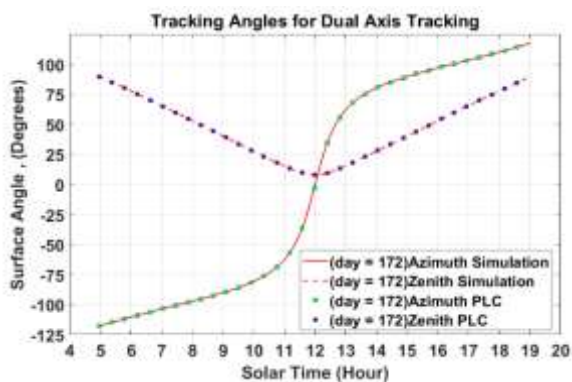


Figure 8: Day_172 simulated and practical results

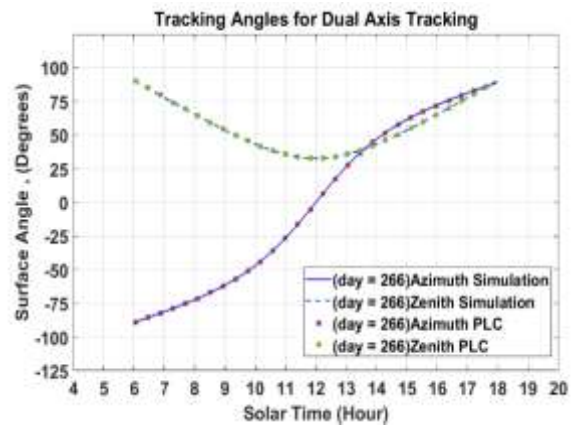


Figure 9: Day_266 simulated and practical results

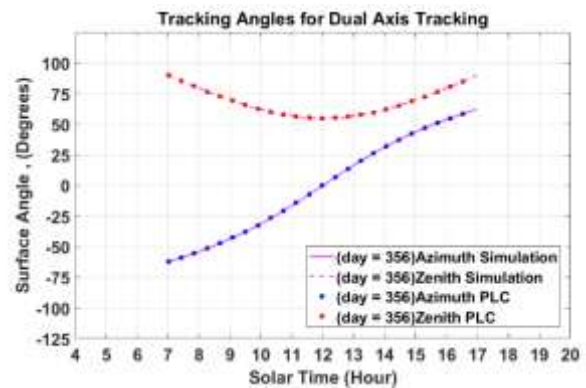


Figure 10: Day_356 simulated and practical results

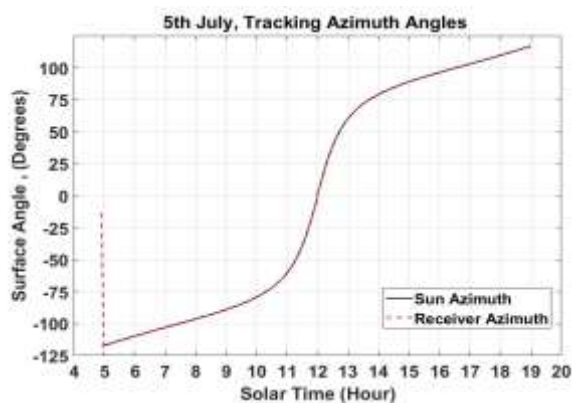


Figure 11: 5th July Azimuth Tracking

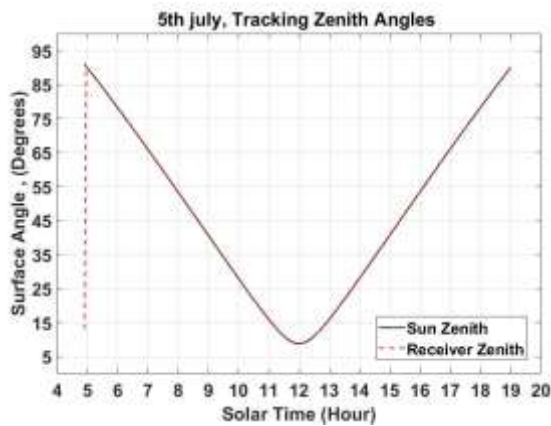


Figure 12: 5th July Zenith Tracking

6. Conclusion

To get the accurate position of the sun at any time of day, the astronomical equations were first implemented in MATLAB than in the programmable logic controller (PLC). It observed that the value of sun zenith angles and azimuth angles got from MATLAB and PLC were approximately the same. A hardware system was designed to track the sun and it controlled by an ON-OFF controller implemented in PLC. According to the results of measurements performed using PLC and logged by using HMI, it was seen that the tracking controller worked efficiently with the maximum observed error of 0.13°. The hardware system designed in this study can easily be used in the sun-tracking system of PV panels, parabolic dish, parabolic trough. Presented work would be enhanced by adding energy measurements to further analyze the efficiency of the solar tracking system.

REFERENCE

1. Lazaroiu, G.C., et al., *Comparative analysis of fixed and sun tracking low power PV systems considering energy consumption*. Energy Conversion and Management, 2015. **92**: p. 143-148.
2. Chaïb, A., M. Kesraoui, and E. Kechadi. *Heliostat orientation system using a PLC based robot manipulator*. in *2013 Eighth International Conference and Exhibition on Ecological Vehicles and Renewable Energies (EVER)*. 2013.
3. Loudadi, M. and H.E. Omari. *Solar tracking systems for solar concentrator field of heliostats - Innovation, performance and adaptation to small-scale applications*. in *2014 International Renewable and Sustainable Energy Conference (IRSEC)*. 2014.

4. Fathabadi, H., *Novel high efficient offline sensorless dual-axis solar tracker for using in photovoltaic systems and solar concentrators*. Renewable Energy, 2016. **95**: p. 485-494.
5. Xing, Z. *Research and design of control system of the solar panel tracking*. in *2016 IEEE Advanced Information Management, Communicates, Electronic and Automation Control Conference (IMCEC)*. 2016.
6. Kumar, N, K. and V. Subramaniam, *Real Time Clock based Energy Efficient Automatic Dual Axis Solar Tracking System*. Vol. 22. 2018. 15-26.
7. Mao, K., F. Liu, and I.R. Ji. *Design of ARM-Based Solar Tracking System*. in *2018 37th Chinese Control Conference (CCC)*. 2018.
8. Shufat, S.A.A., E. Kurt, and A. Hancerlioğulları, *Modeling and Design of Azimuth-Altitude Dual Axis Solar Tracker for Maximum Solar Energy Generation*. 2019, 2019. **8**(1): p. 7 %J International Journal of Renewable Energy Development.
9. Muslim, H., *Solar Tilt Angle Optimization of PV Systems for Different Case Studies*. Vol. 6. 2019.
10. Mousazadeh, H., et al., *A review of principle and sun-tracking methods for maximizing solar systems output*. Renewable and Sustainable Energy Reviews, 2009. **13**(8): p. 1800-1818.
11. Duffie, J.A., *Solar engineering of thermal processes / John A. Duffie, William A. Beckman*, ed. W.A. Beckman. 1991, New York: Wiley.
12. Er, Z. and S. Marangozoğlu, *New Design for Solar Panel Tracking System Based on Solar Calculations*. 2018. 1042-1045.



Determining the Precise Work Area of Agriculture Machinery using Internet of Things and Artificial Intelligence

Dr. Tariq Kamal^{1*}, Asima Bibi¹, Syed Muhammad Usman¹, Khubaib Ahmad¹, Dr. Bilal Habib¹, Dr. Zaka Ullah Zahid², Dr. Muhammad Tufail Khan³, Adil Iqbal¹, and Abdullah Osama¹

1. Department of Computer Systems Engineering, University of Engineering and Technology (UET), Peshawar
 2. Department of Electrical Engineering, University of Engineering and Technology (UET), Peshawar
 3. Department of Mechatronics Engineering, University of Engineering and Technology (UET), Peshawar
- *tkamal@uetpeshawar.edu.pk

Abstract:

Precisely measuring the work area of agriculture farm machinery is important for performing the authentication of machinery usage, efficient allocation of resources, measuring the effect of machinery used on the yield, usage billing, and driver's behavior. The manual measurement, which is a common practice is an error-prone and time-consuming process. The irregular fields make it even more difficult to calculate the work area. An automatic solution that uses smart technology and algorithms that precisely calculate the work area is crucial for the advancement of agriculture. In this work, we have developed a smart system that utilizes the Internet of Things (IoT), Global Positioning System (GPS) and Artificial Intelligence (AI) that records the movement of agriculture machinery and use it to measure the precise work area of its usage. The system couples the nearest neighborhood algorithms with contact-based mechanisms to find the precise work area for different shaped fields and activities. The system was able to record the movement of machinery and calculate its work area, regardless of how many times the machinery runs through a particular field. Our evaluation shows that the system was able to precisely find the work boundaries and calculate the area with a maximum of 9% error for irregular shapes.

Key Words: Area Estimation, Agriculture Machinery, Artificial Intelligence, GPS

1. INTRODUCTION

As the world is progressing towards the fourth Industrial Revolution [1], the use of state-of-the-art technologies including the Internet of Things (IoT) [2], Artificial Intelligence (AI) [3] and Cloud Computing [4] is becoming mainstream. Agriculture yearly contributes a major chunk to the world economy [5]. Modernizing agriculture can drastically increase the production of farms and can cause overall growth in the world economy. Agriculture types of machinery are used to plant, cultivate and harvest the crops on a piece of land.

By measuring the work area of agriculture machinery, we can verify the machinery usage and estimate the cost of operation. Conventionally, a measurement tape is used to manually measure the area of farmland. This is a time-consuming process and very inefficient. The inefficiency increases, even more, when we try to measure the area of a field that is irregular in shape. The shape of the field has a great impact on the calculation of the machinery work area [6].

Typically, people have been using Global Positioning System (GPS) in navigation services

and tracking [7]. The GPS can also be applied to the agriculture domain. It is a satellite-based navigation system that uses a geographic coordinates system to give us the accurate location of a GPS module. The GPS coordinates include the latitudes and longitudes. We utilize GPS to record the movement of agricultural machinery. The GPS data collection itself is a problem. A solution was thought in this paper to efficiently record the GPS data. We use a smart IoT device. The GPS module in combination with cloud technologies is used to record the data in an efficient manner. We faced issues with the data dropping. Also, there were frequent outliers in GPS data that could make the machinery work area calculation very inaccurate.

In this paper, we have implemented several algorithms, which find the precise work area of agriculture machinery. Keeping the problem in view various methods and techniques were studied and ultimately a solution was derived that used Artificial Intelligence (AI). AI was used to detect outliers and discard them; AI enabled us to detect the accurate boundary of the field where the agriculture machinery has completed its work. With accurate boundary detection, we were able to calculate the precise work area of agriculture machinery.



The rest of the paper is structured as follows. Section 2 describes the related work in the agriculture domain that utilizes IoT and other technologies to boost agriculture production. Section 3 describes the use of GPS and AI in agriculture. Section 4 discusses the IoT-cloud platform for data collection, storage and processing. Section 5 formulates a methodology to detect the boundary of the work area of machinery. Determining the boundary leads to the shape of the field and work area estimation. Section 6 outlines the methods used for area calculation. Section 7 shows the accuracy and performance evaluations of the schemes for different field shapes. Concluding remarks and future work is presented in section 8.

2. RELATED WORK

The Internet of Things (IoT) and data analytics (DA) are playing a big role in increasing operational efficiency and productivity [8] [9] [10]. Zhao, J.-c., et al have mentioned that there are several sectors in agriculture that can be monitored with IoT [11]. Elijah, O., et al. has found that to make agricultural decisions, important factors to be known are the shape and work area of farmland [12]. Since the agricultural fields are not always of regular shape, most of the agricultural fields are polygon or irregular structure. By knowing the coordinates of the vertices of a complex polygon, its area can be calculated. In a research article Li, L. explained that a cloud-based global positioning system (GPS) can be used to track location and other information [13].

The field size, shape and working speed can be calculated and reported with the help of AI algorithms. Three main methods are used in the context of agricultural statistics are respondent self-reported land area, compass and rope. Carletto, C., et al. mentioned that Conventionally, a measurement tape is used to manually measure the area of a farmland [14]. Ning, X., et al. developed a farmland measuring device for the measurement of the arbitrary shape of the farmland area [16]. Evaluation of testing shows the average relative error of measurement remains within 5%. This is a time-consuming process and also very inefficient.

The inefficiency increases even more when we try to measure the area of a field that is irregular in shape. The shape of the field has a great impact on the calculation of the machinery work area. For example, the area calculation of a simple rectangular field is easy compared to a very irregular shaped field. Due to frequent outliers in GPS data that could make the machinery work area calculation very inaccurate. Kudo, M., et al concluded that for the shape extraction

framework, in general, most of the convex points exist in the boundary; therefore it was proposed to detect the outliers on an alpha shape basis [17]. Park, J.-S., et al mentioned that Euclidean space is one of the central concepts in computational geometry [18]. Yahya, Z., et al., research shows that convex and concave hulls are useful concepts in area calculations [19]. By considering the results of both concave hull performs better than the convex hull, and to formulate it few algorithms were suggested. Moreira, A., et al concluded that Concave Hull based algorithms; Delaunay triangulation and K-nearest neighbor are the closest methods to be reconnecting the vertices for geometric shape reconstruction [20]. The Delaunay triangulation works the same as the convex hull in the case of 3-dimensional, and it does not retain digging points within Delaunay triangulation. ABDULLAYEVA, A., et al., proposed a k-nearest neighbors approach, where the value of k, the only algorithm parameter used to control the “smoothness” of the final solution [21].

3. GPS AND AI IN AGRICULTURE

GPS is a satellite based navigation system, which uses a geographic coordinate system to give us the accurate location of a GPS module [6]. The geographic coordinates system consists of the longitudes and latitudes. Every location on Earth can be specified using a set of numbers. The longitudes specify the horizontal position (east-west) and the latitudes specify the vertical position (north-south). Both combined pinpoint the exact location on the Earth. GPS is utilized to accurately measure the location of agriculture machinery working in the field. With the GPS coordinates at every instant of work done, we can keep track of the movement of the agriculture machinery. The most feasible way to record the GPS data these days is using smart IOT devices including modern smartphones. Modern smartphones contain a built-in GPS module that could be utilized for data collection purposes.

AI has some very convenient use cases that are revolutionizing the world [3]. It became a very powerful tool, which can be helpful to companies stand out in the competition with their rivals, accomplishing tasks with ease and quick. The use of AI techniques surely reduces the chances of making errors as well as a great help in making critical decisions [22]. AI is making machines smart enough that they could mimic the cognitive functions of the human brain which includes decision making, learning and problem solving. In agriculture, besides seeds, fertilizers and water, agricultural productivity is also dependent on on-farm labor productivity, which in turn is dependent on whether the farmers have access to tools, equipment and machinery to carry out farm operations efficiently. Mechanization,



therefore, plays an important part in improving agriculture productivity. Farm mechanization has an enormous potential to leverage the efforts of farmers and boost crop productivity. By finding the precise work area of agriculture machinery, we can efficiently allocate our resources to increase productivity even further.

In this paper, we discuss a use case where we detect the boundary points of the GPS data that we collect to record the movements of agriculture machinery. By getting the boundary points, we can determine the work area of machinery using AI algorithms.

4. DATA COLLECTION AND STORAGE

In order to calculate the agriculture machinery work area, there needs to be a proper mechanism in place. As shown in Figure 1, our system consists of an IoT module and a cloud module. The cloud module consists of event-handlers, data storage units and AI units. Details of each of the components are given below.

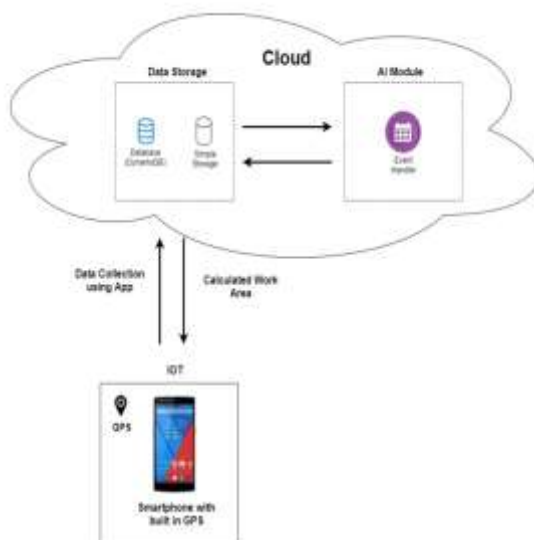


Fig. 1. The system architecture diagram showing communication between IoT devices and Cloud.

4.1 IOT MODULE

The IoT module consists of a smartphone and a GPS. The GPS helps record the movement of the machinery in the field. A mobile application has been developed to record GPS data. The mobile application gives control to the machinery driver to start and stop the recording of the data. While carrying out the study the smartphone is kept with the driver to record the machinery movement. Initially, the data is stored inside the smartphone cache memory and as soon as the smartphone is

connected to the internet, the data is sent over to the cloud platform.

4.2 CLOUD DATA STORE

The data from the IoT module is stored on the cloud for further processing. The cloud has two storage: simple storage and relational database [23]. The simple storage records the data and the relational store records the output of AI algorithms [24].

4.3 AI MODULE

The AI module, which is hosted on the cloud, consists of several algorithms. The algorithms run on the GPS data collected using the IoT module. The AI algorithms mainly perform two tasks: boundary detection and area calculation. More details of each algorithm are given in Section 5.

5. FIELD BOUNDARY DETECTION

The boundary of the work area is calculated from the collected data. The GPS coordinates collected for each study may include all the points showing the agriculture machinery movement. To get the field shape we need to identify the boundary points only. The work area field could be regular or irregular in shape. The boundary detection for the regular shaped field is easy to calculate, while irregular-shaped fields are relatively difficult. After studying several methods, including Delaunay Triangulation and Concave Hull, we were able to find the best algorithm for boundary detection. An overview of each algorithm is presented here. The detailed comparison of Algorithms is presented in evaluation (Section 7) of the paper.

5.1 CONVEX HULL WITH DELAUNAY TRIANGULATION

Delaunay Triangulation is a geometric technique, that could be used to determine the convex hull of a set of points [25]. It performs well for regularly shaped fields, but its accuracy suffers when it comes to the irregularly shaped fields.

5.2 CONCAVE HULL USING KNN

The K-Nearest Neighbor (KNN) Algorithm is a machine learning technique used for classification and regression. We use KNN to determine the Concave Hull of the data points [20]. This gives us the boundary points of the field. This is the best performing algorithm as it works for both the regular and irregular shaped fields. The problem with this method is that it is computationally complex for larger data sets. Therefore, a solution for it was thought out to achieve the boundary points at a faster



rate. The FLANN (Fast Library for Approximate Nearest Neighbors) is a library that contains a collection of algorithms optimized for fast nearest neighbor search in large datasets [26]. The Concave Hull using KNN with FLANN was the best solution to detect the boundary of the GPS dataset, small or large in size. The comparison of Concave Hull using KNN with FLANN and Concave Hull using KNN without FLANN is presented in the evaluation section.

6. FIELD AREA CALCULATION

In this section, we discuss the work area calculation algorithms. We discuss the Delaunay, KNN and Contact-based algorithms along with its merits and demerits. A comparison of these algorithms is shown in the Evaluation section.

6.1 DELAUNAY TRIANGULATION

The Delaunay Triangulation uses a convex based mechanism to find the boundary points of the work activity [25]. The area is then calculated based on the GPS points. Since the algorithm uses a convex hull, it may include the region where activity was not performed. As a result, the calculated area will be large as compared to the actual activity. The algorithm works well for regular shapes and the activities where dense activity was performed but fails to calculate the area of irregular shapes.

6.2 CONCAVE HULL USING KNN WITHOUT FLANN

The Concave Hull uses KNN mechanisms for boundary points detection and is good at calculating the area of fields of different shapes [20]. The algorithm works well for different shapes; however, the calculations can be inaccurate if the field activity was performed around the perimeter or certain points in the field. More points help the algorithm in finding a better approximation of the area, however, as the number of points increases the execution time of algorithm increases exponentially.

6.3 CONCAVE HULL USING KNN WITH FLANN

Since the KNN algorithm suffers from larger execution times, it is combined with a FLANN mechanism [26]. The FLANN removes the unwanted points from the calculation of neighborhood detection, which results in slower execution times. However, as with KNN, this

algorithm suffers from incorrect results if the activity was performed around the perimeter.

6.3.1 CONTACT-BASED

To overcome the shortcoming of Delaunay and KNN, we have developed a contact-based mechanism. The contact-based mechanism uses the GPS latitudes and longitudes to calculate the distance travelled by the machine during the activity. The area is calculated by multiplying the distance travelled with the width of the machinery. This can help us find the precise amount of work performed and will also tell us about the driver's behavior. The Contact-based method will show a very different area calculation if the driver skips parts of the field.

6.3.2 NUMBER OF FIELD RUNS

Sometimes, we are interested in knowing not only the area of field activity but also in the number of times the field runs were performed. The KNN and Contact-Based algorithms can be combined to find the number of field-runs performed. The KNN will find the area covered, and the contact-based algorithm will find the amount of cumulative work. Combining both (Contact Area/KNN Area) will give us the number of runs. This information can be useful in field outcomes and billing.

7. EVALUATION

In this section, we compare the different boundary detection and area calculation algorithms. The algorithms are mainly compared in terms of shape detection, area calculation, and execution performance.

7.1 EXPERIMENTAL SETUP

The results were collected on different farm types of machinery (Cultivator, Rotavator and Laser-leveler). The data from IoT was accumulated into an android smartphone app. The data from the android app was sent using Wi-Fi to AWS cloud, where the AI algorithms were applied to them.

7.2 COMPARISON OF BOUNDARY DETECTION

The algorithms are compared in terms of detecting the boundary of the work area.



Regular Shape 1

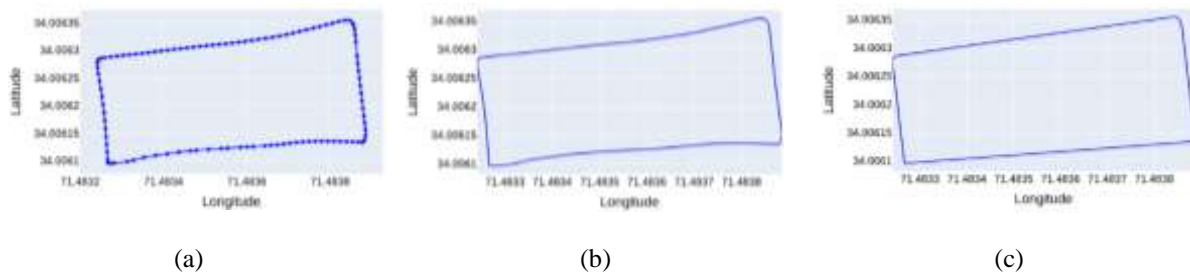


Fig. 2. Comparison of boundary detection algorithms (a) Actual GPS Plots (b) Concave Hull using KNN (c) Convex Hull using Delaunay Triangulation

Regular Shape 2

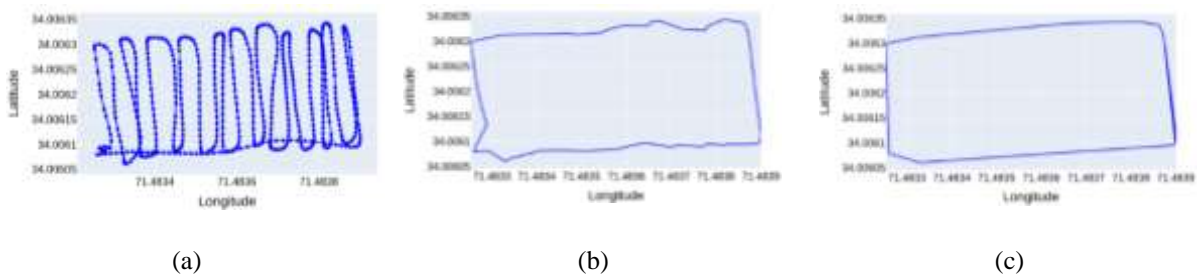


Fig. 3. Comparison of boundary detection algorithms (a) Actual GPS Plots (b) Concave Hull using KNN (c) Convex Hull using Delaunay Triangulation

Irregular Shape 1

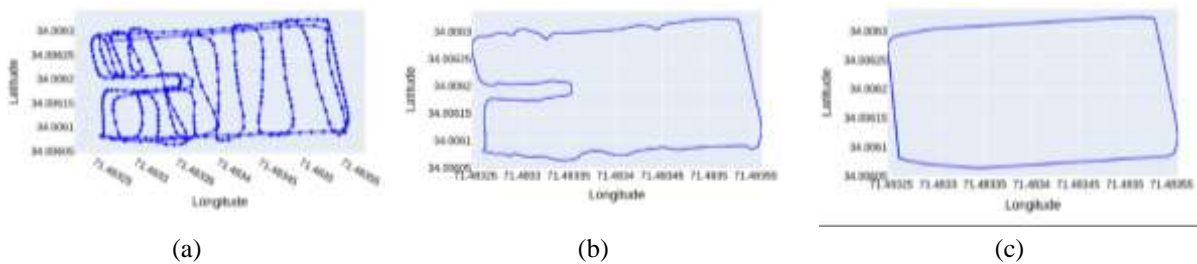


Fig. 4. Comparison of boundary detection algorithms (a) Actual GPS Plots (b) Concave Hull using KNN (c) Convex Hull using Delaunay Triangulation

Irregular Shape 2

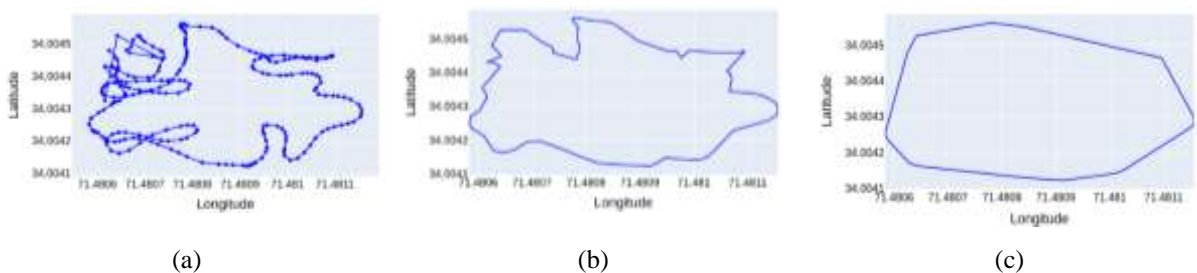


Fig. 5. Comparison of boundary detection algorithms (a) Actual GPS Plots (b) Concave Hull using KNN (c) Convex Hull using Delaunay Triangulation



Figure 2 And Figure 3 shows a comparison of Concave Hull (that uses KNN) with Convex Hull (that uses Delaunay Triangulation). It could be observed that both algorithms performed well for a regular shaped work area. For irregular shape, the concave hull algorithms (KNN) has performed really well determining the boundary points. While Delaunay triangulation fails to identify the edges in detail as shown in Figure 4. Delaunay Triangulation has completely failed to identify the cave like shape, while Concave Hull using KNN performs well. In case of very irregular field shown in Fig. 5, Delaunay Triangulation again failed but Concave Hull using KNN was able to detect most of the shape. It is also important to note the shape formed by Concave is also very close to the actual shape. The Delaunay triangulation is good only for regular shaped fields, while concave hull using KNN performs well, but as the irregularity increases its accuracy is also affected. Thus, the irregularity of shape has a direct effect on the accuracy of boundary detection.

7.3 COMPARISON OF AREA ESTIMATION

Table 1 Regular Shape 1

	Area (meter-square)	Execution Time (seconds)	Area Estimation Error
Actual Area	1240	0	0
Delaunay	1324.4	0.0008	6.8
KNN without FLANN	1239.5	0.114	0.04
KNN with FLANN	1239.7	0.0013	0.02

Table 2 Regular Shape 2

	Area (meter-square)	Execution Time (seconds)	Area Estimation Error
Actual Area	1470	0	0
Delaunay	1622.5	0.0014	10.34
KNN without FLANN	1500.2	4.216	2.04
KNN with FLANN	1500.7	0.0287	2.09

Table 3 Irregular Shape 1

	Area (meter-square)	Execution Time (second)	Area Estimation Error
Actual Area	660	0	0
Delaunay	752.69	0.00144	13.9
KNN without FLANN	622.3	0.998	5.75
KNN with FLANN	683.75	0.0104	3.5

Table 4 Irregular Shape 2

	Area (meter-square)	Execution Time (seconds)	Area Estimation Error
Actual Area	1500	0	0
Delaunay	1970.5	0.00104	31
KNN without FLANN	1619.5	0.389	7.9
KNN with FLANN	1623	0.0134	8.2

The KNN and Delaunay schemes are compared in terms of area estimation. Tables 1 and 2 shows that KNN with and without FLANN shows good performance when calculating the area of regular shapes. The error is less than 3% for all the regular shapes. The Delaunay scheme shows slightly larger errors, in the range of 6% – 11%.

For irregular shapes, shown in Tables 3 and 4, the KNN without FLANN shows a maximum of 8% error. The KNN with FLANN shows a slightly larger error (up to 10%). The increase in error is due to the fact that FLANN removes some points which results in a lower granularity.

Table 4 also shows that for irregular shapes, the error of Delaunay increases up to 31%. The increase in error is largely due to the fact that the convex mechanism is used for approximation.

7.4 COMPARISON OF PERFORMANCE

Table 4 Execution Time comparison, Concave Hull Using KNN without FLANN vs Concave Hull Using KNN with FLANN

Number of Data Points to be processed	Concave Hull using KNN without FLANN (seconds)	Concave Hull using KNN with FLANN (seconds)
100	0.153	0.003
500	0.932	0.028
1000	1.204	0.041
1500	1.246	0.053
2000	3.795	0.067
2500	2.754	0.093
3000	1.429	0.112
3500	2.792	0.135
4000	7.772	0.092
4500	6.272	0.1
5000	6.128	0.148



Concave Hull using the KNN algorithm shows the best performance when detecting the boundaries and calculating the work area. However, it suffers from larger execution times as the number of GPS points is increased as shown in Table 5. To overcome, this, we are using KNN with FLANN. FLANN using neighborhood approximation and reduces the number of comparisons. As a result, the execution times of FLANN-based KNN is may fold less than the KNN mechanism, as elaborated in Table 5.

8. CONCLUSIONS AND FUTURE WORK

The irregularity of the field, driver's behavior and number of field-runs by a machinery have a direct impact on the work area calculation. By getting the machinery work area we can perform the authentication of machinery usage, allocate resources efficiently, calculate the yield per unit area, measure the cost of machinery operation and study the driver's behavior. GPS and AI are good at finding the precise work area of agriculture farm machinery. The convex shape algorithms like Delaunay were good at finding areas of regular shapes but gives inaccurate numbers when dealing with irregular shapes. The concave hull algorithms like KNN were good in the detection of both regular and irregular shapes, however, it was computationally expensive for larger data sets. KNN, when combined with FLANN, showed good accuracy and was computationally cheaper compared to other algorithms. The KNN is a very good solution, but it could show incorrect results when the study is performed around the perimeter only. The functionality of KNN was further extended to irregular and sparse work using a Contact-Based algorithm. The combination also helped find the number of field-runs.

The contact-based area calculation uses a distance mechanism and was helpful in finding the area and number of field-runs. The mechanism expects that the field was covered in good proportion in all regions. If the work was performed around the boundaries (as is the case in Fig 2 and Fig 4), the contact-based mechanism will give incorrect results. Therefore, KNN, Delaunay, KNN with FLYNN and contact-based mechanism are useful only when used in conjunction.

As part of future work, the work can be extended to show a relationship between the number of GPS samples of data points and precision of work area calculation. The boundary detection for a small number of points is difficult to achieve, a technique could be derived to deal with this problem. We can integrate the system in this paper, with a billing

system to estimate the cost of machinery operation using the calculated work area. By measuring the cost of machinery and the net yield produced, we can effectively allocate the resources to increase the production of farms. Studying the driver behavior, we can highlight the practices that cause low yield and effectively introduce the best agriculture machinery operation practices.

REFERENCES

- [1] Forum, W.E. *The future of jobs: Employment, skills and workforce strategy for the fourth industrial revolution*. in Global Challenge Insight Report, World Economic Forum, Geneva. 2016.
- [2] Gubbi, J., et al., *Internet of Things (IoT): A vision, architectural elements, and future directions*. Future generation computer systems, 2013. 29(7): p. 1645-1660.
- [3] Russell, S.J. and P. Norvig, *Artificial intelligence: a modern approach*. 2016: Malaysia; Pearson Education Limited.
- [4] Hayes, B., *Cloud computing*. Communications of the ACM, 2008. 51(7): p. 9-11.
- [5] Alston, J.M. and P.G. Pardey, *Agriculture in the global economy*. Journal of Economic Perspectives, 2014. 28(1): p. 121-46.
- [6] Dong, J., et al. *Multifunctional field area measurement and experimental research based on GPS module*. in 2010 World Automation Congress. 2010. IEEE.
- [7] Parkinson, B.W., et al., *Global positioning system: Theory and applications, Volume II*. 1996: American Institute of Aeronautics and Astronautics.
- [8] Topakci, M., et al., *Improvement of field efficiency measurement system based on GPS for precision agriculture applications*. Journal of Food, Agriculture & Environment, 2010. 8(3-4): p. 288-292.
- [9] Sumathi, K., K. Santharam, and N. Selvalakshmi. *Data Analytics platform for intelligent agriculture*. in 2018 2nd International Conference on I-SMAC (IoT in Social, Mobile, Analytics and Cloud)(I-SMAC) I-SMAC (IoT in Social, Mobile, Analytics and Cloud)(I-SMAC), 2018 2nd International Conference on. 2018. IEEE.
- [10] Jaiganesh, S., K. Gunaseelan, and V. Ellappan. *IOT agriculture to improve food and farming technology*. in 2017 Conference on Emerging Devices and Smart Systems (ICEDSS). 2017. IEEE.
- [11] Zhao, J.-c., et al. *The study and application of the IOT technology in agriculture*. in 2010 3rd



- International Conference on Computer Science and Information Technology*. 2010. IEEE.
- [12] Elijah, O., et al., *An overview of Internet of Things (IoT) and data analytics in agriculture: Benefits and challenges*. IEEE Internet of Things Journal, 2018. 5(5): p. 3758-3773.
- [13] Li, L. *Application of the internet of thing in green agricultural products supply chain management*. in *2011 Fourth International Conference on Intelligent Computation Technology and Automation*. 2011. IEEE.
- [14] Carletto, C., et al. *Cheaper, Faster, and More Than Good Enough: Is GPS the New Gold Standard in Land Area Measurement?* in *Survey Research Methods*. 2017.
- [15] Windarni, V.A., E. Sedyono, and A. Setiawan, *THE EVALUATION OF LAND AREA MEASUREMENT USING GPS TECHNOLOGY*. Jurnal Ilmiah Kursor, 2017. 9(1).
- [16] Ning, X., et al. *Primitive Shape Extraction for Objects in Point Cloud*. in *2017 International Conference on Virtual Reality and Visualization (ICVRV)*. 2017. IEEE.
- [17] Kudo, M., A. Nakamura, and I. Takigawa. *Classification by reflective convex hulls*, 19th International Conference on Pattern Recognition. 2008. IEEE.
- [18] Park, J.-S. and S.-J. Oh, *A new concave hull algorithm and concaveness measure for n-dimensional datasets*. Journal of Information science and engineering, 2012. 28(3): p. 587-600.
- [19] Yahya, Z., et al., *A Concave Hull Based Algorithm for Object Shape Reconstruction*. 2017.
- [20] Moreira, A. and M.Y. Santos, *Concave hull: A k-nearest neighbours approach for the computation of the region occupied by a set of points*. 2007.
- [21] ABDULLAYEVA, A., *Impact of Artificial intelligence on agricultural, healthcare and logistics industries*. Annals of Spiru Haret University. Economic Series, 2019. 19(2): p. 167-175.
- [22] Murase, H., *Artificial intelligence in agriculture*. Computers and Electronics in Agriculture, 2000. 29(1/2).
- [23] Brantner, M., et al. *Building a database on S3*. in *Proceedings of the 2008 ACM SIGMOD international conference on Management of data*. 2008. ACM.
- [24] Sivasubramanian, S. *Amazon dynamoDB: a seamlessly scalable non-relational database service*. in *Proceedings of the 2012 ACM SIGMOD International Conference on Management of Data*. 2012. ACM.
- [25] Field, D.A., *Laplacian smoothing and Delaunay triangulations*. Communications in applied numerical methods, 1988. 4(6): p. 709-712.
- [26] Muja, M. and D.G. Lowe, *Fast approximate nearest neighbors with automatic algorithm configuration*. VISAPP (1), 2009. 2(331-340): p. 2.



A Novel Spherical Actuator for Robotic Shoulder Joint

M. U. Khan^{1*}, M. Rizwan²

1- Al-Khawarzimi Institute of Computer Science, UET, Lahore, Pakistan

2- Department of Mechatronics and Control Engineering, UET, Lahore, Pakistan

*Corresponding Author: umair.khan@kics.edu.pk

Abstract:

The usefulness of robotic limbs can be determined by their performance in real life situations. For a robotic limb to affectively replace a human limb, it should at least mimic its natural range of motion and torque. Currently existing systems fall short in satisfying both or at least one of these parameters. To get the robotic dynamics to be as close as possible to the natural dynamics of a human limb, we have designed a novel spherical actuator in place of standard motors and mechanical joints. The designed machine can perform rotation around three separate axis independently and simultaneously, while providing a maximum torque of 1.3Nm.

Keywords: Spherical Motor; Magnetic Field Strength; Torque; Degrees-of-Freedom

1. Introduction

Although most machines can work faster and bear much more load than humans, scientists have always tried to make their movements as close to biological beings as possible. Humanoid robots are results of such efforts. Humanoid limbs might be able to lift very heavy loads but they have a serious disadvantage when it comes to fluidity and range of motion. A human shoulder is capable of rotation along three separate axis, each with different range of rotation. And in humanoid robotic arms, to move or rotate a joint in multiple directions, more than one actuators are required, each pertaining to a certain specific degree of freedom. This brings with itself, a number of drawbacks. The overall size of the machine is increased due to inclusion of multiple motors. And control of multiple motors, for actuation of a single joint, requires more processing cost. In effect, it is not an optimal method of achieving multiple-DoF.

Commercially available motors are linear or rotary with one degree of freedom. But through some recent researches in the past, a new type of actuators has emerged, making rotation possible with multi degrees of freedom. These actuators are often referred to as Spherical Motors having actuation possible with two or three degrees of freedom (DoF) depending upon design. A number of such actuators have been developed by different researchers having different constraints, the details of which are discussed in the following.

An alternative design based on the concept of a spherical motor presents some attractive possibilities by combining pitch, roll, and yaw motion in a single joint. In addition to the compact design, the spherical motor results in relatively simple joint kinematics. In some applications, such as high speed plasma and laser cutting, the demands on the workspace and the force/torque

requirements are low but the end effector is oriented quickly, continuously and isotropically in all directions. Unfortunately, the popular three-consecutive rotational-joints possess singularities within its workspace, which is a major problem in trajectory planning and control. A spherical induction motor was conceptualized in **Error! Reference source not found.** Complicated three phase windings must be mounted in recessed grooves in addition to the rolling supports for the rotor in a static configuration. These and other considerations lead to an investigation of an alternative spherical actuator based on the concept of variable reluctance stepper motor which is easier to manufacture [3]. The trade-off, however, is that a sophisticated control scheme is required. Mashimo et al. constructed an ultrasonic spherical motor capable of 3-DoF [4]. The maneuverability of the design was exceptional but it provided very small amount of torque and thus was unsuitable for high load applications. The mechanical design of a spherical induction motor is complex.

In contrast, a number of other technologies have also been tinkered with to achieve life-like motion in robotic joints. An application of piezoelectric actuator for multi-DoF system was studied by Ying Wu in [5]. Also with recent studies in artificial muscle development, including works by Mirvakili and Hunter in [6] and [7], technology in artificial joints and robotic limbs has advanced by leaps. But still these methods don't provide as much range of motion as required in most applications.

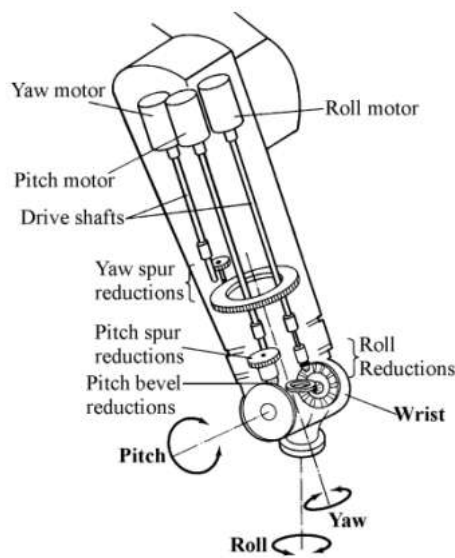


Figure 1. Multi-DoF System with Multiple Motors [1]

Apart from different constructions of spherical motors, researchers have also worked on improving control and different output parameters of these motors. Ankit Bhatia in [8], [9] used a six-stator spherical induction motor for locomotion and providing dynamic stability to a mobile robot. Hongfeng Li in [10] applied thermal network model to analyze how different speed and load influence temperature rise. They thus improve structure of stator for better heat dissipation.

Nagayoshi et al. devised a technique that helps decide current distribution to electromagnets for maximum torque. The devised system was also tested and its results confirmed through experimentation [11]. An improved topology was designed and optimized in [12] for maximization of power to volume ratio in a powered-wheel using NSGA-II, which is a multi-constraint/multi-objective evolutionary algorithm. Hongfeng Li et al., in [13], also analyzed the effects caused by different motor structures on end leakage magnetic field. They performed simulations and then verified the results practically on a spherical motor with its permanent magnets in halback array configuration. Bin Li et al. formulated a methodology for deriving current excitation strategy and verified the results by finite element analysis and through practical operation [14]. A vision-based feedback was used by applying image processing, namely pattern processing algorithms, and then using a PD controller for stabilizing the system [15]. The applied algorithms were able to identify rotor's position in space and thus provided an active feedback to the system. Min Dai et al. investigated characters of air gap flow-field in a magnetically levitated spherical motor [16]. Dependency of the

air gap flow-field was studied on motor's static and dynamic characteristics.

In this research, we focus on removing the discussed drawbacks of existing systems by designing a spherical motor with a novel stator construction. The study includes simulations of magnetic field and output torque based on different coil parameters and subsequently a mathematical model of the optimized system. A PID controller and a unity feedback was also implemented for obtaining closed loop response of the system.

2. Proposed Motor Design

The focus of this research is to develop a humanoid robotic shoulder joint. To achieve this goal, we first have to look at the motion constraints and parameters governing the movement of a healthy human shoulder joint. According to Namdari et al. in [17], an average adult can move his/her arm through about 180° in coronal plane, 200° in sagittal plane and 90° about its own axis. Furthermore, for an individual of average height and mass, the shoulder joint should at least produce 1Nm of torque to move an arm. For a humanoid robot to closely mimic an actual arm, the designed actuator must output similar numbers. In light of the previous researches done in this domain and the designs tested henceforth, a specific pole shape was designed to maximize output torque.

2.1 Rotor

The rotor is spherical in shape with curved magnetic bars stacked side by side. The magnets are arranged with alternating polarities. This configuration ensures that magnetic flux lines are directed radially from the surface of the rotor. The tightly stacked magnets allow for stronger magnetic field in the surrounding area.

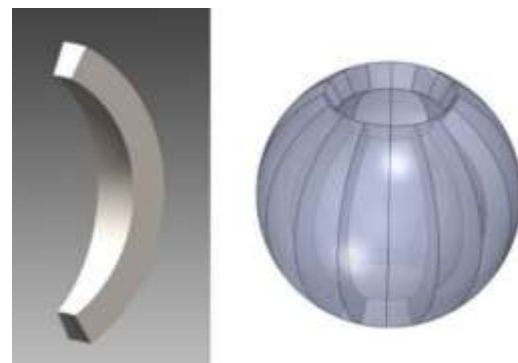


Figure 2. Single and Stacked rotor PMs

Magnets are stacked side by side to form a sphere like structure. The polarities of the magnets can be arranged in different patterns for different magnetic field distributions. The effect of some



arrangements on resultant magnetic field was studied with the help of simulations in EMS for Solidworks. When all the poles are arranged in a unidirectional manner i.e. all magnets have their norths facing outward, the magnetic field plot of the assembly can be represented by the Figure 3. In this case, almost all magnetic field lines are concentrated at the top and bottom edges of the sphere and magnetic field values at points away from edges are almost negligible. Thus, this arrangement will result in a major drawback, as almost no magnetic field lines will pass through the coils, producing no measurable force.

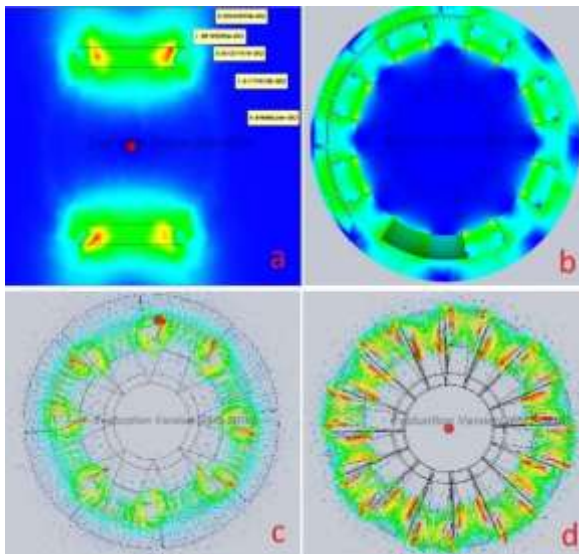


Figure 3. Magnetic Field Intensity plots (a) Unidirectional, (b) Halbach array, (c) Alternating with low pole density, (d) Alternating with higher pole density

On the other hand, if magnets are arranged with alternating polarities, much more magnetic flux lines are passing through the surrounding coils as compared to previous case. Increasing number of poles also increases magnetic field around the rotor. This is due to shorter distance between adjacent pole centers.

Another arrangement, that is sometimes used in certain devices, is Halbach array in which polarities are alternated in steps. This leads to a greater spread of magnetic field. It is seen that although magnetic field strength is spread out over a larger area, the average field strength across the coils goes down due to greater gaps between resultant north and south poles.

Taking into account the four arrangements of rotor poles, it is established that arranging higher density of magnets with alternating polarities results in highest average magnetic field strength

through the surrounding coils and thus, must produce highest amount of torque.

2.2 Stator

In the designed system, the solenoids are in the shape of curved rectangles which encircle the PM sphere. The coils can be wound two ways. The direction 1 shown in Figure 5 allows rotation in coronal and sagittal planes, while direction 2 allows rotation in transverse plane.

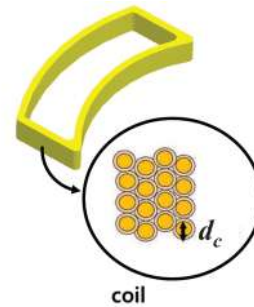


Figure 4. Stator coil shape

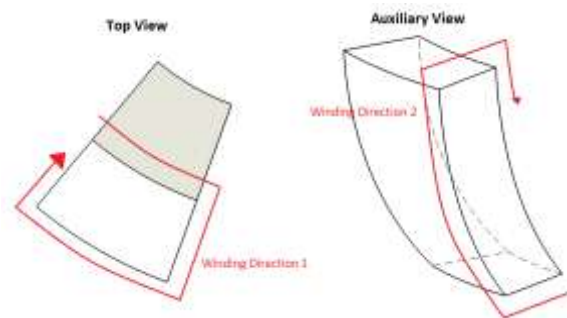


Figure 5. Stator coil winding sense

2.3 Complete 3D Model

The complete model turns out to look like that in Figure 6. Here, only the coils' faces that are in front of the rotor are depicted as the rest of the coil has no significant effect on relevant forces. The stator contains a set of 16 coils and the rotor has an equal number of magnets. The coils and their cores are supported on a flower shaped base. Angles α , β and γ represent rotation along x, y and z-axis respectively.

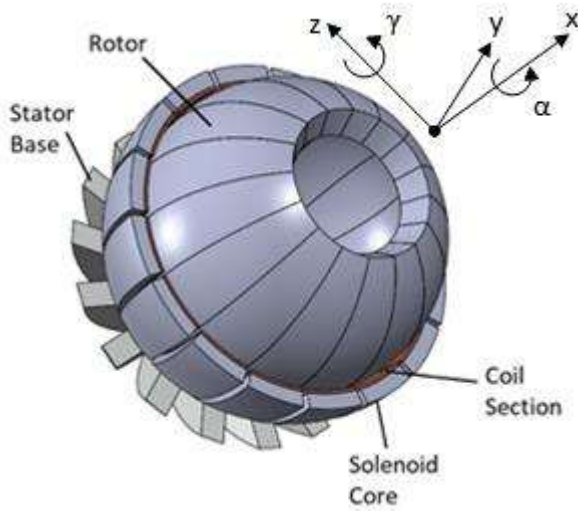


Figure 6. Complete actuator model

3. Inherent Torque of Designed Motor

After establishing a proof of concept, and testing different magnet arrangements, a working design was finalized, assembled and simulated. A set of several parameters was calculated including current density through stator coils, magnetic field density inside the structure and force density etc. The design consisted of 16 PMs arranged in a circular pattern with alternating polarities, a set of 16 coils surrounding the PMs hoisted on a flower shaped base and each coil had an iron powder core. Iron powder core provides much lesser losses than soft iron cores and laminated steel cores. This is due to much smaller path allowance for eddy currents.

To find maximum holding torque in initial position (no rotation in any plane), four pairs of coils were energized with elements of each pair facing each other. Different parameters like wire diameter, number of turns, packing density and coercivity direction of PMs was set and simulation was run to get results. This process was repeated for different angles of rotation to compare how output torque changed with actuator's pose.

As evident from the depicted charged coils, the resultant torque's normal vector should be along z-axis. This is verified from the results table as the y and x-components of the torque are negligible as compared to its z-component. The direction of net torque was verified for different combinations of energized coils. Thus, also verifying that any pose within 3-DoF can be achieved when a specific set of coils is energized to a specific amount.

Rotor's pose is changed i.e. rotation angle about z-axis is gradually increased from 0° to 80° and corresponding maximum torques are calculated as represented in Table 1. To represent how torque is affected by angle of rotation along a single degree of freedom, curve fitting method is implemented based on simulated values and expressions for torque, with respect to rotation, are generated. Expressions (1) and (2), representing second and first order curve fitted polynomial equation respectively, may be used in system's mathematical model.

Table 1. Maximum torque corresponding to rotation about single axis

α (°)	0	20	40	60	80
τ (Nm)	1.35	1.24	1.05	0.85	0.55

$$\tau_{\alpha} \cong -5.584 \times 10^{-5} \alpha^2 - 5.63 \times 10^{-3} \alpha + 1.355 \quad (1)$$

$$\tau_{\alpha} \cong -0.0101 \alpha + 1.407 \quad (2)$$

4. Mathematical Representation

We know that force experienced by a current carrying coil, with n number of turns, inside a magnetic field is represented as following equation [18].

$$f = nI(l \times B) \quad (3)$$

In the proposed design for spherical motor, the carrying current coils are static while the inner magnetic core, housing magnets to generate the magnetic field, is free to rotate. Coils being static, the rotor will experience a force equal in magnitude but opposite in direction to that on stator coils and will rotate accordingly as it is free to move around. Balancing torques for the system will result in equation (4).

$$J \begin{bmatrix} \ddot{\alpha} \\ \ddot{\beta} \\ \ddot{\gamma} \end{bmatrix} + b \begin{bmatrix} \dot{\alpha} \\ \dot{\beta} \\ \dot{\gamma} \end{bmatrix} - NrnlB(\alpha, \beta, \gamma) \begin{bmatrix} I_a \\ I_b \\ I_c \end{bmatrix} = -LF \sin \varphi \quad (4)$$

With J being moment of inertia of rotor, b damping coefficient, N is number of active coils, r is rotor radius, n is the number of turns in coil, l is affective length of stator coil facing the rotor, L is the length of load arm, F is total force applied by the load, φ is incident angle of external force, and α, β, γ are yaw, pitch and roll angles respectively. The net magnetic field strength (B) through the coils is dependent on pose of rotor, so it is represented as a function of α, β and γ . Solving the above equation results in the following relation;



$$\theta(t) = \begin{bmatrix} \alpha \\ \beta \\ \gamma \end{bmatrix} = \frac{J(bt/J-1+e^{-\frac{bt}{J}})(NrnlBI_x-FL\sin\phi)}{b^2} \quad (5)$$

$$\theta(t) = \begin{bmatrix} \alpha \\ \beta \\ \gamma \end{bmatrix} = CBI_x + D \quad (6)$$

$$I_x = \begin{bmatrix} I_a \\ I_b \\ I_c \end{bmatrix} \quad (7)$$

Here, θ is the resultant pose of rotor, C is a time dependent variable and D is a constant.

Representing the system in s-domain, we get;

$$\theta(s) = \frac{NrnlBI_x-FL\sin\phi}{s^2(b+Js)} \quad (8)$$

The torque (τ) induced is represented by the following expression;

$$\tau = NrnlB(I_a\hat{\alpha} + I_b\hat{\beta} + I_c\hat{\gamma}) \quad (9)$$

For simplicity of calculation and analysis, expression (9) can be replaced by (2) to represent rotation about z axis. Thus, for a single degree-of-freedom, the load-free system can also be represented as;

$$J\ddot{\alpha} + b\dot{\alpha} + 0.0101\alpha - 1.407 = 0 \quad (10)$$

4.1 Closed Loop Response

To hold the rotor shaft at a specific orientation, a unity-feedback, closed loop is implemented. Using Matlab, Proportional (K_p), Integral (K_i) and Differential (K_d) coefficients are computed with respect to desired form factor and specific parameters for materials used in the design i.e. neodymium magnets of specific dimensions and copper coils with powdered iron cores. The system is tuned further to acquire a shorter response time and an appropriate transient behavior. After integrating the control and feedback sections in the system equation, its response is plotted for a step input. The overall system transfer function then comes out to be;

$$\theta_{closed\ loop}(s) = \frac{(K_i+s(K_p+K_d s))(2BI_x l r - FL\sin\phi)}{s^3(b+Js)+2BI_l r(K_i+s(K_p+K_d s))-FL(K_i+s(K_p+K_d s))\sin\phi}$$

(11)

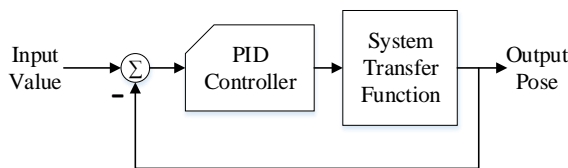


Figure 7. Control loop block diagram

Figure 8 shows the transient closed loop response of controlled system for rotation about a single axis. Although stabilization time is quite reasonable, a slight overshoot occurs which can be eliminated with advanced control techniques.

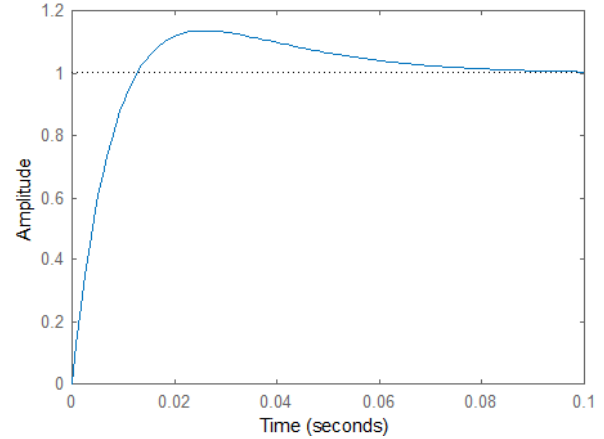


Figure 8. System step response

5. Conclusion

The simulations verify the conceptual design of proposed spherical actuator. Although, the control feedback was applied for actuation of a single degree of freedom, the system can be easily scaled and the models updated to incorporate rotation in two more planes. Simulations also verify that the designed system can rotate about three axis independently or simultaneously. The angle of rotation for two degrees of freedom is limited if a load arm is attached to the rotor. The third degree of freedom remains free-running as motion along this axis is not hindered by surrounding coils.

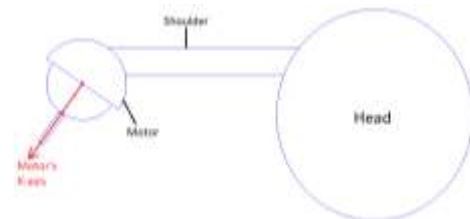


Figure 9. Motor fixture on humanoid shoulder

This actuator works similar to a ball and socket joint and can be used as such in a humanoid robot. The designed actuator can make a +80° to -80° sweep across its y and z-axis and a complete 360° revolution about its x-axis. To make maximum use of its rotation as a shoulder joint, it has to be placed such that its x-axis is angled slightly towards the collar in transverse plane as shown in Figure 9. This enables us to cover most of the volume covered by an actual human shoulder joint.



In addition to that, a maximum torque of 1.3 Nm is quite small for any real world application, so a spherical gear system has to be added at the output stage with a gear ratio respective to the desired torque. This will require some slight changes to shape of rotor shell.

In terms of future prospects, optimization may be performed on the shape of EM poles and the thickness of coils for maximum torque to volume ratio. The PM ball may be fixed and the encircling EMs be made movable to study changes in response time and stability of the machine. Furthermore, the effects of putting EMs on the inner side of the actuator and PMs on the outer side of the assembly may be studied. A spherical gear system may also be designed to couple with the actuator for varying torques and speeds.

REFERENCES

- [1] Wang, J., Mitchell, K., Jewell, G. W., & Howe, D. (2001, May). Multi-degree-of-freedom spherical permanent magnet motors. In *Proceedings 2001 ICRA. IEEE International Conference on Robotics and Automation (Cat. No. 01CH37164)* (Vol. 2, pp. 1798-1805). IEEE.
- [2] Kumagai, M., & Hollis, R. L. (2013, May). Development and control of a three DOF spherical induction motor. In *2013 IEEE International Conference on Robotics and Automation* (pp. 1528-1533). IEEE.
- [3] Li, Z. (2009). Robust control of PM spherical stepper motor based on neural networks. *IEEE Transactions on Industrial Electronics*, 56(8), 2945-2954.
- [4] Mashimo, T., Toyama, S., & Ishida, H. (2009). Design and implementation of spherical ultrasonic motor. *IEEE transactions on ultrasonics, ferroelectrics, and frequency control*, 56(11), 2514-2521.
- [5] Wu, Y., & Zou, Q. (2009). Robust inversion-based 2-DOF control design for output tracking: piezoelectric-actuator example. *IEEE Transactions on Control Systems Technology*, 17(5), 1069-1082.
- [6] Mirvakili, S. M., & Hunter, I. W. (2017, April). A torsional artificial muscle from twisted nitinol microwire. In *Electroactive Polymer Actuators and Devices (EAPAD) 2017* (Vol. 10163, p. 101630S). International Society for Optics and Photonics..
- [7] Mirvakili, S. M., & Hunter, I. W. (2016, April). Bending artificial muscle from nylon filaments. In *Electroactive Polymer Actuators and Devices (EAPAD) 2016* (Vol. 9798, p. 97981L). International Society for Optics and Photonics.
- [8] Seyfarth, G., Bhatia, A., Sassnick, O., Shomin, M., Kumagai, M., & Hollis, R. (2016, May). Initial results for a ballbot driven with a spherical induction motor. In *2016 IEEE International Conference on Robotics and Automation (ICRA)* (pp. 3771-3776). IEEE.
- [9] Bhatia, A., Kumagai, M., & Hollis, R. (2015, May). Six-stator spherical induction motor for balancing mobile robots. In *2015 IEEE International Conference on Robotics and Automation (ICRA)* (pp. 226-231). IEEE.
- [10] Li, H., & Shen, Y. (2015). Thermal analysis of the permanent-magnet spherical motor. *IEEE Transactions on Energy Conversion*, 30(3), 991-998.
- [11] Kasashima, N., Ashida, K., Yano, T., Gofuku, A., & Shibata, M. (2016). Torque control method of an electromagnetic spherical motor using torque map. *IEEE/ASME Transactions on Mechatronics*, 21(4), 2050-2060.
- [12] Fernandes, J. F., Vieira, S. M., & Branco, P. C. (2017). Multiobjective optimization of a shell-like induction spherical motor for a power-assisted wheelchair. *IEEE Transactions on Energy Conversion*, 33(2), 660-669.
- [13] Li, H., & Li, T. (2018). End-effect magnetic field analysis of the halbach array permanent magnet spherical motor. *IEEE Transactions on Magnetics*, 54(4), 1-9.
- [14] Li, B., Zhang, S., Li, G., & Li, H. (2018). Synthesis strategy for stator magnetic field of permanent magnet spherical motor. *IEEE Transactions on Magnetics*, 54(10), 1-5.
- [15] Qian, Z., Li, G., Wang, Q., Guo, X., & Ju, L. (2016, November). Vision-based permanent magnet spherical motor orientation detection and adaptive PD control system. In *2016 19th International Conference on Electrical Machines and Systems (ICEMS)* (pp. 1-5). IEEE.
- [16] Dai, M., Zhang, Y., Zeng, L., Zhu, Z., Sun, J., & Zhang, F. (2018, April). Research on bearing characteristics of air gap flow-field for a maglev spherical motor. In *2018 4th International Conference on Control, Automation and Robotics (ICCAR)* (pp. 296-300). IEEE.
- [17] Namdari, S., Yagnik, G., Ebaugh, D. D., Nagda, S., Ramsey, M. L., Williams Jr, G. R., & Mehta, S. (2012). Defining functional shoulder range of motion for activities of daily living. *Journal of shoulder and elbow surgery*, 21(9), 1177-1183.
- [18] Benegal, R., Karimi, F., Filleter, T., & Sinclair, A. N. (2018). Optimization of periodic permanent magnet configuration in Lorentz-force EMATs. *Research in Nondestructive Evaluation*, 29(2), 95-108.



Vibrational Analysis of Microcantilever Beams using Modeling and Simulation Technique

Dr. Tauseef Aized¹, Sania Azam², Mukhtiar Ahmad³, Amna Azam²

1. University of Engineering & Technology, Lahore
2. Muhammad Nawaz Shareef University of Engineering & Technology, Multan
3. Beijing Institute of Technology, China

*Corresponding Author: saniaazam@ymail.com

Abstract:

Micro-Electro-Mechanical-Systems (MEMS), the tiny devices are capable of sensing, controlling and actuation of the microscale vibrations and trigger the salutary effects on macro scales. Operations of such microsystems are ruled by the oscillations of the microstructures and reliability of the systems is commanded by the sensitivity of the microstructure. The system with higher resonant frequencies show higher sensitivity to the loads and situations being faced. An accurate modal analysis provides the natural frequencies of the system and mode shapes while transient analysis provides the transient response curves which provide the energy dissipation (Damping) mechanism of the system. Transient and Modal Analysis of different beams has been studied in the present work to study the sensitivity of the beams having different geometries (varying length and width, thickness and gap height from the substrate kept constant). The objective is to study the effect of geometric parameters of the beams over their resonance behavior as well as damping phenomenon under different pressures. Resonant frequencies, mode shapes, transient response curves, charts of damping ratios have been obtained by ANSYS Simulations and interesting relations between length and natural frequencies and pressure versus damping have been documented in the paper. The approach used can be useful for other micro and nanoscale structures.

Key Words: MEMS; Resonant Frequencies; Damping; Microbeams

1. Introduction

Micro-Electro-Mechanical-Systems MEMS also known as micro-mechatronic systems include multiple disciplines ranging from mechanical, chemical, electrical engineering to material sciences and instrumentation. The devices perform combined mechanical and electrical functions to control the sensitive devices which find their applications in very important fields like an airport (to sense the prohibited materials), automobiles (for airbag safety sensor) and in biosensors (BP apparatus). Microstructures that may be in the form of micro cantilever beams or micro pipes are the principal elements of such micro systems for sensing operation. Since the sensitivity of the systems is commanded by the dynamics of the microstructure, dynamics study has been the area of interest for many researchers while working for the reliability and accuracy of the system. For example, Xia et al. (2010) studied the geometric parameters of microbeams to check the influences over performance of the suggested design [1]. Ali et al. (2019), Deng et al. (2017), and Amir et al. (2017)

also documented the geometric considerations e.g. effect of length, volume fraction exponent and effects of number of supports over dynamics of the micropipes and evaluated the buckling behavior and natural frequencies [2,3,4]. Ghayesh et al. (2018) studied the effects of size and gradient index with the assumption of power law (material and geometric parameters are uniformly distributed along the length) and it has been concluded large size and GI (gradient index) cause large peak amplitude proving large effect of size [5,6].

Additionally, Ghayesh et al. (2017) investigated the imperfect Timoshenko microbeams under transient analysis and observed the nonlinear vibrations concluding that very small variation in geometric parameters affects the system's qualitative and qualitative response [7].

Akgöz et al. (2013) examined the microbeams for natural frequencies using power law assumption and variable material and cross-section of the beams [8]. Simsek (2015) studied the effect of lengths over vibrations of microbeams with fixed boundary conditions over both sides of the beams contrary to



Akgöz who used the boundary condition of the cantilever (fixed at one end and free to move at other end) [9]. Ghayesh et al. (2017) having a lot of work in microbeams also studied the supercritical instability of microbeams under transient loading. The load consisted of mean value which started from zero and increases up to the supercritical regime. Results obtained in the form of nonlinear FRF curves [10]. Previous researches had been focusing on experimental works that require costly repetitions of processes like redesigning and remanufacturing.

The findings of this study will conduce to its benefits of society considering that MEMS plays an important role in technological progress. The growing demand of innovative industrial applications justifies the need for more effective and life changing approaches to study the design of Micro cantilever beams for the assessment of its performance and reliability. True novelty of the study is its uniqueness in ease with reduced time and cost approach to learn the effects of the geometric parameter over vibrational behavior of the microstructure which has not been explored before. The relationship between length and natural frequency and pressure vs damping has been uncovered using simulation techniques that will be new guidance for the researchers to learn the design of microstructures against its dynamics. Study Effects of length to thickness ratio is presented by Ashraf (2016) and Dang (2018) [11,12] but the effects of length alone are not studied yet which is the focus of this study.

Similarly, damping ratios at different pressures are presented by Sumali (2017) and Ozdoganlar (2005) for air and structural damping of microcantilevers. They provided a baseline for the relations between pressure and structural damping to be compared with the presented study. The results obtained provided a good correspondence with the results already available in the literature [13,14].

2. Methodology

Modeling and simulation technique has been adopted since it prohibits the system from unexpected risks and failures. Beams are modeled in Solid Works and then transferred to the ANSYS for modal and Transient analysis. The steps followed are explained below.

2.1 Modeling:

Two types of modeling techniques are available for microbeams. Beams can be generated by layer by layer addition of beam over attachment and attachment over a substrate. But this kind of

modeling requires introducing joints and connections during simulation which can be a little bit complex.

Another simple technique to generate the microbeams which also has been followed for the present study is to generate the rectangle of whole dimensions accumulatively and remove the excess material leaving behind the beam with required over attachment and substrate.

A rectangle (1000x24.75x20 μm) is generated, excess material is subtracted using cutout command such that only a cantilever beam(800x20x2.5 μm and gap height=2 μm) attached to the substrate is gained at the end of the modeling process.

Three more beams are also constructed following the same procedures. the beams are having different lengths of 700, 600 and 300 microns. The completed microstructure is then transferred to ANSYS for further analysis.

One of the Beam sketches is shown for the demonstration below in Fig. 1

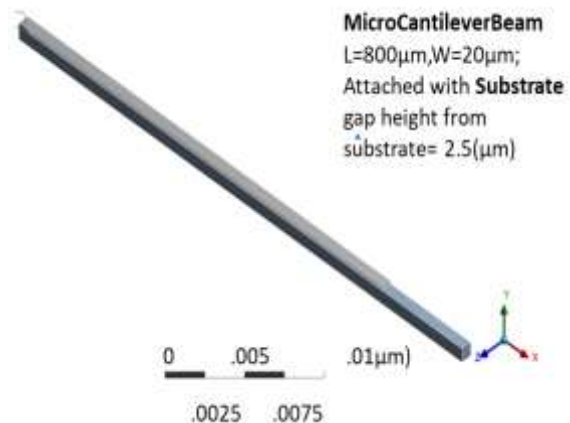


Fig. 1: Microbeam modeled in solid works

2.2 Modal Analysis:

After setting the units system, the first step to follow is to assign the material properties and then fine mesh has been applied to the microstructure.

Beams are assigned the properties of polysilicon and the substrate is assigned with Quartz. Boundary condition of the fixed end at one side and free to move at other has been applied.

The assigned material properties are also given in table 1 below:



Mode shapes and resonant frequencies of all of the microbeams has been attained and demonstrated in Figs. (2-5) and Table 2.

Table 1: Material properties assigned to beam and Substrate

Properties	Beam (Polysilicon)	Substrate (Quartz)
Young's Modulus (Pa)	1.6x10 ¹¹	7.6x10 ¹¹
Poisson's Ratio	0.22	0.17
Density (kg/m ³)	2329	2200

2.3 Transient Analysis

A transient load has been applied in two timesteps; in the first time step the load is applied for one milli second while the second step is about the removal of load and leaving the structure oscillating for ten seconds. Transient response curves have been obtained in nodal Y direction at beam tip at a pressure of 10-10000Pa.

The damping phenomenon is estimated from transient response curves obtained from this analysis and it is visualized in Figs. (6-8).

2.4 Damping Ratio

The damping ratio has been calculated by considering two successive peaks of each, taking their ratio and natural log. The mathematical equations used are shown as (1) & (2).

$$\delta = \ln \frac{x_1}{x_2} \quad (1)$$

$$\xi = \frac{\delta}{\sqrt{2\pi^2 + \delta^2}} \quad (2)$$

where δ = log decrement, x_1 and x_2 are successive peaks of the curves obtained from transient response. and ξ =damping ratio

3. Results and Discussions

3.1 Natural Frequencies:

A significant relation between length and natural frequencies has been concluded from the comparison that is, length and resonant frequencies are inversely related. The microbeams with shorter length showed higher natural frequencies proving about their higher sensitivity. It means it can be concluded that short length beams are good for practical applications

since the highest sensitivity is the requirement in the sensors [11,12]. Ashraf M and Dang V.H have shown the relation between natural frequencies and length to thickness ratio which attests the present derived relations although thickness in the present work has been kept constant and only length has been varied.

Observation of natural frequencies at higher modes provides with the fact that when we increased the length from 100-300 μ m there is less difference in the natural frequencies or it may be said to be negligible but reducing the length from 800 μ m to 300 μ m(meaning the difference of 500 μ m) provided with a significant difference in the results and thus in the sensitivity.

Table 2: Resonance frequencies of microbeams with difference in lengths

L (μ m)	Frequency [Hz]			
	Mode1	Mode2	Mode3	Mode4
800	0.11933x10 ⁵	4.8667x10 ⁵	4.9147x10 ⁵	7.4777x10 ⁵
700	1.5581x10 ⁵	4.8668x10 ⁵	4.9147x10 ⁵	9.7639x10 ⁵
600	2.12 x10 ⁵	4.8668x10 ⁵	4.9147x10 ⁵	1.3284x10 ⁶
300	4.8669x10 ⁵	4.9147x10 ⁵	8.457 x10 ⁵	3.0436x10 ⁶

3.2 Mode Shapes

Mode shapes inform about the shapes of the microbeams in which they are expected to deform.

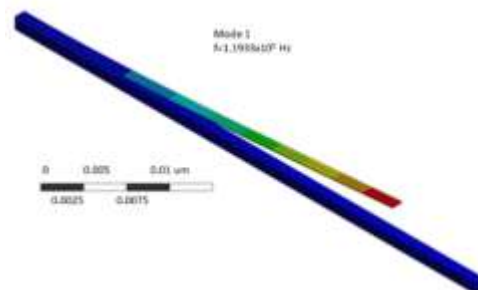


Fig. 2: mode 1 for beam with L=800 μ m

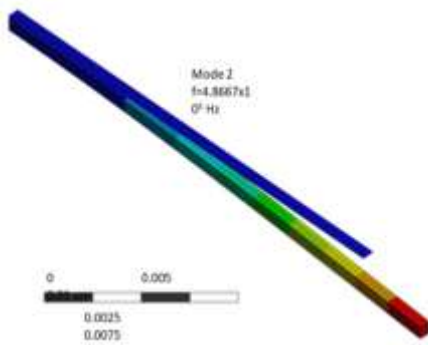


Fig. 3: Mode2

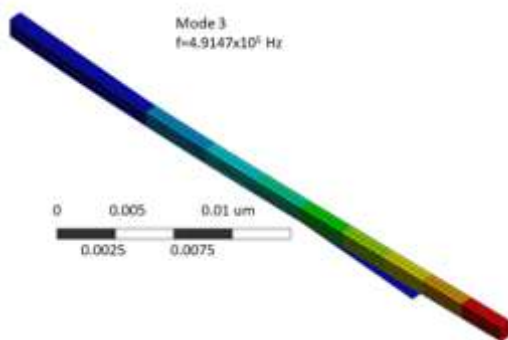


Fig. 4: Mode3

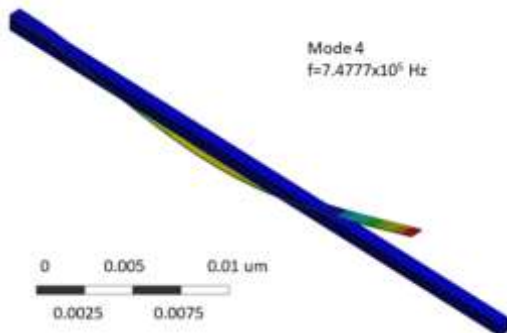


Fig. 5: Mode4

Four mode shapes of only one beam are presented in Figs. (2-5) for the demonstration because of space limitations.

3.3 Transient Response:

Transient response curves obtained from the transient analysis provided with the traces of oscillations decay for all beams. it is concluded that curves that decay faster have a higher resistance to vibration thus proving about high damping and vice versa. A peak is seen in all curves which tell about the appearance

of resonant frequency during vibration. Since curves are obtained at different pressure to view the effect of pressure over dynamics as well as vibration decay mechanisms, it is seen that beams have higher damping at lower pressure and lower damping at higher pressure interestingly providing with the inverse relation between pressure and damping of oscillations [13,14] as it has been deduced by Sumali and Ozdoganlar in their work, they have shown how structural damping varies when pressure is increased. These facts are demonstrated for beams of 800,600 and 300 μ m at pressure varying from 10-10000Pa in Figs (6-8)

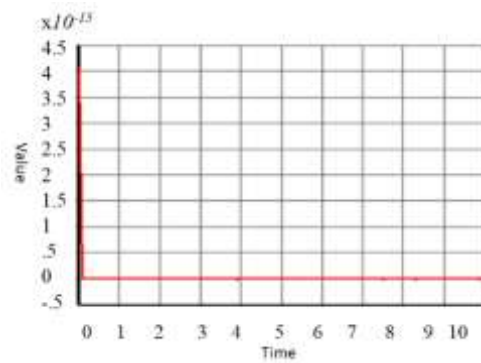


Fig. 6a: Time response curve for beam with 800 μ m at 10Pa

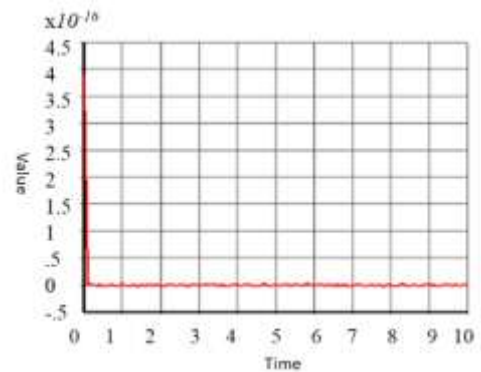


Fig. 6b: For beam with 800 μ m at 10000Pa

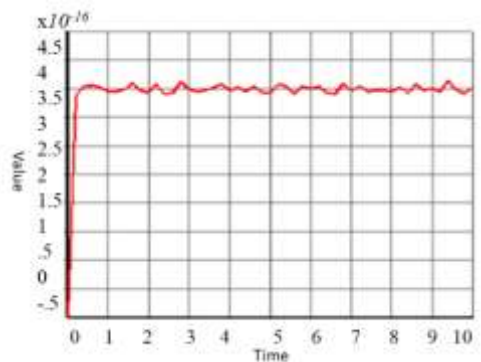


Fig.7a: For beam with 600 μ m at 100Pa

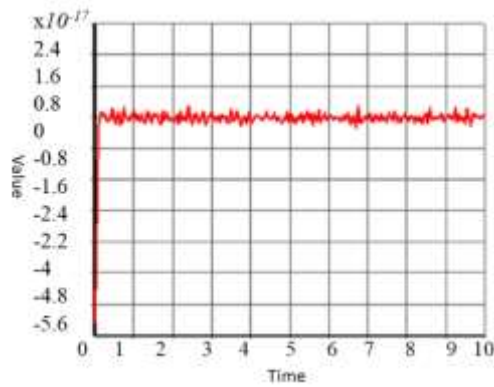


Fig.7b: For beam with 600 μm at 1000Pa

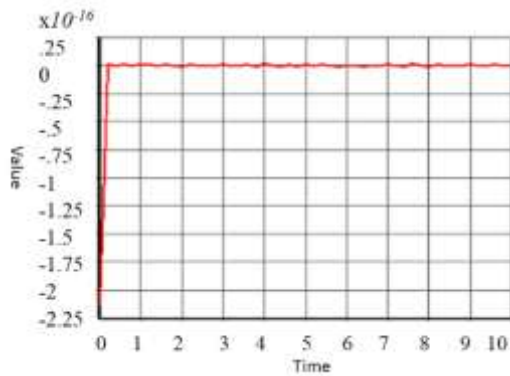


Fig.8a: For beam with 300 μm at 10Pa

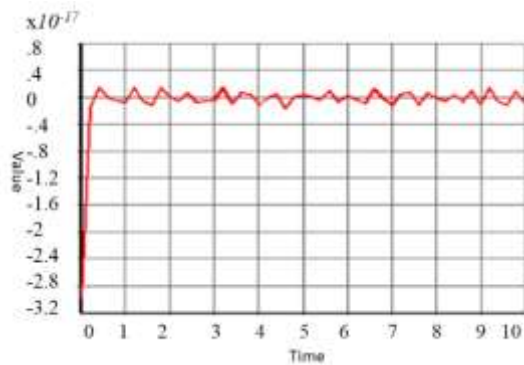


Fig.8b: For beam with $L=300\mu\text{m}$ at 10000Pa

3.4 Damping Ratio

The damping ratios have been calculated using equations (1) & (2) from curves obtained from transient response. The damping ratios also replicate the aforementioned inverse relationship of damping versus pressure.

The facts are demonstrated for beams of 800, 600 and 300micron at a range of pressures in Figs. (9-10) that as we increase the pressure from 0Pa to 10000Pa damping ratio goes on decreasing from 0.25 to 0.05

authorizing the fact that energy dissipates later when the applied pressure is higher.

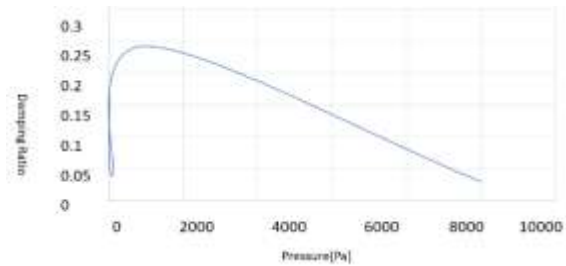


Fig. 9: Damping ratio for beam with $L=800\mu\text{m}$

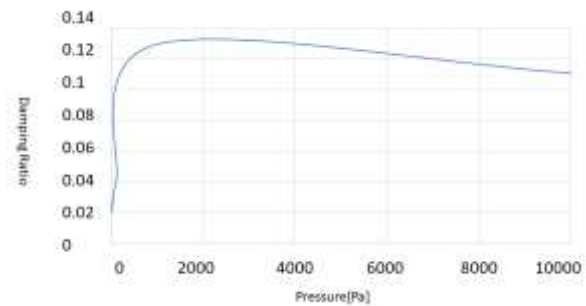


Fig. 10: Damping ratio for beam with $L=600\mu\text{m}$

4. Conclusions

Vibrational analysis of beams has been conducted to view the effect of the length over the sensitivity of the microbeams and to investigate the effects of pressure over damping mechanisms of beams. The results have been documented by figures and charts obtained from modeling and simulation techniques. It has been stated that beams geometry has a significant effect over its sensitivity and it is necessary to count the length of microbeams while designing a sensor based on microcantilever. It is well documented that beams with shorter lengths may prove the best option for the application with higher sensitivity.

Another important finding is about the relationship between pressure and energy dissipation phenomenon which are also found to be inversely related. These facts have been attested at many pressures and the charts of damping ratios have been presented to show the pressure versus damping relations at various pressures.

REFERENCES

- [1] Xia W., Wang L., Yin L., 2010. Nonlinear non-classical microscale beams: Static bending, postbuckling and free vibration. *International*



- Journal of Engineering Science*. Vol. (48). Issue 12. pp 2044-2053. ISSN 0020-7225.
- [2] Farajpour., Ali & Farokhi., Hamed & Ghayesh., Mergen., 2019. Mechanics of Fluid-Conveying Microtubes: Coupled Buckling and Post-Buckling. *Vibration*. Vol. (2). pp 102-115. 10.3390/vibration2010007.
- [3] Deng., Jiaquan & Liu., Yongshou & Liu., Wei.. 2017. Size-dependent vibration analysis of multi-span functionally graded material micropipes conveying fluid using a hybrid method. *Microfluidics and Nanofluidics*. 21. 10.1007/s10404-017-1967-7.
- [4] Dehrouyeh-Semnani., Amir & Nikkhah-Bahrami., Mansour & Yazdi., Mohammad. 2017. On nonlinear stability of fluid-conveying imperfect micropipes.
- [5] Ghayesh, M.H.; Amabili, M.; Farokhi, H. 2013. Three-dimensional nonlinear size-dependent behaviour of timoshenko microbeams. *Int. J. Eng. Sci.*, Vol(71), pp 1–14
- [6] Ghayesh, M.H. **2018**. Mechanics of tapered AFG shear-deformable microbeams. *Microsyst. Technol.* Vol. (24). pp 1743–1754.
- [7] Ghayesh, M.H.; Farokhi, H. **2017**. Parametric vibrations of imperfect timoshenko microbeams. *Microsyst. Technol.* Vol. (23). pp 4917–4929.
- [8] Akgöz, B.; Civalek, Ö. **2013**. Free vibration analysis of axially functionally graded tapered bernoulli–euler microbeams based on the modified couple stress theory. *Compos. Struct.* Vol. (98), pp 314–322.
- [9] Şimşek, M. **2015** Size dependent nonlinear free vibration of an axially functionally graded (AFG) microbeam using he’s variational method. *Compos. Struct.* Vol. (131), pp 207–214.
- [10] Ghayesh, M.H.; Farokhi, H. **2017** Parametric vibrations of imperfect timoshenko microbeams. *Microsyst. Technol.*, Vol. (23), pp 4917–4929
- [11] Ashraf M Zenkour. 2016. Free vibration of a microbeam resting on Pasternak’s foundation via the Green–Naghdi thermoelasticity theory without energy dissipation. *Journal of Low Frequency Noise, Vibration and Active Control*. Vol. 35(4). pp 303–311
- [12] Dang Van Hieu. 2018. Postbuckling and Free Nonlinear Vibration of Microbeams Based on Nonlinear Elastic Foundation. *Mathematical Problems in Engineering*, vol. (2018), Article ID 1031237, 17 pages.
- [13] Ozdoganlar, O. B., B. D. Hansche, et al. 2005. Experimental modal analysis for microelectromechanical systems. *Experimental Mechanics* Vol:45(6): pp: 498-506
- [14] Sumali, H. and T. G. Carne. 2003. Air-Drag Damping on Micro-Cantilever Beams. *Society for Experimental Mechanics. Bethel, America*: pp: 788-794



Vision Based Gesture Controlled Robotic Arm

Saqib Zafar^{1*}, Muhammad Usman¹, Fatima Ahmad^{1*}, Nasir Ahmad¹, Hafiz Farhan Maqbool^{1,2*} Muhammad Imran¹

1. Department of Mechatronics & Control Engineering, University of Engineering & Technology, Lahore (FSD Campus)-38000, Pakistan.

2. Human Centred Robotics Lab (HCRL), National Centre of Robotics and Automation (NCRA) Lahore, Pakistan

*saqibzafar704@gmail.com

*fatimaahmad6220@gmail.com

*farhan.maqbool@uet.edu.pk

Abstract:

Gesture identification has been developed to replace the approach of the conventional controlling mechanism of robots such as joysticks, keypads by hand gesture based controlling. This research focuses on the application of gesture control of the hand for its various configurations. The main element in developing a hand gesture interface is the selection of the hand gestures (or postures) themselves. Hence, this research proposed a system that is accurate in locating some important features of hand in an image processing domain using a web camera to control the robotic arm. This robotic arm has 3 degree-of-freedom (DOF) with finger gripper. It is controlled by different hand gestures movements in front of a camera. Machine vision and image processing techniques are used for hand gesture recognition. The algorithm and its implementation for gesture recognition are presented and the results of different steps of the proposed system are explained.

Key Words: Gesture; Robotic Arm; Image Processing; Recognition

1. Introduction

Speech and gestures are natural, intuitive communication methods/styles of interaction between human and real-world devices [1]. Children utilize gestures as an essential type of communication for interaction with their surroundings [2]. Gestures like movements of the body, expressions of face and finger pointing are different ways for people to express themselves. However, current interface technology rarely adopts such methods when designing human-machine interaction for the purpose of expression [3]. Human-machine interfaces mostly use joysticks, keyboards, and keypads, but such interfaces rarely use gestures. Hand gesture-based interaction commonly uses two types of interface, gloved-based and vision-based [4], [5]. Vision-based interfaces require powerful image processing algorithms to segment the hand from the stationary background and lighting conditions, and to select features to represent gestures that enhance gesture classification accuracy [6], [7]. The user is tethered to the computer in a gloved based technology which compromises the comfort and work-space. Even though, with the introduction of wireless technology in the market, the user still requires wearing some kind of glove or marker.

The rest of the paper is organized as follows: Section 2 discusses the system architecture whereas section 3 describes the algorithm for gesture recognition. Section 4 presents results and discussion followed by the conclusion and future work in sections 5 and 6.

2. System Architecture

The overall architecture of the proposed system is shown in Fig. 1. The proposed system consists of a robotic arm, a webcam, a Laptop, Programming Software, Microcontroller, motors, bridge circuits, and feedback sensors. First, USB webcam takes the image of the human arm and sends it to a computer; software process images to acquire the required gesture and sends robotic arm control signals to the microcontroller through MAX 232 converter. Then, the controller generates motors pulses for stepper motors and dc motor while taking feedback signals from rotation sensors.

The robotic arm to be controlled by hand gestures has four joints; base, shoulder, elbow, and wrist. The Links of robotic joints are made of aluminium and stepper motors are used for links and base movement because it gives an accurate value in step size/angle controlled in the program.



While a dc motor is used for gripper opening and closing as we didn't require step size/angle.

3D Cad model of the robotic arm and manufactured prototype are shown in Fig. 2 and Fig. 3. On the motors control side, three Dual H-bridge circuits are used to control the rotation of stepper motor in a step angle of 1.8 degrees. In order to measure joints' angles for feedback, one 10mm square GS encoder is used for base rotation, two large potentiometers for shoulder and elbow links and a push button switch for grippers are used. To control the stepper motors and dc motor and monitor current angles of joints and base, microcontroller (PIC16F877A) is employed. MAX232 converter is used to communicate serially between the PC and microcontroller. The MAX232 is a dual driver and receiver. It is used to change voltage levels of RX, TX, CTS, and RTS signals. The MAX232 is connected with RS232 female/male 9 pins serial to USB which communicates the signal.

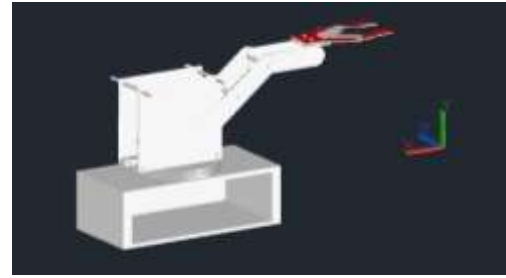


Fig. 2: 3D Cad model of the robotic arm

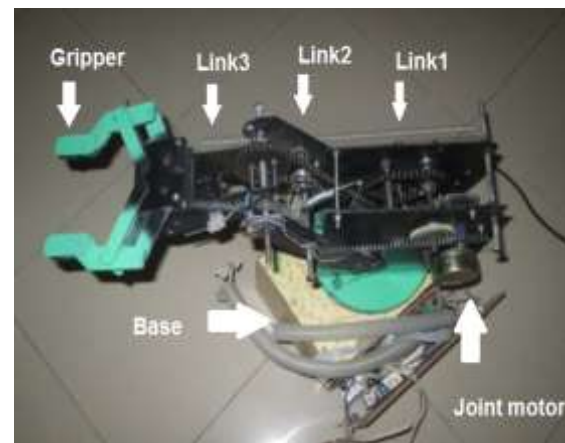


Fig. 3: Actual design of the robotic arm

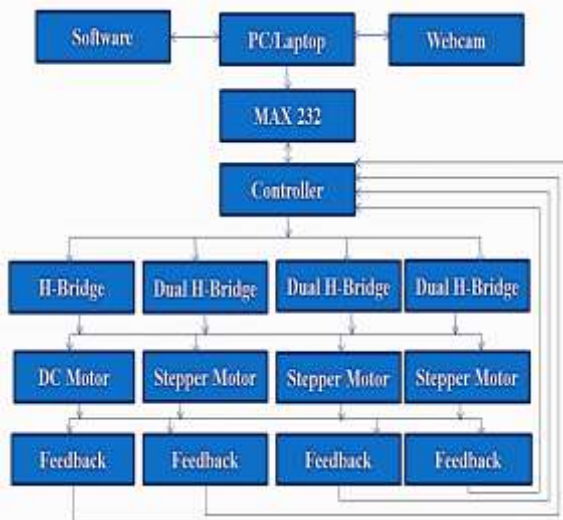


Fig. 1: Architecture of vision-based hand gesture controlled robotic arm

An A4 TECH USB webcam having a camera resolution of 8 Megapixels is mounted on a laptop screen for hand gesture capturing. Fig. 2 shows the CAD model of the robotic arm and Fig. 3 shows the actual design of the robotic arm.

3. Algorithm for Gesture Recognition

Flow diagram of the algorithm for hand gesture recognition is shown in Fig. 4. It starts with image acquisition and ends at gesture labeling. In proceeding paragraphs, each step of the algorithm will be described in detail.

RGB image of a hand in a real-world scenario is captured by a webcam at 20 frames per second. The region of hand needs to be separated from background objects so gestures can be recognized. But binary segmentation of RGB image to get hands region does not work well as threshold value will keep on varying because the RGB color model is easily influenced by ambient light. Therefore, the RGB color space should be transformed into another color space which is insensitive to lighting conditions such as HSV color space to extract human skin areas as shown in Fig. 4.

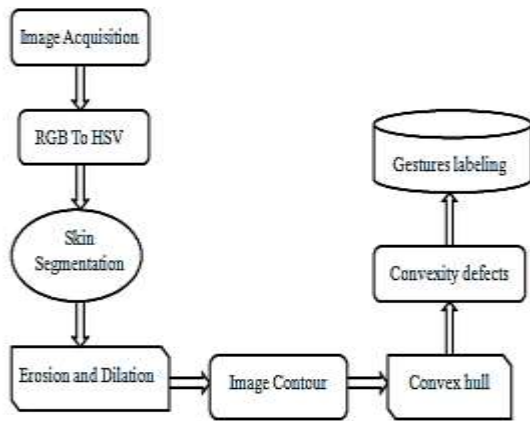


Fig. 4: Flow diagram of the gesture recognition process

As a result of binary segmentation, the skin area was separated out along with some background noise whose Hue Saturation and Value (HSV) values were close to that of the skin. To remove noisy pixels, morphological operation erosion is applied, and image dilation is applied to restore the shape of the hand segment.

A graphical user interface (GUI) has been designed for the proposed system. This GUI is used to visualize the hand gesture, the status of the serial port connection, and interactively adjust various parameters. The GUI is developed in Microsoft Visual Studio 2012 using C programming language and micro C PRO for PIC Microcontroller. Fig. 5. shows GUI.

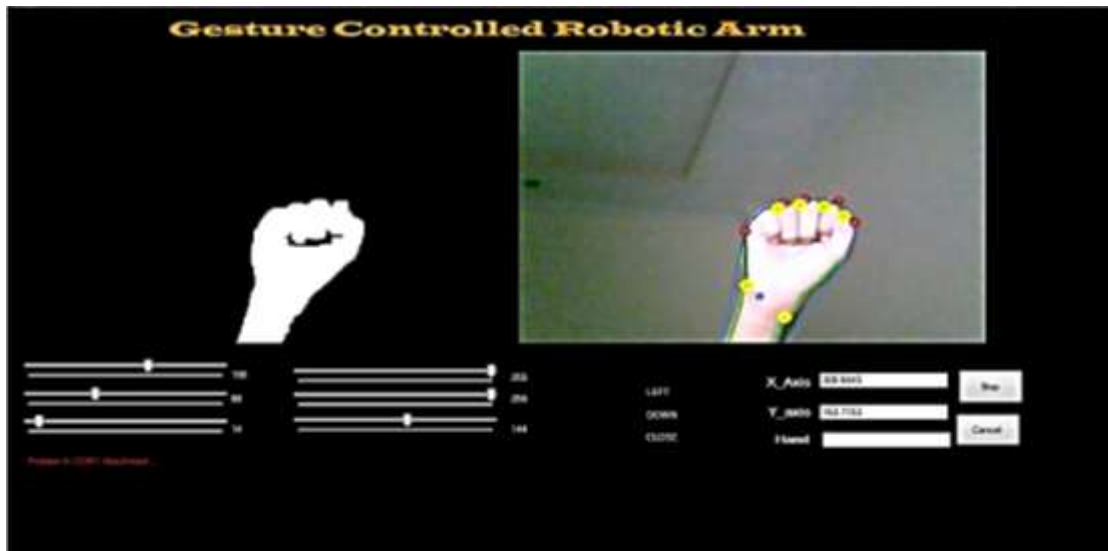


Fig. 5: Graphical User Interface of the system

At first step, image acquisition is performed by using a webcam. It takes an RGB image and displays it on the right portion of the screen. Then the skin color is adjusted for image segmentation by moving scrolls that are present on a software screen and the segmented image of the hand is displayed on the left portion

For two sets in Z^2 , A and B , the dilation and erosion of A by B are denoted by following relations;

$$A \oplus B = \{z | (\hat{B})_z \cap A \neq \phi\} \quad \square \square \square$$

$$A \ominus B = \{z | (B)_z \subseteq A\} \quad \square \square \square$$

When the user presses 'Open' button to open a serial port connection to send joint angles

commands data to a microcontroller to drive the robotic arm to respective pose. Upon successful execution, 'Close' button is pressed to disable webcam and exit the GUI window. The GUI is user-friendly as it shows an error message "Problem in COM1 attachment" if the robotic arm is not connected to PC/Laptop.



4. Results and Discussion

Fig. 6 shows the result of the RGB image of hand acquired by the webcam from the real world.

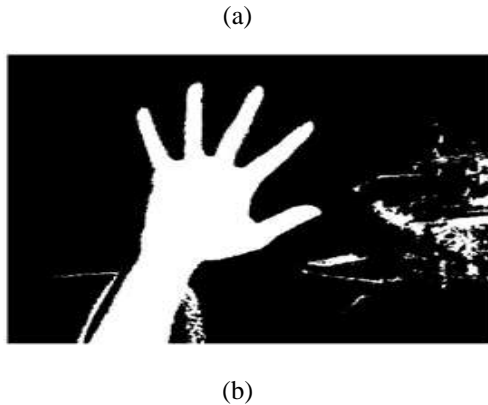


Fig. 6: (a) original image (b) binary image of the original image

Fig. 7 shows the application of erosion once and dilation twice as significant noise has been eliminated from the binary image.

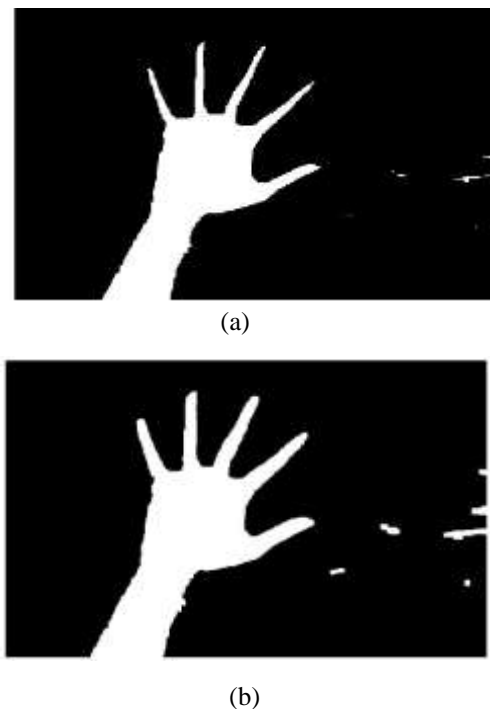


Fig. 7: (a) Erosion Process (b) Dilation Process

Now, all the contours of regions are to be found so that a small area can be neglected, and the forearm area is focused in the image. It can be accomplished by comparison of the length of their contours as the hand possesses the longest contour. Unlike the connected component, tracing the whole pixels in an area is not necessary for contour

finding, only boundary pixels will be visited. The advantage is to lower computation cost and finding the contour information as required. In this paper, we used Theo Pavlidis' Algorithm [8] to find contours. It works very well on 4-connected patterns which the forearm contours are always tending to be.

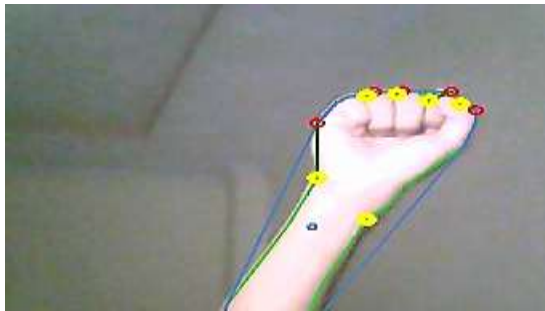


Next, the convex hull for the contour of the forearm is generated by applying a three-coin algorithm proposed by Graham and Yao [9] as shown in Fig.8. Usually, the arm part has a smooth contour while the hand part possesses multiple convex and concave contours.

Observation of the contours and its convex hull reveals that the areas which the convex hull contains but is not included in the contour are termed as the convexity defects. Convexity defect provides us very useful information to understand the shape of a contour. In many situations' contours of forearm are often being found that the convexity defects are around the palm. Many characteristics of complex contours can be shown by convexity defects. The purple point is obviously the point with the longest distance to the defect's convex hull edge. And the length of the purple line is the depth of the purple point. Since the depth of the purple is the longest, it will also be the depth of the convexity defect. And the purple point is the depth point. Fig. 8 shows all the depth points of a forearm contour.



(a)



(b)

Fig. 8: Convex hull of hand contour a) open palm, b) close palm

The depth points are represented in yellow. Since there are 6 depth points shown in figure 8, so there are 6 convexity defects in the forearm contour. Only six convexity defects can be seen with human eyes while the rest of them are too small to be seen. Since the fingertips connect the convex hull edge, it would be easy to create a very small convexity defect if there is a concave contour. We should regardless of such convexity defects and take the convexity defects with the large area as what we are interested in. The large convexity defects also have a long depth. So we need to check the depth of all the convexity defects. If the depth is longer than a certain threshold, we draw the depth point of it. If it's no longer than a certain threshold, the defect will be ignored.

By observing the depth points in many different gestures, we noticed that the depth points are tending to be around the hand palm. There are few conditions in which estimations are needed to be modified. When the number of depth points is two or less, the estimation of palm could not be right. We include the most elevated point in the shape as an additional depth point. Often, the depth points adjacent to the wrist may slip away; which will cause the wrong estimation of palm. So, we use the scroll bar to adjust HSV. This will limit the impact of the slipped point. Another occasion is experienced when the finger is bowed, an undesired fingertip will be found. A threshold of $0.0077 * \text{perimeter}$ is set for those unwanted fingertips. The experimental result shows that our method is not highly accurate but offers a low computation cost.

The experimental setup is depicted in Fig. 9 where the robotic arm, webcam, and laptop are connected together. In our experiment, we performed all defined gestures and robotic arm followed hand movement as our hand moves left, the robotic arm also moves towards left and with the hand moving right, the robotic arm also moves towards the right and so on. The gripper can be opened or closed with the opening and closing of a hand. This was depicted in Fig. 10; where the gripper is in a closed position with hand in a closed position as well.

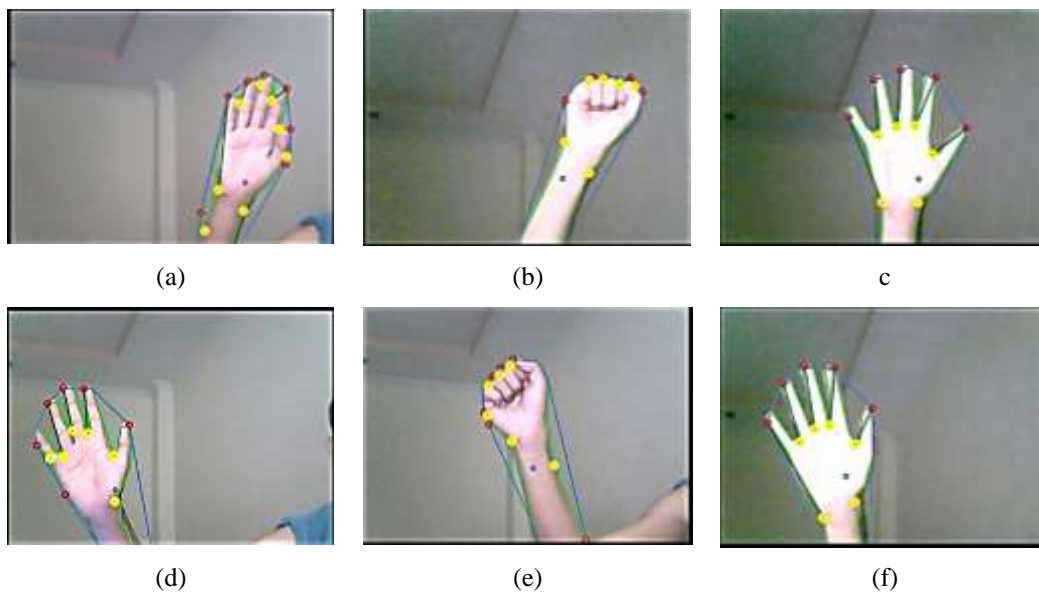


Fig. 9: a) Left, down, open gesture b) Left, up, close gesture c) Left, up, open gesture d) Right, down, open gesture e) Right, up, close gesture f) Right, up, open gesture



Fig. 10: Hardware and software interaction left down close gesture

5. Conclusion

This study presents the development of a 3DOF robotic arm that is controlled through gestures using computer vision techniques. The system is composed of a webcam, a robotic arm, a laptop/PC, PIC microcontroller, motor driving circuitry, and wearable sensors. The robotic arm consisted of three revolute joints; base, arm and two fingers gripper end effector. Pavlidis algorithm is applied to search for the contours in the image and the three-coin algorithm is used to find the convex hull. After comparing the contour and its convex hull and all the depth points of convexity defects are found. By observing the depth points in many different gestures, different hand gestures are identified such as hand opening, hand closing. The experimental results show that our robotic arm follows these hand gestures for its various configurations. The proposed technique can potentially be used as an alternative approach to the conventional controlling mechanism of robots such as using keypad or joysticks.

6. Future Work

The proposed system assumed the input data to be the arm in this study; one can apply hand or arm recognition and hence the system can be used in more flexible conditions. Future work includes the implementation of the proposed system using two cameras to locate hand features more accurately. In addition, to find the exact rotation of the forearm

and to avoid the problem of overlapping of hand the depth information will also be included.

REFERENCES

- [1] H. I. Stern, J. P. Wachs and Y. Edan, "Optimal Hand Gesture Vocabulary Design Using Psycho-Physiological and Technical Factors," *7th International Conference on Automatic Face and Gesture Recognition (FGR06)*, Southampton, 2006, pp. 257-262. DOI: 10.1109/FGR.2006.84G.
- [2] S. W. Goodwyn and L. P. Acredolo, "Encouraging symbolic gestures: A new perspective on the relationship between gesture and speech," *New Directions for Child and Adolescent Development*, 1998(79), 61-73.
- [3] J. Rasmussen, "Information Processing and Human-Machine Interaction: An Approach to Cognitive Engineering", North-Holland Series in System Science and Engineering, 12. New York: North-Holland, 1986.
- [4] V. I. Pavlovic, T. S. Huang and R. Sharma, "Visual Interpretation of Hand Gestures for Human-Computer Interaction: A Review," in *IEEE Transactions on Pattern Analysis & Machine Intelligence*, vol. 19, no. , pp.677-695,1997. DOI:10.1109/34.598226J.
- [5] M. Yeasin, and S. Chaudhuri, "Visual understanding of dynamic hand



- gestures" Pattern Recognition, 33(11), pp.1805-1817, 2000.
- [6] J. Triesch and C. Von Der Malsburg, "A gesture interface for human-robot-interaction," *Proceedings Third IEEE International Conference on Automatic Face and Gesture Recognition*, Nara, 1998, pp. 546-551. DOI: 10.1109/AFGR.1998.6710051.
- [7] T. Darrell, A. P. Pentland, A. Azarbajejani and C. R. Wren, "Pfinder: Real-Time Tracking of the Human Body," in *IEEE Transactions on Pattern Analysis & Machine Intelligence*, vol. 19, no. , pp. 780-785, 1997. DOI:10.1109/34.598236
- [8] T. Pavlidis, "Algorithms for Shape Analysis of Contours and Waveforms," in *IEEE Transactions on Pattern Analysis & Machine Intelligence*, vol.2,no.,pp.301-312, 1980. DOI:10.1109/TPAMI.1980.4767029
- [9] R.L. Graham, and F.F. Yao, Finding the convex hull of a simple polygon. *Journal of Algorithms*, 4(4), pp.324-331, 1983. DOI:10.1016/0196-6774(83)90013-5



ABSTRACTS



Assessment of Rain Water Harvesting System (Case study Sheikhul Bandi Abbottabad)

Mujahid Khan, Syed Adnan Shah, Ikramullah qayuum, Ashar Iqbal

Abstract:

The life of the inhabitants of the globe is greatly dependant on water. Providing portable water to communities is of prime interest. Scarcity of water is a threat in near future in Pakistan. There is a need to search for alternate sources of water to fulfil the community requirement. Rainwater Harvesting (RWH) system is a better alternative. Keeping in view the vast application of this system, it is adopted as an alternative source of water in a village of Abbottabad city where there is scarcity of water. According to Public Health Engineering Department (PHED), the currently available gravity system and three tube wells are not sufficient to supply water to all the population. For this study, first, the rainfall data is collected and then by using the principle of rainwater harvesting system, the quantity of available water is calculated. The calculations were made using SCS curve number method using mean monthly rainfall depth. From calculation, we found that not only for current population but for population in 2028 can also be served by storing the water that we get from Rainwater Harvesting system if stored in a reservoir. But after 20 years i.e. in 2038, there will be deficiency of 146, 449 gallons per day of water for entire community which can easily be arranged from a small tube well. Therefore, on the basis of this study, it was recommended to the PHED of Abbottabad city to store the rainwater in a reservoir so that it can be easily utilised.

Selective exhaust gas recirculation for natural gas-fired power plant coupled with CO₂ capture system

Yamina Qureshi¹, Usman Ali¹

1- Department of Chemical Engineering, University of Engineering and Technology, G.T. Rd, Lahore 54890, Pakistan (yaminaqureshi@gmail.com)

Abstract:

Fossil fuels play a significant role in increasing energy demand, which is the primary cause of anthropogenic CO₂ emanations. CO₂ is the main greenhouse gas and has an impact on global climate change, so it is becoming necessary to capture and store CO₂. Process simulation of 606 MW NGCC power plant accompanied by CO₂ capture plant is designed and integrated for 90 % CO₂ capture efficiency. Decarbonizing from NGCC power plant is challenging due to low CO₂ content (~3-4 vol. %) and a high flow rate of flue gas. By revamping the capture plant with the SEGR scheme, selective CO₂ is recycled back with ambient air to the inlet of the feed compressor. SEGR enhances CO₂ concentration to around 13-14 vol.% compared to 6.6 vol.% at 35 % EGR ratio and keeping minimum O₂ content at 16 vol.% in the combustor while SEGR maintains at approximate 19 vol.%. Thus, SEGR offers more stable combustion with a higher CO₂ concentration in the flue gas. In this research work, the integration of NGCC plant coupled with an amine capture plant in Aspen plus is exploited. Further, the effect of series, parallel, and combined S-EGR configuration are analyzed. The results indicate that for hybrid configuration, CO₂ contents are enhanced to 18 vol.% while for parallel flow operating at 70% recirculation ratio and for series flow CO₂ contents increase above 13-14 vol.%. The specific reboiler duty for hybrid, parallel, and series configuration reduces to 3.32, 3.42, and 3.56 MJ/kg CO₂, respectively.



Thermal Investigation of Nanofluids in Heat Exchanger using Two Phase Approach

M Mubashir Farid¹, Tauseef Aized Khan², Shahid Farooq³

- 1- School of Mechanical Engineering, University of Engineering and Technology Lahore, Pakistan
- 2- School of Mechanical Engineering, University of Engineering and Technology Lahore, Pakistan
- 3- School of Mechanical Engineering, University of Engineering and Technology Lahore, Pakistan

Abstract:

This paper investigates the effect of nanofluids on heat transfer via flat-tube heat exchanger under the boundary condition of constant heat flux using Computational fluid analysis. Three nanofluids Titanium Oxide (TiO₂)/water, Aluminum Oxide (Al₂O₃)/water and Silicon oxide (SiO₂) were used with nanoparticles of diameter 10 nm. A two phase approach with a mixture model is adopted in computational fluid analysis. The heat transfer co-efficient was calculated at Reynolds number 1750 utilizing various different volume concentrations, 0.1%, 0.3%, 0.5%, 0.7%, of nanoparticles. It was observed that an increase in the concentration of the nanoparticles resulted in an increase in the value of heat transfer co-efficient. The results observed at 0.7% volume concentration, using two phase approach, showed 4.09%, 6% and 7.9% enhancement in heat transfer co-efficient for TiO₂/water, SiO₂/water and Al₂O₃/water respectively when compared with the results of single-phase technique.

Numerical investigation of thermo-hydraulic characteristics of an indirect evaporative cooler

Attiq ur Rehman¹, Qamar Mahboob¹, Muhammad Asim¹, Muhammad Sajid Kamran¹, Jawad Sarwar¹

1- Department of Mechanical Engineering UET Lahore

Abstract:

The use of the air conditioning is increasing day by day; therefore, some new techniques are much needed which are efficient at low cost. So, in this study, the indirect evaporative cooling system was analyzed on the bases of velocity magnitude, temperature differences and geometrical changes. A 3-D doubled channel is simulated having two separate inlets for cold air and hot air. The air flow was parallel and crossing of air from one channel to other was made possible by using a plate having holes in it. Simulations results shows that by maintaining the proper velocity magnitude and temperature the final change in cooling is increased at constant humidity level. But by obtaining the better results it is necessary to have a precise hole size of the middle-used plate which is providing as a medium or plate form for all these cooling changes. It is shows that the velocity magnitude of the system and the relative humidity both are best fit for our 3-D model at 0.1 m/s.



Visualization of Heliostat field of solar thermal tower power plant using virtual reality (VR) technologies

Kamran Mahboob^{1,2}, Muhammad Awais², Ahsan Naseem², Malik Safi Ullah², Awais Khan¹, Tauseef Azid¹

1- Dept. of Mechanical Engineering, University of Engineering and Technology Lahore, Pakistan
(mahboobcct@gmail.com)

2- Dept. of Mechanical Engineering, Chenab College of Engineering and Technology Gujranwala, Pakistan

Abstract:

An important part of global energy depends on the development of the solar industry. To date, we have noticed the shift of fossil fuels energy into renewable energy. The past decade has shown significant progress in computer science and CAD is increasingly used for design and development. Visualization of the data generated from the modeled in the CAD program plays an important role in the creation of state of the art designs. An important limitation during the design phase is the visualization of three-dimensional geometry. This article attempts to illustrate use of VR technologies in solar thermal power plant development. This article analyzes various strategies and methods for visualization of CAD models in virtual reality. An Android phones interfaced with desktop computers as well as head movement control strategies are discussed. It is concluded that VR technologies can help in visualization as well as in development of field of solar thermal power plant having minimum design related issues.

Passive Temperature Excursion of Lithium Ion Batteries

Waqas Ahmed¹, Abid Hussain¹, Muhammad Rizwan¹

1- Department of Mechanical Engineering, University of Engineering & Technology Taxila, Pakistan.
(abid.hussain@uettaxila.edu.pk)

Abstract:

Energy plays a significant role in the advancement of a nation both socially and financially. Utilization of energy from renewable sources is the main research focus in order to reduce dependency on conventional fuels. Keeping in view of the fact, battery hybrid vehicles are rapidly replacing conventional vehicles. Lithium ion battery is an integral part of battery electric vehicles due to their high energy and power density. Their efficiency is drop due to rise in temperature of battery pack. Achievement is to maintain battery within permissible temperature limits. In current study efficient thermal management (graphene coated nickel foam paraffin composite) are examined experimentally for highly powered Li-ion batteries. Experimental model carries six Panasonic 18650B 3400 mAh lithium ion energy cells which were connected in series. Four other thermal management modes were compared, and their results were evaluated. By utilizing graphene coated nickel foam paraffin composite 34% reduction in temperature of battery pack is achieved. While 1% decreases in temperature of battery enhance the life of battery two months. So, graphene coated nickel foam paraffin composite is feasible option for thermal management of lithium ion battery pack.



Comparison of Flow-Solvers: Linear Vortex Lattice Method and Higher-Order Panel Method with Analytical and Wind Tunnel Data

Tahura Shahid¹, Faiza Sajjad¹, Muneeb Ahsan², Shuaib Salamat¹, Jehanzeb Masud²

1- AvRID, PAC Kamra.

2- Air University, Islamabad.

Abstract:

Two induced drag analysis techniques, Vortex Lattice Method (VLM) and panel method are renowned for inviscid aerodynamic computations and are widely used in aerospace industry and academia. In order to demonstrate applicability of potential flow theory and to establish an extensive correlation of linearized, attached potential flow-solver codes for estimating lift and induced drag, a generic rectangular wing planform is analyzed. Due to wide range of applicability in conceptual design, the two solvers are compared for accuracy, computational time and input controllability to find an optimum solver that can predict inviscid aerodynamics accurately and efficiently but with least amount of time. VLM-based code is founded upon the Laplace equation. It approximates a three-dimensional wing into a two-dimensional planform, making it apposite for moderate aspect ratio and thin-airfoil aircraft. A modified VLM is used that takes suction parameter, calculated analytically, as an input to capture three-dimensional leading-edge thrust and vortex lift effects. On the contrary, the higher-order panel method, takes the complete wing surface and changes the wake orientation to model modified flow in order to better predict the effects of downwash. These codes, allow computation in both subsonic and supersonic regimes, as they include Prandtl-Glauert compressibility correction. The rectangular wing is generated with identical number of panels and networks for coherent comparison. Distinguishable pre-processing techniques are utilized and similar boundary conditions and flow conditions are maintained over the surface that are then given to solvers. The induced drag polar is plotted and compared with wind tunnel and analytical data.

Design and Analysis of Combined Darrieus Savonius Wind Turbine

Muneeb Ahsan¹, Syed Hassan Raza², Nadeem Shafi Khan²

1- Air University, Aerospace and Aviation Campus, Kamra (muneebahsan@live.com)

2- College of Aeronautical Engineering, Risalpur

Abstract:

With a rapidly growing demand of energy, finding and using advanced and non-conventional energy sources is inevitable. Wind power is a primary source of alternate energy which would otherwise go wasted if not extracted through some mechanical means. Lift-based vertical-axis wind turbines such as Darrieus turbines are capable of producing large amounts of energy with a much simpler mechanism than conventional horizontal-axis wind turbines making them more cost-effective. However, Darrieus wind turbines lack the self-start capability due to low lift and higher required torque at start-up. Combining the Darrieus wind turbine with the drag-driven Savonius turbine gives it self-start capability. In this study, design and performance for the combined Darrieus and Savonius rotor have been analyzed; keeping in view the construction difficulties in mind. This paper discusses the design of an H-rotor Darrieus turbine; whereby the design methodology follows the trend analysis technique for parametric analysis of the turbine, and then incorporates the Savonius rotor to give it a self-start capability.



Design a Solar Powered Air Conditioning system

M Rizwan Mehboob¹, M Imran Mehboob¹ and Sumera Mehboob²

- 1- Student, Mechanical Engineering Department, University of Engineering and Technology, Lahore, Pakistan (engr.rizwan.mehboob@gmail.com)
- 2- Student, Department of Chemistry, University of Education, Division of Science and Technology, Township Lahore, Pakistan

Abstract:

Limited resources and infrastructure in Pakistan have caused a dire energy shortage. Air conditioning alone accounts for more than 70 % of electrical power consumption. This has increased the cost of electricity and energy power infrastructure. Vapor compression systems are the most used air conditioning systems in the world. They operate on chlorofluorocarbons, CFC which are directly responsible for ozone depletion and devastating climate changes. Solar is an immense power source with 1.8×10^{11} MW of energy reaching the earth's surface, which is much higher than current energy demand of the world. By using solar energy to power air conditioner, we can greatly reduce the energy shortage and environmental issues whilst increase energy security. The aim of this thesis is to design and fabricate a solar powered vapor absorption system. This research contains detail design calculation of individual components of vapor absorption system. The generator is designed in the form of a shell and tube heat exchanger, thermal analysis is performed to provide overall heat transfer coefficient, tube lengths and other parameters. Stress analysis is carried out to calculate shell thickness. Overall heat transfer coefficient, tube lengths and fin geometry for the condenser and evaporator are calculated using thermal analysis. Capillary tube length was calculated using pressure drop calculation. Double pipe heat exchanger was designed by performing a thermal analysis to calculate the necessary tube length. Absorber was designed by performing a thermal analysis to calculate the length of tubes. Design calculation for solar dish were completed to provide focal length, aperture area and depth. Detailed drawing of all the components are made on SOLIDWORKS software. This research contains detailed information on the fabrication procedures of all the individual components according to the design specifications. The proposed designed will cut down on the consumption of electricity to a mere few watts and eliminate pollutant emission.

Computational Investigation of Turbulent Flow through Fractal Plates by Using COMSOL Multi-physics 5.2a

Hassan Raza¹, Ghulam Abbas Gohar², Muhammad Shahid Nazeer², Ali Zahid², Muhammad Muzammil Nazeer², Muhammad Saeed², Rashid Hussain Asif², Shiekh Adnan Atta²

- 1- Department of Mechanical Engineering , The Hong Kong Polytechnic University , Hong Kong (engrhassan21@gmail.com)
- 2- Department of Mechanical Engineering , COMSATS University Islamabad , Sahiwal Campus

Abstract:

This report is related to the Computational Fluid Dynamics (CFD) analysis of a turbulence loss in a pipe with various designs of fractal plates using COMSOL Multi-physics 5.2a. COMSOL Multi-physics 5.2a is a general-purpose finite element-modelling package for numerically solving a wide variety of mechanical problems. In this simulation comparison between conventional orifice and fractal plate orifice is performed. By using conventional orifice in a pipe of flow the maximum pressure drop occurs. To overcome pressure drop, a new design of orifice is proposed to reduce the pressure drop in a pipe. Various designs of orifice called fractal plate have been designed and analysed by applying pressure 50 Pa and 10 Pa and inlet of pipe. New designed fractal plates are named as S-1 Series, S-2 Series, S-3 Series and S-4 Series. Apply various pressure range from 10Pa to 50Pa on these series pressure drop was measured and concluded from these analysis, that S-4 Series is better as compared to other series pressure drop is minimum because retardation of fluid flow produced minimum as compared to other series. Retardation reduced because of the maximum area for passes to fluid flow in a pipe. In this Series, pressure drop is 28% lower on the same test conditions.



Causes, Effects and Prevention Techniques for Smog in Pakistan

Syed Ubaid Ur Rehman¹, Dr. Tauseef Aized¹, Syed Muhammad Sohail Rehman¹, Syed Junaid Ur Rehman²

1- Department of Mechanical Engineering, University of Engineering & Technology, Lahore
(surehman2011@gmail.com)

2- Department of Food Sciences and Technology, Khwaja Fareed University of Engineering and Information Technology, Rahimyar Khan

Abstract:

Air Quality Index of urban areas in major cities of Pakistan has become serious public health concern for last five years. Purpose of this research work is to analyze the smog contributing factors, their effects and prevention techniques. Lack of plantation, vehicular emission, burning of crops residue, emission from industrial units and brick kilns are major contributing factors. Using of non-renewable fuels also cause of air contamination. In the month of October, November and December, upper Punjab (Lahore, Faisalabad and Gujranwala divisions) face acute (up 635 AQI) level of smog. High concentration of PM-2.5 particulate matter in the air is hazardous for human health. It causes numerous health issues including eyes sour, burning of throat, respiratory problems. Results indicate that transport sector contributing 43% of total smog emission. Industrial sector and agriculture contribute 25% and 20% respectively. Prevention techniques were employed to protect the human lives and overall effect of smog on biodiversity. Government of Pakistan should take notice to tackle the situation on emergency bases. Brick kiln and open burning of crops residue should be banned (especially in the month of October and November). Also reduce the consumption of non-renewable fuels and should transfer their dependency on renewable resources. Tree plantation campaign should be started on priority bases.

ICME 20115: Analysis of the Spiral Bladed Vertical Axis Wind Turbine using Subsonic Wind Tunnel

Roshan Manghwar¹, Tanweer Hussain¹, Imran Nazir², Muhammad Sharif Jamali¹

1- Department of Mechanical Engineering, Mehran University of Engineering and Technology Jamshoro
(roshankarmani@gmail.com)

2- Department of Chemical Engineering, Mehran University of Engineering and Technology Jamshoro

Abstract:

In order to meet the high energy requirements, by considering the challenges being faced by VAWT's for energy generation at large scale, analysis was carried out for spiral bladed vertical axis wind turbine. The analysis was carried out using low speed open-circuit subsonic wind tunnel. Firstly, the wind tunnel was tested for accurate measurement on the basis of the available airfoil models at different wind speeds. After that, 3D printed models of spiral bladed vertical axis wind turbines with two and three blades were tested at different wind speeds. Results showed the significant increase in the output power as compared to the conventional designs of the VAWT's. In addition, the cut-in and cut-off speeds were calculated to analyze the dynamic stability of the turbine. We evaluated the relationship of wind speed with rpm and torque of the turbine.



Scenario Analysis of the Potential for CO₂ Mitigation and Energy Efficiency in Cement Industry of Pakistan Using LEAP

Amjad ullah khan¹, M. Bilal Sajid¹

1- US Pakistan Centers for Advanced Studies in Energy NUST Islamabad Pakistan
(amjadullahkhan64@gmail.com)

Abstract:

The cement industry of Pakistan is a huge consumer of energy, consuming approximately 1.7 Thousand GWh electrical and 209.3 Million GJ thermal energy respectively during base year 2018. Moreover, due to frequent use of carbon-intensive kiln fuel such as coal and petroleum coke, the cement industry of Pakistan is responsible for various types of atmospheric emissions like NO_x, ammonia, PM (Dust). Cement production in Pakistan is alone responsible for 19.5 Million metric Tons of CO₂ equivalent GHG emissions. Pakistan the 12th most vulnerable country to global warming in the world, needs to reduce the cement production adverse effect. Growth rate of 3.6% is projected for cement production in Pakistan, due to urbanization, population growth, and future mega projects such as CPEC, which will cause 56.3 Million Metric Tons of CO₂ up to 2048, which needs to be mitigate to reduce the environmental impacts of cement industry. This study investigates the impacts of various policies on CO₂ emission and energy consumption reduction from Pakistan cement industry using long range energy alternative planning system (LEAP). The current and future energy demand and emission is defined for analysis period of 30 years (2018-2048). Three different scenario business as usual (BAU), Efficient production (EFF) and Alternative Fuels (ALT) is considered to estimate the overall effect of cement production up to 2048. The results indicate that in 2048 CO₂ equivalent emission and overall energy consumption would reach to 56.3 Million metric tons and 622.4 Million GJ respectively in BAU scenario. However, Replacement of Coal with 40% Natural gas and 10% Biomass would result in 27 Million Metric ton CO₂ equivalent emission (50% reduction) up to year 2048. Similarly implementing various energy efficiency measures would result 1.7 Thousand GWh electrical energy saving (34% reduction) and 6.1 Million GJ (1% reduction) of overall energy saving. Additionally, Using ORC for a 5-stage preheater has a capacity of producing 48MW electrical power. Installation of electrostatic precipitators can reduce the dust emission to reduce the adverse environmental impacts of the Cement industry of Pakistan.



Fe-Polyphenol Complex Dyes for DSSCs

Soner Çakar¹ and Mahmut Özacar^{1,2*}

¹Zonguldak Bulent Ecevit University, Science & Arts Faculty, Department of Chemistry, 67100 Zonguldak, Turkey.

²Sakarya University, Biomedical, Magnetic and Semiconductor Materials Application and Research Center (BIMAS-RC), 54187 Sakarya, Turkey.

*Corresponding author e-mail: mozacar@sakarya.edu.tr

Abstract

Solar energy is environmental and clean energy sources and it is potential alternatives for fossil fuels [1]. The solar cells are electrochemical devices as converting from solar energy to electricity. Dye sensitized solar cells (DSSCs) were firstly invented in 1991 by Oreagan and Gratzel [2]. Typically, DSSCs have consist of four main components as follows; a photoanode (wide band gap metal oxide semiconductor), a dye sensitizer (organometallic or organic dye), an electrolyte (redox couple) and a counter electrode (catalyst). In two decades, the researchers' efforts have focused on DSSCs based different sensitizers due to the environmental friendless and low-cost production [3]. Many of researchers have improvement separately different types of dyes, but these dyes have insufficient and researchers looking for a new type dyes and/or alternatives. In this work we have proposed polyphenols and Fe-polyphenols as alternative sensitizers in DSSCs applications. Additionally, we have used TiO₂ nanoparticles as photoanode, I⁻/I₃⁻ redox couple as electrolyte and Pt coated FTO glass as counter electrode. The polyphenol based solar cells have three advantages as follows; low-cost, non-toxic and easy prepared system. The polyphenols have secondary metabolism in various plants. The efficiency of solar cells using Polyphenols as sensitizer was 0.96%, while the efficiency of solar cells increased to 2.09% when Fe-polyphenols were used as sensitizers. The obtained results are strongly supported the prospects for successfully application of DSSCs based on natural dye system and indicate the importance of molecular complexation design for natural dye system to produce highly efficient DSSCs.

Keywords: DSSCs, polyphenol, Fe-polyphenol complex, TiO₂.

Acknowledgments

M.O. thanks to Turkish Academy of Sciences (TUBA) for partial support.

References

- [1] Wang, X.F., Tamiaki, H., Kitao, O., Ikeuchi, T., Sasaki, S.I., J. Power Sources 242 (2013) 860–864.
- [2] B. O'Regan, M. Gratzel, Nature, 353 (1991) 737-740.
- [3] Çakar, S., Güy, N., Özacar, M., Fındık, F., Electrochim. Acta 209 (2016) 407–422.



Photoelectrochemical Water Splitting with Ag₂CrO₄/g-C₃N₄/MnFe₂O₄ Nanocomposite

Keziban Atacan¹, Nuray Güy² and Mahmut Özacar^{1,2*}

¹Sakarya University, Biomedical, Magnetic and Semiconductor Materials Application and Research Center (BIMAS-RC), 54187 Sakarya, Turkey.

²Sakarya University, Science & Arts Faculty, Department of Chemistry, 54187 Sakarya, Turkey.

*Corresponding author e-mail: mozacar@sakarya.edu.tr

Abstract

Photoelectrochemical (PEC) water splitting technology is one of the brightest technologies for producing hydrogen gas to secure supply of energy and has attracted significant interest [1]. The spinel ferrites which were commonly active in the visible light range with the empirical formula AFe₂O₄ (A = Mn, Ni, Cu, Co, Zn) were studied as photoreduction catalysts for H₂ production [2]. Among them, semiconductor metal oxides with ferrites are influential materials to enhance the stability, catalytic efficiency and hinder the agglomeration of ferrite nanoparticles [3]. Ag₂CrO₄ which has a narrow band gap of ~1.80 eV is a new photocatalyst [4]. Preparation and application of magnetic photocatalysts with advantages of low operational costs, short separation time and simple technical requirements are effective strategy [5].

Herein, we discovered that Ag₂CrO₄/g-C₃N₄/MnFe₂O₄ nanocomposite possesses high catalytic performance under visible light using PEC water splitting. Firstly, ternary nanocomposite was synthesized and characterized with X-ray diffraction (XRD), UV-Vis diffuse reflectance spectra (DRS) and Fourier transform-infrared (FTIR) spectroscopy. Secondly, the powder Ag₂CrO₄/g-C₃N₄/MnFe₂O₄ nanocomposite was electrophoretically deposited onto indium tin oxide (ITO) coated glass substrate for PEC hydrogen evolution. Finally, the hydrogen production was evaluated under visible light irradiation.

Keywords: Ag₂CrO₄, g-C₃N₄, MnFe₂O₄, photoelectrochemical water splitting, photocatalyst.

Acknowledgments

M.O. thanks to Turkish Academy of Sciences (TUBA) for partial support.

References

- [1] Atacan, K., Topaloğlu, B., Özacar, M., Applied Catalysis A: General 564 (2018) 33-42.
- [2] Helaili, N., Mitran, G., Popescu, I., Bachari, K., Marcu, I.C., Boudjemaa, A., J. Electroanal. Chem. 742 (2015) 47-53.
- [3] Vignesh, K., Suganthi, A., Min, B.K., Kang, M., J. Mol. Catal. A Chem. 395 (2014) 373-383.
- [4] Güy, N., Özacar, M., J. Photochem. & Photobiol. A Chem. 370 (2019) 1-11.
- [5] Jing, L., Xu, Y., Qin, C., Liu, J., Huang, S., He, M., Xu, H., Li, H., Mater. Res. Bull. 95 (2017) 607-615.



Photocatalytic Degradation of Rhodamine B with CuFe₂O₄/Tannin/ZnO Magnetic Nanocomposite under Visible Light

Keziban Atacan¹, Nuray Güy² and Mahmut Özacar^{1,2*}

¹Sakarya University, Biomedical, Magnetic and Semiconductor Materials Application and Research Center (BIMAS-RC), 54187 Sakarya, Turkey.

²Sakarya University, Science & Arts Faculty, Department of Chemistry, 54187 Sakarya, Turkey.

*Corresponding author e-mail: mozocar@sakarya.edu.tr

Abstract

Water pollution has a great influence on natural ecological balance and also considered a threat to human health [1]. Many different strategies have been developed for the solution of these problems such as coagulation, flocculation, membrane filtration, adsorption and specially the photocatalysis [2]. Spinel ferrites are compounds with the general formula MFe₂O₄, in which M is a metal. They are good candidates as photocatalysts owing to their relatively narrow band gap, which enables them to absorb visible light [3]. Furthermore, magnetic nanoparticles have been commonly used in the photocatalysis because of their advantage of magnetic recyclability and reusability [4]. ZnO is one of the most used semiconductor photocatalysts with superior properties such as surface properties, chemical stability, low cost and nontoxicity [5].

In this study, magnetically separable CuFe₂O₄/Tannin/ZnO ternary nanocomposite was prepared. The X-ray diffraction (XRD), UV-vis diffuse reflectance spectra (DRS) and Fourier transform-infrared (FTIR) spectroscopy were applied to characterize structure properties of the resultant photocatalysts. The photocatalytic performance of CuFe₂O₄/Tannin/ZnO magnetic nanocomposite was evaluated by degradation of Rhodamine B (Rh-B). The photocatalytic activity of the composite and reusability are found to be very high.

Keywords: CuFe₂O₄, ZnO, magnetic nanoparticle, photocatalyst, Rhodamine B.

Acknowledgments

M.O. thanks to Turkish Academy of Sciences (TUBA) for partial support.

References

- [1] Wan, J., Zhang, C., Zeng, G., Huang, D., Hu, L., Huang, C., Wu, H., Wang, L., J. Hazardous Material 320 (2016) 278-288.
- [2] Güy, N., Özacar, M., International J. Hydrogen Energy 43 (2018) 8779-8793.
- [3] Díez-García, M.I., Lana-Villarreal, T., Gómez, R., ChemSusChem 9 (2016) 1504-1512.
- [4] Ge, M., Liu, W., Hu, X.R., Li, Z.L., J. Physics and Chemistry of Solids 109 (2017) 1-8.
- [5] Güy, N., Atacan, K., Karaca, E., Özacar, M., Solar Energy 166 (2018) 308-316.



Optimization of a Geothermal Multi-Generation Energy System: Energy, Exergy and Cost for Use in Coastal and Tropical Environments

Asif Mansoor¹, Tahir A. H. Ratlamwala¹, Muhammad A.M. Abdulmannan¹, Zaeem Shabbir¹, Muhammad S. Idrees¹, Sohail B. Qureshi¹

1- Pakistan Navy Engineering College, National University of Sciences and Technology, Pakistan
(enr.mabd@gmail.com)

Abstract:

A considerable increase in global warming and climate change has seen in recent years; Resulting in effects as desertification of agricultural lands, changes in monsoon season, increase of floods, filling of land by rising sea level etc. At the same time, energy requirements are growing with the exponential increase of population, which most of the demand is covered by energy produced through fossil fuels. Fossil fuels has major drawback of releasing substantial amount of carbon emission, which is a major player in deteriorating the environment. As a result, extensive research is carrying on nowadays on utilizing renewable energy resources which provides clean energy with decreased emissions. In this paper, a multi-generation system is proposed to produce five outputs: electricity, hot water, cooling, drying-air and fresh water. Aim of the research is to design a stand-alone multi-generation system that can fulfill the energy needs of a small scale community/industry in the coastal or tropical areas in the region. This system uses isobutane-based, organic rankine cycle driven primarily from low/ moderate temperature geothermal resource to produce more than 0.8 MW of power and 150 tons of cooling capacity. Energy, exergy and cost analysis has been carried out to optimize the system. Being a coupled system, it maintains an efficiency of more than 20% under all ambient conditions with an overall exergic efficiency of more than 65%. Moreover, the effects of changing environmental temperature, changes in temperature of geo-water as well as effects of three different refrigerants have also been studied.

Transformation of gasoline two-wheeler to electric two-wheeler; Energy and Environment perspective

Waqas Nazir Awan^{1*}, Tanzeel Ur Rashid¹, Talal Bin Ahmed¹, Ubaid Ur Rehman¹, Sher Asif Khan¹, Muhammad Uzair Shah¹, Muhammad Hameed Ul Din²

1- Mechanical Engineering Department, University of Engineering and Technology, Taxila
EngineerWaqasMalik@gmail.com

2- Mechanical Engineering Department, University of Lahore, Lahore

Abstract:

Pakistan is the world fifth biggest market for two-wheeler, sold 2.3 million two-wheelers in 2017, but almost all share relay on conventional internal combustion engine (ICE) technology. The ICE technology consumes gasoline fuel which emits carbon dioxide and other pollutant. Now government of Pakistan is planning to overcome harmful pollution, produced by transport and other sectors. Our project focuses on the transformation of conventional ICE technology with an electric technology to analyses energy demand and carbon footprint. Due to scope of this paper, we are limited to transformation of 70cc technology to electric scooter only. After the transformation, we analyzed it in term of energy, environment, technology, management, social and business perspective. By penetrating 30 percent electric two-wheeler up to 2030, we may save overall 550 million litres or 19.4 PJ (0.45 MTOES) of energy, reduce 6.3million metric tons of carbon footprint.



Energy Management Practices of Pakistan's Glass Manufacturing Industry

Arslan Yousaf¹, Tauseef Aized Khan¹

1- Department of Mechanical Engineering UET Lahore (m.arslanyousaf@yahoo.com)

Abstract:

The ultimate objective of this study is energy management and energy efficiency improvement among glass industries in Pakistan. The ultimate goal is to deal with multiple issues that are associated with energy management practices that are among glass industry. The detailed analysis of glass industries is generally based on factors like technical measures need to deal with cost effective steps with non-performing components. This paper is a detailed study of improved energy efficiency and energy resource utilization in glass manufacturing industry. There are factors that's associated with energy efficiency but there is lack of awareness linked with energy management techniques in industrial professionals. In this paper a step by step guide and improvement plan have been discussed with seen a certain improvement by percentage of 12-14% in energy resources like gas, electricity and compressed air. Overall electricity expense usually deals with multiple expenditures that are associated with compressors, blowers, electric boosters in furnace. Whereas, in glass industry deals with gas utilization in furnace, annealing Lehr and sand dryer. The overall investigation of energy consumption at multiple sectors and its growth by time as to understand overall consumption by energy and its utilization in future needs of industry whereas it's technical development. There is huge potential of Pakistan's export market as readily available Raw Materials, Human Resources and Strong local and international market of increasing demand of household glass, construction industry and electronics industry.

Energy Improvement Strategies in Coal Fired Chain Grate Boiler

Mr. Muhammad Khalil¹, Abid Hussain¹

1- Department of Mechanical Engineering, University of Engineering and Technology Taxila, Pakistan
(abid.hussain@uettaxila.edu.pk)

Abstract:

Gross calorific values (GCV) of coal are necessary characteristics which perform a key role in the boiler performance for generating the steam. Steam generation of boiler can be improved by using the coal of different gross calorific values (GCV) and also use of different size of coal in relevant combustion process. In this study, the generation of steam with the combustion of coal in chain grate boiler is examined. The combustion of coal with different gross calorific values and size 0-50 mm of coal for steam flow rate was studied. A comparative steam generation analysis is made on gross calorific value of coal. The effect of Pressure of steam and temperature of feed water on efficiency of boiler are experimentally considered. If the pressure of steam increases, the efficiency of the boiler also increases. Due to increases in pressure of steam, the enthalpy of steam also increases. Due to heat transfer, preheated the boiler feed water in economizer and back to the boiler with high temperature. This reduce the amount of heat which uses in the boiler. Because of heat transfer in economizer, we can decrease fuel usage by 5 to 10%. This analysis inform that for better efficiency with the lowest gross calorific value (GCV) of coal is an important input for any country's socio economic development. Experimental results show that a minor development in the productivity of the boiler with lowest gross calorific value (GCV) of coal can increase efficiency of the boiler by 15-20% and also minimize the CO₂ emissions.



Energy and Exergy Analyses of Multi-Generation System using Renewable Energy

Tahir Abdul Hussain Ratlamwala¹, Jahanzeb Javed²

1- Faculty of Engineering Sciences, National University of Sciences and Technology, Islamabad, Pakistan
(tahir.ratlamwala@pnec.nust.edu.pk)

Abstract:

The following study investigates the design and analysis of Multi-Generation system. Renewable energy (Solar) is used as an energy input into the system that will produce electricity, heating, cooling and dehumidification of air. The system comprises of Co-generation power cycle, double effect vapor absorption cooling system. The results are obtained using Energy and Exergy analysis, the Efficiency of Power cycle is found to be 50.64% producing a net power of 0.216 MW. The COP and Exergy efficiency of the cooling system is found to be 1.103 and 26.14% respectively. The complete system is analyzed by using EES software that includes Energy and Exergy analysis. The other parameters of the system are analyzed and concluded through graphs and tables.



Analysis of Wind Turbine Blade's material using simulation

Saad Imran¹, Hamza Riaz²

1- University of Engineering and Technology, Lahore (Saadimran207@gmail.com)

2- University of Engineering and Technology, Lahore

Abstract:

The geometry and material of wind turbine blade plays a crucial role in determining the efficiency and durability of wind turbine itself. So, it is beneficial to use such a kind of material that has better structural properties and durability. Not only good mechanical properties but should be light weight and more industrially feasible to manufacture. Initially wind turbine blades are mostly manufactured using epoxy glass as it was cheaper and easily available. But later it showed that by using epoxy carbon, the durability could be increased significantly of the blades. In this paper with the help of the computer modelling and ANSYS it is showed that carbon nano tube reinforced epoxy carbon (i.e. epoxy carbon material has an additional layer of carbon nanotube) materials when subjected to same conditions as that of epoxy carbon alone, lays better durability considering the factors like total deformation, shear stresses, Von-Misses Stresses, Normal stresses and Directional deformation.

Design and Experimentation of Sevonius Vertical Axis Wind Turbine for Roadside Applications

Muhammad Rizwan^{1*}, Abid Hussain¹, Waqas Ahmed¹

1- Department of Mechanical Engineering, University of Engineering and Technology Taxila, Pakistan
(mrjaved1996@gmail.com)

Abstract:

Electricity shortfall is a major problem for Pakistan nowadays. Government is looking for cheap and long lasting sources of electricity generation. To overcome this problem renewable energy is a vital source. Wind energy is a cheap and pollution free source of renewable energy. Pakistan has great potential of wind along the coastal line. We can also use our roads other than coastal area to produce wind energy. There are different wind turbines available in the market, but for roadside application the most suitable is sevonius vertical axis wind turbine. Sevonius turbine uses the wind thrust of passing vehicles to produce energy. Sevonius turbine with 2 blades along with the pulleys belt drive system to transmit motion is used. The sevonius wind turbine was designed for 75 watts. The efficiency of normally designed sevonius turbine is about 40%. Its efficiency can be enhanced using light weight blade material with suitable drive system.



Design and Fabrication of Conductive Polymer Strain Sensor

Bakhtawar Maqsood¹, Muzamil Bokhari¹, Ajab Khan Kasi¹

1- Department of Physics, University of Balochistan, Quetta, Pakistan (bakhtawar.phy@gmail.com)

Abstract:

The demand for soft, wearable, stretchable and smart sensors is augmenting because of their flexibility, precision and direct interaction with any medium like fabrics and the human body. Smart strain sensors are highly flexible and sensitive. Stretchable strain sensors can directly mount on clothes (fabrics) or easily attached to the human skin for motion detection very precisely. Herein, we report a very sensitive, stretchable and flexible strain sensor based on a nanocomposite of gold nanoparticles (AuNPs) and elastic microstructure polymer (EMP). Thin-film of AuNPs embedded between the two layers of EMP like sandwich structure. Polymer-based strain sensors can sense the bending angle up to 0° to 160°. The strain sensor based on AuNPs elastomeric nanocomposite shows tunable gauge factor (GF) 1.5 to 20 with 75% stretchability, 5s of response instancethe and very low creep because of superconductivity of gold. When deformed or stretched the AuNPs displace from their original position, this causes a change in resistance which makes it capable of measuring strain. The high flexibility, sensitivity, and repeatability of AuNPs based elastic strain sensor make it extremely auspicious for microelectromechanical systems, soft sensors, nanogenerators, smart electronic devices transparent electrodes, and orthotics. Because of the quick response, simplicity, periodicity and accuracy, this flexible strain sensor is best for very precise strain mapping.

Modified and Cost-Efficient Design of the Permeameter Utilizing Indigenous Resources

Ghous Baksh¹, Hoor Ul Ain¹, Rabia Basry¹, Nayab Fareed¹ and Atif Ismail¹

1. Department of Geological Engineering, University of Engineering and Technology Lahore
(ghousbuksh65@gmail.com)

Abstract:

Permeability is one of the most important properties of porous media required to characterize any reservoir rock. The measurement of permeability using permeameter considered the most reliable indicator of the flowing ability of the medium in geological engineering. Highly complex and costly international instruments are available to measure the permeability. The scope of research at the undergraduate level requires a simple and cost-effective instrument to cover the purpose of measurement of permeability. In this work, permeameter is designed on the basis of 2D and 3D modeling using a computer-aided approach. Improvement in the fabrication of the apparatus is suggested in terms of auto Klinkenberg correction and the pressure-strength relationship of the rock. For analysis of the cost of the permeameter, the price of the indigenous available parts used in the designed model is compared with international available resources. The comparison shows that imported parts enhance the price almost up to 35 % percent greater as compared to locally available parts if we ignore the other than fabrication factors.



Functional Reverse Engineering of Machine Tools

Wasim Ahmed Khan¹

1- Faculty of Mechanical Engineering GIK Institute of Engineering Sciences and Technology Topi-23640,
Khyber Pakhtunkhwa, Pakistan (wasim@giki.edu.pk)

Abstract:

The purpose of this talk is to persuade academia to develop capacity building in strategic and non-strategic machine tool technology, and machinery in other sectors. Strategic machines can produce non-strategic machines and any other discrete product. Nonstrategic machines directly or indirectly produce machines used in production of food, apparel and shelter. Functional Reverse Engineering of Machine Tools and Equipment is meant for acquiring self-sufficiency in discrete manufacturing sector. The same process is applicable to other sectors as well. Functional reverse engineering is a redesign and manufacturing procedure that does not violate anybody's intellectual property rights and allows incorporation of innovative features making the discrete product under consideration more viable for the client. Pakistan being one of the Next Eleven emerging markets, requires focus on more exports from the country and lessen the burden of imports. To achieve this and to move on to BRICS nations, the country has to have the capacity to develop machinery in sectors such as machine tools, construction, food processing and packaging, textile, automobiles, home appliances, energy, biomedical engineering etc. The Faculty of Mechanical Engineering at the GIK Institute is fully aware of this necessity and the Machine Tool Research Group at the GIK Institute has spent three years working in this area. The responsibility of the group is to provide a general model for an enterprise of functional reverse engineering that can generate profit in less focused but advance areas of research and development in the country and share the model with peers working in other sectors. The work is being done with the support of Directorate of Science and Technology, Department of Science and Technology, Government of Khyber Pakhtunkhwa and GIK Institute.

Design and Fabrication of Aluminum Anodizing Process

Saud Bin Zafar¹, Saadullah¹, Sajeel Tariq¹, Rao Muhammad Hamza¹

1- Department of Mechanical Engineering (miansaud30@gmail.com)

Abstract:

Anodizing is an electrochemical process that converts the metal surface into an anodic oxide finish. This project deals with the anodizing of aluminum metal. The general principles of anodizing is to enhance surface finish of the components, also to increase their wear resistance, improve abrasion resistance, boosts their adhesive bonding and to build up a corrosion resistant layer as a byproduct. This project includes the designing and fabrication of anodizing system. To achieve the aims and targets of this project, various research papers and articles have been studied, for instance to attain high wear resistance, various parameters are altered like voltage, current, time, type of electrolyte, concentration of the electrolyte and temperature of electrolyte. The methodology contains pretreatment operations which involves the cleaning processes like degreasing, pickling, desmutting at optimum conditions. After then Anodizing takes place by generating an anodic oxide film on the surface of aluminum metal. Finally the flow of the process ends with the post treatment operations like dying and hot sealing, for improving the appearance of the component and for filling up the pores of the component. There are many products for automotive, medical or kitchen applications where appearance is not unimportant but resistance to wear processes and/or cleaning using aggressive chemical agents are particularly demanding of the properties of anodized aluminum. Moreover, one of the industrial problem is to be solved in this project like in automobiles, the master



piston cylinders of hydraulic brake system must be anodized in order to improve its wear resistance before its application in automobiles, to increase its lifespan. Briefly, this project elaborates the accomplishments of the component after anodizing it by modifying the parameters involved in the process.



Design and Fabrication of Charpy Impact Testing Machine

Muhammad Zeeshan¹, Ismail Khan², Muhammad Owais¹, Adam Khan¹

1- Department of Mechanical Engineering, University of Engineering and Technology Peshawar 25120, KPK, Pakistan (zarafzee@gmail.com)

Abstract:

In the manufacturing of different parts of locomotive like wheels, connecting rods and other things like coins where these components are exposed by a sudden force known as impact force. Where such loads are subjected suddenly which result in inducing stress in such components and these forces (load) are greater and larger than the stress produce by progressive load. Hence that's why impact tests are conducted to check the absorbing shock capacities of different types of materials that are subjected to applied sudden loads. The output of these test are expressed in terms like (1) Rupture energy (2) Modulus of rupture and (3) Notch impact strength. This type of Charpy Impact Testing machine is selected for the Metals having capacity of 130J and can be manufacture after different stages of designing the machine and then it is to be fabricated according to the Standards i.e. American Society for Testing and Materials (ASTM) ASTM E23,E1823,E2298 and ASTM A370-NIST (national institute of standards and technology) and ISO148-1(International Organization for Standardization) after that the specimen of mild steel that is selected to be tested is also be according to the ASTM A370 and ISO148 the specimen is to be go through heat treatment processes (Annealing, Quenching, Normalizing, Tempering). After that a series of testing is performed of this specimen and that gives different result which is used to find the relative toughness of the material and the energy needed to fracture and breakdown a material and it is used in order to measure the yield strength of different materials. Also the strain rate may be studied and can be analyzed for its effect on fracture and it gives the relative properties of different materials such as toughness, percent ductility, percent brittleness, notch sensitivity and impact strength.

Application of Total Productive Maintenance (TPM) Technique in Improved Productivity of Industrial Equipment: A case study from Pakistan

Hamid Minhas¹, Usman Ghani², Shar Noor³, Muhammad Usman⁴, and Zain Ul Hassan⁴

1- Department of Industrial Engineering, University of Engineering and Technology, Peshawar, (minhas.mech@gmail.com)

2- Department of Mechanical Engineering, University of Engineering and Technology, Peshawar, Jalozi, Campus,

3- Department of Industrial Engineering, University of Engineering and Technology, Peshawar,

4- Department of Mechanical Engineering, University of Engineering and Technology, Lahore,

Abstract:

One of the most important technical key performance indicators (KPIs) is the overall equipment effectiveness (OEE) which is used to achieve set goals in manufacturing. The productivity of any manufacturing process highly depends on this globally accepted factor. Also, producing better quality and cost-effective products is a fundamental need to remain competitive in any consumer market. Thus, many techniques which include Total Quality Management (TQM), Total Productive Maintenance (TPM) and Lean Manufacturing are developed to eliminate any wastage in manufacturing processes and produce economical products by enhancing OEE. Maximization of the efficiency of equipment i.e. to eliminate the losses impedes the improvement of efficiency. These losses are the real problems, therefore in this research, multiple factors have been analysed which affect the productivity and Overall Equipment Efficiency (OEE). A case study of local industry has been discussed and reported for future industrial processes in perspective of maintenance.



Productivity Enhancement of a Process Industry using Value Stream Mapping

Asif Mahmood¹, Dr. Tauseef Aized², Shoaib Muhammad³

1- University of Engineering and Technology, Lahore (asifmahmoode@gmail.com)

2- University of Engineering and Technology, Lahore

3- University of Engineering and Technology, Lahore

Abstract:

Customer expects short lead time in demand delivery. In order to reduce the lead time, it is vital to analyze production layout of process industry. In this paper, Value Stream Mapping as a lean technique is applied in a tire manufacturing industry that is in Lahore, Pakistan. Because, it is a key tool to identify opportunities in production layout. Based on current state, the non-value-added time was marked out in terms of large changeover time and unnecessary movements. By introducing quick changeover and U-shaped configuration of equipment, that is reduced lead time and delays in deliveries. As a result of changes, the productivity is increased. Furthermore, it will certainly increase the potential customers and market share, that's ultimate vision of any industry.

Minimization of warpage in Plastic Part using Response Surface Methodology

Awais Ahmad Khan, Ramsha Kanwal, Muhammad Ismail Najib, Ghulam Moeenuddin, Hira Syed, Arooba Malik, Basit Mehmood, Muhammad Tahir Arshad

Mechanical Engineering Department, University of Engineering & Technology, Lahore, Pakistan

Abstract:

Plastic injection molding has being commonly used for the production of diversity of products. Warpage is currently a problem in plastic industry and there are no easily available methods to measure the warpage produced in plastics parts. The work presented in the article deals with optimization of injection molding parameters in plastic industries. The objective is to find out the optimized numerical values of four critical parameters of injection molding: mold temperature, melt temperature, Injection time and cooling time so that warpage (differential shrinkage) could be minimized. The methodology adopted to achieve this goal was based on simulation using Moldflow software and optimization of controlling parameters. Poly Plast Custom Molders was selected and a Mud-Guard of CD-70 bike made of polypropylene material was inspected for warpage using a range of values for parameters on Mold Flow Software and ultimately analyzing the results on Minitab Software using Response Surface Method. The results obtained shows that the warpage response is minimum at a high level of Injection time and low level of melt temperature. Mold Temperature has small effect and there is no effect due to cooling time.



Implementation of Lean Six Sigma in an Air Conditioning Industry: A case study

Arshad Khan¹, Ali.Hasnain¹, M.U Malkana¹

1- Department of Mechanical Engineering, University of Engineering & Technology, Lahore, Pakistan
(Arshad.uet555@gmail.com)

Abstract:

This paper reports the impact of implementation of Lean Six Sigma (LSS) in an Air Conditioning industry. A well-known framework of Six Sigma “DMAIC” used in this research paper. DMAIC stands for Define, Measure, Analyze, Improve and Control. During this research, the problem of material rejection, high manpower (Low UPMH) and safety issues examined. Design modification of outdoor unit testing power code is the core activity of this examination. At the end of this examination, a single solution provided for the problem and the improved solution implemented practically. The calculation made during examination of problem and solution, which shows that on implementation of LSS UPMH increased by 2% (from 0.96 to 0.98). In addition, LSS help to reduce the material rejection by 100 % in both thimble and terminal Block as it eliminates the use of thimbles and screws. The process shifted to single workstation, before it was performing at three different stations due to which the process cycle time reduced from 45 sec to 17 sec.

Improving the Efficiency of Assembly Line using Line Balancing and Work Study Method in a Manufacturing Industry

Fareed Alam Chishti¹

1- Department of Mechanical Engineering, University of Engineering and Technology Lahore, Pakistan.
(fareed.alam991@gmail.com)

Abstract:

This study aims to improve the efficiency of a portion of manual assembly line in a well-known refrigerator manufacturing industry of Pakistan. The techniques employed in this study are line balancing and work study method. Firstly, takt time for desired production and cycle time of each operation was calculated and measured using stopwatch. The operation whose cycle time was exceeding takt time was broken down into tasks and redistributed with other workstation to keep its cycle time within takt time limit. Thus, improving the line efficiency from 70.12% to 84.77% by eliminating the bottleneck operation. Also, macro motion study of a worker was conducted using man type flow chart and worker efficiency was improved by 12%. This was outcome of identifying non-value-added activities and eliminating them from operation.



Design Modification of Power Cord of an Air Conditioner's Indoor Unit to Improve Productivity through Implementation of Lean Six Sigma

Ali Hasnain^{1,*}, J. Sarwar¹, A. Khan¹, Q.Z.Ahan¹, Awais A.Khan¹

1- Department of Mechanical Engineering, University of Engineering & Technology, Lahore, Pakistan;
(alihanain41@gmail.com)

Abstract:

This paper implements combined tool Define, Measure, Analyze, Improve and Control (DMAIC) of lean and six sigma in a home appliances industry. In this research work, the problem of no start of indoor unit in testing room is examined. Design modification of indoor power cord which is used during indoor testing is the main objective of this research work. At the end of the problem examination, solution of changing indoor power cord design is suggested and implemented. After implementation, a problem of spring buckling occur which is then improve by changing the design of spring from cylindrical to conical. Calculation is made in this research work after complete examination of the problem which shows that Lean Six Sigma (LSS) implementation improve Unit per Hour (UPH). LSS implementation also helped to eliminate the use of screws completely due to which process become simplified and cycle time reduced.

Implementation of lean six sigma to improve changeover time, machine availability and productivity

Arshad khan¹, J. Sarwar¹, A. Hasnain¹, Q. Z. Ahsan¹, and Awais A.Khan¹

1- Department of Mechanical Engineering, University of Engineering & Technology, Lahore, Pakistan;
(arshad.uet555@gmail.com)

Abstract:

In this work, a problem of low productivity, less availability of expending machine and high changeover time, are investigated and improved by implementing lean six sigma tools. A combined tool of Lean and Six Sigma referred as Define, Measure, Analyze, Improve and Control (DMAIC) is used. The implementation of DMAIC tool shows that the design of a new trolley and color coding of machines are required. The result shows that the new trolley design and color coding of machines enhances the productivity and machine availability and reduces the changeover time. Model changeover time is reduced by 35%, machine availability is increased by 10% and productivity is increased by 15%. Furthermore, the distance travelled by the workers during model change overt is reduce by 93% (from 86 meter to 6 meter).



Design and Development of Cost Effective Prosthetic Hand using four stage gear Reduction with Infinite Fatigue Life

Usman Ali Khan¹, Saman Khan¹, M. Areeb Usman¹, Mohsin Ali¹, Umar S. Khan^{1,2}, Mohsin I. Tiwana^{1,2}

1- Department of Mechatronics Engineering, College of Electrical and Mechanical Engineering (CEME), National University of Sciences and Technology Islamabad, Pakistan (usman_260@yahoo.com)

2- National Centre of Robotics and Automation

Abstract:

The paper is based on the design, analysis and development of cost effective single DOF motor actuated prosthetic hand with infinite fatigue life. In developing countries like Pakistan where people have not enough buying power, demand the cost effective solutions. Importing devices like prostheses costs a lot which makes it unaffordable and also difficult to repair in case of fault. This paper discusses the development of a cost effective solution of upper limb prostheses which can be fabricated locally and is competitive with the pre-existing products. Local fabrication makes the prostheses affordable for most the people. Upper limb amputees will use the hand to perform their daily tasks independently. Hand is designed to have high gripping force of 88N, opening/closing time of 1.2 sec and maximum opening of 120mm which is comparable with the state of the art hand made by German company Otto Bock. 4 stage gear reduction is used to transfer force from motor to the gripping jaws of hand. A detailed stress analysis is conducted using extensive software simulations which confirm durability and infinite fatigue life of the hand. Weight of the hand is also reduced to 320 grams by selecting optimum materials using simulation results. Efficient and simple design, fabricated using local parts and manufacturing processes ensure the cost effectiveness of the hand which encourages amputees to use the hand. The hand is rigorously tested on two patients using EMG control circuitry and they are using the hand in their routine tasks.

Study of the Recent Developments and Trends of End-Effector Design for Fruit Harvesting Robot from 2013-2019

Sadaf Jamshed¹, Tauseef Aized²

1- Department of Mechanical Engineering UCP Lahore (sadaf.zeeshan@ucp.edu.pk)

2- Department of Mechanical Engineering UET Lahore

Abstract:

In the recent years, automation in the field of agriculture has grown exponentially. Fruit harvesting robots is one such area that has seen many advancements in the past ten years. With the improved sensors and technology, development of an optimized commercial model of fruit harvesting robot seems very promising. A lot of work is also done for optimizing end effector design as well. New techniques and gripper design combinations has been tried for various fruits. Various tests have been conducted to manage gripper force and pressure to avoid fruit damage. However, with all this research done there is no paper available which reviews the latest trends of end effector especially for fruit harvesting robots. This paper aims at highlighting all the recent developments made in gripper designs for fruit harvesting robots. All successfully tested designs are discussed systematically. The paper will assist in providing a guideline for an optimum gripper design for fruit harvesting robot.



IOT based DATA Acquisition, Control and Performance Monitoring of 4-Stroke Diesel Engine

Muhammad Imran¹, S.M. Umair Rasheed¹, Tauseef Aized², Arslan Ahmad Chattha¹, Ifrikhar Tumrani¹, Hassan Tanveer¹, Muhammad Furqan¹

1- Department of Mechatronics and Control Engineering, University of Engineering and Technology
Lahore, Faisalabad Campus (engrimran23@gmail.com)

2- Department of Mechanical Engineering, University of Engineering and Technology Lahore

Abstract:

IOT is the latest emerging technology of the Physical things connected with Internet. It helps us to acquire, monitor data and Control parameters over the internet from far off location. In this paper, we are using a 4-stroke diesel engine connected with an instrumentation frame for local monitoring of engine parameters. The GUI of Versatile data Acquisition software (VDAS) is also used for local monitoring of engine parameters which is connected with instrumentation frame. The instrument frame is connected with Arduino, which is then connected with internet through Blynk App which is used to acquire, monitor and Control the engine parameters over internet from anywhere in the world. Controlling the torque and speed of the 4-stroke diesel engine by using continuous control action (closed loop system).

Optimized Sorting Robotic Arm: (Design for processing industry)

Muhammad Ihtisham Amin¹, Muhammad Adeel Hafeez¹, Adeel Ahmad¹

1- Chenab College of Engineering and Technology Gujranwala, Pakistan (Amin.Ihtisham9@gmail.com)

Abstract:

Automation has become a major part of different industrial processes due to its better accuracy and untired working. A robotic arm is an essential part of many industries as well as commercial automation processes. In this paper, we have proposed a model for the robotic arm that can detect the object on the production conveyor belt, recognize the object based on its color and transfer it to the supply conveyor belt. To detect and recognize the objects, simple infrared (IR) sensor and color sensor (CS) are used which are quite inexpensive compared to camera-based detectors and they are easy to implement due to the absence of highly computational image processing techniques. We achieved 93.26% accuracy for color detection in the presence of confusing colors. Commended to achieved angle accuracy for placing the object to the supply belt is 93.94%, while this model is almost 15 seconds faster than the manually controlled robotic arms. The response time of the manual and proposed models is roughly calculated by making multiple trails.



Smart Visitor's Management System through ID Card in Pakistan

Ayesha Siddiqa^{1,2}, Usman Sheikh², Aneeq Asif², Zainab Riaz², Ali Asghar²

- 1- Department of Mechatronics and Control Engineering, University of Engineering and Technology Lahore (siddiqayesha97@gmail.com)
- 2- Department of Mechatronics and Control Engineering, University of Engineering and Technology Lahore (Faisalabad Campus), Pakistan.

Abstract:

This paper presents a prototype smart visitors management system that is designed for the collection as well as data storage of visitors which could facilitate the security departments. The proposed method mainly integrates into two components; firstly, visitors fill the online appointment form and they will receive a confirmation message. Notification of confirmation allows a visitor to visit that specific firm or industry. Secondly, before entry visitors must press IN on a GUI based touchpad and simultaneously enter the ID-card which will be scanned on both sides. After visiting, visitors must have to press EXIT and enter the visiting card for leaving the industry to collect the deposited ID card. To enhance security, we developed three crossmatches. Firstly, the username is cross matched with online data. Secondly, through the password which was sent to the user via GSM and thirdly, the crosscheck of CNIC number. In this way, the data of visitors has been collected and saved into excel. This saved data remains stored for information of visitors as well as for security purposes. In this way, our designed system will provide an ideal solution to the security department that are faced by manually entering data.

Automated Fruit Harvesting System using Digital Image Processing for Indoor Environment

Samrina Sarwar¹, Aisha Kanwal¹, Shaban Arshad¹, Zainab Riaz¹, Ali Usama¹, Usman Sheikh²

- 1- Department of Mechatronics and Control Engineering, University of Engineering and Technology Lahore, Pakistan (simimeher114@gmail.com)
- 2- Faculty of Mechatronics and Control Engineering, University of Engineering and Technology Lahore, Pakistan

Abstract:

Manual fruit and vegetable harvesting method involves problems like labour cost, harvesting unripened fruit, less efficient, low production rate and less accuracy. The solution of these problems is in mechanization which involves harvesting robots and harvesting machines. Tomato is one of the major vegetable fruits and its harvesting in green house is also a time-consuming process because in green house suitable environment is provided to get maximum production. This paper includes an attempt to design a mobile robot which can efficiently pluck the ripened tomatoes one by one and place them in carrier. The robot has a robotic arm, end effector and a camera fitted on end effector for recognition purpose. A control system for the control of robotic arm is designed so that it can move vertically upward to the required height and also in the horizontal direction to reach the target. The arm has rotational plucking gripper to cut and hold the tomato. To avoid obstacles in the way of robot, ultrasonic sensor has been used. Image processing techniques based on colour and shape to differentiate between ripened and unripened tomatoes have been used which is efficient method to identify ripened tomatoes because it is much accurate as well as easiest method as compared to other. All the operations performed are automatic, so there are very small chances of error & the problems that we face in manual harvesting.



IoT Based Automatic Street Lights and Car Parking System

Engr. Saif Ullah¹, Engr. Jalal Khan¹, Dr. Mushtaq Ahmad Khan²

- 1- Department of Telecommunication Engineering, University of Engineering and Technology Mardan, (engrsaifullah729@gmail.com)
- 2- Lecturer, Department of Basic Sciences, University of Engineering and Technology Mardan

Abstract:

Pakistan is suffering with a shortage of energy whereas a considerable amount of energy is consumed by a large number of existing manual street lights just for illumination, nothing else. An automatic street lights system is introduced which uses cheaper and less power consuming LEDs with good performance, and other features like speed detection, number plate recognition, weather forecasting and emergency alarming in case of fire or fog. Nowadays traffic jam is a major issue due to parking mismanagement. People wander in search of parking places which are often not available. Automatic car parking system consists IR sensors, LCD and an Android Application. Arduino Mega is used for automatic street lights system and Arduino UNO for automatic car parking system. For providing connectivity between sensors and android application and server, there is Wi-Fi module ESP8266 which is cheaper and very fast. Using a Wi-Fi module, it is easy to send the data of sensors to an android application named "Blynk" and a server named "ThingSpeak". One can see this data anytime from anywhere.

Image processing and Data storage for fire Alarm

Zainab Riaz¹, Aneeq Asif¹, Aysha Saddiq¹, Ali Asghar¹, Waqas Arshad¹, Muhammad Zia Ur Rahman¹

- 1- Department of Mechatronics and Control Engineering, Faisalabad Campus, University of Engineering and Technology Lahore

Abstract:

This paper explains the algorithm for fire alarm for the purpose of safety from any loss and property damage. Here, the designed algorithm is for the comparison of captured pictures. The purpose of comparison is to validate our results. In captured pictures, there may exist fire colour in pictures, which is the indication of fire in that specific area. Captured pictures are stored in folder and its path is stored in excel. We observed the indication of fired picture through fire alarm. When the fire is diminished, we used reset button to stop the buzzer and to monitor the system again. The path of those pictures as well as the time and date of captured pictures will remain store in excel for later study of the failure of the system and also for the record purposes.



An Approach to Measure Key Performance Indicators for Linear Servo Actuators

Naveed Riaz¹, Faisal Rehman²

1- National University of Sciences & Technology Pakistan, engrnaveedriaz@gmail.com

2- National University of Sciences & Technology Pakistan

Abstract:

Linear Servo actuators are commonly used in various automated systems and are very desirable for high dynamic load applications. This paper investigates the influence of different key performance indicators that govern the performance of linear servo actuators. The critical performance parameters are identified, calculated and analyzed. The factors that affect these functional parameters are considered in detail. The inertial subsystem of linear actuator was created using lumped system approach. The mechanical linkage between individual components of actuator is derived using governing mathematical equations. The influential parameters including slew rate, dead-band and mechanical backlash are evaluated using loading test setup by considering the appropriate actuator drive. In the end, open loop testing is performed to find these parameters.

Voice Recognition based Operation Theatre Assistive Robot

Arslan Ahmad¹, Amr Fazeel Baig¹, Iram Liaquat¹, Samavia Noor¹, Syed Muhammad Umer²,

1- Engineer from the Department of Mechatronics and Control Engineering, University of Engineering and Technology, Lahore (FC)

2- Lecturer in the Department of Mechatronics and Control Engineering, University of Engineering and Technology, Lahore (FC) (s.m.umer@uet.edu.pk)

Abstract:

This article describes the design and analysis of an assistive robot with 4-axes articulated robotic manipulator. The current work is undertaken by considering various medically used robots to design and fabricate a 4-DOF robotic arm. Forward kinematic model has been presented in order to determine the end effector's position and orientation. This analysis is useful for path tracking and trajectory following of a surgical robot or assistive robot with 'pick and place' application of surgical tools using voice recognition. Based on this analysis, a researcher can develop a path tracking behaviour of an end-effector in complicated workspace. We have succeeded in recognizing the voice of a person (in a noise free environment) and hence picking the same tool as spoken by the person and placing it in his hands using colour recognition methods and then returning to its initial position. The simple plan of this project was to make a prototype to work in an operation theatre environment, which is a noise free environment. This prototype can recognize the voice of surgeon and understand the name of the tool spoken by the surgeon through a series of training of VRM. As soon as it understands the tool name, the respective tool tray comes to the top by using elevator mechanism. Meanwhile, the arm moves in the specific manner as programmed and picks up the tool and moves towards the doctor's hand, and through colour recognition of the gloves, it places precisely in the hands of the doctor. A series of testing and troubleshooting took place and different types of hurdles and barriers were encountered during the process, like motor damaging, friction factors, and wiring issues.



Towards the development of an Intelligent Smart Cane for Visually Impaired People

Rabia Samreen¹, Rimsha Perveen¹, Rida Fatima¹, Fatima Ahmad¹, Saqib Zafar¹, Aamir Mehmood¹, Hafiz Farhan Maqbool¹

1- Department of Mechatronics & Control Engineering, University of Engineering & Technology, Lahore (FSD Campus)-38000 (saqibzafar704@gmail.com)

Abstract:

Visually impaired people face difficulties while interacting with their environment because most of the people use a traditional cane for their mobility from one place to another. Traditional cane could not help them to detect obstacles. This paper presents the development of an intelligent smart cane for visually impaired people that detects the obstacle and alerts them through voice command. Moreover, this cane also detects the even and uneven surface of terrain and provides the direction information through vibrations of vibratory motors mounted the handle of cane. The system enables the user to move from one place to another with ease and confidence similar to as sighted person. The whole system is designed to be small, lightweight and is tested in conjunction with the white cane. The experimental results have shown that the proposed system could potentially be used for the visually impaired people with quite ease and avoiding human dependency.

Human-robot teams in industrial assembly

Ali Ahmad Mali¹, Bilal Ahmad²

1- University of Southern Denmark, Sønderborg, Denmark (alimalik@mci.sdu.dk)

2- University of Management & Technology, Lahore, Pakistan

Abstract:

The paper discusses the future of industrial assembly with human-robot teams. An industrial case of a manufacturing company is presented to develop a human-robot assembly workstation. A structured design method is documented for developing HRC production systems. Distribution of assembly tasks between human and robot is discussed. Human-robot virtual simulation models as digital prototype are developed for validation of the design of human-robot production system. Digital twins as simulation models with a lifecycle approach are explored for their usefulness in dealing operational complexity of human-robot manufacturing team. The digital twin extends the use of virtual simulation models developed in the design phase of a production system to operations for real-time control, dynamic skill-based tasks allocation between human and robot, sequencing of tasks and developing robot program accordingly.



Design of G Code Interpreter Algorithm for CNC Machines

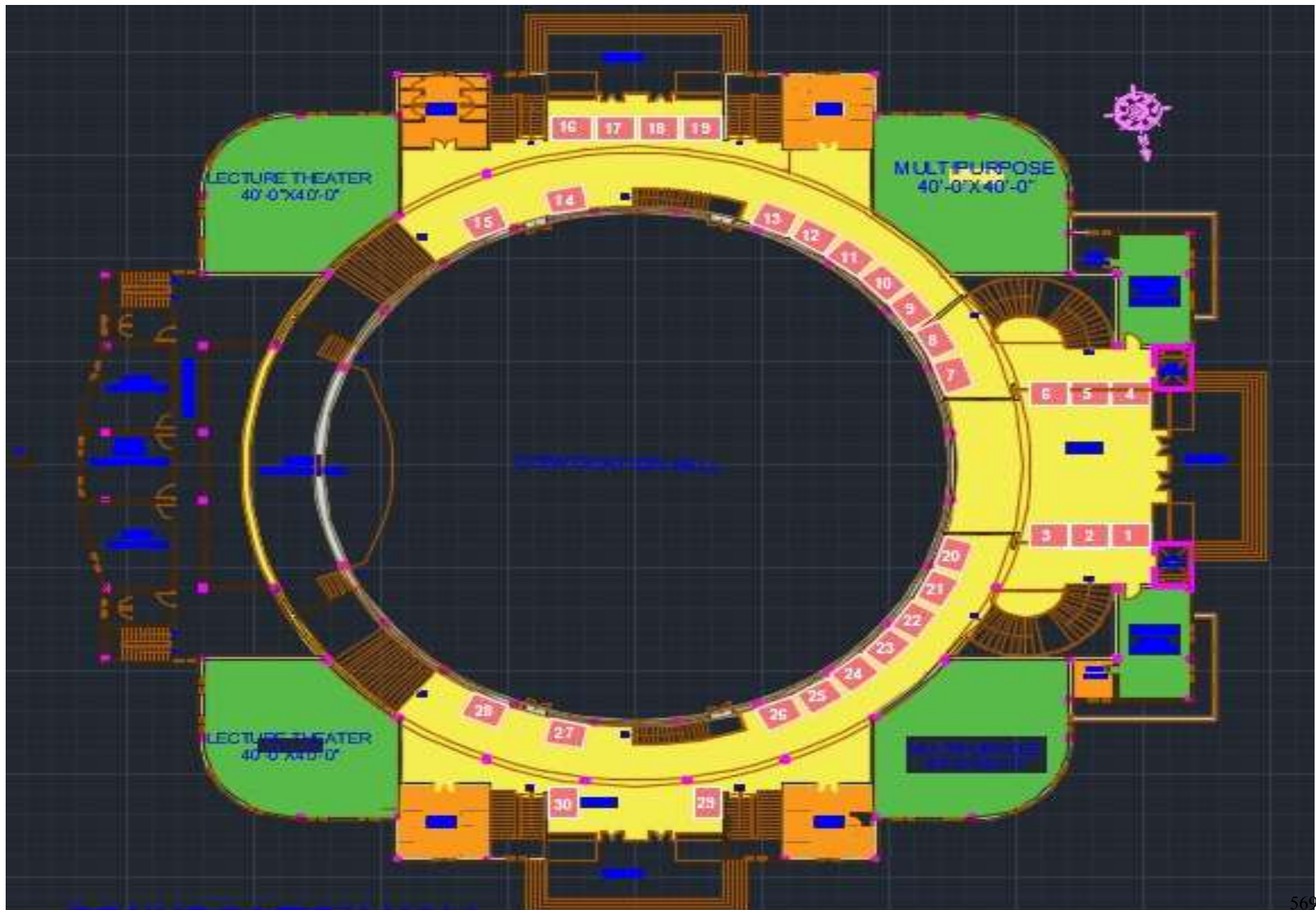
Muhammad Ali Bhutto¹, Asif Ullah¹, Wasim A.Khan¹, Khalid Rehman¹

1- Faculty of Mechanical Engg. Ghulam Ishaq Khan Institute of Engg. & Technology, Topi, Swabi, Pakistan,
(asif.ullah@giki.edu.pk)

Abstract:

Computer Numerical Control (CNC) machines are electro-mechanical devices that control machine tools via computer programming inputs. The programming of the CNC machines is commonly referred to as part programming or G Code programming. In order to decode the part program into electric signals to achieve the axes' motion, CNC machines require an efficient software system that can interpret the part program into the information understandable for the actuators and other mechanical hardware. In this paper, the design of a G code interpreter algorithm using ISO 6983-1:2009 standard has been presented. The interpreter algorithm has been divided into three parts: command identification, command formation and command execution. Each cycle presents and discusses the respective algorithm for all the functions such as sequence number (N), preparatory (G), miscellaneous (M), axes (x, y, z), feed rate (F), spindle speed (S) and tool (T) functions. Experiments were conducted on a prototype CNC router to validate the proposed interpreter algorithm thus proving the feasibility of its application. Furthermore, it was compared to open source interpreters to determine its availability, reliability and efficiency.

EXHIBITION MAP, UET MAIN AUDITORIUM





**UNIVERSITY OF ENGINEERING
AND TECHNOLOGY, LAHORE**

Grand Trunk Road
Lahore, Pakistan